

# Water balance

from mountain glacier scale to ice  
sheet scale

With focus on Mittivakkat Gletscher, Southeast Greenland,  
and the Greenland Ice Sheet



January 9, 2015  
Doctoral Thesis

Sebastian H. Mernild, Ph.d.





# Water balance

from mountain glacier scale to ice  
sheet scale

With focus on Mittivakkat Gletscher, Southeast Greenland,  
and the Greenland Ice Sheet

Doctoral Thesis

Sebastian H. Mernild, Ph.d.  
Glaciology and Climate Change Laboratory  
Center for Scientific Studies/Centro de Estudios Cientificos  
Av. Arturo Prat 514  
Valdivia, Chile  
[smernild@gmail.com](mailto:smernild@gmail.com)

Research sponsored by the following institutions:



The water that runs to the Arctic sea,  
Ought to balancing P minus E.  
While all of us know this has to be true,  
Why then, we ask, are our budgets askew?

Its tough to assess the land-ocean link,  
When data on precip. and snowfall just stink.  
It's also hard to attain our goals,  
From streamflow records with numerous holes.

Rawinsonde data can help in this matter,  
But estimates also contain ample scatter.  
Is numerical weather prediction a cure?  
Some of us think so, others aren't sure.

Similar problems abound in the sea,  
Where fluxes of fresh and of salt don't agree.  
A Svedrup here and a Svedrup there,  
Add it all up and it's really scare.

How do we measure the average rate?  
Of freshwater export out of Fram Strait?  
And how do the volumes of sea ice and brine,  
Affect the strength of the halocline?

The Atlantic inflow, where does it go?  
Does the import have links with the NAO?  
This is an issue that needs lots of thinking,  
Likely combined with needed drinking.

To conclude, it seems that we still don't know,  
Just how to balance the H<sub>2</sub>O.  
But as the modeling crowd might say with inflection,  
Let's try and do it without flux correction.

Mark C. Serreze (1998)  
Workshop summary

## Table of Contents

<b>Preface and acknowledgement</b>	<b>1</b>
<b>Dansk Resume</b>	<b>3</b>
<b>Abstract</b>	<b>5</b>
<b>1. Introduction</b>	<b>7</b>
1.1 Climate and Cryosphere	7
1.2 Objectives, content, and structure	8
1.2.1 Objective	8
1.2.2 Content and structure	9
<b>2. Arctic as an integrated system</b>	<b>13</b>
2.1 The integrated Arctic system	13
2.2 The water balance	14
2.3 Mass-balance and hydrological observations in Greenland	16
2.4 Mittivakkat Gletscher – an ice and water balance laboratory	17
2.4.1 80 years of research of Mittivakkat Gletscher and the surrounding area	17
2.4.2 Earlier model simulations of Mittivakkat Gletscher and the surrounding area	19
2.4.3 SnowModel and its subprograms	21
2.4.4 SnowModel code developments for Greenland studies	23
2.4.5 Mass-balance, AAR, out of balance conditions, area, and volume change	25
2.5 Greenland Ice Sheet	27
2.6 Test of SnowModel for the Greenland simulations	28
<b>3. Glacier and ice caps</b>	<b>31</b>
3.1 Mittivakkat Gletscher in coastal Southeast Greenland	31
3.1.1 Climate conditions in coastal Greenland including at the Mittivakkat Gletscher region	31
3.1.2 Mittivakkat Gletscher observations	33
3.1.3 Mittivakkat Gletscher SMB, temperature inversion, and runoff routing modeling	40
3.2 GIC in a northern North Atlantic, Northern Hemispheric, and global perspectives	46
3.3 GIC conclusion	50
<b>4. The Greenland Ice Sheet</b>	<b>53</b>
4.1 GrIS surface melt, surface mass-balance, and runoff conditions	53
4.2 Water balance case studies from Sermilik Fjord	60
4.3 GrIS conclusion	61
<b>5. Conclusion and perspective for future work</b>	<b>65</b>
5.1 Summary of main scientific contributions	65
5.2 Mass-balance and runoff observations and modeling issues for future research	66
<b>References</b>	<b>69</b>

## Appendices: Publications [1]–[19]

- [1] Mernild, S. H., Hanna, E., Yde, J. C., Cappelen, J., and Malmros, J. K. 2014. Coastal Greenland air temperature extremes and trends 1890–2010: Annual and monthly analysis. *International Journal of Climatology*, 34, 1472–1487, doi: 10.1002/joc.3777.
- [2] Mernild, S. H., Hanna, E., McConnell, J. R., Sigl, M., Beckerman, A. P., Yde, J. C., Cappelen, J., and Steffen, K. 2014. Greenland precipitation trends in a long-term instrumental climate context (1890–2012): Evaluation of coastal and ice core records. *International Journal of Climatology*, doi:10.1002/joc.3986.
- [3] Mernild, S. H., Hansen, B. U., Jakobsen, B. H., and Hasholt, B. 2008. Climatic conditions at the Mittivakkat Glacier catchment (1994–2006), Ammassalik Island, SE Greenland, and in a 109-year perspective (1898–2006). *Geografisk Tidsskrift-Danish Journal of Geography*, 108(1), 51–72.
- [4] Mernild, S. H., Knudsen, N. T., Lipscomb, W. H., Yde, J. C., Malmros, J. K., Jakobsen, B. H., and Hasholt, B. 2011. Increasing mass loss from Greenland's Mittivakkat Gletscher. *The Cryosphere*, 5, 341–348, doi:10.5194/tc-5-341-2011.
- [5] Mernild, S. H., Knudsen, N. T., Hoffman, M. J., Yde, J. C., Lipscomb, W. H., Hanna, E., Malmros, J. K., and Fausto, R. S. 2013. Volume and Velocity changes at Mittivakkat Gletscher, Southeast Greenland, 1994–2012. *Journal of Glaciology*, 59(216), 660–670, doi:10.3189/2013JoG13J017.
- [6] Mernild, S. H., Pelto, M., Malmros, J. K., Yde, J. C., Knudsen, N. T., and Hanna, E. 2013. Identification of ablation rate, ELA, AAR, and net mass balance using transient snowline variations on two Arctic glaciers. *Journal of Glaciology*, 59(216), 649–659, doi:10.3189/2013JoG12J221.
- [7] Mernild, S. H., Malmros, J. K., Yde, J. C., Knudsen, N. T., Wilson, R., Hanna, E., Fausto, R. S., As, Van D. 2014. Albedo decline on Greenlands Mittivakkat Gletscher. *International Journal of Climatology*, doi: 10.1002/joc.4128.
- [8] Mernild, S. H., Liston, G. E., Kane, D. L., Hasholt, B. and Knudsen, N. T. 2008. Snow, runoff, and mass balance modelling for the entire Mittivakkat Glacier (1998–2006), Ammassalik Island, SE Greenland. *Geografisk Tidsskrift-Danish Journal of Geography*, 108(1), 121–136.
- [9] Mernild, S. H. and Liston, G. E. 2010. The influence of air temperature inversion on snow melt and glacier surface mass-balance simulations, SW Ammassalik Island, SE Greenland. *Journal of Applied Meteorology and Climate*, 49(1), 47–67.
- [10] Liston, G. E. and Mernild, S. H. 2012. Greenland freshwater runoff. Part I: A runoff routing model for glaciated and non-glaciated landscapes (HydroFlow). *Journal of Climate*, 25(17), 5997–6014.
- [11] Mernild, S. H., Malmros, J. K., Yde, J. C., and Knudsen, N. T. 2012. Multi-decadal marine and land-terminating glacier retreat in Ammassalik region, Southeast Greenland. *The Cryosphere*, 6, 625–639, doi:10.5194/tc-6-625-2012.
- [12] Mernild, S. H., Lipscomb, W. H., Bahr, D. B., Radić, V., and Zemp, M. 2013. Global glacier retreat: A revised assessment of committed mass losses and sampling uncertainties. *The Cryosphere*, 7, 1565–1577, doi:10.5194/tc-7-1565-2013.

- [13] Mernild, S. H., Hanna, E., Yde, J. C., Seidenkrantz, M.-S., Wilson, R., and Knudsen, N. T. 2014. Atmospheric and oceanic influence on mass-balance trends of northern North Atlantic region land-terminating glaciers. *Geografiska Annaler: Series A, Physical Geography*, 96, 561–577, doi:10.1111/geoa.12053.
- [14] Mernild, S. H., Liston, G. E., and Hiemstra, C. A. 2014 Northern Hemisphere glaciers and ice caps surface mass balance and contribution to sea-level rise. *Journal of Climate*, 27(15), 6051–6073, doi.org/10.1175/JCLI-D-13-00669.1.
- [15] Mernild, S. H., Liston, G. E., Hiemstra C. A., and Steffen, K. 2008. Surface Melt Area and Water Balance Modeling on the Greenland Ice Sheet 1995–2005. *Journal of Hydrometeorology*, 9(6), 1191–1211.
- [16] Mernild, S. H., Mote, T., and Liston, G. E. 2011. Greenland Ice Sheet surface melt extent and trends, 1960–2010. *Journal of Glaciology*, 57(204), 621–628.
- [17] Mernild, S. H. and Liston, G. E. 2012. Greenland freshwater runoff. Part II: Distribution and trends, 1960–2010. *Journal of Climate*, 25(17), 6015–6035.
- [18] Mernild, S. H., Liston, G. E., Hiemstra, C. A. and Christensen, J. H. 2010. Greenland Ice Sheet surface mass-balance modeling in a 131-year perspective 1950–2080. *Journal of Hydrometeorology*, 11(1), 3–25.
- [19] Mernild, S. H., Howat, I. M., Ahn, Y., Liston, G. E., Steffen, K., Jakobsen, B. H., Hasholt, B., Fog, B., and van As, D. 2010. Freshwater flux to Sermilik Fjord, SE Greenland. *The Cryosphere*, 4, 453–465, doi:10.5194/tc-4-453-2010.



## Preface and acknowledgement

The work presented in this thesis: ‘*Water balance from mountain glacier scale to ice sheet scale – with focus on Mittivakkat Gletscher, Southeast Greenland, and the Greenland Ice Sheet*’, together with the 19 publications published until 2014, form the material submitted for evaluation for the degree of *doctor scientiarum* (dr. scient.) at the University of Copenhagen. Each of these papers have been published in peer reviewed scientific journals. None of the published papers have previously been under evaluation for an academic degree in Denmark, or externally. The papers are referenced by the numbers [1]–[19].

In this report I have assembled and summarized my most important scientific contributions to the understanding of the climate impact on the hydrological cycle and the water balance (the water balance components) from mountain glaciers in Greenland and the Greenland Ice Sheet (GrIS). The contributions are based on observations, model code developments, and model simulations. This has been my research interest for many years. The wider objective of my research concerns the impact from climate change on glaciers, ice caps, and ice sheets and their contributions to the contemporary global sea-level rise.

I wish to acknowledge colleagues and managements at the three international research institutions, where I have been affiliated after moving to the US and leaving Denmark behind in 2006. At the University of Alaska Fairbanks (UAF), Alaska, at the International Arctic Research Center (IARC), I was given the opportunity to explore and develop GrIS surface mass-balance (SMB) models at a time when ice sheet SMB models – when combined full energy balance, blowing-snow distribution, multi-layer snowpack, and runoff routing models – were still in their infancy. This taught me the potential of such an interesting modeling field. At Los Alamos National Laboratory (LANL), New Mexico, at the Climate, Ocean, and Sea Ice Modeling Group (COSIM), I was then encouraged to further develop modeling tools in relation to snow and freshwater runoff from mountain glaciers and ice sheets, testing these against observations. This taught me the limitations of models, and how important it is to compare and verify simulations with observations. Finally, the Center for Scientific Studies/Centro de Estudios Científicos (CECs), Chile, at the Glaciology and Climate Change Laboratory, has inspired me to look into holistic perspectives and given me the opportunity to compare my knowledge from the Arctic area with knowledge from other glacierized regions. All three affiliations have provided inspiring scientific environments in different ways and have given me the opportunity to collaborate on broader international research projects, and to build-up an international network across continents.

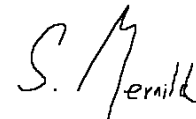
This scientific journey would not have been possible without the interaction from esteemed colleagues around the world. Colleagues I acknowledge for our interesting discussions and friendships. Specifically, I want to thank the following for inspiring and motivating collaborations over the years: Glen E. Liston (Colorado State University), Larry Hinzman (IARC), Christopher A. Hiemstra (CRREL), Edward Hanna (University of Sheffield), Konrad Steffen (Swiss Federal Institute for Forest, Snow and Landscape Research), Matthew W. Hecht (LANL), William H. Lipscomb (LANL), David M. Holland (New York University), Andrew P. Beckerman (University of Sheffield), Bent Hasholt

(University of Copenhagen), Jacob C. Yde (Sogn and Fjordane University College), Jens Hesselbjerg Christensen (DMI), and Niels Tvis Knudsen (Aarhus University).

Last, but not least, my deepest and humble gratitude goes to my family, and especially to Birgitte, Frederik, and Benedikte for their willingness to live abroad, support, patience, consistent good humor, and for accepting that I have always been too busy with my research.

*“The journey of a thousand miles begins with a single step.”*  
— Lao Tzu, philosopher and poet of ancient China.

Yokohama, Japan  
January 9, 2015

A handwritten signature in black ink, appearing to read 'S. H. Mernild'. The signature is stylized, with the first letters of the first and last names being prominent.

Sebastian H. Mernild



## Dansk Resume

De 19 publikationer samt materialet i denne *dr. scient.* afhandling er en række videnskabelige forskningsstudier baseret på observationer, modeludvikling og computersimuleringer på og omkring Mittivakkat Gletscheren i Sydøstgrønland. Denne er den eneste lokale gletscher i Grønland, hvorfra der eksisterer lange observerede tidsserier af meteorologiske data, massebalancedata, afstrømningsdata og målinger af gletscherfrontbeliggenheder. Disse data perspektiveres til gletscher-, iskappe- og klimaforhold i den nordlige del af den nordatlantiske region, til indlandsisen samt til andre gletschere og iskapper på kloden. Publikationerne har bidraget til at udvide vores forståelse af og viden indenfor atmosfære-landoverfladeinteraktioner i relation til gletscherrand-, areal- og volumenændringer samt til sne, gletscher og hydrologiske processer og vandbalancebudgetter ved lokale gletschere i Sydøstgrønland, ved Grønlands indlandsis og i Grønland som helhed. Overordnet skal disse data ses i relation til at kvantificere vandbalancebudgettet til det omkringliggende hav – fra gletscherskala til indlandsisskala i relation til ændringer i det globale havniveau.

Afhandlingen er inddelt i forskellige kapitler. *Kapitel 1* giver en introduktion til de ovenfor beskrevne emner samtidig med, at formålet med afhandlingen defineres. *Kapitel 2* præsenterer og diskuterer relevante dele af forskningshistorien ved og omkring Mittivakkat Gletscheren, samt de igangværende og tidligere relevante projekter og metoder, der har været anvendt til bestemmelsen af bl.a. klimatiske, glaciologiske og hydrologiske forhold, herunder massebalance- og afstrømningsforhold ved gletscheren. *Kapitel 3* indeholder et resume og en diskussion af observerede ændringer af bl.a. Mittivakkat Gletscherens randbeliggenhed og areal, albedoforandringer og forhold omhandlende det faktum, at gletscheren er 'ude af ligevægt' med de nuværende klimatiske forhold. Desuden indeholder kapitlet en præsentation og en diskussion af både observerede og computersimulerede klima, sne, overflademassebalance- og afstrømningsforhold og processer på og fra Mittivakkat Gletscheren sammenlignet med gletschere og iskappeforhold fra andre lokaliteter (udenfor Grønland). *Kapitel 4* præsenterer og diskuterer indlandsisens simulerede arealafsmeltnings-, overflademassebalance- og afstrømningsforhold samt et fremtidigt potentielt 'tipping point' for den. Den nuværende spaciotorporale fordeling af ferskvand til de nærliggende fjord- og havområder – fra indlandsisen og lokale gletschere (fra Grønland som helhed) – bliver også belyst for at synliggøre fordelingen af afstrømningen fra land til hav samt dets bidrag til det globalt stigende havniveau.

Mine væsentligste forskningsbidrag til ny videnskabelig viden ligger indenfor de følgende fire områder:

- *Observationer af lokale gletschere i Grønland.* Observationer af Mittivakkat Gletscherens rand-, area-, albedo-, massebalance- og afstrømningsforhold er af høj videnskabelig værdi for vores forståelse af lokale gletschere og disses forhold i det randnære område i Grønland, udenfor indlandsisen, herunder deres indflydelse på de hydrologiske forhold og vandbalancebudgetter, specielt i en tid, hvor klimaet er under forandring – gående både mod varmere og mere tørre forhold.

- *Modeludvikling og simulering af lokale gletscherforhold i Grønland.* Modeludviklingen af programmerne SnowModel (et modelværktøj, der udover at simulere meteorologiske forhold, snefordeling og -udvikling også er i stand til at beregne sne- og gletscherisoverfladeafsmeltning) og HydroFlow (et modelværktøj til beregning af smeltevandets rute gennem snepakken, gletscherisen og gennem landskabet ud til kysten) samt simuleringer har bibragt os ny indsigt i klimaets indflydelse på Mittivakkat Gletscherens overflademassebalanceforhold, herunder indflydelse på såvel sne- og gletscherforhold stammende fra tilstedeværelsen af inversionslag, samt i den spatiotemporale fordeling af afstrømningsforhold og disses indflydelse på vandbalancebudgettet.
- *Opskallering af gletscher- og iskappeforhold.* Med fokus på gletscher- og iskappemassebalanceforhold og -tendenser er disse blevet analyseret og sammenlignet: (a) for den nordlige del af den nordatlantiske regions vedkommende, inklusive Mittivakkat Gletscheren, med variationer i storskala atmosfæriske og oceanografiske forhold; og (b) for den nordlige halvkugles vedkommende og globalt i relation til gletscher- og iskappebidraget til det globalt stigende havniveau. Også ude af ligevægts forhold i gletschere og iskapper er blevet bestemt, i relation til det fremtidige gletscher- og iskappebidrag til det globalt stigende havniveau.
- *Modellering af indlandsisens overflade- samt afstrømningsforhold.* Simulering af indlandsisens smelte- og overflademassebalanceforhold i såvel nutidige som fremtidige tidsperspektiver (1950/1960 til 2080). Modellerne SnowModel og HydroFlow gav f.eks. ny indsigt i den spatiotemporale fordeling af afstrømningen fra Grønland til havet (både direkte fra indlandsisen og fra det kystnære område mellem indlandisen og oceanet).

## Abstract

The 19 publications and material presented in this thesis emphasize my research conducted on the Mittivakkat Gletscher in Southeast Greenland (the only mountain gletscher in Greenland for which there exist long-term observed time series of meteorological data, net mass-balance, freshwater runoff, and glacier front fluctuations), and externally on glaciers and ice caps (GIC) in the northern North Atlantic region, on both the Northern Hemisphere and globally, and on the Greenland Ice Sheet (GrIS). The publications represent an improvement in our understanding of atmosphere-land interactions related to snow, ice, hydrological processes and cycle, and water balance from Greenland – from glacier scale to ice sheet scale – to its surroundings. The publications present a description of the climate conditions at Mittivakkat Gletscher (with perspective to overall Greenland conditions); Mittivakkat Gletscher mass changes from observations and model applications; together with model simulations of GIC externally, and on the GrIS.

The thesis is divided into several chapters, where relevant parts from the research history from the Mittivakkat region and on the Mittivakkat Gletscher are described, including ongoing observational projects and used methods (Chapter 2). The Mittivakkat Gletscher margin and area fluctuations, albedo changes, and ‘out of balance’ conditions (committed mass loss) were observed. Snow, surface mass-balance (SMB), and runoff were both observed and modeled for Mittivakkat Gletscher (Chapter 3), and compared to GIC externally. For the GrIS, the melt extent, SMB, and runoff were modeled – including the spatiotemporal distribution of runoff to the adjacent seas –, and its application to emphasize the link between terrestrial freshwater fluxes from GIC and GrIS to fjords, and its subsequent mass contribution to global sea-level change (Chapter 4).

My main contributions to scientific knowledge have been in the following research areas:

- *Greenland mountain glacier observations.* The Mittivakkat Gletscher observations are scientifically valuable for our understanding of long-term mountain glacier behavior and its impact on the water balance during changing climate conditions in coastal Greenland – during a period with a warming and drying climate.
- *Greenland mountain glacier model code development and simulations.* The SnowModel and HydroFlow code developments and simulations brought new insight into the climate impact on Mittivakkat Gletscher SMB conditions, impacts from simulations of air temperature inversion on snow and glacier conditions, and to the spatiotemporal distribution of runoff and its impact on the water balance.
- *GIC upscaling* with a focus on present GIC net mass-balance conditions and trends for the northern North Atlantic region related to variabilities in large-scale climatic and oceanic indices, and for the Northern Hemisphere and globally, related to GIC net mass-balance contributions to sea-level rise. Further, new insights were obtained on GIC out of balance conditions and the future committed GIC area and volume mass loss with regards to mean sea-level changes.

- *Greenland Ice Sheet surface and runoff modeling*. Modeling of the GrIS surface melt extent and surface mass-balance conditions in both present and future time perspectives (1950/1960 through 2080). The developed HydroFlow model provided new insights regarding the spatiotemporal distribution of terrestrial runoff from Greenland (from the GrIS and from the land strip area) to the adjacent seas.

## 1. Introduction

### 1.1 Climate and Cryosphere

*“The cryosphere, comprising snow, river and lake ice, sea ice, glaciers, ice shelves and ice sheets, and frozen ground, plays a major role in the Earth’s climate system through its impact on the surface energy budget, the water cycle, primary productivity, surface gas exchange and sea level. The cryosphere is thus a fundamental control on the physical, biological and social environment over a large part of the Earth’s surface. Given that all of its components are inherently sensitive to temperature change over a wide range of time scales, the cryosphere is a natural integrator of climate variability and provides some of the most visible signatures of climate change.”*

(Vaughan et al. 2013)

The above quote presents the components of the cryosphere in the Earth’s climate system and its impact on different physical subjects e.g., the surface energy budget, the water cycle, and sea-level rise as summarized in the beginning of Chapter 4 “Observations: Cryosphere” taken from the Fifth Assessment Report (AR5) of the Intergovernmental Panel on Climate Change (IPCC) published in 2013.

Warming of the climate system is unequivocal, and since the 1950s, many of the observed changes in Earth’s climate system and in the cryosphere, as mentioned in the quote, are unprecedented over decades to millennia (IPCC 2013; Summary for Policymakers (SPM)). The atmosphere and ocean have warmed, and subsequently the cryosphere has changed. For instance, Pan-Arctic spring snow cover has decreased in extent and in duration (Brown et al. 2010; Callaghan et al. 2011; Liston and Hiemstra 2011), terrestrial-terminating glaciers have thinned and receded and are an important component in the high-latitude hydrological cycle and water balance (Gardner et al 2013; [14]), and river flow has increased (Shiklomanov and Lammers 2009; Overeem and Syvitski 2010; [10]). Also, the global sea-level has risen (Church et al. 2013), providing some of the most visible consequences of climate change.

Climate change and the effects of climate change have been particularly pronounced in the Arctic region (Hartmann et al. 2013), where cryospheric elements are present. The Arctic is undergoing a system-wide response to the altered climatic state. Changes in the Arctic climate play a non-insolated role in the global climate system: it both affects and is affected by the global climate change through multiple complex interactions. Changes in the Arctic will therefore have far-reaching consequences for, and feedbacks to, the entire Earth system (McGuire et al. 2006).

Analyses of climate measurements have indicated that the global average combined temperature of ocean and land surface air has on average increased by 0.85°C over the period 1880 through 2012, and that warming occurred more intensively at northern latitudes, including for Greenland, than elsewhere (McBean et al. 2005; IPCC 2013, SPM), especially in winter and spring (e.g., Hanna et al. 2012). For Greenland, the first decade of the new millennium had the highest mean annual air temperature (MAAT) on record (this has also been confirmed at the global scale by Hansen et al. (2010)), and the highest number of MAAT warm extremes [1]. The on average increasing temperatures have been accompanied by an on average increasing precipitation for Arctic latitudes (e.g.,

Hartmann et al. 2013; Hinzman et al. 2013) and for Greenland, covering spatiotemporal variability within relatively short distances and periods (e.g., [2] [3]).

In the coming ~85 years – towards the end of the 21<sup>st</sup> century – climate models estimate that the global mean surface air temperature will increase by between 0.3–4.8°C based on the different Representative Concentration Pathway (RCP) scenarios: Air temperatures are predicted to increase beyond 2100 (IPCC 2013; SPM). The Arctic region is expected to warm more rapidly than the global mean (Collins et al. 2013; Kirtman et al. 2013). The increasing temperature will be accompanied by on average increasing of precipitation towards the end of the 21<sup>st</sup> century of more than 50 % in the Arctic regions (Kattsov et al. 2007; Bintanja and Selten 2014), with substantial spatial variability in precipitation patterns (Collins et al. 2013).

Based on the ongoing and future expected changes in climate conditions (highlighted above), together with the inherent sensitivity of the cryosphere to temperature and precipitation changes over a wide range of time scales, we are – as a scientific community – facing enormous challenges to continue improving our understanding of past and present cryospheric conditions and processes in order to better predict future changes. For example, regarding GIC a very small fraction of Earth’s approximately estimated 200,000 GIC (e.g., Pfeffer et al. 2014) have been mass-balance observed, of which about 70 have uninterrupted records of 20 years or more (Dyurgerov 2010; WGMS 2012; [12]).

To predict the impact from a future changing climate, we need to understand the present and past processes and conditions. Such challenges include an extended understanding of GIC and GrIS, including their mass-balance and freshwater runoff processes, changes, climate sensitivity, and subsequent impacts on micro-, local-, regional-, hemispheric-, global-scales, since GIC and GrIS are reservoirs of water from a hydrological perspective and important regulators of water availability and future contributors to eustatic sea-level rise.

This thesis deals with analyses of climate impacts on the Mittivakkat Gletscher, which is the only mountain glacier in Greenland for which there exists long-term observations of meteorological data, net mass-balance, runoff, and glacier front fluctuations (with regards to GIC in Greenland and externally) and on the GrIS through observations, model code development, and model simulations to improve our understanding of atmosphere-land interactions related to snow, ice, hydrological processes, hydrological cycle, and the water balance. Computer based GIC and GrIS snow, SMB, and runoff models have been developed and applied, since: 1) the demand to develop model routines increases with the increasing pressure to realistically understand and describe complicated physical atmosphere-snow-ice-water-processes and interactions; and 2) because observations of climate, snow, ice, and hydrological processes have typically not been possible over large areas in Greenland due to impassable terrain, remote locations, and harsh climatic conditions.

## 1.2 Objective, content, and structure

### 1.2.1 Objective

The objective of this thesis is to present the combined contribution to scientific knowledge of the research presented in the 19 publications – publications related to *physical GIC and GrIS hydrological conditions and water budgets*. In order to accomplish

these objectives the thesis is divided into several chapters with the aim of presenting my research contributions within the overall framework of: 1) GIC margin and area fluctuations, albedo changes, out of balance conditions (committed mass loss), and snow, SMB, and runoff observations and modeling for Greenland's Mittivakkat Gletscher representative for GIC in Southeast Greenland with regards to GIC externally; and 2) GrIS melt extent, SMB, and runoff modeling (including the spatiotemporal distribution of runoff to the adjacent seas), and its application to emphasize the link between terrestrial freshwater fluxes from GIC and GrIS to fjords and adjacent seas, and its subsequent mass contribution to global sea-level change. This is to improve our understanding of atmosphere-land interactions related to snow, ice, hydrological processes, and the water balance from Greenland to its surroundings.

The research is presenting present day GIC and GrIS surface mass-balance conditions covering the period 1950/1960 through 2014 during a period where intensive warming occurred at northern latitudes; and examples of GrIS surface hydrological conditions predicted towards 2080 forced by regional climate model (RCM) data.

### 1.2.2 Content and structure

Chapter 2 presents and discusses recent cryospheric research in Greenland in relation to the different ongoing mass-balance and hydrometric GIC and GrIS monitoring programs. The different GIC and GrIS observation and calculation methods, model applications, model code developments, and model tests used in the presented publications [4]–[19] are described and discussed to emphasize the methods used for estimating snow and ice surface melt, surface mass-balance conditions, freshwater runoff, the hydrological processes, and the water balance budget for the Mittivakkat Gletscher and the GrIS.

Chapter 3 focuses on the Mittivakkat Gletscher. Initially a historical overview of the Mittivakkat Gletscher is presented. Mass balance conditions (winter, summer, and net mass balances), margin and area fluctuations, ice thickness, volume, surface velocity, transit snow line (TSL), the equilibrium-line altitude (ELA), accumulation-area ratio (AAR), surface albedo changes and out of balance conditions are elucidated and discussed. Mittivakkat Gletscher conditions estimated either from observations or model simulations are discussed. Finally, the Mittivakkat Gletscher conditions are compared against different broad-scale studies: GIC margin and area fluctuations from the Ammassalik region (around the Sermilik Fjord), Southeast Greenland, net mass-balance conditions for GIC in the northern North Atlantic region (linked to large-scale atmospheric and oceanic indices) and on the Northern Hemisphere, and out of balance conditions for GIC globally. This chapter is based on the publications [1]–[10] which deal with the different Mittivakkat Gletscher studies, and [11]–[14] which deal with regional-, hemispheric-, and global-scales GIC studies.

Chapter 4 focuses on GrIS surface simulations, including melt conditions (extent and duration) and water balance components (precipitation, evaporation, sublimation, runoff, and SMB), and the spatiotemporal pattern of GrIS and coastal Greenland distributed runoff to the adjacent oceans. The surface melt conditions and water balance components are simulated for 1995–2005 and 1960–2010 forced by automatic weather station (AWS) data and for 1950–2080 forced by RCM data evaluating the projected future water balance for the GrIS. Finally, on a regional scale a case study about the Sermilik Fjord (an icefjord), is included to emphasize the current overall freshwater flux, and individual contributions from runoff, ice discharge, subglacial geothermal and frictional, and rain on the fjord surface area. This chapter is based on publications

**Table 1:** The structure and content of the thesis divided by publications, chapters, and research topics.

Publication	Chapter	Element	Geography	Research topic	Period	
[1]	3	Climate change	Greenland margin area	Surface air temperature and link to temperature extremes	1890–2010	
[2]			GrIS and Greenland margin area	Precipitation	1890–2012	
[3]			Mittivakkat Gletscher region	AWS data analyze linked to synoptic data	1994–2006 and 1898–2006	
[4]		Glacier and ice caps	Mittivakkat Gletscher, Mittivakkat Gletscher catchment, and surrounding area	Mass balance, out of balance conditions, margin recession <sup>†</sup>	1996–2010 <sup>†</sup> 1900–2010	
[5]				Volume, mean ice thickness, surface velocity <sup>§</sup>	1986–2011 <sup>§</sup> 1996–2011	
[6]				Ablation rates, TSL, EL, AAR, out of balance	1999–2012	
[7]				Surface albedo, mass balance, ELA	2000–2013	
[8]				Precipitation, snow, evaporation, sublimation, SMB, and runoff modeling	1998–2006	
[9]				Air temperature inversion model code development, and modeling	1999–2006	
[10]				Runoff routing and multi snowpack model code development and modeling	2003–2010	
[11]				GIC regional-, hemispheric-, and global-scales	Regional GIC and GrIS front and area fluctuations	1972–2011
[12]					Global GIC mass balance, AAR, out of balance conditions	1971–2010
[13]					Regional GIC mass balance linked to atmospheric and oceanic circulation indices	1970–2009
[14]					Northern Hemisphere GIC temperature, precipitation, sublimation, evaporation, SMB, and runoff modeling	1979–2009
[15]	4	Greenland Ice Sheet and Greenland	GrIS and Greenland	Melt extent, internal storage, Precipitation, SMB, evaporation, sublimation, and runoff modeling	1995–2005	
[16]				Surface melt extent modeling	1960–2010	
[17]				Internal storage, precipitation, SMB, runoff (GrIS), runoff spatial distribution modeling (Greenland)	1960–2010	
[18]				Melt extent, internal storage, precipitation, evaporation, sublimation, SMB, and runoff modeling	1950–2080	
[19]				GrIS and Greenland: Sermilik Fjord (case studies)	Sermilik Fjord: Freshwater flux: modeled freshwater runoff and observed ice discharge	1999–2008

[15]–[18] all dealing with the entire GrIS (and [17] the entire Greenland), where [19] deals specifically with the Sermilik Fjord catchment.

Finally, Chapter 5 contains conclusions and perspectives for future work regarding GIC in Greenland and the GrIS.



The structure of the content of this thesis is not organised according to the chronology of my publications [1] to [19], but instead divided into subjects related to GIC and then GrIS issues. Table 1 summarizes the structure and content of the thesis.



## 2. Arctic as an integrated system

### 2.1 The integrated Arctic system

The Arctic region is complex and is in rapid transformation, due to changes in climate (e.g., Bring and Destouni 2014). Although much remains to be learned about the Arctic and its component processes, many of the most urgent scientific, engineering, and social questions can only be approached through a broader system perspective (Hinzman et al. 2013). As in other ecosystems, the Arctic components are interdependently linked to one another, and inherently interconnected with the broader global system (e.g., Roberts et al. 2010; Saito et al. 2013). The different atmospheric, surface, and subsurface components, processes, and feedback pathways for the Arctic are schematically illustrated in Figure 1 – all affecting short and long term changes in the atmospheric, terrestrial, or marine environments.

A significant part of this unique Arctic complex system is the *cryosphere* comprising e.g., snow, glaciers, and an ice sheet which influences the Earth's dynamic climate system through its different impacts on e.g., the surface energy balance, the water

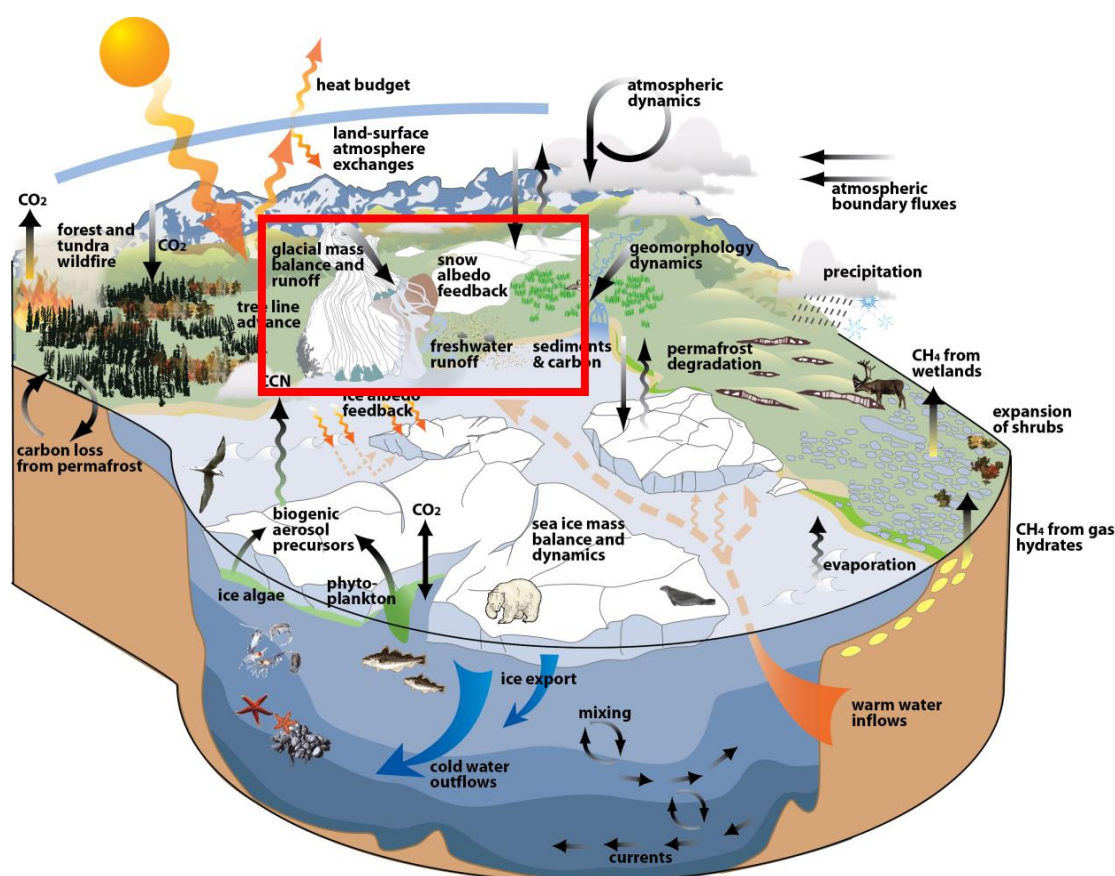


**Figure 1:** Schematic illustration of Arctic as a tightly coupled system, influenced by components, processes, and feedback pathways between the atmosphere, surface, and subsurface – between the atmosphere, terrestrial, and marine environments. The bold red rectangle highlights the cryospheric part of the Arctic region comprising snow, glaciers, and ice sheets influencing the surface energy budget, freshwater budget, sea-level, and Atlantic meridional overturning circulation. The figure is modified from Hinzman et al. (2013).

cycle, and sea-level change, but which is also affected by global climate changes through multiple complex interactions. To better visualize these cryospheric interactions on a detailed scale related to glaciers and ice sheets, Figure 2 illustrates in a schematic way the different atmosphere-ice and ice-ocean components, processes, and interactions associated with estimating net mass-balance conditions (accumulation and ablation conditions) here shown for a marine-terminating glacier. Importantly, these processes and interactions vary both in time and space. To better understand these processes and interactions, and to quantify the various accumulation and ablation components illustrated in Figure 2, Greenland can be characterized as a unique place – as a field laboratory – for such studies.

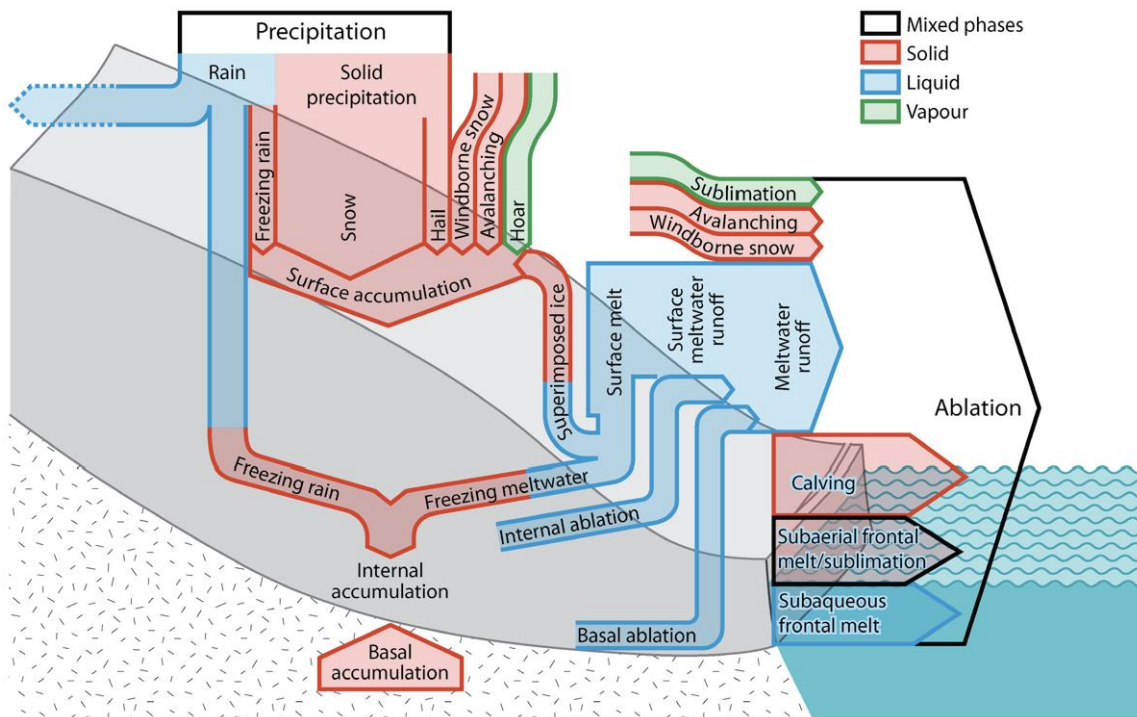


**Figure 2:** Schematic illustration of the different accumulation and ablation components of a marine-terminating glacier. The color codes indicate the different phases from mixed (black), solid (red), liquid (blue), and vapour fluxes (green). The arrows have arbitrary widths and do not indicate physical pathways of mass transfer. The figure is from Cogley et al. (2011).

## 2.2 The water balance

The glacier accumulation and ablation components (UNESCO 1992) schematically illustrated in Figure 2 can be solved based on the hydrological method (Equation 1). Here, the yearly surface water balance equation is illustrated initially for a land-terminating glacier (by not including dynamical mass loss) (Equation 1) [8] [10] [14] [15] [17] [18], which can be described as follows:

$$P - (E + Su) - R \pm \Delta S = 0 \pm \eta \quad (1)$$

where,  $P$  (mm water equivalent (w.e.)) is precipitation input from snow and rain (and possibly from condensation, blowing snow, and avalanches),  $E$  (mm w.e.) is evaporation

(liquid to gas phase flux of water),  $Su$  (mm w.e.) is sublimation (solid to gas phase with no intermediate liquid stage),  $R$  (mm w.e.) is surface runoff,  $\Delta S$  (mm w.e.) is change in storage ( $\Delta S$  is also referred to as SMB, or as net mass-balance ( $B_a$ ) in the literature) i.e., changes in glacier storage and snowpack storage. The parameter  $\eta$  is the water balance discrepancy (error). The error term should be 0 or small if the components:  $P$ ,  $E$ ,  $Su$ ,  $R$ , and  $\Delta S$  have been determined accurately. Also,  $\Delta S$  is often calculated as the residual value, and if so, the balance discrepancy is then set to be zero, and the errors are therefore shunted into the residual term. In Equation 1,  $P$  is calculated as positive and  $E$ ,  $Su$ , and  $R$  are considered negative for a glacier.

For marine-terminating glaciers (Figure 2; by including dynamical mass loss) the water balance equation (Equation 2) can be expanded and described as follows:

$$P - (E + Su) - R - Id \pm \Delta S = 0 \pm \eta \quad (2)$$

where,  $Id$  is dynamical mass loss from glacier front ablation taking into account calving, subaerial frontal melt and sublimation, and subaqueous frontal melt (Figure 2). In [15] [19], for example, the mass loss contribution from observed ice discharge was taken into account, when estimating the freshwater fluxes and the water balance.

The components regarding to e.g., the basal glacier conditions (Figure 2) are not included in Equation 2. As an example, in [19] basal glacier conditions such as subglacial geothermal melting and subglacial frictional melting due to basal ice motion were calculated to account for ~1 % of the terrestrial freshwater flux to e.g., Sermilik Fjord. Due to this relatively minor contribution from the terrestrial freshwater flux it has been ignored from Equation 2.

In practical work the hydrological method can be applied e.g., for an individual glacier, and an ice sheet, but also for an individual drainage basin (e.g., Mernild and Hasholt 2006; Mernild et al. 2008a, 2008b; Hasholt et al. 2008a). However, the method does not provide any information on the spatial distribution of components or gradients (Cogley et al. 2011).

In Table 2, the different water balance components estimated in each individual publication are shown to illustrate whether the entire water balance or only parts of it are presented. Also, to illustrate whether the individual water balance components are estimated based on observations, simulations, or as a residual (for the latter it will only be  $\Delta S$ ).

**Table 2:** Calculation methods used in the different publications for estimating the water balance components and subsequently the water balance budget. The letters indicate whether the water balance components are: observed (O), model simulated (S), calculated as a residual term (R), not calculated (N), based on literature value (L), or not included in the publication (-).

	GIC							GrIS and Greenland							
	Mittivakkat Gletscher, Mittivakkat Gletscher catchment, and surrounding area				GIC regional-, hemispheric-, And global-scales			GrIS and Greenland				Sermilik Fjord (case studies)			
	[4]	[5]	[6]	[7]	[8]	[9]	[10]	[12]	[13]	[14]	[15]	[16]	[17]	[18]	[19]
$P$	-	O <sup>†</sup>	O <sup>†</sup>	O <sup>†</sup>	S	S	S	-	-	S	S	-	S	S	S
$E$	-				S	S	S	-	-	S	S	-	S	S	S
$Su$	-	O <sup>§</sup>	O <sup>§</sup>	O <sup>§</sup>	S	S	S	-	-	S	S	-	S	S	S
$R$	-				S	S	S	-	-	S	S	S*	S	S	S
$Id$	-	-	-	-	-	-	-	-	-	-	L	-	-	-	O
$\Delta S$	O	O	O	O	R	R	R	O	O	R	R	-	R	R	-
$H$	-	-	-	-	N	N	N	-	-	N	N	-	N	N	-

Here, reported as <sup>†</sup>winter mass-balance, <sup>§</sup>summer mass-balance, and as <sup>\*</sup>surface melt.

## 2.3 Mass-balance and hydrological observations in Greenland

Around ~85 % of Greenland is covered by the GrIS (the largest terrestrial reservoir of permanent snow and ice in the Northern Hemisphere, equal to ~7.4 m sea-level equivalent (SLE); ~1.7 million km<sup>2</sup> in area and nearly 3,000 m thick) and by ~20,000 individual GIC dynamically disconnected from the GrIS (Pfeffer et al. 2014; Radić et al. 2014), covering an area of ~89,300 ± 2,800 km<sup>2</sup> (Rastner et al. 2012). Out of these thousands of GIC, which are located in the land strip area between the GrIS margin and the ocean, only a few GIC currently have ongoing “long-term” operational mass-balance programs to quantify GIC accumulation, ablation, and net mass-balances. For the Arctic in total there are ~25–30 operational GIC net mass-balance programs (WGMS 2012).

These operating GIC net mass-balance programs in Greenland are located in eastern Greenland, on the A. P. Olsen Iskappe (74.6°N, Zackenberg, East Greenland), where the monitoring program has been ongoing continuously since 2008 operated by the Geological Survey of Denmark and Greenland (GEUS) (Larsen et al. 2012), Freya Gletscher (74.4°N, Clavering Island, East Greenland) since 2007 by Austrian Polar Research Institute (Hynek et al. 2014), and Mittivakkat Gletscher (65.7°N, Ammassalik Island Southeast Greenland) since 1995 by Aarhus University and University of Copenhagen (where both N. T. Knudsen and S. H. Mernild were Principal Investigators from 2009 through 2013), and subsequently by GEUS. However, recently (in 2012), for example, operational mass-balance programs were initiated on Qaanaaq Gletscher, which is a part of the Qaanaaq Iskappe (74.4°N, Qaanaaq, Northwest Greenland) by Hokkaido University (Sugiyama et al. 2014; pers. com S. Sugiyama, January 2015), and on Qassinnguit Gletscher (64.1°N, Nuuk/Kobberfjord, West Greenland) by Asiaq (Abermann et al. 2014). Mittivakkat Gletscher is the only continuously long-term mass-balance observed glacier in Greenland [4]–[6], having the most extensive published series of glacier in-situ measurements (Knudsen and Hasholt 2004, 2008; Kargel et al. 2012). All observed GIC are land-terminating GIC and therefore influenced directly by atmospheric conditions, and not by a combination of atmospheric and oceanic conditions.

On the GrIS, mass-balance programs e.g., at the K-transect has been operated since 1990 (by Utrecht University), located ~20–25 km east of the town Kangerlussuaq (67.0°N; West Greenland). Here, AWS parameters are measured and SMB estimated at individual points along the transect from ~340 m above sea level (a.s.l.) to ~1,500 m a.s.l. (van de Wal et al. 2005, 2012; van den Broeke et al., 2008a, 2008b, 2008c; [16] [17]). Also, AWS parameters and mass-balance are measured in the GrIS ablation zone through e.g., the PROMICE project (operated by GEUS) (an overview of the different GrIS mass-balance locations can be found in: [http://promice.org/Newsletter\\_07.pdf](http://promice.org/Newsletter_07.pdf)), and on the ice sheet through the Greenland Climate Network (GC-Net) (operated by University of Colorado: [www.cires.colorado.edu/science/groups/steffen/gcnet/](http://www.cires.colorado.edu/science/groups/steffen/gcnet/)) [15]–[17] [19].

Along the Greenlandic coast, at least eight “long-term” permanent hydrometric monitoring stations are operating, measuring the outlet runoff from GIC and GrIS catchments to the fjords and adjacent seas. Runoff at the outlet represents an integrated response of the upstream watershed to precipitation and other hydrometeorological processes like snow and glacier melt, to snow cold content, and to glaciological processes like englacial bulk water storage and release, instead of just the climate impact on snow and ice conditions [10] [17]. These hydrological stations are spread out around

the margin of Greenland and located at Zackenberg (74.5°N, Northeast Greenland, operated since 1996 by Aarhus University) (e.g., Mernild et al. 2007, 2008b; Hasholt et al. 2008a; ZERO Annual Reports: [www.zackenberg.dk](http://www.zackenberg.dk)), Mittivakkat Gletscher catchment (65.7°N, Southeast Greenland, since early-1990s by University of Copenhagen) (Hasholt and Mernild 2006; Mernild and Hasholt 2006; [10]), Nuuk/Kobberfjord catchment (64.1°N, West Greenland, since 2007/2008 by Aarhus University) (NERO Annual Reports; [www.nuuk-basic.dk](http://www.nuuk-basic.dk)), Tasersiaq catchment (66.2°N, West Greenland, since 1975 by Asiaq) ([www.asiaq.gl](http://www.asiaq.gl)), Akuliarusiarsuup Kuua River (67.1°N, West Greenland, since 2008) (Rennermalm et al. 2012, 2013), Kangerlussuaq catchment outlet (67.0°N, West Greenland, since 2007) (e.g., Mernild et al. 2008c, 2011; van As et al. 2012; Hasholt et al. 2013; Mikkelsen et al. 2013; Mikkelsen 2014), Tasersuaq near Sisimiut (66.9°N, West Greenland, 1977–2010 by Asiaq and hereafter by Nukissiorfiits) ([www.nukissiorfiit.gl](http://www.nukissiorfiit.gl)), and Thule (76.5°N, Northwest Greenland, since 2004 by University of Alaska) (unpublished). Such observed runoff time series have limitations since they only span parts of the runoff season, and all together transfer less than 1 % of the Greenland runoff to adjacent seas [17].

In general, these mass-balance and runoff observational limitations result in restricted observational knowledge about the glaciological and hydrological conditions and interactions in Greenland. This is a serious impediment to our detailed understanding of hydrological processes and water balances from GIC and GrIS, and subsequent changes in ice volume and their coupling with climate change – especially because: 1) the increase in GIC and GrIS net mass loss and surface runoff since the early 1990s has followed atmospheric warming (e.g., Hanna et al. 2008; [18]; Box and Colgan 2013; Church et al. 2013; Vaughan et al. 2013), where the GrIS net mass-balance, for example, was close to equilibrium during the relatively cold 1970s and 1980s (e.g., Rignot et al. 2008); and 2) the freshwater runoff since the early 1990s to the late-2000s has been estimated to have explained approximately half of the recent mass loss of the GrIS, with iceberg calving generating the other half (e.g., Zwally and Giovinetto 2001; van den Broeke 2009; Straneo et al. 2013). For 2009 to 2012, however, freshwater runoff has been estimated to explain around two-thirds of the mass loss of the GrIS (Enderlin et al. 2014). In comparison, for example, existing analyses of Greenland, and of Arctic in general, GIC area fluctuations are more numerous, based on historical accounts, aerial photography, and satellite images spanning different time intervals from the early twentieth century to present day (e.g., Sharp et al. 2003; Ananicheva et al. 2006; Glazovsky and Marcheret 2006; Dowdeswell et al. 2007; Anderson et al. 2008; Paul and Svoboda 2009; Barrand and Sharp 2010; Bolch et al. 2010; Andreassen et al. 2012; Bjørk et al. 2012; [11]; Shahgedanove et al. 2012).

However, due to the net mass-balance and runoff observational limitations of GrIS and GIC in Greenland, the Mittivakkat Gletscher is so far the *only* mountain glacier in Greenland, where the possibility of linking continuously long-term climate records with net mass-balance and hydrological observations is present to identify, monitor, quantify, and determine processes and interactions regarding water budget conditions in a present warming climate.

## 2.4 Mittivakkat Gletscher – an ice and water balance laboratory

### 2.4.1 80 years of research of Mittivakkat Gletscher and the surrounding area

The Mittivakkat Gletscher (a temperate glacier; 26.2 km<sup>2</sup>; ranging from ~160–880 m a.s.l. 65°41'N, 37°48'W; Figure 3), and the adjacent area around the glacier – the



Sermilik area – has geographically been the target area for several scientific expeditions since 1933 (Hasholt and Jakobsen 2008). Based on the earliest scientific glacier work on Mittivakkat Gletscher in 1933 conducted by the geologist Keld Milters, led by the polar researcher Knud Rasmussen during his Seventh Thule Expedition, Mittivakkat Gletscher was during the International Geophysical Year (IGY) 1957/1958 picked as one of the Danish focus sites for Arctic research. Between IGY and 1970, expeditions to Mittivakkat Gletscher were conducted to demonstrate the relationships between climate induced ablation variations and freshwater runoff. In 1970 a permanent field station – *the Sermilik Station* – was established by University of Copenhagen (Fristrup 1970) (and reconstructed in 1973 after a snow avalanche destroyed it in 1972) to intensify the scientific research on glaciology and glacially driven geomorphological processes, and more broadly on physical geographical processes in a “typical” Arctic landscape: a landscape including a glaciated area, proglacial valley/outwash plain, and delta/coastal zone, with the purpose of identifying, monitoring, quantifying, and determining their relative importance and variability (Hasholt and Jakobsen 2008).

In 1993 and 1997, permanent AWS were installed by University of Copenhagen in the Mittivakkat Gletscher catchment on a nunatak near the Mittivakkat equilibrium-line

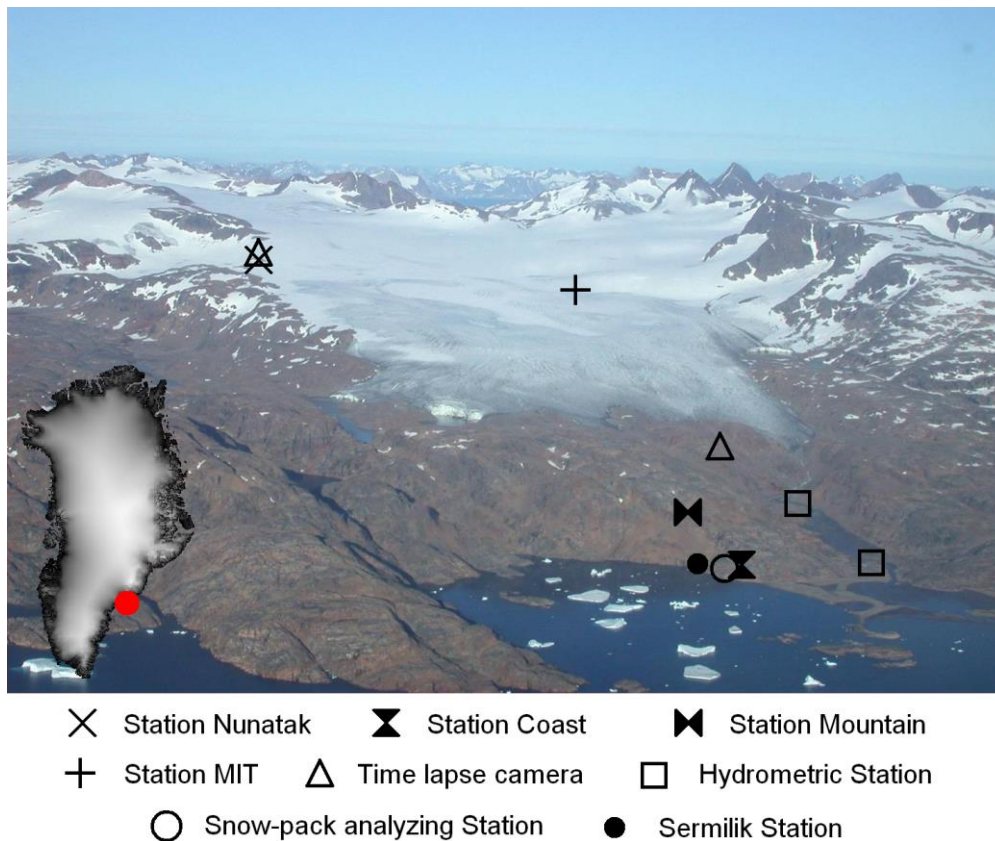


**Figure 3:** The Mittivakkat Gletscher in 2006, when the distance between the glacier margin and the coast was approximately 1,500 m. Symbols for the location of AWS, hydrometric stations, time lapse cameras, the snow station, and the Sermilik Station are illustrated. The photo is taken toward ESE with Sermilik Fjord in the foreground and the Irminger Sea in the background. The Mittivakkat Gletscher is located in the Low Arctic (Born and Böcher 2001), on the western central part of the Ammassalik Island, approximately 10–12 km northwest of the town Tasiilaq and 50 km east of the eastern margin of the GrIS, separated from the mainland by the 10–15 km wide Sermilik Fjord. The inset figure indicates the general location of the Mittivakkat Gletscher within the Eastern Greenland. The photo is modified from [4].



altitude (ELA; the ELA is the spatially averaged elevation of the equilibrium line, defined as the set of points on the glacier surface where the net mass balance is zero) (515 m a.s.l.; 65°42.3'N, 37°48.7'W; named: Station Nunatak) and in the coastal zone (25 m a.s.l.; 65°40.8'N, 37°55.0'W; named: Station Coast) (Hasholt et al. 2004; [7]–[10]), in order to provide information about the climate conditions and gradients. Climatic observations were recorded sporadically until 1993. In 1995 the present ongoing observational glacier mass-balance program (based on the direct glaciological method; Østrem and Brugman 1991) was established covering 16.3 km<sup>2</sup> of the Mittivakkat Gletscher area (Knudsen and Hasholt 2004; [4] [5]) (comparable SMB estimates are not available for any other GIC peripheral to the GrIS), and time lapse cameras were installed to visualize snow, ice, and hydrological runoff conditions (Hasholt and Mernild 2004; Mernild and Hasholt 2006; Mernild et al. 2006b). Ultrasonic sensors were operated in the proglacial valley downstream from the Mittivakkat Gletscher – one near the glacier outlet (since 2004; 65°40.7'N, 37°54.7'W; named Station Lars) and one at the catchment outlet (since 1993; 65°40.6'N, 37°54.7'W; named: Station Isco (at the outlet 72–78 % of the upstream area was glacier covered [10])) to monitor the river stage level during the runoff season and the variation in snow depth accumulation during snow covered periods when the river was frozen. The river discharge was discontinuously measured at Station Isco until 1993, and almost continuously every year thereafter, however, missing for several years in the 2000s [11]. Measurements only span parts of the runoff season as discharge observations were lacking both in the beginning and at the end of the runoff season (Hasholt and Mernild 2004; Mernild 2006; Mernild et al. 2006a; Mernild and Hasholt 2006). Furthermore, in 2009 additional AWS were installed (192 m a.s.l.; 65°41.0'N, 37°54.6'W; named Station Mountain and 510 m a.s.l.; 65°41.3'N, 37°49.3'W; named Station MIT) and in 2010 a snow-pack analyzing station (9 m a.s.l.; 65°40.8'N, 37°55.0'W) was installed in the coastal zone to provide continuous information regarding the snowpack density and liquid water content conditions (snowpack data are unpublished) (Figure 3).

Since the early 1990s, due to the establishment of permanent research monitoring installations, scientific research at the Mittivakkat Gletscher and in the surrounding area has been intensified, and more so since the Sermilik Stations joined several international research networks, most recently the EU funded InterAct program: an international network for terrestrial research and monitoring in the Arctic ([www.eu-interact.org](http://www.eu-interact.org)).

#### 2.4.2 Earlier model simulations of Mittivakkat Gletscher and the surrounding area

In Greenland, due to the harsh climate conditions, terrain, and remote locations of GIC, extensive observations of e.g., meteorological data, snow accumulation, snow distribution, snow density, snow melt, glacier melt, glacier net mass-balance, and freshwater runoff are very limited. Different model systems have therefore been developed and applied initially on well-monitored locations – such as the Mittivakkat Gletscher – then later, for example, used to simulate the spatiotemporal variations in meteorological, snow, ice, hydrological processes, and the water balance for ungauged basins and/or for the GrIS.

Therefore, on the Mittivakkat Gletscher different conceptual hydrological models such as the Time-Area model (Mernild et al. 2006a), NAM (a lumped Rainfall-Runoff model) (DHI 2003a, 2003b), and a numerical runoff-sediment model (based on lumped-elements) (Fausto et al. 2012) were initially used to simulate the temporal variability in point discharge – the runoff hydrograph – at the Mittivakkat Gletscher catchment outlet, together with suspended sediment concentrations.

The Time-Area model is a runoff model, where the hourly runoff hydrograph is simulated based on the sum of flow-contributions (from rain, snow melt, and ice melt) from a subdivision of the catchment, defined by time contours (isochrones), which are lines of equal flow time to the point where discharge is required (Shaw 1999). Thus, for the Mittivakkat Gletscher, modifications were implemented in the Time-Area model, by dividing the model into 100-m surface elevation bands, rather than isochrones, and by using experimental average flow times through the different components (snow, firn, and ice) (Mernild 2006; Mernild et al. 2006a). The Time-Area model simulated hourly runoff was tested against independent observed runoff from the Mittivakkat Gletscher catchment with acceptable results ( $r^2 = 0.85$ , where  $r^2$  is the square of the linear correlation coefficient). This indicates that the model is useful for site-specific and case-specific runoff purposes, and not beyond that, for which the model has not been empirically tested. Even though the Time-Area model is not developed for glaciers and therefore does not take into account routines related to e.g., glacier dynamics, changes in the internal drainages system (hydrological response), internal water storage and release, and receiving/delivering of water from neighboring glacier catchments, the model was, however, useful as a test to estimate the hourly runoff hydrograph of limited time periods from both a fully snow-covered Mittivakkat Gletscher in May 2005 and a partially snow-covered glacier in August 2004.

Further, a NAM model was set up and used on the Mittivakkat Gletscher to simulate the daily runoff hydrograph (1993–2004), including for the periods at the beginning and at the end of the runoff season, where direct measurements were not possible causing uncertainties in the yearly water balance calculations (Mernild and Hasholt 2006). The NAM model is a conceptual lumped model – a three linear reservoirs model. NAM was originally developed for glacier-free landscapes, and therefore, from a glacier-hydrological perspective the model has limitations in its description of the water routing processes through snow, firn, and ice (as also illustrated for the Time-Area model). The NAM model uses simple quantitative routines to estimate snow conditions; including snow storage and melt. The snowmelt is calculated using the positive degree-day approach, assuming an empirical relationship between air temperature (sensible heat) and surface melt rates (DHI 2003a, 2003b). The NAM model simulated daily runoff was tested against independent observed runoff, where the timing and magnitude of simulated runoff in general were in good accordance with observed discharge ( $r^2 = 0.77$ ) (Mernild and Hasholt 2006). This indicates that the NAM model is useful for site-specific and case-specific catchment runoff purposes, and not assumed to be valid for simulations of internal processes within the catchment.

Also, a numerical runoff-sediment model (based on lumped-elements) was set up and used together with an early version of SnowModel [8] (without SnowPack-ML [10] [17], HydroFlow [10] [17], air temperature inversion [9], and physical routines for the spatial and temporal variability in snow albedo (Mernild et al. 2010a)) for the Mittivakkat Gletscher to simulate daily runoff and subsequent suspended sediment concentration and transport using a constant idealized glacier drainage system (2003–2005) (Fausto et al. 2012). The idealized hydraulic-circuit drainage system followed Clarke (1996) and includes three elements constant in size and structure constrained by average flow times (Mernild 2006): 1) a crevasse feeder (a discharge and storage volume) leading meltwater from the glacier surface to the bedrock; 2) a subglacial channel system leading meltwater and suspended sediment towards a subglacial storage; and 3) a channel system leading meltwater and suspended sediment to the glacier margin (Clarke 1996). The simulated suspended sediment concentration were tested against independent observations, indicating correlations between 0.63–0.89, also capturing most of the large sediments

spikes associated with high melting events (Fausto et al. 2012). This model is useful for site-specific and case-specific issues, and will as such need validation if used elsewhere for simulating glacial runoff and sediment concentrations.

The mechanisms that connect climate, glacier surface conditions, ice dynamics, and internal hydrology are still weakly understood, for example, routing and storage of meltwater and liquid precipitation through glacier ice, and transforming the input contributions into a runoff hydrograph at the terminus based on seasonal changes in hydrological response and delay (e.g., Lemke et al. 2007; van den Broeke et al. 2008; Nick et al., 2009; [10] [17]). In spite of this and earlier snow, SMB, and runoff studies at the Mittivakkat Gletscher, there is growing recognition that accurate representations of the spatial snow distribution and SMB, internal drainage and storage, and flow processes are essential to realistically assess the impact of climate changes on the Mittivakkat Gletscher and its runoff. Simple and crude conceptual runoff models have described the glacier drainage system differently and some as a system of linear reservoirs, with different storage properties (Mernild et al. 2006a; Mernild and Hasholt 2006; Fausto et al. 2012). With the purpose of simulating runoff from a glacierized basin, these models omit many of the key physical processes. Such processes have, for example, been tailored to a site-specific glacier, for example, to the Trapridge Glacier, Yukon Territory, Canada, where glacier surface ablation (estimated through a temperature-index parameterization), glacier surface runoff, englacial water transport, subglacial drainage, and subsurface groundwater flow were linked (Flowers et al. 2002a, 2002b). For Mittivakkat Gletscher, to solve some of these runoff challenges a multilayer snowpack model (SnowPack-ML) [10] and a gridded runoff routing model (HydroFlow) were developed [10] [17] and implemented in SnowModel (Liston and Elder 2006a, 2006b; Mernild et al 2006b) to simulate the spatiotemporal distribution in runoff hydrographs.

### 2.4.3 SnowModel and its subprograms

SnowModel is a *state-of-the-art* spatially distributed snow and ice evolution and hydrological modeling system, and an aggregation of six submodels: MicroMet, EnBal, SnowTran3D, SnowPack-ML, HydroFlow, and SnowAssim [8] [9] [10] [14]–[19] (Figure 4).

*MicroMet* is a quasi-physically based high-resolution meteorological distribution model (Liston and Elder 2006b; Mernild et al 2006b), and designed to produce the meteorological forcing distributions of air temperature, relative humidity, wind speed, wind direction, precipitation, solar and longwave radiation, and surface pressure required for SnowModel. MicroMet uses elevation-related interpolations to modify air temperature, humidity, and precipitation following Kunkel (1989), Walcek (1994), Dodson and Marks (1997), and Liston et al. (1999). Temperature and humidity distributions are defined to be compatible with the observed lapse rates. Wind flow in complex topography is simulated following Ryan (1977) and Liston and Sturm (1998). Solar radiation variations are calculated using elevation, slope, and aspect relationships (Pielke 2002). Incoming longwave radiation is calculated while taking into account cloud cover and elevation-related variations following Iziomon et al. (2003). Precipitation is distributed following Thornton et al. (1997). In addition, any data from more than one location, at any given time, is spatially interpolated over the domain using a Gaussian distance-dependent weighting function and interpolated to the model grid using the Barnes objective analysis scheme (Barnes 1964, 1973; Koch et al. 1983).

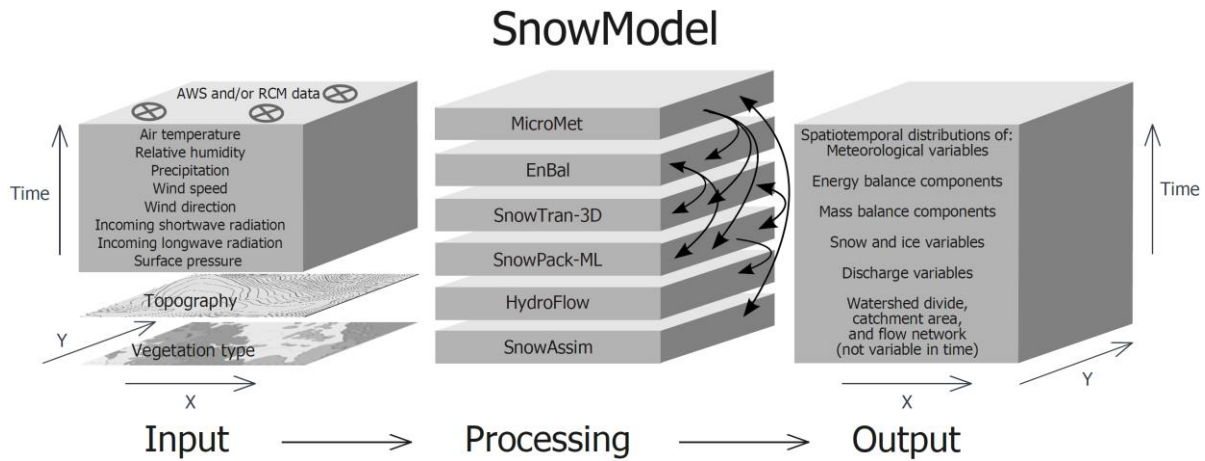


**Figure 4:** A schematic illustration of SnowModel and its six submodels and how the submodels interact with one another, including the required input data, and an example of the output datasets.

*Enbal* is a full energy surface exchange and melt model (Liston 1995; Liston et al. 1999), which simulates surface (skin) temperatures, and energy and moisture fluxes in response to observed and/or modeled near-surface atmospheric conditions provided by MicroMet. The turbulent exchange of sensible heat and latent heat, the conductive energy transport to or from the underlying surface, and the energy flux available for melt are calculated using a surface energy balance model of the form (Equation 3):

$$(1-\alpha)Q_{si} + Q_{li} + Q_{le} + Q_h + Q_e + Q_c = Q_m \quad (3)$$

where,  $Q_{si}$  ( $\text{W m}^{-2}$ ) is the solar radiation reaching Earth's surface,  $Q_{li}$  ( $\text{W m}^{-2}$ ) is the incoming longwave radiation,  $Q_{le}$  ( $\text{W m}^{-2}$ ) is the emitted longwave radiation,  $Q_h$  ( $\text{W m}^{-2}$ ) is the turbulent exchange of sensible heat,  $Q_e$  ( $\text{W m}^{-2}$ ) is the turbulent exchange of latent heat,  $Q_c$  ( $\text{W m}^{-2}$ ) is the conductive energy transport,  $Q_m$  ( $\text{W m}^{-2}$ ) is the energy flux available for melt, and  $\alpha$  is the surface albedo. Over virtually all snow and ice GIC surfaces, the incoming solar radiation is the primary source of energy melting snow and ice by an order of magnitude more than that provided by sensible heat flux associated with air temperature (Liston and Hiemstra 2011; [17]).

*SnowTran-3D* is a three-dimensional surface model for snow redistribution by wind and snow depth evolution (deposition and erosion) from wind-blown snow, based on a mass-balance equation that describes the temporal variation of snow depth at each grid cell within the simulation domain. Deposition and erosion, which lead to changes in snow depth (Equation 4), are the result of changes in horizontal mass-transport rates of saltation,  $Q_{salt}$  ( $\text{kg m}^{-1} \text{s}^{-1}$ ); changes in horizontal mass-transport rates of turbulent suspended snow,  $Q_{turb}$  ( $\text{kg m}^{-1} \text{s}^{-1}$ ); sublimation of transported snow particles,  $Q_v$  ( $\text{kg m}^{-2} \text{s}^{-1}$ ); and the water equivalent precipitation rate,  $P$  ( $\text{m s}^{-1}$ ). Combined, the time rate of change in snow depth,  $\zeta$  (m), is:

$$\frac{d(\rho_s \zeta)}{dt} = \rho_w P - \left( \frac{dQ_{salt}}{dx} + \frac{dQ_{turb}}{dx} + \frac{dQ_{salt}}{dy} + \frac{dQ_{turb}}{dy} \right) + Q_v \quad (4)$$

where,  $t$  (s) is time,  $x$  (m) and  $y$  (m) are the horizontal coordinates in the west-east and south-north directions, respectively, and  $\rho_s$  and  $\rho_w$  ( $\text{kg m}^{-3}$ ) are snow and water density, respectively. At each time step, Equation 4 is solved for each individual grid cell within the domain and is coupled to the neighboring cells through the spatial derivatives ( $d/dx$ ,  $d/dy$ ) (Liston and Sturm 1998, 2002; Liston et al. 2007).

*SnowPack-ML* is a multilayer snowpack evolution model simulating snowpack temperature and density evolution, and snowpack ripening in response to precipitation and melt fluxes defined by MircoMet and Enbal over time, regarding snow temperature and the weight of the overlying snow [10]. In addition, SnowPack-ML simulates the surface meltwater that percolates into, and refreezes within, snow and firn layers as a function of the cold content (the temperature below freezing), and snow and ice permeability, which makes for an important contribution to the evolution of snow and ice densities and subsequently the moisture available for runoff [10].

*HydroFlow* is a gridded linear-reservoir runoff routing model developed to simulate the linkages between runoff production from land-based snowmelt and icemelt processes and the associated freshwater fluxes to downstream areas and surrounding oceans, based on both a slow flow system (transport of water within the individual grid cell to the routing network; identical to flow conditions through the snowpack) and a fast flow system (transport of water between the individual grid cells in the routing network; identical to flow conditions through the glacier ice) [10] [17] (see further below). HydroFlow creates the watershed divide, drainage catchment, and a flow network that links the individual grid cells that make up the simulation domain, and simulates runoff hydrographs at each individual grid cell. The flow time through the fast flow grid system is constrained by observed average flow times (Mernild 2006).

*SnowAssim* is a model available to assimilate field observed datasets and datasets from remote sensing (Liston and Hiemstra 2008).

#### 2.4.4 SnowModel code developments for Greenland studies

SnowModel was originally developed for glacier- and ice-free landscapes. Model modifications were initially implemented and used to: 1) simulate glacier-ice melt and net mass-balance after the winter snow accumulation had ablated; and 2) adjust underestimated observed AWS solid precipitation (adjustment routines were based on iterative procedures) until the model simulated winter mass-balance matched the observed winter mass-balance for Mittivakkat Gletscher (Mernild et al. 2006b). Earlier by Hasholt et al. (2003) the subprogram SnowTran-3D was used to elucidate the snow distribution on the Mittivakkat Gletscher, for the year 1997/1998. Further, physical routines for the spatial and temporal variability in snow albedo according to surface snow characteristics were implemented in SnowModel (Mernild et al. 2010a; using Douville et al. (1995) and Strack et al. (2004)), together with routines for air temperature distribution during periods with inversion [9]. To expand our knowledge about albedo conditions on the Mittivakkat Gletscher, a MODerate Imaging Spectroradiometer (MODIS) albedo study (500-m horizontal grid) compared to ground observations has been conducted [7] – these albedo findings related to surface air temperature conditions are, for example, scheduled to be implemented in SnowModel/EnBal.

To account for the role of surface meltwater percolating into and refreezing within the snowpack – making an important contribution to the evolution of snow and ice densities and moisture available for runoff – a multilayer snow model was developed that simulates the refreezing of meltwater as a function of snow and ice permeability and cold

content. Such, a multilayer snowpack model (SnowPack-ML) was developed [10], implemented, and used in SnowModel, in combination with HydroFlow.

HydroFlow, a gridded linear-reservoir runoff routing model was developed to simulate the linkages between runoff production from land-based snowmelt and icemelt processes and the associated freshwater fluxes to downstream areas and surrounding oceans [10]. Compared to earlier model studies at Mittivakkat Gletscher, and at other mountain glaciers (e.g., Hock and Jansson 2005), these used models are relatively simple representations of a complex natural system. Based on the developed HydroFlow routines, we are able to estimate the spatial distribution of the watershed divides, the size of the drainage area, the flow network, the time evolution and spatial distribution of different water transport mechanisms, and the runoff transient times. The watershed divides, the drainage area, and the flow network were controlled exclusively by the surface topography [10], since the role of bedrock topography in controlling the potentiometric surface and associated flow direction is secondary [17, Equation 4] (Cuffey and Patterson 2010). This is because it appears to be acceptable owing to the smoothness of the surface [17]. Further, based on HydroFlow we are able to simulate the temporal and spatial variability in runoff hydrographs at each grid cell within the simulation domain, including for each individual watershed outlet [10]. HydroFlow was developed on the Mittivakkat Gletscher (2003–2010), where simulated runoff hydrographs were tested against observed hydrographs with substantial correlations (between  $r^2 = 0.63$  and  $0.77$ ) at the glacier catchment outlet [10], reproducing observed runoff in both timing and volume.

Still there are numerous water transport-related processes that are not explicitly included in the HydroFlow model simulations – processes that remain less understood and, for example, delay or reduce water export to the surrounding seas (e.g., Rennermalm et al. 2013). HydroFlow for example, as with most other runoff models, omits processes such as temporal variations in: 1) englacial bulk water storage and release, including drainage from glacial surges and drainage of glacial-dammed water (long-term build-up of storage followed by short-term release); 2) melt contributions from internal glacial deformation, geothermal heat, basal sliding, and the internal drainage system as it evolves during the melt season; 3) englacial water flow between neighboring catchments; and 4) open channel stream flow routing. In addition, SnowModel is not a dynamic glacier model, and routines for simulating changes in glacier area, size, thinning, and subsequent changing hypsometry, are not yet represented within the modeling system [10]. Further, SnowModel assumed one-way atmospheric forcing where the atmospheric conditions were prescribed at each time step. However, the merging of SnowModel with both Snowpack-ML and HydroFlow is a step forward in comparison to the models that have previously been applied on the Mittivakkat Gletscher and on other mountain glaciers (see e.g., Jansson et al. 2003; Hock and Jansson 2005), to simulate glacier runoff hydrographs.

SnowModel/HydroFlow was further used on the Northern Hemisphere ( $>25^\circ\text{N}$ ) to simulate GIC water balance conditions (Equation 1) and net mass-balance contribution to sea-level rise, for all individual GIC greater or equal to  $0.5 \text{ km}^2$  [14] (based on 1-km horizontal grid, 3-h time step, and the Randolph Glacier Inventory (RGI) v.2.0 (Arendt et al. 2012)). This model study is the first of its kind and more detailed – simulating subdiurnal time steps – than earlier studies (e.g., Hock et al. 2009), where a simplified monthly global grid-based degree-day approach ( $1^\circ \times 1^\circ$ ) was used, and than Marzeion et al. (2012), where simulated SMB for individual GIC (RGI v. 1.0) was estimated based on monthly climate forcing using air temperature as a proxy for the energy available for melt. Further, SnowModel/HydroFlow was used to simulate (5-km horizontal grid) the GrIS surface mass-balance conditions, watershed divides, drainage catchments, flow network,

and subsequently the spatial runoff magnitudes and distribution from Greenland – including from ungauged basins in the land strip area between the ice margin and the ocean – to the adjacent fjord and seas, and their changes throughout 1960–2010 [17].

#### 2.4.5 Mass-balance, AAR, out of balance conditions, area, and volume change

Knudsen and Hasholt (2004, 2008) published observed Mittivakkat Gletscher net mass-balance data from 1995/1996 to 2005/2006. Hereafter, the net mass-balance time series have been continuously updated by [4] [5] [7] [8] for the period 1994/1995 to 2013/2014, together with the observed ELA and accumulation area ratio (AAR) time series. These net mass-balance and AAR time series for the Mittivakkat Gletscher, together with radar volume (Knudsen and Hasholt 1999) and area observations [11] were used to emphasize the climate impact on the glacier conditions, on mean ice thickness and volume changes, and subsequently used to estimate the out of balance conditions [4], and how much the Mittivakkat Gletscher is likely to lose in the future, of its current area and volume even in the absence of future climate change. Also, based on the mass-balance program – the positions of the individual stakes in the network (a network varying from 47 stakes in 1998 and 2001 to 18 for the years 2008–2014) –, the surface velocity and its deceleration was estimated (confirmed by the shallow ice approximation) and linked to a decrease in ice thickness and to changes in basal sliding associated with changing subglacial hydrological conditions [5].

The *out of balance* calculations were done based on the AAR method developed by Bahr et al. (2009), where a glacier in balance with the climate has an AAR value equal to its equilibrium value,  $AAR_0$ .  $AAR_0$  was estimated based on a linear regression between AAR and SMB:  $AAR = SMB * m + AAR_0$ , where  $m$  is the slope. Zero values of AAR were excluded from the regression since AAR and SMB are not linear related when net ablation occurs everywhere on the glacier [4] [12]. Also, following Dyurgerov et al. (2009), we assumed that  $AAR_0$  does not change in time for each individual GIC [12]. Glaciers with  $AAR < AAR_0$  will retreat from lower elevations, typically over several decades or longer; until the AAR returns to the equilibrium value [12]. The AAR method does not directly predict rates of retreat and thinning. From the ratio (Equation 5a):

$$\alpha_r = AAR/AAR_0 \tag{5a}$$

the fractional changes ( $\alpha_r$ ) in area ( $p_A$ : Equation 5b) and volume ( $p_V$ : Equation 5c) required to reach equilibrium with a given climate can be estimated:

$$p_A = \alpha_r - 1 \tag{5b}$$

$$p_V = \alpha_r^\gamma - 1 \tag{5c}$$

where,  $\gamma$  is the exponent in the glacier volume ( $V$ )-area ( $A$ ) scaling relationship (Equation 5d):

$$V = cA^\gamma. \tag{5d}$$

Theory suggests the following scaling parameters:  $c = 0.033 \text{ km}^{3-2\gamma}$ , and  $\gamma = 1.375$  for glaciers and  $\gamma = 1.25$  for ice caps (Bahr 1997; Bahr et al. 1997; [12]). However, in Bahr et al. (2009) for glaciers  $\gamma = 1.36$  was empirically estimated [4].

The transit snowlines (TSL) were estimated from high spatial resolution Landsat imagery (30-m grid) on Mittivakkat Gletscher [6], to determine the snow ablation rates, TSL migration rate, ELA, AAR, where ELA is the altitude of the snowline at the end of the ablation season. The satellite derived-ELA were further used to estimate the end date of the ablation season (to verify the date of net mass-balance observations), and AAR were combined with net mass-balance data to estimate the Mittivakkat Gletscher out of balance conditions. This illustrates an alternative way to estimate the out of balance conditions, if AAR are not available from direct ground observations [6]. To compare, a similar study was done for the Lemon Creek Glacier (11.6 km<sup>2</sup>; 58°23.0'N, 134°24.0'W), Southeast Alaska, to highlight how useful these methods were in different Arctic climate settings for estimating TSL, ELA, AAR, and out of balance conditions [6].

Not only for the Mittivakkat Gletscher [4], but also for all observed GIC globally ( $n = 144$ ), where both net mass-balance and AAR time series were available [12], the out of balance conditions and committed area and volume loss were estimated, and divided into regional estimates following the Earth's glaciated regions (in total 16 regions e.g., Pfeffer et al. 2014) to illustrate the geographical variability. The committed global GIC volume loss to sea-level rise was estimated (2001–2010), accepting that undersampling is a significant problem for studies – not only for this study [12] but for all methods – that project global sea-level rise from GIC. Here, uncertainties regarding biases were taken into account, suggesting undersampling and geographical issues to be a source of bias, where the GIC size distribution is, however, not a large source of bias [12]. To reduce the uncertainties, more GIC net mass-balance and AAR observations are needed, and especially in the poor sampled regions such as Greenland, Alaska, Arctic Canada.

Further, the observed Mittivakkat Gletscher net mass-balance time series was used together with observed net mass-balance time series from 28 land-terminating GIC from the northern North Atlantic region (from Iceland, Scandinavia, and Svalbard), in order to analyze the spatiotemporal variability in net mass-balance (1970–2009). This study is important for our understanding, since variations in net mass-balance are related to both surface weather conditions and to atmospheric and oceanic circulations like, for example, the Atlantic Multidecadal Oscillation (AMO), North Atlantic Oscillation (NAO), Arctic Oscillation (AO), and Greenland Blocking Index (GBI) [13]. This analysis was conducted to explore statistical relationships and physical relations between net mass-balance conditions and large-scale atmospheric and oceanic circulation indices for the northern North Atlantic region.

Area and margin changes for the Mittivakkat Gletscher [4] [11] and for 35 land-terminating GIC peripherally and dynamically disconnected to the GrIS in the Ammassalik region (around the Sermilik Fjord) were estimated, together with land- and marine-terminating outlet glaciers from the GrIS (1972–2010) [11]. This was done based on Landsat imagery in order to emphasize the differences in GIC area and margin changes within a specific area, and differences in margin changes between land-terminating GIC, and land- and marine-terminating outlet glaciers from the GrIS (the latter influenced both by atmospheric and oceanic forcing). The differences in margin recession were compared to observed atmospheric air temperatures, precipitation, and reconstructed ocean water temperatures at a depth of 400 m in the Irminger Sea [11].



## 2.5 Greenland Ice Sheet

For the GrIS, SnowModel was set up (5-km horizontal grid; 1-d time step) and used to simulate and quantify present day surface melt extent and surface water balance conditions (Equation 1), including internal refreezing (storage) for 1995–2005 [15] and for 1960–2010 [16] [17]. These simulations were forced based on AWS data from both inside and outside the ice sheet – from up to 56 different AWS from the PROMICE project, K-transect, GC-Net project, Sermilik Station, and the Danish Meteorological Institute (DMI) Synoptic AWS [17]. Also, the variability in ELA and melt index (above 2,000-m in elevation; the melt index is defined as the melting area times the number of melting days) were simulated. Since SnowModel is a surface model, net mass-balance data were linked to observed bottom melting and calving estimates, to give a first hand estimate of the average GrIS mass-balance for 1995–2005 [15].

To simulate the spatial distribution of freshwater runoff to adjacent seas, together with site-specific hydrographs for each individual catchment in Greenland (for the GrIS HydroFlow identified ~400 and for Greenland in total ~3,150 individual drainage catchments [17]), the developed SnowPack-ML and HydroFlow submodels were used together with SnowModel [17]. The same SnowModel setup [17] was used by the IPCC AR5 (Chapter 13, Sea level Change: Figure 13.5 and Table 13.2) together with four SMB modeling systems (using AWS data and RCM data) to evaluate the GrIS SMB conditions for 1960–2010 (Church et al. 2013).

Further, the SnowModel GrIS simulated melt extent, runoff, and SMB were linked to large-scale oceanic circulation indices, the AMO index [16] [17] [20] to emphasize statistical relationships and physical relations, since sea-surface warming trends are potential drivers of ongoing GrIS changes. Also, the impact from global dust veils generated by volcanic activity was linked to GrIS melt extent, SMB, and runoff conditions [16] [17].

Fluctuations in the GrIS SMB, runoff, and mass-balance are of considerable importance to the global eustatic sea-level rise, the Atlantic meridional overturning circulation (AMOC) (Rahmstorf et al. 2005; Weijer et al. 2012; see also Workshop Summary Serreze (1998)), and subsequently on the climate system (Bryden et al. 2005). SnowModel was used (5-km horizontal grid; 1-d time step) to simulate variations in GrIS melt extent, SMB, and freshwater runoff for 1950–2080 [18]. These SnowModel simulations were forced with the IPCC A1B scenario (which is closest to the RCP6 scenario used in IPCC AR5), modeled by the HIRHAM4 RCM using boundary conditions from the ECHAM5 atmospheric-ocean general climate model (AOGCM) – an AOGCM model realistically describing the present-day conditions in the Arctic, and around Greenland in particular (Walsh et al. 2008; Stendel et al. 2008). Based on the results from Walsh et al. (2008), the AOGCM used is a sensible choice, when only one realization is offered [18]. This model study [18] was used by the IPCC AR5 (Chapter 13, Sea level Change: Table 13.4) together with a dozen of other models to predict the contribution to sea-level rise from changes in GrIS SMB during the 21<sup>st</sup> century (Vaughan et al. 2013).

On a regional catchment scale – to understand the freshwater fluxes from Greenland – a SnowModel case study was conducted [19] for the Sermilik Fjord (1999–2008). The terrestrial contribution to the fjord was estimated based on SnowModel simulated freshwater runoff combined with ice discharge observations (updated from Howat et al. 2005, 2007), estimated subglacial geothermal and frictional melting due to basal ice motion, and rain on the fjord surface area, because the freshwater flux exerts an

important influence on the circulation and stratification of adjacent fjords (Straneo et al. 2013). Circulation, flow variability, and melting from icebergs in Sermilik Fjord (Sutherland et al. 2014) were not included in the water balance budget. Also, the fraction of runoff compared to the overall fluxes was estimated. The Sermilik Fjord was chosen because it includes one of the four biggest ice streams in Greenland, the Helheim Glacier (e.g., Howat et al. 2011; Khan et al. 2014). For the Sermilik Fjord the runoff flux variability was simulated based on AWS data (from the PROMICE and GC-Net projects, the Sermilik Station and the DMI synoptic AWS) [19] and combined with ice discharge observations from Helheim, Fenris, and Midgård Glaciers (1999–2008) [19].

## 2.6 Test of SnowModel for the Greenland simulations

Earth science models can be a relatively simple or sophisticated description of reality – in this case of the GIC and GrIS – in terms of verbal description, equations, and the governing relationship that purports to describe the reality (Refsgaard 2007). SnowModel is such a relatively sophisticated model, which includes both mathematical and physical descriptions (equations) and certain interactions between equations (Figure 4) to analyze the specific hypothesis or theory [8]–[10] [14]–[19]. Such a model should be tested against independent field observations and be subject to critical review to indicate that the model is accepted as valid for the specific hypothesis and theory. In Table 3 examples of different independent test results have been summarized for Greenland SnowModel studies conducted throughout the years, used as a measure of the capability of the model to perform the task for which it is specifically intended. Even though a model is: 1) accepted valid for the specific scientific purpose, it is not proof that the model is true – will perform physically right – for all the sub-processes leading up to the purpose, as for example the conceptual Time-Area model (Mernild et al. 2006a) and the NAM model (Mernild and Hasholt 2006); and 2) performing well with substantial correlation at gauging stations it does not, for example, ensure a good performance at sites upstream of those stations (Refsgaard 2007).

In Table 3, a summary of different SnowModel test results are shown (tested against independent field observations through different Greenland studies), to highlight the capability of the model to perform with regards to meteorological and melting conditions (air temperature, wind speed, relative humidity, precipitation, melt index, and melt extent) (Mernild et al. 2008a, 2008b, 2010a) [16], snow processes (snow depth; SWE (snow water equivalent) depth; snow extent) (Hasholt et al. 2003; Mernild et al. 2006b, 2007, 2008a, 2010), glacier ice processes (glacier winter, summer, and net mass-balance; location of ELA) (Mernild et al. 2006b, 2008a) [14], and hydrological runoff processes (discharge) [10]. Overall, the SnowModel tested parameters perform well (Table 3). Due to its high-resolution meteorological distribution model (including a physical inversion scheme), the energy balance for surface energy exchange and melt (including a physical albedo scheme), the blowing snow model (also taking into account blowing snow sublimation and the establishment of e.g., snow drifts), the multi-layer snowpack model (taking into account vertical changes in snow temperature, density, and water content), and the gridded runoff routing model, SnowModel is probably at present one of the most physically correct snow and ice surface models. This is particularly true when simulating: 1) GIC snow and surface ice conditions compared to other GIC models e.g., Hock et al. (2009); Marzeion et al. (2012); Schaefer et al. (2013); and 2) GrIS surface conditions compared to e.g., Box et al. (2009); Ettema et al. (2009); Hanna et al. (2011); Fyke et al.

(2014), where, for example, some of these listed models uses a grid-based degree-day approach and simplified snowpack and blowing-snow models.

**Table 3:** Examples of the different SnowModel validation studies (based on available field observations) for the Mittivakkat Gletscher catchment, the Zackenberg Glacier catchment, Northern Hemisphere, and from the GrIS. The table is updated from Mernild et al. (2009).

Validation of SnowModel routines against observations				
	Parameter	Discrepancy between modeled and observed	Time period	Reference
Mittivakkat Gletscher Catchment	Average SWE depth:	Maximum 1 %	May 1997/1998	Hasholt et al. 2003
	Point snow depth:	Maximum 7 %	Aug 2004 and May/June 2005	Mernild et al. 2006b
	- Winter mass-balance - Summer mass-balance - Net mass-balance - Location of ELA	Maximum 4 % Maximum 7 % Maximum 3 % Maximum 100 m in elevation	1999/2000 to 2003/2004	Mernild et al. 2006b
	Discharge	Average 0.03-0.14 m <sup>3</sup> s <sup>-1</sup> and maximum 3.10-5.25 m <sup>3</sup> s <sup>-1</sup>	2003 through 2010	[10]
Zackenberg Glacier catchment	Average end-of-winter SWE depth	Maximum 6 %	2004 and 2005	Mernild et al. 2007 and 2008b
	Snow extent based on depletion curves	Maximum 5 %	2000 through 2002	Mernild et al. 2007 and 2008b
	Snow extent based on satellite image	7 %	June 2002	Mernild et al. 2007
Northern Hemisphere GIC	Net mass-balance (leave-one-out cross validation)	Root mean square error 0.43 m w.e.	1979 through 2009	[14]
GrIS	Average meteorological data: - air temperature - wind speed - relative humidity - precipitation	0.2 °C 0.2 m s <sup>-1</sup> 0.1 % 1.0 mm w.e.	1995 through 2005	[15]
	End-of-season satellite-derived surface melt extent	Average 4 % and maximum distance of 160 km between modeled and satellite-derived melt and non-melt boundaries	1995 through 2005	[15]
	End-of-season satellite-derived surface melt extent	Average 40 ± 35 km and maximum ~160 km	2010	[16]
	Mean annual satellite-derived surface melt extent	0.4 × 10 <sup>5</sup> km <sup>2</sup>	1979 through 2010	[16]
	Melt-Index	Modeled results are consistent with observations	1995 through 2005	[15]
	Location of ELA	Average 35 m a.s.l. and maximum 425 m a.s.l.	1995 through 2005	[15]
	Average meteorological data (the explained variance): - air temperature - wind speed - precipitation - relative humidity  SWE depth	84–87 % 49–55 % 49–69 % 48–63 %  1 %	2000 through 2007	Mernild et al. 2011
	End-of-season satellite-derived surface melt extent	Average 7.8 ± 5.1 and maximum ~22 km		
SWE depth Mean ELA Daily ranked runoff (the explained variance)	1 % 50 m in elevation 0.86–0.97	2009 through 2013	Mernild et al. 2015	

### 3. Glacier and ice caps

#### 3.1 Mittivakkat Gletscher in coastal Southeast Greenland

##### 3.1.1 Climate conditions in coastal Greenland including at the Mittivakkat Gletscher region

The climate in coastal Greenland is changing [1]–[3], where the surface air temperature along the west coast of Greenland has faced strong warming, especially during winter ( $>10^{\circ}\text{C}$  since 1991), and less warming along the east coast (Hanna et al. 2012). Simultaneously precipitation has on average for coastal Greenland been increasing  $1.3\text{ mm w.e. yr}^{-1}$  (since 1961), even though huge variability exists over short distances and time periods [2] [3].

The climate around the Mittivakkat Gletscher region is affected both by the surface weather conditions and large-scale oceanic and atmospheric circulations [3] [13]. For the Mittivakkat Gletscher catchment and the town Tasiilaq (located  $\sim 10\text{--}12\text{ km}$  southeast of the Mittivakkat Gletscher) observed AWS and synoptic data indicate increasing temperatures over the last decades (Table 4). For Station Nunatak and Station Coast (Figure 3) MAAT was  $-2.4^{\circ}\text{C yr}^{-1}$  and  $-0.8^{\circ}\text{C yr}^{-1}$ , respectively. At both stations MAAT increased  $0.10^{\circ}\text{C yr}^{-2}$  and  $0.05^{\circ}\text{C yr}^{-2}$  (1998–2006) [3], respectively. For the time period almost similar to the Mittivakkat Gletscher observed net mass-balance period MAAT was  $-2.1^{\circ}\text{C yr}^{-1}$  (1994–2013) and  $-0.7^{\circ}\text{C yr}^{-1}$  (1998–2013), and increased by  $0.10^{\circ}\text{C yr}^{-2}$  (1994–2013) and  $0.07^{\circ}\text{C yr}^{-2}$  (1997–2013) (unpublished data), respectively (Table 4). For Tasiilaq, MAAT was  $-0.2^{\circ}\text{C yr}^{-1}$  and increased  $0.06^{\circ}\text{C yr}^{-2}$  (1994–2013) (Cappelen 2013a, 2013b; Mernild et al. 2012a; [1] [3]) (Table 4), and for other coastal stations in Southeast Greenland and at the Summit station at the top of the GrIS (3,208 m a.s.l.) increasing MAAT has also been observed [4]. Simultaneously a negative trend in observed annual precipitation has been observed for Tasiilaq [3] of  $-17\text{ mm w.e. yr}^{-2}$  (1991–2012) and  $-54\text{ mm w.e. yr}^{-2}$  (2001–2012) [2] (Table 4). Divided into seasons, the summer mean surface air temperature (June through August) and winter precipitation (September through May) faced increasing and decreasing trends, respectively, similar compared to the overall trends in MAAT and annual precipitation [4]. For Tasiilaq, higher MAAT has generally been associated with lower annual precipitation for the period where Mittivakkat has been mass-balance observed. Also, since 1900 the Tasiilaq temperature variability has almost been in anti-phase with the precipitation anomaly (Mernild et al. 2012). The last decade 2001–2010 was further the period with the highest number of MAAT warm extremes since 1890 [1] (Table 4), but also on average the warmest decade for Tasiilaq on record – a decade warmer than the early twentieth century warm period in the 1930s and 1940s [1].

Even though the climate for the region around the Mittivakkat Gletscher generally has been associated with increasing MAAT and decreasing annual precipitation sum over the last decades, local variabilities in climate conditions within the Mittivakkat Gletscher catchment are pronounced [3] [9]. The lowest part of the catchment (below approximately 300 m a.s.l.) (Figure 3) is highly dominated by air temperature inversion (84 % of the time) due to the effect of sea breezes [3] [9]. This is associated with the adjacent relatively low temperature and frequently ice-choked Sermilik Fjord as a result of the thermal differences between land and ocean (Hosler 1961; Milionis and Davies 2008). Based on the meteorological observations from Station Coast and Station Nunatak – two stations

**Table 4:** Overview of the different meteorological and Mittivakkat Gletscher conditions and changes based on observation and model simulations presented in [1] [3]–[10] [12].

Parameter	Location	Time period	Mean or range	Change	Reference
Observations					
MAAT	Station Nunatak	1998–2006 1994–2013	-2.4°C -2.1°C	0.10°C yr <sup>-2</sup> 0.10°C yr <sup>-2</sup>	[3]
MAAT	Station Coast	1998–2006 1998–2013	-0.8°C -0.7°C	0.05°C yr <sup>-2</sup> 0.07°C yr <sup>-2</sup>	[3]
MAAT	Station Tasiilaq	1994–2013	0.2°C	0.06°C yr <sup>-2</sup>	[1] [3]
MAAT warm extremes	Station Tasiilaq	2001–2010	The decade with the highest number of warm extremes	-----	[1]
Extension of the thawing period	Station Nunatak Station Coast	1994–2006 1998–2006	101 (1994) to 151 d (2006) 144 (1998) to 149 d (2006)	50 d 5 d	[3]
Annual precipitation Sum (corrected)	Station Tasiilaq	1991–2012 2001–2012	1,257 ± 232 mm w.e. yr <sup>-1</sup> 1,276 ± 300 mm w.e. yr <sup>-1</sup>	-17 mm w. e. yr <sup>-2</sup> -54 mm w. e. yr <sup>-2</sup>	[2]
Net mass-balance	Mittivakkat Gletscher	1995/1996–2010/2011 1995/1996–2013/2014	-0.97 ± 0.75 m w.e. yr <sup>-1</sup> -1.00 ± 0.70 m w.e. yr <sup>-1</sup>	-0.09 m w.e. yr <sup>-2</sup> -0.06 m w.e. yr <sup>-2</sup>	[5]
ELA	Mittivakkat Gletscher	1995/1996–2013/2014	~750 m a.s.l.	From 390 to >930 m a.s.l.	[4]–[6]
AAR	Mittivakkat Gletscher	1995/1996–2013/2014	0.15	-----	[5] [6] [12]
EBY mean glacier-wide albedo	Mittivakkat Gletscher	2000–2013	0.43–0.33	-0.10	[7]
Snow albedo	Station Nunatak Station MIT Station Coast	1995–2007 2009–2012 1997–2007	-----	-0.3 per 1°C of warming -0.3 per 1°C of warming -0.5 per 1°C of warming	[7]
Terminus along the dominant flow line	Mittivakkat Gletscher	1900–2010	-----	-16 m yr <sup>-1</sup>	[4]
Surface area	Mittivakkat Gletscher	1986–2011	31.6 km <sup>2</sup> (1986) 26.2 km <sup>2</sup> (2011)	-17 %	[11]
Mean ice thickness loss	Mittivakkat Gletscher	1995/1996–2010/2011 1995/1996–2013/2014	97 ± 15 m (2011) 93 ± 14 m (2014)	-18 m w.e. (-15 %, since 1994) -22 m w.e. (-19 %, since 1994)	[4] [5]
Ice volume	Mittivakkat Gletscher	1986–2011	3.7 ± 0.5 km <sup>3</sup> (1986) 3.3 ± 0.5 km <sup>3</sup> (1999) 2.6 ± 0.5 km <sup>3</sup> (2011)	-1.1 km <sup>3</sup> or -30 %	[4] [5]
Ice surface velocity	Mittivakkat Gletscher	1995/1996–2010/2011	Maximum mean: 22 m s <sup>-1</sup> Mean: 8 m s <sup>-1</sup> yr <sup>-1</sup>	-30 %	[5]
Out of balance: area Out of balance: volume	Mittivakkat Gletscher	1995/1996–2010/2011 1995/1996–2010/2011	-50–70 % -60–80 %	-----	[4] [6]
SnowModel simulations					
SMB	Mittivakkat Gletscher	1998–2006	-900 ± 470 mm w.e. yr <sup>-1</sup>	-46 mm w.e. yr <sup>-2</sup>	[8]
Precipitation	Mittivakkat Gletscher	1998–2006	1,490 ± 150 mm w.e. yr <sup>-1</sup>	-16 mm w.e. yr <sup>-2</sup>	[8]
Evaporation and sublimation	Mittivakkat Gletscher	1998–2006	-250 ± 30 mm w.e. yr <sup>-1</sup>	0 mm w.e. yr <sup>-2</sup>	[8]
Surface runoff	Mittivakkat Gletscher	1998–2006	-2,140 ± 410 mm w.e. yr <sup>-1</sup>	30 mm w.e. yr <sup>-2</sup>	[8]
Impact on net mass-balance with or without air temperature inversion routines	Mittivakkat Gletscher and nearby glaciers (n = 19)	1998–2006	~20 % less negative net mass-balance by including inversion routines	-----	[9]
Runoff days, runoff volume, and runoff part of glacier loss	Mittivakkat Gletscher basin	2003–2010	200 ± 20 d -40.9 ± 13.7 × 10 <sup>6</sup> m <sup>3</sup> yr <sup>-1</sup> 40 % of runoff from mass loss	30 d -2.9 × 10 <sup>6</sup> m <sup>3</sup> yr <sup>-2</sup>	[10]
Runoff volume	Mittivakkat Gletscher basin	1993–2010 NAM: 1993–2004 HydroFlow: 2003–2010	-33.3 ± 12.6 × 10 <sup>6</sup> m <sup>3</sup> yr <sup>-1</sup>	-1.7 × 10 <sup>6</sup> m <sup>3</sup> yr <sup>-2</sup>	[10] (Mernild and Hasholt 2006)

influenced by the same large-scale weather patterns – the observed mean annual incoming solar radiation at Station Coast was about 10 % lower than at Station Nunatak (1994/1997–2006) [3]. This difference in incoming solar radiation is probably caused by increasing and higher percentages of dense clouds and sea fog in the coastal area [3]. Further, regarding air temperature lapse rates, the sea breezes are strongly controlling the lapse rates within the catchments by indicating positive lapse rates during June through August, and negative lapse rates during September through May (Mernild et al 2006b, [3]).

Observations of precipitation (1999–2006) within the Mittivakkat catchment indicate a range from ~1,300–1,400 mm w.e. yr<sup>-1</sup> at Station Coast to ~1,700–1,800 mm w.e. yr<sup>-1</sup> at Station Nunatak, where ~50 % and ~80 % of the precipitation fell as solid precipitation, respectively [3]. For Tasiilaq, the (un)corrected precipitation was (~800–900 mm w.e. yr<sup>-1</sup>) ~1,200–1,300 mm w.e. yr<sup>-1</sup> (1991–2012) (Cappelen 2013a, 2013b; Mernild et al 2012 [2] [3]) (Table 4), indicating variabilities in precipitation among stations even within relatively short distances. In general for coastal Greenland, precipitation decreased with increasing latitude from ~2,250 mm w.e. yr<sup>-1</sup> at Ikerasassuaq (on the east coast in the far south (60.1°N), an area highly affected by synoptic cyclone passages passing close to Iceland) to ~300 mm w.e. yr<sup>-1</sup> at Danmarkshavn (76.7°N) in northeast Greenland, and with increasing distance from the coast inland towards the ice-sheet margin [2]. This is, for example, in contrast to Bales et al. (2009), who for short distances near the coast, due to orographic enhancements, noted an increase in precipitation towards inland areas in Southeast Greenland. Overall, between the coastal regions the GrIS precipitation trends showed an antiphase variability [2].

### 3.1.2 Mittivakkat Gletscher observations

The Mittivakkat Gletscher has since the long-term mass-balance observations began in 1996 faced positive net mass-balance values in 1996 and 2003. Otherwise, Mittivakkat Gletscher has faced negative net mass-balance values in 17 out of 19 years (Figures 5 and 6). Data collected from 1996 through 2014 shows that the observed Mittivakkat Gletscher mean net mass-balance is  $-1.00 \pm 0.70$  m w.e. yr<sup>-1</sup>, and  $-0.97 \pm 0.75$  m w.e. yr<sup>-1</sup> for 1996–2011[5] (Table 4). The mean observed winter balance was  $1.17 \pm 0.20$  m w.e. yr<sup>-1</sup> and the mean summer balance was  $-2.00 \pm 0.38$  m w.e. yr<sup>-1</sup> (winter and summer balances were measured for 13 out of the last 19 years) [4]–[7]. The net mass-balance changed on average  $-0.09$  m w.e. yr<sup>-2</sup> (1995/1996–2010/2011) [5] and by  $-0.06$  m w.e. yr<sup>-2</sup> (1995/1996–2013/2014) (Table 4). A spatial variation in winter, summer, and net mass-balances are shown in [5], indicating increasing mean winter accumulation with increasing elevation, decreasing mean summer ablation with increasing elevation, and decreasing mean net loss with increasing elevation, as expected [5]. Changes over time indicate the largest spatial annual change in winter balance to occur along the centerline and at high elevations (presumably due to an increase in wind speed [3] and snow redistribution), in summer balance towards the margins and most pronounced in the southern part (presumably due to convection of heat from the surrounding areas), and in net mass-balance in the margin areas in the south and along the center line, even though the general pattern is inhomogeneous (this is a combined effect of changes in winter and summer balances) [5]. For net mass-balance comparison the observed mass-balance for the Freya Gletscher was  $-0.71 \pm 0.41$  m w.e. yr<sup>-1</sup> (2008–2013) (WGMS 2013 and pers. com. D. Binder), indicating as well a net mass loss for Freya Gletscher in Northeast Greenland, however, not in the same order of magnitude as the mass loss from Mittivakkat

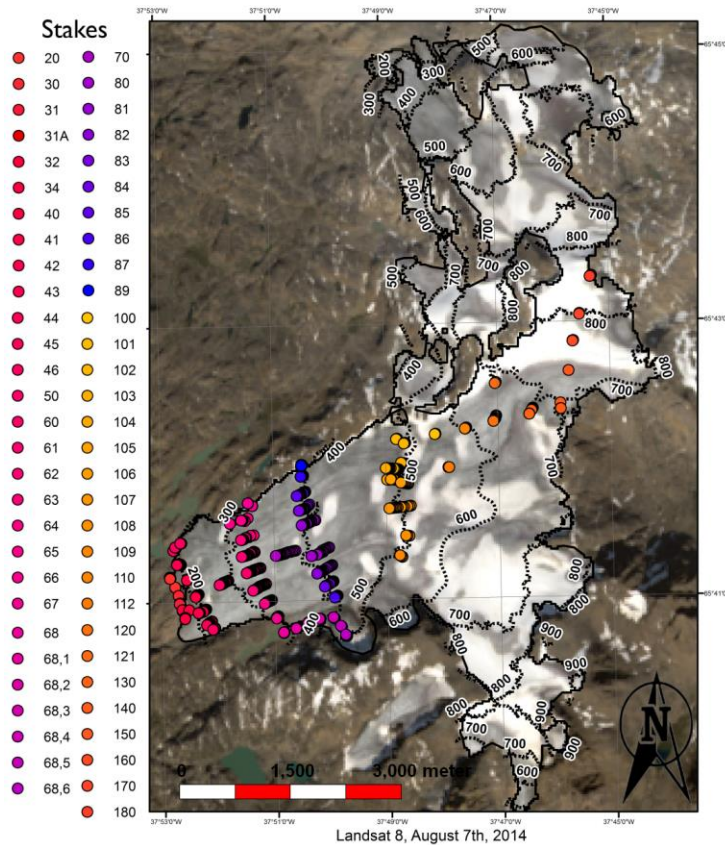


**Figure 5:** Mittivakkat Gletscher including topographic map (100 m contour intervals), and circles illustrating all the stake locations for the glacier observation program. The stake colors on the glacier surface correspond to the stake numbers illustrated to the left, where the low numbers correspond to the stakes at the low-elevation part of the glacier, and the converse. Background photo: Landsat 8, August 7, 2014.

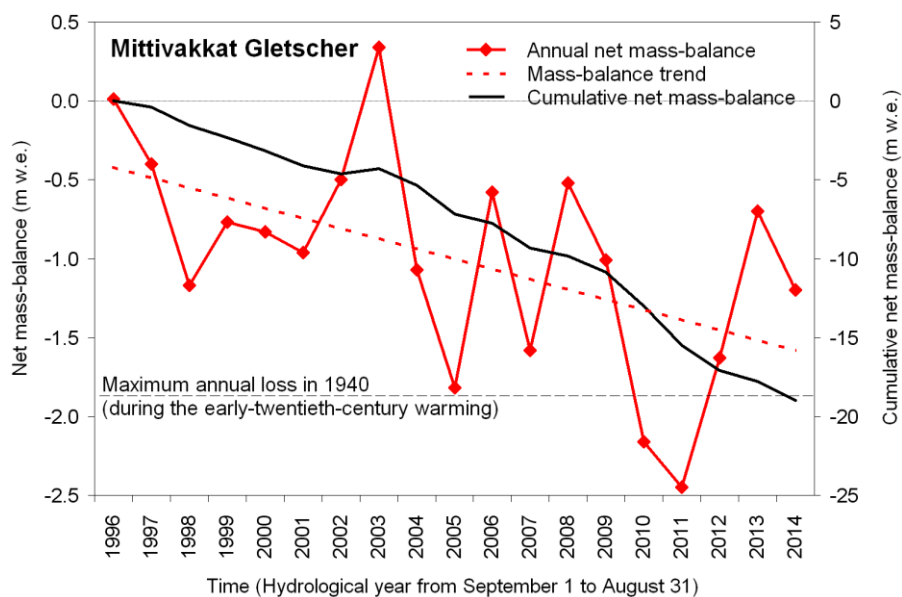


**Figure 6:** Observed net mass-balance and cumulative net mass-balance for the Mittivakkat Gletscher from 1996 through 2014 (updated from Knudsen and Hasholt 2008; [4]–[7]). Also, illustrated in the maximum annual loss of 1.87 m w.e. in 1940 during the early-twentieth-century warming period obtained in a model simulation from 1898 through 1993 (Mernild et al. 2008a).



Gletscher (for the same period Mittivakkat Gletscher had  $-1.41 \pm 0.79$  m w.e.  $\text{yr}^{-1}$ ). A comparison against observed net mass-balance data from the A.P. Olsen Iskappe is at present however not possible, since data is too poorly constrained – and therefore not available (pers. com., M. Citterio (Principal Investigator on the A. P. Olsen Iskappe mass-balance project), September 2014).

In 2010/2011 Mittivakkat Gletscher experienced an average observed maximum net mass-balance loss of 2.45 m w.e., which is around 2 % of the total glacier volume [4]. The maximum loss in 2010/2011, and in 2009/2010 of 2.16 m w.e. exceeded (insignificantly) the maximum loss of 1.87 m w.e. in 1940 during the early twentieth century warm period (data obtained in a model simulation of the Mittivakkat Gletscher net mass-balance from 1898 through 1993) (Mernild et al. 2008a) (Figure 6). The overall trend in net mass-balance for Mittivakkat Gletscher since 1996 has been towards more negative values (Figure 6) for a period where the trend has been towards higher mean summer temperatures (including an extension in the thawing period for both Station Nunatak (50 d) and Station Coast (5 d) [3]) (Table 4) and less winter precipitation [1]–[4]. The years 1996 and 2003 (with positive net mass-balance) were, however, associated with an unusual high winter precipitation and mean summer temperatures. The ELA for Mittivakkat Gletscher has been ranging between 390 m a.s.l. to more than 930 m a.s.l. (1997/1998, 2000/2001, 2004/2005, 2006/2007, 2009/2010, and 2010/2011); with an average change from 500 m a.s.l. to 750 m a.s.l. (over the period 1996 through 2014) [4]–[6]. The average AAR is currently estimated to be 0.15 [5] [6] [12] (Table 4).

Together with a change in ELA and net mass-balance the Mittivakkat Gletscher mean glacier-wide surface albedo at the end of the mass-balance year (EBY) (27/28 July to 12/13 August) has changed [7] (Figure 7). Changes in the EBY mean glacier-wide albedo correlates significantly with changes in winter, summer, and net mass-balances (2000–2013) [7]. From 2000 through 2013 a significant change in EBY mean glacier-wide albedo occurred of -0.10 (from 0.43 to 0.33) for Mittivakkat indicating that the surface became less reflective (i.e. darker) (Table 4), where the greatest decline of 0.25 (from 0.46 to 0.21) occurred near the ELA (Figure 7). ELA is an important surface cover and albedo transitional zone [7]. Since albedo is defined as the reflected fraction of incoming solar shortwave radiation at the surface, a mean albedo drop of 0.10 indicates that more energy is absorbed and available for ablation, and subsequently for the surface mass-balance conditions, leading to accelerated net mass loss in the melt-albedo feedback. In general for Station MIT, the EBY observed bare ice albedo reached  $\sim 0.3$  just exceeding values observed for proglacial bedrock of  $\sim 0.2$  [7]. For all the three AWS Station Coast, Station Nunatak, and Station MIT, snow albedo time series indicate at the same time of year, for example, on April 1<sup>st</sup> or May 1<sup>st</sup> lower albedo values at the coastal station, than on the glacier and the nunatak, due to warmer temperature conditions at the coast, than on the glacier [3]. For the three AWS snow albedo generally changed with increasing air temperatures, most pronounced at the coastal station of -0.5 per 1°C of warming (1997–2007) and less on Mittivakkat (2009–2012) and on the nunatak of -0.3 per 1°C of warming (1995–2007) (Table 4). This was due to e.g., variations in the saturated state of the snowpack, meltwater ponding, and snow grain crystal metamorphism. For comparison a decrease in albedo has also been observed for the whole GrIS. Stroeve (2001) observed an overall downward trend in GrIS albedo (insignificant) in agreement with trends in melt and precipitation. Box et al. (2012) and Tedesco et al. (2013) showed that the mean GrIS-wide albedo (June–August) changed -0.07, from 0.75 in 2000 to 0.68 in 2012 [7] – for 2014, however, the mean GrIS-wide albedo was 0.70 (Tedesco et al. 2014). It is expected that GIC peripheral to the ice sheet would on average show greater albedo decline than the

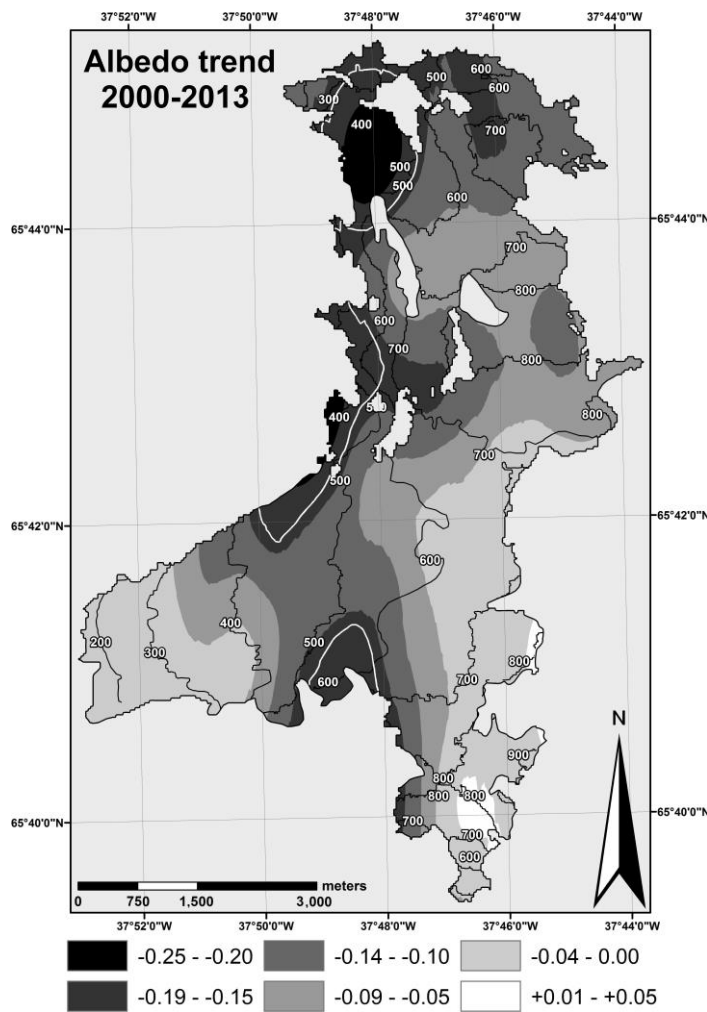


**Figure 7:** Mean MODIS-derived interpolated spatial end of mass-balance year albedo trend for MG for 2000 through 2013, including 100-m contour elevation intervals. The white bold lines indicate the margin for significant trends in albedo, where values below are significant [7]. The figure is modified from [7].

entire GrIS due to greater warming resulting from ocean warming and newly exposed, darker surrounding surfaces [7].

Not only have net mass-balance changes been estimated for Mittivakkat Gletscher, but also changes in the glacier terminus and surface area have been elucidated. Due to variations in topography (shadow effects from surrounding mountains), climate, and dynamic processes within the glacier, the terminus has changed by on average  $-15 \text{ m yr}^{-1}$  (1900–2010) since its historic maximum extent during the Little Ice Age (Figure 8) (Table 4) [4]. For comparison, for East Greenland north of Ammassalik region ( $68\text{--}72^\circ\text{N}$ ), land-terminating GIC peripheral to the GrIS changed on average by  $-10 \text{ m yr}^{-1}$  (2002–2009) for a wide range of GIC sizes (Kargel et al. 2012), and, for example, for West Greenland for Disko Island on average  $-8 \text{ m yr}^{-1}$  for non-surging GIC and  $-20 \text{ m yr}^{-1}$  for quiescent phase surge-type GIC (Yde and Knudsen 2007).

Regarding changes in glacier surface area, the Mittivakkat Gletscher area was estimated for the years 1986 ( $31.6 \text{ km}^2$ ), 1999 (29.6), and 2011 (26.2) emphasizing an area change of  $-17 \%$  [11] (Table 4). The Mittivakkat Gletscher area recession is in line but

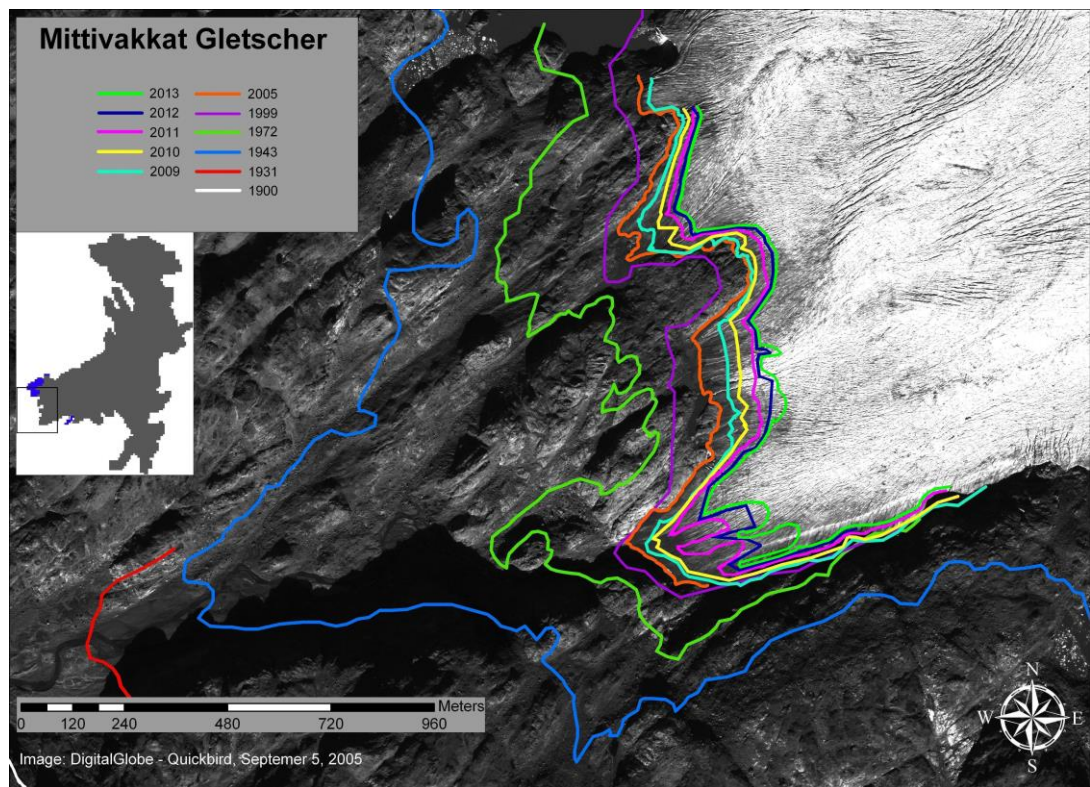


**Figure 8:** The location of the Mittivakkat Gletscher margin delineated as thick lines for 1900, 1931, 1943, 1972, 1999, 2005, 2009–2013. The 1900 LIA trimline (white line) was estimated from field observations (Hasholt et al. 2008b; Humlum and Christiansen 2008) and is partly shown in the lower left corner of the satellite image. The Mittivakkat Gletscher outline is shown on the left with a black square indicating the photographic area. Background photo: DigitalGlobe, Quickbird, 2005. The satellite image is modified from [4].

slightly lower than the area recession for 35 peripheral GIC from the Ammassalik area, where a mean recession of  $-27 \pm 24$  % occurred between 1986 and 2011 [11]. For the Ammassalik area, there are examples of five glaciers that completely melted away, and three glaciers (all facing west) that had a net area increase from 1986 to 2011 [11]. Similar observations of widespread retreat of peripheral GIC in Southeast Greenland over the past few decades has been presented by Bjørk et al. (2012), but also that many land-terminating GIC underwent a more rapid retreat during the early twentieth century warm period, than in the 2000s. For land-terminating GIC around the Arctic, mean net area retreat occurred with examples of -22 % (1958/1960–2006/2008) for Yukon Territory (Berrand and Sharp 2010), -11 % (1985–2005) British Columbia (Bolch et al. 2010), -55 % (1958–2005) Interior northern Baffin Island (Anderson et al. 2008), -13 % (1920–2000) Southeast Baffin Island (Paul and Svoboda 2009), -23 % (1930–2013) and -12 % (1965–2010) Jotunheimen and Breheimen Regions, Southern Norway (Andreassen et al. 2008), -13 % for the ten largest glaciers in Norway (1900s–1999/2006) (Andreassen et al. 2012), -22 % (1953/1960–2000) Northern Polar Urals (Shahgedanove et al. 2012), -19 % (1945–2002/2003) Suntar Khayata Region in North Asia (Ananicheva et al. 2006), and -67 % (1950s–2003) Koryak Upland near Kamchatka Peninsula (Ananichava and Kapustin 2010).

Further, for the Ammassalik area a net area recession was observed for the GrIS land-terminating and marine-terminating parts, where the land-terminating GrIS (and GIC) reflects lower marginal and area changes than the marine-terminating GrIS outlet glaciers [11]. The differences in marginal and area changes between GrIS marine and land-terminating glaciers could be caused by marine-terminating outlet glaciers having been influenced by changes in the force balance due to thinning, reduced resistive force, and speed-up as a combination of increasing mean air temperature and ocean temperatures, where the land-terminating parts were only influenced by atmospheric conditions [11]. In [11] it is shown, that marine-terminating frontal recession rates and decreasing area exposure rates are synchronous with both increasing MAAT (from Tasiilaq) and reconstructed annual ocean water temperature at 400 m depth in the Irminger Sea, penetrating into the Sermilik Fjord and exposing the lower part of glaciers such as Helheim and Fenris to warm waters with temperatures up to 4°C (Johannessen et al. 2011). Also, frontal retreats have been seen elsewhere in Greenland from e.g., 210 marine-terminating glaciers (all having a front wider than 1 km), where 90 % of the glaciers retreated between 2000–2010 (Howat and Eddy 2011), and area exposure retreat from 39 of the widest marine-terminating glaciers, where the cumulative area loss was ~1,370 km<sup>2</sup> between 2000–2010 (Box and Decker 2011).

Figure 6 shows the Mittivakkat Gletscher cumulative net mass-balance from 1995/1996 to 2013/2014, where the total change is estimated to be -19 m w.e. Based on the Mittivakkat Gletscher 1994 estimated radar volume, the mean ice thickness was estimated to be 115 m (Knudsen and Hasholt 1999). Based on the cumulative net mass-balances the mean Mittivakkat Gletscher ice thickness was estimated to be  $97 \pm 15$  m in 2011 (where the uncertainties are assumed equal to the mass-balance method uncertainty of  $\pm 15$  %), identical to a mean ice thickness change of -15 % [5] (Table 4). In 2014 the mean ice thickness was estimated to be  $93 \pm 14$  m, identical to a mean ice thickness change of -19 %. This 2014-mean ice thickness value was independently confirmed in Yde et al. (2014), where the Mittivakkat Gletscher mean ice thickness based on ground penetrating radar observations in 2012 was estimated to be 90 m. On individual stake level the vertical strain ([5]; Equations 1–3) was able to compensate for ~60 % of the surface elevation change due to SMB in the lower part of Mittivakkat Gletscher, and ~25 % in the upper part [5]. If the glacier was in equilibrium with the present day climate, the vertical strain would be equal, and of opposite sign, to SMB. The large discrepancy in the magnitudes of the two processes is an indicator of the disequilibrium of the Mittivakkat Gletscher [5].

Based on the establishment of the point glacier stake mass-balance program on Mittivakkat Gletscher, the stakes were also used to calculate the spatial mean surface velocity field (since 1996). A maximum mean surface velocity was observed where the ice was thickest (similar trends in ice velocity were observed in e.g., Sugiyama et al. 2014), at a maximum of  $22 \text{ m s}^{-1}$  [5] (Table 4), and decreasing towards the margins due to thinner ice and drag from the valley walls, as expected. Because of the thinning in mean ice thickness, the annual mean Mittivakkat Gletscher ice surface velocity changed by -30 % (Table 4), which was fully explained by the dynamic effect of ice thinning (also confirmed using the shallow ice approximation), with uncertainty [5]. An alternative explanation for the reduction in annual mean surface velocity could be that changes in subglacial hydrology from increased surface melting over the study period have led to an earlier and more extensive development of channelized drainage and subsequent decrease in sliding each summer (e.g., Schoof 2010; Sundal et al. 2011). However, it appears that changes in melt only have a minor impact on the deceleration of the annual mean surface velocity [5]. Similar conclusions have been emphasized outside Greenland, at a long-term observed

glacier, Glacier d'Argentière, France, where 20 years of ice thickening and acceleration was followed by 30 years of thinning and deceleration [5].

The observed Mittivakkat Gletscher surface area change and the mean ice thickness changes were used to estimate changes in the glacier volume – a volume estimated to change by  $-1.1 \text{ km}^3$ , or  $-30 \%$  from 1986 through 2011 (Table 4). This indicates that Mittivakkat Gletscher changed in volume from  $3.7 \pm 0.5 \text{ km}^3$  (1986; the 1986 mean ice thickness was estimated by adding the cumulative mass balance during 1986–1994, based on modeled Mittivakkat Gletscher annual mass-balance data from Mernild et al. (2008a), to the 1994 mean ice thickness) to  $2.6 \pm 0.4 \text{ km}^3$  (2011) [5]. In Yde et al. (2014) the volume change was only estimated for the mass-balance observed part of Mittivakkat Gletscher (not from the entire glacier complex) and only from 1994 to 2012 ( $-0.58 \text{ km}^3$ ). Changes in glacier volume indicate that a portion of the freshwater runoff from the glacier will be explained by the net mass-balance loss, influencing the hydrological processes and budget in the catchment. It is confirmed [11] [17] that runoff on catchment scale are strongly influenced by the fraction of GIC cover and by the net mass-balance conditions. Also, previous studies in Greenland and in the circumpolar Arctic by e.g., Kane and Yang (2004) and Hasholt and Mernild (2008) have shown that glaciers have a dominant influence on the water balance in glaciated areas compared to non-glaciated areas, often producing surpluses of melting and runoff exceeding precipitation.

Due to the illustrated changes in surface air temperature from Tasiilaq and other coastal stations in Southeast Greenland [4], together with changes in glacier area for the Ammassalik region [11] and for Southeast Greenland (Bjørk et al. 2012), it is suggested that the Mittivakkat Gletscher volume trend is not merely a local phenomenon but is indicative of glacier change in a broader region [4] [5]. Since direct measurements of glacier volumes in Greenland, and elsewhere, are limited in number, volume change estimates based on scaling functions (e.g., Bahr 1997; Bahr et al. 1997, 2009; Grinsted 2013) or model simulations (e.g., Marzeion et al. 2012; Radić et al. 2014) have been conducted to estimate: 1) the water balance; and 2) broader scale crucial projections of the GIC mass-balance contribution to global sea-level change.

The observed net mass-balance and AAR conditions for Mittivakkat Gletscher (1996–2011) were used (see Section 2.4.5) to calculate the out of balance conditions, and the committed area and volume loss based on the AAR method [4] [6]. AAR varies greatly from one year to another, however, for a period long enough to filter out extremes but shorter than the timescale of adjustment to glacier equilibrium [4], it gives a measure of the health of the glacier (Cogley et al. 2011). Based on both direct net mass-balance and ELA observations and direct net mass-balance and satellite-derived ELA a range in the Mittivakkat Gletscher out of balance conditions was calculated. For Mittivakkat Gletscher to return to equilibrium it must thin, retreat, and lose additional mass (and subsequently change its hypsometry). At present the Mittivakkat Gletscher is significantly out of balance due to present day climate conditions. Mittivakkat is likely to lose around 50–70 % of its area and 60–80 % of its volume [4] [6] (Table 4), typically over several decades or longer if current climate conditions in the region persist. However, if using the  $\gamma$  value (3.14) (Equation 5c) estimated specifically for Mittivakkat Gletscher (a value outside the range of the Bahr 1997 and Bahr et al. (1997, 2009) estimated values) (Yde et al. 2014), Mittivakkat is likely to lose  $>90 \%$  of its volume to return to equilibrium. So far, Mittivakkat Gletscher is the only mountain glacier in Greenland for which the out of balance conditions have been estimated, and therefore are of valuable information regarding future expected changes in area and volume. For comparison similar calculations were conducted for a specific glacier in Alaska, Lemon Creek Glacier [6], and also for all mass-balance and AAR observed GIC on Earth ( $n = 144$ ) [12]. On average,

mass-balance and AAR observed GIC within all of Earth's 16 GIC regions were on a regional scale out of balance [12], taking uncertainties regarding undersampling problems such as sparse observations and geographically biased GIC into account. On a global scale GIC are on average committed to an additional loss of  $32 \pm 12$  % of their area and  $38 \pm 16$  % of their volume to be in equilibrium with the present day climate. These losses will in the future, on local to regional scales, have an impact on the hydrological processes and the water balance, and subsequently on global sea-level rise [12]. Based on the global observed GIC data set, the projected GIC loss implies a global mean sea-level rise of  $163 \pm 69$  mm SLE [12] (see more in Section 3.2).

The output based on the different observational programs and calculations on and around the Mittivakkat Gletscher analyzed in [1]–[7] generally illustrates for the last decades or more: 1) increasing surface air temperature (both MAAT and mean summer temperature); 2) decreasing precipitation (both annually and for the winter season); 3) negative Mittivakkat net mass-balance and a net mass-balance trend towards more negative values; 4) higher elevated location of ELA and a low AAR; 5) drop in mean glacier-wide albedo; 6) glacier terminus retreat; 7) glacier surface area recession; 8) lower mean ice thickness; 9) surface velocity slow down; 10) decreasing glacier volume; and 11) a Mittivakkat Gletscher out of balance with present day climate conditions (Table 4). Such information is important and unique for our understanding of climate change and the climate impact on the Mittivakkat Gletscher (and glaciers in the surrounding area) and subsequently on the hydrological processes and the water balance. The observations indicate that Mittivakkat Gletscher has been retreating over recent decades, and is committed to additional area and volume loss in the future, typically over several decades or longer (if current climate conditions in the region persist), to return to equilibrium.

Also, such observations are useful from a modeling perspective for the verification of developed model processes and simulations. In the following section model results from different kinds of SnowModel code developments and simulations on Mittivakkat Gletscher and the surrounding area will be highlighted. Overall, to provide us with an understanding of the present-day hydrological conditions and the water balance [8]–[10], there is a clear need to explore issues associated with data sparseness and modeling capabilities.

### 3.1.3 Mittivakkat Gletscher SMB, temperature inversion, and runoff routing modeling

Several SnowModel code developments and simulations were conducted for the entire Mittivakkat Gletscher to elucidate the snow accumulation processes, snow and ice ablation processes, and SMB conditions (Equation 1) [8]. Also, the influence from air temperature inversion on the glacier surface [9], the runoff routing conditions from Mittivakkat Gletscher and the non-glaciated landscapes to the coastline were simulated [10].

For the Mittivakkat Gletscher the surface mass balance conditions were simulated (Equation 1), including the winter processes related to the spatial distribution and evolution of snow accumulation, snow-blowing sublimation, evaporation, snow and ice surface melt, surface runoff, and SMB changes on the Mittivakkat Gletscher for 1998–2006 forced with AWS data from Stations Nunatak and Coast (Figure 3). Observed Mittivakkat winter mass-balance data were used for model calibration and validation (Mernild et al. 2006b), since gauging stations underestimate the true amount of solid



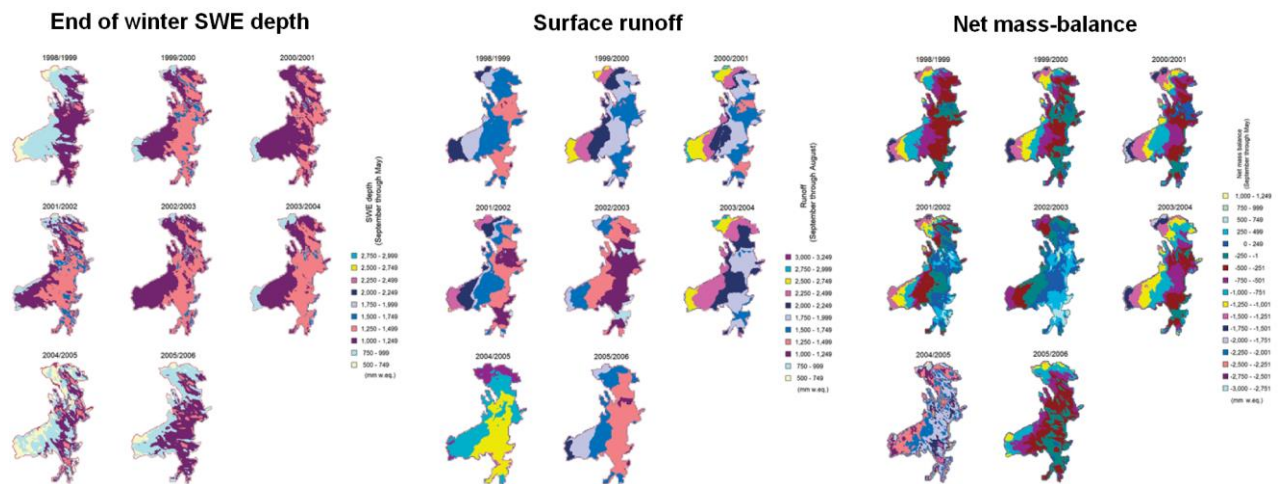


**Figure 9:** Spatial distribution of end of winter SWE depth (May 31), surface runoff, and net mass-balance for the entire Mittivakkat Gletscher following the hydrological period from September 1 to August 31. The SnowModel simulations cover the years from 1998/1999 through 2005/2006 [8].

precipitation due to wind-induced undercatch, wetting losses, and trace amounts (Yang et al. 1998, 1999; Rasmussen et al. 2012; [2] [8]). For the Mittivakkat Gletscher the spatial modeled end-of-winter snow accumulation increased with increasing elevation (similar to observations [5]) up to 700–800 m a.s.l. in response to changes in elevation, topography, and in the dominating wind direction. Maximum snow deposition occurred on the lee side of the ridge east and south of the glacier [8], regarding the snow-blowing processes simulated in SnowModel’s submodel SnowTran-3D. The end-of-summer cumulative surface runoff decreased with increasing elevation (similar trend occurred for the total ablation [5]), where the minimum sum of runoff was simulated on the shadowed side of the ridges. The average Mittivakkat Gletscher simulated net mass-balance was  $-900 \pm 470$  mm w.e.  $\text{yr}^{-1}$  for the entire glacier (1998–2006) (Table 4) [8]. For the mass-balance observed area of Mittivakkat the observed net mass-balance was  $-770 \pm 670$  mm w.e.  $\text{yr}^{-1}$ , and  $-780 \pm 500$  mm w.e.  $\text{yr}^{-1}$  based on simulations [8]. In Figure 9, the spatial distribution of end-of-winter SWE depth, surface runoff, and net mass-balance are shown. The simulated Mittivakkat Gletscher water balance components were for precipitation:  $1,490 \pm 150$  mm w.e.  $\text{yr}^{-1}$ , evaporation and sublimation:  $-250 \pm 30$  mm w.e.  $\text{yr}^{-1}$ , and surface runoff:  $-2,140 \pm 410$  mm w.e.  $\text{yr}^{-1}$  (1998–2006) [8] (Table 4). For nearby Mittivakkat Gletscher catchments without glacier cover, runoff was estimated to be in the range of 1,200–1,400 mm w.e.  $\text{yr}^{-1}$  (Hasholt and Mernild 2008), following the spatial and temporal variability in precipitation. The simulations surely indicate that the Mittivakkat Gletscher has a dominant influence on the water balance compared to neighboring non-glaciated catchments, where  $\sim 40$  % of the runoff is estimated to come from Mittivakkat net mass loss (Table 4).

As briefly stated in Section 3.1 the Mittivakkat Gletscher region is highly influenced by air temperature inversion due to the effect of sea breezes. This is a result of the thermal differences between land and ocean (Hosler 1961; Milionis and Davies 2008), because of the adjacent relatively low temperature and frequently ice-choked Sermilik Fjord. Most climate models do not include routines for simulating the impact on snow and on net mass-balances from air temperature inversion, even though air temperature inversion is a common thing all over the coastal Arctic [9] (including, for example, for

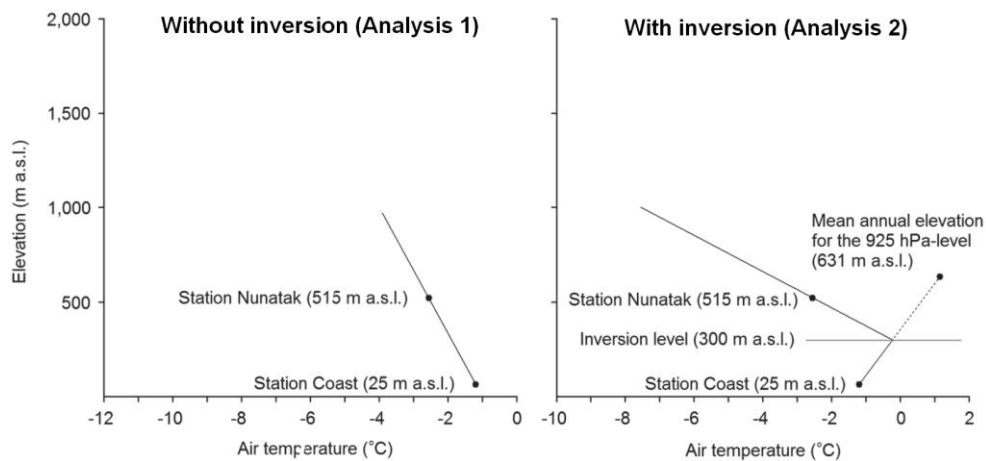


**Figure 10:** A schematic illustration of the air temperature lapse rates used in SnowModel for simulations without routines for air temperature inversion (Analysis 1) and with inversion (Analysis 2) [8]. For simulations with inversion the inversion level was set at 300 m a.s.l. according to observations. In general for the inversion simulations air temperature increased with height up to the inversion level, and above the temperature decreased. The temperatures at the 925 hPa-level were measured from the Station Tasilaq radiosonde observations.

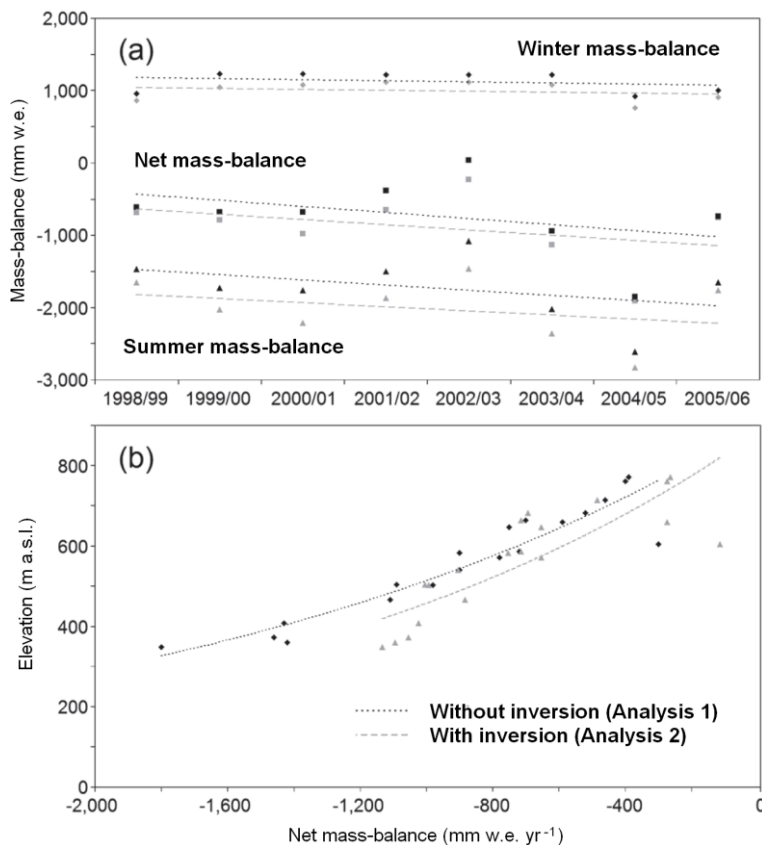


**Figure 11:** (a) SnowModel simulated mean winter, summer, and net mass-balances for the glaciers ( $n = 19$ ) in the domain from 1988/1999 through 2005/2006 both without routines for air temperature inversion (Analysis 1) and with inversion (Analysis 2); and (b) average simulated glacier net mass-balance plotted against the average glacier elevation both without routines for air temperature inversion and with inversion routines. The figure is modified from [9].



Zackenberg (Hansen et al. 2008)). Inversion is likely to have a serious impediment on hydrological research efforts. Model routines taking into account air temperature inversion layer were developed and implemented in SnowModel [9] to improve and realistically describe temperature conditions and to understand the impacts from air temperature inversion on snow accumulation, ablation, and glacier net mass-balance (Figure 10). For the Mittivakkat area the inversion was observed and modeled to occur during 84 % of the simulation period. This inversion frequency (84 %) is almost similar with the inversion frequency of 85–99 % found for Alaskan and Canadian Arctic Stations (e.g., Kahl 1990; Kahl et al. 1992; Kadygrov et al. 1999). Modeled air temperature inversions were determined not to occur during days with strong winds ( $> 8 \text{ m s}^{-1}$ ) and/or high precipitation rates ( $> 10 \text{ mm w.e. d}^{-1}$ ) because of the potential for inversion breakup [9]. To emphasize the influence of air temperature inversion, two simulations were performed: one without accounting for temperature inversion (named: Analyze 1) and one assuming that temperature inversions occur from sea-level to 300 m a.s.l. and are present 84 % of the time during the simulation period (named: Analyze 2). To illustrate the impact from the SnowModel developed air temperature inversion routines, snow accumulation and snow and ice ablation from the Mittivakkat Gletscher and numerous small coastal marginal glaciers ( $n = 19$ ) on the southwestern part of Ammassalik Island were simulated

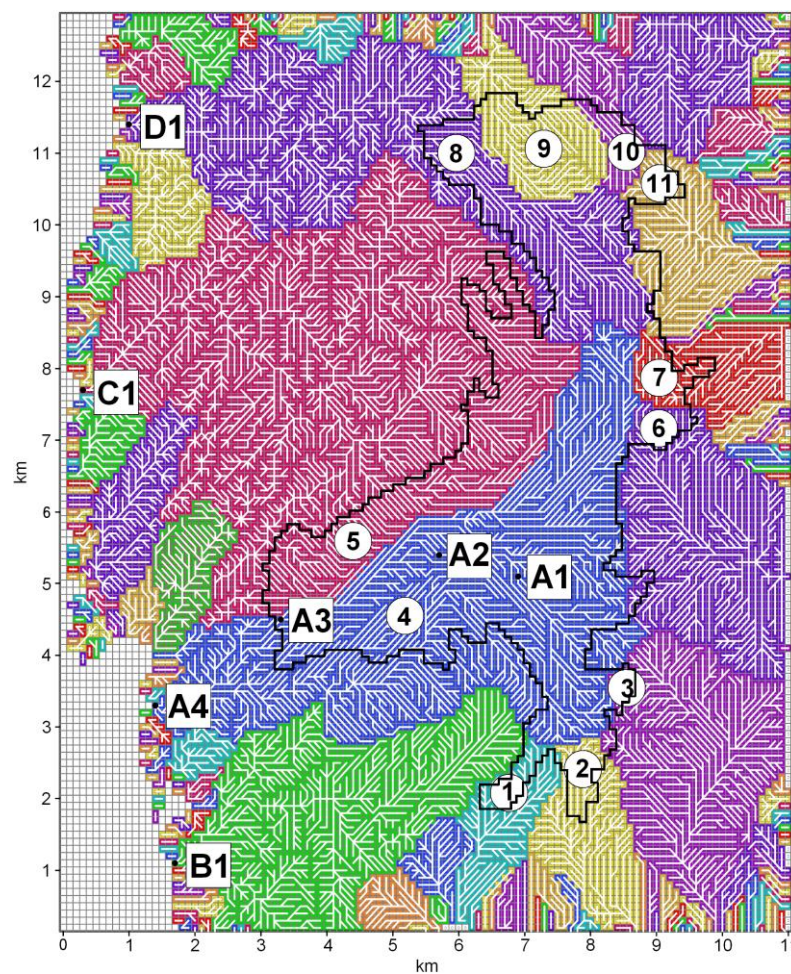


**Figure 12:** Mittivakkat Gletscher complex (represented by the bold line) and HydroFlow simulated individual glacier basins (Area 1 to 11) (represented by different colors), stream/river flow network (represented by white lines), and locations B1, A4, C1, and D1 for simulated catchment outlet hydrographs, and A3, A2, and A1 for catchment upstream locations [10].

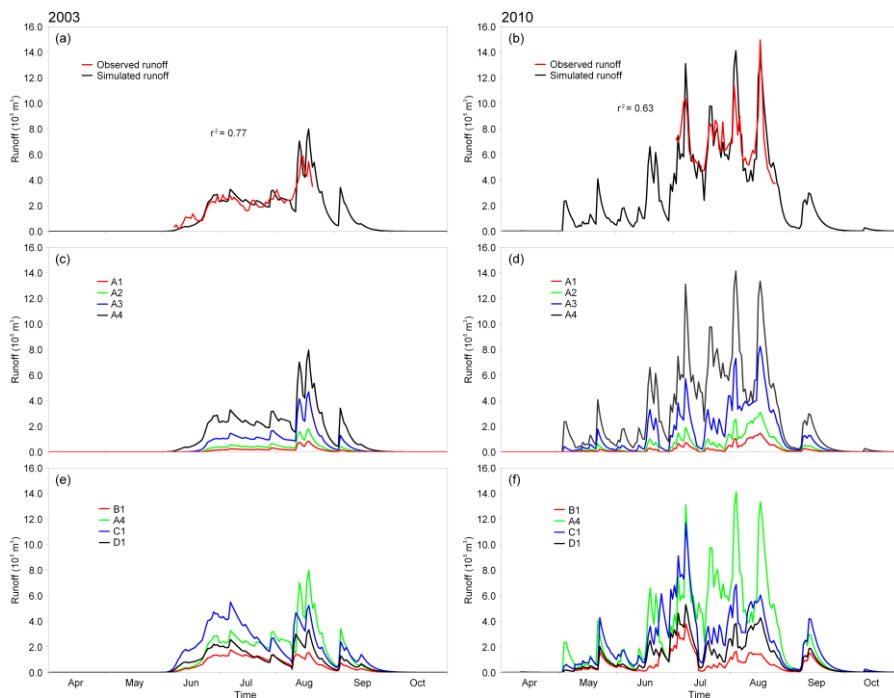


**Figure 13:** (a) Simulated (black line) and observed runoff (red line) at location A4 for 2003 (the year with the second lowest cumulative runoff) and (b) 2010 (the year with the highest cumulative runoff); (c) and (d) simulated hydrographs at different locations upstream for outlet A4; and (e) and (f) simulated hydrographs at outlets B1, A4, C1, and D1 to the Sermilik Fjord (for outlet locations see Figure 12) [10].

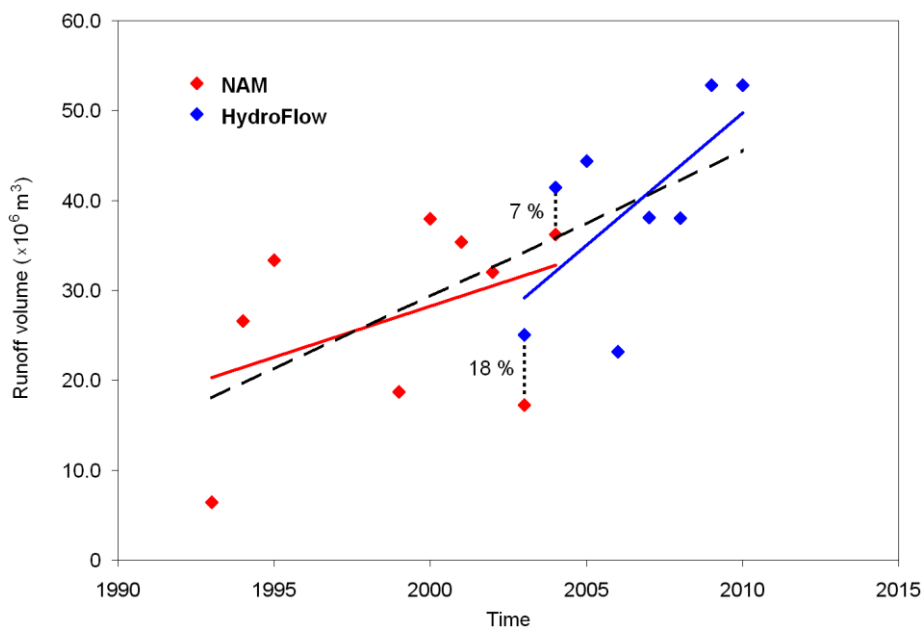


**Figure 14:** Mittivakkat Gletscher catchment simulated runoff 1993–2010. From 1993–2004 runoff was simulated based on the NAM model (Mernild and Hasholt 2006), and 2003–2010 based on HydroFlow [10]. Trend lines are shown for each model-estimated runoff, and for the entire period (black dashed line). Also, for 2003 and 2004, the years where runoff has been simulated based on each individual model, the runoff difference is added to the figure: in 2003 the difference was 18 % and in 2004 it was 7 %.

(1998/1999–2005/2006). The inversion model produced air temperature distributions with warmer lower-elevation areas and cooler higher-elevation areas than without inversion routines because of the use of cold sea-breeze-based temperature data from underneath the inversion (in Figure 10, a schematic illustration of Analyze 1 and 2 distributed air temperature is illustrated). By ignoring routines for air temperature inversion it could create errors of up to two weeks for snowmelt in the lower areas and up to one–three weeks for snowmelt in the higher-elevated areas of the simulation domain, and an average glacier net mass loss difference of ~20 % [10] (a ~20 % less negative net mass-balance by including inversion routines) (Figure 11) (Table 4), influencing the water balance. Such model air temperature inversion simulations in Greenland are the first of their kind, and for a realistic description of the temperature distributions in coastal landscapes, such routines are essential for snow and ice melt and net mass-balance simulations.

SnowModel has been able to simulate fluctuations and trends in Mittivakkat Gletscher surface mass-balance components, both with and without the influence from air temperature inversion in a comprehensive way [8] [9]. Also, based on HydroFlow, the linkages between runoff production from land-based snowmelt and icemelt processes and the associated freshwater flux to downstream areas and surrounding fjords and oceans were estimated [10]. Further, to do so, HydroFlow estimated the watershed divides, catchment areas, and flow networks, and SnowModel/SnowPack-ML estimated snowpack evolution, distribution, and water flow residence time from changes in snow- and ice-covered fractions for glaciers and glacier-free areas within the domain. HydroFlow divided, for example, the Mittivakkat Gletscher into 11 individual drainage basins, emphasizing that around 80 % of the glacier area drained into the Sermilik Fjord (Figure 12), and also that a watershed divide separated the main glacier part into two basins (basin #4 and #5) (Figure 12). Based on tracer observations, glacier subsurface (englacial and subglacial) water flow between neighboring glacier basins (basins #4 and #5) occurred due to englacial fractures such as crevasses and moulins (Mernild 2006, Mernild et al. 2006a). This is expected, however, to only have a minor influence on the outlet hydrograph [19]. Overall based on the runoff simulations, it is clear, that runoff from the different catchments was clearly influenced by the fraction of glacier cover, and glacier cover at low elevations. It also shows that daily simulated runoff variations and peaks compared reasonably well with observed runoff time series ( $r^2$ -values of 0.77 and 0.63) [10] (Figure 13). In the 8-year time period (2003–2010), the mean annual glacier runoff period was  $200 \pm 20$  d, and increased (significantly) by approximately 30 d (Table 4). The number of days with runoff greater than average increased by 15 d from 70 d (2003) to 85 d (2010), indicating in general more days with greater discharge to the Sermilik Fjord [10]. All together the mean annual runoff volume increased by  $54.9 \times 10^6 \text{ m}^3$  for the Mittivakkat Gletscher region (2003–2010) (Figure 13), and from the outlet of the Mittivakkat Gletscher basin #4 (Figure 12) by  $2.9 \times 10^6 \text{ m}^3 \text{ yr}^{-2}$  (2003–2010) (Table 4). Also, from basin #4 the simulations indicate that the Mittivakkat Gletscher has a dominant influence on the water balance, where ~ 35 % of the simulated runoff came from net mass-balance loss. When combining Mittivakkat Gletscher catchment HydroFlow simulated runoff (2003–2010) with earlier NAM simulated runoff (1993–2004) (Mernild and Hasholt 2006), an increasing runoff trend occurred (Figure 14). It is notable, for the years 2003 and 2004, where simulated runoff values occur from both model systems, that runoff simulated in HydroFlow was respectively ~20 % ( $7.8 \times 10^6 \text{ m}^3$ ) and ~7 % ( $5.2 \times 10^6 \text{ m}^3$ ) higher compared to NAM simulated runoff (this could e.g., be due to the use of the positive degree-day approach in NAM) (Figure 14). Overall for the period 1993–2010 the combined model estimated annual runoff was on average  $33.3 \pm 12.6 \times 10^6 \text{ m}^3 \text{ yr}^{-1}$ , increasing annually by  $\sim 1.7 \times 10^6 \text{ m}^3 \text{ yr}^{-2}$  (Table 4).

Based on the already known observed Mittivakkat Gletscher conditions, simulations were conducted to describe in detail the spatiotemporal accumulation (snow accumulation) and ablation processes (evaporation, sublimation, and runoff), but also to emphasize the temporal distribution in freshwater runoff, since observed runoff only span parts of the runoff season, and that the glacier has a dominant influence on the water balance compared to neighboring non-glaciated catchments, where e.g., ~35–40 % of the Mittivakkat Glacier simulated runoff came from net glacier loss.

To highlight if the overall trends in observed and simulated net mass-balance conditions for Mittivakkat Gletscher – leaned towards a more negative net mass-balance – and out of balance conditions are site-specific issues, external glacier net mass-balance and out of balance conditions from the northern North Atlantic region [13], the Northern Hemisphere [14], and globally [12] were estimated based on both observations and model simulations and used for comparison.

### **3.2 GIC in a northern North Atlantic, Northern Hemispheric, and global perspectives**

GIC net mass-balance conditions and trends might be forced both with surface weather conditions and large-scale atmospheric and oceanic circulations [13]. On a regional scale for the northern North Atlantic region (based on net mass-balance mountain GIC observations from Southeast Greenland (from Mittivakkat Gletscher), Iceland, Scandinavia, and Svalbard,  $n = 29$ ) [13], Northern Hemispheric scale (based on net mass-balance simulations of every individual GIC) [14], and global scale (based on all GIC with both net mass-balance and AAR observations,  $n = 144$ ) [12], time series of GIC net mass-balance observations have been analyzed. These three studies are emphasizing e.g., on average increasing net mass loss over recent decades (since the early 1970s), and that the net mass-balance was most negative on average during the first decade of the twenty-first century.

To emphasize on a regional scale the influence from surface weather conditions and large-scale atmospheric and oceanic conditions, the northern North Atlantic region variations in observed GIC net mass-balance were significantly correlated with NASA's Goddard Institute for Space Studies (GISS) regional near-surface air temperatures (Hansen et al. 2010; Erlykin et al. 2012) and the Atlantic Multidecadal Oscillation (AMO) time series (updated from Kaplan et al. 1998), individually [13]. AMO is an expression of fluctuating mean sea-surface temperatures in the North Atlantic region. For example, according to Chylek et al. (2009), Arctic surface air temperatures (on land) are highly correlated with the AMO, which are physically linked to GIC summer balance conditions and subsequent net mass-balance conditions [13]. A positive AMO index indicates relatively high surface air temperature and less precipitation at high latitudes (subsequent relatively high net mass-balance loss), and a negative AMO index indicates relatively low surface air temperature and a higher precipitation (subsequent relatively low net mass-balance loss) (Mernild et al. 2012) [13]. As an example, it could be noted for the AMO index that high GIC mass-balance loss occurs during periods when the North Atlantic and Northwest Europe are characterized by positive temperature anomalies (e.g., Trenberth et al. 2007; Hansen et al. 2010). Sub-dividing the northern North Atlantic region into individual GIC net mass-balance time series (for 2000–2009, a period where data are well represented) for Southeast Greenland, Iceland, Scandinavia, and Svalbard, the subdivision indicates spatial variability in mean GIC net mass-balance from ~-860 mm w.e. yr<sup>-1</sup> for Southeast Greenland and Iceland to ~-380 mm w.e. yr<sup>-1</sup> for Scandinavia and Svalbard

[13]. On average more than two times less net mass-balance loss occurred for GIC in Scandinavia and Svalbard than for GIC in Iceland and Southeast Greenland. For both Iceland and Scandinavia, variations in the North Atlantic Oscillation (NAO) (Hurrell and van Loon 1997) are significant for net mass-balance variations [13], where NAO is an atmospheric circulation indices, and therefore a good measure of airflow and jet-stream variability (e.g., Overland et al. 2012) of moisture transport from the North Atlantic onto Northwest Europe (Dickson et al. 2000; Rogers et al. 2001) [13]. For Iceland and Scandinavia the difference in net mass-balance between relatively dry winters (Iceland conditions) and wet winters (Scandinavia conditions) is an issue. In relatively dry winters, the diminished end-of-winter snow accumulation melts relatively fast during the spring warming, and will promote ablation of the underlying ice; the ice surface albedo facilitates a stronger radiation driven mass loss due to the lower albedo for ice than for snow (Stroeve et al. 2005). Conversely, for relatively wet winters the enhanced end-of-winter snow accumulation, especially when coupled with frequent summer precipitation snow events, keeps the albedo high [17]. In wet/snowy years, it therefore generally takes longer to melt the snowpack than in less wet/snowy years, thus delaying the start of ablation of the underlying ice. Also, the greater than normal liquid precipitation fraction during warm years tends to increase snowpack ablation since heat is introduced by rain and by lowering the surface albedo [7] [13]. Even though differences occur in GIC net mass-balance values between Southeast Greenland and Iceland on the one hand and Scandinavia and Svalbard on the other hand, the individual sub-regional net mass-balance trends on average indicate increasing mass loss since 1970, and onward [13].

For the Northern Hemisphere based on – the highest achievable spatial (1-km horizontal grid) and temporal resolutions (3-h time step) – mountain GIC surface mass-balance conditions (including precipitation, sublimation, evaporation, SMB, and surface runoff) and changes were simulated for each individual GIC. In Figure 15, the GIC surface mass-balance conditions and changes are plotted against latitude and elevation illustrating variability in both space and time for GIC north of 25°N. On a regional scale – for all 15 individual GIC regions on the Northern Hemisphere (defined by Radić and Hock 2010; Pfeffer et al. 2014) (Figure 16) –, the GIC faced mean negative cumulative GIC net mass-balance (1979–2009) [14], for a period where the GIC MAAT, mean summer air temperature, and runoff increased [14, Table 2]. From a water balance perspective, regional variabilities occurred in GIC SMB, where the overall trends for all 15 regions, for example, showed a mean GIC SMB of  $-0.19 \pm 0.03$  m w.e. yr<sup>-1</sup> for the first decade (1979–1989) and  $-0.57 \pm 0.11$  m w.e. yr<sup>-1</sup> for the last decade (1999–2009), and a mean runoff of  $1.73 \pm 0.04$  m w.e. yr<sup>-1</sup> and  $2.06 \pm 0.07$  m w.e. yr<sup>-1</sup>, respectively [14]. For Greenland specifically, the mean GIC SMB was  $-0.14 \pm 0.13$  m w.e. yr<sup>-1</sup> (1979–1989) and  $-0.39 \pm 0.05$  m w.e. yr<sup>-1</sup> (1999–2009), and the mean runoff was  $0.45 \pm 0.12$  m w.e. yr<sup>-1</sup> and  $0.80 \pm 0.03$  m w.e. yr<sup>-1</sup>, respectively [14]. For Greenland this indicates, that ~30 % of the simulated runoff came from net GIC mass-balance loss (1979–1989), and ~50 % (1999–2009); for the Northern Hemisphere the values were ~10 % and ~30 %, respectively. From a sea-level rise perspective, the GIC SMB contribution was on average largest from Alaska (equal to 23 % of the total GIC Northern Hemispheric contribution) and Greenland (12 %) (1979–2009), and for the last decade (1999–2009) for Alaska (19 %), Arctic Canada North (Ellesmere Island) (14 %), and Greenland (13 %). For both periods the SMB contribution to sea-level rise was smallest for Caucasus (<1 %) [14]. The overall GIC SMB contribution to sea-level rise was  $0.51 \pm 0.16$  mm SLE yr<sup>-1</sup> for 1979–2009 and ~40 % higher  $0.71 \pm 0.15$  mm SLE yr<sup>-1</sup> for 1999–2009 for Northern Hemispheric GIC. For Greenland specifically the GIC SMB values were  $0.06 \pm 0.02$  mm SLE yr<sup>-1</sup> and 56 % higher  $0.09 \pm 0.01$  mm SLE yr<sup>-1</sup> (not taking calving from GIC into account), respectively



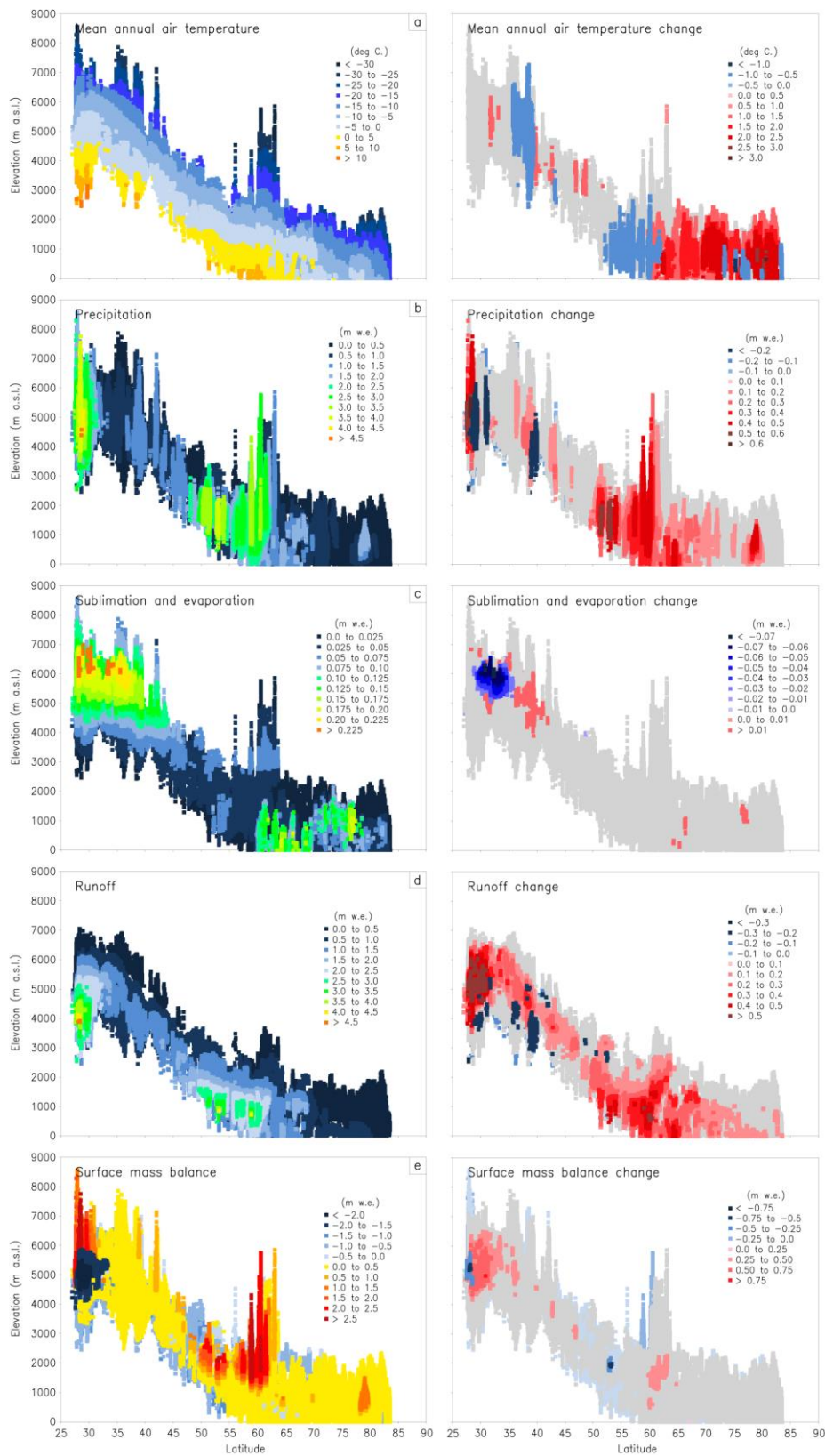


**Figure 15:** Latitude versus elevation for mean (1979–2009) and changes (1979–89 minus 1999–2009): (a) MAAT, (b) precipitation, (c) sublimation and evaporation, (d) runoff, and (e) SMB for all individual GIC covered grid cells ( $n = 543,389$ ). Insignificant changes (in the right column) are highlighted in gray color [14].

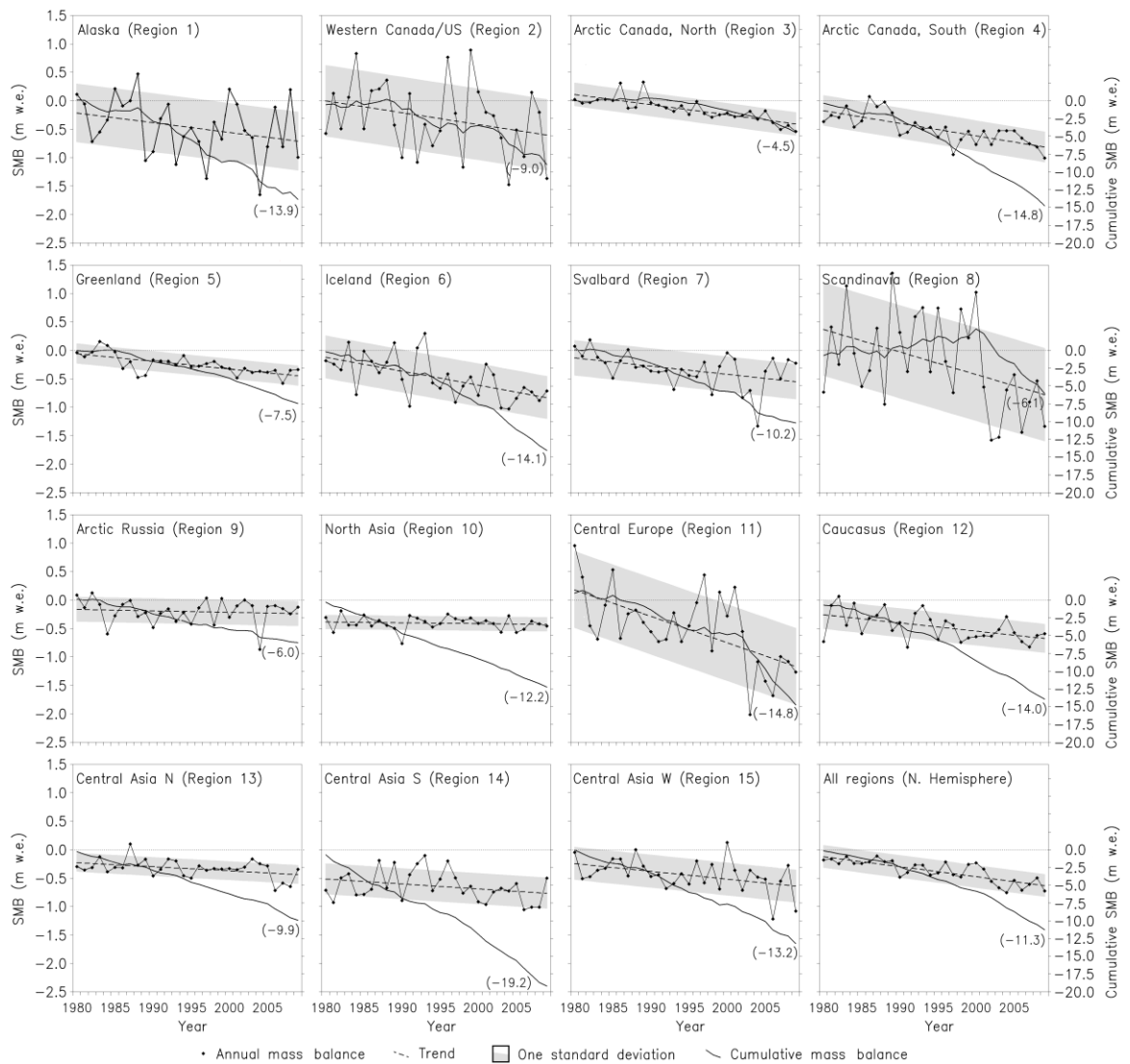


**Figure 16:** Regional breakdown of GIC SMB and cumulative SMB time series for 1979–2009, including linear regression, for the 15 glacier regions north of 25°N [14].

[14]. A value in the range of the estimated mass change of  $0.08 \pm 0.03$  mm SLE  $\text{yr}^{-1}$  (October 2003 through March 2008) from Bolch et al. (2013). In other studies, Marzeion et al. (2012) estimated for 1902–2009 the global GIC mass loss sum to be  $114 \pm 5$  mm SLE, equal to an annual average of 1.06 mm SLE; Kaser et al. (2006) found  $0.77 \pm 0.26$  mm SLE (1991–2004), Gardner et al. (2013) calculated  $0.71 \pm 0.08$  mm SLE (2003–2009), and Hock et al. (2009) estimated  $0.50 \pm 0.18$  mm SLE (1961–2004). Also, several analyses (Dyurgerov and Meier 2005; Kaser et al. 2006; Meier et al. 2007; Cogley 2009a, 2012) based on direct and geodetic measurements suggest that GIC net mass-balance loss is currently raising global mean sea level by about 1 mm SLE  $\text{yr}^{-1}$  [12], which is around one-third of the total rate of altimetry-based sea-level rise of  $3.3 \pm 0.4$  mm SLE  $\text{yr}^{-1}$  (1993–2007) (Cazenave and Llovel 2010) (in Hanna et al. (2013b) the total rate was however estimated to  $3.11 \pm 0.56$  mm SLE  $\text{yr}^{-1}$  (1992/1993–2008/2011) and in Church et al. (2013) to  $\sim 3.2$  mm SLE  $\text{yr}^{-1}$  (1993–2000)). The calculated GIC mass balance contribution to sea-level rise clearly varies depending on the used method. The

SnowModel simulations only calculate SMB net loss from Northern Hemisphere GIC (from 75 % of the global GIC area; Radić et al. 2014). Therefore, global GIC SMB contribution to sea-level rise would likely be higher than the mean annual SnowModel estimated of  $0.71 \pm 0.15$  mm SLE (1999–2009) when adding SMB contributions for the Southern Hemisphere GIC, loss rates from calving GIC and ice sheets, loss rates from subglacial geothermal melting and subglacial frictional melting due to basal ice motion [14], and from ocean thermal expansion (Church et al. 2013).

Due to present day GIC net mass-balance and AAR observations (2001–2010) the out of balance conditions were estimated ( $n = 144$ ). The calculations indicate that GIC are committed to additional losses of  $32 \pm 12$  % of their area and  $38 \pm 16$  % of their volume if the future climate resembles the climate of the past [12]. These losses will have an impact on the water balance, and imply a GIC global mean sea-level rise of  $163 \pm 69$  mm SLE (assuming a total GIC volume of 430 mm SLE; Huss and Farinotti 2012) (other studies have estimated the global GIC volume to: 350 mm SLE (Grinsted 2013), 410 mm SLE (Vaughan et al. 2013), and 520 mm SLE (Radić et al. 2014)). Regional variabilities occur in out of balance conditions between the different GIC regions. Typically, regions such as Greenland, Central Europe (the Alps), and Scandinavia are most out of balance with present day climate conditions whereas New Zealand, Antarctica, and Alaska are less out of balance [12, Table 1].

### 3.3 GIC conclusion

Since 1933, the Mittivakkat Gletscher in Southeast Greenland has been a geographical scientific focus area of identifying, monitoring, quantifying, and determining physical processes regarding e.g., climatology, glaciology, and hydrology, and intensively so since 1993 when the first permanent monitoring programs were installed by University of Copenhagen. Mittivakkat is the *only* long-term mass-balance observed mountain glacier in Greenland, and therefore of high scientific interest for understanding glacier behaviour in a warming climate, and its subsequent impact on the hydrological processes and the water balance. If the Mittivakkat Gletscher programs – the climate, glacier, and hydrological programs – had not been established in the early and mid-1990s and maintained ever since, today we would have limited information and knowledge about mountain glacier conditions in Greenland, from a climate change perspective. Thanks to these established programs, the Mittivakkat Gletscher is today a *climate and ice field laboratory*, which has given us the opportunity to understand the behavior of a Greenlandic mountain glacier under warming and drying climate conditions.

The Mittivakkat Gletscher has on average faced an observed negative net mass-balance of  $-1.00 \pm 0.70$  m w.e.  $\text{yr}^{-1}$  (1995/1996–2013/2014), and an overall trend towards more negative mass-balance values. These mass-balance conditions have been influenced by on average increasing MAAT and mean summer air temperatures and simultaneously decreasing annual and winter precipitation sums. The observed Mittivakkat Gletscher changes are evident, illustrating over time a change in ELA to higher elevations of  $\sim 750$  m a.s.l., a low AAR of 0.15, a drop in EBY mean glacier-wide albedo of 10 % (2000–2013), an average margin change of  $\sim 15$  m  $\text{yr}^{-1}$  (1900–2010), a surface area change of -17 % (1986–2011), a mean ice thickness change of -19 % (1994–2014), a mean ice surface velocity change of -30 %, a glacier volume change of -30 %, and out of balance conditions, where Mittivakkat is likely to lose 50–70 % of its area and 60–80 % of its volume typically over several decades or longer if the current climate conditions in the region persist (Table 4). On the modeling side the Mittivakkat Gletscher surface mass-



balance conditions have been simulated in SnowModel, indicating a mean precipitation of  $1,490 \pm 490$  mm w.e.  $\text{yr}^{-1}$ , evaporation and sublimation of  $-250 \pm 30$  mm w.e.  $\text{yr}^{-1}$ , surface runoff of  $-2,140 \pm 410$  mm w.e.  $\text{yr}^{-1}$ , and SMB of  $-900 \pm 470$  mm w.e.  $\text{yr}^{-1}$  (1998–2006), and subsequently, based on the developed runoff routing model HydroFlow, an annual runoff period of  $200 \pm 20$  d, an increase in the runoff period of  $\sim 30$  d and in volume of  $\sim 2.9 \times 10^6$   $\text{m}^3$   $\text{yr}^{-2}$  for the main part of Mittivakkat Gletscher, and that  $\sim 35$ – $40$  % of the runoff volume will come from net glacier loss.

These Mittivakkat Gletscher findings are unique for our understanding of glacier behaviour under climate warming in Southeast Greenland, and it clearly illustrates that Mittivakkat Gletscher on average is losing mass, thinning, and retreating, and subsequently having an impact on the hydrological processes and the water balance, since a portion of the glacier runoff originates from net glacier loss. To analyze whether these net mass-balance and out of balance findings only occurred for Mittivakkat Gletscher, studies of external GIC conditions were conducted. These studies show, that GIC in the northern North Atlantic region on average also faced increasing net mass-balance loss, even though sub-regional mass-balance variability occurred between East Greenland, Iceland, Scandinavia, and Svalbard. Also, for the Northern Hemisphere and the globe in general, a mean GIC mass-balance trend towards more negative mass-balance values occurred, however variabilities between glacier regions occurred. On a global mean GIC scale it has been stated, that GIC are out of balance with the present climate conditions, for example, illustrated for Mittivakkat, however not in the same range of magnitude as for Mittivakkat Gletscher. The Mittivakkat Gletscher net mass-balance and out of balance trends seems overall to follow the northern North Atlantic, Northern Hemispheric, and global trends. Therefore, there is cause to believe, that the findings at Mittivakkat Gletscher, like the on average higher ELA, margin and area retreat, mean ice thickness and volume thinning, surface velocity slowing down, and mass loss are not a single Mittivakkat Gletscher issue, but probably issues also relevant for GIC elsewhere in e.g., Greenland and northern North Atlantic even though changes in GIC are not uniformly distributed. It is, as an example, shown that a spatiotemporal mass-balance variability occurred for maritime GIC in Scandinavia in 1990s (e.g., Nesje et al. 2000) and for GIC in Karakorum in 2000s (e.g., Hewitt 2005; Gardelle et al. 2012) due to changes in, climate patterns, and subsequent changes in winter accumulation and/or summer ablation conditions.



## 4. The Greenland Ice Sheet

### 4.1 GrIS surface melt, surface mass-balance, and runoff conditions

The GrIS is the largest reservoir of permanent snow and ice in the Northern Hemisphere (e.g., AMAP 2009, 2011), and is highly sensitive to climate changes (e.g., Bamber et al. 2001; Box et al. 2006, 2012; Hanna et al. 2013). The GrIS net mass-balance loss has increased since 1980s (e.g., Rignot et al. 2011; Shepherd et al. 2012; Box and Colgan 2013; Church et al. 2013; Hanna et al. 2013), where mass-loss until around 2000 was largely caused by SMB and hereafter both by SMB and ice dynamics (Hurkmans et al. 2014). For 2009 to 2012, however, freshwater runoff has been estimated to explain around two-third of the mass loss of the GrIS (Enderlin et al. 2014).

To better understand the hydrological processes and the surface water balance for the GrIS, different studies have (since Benson (1962) and Bauer (1968) first estimated the mass-balance components) been conducted to emphasize the climate impact on the GrIS melt and mass-balance components (e.g., Box and Steffen 2001; Box et al. 2004, 2006; Hanna et al. 2005, 2006, 2008, 2009, 2011, 2013, 2014; Fettweis et al. 2005, 2008, 2011, 2013; Fettweis 2007; Tedesco 2007; Bales et al. 2009; Ettema et al. 2009; Sørensen et al. 2011; Tedesco et al. 2011; Kjær et al. 2012; Box and Colgan 2013; Vernon et al. 2013; Csatho et al. 2014; Fyke et al. 2014; [15]–[18]).

For estimating the GrIS mass-balance components the duration, extent, and rates of surface melting are important factors [16]; as an example the increase in GrIS runoff (1960–2010) was estimated based on an 87 % increase in melt extent, an 18 % increase in melt duration, and a 5 % decrease in melt rates [17] (the results were scaled to 100 % to provide a relative measure of melt extent, duration, and rates in governing the changes in runoff). An altered melting regime can produce substantial differences in surface albedo and energy and moisture balances, especially because of an expansion of the wet snow area (wet snow absorbs up to three times more incident solar energy than dry snow (Steffen 1995)), and the bare ice area (albedo for bare ice is (0.35–0.65), and much less than for snow (0.60–0.85)) (Cuffey and Paterson 2010). Therefore, an altered melt regime can e.g., influence the GrIS snow, SMB, supraglacial lake, and runoff conditions and subsequently the dynamic and subglacial GrIS sliding processes. Mechanisms that link climate, surface hydrology, internal drainage and refreezing, and ice dynamics are still poorly understood, and numerical ice-sheet models do not simulate these changes realistically (Nick et al. 2009) [16]. However, since the publication of IPCC AR4 in 2007, ice-sheet models have been improved and do not overly rely on simplified physics, which now allows them to simulate initially simple couplings between ice-sheets, ice streams, and ice shelves in relation to atmospheric and oceanic influences (e.g., Hanna et al. 2013), and therefore probably be able to come up with more realistic evaluations of the GrIS mass-loss contribution to sea-level rise.

Since the satellite era goes back to 1979; we have limited spatial information about melting conditions and extremes before that period, however e.g., shallow firn cores from the dry snow region of the GrIS show that wide-spread surface melt occurred in 1889 (Keegan et al. 2014). Based on SnowModel, GrIS melting conditions were simulated for the period 1960–2010 [16], unfortunately not including the exceptional 2012-melting event (on 12 July; the first widespread melt event during the satellite era (Keegan et al.

2014)) forced by a blocking high-pressure feature in the mid-troposphere forming a heat dome over Greenland that led to the widespread surface melting (Hanna et al. 2014). This exceptional 2012-melt event was, however, then simulated by SnowModel in Hanna et al. (2014) showing that surface melt covered 90 % of the GrIS surface area, which concurs with the 95–98 % melt cover extent from Nghiem et al. (2012) and Hall et al. (2013). This melt event created extreme proglacial river runoff at the Kangerlussuaq catchment outlet and subsequent infrastructural collapse (around 10–13 July, 2012) (Mernild et al. 2012b; Mikkelsen 2014) – meltwater mainly generated from the lower part of the GrIS accumulation zone and the ablation zone, and less (<2 %) from stored water in supraglacial lakes (Mikkelsen 2014).

For 1960–2010, however, the mean annual GrIS simulated melt extent was  $15 \pm 5$  % ( $\sim 2.6 \pm 0.8 \times 10^5 \text{ km}^2 \text{ yr}^{-1}$ ), where the mean melt extent for 1960–1972 changed by an average of -6 % (equal to a change in the melt period of  $-3 \text{ d yr}^{-1}$ ), and for 1973–2010 by an average of 13 % (equal to  $2 \text{ d yr}^{-1}$ ) (Table 5) – a simulated trend which (after 1979) is in agreement with satellite-derived melt extent conditions [16]. The maximum annual modeled melt extent was in 2010 (52 %;  $\sim 9.5 \times 10^5 \text{ km}^2$ ) and the minimum in

**Table 5:** Modeled mean and trends in GrIS melt and surface water balance elements: precipitation, evaporation, sublimation, runoff, and SMB, and Greenland runoff forced by observed AWS and Regional Climate Model data [15]–[18]. The  $\pm$  equals one standard deviation.

Reference	[15]	[16]	[17]	[18]		
Location	GrIS	GrIS	GrIS and Greenland	GrIS		
Time period	1995–2005 $\text{km}^3 \text{ yr}^{-1}$ (mm w.e. $\text{yr}^{-1}$ )	1960–2010	1960–2010 $\text{km}^3 \text{ yr}^{-1}$ (annual change $\text{km}^3 \text{ yr}^{-2}$ )	1950–2080 $\text{km}^3 \text{ yr}^{-1}$	2040–2049 $\text{km}^3 \text{ yr}^{-1}$	2070–2080 $\text{km}^3 \text{ yr}^{-1}$
Forcing	AWS data			RCM		
Mean melt extent	-----	$15 \pm 5$ %	-----	792,000 $\text{km}^2$ 43 %	934,000 $\text{km}^2$ 51 %	1,025,000 $\text{km}^2$ 56 %
Minimum and maximum annual melt extent	-----	52 % (2010) 17 % (1972)	-----	-----	-----	-----
Melt extent trends	-----	-6 % (1960–1972) 13 % (1973–2010)	-----	$\sim 90$ % increase	-----	-----
Melt day trends	-----	-3 $\text{d yr}^{-1}$ (1960–1972) 2 $\text{d yr}^{-1}$ (1973–2010)	-----	Average increase of 29 days	-----	-----
Precipitation or net precipitation <sup>§</sup>	$643 \pm 35$ (345 $\pm$ 19)	-----	$489 \pm 53^{\text{§}}$ (1.5)	$677.3 \pm 89.7$	$698.3 \pm 96.1$	$770.2 \pm 100.6$
Evaporation	$-58 \pm 6$ (31 $\pm$ 3)	-----	-----	$-157.7 \pm 25.7$	$-177.6 \pm 16.8$	$201.8 \pm 18.9$
Sublimation	$-52 \pm 6$ (28 $\pm$ 3)	-----	-----			
Internal storage	-----	-----	$129 \pm 29$ (25 %)	-----	-----	-----
Runoff	$-392 \pm 58$ (211 $\pm$ 31)	-----	$-333 \pm 75$ (69 %*) (3.8)	$-442.1 \pm 134.4$	$-529.2 \pm 37.0$	$667.7 \pm 47.6$
SMB	$141 \pm 83$ (75 $\pm$ 44)	-----	$156 \pm 82$ (-2.3)	$79.3 \pm 128.9$	$-8.5 \pm 75.8$	$-99.3 \pm 103.1$
GrIS mass-balance	$-257 \pm 81$ (-133 $\pm$ 44)	-----	-----	-----	-----	-----
Land strip area runoff	-----	-----	$148 \pm 41$ (31 %*) (0.1)	-----	-----	-----
Total Greenland runoff	-----	-----	$481 \pm 85$ (3.9)	-----	-----	-----

<sup>§</sup> Net precipitation: Precipitation minus evaporation and sublimation. \* Percentage of total runoff from Greenland.

1972 (17 %;  $\sim 3.1 \times 10^5 \text{ km}^2$ ) [16] (Table 5). The simulated trends in melt extent were similar to the smoothed trend of the AMO index [16]. Overall the melt simulations clearly show that the GrIS melt extent has been increasing over recent decades, with several records being set together with an extension of the melting period [16].

For the GrIS, the ELA was simulated for 1995–2005 showing variability between the western and eastern parts of GrIS, due to changes in local topography [15]. For example, on the western GrIS, the ELA varies from around 800 m a.s.l. ( $81^\circ\text{N}$ ) to around 1,600 m a.s.l. ( $69^\circ\text{N}$ ), and on the eastern GrIS from 600 m a.s.l. ( $81^\circ\text{N}$ ) to 1,400 m a.s.l. ( $69^\circ\text{N}$ ) [15]. A lower elevated ELA with increasing latitude is in line with other studies e.g., Zwally and Giovinetto (2001) and Box et al. (2004). For this short ten-year period the ELA for both the western and eastern parts of the GrIS was modeled to increase in elevation by around  $40 \text{ m a.s.l. yr}^{-1}$  [15]. Also, for the 1950–2080 GrIS SMB simulations (based on the A1B scenario modeled by the HIRHAM4 RCM using boundary conditions from ECHAM5 AOGCM) [18], the ELA was simulated to increase in elevation from on average  $1,158 \pm 343 \text{ m a.s.l. (1950–1959)}$  to  $2,056 \pm 413 \text{ m a.s.l. (2070–2080)}$  [18], emphasizing a decreasing accumulation zone and an increasing ablation zone over time for the GrIS. Such a trend was confirmed in Vernon et al. (2013). In Leeson et al. (2015) it was, for example, emphasized that an increasing future ablation zone could indicate the development of supraglacial lakes at higher elevations, with a potential to deliver water and heat to the base of the GrIS influencing the ice flow through enhanced basal lubrication and warming of the ice.

In Table 5 SnowModel simulated GrIS surface mass-balance components are summarized for the different periods emphasized in [16]–[18]. Common for the different surface mass-balance simulations are on average increasing accumulation (precipitation) (with the possibility of decreasing trends over short time periods e.g., 1995–2005), increasing ablation (evaporation, sublimation, and runoff) and decreasing SMB. Regarding GrIS SMB the spatial distribution showed slightly positive SMB values at the interior (up to  $\sim 200 \text{ mm w.e. yr}^{-1}$ , averaging  $\sim 60 \text{ mm w.e. yr}^{-1}$ ), where the lowest values occurred in the southwestern part (below  $-3,000 \text{ mm w.e. yr}^{-1}$ ) and highest values in the southeastern part (above  $1,000 \text{ mm w.e. yr}^{-1}$ ), due to synoptic cyclone passages [2]. A similar pattern in modeled spatial SMB conditions was seen in e.g., Box et al. (2006) and Fettweis (2007). For the period 1995–2005, the SnowModel simulated GrIS SMB of  $141 \pm 83 \text{ km}^3 \text{ yr}^{-1}$  was linked to values of bottom melting by geothermal heating (Church et al. 2001) and iceberg calving (Rignot and Kanagaratnam 2006) to give a first hand estimate of the average GrIS mass-balance for 1995–2005 (Table 5) [15]. This composite GrIS mass-balance estimate indicates that the average GrIS net mass-balance was  $-257 \pm 83 \text{ km}^3 \text{ yr}^{-1}$  (equal to  $\sim 0.7 \text{ mm SLE yr}^{-1}$ ) (1995–2005) (Table 5) (where  $362.5 \text{ Gt yr}^{-1} = 1 \text{ mm SLE yr}^{-1}$  (Hanna et al. 2013)), which is in the range of different estimates from, for example, the GRACE (Gravity Recovery and Climate Experiment) satellite, mass-budgets, and laser altimetry (e.g., Rignot et al. 2008; AMAP 2011; Hanna et al. 2013; Velicogna and Wahr 2013; Csatho et al. 2014), however, in the low end. These studies show a clear trend and a large spread in GrIS mass change over the last two decades, for example, of  $-51 \pm 65 \text{ Gt yr}^{-1}$  (1990s) ( $\sim 0.1 \text{ mm SLE yr}^{-1}$ ) and  $-263 \pm 30 \text{ Gt yr}^{-1}$  (2005–2010) ( $\sim 0.7 \text{ mm SLE yr}^{-1}$ ), from the use of different technical differences and measurement epochs (Hanna et al. 2013) (an increase in GrIS mass-balance contribution to eustatic sea-level was also seen in e.g., Box and Colgan (2013)). But also, that the GrIS mass-loss has migrated clockwise (from Southeast Greenland) around the ice margin to progressively affect the entire ice sheet margin (Velicogna and Wahr 2013). For almost

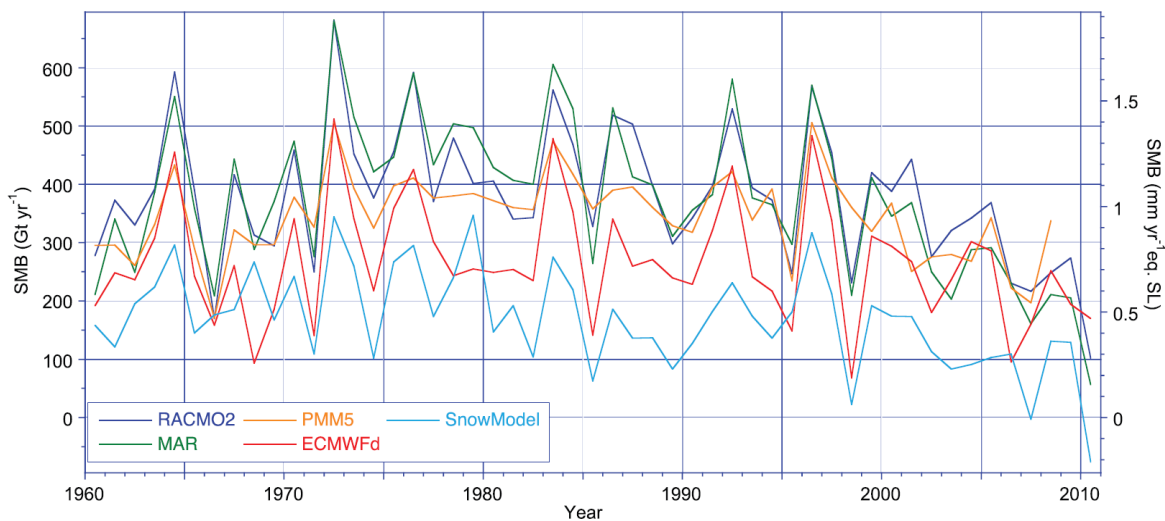


**Figure 17:** Time series of mean annual GrIS SMB, simulated by five different modeling systems for the period 1960–2010. The SnowModel GrIS SMB simulations (turquoise color) originate from [17]. The Figure is from the IPCC AR5 Report, Chapter 13 (Church et al. 2013).

the same period 2000–2010 marine-terminating glaciers retreated (Howat and Eddy 2011, Box and Decker 2011, [11]), where, for example, marine-terminating glaciers for Southeast Greenland retreated more rapidly in the 2000s than in the 1930s during the early twentieth century warm period (Bjørk et al. 2012). Other GrIS mass-balance studies, for example, the CryoSat-2 estimated the GrIS mass change to be  $-375 \pm 24 \text{ km}^3 \text{ yr}^{-1}$  (2011–2014) ( $\sim 1.0 \text{ mm SLE yr}^{-1}$ ) (Helm et al. 2014), where GRACE estimated the mass change for September 2011/September 2012 to be  $-575 \pm 95 \text{ km}^3$  ( $\sim 1.6 \text{ mm SLE yr}^{-1}$ ) (Box et al. 2012; pers com. J. Wahr, September 2013), with e.g., no significant loss during the summer 2013 (therefore, for the period June 2013 through June 2014 the GRACE estimated mass change was  $-6 \text{ Gt}$  – a negligible mass loss compare to other years (Tedesco et al. 2014)). For 2014 the summer loss was of the same order as the summertime mass loss in most prior years, through notably less than the mass loss in the huge melt years of 2010 and 2012 (pers com. J. Wahr, December 2014); The negligible June 2013 through June 2014 mass loss seems likely to be an anomaly, rather than the start of some new mode of mass balance behavior of the GrIS.

The GrIS mass change for approximately the first decade of the new millennium exceeded the maximum GrIS change of around  $-200 \text{ Gt yr}^{-1}$  in the early-1930s (reconstructed values from Box and Colgan 2013; Figure 6), indicating higher mass loss values now than during the early twentieth century warm period.

Combining the GrIS mass-balance eustatic sea-level contribution ( $\sim 0.7 \text{ mm SLE yr}^{-1}$ ) with the Greenland GIC mass-balance contribution ( $\sim 0.1 \text{ mm SLE yr}^{-1}$ ) [14] (Bolch et al. 2013) for 2000–2010, the mass-loss from Greenland to sea-level rise seems to be in the range of  $\sim 0.8 \text{ mm SLE yr}^{-1}$ . This is about one quarter of the mean 1993–2010 global sea-level rise of  $\sim 3.2 \text{ mm SLE yr}^{-1}$ , where the ocean thermal expansion is in the range of  $\sim 1 \text{ mm SLE yr}^{-1}$  out of  $\sim 3.2 \text{ mm SLE yr}^{-1}$  (Church et al. 2013).

In Figure 17, for the time period 1960–2010 SnowModel simulated GrIS SMB are compared (in the IPCC AR5 Report; Chapter 13, Sea level Change: Figure 13.5 and Table 13.2) (Church et al. 2013) against four different SMB modeling systems using either the degree day approach or the energy balance forced by either by RCM data or AWS data to

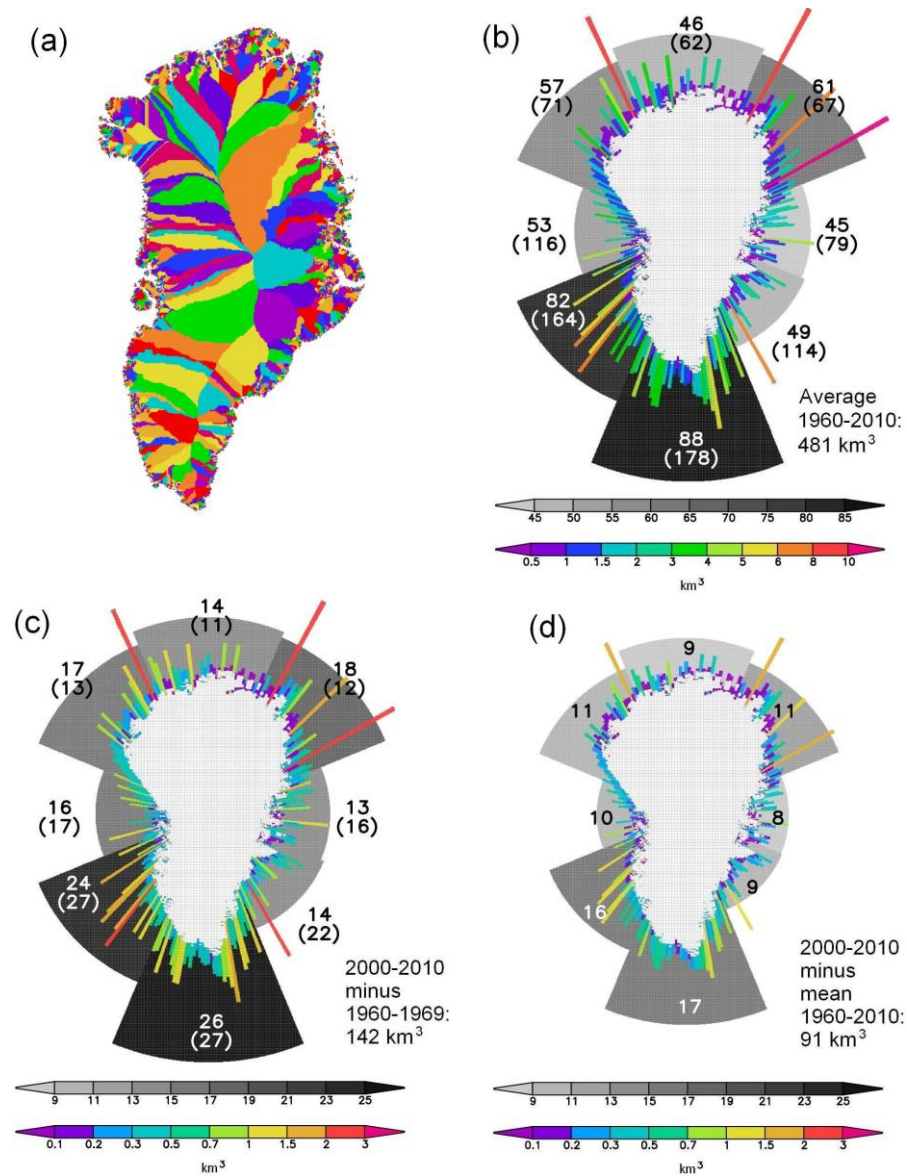


**Figure 18:** (a) HydroFlow simulated individual Greenland drainage basins (in total for Greenland there are ~3,150 individual basins and for GrIS ~400); (b) spatial distribution of simulated runoff from Greenland's individual drainage basins [each radial colored bar represents the accumulated runoff of 10 catchments located side by side (in total there are 316 radial bars); this was done to simplify the presentation of spatial runoff trends, since 85% of all catchments are equal or below 250 km<sup>2</sup>], and from the eight sectors (north, northeast, east, etc.), to the adjacent seas: (a) mean annual Greenland runoff for 1960–2010, where the numbers in brackets indicate the length of the discharge season (in days) for each region; (b) the difference between 2000–2010 mean annual Greenland runoff and the 1960–1969 runoff, where the numbers in brackets indicate the increase in the length (in days) of the discharge season for each region; and (c) the difference between 2000–2010 mean annual Greenland runoff and the 1960–2010 mean. The regional runoff numbers for each sector have been used to scale the radial distance of each gray wedge from the coast to the outside of the wedge and not from the center of Greenland to the outside of the wedge. So, for example, the 53 and 57 wedge in Fig. b ends are a similar distance from the coast but have very different total wedge sizes [and 49 and 45 are similar (Fig. b) because the coast is a similar distance from the center of the projection]. Greenland is slightly distorted from our traditional view in this radial projection. The figure is modified from [17].



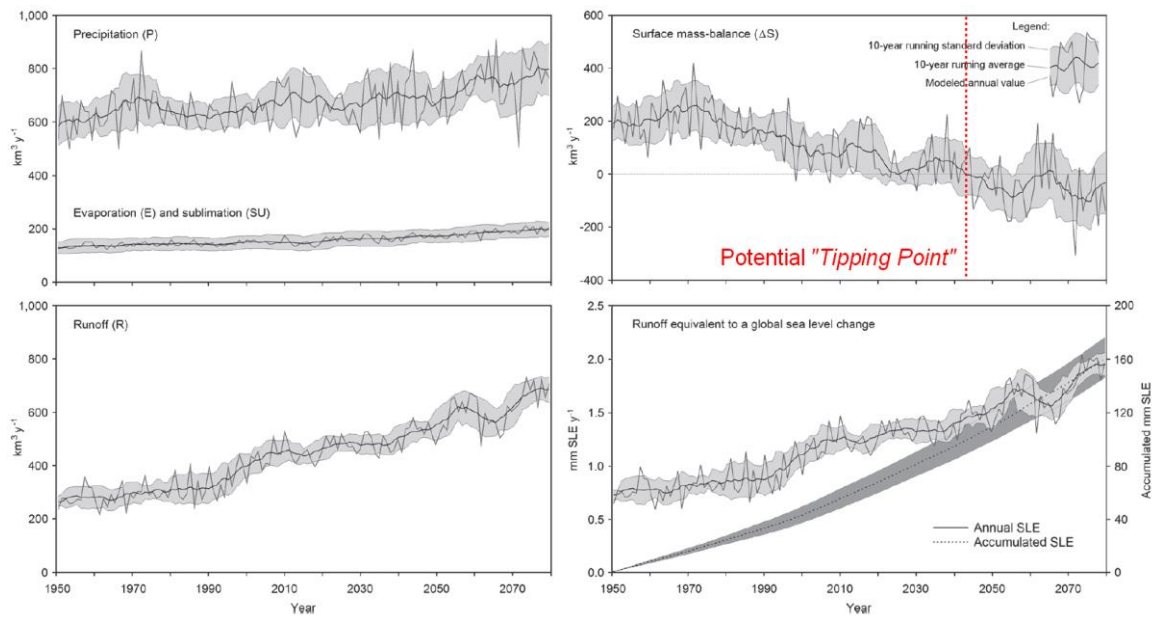


**Figure 19:** Time series for the simulated GrIS precipitation, evaporation, sublimation, runoff, and SMB and annual and accumulated contribution to the global sea-level change for 1950–2080. The figure is modified from [18].

evaluate the GrIS SMB conditions. For 1960–2010 the SnowModel simulated GrIS SMB was on average  $156 \pm 82 \text{ km}^3 \text{ yr}^{-1}$  (Table 5), heading towards  $86 \pm 72 \text{ km}^3 \text{ yr}^{-1}$  for the first decade of the new millennium (2000–2010) [17]. In Figure 17 the five individual GrIS SMB time series are illustrated. The SnowModel simulated GrIS SMB time series follows the variability and trend in SMB time series compared to the other four models, however the SnowModel estimated SMB time series (forced with AWS data) is low – around 35 to 40 % lower than the output from the other four models (Church et al. 2013). This difference is probably mainly related to the fact that SnowModel uses a full energy balance, a multi-layer snowpack, and a blowing-snow model together with the challenges in measuring AWS snow precipitation, which for Arctic, including Greenland can be related with huge uncertainty (e.g., Yang et al. 1998, 1999; Rasmussen et al 2012). Regarding the SnowModel simulated SMB, the variability in this time series (Figure 17) related to impacts from major volcanic eruptions (e.g., Agung, Indonesia (1963), El Chichón, Mexico (1982) and Pinatubo, Philippines (1991)), do not appear to have a significant impact (neither on the the melt extent), even though, as stated by Hanna et al. (2005), global dust veils generated by volcanic activity might cool the polar regions and suppress ice-sheet melt [16] [17].

Based on SnowModel and the HydroFlow routing model code developments, the spatial distribution of runoff was estimated from Greenland (Figure 18), including from the GrIS for 1960–2010 (Table 5). For 1960–2010 the mean Greenland runoff was  $481 \pm 85 \text{ km}^3 \text{ yr}^{-1}$  [17], where ~30 % ( $148 \pm 41 \text{ km}^3 \text{ yr}^{-1}$ ) of the runoff from Greenland to the surrounding seas originated from the land strip area and ~70 % ( $333 \pm 75 \text{ km}^3 \text{ yr}^{-1}$ ) of the runoff from the GrIS. For the GrIS the internal storage was  $129 \pm 29 \text{ km}^3 \text{ yr}^{-1}$  (by not including snowpack routines of retention/refreezing in SnowModel it would lead to an runoff overestimation of ~25 % [17], which is in the same range as values in e.g. Hanna et al. (2005, 2008), but below values in Ettema et al. (2009)). In Bamber et al. (2012) the Greenland runoff was simulated using the RCM RACMO2 (Ettema et al. 2009) to  $416 \pm$



$57 \text{ km}^3 \text{ yr}^{-1}$  (1960–2010), where ~60 % originated from the ice sheet and ~40 % from the land strip area. These values are on average almost identical to the SnowModel/HydroFlow simulated runoff values. Regarding the annual runoff variability, years with relatively high HydroFlow simulated Greenland runoff were equal to a positive AMO index, and vice versa for years with relatively low Greenland runoff volume. It was shown by Chylek et al. (2010), that the Arctic detrended temperatures were highly correlated with AMO, indicating the Atlantic Ocean as a possible source of Arctic climate variability.

For Greenland, the average runoff (1960–2010) was greater from the western half of Greenland  $263 \text{ km}^3 \text{ yr}^{-1}$  (equals 55 % of the total runoff), than from the eastern half of Greenland  $218 \text{ km}^3 \text{ yr}^{-1}$  (45 %), indicating an insignificant difference between West and East Greenland [17]. On a regional scale the greatest runoff amount came from the southern and southwestern parts of Greenland, and lowest runoff from the eastern and southeastern parts of Greenland (Figure 18) – suggesting that regions with relatively high runoff are synchronous with relatively low end-of-winter snow accumulation and vice versa [17]. This regional runoff distribution from Greenland seems in general to be in agreement with Lewis and Smith (2009). The spatial distribution of runoff from Greenland (Figure 18) based on a division of Greenland into individual drainage basins, highly illustrates that the variability in catchment runoff to the surrounding seas varied according to catchment size, ice sheet and GIC elevation range, and ice sheet and GIC areal coverage, where the 1960–2010 average simulated discharge for these drainage catchments varied from 0.01 to  $10.1 \text{ km}^3 \text{ yr}^{-1}$  (Figure 18) [17]. The spatial variability in catchment runoff indicates that for approximately half of the basins the simulated runoff ranged from 0.01 to  $1.0 \text{ km}^3 \text{ yr}^{-1}$  (1960–2010) and contributed 15 % of the total Greenland runoff. In contrast, 15 % of the catchments – catchments with a relatively large ice sheet and/or GIC areal coverage – had a mean annual runoff greater than  $2.5 \text{ km}^3 \text{ yr}^{-1}$  and contributed 40 % of the Greenland runoff to the adjacent seas [17]. Over the period 1960–2010 the Greenland runoff were simulated to increase  $3.9 \text{ km}^3 \text{ yr}^{-2}$  in total, where a change of  $3.8 \text{ km}^3 \text{ yr}^{-2}$  originated from the GrIS and  $0.1 \text{ km}^3 \text{ yr}^{-2}$  from the strip area (Table 5). Also, the simulations further showed pronounced runoff increases in the southern and southwestern parts and the lowest increase in the northwestern part [17]. Such changes in Greenland runoff over time as illustrated, indicates that runoff from a sea-level perspective will increase from  $1.2 \pm 0.2 \text{ mm SLE yr}^{-1}$  (1960–1969) to  $1.6 \pm 0.2 \text{ mm SLE yr}^{-1}$  (2000–2010), averaging  $1.3 \pm 0.2 \text{ mm SLE yr}^{-1}$  [17].

In the time period from 1950 towards 2080, it is, for example, projected based on SnowModel GrIS simulations forced with the A1B scenario (modeled by the HIRHAM4 RCM), that an increase of ~90 % in GrIS melt extent might occur from  $469,000 \text{ km}^2$  (1950–1959) to  $1,025,000 \text{ km}^2$  (2070–2080) [18] (Table 5), with a risk of widespread melt events to occur almost annually by the end of the century (Keegan et al. 2014). Further, an increase in melt index (above 2000-m elevation) of ~140 % and an increase in the melt duration of 29 d is projected to occur (Table 5) [18]. It is further projected that the annual GrIS precipitation, evaporation and sublimation, and runoff will increase on average (Figure 19). Regarding precipitation a mean of  $\sim 680 \pm 90 \text{ km}^3 \text{ yr}^{-1}$  will occur (1950–2080), with an increase from  $\sim 600 \pm 70 \text{ km}^3 \text{ yr}^{-1}$  (1950–1959) to  $\sim 770 \pm 100 \text{ km}^3 \text{ yr}^{-1}$  (2070–2080) [18], and evaporation and sublimation a mean of  $\sim 160 \pm 25 \text{ km}^3 \text{ yr}^{-1}$  will occur (1950–2080), with an increase from  $\sim 140 \pm 20 \text{ km}^3 \text{ yr}^{-1}$  (1950–1959) to  $\sim 200 \pm 20 \text{ km}^3 \text{ yr}^{-1}$  (2070–2080) [18]. For runoff, mean GrIS runoff of  $\sim 440 \pm 135 \text{ km}^3 \text{ yr}^{-1}$  will occur (1950–2080), with an increase from  $\sim 285 \pm 35 \text{ km}^3 \text{ yr}^{-1}$  (1950–1959) to  $\sim 670 \pm 50 \text{ km}^3 \text{ yr}^{-1}$  (2070–2080) (Figure 19). Such a change in runoff over time indicates that runoff from a sea-level perspective will increase from  $0.79 \pm 0.10 \text{ mm SLE yr}^{-1}$  (1950–1959) to

$1.85 \pm 0.08$  mm SLE  $\text{yr}^{-1}$  (2070–2080) [18], indicating a cumulative GrIS runoff of  $\sim 160$  mm SLE for the entire simulation period (Figure 19) [18]. Also, it is projected that the SMB loss will enhance by  $\sim 330$   $\text{km}^3$ , indicating that the GrIS will have continuously positive SMB conditions until early-2040s. For 2040–2049 the mean GrIS SMB was estimated to be  $\sim -10 \pm 75$   $\text{km}^3 \text{yr}^{-1}$  (Table 5) [18]. Hereafter, on a mean decadal scale the GrIS SMB will be negative or close to zero, and continuously negative on an annual scale from mid-2060s and onwards to 2080 [18]. The potential for irreversible processes to occur on the GrIS is possible when the SMB is continuously negative year after year. The GrIS will, during continuously negative SMB, lose mass and eventually results in its stepwise diminishing (Bamber et al. 2009). Therefore, there is a reason to think, that the GrIS according to [18] based on the A1B scenario will likely face by definition a potential ‘tipping point’ between early-2040 and mid-2060 (Figure 19) due to the continuously negative SMB [18]. These simulated SnowModel GrIS SMB conditions are compared (in the IPCC AR5 Report; Chapter 13, Sea level Change: Table 13.4) (Church et al. 2013) against other GrIS SMB studies during the 21<sup>st</sup> century, and recalculated into sea-level contributions. The SnowModel simulated GrIS SMB values [18] show to be within the same range as the other listed studies in the IPCC AR5 Report.

The output from the different GrIS surface modeling studies analyzed in [15]–[18] clearly illustrates, that the GrIS has faced on average increasing melt extent and melt duration, and a higher located ELA, but also that the melt trends and the ELA are expected to increase in content and in elevation towards 2080. From a water balance perspective the SnowModel simulated GrIS surface mass-balance conditions and trends (1960–2010) are in line with previous studies e.g., Vernon et al. 2013 and the IPCC AR5 Report (Church et al. 2013), indicating on average increasing precipitation, evaporation, sublimation, runoff, and a drop in SMB. However, the SMB is still indicating positive annual values (Table 5), during a period (1960–2010) where warming had occurred more intensively at northern latitudes, including for Greenland, than elsewhere (McBean et al. 2005; IPCC 2013, SPM). On the runoff side, the Greenland simulated runoff indicated that 70 % of the Greenland runoff originated from the GrIS, and 30 % from the land strip area. Due to the spatial distribution of runoff, 55 % drained to the west and 45 % to the east. Towards 2080, a positive GrIS SMB is expected to occur until early-2040 and hereafter continuously negative after the mid-2060s. In the 1950–2080 period GrIS runoff is expected to increase cumulatively to what equals  $\sim 160$  mm SLE.

Not only is the spatiotemporal runoff distribution of interest for the entire Greenland, to better understand the terrestrial output to the adjacent seas (Figure 18) and the link to hydrographic conditions like, for example, the AMOC and subsequently the climate system (Bryden et al. 2005; Rahmstorf et al. 2005; Weijer et al. 2012), but also on a region scale for individual fjord systems. Therefore, for example, a case study estimating the freshwater fluxes such as runoff, ice discharge, subglacial geothermal and frictional melting due to basal ice motion and precipitation on the fjord surface area was conducted [19].

## 4.2 Water balance case studie from Sermilik Fjord

On a regional scale – on an icefjord catchment scale – terrestrial inputs of freshwater flux to the Sermilik Fjord, Southeast Greenland, were estimated [19]. Terrestrial freshwater fluxes from Greenland to fjords exert an important influence on the hydrographic conditions near the glacier-ocean boundary at the GrIS margin, and also on

**Table 6:** *Freshwater fluxes to Sermilik Fjord, Southeast Greenland [19].*

Reference	[19]
Location	Sermilik Fjord Catchment
Time period	1999–2008
Freshwater flux	$40.4 \pm 4.9 \text{ km}^3 \text{ yr}^{-1}$
Runoff	$4.6 \pm 0.7 \text{ km}^3 \text{ yr}^{-1}$ (11 %)
Ice discharge, overall	$33.9 \pm 4.1 \text{ km}^3 \text{ yr}^{-1}$ (85 %)
Ice discharge, Helheim Glacier	$25.9 \pm 2.6 \text{ km}^3 \text{ yr}^{-1}$ (65 %)
Ice discharge, Fenris Glacier	$2.5 \pm 0.5 \text{ km}^3 \text{ yr}^{-1}$ (6 %)
Ice discharge, Midgård Glacier	$5.5 \pm 1.0 \text{ km}^3 \text{ yr}^{-1}$ (14 %)
Precipitation on fjord surface area	$1.4 \pm 0.1 \text{ km}^3 \text{ yr}^{-1}$ (3 %)
Subglacial geothermal	$0.01 \text{ km}^3 \text{ yr}^{-1}$ (>0.03 %)
Frictional melting due to basal ice motion	$0.5 \text{ km}^3 \text{ yr}^{-1}$ (1 %)

the circulation and stratification within the fjords and the adjacent oceans, including on the AMOC (e.g., Rahmstorf et al. 2005; Straneo et al. 2011; Weijer et al. 2012). At present, there is limited quantitative information about the terrestrial spatiotemporal patterns of drainage basins and associated ice discharge and runoff fluxes to fjord systems in Greenland. However, variations in ice discharge and increasing mass loss have been observed recently at four of Greenland's largest ice streams: Jakobshavn Isbræ, Helheim Glacier, Kangerdlugssuaq Glacier, and the Northeast Greenland ice stream (Luckman et al. 2006; van den Broeke 2009; Howat et al 2011; Khan et al. 2014). The processes driving the variations in ice discharge and increasing mass loss are still poorly understood (Straneo et al. 2012), even though ice sheet models have been improved and do not over rely on simplified physics (Hanna et al. 2013). One leading hypothesis is that variations in ice discharge and increasing mass loss is caused by increased submarine melting at the glacier terminus, leading to thinning and ungrounding of the floating ice tongue, and reduction in the frontal buttressing to glacier flow (Thomas 2004; Holland et al. 2008; Motyka et al. 2011; Straneo et al. 2012).

In the Sermilik Fjord, the terrestrial inputs of freshwater flux were estimated (1999–2008), indicating ice discharge to be the dominant source of freshwater in the water balance budget [19]. A mean freshwater flux of  $40.4 \pm 4.9 \text{ km}^3 \text{ yr}^{-1}$  was found, where 85 % originated from ice discharge (65 % alone from Helheim Glacier), 11 % from terrestrial surface runoff (from melt water and rain), 3 % from precipitation at the fjord surface area, and 1 % from subglacial geothermal and frictional melting due to basal ice motion (Table 6). The simulated Sermilik Fjord surface runoff varied on an annual scale, ranging in volume from  $2.9 \pm 0.4 \text{ km}^3$  in 1999 to  $5.9 \pm 0.9 \text{ km}^3$  in 2005 [19]. The catchment runoff from the Helheim Glacier accounted on average for 25 % of the total runoff to Sermilik Fjord. The runoff distribution from the different sub-catchments suggested a strong influence from the spatial variation in glacier coverage, indicating high runoff volumes, where glacier cover was present at low elevations, as also stated in the HydroFlow studies [10] [17]. For fjord catchments, which are not influenced by continuous freshwater fluxes from ice streams, the spatiotemporal variation in runoff plays a dominant role in the water balance.

### 4.3 GrIS conclusion

From 1950/1960 to 2010/2080 [15]–[18] the GrIS has faced in general, increasing simulated melt extent, melt duration, a higher located ELA, an increasing ablation area,

and a decreasing accumulation area. These illustrated changes in GrIS surface conditions have happened at the same time (more or less) where the observed mean GrIS-wide albedo dropped by 0.07 (2000–2012) (Box et al. 2012; Tedesco et al. 2013). For the period 1960–2010 the annual simulated precipitation (accumulation) has changed over time, indicating on average increasing annual precipitation (however not for the period 1995–2005) [15]. At the same time (1960–2010) the simulated GrIS ablation has increased (evaporation, sublimation, and runoff), overall indicating a positive SMB for the GrIS. The SnowModel simulated mean GrIS SMB was  $156 \pm 82 \text{ km}^3 \text{ yr}^{-1}$  for 1960–2010 [17], and  $141 \pm 83 \text{ km}^3 \text{ yr}^{-1}$  for 1995–2005 [15]. When combining the simulated 1995–2005 mean positive SMB with observed contributions of bottom melting by geothermal melting and iceberg calving (as a first hand estimate), the GrIS is currently losing a mass of  $257 \pm 82 \text{ km}^3 \text{ yr}^{-1}$  (equal to  $\sim 0.7 \text{ mm SLE yr}^{-1}$ ) [15]. A mass loss value which is within the range of other GrIS mass-balance estimates (e.g., AMAP 2011; Hanna et al. 2013; Csatho et al. 2014), where, for example, the CryoSat-2 estimated GrIS mass loss for 2011–2014 was  $375 \pm 24 \text{ km}^3 \text{ yr}^{-1}$  (Helm et al. 2014), and GRACE estimate September 2011/September 2012 loss was  $575 \pm 95 \text{ km}^3$  (Box et al. 2012; pers. com J. Wahr, September 2013), with no significant loss during the summer 2013. For 2014 the summer loss value was of the same order as the summertime mass loss in most prior years, through notably less than the mass loss in the huge melt years of 2010 and 2012 (pers com. J. Wahr, December 2014).

Combining the GrIS mass-balance eustatic sea-level contribution with the Greenland GIC mass-balance contribution [14] (2000–2010), the overall Greenland mass-loss to sea-level rise was in the range of  $\sim 0.8 \text{ mm SLE yr}^{-1}$ , about one quarter of the mean 1993–2010 global sea-level rise of  $\sim 3.2 \text{ mm SLE yr}^{-1}$  (Church et al. 2013).

When looking only at the GrIS surface mass-balance conditions (by not including dynamical mass loss) the ice sheet is gaining mass (1960–2010), having a positive SMB [17]. Positive SMB conditions were also emphasized in the IPCC AR5 Report (Chapter 13; Church et al. 2013), where SnowModel simulated SMB time series were compared against simulated output data from different SMB models, all indicating positive SMB conditions from 1960–2010. Regarding future expected changes in the GrIS SMB, based on the A1B Scenario (which is closest to the RCP6 Scenario used in IPCC AR5), it is expected that the GrIS SMB will be continuously positive until early 2040s [18]. Hereafter, the mean decadal simulated GrIS SMB will be negative or close to zero, and continuously negative on an annual scale from mid-2060s and onwards to 2080 [18]. Due to the continuously negative SMB values and by use of the definition by Bamber et al. (2009) there is a reason to think, that the GrIS will face ‘tipping point’, and hereafter eventually result in its diminishing.

From a GrIS runoff perspective the runoff has increased over the period from 1960–2010, and it is projected to increase towards 2080 [17] [18]. For 1960–2010 the spatial distribution of runoff was simulated by HydroFlow, emphasizing, for example, that 70 % of the Greenland runoff originated from the GrIS, and the remaining  $\sim 30$  % from the land strip area, but also, that 55 % of the total Greenland runoff of  $481 \pm 85 \text{ km}^3 \text{ yr}^{-1}$  drained to the west, and 45 % to the east [17], with the greatest regional runoff changes in the southern and southwestern parts of Greenland (1960–2010). By not including snowpack routines of retention/refreezing in SnowModel, it would lead to a runoff overestimation of  $\sim 25$  %. On a regional scale, for example, for an icefjord, the Sermilik Fjord, Southeast Greenland, it is estimated that the spatial distribution of runoff counts for 11 % and ice discharge for 85 % of the overall freshwater flux to the fjord, compared to fjords without iceberg calving, where runoff plays a dominant role in the water balance. Beside this spatial division, it further indicates that temporal variations in GrIS runoff and GrIS melt extent is similar to the smoothed trend of the AMO index, where, for example, a

positive AMO index equalled years with relatively high Greenland runoff volume and vice versa [17], and a decreasing AMO index equalled a drop in GrIS melt extent and vice versa [16].



## 5. Conclusions and perspectives for future work

### 5.1 Summary of main scientific contributions

The contributions to science knowledge in the papers of the present thesis are highlighted and discussed in the previous chapters. The main contributions have been in the following research areas:

- *Greenland mountain glacier observations.* Since Mittivakkat Gletscher is the *only* long-term mass-balance observed mountain gletscher in Greenland [4]–[7] observations of net mass-balance conditions (winter, summer, and net mass-balances), together with observations of ELA, AAR, surface albedo, margin, area, surface velocity, mean ice thickness, volume, and runoff changes, and out of balance conditions are new findings and scientifically valuable for our understanding of glacier behavior, and its impact on the water balance during changing climate conditions in coastal Greenland – during a period with a warming and a drying climate [1]–[3].

- *Greenland mountain glacier model code development and simulations.* The Mittivakkat Gletscher SnowModel code developments and simulations brought new insights into the climate impact on surface mass-balance conditions, from precipitation, evaporation, sublimation, surface runoff, and SMB [8], and the impacts from simulations of air temperature inversion on snow and glacier ice melting conditions [9]. The development of the program HydroFlow provided insights into the spatiotemporal distribution of runoff from the Mittivakkat Gletcher catchment, and its impact on the water balance [10].

- *GIC upscaling.* The publications focusing on upscaling present valuable insight regarding GIC net mass-balance conditions and trends for the northern North Atlantic region related to variabilities in large-scale climatic and oceanic indices [13], and for the Northern Hemisphere from a GIC water balance perspective also related to net mass-balance contributions to sea-level rise [14]. Further, new insight was brought regarding the GIC out of balance conditions on both regional and global scales and the future committed GIC area and volume mass-loss regarding e.g., mean sea-level rise [12].

- *Greenland Ice Sheet modeling.* Modeling of the GrIS conditions brought insight into surface melting and surface mass-balance conditions in both present and future time periods regarding the water balances [15]–[18]. The developed HydroFlow model provided new insight regarding the spatiotemporal distribution of terrestrial runoff from Greenland (from the GrIS and also from the land strip area) to the adjacent seas. On a regional fjord catchment scale the total input of terrestrial freshwater flux was estimated, where spatial simulated runoff was combined with ice discharge estimates for outlet glaciers, bringing new insight to the freshwater input to icefjords [19] since freshwater fluxes exert an important influence on the circulation and stratification of adjacent fjords.

These main contributions to scientific knowledge about GIC and ice sheet mass-balance conditions, would probably never have been possible without the knowledge I gained from working on a mountain glacier scale (on the Mittivakkat Gletscher and GIC

simulations) [3]–[14] before I started working (and during my work) with simulations of the GrIS [15]–[19].

## 5.2 Mass-balance and runoff observations and modeling issues for future research

GIC and GrIS mass-balance and runoff observations and modeling have expanded over the last several decades as the demand to understand and describe complicated physical atmosphere-snow-ice-water-processes and interactions has increased. Even though we over the last decades have gained information about GIC and the GrIS surface mass-balance, runoff, and mass-balance conditions, there is still research to be conducted with the purpose of identifying, monitoring, quantifying, and determining processes, variabilities, and interactions regarding hydrological processes and the water balance related to GIC and the GrIS.

To continue the path (“The Journey”, as stated by Lao Tzu in the Preface; Page 2) I have been following over the last many years, emphasizing the hydrological processes and the water balance from both mountain GIC in Greenland and the GrIS, the following list (shown below) should not assume to cover all the most important research issues regarding to e.g., observations and modeling during the coming years. The list rather represents research issues which I from a personal perspective, and in line with the work presented here, find of interest and fundamental for a better understanding of the processes behind GIC and GrIS surface mass-balance and runoff conditions from local to hemispheric perspectives.

- Continue the albedo observations on Mittivakkat Gletscher [7] and subsequently on mountain glaciers in Greenland to better understand the spatiotemporal variation in snow and ice albedo, for example, for the improvement of the snow and ice albedo routines in SnowModel. During the last years of field campaigns on Mittivakkat we have observed variations in surface algal communities causing a darkening of the ice. To better understand the influence of this darkening on the surface albedo, a field program was initiated in August 2014.

- To increase our knowledge of mountain glaciers in Greenland, additional observational net mass-balance and runoff programs should be installed (programs also useful for model validation), especially in the western and northern parts of Greenland. So far, for example, all three operating mass-balance programs in Greenland are located in eastern Greenland [4]–[10].

- GIC are reservoirs of water, and our knowledge about future GIC mass-balance and runoff projections are limited. In addition to the already published GIC model study [14], a study about future runoff conditions might be valuable to improve our understanding of individual GIC behaviour: Such study will be the first to quantify, for example, the runoff *Tipping Points* for GIC. After the occurrence of the runoff *Tipping Point* the annual GIC runoff amount will on average decline as reductions in glacier area outweigh the effect of glacier melting (AMAP 2011). Based on these future simulations, within what range of years can we expect the runoff *Tipping Point* to occur for individual GIC?

- The code development of the *IceHydro/HydroFlow* freshwater runoff routing model could be coupled with a dynamic ice sheet model to provide a link between surface



hydrology – and subsequently englacial and subglacial hydrology – and ice sheet dynamics.

- To better understand the link between the freshwater flux (and the HydroFlow spatiotemporal simulated runoff variability) and the hydrographic conditions near the GrIS glacier-ocean boundaries, there is a potential for doing so for Ilulissat Icefjord, West Greenland, and Sermilik Fjord, Southeast Greenland, due to, for example, quasi-continuous water salinity and temperature observations obtained by ringed seals near tidewater glacier margins ([http://efdl\\_5.cims.nyu.edu/srdl\\_seals/overview.html](http://efdl_5.cims.nyu.edu/srdl_seals/overview.html)). Instrumented seals provide a novel platform to examine the impacts from terrestrial freshwater on the otherwise inaccessible waters beneath the dense ice melangé within the first 0–10 km of the calving front.

- The spatiotemporal distribution of freshwater runoff from Greenland [17] might have an effect on the North Atlantic oceanic conditions, including the AMOC (Rahmstorf et al. 2005), and their impacts on the climate system (Bryden et al. 2005). The HydroFlow modeling tool is capable of providing the missing connection between terrestrial water fluxes and ocean circulation features such as the AMOC. Historically, the representation of Greenland freshwater discharge into the oceans has been either nonexistent or unrealistically simplistic. For example, ocean models have traditionally placed the freshwater runoff flux directly into the midocean areas (Weijer et al. 2012) rather than accurately accounting for the spatial and temporal distributions of actual Greenland runoff.



## References

- Abermann, J., van As, D., Petersen, D., and Nauta, M. 2014. A new glacier monitoring site in West Greenland. Abstract AGU Fall meeting, December 2014.
- AMAP 2009. The Greenland Ice Sheet in a Changing Climate: Snow, Water, Ice and Permafrost in the Arctic (SWIPA) 2009. By: Dahl-Jensen, D., Bamber, J., Bøggild, C. E., Buch, E., Christensen, J. H., Dethloff, K., Fahnestock, M., Marshall, S., Rosing, M., Steffen, K., Thomas, R., Truffer, M., van den Broeke, M., and van der Veen, C. J. Arctic Monitoring and Assessment Programme (AMAP), Oslo. 115 pp.
- AMAP 2011. Snow, Water, Ice, and Permafrost in the Arctic (SWIPA): Climate Change and the Cryosphere. Arctic Monitoring and Assessment Programme (AMAP). Oslo, Norway. Xii + 538 pp.
- Ananicheva, M. D., Kapustin, G. A., and Koreysha, M. M. 2006. Glacier changes in the Suntar-Khayate mountains and Chersky Range from the glacier inventory of the USSR and satellite images 2001–2003. *Data of Glaciological Studies*, 101, 163–169.
- Ananicheva, M. D. and Kapustin, G. 2010. Change of glacier state in mountain regions of the Russian sub-arctic: assessment by satellite imagery and aerial photography in the USSR glacier inventory [in Russian; English summary on last page]. Russian contribution into IPY, 2007-2008, 3, *Cryosphere*, 19–26.
- Anderson, R. K., Miller, G. H., Briner, J. P., Lifton, N. A., and DeVogel, S. B. 2008. A millennial perspective on Arctic warming from C-14 in quartz and plants emerging from beneath ice caps. *Geophysical Research Letters*, 35, L01502.
- Andreassen, L. M., Paul, F., Kaab, A., and Hausberg, J. E. 2008. Landsat-derived glacier inventory for Jotunheimen, Norway, and deduced glacier changes since the 1930s. *The Cryosphere*, 2, 131–145.
- Andreassen, L. M., Winsvold, S. H., Paul, F., and Hausberg, J. E. 2012. Inventory of Norwegian Glaciers. (eds.) Andreassen, L. M. and Winsvold, S. H. Norwegian Water Resources and Energy Directorate, pp. 1–242.
- Arendt, A. and Coauthors 2012. Randolph Glacier Inventory (v2.0): A dataset of global glacier outlines. Global Land Ice Measurements from Space, Boulder Colorado, digital media (with area corrections downloaded 2012). [Available online at <http://www.glims.org/RGI/>.]
- Bahr, D. B. 1997. Global distribution of glaciers properties: A stochastic scaling paradigm. *Water Resources Research*, 33, 1669–1679.
- Bahr, D. B., Dyurgerov, M., and Meier, M. F. 2009. Sea-level rise from glaciers and ice caps: A lower bound. *Geophysical Research Letters*, 36, L03501.
- Bahr, D. B., Meier, M. F., and Peckham, S. D. 1997. The physical basis of glacier volume-area scaling. *Journal of Geophysical Research*, 102, 20355–20362.
- Bales, R. C., Guo, Q., Shen, D., McConnell, J. R., Du, G., Burkhart, J. F., Spikes, V. B., Hanna, E., and Cappelen, J. 2009. Annual accumulation for Greenland updated using ice core data developed during 2000–2006 and analysis of daily coastal meteorological data. *Journal of Geophysical Research*, 114, D06116, doi: 10.1029/2008JD011208.
- Bamber, J. L., Ekholm, S. and Krabill, W. B. 2001. A new, highresolution digital elevation model of Greenland fully validated with airborne laser altimeter data. *Journal of Geophysical Research*, 106(B4), 6733–6745.
- Bamber, J. L., Steig, E., and Dahl-Jensen, D. 2009. What is the tipping point for the Greenland Ice Sheet. C15, Nuuk Climate Days, Changes of the Greenland Cryosphere Workshop & The Arctic Freshwater Budget International Symposium. Nuuk, Greenland, 25–27 August 2009.
- Bamber, J. L., van den Broeke, M., Ettema, J., and Lenaerts, J. 2012. Recent large increases in freshwater fluxes from Greenland into the North Atlantic. *Geophysical Research Letters*, 39, L19501.
- Barnes, S. L. 1964. A technique for maximizing details in numerical weather map analysis. *Journal of Applied Meteorology*, 3, 396–409.

- Barnes, S. L., 1973. Mesoscale objective analysis using weighted time series observations. NOAA Tech. Memo. ERL NSSL-62, National Severe Storms Laboratory, Norman, OK, 60 pp.
- Barrand, N. E. and Sharp, M. J. 2010. Sustained rapid shrinkage of Yukon glaciers since the 1957–1958 International Geophysical Year. *Geophysical Research Letters*, 37, L07501.
- Bauer, A. 1968. Nouvelle estimation du bilan de masses de L’Inlandsis du Groenland. *Deep-Sea Res.*, 14, 13–17.
- Benson, C. S. 1962. Stratigraphic studies in the snow and firn of Greenland Ice Sheet. U.S. Army SIPRE Research Rep. 70, 93 pp.
- Bolch, T., Menounos, B., and Wheate, R. 2010. Landsat-based inventory of glaciers in western Canada, 1985–2005. *Remote Sensing of Environment*, 114, 127–137.
- Bolch, T., Sorensen, L. S., Simonsen, S. B., Molg, N., Machguth, H., Rastner, P., and Paul, F. 2013. Mass loss of Greenland’s glaciers and ice caps 2—3-2008 revealed from ICESat laser altimetry data. *Geophysical Research Letters*, 40, 875–881.
- Born, E. W. and Böcher, J. 2001. The Ecology of Greenland. Nuuk. Ministry of Environment and Natural Resources. 429 pp.
- Box, J. E. 2002. Survey of Greenland instrumental temperature records: 1873–2001. *International Journal of Climatology*, 22, 1829–1847.
- Box, J. E., Bromwich, D. H., and Bai, L.-S. 2004. Greenland ice sheet surface mass balance 1991–2000: Application of Polar MM5 mesoscale model and in situ data. *Journal of Geophysical Research*, 109, D16105.
- Box, J. E., Bromwich, D. H., Veenhuis, B. A., Bai, L.-S., Stroeve, J. C., Rogers, J. C., Steffen, K., Haran, T., and Wang S.-H. 2006. Greenland ice sheet surface mass balance variability (1988–2004) from calibrated Polar MM5 output. *Journal of Climate*, 19, 2783–2800.
- Box, J. E., Cappelen, J., Chen, C., Decker, D., Fettweis, X., Mote, T., Tedesco, M., van de Wal, R. S. W., and Wahr, J. 2012. Greenland Ice Sheet. In Jeffries, M. O., Richter-Menge, J. A., and Overland, J. E. (Eds). Arctic Report Card 2012, <http://www.arctic.noaa.gov/reportcard>.
- Box, J. E. and Colgan, W. 2013. Greenland Ice Sheet Mass Balance Reconstruction. Part III: Marine Ice Loss and Total Mass Balance (1840–2010). *Journal of Climate*, 26, 6990–7002.
- Box, J. E. and Decker, D. T. 2011. Greenland marine-terminating glacier area changes: 2000–2010. *Annals of Glaciology*, 52, 91–98.
- Box, J. E. and Steffen, K. 2001. Sublimation estimates for the Greenland ice sheet using automated weather station observations. *Journal of Geophysical Research*, 106 (D24), 33965–33982.
- Box, J. E., Yang, L., Bromwich, D. H., and Bai, L. S. 2009. Greenland ice sheet surface air temperature variability: 1840–2007. *Journal of Climate*, 22, 4029–4049.
- Bintanja, R. and Selten, F. M. 2014. Future increases in Arctic precipitation linked to local evaporation and sea-ice retreat. *Nature*, 509, 479–482.
- Bjørk, A. A., Kjær, K. H., Korsgaard, N. J., Khan, S. A., Kjeldsen, K. K., Andresen, C. S., Box, J. E., Larsen, N. K., and Funder, S. 2012. An areal view of 80 years of climate-related glacier fluctuations in Southeast Greenland. *Natur Geoscience*, 5, 427–432.
- Bring, A. and Destouni, G. 2014. Arctic Climate and Water Change: Model and Observation Relevance for Assessment and Adaption. *Surveys in Geophysics*, 35, 853–877.
- Brown, R., Derksen, C., and Wang, L. 2010. A multi-data set analysis of variability and change in Arctic spring snow cover extent, 1967–2008. *Journal of Geophysical Research*, 115, D16111.
- Bryden, H. L., Longworth, H. R., and Cunningham, S. A. 2005. Slowing of the Atlantic meridional overturning circulation at 25°N. *Nature*, 438, 655–657.
- Callaghan, T. V., Johansson, M., Brown, R. D., Groisman, P. Y., Labba, N., Radionov, V., Barry, R. G., Bulygina, O. N., Essery, R. L. H., Frolov, D. M., Golubev, V. N., Grenfell, T. C., petrushina, M. N., Razuvaev, V. N., Robinson, D. A., Romanov, P., Shindell, D., Shmakin, A. B., Sokratov, S. A., Warren, S., and Yand, D. 2011. The changing face of Arctic snow cover: a synthesis of observed and projected changes. *Ambio*, 40, 17–31.
- Cappelen, J. (ed). 2013a. Greenland – DMI historical climate data collection 1873–2012 - with Danish abstracts. DMI Technical Report 13-04, Copenhagen, 74, [www.dmi.dk/dmi/tr13-04](http://www.dmi.dk/dmi/tr13-04).

- Cappelen, J. (ed). 2013b. Weather and climate data from Greenland 1958–2012 - observation data with description. DMI Technical Report 13-11, Copenhagen, 23, [www.dmi.dk/dmi/tr13-11](http://www.dmi.dk/dmi/tr13-11).
- Cazenave, A. and Llovel, W. 2010. Contemporary sea level rise. *Annual Review of Marine Science*, 2, 145–173.
- Church, J. A., Clark, P. U., Cazenave, A., Gregory, J. M., Jevrejeva, S., Levermann, A., Merrifield, M. A., Milne, G. A., Nerem, R. S., Nunn, P. D., Payne, A. J., Pfeffer, W. T., Stammer, D., and Unnikrishnan, A. S. 2013. Sea Level Change. In: *Climate Change 2013: The Physical Science Basis. Contribution of Working Group I to the Fifth Assessment Report of the Intergovernmental Panel on Climate Change* [Stocker, T. F., Qin, D., Plattner, G.-K., Tignor, M., Allen, S. K., Boschung, J., Nauels, A., Xia, Y., Bex, V., and Midgley, P. M. (eds.)]. Cambridge University Press, Cambridge, United Kingdom and New York, NY, USA.
- Church, J. A., Greory, J. M., Huybrechts, P., Kuhn, M., Lambeck, C., Nhuan, M. T., Qin, D., and Woodworth, P. L. 2001. Change in sea level. *Climate Change 2001: The Scientific Basis*. Houghton, J. T. et al., Eds., Cambridge University Press, 639–694.
- Chylek, P., Folland, C., Lesins, G., Wang, M. and Dubey, M. 2009. Arctic air temperature change amplification and the Atlantic multidecadal oscillation. *Geophysical Research Letter*, 36, L14801.
- Chylek, P., Folland, C. K., Lesins, G., and Dubey, M. K. 2010. Twentieth century bipolar seesaw of the Arctic and Antarctic surface air temperatures. *Geophysical Research Letters*, 37, L08703.
- Cogley, J. G. 2009a. Geodetic and direct mass-balance measurements: comparison and joint analysis. *Annals of Glaciology*, 50, 96–100.
- Cogley, J. G. 2009b. A more complete version of the World Glacier Inventory. *Annals of Glaciology*, 50, 32–38.
- Cogley, J. G. 2012. The Future of the World’s Glaciers, in: *The Future of the World’s Climate*, edited by: Henderson-Sellers, A. and McGuffie, K., 197–222, Elsevier, Amsterdam, 2012.
- Cogley, J. G., Hock, R., Rasmussen, L. A., Arendt, A. A., Bauder, A., Braithwaite, R. J., Jansson, P., Kaser, G., Möller, M., Nicholson, L. and Zemp, M. 2011. Glossary of Glacier Mass Balance and Related Terms. *IHP-VII Technical Documents in Hydrology*, No. 86, IACS Contribution No. 2, UNESCO-IHP, Paris, pp 124.
- Collins, M., Knutti, R., Arblaster, J., Dufresne, J.-L., Fichefet, T., Friedlingstein, P., Gao, X., Gutowski, W. J., Johns, T., Krinner, G., Shongwe, M., Tebaldi, C., Weaver, A.J., and Wehner, M. 2013. Long-term Climate Change: Projections, Commitments and Irreversibility. In: *Climate Change 2013: The Physical Science Basis. Contribution of Working Group I to the Fifth Assessment Report of the Intergovernmental Panel on Climate Change* [Stocker, T. F., Qin, D., Plattner, G.-K., Tignor, M., Allen, S. K., Boschung, J., Nauels, A., Xia, Y., Bex, V., and Midgley, P. M. (eds.)]. Cambridge University Press, Cambridge, United Kingdom and New York, NY, USA.
- Clarke, G. K. C. 1996. Lumped-element model for subglacial transport of solute and suspended sediment. *Annals of Glaciology*, 22, 152–159.
- Csatho, B. M., Schenk, A. F., van der Veen, C. J., Babonis, G., Duncan, K., Rezvanbehbahani, S., van den Broeke, M. R., Simonsen, S. B., Nagarajan, S., and van Angelen, J. H. 2014. Laser altimetry reveals complex pattern of Greenland Ice Sheet dynamics. *Proceedings of the National Academy of Sciences*, doi:10.1073/pnas.1411680112.
- Cuffey, K. M. and Paterson, W. S. B. 2010. *The Physics of Glaciers*. Fourth Edition. Elsevier, pp. 693.
- DHI Water and Environment 2003a. MIKE 11 Reference Manual, DHI Water and Environment, Denmark.
- DHI Water and Environment 2003b. MIKE 11 User Guide, DHI Water and Environment, Denmark.
- Dickson, R. R., Osborn, T. J., Hurrell, J. W., Meincke, J., Blindheim, J., Adlandsvik, B., Vinje, T., Alekseev, G., and Maslowski, W. 2000. The Arctic Ocean response to the North Atlantic Oscillation. *Journal of Climate*, 13, 2671–2696.

- Dodson, R., and Marks, D. 1997. Daily air temperature interpolation at high spatial resolution over a large mountainous region. *Climate Research*, 8, 1–20.
- Douville, H., Royer, J. F. and Mahfouf, J. F. 1995. A new snow parameterization for the Meteo-France climate model. Part 1. Validation in stand-alone experiments. *Climate Dynamic*, 12(1), 21–35.
- Dowdeswell, E. K., Dowdeswell, J. A., and Cawkwell, F. 2007. On the glaciers of Bylot Island, Nunavut, Arctic Canada. *Arctic, Antarctic, and Alpine Research*, 29, 402–411.
- Dyurgerov, M., Meier, M. F., and Bahr, D. B. 2009. A new index of glacier area change; a tool for glacier monitoring. *Journal of Glaciology*, 55(192), 710–716
- Dyurgerov, M. B. 2010. Data of glaciological studies—Reanalysis of glacier changes: From the IGY to the IPY, 1960–2008. Publication 108, Institute of Arctic and Alpine Research, 116 pp.
- Dyurgerov, M. B. and Meier, M. F. 2005. Glaciers and the Changing Earth System: A 2004 Snapshot, Occas. Paper 58, 117 pp., Institute of Arctic and Alpine Research, Boulder, Colorado.
- Enderlin, E. M., Howat, I. M., Jeong, S., Hoh, M.-J., van Angelen, J. H., and van den Broeke, M. R. 2014. An improved mass budget for the Greenland ice sheet. *Geophysical Research Letters*, 41(3), 866–872.
- Erlykin, A. D., Wolfendale, A. W. and Hanna, E., 2012. Global warming – some perspectives. *Journal of Environmental Science and Engineering*, B1, 2(4), 499–509.
- Ettema, J., van den Broeke, M. R., van Meijgaard, E., van den Berg, W. J., Bamber, J. L., Box, J. E., and Bales, R. C. 2009. Higher surface mass balance of the Greenland ice sheet revealed by high-resolution climate modeling. *Geophysical Research Letters*, 36, L12501.
- Fausto, R. S., Mernild, S. H., Hasholt, B., Ahlstrøm, A. P. and Knudsen, N. T. 2012. Modelling suspended sediment concentration and transport for the hydrological years 2004–2006, Mittivakkat Glacier, Southeast Greenland. *Arctic, Antarctic, and Alpine Research*, 44(3), 306–318, doi:10.1657/1938-4246-44.3.
- Fettweis X. 2007. Reconstruction of the 1979–2006 Greenland ice sheet surface mass balance using the regional climate model MAR. *The Cryosphere*, 1, 21–40.
- Fettweis, X., Franco, B., Tedesco, M., van Angelen, J. H., Lenaerts, J. T. M., van den Broeke, M. R., and Gallee, H. 2013. Estimating the Greenland ice sheet surface mass balance contribution to future sea level rise using the regional atmospheric climate model MAR. *The Cryosphere*, 7, 469–489.
- Fettweis, X., Gallee, H., Lefebvre, L., van Ypersele, J.–P. 2005. Greenland surface mass balance simulated by a regional climate model and comparison with satellite derived data in 1990–1991. *Climate Dynamics*, 24, 623–640.
- Fettweis, X., Hanna, E., Gallee, H., Huybrechts, P., and Erpicum, M. 2008. Estimation of the Greenland ice sheet surface mass balance during 20th and 21st centuries. *The Cryosphere*, 2, 117–129.
- Fettweis, X., Tedesco, M., van den Broeke, M. R., and Ettema, J. 2011. Melting trends over the Greenland ice sheet (1958–2009) from spaceborne microwave data and regional climate models. *The Cryosphere*, 5, 359–375.
- Flowers, G. E. and Clarke, G. K. C. 2002a. A multicomponent coupled model of glacier hydrology. 1. Theory and synthetic examples. *Journal of Geophysical Research*, 107(B11), 2287.
- Flowers, G. E. and Clarke, G. K. C. 2002b. A multicomponent coupled model of glacier hydrology. 2. Application to Trapridge Glacier, Yukon, Canada. *Journal of Geophysical Research*, 107(B11), 2288.
- Fristrup, B. 1970. New Geographical Station in Greenland. *Geografisk Tidsskrift-Danish Journal of Geography*, 69, 199–203.
- Fyke, J. G., Vizcaino, M., Lipscomb, W., and Price, S. 2014. Future climate warming increases Greenland ice sheet surface mass balance variability. *Geophysical Research Letters*, 41(2), 470–475.
- Gardelle, J., Berthier, E., and Arnaud, Y. 2012. Slight mass gain of Karakoram glaciers in the early twenty-first century. *Nature Geoscience*, 5, 322–325.

- Gardner, A. S., Moholdt, G., Cogley, J. G., Wouters, B., Arendt, A. A., Wahr, J., Berthier, E., Hock, R., Pfeffer, W. T., Kaser, G., Ligtenberg, S. R. M., Bolch, T., Sharp, M. J., Hagen, J. O., van den Broeke, M. R., and Paul, F. A. 2013. Reconciled estimate of glacier contributions to sea level rise: 2003 to 2009, *Science*, 340, 852–857.
- Glazovsky, A. and Macheret, Y. 2006. Eurasian Arctic. In: Kotlyakov V M (Ed.). Glaciation in north and central Eurasia in present time. [in Russian with English summary], pp. 97–114 and 438–445, Nauka, Moscow.
- Grinsted, A. 2013. An estimate of global glacier volume. *The Cryosphere*, 7, 141–151.
- Hall, D. K., Comiso, J. C., DiGirolamo, N. E., Shuman, C. A., Box, J. E., Koenig, L. S. Variability in the surface temperature and melt extent of the Greenland ice sheet from MODIS. *Geophysical Research Letters*, 40(10), 2144–2120.
- Hanna, E., Cappelen, J., Fettweis, X., Huybrechts, P., Luckman, A., and Ribergaard, M. H. 2009. Hydrologic response of the Greenland Ice Sheet: the role of oceanographic forcing. *Hydrological Processes*, 23(1), 7–30.
- Hanna, E., Fettweis, X., Mernild, S. H., Cappelen, J., Ribergaard, M., Shuman, C., Steffen, K., Wood, L., and Mote, T. 2014. Atmospheric and oceanic climate forcing of the exceptional Greenland Ice Sheet surface melt in summer 2012. *International Journal of Climatology*, 34, 1022–1037.
- Hanna, E., Huybrechts, P., Cappelen, J., Steffen, K., Bales, R. C., Burgess, E. W., McConnell, J. R., Steffensen, J. P., van den Broeke, M., Wake, L., Bigg, G. R., Griffiths, M., and Savas, D. 2011. Greenland Ice Sheet surface mass balance 1870 to 2010 based on Twentieth Century Reanalysis, and links with global climate forcing. *Journal of Geophysical Research Atmosphere*, 116, D24121.
- Hanna, E., Huybrechts, P., Janssens, I., Cappelen, J., Steffen, K., and Stephens, A. 2005. Runoff and mass balance of the Greenland ice sheet: 1958–2003. *Journal of Geophysical Research*, 110, D13108.
- Hanna, E., Huybrechts, P., Steffen, K., Cappelen, J., Huff, R., Shuman, C., Irvine-Fynn, T., Wise, S., and Griffiths, M. 2008. Increased runoff from melt from the Greenland ice sheet: A response to global warming. *Journal of Climate*, 21, 331–341.
- Hanna, E., McConnell, J., Das, S., Cappelen, J., and Stephens, A. 2006. Observed and modelled Greenland Ice Sheet snow accumulation, 1958–2003, and links with regional climate forcing. *Journal of Climate*, 19(3), 344–358.
- Hanna, E., Mernild, S. H., Cappelen, J., and Steffen, K. 2012. Recent warming in Greenland in a long-term instrumental (1881–2012) climatic context. Part 1: Evaluation of surface air temperature records. *Environmental Research Letters*, 7, 045404.
- Hanna, E., Navarro, F. J., Pattyn, F., Domingues, C., Fettweis, X., Ivins, E., Nicholls, R. J., Ritz, C., Smith, B., Tulaczyk, S., Whitehouse, P., and Zwally, J. 2013b. Ice-sheet mass balance and climate change. *Nature*, 498, 51–59.
- Hansen, J., Ruedy, R., Sato, M., and Lo, K. 2010. Global surface temperature change. *Reviews of Geophysics*, 48, RG4004.
- Hansen, B. U., Sigsgaard, C., Hinkler, J., Mernild, S. H., Petersen, D., Rasch, M., Tamstorf, M. P., Hasholt, B., Rasmussen, L., and Cappelen, J. 2008. Present day climate at Zackenberg. In High-Arctic Ecosystem Dynamics in a Changing Climate: Ten years of monitoring and research at Zackenberg Research Station, Northeast Greenland. (eds) Meltofte H., Christensen, T. R., Elberling, B., Forchhammer, M. C. & Rasch, M. Hydrology and Transport of Sediment and Solutes at Zackenberg. *Advances in Ecological Research*, 40, 197–221.
- Hartmann, D. L., Klein Tank, A.M.G., Rusticucci, M., Alexander, L.V., Brönnimann, S., Charabi, Y., Dentener, F. J., Dlugokencky, E. J., Easterling, D. R., Kaplan, A., Soden, B. J., Thorne, P. W., Wild, M., and Zhai, P. M. 2013. Observations: Atmosphere and Surface. In: Climate Change 2013: The Physical Science Basis. Contribution of Working Group I to the Fifth Assessment Report of the Intergovernmental Panel on Climate Change [Stocker, T. F., Qin, D., Plattner, G.-K., Tignor, M., Allen, S. K., Boschung, J., Nauels, A., Xia, Y., Bex, V., and Midgley, P. M. (eds.)]. Cambridge University Press, Cambridge, United Kingdom and New York, NY, USA.

- Hasholt, B., Hansen, B. U., Humlum, O. and Mernild, S. H. 2004. Meteorological stations at the Sermilik Station, southeast Greenland – physical environment and meteorological observations 2002. *Geografisk Tidsskrift-Danish Journal of Geography*, 104(2), 47–58.
- Hasholt, B., and Jakobsen, B. H. 2008. 75 years of research at the Sermilik Station: 1933–2008. *Geografisk Tidsskrift-Danish Journal of Geography*, 108, 1–4.
- Hasholt, B., Kruger, J., and Skjerna, L. 2008b. Landscape and sediment processes in a proglacial valley, the Mittivakkat Glacier area, Southeast Greenland. *Geografisk Tidsskrift-Danish Journal of Geography*, 108(1), 97–110.
- Hasholt, B., Liston, G. E., and Knudsen, N. T. 2003. Snow distribution modelling in the Ammassalik region, southeast Greenland. *Nordic Hydrology*, 34, 1–16.
- Hasholt, B., and Mernild, S. H. 2004. Estimation of water balance in and around the Mittivakkat Glacier basin, Ammassalik Island, southeast Greenland, in: Northern Research Basins Water Balance, Edited by Kane, D. L. and Yang, D., Wallingford, UK. *IAHS*, 290, 129–142.
- Hasholt, B. and Mernild, S. H. 2006. Glacial erosion and sediment transport in the Mittivakkat Glacier catchment, Ammassalik island, southeast Greenland, 2005. *IAHS*, 306, 45–55.
- Hasholt, B., and Mernild, S. H. 2008. Hydrology, sediment transport and water resources of Ammassalik Island, SE Greenland. *Geografisk Tidsskrift-Danish Journal of Geography*, 108(1), 73–95.
- Hasholt, B., Mernild, S. H., Sigsgaard, C., Elberling, B., Petersen, D., Jakobsen, B. H., Hansen, B. U., Hinkler, J., and Søgaard, H. 2008a. Hydrology and Transport of Sediment and Solutes at Zackenberg. In High-Arctic Ecosystem Dynamics in a Changing Climate: Ten years of monitoring and research at Zackenberg Research Station, Northeast Greenland. (eds) Meltofte H., Christensen, T. R., Elberling, B., Forchhammer, M. C. and Rasch, M. Hydrology and Transport of Sediment and Solutes at Zackenberg. *Advances in Ecological Research*, 40, 111–149.
- Hasholt, B., Mikkelsen, A. B., Nielsen, M. H., and Larsen, M. A. D. 2013. Observations of runoff and sediment and dissolved loads from the Greenland Ice Sheet at Kangerlussuaq, West Greenland, 2007 to 2010. *Zeitschrift für Geomorphologie*, 57(2), 3–27.
- Helm, V., Humbert, A., and Miller, H. 2014. Elevation and elevation change of Greenland and Antarctica derived from CryoSat-2. *The Cryosphere*, 8, 1–21.
- Hewitt, K. 2005. The Karakoram Anomaly? Glacier Expansion and the ‘Elevation Effect,’ Karakoram Himalaya. *Mountain Research and Development*, 25(4), 332–340.
- Hinzman, L. D., Deal, C., McGuire, D. A., Mernild, S. H., Polyakov, I., and Walsh, J. 2013. Trajectory of the Arctic as an Integrated System. *Ecological Applications*, 23(8), 1837–1868.
- Hock, R. and Jansson, P. 2005. Modeling glacier hydrology. Encyclopedia of Hydrological Sciences, Vol. 4, Anderson, M. G. and McDonnell, J. (Eds.). John Wiley & Sons, Ltd, pp. 2647–2655.
- Hock, R., de Woul, M., Radić, V., and Dyurgerov, M. 2009. Mountain glaciers and ice caps around Antarctica make a large sea-level rise contribution. *Geophysical Research Letters*, 36, L07501.
- Holland, D. M., Thomas, R. H., de Young, B., Ribergaard, M. H., and Lyberth, B. 2008. Acceleration of Jakobshavn Isbræ triggered by warm subsurface ocean waters. *Nature Geoscience*, 1(10), 659–664.
- Hosler, C. R. 1961. Low level inversion frequency in the contiguous United States. *Monthly Weather Review*, 89, 310–339.
- Howat, I. M. and Eddy, A. 2011. Multi-decadal retreat of Greenland’s marine-terminating glaciers. *Journal of Glaciology*, 57, 389–396.
- Howat, I. M., Joughin, I., and Scambos, T. 2007. Rapid changes in ice discharge from Greenland outlet glaciers. *Science*, 315, 1559, doi:10.1126/science.1138478, (advanced publication in Science Express on 8 February 2007).
- Howat, I. M., Joughin, I., Tulaczyk, S., and Gogineni, S. 2005. Rapid retreat and acceleration of Helheim Glacier, East Greenland, *Geophysical Research Letters*, 32, L22502, doi:10.1029/2005GL024737.



- Howat, I. M., Ahn, Y., Joughin, I., van den Broeke, M. R., Lenaerts, J. T. M., and Smith, B. 2011. Mass balance of Greenland's three largest outlet glaciers, 2000–2010. *Geophysical Research Letters*, 38, L12501, doi:10.1029/2011GL047565.
- Humlum, O. and Christiansen, H. H. 2008. Geomorphology of the Ammassalik Island, SE Greenland. *Geografisk Tidsskrift-Danish Journal of Geography*, 108(1), 5–20.
- Hurkmans, R. T. W. L., Bamber, J. L., Davis, C. H., Joughin, I. R., Khvorostovsky, K. S., Smith, B. S., and Schoen, N. 2014. Time-evolving mass loss of the Greenland Ice Sheet from satellite altimetry. *The Cryosphere*, 8, 1725–1740.
- Hurrell, J. W. and van Loon, H., 1997. Decadal variations in climate associated with the North Atlantic oscillation, *Climate Change*, 36, 301–326.
- Huss, M. and Farinotti, D. 2012. Distributed ice thickness and volume of all glaciers around the world. *Journal of Geophysical Research*, 117, F04010.
- Hynek, B., Weyss, G. Binder, D., Schöner, W. 2014. Mass Balance of Freya Glacier, 2007/2008 - 2012/2013. *Pangea*, doi:10.1594/PANGAEA.831035.
- IPCC, 2013, Summary for Policymakers. In: Climate Change 2013: The Physical Science Basis. Contribution of Working Group I to the Fifth Assessment Report of the Intergovernmental Panel on Climate Change [Stocker, T.F., Qin, D., Plattner, G.-K., Tignor, M., Allen, S. K., Boschung, J., Nauels, A., Xia, Y., Bex V., and Midgley, P.M. (eds.)]. Cambridge University Press, Cambridge, United Kingdom and New York, NY, USA.
- Iziomon, M. G. Mayer, H., and Matzarakis, A. 2003. Downward atmospheric longwave irradiance under clear and cloudy skies: Measurement and parameterization. *Journal of Atmospheric and Solar-Terrestrial Physics*, 65, 1107–1116.
- Jansson, P., Hock, R., and Schneider, T. 2003. The concept of glacier storage: a review. *Journal of Hydrology*, 282, 116–129.
- Johannessen, O. M., Korabely, A., Miles, V., Miles, M.W., and Solberg, K. E. 2011. Interaction Between the Warm Subsurface Atlantic Water in the Sermilik Fjord and Helheim Glacier in Southeast Greenland. *Surveys in Geophysics*, 32, 387–396, doi:10.1007/s10712-011-9130-6.
- Kadygrov, E. N., Viazankin, A. S., Westwater, E. R., and Widener, K. B. 1999. Characteristics of the low-level temperature inversion at the Northern Slope of Alaska on the based of microwave remote sensing data. *Proc. Ninth ARM Science Team Meeting*, San Antonio, TX, Dept. of Energy, 1–7.
- Kahl, J. D. 1990. Characteristics of the low-level temperature inversion along the Alaska Coast. *International Journal of Climatology*, 10, 537–548.
- Kahl, J. D., Serreze, M. D., and Schnell, R. C. 1992. Tropospheric low-level temperature inversions in the Canadian Arctic. *Atmosphere–Ocean*, 30, 511–529.
- Kane, D. L., and Yang, D. 2004. Overview of water balance determinations for high latitude watersheds. Northern Research Basins Water Balance. *IAHS*, 290, 1–12.
- Kaplan, A., Cane, M. A., Kushnir, Y. and Clement, A. C. 1998. Analyses of global sea surface temperatures 1856–1991. *Journal of Geophysical Research*, 103, 18575–18589.
- Kargel, J. S., Ahlstrøm, A. P., Alley, R. B., Bamber, J. L., Benham, T. J., Box, J. E., Chen, C., Christoffersen, P., Citterio, M., Cogley, J. G., Jiskoot, H., Leonard, G. J., Morin, P., Scambos, T., Sheldon, T., and Willis, I. 2012. Brief communication Greenland's shrinking ice cover: “fast times” but not that fast. *The Cryosphere*, 6, 533–537.
- Kaser, G., Cogley, J. G., Dyurgerov, M. B., Meier, M. F., and Ohmura, A. 2006. Mass balance of glaciers and ice caps: Consensus estimates for 1961–2004. *Geophysical Research Letters*, 33, L19501.
- Kattsov, V. M., et al. 2007. Simulation and projection of Arctic freshwater budget components by the IPCC AR4 global climate models. *Journal of Hydrometeorology*, 8, 571–589.
- Keegan, K. M., Albert, M. R., McConnell, J. R., and Baker, I. 2014. Climate change and forest fires synergistically drive widespread melt events of the Greenland Ice Sheet. *Proceedings of the National Academy of Sciences*, 111(22), 7964–7967.
- Khan, S. A., Kjær, K. K., Bevis, M., Bamber, J. L., Wahr, J., Kjeldsen, K. K., Bjørk, A. A., Korsgaard, N. J., Stearns, L. A., van den Broeke, M. R., Liu, L., Larsen, N. K., and Muresan,

- I. S. 2014. Sustained mass loss of the northeast Greenland Ice sheet triggered by regional warming. *Nature Climate Change*, doi:10.1038/nclimate2161.
- Kirtman, B., Power, S. B., Adedoyin, J. A., Boer, G. J., Bojariu, R., Camilloni, I., Doblas-Reyes, F. J., Fiore, A. M., Kimoto, M., Meehl, G. A., Prather, M., Sarr, A., Schär, C., Sutton, R., van Oldenborgh, G. J., Vecchi G., and Wang, H. J. 2013. Near-term Climate Change: Projections and Predictability. In: *Climate Change 2013: The Physical Science Basis. Contribution of Working Group I to the Fifth Assessment Report of the Intergovernmental Panel on Climate Change* [Stocker, T. F., Qin, D., Plattner, G.-K., Tignor, M., Allen, S. K., Boschung, J., Nauels, A., Xia, Y., Bex, V., and Midgley, P. M. (eds.)]. Cambridge University Press, Cambridge, United Kingdom and New York, NY, USA.
- Knudsen, N. T. and Hasholt, B. 1999. Radio-echo sounding at the Mittivakkat Gletscher, southeast Greenland. *Arctic, Antarctic, and Alpine Research*, 31(3), 321–328.
- Knudsen, N. T. and Hasholt, B. 2004. Mass balance observations at Mittivakkat Glacier, southeast Greenland 1995–2002. *Nordic Hydrology*, 35, 381–390.
- Knudsen, N. T. and Hasholt, B. 2008. Mass balance observations at Mittivakkat Glacier, Ammassalik Island, Southeast Greenland 1995–2006. *Geografisk Tidsskrift-Danish Journal of Geography*, 108(1), 111–120.
- Koch, S. E., DesJardins, M., and Kocin, P. J. 1983. An interactive Barnes objective map analysis scheme for use with satellite and conventional data. *Journal of Applied Meteorology*, 22, 1487–1503.
- Kunkel, K. E. 1989. Simple procedures for extrapolation of humidity variables in the mountains western United States. *Journal of Climate*, 2, 656–669.
- Kjær, K. H. and others 2012. Aerial Photographs Reveal Late-20<sup>th</sup>-Century Dynamic Ice Loss on Northwestern Greenland. *Science*, 337, 569–573.
- Larsen, S. H., Citterio, M., Hock, R., and Ahlstrom, A. P. 2012. Mass and surface energy balance of A.P. Olsen ice cap, NE Greenland, from observations and modeling (1995–2011). AGU Fall abstract C23B-0660.
- Leeson, A. A., Shepherd, A., Briggs, K., Howat, I., Fettweis, X., Morlighem, M., Rignot, E. 2015. Supraglacial lakes on the Greenland ice sheet advance inland under warming climate. *Nature Climate Change*, 5, 51–55.
- Lemke, P. and Coauthors 2007. Observations: Changes in snow, ice and frozen ground. *Climate Change 2007: The Physical Science Basis*, S. Solomon et al., Eds., Cambridge University Press, 337–383.
- Lewis, S. M., and L. C. Smith, 2009: Hydrological drainage of the Greenland ice sheet. *Hydrological Processes*, 23, 2004–2011, doi:10.1002/hyp.7343.
- Liston, G. E. 1995. Local advection of momentum, heat, and moisture during the melt of patchy snow covers. *Journal of Applied Meteorology*, 34, 1705–1715.
- Liston, G. E. and Elder, K. 2006a. A distributed snow-evolution modeling system (SnowModel). *Journal of Hydrometeorology*, 7, 1259–1276.
- Liston, G. E. and Elder, K. 2006b. A meteorological distribution system for high-resolution terrestrial modeling (MicroMet). *Journal of Hydrometeorology*, 7, 217–234.
- Liston, G. E., Haehnel, R. B., Sturm, M., Hiemstra, C. A., Berezovskaya, S., and Tabler, R. D. 2007. Simulating complex snow distributions in windy environments using SnowTran-3D. *Journal of Glaciology*, 53, 241–256.
- Liston, G. E. and Hiemstra, C. A. 2008. A simple data assimilation system for complex snow distributions (SnowAssim). *Journal of Hydrometeorology*, 9, 989–1004.
- Liston, G. E. and Hiemstra, C. A. 2011. The changing cryosphere: Pan-Arctic snow trends (1979–2009). *Journal of Climate*, 24, 5691–5712.
- Liston, G. E. and Mernild, S. H. 2012 [10]. Greenland freshwater runoff. Part I: A runoff routing model for glaciated and non-glaciated landscapes (HydroFlow). *Journal of Climate*, 25(17), 5997–6014.
- Liston, G. E. and Sturm, M. 1998. A snow-transport model for complex terrain. *Journal of Glaciology*, 44, 498–516.

- Liston, G. E. and Sturm, M. 2002. Winter precipitation patterns in Arctic Alaska determined from a blowing-snow model and snow depth observations. *Journal of Hydrometeorology*, 3, 646–659.
- Liston, G. E., Winther, J.-G., Bruland, O., Elvehøy, H. and Sand, K. 1999. Below surface ice melt on the coastal Antarctic ice sheet. *Journal of Glaciology*, 45, 273–285.
- Luckman, A. T., Murray, T., de Lange, R., and Hanna E. 2006. Rapid and synchronous ice-dynamic changes in East Greenland. *Geophysical Research Letters*, 33, L03503, doi:10.1029/2005GL025428.
- Marzeion, B., Cogley, J. G., Richter, K., and Pakes, D. 2014. Attribution of global glacier mass loss to anthropogenic and natural causes. *Science*, 345(6199), 919–921.
- Marzeion, B., Jarosch, A. H., and Hofer, M. 2012. Past and future sea-level change from the surface mass balance of glaciers. *Cryosphere*, 6, 1295–1322.
- McBean, G., Alekseev, G., Chen, D., Foerland, E., Fyfe, J., Groisman, P. Y., King R., Melling, H., Vose, R., Whitfield, P. H. (2005). Arctic climate: past and present. In: Arctic climate impact assessment. Cambridge University Press, Cambridge, pp. 21–60.
- McGuire, A. D., Chapin, F. S., Walsh, J. E., and Wirth, C. 2006. Integrated regional changes in Arctic climate feedbacks: implications for the global climate system. *Annual Review of Environment and Resources*, 31, 61–91.
- Meier, M. F., Dyurgerov, M. B., Rick, U. K., O’Neel, S., Pfeffer, W. T., Anderson, R. S., Anderson, S. P., and Glazovsky, A. F. 2007. Glaciers dominate eustatic sea-level rise in the 21<sup>st</sup> century. *Science*, 317, 1064–1067.
- Mernild, S. H. 2006. The internal drainage system of the lower Mittivakkat Glacier, Ammassalik Island, SE Greenland. *Geografisk Tidsskrift-Danish Journal of Geography*, 106(1), 13–24.
- Mernild, S. H., Hanna, E., McConnell, J. R., Sigl, M., Beckerman, A. P., Yde, J. C., Cappelen, J., and Steffen, K. 2014 [2]. Greenland precipitation trends in a long-term instrumental climate context (1890–2012): Evaluation of coastal and ice core records. *International Journal of Climatology*, doi:10.1002/joc.3986.
- Mernild, S. H., Hanna, E., Yde, J. C., Cappelen, J., and Malmros, J. K. 2014 [1]. Coastal Greenland air temperature extremes and trends 1890–2010: Annual and monthly analysis. *International Journal of Climatology*, 34, 1472–1487.
- Mernild, S. H., Hanna, E., Yde, J. C., Seidenkrantz, M.-S., Wilson, R., and Knudsen, N. T. 2014 [13]. Atmospheric and oceanic influence on mass-balance trends of northern North Atlantic region land-terminating glaciers. *Geografiska Annaler: Series A, Physical Geography*, 96, 561–577, doi:10.1111/geoa.12053.
- Mernild, S. H., Hansen, B. U., Jakobsen, B. H., and Hasholt, B. 2008 [3]. Climatic conditions at the Mittivakkat Glacier catchment (1994–2006), Ammassalik Island, SE Greenland, and in a 109-year perspective (1898–2006). *Geografisk Tidsskrift-Danish Journal of Geography*, 108(1), 51–72.
- Mernild, S. H. and Hasholt, B. 2006. Climatic control on river discharge simulations, Mittivakkat Glacier catchment, Ammassalik Island, SE Greenland. *Nordic Hydrology*, 37(4–5), 327–346.
- Mernild, S. H., Hasholt, B., Kane, D. L., and Tidwell, A. C. 2008. Jökulhlaup Observed at Greenland Ice Sheet. *Eos Trans. AGU*, 99(35), 321–322.
- Mernild, S. H., Hasholt, B. and Liston, G. E. 2006. Water flow through Mittivakkat Glacier, Ammassalik Island, SE Greenland. *Geografisk Tidsskrift-Danish Journal of Geography*, 106(1), 25–43.
- Mernild, S. H., Hasholt, B., and Liston, G. E. 2008b. Climatic control on river discharge simulations, Zackenberg River Drainage basin, NE Greenland. *Hydrological Processes*, 22, 1932–1948.
- Mernild, S. H., Howat, I. M., Ahn, Y., Liston, G. E., Steffen, K., Jakobsen, B. H., Hasholt, B., Fog, B., and van As, D. 2010 [19]. Freshwater flux to Sermilik Fjord, SE Greenland. *The Cryosphere*, 4, 453–465, doi:10.5194/tc-4-453-2010.
- Mernild, S. H., Kane, D. L., Hansen, B. U., Jakobsen, B. H., Hasholt, B. and Knudsen, N. T. 2008a. Climate, glacier mass balance, and runoff (1993–2005) for the Mittivakkat Glacier

- catchment, Ammassalik Island, SE Greenland, and in a long term perspective (1898–1993). *Hydrology Research*, 39(4), 239–256.
- Mernild, S. H., Knudsen, N. T., Hoffman, M. J., Yde, J. C., Lipscomb, W. H., Hanna, E., Malmros, J. K., and Fausto, R. S. 2013 [5]. Volume and Velocity changes at Mittivakkat Gletscher, Southeast Greenland, 1994–2012. *Journal of Glaciology*, 59(216), 660–670, doi:10.3189/2013JoG13J017.
- Mernild, S. H., Knudsen, N. T., Lipscomb, W. H., Yde, J. C., Malmros, J. K., Jakobsen, B. H., and Hasholt, B. 2011 [4]. Increasing mass loss from Greenland's Mittivakkat Gletscher. *The Cryosphere*, 5, 341–348, doi:10.5194/tc-5-341-2011.
- Mernild, S. H., Lipscomb, W. H., Bahr, D. B., Radić, V., and Zemp, M. 2013 [12]. Global glacier retreat: A revised assessment of committed mass losses and sampling uncertainties. *The Cryosphere*, 7, 1565–1577.
- Mernild, S. H. and Liston, G. E. 2010 [9]. The influence of air temperature inversion on snow melt and glacier surface mass-balance simulations, SW Ammassalik Island, SE Greenland. *Journal of Applied Meteorology and Climate*, 49(1), 47–67.
- Mernild, S. H. and Liston, G. E. 2012 [17]. Greenland freshwater runoff. Part II: Distribution and trends, 1960–2010. *Journal of Climate*, 25(17), 6015–6035.
- Mernild, S. H., Liston, G. E., Hasholt, B., and Knudsen, N. T. 2006a. Snow distribution and melt modeling for Mittivakkat Glacier, Ammassalik Island, Southeast Greenland. *Journal of Hydrometeorology*, 7, 808–824.
- Mernild, S. H., Liston, G. E., and Hiemstra, C. A. 2014 [14]. Northern Hemisphere glaciers and ice caps surface mass balance and contribution to sea-level rise. *Journal of Climate*, 27(15), 6051–6073.
- Mernild, S. H., Liston, G. E., Hiemstra, C. A. and Christensen, J. H. 2010 [18]. Greenland Ice Sheet surface mass-balance modeling in a 131-year perspective 1950–2080. *Journal of Hydrometeorology*, 11(1), 3–25.
- Mernild, S. H., Liston, G. E., Hiemstra C. A., and Steffen, K. 2008 [15]. Surface Melt Area and Water Balance Modeling on the Greenland Ice Sheet 1995–2005. *Journal of Hydrometeorology*, 9(6), 1191–1211.
- Mernild, S. H., Liston, G. E., Hiemstra, C. A., Christensen, J. H., Stendel, M., and Hasholt, B. 2011. Surface mass-balance and runoff modeling using HIRHAM4 RCM at Kangerlussuaq (Søndre Strømfjord), West Greenland, 1950–2080. *Journal of Climate*, 24(3), 609–623.
- Mernild, S. H., Liston, G. E., Hiemstra, C. A., Steffen, K., Hanna, E., and Christensen, J. H. 2009. Greenland Ice Sheet surface mass-balance modeling and freshwater flux for 2007, and in a 1995–2007 perspective. *Hydrological Processes*, doi:10.1002/hyp.7354.
- Mernild, S. H., Liston, G. E., Kane, D. L., Hasholt, B. and Knudsen, N. T. 2008 [8]. Snow, runoff, and mass balance modelling for the entire Mittivakkat Glacier (1998–2006), Ammassalik Island, SE Greenland. *Geografisk Tidsskrift-Danish Journal of Geography*, 108(1), 121–136.
- Mernild, S. H., Liston, G. E., Steffen, K., and Chylek, P. 2010. Meltwater flux and runoff modeling in the ablation area of the Jakobshavn Isbræ, West Greenland. *Journal of Glaciology*, 56(195), 20–32.
- Mernild, S. H., Malmros, J. K., Yde, J. C., and Knudsen, N. T. 2012 [11]. Multi-decadal marine and land-terminating glacier retreat in Ammassalik region, Southeast Greenland. *The Cryosphere*, 6, 625–639, doi:10.5194/tc-6-625-2012.
- Mernild, S. H., Malmros, J. K., Yde, J. C., Knudsen, N. T., Wilson, R., Hanna, E., Fausto, R. S., As, Van D. 2014 [7]. Albedo decline on Greenlands Mittivakkat Gletscher. *International Journal of Climatology*, doi: 10.1002/joc.4128.
- Mernild, S. H., Malmros, J. K., Eriksen, J., and Rasmussen, L. 2012b. Den grønlandsk flom (in Danish). *Vejret*, 132, 1–7.
- Mernild, S. H., Mote, T., and Liston, G. E. 2011 [16]. Greenland Ice Sheet surface melt extent and trends, 1960–2010. *Journal of Glaciology*, 57(204), 621–628.
- Mernild, S. H., Pelto, M., Malmros, J. K., Yde, J. C., Knudsen, N. T., and Hanna, E. 2013 [6]. Identification of ablation rate, ELA, AAR, and net mass balance using transient snowline

- variations on two Arctic glaciers. *Journal of Glaciology*, 59(216), 649–659, doi:10.3189/2013JoG12J221.
- Mernild, S. H., Seidenkrantz, M.-S., Chylek, P., Liston, G. E., and Hasholt, B. 2012a. Climate-driven fluctuations in freshwater to Sermilik Fjord, East Greenland, during the last 4000 years. *The Holocene*, 22(2), 155–164.
- Mernild, S. H., Sigsgaard, C. Rasch, M., Hasholt, B., Hansen, B. U., Stjernholm, M. and Petersen, D. 2007. Climate, river discharge and suspended sediment transport in the Zackenberg River Drainage Basin and Young Sund/Tyrolerfjord, Northeast Greenland, 1995–2003. In Rysgaard, S. and Glud, R. N. (Eds.), Carbon cycling in Arctic Marine ecosystems: Case study Young Sound, *Meddr. om Grønland, BioScience*, 58, 24–43.
- Mikkelsen, A. B., 2014. Freshwater discharge and sediment transport to Kangerlussuaq Fjord, West Greenland – Processes, modeling and implications. Ph.D. dissertation. Department of Geosciences and Natural Resource Management, Faculty of Science, University of Copenhagen.
- Mikkelsen, A. B., Hasholt, B., Knudsen, N. T., and Nielsen, M. N. 2013. Jokulhlaups and sediment transport in Watson River, Kangerlussuaq, West Greenland. *Hydrological Research*, 41(1), 58–67.
- Millionis, A. E. and Davies, T. D. 2008. A comparison of temperature inversion statistics at a coastal and a non-coastal location influenced by the same synoptic regime. *Theoretical and Applied Climatology*, 94, 225–239.
- Motyka, R. J., Truffer, M., Fahnestock, M., Mortensen, J., Rysgaard, S., and Howat, I. 2011. Submarine melting of the 1985 Jakobshavn Isbræ floating tongue and the triggering of the current retreat. *Journal of Geophysical Research*, 116(F1), F01007, doi:10.1029/2009JF001632.
- Nesje, A., Lie, O., and Dahl, S. O. 2000. Is the North Atlantic Oscillation reflected in Scandinavian glacier mass balance records? *Journal of Quaternary Science*, 15, 587–601.
- Nghiem, S. V., Hall, D. K., Mote, T. L., Tedesco, M., Albert, M. R., Keegann, K., Shuman, C. A., DiGirolamo, N. E., and Neumann, G. 2012. The extreme melt across the Greenland ice sheet in 2012. *Geophysical Research Letters*, 39, L20502.
- Nick, F. M., Vieli, A., Howat, I. M. and Joughin, I. 2009. Large-scale changes in Greenland outlet glacier dynamics triggered at the terminus. *Nature Geoscience*, 2(2), 110–114.
- Overeem, I. and Syvitski, J. P. M. 2010. Shifting discharge peaks in Arctic rivers, 1997–2007. *Geografiske Annaler, Series A Physical Geography*, 92, 285–196.
- Overland, J. E., Francis, J., Hanna, E. and Wang, M. 2012. The recent shift in early summer arctic atmospheric circulation. *Geophysical Research Letters*, 39, L19804.
- Paul, F. and Svoboda, F. 2009. A new glacier inventory on southern Baffin Island, Canada, from ASTER data: II. Data analysis, glacier change, and application. *Annals of Glaciology*, 50, 22–31.
- Pfeffer, T. W., Arendt, A. A., Bliss, A., Bolch, T., Cogley, J. G., Gardner, A. S., Hagen, J.-O., Hock, R., Kaser, G., Kienholtz, C., Miles, E. S., Moholdt, G., Molg, N., Paul, F., Radić, V., Rastner, P., Raup, B. H., Ricj, J., Sharp, M. J., The Randolph Consortium, 2014. The Randolph Glacier Inventory: a globally complete inventory of glaciers. *Journal of Glaciology*, 60(221), 537–552.
- Pielke, R. A., Sr. 2002. Mesoscale Meteorological Modeling. Academic Press, 676 pp.
- Radić, V., Bliss, A., Beedlow, A. C., Hock, R., Miles, E., and Cogley, J. G. 2014. Regional and global projection of twenty-first century glacier mass changes in response to climate scenarios from global climate models. *Climate Dynamics*, 42, 37–58.
- Radić, V., and Hock, R. 2010. Regional and global volumes of glaciers derived from statistical upscaling of glacier inventory data. *Journal of Geophysical Research*, 115, F01010, doi: 10.1029/2009JF001373.
- Rahmstorf, S. and Coauthors, 2005. Thermohaline circulation hysteresis: A model intercomparison. *Geophysical Research Letters*, 32, L23605, doi:10.1029/2005GL023655.
- Raper, S. C. B. and Braithwaite, R. J. 2006. Low sea level rise projections from mountain glaciers and icecaps under global warming. *Nature*, 439, 311–313.

- Rasmussen, R., Baker, B., Kochendorfer, J., Meyers, T., Landolt, S., Fischer, A. P., Black, J., Theriault, J. M., Kucera, p., Gochis, D., Smith, C., Nitu, R., Hall, M., Ikeda, K., and Gutmann, E. 2012. How well are we measuring snow? The NOAA/FAA/NCAR Winter Precipitation Test Bed. *BAMS*, 811–829.
- Rastner, P., Bolch, T., Molg, N., Machguth, H., Le Bris, R. and Paul, F. 2012. The first complete inventory of the local glaciers and ice caps on Greenland. *Cryosphere*, 6(6), 1483–1495.
- Rau, F., Mauz, F., Vogt, S., Khalsa, S. J. S., and Raup, B. 2005. Illustrated GLIMS Glacier Classification Manual—Glacier Classification Guidance for the GLIMS Glacier Inventory, version 1 (2005-02-10), 36 pp.
- Refsgaard, J. C. 2007. Hydrological Modelling and River Basin Management. Doctoral Thesis, Danmarks og Grønlands Geologiske Undersøgelser – Særudgivelse. Danish Ministry of the Environment. pp 84.
- Rennermalm, A. K., Smith, L. C., Chu, V. W., Box, J. E., Forster, R. R., van den Broeke, M. R., van As, D., and Moustafa, S. E. 2013. Evidence of meltwater retention within the Greenland ice sheet. *The Cryosphere*, 7, 1433–1455.
- Rennermalm, A. K., Smith, L. C., Chu, V. W., Forster, R. R., Box, J. E., and Hagedorn, B. 2012. Proglacial river stage, discharge, and temperature dataset from the Akuliarusiarsuup Kuua River north tributary, Southwest Greenland, 2008-2011. *Earth System Science Data*, 4, 1–12.
- Roberts, A., Hinzman, L. D., Walsh, J. E., Holland, M., Cassano, J., Doscher, R., Mitsudera, H., and Sumi, A. 2010. A science plan for regional Arctic system modeling, a report to the National Science Foundation from the International Arctic Science Community. International Arctic Research Center Technical Papers 10-0001. International Arctic Research Center, University of Alaska, Fairbanks, Alaska, USA.
- Rignot, E., Box, J. E., Burgess, E., and Hanna, E. 2008. Mass balance of the Greenland ice sheet from 1958 to 2007. *Geophysical Research Letters*, 35, L20502, doi:10.1029/2008GL035417.
- Rignot, E., and Kanagaratnam, P. 2006. Changes in the velocity structure of the Greenland Ice Sheet. *Science*, 311, 986–990.
- Rignot, E., Velicogna, I., van den Broeke, M. R., Monaghan, A., and Lenaerts, J. 2011. Acceleration of the contribution of the Greenland and Antarctic ice sheets to sea level rise. *Geophysical Research Letters*, 38, L05503.
- Rogers, A. N., Bromwich, D. H., Sinclair, E. N. and Cullather, R. I., 2001. The atmospheric hydrological cycle over the Arctic basins from reanalysis. Part II: Interannual variability. *Journal of Climate*, 14, 2414–2429.
- Ryan, B. C. 1977. A mathematical model for diagnosis and prediction of surface winds in mountains terrain. *Journal of Applied Meteorology*, 16, 1547–1564.
- Saito, K., Zhang, T., Yang, D., Marchenko, S., Barry, R. G., Romanovsky, V., and Hinzman, L. D. 2013. Influence of the physical terrestrial Arctic in the eco-climate system. *Ecological Applications*, 23, 1778–1797.
- Schaefer, M., Hachguth, H., Falvey, M., and Casassa, G. 2013. Modeling past and future surface mass balance of the Northern Patagonia Icefield. *Journal of Geophysical Research, Earth Surface*, 118, doi:10.1002/jgrf.20038.
- Schoof, C. 2010. Ice-sheet acceleration driven by melt supply variability. *Nature*, 468(7325), 803–806.
- Serreze, M. C. 1998. The freshwater budget to the Arctic Ocean (Workshop Summary). The Freshwater Budget of the Arctic Ocean. Ed. Lewis, E. L. Jones, P. E., Lemke, P., Prowse, T. D., Wadhamn, P. Nato Science Series, 2. Environmental Security, Vol .2, xiii.
- Shahgedanova, M., Nosenko, G., Bushueva, I., and Ivanov, M. 2012. Changes in area and geodetic mass balance of small glaciers, Polar Urals, Russia, 1950–2008. *Journal of Glaciology*, 58(211), 953–964.
- Sharp, M. J., Copland, L., Filbert, K., Burgess, D., and Williamson, D. 2003. Recent changes in the extent and volume of Canadian Arctic glaciers. Snow Watch 2002 Workshop and Assessing Global Glacier Recession, Glaciological Data report, pp. 73–75. NSIDE/WDC for Glaciology, Boulder, Colorado.
- Shaw, E. 1996. Hydrology in Practice. London. Chapman & Hall. Thrid editon (reprinted).

- Shepherd, A. and others 2012. A Reconciled Estimate of Ice-Sheet Mass Balance. *Science*, 338, 1183–1189.
- Shiklomanov, A. I., and Lammers, R. B. 2009. record Russian river discharge in 2007 and the limits of analysis. *Environmental Research Letter*, 4, 045015.
- Steffen, K. 1995. Surface energy exchange at the equilibrium line on the Greenland ice sheet during onset of melt. *Annals of Glaciology*, 21, 13–18.
- Stendel, M., Christensen, J. H., and Petersen, D. 2008. Arctic climate and climate change with a focus on Greenland. *Advances in Ecological Research*, 40, 13–43.
- Strack, J. E., Liston, G. E., and Pielke, R. A. S. 2004. Modeling snow depth for improved simulation of snow–vegetation–atmosphere interactions. *Journal of Hydrometeorology*, 5(5), 723–734.
- Straneo, F., Curry, R. G., Sutherland, D. A., Hamilton, G. S., Cenedese, C., Våge, K., and Sterns, L. A. 2011. Impact of fjord dynamics and glacial runoff on the circulation near Helheim Glacier. *Nature Geoscience*, 4, 322–327.
- Straneo, F., Heimbach, P., Sergienko, O., Hamilton, G., Catania, G., Griffies, S., Hallberg, R., Jenkins, A., Joughin, I., Motyka, R., Pfeffer, W. T., Price, S. F., Rignot, E., Scambos, T., Truffer, M., and Veili, A. 2013. Challenges to understanding the dynamic response of Greenland’s marine terminating glaciers to oceanic and atmospheric forcing. *BAMS*, 8, 1131–1144, doi:10.1175/BAMS-D-12-00100.1.
- Straneo, F., Sutherland, D. A., Holland, D., Gladish, C., Hamilton, G. S., Johnson, H. L., Rignot, E., Xu, Y., and Koppen, M. 2012. Characteristics of ocean waters reaching Greenland’s glaciers. *Annals of Glaciology*, 53(60), 202–210.
- Stroeve, J. 2001. Assessment of Greenland albedo variability from the advanced very high resolution radiometer Polar Pathfinder data set. *Journal of Geophysical Research, Atmosphere*, 106(D24), 33989–34006.
- Stroeve, J., Box, J. E., Gao, F., Liang, S., Nolin, A. and Schaaf, C. 2005. Accuracy assessment of the MODIS 16-day albedo product for snow: comparisons with Greenland in situ measurements. *Remote Sensing of Environment*, 94, 46–60.
- Sugiyama, S. Sakakibara, D., matsuno, S., Yamaguchi, S., Matoba, S., and Aoki, T. 2014. Initial field observations on Qaanaaq ice cap, northwestern Greenland. *Annals of Glaciology*, 55(66), 25–33.
- Sundal, A.V., Shepherd, A., Nienow, P., Hanna, E., Palmer, S., and Huybrechts, P. 2011. Melt-induced speed-up of Greenland ice sheet offset by efficient subglacial drainage. *Nature*, 469(7331), 521–524.
- Sutherland, D. A., Roth, G. E., Hamilton, G. S., Mernild, S. H., Stearns, L. A., and Straneo, F. 2014. Quantifying flow regimes in a Greenland glacial fjord using iceberg drifters. Accepted, *Geophysical Research Letters*.
- Sørensen, L. S. et al. 2011. Mass balance of the Greenland Ice Sheet (2003-2008) from ICESat data – the impact of interpolation, sampling and firn density. *The Cryosphere*, 5(1), 173–186.
- Tedesco, M. 2007. A new record in 2007 for melting in Greenland. *Eos*, 88(39), 383.
- Tedesco, M. and 7 others. 2011. The role of albedo and accumulation in the 2010 melting record in Greenland. *Environmental Research Letters*, 6, 014005.
- Tedesco, M., Box, J. E., Cappelen, J., Fettweis, X., Mote, T., van de Wal, R. S. W., Smeets, C. J. P. P., and Wahr, J. 2014. Greenland Ice Sheet. In Jeffries, M. O., Richter-Menge, J. A., and Overland, J. E. (Eds). Arctic Report Card 2014, <http://www.arctic.noaa.gov/reportcard>.
- Tedesco, M., Fettweis, X., Mote, T., Wahr, J., Alexander, P., Box, J. E., and Wouters, B. 2013. Evidence and analysis of 2012 Greenland records from spaceborne observations, a regional climate model and reanalysis data. *The Cryosphere*, 7, 615–630.
- Thomas, R. H. 2004. Force-perturbation analysis of recent thinning and acceleration of Jakobshavn Isbræ, Greenland. *Journal of Glaciology*, 50(168), 57–66.
- Thornton, P. E., Running, S. W., and White, M. A. 1997. Generating surfaces of daily meteorological variables over large regions of complex terrain. *Journal of Hydrology*, 190, 214–251.

- Trenberth, K. E., Jones, P. D., Ambenje, P., Bojariu, R., Easterling, D., Klein tank, A., Parker, D., Rahimzadeh, F., Renwick, J. A., Rusticucci, M., Soden, B. and Zhai, P. 2007. Observations: surface and atmospheric climate change. In: Solomon, S., Qin, D., Manning, M., Chen, Z., Marquis, M., Averyt, K.B., Tignor, M. and Miller, H.L. (eds), *Climate Change 2007: The Physical Science Basis*. Contribution of Working Group I to the Fourth Assessment Report of the Intergovernmental Panel on Climate Change Cambridge University Press, Cambridge, UK and New York, USA.
- UNESCO 1992. International Glossary of Hydrology. UNESCO, World Meteorological Organisation, ISBN 92-63-02385, Pp 461.
- Vernon, C. L., Bamber, J. L., Box, J. E., van den Broeke, M. R., Fettweis, X., Hanna, E. and Huybrechts, P. 2013. Surface mass balance model intercomparison for the Greenland ice sheet. *The Cryosphere*, 7, 599–614.
- Van As, D., Hubbard, A. L., Hasholt, B., Mikkelsen, A. B., van den Broeke, M. R., and Fausto, R. S. 2012. Large surface meltwater discharge from the Kangerlussuaq sector of the Greenland ice sheet during the record-warm year 2010 explained by detailed energy balance observations. *The Cryosphere*, 6, 199–209.
- van de Wal, R. S. W., Boot, W., Smeets, C. J. P. P., Snellen, H., van den Broeke, M. R., and Oerlemans, J. 2012. Twenty-one years of mass balance observations along the K-transect, West Greenland. *Earth System Science Data*, 5, 351–363.
- van de Wal, R. S. W., Greuell, W., van den Broeke, M. R., Reijmer, C. H., and Oerlemans, J. 2005. Surface mass-balance observations and automatic weather station data along a transect near Kangerlussuaq, West Greenland. *Annals of Glaciology*, 42, 311–316.
- van den Broeke, M. R., Bamber, J., Ettema, J., Rignot, E., Schrama, E., van de Berg, W. J., van Meijgaard, E., Velicogna, I., and Wouters, B. 2009. Partitioning recent Greenland mass loss. *Science*, 326, 984–986.
- van den Broeke, M., Smeets, P., Ettema, J., and Munneke, P. K. 2008a. Surface radiation balance in the ablation zone of the west Greenland ice sheet. *Journal of Geophysical Research*, 113, D13105.
- van den Broeke, M., Smeets, P., and Ettema, J. 2008c. Surface layer climate and turbulent exchange in the ablation zone of the west Greenland ice sheet. *International Journal of Climatology*, 2309–2323.
- van den Broeke, M., Smeets, P., Ettema, J., van der Veen, C., van de Wal, R., and Oerlemans, J. 2008b. Partitioning of melt energy and meltwater fluxes in the ablation zone of the west Greenland ice sheet. *The Cryosphere*, 2, 179–189.
- Vaughan, D. G., Comiso, J. C., Allison, I., Carrasco, J., Kaser, G., Kwok, R., Mote, P., Murray, T., Paul, F., Ren, J., Rignot, E., Solomina, O., Steffen, K. and Zhang, T. 2013. Observations: Cryosphere. In: *Climate Change 2013. The Physical Science Basis. Contribution of Working Group I to the Fifth Assessment Report of the Intergovernmental Panel on Climate Change* [Stocker, T.F., D. Qin, G.-K. Plattner, M. Tignor, S.K. Allen, J. Boschung, A. Nauels, Y. Xia, V. Bex and P.M. Midgley (eds.)]. Cambridge University Press, Cambridge, United Kingdom and New York, NY, USA.
- Velicogna, I and Wahr, J. 2013. Time-variable gravity observations of ice sheet mass balance: Precision and limitations of the GRACE satellite data. *Geophysical Research Letters*, 40(12), 3055–3065.
- Walcek, C. J., 1994. Cloud cover and its relationship to relative humidity during a spring midlatitude cyclone. *Monthly Weather Review*, 122, 1021–1035.
- Walsh, J. E., Chapman, W. L., Romanovsky, V., and Christensen, J. H. 2008. Global climate model performance over Alaska and Greenland. *Journal of Climate*, 21, 2156–2174.
- Weijer, W., Maltrud, M. E., Hecht, M. W., Dijkstra, H. A., and Kliphuis, M. A. 2012. Response of the Atlantic Ocean circulation to Greenland Ice Sheet melting in a strongly-eddy ocean model. *Geophysical Research Letters*, 39, L09606.
- World Glacier Monitoring Service (WGMS) 2012. *Fluctuations of Glaciers 2005-2010 (Vol. X)*, edited by: Zemp, M., Frey, H., Gärtner-Roer, I., Nussbaumer, S. U., Hoelzle, M., Paul, F., and



- Haerberli W., ICSU (WDS) / IUGG (IACS) / UNEP / UNESCO / WMO, Zurich, Switzerland, 336 pp., Publication based on database version: doi:10.5904/wgms-fog-2012-11.
- World Glacier Monitoring Service (WGMS) 2013. Glacier mass balance bulletin 2010-2011 (Bulletin No. 12), edited by: Zemp, M., Nussbaumer, S. U., Naegeli, K., Gärtner-Roer, I., Paul, F., Hoelzle, M., and Haerberli W., ICSU (WDS) / IUGG (IACS) / UNEP / UNESCO / WMO, Zurich, Switzerland, 106 pp., Publication based on database version: doi:10.5904/wgms-fog-2013-11.
- Yang, D., Goodison, B. E., Metcalfe, J. S., Golubev, V. S., Bates, R., Pangburn, T., and Hanson, C. L. 1998. Accuracy of NWS 8 standard nonrecording precipitation gauge: Results and application of WMO intercomparison. *Journal of Atmospheric and Oceanic Technology*, 15, 54–68.
- Yang, D., Ishida, S., Goodison, B. E., and Gunter, T. 1999. Bias correction of daily precipitation measurements for Greenland. *Journal of Geophysical Research*, 104(D6), 6171–6181.
- Yde, J. C. and Knudsen, N. T. 2007. 20th-century glacier fluctuation on Disko Island (Qeqertarsuaq), Greenland. *Annals of Glaciology*, 46, 209–214.
- Yde, J. C., Gillespie, M. K., Løland, R., Ruud, H., Mernild, S. H., de Villiers, S., Knudsen, N. T., and Malmros, J. K. 2014. Volume measurements of Mittivakkat Gletscher, southeast Greenland. *Journal of Glaciology*, 60(224), 1199–1207, doi:10.3189/2014JoG14J047.
- Zwally, H. J. and Giovinetto, M. B. 2001. Balance mass flux and ice velocity across the equilibrium line in drainage systems of Greenland. *Journal of Geophysical Research*, 106(D24), 33, 33717–33728.
- Østrem, G. and Brugman, M. 1991. Glacier mass-balance measurements: a manual for field and office work. NHRI Science Report 4. Environment Canada. National Hydrology Research Institute, Saskatoon, Sask.

[1]

Mernild, S. H., Hanna, E., Yde, J. C., Cappelen, J., and Malmros, J. K. 2014. Coastal Greenland air temperature extremes and trends 1890–2010: Annual and monthly analysis. *International Journal of Climatology*, 34, 1472–1487, doi: 10.1002/joc.3777.

Reprinted with permission from Wiley

# Coastal Greenland air temperature extremes and trends 1890–2010: annual and monthly analysis

Sebastian H. Mernild,<sup>a,b,\*</sup> Edward Hanna,<sup>c</sup> Jacob C. Yde,<sup>d</sup> John Cappelen<sup>e</sup> and  
Jeppe K. Malmros<sup>b</sup>

<sup>a</sup> *Climate, Ocean, and Sea Ice Modeling Group, Computational Physics and Methods, Los Alamos National Laboratory, Los Alamos, NM, USA*

<sup>b</sup> *Glaciology and Climate Change Laboratory, Center for Scientific Studies/Centro de Estudios Científicos (CECs), Valdivia, Chile*

<sup>c</sup> *Department of Geography, University of Sheffield, Sheffield, UK*

<sup>d</sup> *Faculty of Engineering and Science, Sogn og Fjordane University College, Sogndal, Norway*

<sup>e</sup> *Danish Meteorological Institute, Copenhagen, Denmark*

This article has been contributed to by US Government employees and their work is in the public domain in the USA

**ABSTRACT:** We use observed air temperature data series from 14 meteorological stations in coastal Greenland (located all around the Greenland Ice Sheet) for 1960–2010, where long-term records for five of the stations extend back to 1890, to illustrate the annual and monthly temporal and spatial distribution of temperature extremes, with the main focus on the latest decade 2001–2010 (2000s). We find that the 2000s had the highest number of mean annual air temperature (MAAT) warm extremes, and the 1890s the highest number of cold extremes, and that a high (low) positive North Atlantic Oscillation (NAO) Index equals a high number of cold (warm) extreme events. For the 2000s the number of warm extremes was significantly higher by around 50% than the number in the 1940s (the early twentieth century warm period): the latter being the decade with the second highest occurrence of MAAT warm extremes. Since 1960, based on MAAT the number of cold extremes has overall decreased on the decadal timescale, besides a peak in 1980s, while warm extremes have increased, leading to a higher occurrence of extremes (cold plus warm extremes): an almost similar pattern occurred for monthly mean temperatures and monthly mean daily maximum and minimum temperature datasets. Furthermore, a division of Greenland into east and west sectors shows that the occurrence of cold (warm) extremes was more pronounced in the East than in the West in the 1960s and 1970s (mid-1980s to the 2000s).

**KEY WORDS** annual and monthly values; extreme temperature observations; Greenland; mean, maximum, and minimum temperature observations

Received 20 October 2012; Revised 1 May 2013; Accepted 30 May 2013

## 1. Introduction

The first decade of the new millennium (2001–2010) was the warmest globally on record (Hansen *et al.*, 2010) and likely to have been warmer than any other decade within the last thousand years (IPCC, 2007). Statistical analysis of observed data, climate models, and physical reasoning indicate that some types of extreme weather events, notably heatwaves, will greatly increase in number in a warming climate, and have already begun to do so (Coumou and Rahmstorf, 2012). Not only will the number of warm extremes increase, but also the number of cold extremes is likely to decrease contemporaneously. Even if the probability distribution of temperatures is otherwise unchanged as it

is shifted towards warmer conditions, the overall number of extremes (warm plus cold) will increase (Rahmstorf and Coumou, 2011). A changing climate may also be expected to lead to changes in frequency, intensity, spatial extent, duration, and timing of extreme weather and climate events (IPCC, 2012, Summary, p. 7). Donat and Alexander (2012) used a global observational dataset of daily temperatures to show that both daytime (daily maximum) and nighttime (daily minimum) temperatures have become higher over the past 60 years: changes were greater for daily minimum than for daily maximum temperatures. Similar trends were observed for Greenland by Hanna *et al.* (2013).

In an effort to understand climate extremes and their link to climate warming, attempts to quantify observed changes in climate have been made based on climate extremes indices (e.g. Karl *et al.*, 1996). As a first glance to understand and map possible trends and long-term variations in a variety of these indicators, including those found in observed air temperature and precipitation, the U.S. Climate Extremes Index (CEI) was developed by Karl *et al.* (1996) and revised by Gleason *et al.* (2008).

\*Correspondence to: S. H. Mernild, Glaciology and Climate Change Laboratory, Center for Scientific Studies/Centro de Estudios Científicos (CECs), 5110466 Valdivia, Chile. E-mail: mernild@cecs.cl

Correction added 7 August 2013 after original online publication: John Cappelen was erroneously omitted from the author list and has been reinstated.

The CEI was designed not only to identify causes and origins of variability and changes in extremes (Gleason *et al.*, 2008), but also to provide information on the fraction of the contiguous United States – i.e. the spatial extent – that experienced extreme conditions during any giving year or period.

The CEI inspired the authors to use one of its components – the air temperature part – for this Greenland study in order to map changes in the Greenland temperature on annual and monthly scales, and therefore to identify the fraction of the distribution experiencing extreme conditions. The primary focus here is restricted to one of the CEI indicators – surface air temperature (2 m) – since information about the other CEI indicators (Gleason *et al.*, 2008): extreme 1-day precipitation, days with/without precipitation, and the Palmer Drought Severity Index is for this region either non-existent, sparse, or suffers from great uncertainties (e.g. precipitation gauges significantly underestimate solid precipitation in windy environments (Allerup *et al.*, 1998; Yang *et al.*, 1998; Liston and Sturm, 2002, 2004), and are therefore not included in this study).

For estimating *climate extremes*, the following definition has commonly been used: “the occurrence of a value of a climate variable above (or below) a threshold value near the upper (or lower) ends of the range of observed values of the variable” (IPCC, 2012; Summary Section, p. 5). Gleason *et al.* (2008) and Lubchenco and Karl (2012) made this definition quantitative, specifying extreme temperature conditions to be defined as occurrences that fall outside the 90th and the 10th percentile values of the period of record. This well-accepted definition will be applied in this study to analyse temperature extremes in Greenland based on annual, seasonal, and monthly time series of mean, maximum, and minimum daily temperatures. What is considered to be extreme values is by definition based on past experience, where a change in climate moves us out of the familiar range (Coumou and Rahmstorf, 2012).

Here, we ask the questions: (1) Is the 2000s (2001–2010) on average the decade with the most warm extremes on record since 1890 for coastal stations in Greenland, and does the overall occurrence of cold and warm extremes closely follow the overall mean temperature trend? (2) What are the temporal and spatial distributions of cold and warm extremes on annual and monthly timescales for coastal Greenland during 1961–2010, focusing on the recent warm decade of the 2000s? (3) Has the overall number of extreme events (warm plus cold extremes) increased since 1961, and is the number of extreme events highest for the 2000s? and (4) Is there a regional difference between West Greenland and East Greenland in the occurrence of cold and warm extremes for 1961–2010?

To answer question one, long-term mean annual air temperature (MAAT) observations from five coastal stations in Greenland (1890–2010; Figure 1) are analysed in an effort to quantify, on the annual timescale, the proportion of stations which experienced temperatures outside

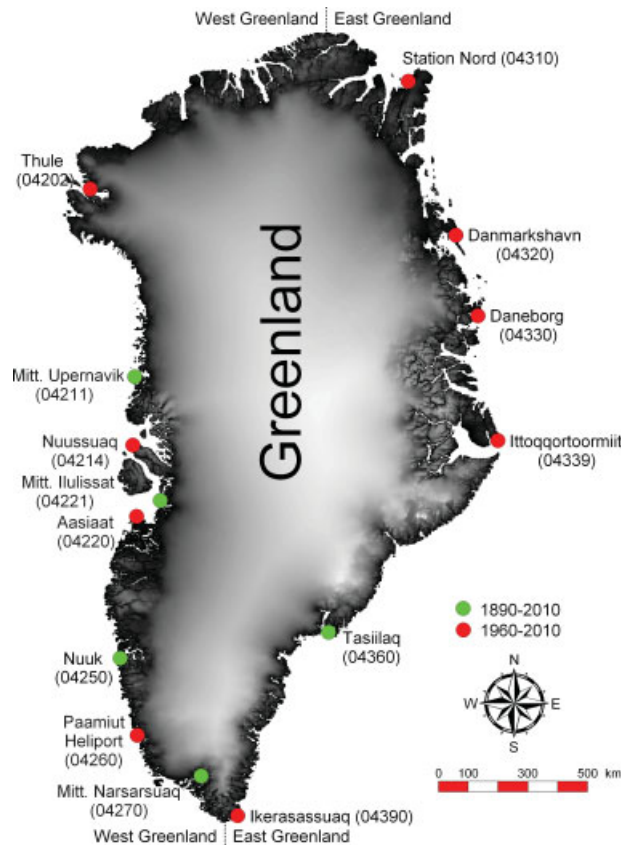


Figure 1. Greenland, including the Greenland Ice Sheet (GrIS), and the location of 14 meteorological stations in the coastal zone recording air temperature. At the green circles air temperature time series are used from 1890 through 2010 (except for Tasiilaq, 1895 through 2010), and at the red circles from 1960 through 2010 (except for Ittoqqortoormiit, 1980 through 2010). The station numbers in the brackets correspond to the World Meteorological Organization (WMO) numbers.

the 10th–90th percentile range, and especially to compare the 2000s with the early twentieth century warm period in the 1930s and 1940s. In addition, in order to address questions two and three, this study presents a detailed temporal and spatial analysis of temperature observations from 14 stations covering the five decades from the 1960s to 2000s, emphasizing changes in the occurrence of temperatures outside the 10th–90th percentile range on annual (based on observed MAAT compiled from generally 3-hourly observations) and on annual mean daily maximum and minimum temperatures [annual values calculated based on daily maximum (highest daytime temperature) and minimum temperatures (lowest nighttime temperature)] and monthly timescales (based on observed monthly mean temperature and monthly mean daily maximum and minimum temperatures). Regarding question four, the regional patterns of cold and warm extremes in West Greenland and East Greenland are analysed in an effort to quantify trends and discrepancies on either side of the ice sheet, relating these to different climate mechanisms and trends (e.g. Jones *et al.*, 1999), based on observed MAAT, monthly mean daily mean, and monthly mean daily maximum and minimum temperatures.

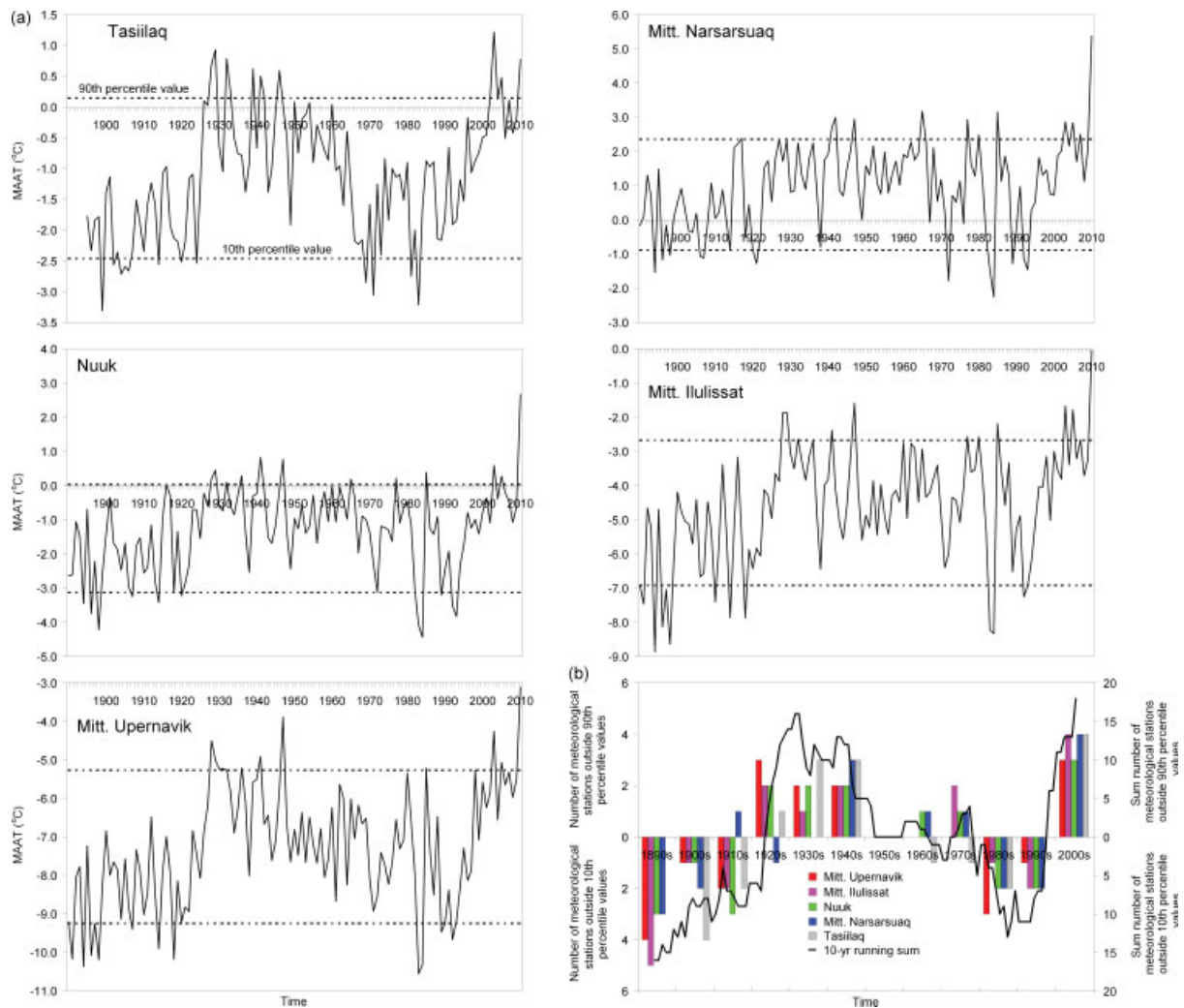


Figure 2. (a) MAAT time series for the five long-term meteorological stations in coastal Greenland (1891–2010) (see Figure 1 for locations). Also shown for each station are the 90th and 10th air temperature percentile values (horizontal dotted lines). (b) The number of years on the decadal timescale (1891–1900, 1901–1910, etc.) that each station is outside the 90th percentile (warm extremes) and 10th percentile (cold extremes), including a 10-year running sum.

## 2. Data and methodology

In order to determine the percentage of meteorological stations experiencing extreme surface air temperatures, observed 2-m temperature data were compiled from 14 long-running Danish Meteorological Institute (DMI) climate stations located surrounding the Greenland Ice Sheet in coastal Greenland (Cappelen, 2011).

Observed air temperature data were used only for those stations for which daily data were at least 80% complete of each month of record – the completeness threshold was selected to maximize the spatial coverage and to minimize uncertainties in trends based on reduced availability of meteorological station data (Gleason *et al.*, 2008). Where data were missing on the daily to weekly timescale, different data-filling procedures were conducted as described in detail by Liston and Elder (2006): (1) for missing data segments of less than 24 h, missing values were determined as an average of the values from 24 h before and after to preserve the diurnal cycle and (2) for missing data segments longer

than 24 h, the time series prediction was made using an autoregressive integrated moving average (ARIMA) model (Box and Jenkins, 1976; Walton, 1996), to forecast into the missing segment using data preceding the missing segment and hindcast into the missing segment using data following the missing segment (both using data spans equal in length to the missing-data span): the two results were then linearly interpolated across the data gap and linearly weighted (Liston and Elder, 2006).

In climate studies, including temperature extreme analysis, it is essential that temperature time series are as homogeneous as possible so that a time series results solely from variations in climate (Tuomenvirta *et al.*, 2000) and not from non-climatic causes such as changes in station location and elevation, instrumentation, and observing practices (Heino, 1994). Standard normal homogeneity tests for climatological data were therefore conducted based on Steffensen *et al.* (1993) and Steffensen (1996), if not already done by DMI (Cappelen *et al.*, 2000; Cappelen, 2011), to test and adjust



Table 1. The decadal sum of warm and cold extremes and the overall occurrence of extremes: cold plus warm extremes for the five long-term meteorological stations in coastal Greenland (1891–2010).

Decade	Number of warm extremes	Number of cold extremes	Overall occurrence of extremes: sum of warm and cold extremes
1890s	0	15	15
1900s	0	9	9
1910s	1	9	10
1920s	8	1	9
1930s	8	0	8
1940s	12	0	12
1950s	0	0	0
1960s	2	1	3
1970s	4	1	5
1980s	0	10	10
1990s	0	7	7
2000s	18	0	18

time series against neighbouring stations, which have been influenced by non-climatic changes and long-term environmental effects (e.g. changes in surrounding vegetation) over time. Within the last 20 years the majority of the DMI meteorological stations used in this study have had fixed locations and automation and new instruments have not influenced the time series (Boas and Wang, 2011), and only five have been relocated: Ittoqqortoormiit (2005), Tasiilaq (2005), Paamiut Heliport (2007), Mitt. Upernavik (2000), and Thule (2000) (Boas and Wang, 2011; Cappelen, 2013a). Therefore, based on the homogeneity tests of the time series and the uncertainties in air temperature observations, it is expected that the overall uncertainty in the air temperature dataset is about 0.1 °C (Cappelen, 2013a, 2013b).

Five of the fourteen stations cover the period 1890–2010 (except for Tasiilaq, which spans 1895–2010) (Cappelen, 2011): these five stations are located in Southeast, South, Southwest, and West Greenland. All 14 stations cover the period 1961–2010 [except for Ittoqqortoormiit, which is missing data from 1961–1980 (20 years); Nauyasuuq, 1972–1981 (10 years); Daneborg 1975–1979 (5 years) and 2007–2009 (3 years); Station Nord 1972–1975 (4 years); Nuuk 1991–1994 (4 years); and Ikerasassuaq 1980 (1 year)] (Cappelen *et al.*, 2000, updated; Boas and Wang, 2011) (Figure 1). Considering the main dataset from 1961 through 2010 (based on annual air temperature data from the 14 DMI climate stations) only 47 years out of 700 years equivalent of data were missing, meaning that less than 7% of the dataset was excluded.

We applied standard descriptive statistics, including mean, standard deviation, minimum, and maximum, as well as linear regression trends, to evaluate evidence of records, changes, and trends for the various decades 1961–1970, 1971–1980, etc., and for the entire study period.

### 3. Results and discussion

#### 3.1. Long-term observed MAAT time series 1890–2010 versus 2001–2010

For the five long-term meteorological stations in Greenland: Tasiilaq, Mitt. Narsarsuaq, Nuuk, Mitt. Ilulissat, and Mitt. Upernavik (Figures 1 and 2(a)) temperature time series (1890–2010) indicated on average increasing MAAT from 1890 through mid-1930s and mid-1980s through present, and decreasing MAAT in between the two periods (mid-1930s through mid-1980s) – temperature trends also confirmed by Box (2002) and Hanna *et al.* (2013, 2012). For the same period 1890–2010 the annual number of warm extremes and cold extremes (dotted lines, Figure 2(a)) varied simultaneously with observed MAAT time series (Figure 2(b)), illustrating a transition – a decrease in the annual number of cold extremes and a subsequent increase in the number of warm extremes for both 1890 through the mid-1930s and the mid-1980s through present, and vice versa for the mid-1930s through the mid-1980s (Figure 2(b)).

For the decades of the 1920s, 1930s, and 1940s, nearly all five long-term stations had MAAT values greater than the 90th percentile, with decadal sums of years with warm extremes of 8, 8, and 12, respectively (Table 1). This means that during the 1940s the five meteorological stations experienced annual MAAT warm extremes 12 times (Figure 2(b) and Table 1), or on average around 24% of the time at the stations. Before the 1920s the decadal sums of meteorological stations with cold extremes were 15, 9, and 9 for the 1890s, 1900s, and 1910s, respectively (Table 1). This indicates that annual MAAT cold extremes occurred 15 times for 1890s (or, on average around 30% of the time at the stations), which was the decade with the highest frequency of cold extremes during the last 120 years. Also, in each of the two periods 1890 to mid-1930s and mid-1980s to 2010 the maximum increasing slopes for the 10-year running sum curve (Figure 2(b)) (estimated based on linear regression) were 2.4 (during 1921–1931) and 2.5 stations per year (during 1993–2005), respectively. This illustrates that rapid shifts from MAAT cold extremes to MAAT warm extremes can occur within only 11–13 years. If the calculation is based on a 5-year running mean the shifts occur within 10–13 years, indicating that this time range is independent of the time span of the running mean.

A comparison was made between the decadal number of MAAT warm extremes in the 1930s (8) and the 1940s (12) with the 2000s (18) for coastal Greenland (Table 1), with the finding that the occurrence of warm extremes was around 50% higher during the 2000s. This is significantly higher at the 97.5% significance level based on the null hypothesis than for the 1930s and 1940s, which were respectively the third and second mean warmest decades. Even if the sum of meteorological stations with warm extremes is calculated based on a 10-year running sum (Figure 2(b)), the 2000s still had the highest sum of MAAT warm extremes (18), while the

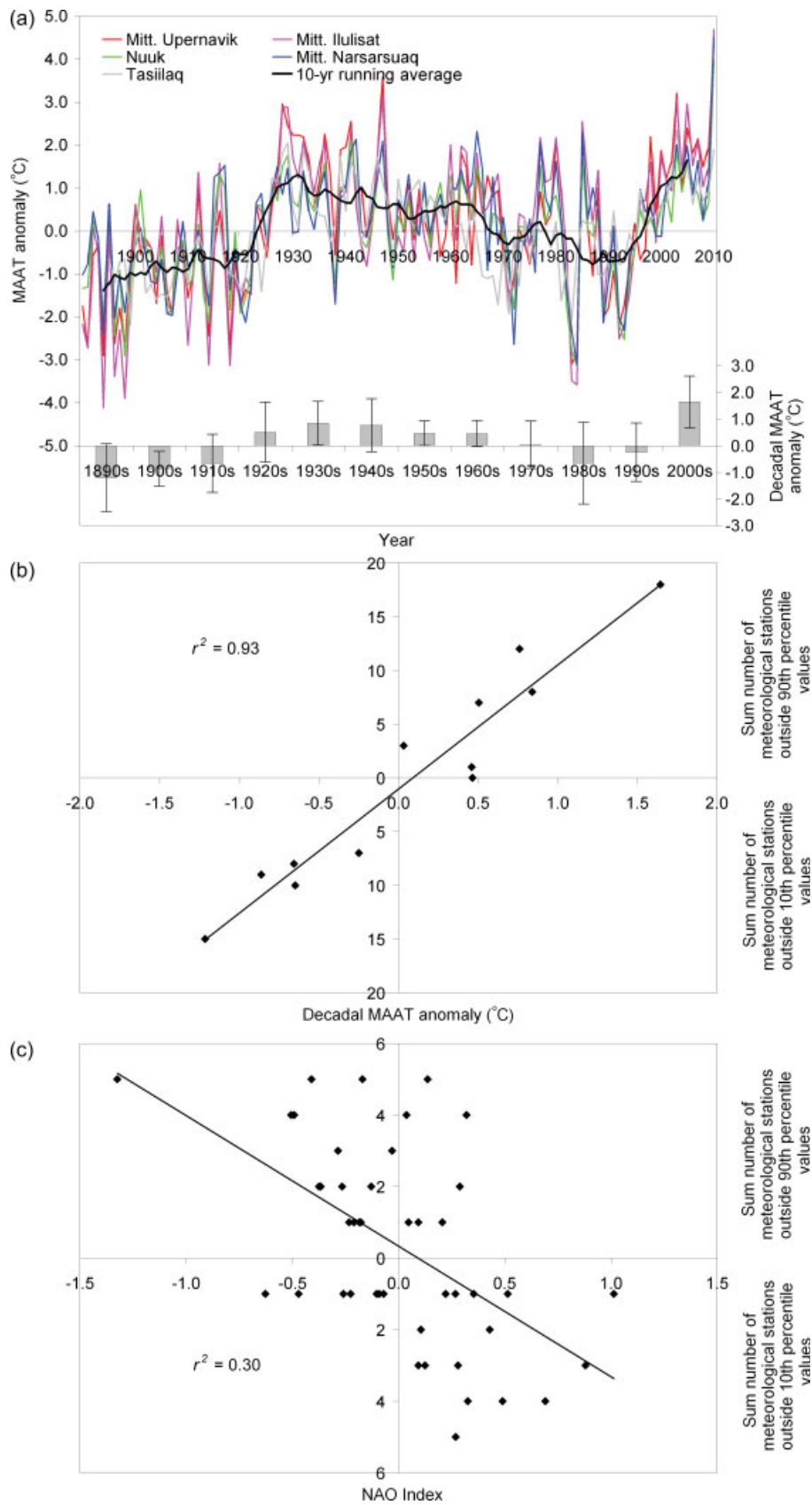


Figure 3. (a) MAAT anomaly for the five stations, including 10-year running average, and mean decadal (1891–1900, 1901–1910, etc.) MAAT anomaly with one standard deviation for the five stations (illustrated in the histogram). (b) Linear regression between mean decadal MAAT anomaly and the number of extreme years on decadal scale. (c) Linear regression between NAO Index and the number of extreme years on decadal scale (years with zero number of extremes are excluded from the regression).

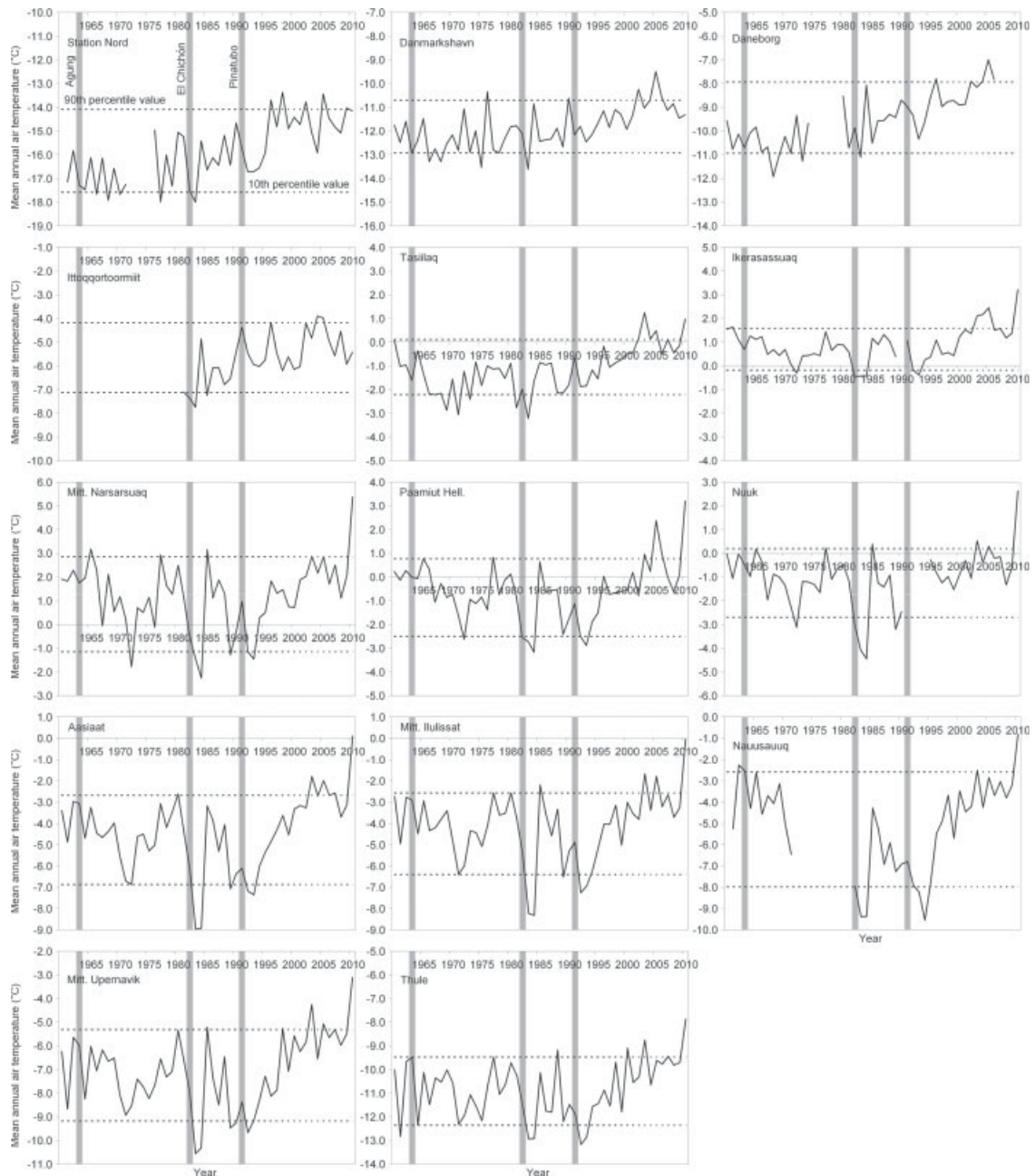


Figure 4. MAAT time series 1961–2010 for all 14 meteorological stations (see Figure 1 for location). Also shown are the 90th and 10th air temperature percentile values (horizontal dotted lines), and the major episodic volcanic eruptions of Agung, Indonesia (1963), El Chichon, Mexico (1982), and Pinatubo, Philippines (1991) (illustrated by grey columns).

highest sums for the earlier warm period centred on 1931 (covering the period 1927–1936) and 1932 (1928–1937) both were 16 (Figure 2(b)).

Figure 3(a) illustrates time series of the MAAT anomaly for the five long-term meteorological stations in coastal Greenland, showing that on the decadal timescale (the ordinate on the histogram) the highest MAAT occurred in the 2000s (this has also been confirmed at the global scale by Hansen *et al.* (2010)). Figure 3(a) also shows (lower panel) the decadal mean temperatures for the 1930s and 1940s – these two decades were before 2000 the warmest decades in Greenland over the last century (Box, 2002).

It has previously been stated by Coumou and Rahmstorf (2012) that the number of warm extremes has increased in a warming climate. For Greenland, the observed warming in MAAT confirmed this, where a strong (significant) correlation of  $r^2 = 0.93$  (where  $r^2$  is square of the linear correlation coefficient) exists between the decadal MAAT anomaly and the decadal sum number of meteorological stations with warm and cold extreme events for the period 1891–2010 (Figure 3(b)). As it is expected that the MAAT for Greenland will continue to increase on average in the future (Stendel *et al.*, 2008), it therefore follows that the number of warm extremes will increase. However, both Chylek *et al.* (2009) and



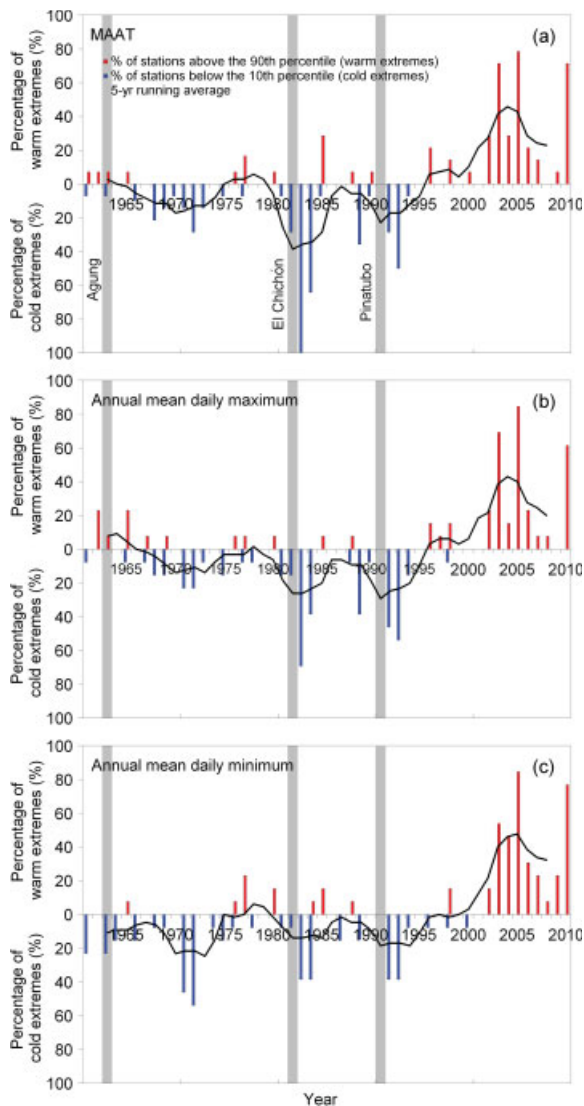


Figure 5. Time series of the annual percentage of meteorological stations outside the 90th and 10th air temperature percentile from 1961 through 2010: (a) MAAT; (b) annual mean daily maximum; and (c) annual mean daily minimum. The red columns indicate the annual percentage of warm extremes, and the blue columns the cold extremes. The black curves represent 5-year running average values. Also, shown are the major episodic volcanic eruptions of Agung, Indonesia (1963), El Chichón, Mexico (1982) and Pinatubo, Philippines (1991) (illustrated by grey columns).

Wu *et al.* (2011) have stated that around one third of changes in Arctic climate might be due to a shifting oceanic regime, and that the AMO (Atlantic Multidecadal Oscillation) might be a key factor influencing Arctic climate.

Regarding the North Atlantic Oscillation (NAO; Hurrell and van Loon, 1997) Index (estimated based on the mean sea-level pressure difference between the Azores High and Icelandic Low) and the annual number of meteorological stations with warm and cold extreme events for the period 1891–2010, a significant correlation of  $r^2 = 0.30$  exists (Figure 3(c)). According to Hurrell (1995) a positive NAO Index is associated with

cold (mild and wet) conditions in Greenland (Scandinavia), while a negative NAO Index equals mild (cold and dry) conditions in Greenland (Scandinavia). These NAO trends for Greenland correspond with the number of cold and warm extremes, where a high positive NAO Index overall equals a high number of cold extreme events and vice versa (Figure 3(c)).

### 3.2. Observed MAAT time series and distribution of cold and warm extremes during 1961–2010

As the 2000s contain both the average highest MAAT and the highest frequency of MAAT warm extremes on decadal scale since 1890 (based on five long-term temperature observations; Figure 3(a) and (b), surface air temperature observations from 14 coastal stations (Figure 1) have been analysed to focus in detail on the five decades (1961–2010) leading up to the warmest decade on record (2001–2010). All 14 temperature time series show increasing MAAT (Figure 4), where on average, the observed air temperature for coastal Greenland increased significantly by  $0.25 \pm 0.20^\circ\text{C decade}^{-1}$  (which is outside the uncertainty range) ( $r^2 = 0.13$ ,  $p < 0.05$ , where  $p$  is the level of significance, 1961–2010) (here and below, the  $\pm$  standard deviations are included) (Figure 4), which was around twice as much as the global mean temperature increase of  $0.14^\circ\text{C decade}^{-1}$  (1961–2010) based on the Goddard Institute for Space Studies (GISS) global temperature dataset (Hansen *et al.*, 2010).

In Figure 4 the individual MAAT time series are shown for the 14 coastal meteorological stations, all indicating trends towards a warmer climate, with an increasing number of warm extremes and a decreasing number of cold extremes after 1961 (Figure 5 and Table 2). According to Hanna *et al.* (2012), this warming was related to increases in both the AMO Index and Greenland Blocking Index (GBI; Fang (2004)). Subsequently, in Figure 5 the annual percentages of extremes are shown for all meteorological stations, illustrating individually for MAAT, annual mean daily maximum, and annual mean daily minimum (Figure 5(a)–(c) and Table 2) that the 2000s were far more extreme than earlier decades (1961–2000), due to the percentage of stations with warm extremes. For example, in the years 2003, 2005, and 2010 (based on the MAAT time series; Figure 5(a)) more than 70% (at least 10 out of 14 stations) of the stations observed warm extremes, with this proportion being 32% on average for the 2000s (Figure 5(a) and Table 2). The years 2003, 2005, and 2010 were the top 3 years regarding the highest percentage of warm extremes in the coastal Greenland observations since 1961, and are within the top 7 years globally according to GISS temperature dataset; for both Greenland and the global dataset the year 2010 had the highest MAAT. Conversely, for the 1980s 25% of the stations on average faced cold MAAT extremes (Figure 5(a) and Table 2), and the individual years 1983 and 1984 had record cold extremes of 100 and 64%, respectively. The years 1983 and 1984 had, according to the coastal observations, the two lowest

Table 2. The decadal mean percentages of warm and cold extremes for 1961–1970, 1971–1980, etc., and the overall occurrence of extremes: cold plus warm extremes.

Data	Parameter	1961–1970	1971–1980	1981–1990	1991–2000	2001–2010
MAAT	Percentage of warm extremes (%)	3	4	4	4	32
	Percentage of cold extremes (%)	7	7	25	9	0
	Overall occurrence of extremes: sum of warm and cold extremes (%)	10	11	29	13	32
Annual mean daily maximum	Percentage of warm extremes (%)	7	2	2	4	29
	Percentage of cold extremes (%)	5	8	19	12	0
	Overall occurrence of extremes: sum of warm and cold extremes (%)	12	10	21	16	29
Annual mean daily minimum	Percentage of warm extremes (%)	1	5	3	2	36
	Percentage of cold extremes (%)	9	14	12	11	0
	Overall occurrence of extremes: sum of warm and cold extremes (%)	10	19	15	13	36

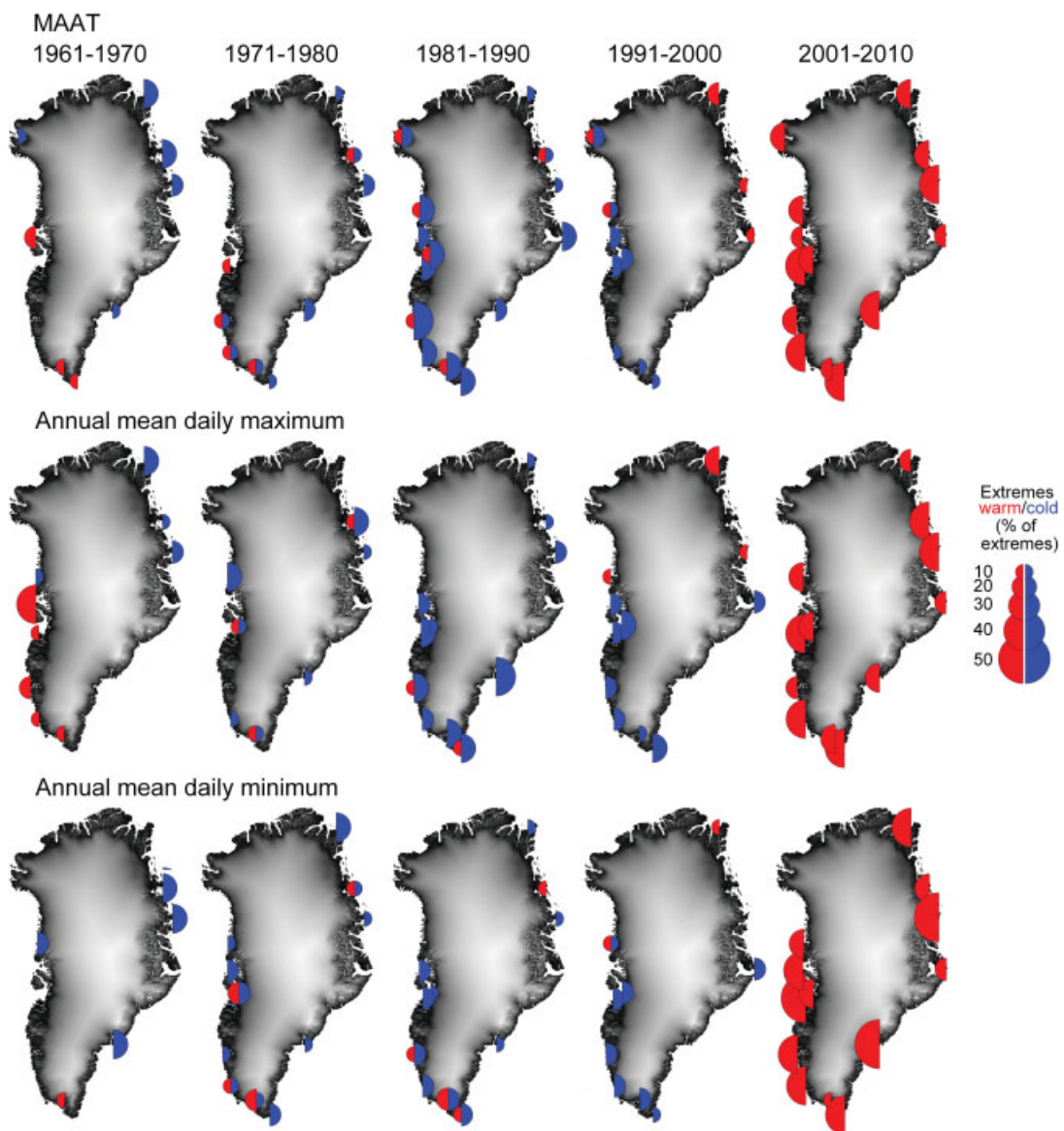


Figure 6. Spatial distribution of the mean decadal percentage (1961–1970, 1971–1980, etc.) of warm extremes (red half circles) and cold extremes (blue half circles) based on MAAT (top), annual mean daily maximum (centre), and annual mean daily minimum (bottom) from 1961 through 2010.

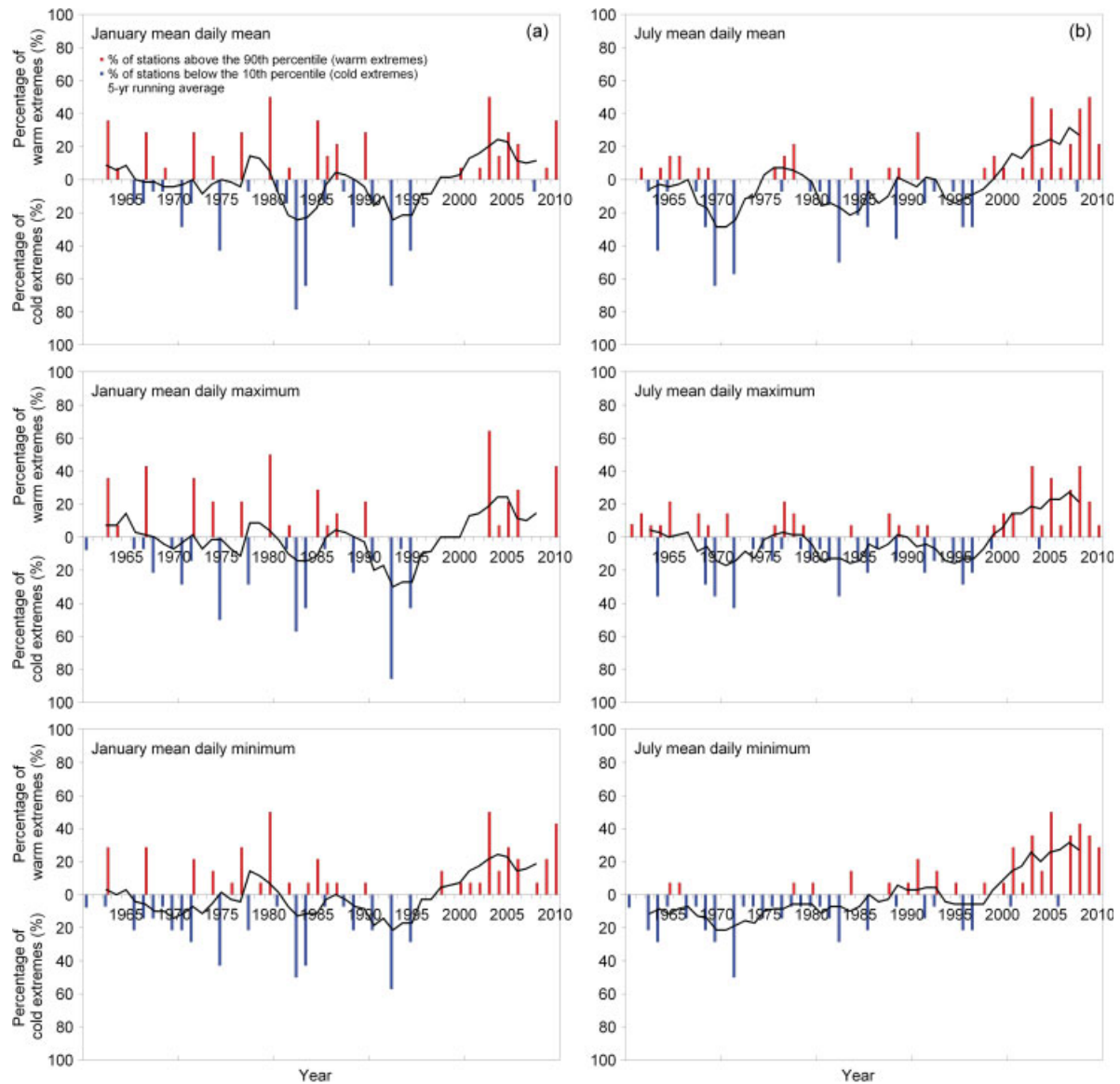


Figure 7. Time series of the annual percentage of warm extremes and cold extremes from 1961 through 2010, illustrated annually: (a) for January mean daily mean and January mean daily maximum and minimum and (b) for July.

MAAT values since 1960, a feature which is not consistent with the global GISS temperature dataset. Also, for the annual mean daily maximum (Figure 5(b)) and minimum time series (Figure 5(c)), the distributions and trends of cold and warm extremes (1961–2010) significantly follow (97.5% quartile; based on the null hypothesis) the described MAAT conditions. However, notable differences in the results between the MAAT and mean daily minimum and mean daily maximum temperature time series occurred. For the annual mean daily minimum time series (Figure 5 and Table 2), the decadal mean percentage of warm extremes in the 2000s (36%) was greater than the percentage for the annual mean daily maximum time series (29%), indicating that warm extremes occurred more often for the annual mean daily minimum time series than the maximum time series. For the 1960s and 1970s the decadal mean percentages of cold extremes were greater for the annual mean daily minimum time

series (9 and 14%), than for the annual mean daily maximum time series (5 and 8%) (Table 2). These differences in the cold and warm extreme patterns between the two time series are less pronounced compared with the global air temperature trends as described by Donat and Alexander (2012), where the distribution of both daily maximum and minimum temperatures shifted towards significantly higher temperatures from 1951–1980 to 1981–2010, and more importantly, that changes in temperature were greater for daily minimum (nighttime) than for daily maximum (daytime) temperatures. This global temperature trend illustrated by Donat and Alexander (2012) is followed by the annual mean daily maximum and minimum warm and cold extreme trends shown for Greenland's coastal stations, as the highest frequency of warm extremes for 2000s was observed in the annual mean daily minimum time series (Figure 5 and Table 2).

Table 3. Decadal mean percentages of warm and cold extremes for 1961–1970, 1971–1980, etc. for January and July based on daily mean, mean daily maximum, and mean daily minimum. Also, the overall occurrence of extremes: cold plus warm extremes are shown.

Month	Data	Parameter	1961–1970	1971–1980	1981–1990	1991–2000	2001–2010
January	Mean daily mean	Percentage of warm extremes (%)	8	12	11	1	16
		Percentage of cold extremes (%)	4	9	21	12	1
		Overall occurrence of extremes: sum of warm and cold extremes (%)	12	21	32	13	17
	Mean daily maximum	Percentage of warm extremes (%)	9	13	8	0	16
		Percentage of cold extremes (%)	5	12	14	15	0
		Overall occurrence of extremes: sum of warm and cold extremes (%)	14	25	22	15	16
	Mean daily minimum	Percentage of warm extremes (%)	6	13	6	2	20
		Percentage of cold extremes (%)	9	11	14	11	0
		Overall occurrence of extremes: sum of warm and cold extremes (%)	15	24	20	13	20
July	Mean daily mean	Percentage of warm extremes (%)	6	4	2	6	25
		Percentage of cold extremes (%)	16	7	16	9	1
		Overall occurrence of extremes: sum of warm and cold extremes (%)	22	11	18	15	26
	Mean daily maximum	Percentage of warm extremes (%)	8	6	3	4	21
		Percentage of cold extremes (%)	10	10	11	11	1
		Overall occurrence of extremes: sum of warm and cold extremes (%)	18	16	14	15	22
	Mean daily minimum	Percentage of warm extremes (%)	1	1	3	6	28
		Percentage of cold extremes (%)	14	12	8	6	1
		Overall occurrence of extremes: sum of warm and cold extremes (%)	15	13	11	12	29

Overall, since the 1960s for the three time series – MAAT, and the annual mean daily maximum and minimum temperatures – the number of cold extremes has on average decreased on the decadal timescale (besides a peak in 1980s for MAAT and annual mean daily maximum and a peak in 1970s for annual mean daily minimum), while the occurrence of warm extremes has on average increased even more, leading to a significant increase in extremes and a higher occurrence of total extremes (cold plus warm extremes) (Figure 5(a)–(c), and Table 2): a trend in keeping with the findings of Rahmstorf and Coumou (2011).

The increased aerosol content in the atmosphere caused by major episodic volcanic eruptions seems to have an impact on the coastal observed MAAT (Figure 4; see also Hanna *et al.*, 2005), and therefore both the proportion of cold extremes based on MAAT and the annual mean daily maximum and minimum temperatures exist (Figure 5). For all coastal stations MAAT decreased for approximately 1–3 years immediately following the El Chichon, Mexico (1982) and Pinatubo, Philippines (1991) volcanic eruptions, whereas for Agung, Indonesia (1963) this signal is much less striking (Figure 4). It has previously been indicated, e.g. by Hanna *et al.* (2005), that global dust veils generated by volcanic activity cool the Greenland Ice Sheet air temperature. The percentage of cold extremes is also clearly statistically linked with, and therefore most likely influenced by volcanic

eruptions (Figure 5). In the years immediately after El Chichon and Pinatubo eruptions, the percentage of cold extremes for MAAT increased from 64 to 100% and 29 to 50%, respectively (Figure 5a); these are the two main periods with the highest proportions of cold extremes. Also, for the annual mean daily maximum and minimum time series the percentage of cold extremes changed immediately after the Chichon and Pinatubo (Figure 5(b) and (c)); here, however, in contrast to the discussion above about Greenland and global day/night temperature trend differences, the percentages of cold extremes were greatest for the annual mean daily maximum time series and smallest for the annual mean daily minimum time series, since volcanic cooling effect is mainly to block solar radiation, i.e. is predominately a daytime effect.

Turning our attention to regional variations, the distribution of cold and warm extremes for coastal Greenland is illustrated in Figure 6 for MAAT, and annual mean daily maximum and minimum temperatures. For each decade (1961–1970, 1971–1980, etc.) the spatial variability of cold and warm extremes follows the average trends illustrated in Figure 5 and Table 2, showing that coastal meteorological stations in the 1970s, 1980s, and 1990s spatially faced a high percentage of cold extremes (more pronounced in West and Southwest Greenland), whereas stations in the 2000s a high percentage of warm extremes. Also, characteristic



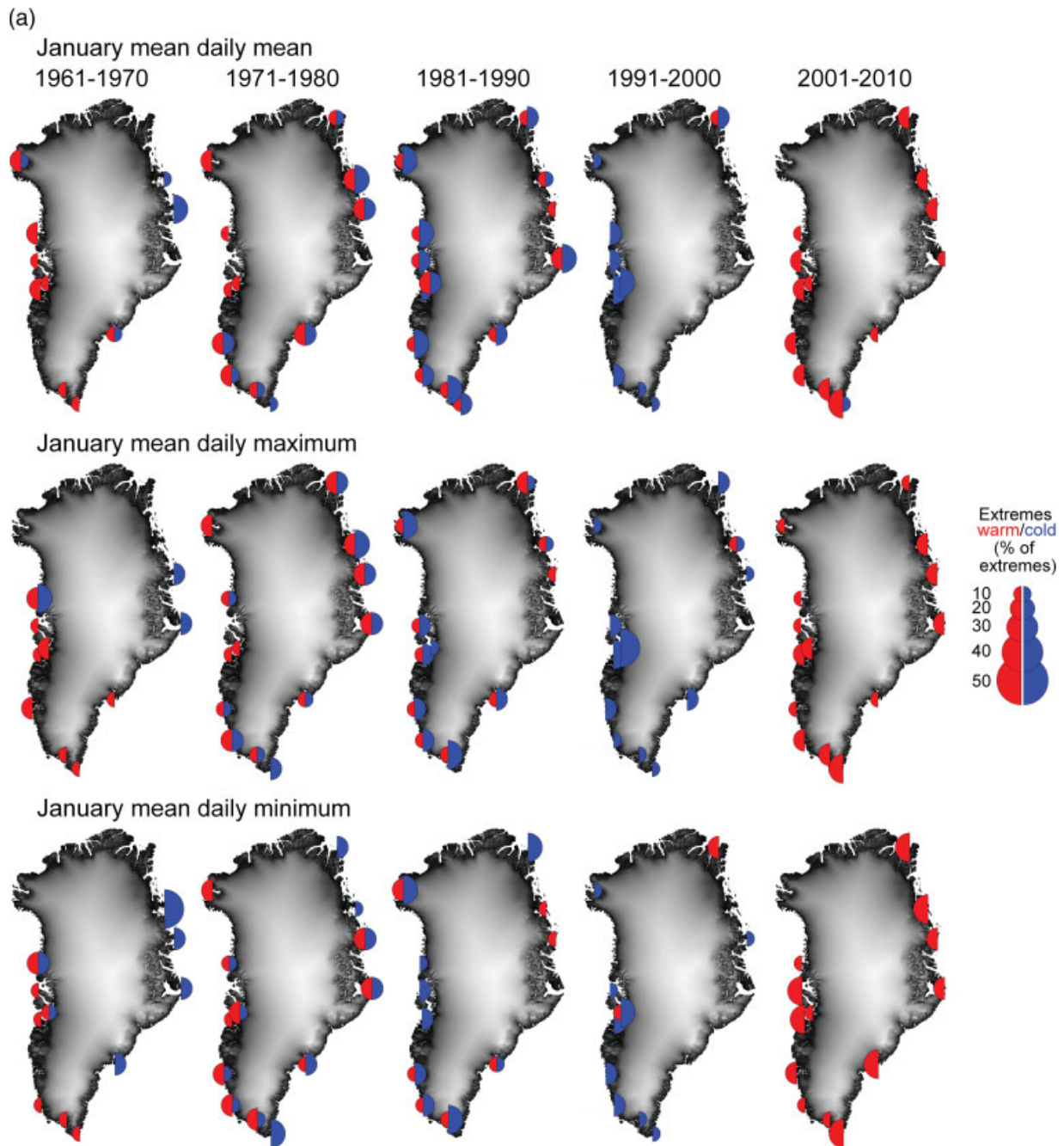


Figure 8. (a) An example of the spatial distribution of the mean monthly warm extremes (red half circles) and cold extremes (blue half circles) illustrated for January, based on January mean daily mean (top), January mean daily maximum (centre), and January mean daily minimum (bottom) on decadal scale (1961–1970, 1971–1980, etc.) from 1961 through 2010. (b) An example of the spatial distribution of the mean monthly warm extremes (red half circles) and cold extremes (blue half circles) illustrated for July, based on July mean daily mean (top), July mean daily maximum (centre), and July mean daily minimum (bottom) on decadal scale (1961–1970, 1971–1980, etc.) from 1961 through 2010.

of the spatial distribution – whether it is the MAAT, the annual mean daily maximum or mean daily minimum dataset – is that stations within a specific decade might have experienced both cold and warm extremes, but also that specific parts of coastal Greenland have been dominated by either cold or warm extremes such as the MAAT values during the 1990s and the annual mean daily maximum during the 1960s. For the MAAT in the 1990s, the northeast (west) part of Greenland was dominated by warm (cold) extremes. The opposite

occurred for the annual mean daily maximum dataset in the 1960s, where southwest (northeast) Greenland was dominated by warm (cold) extremes.

### 3.3. Monthly distribution of cold and warm extremes 1961–2010

On the monthly timescale (Figure 7 and Table 3) – here illustrated as an example for the months January and July – the distribution of both cold and warm extreme time series (the monthly mean daily mean, maximum,

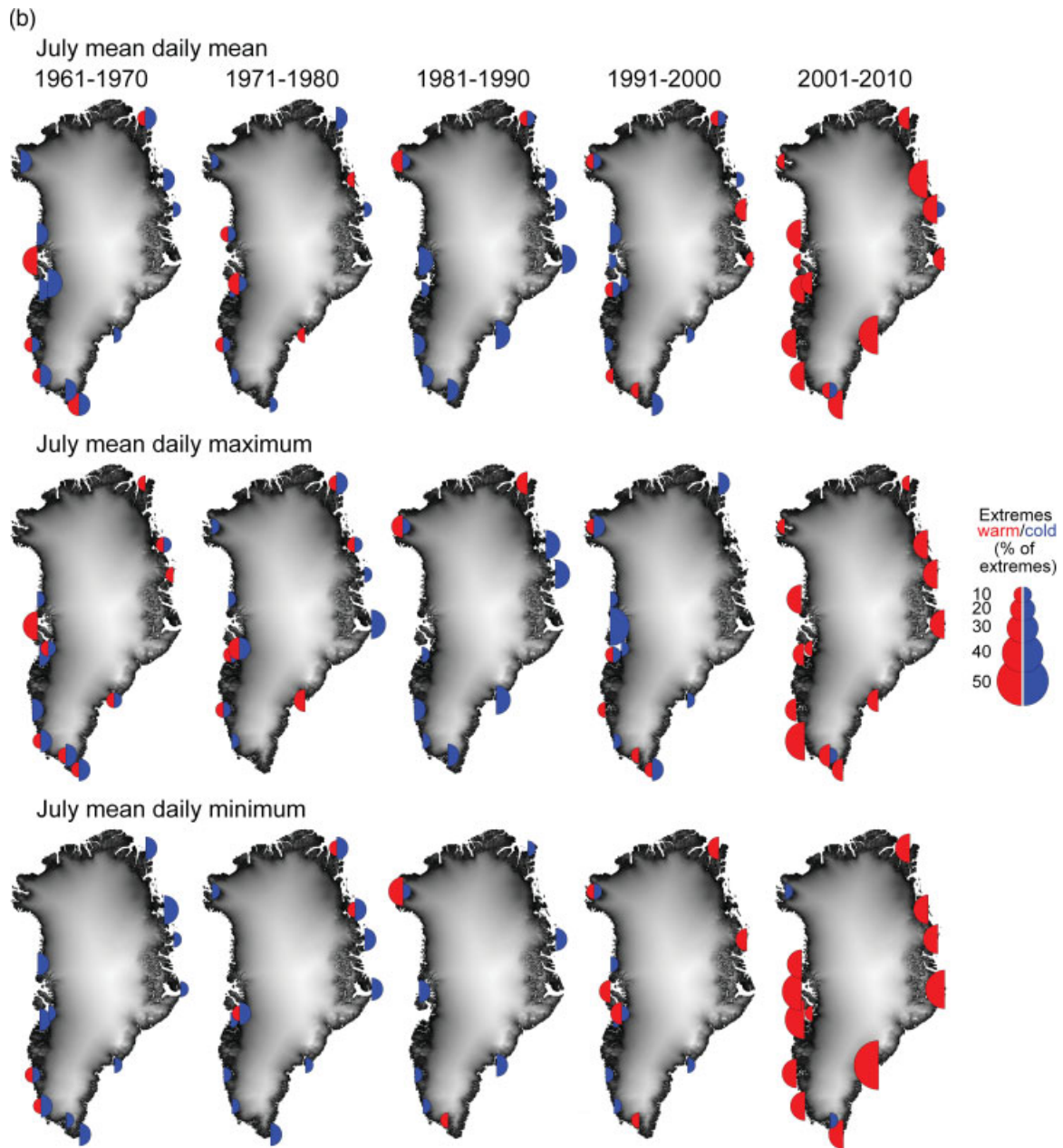


Figure 8. (continued)

and minimum) seems to be in line with the annual time series illustrated in Figure 5, with the highest percentage of cold extremes in the 1970s, 1980s, and 1990s, and the highest percentage of warm extremes in the 2000s. The same monthly trend for January and July applies for the spatial distribution of extremes (Figure 8(a) and (b)), where the spatial distribution of cold extremes dominated coastal Greenland in the 1970s and 1980s, and warm extremes in the 2000s. Furthermore, in Figure 9(a)–(c) monthly time series for January to December are illustrated on the decadal scale, showing the variability of cold and warm extremes based on monthly mean daily mean, maximum, and minimum temperatures. Also at the individual monthly scale, the monthly trends throughout the study period seem to follow each other – heading

towards lower percentages of cold extremes and higher percentage of warm extremes. An inter-comparison between monthly values indicates a variation in the percentage of extremes of  $\sim 10\%$ , except for the monthly cold extremes in the 2000s, which were close to zero for all months. The only season, which seems to differ from the general pattern, is the winter season (December through February), illustrated in green in Figure 9) for the 1980s, where the percentages of warm extremes were insignificantly higher compared with other seasons.

#### 3.4. East and West Greenland cold and warm extremes 1961–2010

Not only does the spatial distribution of stations indicate a pattern in extreme events (Figures 6 and 8),

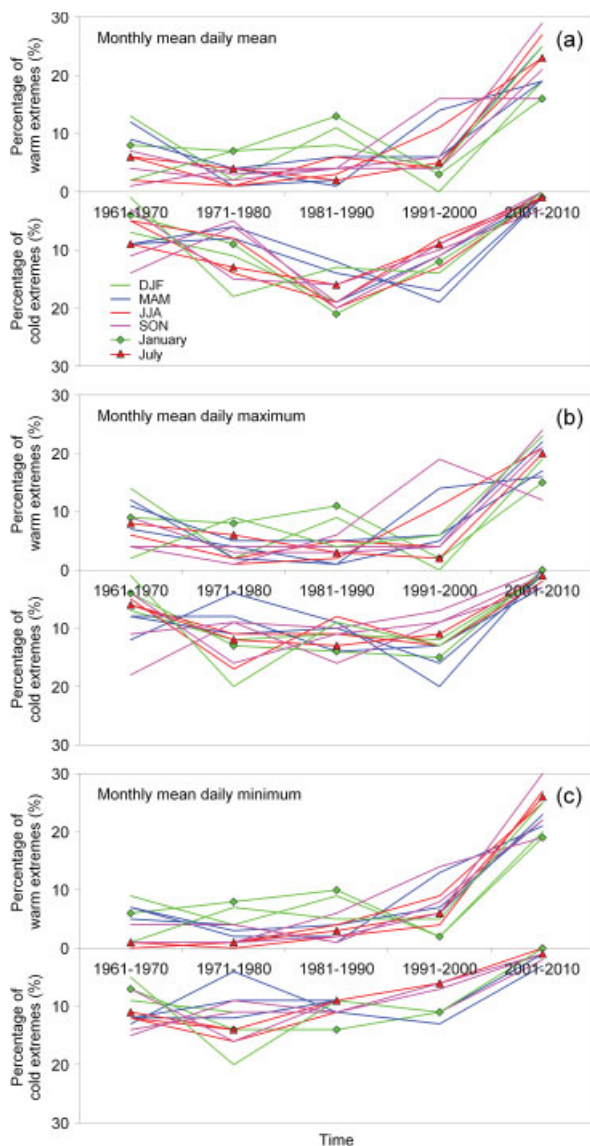


Figure 9. Time series of the percentage of warm extremes and cold extremes from 1961 through 2010, illustrated for January through December on: (a) monthly mean daily mean temperature data; (b) monthly mean daily maximum; and (c) monthly mean daily minimum. The colour codes follow December through February (DJF) (winter), March through May (MAM) (spring), June through August (JJA) (summer), and September through November (SON) (autumn), where January and July are highlighted as examples (for time series of January and July, see Figure 7).

but also this is emphasized by the division of Greenland into east and west sectors separated by the main ice sheet divide (Figure 1): For the East Greenland sector (based on six stations) the temperature increase was on average  $0.45 \pm 0.20 \text{ }^\circ\text{C decade}^{-1}$ , and only  $0.18 \pm 0.07 \text{ }^\circ\text{C decade}^{-1}$  for the West Greenland sector (based on eight stations; Figure 1) (trends, which both are outside the observed uncertainty range), indicating a significant (97.5% quartile; based on the null hypothesis) difference in the temperature increase between East and West Greenland – this temperature difference is further illustrated, where a deeper cooling in West/Southwest Greenland, than East Greenland, occurred in the 1980s

and 1990s, where the cooling is NAO-related (Hanna and Cappelen, 2003). The division of Greenland into these two sectors indicates that East Greenland coastal stations in the 1960s and 1970s (1990s and 2000s) faced a higher percentage of MAAT cold (warm) extremes than West Greenland (Figure 10). That East Greenland faced proportionately more extreme temperature conditions than West Greenland (Figure 10) during the period 1961–2010 is in line with the temperature trends for the two individual regions (Jones *et al.*, 1999), since a relatively rapidly warming climate leads to a marked increase in the number of extreme events (notably warm extremes) (Coumou and Rahmstorf, 2012), but is probably also in line with differences in NAO teleconnections between East and West Greenland (Hanna and Cappelen, 2003; Hanna *et al.*, 2012), and changes in Arctic sea ice coverage (Stendel *et al.*, 2008; Mernild *et al.*, 2010), and subsequent change in the surface albedo and the surface radiation budget.

On the monthly timescale for both East and West Greenland (Figure 11(a)–(c)) the distribution of both cold and warm extreme time series is illustrated based on monthly mean daily mean, maximum, and minimum surface air temperatures. Generally for East and West Greenland, respectively, the monthly mean daily mean time series illustrates a dominance of cold extremes in the 1970s and 1980s, and in the 1980s and 1990s. For East Greenland and West Greenland the highest percentage of monthly warm extremes and the lowest percentage of monthly cold extremes, both occurred in the 2000s. Also at the individual monthly scale, different monthly trends throughout the study period seem overall to follow each other – heading towards a lower percentage of cold extremes and higher percentage of warm extremes. For the monthly mean daily maximum and minimum time series the trend in the cold extremes is different between East and West Greenland (Figure 11(b) and (c)): for East Greenland from the 1960s to 2000s the trend in the percentage of cold extremes steadily decreased towards zero in 2000s, whereas for West Greenland the trend was opposite, where the percentage of cold extremes increased somewhat from the 1960s to 1990s, and thereafter decreased towards zero in the 2000s.

#### 4. Conclusion and summary

Greenland temperature time series for stations located around the margin of the ice sheet reveal unambiguously that since 1890 the coastal number of warm extremes was highest for the 2000s – even when compared with the Early Twentieth Century Warm Period in the 1930s and 1940s, the 2000s had an extended occurrence of annual warm extremes of at least 50%. The probability of high extreme temperatures greatly increases in a warming climate, which is in accordance with our results showing this trend; in addition we observe robust rapid shift from dominant cold to warm extremes, which occur within (climatically) relatively short 10–13 year periods. It is illustrated that a high positive NAO Index overall



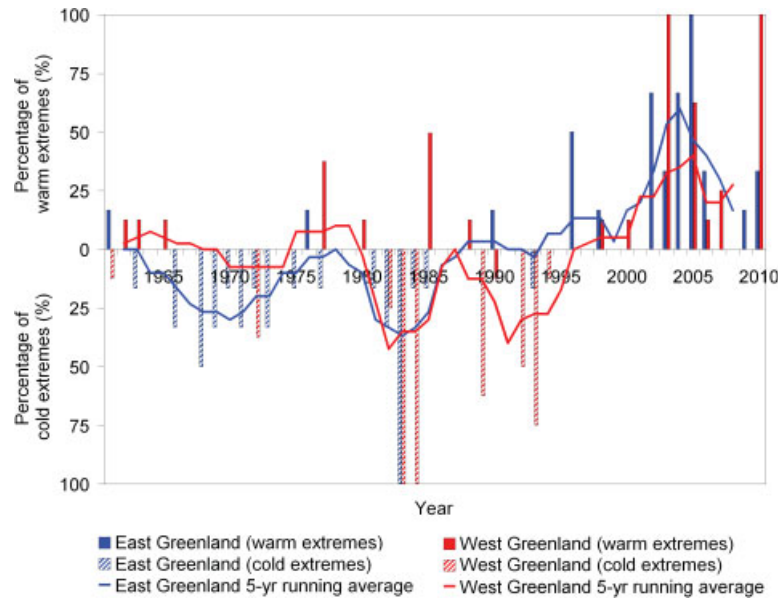


Figure 10. Annual time series from 1961 through 2010 of the percentage of warm extremes and cold extremes based on MAAT for both East Greenland (blue colours) and West Greenland (red colours). The division between East and West Greenland is illustrated in Figure 1.

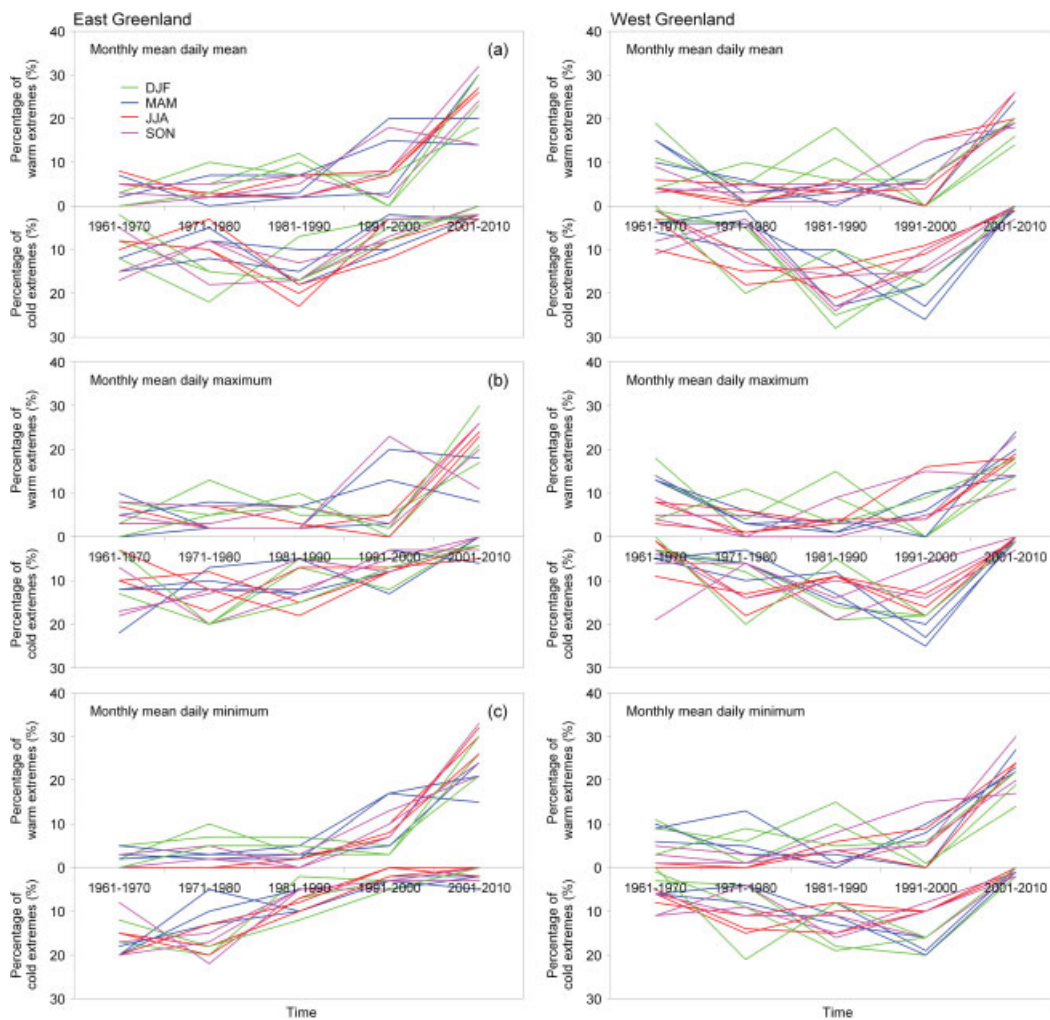


Figure 11. Decadal time series (1961–1970, 1971–1980, etc.) of the percentage of warm extremes and cold extremes for both East and West Greenland (the division between East and West Greenland is illustrated in Figure 1): (a) for monthly mean daily mean; (b) monthly mean daily maximum; and (c) monthly mean daily minimum.



equals a high number of cold extreme events, and vice versa.

Not only did the percentage of warm extremes increase from 1960 to 2010 for coastal Greenland but also the number of cold extremes decreased as well, leading to an overall higher percentage of total extremes (cold plus warm extremes). A similar trend has been confirmed based on CEI for the United States (Gleason *et al.*, 2008), where observations over the past decades illustrate that the area experiencing above-average temperature has been on the rise, with infrequent occurrence of significantly below-average temperatures.

A division of Greenland into east and west sectors separated by the main ice sheet divide shows that the occurrence of cold (warm) extremes was more pronounced in the East than in the West in the 1960s and 1970s (mid-1980s to the 2000s), probably in line with differences in NAO teleconnections on each side of the ice sheet divide. Moreover, we have shown that the recent climate warming was delayed a decade or so on the west side of Greenland compared with in the east.

## Acknowledgements

This work was supported by the Earth System Modeling Program and by the Scientific Discovery for Advanced Computing (SciDAC) Program within the U.S. Department of Energy's Office of Science and by a Los Alamos National Laboratory (LANL) Director's Fellowship. LANL is operated under the auspices of the National Nuclear Security Administration of the U.S. Department of Energy under Contract No. DE-AC52-06NA25396), and partly from the European Community's Seventh Framework Programme under grant agreement No. 262693. Special thanks are given to the Danish Meteorological Institute (DMI) for providing observed meteorological station data. GBI data were derived from the 20CR Reanalysis dataset provided by the NOAA-ESRL Physical Sciences Division, Boulder Colorado on their Web site at <http://www.esrl.noaa.gov/psd/>.

## 5. Conflict of interest

SHM compiled the dataset and analysed the data. SHM, EH, and JCY wrote the manuscript. JC and JKM contributed to the discussion of results and writing of the text.

## References

Allerup P, Madsen H, Vejen F. 1998. Estimating true precipitation in arctic areas. Nordic Hydrological Programme, NHP Report 44, Nordic Hydrological Conference, Helsinki.

Boas L, Wang P. R. 2011. Weather and climate data from Greenland 1958–2010 observation data with description. Danish Meteorological Institute Technical Report 11-10, DMI, Copenhagen, 22.

Box JE. 2002. Survey of Greenland instrumental temperature records: 1873–2001. *International Journal of Climatology* **22**: 1829–1847.

Box GEP, Jenkins GM. 1976. Time Series Analysis, Forecasting, and Control. Holden-Day, 575.

Cappelen J. 2011. DMI monthly climate data collection 1768–2010, Denmark, The Faroe Islands and Greenland. Danish Meteorological Institute, Technical Report 11-05, DMI, Copenhagen, 54, <http://www.dmi.dk/dmi/tr11-05.zip> (data).

Cappelen J (ed). 2013a. Greenland – DMI historical climate data collection 1873–2012 – with Danish abstracts. DMI Technical Report 13-04, Copenhagen, 74, [www.dmi.dk/dmi/tr13-04](http://www.dmi.dk/dmi/tr13-04).

Cappelen J (ed). 2013b. Weather and climate data from Greenland 1958–2012 - observation data with description. DMI Technical Report 13-11, Copenhagen, 23, [www.dmi.dk/dmi/tr13-11](http://www.dmi.dk/dmi/tr13-11).

Cappelen J, Jorgensen BV, Laursen EV, Stannius LS, Thomsen RS. 2000. The observed climate of Greenland 1958–99 – with climatological standard normals, 1961–90. Danish Meteorological Institute Technical Report 00-18, DMI, Copenhagen, 152, [http://www.dmi.dk/dmi/tr00-18-data\\_files.zip](http://www.dmi.dk/dmi/tr00-18-data_files.zip) (data).

Chylek P, Folland C, Lesins G, Wang M, Dubey M. 2009. Arctic air temperature change amplification and the Atlantic Multi-decadal Oscillation. *Geophysical Research Letters* **36**: L14801. DOI: 10.1029/2009GL038777.

Coumou D, Rahmstorf S. 2012. A decade of weather extremes. *Nature Climate Change* **2**: 491–496. DOI: 10.1038/nclimate1452

Donat MG, Alexander LV. 2012. The shifting probability distribution of global daytime and night-time temperatures. *Geophysical Research Letters* **39**: L14707. DOI: 10.1029/2012GL052459.

Fang Z-F. 2004. Statistical relationship between the northern hemisphere sea ice and atmospheric circulation during wintertime. In *Observation, Theory and Modeling of Atmospheric Variability*, Zhu X (ed). World Scientific Series on Meteorology of East Asia. World Scientific Publishing Company: Singapore; 131–141.

Gleason KL, Lawrimore JH, Levinson DH, Karl TR, Karoly DJ. 2008. A revised U.S. Climate Extreme Index. *Journal of Climate* **21**: 2124–2137.

Hanna E, Cappelen J. 2003. Recent cooling in coastal southern Greenland and relation with the North Atlantic Oscillation. *Geophysical Research Letters* **30**(3): 1132. DOI: 10.1029/2002GL015797.

Hanna E, Huybrechts P, Janssens I, Cappelen J, Steffen K, Stephens A. 2005. Runoff and mass balance of the Greenland Ice Sheet: 1958–2003. *Journal of Geophysical Research* **110**: D13108. DOI: 10.1029/2004JD005641.

Hanna E, Mernild SH, Cappelen J, Steffen K. 2012. Recent warming in Greenland in a long-term instrumental (1881–2012) climatic context. Part 1: evaluation of surface air temperature records. *Environmental Research Letters* **7**: 045404. DOI: 10.1088/1748-9326/7/4/045404.

Hanna E, Jones JM, Cappelen J, Mernild SH, Wood L, Steffen K, Huybrechts P. 2013. Discerning the influence of North Atlantic atmospheric and oceanic forcing effects on 1900–2010 Greenland summer climate and melt. *International Journal of Climatology* **33**: 862–888. DOI: 10.1002/joc.3475.

Hansen J, Ruedy R, Sato M, Lo K. 2010. Global surface temperature change. *Reviews of Geophysics* **48**: RG4004.

Heino R. 1994. Climate in Finland during the period of meteorological observations. Finnish Meteorological Institute Contribution, No. 12, Finnish Meteorological Institute, 209.

Hurrell JW. 1995. Decadal trends in the North Atlantic Oscillation: regional temperatures and precipitation. *Science* **269**: 676–679. DOI: 10.1126/science.269.5224.676.

Hurrell JW, van Loon H. 1997. Decadal variations in climate associated with the North Atlantic Oscillation. *Climatic Change* **36**: 301–326.

IPCC. 2007. Summary for policymakers. In *Climate Change 2007, The Physical Science Basis, Contribution of Working Group I to the Fourth Assessment Report of the Intergovernmental Panel on Climate Change*, Solomon S, Qin D, Manning M, Chen Z, Marquis M, Averyt KB, Tignor M, Miller HL (eds). Cambridge University Press: Cambridge, UK and New York, USA.

IPCC. 2012. Managing the risks of extreme events and disasters to advance climate change adaptation. In *A Special Report of Working Groups I and II of the Intergovernmental Panel on Climate Change*, Field CB, Barros V, Stocker TF, Qin D, Dokken DJ, Ebi KL, Mastrandrea MD, Mach KJ, Plattner G-K, Allen SK, Tignor M, Midgley PM (eds). Cambridge University Press: Cambridge, UK, and New York, USA; 582.

Jones PD, New M, Parker DE, Martin S, Rigor IG. 1999. Surface air temperature and its changes over the past 150 years. *Reviews of Geophysics* **37**(2): 173–199.

Karl TR, Knight RW, Easterling DR, Quayle RG. 1996. Indices of climate change for the United States. *Bulletin of the American Meteorological Society* **77**(2): 279–292.

- Liston GE, Elder K. 2006. A meteorological distribution system for high-resolution terrestrial modeling (MicroMet). *Journal of Hydrometeorology* **7**(2): 217–234.
- Liston GE, Sturm M. 2002. Winter precipitation patterns in Arctic Alaska determined from a blowing-snow model and snow-depth observations. *Journal of Hydrometeorology* **3**: 646–659.
- Liston GE, Sturm M. 2004. The role of winter sublimation in the Arctic moisture budget. *Nordic Hydrology* **35**(4): 325–334.
- Lubchenco J, Karl TR. 2012. Predicting and managing extreme weather events. *Physics Today* **65**(3): 31–37.
- Mernild SH, Liston GE, Hiemstra CA, Christensen JH. 2010. Greenland Ice Sheet surface mass-balance modeling in a 131-year perspective 1950–2080. *Journal of Hydrometeorology* **11**(1): 3–25.
- Rahmstorf S, Coumou D. 2011. Increase of extreme events in a warming world. *Proceedings of the National Academy of Sciences* **108**(44): 17905–17909. DOI: 10.1073/pnas.1101766108.
- Steffensen P. 1996. Standard Normal Homogeneity test for Windows. User Guide. Danish Meteorological Institute Technical Report 96–13, DMI, Copenhagen, 35.
- Steffensen P, Larsen FL, Cappelen J. 1993. Homogeneity test of climatological data. Danish Meteorological Institute Technical Report 93–12, DMI, Copenhagen, 22.
- Stendel M, Christensen JH, Petersen D. 2008. Arctic Climate and Climate Change with a Focus on Greenland. *Advances in Ecological Research* **40**: 13–43. DOI: 10.1016/S0065-2504(07)00002-5.
- Tuomenvirta H, Alexandersson H, Drebs A, Frich P, Nordli PO. 2000. Trends in the Nordic and Arctic temperature extremes and ranges. *Journal of Climate* **13**: 977–990.
- Walton TL Jr. 1996. Fill-in of missing data in univariate coastal data. *Journal of Applied Statistics* **23**: 31–39.
- Wu Z, Huang NE, Wallace JM, Smoliak BV, Chen X. 2011. On the time-varying trend in global-mean surface temperature. *Climate Dynamics* **37**: 759–773. DOI: 10.1007/s00382-011-1128-8.
- Yang D, Goodison BE, Metcalfe JR, Golubev VS, Bates R, Pangburn T, Hanson CL. 1998. Accuracy of NWS 8 standard nonrecording precipitation gauge: results and application of WMO intercomparison. *Journal of Atmospheric and Oceanic Technology* **15**: 54–68.

[2]

Mernild, S. H., Hanna, E., McConnell, J. R., Sigl, M.,  
Beckerman, A. P., Yde, J. C., Cappelen, J., and Steffen, K.  
2014. Greenland precipitation trends in a long-term instrumental  
climate context (1890–2012): Evaluation of coastal and ice core  
records.  
International Journal of Climatology, doi:10.1002/joc.3986.

Reprinted with permission from Wiley

# Greenland precipitation trends in a long-term instrumental climate context (1890–2012): evaluation of coastal and ice core records

Sebastian H. Mernild,<sup>a,b,\*</sup> Edward Hanna,<sup>c</sup> Joseph R. McConnell,<sup>d</sup> Michael Sigl,<sup>d</sup> Andrew P. Beckerman,<sup>e</sup> Jacob C. Yde,<sup>f</sup> John Cappelen,<sup>g</sup> Jeppe K. Malmros<sup>a</sup> and Konrad Steffen<sup>h,i,j</sup>

<sup>a</sup> *Glaciology and Climate Change Laboratory, Center for Scientific Studies/Centro de Estudios Científicos (CECs), Valdivia, Chile*

<sup>b</sup> *Climate, Ocean, and Sea Ice Modeling Group, Computational Physics and Methods, Los Alamos National Laboratory, NM, USA*

<sup>c</sup> *Department of Geography, University of Sheffield, UK*

<sup>d</sup> *Desert Research Institute, Reno, NV, USA*

<sup>e</sup> *Department of Animal and Plant Sciences, University of Sheffield, UK*

<sup>f</sup> *Faculty of Engineering Science, Sogn og Fjordane University College, Sogndal, Norway*

<sup>g</sup> *Data and Climate, Danish Meteorological Institute, Copenhagen, Denmark*

<sup>h</sup> *Swiss Federal Research Institute WSL, Birmensdorf, Switzerland*

<sup>i</sup> *Institute for Atmosphere and Climate, Swiss Federal Institute of Technology, Zurich, Switzerland*

<sup>j</sup> *Architecture, Civil and Environmental Engineering, Ecole Polytechnique Federal de Lausanne, Switzerland*

**ABSTRACT:** Here, we present an analysis of monthly, seasonal, and annual long-term precipitation time-series compiled from coastal meteorological stations in Greenland and Greenland Ice Sheet (GrIS) ice cores (including three new ice core records from ACT11D, Tunu2013, and Summit2010). The dataset covers the period from 1890 to 2012, a period of climate warming. For approximately the first decade of the new millennium (2001–2012) minimum and maximum mean annual precipitation conditions are found in Northeast Greenland (Tunu2013 *c.* 120 mm water equivalent (w.e.) year<sup>-1</sup>) and South Greenland (Ikerasassuaq; *c.* 2300 mm w.e. year<sup>-1</sup>), respectively. The coastal meteorological stations showed on average increasing trends for 1890–2012 (3.5 mm w.e. year<sup>-2</sup>) and 1961–2012 (1.3 mm w.e. year<sup>-2</sup>). Years with high coastal annual precipitation also had a: (1) significant high number of precipitation days ( $r^2 = 0.59$ ); and (2) high precipitation intensity measured as 24-h precipitation ( $r^2 = 0.54$ ). For the GrIS the precipitation estimated from ice cores increased on average by 0.1 mm w.e. year<sup>-2</sup> (1890–2000), showing an antiphase variability in precipitation trends between the GrIS and the coastal regions. Around 1960 a major shift occurred in the precipitation pattern towards wetter precipitation conditions for coastal Greenland, while drier conditions became more prevalent on the GrIS. Differences in precipitation trends indicate a heterogeneous spatial distribution of precipitation in Greenland. An Empirical Orthogonal Function analysis reveals a spatiotemporal cycle of precipitation that is linked instantaneously to the North Atlantic Oscillation and the Atlantic Multidecadal Oscillation and with an ~6 years lag time response to the Greenland Blocking Index.

**KEY WORDS** climate; Greenland; ice core; observations; precipitation; weather stations

*Received 13 December 2013; Revised 24 February 2014; Accepted 25 February 2014*

## 1. Introduction

During the last decade attention has been on climate change and its present and potential future impact on the mass balances of the Greenland Ice Sheet (GrIS) and peripheral glaciers and ice caps (GIC) (Steffen and Box, 2001; Hanna *et al.*, 2005, 2006, 2008, 2011, 2013a, 2013b; Box *et al.*, 2006; Fettweis *et al.*, 2008; Bales *et al.*, 2009; Ettema *et al.*, 2009; van den Broeke *et al.*, 2009; Radić and Hock, 2011; Mernild *et al.*, 2010a, 2011a, 2011b, 2013a, 2013b; Marzeion *et al.*, 2012; IPCC, 2013: Chapters 4

and 13), and freshwater (river) runoff from Greenlandic glacier-covered catchments (Mernild *et al.*, 2010b, 2011c; Mernild and Liston, 2012; Rennermalm *et al.*, 2012; Mikkelsen *et al.*, 2013). Mass-balance changes are the sum of surface accumulation (precipitation), surface ablation (evaporation, sublimation, and runoff), and wastage processes (calving), and are to a large extent influenced by changes in Greenlandic climate and ocean temperatures (Straneo *et al.*, 2010, 2013; Hanna *et al.*, 2009, 2013c).

An improved and updated understanding of precipitation conditions in Greenland is relevant not only to climatologists but also to glaciologists, hydrologists, ecologists and the wider population due to, e.g. the potential for hydropower production in Greenland. Therefore, the motivation for this Greenland precipitation analysis is to include both the coastal zone (the land area between the

\* Correspondence to: S. H. Mernild, Glaciology and Climate Change Laboratory, Center for Scientific Studies/Centro de Estudios Científicos (CECs), Av. Arturo Prat 514, 5110466 Valdivia, Chile. E-mail: smernild@gmail.com

ocean and GrIS, including several thousand GIC) and the GrIS for climatological normal periods, to enlarge our knowledge, which will contain an expanded update of earlier comprehensive Greenland climate and precipitation studies (1958–2005) (Yang *et al.*, 1999; Steffen and Box, 2001; Hanna *et al.*, 2006; Bales *et al.*, 2009). This study is timely given the recent rapid changes in Greenland climatology (Hanna *et al.*, 2012, 2013a; Mernild *et al.*, 2013c) and GrIS and GIC mass balances (Box *et al.*, 2012; Liston and Mernild, 2012; Hanna *et al.*, 2013b) that have occurred over the past few decades.

Here, we present long-term monthly, seasonal, and annual precipitation time series from near-coastal meteorological stations in Greenland (1890–2012) and GrIS ice cores (1890–2011). We examine climatological normal periods and shorter recent periods in order to provide evidence of climate change and variability in precipitation patterns. Also, we analyze the coastal precipitation intensity – expressed as the highest 24-h precipitation – and the number of precipitation days in relation to the precipitation sum, and the occurrence and trends of driest and wettest conditions on monthly, seasonal, and annual time-scales. Finally, we employ an Empirical Orthogonal Function (EOF) analysis to evaluate the patterns of temporal and spatial precipitation variations, and combine these with cross-correlations to relate the Greenland precipitation patterns to atmospheric circulation indices: the North Atlantic Oscillation (NAO), the Atlantic Multidecadal Oscillation (AMO), and the Greenland Blocking Index (GBI).

This paper follows the analytical structure of Hanna *et al.* (2012b), where long-term near-coastal surface air temperature records were analyzed on monthly, seasonal, and annual time-scales. To keep the analyses similar, our precipitation datasets were analyzed on a seasonal scale using standard 3-month meteorological seasons: December through February (DJF: winter), March through May (MAM: spring), June through August (JJA: summer), September through November (SON: autumn).

## 2. Precipitation dataset and analysis

### 2.1. Near-coastal precipitation records

Coastal precipitation data were measured at fourteen Greenland synoptic weather stations operated by Danish Meteorological Institute (DMI) (Cappelen, 2013a, 2013b) (Figure 1). Technical weather station details, including details of locations and running time periods, for the stations used herein are illustrated in Table 1. The coastal precipitation data have been quality controlled (initially subject to visual examination) and homogenized using the standard normal homogeneity test (Steffensen *et al.*, 1993; Steffensen, 1996), and compared with neighboring station records where data are available (Cappelen, 2013a). Where the homogeneity test was not conducted by DMI, it was specifically done for this study (this was the case for the stations Nuuk, Ittoqqortoormiit, and Tasiilaq). Periodic gaps in the coastal dataset were filled using linear

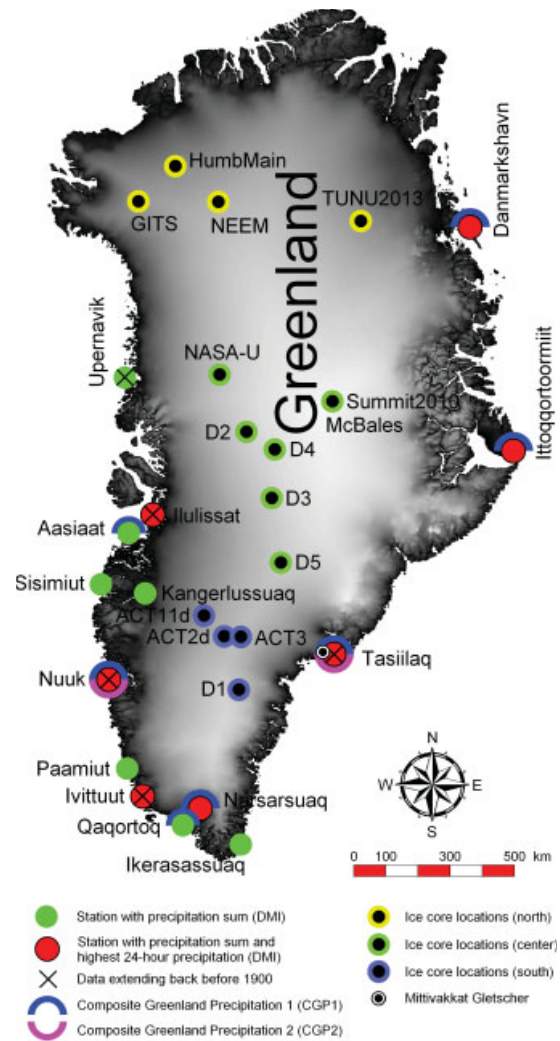


Figure 1. Location map of Greenland Danish Meteorological Institute coastal climate stations and ice core locations used in this study.

correlation against the nearest coastal station. Bales *et al.* (2009) stated that this method provides the best available estimate for gap filling, even though the stations might be several hundreds of kilometers apart. Five of the coastal station sites Upernavik, Ilulissat, Nuuk, Ivittuut, and Tasiilaq (Figure 1) all have observed precipitation records extending back before 1900, giving a reasonable long-term distribution of precipitation patterns in the coastal zone from Northwest Greenland (Upernavik) going south to Southeast Greenland (Tasiilaq). The other station records extend back to around 1961, except for Kangerlussuaq (1976–2012).

Coastal precipitation was measured using the manual Danish Hellmann-type gauges (200 cm<sup>2</sup> opening) placed with their orifices *c.* 2.5 m above the ground surface and equipped with a Nipher shield to minimize undercatch due to drifting snow (Allerup *et al.*, 2000), or the automatic Geonor and Pluvio gauges (having the same opening area, distance above the ground, and shield as the Hellmann gauges). The observed precipitation dataset was bias-corrected following Allerup *et al.* (1998, 2000) due



Table 1. Details of the coastal Greenland meteorological stations used in this study.

Station	DMI operated meteorological stations with the World Meteorological Organization (WMO) code	Latitude (°N)	Longitude (°W)	Available data period	Precipitation parameters	Mean precipitation bias correction factor
Upernavik	34210/04210/04211	72.78	56.13	Jan 1890–Dec 1980	Sum	1.55
Aasiaat*	04220	68.70	52.75	Jan 1958–present	Sum	1.56
Ilulissat	34216/04216/04221	69.23	51.07	Jan 1890–Dec 1984	Sum highest 24-h	1.43
Sisimiut	4230/4234	66.92	53.67	Jan 1961–present (excl. 1993–2001 and 2004–2008)	Sum	1.54
Kangerlussuaq*	04231	67.02	50.70	Jan 1976–present	Sum	1.46
Nuuk***	34250/04250	64.17	51.75	Jan 1890–present	Sum highest 24-h†	1.54
Paamiut	04260	62.00	49.67	Jan 1958–Aug 1992	Sum	1.37
Ivittuut	34262	61.20	48.18	Jan 1890–Dec 1960	Sum highest 24-h	1.36
Narsarsuaq*	04270	61.17	45.42	Jan 1961–present	Sum highest 24-h	1.27
Qaqortoq*	04272	60.72	46.05	Jan 1961–present	Sum	1.33
Danmarkshavn*	04320	76.76	18.67	Jan 1949–present	Sum highest 24-h	1.74
Ittoqqortoormiit*	34339/04339	70.48	21.95	Jan 1950–present	Sum highest 24-h	1.48
Tasiilaq***	34360/04360	65.60	37.63	Jan 1898–present	Sum highest 24-h	1.46
Ikerasassuaq	04390	60.05	43.15	Jan 1958–present (excl. 1981–1992)	Sum	1.47
Mean and standard deviation	–	–	–	–	–	1.47 ± 0.12

\*CGP1 (1961–2012).

\*\*CGP2 (1890–2012).

†The highest 24-h precipitation rate covers the period 1922 through 2012.

to systematic errors such as wind-induced undercatch (because of wind field deformation and turbulence from the measurement instrument) and wetting losses [water subject to evaporation from the surface of the inside walls of the precipitation gauge after a precipitation event and water retained on the walls of the gauge and its containers after its emptying (Goodison *et al.*, 1989; Metcalfe *et al.*, 1994)]. The mean bias correction multiplier for under-caught precipitation was  $1.47 \pm 0.12$  (where  $\pm$  henceforth equals one standard deviation) for all 14 stations (Table 1), ranging from 1.48–1.74 in the northern part of coastal Greenland to 1.27–1.56 in the southern part. These correction intervals correspond to results from Yang *et al.* (1999), who reported total annual gauge bias corrections of 1.50–1.75 in the northern part and 1.20–1.40 in the southern part for the Hellmann gauge-measured precipitation. In their analysis, Yang *et al.* (1999) included wind-induced undercatch, wetting losses, and trace amounts. The latter is a measurement of precipitation of less than 0.1 mm, which is below the resolution of the gauge measurement. The bias correction was highest where the percentage of snow in total annual precipitation was greatest, varying from *c.* 70–80% in the northern part of Greenland to *c.* 30–40% in the southern part. This regional disparity corresponds with progressively higher temperatures from north to south. This has also been confirmed by, e.g. Yang *et al.* (1999) and Bales *et al.* (2009). Henceforth, bias corrected precipitation will be referred to as *precipitation*.

We calculate mean annual sums of coastal precipitation from seven stations asterisked (\*) in Table 1 to construct

a coastal composite Greenland precipitation (CGP1) time series from 1961 to 2012 (shown as an anomaly in Figure 2(a)): Out of the seven station time series, 351 of 364 (96%) annual precipitation values were present and used for the CGP1 time series. Where data were missing (4%) the mean annual CGP1 sums were calculated only based on available data. In addition, we construct a composite coastal Greenland precipitation (CGP2) time series from 1900 to 2012 based on sums from the only two long-term coastal stations covering the entire period asterisked (\*\*) in Table 1: Nuuk (1890–2012) and Tasiilaq (1898–2012) (Figure 2(a)). For the CGP2 1900–2012 time series 84% of the data were present and used for the years where mean annual precipitation data were present for both Nuuk and Tasiilaq. CGP2 has the advantage of illustrating the coastal composite precipitation changes for parts of the southern half of Greenland since 1898, through two periods during the 1930s–1940s and 1990s–2012, where regional warming is acknowledged (Chylek *et al.*, 2006; Hanna *et al.*, 2012). However, quite often precipitation trends are opposite in southeast and southwest Greenland and have different climatic forcing functions. Precipitation in southeast Greenland is generally affected by the cyclonicity between Iceland and Greenland, whereas precipitation in southwest Greenland is often dominated by low pressures forming in the Labrador Sea (Hanna *et al.*, 2006).

## 2.2. Ice core estimated precipitation records

Precipitation from the GrIS was estimated from annual layer water-equivalent thicknesses from 15 ice cores

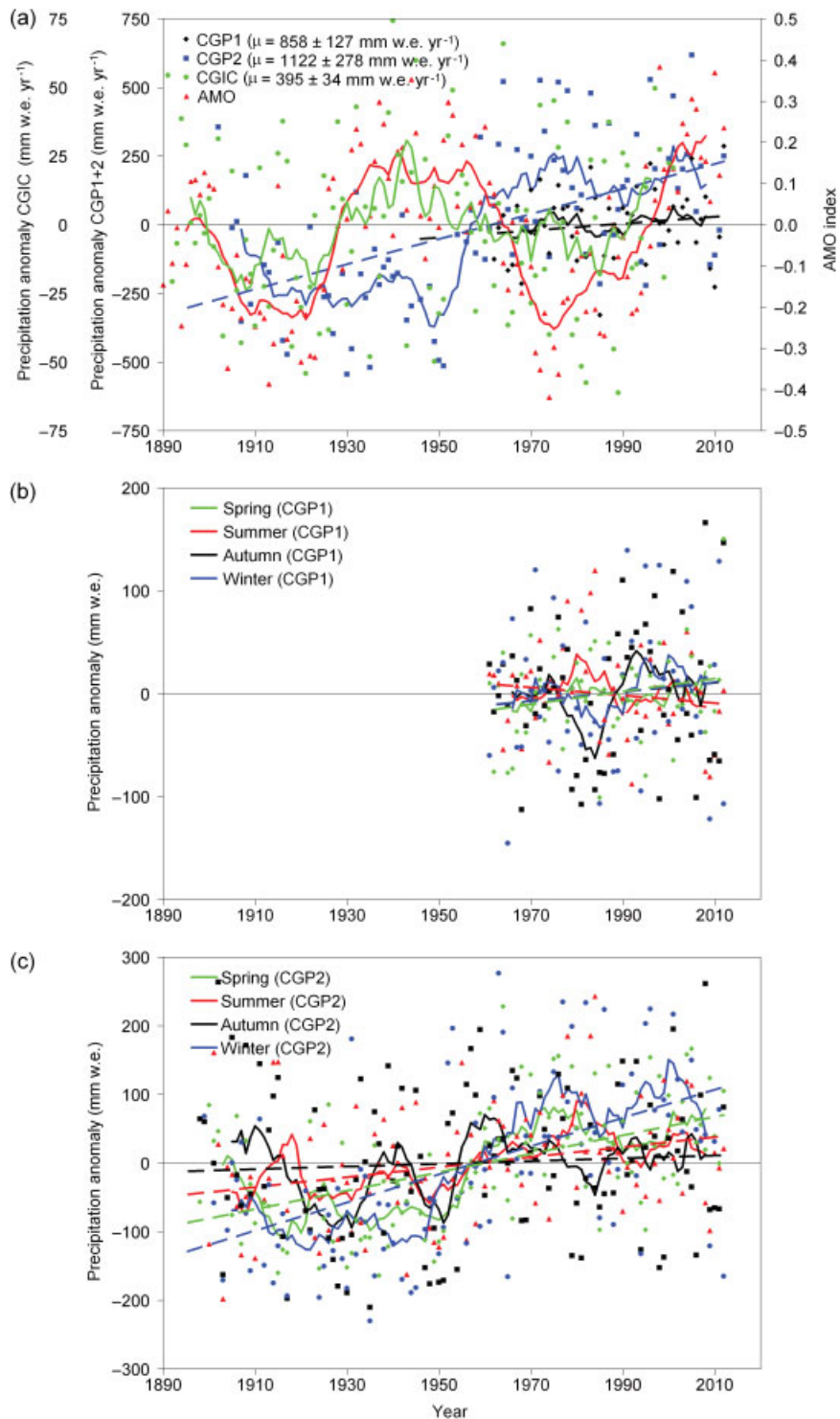


Figure 2. Time-series of Greenland precipitation anomaly sum from coastal stations and from GrIS ice cores, where dots represent the annual precipitation, including 10-year running means and trend lines: (a) coastal composite mean annual precipitation (CGP1) (Aassiat, Nuuk, Narsarsuaq, Qaqortoq, Danmarkshavn, Ittoqqortoormiit, and Tasiilaq; 1961–2012) and CGP2 (Nuuk and Tasiilaq; 1900–2012), composite GrIS ice core mean annual precipitation (CGIC), and AMO; (b) composite mean seasonal CGP1; and (c) composite mean seasonal CGP2. Note the different scales on the ordinate.

(Figure 1 and Table 2). These ice-core time-series provide a spatial GrIS net solid precipitation (i.e. net accumulation) distribution from 1890–2010 for the Tunu2013 and ACT11d ice cores, 1890–2009 (Summit2010), 1890–2003 (ACT2d and ACT3), 1890–2002 (McBales,

D4, and D5), 1890–2001 (NEEM-2008-S3), 1890–1998 (D1, D2, and D3), 1890–1995 (GITS), and 1890–1994 (HumbMain and NASA-U). This method for determining GrIS net solid precipitation does take into account the effects of evaporation and sublimation and would therefore

Table 2. Details of the Greenland Ice Sheet ice cores used in this study.

Ice core	Latitude (°N)	Longitude (°W)	Available data period
HumbMain	78.5	56.8	1890–1994
NASA-U	73.8	49.5	1890–1994
GITS	77.1	61.0	1890–1995
D1	64.5	43.5	1890–1998
D2	71.8	46.2	1890–1998
D3	69.8	44.0	1890–1998
D4	71.4	44.0	1890–2002
D5	68.5	42.9	1890–2002
NEEM-2008-S3	77.5	51.1	1890–2001
McBales	72.5	38.3	1890–2002
ACT2d	66.0	45.2	1890–2003
ACT3	66.0	43.6	1890–2003
Summit2010	72.5	38.3	1890–2009
TUNU2013	78.0	34.0	1890–2010
ACT11d	66.5	46.3	1890–2010

potentially underestimate the actual annual total precipitation. Evaporation is almost negligible at the interior of the GrIS due to daily near-surface air temperatures and mean annual near-surface air temperatures below the freezing point ( $-32$  to  $-25$  °C year<sup>-1</sup>, 1950–2011) (McGrath *et al.*, 2013), where sublimation is likely to be the primary cause of ablation. Surface mass balance simulations indicate that sublimation loss constitutes about 8% (1960–2010) of the annual GrIS precipitation (Mernild *et al.*, 2008a; Mernild and Liston, 2012). Therefore, to compensate for the sublimation and evaporation loss annual GrIS net precipitation was adjusted (in line with previous work by Bales *et al.*, 2009) by adding 8%. Therefore, the GrIS ice-core corrected net solid precipitation will henceforth be referred to as *precipitation*.

From 1890 to 1994, 100% coverage of annual ice core estimated precipitation values were present for all 15 ice core time series. From 1995 to 2000, 67 of 90 (74%) annual precipitation values were present and used, whereas from 2001 to 2010 only 42 of 150 (28%) were available. This decreasing amount of available ice core data through time is in contrast to the increasing amount of data from coastal weather stations, where the majority of observations are available for 1961 to 2012. Based on the ice-core estimated precipitation dataset (from all 15 ice cores) we present a composite GrIS ice core precipitation (CGIC) time-series from 1890 to 2000 (shown as an anomaly in Figure 2(a)), however CGIC time-series might be biased after 1995 due to incomplete ice core time-series. Due to low coverage of available ice core data, the latest decade (2001–2010) was excluded from the CGIC time-series.

Ice cores were collected from higher elevation (>2000 m) sites widely distributed around the GrIS (Figure 1). Details on the collection and measurement techniques used to develop many of the ice core accumulation records have previously been presented (Bales *et al.*, 2009; Hanna *et al.*, 2006, 2011). Hence, here we focus on the development of three new ice core records: ACT11D, Tunu2013, and Summit2010. All three ice

cores were collected without drilling fluid using an electromechanical drill. The ~1-m long cores were returned frozen to the laboratory (in Reno, Nevada), where they were cut into longitudinal samples with cross sections  $\sim 0.032 \times \sim 0.032$  m. The longitudinal samples were analyzed for a broad range of ~35 elements, chemical species, and water isotopes using a unique continuous ice core melter system (McConnell *et al.*, 2002, 2007). While nearly all parameters show distinct annual cycles, we primarily used non sea-salt sulfur, calcium, sodium, black carbon, and deuterium to count annual layers. Well-known, dated volcanic horizons were used to confirm the annual layer counts (Sigl *et al.*, 2013). Uncertainty in the annual dating is estimated to be <2 year for the Tunu2013 and Summit2010 records, which were collected in the dry snow zone of the GrIS. ACT11d was collected in the percolation zone, where meltwater forming at the surface percolates into the snowpack before refreezing, thereby mixing the preserved chemical record. Percolation at the ACT11d site generally is limited to much less than the thickness of the annual snow layer so perturbation of the record is limited. We estimate the annual dating uncertainty at ACT11d as well to be <2 years. Annual net accumulation in water equivalent was determined from the difference in depth between two annual markers after converting the chemical records from snow depth to water equivalent depth. Previous studies using continuous measurements of closely spaced ice cores suggest that due to surface undulations on the ice sheet the uncertainty in annual accumulation measurements from a single ice core record is ~30 mm w.e. year<sup>-1</sup> (McConnell *et al.*, 2000).

### 2.3. Statistical calculations

We applied standard descriptive statistics such as mean values, standard deviation and extreme (minimum and maximum) values. In addition, linear regression analysis was used to evaluate evidence of changes and trends for the various climatological normal periods overlapping by 10-year intervals (e.g. 1961–1990, 1971–2000, etc.). Shorter recent periods of interest, e.g. 1991–2012 and 2001–2012, were also included in these calculations. To test for possible relations and trends, all correlations labeled as ‘significant’ are at or above the 95% confidence level ( $p < 0.05$ ; where  $p$  is level of significance, indicating that there is <5% probability that such a correlation between the two time series was produced by chance). Such calculations are based on the null hypothesis. Also, we use a 10-year running average (5 years back in time and 4 years forward in time) analysis to illustrate the general variability and periods of years with low/high sums of precipitation.

Further, we analyzed the spatiotemporal patterns of precipitation using the Empirical Orthogonal Function (EOF) method. EOF analysis treats the time by spatial location precipitation as a matrix and ordines these data using singular value decomposition to return major axes of variation in precipitation (the number of axes is the same as the number of precipitation time series). The eigenvectors



associated with such an analysis are linked to the spatial locations and reveal relationships between the sites and the major axes. All data were centered at zero and scaled to unit variance.

We then used cross-correlation functions to reveal the relationship between the summarizing EOF functions and three large-scale climatic indices: the North Atlantic Oscillation obtained from Hurrell and van Loon (1997; [http://gcmd.nasa.gov/records/GCMD\\_NCAR\\_NAO.html](http://gcmd.nasa.gov/records/GCMD_NCAR_NAO.html)) (i.e. the mean sea-level pressure difference between the Azores and Iceland), the Atlantic Multidecadal Oscillation updated from Kaplan *et al.* (1998; <http://www.esrl.noaa.gov/psd/data/timeseries/AMO/>) [i.e. the expression of fluctuating mean sea-surface temperature (SST) in the North Atlantic region, illustrating alternating multidecadal periods of cool and warm SST anomalies throughout the North Atlantic Ocean (Schlesinger and Ramankutty, 1994; Kerr, 2000; Knudsen *et al.*, 2011)], and the Greenland Blocking Index (obtained from Fang, 2004; Hanna *et al.*, 2013a, 2013c), which is defined as the normalized values of the 500 hPa mean geopotential height over the GBI domain 60°N–80°N and 20°W–80°W. The cross correlation function reveals contemporary or lagged correlations between the indices and the EOF descriptions of the spatiotemporal precipitation pattern, helping to add insight into the forces driving the spatiotemporal precipitation patterns on Greenland. We estimated the cross correlations for each index as the *x*-variable and the EOFs as *y*-variables, so that positive correlations are interpreted as the EOF summary of precipitation lagging behind the indices.

### 3. Results and discussions

#### 3.1. Annual precipitation trends

Mean annual coastal precipitation for the most recent 2001–2012 period ranged from 302 ± 94 mm water equivalent (w.e.) year<sup>-1</sup> at Danmarkshavn in Northeast Greenland to 2283 ± 576 mm w.e. year<sup>-1</sup> at Ikerasassuaq, on the east coast in the far south (Table 3). On the GrIS mean annual precipitation for this period ranged from 123 ± 22 mm w.e. year<sup>-1</sup> at Tunu2013 (in the northeast) to 378 ± 64 mm w.e. year<sup>-1</sup> at ACT11d (in the southwest close to Kangerlussuaq) (Table 4). At Ikerasassuaq, the precipitation pattern is highly affected by synoptic cyclone passages passing close to Iceland, which typically set up a prevailing easterly airflow towards the southeast coast of Greenland, with orographic enhancement of resulting precipitation (Hanna *et al.*, 2006; Bales *et al.*, 2009). In general, the mean annual coastal precipitation decreased with increasing latitude (a similar trend occurred for the GrIS) and with increasing distance from the coast inland towards the ice-sheet margin. As an example, in both West Greenland between Sisimiut (at the coast) and Kangerlussuaq (*c.* 130 km east of Sisimiut and *c.* 25 km from the ice-sheet margin) and South Greenland between Qaqortoq (at the coast) and Narsarsuaq (*c.* 60 km northeast of Qaqortoq and *c.* 30 km from

Table 3. Annual precipitation totals and standard deviations (mm w.e. year<sup>-1</sup>) at coastal DMI Greenland climate stations for climatological normal and shorter recent periods.

Year	Upernavik	Aasiaat	Ilulissat	Sisimiut	Kangerlussuaq	Nuuk	Paamiut	Ivittuut	Narsarsuaq	Qaqortoq	Danmarkshavn	Ittoqqortoormiit	Tasiilaq	Ikerasassuaq
2001–12	–	541 ± 144	–	631 ± 250	258 ± 63	1369 ± 339	–	–	791 ± 229	1217 ± 432	302 ± 94	635 ± 133	1257 ± 232	2283 ± 576
1991–2012	–	497 ± 128	–	624 ± 233	256 ± 60	1297 ± 312	–	–	830 ± 221	1358 ± 374	321 ± 90	605 ± 132	1276 ± 300	2191 ± 482
1981–2012	–	501 ± 113	–	650 ± 197	242 ± 63	1225 ± 318	–	–	828 ± 233	1301 ± 380	314 ± 97	574 ± 170	1316 ± 308	–
1971–2000	–	494 ± 100	–	616 ± 144	–	1130 ± 235	–	–	817 ± 230	1262 ± 336	301 ± 103	624 ± 237	1437 ± 371	–
1961–90	–	474 ± 112	–	593 ± 148	–	1159 ± 223	1201 ± 273	–	783 ± 219	1138 ± 290	246 ± 100	660 ± 245	1425 ± 364	–
1951–80	373 ± 87	–	368 ± 78	–	–	1129 ± 246	–	–	–	–	242 ± 103	687 ± 224	1338 ± 385	–
1941–70	358 ± 86	–	377 ± 112	–	–	993 ± 329	–	–	–	–	–	–	1148 ± 310	–
1931–60	293 ± 74	–	371 ± 121	–	–	800 ± 246	–	1721 ± 390	–	–	–	–	1081 ± 269	–
1921–50	374 ± 92	–	368 ± 122	–	–	753 ± 190	–	1702 ± 425	–	–	–	–	1011 ± 242	–
1911–40	376 ± 107	–	353 ± 105	–	–	750 ± 188	–	1619 ± 435	–	–	–	–	1051 ± 277	–
1901–30	343 ± 122	–	362 ± 85	–	–	752 ± 192	–	1405 ± 272	–	–	–	–	1142 ± 372	–
1891–1920	376 ± 158	–	334 ± 98	–	–	813 ± 242	–	1473 ± 277	–	–	–	–	–	–
1891–1910	375 ± 178	–	302 ± 69	–	–	892 ± 236	–	1507 ± 296	–	–	–	–	–	–

Table 4. Annual ice core estimated precipitation totals and standard deviations (mm w.e. year<sup>-1</sup>) for climatological normal and shorter recent periods.

Year	HumbMain	NASA-U	GITS	D1	D2	D3	D4	D5	NEEM-2008-S3	McBales	ACT2d	ACT3	Summit 2010	TUNU 2013	ACT11d
2001–10	–	–	–	–	–	–	–	–	–	–	–	–	243 ± 54	123 ± 22	378 ± 64
1991–2010	–	–	–	–	–	–	–	–	–	–	–	–	248 ± 46	131 ± 24	421 ± 82
1981–2010	–	–	–	–	–	–	–	–	–	–	–	–	246 ± 42	131 ± 23	407 ± 78
1971–2000	–	–	–	823 ± 139	484 ± 92	440 ± 80	452 ± 88	415 ± 87	229 ± 49	240 ± 38	424 ± 102	741 ± 131	245 ± 33	129 ± 24	409 ± 74
1961–90	156 ± 38	380 ± 80	383 ± 87	791 ± 150	484 ± 83	449 ± 73	446 ± 88	408 ± 75	227 ± 51	237 ± 31	405 ± 86	720 ± 143	236 ± 37	124 ± 23	400 ± 63
1951–80	151 ± 34	390 ± 73	409 ± 117	803 ± 153	491 ± 53	460 ± 73	452 ± 58	411 ± 81	226 ± 49	239 ± 40	410 ± 77	725 ± 137	240 ± 39	122 ± 20	406 ± 64
1941–70	145 ± 33	381 ± 76	393 ± 123	811 ± 185	495 ± 67	485 ± 74	461 ± 62	417 ± 68	217 ± 46	244 ± 40	412 ± 67	735 ± 125	245 ± 47	125 ± 21	408 ± 68
1931–60	151 ± 37	376 ± 84	412 ± 137	856 ± 188	498 ± 77	491 ± 81	466 ± 76	426 ± 71	208 ± 37	250 ± 41	426 ± 68	754 ± 122	252 ± 49	128 ± 25	376 ± 72
1921–50	153 ± 36	365 ± 88	406 ± 108	897 ± 203	480 ± 87	472 ± 78	452 ± 87	403 ± 77	209 ± 38	240 ± 43	421 ± 70	764 ± 134	243 ± 49	121 ± 26	360 ± 66
1911–40	152 ± 37	363 ± 97	414 ± 105	862 ± 184	483 ± 93	472 ± 86	450 ± 89	403 ± 82	219 ± 48	234 ± 46	411 ± 77	742 ± 119	240 ± 49	127 ± 31	349 ± 64
1901–30	162 ± 49	353 ± 95	368 ± 89	824 ± 181	478 ± 88	464 ± 85	446 ± 80	382 ± 78	216 ± 46	223 ± 58	407 ± 65	722 ± 114	236 ± 46	119 ± 27	348 ± 59
1891–1920	156 ± 49	364 ± 96	388 ± 98	801 ± 197	499 ± 84	490 ± 81	460 ± 77	400 ± 72	213 ± 52	234 ± 55	404 ± 62	716 ± 132	244 ± 49	121 ± 27	359 ± 67
1891–1910	168 ± 53	363 ± 93	393 ± 104	804 ± 217	497 ± 75	490 ± 71	459 ± 77	397 ± 75	204 ± 45	238 ± 60	410 ± 56	706 ± 152	243 ± 47	112 ± 17	362 ± 68

the ice-sheet margin), the mean annual precipitation sum decreased from 631 ± 250 to 258 ± 63 mm w.e. year<sup>-1</sup> and 1217 ± 432 to 791 ± 229 mm w.e. year<sup>-1</sup> (2001–2012), respectively. Similar coastal-to-inland precipitation trends also existed for other periods 1961–1990 to 1991–2012 for which data are available (Table 3), and are likely explained by prevailing wind circulation (e.g. katabatic winds draining downslope from the ice-sheet interior), distance from the oceanic moisture source and the orographic effect of near-coastal mountains – the latter being especially important in Southeast Greenland. We would therefore expect similar coastal-to-inland precipitation trends elsewhere along the Greenland coast. This is in contrast to previous work by Bales *et al.* (2009), who for short distances near the coast, due to orographic enhancements (and the use of high spatial resolution radar profiles), noted an increase in precipitation towards inland areas in Southeast Greenland.

The mean annual coastal precipitation sums for the most recent 2001–2012 period for the only two long-term precipitation time series Nuuk and Tasiilaq (1901–2012) yield the highest mean precipitation sum of 1369 ± 339 for Nuuk and one of the highest mean precipitation sums of 1257 ± 232 mm w.e. year<sup>-1</sup> for Tasiilaq, with both locations significantly (*p* < 0.01) above the mean annual precipitation sums of the warm 1930s–1940s depicted by the 1921–1950 and 1931–1960 climatological normal periods (Table 3). On an annual timescale, Aasiaat, Sisimiut, and Qaqortoq recorded their maximum annual precipitations in 2012, and Nuuk recorded its maximum annual precipitation in 2005 (highlighted in bold in Table 7). This is in contrast to the annual precipitation trends on the GrIS where no annual maximum or minimum precipitation occurred for the most recent decade (Table 8). Further, the three long-term ice core time series: Summit2010, Tunu2013, and ACT11d showed no significant trends or differences in precipitation sums between the most recent period and the sums of the warm 1930s–1940s (depicted by the 1921–1950 and 1931–1960 normal periods) (Table 4 and Figure 3(a)).

For the CGP2 time series (1900–2012) (Figure 2(a)), based on a 10-year running mean, below-average coastal precipitation occurred continuously until the late 1950s, and thereafter continuously above average. The mean difference was *c.* 500 mm w.e. year<sup>-1</sup> in the running average, with a maximum running average difference more than 650 mm w.e. year<sup>-1</sup> (for annual precipitation values the difference between extreme dry and wet conditions was above 1160 mm w.e. year<sup>-1</sup>), and almost matching – in antiphase (from 1925–1995; *r*<sup>2</sup> = 0.58) – the running mean variability in the AMO index (Figure 2(a)). The rapid 1950s phase change indicates that major changes in precipitation patterns over Greenland may occur even over short time periods of ~10 years. The antiphase CGP2-AMO relation shown here is similar to that depicted in Mernild *et al.* (2012) between the Tasiilaq annual precipitation sum and the AMO index time series, while the Tasiilaq annual air temperature time series overall was in phase with the AMO index time series. As well as for

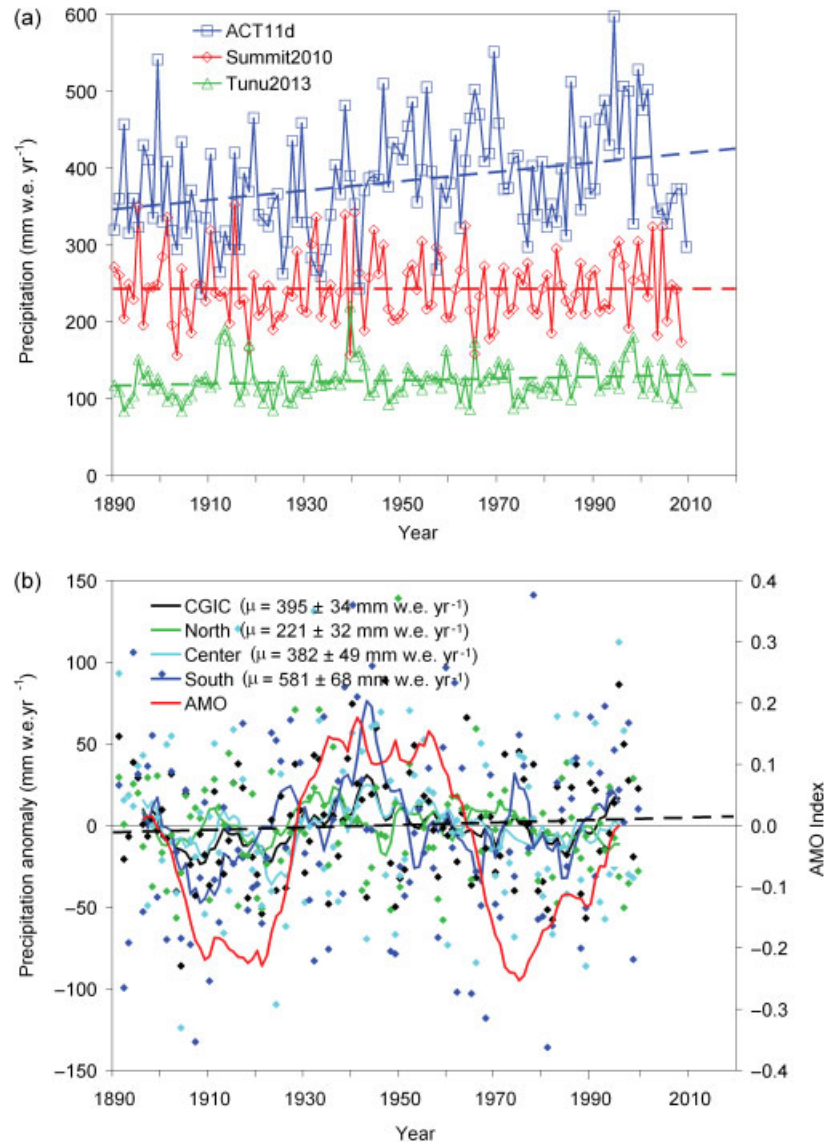


Figure 3. Time-series of GrIS ice core estimated annual precipitation, including 10-year running mean, trend lines, and AMO: (a) three examples of ice core estimated precipitation sum covering the period 1890 through 2009/2010; and (b) composite mean annual ice-core estimated precipitation anomaly time series for the GrIS and the three sectors: north, center, and south (1890–2000) (for location of the sectors, see Figure 1).

Nuuk, the annual precipitation sum was almost matching ( $r^2 = 0.45$ , square of the linear correlation coefficient;  $p < 0.01$ ) – in antiphase (from 1925–1995) – the running mean variability in the AMO index. For the annual CGP1 time series (1961–2012) only minor variations (a maximum difference in running average of  $115 \text{ mm w.e. year}^{-1}$  and in annual values of  $615 \text{ mm w.e. year}^{-1}$ ) occurred during periods with negative (1965–1995) and positive (1996–2012) AMO index.

For the CGIC time series (1890–2000) (Figure 2(a)), based on a 10-year running mean, the average GrIS precipitation almost followed the running mean variability in the AMO index (before the late-1920s the CGIC and AMO curves were both below average, during the period from the 1920s to the mid-1960s the curves were above average, and on average below average from the mid-1960s to the mid-1990s) illustrating a GrIS ice core estimated

precipitation regime in antiphase with the coastal precipitation regime. On the regional scale, a division of the GrIS ice core time series into three regions (north, centre and south; Figure 1) showed that the same overall patterns occurred. However, a gradient in mean values was shown from the northern region of  $221 \pm 120 \text{ mm w.e. year}^{-1}$  to the southern region of  $588 \pm 229 \text{ mm w.e. year}^{-1}$  (1890–2000) (Figure 3(b)).

At the individual coastal station scale for the most recent 2001–2012 period, the greatest overall positive and negative trends in observed annual precipitation occurred for Sisimiut and Tasiilaq of  $48.5 \text{ mm w.e. year}^{-2}$  (and a percentage change of 130% of the initial precipitation value) and  $-53.9 \text{ mm w.e. year}^{-2}$  (–40%), respectively (both significant;  $p < 0.01$ ) (Table 5). The spatial distribution of the precipitation trends for all the coastal meteorological stations is heterogeneous, depicting both increasing and

Table 5. Greenland coastal annual precipitation trends (mm w.e. year<sup>-2</sup>) for climatological normal and shorter recent periods.

Year	Upernavik	Aasiaat	Ilulissat	Sisimiut	Kangerlussuaq	Nuuk	Paamiut	Ivittuut	Narsarsuaq	Qaqortoq	Danmarkshavn	Ittoqqortoormiit	Tasiilaq	Ikerasassuaq
2001–12	–	<b>25.1</b>	–	<b>48.5</b>	–2.8	–7.6	–	–	1.8	–29.7	4.9	1.0	– <b>53.9</b>	24.8
1991–2012	–	<b>11.0</b>	–	<b>20.5</b>	0.6	14.4	–	–	–6.1	– <b>24.6</b>	–3.5	3.8	– <b>17.3</b>	16.5
1981–2012	–	3.2	–	0.7	1.9	<b>12.9</b>	–	–	–1.2	0.1	–0.1	4.5	–10.9	–
1971–2000	–	–1.0	–	5.5	–	3.8	–	–	5.0	<b>19.7</b>	<b>3.6</b>	– <b>11.1</b>	– <b>16.7</b>	–
1961–90	–	<b>6.5</b>	–	<b>6.5</b>	–	– <b>8.6</b>	6.0	–	3.3	1.4	<b>4.8</b>	– <b>9.8</b>	5.8	–
1951–80	<b>4.9</b>	–	<b>4.1</b>	–	–	8.3	–	–	–	–	–0.1	7.2	<b>22.8</b>	–
1941–70	<b>6.7</b>	–	–2.7	–	–	<b>23.8</b>	–	–	–	–	–	–	11.3	–
1931–60	0.7	–	1.0	–	–	5.5	–	– <b>22.3</b>	–	–	–	–	5.1	–
1921–50	– <b>11.0</b>	–	<b>5.2</b>	–	–	–5.1	–	9.3	–	–	–	–	2.3	–
1911–40	0.7	–	– <b>4.3</b>	–	–	3.6	–	<b>24.3</b>	–	–	–	–	–7.2	–
1901–30	<b>6.0</b>	–	–1.2	–	–	–4.6	–	–3.5	–	–	–	–	– <b>22.5</b>	–
1891–1920	–4.7	–	<b>6.8</b>	–	–	– <b>22.0</b>	–	– <b>12.7</b>	–	–	–	–	–	–
1891–1910	– <b>23.4</b>	–	<b>7.7</b>	–	–	– <b>25.6</b>	–	– <b>16.9</b>	–	–	–	–	–	–

Significant trends ( $p < 0.05$ ) are highlighted in bold type.

decreasing trends. This is evident even for relatively short distances between the stations, probably due to a combination of both local and regional weather conditions. For example, the Sisimiut precipitation trend (2001–2012; see above) shows a significant increase but for the same time there was no significant trend at Kangerlussuaq, located 130 km inland. For the same time period, Narsarsuaq and Qaqortoq had insignificant trends, respectively. It is also noteworthy that for none of the normal periods did all coastal stations simultaneously record either positive or negative precipitation trends; similar heterogeneous trend patterns occurred for the GrIS ice core estimated precipitation time series, including the three ice cores: Summit2010, Tunu2013, and ACT11d covering the latest decade (Table 6). This variability illustrates complex temporal and spatial precipitation patterns in Greenland. However, for the CGP1 (1961–2012), CGP2 (1900–2012), and CGIC (1890–2000) anomaly time series the annual precipitation increased on average by 1.3 mm w.e. year<sup>-2</sup> (insignificant), 3.5 mm w.e. year<sup>-2</sup> (significant,  $p < 0.01$ ), and 0.1 mm w.e. year<sup>-2</sup> (insignificant) (Figures 2(a) and 3), respectively. These overall upward trends may indicate that the amount of precipitation across Greenland is increasing in a warming climate. This is in accordance with rising temperatures documented in previous published Greenland climatological analyses such as Hanna *et al.* (2012).

### 3.2. Annual temporal and spatial precipitation conditions

The complex, spatially variable Greenland precipitation trends are captured effectively by the EOF analysis. The first two modes EOF1 (the uniform patterns) and EOF2 (the spatially segregated patterns), represent 46% and 12%, respectively, of the squared covariance. They reveal two potential patterns (Figure 4(a) and (b)), where only EOF1 is statistically significant. However, we report the patterns for both EOF modes for comparative purposes.

Visible via the smoothing line (10-year running mean) in Figure 4(a), EOF1 was positive between 1900–1930 and 1960–1980 and negative between 1930–1960, and 1980–2012. Figure 5 presents the eigenvectors associated with each EOF, capturing specific relationships with the EOFs for each location. The overwhelming negative correlation values for EOF1 (Figure 5(a)) indicate a negative correlation with patterns of precipitation and EOF1 for almost all sites (except for three locations which were positively correlated with EOF1). This suggests variability in Greenland precipitation conditions over time (see Figure 4(a)), and the most recently (since 1980) wetter conditions. The three locations with positive EOF1 values are Ikerasassuaq, Ittoqqortoormiit, and Danmarkshavn (Figure 5(a)), all located in coastal South and East Greenland. They stand out as possibly belonging to a different precipitation regime. We suggest that this EOF1 captures a spatially consistent signature by virtue of the overwhelmingly negative eigenvectors, though there are sites near zero (D1, Neem-2008-S3, and Tunu2013) that join the three positive EOF1 values to generate a pattern in space and time for Greenland.



Table 6. Greenland Ice Sheet ice core estimated annual precipitation trends (mm w.e. year<sup>-2</sup>) for climatological normal and shorter recent periods.

Year	HumbMain	NASA-U	GITS	D1	D2	D3	D4	D5	NEEM-2008-S3	McBales	ACT2d	ACT3	Summit 2010	TUNU 2013	ACT11d
2001–10	–	–	–	–	–	–	–	–	–	–	–	–	–7.3	0.8	<b>–15.4</b>
1991–2010	–	–	–	–	–	–	–	–	–	–	–	–	–1.1	–0.6	<b>–7.9</b>
1981–2010	–	–	–	–	–	–	–	–	–	–	–	–	0.1	–0.1	–0.2
1971–2000	–	–	–	–1.3	1.1	1.4	1.3	2.1	0.1	0.8	0.4	–1.0	0.7	<b>1.2</b>	<b>3.9</b>
1961–90	1.2	–2.2	<b>–4.2</b>	1.0	–0.7	<b>–0.2</b>	–0.4	0.2	–1.3	–0.3	0.2	2.3	0.3	0.5	–1.9
1951–80	–0.5	0.9	–1.0	3.8	–0.8	<b>–3.8</b>	–1.0	–2.4	–0.2	–1.1	–0.6	1.7	–0.8	–0.5	–1.0
1941–70	0.0	1.0	2.4	<b>–7.0</b>	–0.5	–1.7	–1.2	0.0	0.8	–0.8	–1.9	<b>–6.6</b>	<b>–1.7</b>	–0.1	<b>2.8</b>
1931–60	–0.7	–0.4	–3.8	–2.9	–1.4	–0.6	–0.9	–0.7	0.3	–1.0	–0.5	1.6	–0.3	–0.2	<b>3.4</b>
1921–50	–1.2	1.4	–0.8	–1.5	1.7	1.7	2.2	1.6	–0.5	1.2	0.8	2.6	1.0	0.8	<b>3.1</b>
1911–40	0.9	0.8	<b>4.6</b>	3.6	–0.1	–0.5	0.4	1.4	–1.1	<b>1.6</b>	2.4	0.8	–0.1	–0.1	0.7
1901–30	–1.2	–1.0	2.3	<b>6.6</b>	–2.2	–1.4	–1.8	–0.4	0.8	0.4	–0.2	<b>4.5</b>	–0.7	0.1	1.0
1891–1920	–0.1	–1.5	<b>–3.7</b>	–3.1	–0.9	–1.7	–1.1	–0.8	0.2	–0.5	–0.1	–0.1	–0.6	1.3	–0.8
1891–1910	<b>5.3</b>	–4.9	–8.9	–8.5	–3.8	<b>–5.4</b>	–3.8	–3.7	<b>–2.5</b>	–0.9	1.1	–2.8	–1.8	0.1	–2.8

Significant trends ( $p < 0.05$ ) are highlighted in bold type.

For EOF2 (Figures 4(b), (d), and 5(b)), a much more substantial separation between the interior and the coastal precipitation regimes are suggested. For example, 11 out of 15 ice core locations at the interior had a positive correlation with EOF2, while eight out of 14 station locations in the coastal zone had negative correlations with EOF2 (Figure 5(b)). As with EOF1, there are some exceptions, since a few ice cores seem to be more similar to the coastal precipitation regime, and a few coastal stations were more similar to the interior precipitation regime (Figure 5(a) and (b)).

Further insight into the drivers of the uniform patterns in EOF1 and spatially segregated patterns in EOF2 are revealed via cross correlations with the NAO index, AMO Index, and GBI (Figure 6). EOF1 (Figure 6(a)) is positively correlated ( $r^2 = 0.20$ ) with NAO and negatively correlated ( $-0.28$ ) with AMO at lag 0, and negatively correlation with the GBI ( $-0.31$ ) at lag 6 (i.e. a lagging time of  $\sim 6$  years). This signal indicates that the general pattern of precipitation shown via EOF1 is linked to current NAO and AMO conditions, and responds inversely to GBI influences  $\sim 6$  years later. The relationship between EOF2, capturing some stark spatial variation between coastal and ice-core patterns and the indices is illustrated in Figure 6(b). The pattern captured in EOF2 is negatively correlated ( $r^2 = -0.40$ ; significant) with NAO at lag 0, negatively correlated with AMO ( $-0.21$ ; significant) at lag 9, and positively correlated with GBI ( $0.30$ ; significant) at lag 7, suggesting a delayed response to both of the climate indices AMO and GBI. The physical mechanism seems not clear, unless this is some kind of response to long-term cycles in AMO and, possibly, GBI.

Overall for the annual analysis, the eigenvectors interpolated across longitudes and latitudes highlight the spatio-temporal pattern of precipitation across Greenland (Figure 4(c) and (d)). For EOF1 the signature of Greenland precipitation indicates three sections: one in northwest, southeast, and northeast Greenland with sites (Figure 4(c)), that all are near zero or positively correlated, and different from the conditions in the interior of the GrIS. This separation between northwest, southeast, and northeast could probably be due to the different climatic forcing functions for Greenland, where precipitation in the northeast may be dominated by changes in the sea-ice content, in the coastal southeast by a combination of synoptic cyclone passages near Iceland and orographic enhancement of precipitation, and in (south)west Greenland by low pressures forming in the Labrador Sea (Hanna *et al.*, 2006). In the interior the signature indicates positively correlated conditions, suggesting that the variability in ice-core estimated precipitation may be influenced by the same overall climatic precipitation and topographical conditions. For EOF2 (Figure 4(b)), the spatially interpolated conditions seem however to have a less clear signature.

### 3.3. Seasonal coastal precipitation trends

On a seasonal timescale, for both winter and spring the mean coastal precipitation sums for the most recent period

PRECIPITATION IN GREENLAND

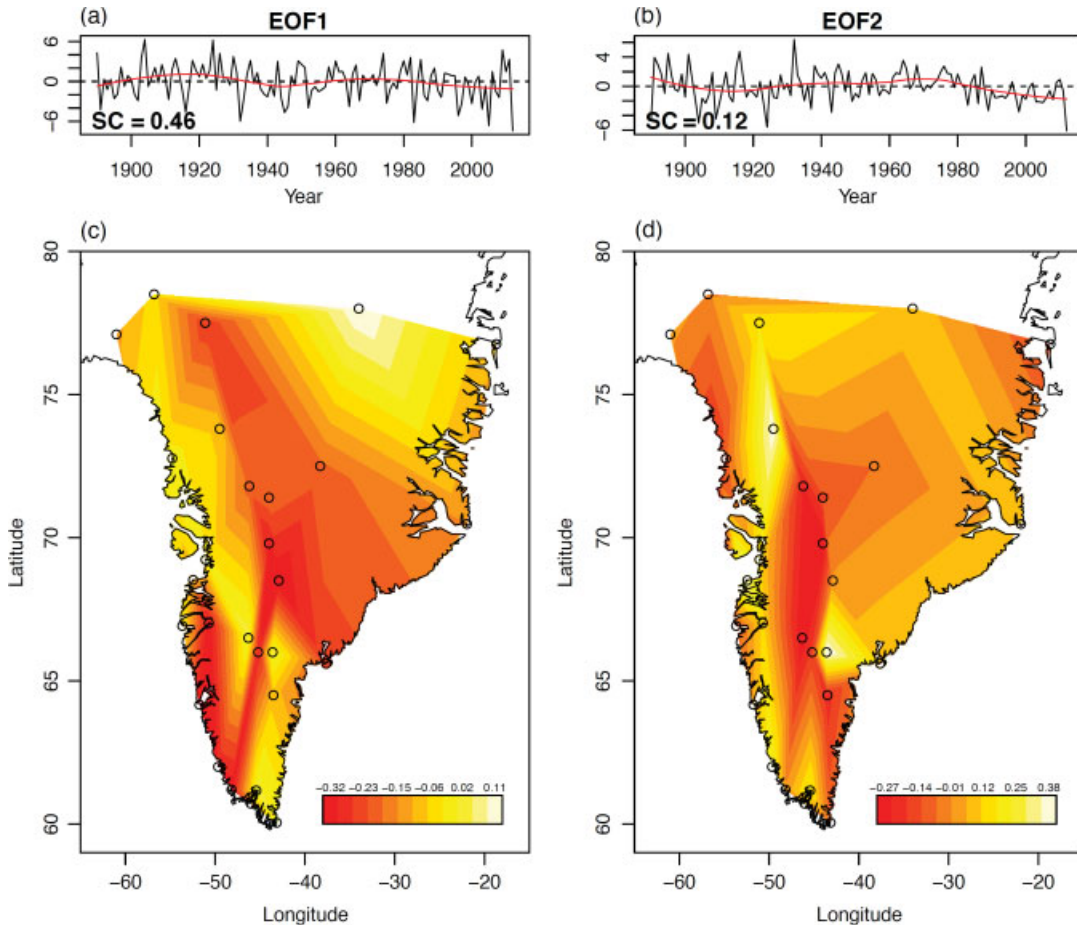


Figure 4. Greenland precipitation time series (1890–2012) based on the empirical orthogonal functions: (a) EOF1; and (b) EOF2. SC equals the square covariance, and maps of the interpolated eigenvectors for (c) EOF1 and (d) EOF2 show the spatiotemporal signature of Greenland precipitation.

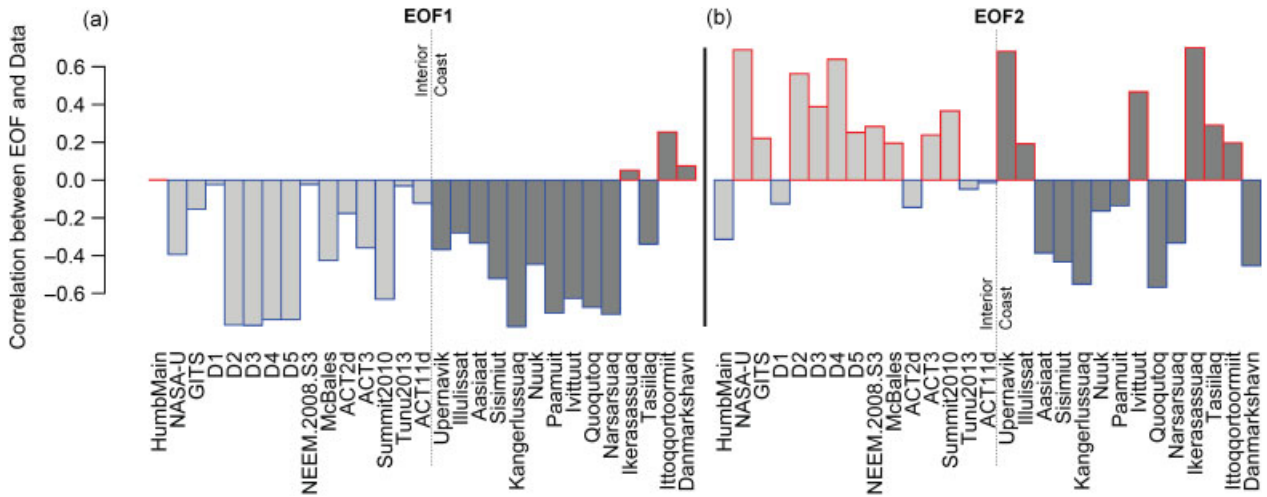


Figure 5. Eigenvector correlation values for each site for both: (a) EOF1; and (b) EOF2.

2001–2012 were lowest for Kangerlussuaq and highest for Ikerassuaq, whereas for both summer and autumn minima were recorded at Danmarkshavn and maximum at Ikerassuaq (Table S1). Also for other periods, Ikerassuaq had maximum seasonal precipitation sums for all four seasons (1991–2012, where data are available), while

the minimum seasonal sums alternated between Danmarkshavn and Kangerlussuaq (1991–2012, and 1981–2012, where data are available). This probably reflects higher temperatures and a convective Labrador Sea influence on Kangerlussuaq precipitation in summer. At Ikerassuaq, the range in mean seasonal precipitation sum (2001–2012)

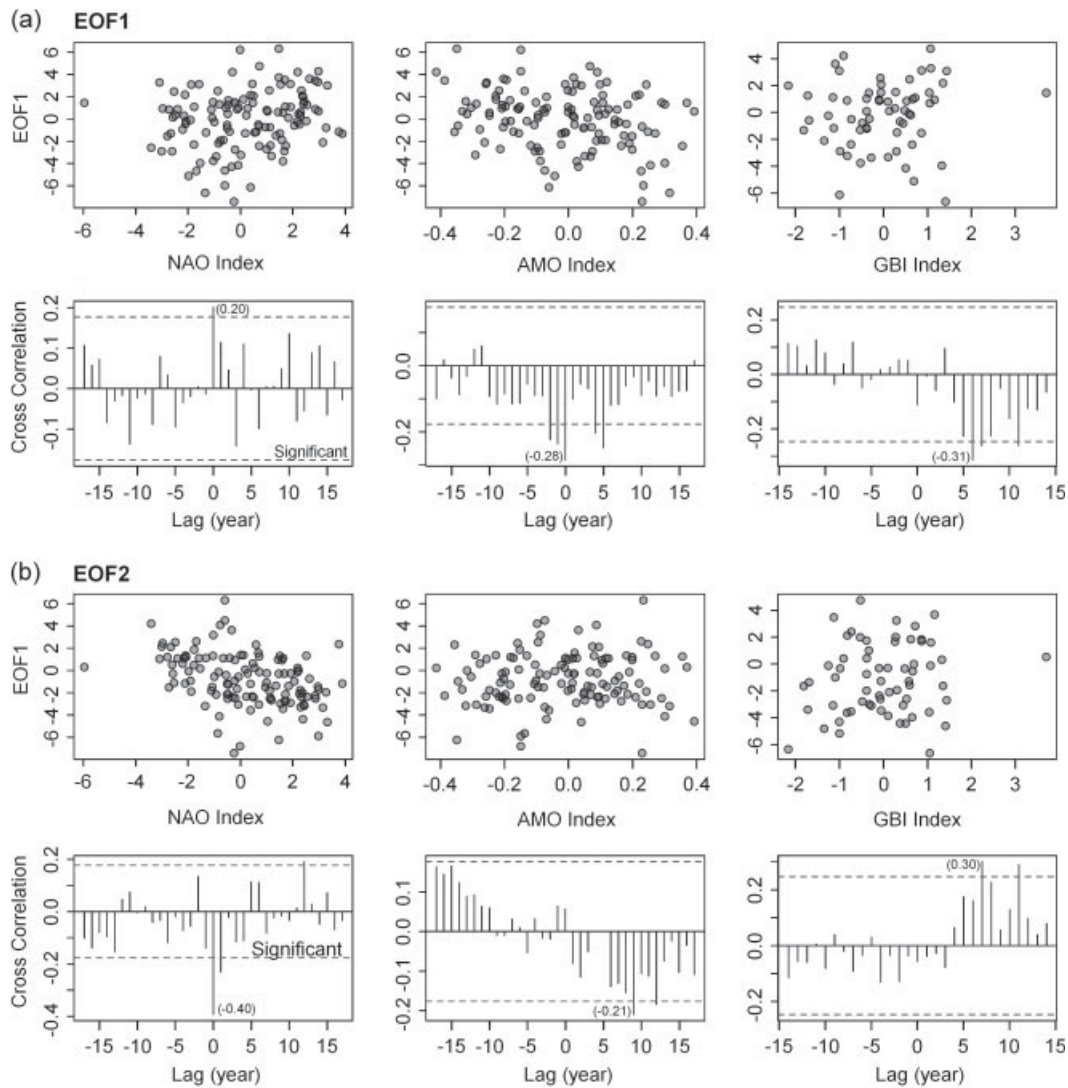


Figure 6. (a) EOF1; and (b) EOF2 cross correlation relationships between the NAO Index, AMO Index, and GBI. The horizontal dashed line indicates the line of significance.

varied from  $553 \pm 289$  mm w.e. in spring to  $695 \pm 232$  mm w.e. in summer (Table S1). For the minimum locations, the winter and spring mean (2001–2012) sums at Kangerlussuaq were  $40 \pm 12$  and  $44 \pm 30$  mm w.e., respectively, and summer and autumn sums at Danmarkshavn were  $51 \pm 33$  and  $56 \pm 20$  mm w.e., respectively. It is worth mentioning that for all four seasons the mean seasonal coastal precipitation sum decreased with increasing latitudes and along the two coastal-to-inland transects from Sisimiut to Kangerlussuaq and Qaqortoq to Narsarsuaq. These overall latitudinal and coastal-to-inland patterns are present not only for the most recent period, but also for the periods 1961–1990 and 1991–2012, where data are available (Table S1).

Also, Nuuk (one of the two stations used in the CGP2 time series) yields for the most recent 2001–2012 period the highest mean precipitation sum for annual and all seasons, whereas for Tasiilaq the spring and winter seasons had the highest mean seasonal precipitation sums for the 1971–2000 climatological normal period, 1961–1990 for

summer, and 1901–1930 for autumn (Table S1). These differences highlight different prevailing precipitation patterns (and probably climatic forcing factors; Hanna *et al.*, 2013a) for Nuuk and Tasiilaq. Also, regarding the record wettest and driest monthly and seasonal conditions for all stations, Kangerlussuaq, Narsarsuaq, Danmarkshavn, and Ikerasassuaq had record-high monthly and seasonal precipitation within the most recent period 2001–2012 (highlighted with bold in Table 7). This is in contrast to Qaqortoq, Ittoqqortoormiit, and Tasiilaq, where precipitation records rarely occurred during the last decade (Table 7).

For the individual seasonal composite coastal Greenland anomaly precipitation time series CGP2 (1900–2012) (Figure 2(c)) the 10-year running average follows the overall annual trend (Figure 2(a)), where all seasons – except for a few years in summer and autumn – were below average up to the late 1950s, and thereafter above average. For all four seasonal anomaly time series a clear shift in the

Table 7. Monthly, seasonal, and yearly driest and wettest precipitation sums at coastal DMI Greenland climate stations (mm w.e. year<sup>-1</sup>).

Station	Jan	Feb	Mar	Apr	May	Jun	Jul	Aug	Sep	Oct	Nov	Dec	Spring (MAM)	Summer (JJA)	Autumn (SON)	Winter (DJF)	Year
Upernavik (Jan 1890–Dec 1980)	Driest 0.0 (1937)	0.0 (1937)	0.0 (1935)	0.0 (1904)	0.0 (1933)	0.0 (1939)	0.0 (1935)	0.0 (1941)	0.0 (1935)	2.5 (1908)	1.4 (1910)	0.0 (1908)	2.0 (1890)	20.2 (1957)	14.7 (1935)	5.3 (1912/13)	133.8 (1911)
	Wettest 82.4 (1979)	142.3 (1901)	98.2 (1900)	105.4 (1978)	96.5 (1895)	112.4 (1916)	204.1 (1908)	162.8 (1907)	156.6 (1967)	149.1 (1899)	176.2 (1969)	87.4 (1893)	178.0 (1896)	254.5 (1908)	310.9 (1895)	233.5 (1896/97)	700.6 (1895)
Aasiaat (Jan 1958–present)	Driest 1.4 (1959)	2.7 (1963)	0.0 (1960)	2.8 (1961)	1.6 (2004)	0.0 (1990)	0.0 (2008)	0.0 (1966)	3.0 (1988)	9.4 (2002)	10.1 (1968)	8.4 (1962)	15.3 (1960)	35.3 (1969)	65.1 (1994)	18.6 (1958/59)	22.3 (1965)
	Wettest 112.8 (1979)	104.5 (1969)	150.0 (1979)	116.4 (1973)	91.7 (1980)	177.4 (1974)	189.4 (1959)	189.4 (1986)	200.1 (1961)	144.5 (1978)	144.3 (1985)	91.4 (1977)	200.9 (1979)	283.8 (1959)	288.0 (2012)	197.5 (1978/79)	755.4 (2012)
Illullissat (Jan 1890–Dec 1984)	Driest 0.3 (1925)	0.0 (1939)	0.4 (1934)	0.9 (1898)	0.0 (1934)	0.0 (1937)	0.6 (1957)	0.0 (1966)	4.8 (1930)	2.7 (1940)	1.1 (1939)	1.9 (1898)	8.2 (1920)	21.5 (1943)	29.7 (1891)	6.6 (1898/99)	185.3 (1896)
	Wettest 62.7 (1949)	95.7 (1948)	72.8 (1949)	152.9 (1973)	97.9 (1948)	133.2 (1942)	144.8 (1944)	171.7 (1935)	230.4 (1967)	141.0 (1978)	114.6 (1969)	104.7 (1940)	212.9 (1973)	238.0 (1942)	285.9 (1957)	208.2 (1948/49)	742.7 (1948)
Sisimiut (Jan 1961–present, minus 1993–2001 and 2004–2008)	Driest 2.9 (1966)	1.7 (1985)	1.9 (1992)	0.8 (1963)	0.6 (1963)	5.4 (1973)	7.9 (1976)	0.5 (1977)	12.4 (1988)	12.2 (1971)	9.4 (1968)	0.0 (1991)	7.4 (1963)	93.9 (1980)	81.5 (1982)	15.5 (1989/90)	260.5 (1992)
	Wettest 106.7 (2010)	123.0 (1988)	94.5 (1987)	175.0 (1973)	114.8 (1982)	170.2 (2004)	166.6 (1972)	211.7 (1986)	299.5 (1976)	147.3 (1972)	142.5 (1971)	173.3 (2010)	215.5 (1973)	321.0 (1981)	389.1 (1986)	223.9 (1969/70)	1003.8 (2012)
Kangerlussuaq (Jan 1976–present)	Driest 0.6 (1990)	0.4 (1989)	0.0 (2006)	0.0 (2011)	0.0 (1995)	0.0 (2000)	2.9 (1999)	0.0 (1977)	4.2 (1995)	2.8 (1985)	1.5 (2006)	0.0 (1985)	2.9 (1995)	27.2 (1980)	32.1 (1995)	5.7 (1989/90)	111.3 (1980)
	Wettest 33.6 (2010)	32.1 (2011)	15.5 (1991)	55.4 (2005)	46.7 (2005)	58.5 (1994)	92.4 (1997)	117.3 (1991)	91.9 (2003)	59.2 (1978)	59.8 (2001)	32.1 (2006)	105.0 (2005)	195.9 (1983)	137.1 (2000)	61.3 (2003/04)	330.0 (1997)
Nuuk (Jan 1890–present)	Driest 3.9 (1939)	0.0 (1933)	0.0 (1909)	0.0 (1902)	0.0 (1911)	0.0 (1913)	0.0 (1933)	0.0 (1966)	1.7 (1948)	6.2 (1917)	4.9 (1931)	0.2 (1946)	16.5 (1930)	13.9 (1903)	56.7 (1951)	19.0 (1939/40)	367.1 (1948)
	Wettest 365.7 (1953)	387.7 (1890)	416.1 (1968)	246.6 (2006)	395.1 (1928)	257.7 (1979)	350.7 (1983)	334.2 (1984)	341.5 (1967)	460.0 (1995)	373.4 (2008)	231.8 (2001)	568.8 (2005)	614.4 (1915)	840.8 (2008)	613.9 (1953/54)	1881.9 (2005)
Paamiut (Jan 1958–Aug 1992)	Driest 1.8 (1966)	9.8 (1982)	8.9 (1962)	4.9 (1961)	6.0 (1968)	7.7 (1974)	1.6 (1992)	0.0 (1858)	34.2 (1968)	4.9 (1968)	25.3 (1974)	6.2 (1978)	84.4 (1985)	122.1 (1958)	96.7 (1968)	70.8 (1959/60)	689.5 (1958)
	Wettest 282.8 (1967)	278.4 (1965)	214.1 (1968)	196.2 (1983)	296.1 (1987)	214.1 (1983)	276.2 (1964)	487.8 (1984)	259.7 (1989)	250.5 (1972)	246.2 (1983)	408.4 (1975)	480.1 (1983)	690.5 (1983)	495.1 (1966)	661.2 (1975/76)	1997.1 (1983)
Ivittuut (Jan 1890–Dec 1960)	Driest 1.8 (1940)	0.0 (1912)	0.7 (1897)	1.2 (1937)	0.0 (1930)	1.9 (1916)	2.3 (1933)	0.0 (1958)	31.4 (1930)	31.3 (1903)	3.1 (1910)	0.0 (1924)	75.4 (1904)	26.6 (1903)	232.9 (1920)	32.3 (1911/12)	758.6 (1924)
	Wettest 484.0 (1891)	607.5 (1932)	520.9 (1938)	297.7 (1938)	398.0 (1903)	396.5 (1934)	358.1 (1945)	354.2 (1915)	513.7 (1939)	508.0 (1944)	431.4 (1933)	272.1 (1952)	826.7 (1929)	669.1 (1937)	1042.4 (1937)	875.0 (1933/34)	2433.0 (1945)
Narsarsuaq (Jan 1961–present)	Driest 0.3 (1966)	0.4 (2010)	0.0 (1962)	2.4 (1989)	3.6 (1974)	0.3 (2008)	0.3 (1992)	0.6 (1966)	5.2 (1981)	0.0 (1968)	2.8 (2002)	4.2 (2000)	32.3 (1962)	90.0 (2009)	24.2 (1968)	18.6 (1965/66)	330.1 (1985)
	Wettest 214.0 (1996)	334.3 (1993)	165.7 (1998)	170.2 (1999)	204.4 (1987)	170.7 (1983)	290.6 (1966)	278.4 (1984)	289.4 (1990)	242.1 (2003)	401.5 (2008)	418.1 (1975)	298.1 (2012)	454.1 (1983)	616.0 (2008)	491.5 (1975/76)	1336.3 (1983)



Table 7. Continued.

Station	Jan	Feb	Mar	Apr	May	Jun	Jul	Aug	Sep	Oct	Nov	Dec	Spring (MAM)	Summer (JJA)	Autumn (SON)	Winter (DJF)	Year
Qaqortoq (Jan 1961–present)	5.7 (1966)	0.7 (1982)	0.0 (1962)	1.7 (1989)	3.5 (1985)	2.7 (2010)	4.1 (1992)	5.7 (1980)	2.1 (1981)	0.8 (1968)	4.0 (2002)	9.3 (2007)	47.1 (1985)	131.2 (1992)	41.3 (1968)	43.0 (1965/66)	530.8 (1985)
	279.3 (1967)	333.7 (1993)	281.1 (1983)	235.8 (1975)	225.5 (1987)	192.5 (1997)	496.0 (1966)	342.8 (1984)	311.6 (1990)	285.4 (1987)	386.2 (2001)	987.4 (1998)	533.7 (1983)	560.8 (1984)	739.3 (1995)	1223.4 (1998/99)	1972.1 (2012)
Danmarkshavn (Jan 1949–present)	1.2 (1975)	0.0 (2010)	0.2 (1962)	0.0 (1962)	0.0 (1997)	0.0 (2012)	0.0 (2010)	0.2 (1973)	0.0 (1962)	0.3 (1960)	0.0 (1952)	0.0 (1952)	4.5 (1962)	7.3 (2010)	6.8 (1951)	6.8 (1950/51)	63.1 (1951)
	161.5 (2006)	82.0 (2008)	106.7 (2012)	82.4 (2006)	34.4 (2009)	57.2 (1954)	86.6 (1986)	110.7 (1990)	182.1 (1955)	99.8 (1957)	141.3 (1991)	108.8 (1957)	147.9 (2011)	161.1 (1998)	244.4 (1991)	289.2 (2005/06)	536.9 (1990)
Ittoqqortoormiit (Jan 1950–present)	3.3 (1955)	1.2 (1965)	6.4 (1992)	0.1 (1988)	0.0 (1958)	0.0 (1982)	0.0 (2001)	0.7 (1977)	0.0 (1981)	3.3 (1983)	0.0 (2010)	2.8 (1985)	26.8 (1953)	28.2 (1950)	18.7 (1983)	58.7 (1985/86)	276.5 (1983)
	189.3 (1974)	261.9 (1982)	189.0 (1976)	147.6 (2004)	139.5 (1970)	157.5 (1953)	153.5 (1970)	198.4 (1982)	264.8 (1959)	461.6 (1976)	221.7 (1993)	300.0 (2007)	329.3 (1976)	340.0 (1969)	564.5 (1976)	421.7 (2010/11)	1246.4 (1976)
Tasiilaq (Jan 1898–present)	4.8 (1948)	1.9 (1957)	11.8 (1940)	2.0 (1950)	2.2 (1941)	0.0 (2012)	0.3 (1954)	1.0 (1943)	3.4 (1948)	16.2 (1935)	13.7 (2010)	5.0 (1930)	122.9 (1915)	37.9 (1924)	111.5 (1935)	38.5 (1930/31)	612.9 (1950)
	565.1 (1972)	594.9 (1932)	552.3 (1964)	258.9 (1909)	339.3 (1903)	194.5 (1953)	251.1 (1901)	300.6 (1947)	342.3 (1996)	687.9 (1914)	409.7 (1902)	383.0 (1970)	693.0 (1964)	534.8 (1901)	1073.8 (1902)	1035.5 (1971/72)	2165.1 (1908)
Ikerassuaq (Jan 1958–present, minus 1981–1992)	43.9 (1993)	8.4 (1960)	9.1 (2001)	33.7 (1996)	18.3 (1993)	10.5 (2012)	30.3 (2000)	25.6 (1997)	72.3 (1999)	33.4 (2004)	58.6 (2010)	68.1 (2007)	173.7 (1993)	223.3 (2000)	396.8 (1980)	216.2 (1994)	1588.5 (1994)
	747.4 (1961)	682.9 (1965)	578.7 (1974)	658.3 (1976)	769.5 (2010)	671.4 (2005)	475.5 (1977)	837.7 (1960)	746.7 (1958)	897.4 (1960)	698.8 (1965)	670.5 (1976)	1391.7 (1975)	1179.4 (1960)	1635.2 (1964)	1876.0 (1976)	4848.1 (1965)

Driest and wettest records since 2000 are highlighted in bold. In case the monthly precipitation is zero for two or more months, the latest year of occurrence is mentioned in brackets.

Table 8. Yearly driest and wettest ice core estimated precipitation sums (mm w.e. year<sup>-1</sup>).

Year	HumbMain	NASA-U	GITS	D1	D2	D3	D4	D5	NEEM-2008-S3	McBales	ACT2d	ACT3	Summit 2010	TUNU 2013	ACT11d
Driest	82 (1901)	193 (1904)	199 (1910)	492 (1893)	301 (1984)	278 (1904)	283 (1989)	220 (1974)	129 (1896)	121 (1902)	243 (1997)	471 (1931)	156 (1904)	83 (1905)	237 (1909)
Wettest	282 (1905)	572 (1915)	876 (1953)	1404 (1894)	724 (1916)	679 (1911)	747 (1932)	608 (1996)	368 (1912)	357 (1905)	645 (1994)	1121 (1972)	352 (1916)	220 (1940)	597 (1995)

The year of occurrence is shown in brackets.

amount of precipitation from relatively dry to wet conditions occurred around 1960. The trend lines in Figure 2(c) indicate (1900–2012) that the greatest seasonal changes in precipitation sum occurred during winter time (20.6 mm w.e. decade<sup>-2</sup>; significant  $p < 0.01$ ), and smallest seasonal changes during autumn (2.0 mm w.e. decade<sup>-2</sup>; insignificant). On a shorter/more recent time frame (1961–2012), the CGP1 seasonal time series indicates increasing coastal seasonal precipitation sums for spring, autumn, and winter in the range of 4.4 to 6.0 mm w.e. decade<sup>-2</sup> (all insignificant), and decreasing sums for summer time of 3.8 mm w.e. decade<sup>-2</sup> (insignificant).

For the specific location near Tasiilaq it is possible to compare precipitation changes with glacier mass-balance observations (from the only long-term observed mountain glacier in Greenland, the Mittivakkat Gletscher 1995/1996 to present (Figure 1); Knudsen and Hasholt, 2008; Mernild *et al.*, 2013b, 2013c). The glacier is located about 10 km west of the Tasiilaq meteorological station. The comparison supports that a clear negative trend occurred based on seasonal changes in autumn, winter and spring precipitation for 1991–2012 (Table S2). These decreasing coastal precipitation trends for autumn, winter, and spring correspond with a decreasing trend in winter (September through May) glacier mass-balance at Mittivakkat Gletscher, illustrating a link between regional climate change and observations of glacier response. This corroborates Mernild *et al.* (2008b) who found a significant linear relationship (1995/96–2002/03) between uncorrected winter precipitation at Tasiilaq and Mittivakkat Gletscher winter balance ( $n = 8$ ,  $r^2 = 0.68$ ,  $p < 0.01$ ), and a less strong (but still statistically significant) relationship ( $n = 8$ ,  $r^2 = 0.55$ ,  $p < 0.025$ ) between mean summer temperature at Tasiilaq and Mittivakkat Gletscher summer balance (1995/1996–2002/2003).

### 3.4. Highest 24-h precipitation and number of precipitation days

The annual coastal precipitation sum is shown in Figure 7 together with the highest 24-h precipitation (a proxy of precipitation intensity) and the annual number of days with precipitation. A high annual precipitation sum corresponds to a high number of precipitation days, and vice versa, as shown using linear regression ( $r^2 = 0.59$  and  $p < 0.01$ ). For the coastal precipitation interval from 0 to 500 mm w.e. year<sup>-1</sup> the range in the annual number of days with precipitation varies between *c.* 50 and 175 days (having a mean and standard deviation of  $96 \pm 32$  days). In comparison, above 1000 mm w.e. year<sup>-1</sup> the range is between *c.* 100 and 200 days ( $153 \pm 23$  days). The difference in mean and standard deviations between the two intervals indicates that for high annual precipitations ( $>1000$  mm w.e. year<sup>-1</sup>) the number of precipitation days was higher but the spread in the number of days was lower, and vice versa for the 0–500 mm w.e. year<sup>-1</sup> interval. Regarding a potential link between the annual precipitation sum and the highest 24-h precipitation, a significant ( $p < 0.01$ ) correlation of 0.54 was found, indicating that years of high annual precipitation tend to have the highest 24-h precipitation (Figure 7).

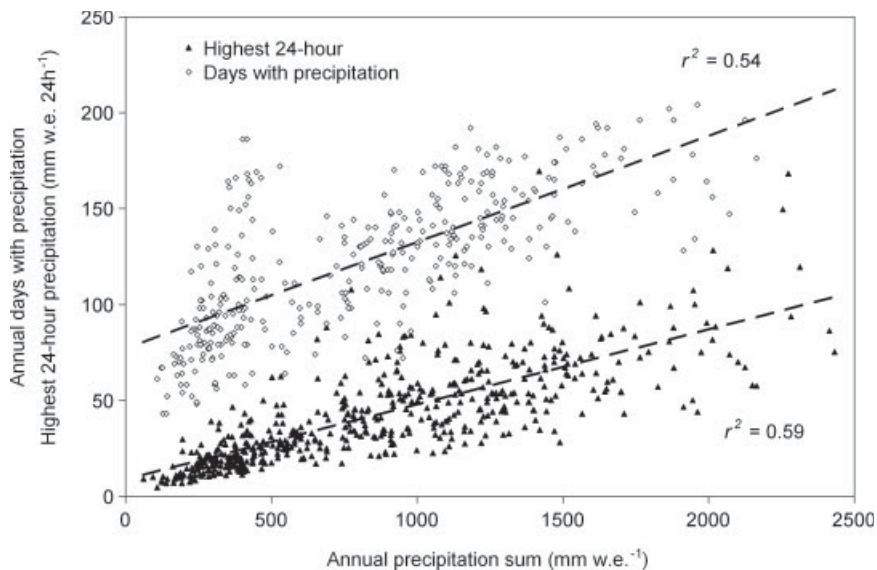


Figure 7. Linear correlations between annual precipitation sum and the highest 24-h precipitation on annual scale and the annual number of days with precipitation, only for the coastal stations marked with red in Figure 1.

#### 4. Conclusions and perspective

In Greenland there is significant variability in precipitation conditions and trends among coastal meteorological stations and ice cores through time since 1890. Precipitation on both annual and seasonal time-scales decreased with increasing latitude and increasing distance from the coast and inland towards the ice-sheet margin, likely explained by the distance from the oceanic moisture source and the orographic effect of near-coastal mountains.

Our EOF analysis provides two insights. First, there is an overall spatiotemporal cycle of precipitation captured in the EOF1 mode that is linked to the NAO and AMO and with an  $\sim 6$  years lag time response to the GBI. All but three records of precipitation are linked to this pattern. Second, there is a clear potentially important separation of coastal and ice-core series that is strongly linked to the NAO, indicating a NAO-driven oscillation between inland and coastal precipitation patterns. We note, however, that while the patterns are clear in the spatial segregation and correlation with NAO, the second EOF2 mode actually captures only a small potentially nonsignificant amount of variation. This might change with a more spatially resolved set of data.

A distinct increase in coastal precipitation occurred around 1960, and coastal precipitation was almost in antiphase with the (running mean) variability in the AMO-index (1925–1995) and the ice-core estimated GrIS precipitation time-series. This indicates that major changes in the mean annual precipitation pattern of around 500 mm w.e. year<sup>-1</sup> can occur within a 5–10 years timeframe. It is important to highlight and understand such rapid changes in the Greenland precipitation patterns to improve the reliability of future climate projections, since such rapid precipitation changes during climate warming may influence coastal glacier mass balance and water budgets, including freshwater runoff from Greenland to the adjacent ocean.

#### Acknowledgements

The ice core data were developed with support from NSF and NASA, including NSF grants 0909541, 1023672, and 1204176 which funded the collection and analyses of a number of recent ice cores records. We gratefully acknowledge assistance from logistics and drilling personnel in the field as well as students and staff in the Reno laboratory, Nevada. Special thanks are given to the Danish Meteorological Institute for providing observed meteorological station data. A.P.B. was funded by CONICYT, Chile (Grant Reference: MEC80120004). The authors have no conflict of interest.

#### Supporting Information

The following supporting information is available as part of the online article:

**Table S1.** (a) spring (MAM); (b) summer (JJA); (c) autumn (SON); and (d) winter (DJF) precipitation sum and standard deviations (mm w.e. year<sup>-1</sup>) at coastal DMI Greenland climate stations for climatological normal and shorter recent periods. The ‘x’ indicates ‘no value’.

**Table S2.** Greenland coastal precipitation; (a) spring (MAM); (b) summer (JJA); (c) autumn (SON); and (d) winter trends (DJF) (mm w.e. year<sup>-2</sup>) for climatological normal and shorter recent periods. Significant trends ( $p < 0.05$ ) are highlighted in bold type.

#### References

- Allerup P, Madsen H, Vejen F. 1998. Estimating true precipitation in arctic areas. In *Proceedings of the Nordic Hydrological Conference*. Helsinki: Nordic Hydrological Programme Report, 44, 1–9.
- Allerup P, Madsen H, Vejen F. 2000. Correction of precipitation based on off-site weather information. *Atmos. Res.* **53**: 231–250.
- Bales RC, Guo Q, Shen D, McConnell JR, Du G, Burkhart JF, Spikes VB, Hanna E, Cappelen J. 2009. Annual accumulation for Greenland updated using ice core data developed during 2000–2006 and analysis

- of daily coastal meteorological data. *J. Geophys. Res.* **114**: D06116, DOI: 10.1029/2008JD011208.
- Box JE, Bromwich DH, Veenhuis BA, Bai L-S, Stroeve JC, Rogers JC, Steffen K, Haran T, Wang S-H. 2006. Greenland ice sheet surface mass balance variability (1988–2004) from calibrated Polar MM5 output. *J. Clim.* **19**: 2783–2800.
- Box JE, Cappelen J, Chen C, Decker D, Fettweis X, Mote T, Tedesco M, van de Wal RSW, Wahr J. 2012. Greenland Ice Sheet (in Arctic Report Card 2012), <http://www.arctic.noaa.gov/reportcard>, 146–158.
- van den Broeke MR, Bamber J, Ettema J, Rignot E, Schrama E, van de Berg WJ, van Meijgaard E, Velicogna I, Wouters B. 2009. Partitioning recent Greenland mass loss. *Science* **326**: 984–986.
- Cappelen J. (ed). 2013a. Greenland – DMI Historical Climate Data Collection 1873–2012 – with Danish Abstracts. DMI Technical report 13-04, Copenhagen, [www.dmi.dk/dmi/tr13-04](http://www.dmi.dk/dmi/tr13-04), 74.
- Cappelen J. (ed). 2013b. Weather and climate data from Greenland 1958–2012 – Observation data with description. DMI Technical report 13-11, Copenhagen, [www.dmi.dk/dmi/tr13-11](http://www.dmi.dk/dmi/tr13-11), 23.
- Chylek P, Dubey MK, Lesins G. 2006. Greenland warming of 1920–1930 and 1995–2005. *Geophys. Res. Lett.* **33**: L11707, DOI: 10.1029/2006GL026510.
- Chylek P, Folland C, Lesins G, Wang M, Dubey M. 2009. Arctic air temperature change amplification and the Atlantic Multidecadal Oscillation. *Geophys. Res. Lett.* **36**: L14801, DOI: 10.1029/2009GL038777.
- Chylek P, Folland C, Lesins G, Dubey M. 2010. Twentieth century bipolar seesaw of the Arctic and Antarctic surface air temperature. *Geophys. Res. Lett.* **37**: L08703, DOI: 10.1029/2010GL042793.
- Ettema J, van den Broeke MR, van Meijgaard E, van den Berg WJ, Bamber JL, Box JE, Bales RC. 2009. Higher surface mass balance of the Greenland ice sheet revealed by high-resolution climate modeling. *Geophys. Res. Lett.* **36**: L12501, DOI: 10.1029/2009GL038110.
- Fang Z-F. 2004. Statistical relationship between the northern hemisphere sea ice and atmospheric circulation during wintertime. In *Observation, Theory and Modeling of Atmospheric Variability*. World Scientific Series on Meteorology of East Asia, Zhu X (ed). World Scientific Publishing Company: Singapore; 131–141.
- Fettweis X, Hanna E, Gallee H, Huybrechts P, Ericum M. 2008. Estimation of the Greenland ice sheet surface mass balance during 20th and 21st centuries. *Cryosphere* **2**: 117–129.
- Folland CK, Palmer T, Parker DE. 1986. Sahel rainfall and worldwide sea temperatures. *Nature* **320**: 602–607.
- Goodison BE, Sevruk B, Klemm S. 1989. WMO solid precipitation measurement intercomparison: objectives, methodology, analysis. IAHS publication, 179, 57–64.
- Hanna E, Huybrechts P, Janssens I, Cappelen J, Steffen K, Stephens A. 2005. Runoff and mass balance of the Greenland ice sheet: 1958–2003. *J. Geophys. Res.* **110**: D13108, DOI: 10.1029/2004JD005641.
- Hanna E, McConnell J, Das S, Cappelen J, Stephens A. 2006. Observed and modelled Greenland Ice Sheet snow accumulation, 1958–2003, and links with regional climate forcing. *J. Clim.* **19**(3): 344–358, DOI: 10.1175/JCLI3615.1.
- Hanna E, Huybrechts P, Steffen K, Cappelen J, Huff R, Shuman C, Irvine-Fynn T, Wise S, Griffiths M. 2008. Increased runoff from melt from the Greenland ice sheet: A response to global warming. *J. Clim.* **21**: 331–341.
- Hanna E, Cappelen J, Fettweis X, Huybrechts P, Luckman A, Ribergaard MH. 2009. Hydrologic response of the Greenland Ice Sheet: the role of oceanographic forcing. *Hydrol. Process.* **23**(1): 7–30, DOI: 10.1002/hyp.7090.
- Hanna E, Huybrechts P, Cappelen J, Steffen K, Bales RC, Burgess EW, McConnell JR, Steffensen JP, van den Broeke M, Wake L, Bigg GR, Griffiths M, Savas D. 2011. Greenland Ice Sheet surface mass balance 1870 to 2010 based on Twentieth Century Reanalysis, and links with global climate forcing. *J. Geophys. Res. Atmos.*, **116**, D24121, DOI:10.1029/2011JD016387
- Hanna E, Mernild SH, Cappelen J, Steffen K. 2012. Recent warming in Greenland in a long-term instrumental (1881–2012) climatic context. Part I: Evaluation of surface air temperature records. *Environ. Res. Lett.*, **7**, 045404, DOI:10.1088/1748-9326/7/4/045404.
- Hanna E, Cappelen J, Fettweis X, Mernild SH, Mote T, Steffen K, Wood L. 2013a. Atmospheric and oceanic climatic forcing of the exceptional Greenland Ice Sheet surface melt in summer 2012. *Int. J. Climatol.*, DOI: 10.1002/joc.3743.
- Hanna E, Navarro FJ, Pattyn F, Domingues C, Fettweis X, Ivins E, Nicholls RJ, Ritz C, Smith B, Tulaczyk S, Whitehouse P, Zwally J. 2013b. Ice-sheet mass balance and climate change. *Nature* **498**: 51–59, DOI: 10.1038/nature12238.
- Hanna E, Jones JM, Cappelen J, Mernild SH, Wood L, Steffen K, Huybrechts P. 2013c. The influence of North Atlantic atmospheric and oceanic forcing effects on 1900–2010 Greenland summer climate and ice melt/runoff. *Int. J. Climatol.* **33**: 862–880, DOI: 10.1002/joc.3475.
- Hurrell JW, van Loon H. 1997. Decadal variations in climate associated with the North Atlantic Oscillation. *Climate Change* **36**: 301–326.
- IPCC. 2013. Summary for policymakers. [http://www.climatechange2013.org/images/uploads/WGIAR5-SPM\\_Approved27Sep2013.pdf](http://www.climatechange2013.org/images/uploads/WGIAR5-SPM_Approved27Sep2013.pdf).
- Kaplan A, Cane MA, Kushnir Y, Clement AC. 1998. Analyses of global sea surface temperatures 1856–1991. *J. Geophys. Res.* **103**: 18575–18589.
- Kerr RA. 2000. A North Atlantic climate pacemaker for the centuries. *Science* **288**: 1984–1985.
- Knudsen NT, Hasholt B. 2008. Mass balance observations at Mittivakkat Glacier, Ammassalik Island, Southeast Greenland 1995–2006. *Danish J. Geograp.* **108**(1): 111–120.
- Knudsen MF, Seidenkrantz M-S, Jacobsen BH, Kuijpers A. 2011. Tracking the Atlantic multidecadal oscillation through the last 8,000 years. *Nat. Commun.* **2**: 178.
- Liston GE, Mernild SH. 2012. Greenland freshwater runoff. Part I: A runoff routing model for glaciated and non-glaciated landscapes (HydroFlow). *J. Clim.* **25**(17): 5997–6014.
- Marzeion B, Jarosch AH, Hofer M. 2012. Past and future sea-level change from the surface mass balance of glaciers. *Cryosphere*, **6**, 1295–1322. DOI: 10.5194/tc-6-1295-2012.
- McConnell JR, Mosley-Thompson E, Bromwich DH, Bales RC, Kyne J. 2000. Interannual variations of snow accumulation on the Greenland Ice Sheet (1985–1996): New observations versus model predictions. *J. Geophys. Res.* **105**: 4039–4046.
- McConnell JR, Lamorey GW, Lambert SW, Taylor KC. 2002. Continuous ice-core chemical analyses using inductively coupled plasma mass spectrometry. *Environ. Sci. Technol.* **36**(1): 7–11.
- McConnell JR, Edwards R, Kok GL, Flanner MG, Zender CS, Saltzman ES, Banta JS, Pasteris DR, Carter MM, Kahl JDW. 2007. 20th century industrial black carbon emissions altered Arctic climate forcing. *Science* **317**: 1381–1384, DOI: 10.1126/science.1144856.
- McGrath D, Colgan W, Bayou N, Muto A, Steffen K. 2013. Recent warming at Summit, Greenland: Global context and implications. *Geophys. Res. Lett.* **40**: 2091–2096, DOI: 10.1002/grl.50456.
- Mernild SH, Liston GE. 2012. Greenland freshwater runoff. Part II: Distribution and trends, 1960–2010. *J. Clim.* **25**(17): 6015–6035.
- Mernild SH, Kane DL, Hansen BU, Jakobsen BH, Hasholt B, Knudsen NT. 2008a. Climate, glacier mass balance, and runoff (1993–2005) for the Mittivakkat Glacier catchment, Ammassalik Island, SE Greenland, and in a long term perspective (1898–1993). *Hydrol. Res.* **39**(4): 239–256.
- Mernild SH, Liston GE, Hiemstra CA, Steffen K. 2008b. Surface Melt Area and Water Balance Modeling on the Greenland Ice Sheet 1995–2005. *J. Hydrometeorol.* **9**(6): 1191–1211.
- Mernild SH, Liston GE, Hiemstra CA, Christensen JH. 2010a. Greenland Ice Sheet surface mass-balance modeling in a 131-year perspective 1950–2080. *J. Hydrometeorol.* **11**(1): 3–25.
- Mernild SH, Liston GE, Steffen K, Chylek P. 2010b. Meltwater flux and runoff modeling in the ablation area of the Jakobshavn Isbræ, West Greenland. *J. Glaciol.* **56**(195): 20–32.
- Mernild SH, Knudsen NT, Lipscomb WH, Yde JC, Malmros JK, Jakobsen BH, Hasholt B. 2011a. Increasing mass loss from Greenland's Mittivakkat Gletscher. *Cryosphere* **5**: 341–348, DOI: 10.5194/tc-5-341-2011.
- Mernild SH, Liston GE, Hiemstra CA, Christensen JH, Stendel M, Hasholt B. 2011b. Surface mass-balance and runoff modeling using HIRHAM4 RCM at Kangerlussuaq (Søndre Strømfjord), West Greenland, 1950–2080. *J. Clim.* **24**(3): 609–623, DOI: 10.1175/2010JCLI3560.1.
- Mernild SH, Mote T, Liston GE. 2011c. Greenland Ice Sheet surface melt extent and trends, 1960–2010. *J. Glaciol.* **57**(204): 621–628.
- Mernild SH, Seidenkrantz M-S, Chylek P, Liston GE, Hasholt B. 2012. Climate-driven fluctuations in freshwater to Sermilik Fjord, East Greenland, during the last 4000 years. *The Holocene* **22**(2): 155–164, DOI: 10.1177/0959683611431215.
- Mernild SH, Hanna E, Yde JC, Cappelen J, Malmros JK. 2013a. Coastal Greenland air temperature extremes and trends 1890–2010: Annual and monthly analysis. *Int. J. Climatol.*, DOI: 10.1002/joc.3777.
- Mernild SH, Knudsen NT, Hoffman MJ, Yde JC, Lipscomb WL, Hanna E, Malmros JK, Fausto RS. 2013b. Volume and Velocity changes at Mittivakkat Gletscher, Southeast Greenland, 1994–2012. *J. Glaciol.* **59**(216): 660–670, DOI: 10.3189/2013JoG13J017.
- Mernild SH, Lipscomb WH, Bahr DB, Radić V, Zemp M. 2013c. Global glacier retreat: A revised assessment of committed mass



- losses and sampling uncertainties. *Cryosphere* **7**: 1565–1577, DOI: 10.5194/tc-7-1565-2013.
- Mernild SH, Pelto M, Malmros JK, Yde JC, Knudsen NT, Hanna E. 2013d. Identification of ablation rate, ELA, AAR, and net mass balance using transient snowline variations on two Arctic glaciers. *J. Glaciol.* **59**(216): 649–659, DOI: 10.3189/2013JoG12J221.
- Metcalfe JR, Ishida S, Goodison BE. 1994. A corrected precipitation archive for the Northwest Territories of Canada, [http://www.usask.ca/geography/MAGS/Data/Public\\_Data/precip\\_corr/pcpncor\\_e.htm](http://www.usask.ca/geography/MAGS/Data/Public_Data/precip_corr/pcpncor_e.htm).
- Mikkelsen AB, Hasholt B, Knudsen NT, Nielsen MN. 2013. Jokulhlaups and sediment transport in Watson River, Kangerlussuaq, West Greenland. *Hydrol. Res.* **41**(1): 58–67.
- Radić V, Hock R. 2011. Regionally differentiated contribution of mountain glaciers and ice caps to future sea-level rise. *Nat. Geosci.* **4**: 91–94.
- Rennermalm AK, Smith LC, Chu VW, Forster RR, Box JE, Hagedorn B. 2012. Proglacial River Dataset from the Akuliarusiarsuup Kuua River Northern Tributary, Southwest Greenland, 2008–2010. *Earth Sys. Sci. Data* **4**: 1–12, DOI: 10.5194/essd-4-1-2012.
- Schlesinger ME, Ramankutty N. 1994. An oscillation in the global climate system of period 65–70 years. *Nature* **367**: 723.
- Sigl M, McConnell JR, Layman L, Maselli O, McGwire K, Pasteris D, Dahl-Jensen D, Steffensen JP, Edwards R, Mulvaney R. 2013. A new bipolar ice core record of volcanism from WAIS Divide and NEEM and implications for climate forcing of the last 2000 years. *J. Geophys. Res.* **118**: 1151–1169, DOI: 10.1029/2012JD018603.
- Steffen K, Box JE. 2001. Surface climatology of the Greenland Ice Sheet: Greenland climate network 1995–1999. *J. Geophys. Res.* **106**(D24): 33951–33964.
- Steffensen P. 1996. Standard normal homogeneity test for Windows. DMI Technical Report 96-13, Copenhagen, 35.
- Steffensen P, Larsen FL, Cappelen J. 1993. Homogeneity test of climatological data. DMI Technical Report 93-12, Copenhagen, 22.
- Straneo F, Hamilton GS, Sutherland DA, Stearns LA, Davidson F, Hammillet MO, Stenson GB, Rosing-Asvid A. 2010. Rapid circulation of warm subtropical waters in a major glacial fjord in East Greenland. *Nat. Geosci.* **3**: 182–186.
- Straneo F, Heimbach P, Sergienko O, Hamilton G, Catania G, Griffies S, Hallberg R, Jenkins A, Joughin I, Motyka R, Pfeffer WT, Price SF, Rignot E, Scambos T, Truffer M, Vieli A. 2013. Challenges to understanding the dynamic response of Greenland's marine terminating glaciers to oceanic and atmospheric forcing. *Bull. Am. Meteorol. Soc.* **8**: 1131–1144, DOI: 10.1175/BAMS-D-12-00100.
- Yang D, Ishida S, Goodison BE, Gunter T. 1999. Bias correction of daily precipitation measurements for Greenland. *J. Geophys. Res.* **104**(D6): 6171–6181, DOI: 10.1029/1998JD200110.

[3]

Mernild, S. H., Hansen, B. U., Jakobsen, B. H., and Hasholt, B. 2008. Climatic conditions at the Mittivakkat Glacier catchment (1994–2006), Ammassalik Island, SE Greenland, and in a 109-year perspective (1898–2006). *Geografisk Tidsskrift-Danish Journal of Geography*, 108(1), 51–72.

Reprinted with permission from Taylor & Francis



# Climatic conditions at the Mittivakkat Glacier catchment (1994–2006), Ammassalik Island, SE Greenland, and in a 109-year perspective (1898–2006)

Sebastian H. Mernild, Birger U. Hansen, Bjarne H. Jakobsen & Bent Hasholt

## Abstract

The present-day climate in the Mittivakkat Glacier catchment (65°N), Southeast Greenland, is investigated spatiotemporally based on time series (13 years, 1994–2006) and standard synoptic climate data from the meteorological station in Tasiilaq (Ammassalik), covering 109 years (1898–2006). Within the catchment, meteorological conditions are monitored at the coast (Station Coast, 25 m a.s.l.) for the period 1998–2006 and in the glacier area (Station Nunatak, 515 m a.s.l.) for 1994–2006. During this 13-year period, solar radiation shows increasing values, averaging  $0.5 \text{ W m}^{-2} \text{ y}^{-1}$ , at the nunatak and decreasing values, averaging  $1.4 \text{ W m}^{-2} \text{ y}^{-1}$ , at the coast. The mean annual solar radiation at Station Coast is  $102 \text{ W m}^{-2} \text{ y}^{-1}$ , which is about 10% lower than at Station Nunatak, and is probably caused by increasing and higher percentages of dense clouds and sea fog in the coastal area. The mean annual air temperature is increasing by  $0.10^\circ\text{C y}^{-1}$  at the nunatak and by  $0.05^\circ\text{C y}^{-1}$  at the coast, extending the thawing periods by about 50 days and 5 days, respectively. A snow-free period of 64 days is observed at the nunatak. The coastal area is highly dominated by air temperature inversion and sea breezes during spring and summer, strongly controlling the lapse rates within the catchments. The glacier area is highly dominated by katabatic fall winds, resulting in an almost total lack of calm periods. The wind speed is highest during winter, with mean average values around  $6.0 \text{ m s}^{-1}$ , and gusts up to  $35.0 \text{ m s}^{-1}$ . The total annual precipitation varies from 1,851 mm w.eq.  $\text{y}^{-1}$  at the nunatak (solid precipitation: 80%, mixed: 6%, and liquid: 14%) to 1,428 mm w.eq.  $\text{y}^{-1}$  at the coast (53%, 31%, and 16%), covering an average positive orographic effect for solid precipitation during winter ( $113 \text{ mm w.eq. } 100 \text{ m}^{-1}$ ) and a negative effect for liquid precipitation during summer ( $-52 \text{ mm w.eq. } 100 \text{ m}^{-1}$ ).

Over the last 109 years (1898–2006) precipitation in the catchment has increased about 85 mm w.eq., covering two significant precipitation-rich periods: 1901–1914 ( $1,560 \text{ mm w.eq. } \text{y}^{-1}$ ) and 1963–1978 ( $1,563 \text{ mm w.eq. } \text{y}^{-1}$ ). Mean annual air temperature in the catchment has generally increased  $0.2^\circ\text{C}$  through the 109-year period, most significantly  $\sim 2.7^\circ\text{C}$  within the last 25 years. The warmest 10-year period since 1898 was 1938–1947, showing an annual average of  $-1.83^\circ\text{C}$ , while 1997–2006 was the warmest 10-year period within the last 60 years, with an annual average of  $-2.10^\circ\text{C}$ .

## Keywords

Arctic; Ammassalik Island; climate; meteorology, Mittivakkat Glacier; 109-year perspective (1898–2006).

Sebastian H. Mernild (Corresponding author)

International Arctic Research Center and Water & Environmental Research Center, University of Alaska Fairbanks, Alaska, USA

E-mail: fxs@uaf.edu

Birger U. Hansen

Bjarne H. Jakobsen

Bent Hasholt

Department of Geography & Geology, University of Copenhagen, Denmark

Geografisk Tidsskrift-Danish Journal of Geography

108(1):51–72, 2008

Climate change is a worldwide phenomenon and one of the most important issues facing modern society. The global mean surface air temperature has increased approximately  $0.6^\circ\text{C}$  over the past century (Lemke et al., 2007), showing the most significant increases over the last 30 years (Serreze et al., 2000). Air temperatures in Greenland reached a maximum in the 1930s, after which cooling prevailed until the early 1980s (Box et al., 2006).

North of  $60^\circ\text{N}$  latitude the average surface air temperature has increased by approximately  $0.09^\circ\text{C decade}^{-1}$ , a change conspicuous in winter months (e.g., Box, 2002; Sturm et al., 2005). It has been suggested that the 1990s was the warmest decade of the past 1,000 years (Crowley, 2000). The warming has been accompanied by a general increase in precipitation in the Arctic of approximately  $1\% \text{ decade}^{-1}$  (ACIA, 2005). Projections suggest continued and proba-



bly accelerated warming during the twenty-first century (IPCC, 2001, 2007).

The Arctic climate is one of the most extreme and important components within the global climate system, and like all other climate systems, it exhibits variability over a wide spectrum of time scales (Hansen et al., 2008). A fundamental problem in understanding climate variability and change is that the different system components have different response times and interact through various feedback processes. The components are never in equilibrium. A warming climate – the occurrence of warmer extreme and seasonal surface climatic conditions – will therefore initiate and evolve a cascade of impacts that affect the Arctic ecosystems e.g., the cryospheric and hydrological processes (Mernild et al., 2008; Hinkler et al., 2008). Presently, the Arctic is experiencing a system-wide response to an altered climatic state (Hinzman et al., 2005). It appears that first-order impacts of a warming climate on the terrestrial ecosystem will result from a longer thawing period combined with possible increases in precipitation (e.g., Anisimov and Fitzharris, 2001; Hinzman et al., 2005; Mernild et al., 2007a). The combined effect generally results in longer snow-free seasons and secondary impacts such as increased melting of glacier ice and snow and a deeper active layer. Effects of a general warming of the Arctic must be seen in a context directly linked to both short and long-term climate derived effects.

No direct measured data on the influence of a general warming on the terrestrial ecosystems in East Greenland are available before the International Geophysical Year (IGY) 1957–58 (also known as the Third International Polar Year (IPY)). As an IPY contribution, the first connected measurements of meteorology and the influence on the terrestrial ecosystems were carried out in the Mittivakkat Glacier catchment (65°N), Ammassalik Island. In 1972, the Sermilik Research Station was established in the Mittivakkat Glacier catchment. Since then, an extensive monitoring program has been supported by the Department of Geography and Geology, University of Copenhagen, to study the climate-landscape processes and their interactions, in a context directly linked to both short- and long-term climate derived effects. To monitor the climate variability, including the expected warming and its influence on ecosystems, several long-term research programs have been established all over the northern polar region over the past two decades. However, at present, the Mittivakkat Glacier catchment (65°N), Low Arctic - SE Greenland, is one of only two catchments on

the entire approximately 3,000 km coast of East Greenland where continuous and automated meteorological monitoring and observations of terrestrial ecosystems responses take place. The other catchment is Zackenberg (74°N), High Arctic - NE Greenland. The very limited number of research programs in East Greenland is explained by the remote terrain, logistic challenges, and harsh climatic conditions. Data covering the last decade offer time scales of daily, seasonal and yearly variations within the study areas, but time scales of multiple decades are much more limited for East Greenland and the Arctic in general. However, the Danish Meteorological Institute (DMI) has been operating a few synoptic climate stations along the coast of East Greenland: Station Nord (81°N) since 1961; Danmarkshavn (76°N) since 1958; Daneborg (74°N) since 1946 (apart from the period 1975–78); Scoresbysund (70°N) since 1980, and Tasiilaq (Ammassalik) (65°N) since 1898.

The aim of this study is to present and discuss the most prominent parameters of the present climate at the Mittivakkat Glacier catchment and focus on the spatiotemporal variations and trends of these parameters for the period 1994–2006, comparing the coastal area and the upper glacier area. Based on the period of detailed observations and supported by synoptic meteorological data from Tasiilaq, we hindcast the variations and trends in air temperature, relative humidity, wind speed, and precipitation in the catchment over a total of 109 years, from 1898 to 2006.

## Study area

The Mittivakkat Glacier catchment (18.4 km<sup>2</sup>) (65°42'N; 37°48'W) (Figure 1) is located at the west coast of the Ammassalik Island, Southeast Greenland, approximately 15 km northwest of the town of Tasiilaq and 50 km east of the eastern margin of the Greenland Ice Sheet (GrIS). The island is separated from the mainland by the 10–15 km wide north-south going Sermilik Fiord. The area is considered to be Low Arctic according to Born and Böcher (2001), and represents a very humid part of Greenland. The catchment is characterized by a strong alpine relief and ranges in elevation from 0 to 973 m a.s.l., with the highest altitudes in the eastern part of the catchment. About 22% of the catchment (~4 km<sup>2</sup>) is ice-free land and is dominated by bare bedrock in the upper parts, and mostly sparsely vegetated loose talus and debris flow deposits in the lower parts. The catchment is covered by parts of the Mittivakkat Glacier complex (78%; ~14.4 km<sup>2</sup>) (Figure 1). The

glacier is temperate, has an average thickness in the catchment of approximately 115 m, and ranges from approximately 160 to 930 m a.s.l. in elevation (Knudsen and Hasholt, 1999; Mernild et al., 2006a). The present glacier terminus is situated about 2 km from the coastline. Since 1933 the glacier terminus has retreated about 1.3 km (approximately  $18 \text{ m y}^{-1}$ ), with a decrease in glacier surface elevation of up to 100 m in the lower part of the ablation area, below 300 m a.s.l. (Knudsen and Hasholt, 2004).

## Data Availability and Methods

The present study is based on meteorological data from 1994–2006 measured within the Mittivakkat Glacier catchment and standard synoptic meteorological data from 1898–2006 recorded at the DMI climate station at Tasiilaq; named Station Tasiilaq (Figure 1).

Since the summer of 1993, a meteorological station, Station Nunatak (Figure 2a), has continuously monitored every third hour the meteorological conditions on a nunatak ( $65^{\circ}42.3'N$ ;  $37^{\circ}48.7'W$ , 515 m a.s.l.) on the northern side of the Mittivakkat Glacier. The station is located close to the Equilibrium Line Altitude (ELA; where annual ablation equals annual accumulation) in order to capture the glacier climate. The following parameters are measured: wind direction (4.0 m above terrain), wind speed and wind gust (2.0 and 4.0 m), air temperature (2.0 and 4.0 m), relative humidity (4.0 m), incoming and reflected (outgoing) short-wave radiation, and net radiation (4.0 m) (e.g., Hasholt et al., 2004; Hasholt and Mernild, 2004). Liquid precipitation (rain) was measured 0.45 m above the ground, approximately the height of the local roughness element (Mernild et al., 2006a). Snow water equivalent (SWE, solid precipitation) was calculated from snow depth sounding observations (Campbell SR50 station) at the nunatak.

In 1997 an additional meteorological station, Station Coast (Figure 2b), was established on the coast, on a small rock hill close to the research station ( $65^{\circ}40.8'N$ ;  $37^{\circ}55.0'W$ , 25 m a.s.l.) in order to record the climate in the coastal region and any diverging trends and orographic effects by comparison with the nunatak station. Since the summer of 1997, the station has continuously monitored at three hour intervals the meteorological conditions in the coastal area. The following sensors were mounted 2.0 m above terrain: wind direction, wind speed, wind gust, air temperature, relative humidity, incoming and reflected (outgoing) short-wave radiation, and net radiation. Liquid

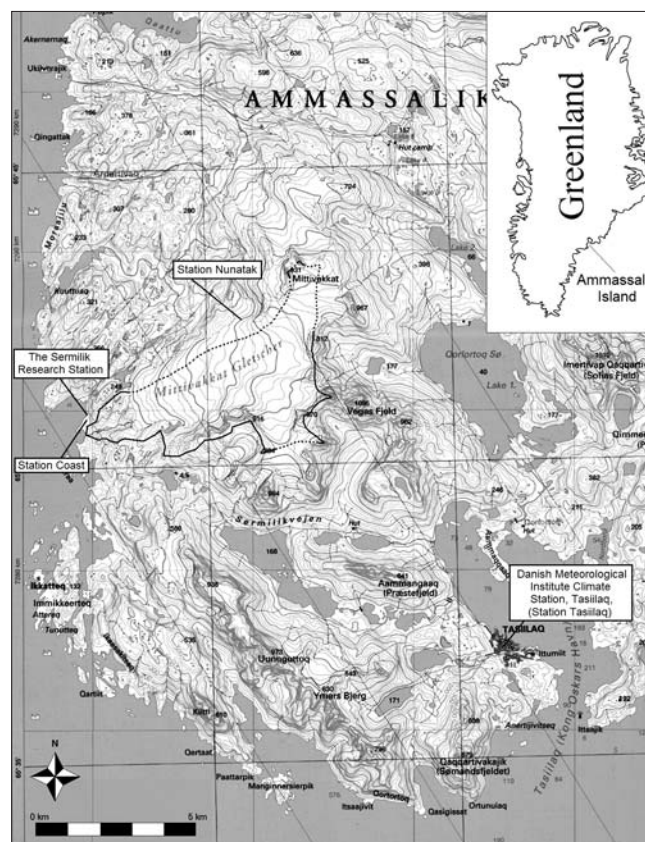


**Figure 1:** Location map showing the Mittivakkat Glacier catchment (18.4 km<sup>2</sup>), Ammassalik Island, including meteorological stations: Station Nunatak (515 m a.s.l.) Station Coast (25 m a.s.l.), and the Danish Meteorological Institute (DMI) climate station in Tasiilaq (Ammassalik), Station Tasiilaq. The dashed line indicates the topographic watershed divide on the Mittivakkat Glacier and the solid line, the topographic watershed divide on bedrock for the Mittivakkat Glacier catchment. The inset figure indicates the general location of the Mittivakkat Glacier catchment within Eastern Greenland (modified from Greenland Tourism).

precipitation was measured 0.45 m above the ground. SWE was calculated by sounding observations during winter at the hydrometric station Isco Island (located close to the coast and approximately 200 m southwest from Station Coast), where the summer river stage variations are measured. Station details, including the types, accuracy, and range of sensors at Station Nunatak and Station Coast, are given in Table 1.

Air temperature inversion occurs in the coastal area of the Mittivakkat Glacier catchment, affecting the air temperature lapse rates in the area. Based on radio-sonde observations in July 2006, the altitude of the air temperature inversions was determined.

In the Arctic, rainfalls in the summer time are gener-

<b>Station Coast, 25m a.s.l. (data recorded since June 1997)</b>			
<b>Parameter</b>	<b>Sensor</b>	<b>Level (m)</b>	<b>Accuracy</b>
Wind direction	Aanderaa Wind Direction Sensor 2053	2.0	$\pm 5^\circ$ (threshold speed $<0.3 \text{ m s}^{-1}$ )
Wind speed / wind gust	Aanderaa Wind Speed Sensor 2740 (three cup rotor)	2.0	$\pm 0.2 \text{ m s}^{-1}$
Air temperature	Aanderaa Air Temperature Sensor 2775	2.0	$\pm 0.1^\circ\text{C}$ (range $-44$ to $+49^\circ\text{C}$ )
Relative humidity	Aanderaa Relative Humidity Sensor 2820	2.0	$\pm 3\%$ RH (range 5 to 100% RH)
Solar radiation (In and Out)	Aanderaa Solar Radiation Sensor 2770 (Pyranometer)	2.0	$< \pm 20 \text{ W m}^{-2}$ (resolution $4 \text{ W m}^{-2}$ )
Net radiation (In and Out)	Aanderaa net Radiation Sensor 2811	2.0	$\pm 20 \text{ W m}^{-2}$ (resolution $4 \text{ W m}^{-2}$ )
Precipitation	Davis Rain Collector II (tipping bucket), sampling area $213 \text{ cm}^2$	0.45	$\pm 4\%$ (0.2 mm at one tip)
Ground temperature	Aanderaa temperature Sensor 3145	-0.1	$\pm 0.1^\circ\text{C}$
<b>Station Nunatak, 515 m a.s.l. (data recorded since July 1993)</b>			
Wind direction	Aanderaa Wind Direction Sensor 2053	2.0	$\pm 5^\circ$ (threshold speed $<0.3 \text{ m s}^{-1}$ )
Wind speed	Aanderaa Wind Speed Sensor 2740 (three cup rotor)	2.0 4.0	$\pm 0.2 \text{ m s}^{-1}$
Air temperature	Aanderaa Air Temperature Sensor 2775	2.0 4.0	$\pm 0.1^\circ\text{C}$ (range $-44$ to $+49^\circ\text{C}$ )
Relative humidity	Aanderaa Relative Humidity Sensor 2820	4.0	$\pm 3\%$ RH (range 5 to 100% RH)
Solar radiation (In and Out)	Aanderaa Solar Radiation Sensor 2770 (Pyranometer)	4.0	$< \pm 20 \text{ W m}^{-2}$ (resolution $4 \text{ W m}^{-2}$ )
Net radiation (In and Out)	Aanderaa net Radiation Sensor 2811	4.0	$\pm 20 \text{ W m}^{-2}$ (resolution $4 \text{ W m}^{-2}$ )
Precipitation	Aanderaa Rain Collector, sampling area $50 \text{ cm}^2$	4.0	$\pm 4\%$ (0.2 mm at one tip)
Ground temperature	Aanderaa temperature Sensor 3145	-0.1 -0.3	$\pm 0.1^\circ\text{C}$

**Table 1:** Sensors at the two meteorological stations: Station Coast and Station Nunatak at the Sermilik Station, Mittivakkat Glacier catchment, East Greenland. A negative level indicates that the instruments are below the surface.

ally characterized by a low intensity (Przybylak, 2003) and are easily significantly underestimated because of aerodynamic errors (e.g., Young et al., 2006). Measuring of snow precipitation is also uncertain, especially under windy and cold conditions (e.g., Yang et al., 1999; Liston and Sturm, 2002, 2004; Serreze and Barry, 2005). Snowfall in the Arctic is most often connected with strong winds and typically takes the form of fine snowflakes (Sturm et al., 1995). As a result, wind easily lifts and redistributes the snowflakes according to exposure and local topography. In Arctic America, snow usually begins to drift at wind speeds above  $5.0 \text{ m s}^{-1}$  (Liston and Sturm, 1998), and it can sometimes be difficult to distinguish between a period of snowfall and a period of drifting snow.

In the present study, the SWE was calculated based on snow depth sounding observations. After noise was removed from the snow depth data (Campbell SR50-data) (Mernild and Hasholt, 2006; Mernild 2006), the observations were fractionated into liquid (rain) precipitation and solid (snow) precipitation at different air temperatures (Førland and Hanssen-Bauer, 2003). For air temperatures below  $-1.5^\circ\text{C}$ , sounding observations represent solid precipitation in 100% of the events, and for temperatures above  $3.5^\circ\text{C}$ , precipitation is liquid for 100% of the events. In between ( $-1.5^\circ\text{C}$  to  $3.5^\circ\text{C}$ ), the fraction of snow and rain (mixed precipitation) is calculated by linear interpolation (Førland and Hanssen-Bauer, 2003). The air temperature recorded at Station Coast is not considered





**Figure 2:** (a) Station Nunatak was established in the summer of 1993 (Photo B. Hasholt); and (b) Station Coast in the summer of 1997 (Photo: S. Mernild).

representative for the temperature at which snowflakes are established. The air temperature at the nunatak (at the higher elevation) is more representative of the air temperature where snowflakes form. Therefore, Station Nunatak temperatures, as the more representative air temperatures, were used for fractionation at both stations.

Measured increases in snow depth at relative humidity  $<80.0\%$  and at wind speeds  $>10.0 \text{ m s}^{-1}$  were removed to distinguish between the situations of real snow accumulation based on precipitation events and blowing snow redistribution, based on experiences from East Greenland (Mernild et al., 2007b, 2007c). The snow depth increases were adjusted using a temperature-dependent snow density (Brown et al., 2003), and an hourly snow pack settling rate (Anderson, 1976); snow settles as it accumulates, and thus the snow depth on the ground is always less than the measured thickness of the initial snowfall. The SWE is expected to be accurate within  $\pm 10\text{--}15\%$  (Mernild et al., 2006a). Further, SWE precipitation from Station Nunatak was compared and calibrated against the Mittivakkat Glacier winter mass balance observations, showing an average underestimated SWE depth of 28% (1998–2002) before adjustment due to the exposed station location on the nunatak (Mernild et al., 2006a, 2008). At Station Tasiilaq, precipitation (1958–2006) was corrected according to Allerup et al. (2000). Before 1958 corrected precipitation was calculated (linear regression) based on observed and corrected precipitation (1958–2006).

Wind speeds measured at 10.0 m at Station Tasiilaq

and a roughness length of 0.1 m were used to calculate the wind speed at 2.0 m above terrain.

SnowModel is a spatially distributed snow pack evolution modeling system simulating accumulation and loss from snow precipitation, blowing snow redistribution, blowing snow sublimation, snow density evolution, snow pack ripening, and snow and ice melt. The model is specifically designed to be applicable over a wide range of snow landscapes and climates (Liston and Elder, 2006b, Mernild et al., 2006a). SnowModel includes a micrometeorological model (MicroMet) (Liston and Elder, 2006a). MicroMet is a quasi-physically-based meteorological distribution model designed to produce high-resolution meteorological forcing distributions of meteorological data into the terrestrial landscape (e.g., air temperature, relative humidity, wind speed, wind direction, precipitation, solar and long wave radiation, and surface pressure). MicroMet uses elevation-related interpolations to modify air temperature, humidity, and precipitation following

Kunkel (1989), Walcek (1994), Dodson and Marks (1997), and Liston et al. (1999). Temperature and humidity distributions are defined to be compatible with the observed lapse rates. Wind flow in complex topography is simulated following Ryan (1977) and Liston and Sturm (1998). Solar radiation variations are calculated using elevation, slope, and aspect relationships (Pielke, 2002). Incoming long-wave radiation is calculated while taking into account cloud cover and elevation-related variations following Iziomon et al. (2003). Precipitation is distributed following Thornton et al. (1997). In addition, any data from more than one location, at a given time, are spatially interpolated over the domain using a Gaussian distance-dependent weighting function and interpolated to the model grid using the Barnes objective analysis scheme (Barnes, 1964, 1973; Koch et al., 1983). SnowModel/MicroMet simulations have been compared against observations in alpine, Arctic, and Antarctic landscapes with reasonable results (Greene et al., 1999; Liston et al., 2000; Hiemstra et al., 2002; Liston and Sturm 2002; Hasholt et al., 2003; Bruland et al., 2004; Mernild et al., 2006a, 2006c, 2007b, 2008a, 2008b).

In order to model meteorological variations and trends (air temperature, relative humidity, wind speed, and precipitation) in the Mittivakkat Glacier catchment covering the last 109 years (1898–2006), data from Station Tasiilaq were used. Before 1958 the climate station in Tasiilaq only recorded air temperature and precipitation, and calculations were only carried out for the period 1958 to 2006.

For the period 1998 to 2006, SnowModel/MircoMet mean daily Mittivakkat Glacier catchment spatially distributed data for air temperature, relative humidity, wind speed, and precipitation were compared (linear regression) with observed meteorological data (air temperature, relative humidity, wind speed, and corrected precipitation) from Station Tasiilaq. Linear regressions for air temperatures ( $R^2 = 0.87$ ;  $p < 0.01$  (where  $p$  is the level of significance)), for relative humidity ( $R^2 = 0.46$ ;  $p < 0.01$ ), and for wind speed ( $R^2 = 0.64$ ;  $p < 0.01$ ) were calculated based on daily values. Calculations for precipitation ( $R^2 = 0.79$ ;  $p < 0.01$ ) were based on total annual precipitation values (TAP). Based on climatologically significant correlations between catchment data and records from Station Tasiilaq, Mittivakkat Glacier catchment meteorological conditions are estimated back to 1898. Further, in the context of the last 109 years (1898–2006), the period 1998 through 2006 is merely 11% of the time series record. Average observed relative humidity (daily) and

precipitation (yearly) from the short period are significantly similar (97.5% fractal) to observations from the long period, while wind speed (daily) and air temperature (daily) are significantly different, illustrating variability in some meteorological parameters through time.

## Results and discussion

### *Overall climatic conditions*

The climate in the Ammassalik area is affected by the GrIS and the East Greenland Polar Sea Current which has a surface temperature close to 0°C throughout the year and which brings along drift ice most of the year. Winters are moderately cold with only short periods of above freezing temperatures. In coastal areas summers are cold too, often with moist and foggy conditions, whereas slightly warmer and sunny conditions are found inland and in the inner parts of the fjords, away from the ocean. Winds and precipitation in the area are strongly affected by lows. Most lows affecting Greenland arrive from directions between south and west, steered by an upper level cyclone, the ‘polar vortex’, in winter centered over the Canadian Cold Pole and in summer less pronounced and situated over the Arctic Ocean (Hansen et al., 2008). The track of a pressure system is of utmost importance for weather conditions at a given position. In front of such a low there are easterly winds towards the coast where the relatively moist air mass is lifted up and causes precipitation on the eastern side of the mountains. On the leeward side of the mountains, the air mass descends and is heated adiabatically  $1^\circ\text{C } 100 \text{ m}^{-1}$ . In East Greenland these foehn winds are called neqqajaaq, and they are registered as strong, relatively warm and dry winds that blow from a mountainous area towards the lowlands. Behind the lows there may be very strong winds from directions between the north and the west. The origin of these air masses is the GrIS; cold air with a high density flow towards the edge of the GrIS. The outflow accelerates when the slope of the interface increases, and the topography may cause canalisation with extremely strong winds at the edge of the ice and in the landscape between the GrIS and the ocean. These sudden changes from calm to gale force can be registered in the study area, and they are known by the Greenlandic word piteraqaq.

### *Meteorological conditions 1994–2006*

#### *Solar radiation, albedo, and snow cover*

The midnight sun line passes through Tasiilaq, while the

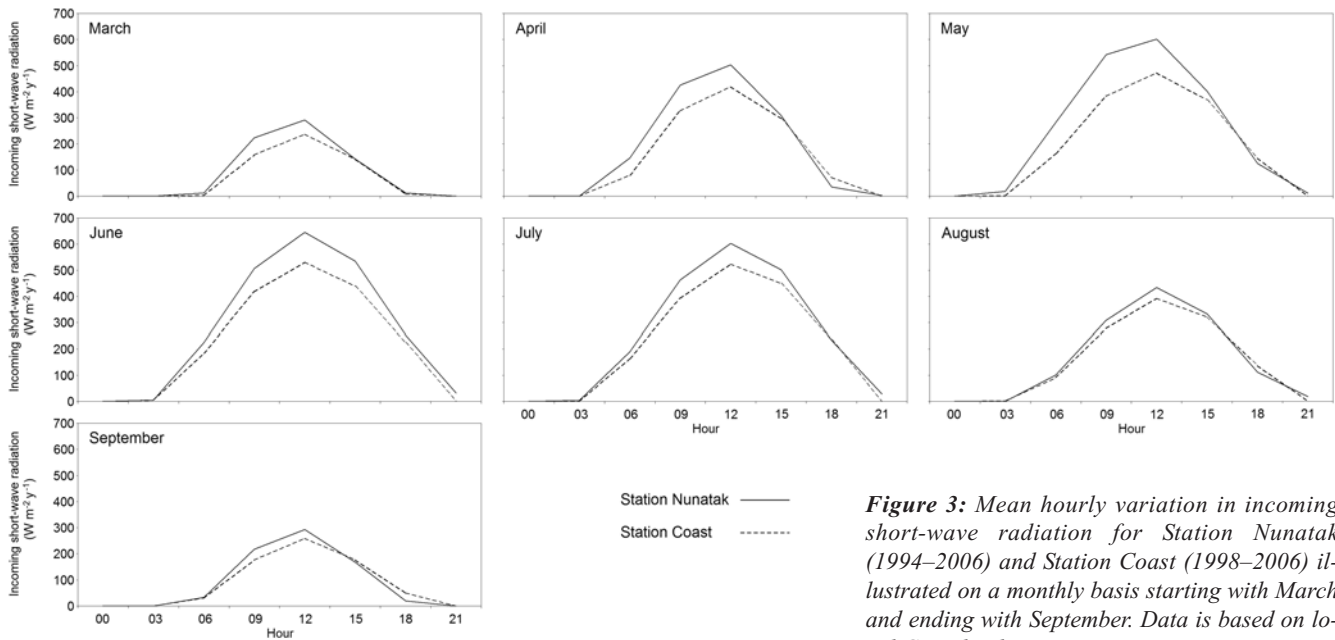


**Figure 3:** Mean hourly variation in incoming short-wave radiation for Station Nunatak (1994–2006) and Station Coast (1998–2006) illustrated on a monthly basis starting with March and ending with September. Data is based on local Greenland winter time.

polar night line is located about 200 km further north. Surrounding topography, slope/aspect of the terrain, and cloud cover have a great influence on the amount of incident (incoming) solar radiation, but geographical latitude is the main factor determining the weather and climate, especially in high latitude arctic regions. Locations at high latitudes receive limited amounts of solar radiation, especially during wintertime. The surface radiation balance ( $W m^{-2}$ ) can be expressed as:

$$Q^* = S_n + L_n = S_{\downarrow} - S_{\uparrow} + L_{\downarrow} - L_{\uparrow} = S_{\downarrow}(1 - \hat{a}) + L_n$$

where  $S_{\downarrow}$  is incoming solar radiation or global radiation,  $S_{\uparrow}$  the reflected solar radiation, the albedo ( $\hat{a}$ ) is the ratio of reflected to incoming solar radiation ( $S_{\downarrow} / S_{\uparrow}$ ), while  $L_{\downarrow}$  and  $L_{\uparrow}$  are the incoming and outgoing terrestrial long-wave fluxes, respectively. Net radiation  $Q^*$  is therefore the surplus or deficit of energy at the surface resulting from net short-wave ( $S_n$ ) and net long-wave ( $L_n$ ) radiative fluxes.

At Station Nunatak, where the surface gently slopes from N, NE, and E towards SW and W; diurnal variations in outgoing solar radiation are measured compared to a horizontal surface. At Station Coast, a large part of the hemisphere is obscured by a mountain to the E and NE of the station, causing a reduction of 10–100  $W m^{-2}$  in the global radiation, which is most pronounced from daily sunrise to noon, from March through September (Figure

3). In periods with dense cloud cover, direct solar radiation is almost reduced, leaving only diffuse radiation (about 20–30% of potential radiation) to reach the surface. In Figure 4a the annual variation in incoming short-wave radiation for Station Nunatak (1994–2006) and Station Coast (1998–2006) is illustrated. At Station Nunatak, increasing solar radiation of approximately  $0.5 W m^{-2} y^{-1}$  is observed ( $R^2 = 0.31$ ,  $p < 0.10$ ), whereas solar radiation decreases at Station Coast by approximately  $1.4 W m^{-2} y^{-1}$  ( $R^2 = 0.46$ ,  $p < 0.05$ ). The mean annual solar radiation is  $113 W m^{-2} y^{-1}$  and  $102 W m^{-2} y^{-1}$  for Station Nunatak (1994–2006) and Station Coast (1998–2006), respectively, indicating approximately 10% lower annual solar radiation in the coastal area probably due to the high frequency of dense clouds or thin sea fog (Figures 4a and 4b), which occur when relatively warm, moist air flows in over a cold surface. Further to the north, at the Zackenberg catchment ( $74^{\circ}N$ ), the mean annual solar radiation close to the coast of Young Sound is  $104 W m^{-2}$ , approximately 8% lower than at Station Nunatak. The slightly lower values are mainly due to the higher geographic latitude and a high summer cloud cover, based on advective sea fog (Mernild et al., 2007a; Hansen et al., 2008). The solar radiation at Station Nunatak (1994–2006) and Station Coast (1998–2006) showed large monthly variations (Figures 4a and 4b) from no incoming radiation during the polar night period, to a mean monthly maximum of  $275 W m^{-2}$  and  $231 W m^{-2}$ , respectively. Variations in albedo at Station



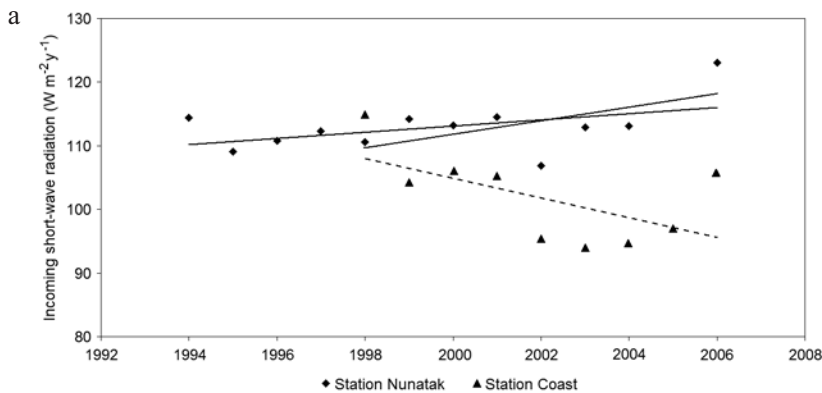
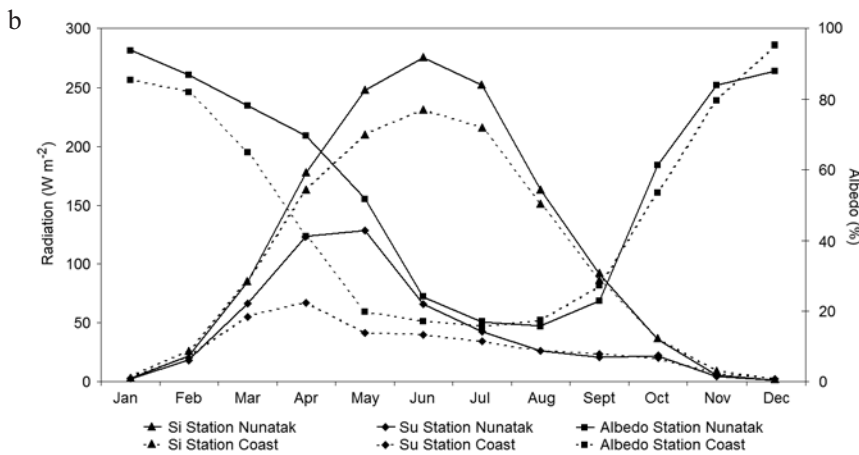


**Figure 4:** (a) Temporal trends in annual incoming short-wave radiation for Station Nunatak (1994–2006) and Station Coast (1998–2006). For Station Nunatak, data from 2005 are missing due to incomplete annual time series; and (b) mean monthly incoming ( $S_i$ ), reflected solar radiation ( $S_u$ ) and albedo at Station Nunatak (1994–2006) and at Station Coast (1998–2006).



Nunatak and Station Coast are also seen in Figure 4b, where low values around 15–20% indicate snow-free periods at the stations. Snow-free conditions occurred approximately four weeks earlier in the coastal area compared to the nunatak. The average monthly patterns of net short-wave radiation, net long-wave radiation, and net radiation are presented in Figure 5 for Station Nunatak and Station Coast. Net long-wave radiation is negative throughout the year, while net radiation is negative during winter months, October through March for Station Nunatak and November through February for Station Coast. In the spring time, net short-wave radiation is 10 to 43  $W m^{-2}$  higher at the coast station compared to the nunatak due to the high albedo from the long-lasting snow cover at the nunatak. In the summer time, the net short-wave radiation is 20 to 25  $W m^{-2}$  lower at the coast station due to the previously mentioned influence of the surrounding topography on the global radiation. The net long-wave radiation at Station Nunatak varies between  $-30$  to  $-50 W m^{-2}$ , which is quite normal for a horizontal Arctic surface, which is snow covered most of the year (Przybylak, 2003). The annual variation of the long-

wave radiation is mainly caused by the melting of the snow. In snow-free periods the difference between surface and atmosphere temperatures increases and is higher than during the snow covered periods. Due to the surrounding high terrain at Station Coast, the net long-wave radiation is very close to zero in the winter period, indicating a small temperature difference between the surface and the

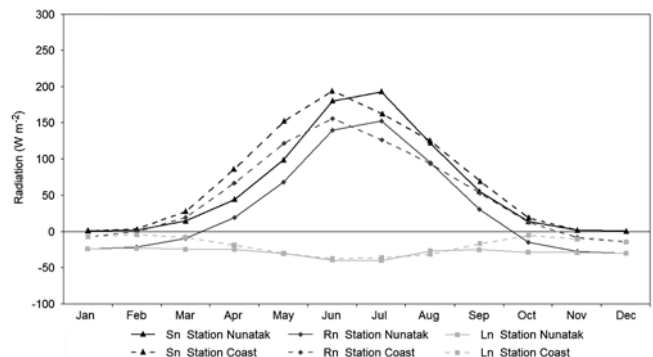


**Figure 5:** Average monthly pattern of net short-wave radiation ( $S_n$ ), net long-wave radiation ( $L_n$ ), and net radiation ( $R_n$ ), where  $R_n = S_n + L_n$  (Equation 1) for Station Nunatak (1994–2006) and Station Coast (1998–2006).

atmosphere/surrounding terrain. The difference of 30 W m<sup>-2</sup> between the two stations in the winter period is quite normal in snow-covered arctic areas if the surrounding terrain has an elevation angle of 25–30 degrees (Plüss et al., 1997). The annual average of the net radiation at Station Coast is 59% higher compared with Station Nunatak, mainly caused by the long-lasting and prevailing snow cover at the latter station. For most Arctic sites, about 50% of the annual solar radiation is reflected before snow melt (Hansen et al., 2008); at Station Nunatak and Station Coast it is around 60% and 40%, respectively.

During the nine-year period (1998–2006), a continuous winter snow cover is established at Station Nunatak between the end of September and the beginning of November, lasting until the end of June/beginning of July. The number of days with snow cover at Station Nunatak has decreased significantly ( $R^2 = 0.77$ ;  $p < 0.01$ ) by 64 days, from a total of 286 snow cover days in 1998/99 to 218 days in 2005/06, indicating a snow-free season 44 days longer in autumn ( $R^2 = 0.59$ ;  $p < 0.05$ ) and a significant 20 days longer in spring ( $R^2 = 0.92$ ;  $p < 0.01$ ). In the Zackenberg catchment (74°N) the length of the snow cover period has also decreased by around 50 days (1995–2003) (Mernild et al., 2007a). At both sites, and probably for East Greenland in general, the decreasing length of the snow cover period is presumably caused by increasing air temperatures and enhanced thawing rates.

#### *Air temperature and degree days*

Air temperature is the most important and therefore also the most often studied climatological parameter. The mean annual air temperature (MAAT) (1998–2006) in the Mittivakkat Glacier catchment is -1.7°C. It is derived by spatial simulations in MicroMet, and based on an input of -2.4°C (2.0 m) at Station Nunatak (1994–2006), and -0.8°C (2.0 m) at Station Coast (1998–2006). The mean air temperature values cover a trend in MAAT from 1998 to 2006, showing a significant ( $R^2 = 0.50$ ;  $p < 0.01$ ) increasing MAAT of 0.10°C y<sup>-1</sup> in the upper glacier area (Station Nunatak) and an increasing temperature in the coastal area of 0.05°C y<sup>-1</sup> (Station Coast) ( $R^2 = 0.07$ ;  $p < 0.10$ ). At Station Tasiilaq, MAAT increased by 0.12°C y<sup>-1</sup> ( $R^2 = 0.25$ ;  $p < 0.10$ ) (Figure 6a) (1998–2006). In the Zackenberg catchment (74°N) observed air temperatures also indicate increasing MAAT of approximately 0.10°C y<sup>-1</sup> (1996–2003) and a warming in all seasons except the spring (March–May) (Mernild et al., 2007a). For Station Nunatak, the mean minimum monthly air temperature is -8.9°C in January and -6.8°C in February for Station Coast,

in contrast to the average warmest month which is July at the nunatak (6.2°C) and August at the coast (5.3°C) (Figures 6b and 6c). Temperature differences in the warmest months between the stations, both in value and time, are probably mostly due to the heat capacity of the Sermilik Fjord, near Station Coast, and the high frequency of dense clouds or thin sea fog in the coastal area. At Station Coast, positive mean daily air temperatures occur from the beginning of May (day of year (DOY) 122) to the beginning of October (DOY 281), and at Station Nunatak, from the end of May (DOY 141) to the end of September (DOY 266) (Figures 6b and 6c). However, the maximum mean daily air temperature occurs at the nunatak (14.8°C; coast: 13.6°C). Figures 6b and 6c show that the absolute maximum positive air temperatures can occur in short periods during winter months, highly related to the occurrence of foehn situations.

The annual range of temperature (i.e. the difference between the highest and lowest mean monthly air temperatures) has in previous studies (e.g., Przybylak, 2003; Hansen et al., 2008) been used to distinguish between three well-defined types of annual cycles in temperatures in the Arctic: (1) maritime, an annual temperature range of 10–15°C; (2) coastal, a range of 15–25°C; and (3) continental, greater than 25°C. The continental type is the most common in the Arctic, representing 80% of the cycles. Figure 6d shows that Station Coast belongs to the maritime type in most years, but recently, in 2005 and 2006, it has moved towards the coastal type, whereas Station Nunatak is a coastal type, except for the maritime conditions in 1996.

Figure 6e illustrates the seasonal variability (December–February, March–May, June–August, and September–November) in air temperature for Station Nunatak (1998–2006) and Station Coast (1998–2006). At Station Nunatak, all seasons show increasing air temperatures ( $R^2 = 0.08$ ,  $p < 0.25$  for December–February;  $R^2 = 0.14$ ,  $p < 0.10$  for March–May;  $R^2 = 0.48$ ,  $p < 0.01$  for June–August; and  $R^2 = 0.05$ ,  $p < 0.25$  for September–November). The increase is most conspicuous for the winter (December through February), 0.10°C y<sup>-1</sup>, and for the spring (March through May), 0.13°C y<sup>-1</sup>, which is in accordance with previous studies for the Arctic area by Box (2002) and Sturm et al. (2005). Less conspicuous increases are seen in summer and autumn periods, showing values of 0.09°C y<sup>-1</sup> and 0.04°C y<sup>-1</sup>, respectively. For Station Coast the seasonal trends are different. Due to the local coastal conditions, decreasing air temperatures are observed during autumn ( $R^2 = 0.42$ ,  $p < 0.05$  for September–November) and

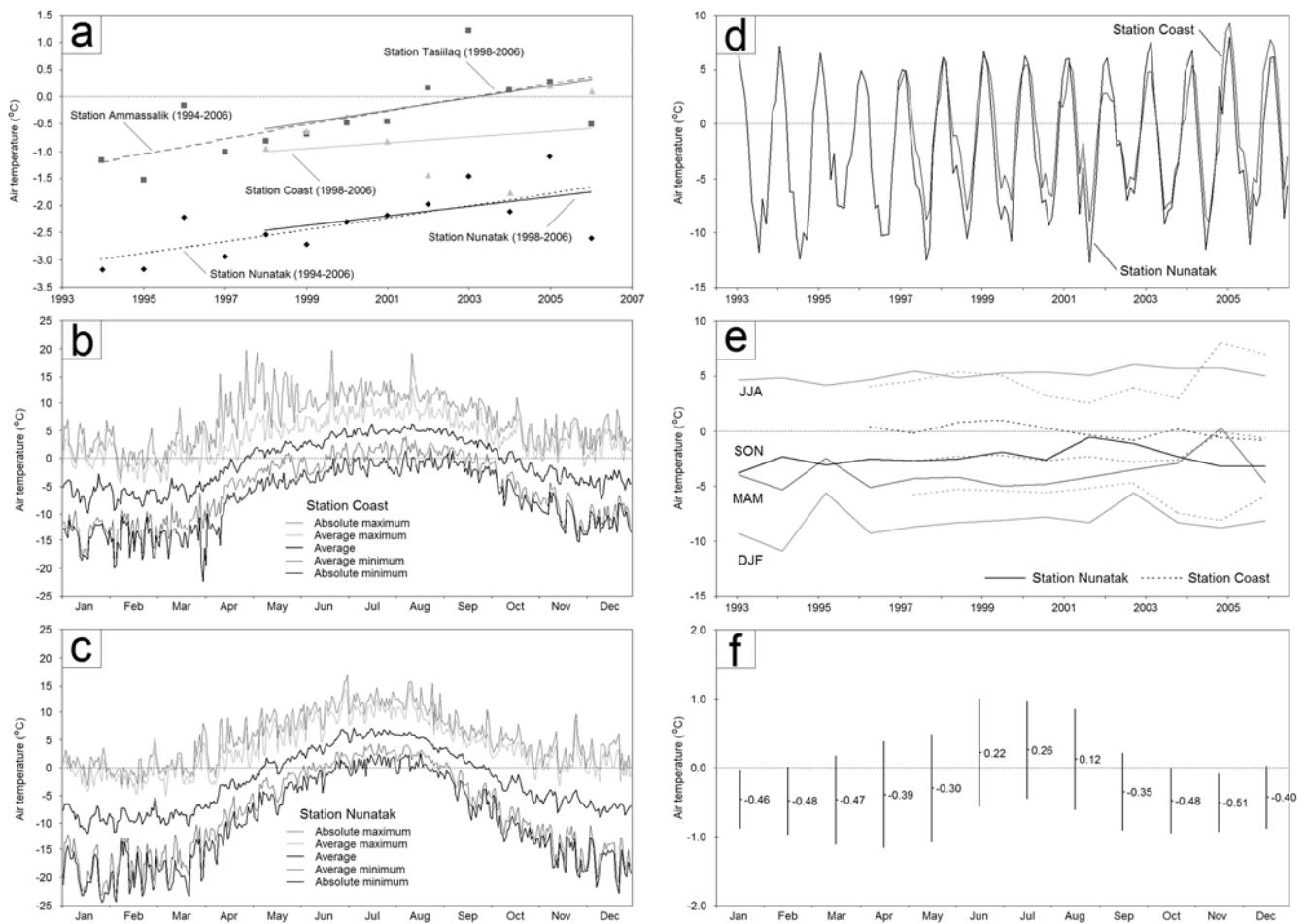


**Figure 6:** (a) Mean annual air temperature (MAAT) at Station Coast (2.0 m) (1998–2006), Station Nunatak (2.0 m) (1994–2006), and Station Tasilaq (2.0 m) (1994–2006); (b) Station Coast absolute and average maximum, average, and absolute and average minimum daily air temperatures (2.0 m) (1998–2006); (c) Station Nunatak absolute and average maximum, average, and absolute and average minimum daily air temperatures (2.0 m) (1994–2006); (d) mean monthly air temperature for Station Coast (2.0 m) and Station Nunatak (2.0 m); (e) seasonal air temperatures at Station Coast (2.0 m) and at Station Nunatak (2.0 m). The abbreviations are DJM (December, January, and February), MAM (March, April, and May), JJA (June, July, and August), and SON (September, October, and November); and (f) mean monthly lapse rates based on air temperature from Station Coast (2.0 m) and Station Nunatak (2.0 m) (1998–2006).

winter ( $R^2 = 0.24$ ,  $p < 0.10$  for December–February), whereas increasing temperatures are seen during spring ( $R^2 = 0.42$ ,  $p < 0.05$  for March–May), and summer ( $R^2 = 0.13$ ,  $p < 0.25$  for June–August) (Figure 6e). For Station Coast, increasing air temperatures are most pronounced during spring,  $0.21^\circ\text{C y}^{-1}$ , and decreasing temperatures, during winter,  $0.18^\circ\text{C y}^{-1}$ . On an annual basis, the MAAT is increasing at both Station Nunatak and Station Coast (Figure 6a).

Mean monthly air temperature lapse rates for the Mitivakkat Glacier catchment based on data from the two stations, Station Nunatak and Station Coast are shown

(Figure 6f). The mean annual air temperature lapse rate was approximately  $-0.3^\circ\text{C } 100 \text{ m}^{-1}$  (1998–2006) (half the value of the adiabatic change:  $-0.65^\circ\text{C } 100 \text{ m}^{-1}$ ), with an average range between the most negative and the most positive mean monthly lapse rate of  $0.74^\circ\text{C } 100 \text{ m}^{-1}$ . February had the lowest average lapse rate ( $-0.48^\circ\text{C } 100 \text{ m}^{-1}$ ), while July had the highest ( $0.26^\circ\text{C } 100 \text{ m}^{-1}$ ) (Figure 6f). The clearly positive average air temperature lapse rates from June to August are influenced by the coastal wind regime. During summer, sea breezes governed by local temperature differences in the heating of sea and land prevail, the relatively cold and foggy air influencing the

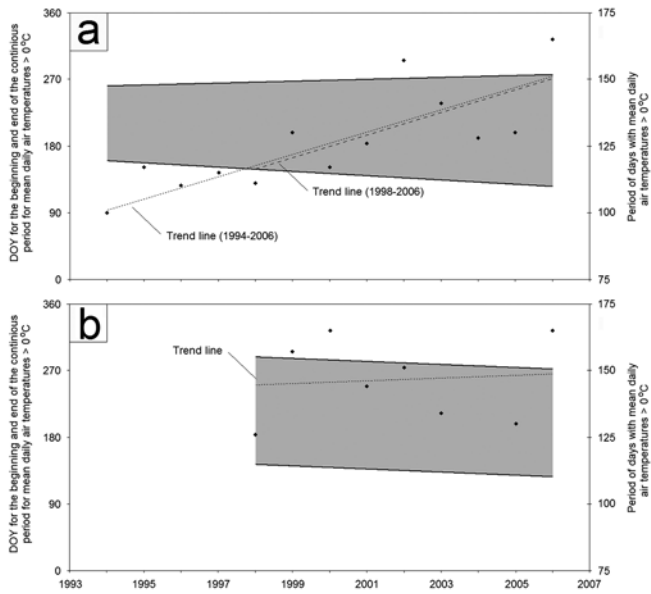


**Figure 7:** Day of year (DOY) for the beginning and the end of the continuous period for mean daily air temperatures above 0°C for: (a) Station Nunatak (1994–2006); and (b) Station Coast (1998–2006). The gray area indicates the yearly period mean daily air temperature above 0°C, and the two full-drawn trend lines indicate the beginning and end of the continuous period (related to the left ordinate). The dotted line indicates the trend line (linear regression) for the number of days with mean daily air temperature above 0°C (right ordinate).

coastal landscapes. The same lapse rate trend is also present for the area for periods without the occurrence of dense clouds or thin fog at the coast (Mernild et al., 2005), and the trend in monthly lapse rates is quite similar to other Arctic coastal areas e.g., the Zackenberg catchment (74°N) (Mernild et al., 2007c; Hansen et al., 2008). The lower parts of the Mittivakkat Glacier catchment, comprising the proglacial valley and the coastal area, are strongly dominated by air temperature inversion shown by frequent situations in which temperatures increase rather than decrease with altitude, affecting the air temperature lapse rates in the catchment. In summer time (June through August), air temperature inversions are estimated to be present in approximately 59% of the observations due to the coastal wind regime. Radio-sonde observations in July 2006 show that air temperature inversions occur at 300 m a.s.l. In winter, the occurrence of temperature inversion decreases probably because sea and land surfaces are much the same, since they are both covered more or less continuously in ice and snow, eliminating local temperature differences in the heating of sea and

land. Higher wind speeds in the catchment during the winter also work against the development of temperature inversion as they promote mixing and destroy the inversion. In the high Arctic Zackenberg catchment (74°N) the yearly occurrence of air temperature inversions are opposite. During the winter months, temperature inversion prevails around 50–80% of the time whereas there is evidence of temperature inversion 10–50% of the time in summer and autumn (Mernild et al., 2007c; Hansen et al., 2008). A similar trend is described by Serreze et al. (1992) as a common feature for the Eurasian Arctic environment.

The number of days with continuous mean daily air temperatures above 0°C is shown on Figures 7a and 7b, in-

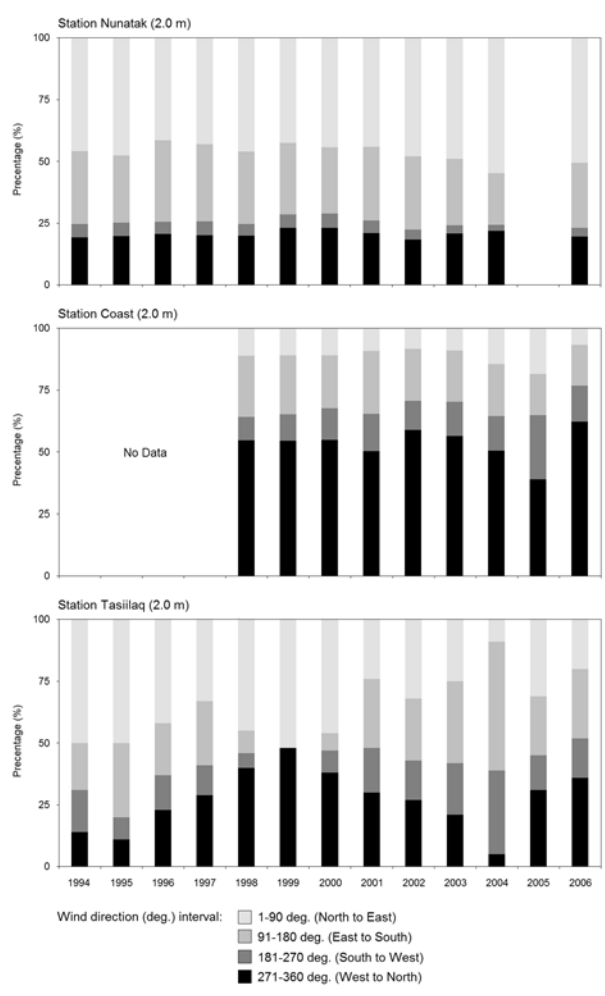


**Figure 8:** The yearly variation in wind direction in percentage (%) at Station Nunatak (2.0 m) (1994–2006), Station Coast (2.0 m) (1998–2006), and Station Tasiilaq (2.0 m) (1994–2006). The wind direction is divided into four intervals: 1–90 degrees (North to East), 91–180 degrees (East to South), 181–270 degrees (South to West), and 271–360 degrees (West to North).



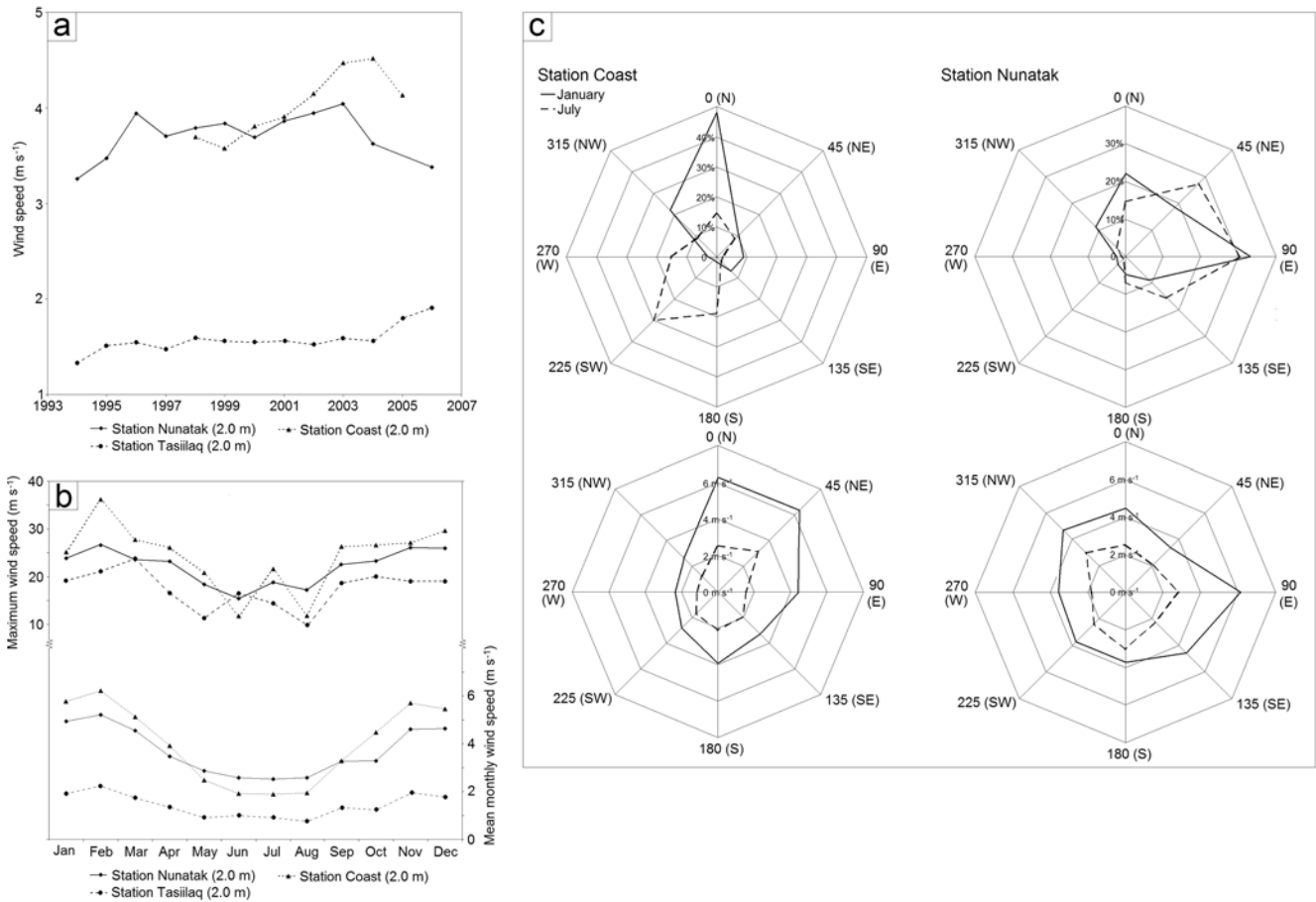


**Figure 9:** (a) Temporal trends in mean annual wind speed as average yearly values (1994–2006) for Station Nunatak (2.0 m), Station Coast (2.0 m), and Station Tasiilaq (2.0 m) (values are missing from 2005 at Station Nunatak and 2006 at Station Coast due to incomplete annual time series). Wind speed is measured at 10.0 m at Station Tasiilaq, but here calculated for 2.0 m based on roughness at 0.1 m; (b) temporal trends in absolute maximum and mean monthly wind speed values for Station Nunatak (1994–2006), Station Coast (1998–2006), and Station Tasiilaq (1994–2006). Notice the change in scale on the ordinate; and (c) mean frequency (%) of wind direction, and mean wind speed ( $m s^{-1}$ ) related to wind direction for January and July at Station Nunatak (1994–2006) and at Station Coast (1998–2006).

dicating a significant ( $R^2 = 0.70$ ,  $p < 0.01$ ) increasing continuous melt period at Station Nunatak and a non-significant increasing melt period at Station Coast. At the nunatak the period was extended by 50 days, from 101 continuous thawing days (1994) to 151 thawing days (2006): resulting in a significant extension of the spring melt by 35 days ( $R^2 = 0.61$ ;  $p < 0.01$ ), and an extension in autumn of 15 days ( $R^2 = 0.29$ ;  $p < 0.025$ ). At Station Coast, the period was extended by an average of five days, from 144 thawing days (1998) to 149 days (2006), comprising a continuous spring melt extended by 17 days ( $R^2 = 0.21$ ;  $p < 0.10$ ), and a shortening of the autumn melt of 12 days ( $R^2 = 0.37$ ;  $p < 0.05$ ). At Zackenberg (74°N) the trend lines (1996–2003) indicate a lengthening of the

thawing season in autumn by 16 days and a shortening in spring by 2 days for a net lengthening of the thawing season of 14 days (Mernild et al., 2007a). The increasing length of the thawing period during the last decade observed for both studied catchments in East Greenland presumably represents a general phenomenon for East Greenland.

The observed increased length of the thawing period in the Mittivakkat catchment from 1994 through 2006 is furthermore reflected in an increasing number of thawing degree days (TDD) per year. The accumulated number of thawing degree days (TDD) is the sum of values of positive mean daily air temperatures (Mernild et al., 2005). TDD is also referred to as PDD (Positive Degree Days).

For Station Nunatak, TDD increased significantly by 50% on average from 495 to 745 ( $R^2 = 0.40$ ;  $p < 0.01$ ), while TDD at Station Coast increased from 570 in 1998 to 894 in 2006, an average increase of 57% ( $R^2 = 0.44$ ;  $p < 0.05$ ). In general, plant growth is strongly related to air temperature, and air temperature is found to be a strong limiting factor for growth potential in Arctic landscapes. Plant growth is insignificant when the daily mean air temperature is below  $5^\circ\text{C}$ , and this temperature has become widely adopted as a threshold air temperature for defining growing degree days (GDD), also called the effective air temperature sum and indicating the potential plant production in the growing season. For Station Nunatak, GDD increased significantly ( $R^2 = 0.40$ ;  $p < 0.01$ ) from 78 to 144 (85% increase) in average, while GDD at Station Coast increased from 53 in 1998 to 108 in 2006 (104% increase) on average ( $R^2 = 0.10$ ;  $p < 0.25$ ).

#### *Wind direction, wind speed, and relative humidity*

Winds in the coastal landscapes of Greenland are partly the result of large-scale atmospheric circulations influenced by pressure gradients. In addition, local geographical factors such as distance from the Arctic Ocean and the GrIS, orographic, and topography (altitude and relief) influence wind direction and speed (e.g., Przybylak, 2003; Mernild et al., 2006b; Hansen et al., 2008). Wind directions at both stations, Station Nunatak and Station Coast, are highly dependent on the orographic conditions. At Station Nunatak cold katabatic fall winds, especially from N to E ( $0\text{--}90$  deg.), dominate around 50% of the time (Figure 8). The frequent katabatic winds also result in the almost total lack of calm periods (only 0.2% at Station Nunatak and 1.2% at Station Coast (Hasholt et al., 2004)). During winter (illustrated by January in Figure 9c) and summer (illustrated by July) the main wind directions are from N to E at Station Nunatak. At Station Coast, winds from W to N ( $270\text{--}360$  deg.) dominate around 50% of the time (Figure 8). The wind direction is influenced by the surrounding topography, and during winter time to some extent by winds from the GrIS canalized through the Sermilik Fjord. Further, the valley northeast of the station may channel cold katabatic winds, especially in the winter: approximately 50% of the time the wind comes from northerly directions (Figure 9c). Due to this tunneling effect, the gusts at Station Coast can be even greater than at Station Nunatak.

During the winter, both sea and land surfaces are mostly covered by ice and snow. Low amounts of absorbed solar radiation over this homogeneous cover of

snow and ice provide small differences in energy partitioning between marine and terrestrial surfaces (Hansen et al., 2008). After terrestrial snowmelt, the land surface warms up, giving rise to large temperature differences between the land and the still frozen sea. This temperature gradient induces a cold and moist daytime sea breeze at Station Coast, mainly coming from S and SW (Figure 9c). As the sea ice starts melting, temperature differences between sea and land decreases, but due to the continuous and high input of solar radiation during mid summer, the sea breeze will still exist, only in a slightly weaker version. Such sea breezes have been found all over the Arctic e.g., along the Alaskan Beaufort Sea Coast (Kozo, 1982a, 1982b), Svalbard (Wojcik and Kejna, 1991), the Hudson Bay area in Canada (Weick and Rouse, 1991), on Disko Island, W Greenland (Hansen et al., 2005), and in Zackenberg, NE Greenland (Hansen et al., 2008).

The mean annual wind speed is  $3.7\text{ m s}^{-1}$  (2.0 m) at Station Nunatak (1994–2006),  $4.1\text{ m s}^{-1}$  (2.0 m) at Station Coast (1998–2006), and  $1.5\text{ m s}^{-1}$  (2.0 m) at Station Tasiilaq (1994–2006). Wind speed data show a non-significant trend of increasing velocities at Station Nunatak, but a significant increasing trend at Station Coast ( $R^2 = 0.71$ ;  $p < 0.01$ ) and at Station Tasiilaq ( $R^2 = 0.67$ ;  $p < 0.01$ ) (Figure 9a), mainly due to increasing wind speed during the winter season (Figure 10). The years 2005 and 2006 show decreasing average annual wind speeds at Station Nunatak and Station Coast, while average wind speeds still increase at Station Tasiilaq. The highest wind speeds occur during winter time (Figures 9b and 10), with mean monthly velocities around  $6.0\text{ m s}^{-1}$  and gust values up to  $35.0\text{ m s}^{-1}$  at Station Nunatak and Station Coast. Furthermore, the gust velocities occur mainly from the dominating wind directions. Strong winds (neqqqjaaq, similar to a foehn wind) occur during winter on the Mittivakkat Glacier, mainly coming from the NE and E, and often followed by cold katabatic winds (piteraqaq). Wind velocities during a piteraqaq can gust to  $85\text{ m s}^{-1}$ .

In the Arctic, snow redistribution is common due to wind drift. At Station Nunatak conditions for drifting snow are present 23%, and at Station Coast, 34% of the year. This means potential monthly winter snow drift up to 41% of the time in February at Station Nunatak and 59% of the time in January and February at Station Coast (Table 2).

The mean annual relative humidity at Station Nunatak during 1998–2006 is 83% (data from 2001–2003 are not included due to a temporal error in recordings), covering a yearly variation from 75% (2000) to 85% (1996). At Sta-



	Jan	Feb	Mar	Apr	May	Jun	Jul	Aug	Sep	Oct	Nov	Dec	Mean
Percentage of blowing snow events (%), Station Nunatak	37	41	33	22	14	10	8	9	18	19	33	33	23
Percentage of blowing snow events (%), Station Coast	59	59	47	35	15	6	6	8	19	44	58	55	34

**Table 2:** Temporal variation in percentage (%) of blowing snow events during the year for Station Nunatak (2.0 m) (1994–2006) and Station Coast (2.0 m) (1998–2006).

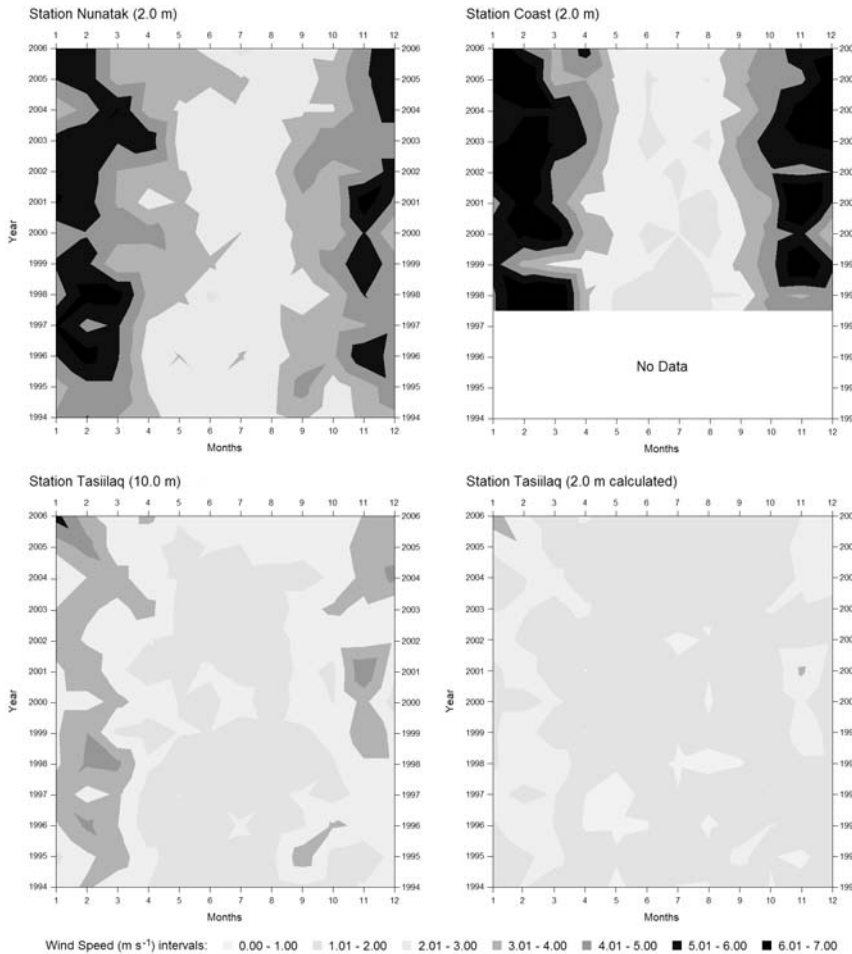


**Figure 10:** Station Nunatak (2.0 m), Station Coast (2.0 m), and Station Tasiilaq (10.0 m and 2.0 m calculated) mean monthly wind speed for the period 1994 through 2006. Wind speed at Station Tasiilaq (2.0 m) is calculated based on roughness at 0.1 m.

tion Coast, the mean annual relative humidity reaches 82%, varying from 76% (1998) to 91% (2003); at Station Tasiilaq, it reaches 80%, varying from 71% (1995) to 84% (1988) (Figure 11a). The highest monthly average relative humidity values at Station Nunatak occur during winter (83%) due to lower air temperatures, whereas the highest values at Station Coast occur during summer (86%) due to sea breezes and the proximity to the fjord (Figure 11b).

### Precipitation

The amount of precipitation over any area depends on the moisture content of the air, the pattern of weather systems affecting the area and the topography, altitude, and character of the underlying surface (Hansen et al., 2008). The

average TAP at Station Nunatak is 1,851 mm w.eq.  $y^{-1}$  (1999–2006), 1,428 mm w.eq.  $y^{-1}$  at Station Coast (1999–2006) (Figures 12a and 12c), and 1,549 mm w.eq.  $y^{-1}$  for the whole Mittivakkat Glacier catchment, derived by spatial simulations in MicroMet. At the DMI climate station in Tasiilaq, the corrected TAP is 1,254 mm w.eq.  $y^{-1}$  (1999–2006) (Figure 12e). Based on a temperature controlled fractionation of precipitation events, solid precipitation represents about 80% of the TAP, mixed precipitation, 6%, and liquid precipitation, 14% at Station Nunatak. At Station Coast, the distribution is 53%, 31%, and 16%, and at Station Tasiilaq, 23%, 46%, and 31%, respectively (Figure 12). After applying a wind speed and a winter glacier mass balance SWE correction, partly due to the exposed station location at the nunatak (Mernild et al.,

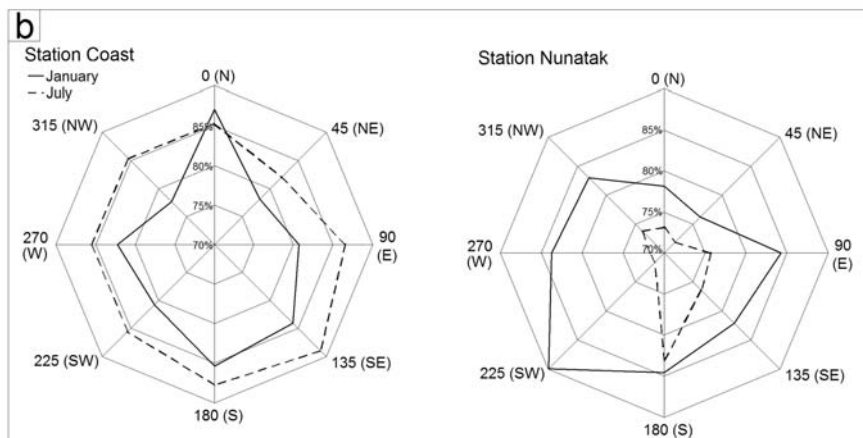
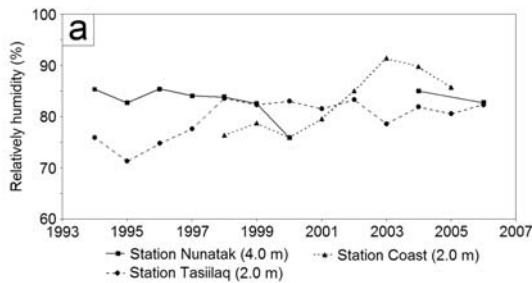


**Figure 11:** (a) Temporal trends in mean annual relative humidity (%) for Station Nunatak (4.0 m) (1994–2006), Station Coast (2.0 m) (1998–2006), and Station Tasiilaq (2.0 m) (1994–2006) (values are missing from 2005 at Station Nunatak and 2006 at Station Coast due to incomplete annual time series). Missing observations in relative humidity at Station Nunatak from 2001 through 2003 is due to temporal error in recordings; and (b) relative humidity related to wind direction for average January and July at Station Nunatak (1994–2006) and at Station Coast (1998–2006).

2006a), the average SWE at Station Nunatak is calculated to 1,503 mm w.eq.  $y^{-1}$  during 1999–2006. At Station Coast, SWE is 947 mm w.eq.  $y^{-1}$ , indicating an average positive orographic effect of 113 mm w.eq. per 100 m for SWE winter precipitation (1999–2006) within the Mittivakkat Glacier catchment. The 113 mm w.eq. SWE per 100 m between the two stations is assumed to be closely related to the orographic influence of Ammassalik Island in general. In previous studies by Mernild et al. (2006a), 99 mm w.eq. per 100 m was estimated for the Mittivakkat catchment. The orographic effect of 113 mm w.eq. per 100 m for SWE precipitation equals an approximately 10% SWE increase per 100 m elevation. Also, previous studies by Hasholt et al. (2003) showed orographic precipitation increases as high as 14% per 100 m for Ammassalik Island. The obtained and improved values in the present study are very close to gradients found and used in mountainous areas such as Svalbard (Humlum, 2002) and Norway (Young et al., 2006). A reverse and negative orographic effect occurs for total average liquid summer precipitation, showing an average negative orographic effect of -52 mm w.eq. per 100 m (1999–2006) (Figures 12a and 12c). This is presumably mostly due to the higher frequency of rain from clouds and fog only reaching the coastal areas, but is probably also affected by anticipated liquid precipitation in early and late summer actually

falling as snow at higher altitudes.

The monthly variation in precipitation at Station Nunatak, Station Coast, and Station Tasiilaq (Figures 12b, 12d, and 12f) shows the highest precipitation values during winter, primarily due to a high cyclonic activity in the period from November to April. Values reach 281 mm w.eq. on the glacier, 175 mm w.eq. at the coast, and 181 mm w.eq. in Tasiilaq. The monthly precipitation shows on average the lowest values after the beginning of snowmelt and during the summer period, when cyclonic activity affecting the area decreases and air temperatures generally increase more rapidly than the humidity. On average, the calculated mixed precipitation is 120 mm (6% of total) at Station Nunatak, 435 mm w.eq. (31% of total) at Station Coast, and 570 mm w.eq. (46% of total) at Station Tasiilaq (Figure 12g), and it mainly occurs in early and late summer in the Mittivakkat catchment, although depending on temperature it may occur all year round. Liquid precipitation at Station Nunatak is 251 mm w.eq. (14% of total), 217 mm w.eq. (16%) at Station Coast, and 390 mm w.eq. (31%) at Station Tasiilaq (Figure 12g). Liquid precipitation occurs mainly from June to September in the Mittivakkat catchment, whereas it generally is seen all year round in Tasiilaq.

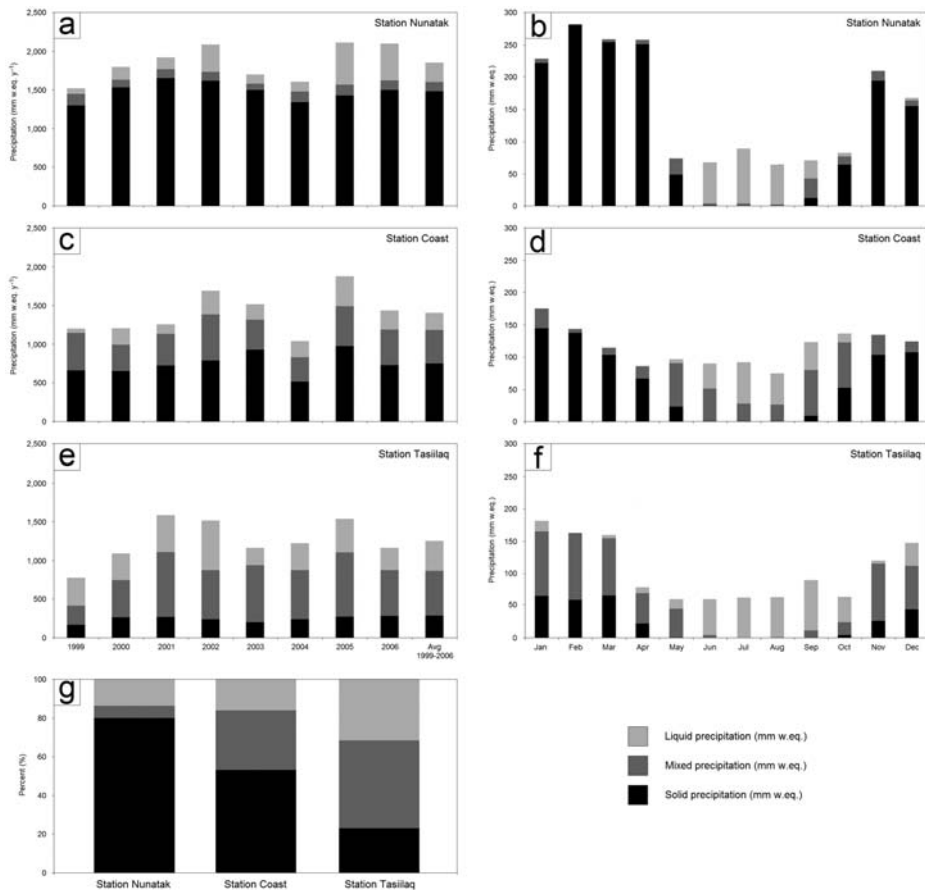


**Figure 12:** Precipitation (liquid, mixed, and solid) (1999–2006) (mm w.eq.) at: (a) Station Nunatak; (c) Station Coast; and (e) Station Tasiilaq. Mean monthly precipitation at: (b) Station Nunatak; (d) Station Coast; and (f) Station Tasiilaq, (g) a separation into liquid, mixed, and solid precipitation in percentage (%) for Station Nunatak, Station Coast, and Station Tasiilaq. Solid precipitation falls as snow when air temperature is below  $-1.5^{\circ}\text{C}$ , liquid precipitation falls as rain when air temperature is above  $3.5^{\circ}\text{C}$ , and mixed precipitation falls as sleet when the air temperature is between  $-1.5$  and  $3.5^{\circ}\text{C}$ . At Station Tasiilaq precipitation is corrected according to Allerup et al. (2000).

*Air temperature, relative humidity, wind speed, and precipitation in a 109-year perspective*

Figure 13a illustrates the calculated variation in MAAT from 1898 through 2006 for the Mittivakkat Glacier catchment. Pronounced periods of warming are observed from 1918 (the end of the Little Ice Age) to 1935 ( $0.12^{\circ}\text{C y}^{-1}$ ;  $R^2 = 0.47$ ;  $p < 0.01$ ) and from 1978 to 2006 ( $0.08^{\circ}\text{C y}^{-1}$ ;  $R^2 = 0.50$ ;  $p < 0.01$ ). Air temperature cooling in the Mittivakkat Glacier catchment prevailed from 1955 to 1978 ( $-0.04^{\circ}\text{C y}^{-1}$ ;  $R^2 = 0.18$ ;  $p < 0.025$ ), and approximately constant temperature conditions occurred from 1898 to 1918 ( $0.02^{\circ}\text{C y}^{-1}$ ;  $R^2 = 0.06$ ;  $p < 0.25$ ) and from 1935 to 1955 ( $-0.02^{\circ}\text{C y}^{-1}$ ;  $R^2 = 0.04$ ;  $p < 0.25$ ). The air temperature trends in the Mittivakkat Glacier catchment are in accordance with observations from other Arctic sites (Serreze et al., 2000; Box, 2006). The overall trend (linear regression) in air temperature over the last 109 years (1898–2006) shows a small increase of  $0.2^{\circ}\text{C}$  ( $R^2 = 0.03$ ;  $p < 0.10$ ) (Figure 13a) for the Mittivakkat Glacier catchment, whereas the temperature trend 15 km away, at the outer coast at the Station Tasiilaq, shows a higher in-

crease of about  $0.7^{\circ}\text{C}$  ( $R^2 = 0.04$ ;  $p < 0.025$ ). Calculated for the last 100 years (1907–2006) and for the last 75 years (1932–2006), the trend lines indicate a decrease in air temperature of  $0.24^{\circ}\text{C}$  ( $R^2 < 0.01$ ;  $p < 0.25$ ) and  $0.91^{\circ}\text{C}$  ( $R^2 = 0.07$ ;  $p < 0.025$ ) (Figure 13a) for the Mittivakkat catchment and Tasiilaq, respectively, but over the last 50 years (1957–2006), air temperatures have increased for the Mittivakkat Glacier catchment by  $0.88^{\circ}\text{C}$  ( $R^2 = 0.08$ ;  $p < 0.025$ ), and significantly, by  $2.66^{\circ}\text{C}$  ( $R^2 = 0.62$ ;  $p < 0.01$ ) over the last 25 years (1982–2006). All four seasons at the Mittivakkat glacier catchment show warming over the 109-year period (Figure 13b), especially during the winter season by  $1.43^{\circ}\text{C}$  ( $R^2 = 0.05$ ;  $p < 0.025$ ). It can be concluded that the warmest average 10-year period within the last 109 years was the period from 1938–1947 ( $-1.83^{\circ}\text{C}$ ), while within the last 60 years, the warmest 10-year period was the period from 1997–2006 ( $-2.10^{\circ}\text{C}$ ) for the Mittivakkat Glacier catchment (Figure 13a). Not only in East Greenland, but also in West Greenland, the 1930s and 1940s constituted the warmest period until now since the termination of the little ice age (Cappelen, 2004).

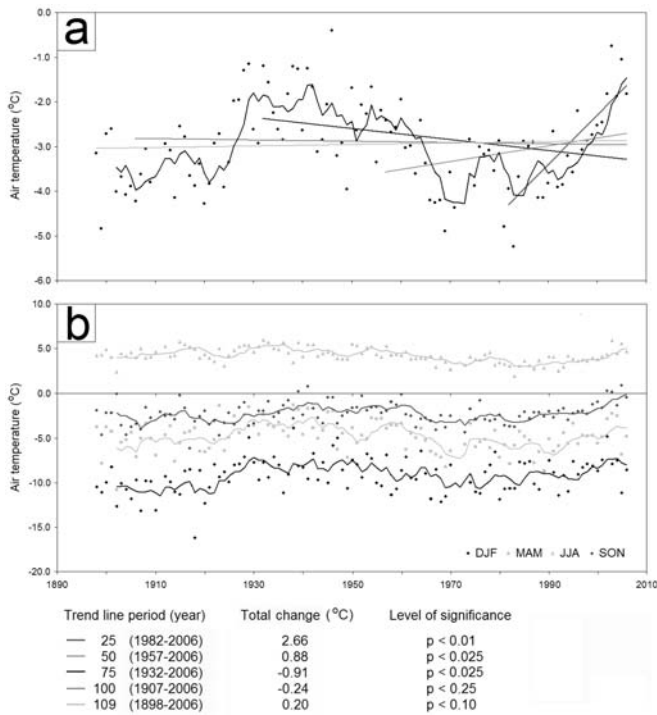


**Figure 13:** (a) Mean annual and five-year running mean annual air temperatures (°C) for the Mittivakkat Glacier catchment for the period 1898–2006, including trend lines for the last 25 years (1982–2006), 50 years (1957–2006), 75 years (1932–2006), 100 years (1907–2006), and 109 years (1898–2006); and (b) mean seasonal and five-year running seasonal air temperatures. The abbreviations are DJM (December, January, and February), MAM (March, April, and May), JJA (June, July, and August), and SON (September, October, and November). Data are missing in the period from September 1910 to August 1911 and from January 1971 to December 1972.

The mean annual relative humidity and wind speed for the Mittivakkat Glacier catchment for the period 1958 to 2006 are shown in Figure 14a. The relative humidity is fairly constant throughout the period, averaging 79%, and varying between 73 to 83%. Over the last 48 years (1959–2006), the humidity trends (linear regression) show an increase for the Mittivakkat Glacier catchment of 0.1% ( $R^2 < 0.01$ ), but over the last 25 years (1982–2006), the trends show an increase of 2.4% ( $R^2 = 0.10$ ;  $p < 0.10$ ), presumably linked to changes in temperature and moisture in air masses reaching the area.

Figure 14b shows the mean annual wind speed in the Mittivakkat catchment. Trends (linear regression) indicate a significant increase for the two calculated periods: 1959–2006 (48 years) and 1982–2006 (25 years). Within the last 48 years and 25 years the wind speed at the Mitti-

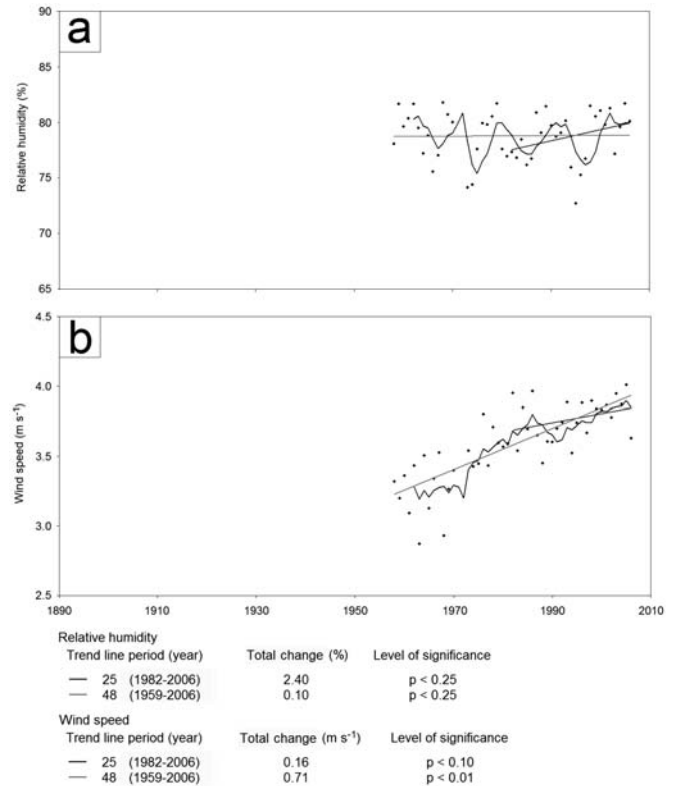


**Figure 14:** Mean annual and five-year running mean annual: (a) relative humidity (%); and (b) wind speed (m s<sup>-1</sup>) for the Mittivakkat Glacier catchment for the period 1998–2006, including trend lines for the last 25 years (1981–2006) and 48 years (1958–2006). Data are missing in the period from January 1971 to December 1972.

vakkat Glacier catchment has increased significantly by 0.71 m s<sup>-1</sup> ( $R^2 = 0.61$ ;  $p < 0.01$ ) and 0.16 m s<sup>-1</sup> ( $R^2 = 0.10$ ;  $p < 0.01$ ), respectively, indicating windier conditions in the catchment.

Figure 15a illustrates the calculated variation in TAP for the Mittivakkat Glacier catchments from 1898 through 2006, averaging 1,454 mm w.eq. y<sup>-1</sup>. The TAP is divided into solid, mixed, and liquid precipitation, averaging 982 mm w.eq. y<sup>-1</sup> (68%), 205 (14%), and 267 (18%), respectively (Figures 15a and 15b). Precipitation-rich periods are observed from 1901 through 1914 (1,560 mm w.eq. y<sup>-1</sup>) and from 1963 through 1978 (1,563 mm w.eq. y<sup>-1</sup>) (Figure 15c). Outside the wet periods, TAP reaches on average 1,400 mm w.eq. y<sup>-1</sup>, which is significantly different from the wet time periods (97.5% fractal). The overall trend (linear regression) in TAP over the last 109 years (1898–2006) shows an increase of 85 mm w.eq. ( $R^2 = 0.02$ ;  $p < 0.05$ ) for the Mittivakkat Glacier Catchment (Figure 15c).



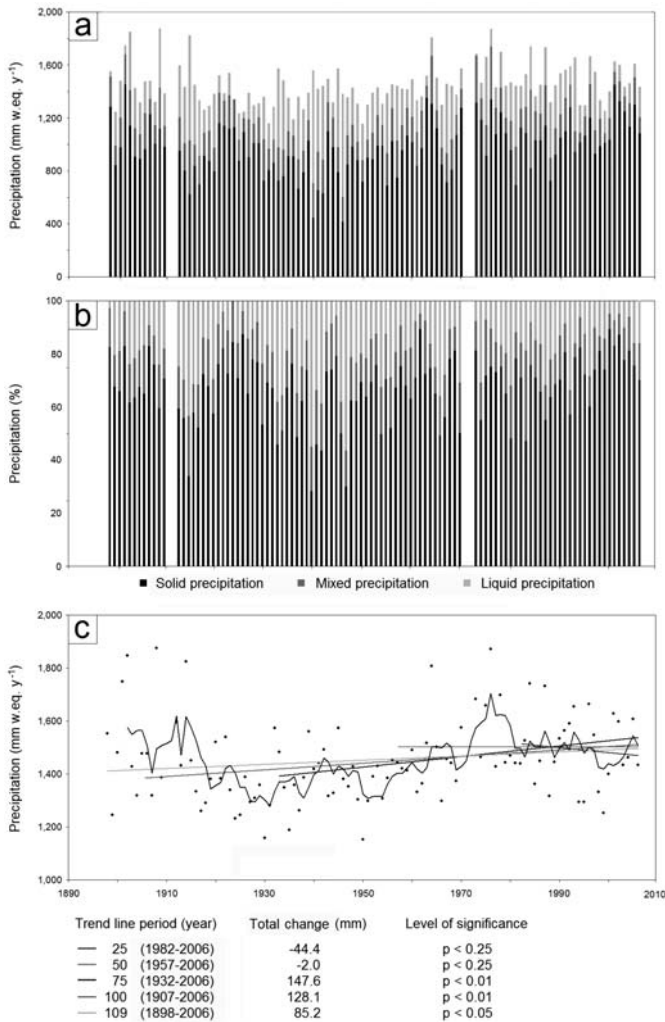


**Figure 15:** Total annual precipitation (TAP) illustrated as solid, mixed, and liquid precipitation for the Mittivakkat Glacier catchment (1898–2006) in: (a) mm w.eq. y<sup>-1</sup>; (b) in percentage (%). Solid precipitation falls as snow when air temperature is below -1.5°C, liquid precipitation falls as rain when air temperature is above 3.5°C, and mixed precipitation falls as sleet when the air temperature is between -1.5 and 3.5°C; and (c) TAP and five-year running mean TAP for the Mittivakkat Glacier catchment for the period 1898–2006, including trend lines for the last 25 years (1982–2006), 50 years (1957–2006), 75 years (1932–2006), 100 years (1907–2006), and 109 years (1898–2006). Data are missing for the periods from September 1910 to August 1911 and from January 1971 to December 1972.

At Station Tasiilaq, the trend in the corrected TAP (1898–2006) shows a higher increase of 281 mm w.eq. ( $R^2 = 0.04$ ;  $p < 0.025$ ); however, TAP over the last 50 years (1957–2006) and the last 25 years (1982–2006) has decreased by 4 mm w.eq. ( $R^2 < 0.01$ ;  $p > 0.25$ ) and 95 mm w.eq. ( $R^2 < 0.01$ ;  $p > 0.25$ ), respectively. The decreasing

TAP trend is probably due to changes in wind direction, from less dominating N and E (0–90 deg.) winds in the 1970s, 1980s, and 1990s to more dominating E to W (90–270 deg.) winds in the years around 2003 to 2006. A recent decreasing TAP trend is also seen for Danmarks-havn, while TAP increased at Station Nord, Scoresbysund, and in the Daneborg/Zackenber region in the period 1985–2006. For Zackenberg (74°N), however, the TAP increased 1.9 mm w.eq. y<sup>-1</sup> in the period 1958–2005 (Hansen et al., 2008). An increase of 281 mm w.eq. at Station Tasiilaq corresponds to an increase of approximately 25 mm w.eq. decade<sup>-1</sup>, and equals about 2% decade<sup>-1</sup>, which is relatively close to values given by ACIA (2005) of about 1% decade<sup>-1</sup> for the Arctic area. For the last 100 years (1907–2006) and 75 years (1932–2006), the trend lines for the Mittivakkat Glacier catchment (Figure 15b) indicate a significant increase in precipitation of 128 mm w.eq. ( $R^2 = 0.06$ ;  $p < 0.01$ ) and 148 mm w.eq. ( $R^2 = 0.09$ ;  $p < 0.01$ ), respectively. For the same periods, the air temperature increased (Figure 13a). Over the last 50 (1957–2006) and 25 years (1982–2006), TAP trends have been decreasing for the Mittivakkat Glacier catchment by 2 mm w.eq. ( $R^2 < 0.01$ ;  $p < 0.25$ ) and 44 mm w.eq. ( $R^2 < 0.01$ ;  $p < 0.25$ ), respectively, analogous to trends at Station Tasiilaq. In the same 50-year and 25-year periods, air temperature, relative humidity, and wind speed have increased in the Mittivakkat catchment.

## Summary

From the above analysis of thirteen years of data (1994–2006) from meteorological stations within the Mittivakkat Glacier catchment on the western part of the Ammassalik Island, Southeast Greenland, we conclude that marked changes can be noted, including increasing mean annual air temperatures both in the glacier area and in the coastal area in the order of 0.10°C y<sup>-1</sup> and 0.05°C y<sup>-1</sup>, respectively. Changes in air temperature impact the thawing period and the length of the snow-free period in the catchment. Due to the close proximity of the catchment to the coast, the area is strongly dominated by air temperature inversion and sea breezes during summer. When data from the Mittivakkat Glacier catchment are compared to other data series in East Greenland e.g., from the Zackenberg catchment (74°N), NE Greenland, it becomes clear that meteorological and snow cover observations in the Mittivakkat catchment probably reflect general changes at the east coast of Greenland. Based on correlations be-

tween data from the Mittivakkat Glacier catchment for the period 1994–2006, and meteorological records from the DMI station in Tasiilaq covering 1898–2006, it has been possible to estimate data for the Mittivakkat Glacier catchment back to 1898. Over this period, meteorological parameters are in accordance with general trends and changes in Arctic climates; this applies especially to the last 25 years, where increasing air temperature, wind speed, relative humidity and summer precipitation are observed, whereas winter precipitation and TAP have decreased slightly.

### Acknowledgements

The authors would like to thank the anonymous reviewer for insightful reviews of this paper. This work was supported by grants from the Department of Geography and Geology, University of Copenhagen, the Danish National Science Research Council (SNF), the University of Alaska Presidential IPY Postdoctoral Foundation, and the University of Alaska Fairbanks (UAF) Office of the Vice Chancellor for Research and carried out during the first author's IPY Post Doc. Program at the UAF. Thanks to John Cappelen, Danish Meteorological Institute (DMI), for providing meteorological station information and data from Tasiilaq. Special thanks to Dr. Glen E. Liston, Cooperative Institute for Research in the Atmosphere (CIRA), Colorado State University, for the use of SnowModel/MircoMet for the meteorological simulations.

### References

- ACIA (2005): Arctic Climate Impact Assessment. Cambridge University Press, 1042 pp.
- Allerup, P., Madsen, H., and Vejen, F. (2000): Correction of observed precipitation in Greenland. XXI Nordic Hydrological Conference 2000, Uppsala 26–30 June. Nordic Association for Hydrology.
- Anderson, E. A. (1976): A point energy balance model of a snow cover. NOAA Tech. Rep. NWS 19, 150 pp.
- Anisimov, O. A. and Fitzharris, B. (2001): Polar regions (Arctic and Antarctic). Pp. 801–841 in: McCarthy, O.F., C.J., Leary, N.A., Dokken, D.J., and Whits, K.S. (eds.): *Climate Change 2001: Impacts, Adaptation, and Vulnerability*. Contribution of Working group II to the Third Assessment Report of the Intergovernmental Panel on Climate Change, Cambridge University Press, Cambridge.
- Barnes, S. L., (1964): A technique for maximizing details in numerical weather map analysis. *J. Appl. Meteor.*, 3, 396–409.
- Barnes, S. L. (1973): Mesoscale objective analysis using weighted timeseries observations. NOAA Tech. Memo. ERL NSSL-62, National Severe Storms Laboratory, Norman, OK, 60 pp.
- Born, E. W. and Böcher, J. (2001): *The Ecology of Greenland*. Nuuk. Ministry of Environment and Natural Resources. 429 pp.
- Box, J. E. (2002): Survey of Greenland Instrumental Temperature Records: 1973–2001. *International Journal of Climatology* 22: 1829–1847.
- Box, J. E., D. H. Bromwich, B. A. Vennhuis, L.-S. Bai, J. C. Stroeve, J. C. Rogers, K. Steffen, T. Haren, and S.-H. Wang, (2006): Greenland ice sheet surface mass balance variability (1988–2004) from calibrated Polar MM5 output. *Journal of Climate* 19: 2783–2800.
- Brown, R. D., Brasnett, B. and Robinson, D. (2003): Gridded North American monthly snow depth and snow water equivalent for GCM evaluation. *Atmosphere-Ocean* 41(1): 1–14.
- Bruland, O., Liston, G. E., Vonk, J., Sand, K. and Killington, A. (2004): Modelling the snow distribution distribution at two High-Arctic sites at Svalbard, Norway, and at a Sub-Arctic site in Central Norway. *Nordic Hydrology* 35(3): 191–208.
- Cappelen, J. (2004): Yearly Mean Temperature for Selected Meteorological Stations in Denmark, the Faroe Islands and Greenland; 1873–2003. Technical Report 04-07. Danish Meteorological Institute, Weather and Climate Information Division. Copenhagen, Pp. 9.
- Crowley, T. J. (2000): Causes of Climate Change over the Past 1,000 Years. *Science*, 289(5777): 270–277.
- Dodson, R., and D. Marks. (1997): Daily air temperature interpolation at high spatial resolution over a large mountainous region. *Climate Res.* 8: 1–20.
- Førland, E. J. and Hanssen-Bauer, I. (2003): Climate variations and implications for precipitations types in the Norwegian Arctic. Met. Report, Norwegian Meteorological Institute, Report No. 24/02, 21 pp.
- Greene, E. M., Liston, G. E. and Pielke, R. A. (1999): Simulation of above treeline snowdrift formation using a numerical snowtransport model. *Cold Reg. Sci. Technol.* 30: 135–144.
- Hansen, B.U., Elberling, B., Humlum, O. and Nielsen, N. (2005): Meteorological trends (1991–2004) at Arctic Station, Central West Greenland (69°15'N) in a 130



- years perspective. *Geografisk Tidsskrift-Danish Journal of Geography* 106(1): 45–56.
- Hansen, B. U., Sigsgaard, C., Rasmussen, L., Cappelen, J., Hinkler, J., Mernild, S. H., Petersen, D., Tamstorf, M., Rasch, M. and Hasholt, B. (2008): Present Day Climate at Zackenberg. *Advances in Ecological Research* 40: 115–153.
- Hasholt, B., Hansen, B. U., Humlum, O. and Mernild, S. H. (2004): Meteorological stations at the Sermilik Station, Southeast Greenland: physical environment and meteorological observations 2002. *Geografisk Tidsskrift-Danish Journal of Geography* 104(2): 47–58.
- Hasholt, B., Liston, G. E. and Knudsen, N. T. (2003): Snow distribution modelling in the Ammassalik region, southeast Greenland. *Nordic Hydrology* 34: 1–16.
- Hasholt, B. and Mernild, S. H. (2004): Estimation of water balance in and around the Mittivakkat Glacier basin, Ammassalik Island, southeast Greenland. 290. Pp 129–142 in: Kane, D. L. and Yang, D. (eds.): Northern Research Basins Water Balance, IAHS Publication.
- Hiemstra, C. A., Liston, G. E. and Reiners, W. A. (2002): Snow Redistribution by Wind and Interactions with Vegetation at Upper Treeline in the Medicine Bow Mountains, Wyoming. *Arctic, Antarctic, and Alpine Research* 34: 262–273.
- Hinzman, L. D., Bettes, N. D., Bolton, W. B., Chapin, F. S., Dyrgerov, M. B., Fastie, C. L., Griffith, B., Hollister, R. D., Hope, A., Huntington, H. P., Jensen, A. M., Jia, G. J., Joergensen, T., Kane, D. L., Klein, D. R., Kofinas, G., Lynch, A. H., Lloyd, A. H., McGuire, A. D., Nelson, F. E., Oechel, W. C., Osterkamp, T. E., Racine, C. H., Romanovsky, V. E., Stone, R. S., Stow, D. A., Sturm, M., Tweedie, C. E., Vourlitis, G. L., Waker, M. D., Walker, D. A., Webber, P. J., Welker, J. M., Winker, K. S., and Yoshikawa, K. (2005): Evidence and implications of recent climate change in Northern Alaska and other Arctic regions. *Climatic Change* 72: 251 – 298.
- Humlum, O. (2002): Modelling late 20<sup>th</sup>-century precipitation in Nordenskiöld Land, Svalbard, by geomorphic means. *Norwegian Journal of Geography* 56: 96–103.
- IPCC (2007) *Climate Change 2007: The Physical Science Basis* (Ed. by S. Solomon, D. Qin, M. Manning, Z. Chen, M. Marquis, K.B. Averyt, M. Tignor and H.L. Miller), Cambridge University Press, Cambridge, United Kingdom and New York, NY, USA, 996 pp.
- Iziomon, M. G., H. Mayer, and A. Matzarakis, (2003): Downward atmospheric longwave irradiance under clear and cloudy skies: Measurement and parameterization. *J. Atmos. Sol.-Terr. Phys.* 65:1107–1116.
- Knudsen, N. T and Hasholt, B. (1999): Radio-echo sounding at the Mittivakkat Gletscher, Southeast Greenland. *Arctic, Antarctic, and Alpine Research* 31(3): 321–328.
- Knudsen, N. T., and Hasholt, B. (2004): Mass balance observations at Mittivakkat Glacier, southeast Greenland 1995–2002. *Nordic Hydrol.* 35: 381–390.
- Koch, S. E., M. DesJardins, and Kocin, P. J. (1983): An interactive Barnes objective map analysis scheme for use with satellite and conventional data. *J. Climate Appl. Meteor.* 22: 1487–1503.
- Kozo, T. L. (1982a): An Observational Study of Sea Breezes Along the Alaskan Beaufort Sea Coast: Part I. *Journal of Applied Meteorology* 21(7): 891–905.
- Kozo, T. L. (1982b): A Mathematical Model of Sea Breezes Along the Alaskan Beaufort Sea Coast: Part II. *Journal of Applied Meteorology* 21(7): 906–924.
- Kunkel, K. E. (1989): Simple procedures for extrapolation of humidity variables in the mountainous western United States. *J. Climate* 2: 656–669.
- Lemke, P., J. Ren, R.B. Alley, I. Allison, J. Carrasco, G. Flato, Y. Fujii, G. Kaser, P. Mote, R.H. Thomas and T. Zhang. (2007): Observations: Changes in Snow, Ice and Frozen Ground. In: *Climate Change 2007: The Physical Science Basis. Contribution of Working Group I to the Fourth Assessment Report of the Intergovernmental Panel on Climate Change* [Solomon, S., D. Qin, M. Manning, Z. Chen, M. Marquis, K.B. Averyt, M. Tignor and H.L. Miller (eds.)]. Cambridge University Press, Cambridge, United Kingdom and New York, NY, USA.
- Liston, G. E. and Elder, K. (2006a): A meteorological distribution system for high resolution terrestrial modeling (MicroMet). *Journal of Hydrometeorology* 7: 217–234.
- Liston, G. E. and Elder, K. (2006b): A distributed snow-evolution modeling system (SnowModel). *Journal of Hydrometeorology* 7: 1259–1276.
- Liston, G. E. and M. Sturm, (1998): A snow-transport model for complex terrain. *J. Glaciol.*, 44, 498–516.
- Liston, G. E. and Sturm, M. (2002): Winter Precipitation Patterns in Arctic Alaska Determined from a Blowing-Snow Model and Snow-Depth Observations. *Journal of Hydrometeorology* 3: 646–659.
- Liston, G. E., and M. Sturm, (2004). The role of winter

- sublimation in the Arctic moisture budget. *Nordic Hydrology* 35(4): 325–334.
- Liston GE, Winther J-G, Bruland O, Elvehøy H, Sand K. (1999): Below surface ice melt on the coastal Antarctic ice sheet. *Journal of Glaciology* 45(150): 273–285.
- Liston, G. E., Winther, J.-G., Bruland, O., Elvehøy, H., Sand, K. and Karlöf, L. (2000): Snow and blue-ice distribution patterns on the coastal Antarctic ice sheet. *Antarctic Science* 12(1): 69–79.
- Mernild, S. H. (2006): Freshwater Discharge From the Coastal Area Outside the Greenland Ice Sheet, East Greenland. Institute of Geography, University of Copenhagen PhD thesis, 387 pp.
- Mernild, S. H. and Hasholt, B. (2006): Climatic control on river discharge simulations from the Mittivakkat Glacier catchment, Ammassalik Island, SE Greenland. *Nordic Hydrology*, 37(4-5): 327–346.
- Mernild, S. H., Hasholt, B. and Hansen, B. U. (2005): Meteorological observations 2003 at the Sermilik Station, Ammassalik Island, Greenland. *Geografisk Tidsskrift-Danish Journal of Geography* 105(1): 49–56.
- Mernild, S. H., Hasholt, B. and Hansen, B. U. (2006b): Meteorological observations 2004 at the Sermilik Station, Ammassalik Island, Greenland. *Geografisk Tidsskrift-Danish Journal of Geography* 106(1): 131–140.
- Mernild, S. H., Hasholt, B. and Liston, G. E. (2006c): Water flow through Mittivakkat Glacier, Ammassalik Island, SE Greenland. *Geografisk Tidsskrift-Danish Journal of Geography* 106(1): 25–43.
- Mernild, S. H., Hasholt, B. and Liston, G. E. (2007b): Climatic control on river discharge simulations, Zackenberg River Drainage Basin, NE Greenland. *Hydrological Processes* DOI: 10.1002/hyp.6777.
- Mernild, S. H., Liston, G. E. and Hasholt, B. (2007c): Snow-distribution and Melt Modeling for Glaciers in Zackenberg River Drainage Basin, NE Greenland. *Hydrological Processes*, 21: 3249–3263. DOI: 10.1002/hyp.6500
- Mernild, S. H., Liston, G. E., Hasholt, B. and Knudsen, N. T. (2006a): Snow Distribution and Melt Modeling for Mittivakkat Glacier, Ammassalik Island, Southeast Greenland. *Journal of Hydrometeorology* 7: 808–824.
- Mernild, S. H., Liston, G. E., and Hasholt, B. (2008a): East Greenland freshwater runoff to the Greenland-Iceland-Norwegian Seas 1999–2004 and 2071–2100. *Hydrological Processes*, DOI: 10.1002/hyp.7061.
- Mernild, S. H., Liston, G. E., Knudsen, N. T., Hasholt, B., and Kane, D. (2008b): Spatial snow distribution, runoff, and mass balance modeling for entire Mittivakkat Glacier (1998–2006), Ammassalik Island, SE Greenland. *Geografisk Tidsskrift-Danish Journal of Geography* 108(1): 121–136.
- Mernild, S. H., Sigsgaard, C., Rasch, M., Hasholt, B., Hansen, B. U., Stjernholm, M. and Petersen, D. (2007a): Climate, river discharge and suspended sediment transport in the Zackenberg River Drainage Basin and Young Sound/Tyrolerfjord, Northeast Greenland. In Rysgaard, S. and Glud, R. N. (eds.), *Carbon cycling in Arctic Marine ecosystems: Case study Young Sound Meddr. om Grønland, BioScience* 58: 24–43.
- Pielke, R. A., Sr. (2002): *Mesoscale Meteorological Modeling*. Academic Press, 676 pp.
- Plüss, C. and Ohmura, A. (1997): Long-wave Radiation on Snow-Covered Mountainous Surfaces, *Journal of Applied Meteorology* 36: 818–824.
- Przybylak, R. (2003): *The Climate of the Arctic*. Kluwer Academic Publishers, Atmospheric and Oceanographic Sciences Library 26, 270 pp.
- Ryan, B. C. (1977): A mathematical model for diagnosis and prediction of surface winds in mountainous terrain. *J. Appl. Meteor.* 16: 571–584.
- Serreze MC and Barry RG. (2005).: *The Arctic Climate System*. Cambridge Atmospheric and Space Science Series: Cambridge; pp. 424.
- Serreze, M. C., Kahl, J. D., and Schnell, R. C. (1992): Low-level Temperature Inversions of the Eurasian Arctic and Comparisons with Soviet Drifting Station Data. *Journal of Climate* 5: 615–629.
- Serreze, M. C., Walsh, J. E., Chapin, F. S., III Osterkamp, T., Dyrgerov, M., Romanovsky, V., Oechel, W. C., Morrison, J., Zhang, T., and Barry, R. G. (2000): Observational evidence of recent change in the northern high latitude environment. *Clim. Change* 46: 159–207.
- Sturm, M., Holmgren, J. and Liston, G.E. (1995): Seasonal Snow Cover Classification System for Local to Global Applications. *J. Climate* 8: 1261–1283.
- Sturm, M., Schimel, J., Michaelson, G., Welker, J. M., Oberbauer, S. F., Liston, G. E., Fahnestock, J., and Romanovsky, V. E. (2005): Winter Biological Processes Could Help Convert Arctic Tundra to Shrubland. *BioScience* 55(1): 17–26.
- Thornton, P. E., S. W. Running, and M. A. White, (1997): Generating surfaces of daily meteorological variables over large regions of complex terrain. *J. Hydrol.*, 190, 214–251.
- Walcek, C. J. (1994): Cloud cover and its relationship to relative humidity during a spring midlatitude cyclone.

- Mon. Wea. Rev. 122: 1021–1035.
- Weick, E.J. and Rouse, W.R. (1991): Advection in the Coastal Hudson Bay Lowlands, Canada. II. Impact of Atmospheric Divergence on the Surface Energy Balance Arctic Alpine Res. 23: 338–348.
- Wojcik, G. and Kejna, M. (1991): TITEL Acta Univ. Wratisl 1213: 351–363.
- Yang, D., Ishida, S., Goodison, B.E. and Gunther, T. (1999): Bias correction of precipitation data for Greenland. Journal of Geophysical Research-Atmospheres 104(D6): 6171–6181.
- Young, K. L., Bolton, W. R., Killingtveit, Å., and Yang, D. (2006): Assessment of precipitation and snowcover in northern research basins. Nordic Hydrology, 37(4–5): 377–391.

[4]

Mernild, S. H., Knudsen, N. T., Lipscomb, W. H., Yde, J. C.,  
Malmros, J. K., Jakobsen, B. H., and Hasholt, B. 2011.  
Increasing mass loss from Greenland's Mittivakkat  
Gletscher.  
The Cryosphere, 5, 341–348, doi:10.5194/tc-5-341-2011.

Reprinted with permission from Copernicus Publications

## Increasing mass loss from Greenland's Mittivakkat Gletscher

S. H. Mernild<sup>1</sup>, N. T. Knudsen<sup>2</sup>, W. H. Lipscomb<sup>3</sup>, J. C. Yde<sup>4,5</sup>, J. K. Malmros<sup>6</sup>, B. Hasholt<sup>6</sup>, and B. H. Jakobsen<sup>6</sup>

<sup>1</sup>Climate, Ocean, and Sea Ice Modeling Group, Computational Physics and Methods, Los Alamos National Laboratory, Los Alamos, New Mexico 87545, USA

<sup>2</sup>Department of Geology, Aarhus University, 8000 Aarhus, Denmark

<sup>3</sup>Climate, Ocean, and Sea Ice Modeling Group, Fluid Dynamics and Solid Mechanics, Los Alamos National Laboratory, Los Alamos, New Mexico 87545, USA

<sup>4</sup>Center for Geomicrobiology, Aarhus University, 8000 Aarhus, Denmark

<sup>5</sup>Sogn og Fjordane University College, 6851 Sogndal, Norway

<sup>6</sup>Department of Geography and Geology, University of Copenhagen, 1350 Copenhagen, Denmark

Received: 22 January 2011 – Published in The Cryosphere Discuss.: 4 February 2011

Revised: 7 April 2011 – Accepted: 8 April 2011 – Published: 14 April 2011

**Abstract.** Warming in the Arctic during the past several decades has caused glaciers to thin and retreat, and recent mass loss from the Greenland Ice Sheet is well documented. Local glaciers peripheral to the ice sheet are also retreating, but few mass-balance observations are available to quantify that retreat and determine the extent to which these glaciers are out of equilibrium with present-day climate. Here, we document record mass loss in 2009/10 for the Mittivakkat Gletscher (henceforth MG), the only local glacier in Greenland for which there exist long-term observations of both the surface mass balance and glacier front fluctuations. We attribute this mass loss primarily to record high mean summer (June–August) temperatures in combination with lower-than-average winter precipitation. Also, we use the 15-yr mass-balance record to estimate present-day and equilibrium accumulation-area ratios for the MG. We show that the glacier is significantly out of balance and will likely lose at least 70% of its current area and 80% of its volume even in the absence of further climate changes. Temperature records from coastal stations in Southeast Greenland suggest that recent MG mass losses are not merely a local phenomenon, but are indicative of glacier changes in the broader region. Mass-balance observations for the MG therefore provide unique documentation of the general retreat of Southeast Greenland's local glaciers under ongoing climate warming.

### 1 Introduction

Greenland has warmed significantly during the past two decades. Summer air temperatures in Greenland's coastal areas increased by an estimated 1.7 °C, on average, from 1991 to 2006 (Comiso, 2006). Mass loss from the Greenland Ice Sheet (GrIS) and from smaller glaciers and ice caps is making a significant and growing contribution to global sea-level rise (Dowdeswell, 2006; Meier et al., 2007; van den Broeke, 2009; Dyurgerov et al., 2009; Mernild et al., 2010). Recent mass-balance estimates for Greenland have focused on the main ice sheet (Hanna et al., 2008; Ettema et al., 2009). In 2010, Greenland experienced record-setting surface melt extent and glacier area loss due to a relatively warm, dry winter followed by an exceptionally warm summer. Mean recorded temperatures were 0.6 to 2.4 °C above the 1971–2000 baseline, with the largest anomalies in the west, where melt rates were the highest since systematic observations began in 1990 (Box et al., 2010; Tedesco et al., 2011). Greenland last experienced comparable conditions in 2007, when high summer temperatures led to increased melting (Mote, 2007; Tedesco, 2007; Steffen et al., 2008), surface mass loss, and freshwater runoff (Mernild and Hasholt, 2009). As the climate has warmed, Greenland's outlet glaciers have accelerated and thinned, and the surface mass balance has become more negative. During the past several years the GrIS is estimated to have lost mass at a rate of more than 200 Gt yr<sup>-1</sup> (Allison et al., 2009).

Comparable estimates are not available for glaciers and ice caps (GIC) peripheral to the main ice sheet. Although GIC have a relatively small total mass (an estimated 4.4 cm



Correspondence to: S. H. Mernild  
(mernild@lanl.gov)



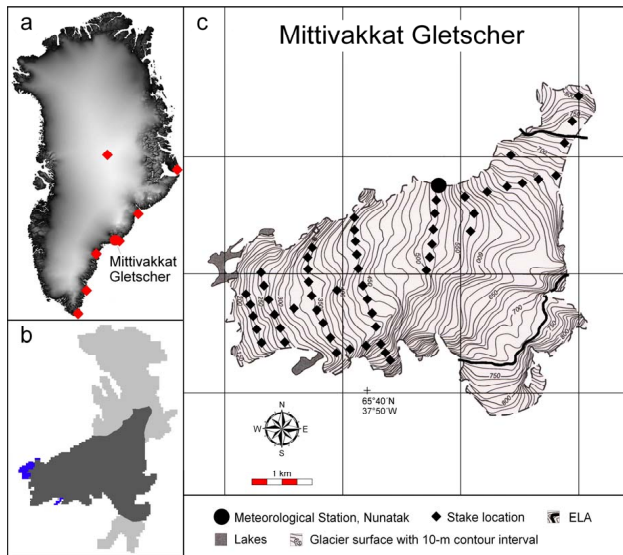


**Fig. 1.** (a) Location of the Mittivakkat Gletscher (red circle) and coastal meteorological stations (red diamonds) in Southeast Greenland; (b) glacier outline where net balance has been observed (dark gray), along with lobes to the north and south (light gray) that lie in distinct drainage basins; and (c) topographic map (10-m contour interval), with a black circle showing the location of the meteorological station at the nunatak on the glacier, black diamonds showing the stake locations for the glacier observation program (due to a high density of crevasses SE of the glacier, no stakes were located there), and black lines showing the average equilibrium line since 1995.

sea-level equivalent for Greenland and 60 cm globally – Radić and Hock, 2010), they are sensitive to surface-mass-balance changes and can equilibrate to climate changes on time scales short compared to ice-sheet response times. The rate of global mean sea-level rise resulting from GIC retreat has been estimated to be  $\sim 1 \text{ mm yr}^{-1}$  (Meier et al., 2007), comparable to that from the Greenland and Antarctic ice sheets combined (Velicogna, 2009). This study provides information about the only local glacier in Greenland (WGMS, 2009) – the Mittivakkat Gletscher in SE Greenland (Fig. 1) – for which there exist long-term observations of both the surface mass balance (since 1995) and glacier front fluctuations (since the maximum Little Ice Age (LIA) extension around 1900). We estimate accumulation-area ratios for the MG to quantify the extent to which the glacier is out of balance with present-day climate, and we suggest that recent MG mass losses are not merely a local phenomenon but are indicative of regional changes.

## 2 Methods and historical data

As a result of harsh climate conditions and logistical difficulties, few reliable long-term observations of mass loss and

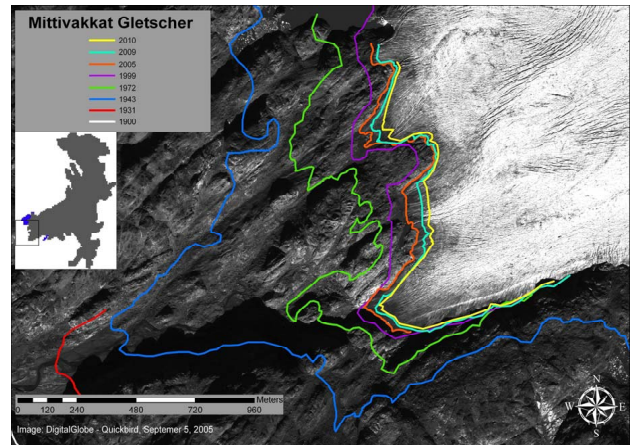


**Fig. 2.** The location of the Mittivakkat Gletscher margin delineated as thick lines for 1900, 1931, 1943, 1972, 1999, 2005, 2009, and 2010. The 1900 LIA trimline (white line) was estimated from field observations (Hasholt et al., 2008; Humlum and Christiansen, 2008) and is partly shown in the lower left corner of the satellite image. The 1931, 1943, and 1972 margins were estimated from aerial photos, the 1999 margin from Landsat 5, and the 2005 margin from Quickbird. The more recent margins 2009 and 2010 were obtained from topographic surveys (Kern Theodolite observations) and GPS measurements. The Mittivakkat Gletscher outline is shown at left with a black square indicating the photographic area (background photo: DigitalGlobe, Quickbird, 2005).

retreat are available for Greenland's peripheral glaciers. The Mittivakkat Gletscher in Southeast Greenland ( $17.6 \text{ km}^2$ ;  $65^\circ 41 \text{ N}$ ,  $37^\circ 48 \text{ W}$ ) is an exception. This glacier and the surrounding landscape have been photographed at regular intervals since 1931, supplemented more recently by topographic surveys. In 1995 the observing program was expanded with the initiation of continuous and annual surface-mass-balance measurements and an automated glacier climate program. These measurements are supplemented by meteorological data from the coastal town of Tasiilaq, 15 km to the southeast.

As illustrated by Figs. 2 and 3 and Table 1, the glacier terminus has retreated by about 1600 m since the maximum LIA extension around 1900 and by 1300 m since 1931. Table 1 shows terminus changes for the intervals noted in Fig. 2, indicating average retreat rates ranging from  $\sim 6 \text{ m yr}^{-1}$  (1999–2005) to  $\sim 24 \text{ m yr}^{-1}$  (1943–1972). The retreat of the MG terminus is influenced by (1) the transition from valley to peak topography as the terminus moves inland from the fjord and the shadow effect from the surrounding mountains (Mernild and Liston, 2010), (2) climate variability, and (3) dynamic processes within the glacier. Therefore, a warming signal from the changing climate may not be seen immediately as a glacier margin retreat. For example, the period from 1931 to 1943 was exceptionally warm, as indicated by mean-annual-air-temperature (MAAT) anomalies in Tasiilaq, but the maximum average retreat rate of  $\sim 24 \text{ m yr}^{-1}$  was observed later, from 1943 to 1972.



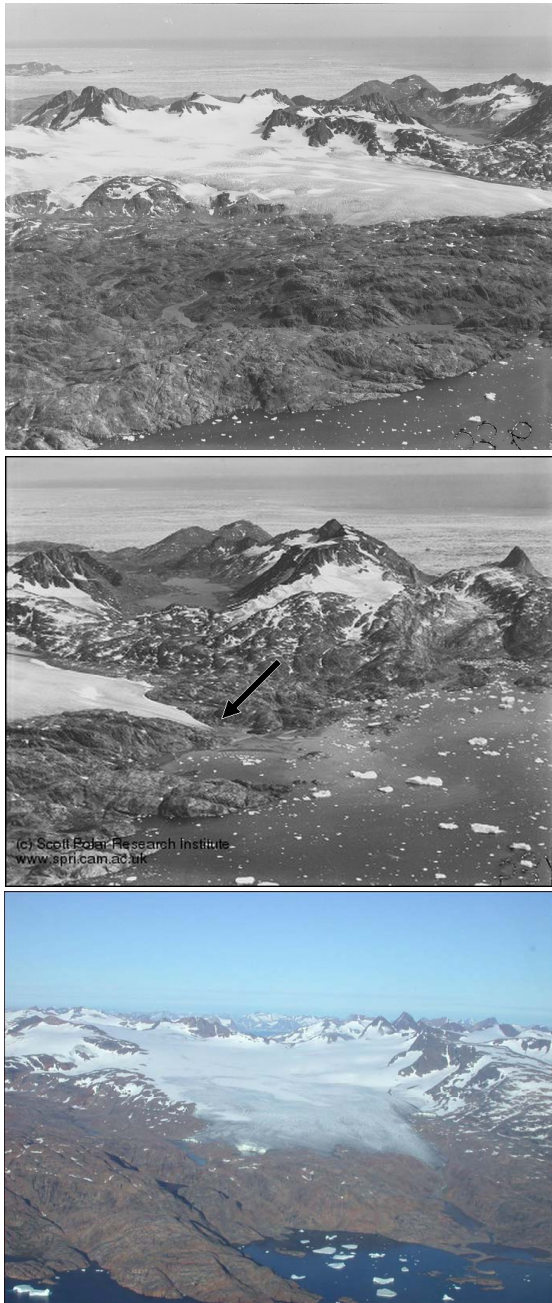


**Fig. 3.** (above, in black and white) Photographs of the Mittivakkat Gletscher in 1931, when the glacier margin, shown by the arrow, was within 200 m of the coastline. The photos are taken toward SSE, with Sermilik Fjord in the foreground and the Irminger Sea in the background (licensed with permission of the Scott Polar Research Institute, University of Cambridge, taken on the British Arctic Air Route Expedition, 1930–1931). (below, in color) Photograph of the MG in 2006, when the glacier margin was approximately 1500 m from the coast. The photo is taken toward ESE (Department of Geography and Geology, University of Copenhagen).

The annual surface mass balance of the MG has been recorded since 1995/96 (Knudsen and Hasholt, 2004, 2008). In 10 out of 15 yr, both winter mass balance (accumulation measured at the end of May) and summer mass balance (ablation measured at the end of August) were observed. The stake method – also known as the “direct glaciological method” (Ostrem and Brugman, 1991) – was used to determine annual variations and trends in ice/snow extent and ice volume and to calculate the equilibrium line altitude (ELA) (the ELA is the spatially averaged elevation of the equilibrium line, defined as the set of points on the glacier surface where the net mass balance is zero). Snow accumulation and snow/ice ablation were measured using cross-glacier stake lines at separations of approximately 500 m. The stakes in each line were 200–250 m apart, and measurements were obtained at a total of 45–50 stakes (Fig. 1c). End-of-winter snow density was measured vertically at 25-cm depth intervals in pits at 250, 500, and 750 m above sea level (a.s.l.). The observed mass balance is considered to be accurate to within  $\sim 15\%$  for the entire glacier, although larger errors may occur locally, particularly in crevassed areas (Knudsen and Hasholt, 2004).

Meteorological conditions at the MG have been recorded since 1995 at an automated weather station operated by the Department of Geography and Geology, University of Copenhagen, located on a small nunatak at 515 m a.s.l., just below the average ELA. Long-term (1900–2010) climate data representative of the region are available from a synoptic meteorological station at 44 m a.s.l., operated by the Danish Meteorological Institute and located 15 km to the southeast of the MG in the outskirts of Tasiilaq.

### 3 Results and discussion

Figure 4 shows the net mass balance of the MG as a function of elevation from 1995/96 to 2009/10, and Fig. 5a shows the average annual net balance for the entire glacier. The glacier mass balance has been negative in 13 out of 15 yr. Table 2 gives the ELA in each year, ranging from 390 m a.s.l. to more than 930 m a.s.l. with an average of about 730 m a.s.l. In several years (1998, 2001, 2005, 2007, and 2010), net ablation was recorded at all elevations between the summit (930 m a.s.l.) and the terminus (180 m a.s.l.).

Data collected during 2009–2010 show that the MG experienced an average surface mass loss of 2.16 m water equivalent (w.e.), or about 2% of the total glacier volume, from September 2009 through August 2010. This was the greatest annual mass loss since the expansion of the observing program in 1995, 0.34 m more than the previous observed record loss in 2005 and significantly above the 15-yr average loss of  $0.87 \pm 0.17 \text{ m yr}^{-1}$  (Fig. 5a). The 2009/10 loss exceeded (insignificantly) the maximum annual loss of 1.87 m w.e. (in 1940, during the early-twentieth-century warming) obtained in a model simulation of the MG surface mass balance from

**Table 1.** Mittivakkat Gletscher terminus changes and Tasiilaq MAAT anomaly for the intervals noted in Fig. 2.

Interval	1900*– 1931	1931– 1943	1943– 1972	1972– 1999	1999– 2005	2005– 2009	2009– 2010	Average, 1900–2010
Mittivakkat Gletscher average terminus changes (m yr <sup>-1</sup> )	-8	-14	-24	-15	-6	-10	-19	-15
Tasiilaq MAAT anomaly (five year running average) (°C)	Maximum	1.07	1.35	0.81	0.26	1.27	0.85	-
	Average	-0.24	0.82	-0.01	-0.55	1.00	0.79	-
	Minimum	-1.05	0.49	1.39	-1.22	0.40	0.73	-

\* The LIA trimline and moraine are estimated from field observations (Hasholt et al., 2008; Humlum and Christiansen, 2008). The trimline is the maximum extension since around 1900.

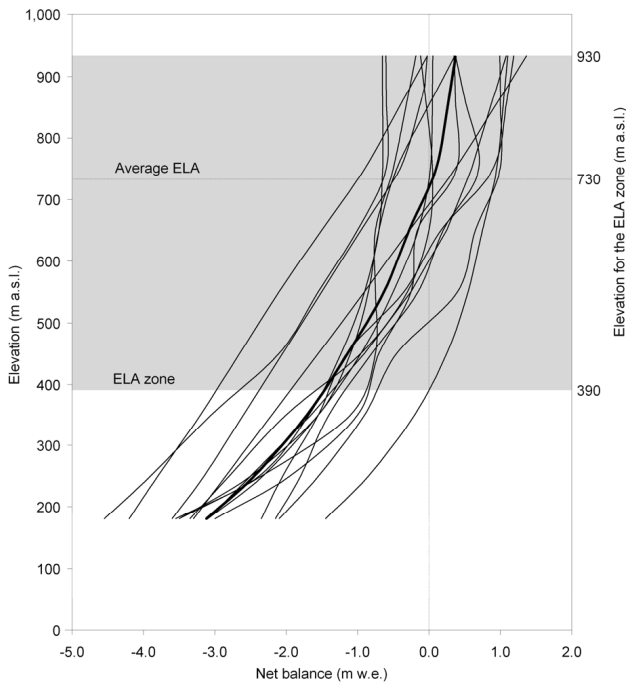


**Fig. 4.** Variation of the net annual mass balance with altitude for the Mittivakkat Gletscher, 1995–2010. The bold line is the average, and the different years are not labeled individually. The net balance data reported here are updated from Knudsen and Hasholt (2008).

1898 to 1993 (Mernild et al., 2008). At the glacier terminus (below 200 m a.s.l.) the observed area-averaged 2010 melt rate was 4.2 m, similar to the values of 4.6 m and 3.6 m observed in 2005 and 2007, respectively, and almost twice the 15-yr average of approximately 2.5 m.

Local meteorological data indicate that higher-than-average temperatures, along with lower-than-average winter precipitation, were primarily responsible for this record mass loss. During the 2010 summer ablation season (June through August) the mean MG air temperature recorded at 515 m a.s.l. was 7.5 °C, and the mean temperature at Tasi-

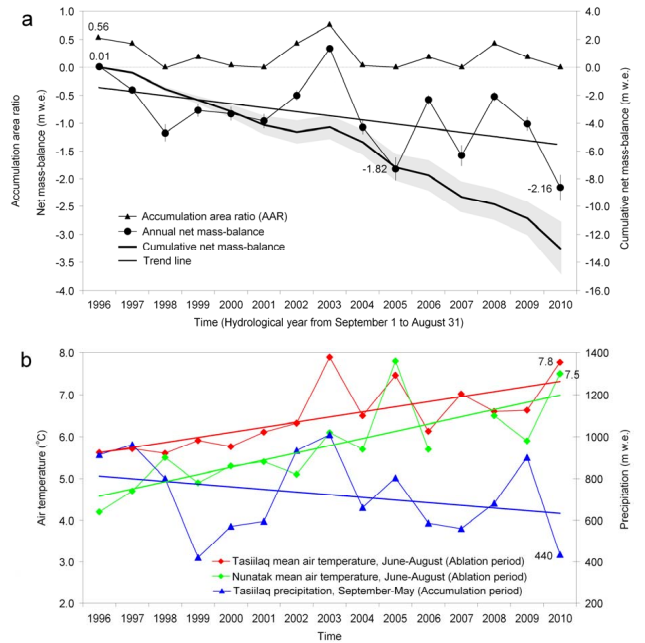


**Fig. 5.** (a) Observed annual mass balance (with 15% error bars), cumulative net mass balance (with a gray zone indicating the 15% error), and accumulation-area ratio for the Mittivakkat Gletscher, 1995–2010. (b) Time series (1995–2010) of observed winter precipitation (September–May) and mean summer air temperature (June–August) from Tasiilaq (44 m a.s.l.) and Station Nunatak (515 m a.s.l.). The straight lines are linear fits to the data; the two temperature trends are statistically significant.

ilaq was 7.8 °C (Fig. 5b). These values are 1.8 °C and 1.4 °C, respectively, above the 1995–2010 average. During the 2009/10 winter accumulation season (September through May), mean temperatures at the MG and Tasiilaq were -3.4 °C and -2.0 °C, respectively, or 1.3 °C and 0.5 °C above average. Uncorrected winter precipitation at Tasiilaq was ~440 mm w.e., or ~260 mm w.e. (~40%) below the 15-yr average (Fig. 5b). Glacier ice was exposed in late June 2010 (Anders Anker Bjørk, personal communication, March

**Table 2.** Annual ELA for Mittivakkat Gletscher, 1995–2010.

Year	ELA (m a.s.l.)
1995/96	500
1996/97	590
1997/98	> 930
1998/99	740
1999/00	650
2000/01	> 930
2001/02	620
2002/03	390
2003/04	850
2004/05	> 930
2005/06	680
2006/07	> 930
2007/08	600
2008/09	690
2009/10	> 930
Average	~ 730

2011), two to three weeks earlier than average. Mernild et al. (2008) found significant relationships ( $p < 0.01$ , where  $p$  is the level of significance) between uncorrected winter precipitation at Tasiilaq and MG winter balance ( $n = 8$ ,  $r^2 = 0.68$ ) and between summer temperature at Tasiilaq and MG summer balance ( $n = 8$ ,  $r^2 = 0.55$ ). High summer temperatures favor increased surface ablation (evaporation, sublimation, and melt). Low winter snowfall leads to earlier exposure of glacier ice and of the previous year's summer snow surface; these surfaces have a lower albedo than fresh snow (Oke 1987), promoting greater solar absorption and increased melting. Although high winter temperatures could contribute to an early start of the melt season by decreasing the “cold content” of the snow (Bøggild et al., 2005), the correlation between winter temperatures and annual mass balance has not been found to be significant (Mernild et al., 2008). Similar weather conditions were observed in 2009/10 throughout Greenland, more pronounced in the west and less so in the northeast (Box et al., 2010; Tedesco et al., 2011).

The general trend for the MG since 1995 has been toward higher summer temperatures, less winter precipitation, and a more negative glacier mass balance (Fig. 5). Summer temperatures have increased significantly ( $p < 0.01$ ) at both meteorological stations, by  $1.7^\circ\text{C}$  at the MG and by  $1.8^\circ\text{C}$  at Tasiilaq. Winter precipitation has declined by  $\sim 230$  mm w.e., although this change is within the variability of the 15-yr record (Fig. 5b). The two years with a slightly positive mass balance, 1995/96 (0.01 m w.e.) and 2002/2003 (0.34 m w.e.), were associated with unusually high winter precipitation (around 1000 mm w.e.) and mean summer temperatures of  $4.2$  and  $6.1^\circ\text{C}$  (Station Nunatak) and  $5.6$  and  $7.9^\circ\text{C}$  (Station Tasiilaq), respectively. Figure 5a shows the cumulative net mass balance for the MG since 1995/96. The total mass

**Table 3.** Area and accumulation-area ratios. The left column lists Mittivakkat Gletscher elevation bands at 100-m intervals; the middle column gives the glacier area located within each band; and the right column gives the estimated AAR when the ELA falls within the given band.

MG elevation bands (m a.s.l.)	Area (km <sup>2</sup> )	AAR
> 930	–	0.00
800–930	0.77	0.04
700–799	2.65	0.19
600–699	3.99	0.42
500–599	2.70	0.56
400–499	3.16	0.75
300–399	2.35	0.89
200–299	1.44	0.97
< 200	0.54	1.00
Total	17.6	–

loss is estimated at  $13.0 \pm 1.9$  m w.e., or 11% of the total ice volume determined in 1994 (Knudsen and Hasholt, 1999). Since 1995 the glacier terminus has retreated by about 110 m, as illustrated by the front observations (Fig. 2 and Table 1).

The recent trends for the MG region are consistent with long-term climate trends since 1900 for Tasiilaq, where the temperature anomaly is almost in anti-phase with the precipitation anomaly (Mernild et al., 2011). During periods with a decreasing trend in precipitation (e.g., from 1900 until the 1930s and 1970 to the present), the temperature trend was increasing, and visa versa. Although there have been periods of higher-than-average precipitation and lower-than-average temperature (Mernild et al., 2011), the MG terminus has retreated continuously since the maximum LIA extension.

The long-term record of surface temperature in Tasiilaq is reproduced in Fig. 6, together with meteorological observations from Southeast Greenland's coastal stations (ranging in elevation from 13 to 88 m a.s.l.), and from the Summit station at the top of the Greenland Ice Sheet (3208 m a.s.l.). MAAT anomalies at Station Tasiilaq are significantly correlated with MAAT anomalies at other coastal stations ( $r^2$  values of 0.61–0.91,  $p < 0.01$ ), and at Summit ( $r^2 = 0.42$ ,  $p < 0.10$ ). These data suggest that recent MG mass losses, which have been driven largely by higher surface temperatures, are representative of the broader region, which includes many hundreds of local glaciers. Observations of glaciers in the Mittivakkat region, including Sermilik Fjord and Ammassalik Island, show terminus retreats comparable to that of MG. These glaciers are almost similar to the MG in size and elevation range.

The accumulation-area ratio (AAR: the ratio of the accumulation area to the area of the entire glacier) has been estimated for the MG each year from 1995/96 to 2009/10 (Fig. 5a), a period long enough to filter out high-frequency interannual variability but significantly shorter than the time scale of adjustment to equilibrium. As shown in Table 3,

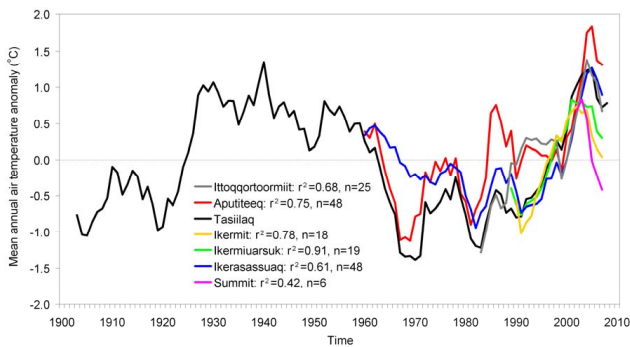


**Fig. 6.** Long-term time series of observed MAAT anomaly (five year running average) from Tasiilaq and other meteorological stations in Southeast Greenland. The  $r^2$  values indicate the correlation between the Tasiilaq anomaly and anomalies from other stations shown in Fig. 1a (Ittoqqortoormiit is farthest north, and Ikerasassuaq is farthest south).

the glacier is partitioned into 100-m elevation bands, and the AAR for a given year is determined based on the glacier area above and below the ELA. The average AAR is 0.15 and can be determined as follows. A linear regression between the AAR and the surface mass balance ( $r^2 = 0.89$ ,  $p < 0.01$ ) gives the relation  $AAR = m \cdot b + AAR_0$ , where  $b$  is the net mass balance ( $\text{m yr}^{-1}$ ),  $m = 0.49 \text{ m}^{-1} \text{ yr}$  is the slope, and  $AAR_0 = 0.61$  is the AAR when  $b = 0$ . Zero values of AAR are excluded from the regression, since AAR and mass balance are not linearly related when net ablation occurs everywhere on the glacier. Based on this regression, the average AAR is defined as the predicted AAR during a year when the mass balance is equal to its 15-yr mean value of  $-0.87 \text{ m yr}^{-1}$ . The resulting average AAR of 0.15 is slightly lower than the 15-yr arithmetic mean AAR of 0.22, which includes several years of strongly negative mass balance and zero AAR.

Glaciers and ice caps (GIC) in equilibrium with local climate typically have an AAR of 0.5–0.6, with a global average of  $0.579 \pm 0.009$  (Dyurgerov et al., 2009). Expected changes in glacier area and volume can be derived from  $\alpha_r = AAR/AAR_0$ , the ratio of the current AAR to its equilibrium value. (Specifically,  $p_s = \alpha_r - 1$  and  $p_v = \alpha_r^\gamma - 1$ , where  $p_s$  is the expected fractional area change,  $p_v$  is the fractional volume change, and  $\gamma = 1.36$  is an empirical constant – Bahr et al., 2009). As stated above, the MG has an  $AAR_0$  of approximately 0.61, close to the global average. The resulting  $\alpha_r = 0.25 \pm 0.08$  implies that the MG will lose about  $75 \pm 8\%$  of its present area and  $85 \pm 7\%$  of its volume (a volume loss of  $\sim 1.5 \pm 0.1 \text{ km}^3$ ) if current climate conditions persist.

#### 4 Summary and conclusion

Local glacier observations in Greenland are rare, and the MG is the only glacier in Greenland for which long-term observations of both the surface mass balance and glacier front fluctuations exist. Since 1995, the general trend for the MG has been toward higher temperatures, less snowfall, and a more negative glacier mass balance, with record mass loss in 2009/10. In 13 of the last 15 yr, the MG had a negative surface mass balance. The two years with a slightly positive balance were associated with unusually high winter precipitation. The MG is significantly out of balance; an analysis of accumulation-area ratios suggests that the glacier will likely lose at least 70% of its current area and 80% of its volume even in the absence of further climate changes.

Bahr et al. (2009) carried out a global analysis of glacier AARs to obtain lower bounds for global sea-level rise associated with expected GIC mass loss. They computed an average  $AAR = 0.44$  from 1997–2006 for a global sample of 86 glaciers and ice caps, and they estimated that GIC must lose at least 27% of their volume (the equivalent of an 18-cm rise in global average sea level) in order to reestablish equilibrium under present-day conditions. None of the 86 glaciers in their dataset is located in Greenland. Given that the average AAR for the MG is well below the global average and is likely to be typical of many of Greenland's peripheral glaciers, observations of the mass balance of Mittivakkat Gletscher are relevant to more informed estimates of future glacier retreat and sea-level rise.

During the last century, mean temperatures in Tasiilaq have been characterized by early-twentieth-century warming (ETCW) from 1900 until the 1930s and late-twentieth-century warming (LTCW) from 1970 to the present, interrupted by several decades of mid-century cooling (Fig. 6). Higher temperatures have generally been associated with lower precipitation, and vice versa (Mernild et al., 2011). Both the ETCW and the mid-century cooling appear to be connected to internal variability in the North Atlantic Ocean (Brönnimann, 2009), whereas it is generally accepted that the LTCW is a regional amplification of global warming driven mainly by increased fossil fuel burning (IPCC, 2007; Chylek et al., 2010). To the extent that the recent warming is anthropogenic in origin, temperatures in the Mittivakkat region are likely to continue to increase, leading to larger area and volume losses than are projected based on the current average AAR, and possibly to the complete melting of the MG and other local glaciers of Southeast Greenland.

*Acknowledgements.* We thank Mauri Pelto, Xavier Fettweis, and two anonymous reviewers for their insightful critiques. This work was supported by grants from the Climate Change Prediction Program and Scientific Discovery for Advanced Computing (SciDAC) program within the US Department of Energy's Office of Science, by a Los Alamos National Laboratory (LANL) Director's Fellowship, and by a fellowship from the LANL Institute for Geophysics and Planetary Physics. LANL is operated under the



auspices of the National Nuclear Security Administration of the US Department of Energy under Contract No. DE-AC52-06NA25396. Field work was supported by grants from the Danish Research Council under the frame program on climate and Arctic landscape processes carried out at the Institute of Geography and Geology, Copenhagen University, and by the Department of Earth Sciences, University of Aarhus. We thank David Bahr, Matthew Hecht, and Wilbert Weijer for helpful comments. Thanks are given to the Danish Meteorological Institute for providing WMO synoptic meteorological data from the East Greenland stations.

Edited by: E. Hanna

## References

- Allison, I., Bindoff, N. L., Bindschadler, R. A., Cox, P. M., de Noblet, N., England, M. H., Francis, J. E., Gruber, N., Haywood, A. M., Karoly, D. J., Kaser, G., Le Qu'ér'e, C., Lenton, T. M., Mann, M. E., McNeil, B. I., Pitman, A. J., Rahmstorf, S., Rignot, E., Schellnhuber, H. J., Schneider, S. H., Sherwood, S. C., Somerville, R. C. J., Steffen, K., Steig, E. J., Visbeck, M., and Weaver, A. J.: The Copenhagen Diagnosis: Updating the World on the Latest Climate Science. The University of New South Wales Climate Change Research Centre (CCRC), Sydney, Australia, 60 pp., 2009.
- Bahr, D. B., Dyurgerov, M., and Meier, M. F.: Sea-level rise from glaciers and ice caps: A lower bound, *Geophys. Res. Lett.*, 36, L03501, doi:10.1029/2008GL036309, 2009.
- Box, J. E., Cappelen, J., Decker, D., Fettweis, X., Mote, T., Tedesco, M., and Van de Wal, R. S. W.: Greenland [in Arctic Report Card 2010], <http://www.arctic.noaa.gov/reportcard>, 2010.
- Brönnimann, S.: Early twentieth-century warming, *Nat. Geosci.*, 2, 735–736, 2009.
- Bøggild, C. E., Forsberg, R., and Reeh, N.: Melt: Water in a transect across the Greenland ice sheet, *Ann. Glaciol.*, 40, 169–173, 2005.
- Chylek, P., Folland, C., Lesins, G., and Dubey, M.: Twenties century bipolar seesaw of the Arctic and Antarctic surface air temperature, *Geophys. Res. Lett.*, 37, L08703, doi:10.1029/2010GL042793, 2010.
- Comiso, J.: Arctic warming signals from satellite observations, *Weather*, 61(3), 70–76, 2006.
- Dowdeswell, J. A.: A changing Greenland Ice Sheet and global sea-level rise, *Science*, 311, 963–964, 2006.
- Dyurgerov, M., Meier, M. F., and Bahr, D. B.: A new index of glacier area change; a tool for glacier monitoring, *J. Glaciology*, 55(192), 710–716, 2009.
- Ettema, J., van den Broeke, M., van Meijgaard, E., van de Berg, M. J., Bamber, J. L., Box, J. E., and Bales, R. C.: Higher surface mass balance of the Greenland Ice Sheet revealed by high resolution climate modeling, *Geophys. Res. Lett.*, 36, L12501, doi:10.1029/2009GL038110, 2009.
- Hanna, E., Huybrechts, P., Steffen, K., Cappelen, J., Huff, R., Shuman, C., Irvine-Fynn, T., Wise, S., and Griffiths, M.: Increased runoff from melt from the Greenland Ice Sheet: a response to global warming, *J. Climate*, 21(2), 331–341, 2008.
- Hasholt, B., Krüger, J., and Skjerna, L.: Landscape and sediment processes in a proglacial valley, the Mittivakkat Glacier area, Southeast Greenland, *Geografisk Tidsskrift*, 108(1), 97–110, 2008.
- Humlum, O. and Christiansen, H. H.: Geomorphology of the Ammassalik Island, SE Greenland, *Geografisk Tidsskrift*, 108(1), 5–20, 2008.
- IPCC: Climate Change. The Physical Science Basis. Contributing of Working Group I to the Fourth Assessment Report of the Intergovernmental Panel on Climate Change, edited by: Solomon, S., Qin, D., Manning, M., Chen, Z., Marquis, M., Averyt, K. B., Tignor, M., and Miller, H. L., Cambridge University Press, Cambridge, United Kingdom and New York, NY, USA, 996, 2007.
- Knudsen, N. T. and Hasholt, B.: Radio-echo Sounding at the Mittivakkat Gletscher, Southeast Greenland, Arctic, Antarctic, and Alpine Research, 31(3), 321–328, 1999.
- Knudsen, N. T. and Hasholt, B.: Mass balance observations at Mittivakkat Glacier, southeast Greenland 1995–2002, *Nord. Hydrol.*, 35, 381–390, 2004.
- Knudsen, N. T. and Hasholt, B.: Mass balance observations at Mittivakkat Glacier, Ammassalik Island, Southeast Greenland 1995–2006, *Geografisk Tidsskrift*, 108(1), 111–120, 2008.
- Meier, M. F., Dyurgerov, M. B., Rick, U. K., O'Neel, S., Pfeffer, W. T., Anderson, R. S., Anderson, S. P., and Glazovsky, A. F.: Glaciers dominate eustatic sea-level rise in the 21st century, *Science*, 317, 1064–1067. doi:10.1126/science.1143906, 2007.
- Mernild, S. H. and Hasholt, B.: Observed runoff, jökulhlaups, and suspended sediment load from the Greenland Ice Sheet at Kangerlussuaq, West Greenland, for 2007 and 2008, *J. Glaciol.*, 55(193), 855–858, 2009.
- Mernild, S. H. and Liston, G. E.: The influence of air temperature inversion on snow melt and glacier surface mass-balance simulations, SW Ammassalik Island, SE Greenland, *J. Appl. Meteorol. Clim.*, 49(1), 47–67, 2010.
- Mernild, S. H., Kane, D. L., Hansen, B. U., Jakobsen, B. H., Hasholt, B., and Knudsen, N. T.: Climate, glacier mass balance, and runoff (1993–2005) for the Mittivakkat Glacier catchment, Ammassalik Island, SE Greenland, and in a long term perspective (1898–1993), *Hydrol. Res.*, 39(4), 239–256, 2008.
- Mernild, S. H., Liston, G. E., Hiemstra, C. A., and Christensen, J. H.: Greenland Ice Sheet surface mass-balance modeling in a 131-year perspective 1950–2080, *J. Hydrometeorol.*, 11(1), 3–25, 2010.
- Mernild, S. H., Seidenkrantz, M.-S., Chylek, P., Liston, G. E., and Hasholt, B.: Climate-driven fluctuations in freshwater to Sermilik Fjord, East Greenland, during the last 4000 years, in press, *The Holocene*, 2011.
- Mote, T. L.: Greenland surface melt trends 1973–2007. Evidence of a large increase in 2007, *Geophys. Res. Lett.*, 34, L22507, doi:10.1029/2007GL031976, 2007.
- Oke, T. R.: *Boundary Layer Climates*. Second Edition, Routledge, 423 pp., 1987.
- Ostrem, G. and Brugman, M.: *Glacier mass balance measurements. A manual for field and office work*, NRHI Science Report, No 4., 224 pp., 1991.
- Radić, V. and Hock, R.: Regional and global volumes of glaciers derived from statistical upscaling of glacier inventory data, *J. Geophys. Res.*, 115, F01010, doi:10.1029/2009JF001373, 2010.
- Steffen, K., Clark, P. U., Cogley, J. G., Holland, D., Marshall, S., Rignot, E., and Thomas, R.: Rapid changes in glacier and ice sheet and their impacts on sea level, in: *Abrupt Climate Change*,

- a Report by the US Climate Change Science Program and the Subcommittee on Global Change Research, US Geological Survey, Reston, VA, 60–142, 2008.
- Tedesco, M.: A new record in 2007 for melting in Greenland, *Eos Trans. AGU*, 88(39), 383, 2007.
- Tedesco, M., Fettweis, X., van den Broeke, M. R., van de Wal, R. S. W., Smeets, C. J. P. P., van de Berg, W. J., Serreze, M. C., and Box, J. E.: The role of albedo and accumulation in the 2010 melting record in Greenland, *Environ. Res. Lett.*, 6, 014005, 1–6, 2011.
- van den Broeke, M., Bamber, J., Ettema, J., Rignot, E., Schrama, E., van de Berg, W. J., van Meijgaard, E., Velicogna, I., and Wouters, B.: Partitioning recent Greenland mass loss, *Science*, 326, 984–986, 2009.
- Velicogna, I.: Increasing rates of ice mass loss from the Greenland and Antarctic ice sheets revealed by GRACE, *Geophys. Res. Lett.*, 36, L19503, doi:10.1029/2009GL040222, 2009.
- WGMS: Glacier Mass Balance Bulletin. Bulletin No. 10 (2006–2007), edited by: Haeberli, W., Gartner-Roer, I., Hoelzle, M., Paul, F., and Zemp, M., ICSU(WDS)/IUGG(IACS)/UNEP/UNESCO/WMO, World Glacier Monitoring Service, Zurich, 96 pp., 2009.



[5]

Mernild, S. H., Knudsen, N. T., Hoffman, M. J., Yde, J. C., Lipscomb, W. H., Hanna, E., Malmros, J. K., and Fausto, R. S. 2013. Volume and Velocity changes at Mittivakkat Gletscher, Southeast Greenland, 1994–2012. *Journal of Glaciology*, 59(216), 660–670, doi:10.3189/2013JoG13J017.

Reprinted with permission from International Glaciological Society

# Volume and velocity changes at Mittivakkat Gletscher, southeast Greenland

Sebastian H. MERNILD,<sup>1,2</sup> Niels T. KNUDSEN,<sup>3</sup> Matthew J. HOFFMAN,<sup>4</sup> Jacob C. YDE,<sup>5</sup> Edward HANNA,<sup>6</sup> William H. LIPSCOMB,<sup>4</sup> Jeppe K. MALMROS,<sup>2</sup> Robert S. FAUSTO<sup>7</sup>

<sup>1</sup>*Climate, Ocean, and Sea Ice Modeling Group, Computational Physics and Methods, Los Alamos National Laboratory, Los Alamos, NM, USA*

<sup>2</sup>*Glaciology and Climate Change Laboratory, Center for Scientific Studies/Centro de Estudios Científicos (CECs), Valdivia, Chile*  
E-mail: mernild@cecs.cl

<sup>3</sup>*Department of Geoscience, Aarhus University, Aarhus, Denmark*

<sup>4</sup>*Climate, Ocean, and Sea Ice Modeling Group, Fluid Dynamics and Solid Mechanics, Los Alamos National Laboratory, Los Alamos, NM, USA*

<sup>5</sup>*Sogn og Fjordane University College, Sogndal, Norway*

<sup>6</sup>*Department of Geography, University of Sheffield, Sheffield, UK*

<sup>7</sup>*Geological Survey of Denmark and Greenland, Copenhagen, Denmark*

**ABSTRACT.** We document changes for Mittivakkat Gletscher, the peripheral glacier in Greenland with the longest field-based observed mass-balance and surface velocity time series. Between 1986 and 2011, this glacier changed by  $-15\%$  in mean ice thickness and  $-30\%$  in volume. We attribute these changes to summer warming and lower winter snow accumulation. Vertical strain compensated for  $\sim 60\%$  of the elevation change due to surface mass balance (SMB) in the lower part, and  $\sim 25\%$  in the upper part. The annual mean ice surface velocity changed by  $-30\%$ , which can be fully explained by the dynamic effect of ice thinning, within uncertainty. Mittivakkat Gletscher summer surface velocities were on average  $50\text{--}60\%$  above winter background values, and up to  $160\%$  higher during peak velocity events. Peak velocity events were accompanied by uplift of a few centimeters.

## INTRODUCTION

In recent decades, glaciers have thinned and receded in many regions of the world (Oerlemans and others, 2007; Cogley, 2012; Leclercq and Oerlemans, 2012). The contribution to sea-level rise due to mass loss from glaciers peripheral to the Greenland and Antarctic ice sheets is comparable to that from the ice sheets themselves and has increased in recent decades (Kaser and others, 2006; Meier and others, 2007; Cogley, 2012). The thousands of glaciers located peripherally to (and disconnected from) the Greenland ice sheet cover an area of  $\sim 89\,300 \pm 2800 \text{ km}^2$  (Rastner and others, 2012), compared with  $\sim 1.7 \times 10^6 \text{ km}^2$  for the continuous ice sheet (Kargel and others, 2012).

Our knowledge of the morphological characteristics, ice dynamics and climate sensitivity of these glaciers is limited (Marzeion and others, 2012). Glacier mass-balance studies often exclude the Greenland peripheral glacier contribution to sea-level rise (e.g. Jacob and others, 2012), even though Yde and Knudsen (2007), Bjørk and others (2012), Kargel and others (2012) and Mernild and others (2012) have documented substantial glacier area recession on Disko Island ( $69\text{--}70^\circ \text{ N}$ ; West Greenland) and in southeast ( $65^\circ \text{ N}$ ) and East Greenland ( $68\text{--}72^\circ \text{ N}$ ). Not only is the glacier area decreasing, but also the annual surface melt extent and the amount of surface melting and freshwater runoff from peripheral glaciers have increased during the past several decades (e.g. Mernild and Hasholt, 2006; Kargel and others, 2012). This trend agrees with observations and modeling of runoff from the Greenland ice sheet (Hanna and others, 2008, 2012a; Mernild and Hasholt, 2009; Mernild and

others, 2010; Mernild and Liston, 2012), where increased surface melting influences glacier dynamics through changes in subglacial hydrology (e.g. Van der Wal and others, 2008; Sundal and others, 2011).

Mittivakkat Gletscher (henceforth MG; Fig. 1), located in the Ammassalik region, is Greenland's only peripheral glacier for which there exist surface mass-balance (SMB) records (since 1995), surface velocity measurements (since 1995), aerial photographs and satellite margin and area observations (since 1900) (Mernild and others, 2011a, 2012; Bjørk and others, 2012). This study analyzes spatial changes in MG's SMB (winter, summer and annual net mass balances) and quantifies the decrease in ice thickness, volume and surface velocity during a 25 year period of climate warming (1986–2011). These new results of ice thickness, volume and surface velocity changes supplement a previous study of MG by Mernild and others (2011a), where the focus was on the relations between frontal glacier recession and recession rates, annual net mass-balance and accumulation-area ratio (AAR) conditions relative to out-of-balance conditions and the committed area and ice volume loss even in the absence of further climate changes.

## STUDY AREA

Mittivakkat Gletscher ( $65^\circ 42' \text{ N}$ ,  $37^\circ 48' \text{ W}$ ;  $26.2 \text{ km}^2$ ) is located in what is considered the Low Arctic (Born and Böcher, 2001), with a local mean annual air temperature of  $-2.2^\circ \text{ C}$  (1993–2011) (Hanna and others 2012b), and mean annual precipitation in the range  $1400\text{--}1800 \text{ mm w.e. a}^{-1}$

(1998–2006) at Tasiilaq (from the Danish Meteorological Institute (DMI) station located  $\sim 15$  km southeast of MG) (Mernild and others, 2008a). The glacier is temperate (i.e. ice at the pressure-melting point), with seasonal temperature excursions in the upper few meters (Knudsen and Hasholt, 1999). Since its maximum extent during the Little Ice Age, MG has undergone almost continuous retreat (Knudsen and Hasholt, 1999; Knudsen and others, 2008; Mernild and others, 2011a). During 1986–2011 the glacier area changed by  $-18\%$ , from  $31.6 \text{ km}^2$  (1986) to  $29.5 \text{ km}^2$  (1999) to  $26.2 \text{ km}^2$  (2011) (Mernild and others, 2012), and the mean surface slope changed from  $0.095 \text{ m m}^{-1}$  ( $=5.4^\circ$ ) to  $0.104 \text{ m m}^{-1}$  ( $5.9^\circ$ ). The area change of MG follows the overall trend of the Ammassalik region, where glaciers on average changed by  $-27 \pm 24\%$  during this period (Mernild and others, 2012).

For MG the annual SMB has been observed for 16 years since 1995/96, and the winter and summer balances for 10 of the last 12 years. The mean annual net mass balance is  $-0.97 \pm 0.75 \text{ m w.e. a}^{-1}$  (1995/96–2010/11), with a mean winter balance of  $1.18 \pm 0.19 \text{ m w.e. a}^{-1}$  and a mean summer balance of  $-1.94 \pm 0.38 \text{ m w.e. a}^{-1}$  (1995/96–2007/08) (Mernild and others 2013). The annual SMB has changed on average by  $-0.09 \text{ m w.e. a}^{-2}$  ( $r^2=0.36$ ;  $p<0.01$ , significant; where  $r^2$  is the explained variance and  $p$  is level of significance; the term ‘significant’ is only used where the relationship is statistically significant at the 10% level or better, based on a linear regression  $t$ -test). The explained variance in the annual winter and summer balances was  $r^2=0.34$ ;  $p<0.05$  and  $r^2=0.01$ ;  $p>0.25$ , respectively. Winter and summer balances were not observed during several years in the later part of the record with highly negative annual SMB. The net balance in 2010/11 was a record setting,  $-2.45 \text{ m w.e.}$ , about two standard deviations below the mean and  $0.29 \text{ m w.e.}$  more negative than the previous observed record low mass balance in 2009/10 (Mernild and others, 2011b).

Since 1995 the equilibrium-line altitude (ELA) has risen from  $\sim 500 \text{ m a.s.l.}$  to  $750 \text{ m a.s.l.}$  (Mernild and others, 2011a). For six years during this time frame the mass balance was negative for the entire glacier: 1997/98, 2000/01, 2004/05, 2006/07, 2009/10 and 2010/11. The average AAR is currently  $\sim 0.15$ .

## DATA AND METHODS

### Thickness and volume

In 1994 the MG surface elevation, bed topography and ice thickness were estimated based on monopulse radio-echo soundings (Knudsen and Hasholt, 1999). The mean MG ice thickness ( $115 \text{ m}$ ) was derived from measurements at 450 positions, spaced  $\sim 100 \text{ m}$  apart along profiles running across the glacier, and  $\sim 300 \text{ m}$  apart along the flowline with a vertical spacing of  $50 \text{ m}$  (two such profiles are illustrated in Fig. 2). The error in measured ice thickness was estimated to be less than  $\pm 5 \text{ m}$  (Knudsen and Hasholt, 1999), giving a relative uncertainty of  $<5\%$  for the mean 1994 ice thickness ( $115 \text{ m}$ ).

In 1995 a glacier observation program was initiated to measure MG’s annual SMB and to map changes in ice thickness. A network of stakes (Fig. 1) was used to measure summer ablation (Fig. 3) based on the direct glaciological method (Østrem and Brugman, 1991; Mernild and others, 2011a). The vertical accuracy of observed annual stake

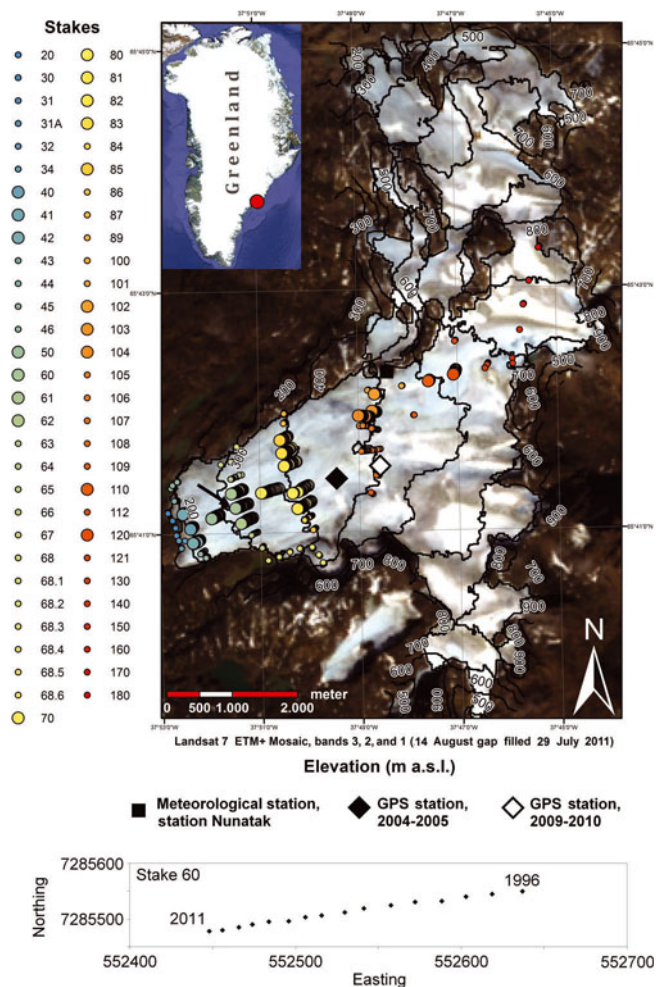


**Fig. 1.** Mittivakkat Gletscher ( $26.2 \text{ km}^2$ ;  $65^\circ 41' \text{ N}$ ,  $37^\circ 48' \text{ W}$ ) including topographic map ( $100 \text{ m}$  contour interval), and circles illustrating the stake locations for the glacier observation program, 1995–2011. The stake colors on the glacier surface correspond to the stake numbers illustrated to the left, where the low numbers correspond to the stakes at the low-elevation part of the glacier, and the converse. The 18 stakes (40, 41, 42, 50, 60, 61, 62, 70, 80, 81, 82, 83, 85, 102, 103, 104, 110 and 120) measured continuously throughout the period are highlighted in bold. Due to a high density of crevasses in the southeastern part of the glacier, no stakes were located there. The meteorological station at the nunatak is shown by a black square, and the GPS station on the glacier by black and white diamonds. The inset indicates the location of MG in southeast Greenland. Below, an example of an annual time series (1996–2011) of stake locations is shown for stake 60, denoted by a black arrow on the map (source: Landsat 7 Enhanced Thematic Mapper Plus (ETM+) Mosaic, 1 August 2009 and 14 August 2011).

mass-balance measurements has been estimated to be within  $5 \text{ cm}$ , or  $<\pm 10\%$  (Østrem and Stanley, 1969). Measurements were obtained at 59 stakes covering  $16.3 \text{ km}^2$  of MG, excluding the crevassed area in the southeastern part of the glacier (this omission is not likely to bias the results, since the surface of the crevassed area follows the general hypsometric distribution in the upper part of MG (Mernild and others, 2006, 2008b)). Since its establishment, the stake network has moved slowly down-glacier by  $50$ – $275 \text{ m}$  (based on calculations, this movement has an insignificant impact on estimates of the mean annual surface velocity). The winter balance was calculated as the difference between the net annual balance and the summer

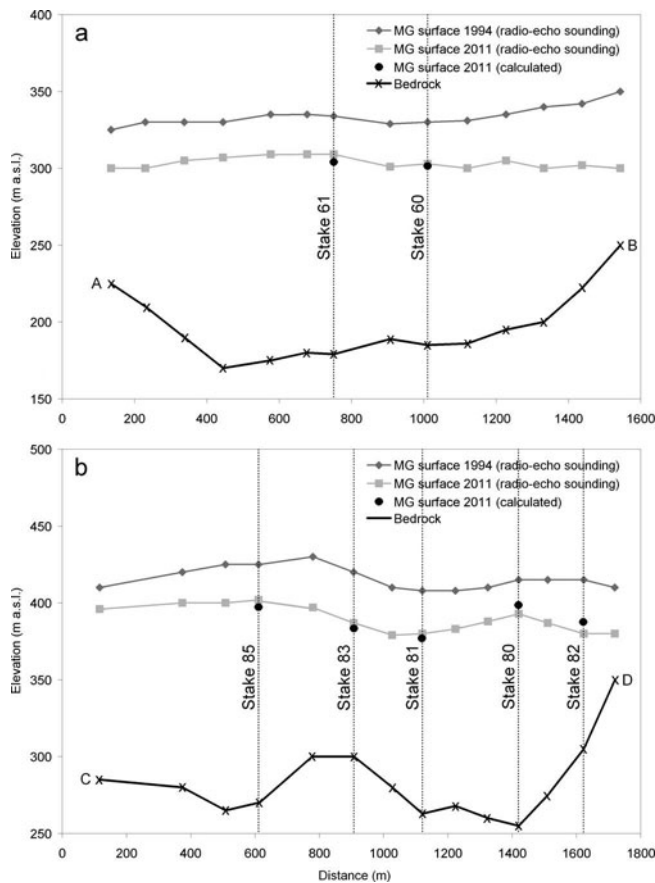


**Fig. 2.** A comparison between the 2011 calculated mean MG thickness and the 2011 and 1994 monopulse radio-echo sounding estimated mean thicknesses at two cross-section locations in the ablation area: (a) at ~300 m a.s.l.; (b) at ~400 m a.s.l. Approximate locations of the cross sections are shown in Figure 7c.

balance. The mass-balance observations are accurate within  $\pm 15\%$  for the entire MG (Fig. 3) (Knudsen and Hasholt, 2004), which is within the uncertainty range suggested by Cogley and Adams (1998) for these methods.

The MG ice volume was calculated for 1986, 1999 and 2011 and based on the satellite-derived glacier extent (from Landsat imagery) multiplied by the mean ice thickness (Mernild and others, 2012). The mean ice thicknesses for 1999 and 2011 were calculated from the observed 1994 mean thickness and the cumulative observed mass balance. To assess the accuracy of the calculations, we compared the 2011 calculated MG thickness against thickness measured in 2011 by monopulse radio-echo sounding along two cross-section profiles (both located in the ablation zone) (Fig. 2). The mean difference in ice thickness between the calculations and radio-echo soundings was on average 2 m (seven stakes, root mean square (rms) = 3 m) (Fig. 2).

The 1986 mean ice thickness was estimated by adding the cumulative mass balance during 1986–94, based on modeled MG annual mass-balance data from Mernild and others (2008c), to the 1994 mean thickness (Fig. 4). The calculated MG annual mass balance was compared against observed mass balance for a control period 1995/96 to 2003/04, indicating an  $r^2$  value of 0.71 (significant,  $p < 0.01$ ) and a difference less than 0.01 m between observed and calculated mass-balance values. The 1986–94 calculation method was extended back to 1981, at which point the mean calculated surface elevation was compared to a 1981 map

(1 : 20 000) of digitized mean surface topography (Knudsen and Hasholt, 1999), indicating an average difference of 2–4 m (rms = 3 m) (not shown).

The MG surface slope was calculated for both 1996 and 2011 for the longitudinal profile along stakes 31, 40, 50, 60, 70, 80, 107, 110, 120, 130 and 140 (Figs 1 and 5).

### Surface ice velocity and thickness changes

Each stake position (Fig. 1) was measured annually, varying from 47 stakes in 1998 and 2001 to 18 stakes for the years 2008–11. Eighteen stakes were measured continuously throughout the period 1995/96–2010/11. Before 2004, the horizontal stake positions were measured by topographic surveys using a theodolite (Kern) with an Electro-optical Distance Meter, having a horizontal uncertainty of less than  $\pm 1$  m. After 2004, stake position was based on a portable single-frequency GPS (Garmin GPS 12 XL) with a relative horizontal uncertainty (std dev.) of about  $\pm 2$ –3 m (similar to a relative uncertainty of approximately  $\pm 10\%$  for maximum annual velocity, and  $\pm 25\%$  for mean velocity). The horizontal  $\pm 2$ –3 m value is based on long time repeated fixed station measurements with the same instrument during several years. The annual stake positions were used to calculate the spatial mean surface velocity field.

Also, a continuous ice surface velocity time series was obtained from a dual-frequency GPS receiver (Javad Laxon GGD160T, operated by the Geological Survey of Denmark and Greenland) positioned near the center of MG (Fig. 1). This time series was used to determine the seasonal variability in ice surface velocity. However, we have access to data only from May 2004 through July 2005 (when the GPS receiver was located at elevations from 462 to 455 m a.s.l.) and from March 2009 through August 2010 (513–509 m a.s.l.). The horizontal and vertical uncertainties in the GPS time series were on average around 3 and 6 mm, respectively.

Thickness changes,  $dh/dt$ , at a point on the glacier are a combination of SMB and vertical strain and can be described by continuity (Cuffey and Patterson, 2010) approximately as

$$dh/dt = b - u_s \tan \alpha + w_s \quad (1)$$

where  $b$  is the SMB,  $u_s$  is the horizontal surface velocity,  $\alpha$  is the surface slope and  $w_s$  is the vertical velocity of a fixed point on the glacier (e.g. the top of a stake). However, our surveys measured the position of the ice surface at each stake, so our observed vertical velocity includes the SMB. Thus, we calculate thickness changes as

$$dh/dt = w_{\text{obs}} - u_s \tan \alpha \quad (2)$$

where  $w_{\text{obs}}$  is the observed vertical velocity measured as the height difference between two successive surveys of the ice surface elevation at the position of a stake. We separate the component of thickness change due to vertical strain rate (emergence velocity,  $w_e$ ) as

$$w_e = dh/dt - b \quad (3)$$

To assess how much of the deceleration in surface velocity can be explained by changes in thickness, the theoretical surface velocity due to deformation at the beginning and end of the study period was calculated using the shallow ice approximation (SIA; Hutter 1983):

$$v_{\text{sia}} = 1/(2A)(\rho g ds/dx)^3 H^4 \quad (4)$$

where  $A$  is the flow law rate factor, taken as



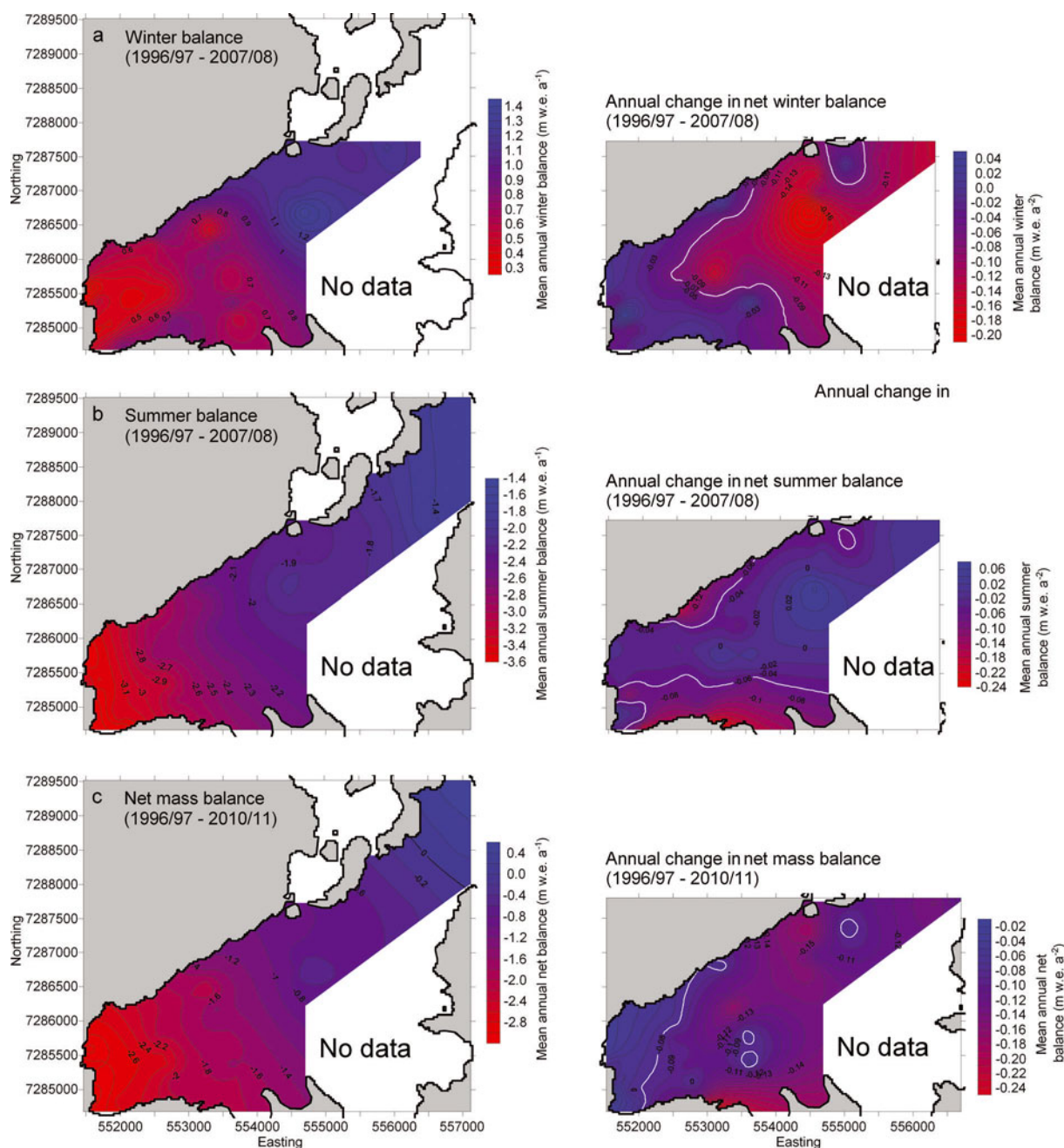


**Fig. 3.** Annual mass-balance distributions and changes at MG: (a) mean winter mass balance and annual change (blue-red shades); (b) mean summer mass balance and annual change; and (c) net annual mass balance and annual change for 1996/97 through 2010/11. The white bold lines (in the right-side panels) indicate the margin for significant annual trends in winter, summer and net mass balances, where values below are significant. The white area has no data, and the margin is based on Landsat 7 ETM+ Mosaic imagery, 1 August 2009 and 14 August 2011.

$2.1 \times 10^{-16} \text{ a}^{-1} \text{ Pa}^{-3}$  for isothermal ice at  $0^\circ\text{C}$  (Cuffey and Paterson, 2010),  $\rho$  is the density of ice taken as  $900 \text{ kg m}^{-3}$ ,  $g$  is acceleration due to gravity,  $9.81 \text{ m s}^{-2}$ ,  $dS/dx$  is the surface slope and  $H$  is the ice thickness. We apply Eqn (4) within the ablation area along the longitudinal profile from stake 31 through stake 80, performing the calculation midway between stake locations, based on the values of thickness, slope and observed velocity averaged between the two adjacent stake locations. This provides a flowline average over  $\sim 3$ – $5$  ice thicknesses, which compensates somewhat for the fact that the SIA ignores longitudinal and lateral stresses that may be important for a mountain glacier. A shape factor is not used because MG is wide relative to its depth (half-width/thickness  $\approx 10$ ).

## RESULTS AND DISCUSSION

### Spatial surface mass-balance and thickness changes

Figure 3 illustrates the mean spatial variations in winter, summer and annual net mass balances. The mean winter balance shows less accumulation at low elevations ( $0.3 \text{ m w.e. a}^{-1}$ ) than at higher elevations ( $>1.4 \text{ m w.e. a}^{-1}$ ) (Fig. 3a), with a mean orographic gradient of  $\sim 0.2 \text{ m w.e. a}^{-1}$  per 100 m increase in elevation (1995/96–2007/08). Figure 3a also illustrates the spatial distribution of the annual change in winter balance, showing that the terminus, the marginal areas at high elevations, and areas near mountain ridges had the smallest decrease, while other areas had an increasing winter balance ( $0.04 \text{ m w.e. a}^{-2}$ ). The largest changes

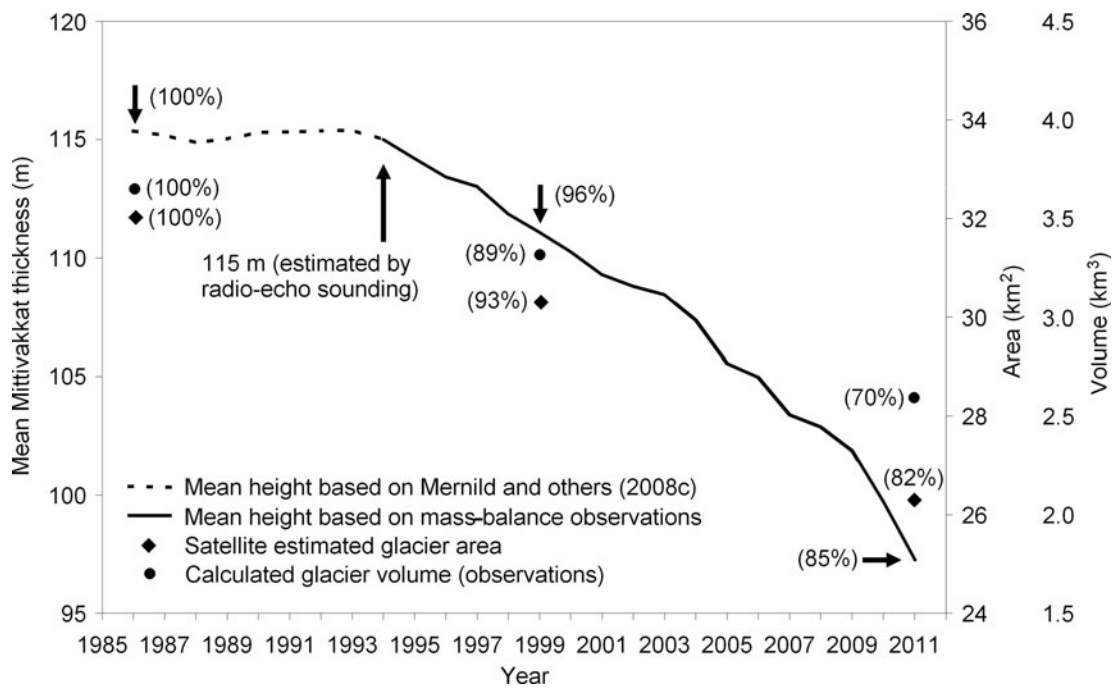


**Fig. 4.** Time series of estimated mean thickness (line), area (diamonds; Mernild and others, 2012) and volume (circles) for MG. The dashed time series is estimated based on MG net mass-balance calculations (Mernild and others, 2008c). The percent of 1986 MG mean height, area and volume (the 1986 values were set to 100%) are shown in parentheses.

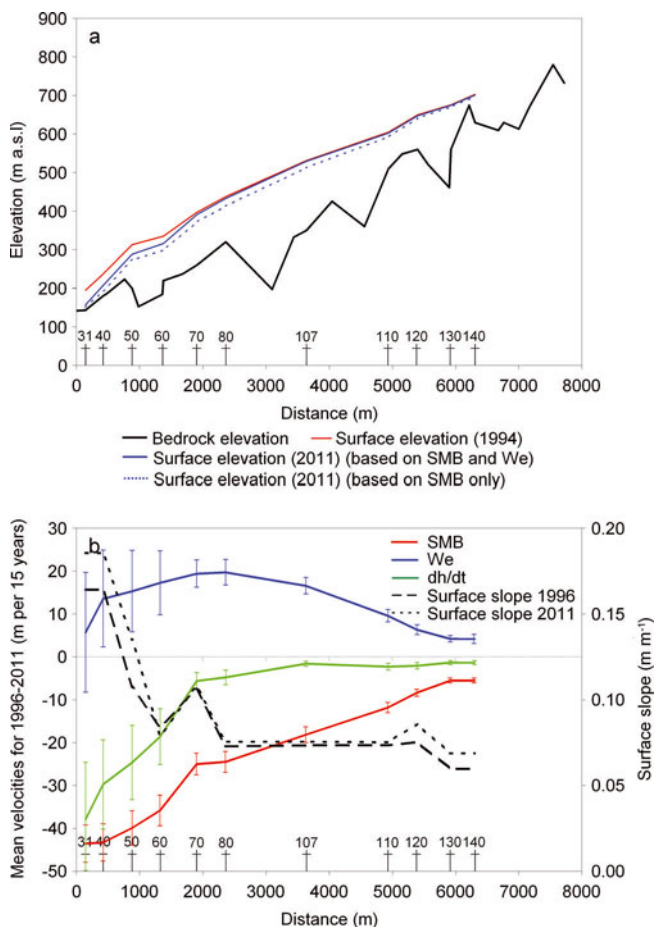


**Fig. 5.** (a) Longitudinal surface elevation for 1994 and 2011, where the 2011 elevation was calculated with and without vertical velocity ( $w_e$ ), showing the positions of stakes 31–140; and (b) longitudinal mean surface slope for 1996 and 2011, SMB,  $w_e$  and  $dh/dt$  including uncertainty bars.

( $-0.20 \text{ m w.e. a}^{-2}$ ) occurred along the center line of the glacier and at higher elevations, most pronounced at  $\sim 500 \text{ m a.s.l.}$ , where significant trends below  $-0.07 \text{ m w.e. a}^{-2}$  occurred (Fig. 3a).

The summer balance shows more ablation at low elevations, and decreasing mass loss towards higher elevations (Fig. 3b), as expected. The summer mass balance varied from  $-3.6 \text{ m w.e. a}^{-1}$  at low elevations to  $-1.4 \text{ m w.e. a}^{-1}$  at high elevations, giving a mean gradient of  $0.3 \text{ m w.e. a}^{-1}$  per 100 m increase in elevation (1995/96–2007/08). Figure 3b illustrates the spatial distribution of the annual change in summer balance, showing the largest change towards the margins, and most pronounced in the southern part of the glacier ( $-0.22 \text{ m w.e. a}^{-2}$ ). Significant trends occurred where the annual trend in summer balance was less than  $-0.06 \text{ m w.e. a}^{-2}$  (Fig. 3b). A possible explanation for the spatial pattern in summer mass-balance change is that the surface albedo was reduced as the margins receded, for example due to aeolian- and englacially transported debris exposed at the ice surface. Additionally, enhanced melting along the margins may have been due to increasing convection of heat from the surrounding areas. Towards the center of the glacier the energy balance will be less affected by these processes.

The net mass balance shows the combined effects of changes in winter and summer balances. The net mass balance shows the lowest values at low elevations ( $-3.0 \text{ m w.e. a}^{-1}$ ) and highest values at higher elevations ( $-0.4 \text{ m w.e. a}^{-1}$ ) (Fig. 3c). The mean net mass-balance gradient was  $0.5 \text{ m w.e. a}^{-1}$  per 100 m (1995/96–2010/11). The annual change in net mass balance is inhomogeneous, with the largest changes in the marginal area in the south ( $-0.24 \text{ m w.e. a}^{-2}$ ) and along the center line (around  $-0.16 \text{ m w.e. a}^{-2}$ ) (Fig. 3c). A significant trend occurred below  $-0.08 \text{ m w.e. a}^{-2}$ . The mass loss at  $\sim 500 \text{ m a.s.l.}$  likely reflects that more ice has recently been exposed in that area



as the snow and firn cover receded up-glacier. Due to the increased ice exposure, a change in surface albedo has occurred from 0.8–0.9 for snow to around 0.4 for bare ice, highly reinforcing the surface melt of MG, especially at mid-to high elevations.

Surface elevation and ice thickness decreased across the glacier from 1995 to 2011 (Fig. 5a and b). Surface elevation changes ( $dh/dt$  calculated from Eqn (2)) for the longitudinal MG profile are  $-5.7 \pm 2.0$  to  $-37.9 \pm 13.3$  m w.e. (averaging  $-23.3 \pm 8.2$  m w.e.) on the lower part of the glacier at stakes 31, 40, 50, 60 and 70, and  $-1.4 \pm 0.5$  to  $-2.3 \pm 0.8$  m w.e. (averaging  $-1.8 \pm 0.6$  m w.e.) on the upper part at stakes 110, 120, 130 and 140 (Fig. 5b, green line). The surface elevation change due to SMB alone was more negative than the total elevation changes:  $-25.0 \pm 2.5$  to  $-43.5 \pm 4.4$  m w.e. (averaging  $-37.5 \pm 3.8$  m w.e.) in the lower part and  $-5.5 \pm 0.6$  to  $-11.8 \pm 1.2$  m w.e. (averaging  $-7.8 \pm 0.8$  m w.e.) in the upper part (Fig. 5b, red line). Vertical strain was able to compensate for  $\sim 60\%$  of the elevation change due to SMB in the lower part,  $\sim 25\%$  in the upper part, and overall on average  $\sim 50\%$  for the longitudinal profile. If the glacier were in equilibrium with climate, vertical strain would be equal, and of opposite sign, to SMB; the large discrepancy in the magnitudes of the two processes is an indicator of the disequilibrium of MG. The vertical strain was unevenly distributed along the longitudinal profile (Fig. 5b, blue line), with the greatest compensation of thinning due to SMB at central elevations at stake 80 ( $w_e = 20$  m) where the mean surface velocity was greatest, and decreasing towards high and low elevations. That vertical strain is strongly positive throughout the region profiled suggests that the accumulation zone must be thinning strongly because the accumulation rates there are low and unlikely to be able to compensate for the transfer of mass to the ablation zone. Due to logistical constraints with working in the accumulation zone, we are unable to measure thinning there, but we are able to document thinning (elevation lowering) at a single point at the upper part of MG (Fig. 6; the nunatak location is illustrated in Fig. 1). Based on repeated markings of the ice margin position, the surface lowered 24 m between 1994 and 2010 at this specific location.

### Volume changes

The glacier-covered area is one of the easiest glacier morphometric quantities to measure (e.g. Bahr, 2011). The surface area of MG was estimated for the years 1986, 1999 and 2011 based on satellite imagery, and the area changed by  $-18\%$  during this period (Mernild and others 2012). For the same period, the estimated mean ice thickness changed by  $-15\%$ , from  $115 \pm 17$  m (1986) to  $110 \pm 17$  m (1999) to  $97 \pm 15$  m (2011) (where the uncertainties are assumed equal to the mass-balance method uncertainty of  $\pm 15\%$ ). Based on observed changes in area cover and mean thickness, the mean volume diminished by  $1.1 \text{ km}^3$  (30%) (Fig. 4), from  $3.7 \pm 0.5 \text{ km}^3$  (1986) to  $3.3 \pm 0.5 \text{ km}^3$  (1999) to  $2.6 \pm 0.4 \text{ km}^3$  (2011). This change in volume occurred contemporaneously with highly significant observed changes in mean annual air temperature (MAAT) of  $0.09^\circ\text{C a}^{-1}$  ( $r^2 = 0.51$ ;  $p < 0.01$ ), mean summer air temperature (June–August) of  $0.09^\circ\text{C a}^{-1}$  ( $r^2 = 0.60$ ;  $p < 0.01$ ) and in mean annual (uncorrected) precipitation of  $-8 \text{ mm w.e. a}^{-2}$  ( $r^2 = 0.08$ ;  $p < 0.10$ ) (1986–2011) at the nearby DMI station in Tasiilaq (Carstensen and Jørgensen, 2011). Climate records from other meteorological stations in southeast

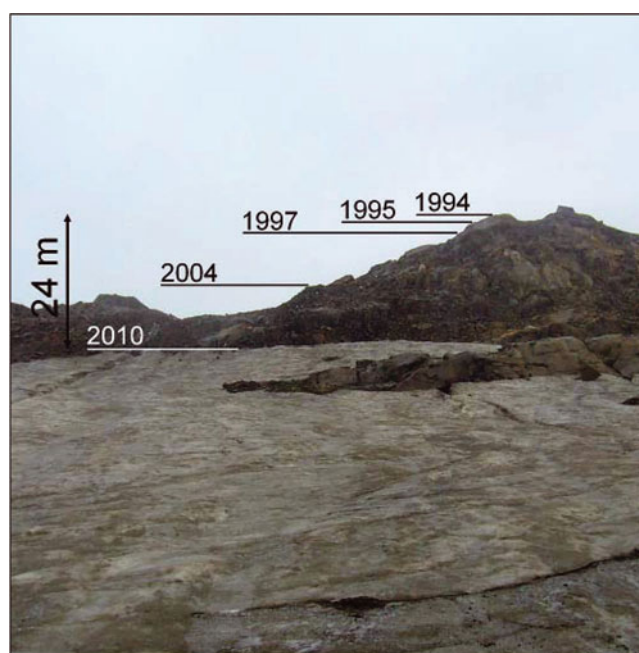


**Fig. 6.** Observed surface elevation lowering from 1994 through 2010 at a nunatak in the upper part of MG (the location of the nunatak, close to the northwestern margin, is marked with a black square in Fig. 1). The lines corresponding to the MG margin location were marked with spray-paint on the nunatak during the indicated summers. The photograph was taken looking south, and the distance from where the photo was taken to the glacier margin (the 2010 line) was approximately 12–13 m (photographs: S.H. Mernild, August 2010).

Greenland show significant increases in MAAT and mean summer air temperature since the early 1980s in the ranges  $0.05\text{--}0.08^\circ\text{C a}^{-1}$  and  $0.02\text{--}0.08^\circ\text{C a}^{-1}$ , respectively, suggesting that the MG trends are not merely a local phenomenon but are indicative of glacier changes in the broader region (Mernild and others, 2011a). Such changes at the broader regional scale have been illustrated by Bjørk and others (2012), highlighting widespread retreat along the southeastern margin of Greenland over the past 80 years, where major retreat occurred not only during the recent warming, but also during and after warming in the early 20th century.

### Surface velocity changes

The surface velocity of MG has been observed since 1996/97 at the stake locations (Fig. 1). Mean surface velocity has a maximum of  $22 \text{ m a}^{-1}$  near the center of the glacier (shown in red in Fig. 7a), and a spatial average of  $8 \text{ m a}^{-1}$ . The velocity at the lateral margins consistent with drag from the valley walls and thinner ice (e.g. Cuffey and Paterson, 2010) was  $\sim 3\text{--}5 \text{ m a}^{-1}$ . The highest surface velocities are observed where the ice is thickest, and at the two cirques to the south of MG. In this context it has to be emphasized that the estimation of the spatial surface velocity field is likely to have a higher degree of uncertainty towards the crevassed parts of the glacier where no direct measurements of velocity are available.

Over the 15 year period (1996/97–2010/11), surface velocity has decelerated across the glacier, by  $>50\%$  in much of the ablation area. However, the change in annual surface velocity has been unevenly distributed across the glacier (Fig. 7b). The greatest deceleration,  $\sim 0.6 \text{ m a}^{-2}$ , is observed on the lower part of the glacier near the margins (a significant

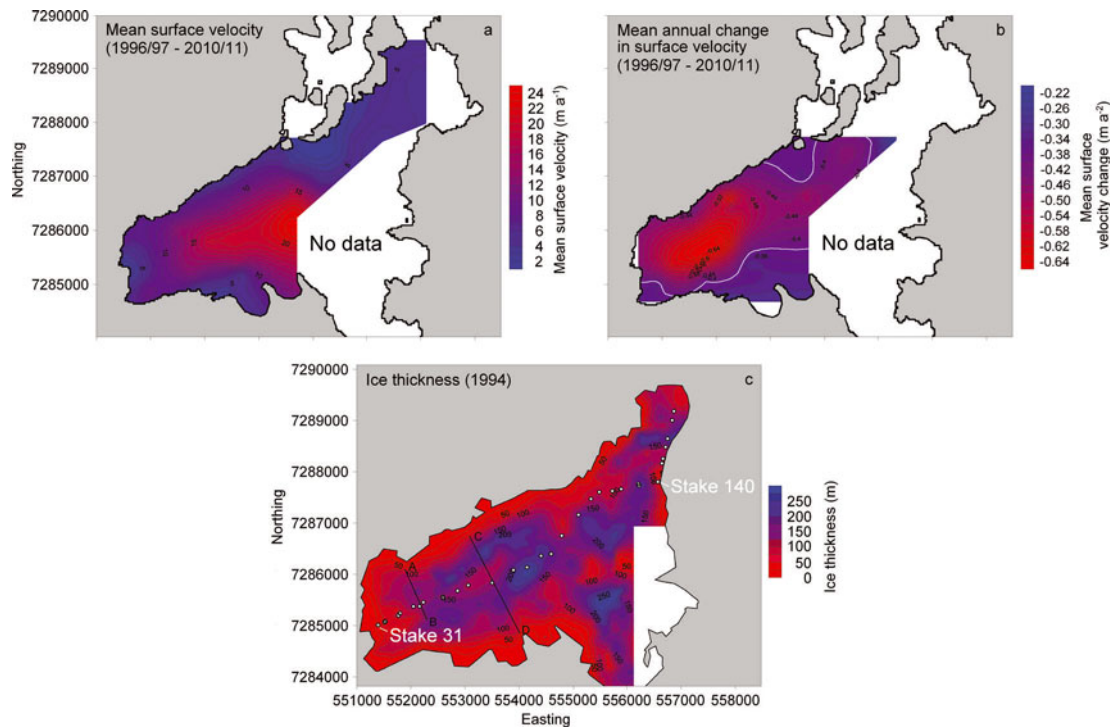


**Fig. 7.** Mittivakkat Gletscher: (a, b) Mean annual surface velocity (a) and mean surface velocity change (b) from 1996/97 to 2010/11. The white bold lines indicate the margin for significant annual trends in surface velocity, where values below are significant. (c) Ice thickness based on radar observations in 1994 (Knudsen and Hasholt, 1999) including the location of the longitudinal profile (white circles) (illustrated in (a, b)) and the two cross-section profiles (illustrated in Fig. 2). The locations of stakes 31 and 140 are marked. No observations were made in the southeastern part of the glacier since this is a heavily crevassed area. The white area has no data, and the margin in (a) and (b) is based on Landsat 7 ETM+ Mosaic imagery 1 August 2009 and 14 August 2011, and in (c) is derived from GPS observations.

deceleration trend occurred below  $0.38 \text{ m a}^{-2}$ ; Fig. 7b), where the greatest thinning has also occurred (Fig. 3c).

The decelerating change in annual surface velocity observed across MG is likely related to the glacier thinning, which will decrease both deformation and sliding (Cuffey

and Paterson, 2010), and slow the transfer of ice to lower elevations, which might buffer the retreat to some extent. An alternative explanation for the reduction in velocity is that changes in subglacial hydrology from increased surface melting over the study period have led to an earlier and more extensive development of channelized drainage and subsequent decrease in sliding each summer (e.g. Schoof, 2010; Sundal and others, 2011).

We assess the deceleration in the theoretical surface velocity that can be explained by changes in thickness, though the calculation of  $v_{\text{sia}}$  (Eqn (4)) has a high degree of uncertainty due to uncertainty in the flow rate factor and the lack of higher-order stresses. The calculations indicate that the observed changes in surface velocity can largely be explained by the thickness changes over the study period (Fig. 8). Our calculation of  $v_{\text{sia}}$  does not include a contribution to surface velocity from sliding, which is typically a large component on temperate glaciers (Weertman, 1957; Cuffey and Paterson, 2010). However, sliding velocity is commonly assumed to vary with ice thickness to a power of 1–3 (Bindschadler, 1983; Clarke, 2005; Cuffey and Paterson, 2010), and, allowing a component of surface velocity due to sliding (e.g. by lowering  $A$ ) with powers that range from 1 to 3, we find that the change in thickness can still explain most of the change in observed velocity without requiring changes in sliding related to hydrology since thickness changes affect sliding in a similar fashion to deformation.

The alternative hypothesis is that the observed surface velocity is due to a reduction in basal sliding associated with changing hydrology. Though meltwater draining to the beds of glaciers can increase sliding initially, once subglacial hydrologic systems adjust to the input, sliding can decrease

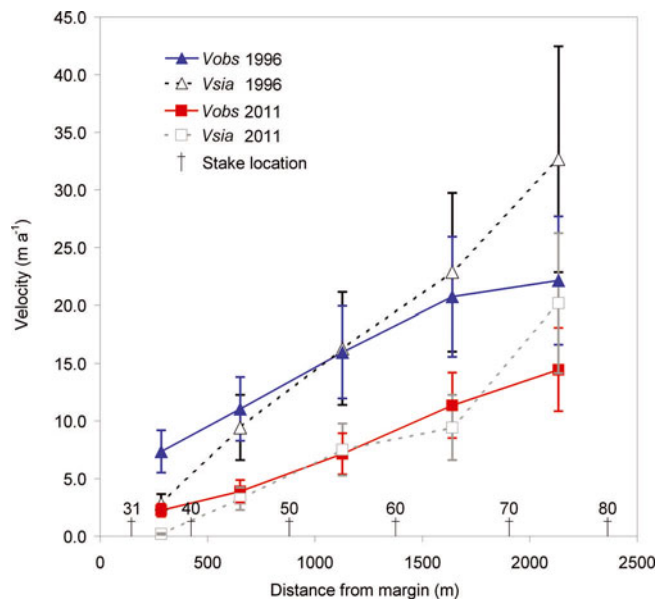


**Fig. 8.** Observed ( $V_{\text{obs}}$ ) and calculated ( $V_{\text{sia}}$ ; Eqn (4)) surface velocities including uncertainty bars for 1996 and 2011 along a longitudinal profile (Fig. 7c) through the ablation zone. Each point is midway between two stake locations which are identified by dagger symbols.

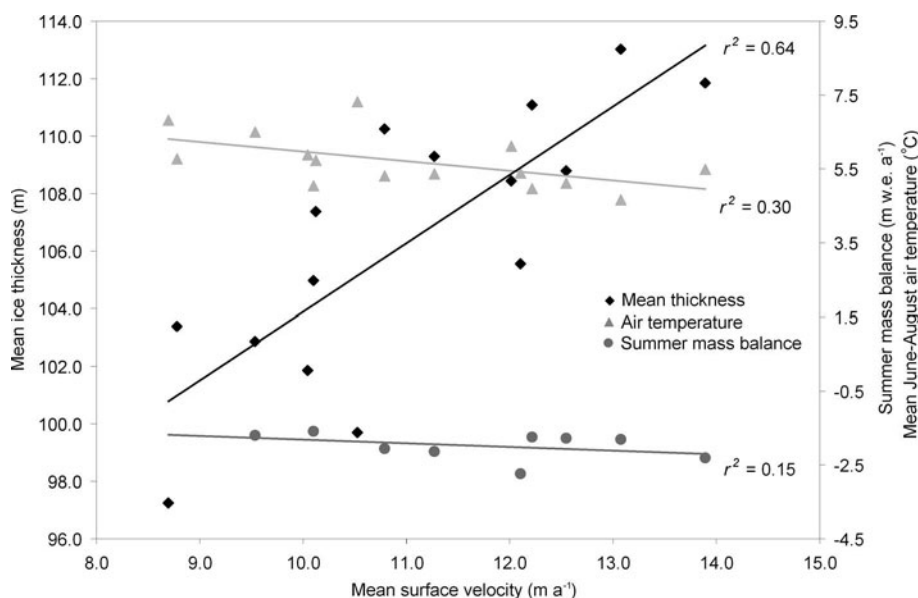


**Fig. 9.** Linear relationship between MG mean annual surface velocity and mean ice thickness (black diamonds) estimated from stake observations, observed summer mass balance (dark gray circles) and observed mean JJA air temperature at station Nunatak (light-gray triangles) from 1996 to 2011.

with sustained meltwater input (Bartholomaeus and others, 2008; Schoof, 2010), potentially leading to lower average summer velocity (Truffer and others, 2005; Vincent and others, 2009; Sundal and others, 2011). Summer mass balance (and by association, melt) has become increasingly negative across MG during the study period (Fig. 3b). However, changes in melt appear to have only a minor impact on surface velocity at the seasonal scale. Summer mass balance and mean June–August (JJA) temperatures, both proxies for melt, are only weakly correlated with mean annual surface velocity ( $r^2=0.15$ , insignificant at  $p<0.25$ , and  $r^2=0.30$ , significant at  $p<0.025$ , respectively), while thickness is relatively strongly positively correlated with surface velocity ( $r^2=0.64$ , significant at  $p<0.01$ ; Fig. 9). Thus changes to summer melt are relatively unimportant, compared with thickness changes, for changes in velocity.

Based on these analyses, we conclude that the observed 15 year slowdown was caused by decreasing ice deformation (and possibly sliding) resulting from glacier thinning, whereas changes to hydrology during that time do not seem to be important. This is consistent with previous studies which found that time periods of decadal lengths are necessary to observe the dynamic effects of thinning. Vincent and others (2009) recorded 20 years of thickening and speed-up followed by 30 years of thinning and slowdown at Glacier d'Argentière, France. In contrast, Müller and Iken (1973) found small ( $\sim 1$  m) thickness changes inadequate to explain annual velocity changes over a 2–3 year period on White Glacier, Arctic Canada.

### Seasonal velocity variations

Daily MG surface velocity was observed during two periods (May 2004 through July 2005, and March 2009 through August 2010) (Fig. 10a) (see Fig. 1 for locations of the GPS stations), illustrating variations in speed at short timescales. For the summer (JJA) the mean ice surface velocity varied between  $0.061 \pm 0.01$  and  $0.066 \pm 0.02$   $\text{m d}^{-1}$ , with a maximum observed daily velocity of  $0.10$   $\text{m d}^{-1}$  (26 June 2005). For the winter (September–May) the velocity varied between

$0.038 \pm 0.01$  and  $0.043 \pm 0.01$   $\text{m d}^{-1}$ . The summer values are 50–60% higher than the winter background values, and up to 160% higher for peak events (Fig. 10a and b). Similar seasonal patterns in ice surface velocity were observed at Flade Isblink ice cap (the largest ice cap in Greenland), northeast Greenland (Palmer and others, 2010), at John Evans Glacier, Nunavut, Canada (Bingham and others, 2003), and at the western land-terminating margin of the Greenland ice sheet, where the peak summer velocity was up to 220% above the winter background velocity (Bartholomew and others, 2010; Hoffman and others, 2011). There is some evidence that increases in water storage are associated with increases in sliding. MG peak velocity events were typically accompanied by uplift of a few centimeters. Similar uplift has been observed for mountain glaciers (e.g. Iken and others 1983; Bartholomaeus and others, 2008; Howat and others, 2008) and the Greenland ice sheet (e.g. Bartholomew and others, 2010; Hoffman and others, 2011; Sole and others, 2011) during speed-up events.

The seasonal pattern in the daily surface velocity demonstrates the spring speed-up, which is common on temperate mountain glaciers, in which the onset of summer melt results in a large increase in velocity that is short-lived despite continued melt throughout the summer (e.g. Iken and others, 1983; Nienow and others, 1998; Anderson and others, 2004). At the beginning of each summer, velocity increase follows increasing air temperature, peaking in early to mid-June. After this initial speed-up, velocity has little clear relationship with air temperature until the end of summer when air temperatures fall to and remain well below  $0^\circ\text{C}$  (Fig. 10). This behavior is consistent with transient speed-up when subglacial water storage is increasing in spring and water inputs encounter an undeveloped drainage system (e.g. Truffer and others 2005; Bartholomaeus and others 2008). The periods 25 July to 5 August 2004, 30 June to 19 July 2009, and 13 June to 18 July 2010 are examples of multi-week periods of increasing temperatures during midsummer accompanied by a slowdown in surface velocity (Fig. 10a), suggestive of



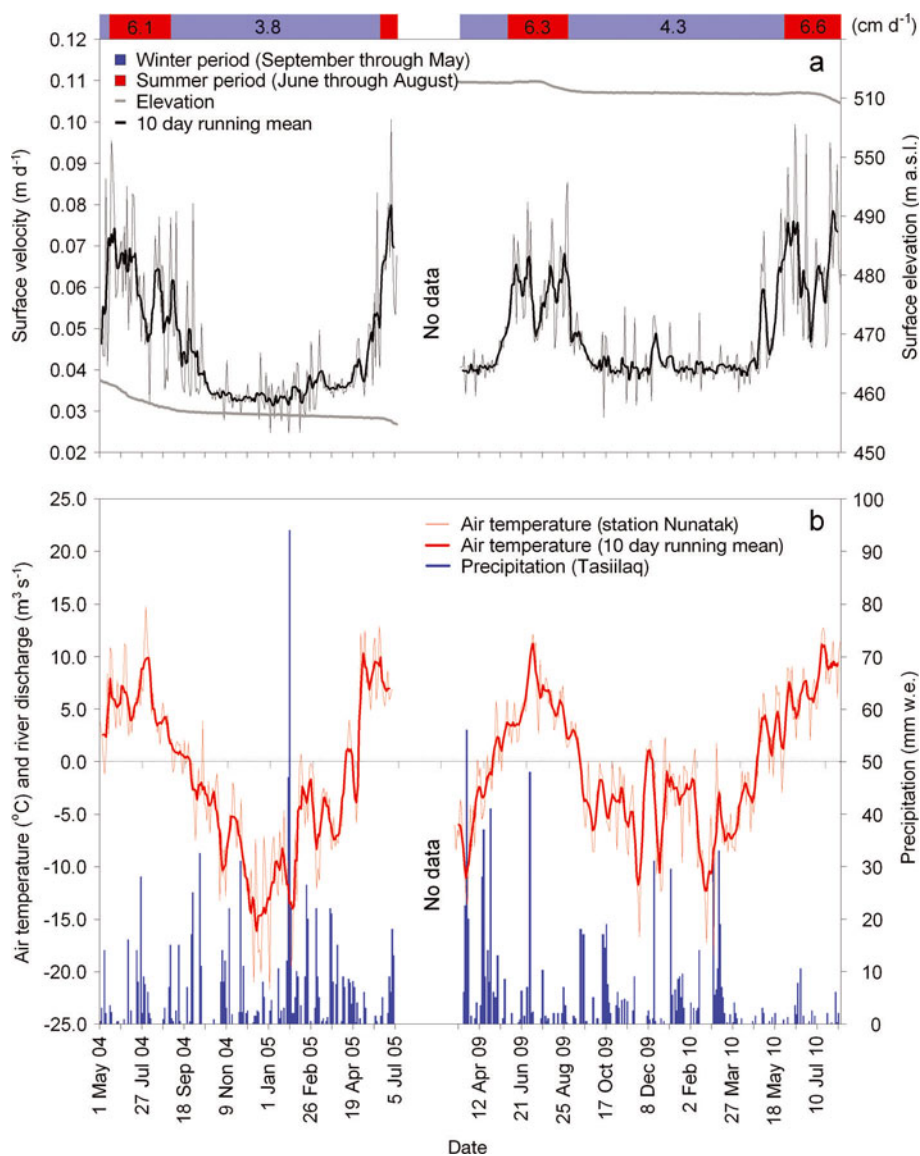


**Fig. 10.** (a) Observed MG seasonal surface velocity at the GPS station. Between 2005 and 2009 the GPS station was moved to a higher elevation on the glacier (see black and white diamonds in Fig. 1 for locations). The mean seasonal surface velocities are also shown, for the winter (September–May; marked with light blue at the top of the figure) and summer (June–August; marked with red). (b) Observed air temperature at station Nunatak and observed precipitation (uncorrected) at station Tasiilaq.

the presence of an efficient subglacial hydrologic system by midsummer. Despite these complex variations in sliding during summer, changes to hydrology over the 15 year study period do not appear to be the primary cause of the observed long-term deceleration (Section 4.3).

## CONCLUSIONS

Direct mass-balance observations from Greenland's peripheral glaciers are rare, and MG is the glacier in Greenland with the longest mass-balance observation time series. We have analyzed spatially distributed winter, summer and annual mass balances and ice surface velocities based on direct observations of MG, along with calculated mean ice thickness and volume changes. We have found unambiguous evidence of ice thinning and slowdown in a warming climate. From 1986 to 2011, surface elevation decreased across the glacier, and the vertical strain rate was able to compensate for  $\sim 50\%$  of the elevation changes due to SMB. We found significant changes in mean ice thickness ( $-15\%$ ),

ice volume ( $-30\%$ ) and mean annual surface velocity ( $-30\%$ ). The decrease in surface velocity was likely a dynamic effect of ice thinning. At the seasonal scale, daily summer surface velocities were 50–60% higher than the winter background values, and up to 160% higher for peak events. The specificity of the MG observations, as presented here, will be crucial for a detailed understanding of the behavior of Greenland's peripheral glaciers, which according to Bjørk and others (2012) and Mernild and others (2012) have exhibited widespread retreat along the southeastern margin of Greenland over the past few decades.

## ACKNOWLEDGEMENTS

We extend a very special thanks to two anonymous reviewers and Mauri Pelto for insightful critique of this paper. This work was partly supported by the Climate Change Prediction Program and by the Scientific Discovery for Advanced Computing (SciDAC) program within the US Department of Energy's Office of Science and by a Los Alamos National

Laboratory (LANL) Director's Fellowship. LANL is operated under the auspices of the National Nuclear Security Administration of the US Department of Energy under contract No. DE-AC52-06NA25396), and partly from the European Community's Seventh Framework Programme under grant agreement No. 262693. We thank the Danish Meteorological Institute for providing World Meteorological Organization synoptic meteorological data from Tasiilaq. N.T.K., S.H.M. and J.C.Y. did the MG mass-balance observations. S.H.M., N.T.K. and M.J.H. planned the study and analyzed the data, S.H.M., M.J.H., N.T.K. and J.C.Y. wrote the manuscript, and J.K.M., W.H.L., E.H. and R.S.F. contributed to the discussion of results and writing of the text.

## REFERENCES

- Anderson RS and 6 others (2004) Strong feedbacks between hydrology and sliding of a small alpine glacier. *J. Geophys. Res.*, **109**(F3), F03005 (doi: 10.1029/2004JF000120)
- Bahr DB (2011) Estimation of glacier volume and volume change by scaling methods. In Singh VP, Singh P and Haritashya UK eds. *Encyclopedia of snow, ice and glaciers*. Springer, Dordrecht
- Bartholomew TC, Anderson RS and Anderson SP (2008) Response of glacier basal motion to transient water storage. *Nature Geosci.*, **1**(1), 33–37 (doi: 10.1038/ngeo.2007.52)
- Bartholomew I, Nienow P, Mair D, Hubbard A, King MA and Sole A (2010) Seasonal evolution of subglacial drainage and acceleration in a Greenland outlet glacier. *Nature Geosci.*, **3**(6), 408–411 (doi: 10.1038/ngeo863)
- Bindschadler R (1983) The importance of pressurized subglacial water in separation and sliding at the glacier bed. *J. Glaciol.*, **29**(101), 3–19
- Bingham RG, Nienow PW and Sharp MJ (2003) Intra-annual and intra-seasonal flow dynamics of a High Arctic polythermal valley glacier. *Ann. Glaciol.*, **37**, 181–188 (doi: 10.3189/172756403781815762)
- Bjørk AA and 8 others (2012) An aerial view of 80 years of climate-related glacier fluctuations in southeast Greenland. *Nature Geosci.*, **5**(6), 427–432 (doi: 10.1038/ngeo1481)
- Born EW and Böcher J (2001) *The ecology of Greenland*. Ministry of Environment and Natural Resources, Greenland, Nuuk
- Carstensen LS and Jørgensen BV (2011) Weather and climate data from Greenland 1958–2010. (DMI Tech. Rep. 11-10) Danish Meteorological Institute, Copenhagen
- Clarke GKC (2005) Subglacial processes. *Annu. Rev. Earth Planet. Sci.*, **33**, 247–276 (doi: 10.1146/annurev.earth.33.092203.122621)
- Cogley JG (2012) The future of the world's glaciers. In Henderson-Sellers A and MacGuffie K eds. *The future of the world's climate*. Elsevier, Waltham, MA, 197–222
- Cogley JG and Adams WP (1998) Mass balance of glaciers other than the ice sheets. *J. Glaciol.*, **44**(147), 315–325
- Cuffey KM and Paterson WSB (2010) *The physics of glaciers*, 4th edn. Butterworth-Heinemann, Oxford
- Hanna E and 8 others (2008) Increased runoff from melt from the Greenland Ice Sheet: a response to global warming. *J. Climate*, **21**(2), 331–341
- Hanna E and 6 others (2012a) The influence of North Atlantic atmospheric and oceanic forcing effects on 1900–2010 Greenland summer climate and ice melt/runoff. *Int. J. Climatol.*, **33**(4), 862–880 (doi: 10.1002/joc.3475)
- Hanna E, Mernild SH, Cappelen J and Steffen K (2012b) Recent warming in Greenland in a long-term instrumental (1881–2012) climatic context: I. Evaluation of surface air temperature records. *Environ. Res. Lett.*, **7**(4), 045404 (doi: 10.1088/1748-9326/7/4/045404)
- Hoffman MJ, Catania GA, Neumann TA, Andrews LC and Rumrill JA (2011) Links between acceleration, melting, and supraglacial lake drainage of the western Greenland Ice Sheet. *J. Geophys. Res.*, **116**(F4), F04035 (doi: 10.1029/2010JF001934)
- Howat IM, Tulaczyk S, Waddington E and Björnsson H (2008) Dynamic controls on glacier basal motion inferred from surface ice motion. *J. Geophys. Res.*, **113**(F3), F03015 (doi: 10.1029/2007JF000925)
- Hutter K (1983) *Theoretical glaciology; material science of ice and the mechanics of glaciers and ice sheets*. D. Reidel, Dordrecht/Terra Scientific, Tokyo
- Iken A, Röthlisberger H, Flotron A and Haeberli W (1983) The uplift of Unteraargletscher at the beginning of the melt season – a consequence of water storage at the bed? *J. Glaciol.*, **29**(101), 28–47
- Jacob T, Wahr J, Pfeffer WT and Swenson S (2012) Recent contributions of glaciers and ice caps to sea level rise. *Nature*, **482**(7386), 514–518 (doi: 10.1038/nature10847)
- Kargel JS and 15 others (2012) Brief communication: Greenland's shrinking ice cover: 'fast times' but not that fast. *Cryosphere*, **6**(3), 533–537 (doi: 10.5194/tc-6-533-2012)
- Kaser G, Cogley JG, Dyurgerov MB, Meier MF and Ohmura A (2006) Mass balance of glaciers and ice caps: consensus estimates for 1961–2004. *Geophys. Res. Lett.*, **33**(19), L19501 (doi: 10.1029/2006GL027511)
- Knudsen NT and Hasholt B (1999) Radio-echo sounding at the Mittivakkat Gletscher, southeast Greenland. *Arct. Antarct. Alp. Res.*, **31**(3), 321–328
- Knudsen NT and Hasholt B (2004) Mass balance observations at Mittivakkat Gletscher, Southeast Greenland 1995–2002. *Nord. Hydrol.*, **35**(4), 381–390
- Knudsen NT, Nønborg P, Yde JC, Hasholt B and Heinemeier J (2008) Recent marginal changes of the Mittivakkat Glacier, Southeast Greenland and the discovery of remains of reindeer (*Rangifer tarandus*), polar bear (*Ursus maritimus*) and peaty material. *Geogr. Tidsskr.*, **108**(1), 137–142
- Leclercq PW and Oerlemans J (2012) Global and hemispheric temperature reconstruction from glacier length fluctuations. *Climate Dyn.*, **38**(5–6), 1065–1079 (doi: 10.1007/s00382-011-1145-7)
- Marzeion B, Jarosch AH and Hofer M (2012) Past and future sea-level change from the surface mass balance of glaciers. *Cryosphere*, **6**(6), 1295–1322 (doi: 10.5194/tc-6-1295-2012)
- Meier MF and 7 others (2007) Glaciers dominate eustatic sea-level rise in the 21st century. *Science*, **317**(5841), 1064–1067 (doi: 10.1126/science.1143906)
- Mernild SH and Hasholt B (2006) Climatic control on river discharge simulations, Mittivakkat Glacier catchment, Ammassalik Island, SE Greenland. *Nord. Hydrol.*, **37**(4–5), 327–346 (doi: 10.2166/nh.2006.018)
- Mernild SH and Hasholt B (2009) Observed runoff, jökulhlaups and suspended sediment load from the Greenland ice sheet at Kangerlussuaq, West Greenland, 2007 and 2008. *J. Glaciol.*, **55**(193), 855–858 (doi: 10.3189/002214309790152465)
- Mernild SH and Liston GE (2012) Greenland freshwater runoff. Part II: distribution and trends 1960–2010. *J. Climate*, **25**(17), 6015–6035 (doi: 10.1175/JCLI-D-11-00592.1)
- Mernild SH, Liston GE, Hasholt B and Knudsen NT (2006) Snow distribution and melt modeling for Mittivakkat Glacier, Ammassalik Island, Southeast Greenland. *J. Hydromet.*, **7**(4), 808–824 (doi: 10.1175/JHM522.1)
- Mernild SH, Hansen BU, Jakobsen BH and Hasholt B (2008a) Climatic conditions at the Mittivakkat Glacier catchment (1994–2006), Ammassalik Island, SE Greenland, and in a 109-year perspective (1898–2006). *Geogr. Tidsskr.*, **108**(1), 51–72
- Mernild SH, Liston GE, Kane DL, Hasholt B and Knudsen NT (2008b) Spatial snow distribution, runoff, and mass balance modelling for entire Mittivakkat Glacier (1998–2006), Ammassalik Island, SE Greenland. *Geogr. Tidsskr.*, **108**(1), 121–136 (doi: 10.1080/00167223.2008.10649578)
- Mernild SH, Kane DL, Hansen BU, Jakobsen BH, Hasholt B and Knudsen NT (2008c) Climate, glacier mass balance and runoff

- (1993–2005) for the Mittivakkat Glacier catchment, Ammassalik Island, SE Greenland, and in a long term perspective (1898–1993). *Hydrol. Res.*, **39**(4), 239–256 (doi: 10.2166/nh.2008.101)
- Mernild SH, Liston GE, Steffen K, Van den Broeke M and Hasholt B (2010) Runoff and mass-balance simulations from the Greenland Ice Sheet at Kangerlussuaq (Søndre Strømfjord) in a 30-year perspective, 1979–2008. *Cryosphere*, **4**(2), 231–242 (doi: 10.5194/tc-4-231-2010)
- Mernild SH and 6 others (2011a) Increasing mass loss from Greenland's Mittivakkat Gletscher. *Cryosphere*, **5**(2), 341–348 (doi: 10.5194/tc-5-341-2011)
- Mernild SH, Knudsen NT and Hanna E (2011b) Mittivakkat Gletscher, SE Greenland. In Richter-Menge J, Jeffries MO and Overland JE eds. *Arctic Report Card*. (NOAA Report 2011) National Oceanic and Atmospheric Administration, Washington, DC <http://www.arctic.noaa.gov/report11>
- Mernild SH, Malmros JK, Yde JC and Knudsen NT (2012) Multi-decadal marine- and land-terminating glacier recession in the Ammassalik region, southeast Greenland. *Cryosphere*, **6**(3), 625–639 (doi: 10.5194/tc-6-625-2012)
- Mernild SH, Pelto MS, Malmros JK, Yde JC, Knudsen NT and Hanna E (2013) Identification of ablation rate, ELA, AAR and net mass balance using transient snowline variations on two Arctic glaciers. *J. Glaciol.*, **59**(216), 649–659
- Müller F and Iken A (1973) Velocity fluctuations and water regime of Arctic valley glaciers. *IASH Publ.* 95 (Symposium at Cambridge 1969 – *Hydrology of Glaciers*), 165–182
- Nienow P, Sharp M and Willis I (1998) Seasonal changes in the morphology of the subglacial drainage system, Haut Glacier d'Arolla, Switzerland. *Earth Surf. Process. Landf.*, **23**(9), 825–843 (doi: 10.1002/(SICI)1096-9837(199809)23:9<825::AID-ESP893>3.0.CO;2-2)
- Oerlemans J, Dyurgerov M and Van de Wal RSW (2007) Reconstructing the glacier contribution to sea-level rise back to 1850. *Cryosphere*, **1**(1), 59–65 (doi: 10.5194/tc-1-59-2007)
- Østrem G and Brugman M (1991) *Glacier mass-balance measurements: a manual for field and office work*. (NHRI Science Report 4) Environment Canada. National Hydrology Research Institute, Saskatoon, Sask.
- Østrem G and Stanley AD (1969) *Glacier mass balance measurements, a manual for field and office work: a guide for personnel with limited backgrounds in glaciology*. Department of the Environment, Inland Waters Branch, Ottawa, Ont.
- Palmer SJ, Shepherd A, Sundal A, Rinne E and Nienow P (2010) InSAR observations of ice elevation and velocity fluctuations at the Flade Isblink ice cap, eastern North Greenland. *J. Geophys. Res.*, **115**(F4), F04037 (doi: 10.1029/2010JF001686)
- Rastner P, Bolch T, Mölg N, Machguth H, Le Bris R and Paul F (2012) The first complete inventory of the local glaciers and ice caps on Greenland. *Cryosphere*, **6**(6), 1483–1495 (doi: 10.5194/tc-6-1483-2012)
- Schoof C (2010) Ice-sheet acceleration driven by melt supply variability. *Nature*, **468**(7325), 803–806 (doi: 10.1038/nature09618)
- Sole AJ and 6 others (2011) Seasonal speedup of a Greenland marine-terminating outlet glacier forced by surface melt-induced changes in subglacial hydrology. *J. Geophys. Res.*, **116**(F3), F03014 (doi: 10.1029/2010JF001948)
- Sundal AV, Shepherd A, Nienow P, Hanna E, Palmer S and Huybrechts P (2011) Melt-induced speed-up of Greenland ice sheet offset by efficient subglacial drainage. *Nature*, **469**(7331), 521–524 (doi: 10.1038/nature09740)
- Truffer M, Harrison WD and March RS (2005) Correspondence. Record negative glacier balances and low velocities during the 2004 heatwave in Alaska, USA: implications for the interpretation of observations by Zwally and others in Greenland. *J. Glaciol.*, **51**(175), 663–664 (doi: 10.3189/172756505781829016)
- Van de Wal RSW and 6 others (2008) Large and rapid melt-induced velocity changes in the ablation zone of the Greenland Ice Sheet. *Science*, **321**(5885), 111–113 (doi: 10.1126/science.1158540)
- Vincent C, Soruco A, Six D and Le Meur E (2009) Glacier thickening and decay analysis from 50 years of glaciological observations performed on Glacier d'Argentière, Mont Blanc area, France. *Ann. Glaciol.*, **50**(50), 73–79 (doi: 10.3189/172756409787769500)
- Weertman J (1957) On the sliding of glaciers. *J. Glaciol.*, **3**(21), 33–38
- Yde JC and Knudsen NT (2007) 20th-century glacier fluctuations on Disko Island (Qeqertarsuaq), Greenland. *Ann. Glaciol.*, **46**, 209–214 (doi: 10.3189/172756407782871558)

MS received 23 January 2013 and accepted in revised form 13 April 2013



[6]

Mernild, S. H., Pelto, M., Malmros, J. K., Yde, J. C., Knudsen, N. T., and Hanna, E. 2013. Identification of ablation rate, ELA, AAR, and net mass balance using transient snowline variations on two Arctic glaciers.

Journal of Glaciology, 59(216), 649–659, doi:10.3189/2013JoG12J221.

Reprinted with permission from International Glaciological Society

# Identification of snow ablation rate, ELA, AAR and net mass balance using transient snowline variations on two Arctic glaciers

Sebastian H. MERNILD,<sup>1,2</sup> Mauri PELTO,<sup>3</sup> Jeppe K. MALMROS,<sup>2</sup> Jacob C. YDE,<sup>4</sup>  
Niels T. KNUDSEN,<sup>5</sup> Edward HANNA<sup>6</sup>

<sup>1</sup>*Climate, Ocean, and Sea Ice Modeling Group, Los Alamos National Laboratory, Los Alamos, NM, USA*

<sup>2</sup>*Glaciology and Climate Change Laboratory, Center for Scientific Studies/Centro de Estudios Científicos (CECs),  
Valdivia, Chile*

*E-mail: mernild@cecs.cl*

<sup>3</sup>*Department of Environmental Science, Nichols College, Dudley, MA, USA*

<sup>4</sup>*Sogn og Fjordane University College, Sogndal, Norway*

<sup>5</sup>*Department of Geoscience, University of Aarhus, Aarhus, Denmark*

<sup>6</sup>*Department of Geography, University of Sheffield, Sheffield, UK*

**ABSTRACT.** Identification of the transient snowline (TSL) from high spatial resolution Landsat imagery on Lemon Creek Glacier (LCG), southeast Alaska, USA, and Mittivakkat Gletscher (MG), southeast Greenland, is used to determine snow ablation rates, the equilibrium-line altitude (ELA) and the accumulation-area ratio (AAR). The rate of rise of the TSL during the ablation season on a glacier where the balance gradient is known provides a measure of the snow ablation rate. On both LCG and MG, snow pits were completed in regions that the TSL subsequently transects. This further provides a direct measure of the snow ablation rates for a particular year. TSL observations from multiple dates during the ablation season from 1998 to 2011 at LCG and 1999 to 2012 at MG were used to explore the consistency of the TSL rise and snow ablation rate. On LCG and MG the satellite-derived mean TSL migration rates were  $3.8 \pm 0.6$  and  $9.4 \pm 9.1 \text{ m d}^{-1}$ , respectively. The snow ablation rates were  $0.028 \pm 0.004 \text{ m w.e. d}^{-1}$  for LCG and  $0.051 \pm 0.018 \text{ m w.e. d}^{-1}$  for MG estimated by applying a TSL–mass-balance-gradient method, and  $0.031 \pm 0.004$  and  $0.047 \pm 0.019 \text{ m w.e. d}^{-1}$  by applying a snow-pit–satellite method, illustrating significant agreement between the two different approaches for both field sites. Also, satellite-derived ELA and AAR, and estimated net mass-balance ( $B_a$ ) conditions were in agreement with observed ELA, AAR and  $B_a$  conditions for LCG and MG.

## 1. INTRODUCTION

There is a strong relationship between annual glacier equilibrium-line altitude (ELA; the ELA is the spatially averaged elevation of the equilibrium line, defined as the set of points on the glacier surface where the annual net mass balance is zero) and net mass balance ( $B_a$ ), and between accumulation-area ratio (AAR: the ratio of the accumulation area to the area of the entire glacier) and  $B_a$  (Dyrgerov, 1996; Hock and others, 2007). For instance, the World Glacier Monitoring Service produces detailed graphs showing the coupling between  $B_a$  and both ELA and AAR on a global scale (WGMS, 2011). Remote-sensing imagery provides a useful tool for identifying the ELA and transient snowline (TSL) in areas where field observations are lacking or on regional scales (Østrem, 1975). The TSL is the location of the transition from snow cover to, for example, bare glacier ice, superimposed ice and firn at a particular time during the ablation season (Østrem, 1975), whereas the ELA is the altitude of the snowline at the end of the ablation season. The transient mass balance (defined as the glacier mass balance from the onset of the accumulation season to a particular time in the following ablation season, and assuming that the specific winter mass balance is not negative anywhere on the glacier) at the TSL is zero (Hock and others, 2007), providing an important reference point for constructing a balance gradient curve. The TSL can be identified near the end of the ablation season using aerial photographs or satellite imagery (Hall

and others, 1989). However, in many years the time-span between available and usable imagery where the TSL is visible at the end of the ablation season can be several weeks. If the migration rate of TSL can be determined along a balance gradient curve and is reasonably consistent, the ELA can be reliably estimated from TSL observations conducted several weeks before the end of the melt season (Pelto, 2011). Observations of TSL from the early part of the ablation season should be excluded from the balance gradient curve because the entire glacier will remain snow-covered (transient AAR=1) until the TSL becomes visible when all snow has melted at one point on the glacier (Hock and others, 2007). The current availability of satellite imagery from many sources ensures coverage late in the ablation season for the most recent years since the early 1990s. Once the AAR– $B_a$  relation is calibrated for a particular glacier, the approach outlined above using TSL–AAR and TSL–ELA observations enables accurate remote monitoring of glacier net mass balance. This is important since glaciers are climate-sensitive, and for understanding and predicting glacier response during climate warming related to, for example, watershed hydrology and global sea-level rise.

Here we explore the capability of satellite imagery to: (1) determine the TSL migration rates throughout the ablation season for two individual glaciers – Lemon Creek Glacier, southeast Alaska, USA (Fig. 1a), and Mittivakkat Gletscher, southeast Greenland (Fig. 1b) – in two different

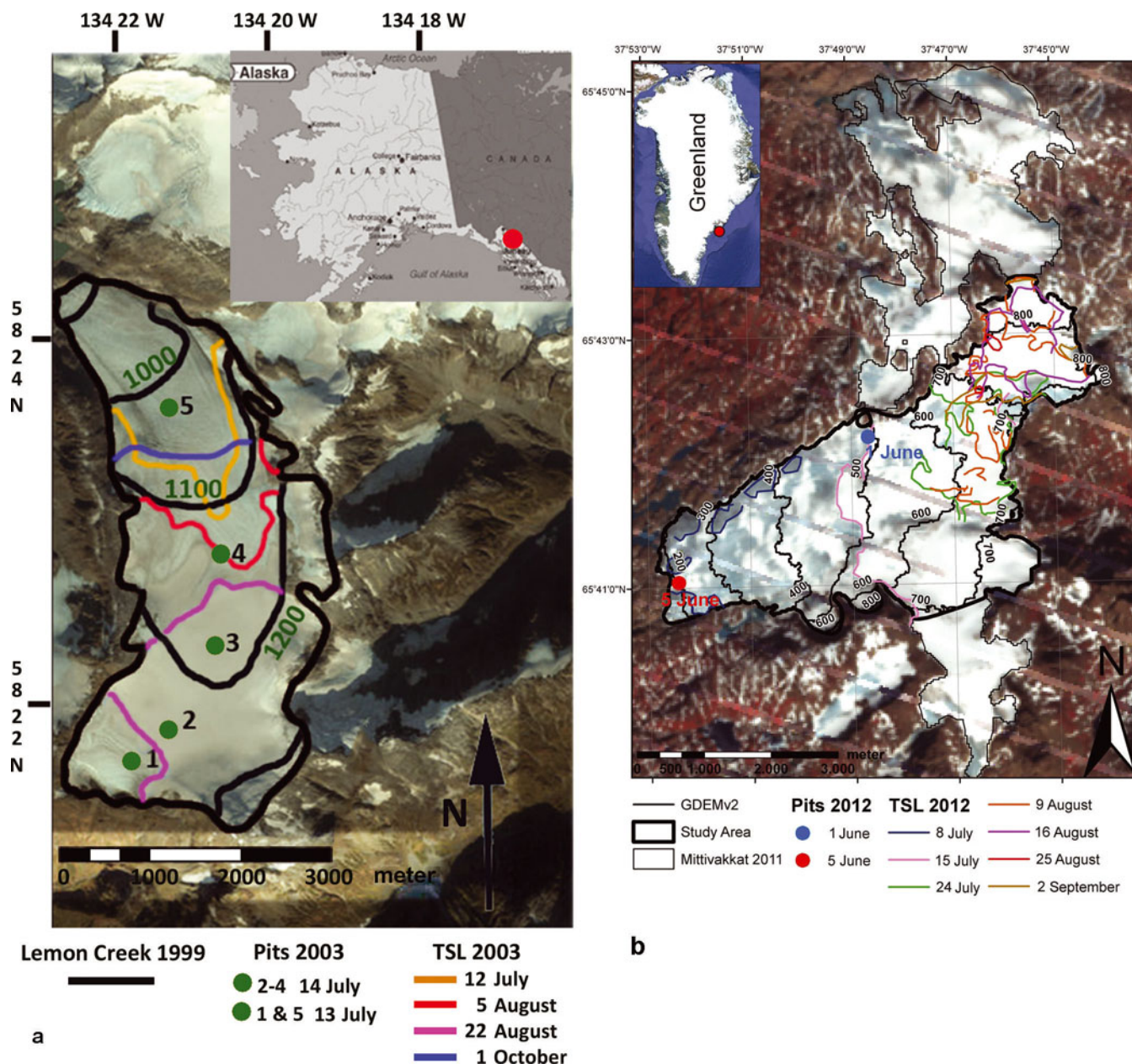


**Fig. 1.** (a) Satellite image of Lemon Creek Glacier (11.6 km<sup>2</sup>) (inset indicates general location of the glacier in southeastern Alaska), with 100 m contour intervals. Green dots (1–5) indicate standard snow-pit locations from 2003, and colored bold lines the seasonal locations of snowlines during the 2003 ablation season. The glacier boundary is for 1999 and estimated from Global Land Ice Measurements from Space (GLIMS; www.glims.org). (b) Satellite image of Mittivakkat Gletscher (26.2 km<sup>2</sup> in total in 2011, and 15.9 km<sup>2</sup> for the observed  $B_a$  study area) (inset indicates general location of the glacier in southeast Greenland), with 100 m contour intervals. The red and the blue dots indicate an example of snow-pit locations from 2012, and the colored bold lines the seasonal locations of snowlines during the 2012 ablation season. The glacier boundary is based on Landsat 7 ETM+ Mosaic imagery (1 August 2009 and 14 August 2011).

Arctic climate settings; (2) estimate snow ablation rates; (3) reconstruct elevation of the ELA based on the TSL–ELA relation; (4) estimate AAR conditions; (5) reconstruct observed  $B_a$  based on a satellite-derived AAR– $B_a$  relation; and (6) estimate the out-of-equilibrium conditions with the present-day climate. At both glaciers, detailed  $B_a$  measurements have been conducted for many years (Miller and Pelto, 1999; WGMS, 2011; Mernild and others, 2012). These data, including the mass-balance gradients and the TSL migration rate (henceforth the *TSL–mass-balance-gradient method*), have been validated by snow ablation rates calculated from snow-pit data (henceforth the *snow-pit–satellite method*) (see Section 3).

## 2. STUDY AREAS

### Lemon Creek Glacier

Lemon Creek Glacier (LCG; 11.6 km<sup>2</sup>; 58°23' N, 134°24' W) is located in the Juneau Icefield in the Coast Range of southeast Alaska (Fig. 1a), and is a temperate valley glacier (Marcus and others, 1995). The  $B_a$  of the LCG has been monitored since 1953 by the Juneau Icefield Research Program (JIRP) (Pelto and Miller, 1990). LCG extends from 820 to 1400 m a.s.l. From the head of the glacier to the mean ELA at 1050–1100 m a.s.l. (1998–2010) (WGMS, 2011) (annual variations in ELA are illustrated in Fig. 2a), the glacier flows northward, and in the ablation zone it turns

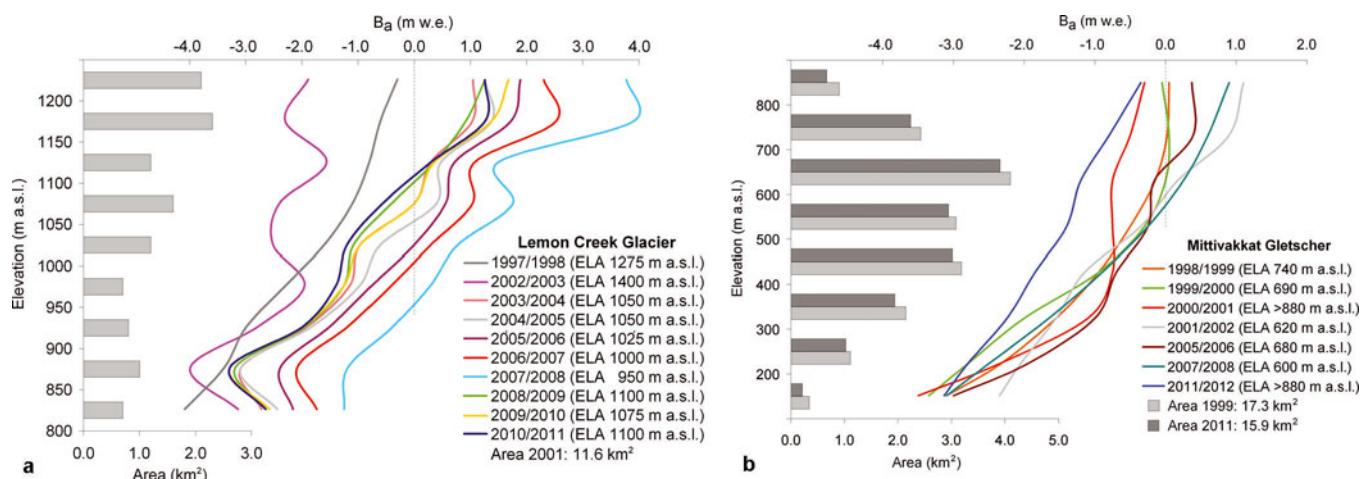


**Fig. 2.** (a) Area elevation band distribution for 2001 derived from Landsat ETM+ Mosaic and observed balance gradients of LCG for 1997/98, 2002/03, 2003/04, 2004/05, 2005/06, 2006/07, 2007/08, 2008/09, 2009/10 and 2010/11, the same years when Landsat TM imagery was obtained to estimate TSL trends (Table 2). (b) Area elevation band distribution for 1999 and 2011 derived from Landsat 7 ETM+ Mosaic and observed balance gradients of MG for 1998/99, 1999/2000, 2000/01, 2001/02, 2005/06, 2007/08 and 2011/12, the same years when Landsat TM/ETM+ imagery was obtained to estimate TSL trends (Table 3).

westward, terminating at  $\sim 820$  m a.s.l. LCG surface slope changes from  $\sim 4^\circ$  in the accumulation area to  $\sim 18^\circ$  at the termini. The glacier terminus retreated on average  $10\text{--}13$  m  $a^{-1}$  between 1998 and 2009. For LCG the observed  $B_a$  was on average  $-0.44$  m w.e.  $a^{-1}$  from 1953 to 2011 and  $-0.51$  m w.e.  $a^{-1}$  from 1996 to 2011 (Pelto and Miller, 1990; WGMS, 2011); winter and summer balances are not determined separately. LCG is located in a sub-Arctic region of temperate maritime climate, with annual precipitation of  $\sim 3000\text{--}4000$  mm and an average annual air temperature at the ELA of  $-1^\circ\text{C}$ .

### Mittivakkat Gletscher

Mittivakkat Gletscher (MG;  $26.2$  km<sup>2</sup> in 2011;  $65^\circ 41' \text{N}$ ,  $37^\circ 48' \text{W}$ ) is located in the Ammassalik region, southeast Greenland (Fig. 1b), and is a temperate glacier (Knudsen and Hasholt, 1999). It extends from 160 to 880 m a.s.l. Since the end of the Little Ice Age around AD 1900, MG has undergone almost continuous retreat (Knudsen and others, 2008; Mernild and others, 2011a), in which the glacier area decreased by 18% (1986–2011) (Mernild and others, 2012), volume decreased by 30% (1986–2011) (Mernild and others, 2013) and the mean surface slope increased from  $0.095$  m  $m^{-1}$  ( $=5.4^\circ$ ) to  $0.104$  m  $m^{-1}$  ( $5.9^\circ$ ) (1986–2011).

For MG the  $B_a$  has been observed for 17 years since 1995/96, and the winter and summer balances individually for only 11 years ( $B_a$  was measured over the study area:  $17.3$  km<sup>2</sup> in 1999 and  $15.9$  km<sup>2</sup> in 2011).  $B_a$  is  $-1.01 \pm 0.74$  m w.e.  $a^{-1}$  (1995/96 to 2011/12), with a mean winter balance of  $1.16 \pm 0.20$  m w.e.  $a^{-1}$  and a mean summer balance of  $-1.99 \pm 0.40$  m w.e.  $a^{-1}$  (1995/96 to 2001/02, 2004/05 to 2005/06, 2007/08 and 2011/12). In 2010/11,  $B_a$  was at a record setting,  $-2.45$  m w.e.: about two standard deviations below the mean, and  $0.29$  m w.e. more negative than the previous observed record low  $B_a$  in 2009/10 (Mernild and others, 2011b). The loss of  $1.63$  m w.e. in 2011/12 was the fourth highest loss since 1995, and three of the four highest recorded  $B_a$  losses have occurred in the last three years included in this study. Since 1995, the mean ELA has risen from around  $500$  m a.s.l. to  $750$  m a.s.l. (Mernild and others, 2011a updated). Figure 2b shows annual variations in ELA.

MG is considered to be located in the Low Arctic (Born and Böcher, 2001), and in a relatively wet and snowy part of Greenland (Mernild and Liston, 2010). An air temperature analysis reveals that the mean annual air temperature for MG was  $-2.2^\circ\text{C}$  (1993–2011) at  $515$  m a.s.l. (Mernild and others, 2008 updated), and a trend analysis of standard seasonal averages shows the following increases in seasonal air temperature for 1993–2011:  $2.9^\circ\text{C}$  in winter,  $0.9^\circ\text{C}$  in spring,  $2.6^\circ\text{C}$  in summer and  $1.0^\circ\text{C}$  in autumn (Hanna and others, 2012). The mean annual precipitation varied in the range  $1400\text{--}1800$  mm w.e.  $a^{-1}$  (1998–2006) (Mernild and others, 2008).

### 3. METHODS

For LCG and MG, respectively, imagery from the satellite platforms Landsat 5 Thematic Mapper (TM) and Landsat 7 Enhanced TM Plus (ETM+) was selected to estimate TSL migration rates, snow ablation rates, ELA and AAR. Below, specific details are illustrated for sensors, band information, scenes used in the analyses, and uncertainties related to the satellite imagery processing (Table 1).

#### Satellite method at Lemon Creek Glacier

The TSL on LCG is readily identifiable on 34 scenes acquired in 1998 and 2003–11, and visualized using the US Geological Survey (USGS) Globalization Viewer software (Table 1). LCG falls in path/row 58/19 and 57/19; all images are false-color RGB (red, green, blue) composites, bands 3, 4 and 5, with a 2% linear stretch applied. The  $7.5$  min quadrangle digital elevation model (DEM) from the United States Geological Survey was used (further information: <http://eros.usgs.gov/#/Guides/dem>). The TSL is manually digitized for each scene. The exception is when the TSL rises to  $1200$  m a.s.l. or is  $<900$  m a.s.l.: in both cases the surface slopes increase, leading to higher error margins. The satellite images were georeferenced in ArcMap 9.3 using five topographically unique reference points. The five ground control points (GCPs) are part of the benchmark survey network for the Juneau Icefield; their position is determined in the field using rapid static and real-time GPS



**Table 1.** Satellite platforms, sensors, band information and scenes used in the analysis related to the satellite study for Lemon Creek Glacier and Mittivakkat Gletscher

	Lemon Creek Glacier	Mittivakkat Gletscher
Platforms	Landsat 5 and 7	Landsat 5 and 7 Terra
Sensors and bands	Landsat TM and ETM+ (bands 3, 4 and 5)	Landsat TM and ETM+ (bands 2, 3 and 5) ASTER GDEM v2
Ground resolution	30 m	30 m, 15 m panchromatic 30 m
Precision	±15 m (horizontal)	±15 m, 7.5 m panchromatic (horizontal) ~±12.5 m (vertical)
Scenes (survey years and dates)*	LT50580191998211PAC00 LT50580191998259PAC00 LT50580192003193PAC00 LE70580192003217EDC02 LT50570192003234PAC00 LE70570192003274EDC02 LE70570192004197EDC01 LT50570192004221PAC00 LE70570192004229EDC02 LT50570192004237PAC00 LE70570192004245EDC02 LE70570192004293EDC01 LE70580192005222EDC00 LE70570192005167EDC00 LT50570192006210PAC01 LT50570192006258PAC01 LE70580192006289EDC00 LE70580192007196EDC00 LE70580192007228EDC00 LT50570192007245PAC01 LT50570192007261PAC00 LT50570192007277PAC00 LT50570192008184PAC01 LT50570192008232PAC01 LE70570192009194EDC00 LE70580192009217SGS02 LT50580192009241PAC01 LT50580192009257PAC00 LT50570192010189PAC01 LT50580192010228GLC00 LT50580192010260GLC00 LT50580192010276GLC01 LT50570192011192PAC00 LE70580192011255EDC00	LE72300141999211SGS00 LE72310141999250AGS00 LE72320141999193EDC00 LE72320141999241EDC00 LE72310142000173SGS00 LE72310142000253EDC00 LE72320142000228AGS00 epp232r014_7f20010701 LE72310142001271EDC00 LE72320142001182AGS00 LE72320142001214AGS00 LE72310142002210EDC00 LE72320142002217EDC00 LE72310142006205EDC00 LE72320132006244EDC00 LE72320142006180EDC00 LE72320142006244EDC00 LE72320142006260EDC00 LE72310142008227EDC00 LE72310142008275EDC00 LE72320142008170EDC00 LE72320142008202EDC00 LE72310142012190EDC00 LE72320142012197EDC00 LE72310142012206EDC00 LE72310142012222EDC00 LE72320142012229EDC00 LE72310142012238EDC00 LE72320142012245EDC00
TSL elevation error	<±5–15 m (vertical)	<±14.7 m (vertical) –

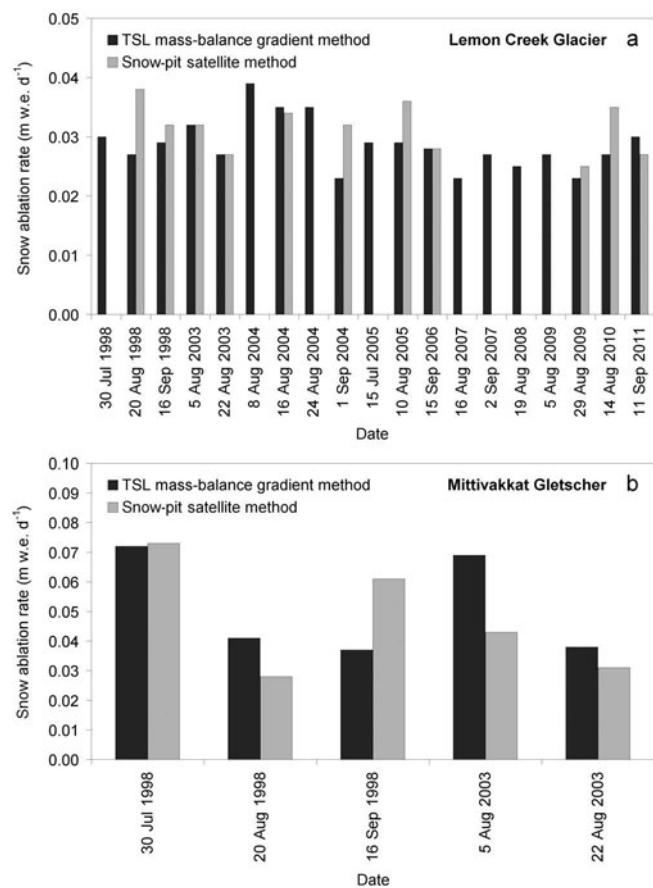
\*Information is inherent in the scene name, for example in LE70580192011255EDC00, with sensor LE7, path 058, row 019, year 2011, Julian day 255 and processing quality notes EDC00.

equipment with an accuracy of 0.01 m horizontally and 0.05 m vertically. The registration errors between the Landsat 5 TM and 7 ETM+ products were 24 m root-mean-square error (RMSE) based on five GCPs. The image spatial resolution of 30 m and the registration of 24 m combined with mean surface gradients of 0.04–0.08 m m<sup>-1</sup> yields an error of ±1–4 m in TSL elevation, with a mean of 1.56 m. The data frame containing imagery and base map was transformed to North American Datum (NAD) 1983, Universal Transverse Mercator (UTM) zone 8N to ensure spatial accuracy for measurements.

### Satellite method at Mittivakkat Gletscher

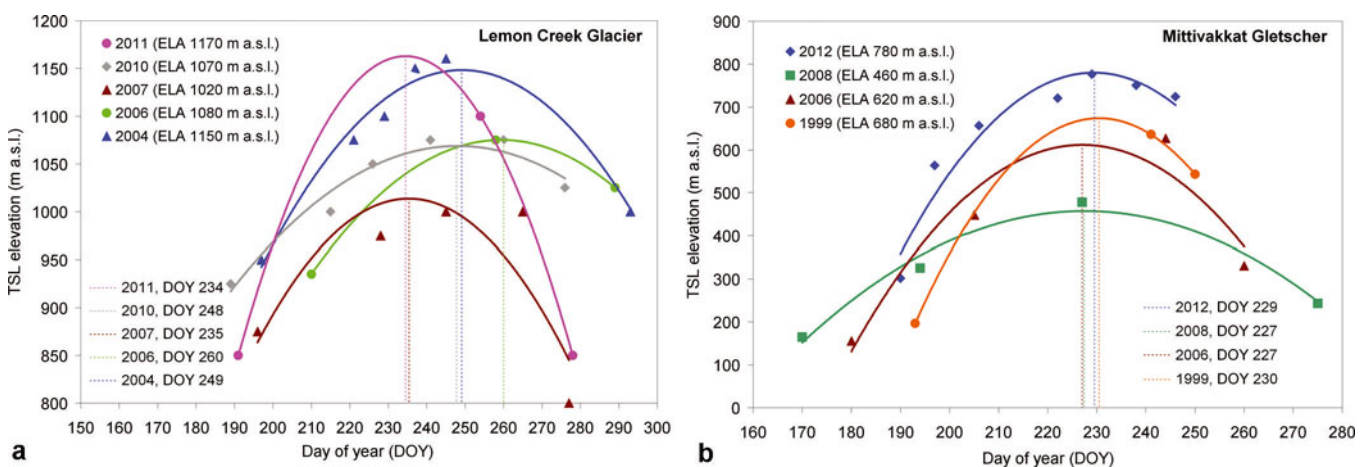
For MG the satellite imagery data were available through the USGS 'EarthExplorer' online database. The area of MG is covered by two Landsat overpasses path/row 231/14 and 232/14. The TSL on MG was identified using imagery from Landsat 5 TM and 7 ETM+ having a ground resolution of 30 m (Table 1). The TSL was manually digitized from the 26 scenes (Table 3, further below) by composing a false-color

image from bands 2, 3 and 5, to maximize the snow-cover contrast in the image. A DEM was extracted from the Advanced Spaceborne Thermal Emission and Reflection Radiometer (ASTER) Global Digital Elevation Model Version 2 (GDEM v2), providing a vertical average precision of ~12 m over Greenland (Tachikawa and others, 2011). The vertical error is expected to be closer to the GDEM v2 standard ±8.7 m precision due to the gentle slope of the majority of the glacier from where the measurements were taken (Tachikawa and others, 2011). The lateral error associated with GDEM v2 is a little more than half a pixel (17 m). ASTER GDEM v2 is a product of the US Ministry of Economy, Trade, and Industry and NASA. The overall registration errors between the Landsat 5 TM and 7 ETM+ products were measured to be 21 m RMSE based on 31 GCPs (first order). The differences between ASTER GDEM v2 and Landsat 5 TM were 22 m RMSE based on 25 GCPs, and between ASTER GDEM v2 and Landsat 7 ETM+ were 20 m RMSE (23 GCPs). The vertical error produced by the registration errors was found to be 1.8–3.1 m, averaging



**Fig. 3.** Estimated snow ablation rates for LCG (a) and MG (b) based on the TSL–mass-balance-gradient method and the snow-pit–satellite method (Tables 2 and 3).

2.2 m, with a spatial resolution of 30 m and mean surface gradients of 0.06–0.10 m m<sup>-1</sup>. The data for MG were projected in World Geodetic System 1984 (WGS84), UTM zone 24N. The accuracy of the Landsat imagery was validated by in situ GPS measurements taken in the field from several years, and all measurements were within half a pixel (15 m) (Mernild and others, 2012).



**Fig. 4.** (a) Satellite-derived LCG TSL elevations throughout five summer periods: 2004, 2006, 2007, 2010 and 2011. Only summer periods are shown from where TSL was estimated by satellite at least three times, including at the beginning of the accumulation season. The ELA is well estimated by TSL observations, except in 2011 when no observations occur within 15 days of the end of the melt season. (b) Satellite-derived MG TSL elevations throughout four summer periods: 1999, 2006, 2008 and 2012. Only summer periods are shown from where TSL was estimated by satellite at least three times, including the beginning of the accumulation season.

## Calculations

For LCG and MG the snow ablation rates were calculated based on both the TSL–mass-balance-gradient method and the snow-pit–satellite method (Fig. 3a and b). For the TSL–mass-balance-gradient method snow ablation rates were calculated from the rise in TSL (Tables 2 and 3), where the TSL migration rates were multiplied with the field-determined balance gradients near the TSL. For the snow-pit–satellite method, the snow ablation rates were calculated based on observed snow loss in snow pits (Tables 2 and 3), where the snow depths were divided by the time interval for the TSL to transect the snow pits. For example, if the snowpack depth on 1 July in a snow pit was 1.4 m w.e., and on 12 August the TSL reached the snow pit, then it took 42 days to ablate 1.4 m w.e. of snow, yielding the snow ablation rate. At LCG, snow-pit excavations were conducted for the years 1998 and 2003–12 (Table 2) and at MG for the years 1999, 2000–02, 2006, 2008 and 2012 (Table 3).

The annual ELAs for LCG and MG were estimated based on second-order polynomial regression between the TSL elevation and the TSL date (remembering that for any specific date of TSL observation the transient mass balance at the TSL is zero), where ELA faces the highest calculated TSL at the end of the ablation season (Fig. 4a and b). In many years the time difference between available and usable imagery where the TSL is visible at the end of the ablation season can be several weeks, which is why the approach of utilizing a second-order polynomial regression is an advantage. The annual AAR was calculated from the estimated ELA. Both glaciers were partitioned into elevation bands (LCG 50 m elevation bands and MG 100 m elevation bands), and the AAR for a given observed year was determined based on the glacier area above and below the ELA: for LCG a fixed area of 11.6 km<sup>2</sup> was used for the entire period, and for MG an assumed linearly decreasing area from 17.3 km<sup>2</sup> (1999) to 15.9 km<sup>2</sup> (2011) was used.

To reconstruct the LCG and MG  $B_a$ , linear regressions between the estimated AAR and observed  $B_a$  were used (for the entire MG the  $B_a$  is considered to be accurate within ~15% (Knudsen and Hasholt, 2004; Mernild and others, 2011a)). A linear regression between the AAR and  $B_a$



**Table 2.** Dates and elevation of TSL observations on LCG. The TSL elevation rate is the mean daily rise in TSL elevation since the previous observation date at least 15 days earlier. Snow-pit depth (SWE) is from the original mid-July excavation on the date indicated; the accumulated snow has completely ablated. Snow ablation rate is the ablation needed to remove the snow-pit accumulation by the observation date

Year	Observation date (number of days between observations)	Mean TSL  m a.s.l.	TSL elevation rate (mean for ablation season, where >1 observation)  m d <sup>-1</sup>	Snow-pit depth, elevation and date	Snow ablation rate	
					TSL–mass-balance- gradient method m w.e. d <sup>-1</sup>	Snow-pit–satellite method m w.e. d <sup>-1</sup>
1998	11 Jul	950 ± 5				
	30 Jul (19)	1025 ± 5	3.9		0.030	
	20 Aug (21)	1100 ± 5	3.6	1.5 m at 1085 m a.s.l. on 11 Jul	0.027	0.038
	16 Sep (27)	1200 ± 10	3.9 (3.8 ± 0.2)	1.8 m at 1200 m a.s.l. on 11 Jul	0.029	0.032
2003	12 Jul	1040 ± 5				
	5 Aug (24)	1110 ± 5	3.3	0.8 m at 1085 m a.s.l. on 11 Jul	0.032	0.032
	22 Aug (17)	1170 ± 5	3.5 (3.4 ± 0.1)	1.0 m at 1160 m a.s.l. on 15 Jul	0.027	0.027
2004	15 Jul	950 ± 5				
	8 Aug (24)	1075 ± 5	5.2		0.039	
	16 Aug (8)	1100 ± 5	4.7	1.3 m at 1085 m a.s.l. on 9 Jul	0.035	0.034
	24 Aug (8)	1150 ± 5	4.7		0.035	
	1 Sep (8)	1160 ± 5	3.1 (2.9 ± 0.9)	1.6 m at 1160 m a.s.l. on 11 Jul	0.023	0.032
2005	19 Oct (48)	1000 ± 5	-3.3			
	18 Jun	850 ± 5				
	15 Jul (27)	960 ± 5	3.9		0.029	
2006	10 Aug (26)	1050 ± 5	3.9 (3.9 ± 0.0)	1.3 m at 1070 m a.s.l. on 5 Jul	0.029	0.036
	29 Jul	935 ± 5				
2007	15 Sep (48)	1075 ± 5	3.0	2.0 m at 1070 m a.s.l. on 12 Jul	0.028	0.028
	16 Oct (31)	1025 ± 5	-1.6			
	15 Jul	875 ± 5				
2008	16 Aug (32)	975 ± 5	3.1		0.023	
	2 Sep (17)	1000 ± 5			0.027	
	22 Sep (20)	1000 ± 5				
	4 Oct (12)	800 ± 15	-15.4			
	2 Jul	800 ± 5				
2009	19 Aug (48)	925 ± 5	3.4		0.025	
	13 Jul	900 ± 5				
	5 Aug (23)	975 ± 5	3.6		0.027	
2010	29 Aug (24)	1050 ± 5	3.0 (3.3 ± 0.4)	1.2 m at 1025 m a.s.l. on 12 Jul	0.023	0.025
	14 Sep (16)	1060 ± 5				
	8 Jul	925 ± 5				
	3 Aug (26)	1000 ± 5	3.8			
2011	14 Aug (11)	1050 ± 5		1.2 m at 1025 m a.s.l. on 10 Jul	0.027	0.035
	29 Aug (15)	1075 ± 5				
	17 Sep (19)	1075 ± 5				
	3 Oct (16)	1025 ± 5	-3.1			
	10 Jul	850 ± 5				
2011	11 Sep (63)	1100 ± 5	4.0	1.8 m at 1085 m a.s.l. on 4 Jul	0.030	0.027
	5 Oct (24)	850 ± 15	-10.0			
Average	–	–	3.8 ± 0.6*	–	0.028 ± 0.004 <sup>†</sup>	0.031 ± 0.004

\*Mean TSL elevation rate was calculated based on positive rates.

<sup>†</sup>Average and standard deviations were only calculated for years with data available from both glaciers.

gives the relation

$$AAR = s \cdot B_a + AAR_0 \quad (1)$$

where  $s$  is the slope and  $AAR_0$  is the AAR when  $B_a = 0$ . Zero values of AAR were excluded from the regression (only MG experienced years where  $AAR = 0$ ), since AAR and  $B_a$  are not linearly related when net ablation occurs all over the glacier surface (Mernild and others, 2011a). Additional information about the LCG  $B_a$  program and methods is provided by Marcus and others (1995), Sapiano and others (1998) and Miller and Pelto (1999), and about the MG  $B_a$  program by Knudsen and Hasholt (2008) and Mernild and others (2011a).

## 4. RESULTS AND DISCUSSION

### Snow ablation rates and ELA reconstruction

The TSL for LCG was observed for 39 dates during the period that defines 25 time periods during which satellite observations are at least 15 days apart (Table 2). For MG the numbers were 25 dates within 11 time periods (Table 3). For LCG the observed positive TSL migration rates varied from  $2.9 \pm 0.9 \text{ m d}^{-1}$  (for the 2004 ablation season) to  $3.9 \pm 0.0 \text{ m d}^{-1}$  (2005) (having a migration rate of up to  $5.2 \text{ m d}^{-1}$  between subsequent satellite observations), with a mean for all ablation periods of  $3.8 \pm 0.6 \text{ m d}^{-1}$  (positive rates indicate when TSL is moving towards higher elevations, and, here

**Table 3.** Dates, mean elevation and standard deviation of satellite-derived TSL on MG. Also shown are observed snow-pit and estimated snow ablation values. Where the TSL elevation rate is negative it indicates that the TSL has moved down-glacier. For the years 2000, 2001, 2002 and 2008, no snow ablation rates are estimated, either because of an insufficient number of snow pits or no available Landsat imagery for estimating TSL

Year	Observation date (number of days between observations)	Mean TSL  m a.s.l.	TSL elevation rate (mean for ablation season, where >1 observation)  m d <sup>-1</sup>	Snow-pit depth, elevation and date	Snow ablation rate	
					TSL–mass-balance- gradient method m w.e. d <sup>-1</sup>	Snow-pit–satellite method m w.e. d <sup>-1</sup>
1999	12 Jul	197 ± 35		3.64 m at 270 m a.s.l. on 31 May	0.072	0.073
	29 Aug (48)	636 ± 61	9.2	2.16 m at 483 m a.s.l. on 27 May	0.041	0.028
	7 Sep (9)	544 ± 24	-10.3	2.60 m at 670 m a.s.l. on 28 May		
2000	21 Jun	159 ± 29		3.88 m at 519 m a.s.l. on 27 May	0.037	0.061
	15 Aug (55)	477 ± 27	5.7			
2001	9 Sep (25)	613 ± 34	5.5 (5.6 ± 0.1)			
	1 Jul	287 ± 16		1.42 m at 225 m a.s.l. on 30 May		
2002	2 Aug (32)	472 ± 25	5.6	2.64 m at 510 m a.s.l. on 29 May		
	27 Jul	490 ± 22		2.27 m at 185 m a.s.l. on 29 May		
2006	5 Aug (9)	486 ± 26	-0.5	2.50 m at 500 m a.s.l. on 26 May		
	29 Jun	156 ± 23		1.20 m at 209 m a.s.l. on 6 Jun	0.069	0.043
	24 Jul (25)	449 ± 20	11.6			
2008	1 Sep (39)	627 ± 41	4.6 (8.1 ± 5.0)			
	17 Sep (16)	332 ± 29	-18.4			
	18 Jun	165 ± 28				
	12 Jul (24)	326 ± 13	6.7			
2012	14 Aug (33)	479 ± 28	4.6 (5.7 ± 1.5)			
	1 Oct (48)	244 ± 20	-5.3			
	8 Jul	302 ± 75		1.88 m at 199 m a.s.l. on 5 Jun		
	15 Jul (7)	563 ± 94	37.3	1.32 m at 496 m a.s.l. on 1 Jun	0.038	0.031
	24 Jul (9)	657 ± 51	10.5			
Average			9.4 ± 9.1*		0.051 ± 0.018	0.047 ± 0.019

\*Mean TSL elevation rate was calculated based on positive rates.

and below, ± is stated as plus or minus one standard deviation). At the beginning of the accumulation season, negative LCG TSL migration rates occurred within the range -1.6 to -15.4 m d<sup>-1</sup> (Table 2), indicating a lowering in the TSL elevation between September and October. The mean TSL migration rate on LCG of 3.8 m d<sup>-1</sup> compares well with the mean migration rate of 3.7 m d<sup>-1</sup> on nearby Taku Glacier (Pelto, 2011), a temperate maritime valley glacier located in the Juneau Icefield (671 km<sup>2</sup>; 58.4° N, 134.1° W), ~20 km to the northeast of LCG. The larger area of Taku Glacier allows the use of high temporal resolution Moderate Resolution Imaging Spectroradiometer (MODIS) imagery for accurate TSL identification. This provides additional dates closer to the end of the ablation season, and allows application of the TSL migration rate for well-constrained estimates of the snow ablation rates and the location (elevation) and date of the annual ELA.

For MG the observed positive TSL migration rates varied from 5.6 ± 0.1 m d<sup>-1</sup> (for the 2000 ablation season) to 14.9 ± 15.1 m d<sup>-1</sup> (2012) (having a migration rate up of to 37.3 m d<sup>-1</sup> between subsequent satellite observations), with a mean for all ablation periods of 9.4 ± 9.1 m d<sup>-1</sup> (Table 3). At the beginning of the MG accumulation season, from the end of August to September/October, TSL migration rates ranged from -0.5 to -18.4 m d<sup>-1</sup>, illustrating the lowering rate of the TSL (Table 3). The TSL migration rate was used to determine

snow ablation rates using both methods: the TSL–mass-balance-gradient method and the snow-pit–satellite method (see Section 3). For LCG, based on the TSL–mass-balance method, the snow ablation rates varied from 0.023 to 0.039 m w.e. d<sup>-1</sup>, averaging 0.028 ± 0.004 m w.e. d<sup>-1</sup>, whereas snow ablation rates based on the snow-pit–satellite method varied from 0.025 to 0.038 m w.e. d<sup>-1</sup>, averaging 0.031 ± 0.004 m w.e. d<sup>-1</sup> (Fig. 3a; Table 2). The JIRP ablation measurements for LCG during the 2004–10 ablation seasons, over a total period of 162 days, yield a mean snow ablation rate of 0.031 m w.e. d<sup>-1</sup>, which is in accordance with calculations: the estimated snow ablation rates for LCG were significantly identical (97.5% quartile; based on the null hypothesis). The similarity of the TSL and field snow ablation rates supports the concept that remote-sensing TSL observations (which can be extended over longer time periods and are not simple point measurements), together with field snow-pit observations, offer a useful approach for estimating annual ablation rates, which are important in assessing changes in glacier mass balance in the Juneau Icefield region.

For MG the snow ablation rates showed more variability than for LCG, with rates in the range 0.037–0.072 m w.e. d<sup>-1</sup>, averaging 0.051 ± 0.018 m w.e. d<sup>-1</sup> (based on the TSL–mass-balance-gradient method), and 0.028–0.073 m w.e. d<sup>-1</sup>, averaging 0.047 ± 0.019 m w.e. d<sup>-1</sup> (based on the snow-pit–satellite method) (Fig. 3b; Table 3). However, the estimated

**Table 4.** Observed and TSL satellite-derived AAR for LCG (1998–2011) and MG (1999–2012)

Year	LCG		MG	
	Observed AAR (WGMS, 2011 updated)*	TSL satellite-derived AAR*	AAR from mass-balance observations (Mernild and others, 2011b updated)†	TSL satellite-derived AAR‡
1997/98	0.07	–	–	–
1998/99	0.68	–	0.18	0.24
1999/2000	0.82	–	0.05	–
2000/01	0.77	–	0.00	–
2001/02	0.67	–	0.41	–
2002/03	0.05	–	0.75	–
2003/04	0.59	0.28	0.05	–
2004/05	0.61	–	0.00	–
2005/06	0.68	0.47	0.18	0.38
2006/07	0.72	0.63	0.00	–
2007/08	0.80	–	0.41	0.63
2008/09	0.64	–	0.18	–
2009/10	0.50	0.50	0.00	–
2010/11	0.43	0.20	0.00	–
2011/12	–	–	0.00	0.07
Average and std dev.	0.57 ± 0.24 0.58 ± 0.12§	0.42 ± 0.17§	0.16 ± 0.22 0.19 ± 0.17§	0.33 ± 0.24§

\*LCG AAR was estimated based on a fixed area of 11.4 km<sup>2</sup> (2001) (Fig. 2a).

†The observed MG AAR was calculated based on a fixed area of 17.6 km<sup>2</sup>.

‡MG AAR was estimated based on an assumed linearly decreasing area from 17.3 km<sup>2</sup> (1999) to 15.9 km<sup>2</sup> (2011) (Fig. 2b).

§Average and standard deviations were calculated for years where data are available from both glaciers.

snow ablation rates for MG were significantly identical (97.5% quartile; based on the null hypothesis). At MG no direct field snow ablation measurements have been conducted to validate the estimated snow ablation values, but in future mass-balance model simulations the calculated snow ablation rates have the potential to be compared against simulated ablation rates. Mernild and others (2006) presented simulated daily snow and ice melt rates using the modeling software package SnowModel (Liston and Elder, 2006; Mernild and others, 2010; Liston and Mernild, 2012) for the period 1999–2004, and these simulated rates (0.03–0.04 m w.e. d<sup>-1</sup>) were on average slightly lower than the estimated snow ablation rates presented in this study (Fig. 3b). A reason for this could be that the TSL–mass-balance-gradient and snow-pit–satellite methods concern the ablation rate of the snowpack (melt, evaporation and sublimation), whereas SnowModel simulations only include surface melt rates from the snowpack and the bare glacier ice (SnowModel simulations forced by mean daily climate data).

The satellite-derived TSL and dates for LCG and MG provide a dataset for estimating the annual ELA and the date of the end of the ablation season. In Figure 4a and b, seasonal variations of TSL are shown for LCG (2004, 2006, 2007, 2010 and 2011) and MG (1999, 2006, 2008 and 2012). A second-order polynomial regression between the day of year (DOY) and TSL on an annual scale indicates that ELA for LCG varies between 1020 m a.s.l. in 2007 and 1170 m a.s.l. in 2011, and the ablation seasons ended between DOY 234 (22 August) and DOY 260 (17 September) for the years where satellite-derived TSL observations through and beyond the ablation season were available. These estimated ELA conditions for LCG are in accordance with annual fieldwork observations (Fig. 2a), although ELA is overestimated on average by ~50 m a.s.l. compared to direct observations; much of this overestimation occurred from 2011, where no TSL observations were available within

15 days of the end of the melt season. For MG, the estimated annual ELA was located between 460 m a.s.l. (2008) and 780 m a.s.l. (2012), and the ablation season ended between DOY 227 (15 August) and DOY 230 (18 August). The estimated ELA was significantly identical to MG annual field observations (97.5% quartile; based on the null hypothesis), although the estimated ELA was on average underestimated by ~90 m a.s.l. (Fig. 2b), giving reason to believe that the method presented here is useful for ELA estimations at both MG and LCG. For the years 1999, 2006, 2008 and 2012 the MG ablation season ended within 3–4 days in mid-August. At MG the  $B_a$  observations are conducted in early/mid-August, which seems to be a good time for capturing the majority of the ablation season (at least for the four years 1999, 2006, 2008 and 2012 as illustrated in Fig. 4b); however, surface melt occurred considerably later in particular years (e.g. until late October in 2010 and late September in 2012).

### AAR and $B_a$ reconstruction

AAR varies greatly from one year to another (Table 4); however, for a period long enough to filter out extremes but shorter than the timescale of adjustment to glacier equilibrium, it gives a measure of the health of the glacier (Cogley and others, 2011). For LCG, observed AAR varied between 0.07 (1998) and 0.82 (2000) for the period 1997/98 to 2011/12, averaging  $0.57 \pm 0.24$ , while AAR for MG varied between 0.75 (2003) and 0.00 (e.g. 2012) for the period 1998/99 to 2011/12, averaging  $0.15 \pm 0.22$  (Table 4). MG experienced AAR = 0 six times within the last 14 years, including the three most recent years in this study (2010, 2011 and 2012). According to Dyurgerov and others (2009), glaciers and ice caps in equilibrium with the local climate typically have an AAR of 0.5–0.6, with a global average of  $0.579 \pm 0.009$ . Pelto (2010) identified that glaciers having a frequent AAR = 0 lack a persistent accumulation zone and cannot survive.

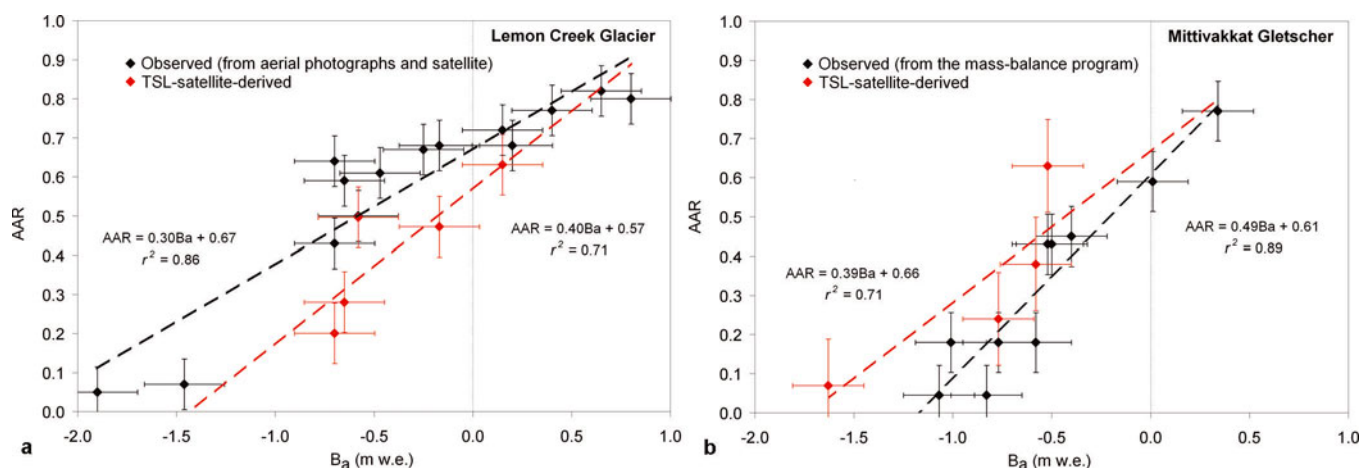


**Fig. 5.** (a) LCG observed AAR and  $B_a$  trend line (dashed black line) from 1997/98 to 2010/11, and TSL satellite-derived AAR and observed  $B_a$  trend line (dashed red line) based on data from 2003/04, 2005/06, 2006/07, 2009/10 and 2010/11. Also illustrated are standard errors for each dataset. (b) MG observed AAR and  $B_a$  trend line (dashed black line) from 1995/96 to 2011/12 (zero values of AAR are excluded from the regression, as AAR and  $B_a$  are only linearly related when ELA is located within the elevation range of the glacier), and TSL satellite-derived AAR and observed  $B_a$  trend line (dashed red line) based on data from 1998/99, 2005/06, 2007/08 and 2011/12. Also illustrated are standard errors for each dataset.

In Table 4, annual TSL satellite-derived AAR values are listed for LCG (2004, 2006, 2007, 2010 and 2011) and MG (1999, 2006, 2008 and 2012) and compared against field observations. For LCG the TSL satellite-derived method on average underestimated AAR by 0.16 (16%) compare to observations, and for MG AAR overestimated on average by 0.14 (14%), but since the respective error bars overlap, there is no significant difference. In Figure 5a and b, TSL satellite-derived AAR is plotted against  $B_a$  for LCG and MG. The TSL satellite-derived AAR  $B_a$  trend lines (red lines) follow observed values and trend lines (black lines). If additional observations are added to the trend lines,  $B_a$  can be substituted by the satellite observations, once sufficient data exist to better constrain late-season TSL behavior and hence annual AAR determination. Based on the LCG satellite-derived AAR and  $AAR_0$  conditions (Fig. 5a), expected changes in the LCG area and volume can be derived from

$$\alpha_r = AAR/AAR_0 \quad (2)$$

the ratio of the current AAR to its equilibrium value. The fractional changes in area ( $p_s$ ) and in volume ( $p_v$ ) are calculated from

$$p_s = \alpha_r - 1 \quad (3)$$

$$p_v = \alpha_r^\gamma - 1 \quad (4)$$

where  $\gamma = 1.36$  for valley glaciers, derived empirically and from theory (Bahr and others, 2009). Based on the LCG trend between the TSL satellite-derived AAR and  $B_a$ , LCG has an estimated  $AAR_0$  of 0.57 that is comparable to the observed  $AAR_0$  value of 0.67 (Fig. 5a). Dyurgerov and others (2009) computed  $AAR_0$  for 86 glaciers and ice caps by using linear regression between AAR and  $B_a$ , showing an average value of  $0.58 \pm 0.01$ . The resulting LCG AAR (0.42; Table 4) and  $AAR_0$  values (0.57; Fig. 5a) (based on the TSL satellite-derived AAR relationship to  $B_a$ ) indicate that LCG will lose  $26 \pm 3\%$  of its present area and  $34 \pm 3\%$  of its volume typically over several decades or longer if current climate conditions in the region of LCG persist. Based on observed AAR (0.57; Table 4) and  $AAR_0$  (0.67; Fig. 5a), LCG will respectively lose  $15 \pm 1\%$  and  $20 \pm 2\%$ . Similar area and

volume fraction calculations were conducted for MG, indicating that MG based on the TSL satellite-derived AAR (0.33; Table 4) and  $AAR_0$  (0.66; Fig. 5b) will lose about  $50 \pm 6\%$  of its present area and  $61 \pm 5\%$  of its volume if current climate conditions in southeast Greenland persist. MG is significantly out of balance with climate, and far below the global AAR mean, and will likely lose a significant amount of its current area and volume even in the absence of further climate changes. Based on  $\alpha_r$  calculations from observations in Mernild and others (2011a) ( $AAR = 0.16$  (Table 4) and  $AAR_0 = 0.61$  (Fig. 5b)), MG will lose  $74 \pm 8\%$  of its current area and  $84 \pm 7\%$  of its volume over several decades or longer if current climate conditions persist. For both glaciers the satellite-estimated fractional area and volume losses seem to point out the extent to which the glaciers are out of balance with present-day climate observations.

An expansion of the study by adding satellite-derived annual glacier conditions, i.e. ELA, AAR and  $B_a$ , is desirable to better quantify the presented relationships, to increase accuracy and further validate the findings at LCG and MG. Also, so-called 'transient' area-averaged mass balances can be computed and related to concurrent transient ELA and AAR values; this method assumes that the relationship between transient values of mass balance and ELA and AAR in the course of one season is identical to the relationship between  $B_a$  and ELA and AAR at the end of the mass-balance year over many years (Hock and others, 2007).

## 5. CONCLUSIONS

Snow ablation rates determined from observations of TSL migration by Landsat imagery and the balance gradient (from the TSL-mass-balance-gradient method) agree significantly with field measurements of snow ablation using stakes and snowpack loss identified directly at snow-pit locations from TSL variation (from the snow-pit-satellite method), varying on average in the ranges 0.028–0.031 and 0.047–0.051 m w.e. d<sup>-1</sup> for LCG and MG, respectively. This supports the utility of using TSL observations to estimate ELA

and AAR conditions on LCG and MG, but also at seasonal scale for LCG and MG if a relationship between transient mass balance, ELA and AAR values occurs. It is likely this will be useful for assessing nearby glaciers where field data are lacking but which share a similar rate of TSL rise, as this would indicate a similar balance gradient, which is not unusual for glaciers in the same climate setting (Braithwaite and Raper, 2007). For LCG the estimated ELA varied between 1020 and 1170 m a.s.l., and for MG between 480 and 780 m a.s.l. For both glaciers the estimated ELA and AAR were in accordance with annual fieldwork observations, indicating that the method presented here is useful for ELA and AAR estimations, but also for estimating out-of-balance conditions, where MG is significantly out of balance with present-day climate, and LCG less so.

## ACKNOWLEDGEMENTS

This work was supported by the Earth System Modeling program and by the Scientific Discovery for Advanced Computing (SciDAC) program within the US Department of Energy's Office of Science and by a Los Alamos National Laboratory (LANL) Director's Fellowship. LANL is operated under the auspices of the National Nuclear Security Administration of the US Department of Energy under contract No. DE-AC52-06NA25396, and partly from the European Community's Seventh Framework Programme under grant agreement No. 262693. The LCG mass-balance data would not exist without the leadership of JIRP directors Maynard Miller, Jay Fleischer and Jeff Kavanaugh. We also thank the May/June 2012 Mittivakkat Gletscher field crew for collecting winter balance and snow-pit data. S.H.M., J.K.M. and M.P. compiled the dataset and analyzed the data, and S.H.M. and M.P. wrote the manuscript. J.C.Y., J.K.M., N.T.K. and E.H. contributed to the discussion of results and writing of the text.

## REFERENCES

- Bahr DB, Dyurgerov M and Meier MF (2009) Sea-level rise from glaciers and ice caps: a lower bound. *Geophys. Res. Lett.*, **36**(3), L03501 (doi: 10.1029/2008GL036309)
- Born EW and Böcher J (2001) *The ecology of Greenland*. Ministry of Environment and Natural Resources, Greenland, Nuuk
- Braithwaite RJ and Raper SCB (2007) Glaciological conditions in seven contrasting regions estimated with the degree-day model. *Ann. Glaciol.*, **46**, 297–302 (doi: 10.3189/172756407782871206)
- Cogley JG and 10 others (2011) *Glossary of glacier mass balance and related terms*. (IHP-VII Technical Documents in Hydrology 86) UNESCO–International Hydrological Programme, Paris
- Dyurgerov M (1996) Substitution of long-term mass balance data by measurements of one summer. *Z. Gletscherkd. Glazialgeol.*, **32**, 177–184
- Dyurgerov M, Meier MF and Bahr DB (2009) A new index of glacier area change: a tool for glacier monitoring. *J. Glaciol.*, **55**(192), 710–716 (doi: 10.3189/002214309789471030)
- Hall DK, Chang ATC, Foster JL, Benson CS and Kovalick WM (1989) Comparison of *in situ* and Landsat derived reflectance of Alaskan glaciers. *Remote Sens. Environ.*, **28**, 23–31 (doi: 10.1016/0034-4257(89)90102-8)
- Hanna E, Mernild SH, Cappelen J and Steffen K (2012) Recent warming in Greenland in a long-term instrumental (1881–2012) climatic context: I. Evaluation of surface air temperature records. *Environ. Res. Lett.*, **7**(4), 045404 (doi: 10.1088/1748-9326/7/4/045404)
- Hock R, Kootstra D-S and Reijmer C (2007) Deriving glacier mass balance from accumulation area ratio on Storglaciären, Sweden. *IAHS Publ.* 318 (Symposium at Foz do Iguaçu 2005 – *Glacier Mass Balance Changes and Meltwater Discharge*), 163–170
- Knudsen NT and Hasholt B (1999) Radio-echo sounding at the Mittivakkat Gletscher, southeast Greenland. *Arct. Antarct. Alp. Res.*, **31**(3), 321–328
- Knudsen NT and Hasholt B (2008) Mass balance observations at Mittivakkat Gletscher, Southeast Greenland 1995–2006. *Geogr. Tidsskr.*, **108**(1), 111–120
- Knudsen NT, Nønborg P, Yde JC, Hasholt B and Heinemeier J (2008) Recent marginal changes of the Mittivakkat Glacier, Southeast Greenland and the discovery of remains of reindeer (*Rangifer tarandus*), polar bear (*Ursus maritimus*) and peaty material. *Geogr. Tidsskr.*, **108**(1), 137–142
- Liston GE and Elder K (2006) A distributed snow-evolution modeling system (SnowModel). *J. Hydromet.*, **7**(6), 1259–1276 (doi: 10.1175/JHM548.1)
- Liston GE and Mernild SH (2012) Greenland freshwater runoff. Part I: a runoff routing model for glaciated and nonglaciated landscapes (HydroFlow). *J. Climate*, **25**(17), 5997–6014 (doi: 10.1175/JCLI-D-11-00591.1)
- Marcus MG, Chambers FB, Miller MM and Lang M (1995) Recent trends in the Lemon Creek Glacier, Alaska. *Phys. Geogr.*, **16**(2), 150–161
- Mernild SH and Liston GE (2010) The influence of air temperature inversions on snow melt and glacier surface mass-balance simulations, Ammassalik Island, Southeast Greenland. *J. Appl. Meteorol. Climatol.*, **49**(1), 47–67 (doi: 10.1175/2009JAMC2065.1)
- Mernild SH, Liston GE, Hasholt B and Knudsen NT (2006) Snow distribution and melt modeling for Mittivakkat Glacier, Ammassalik Island, Southeast Greenland. *J. Hydromet.*, **7**(4), 808–824 (doi: 10.1175/JHM522.1)
- Mernild SH, Hansen BU, Jakobsen BH and Hasholt B (2008) Climatic conditions at the Mittivakkat Glacier catchment (1994–2006), Ammassalik Island, SE Greenland, and in a 109-year perspective (1898–2006). *Geogr. Tidsskr.*, **108**(1), 51–72
- Mernild SH, Liston GE, Steffen K and Chylek P (2010) Meltwater flux and runoff modeling in the ablation area of Jakobshavn Isbræ, West Greenland. *J. Glaciol.*, **56**(195), 20–32 (doi: 10.3189/002214310791190794)
- Mernild SH and 6 others (2011a) Increasing mass loss from Greenland's Mittivakkat Gletscher. *Cryosphere*, **5**(2), 341–348 (doi: 10.5194/tc-5-341-2011)
- Mernild SH, Knudsen NT and Hanna E (2011b) Mittivakkat Gletscher, SE Greenland. In Richter-Menge J, Jeffries MO and Overland JE eds. *Actic Report Card*. (NOAA Report 2011) National Oceanic and Atmospheric Administration, Washington, DC <http://www.arctic.noaa.gov/report11/>
- Mernild SH, Malmros JK, Yde JC and Knudsen NT (2012) Multi-decadal marine- and land-terminating glacier recession in the Ammassalik region, southeast Greenland. *Cryosphere*, **6**(3), 625–639 (doi: 10.5194/tc-6-625-2012)
- Mernild SH and 7 others (2013) Volume and velocity changes at Mittivakkat Gletscher, southeast Greenland. *J. Glaciol.*, **59**(216), 660–670
- Miller MM and Pelto MS (1999) Mass balance measurements on the Lemon Creek Glacier, Juneau Icefield, Alaska 1953–1998. *Geogr. Ann. A*, **81**(4), 671–681
- Østrem G (1975) ERTS data in glaciology – an effort to monitor glacier mass balance from satellite imagery. *J. Glaciol.*, **15**(73), 403–415
- Pelto MS (2010) Forecasting temperate alpine glacier survival from accumulation zone observations. *Cryosphere*, **4**(1), 67–75 (doi: 10.5194/tc-4-67-2010)
- Pelto M (2011) Utility of late summer transient snowline migration rate on Taku Glacier, Alaska. *Cryosphere*, **5**(4), 1127–1133 (doi: 10.5194/tc-5-1127-2011)

Pelto MS and Miller MM (1990) Mass balance of the Taku Glacier, Alaska from 1946 to 1986. *Northwest Sci.*, **64**(3), 121–130

Sapiano JJ, Harrison WD and Echelmeyer KA (1998) Elevation, volume and terminus changes of nine glaciers in North America. *J. Glaciol.*, **44**(146), 119–135

Tachikawa T and 12 others (ASTER GDEM Validation Team) (2011) *ASTER Global Digital Elevation Model Version 2 – summary of validation results*, NASA Land Processes. NASA Distributed

Active Archive Center, Joint Japan–US ASTER Science Team, [http://www.jspacesystems.or.jp/ersdac/GDEM/ver2Validation/Summary\\_GDEM2\\_validation\\_report\\_final.pdf](http://www.jspacesystems.or.jp/ersdac/GDEM/ver2Validation/Summary_GDEM2_validation_report_final.pdf)

World Glacier Monitoring Service (WGMS) (2011) *Glacier Mass Balance Bulletin No. 11 (2008–2009)*, ed. Zemp M, Nussbaumer SU, Gärtner-Roer I, Hoelzle M, Paul F and Haeberli W. ICSU(WDS)/IUGG(IACS)/UNEP/UNESCO/WMO, World Glacier Monitoring Service, Zürich

*MS received 17 November 2012 and accepted in revised form 12 April 2013*



[7]

Mernild, S. H., Malmros, J. K., Yde, J. C., Knudsen, N. T., Wilson, R., Hanna, E., Fausto, R. S., As, Van D. 2014. Albedo decline on Greenlands Mittivakkat Gletscher. International Journal of Climatology, doi: 10.1002/joc.4128.

Reprinted with permission from Wiley

# Albedo decline on Greenland's Mittivakkat Gletscher in a warming climate

Sebastian H. Mernild,<sup>a\*</sup> Jeppe K. Malmros,<sup>a,b</sup> Jacob C. Yde,<sup>c</sup> Ryan Wilson,<sup>a</sup>  
Niels T. Knudsen,<sup>d</sup> Edward Hanna,<sup>e</sup> Robert S. Fausto<sup>f</sup> and Dirk van As<sup>f</sup>

<sup>a</sup> *Glaciology and Climate Change Laboratory, Center for Scientific Studies/Centro de Estudios Científicos (CECs), Valdivia, Chile*

<sup>b</sup> *Department of Geosciences and Natural Resource Management, University of Copenhagen, Denmark*

<sup>c</sup> *Sogn og Fjordane University College, Sogndal, Norway*

<sup>d</sup> *Department of Geoscience, University of Aarhus, Denmark*

<sup>e</sup> *Department of Geography, University of Sheffield, UK*

<sup>f</sup> *Geological Survey of Denmark and Greenland (GEUS), Copenhagen, Denmark*

**ABSTRACT:** Albedo is one of the parameters that govern energy availability for snow and ice surface ablation, and subsequently the surface mass balance conditions of temperate glaciers and ice caps (GIC). Here, we document snow and ice albedo changes for Mittivakkat Gletscher (MG) in Southeast Greenland (2000–2013), for which an 18-year record of direct surface mass balance measurements exists. The MODerate Imaging Spectroradiometer (MODIS MCD43A3) albedo product was used to study MG's snow and ice albedo, evaluated against supraglacial automatic weather station (AWS) observations. In general, by the end of the mass balance year (EBY), MG's AWS observed bare ice albedo reached ~0.3 only just exceeding values observed for proglacial bedrock (~0.2). The analysis reveals negative mean trends in the MODIS-derived MG EBY albedo for the period 2000–2013 with a significant decline in mean glacier-wide albedo of 0.10. The greatest decline in albedo, of 0.25, occurred near the equilibrium line altitude (ELA), an important surface cover and albedo transitional zone. The EBY albedo correlates significantly with ELA and net winter and summer glacier mass balance records.

**KEY WORDS** albedo; Greenland; Mittivakkat Gletscher; MODIS; radiation

*Received 22 February 2013; Revised 18 May 2014; Accepted 14 July 2014*

## 1. Introduction

Surface albedo is defined as the reflected fraction of incoming solar shortwave radiation at the surface (e.g. Dumont *et al.*, 2012). For snow and ice surfaces, spatiotemporal albedo variability governs the energy available for ablation, and subsequently the surface mass balance conditions (e.g. Hock, 2005; Six *et al.*, 2009). The albedo of glaciers and ice caps (GIC) is highly variable in space and time with common values for snow and ice surfaces ranging from ~0.9 for fresh dry snow to ~0.2 for debris-rich ice (e.g. Cuffey and Paterson, 2010, p. 146). Several studies have investigated snow and ice surface albedo conditions and the existence of albedo feedback mechanisms (Dozier *et al.*, 1981; Takeuchi *et al.*, 2001; Liang *et al.*, 2005; Oerlemans *et al.*, 2009; Bøggild *et al.*, 2010; Gardner and Sharp, 2010; Box *et al.*, 2012a, 2012b; Dumont *et al.*, 2012; Stibal *et al.*, 2013; Tedesco *et al.*, 2013; van As *et al.*, 2013; Wright *et al.*, 2014). For these two surface types, temporal changes in albedo have been related to a number of factors. Deposits of black

carbon particles, dust (anthropogenic and/or naturally sourced), and englacial melt-out debris, for example, have been shown to decrease albedo. Snow/ice albedo decreases have also been related to microbial activity (including algae and cyanobacteria), snow grain crystal metamorphism, bare ice exposure, meltwater ponding, precipitation partitioning (fraction of precipitation falling as rain or snow), and variations in the saturation state of the snowpack.

Obtaining systematic albedo ground measurements from snow and ice surfaces can be challenging and time consuming. In this respect, terrestrial/aerial photography and satellite remote sensing have proven to be efficient sources of data (Knap *et al.*, 1999a, 1999b; Klok *et al.*, 2003; Corripio, 2004; Greuell and Oerlemans, 2004, 2005; Liang *et al.*, 2005; Stroeve *et al.*, 2006; Tedesco and Kokhanovsky, 2007; Dozier *et al.*, 2009; Zege *et al.*, 2011; Wright *et al.*, 2014). As an example, the MODerate Imaging Spectroradiometer (MODIS) MOD10A1 and MCD43A albedo products have been used for studies on the Greenland Ice Sheet (GrIS) showing that ice sheet-wide average June–August albedo had declined from 2000 to 2012 (Box *et al.*, 2012a; Stroeve *et al.*, 2013; Tedesco *et al.*, 2013). This decline in area-average albedo may have initiated a positive melt-albedo feedback accelerating mass loss [indicates that the surface became

\* Correspondence to: S. H. Mernild, Glaciology and Climate Change Laboratory, Center for Scientific Studies/Centro de Estudios Científicos (CECs), Av. Arturo Prat 514, 5110466 Valdivia, Chile. E-mail: mernild@cecs.cl

less reflective (i.e. darker) over time: as a consequence, more incoming shortwave solar radiation was absorbed and thus contributing to surface ablation, leading to accelerated mass loss in the melt-albedo feedback]. Wang *et al.* (2012) questioned these findings, attributing the decline in albedo to errors introduced by degrading of the MODIS instrument's sensitivity. However, Box *et al.* (2012b) and Stroeve *et al.* (2013) discounted this problem through comparison of the MODIS MOD10A1 and the MCD43 dataset, respectively, with GC-Net ground truth *in situ* albedo observations distributed across the GrIS (Tedesco *et al.*, 2013).

In Greenland, several thousand GIC exist that are irregularly distributed around the periphery of the ice sheet (Arendt *et al.*, 2012). Similar to the ice sheet itself, these peripheral GIC have undergone dynamic thinning, frontal recession, and mass loss over the past few decades (Jiskoot *et al.*, 2003; Mernild *et al.*, 2006, 2012; Yde and Knudsen, 2007; Kargel *et al.*, 2012). Despite these morphometric changes, GIC albedo conditions and the subsequent links and feedbacks to changes in glacier mass balance and equilibrium line altitude (ELA; the spatially averaged elevation of the equilibrium line, defined as the set of points on the glacier surface where the net mass balance is zero) remain to be examined in detail. Examination of these links is important, as GIC are contributors to eustatic sea-level rise, and regulators of water availability around the world (e.g. Hock *et al.*, 2009; Gardner *et al.*, 2013).

This study provides information about a local glacier in Greenland, the Mittivakkat Gletscher (MG) located in Southeast Greenland (Figure 1), for which mass balance (since 1995) and glacier front observations (since 1900) exist (Mernild *et al.*, 2011). The primary objectives for this study are to quantify and understand: (1) the seasonal variability in albedo based on *in situ* observations (1995–2013) and the albedo's sensitivity to near-surface air temperature and precipitation changes; (2) the spatiotemporal interannual variability of the MODIS-derived albedo for 2000–2013; (3) the annual trends in MG-wide average albedo and the maximum average albedo change; and (4) the statistical relationships between albedo and net mass balance ( $B_a$ ), winter mass balance ( $B_w$ ), summer mass balance ( $B_s$ ), and ELA conditions. Focus will be put on albedo conditions at the end of the mass balance year (EBY), as it is hypothesized that glacier surface albedo at the EBY may provide a valuable proxy for the annual mass balance conditions (e.g. Dumont *et al.*, 2012).

## 2. Study area

MG (26.2 km<sup>2</sup> in 2011; 65°41'N, 37°48'W) is a temperate glacier (Knudsen and Hasholt, 1999) located in the Ammassalik region, Southeast Greenland (Figure 1). Since 1931, MG has been observed at regular intervals by means of field observations, aerial photography, and satellite imagery. From 1931, the glacier terminus has retreated horizontally by ~1300 m (Mernild *et al.*, 2011). MG is currently situated in an elevation range between 160 and

880 m above sea level (a.s.l.) (Figure 1). *In situ*  $B_a$  observations over the study area of 17.3 km<sup>2</sup> (in 2011) have been conducted annually since 1995, and both  $B_w$  and  $B_s$  have been measured for 12 of 18 years. The mean 1995–2013  $B_a$  was  $-0.99 \pm 0.72$  m water equivalent (w.e.) year<sup>-1</sup> (where  $\pm$  henceforth equals one standard deviation) (Mernild *et al.*, 2013a, 2013b), having a significant  $B_a$  trend of  $-0.07$  m w.e. year<sup>-2</sup>. The 1995–2013 MG  $B_w$  and  $B_s$  were  $1.17 \pm 0.20$  and  $-2.00 \pm 0.38$  m w.e. year<sup>-1</sup>, respectively. The negative  $B_a$  is also apparent at the ELA, which has risen from around 500 to 750 m a.s.l. since 1995 (Mernild *et al.*, 2013b).

Surface impurities are mainly observed on the lower part of the MG's ablation zone. They likely originate from windblown sediment, englacially transported debris originally deposited higher up on the glacier, and supraglacial avalanche deposits from the surrounding peaks. They tend to form millimetre- to centimetre-scale aggregates (cryoconite) that melt into the ice and snow surface, creating characteristic cryoconite holes (Figure 2(a)). Similar surface impurities are also observed on the upper accumulation zone but to a lesser extent (Figure 2(b)).

Three automatic weather stations (AWSs) are active in the MG area (Figure 1): Station MIT of the PROMICE network (463–450 m a.s.l. from May 2009 to August 2012, 65°41.6'N; 37°49.5'W–65°41.5'N; 37°49.6'W), Station Nunatak (515 m a.s.l. from March 1995 to November 2007, 65°42.3'N; 37°48.7'W), and Station Coast (25 m a.s.l. from March 1997 to November 2007, 65°40.8'N; 37°55.0'W). The near-surface mean annual air temperature (MAAT) for MG was  $-1.2$  °C (2000–2013) (Hanna *et al.*, 2012, updated). A linear trend analysis of MAAT shows an average air temperature increase of 0.7 °C for 2000–2013. The corrected mean annual precipitation, measured at the Danish Meteorological Institute (DMI) Tasiilaq station located ~10 km southeast of MG was  $1250 \pm 230$  mm w.e. year<sup>-1</sup> (2000–2012) (Mernild *et al.*, 2014), and exhibits a trend of  $-53.9$  mm w.e. year<sup>-2</sup> for 2000–2012 (based on a linear trend analysis).

## 3. Methods

### 3.1. MODIS-derived albedo

The MCD43A3 product is a combined TERRA and AQUA product produced every 8 days containing 16-day mean albedo values derived from radiometrically corrected sensor data. Each consecutive composite overlaps every 8 days.

The MODIS pixels covering MG were: (1) extracted using a glacier mask obtained from 1999 Landsat 5 Thematic Mapper classification (30-m increment) (for further detail see Mernild *et al.*, 2012); and (2) spatially interpolated using an ordinary kriging method to illustrate the smoothed 16-day mean smooth EBY albedo conditions. The albedo trends for the 14-year period (2000–2013) were calculated on a pixel basis. Only pixel time series having 10 or more years of data were used during the

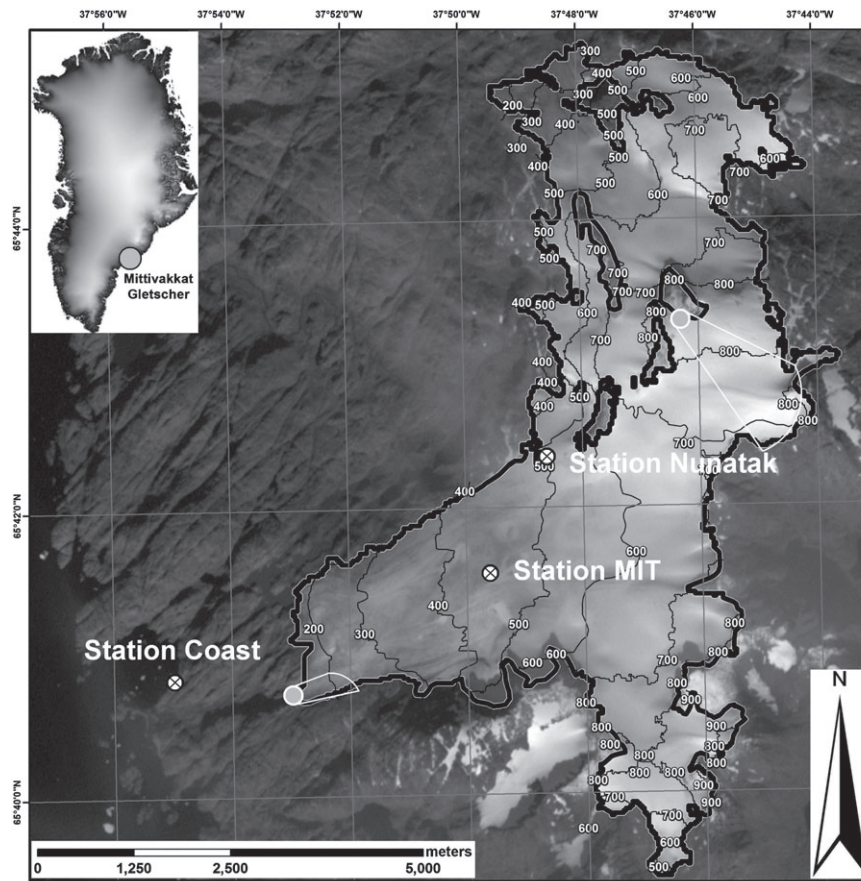


Figure 1. Landsat 7 Enhanced Thematic Mapper Plus (ETM+) image of the Mittivakkat Gletscher, 7 September 1999, with 100-m contour interval. The inset figure indicates the general location of the Mittivakkat Gletscher region in Southeast Greenland. The three AWSs that measure solar radiation are indicated [Station MIT (450 m a.s.l.), Station Nunatak (515 m a.s.l.), and Station Coast (25 m a.s.l.)], as well as the locations where the photos in Figure 2 were taken.

trend analysis. In total, 86% of all pixels were included in the analysis.

As the MOD10A product only provides blue-sky (actual) albedo for snow and ice, the MCD43A product used here provides white-sky albedo (albedo in the absence of a direct component when the diffuse component is isotropic) (Stroeve *et al.*, 2005), black-sky albedo [albedo in the absence of a diffuse component, which is a function of solar zenith angle (SZA)], and reflectance's for all surface types. The MCD43A is corrected using the Nadir MODIS Bi-Directional Reflectance Function (BDRF) Adjusted Reflectance (NBAR) and calculated to present surface reflectance values at local solar noon (Schaaf *et al.*, 2002). When the surface values are not available to obtain a magnitude inversion, a backup algorithm is performed (Schaaf *et al.*, 2002). Full information on these MODIS albedo pre-processing procedures is documented in the studies by Lucht (1998), Lucht *et al.* (2000), Schaaf *et al.* (2002) and Salomon *et al.* (2006).

The MG MODIS data were obtained yearly (2000–2013) for the 16-day mean period 27/28 July–12/13 August (Table 1). This specific 16-day period was chosen as it encompasses the EBY and the maximum height of the transient snowline. According to Mernild *et al.* (2013b) the net balance year ends between

15 and 18 August (based on available transient snow line observations from the years 1999, 2006, 2008, and 2012: the only 4 years where it was possible based on available transient snow lines to estimate the time for the EBY).

In order to derive blue-sky albedo from the MCD43A product, the fractional proportion of the black-sky component was calculated for each re-projected MODIS pixel. This was performed by integrating methodology developed by Weiss and Norman (1985) with the revised optical air mass tables produced by Kasten and Young (1989). The ratio between the MODIS-derived black-sky and white-sky albedo varied over the observation period changing from an average black-sky albedo of  $0.43 \pm 0.07$  and  $0.57 \pm 0.07$  for 8/9 May to 24/25 May periods, respectively, to  $0.84 \pm 0.04$  and  $0.16 \pm 0.04$  for 27/28 July to 12/13 August periods, respectively, indicating less diffuse radiation in the summer season (Table 2). These differences can be attributed to seasonal changes in the thickness of the atmosphere mainly caused by natural variations in the SZA (Schaaf *et al.*, 2011).

The albedo signal is affected by surface slope, roughness, and shadows from surrounding mountains. Consequently, five pixels from MG were excluded from the analysis. Wright *et al.* (2014) stated that sloping surfaces can alter the measured albedo, resulting in an



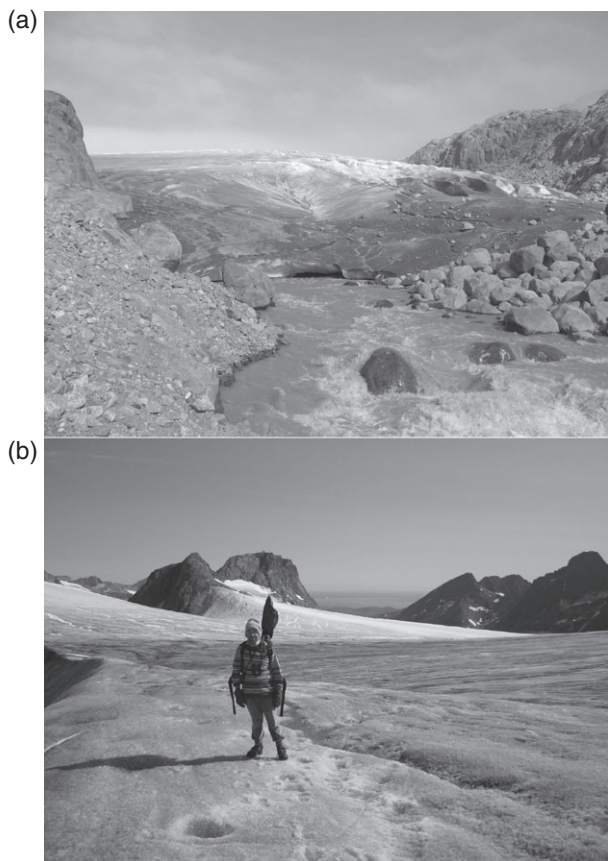


Figure 2. (a) The MG margin with debris cover. The photo was taken looking east, and the distance to the margin is 50–70 m (Photo: Mernild, 2011). (b) The upper part of Mittivakkat Gletscher. The photo was taken looking southeast towards the Irminger Sea, and the distances from the foreground to the mountains in the background are approximately 2 km (Photo: Hanna, 2012).

apparent albedo that is different from the albedo of a flat surface (based on observations from the GrIS). According to Strahler *et al.* (1999) such a range is within 10%. However, when comparing year-to-year albedo changes (on the same dates in each of the 14 years, i.e. with the same solar angle) on a corresponding pixel basis – as performed in this study – slope and surface roughness effects are expected to be the same, together with the systematic signal-to-noise errors, and therefore becomes less relevant as temporal changes in these parameters during the observation periods are minimal. Mernild *et al.* (2013a) report that the mean annual change in surface slope for the lower half of MG was  $0.02^\circ \text{ year}^{-1}$  (1986–2011). An annual mean change which is insignificant in a year-to-year albedo change evaluation.

### 3.2. Observed radiation and albedo calculations

The three AWSs measured incoming solar shortwave radiation (Si) and reflected solar radiation (Su) were done at hourly time steps at 2-m level for the Station Coast, 2.7-m level for the Station MIT, and 4-m level for the Station Nunatak. The accuracy regarding the Si and Su measurements (Aanderaa Solar Radiation Sensor 2770) for Station Nunatak and Station Coast was

within  $\pm 20 \text{ W m}^{-2}$  (Mernild *et al.*, 2008), and for Station MIT  $\pm 10\%$  [as quoted by the radiometer manufacturer (<http://s.campbellsci.com/documents/us/manuals/cnr1.pdf>)].

Albedo was calculated as

$$\text{albedo} = \Sigma \text{Su} / \Sigma \text{Si} \quad (1)$$

between the daily sum of Su and sum Si (and for Station MIT  $\Sigma \text{Su}_{\text{corrected}} / \Sigma \text{Si}_{\text{corrected}}$ , see below). As Station MIT is positioned on the dynamic glacier surface in contrast to Stations Coast and Nunatak, which are placed on a horizontal rock, the observed time series were corrected using measured tilt. For this procedure, the tilt correction method developed by van As (2011) was used, indicating a tilt correlation impact of +0.02 on the albedo values. Data from Station MIT were omitted mainly from September/October through March/April, when the angle between the sun and the radiometer is greater than  $70^\circ$  (Stroeve *et al.*, 2006). For 2013, the majority of the Station MIT albedo time series was omitted because the station had tilted. The Stations Nunatak and Coast observed radiation data were omitted from November through February because low sun angles in winter prevent the accurate calculation of albedo.

Observed AWS mean monthly albedo time series for Station MIT (April–July), Station Nunatak (March–May), and Station Coast (March–April) – covering the period of available radiation data and snow on the ground – were compared against near-surface mean monthly air temperature time series. This was performed based on linear regression to determine the melt-albedo feedback for the spring and summer snowmelt seasons.

### 3.3. Evaluation of MODIS-derived albedo

A point-grid evaluation at Station MIT of MODIS-derived albedo (Figure 3; see black bold square) was conducted as an average over the MODIS 16-day albedo product periods from 8/9 May to 24/25 May and 16/17 May to 1/2 June (both end of winter period) and 27/28 July to 12/13 August (the EBY), where data were available for both datasets (2009–2012) (Figure 4). According to Liang *et al.* (2002), point-grid verification is not suitable for pixels of more than  $1 \text{ km}^2$  covering heterogeneous landscapes. However, the mean MODIS-derived albedo and the mean Station MIT corrected albedo are statistically identical with, for example, end of mass balance means of  $0.34 \pm 0.05$  and  $0.28 \pm 0.13$ , respectively. Additionally, a root mean square error (RMSE) of 0.095 was obtained for all three periods, even though the AWS albedo was measured under all-sky conditions in comparison with MODIS-derived albedo which was based solely on clear-sky conditions. This RMSE is slightly greater than the RMSE reported by Stroeve *et al.* (2006) of 0.067, where MODIS MOD10A1 was validated using GrIS GC-Net AWS data (Steffen *et al.*, 1996), and the RMSE of 0.079 reported by van As *et al.* (2013) was validated against PROMICE AWS data (Ahlstrøm *et al.*, 2008) from the GrIS. Overall the radiometer point-corrected albedo indicated larger variability than MODIS, with the greatest annual difference at

Table 1. Satellite platforms, sensors, band information, and scenes used in the analysis of albedo at Mittivakkat Gletscher.

Platform	Terra and Aqua
Sensor	Moderate Resolution Radiometer (MODIS)
Ground resolution	500 by 500 m
Scenes	MCD43A3.MRTWEB.A2000209.005.Albedo_BSA_shortwave MCD43A3.MRTWEB.A2000209.005.Albedo_WSA_shortwave MCD43A3.MRTWEB.A2001209.005.Albedo_BSA_shortwave MCD43A3.MRTWEB.A2001209.005.Albedo_WSA_shortwave MCD43A3.MRTWEB.A2002209.005.Albedo_BSA_shortwave MCD43A3.MRTWEB.A2002209.005.Albedo_WSA_shortwave MCD43A3.MRTWEB.A2003209.005.Albedo_BSA_shortwave MCD43A3.MRTWEB.A2003209.005.Albedo_WSA_shortwave MCD43A3.MRTWEB.A2004209.005.Albedo_BSA_shortwave MCD43A3.MRTWEB.A2004209.005.Albedo_WSA_shortwave MCD43A3.MRTWEB.A2005209.005.Albedo_BSA_shortwave MCD43A3.MRTWEB.A2005209.005.Albedo_WSA_shortwave MCD43A3.MRTWEB.A2006209.005.Albedo_BSA_shortwave MCD43A3.MRTWEB.A2006209.005.Albedo_WSA_shortwave MCD43A3.MRTWEB.A2007209.005.Albedo_BSA_shortwave MCD43A3.MRTWEB.A2007209.005.Albedo_WSA_shortwave MCD43A3.MRTWEB.A2008209.005.Albedo_BSA_shortwave MCD43A3.MRTWEB.A2008209.005.Albedo_WSA_shortwave MCD43A3.MRTWEB.A2009209.005.Albedo_BSA_shortwave MCD43A3.MRTWEB.A2009209.005.Albedo_WSA_shortwave MCD43A3.MRTWEB.A2010209.005.Albedo_BSA_shortwave MCD43A3.MRTWEB.A2010209.005.Albedo_WSA_shortwave MCD43A3.MRTWEB.A2011209.005.Albedo_BSA_shortwave MCD43A3.MRTWEB.A2011209.005.Albedo_WSA_shortwave MCD43A3.MRTWEB.A2012209.005.Albedo_BSA_shortwave MCD43A3.MRTWEB.A2012209.005.Albedo_WSA_shortwave MCD43A3.MRTWEB.A2013209.005.Albedo_BSA_shortwave MCD43A3.MRTWEB.A2013209.005.Albedo_WSA_shortwave MCD43A3.A2009129.h16v02.005.2009151200540.hdf MCD43A3.A2009137.h16v02.005.2009156184642.hdf MCD43A3.MRTWEB.A2009209.005.Albedo_BSA_shortwave MCD43A3.MRTWEB.A2009209.005.Albedo_WSA_shortwave MCD43A3.A2010129.h16v02.005.2010148061028.hdf MCD43A3.A2010137.h16v02.005.2010159073811.hdf MCD43A3.MRTWEB.A2010209.005.Albedo_BSA_shortwave MCD43A3.MRTWEB.A2010209.005.Albedo_WSA_shortwave MCD43A3.A2011129.h16v02.005.2011152140344.hdf MCD43A3.A2011137.h16v02.005.2011158141322.hdf MCD43A3.MRTWEB.A2011209.005.Albedo_BSA_shortwave MCD43A3.MRTWEB.A2011209.005.Albedo_WSA_shortwave MCD43A3.A2012129.h16v02.005.2012153075603.hdf MCD43A3.A2012137.h16v02.005.2012160212919.hdf MCD43A3.MRTWEB.A2012209.005.Albedo_BSA_shortwave MCD43A3.MRTWEB.A2012209.005.Albedo_WSA_shortwave MCD43A3.MRTWEB.A2013209.005.Albedo_BSA_shortwave MCD43A3.MRTWEB.A2013209.005.Albedo_WSA_shortwave

the EBY of 0.14 (2009). This difference of MODIS albedo is most likely caused by factors such as:

1. The spatial comparison between a point value and a pixel value, with the possibility of having mixed pixels across different surface conditions. Point observations tend to have a greater variability as they are more sensitive to local changes in snow grain metamorphism and ice surface exposure, whereas grid cell observations cover a greater area. This is supported by the

difference in standard deviation between the two time series (Figure 4). Differences are especially clear when the point-grid-albedo-comparison was done during a ‘transition zone’, where glacier surface properties over the ablation season changes from, for example, dry snow zone condition or wet-snow zone conditions to bare ice conditions [for the different zones and conditions, see Cuffey and Paterson (2010, p. 14)].

2. The uncertainties in using MODIS due to a systematic increasing bias at SZA above 55°N (e.g. Wang



Table 2. The ratio between the MODIS-derived black-sky and white-sky albedo. The 2-day span is because of leap year.

	8/9 May to 24/25 May	16/17 May to 1/2 June	27/28 July to 12/13 August
Black-sky albedo	$0.43 \pm 0.07$	$0.51 \pm 0.03$	$0.84 \pm 0.04$
White-sky albedo	$0.57 \pm 0.07$	$0.49 \pm 0.03$	$0.16 \pm 0.04$

and Zender, 2010). According to Schaaf *et al.* (2011), Wang and Zender (2010) erroneously conclude that the accuracy deteriorates for SZA above  $55^{\circ}\text{N}$  and often becomes physically unrealistic above  $65^{\circ}\text{N}$ . Once the quality flags are considered, comparisons demonstrate that the MODIS product performs well when used out of the recommended limit of  $65^{\circ}\text{N}$  SZA.

Our comparison (Figure 4) suggests that the use of MODIS-derived albedo is appropriate for estimating the EBY (16-day) mean MG albedo at Station MIT, including its annual variability and the surface albedo conditions for MG in general.

To test for possible relations, all correlation trends labelled as 'significant' are equal to or above the 95% confidence level ( $p < 0.05$ ; where  $p$  is significance level).

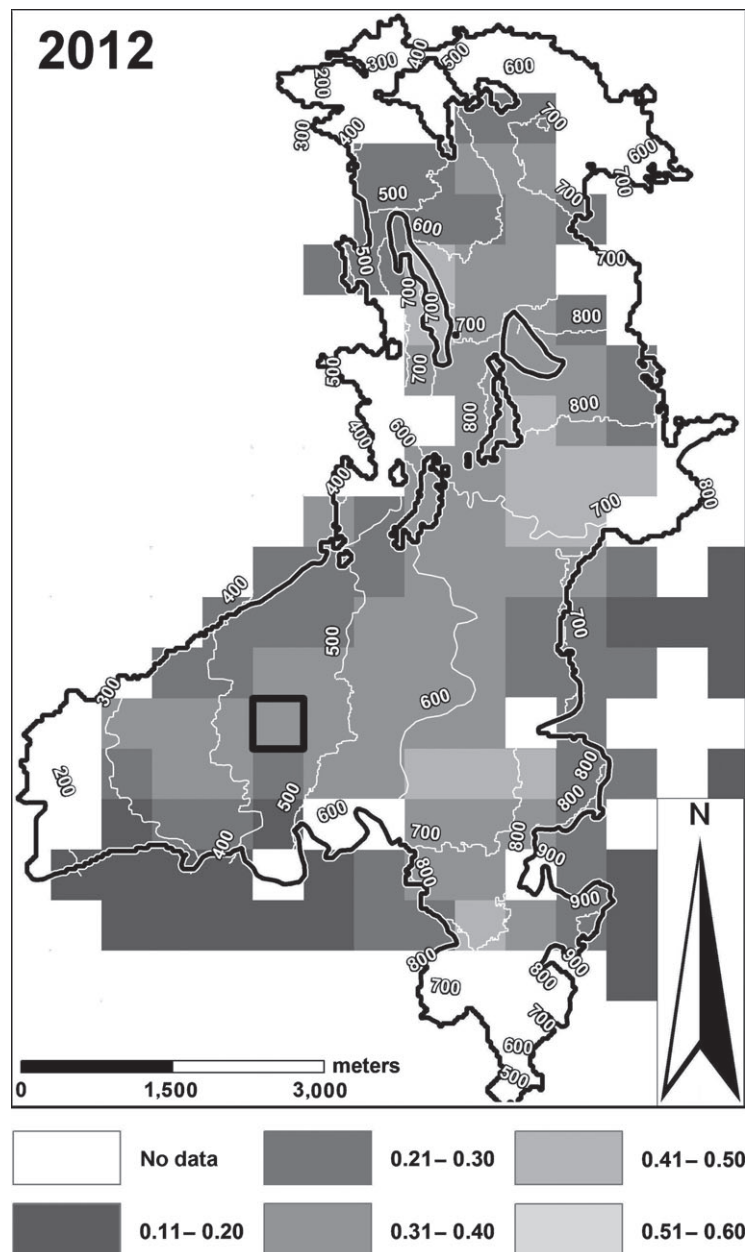


Figure 3. An example of the 16-day mean end of mass balance year MODIS-derived albedo for MG for 2012 on a  $500 \times 500$  m grid. The grid cell where Station MIT is positioned is indicated (see black bold square) and 100-m contour elevation intervals are illustrated.

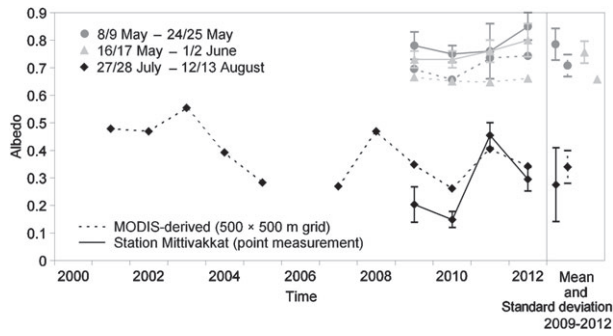


Figure 4. Time series of the mean end of mass winter balance (8/9 May–24/25 May and 16/17 May–1/2 June) and end of mass balance year (27/28 July–12/13 August) Station MIT observed albedo and MODIS-derived albedo for the Station MIT grid cell. Mean and standard deviation are calculated for the common period, and also for individual years for the Station MIT time series.

### 3.4. Mass balance observations

At MG the stake measurements were used to determine variations in mass balance and the position of the ELA. Snow accumulation and snow and ice ablation were measured with cross-glacier stake lines approximately 500 m apart. The stakes in each line were 200–250 m apart, and measurements were obtained from a total of 47 stakes in 1998 and 2001 and 18 stakes continuously from 2008 to 2011 (for location of the stakes see Figure 1 in Mernild

*et al.*, 2011, 2013a). End of winter snow density was measured vertically at 25-cm depth interval in pits located at 250, 500, and 750 m a.s.l. The mass balance observations are considered to be accurate within  $\pm 340$  mm w.e. year<sup>-1</sup> for the entire glacier (Zemp *et al.*, 2013).

## 4. Results and discussions

### 4.1. AWS observed albedo time series

Figure 5(a)–(c) illustrates the mean daily Si and Su time series from Station MIT (2009–2012), Station Nunatak (1995–2007), and Station Coast (1997–2007). The mean daily Si and mean daily maximum Si were both lower by  $\sim 10$ –20% at the coast and on the lower parts of MG due to the local prevailing atmospheric conditions in the area (Mernild and Liston, 2010) compared to the central part of MG. Mean and maximum Si was 177 and 239  $W m^{-2}$ , 200 and 256  $W m^{-2}$ , and 217 and 265  $W m^{-2}$  at Station Coast, Station Nunatak, and Station MIT, respectively (covering the period March–August for all stations). This variability in Si between stations is likely caused by clouds and fog in the Sermilik Fjord (Mernild *et al.*, 2008). Variability in Su may be the result of variations in surface conditions, such as snow cover, bare ice, and wet/dry bedrock.

Figure 5(d) presents the three AWS mean albedo time series. Regarding albedo variability from March to July,

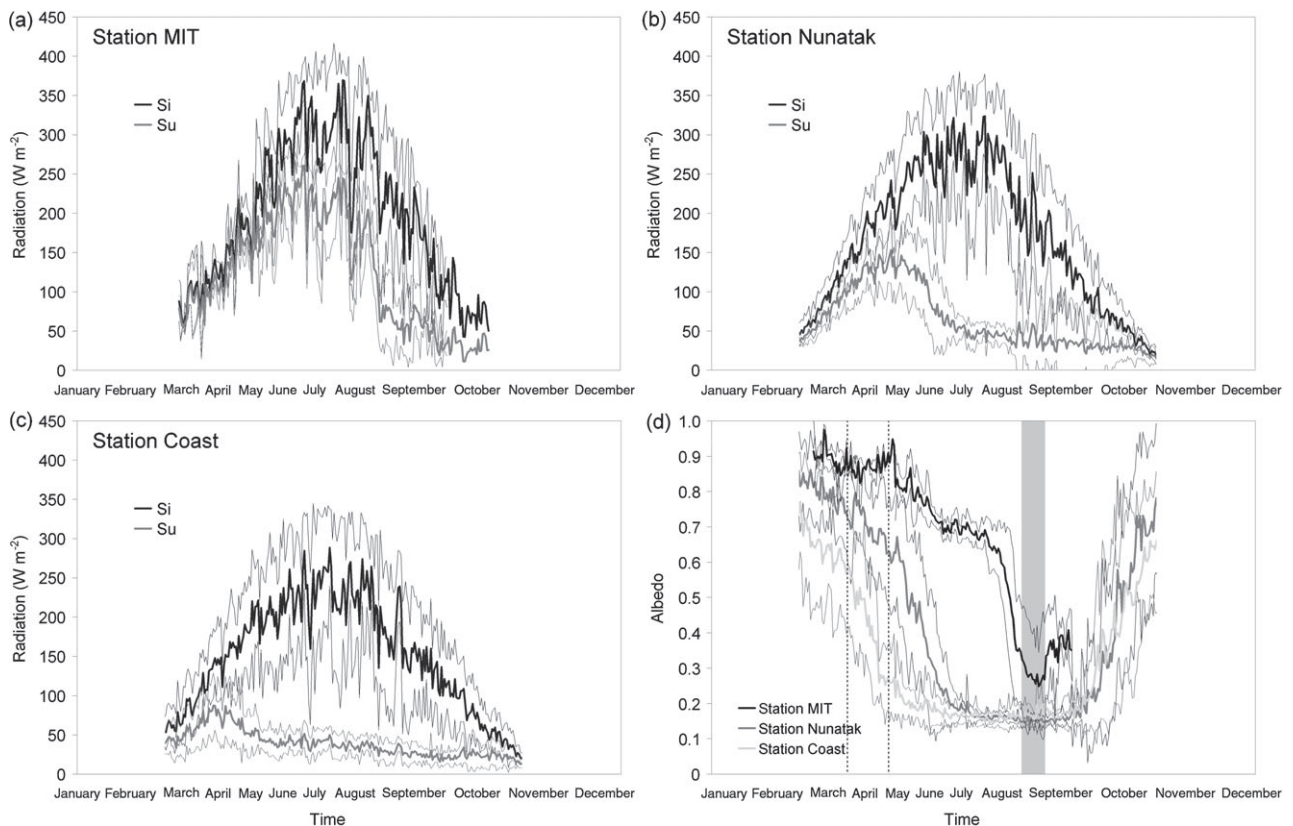


Figure 5. Mean time series of incoming shortwave radiation (Si) and reflected solar radiation (Su) for: (a) Station MIT (2009–2012); (b) Station Nunatak (1995–2007); (c) Station Coast (1997–2007); and (d) mean time series of albedo for the Stations MIT, Nunatak, and Coast. The thin grey lines indicate  $\pm 1$  standard deviation. The vertical grey bar in (d) illustrates the MODIS albedo time stamp at the EB, and the dotted black lines indicate the dates 1 April and 1 May.

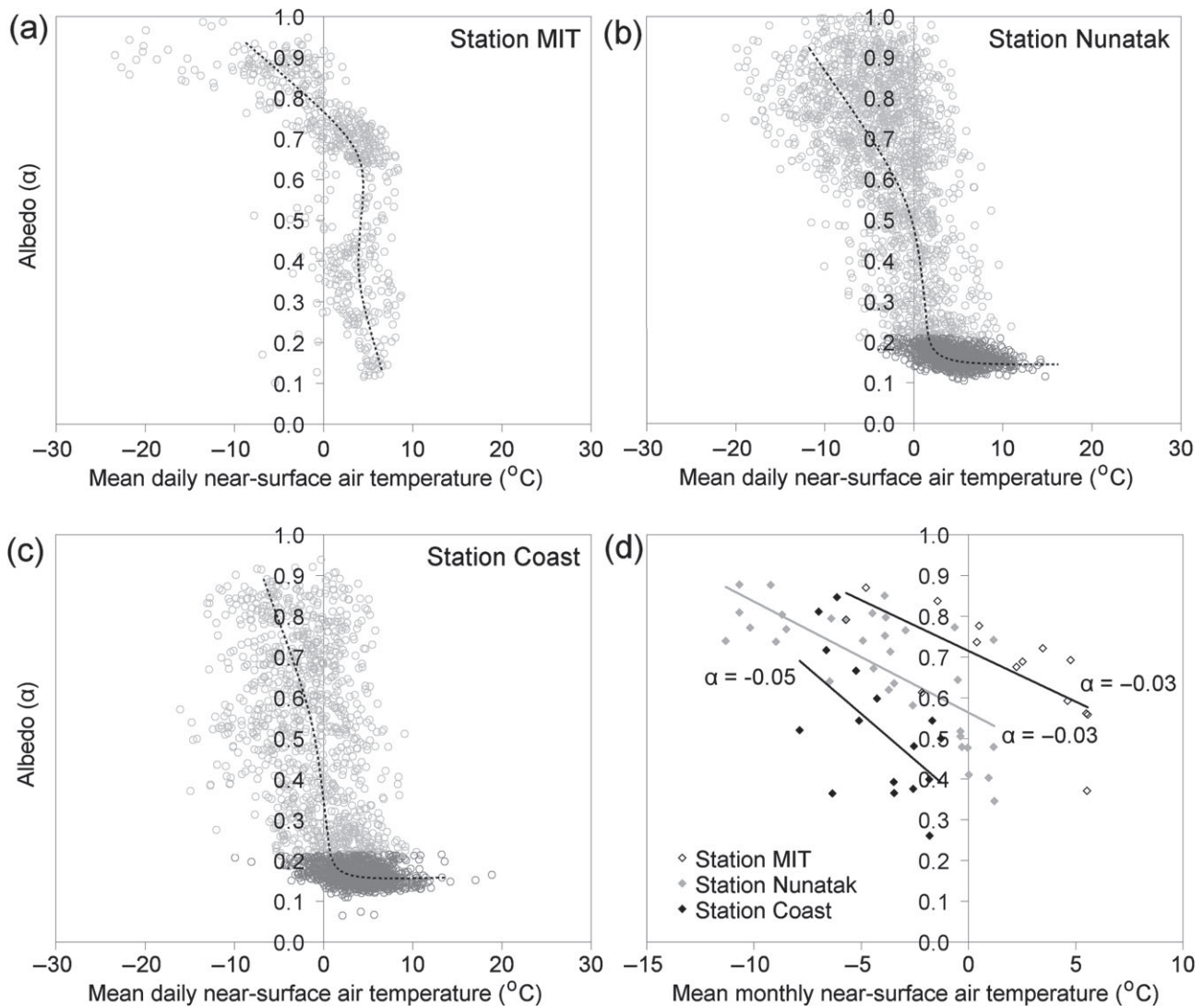


Figure 6. Daily mean albedo *versus* air temperature at the three meteorological stations: (a) Station MIT (2009–2012); (b) Station Nunatak (1995–2007); and (c) Station Coast (1997–2007). The decline in mean albedo with increasing temperature is illustrated by the smoothed hyperbolic curve (dotted lines), and the dark grey clusters for Station Nunatak and Station Coast are albedo observations for bedrock; and (d) mean monthly albedo *versus* air temperature for the period of potential snowmelt in spring and summer: Station MIT (April–July), Station Nunatak (March–May), and Station Coast (March–April).  $\alpha$  is the slope of the linear regression.

albedo is shown to be higher in the central part of MG than at the coast which is likely a consequence of lower melt rates and shorter snow-free conditions at higher elevations (Mernild *et al.*, 2008). At Station Coast snow-free conditions occur on average 5–7 weeks earlier than at Station Nunatak (1994–2006). As an example of this spatial variability, the mean observed albedo on 1 April was  $0.92 \pm 0.02$  for Station MIT,  $0.74 \pm 0.11$  for Station Nunatak, and  $0.57 \pm 0.17$  for Station Coast and  $0.90 \pm 0.03$ ,  $0.61 \pm 0.15$ , and  $0.26 \pm 0.08$  on 1 May (Figure 5(d)), respectively. For both Stations Coast and Nunatak, the albedo time series stabilized at a minimum level of  $\sim 0.2$  in early May and late June/early July, respectively. This was most likely due to the ablated snow cover and subsequently exposed bedrock. On the surface of MG, at Station MIT, the decline in albedo occurred later than at the two bedrock locations, reaching a minimum of  $\sim 0.3$  for bare ice [similar to albedo values for clean ice of 0.30–0.46

(Cuffey and Paterson, 2010)] in early/mid August, the period we defined as the EBY. This difference in minimum albedo between the stations occurred until the first snow-fall in late summer/early autumn. Hereafter, the albedo rose for all three stations (Figure 5(d)).

#### 4.2. Albedo sensitivity to surface air temperature

Absorbed incoming solar radiation is the primary source of melting energy for snow and ice covered surfaces at high latitudes (e.g. Liston and Hiemstra, 2011). In such locations, the melt-albedo feedback is initiated by energy fluxes that respond to changes in temperature, such as downward longwave radiation and turbulent heat fluxes (van As *et al.*, 2013). Air temperatures are not only strongly correlated with surface melt rates, melt extent, and the fraction of precipitation falling as rain *versus* snow, but also with snow and ice surface albedo. Warming can affect albedo, even without removing snow and



ALBEDO DECLINE

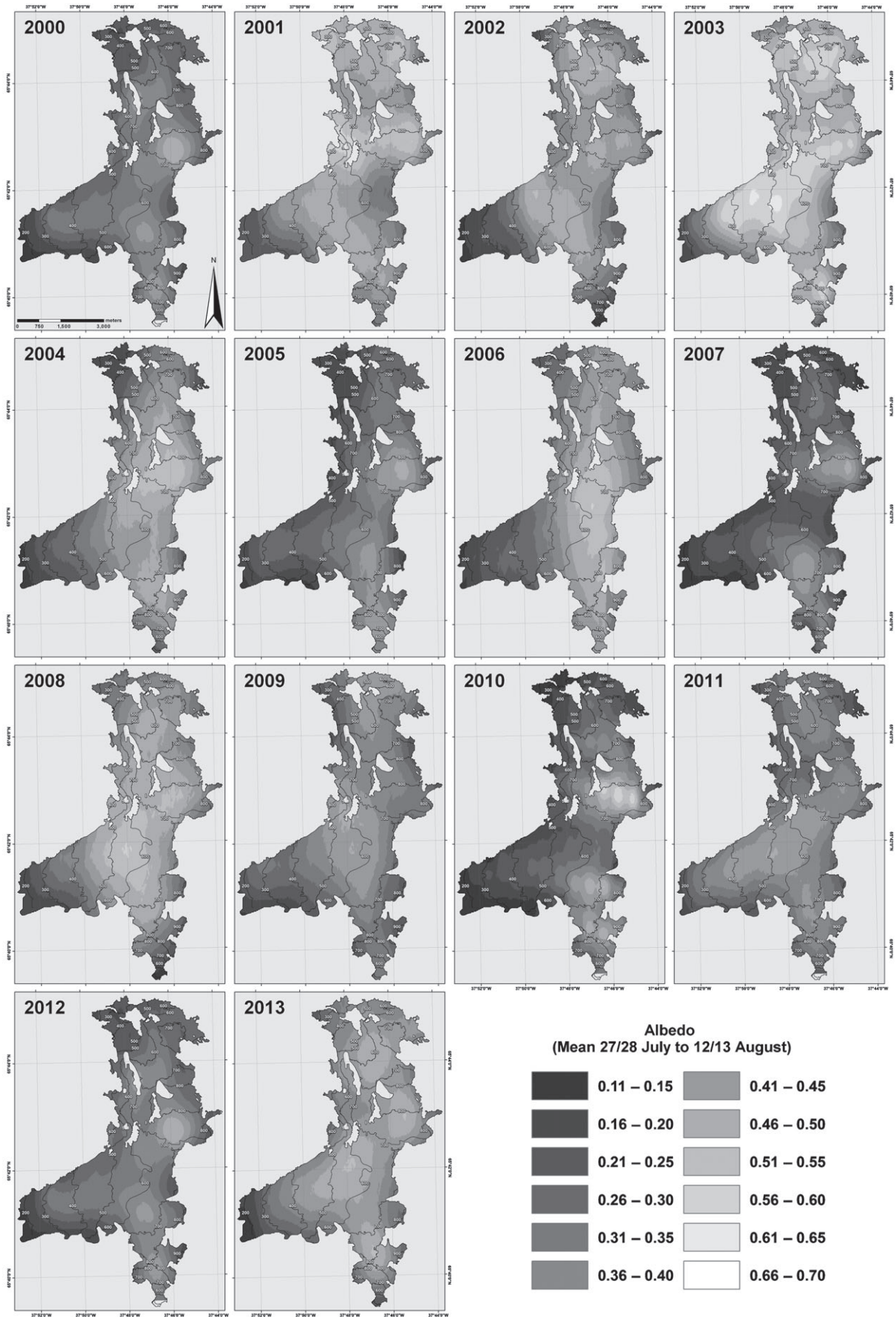


Figure 7. MODIS-derived spatial end of mass balance year mean albedo for MG from 2000 through 2013. The 100-m contour elevation intervals are illustrated.

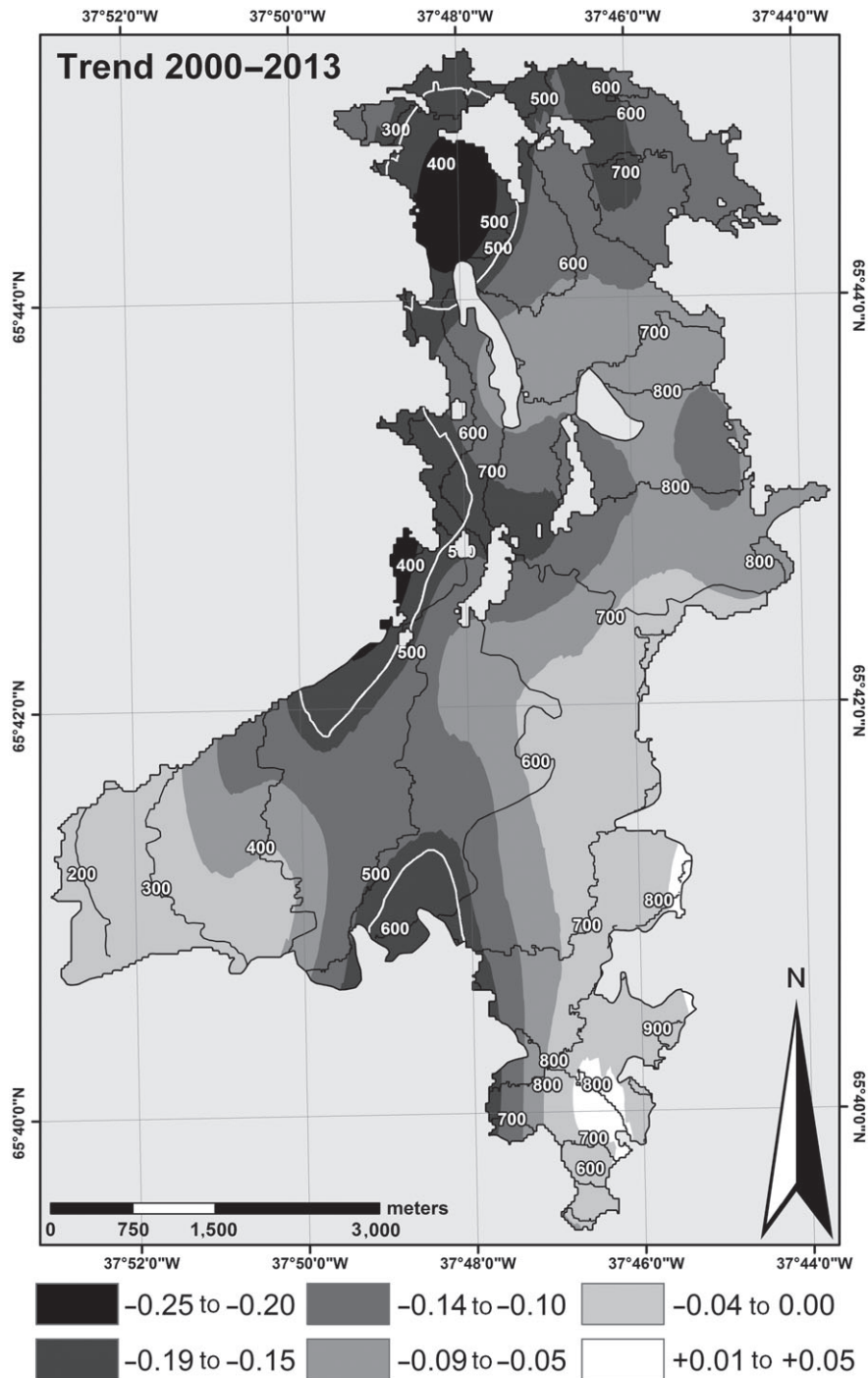


Figure 8. Mean MODIS-derived spatial end of mass balance year albedo trend for MG for 2000 through 2013, including 100-m contour elevation intervals. The white bold lines indicate the margin for significant trends in albedo, where values below are significant.

ice cover, in several ways. Albedo reductions, for example, can be initiated by heat-driven snow grain metamorphism (e.g. Warren, 1982; Dozier *et al.* 2009) and by development of small-scale supraglacial meltwater-filled features on the bare ice surface. Snow and ice albedo reductions can also result from warming-induced increases in the fraction of liquid precipitation (Box *et al.*, 2012b). Subsequent increases of melt/rain water content have been shown to reduce snowpack cold content (due to release of latent heat) (e.g. Trabant and Mayo, 1985; Kane *et al.*,

1991; Conway and Benedict, 1994) and change snow grain size/shape and snow liquid content (e.g. Dumont *et al.*, 2012), again resulting in albedo lowering.

This melt-albedo feedback mechanism, where ice and snow melt accelerates albedo lowering which subsequently melt increase, results in a self-initiating snow/ice ablation throughout the ablation season until fresh snowfall occurs in late summer/early autumn. The melt-albedo feedback can be expressed as the relation between increasing near-surface air temperatures

and decreasing albedo, and is examined for the three AWS's (Figure 6). For all three stations, the snow albedo generally decreased with increasing air temperatures (Figures 6(a)–(c)), following different mean smoothed hyperbolic curves. Linear relations for monthly mean values suggest that 1 °C of warming in the near-surface air temperature leads to an average snow albedo reduction of 0.03–0.05 [this compares to 0.034 for the ablation area and 0.002 for the accumulation area of the GrIS (2000–2011) (Box *et al.*, 2012b)]. At MG, the albedo is generally low when near-surface air temperature is high (Figure 6(d)). For Stations MIT and Nunatak, the trend in snow albedo reduction is similar (March–July). However, an average lowering in albedo of ~0.1 occurred for Station Nunatak, probably due to the impacts of wind-blown impurity depositions originating from weathering of the Nunatak. Not only is the snow albedo reduction for Station Coast greater than the reduction for both Stations MIT and Nunatak, but the albedo is also lower for any given individual monthly air temperature (Figure 6(d)). These spatial differences in snow albedo conditions may be the result of increasing cloud and sea fog percentages (originating from the Sermilik Fjord), higher coastal temperatures compared to the central part of the MG, and a greater fraction of precipitation falling as rain *versus* snow in the coastal area (Mernild *et al.*, 2008).

#### 4.3. Spatial and interannual variability in EBY albedo

On Figure 7, the spatial MG MODIS-derived EBY mean albedo is illustrated for each year from 2000 to 2013. For all years, albedo was generally lowest at low-lying elevations with values of 0.11–0.15 [similar to debris-rich ice (Cuffey and Paterson, 2010)], rising with increasing elevation to albedo values of 0.66–0.70. A decrease in albedo occurred at the highest elevation locations close to the eastern glacier margin. This decrease can probably be attributed to windblown dust or rock avalanches from the surrounding peaks (shown in Figure 2(b)). Overall, 2003 was the year with the relatively highest average albedo value ( $0.49 \pm 0.09$ ) and 2007 ( $0.26 \pm 0.08$ ) was the year with the lowest average albedo.

MG albedo change from 2000 to 2013 was largest (below –0.10) in the central part of the glacier between 400 and 650 m a.s.l., covering approximately an area of 9 km<sup>2</sup> (Figure 8). This elevation range coincides with that of the ELA in recent years (from around 500 to 750 m a.s.l.). The large decline in albedo in this area is thus expected to be related to the ascent of the ELA and snowline migration. Qu and Hall (2007) concluded that albedo changes were associated more with a loss in seasonal snow cover than changes related to snow metamorphosis. The significant declines in albedo occurred where the change in albedo was below –0.17. This occurred in the elevation range from 450 to 600 m a.s.l., covering 8% of MG (2.1 km<sup>2</sup>). The smallest changes in albedo occurred where MG was either snow covered during the entire observation period, in the high-elevation accumulation zone or constituted of exposed glacier ice in the low-elevation ablation zone

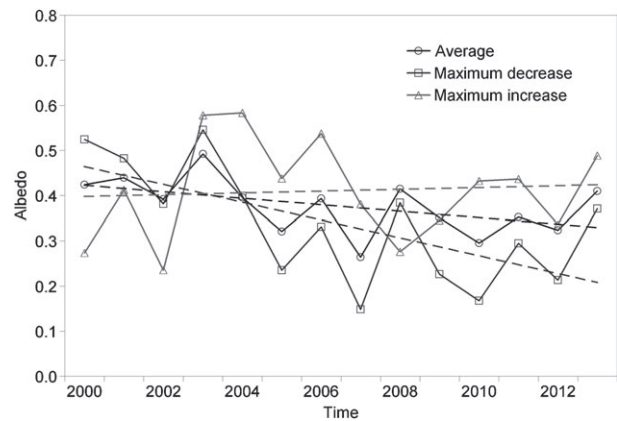


Figure 9. Time series of MG MODIS-derived end of mass balance year average, maximum decrease, and maximum increase in albedo from 2000 through 2013.

(Figure 8). A similar pattern of albedo lowering was seen for the ablation zone of the GrIS (Bøggild *et al.*, 2010), where emergence and melting of ice in the ablation zone resulted in a dusty surface layer.

In Figure 9, the MG MODIS-derived EBY albedo is illustrated, showing both decreasing and increasing albedo trends based on linear regression from 2000 to 2013. The maximum increase for a glacier MODIS pixel was 0.02 (insignificant), varying from 0.40 to 0.42 (Figure 9). This occurred at 820 m a.s.l. (Figure 8), an area prone to snow redistribution. The maximum decrease in albedo was 0.25 (significant), reducing from 0.46 to 0.21 (Figure 9). This maximum decrease occurred at 440 m a.s.l., where MG changed from an end-of-season snow cover to subsequent end-of-season bare ice cover (Figure 8). The average albedo for MG declined throughout the observation period, the lowest value being reached in 2013. On average, the albedo declined (significantly) from 0.43 to 0.33 (Figure 9), indicating an annual trend of  $-0.007 \text{ year}^{-2}$ . Consequently, on average 10% more incoming solar short-wave radiation became available for surface ablation at the end of the melt season. This decrease in albedo occurred simultaneously with a mean increase in MG near-surface MAAT of 0.7 °C (2000–2013), supporting the occurrence of the theorized melt-albedo feedback.

A decrease in albedo has also been observed for the whole GrIS. Stroeve (2001) observed an overall downward trend in GrIS albedo (insignificant) in agreement with trends in melt and precipitation. Box *et al.* (2012a) and Tedesco *et al.* (2013) showed that the GrIS average albedo (June–August) declined from 0.75 in 2000 to 0.68 in 2012 in July. It is expected that local GIC would on average show greater albedo decline than the entire GrIS due to greater warming (resulting from ocean warming and newly exposed, darker surrounding surfaces). In relative terms, GIC probably also have larger areas relatively of exposed glacier surface ice impurities and supraglacial meltwater-filled features (e.g. Dumont *et al.*, 2012; Tedesco *et al.*, 2013), supporting the melt-albedo feedback tendency towards less reflectivity.



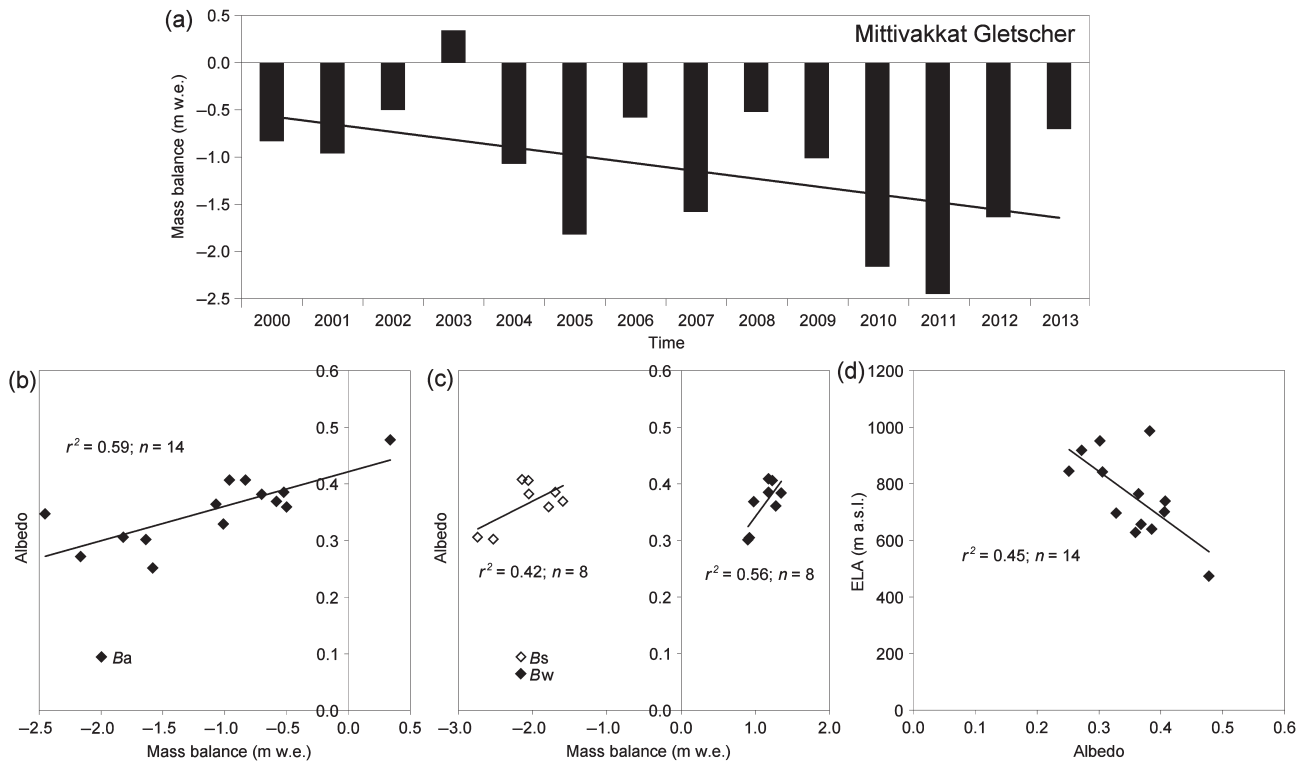


Figure 10. (a) Observed annual Mittivakkat Gletscher mass balance; (b) Mittivakkat Gletscher mean EBY MODIS-derived albedo *versus* Ba (1999/2000–2010/2013); (c) mean MODIS-derived albedo *versus*  $B_s$  and  $B_w$ ; and (d) MODIS-derived albedo *versus* ELA elevation.

#### 4.4. Albedo, mass balance, and ELA

For temperate GIC, surface albedo is closely related to mass balance (Hock, 2005; Six *et al.*, 2009; Dumont *et al.*, 2012), and albedo values at the end of the ablation season are related to annual balance conditions (Dumont *et al.*, 2012). In Figure 10(a),  $B_a$  is illustrated for the period 2000 through 2013 indicating a mean trend of  $-0.08 \text{ m.w.e. year}^{-2}$  (significant). Additionally, in Figure 10(b) the EBY albedo is plotted against  $B_a$ , and in Figure 10(c) against both  $B_w$  and  $B_s$ . For MG, average albedo is shown to correspond based on linear regression, with  $B_a$ ,  $B_w$ , and  $B_s$  values. Overall, changes in end of melt season albedo can explain 59% ( $r^2 = 0.59$ ) of the variability in  $B_a$ , 42% in  $B_s$ , and 56% in  $B_w$  (these are significant correlations). Furthermore, high MG winter balance  $B_w$  reduces the  $B_s$  as more time is required to melt a thicker snow cover during the summer season (Knudsen and Hasholt, 2008). This explains why  $B_w$  is more closely related to the EBY albedo than  $B_s$ . The highest correlation between seasonal mass balances and albedo, however, is found for albedo and  $B_w$ . This strong correlation emphasizes the importance of changes in  $B_w$ , probably because the divide between the accumulation zone and the ablation zone is characterized by greatly contrasting albedo values which complicates the relationship in summer. Finally, the EBY albedo and ELA are inversely correlated ( $r^2 = 0.45$ ; significant), where a minimum albedo for MG corresponds to a relatively large bare ice area and a relatively high ELA.

Peripheral GIC in Greenland are undergoing contemporary mass loss, thinning and recession (Jiskoot *et al.*, 2003; Mernild *et al.*, 2006, 2012; Yde and Knudsen, 2007; Kargel *et al.*, 2012). Such losses have been enhanced by a recent period of record warming (Hansen *et al.*, 2010; Hanna *et al.*, 2014). In light of these glaciological and climatic changes, the monitoring of surface albedo has become increasingly important. More knowledge is needed on regression scale variability in albedo changes in order to extrapolate singular glacier information to larger areas. Also, greater insight into the albedo-changing potential of supraglacial algae and cyanobacteria is needed to help understand the consequences of resulting biogenic feedback mechanisms on glacier melt rates (Hodson *et al.*, 2010; Yallop *et al.*, 2012).

#### 5. Conclusions

The average albedo of MG at the EBY decreased from 0.43 to 0.33 from 2000 to 2013. As a consequence increasing amounts (10%) of solar shortwave radiation were absorbed at the surface, contributing to surface ablation, snow metamorphosis, and bare ice exposure at the EBY. Albedo variability explains 59% of the variability in the annual mass balance, supporting the hypothesis that glacier surface albedo at the EBY is related to annual mass balance (e.g. Dumont *et al.*, 2012). The decline in albedo is consistent with studies of the GrIS (Box *et al.*, 2012a; Tedesco *et al.*, 2013). Average MG albedo reduced by up to 0.25 over 14 years. The trend in albedo has a

distinct spatial pattern: the greatest reduction occurred in the central part of the glacier, where the ELA has migrated upward replacing snow-covered areas with darker bare ice.

## Acknowledgements

This work was supported by the European Union Seventh Framework Program (FP7/2007–2013) under grant agreement No. 262693 (Project GALOB: Glacier Albedo Observations in SE Greenland), and by Centro de Estudios Científicos (CECs), which is funded by the Chilean Government through the Centers of Excellence Base Financing Program of CONICYT. We thank University of Copenhagen, Department of Geosciences and Natural Resource Management for providing meteorological data from both Station Nunatak and Station Coast. No authors have conflict of interest.

## References

- Ahlström AP, Andersen SB, van As D, Citterio M, Fausto RS, Nielsen S, Jepsen HF, Kristensen SS, Christensen EL, Stenseng L, Forsberg R, Hanson S, Petersen D. 2008. A new programme for monitoring the Greenland ice sheet mass loss. *GEUS Bull. Ser. Rev. Surv. Activities* **15**: 61–64.
- Arendt A, Bolch T, Cogley JG, Gardner A, Hagen J-O, Hock R, Kaser G, Pfeffer WT, Moholdt G, Paul F, Radic V, Andreassen L, Bajracharya S, Beedle M, Berthier E, Bhabri R, Bliss A, Brown I, Burgess E, Burgess D, Cawkwell F, Chinn T, Copland L, Davies B, de Angelis H, Dolgova E, Filbert K, Forester R, Fountain A, Frey H, Giffen B, Glasser N, Gurney S, Hagg W, Hall D, Haritashya UK, Hartmann G, Helm C, Herreid S, Howat I, Kapustin G, Khromova T, Kienholz C, Koenig M, Kohler J, Krieger D, Kutuzov S, Lavrentiev I, LeBris R, Lund J, Manley W, Mayer C, Miles E, Li X, Menounos B, Mercer A, Moelg N, Mool P, Nosenko G, Negrete A, Nuth C, Pettersson R, Racoviteanu A, Ranzi R, Rastner P, Rau F, Rich J, Rott H, Schneider C, Selkverstov Y, Sharp M, Sigursson O, Stokes C, Wheate R, Winsvold S, Wolken G, Wyatt F, Zheltyhina N. 2012. *Randolph Glacier Inventory [v2.0]: A Dataset of Global Glacier Outlines. Global Land Ice Measurements from Space*. Digital Media: Boulder, CO.
- van As D. 2011. Warming, glacier melt and surface energy budget from weather station observations in the Melville Bay region of northwest Greenland. *J. Glaciol.* **57**(202): 208–220.
- van As D, Fausto R, Colgan WT, Box JE, Ahlstrom AP, Andersen SB, Andersen ML, Charalampidis C, Citterio M, Edelvang K, Jensen TS, Larsen SH, Machguth H, Nielsen S, Veicherts M, Weidick A. 2013. Darkening of the Greenland ice sheet due to the melt-albedo feedback observed at PROMICE weather stations. *Geol. Surv. Den. Green. Bull.* **28**: 69–72.
- Bøggild CE, Brandt RE, Brown KJ, Warren SG. 2010. The ablation zone in northeast Greenland: ice types, albedos and impurities. *J. Glaciol.* **56**(195): 101–113.
- Box JE, Cappelen J, Chen C, Decker D, Fettweis X, Mote T, Tedesco M, van de Wal RSW, Wahr J. 2012a. Arctic Report Card 2012, Greenland Ice Sheet, NOAA Report, NOAA, Washington, DC, 25 pp.
- Box JE, Fettweis X, Stroeve JC, Tedesco M, Hall DK, Steffen K. 2012b. Greenland ice sheet albedo feedback: thermodynamics and atmospheric drivers. *Cryosphere* **6**: 821–839, doi: 10.5194/tc-6-821-2012.
- Conway H, Benedict R. 1994. Infiltration of water into snow. *Water Resour. Res.* **30**(3): 641–649.
- Corripio J. 2004. Snow surfaces albedo estimation using terrestrial photography. *Int. J. Remote Sens.* **25**: 5705–5729, doi: 10.1080/01431160410001709002.
- Cuffey KM, Paterson WSB. 2010. *The Physics of Glaciers*. Elsevier: Oxford, UK, 693 pp.
- Dozier J, Schneider SR, McGinnis DF. 1981. Effect of grain size and snowpack water equivalence on visible and near-infrared satellite-observations of snow. *Water Resour. Res.* **17**: 1213–1221, doi: 10.1029/WR017i004p01213.
- Dozier M, Arnaud Y, Six D, Corripio J. 2009. Retrieval for glacier surface albedo using terrestrial photography. *La Houille Blanche* **2**: 102–118, doi: 10.1051/lhb/2009021.
- Dumont M, Gardelle J, Sirguey P, Guillot A, Six D, Rabatel A, Arnaud Y. 2012. Linking glacier annual mass balance and glacier albedo retrieved from MODIS data. *Cryosphere* **6**: 1527–1539, doi: 10.5194/tc-6-1527-2012.
- Gardner AS, Sharp MJ. 2010. A review of snow and ice albedo and the development of a new physically based broadband albedo parameterization. *J. Geophys. Res.* **115**: F01009, doi: 10.1029/2009JF001444.
- Gardner AS, Moholdt G, Cogley JG, Wouters B, Arendt AA, Wahr J, Berthier E, Hock R, Pfeffer WT, Kaser G, Ligtenberg SRM, Bolch T, Sharp MJ, Hagen JO, van den Broeke MR, Paul FA. 2013. Reconciled estimate of glacier contributions to sea level rise: 2003 to 2009. *Science* **340**(6134): 852–857.
- Greuell W, Oerlemans J. 2004. Narrow-to-broadband conversion for glacier ice and snow: equations based on modeling and ranges of variability of the equations. *Remote Sens. Environ.* **89**: 95–105, doi: 10.1016/j.rse.2003.10.010.
- Greuell W, Oerlemans J. 2005. Validation of AVHRR- and MODIS-derived albedos of snow and ice surfaces by means of helicopter measurements. *J. Glaciol.* **51**(172): 37–48.
- Hanna E, Mernild SH, Cappelen J, Steffen K. 2012. Recent warming in Greenland in a long-term instrumental (1881–2012) climatic context: I. Evaluation of surface air temperature records. *Environ. Res. Lett.* **7**(4): 045404, doi: 10.1088/1748-9326/7/4/045404.
- Hanna E, Fettweis X, Mernild SH, Cappelen J, Ribergaard MH, Shuman CA, Steffen K, Wood L, Mote TL. 2014. Atmospheric and oceanic climate forcing of the exceptional Greenland ice sheet surface melt in summer 2012. *Int. J. Climatol.* **34**: 1022–1037, doi: 10.1002/joc.3743.
- Hansen J, Ruedy R, Sato M, Lo K. 2010. Global surface temperature change. *Rev. Geophys.* **48**: RG4004, doi: 10.1029/2010RG000345.
- Hock R. 2005. Glacier melt: a review of processes and their modeling. *Prog. Phys. Geogr.* **29**: 362–391, doi: 10.1191/0309133305pp453ra.
- Hock R, de Woul M, Radić V, Dyurgerov M. 2009. Mountain glaciers and ice caps around Antarctica make a large sea-level rise contribution. *Geophys. Res. Lett.* **36**: L07501, doi: 10.1029/2008GL037020.
- Hodson AJ, Boggild C, Hanna E, Huybrechts P, Langford H, Cameron K, Houldsworth A. 2010. The cryoconite ecosystem on the Greenland ice sheet. *Ann. Glaciol.* **51**(56): 123–129.
- Jiskoot H, Murray T, Luckman A. 2003. Surge potential and drainage-basin characteristics in East Greenland. *Ann. Glaciol.* **36**: 142–148.
- Kane DL, Hinzman LD, Benson CS, Liston GE. 1991. Snow hydrology of a headwater Arctic basin: 1. Physical measurements and process studies. *Water Resour. Res.* **27**(6): 1099–1109.
- Kargel JS, Ahlström AP, Alley RB, Bamber JL, Benham TJ, Box JE, Chen C, Christoffersen P, Citterio M, Cogley JG, Jiskoot H, Leonard GJ, Morin P, Scambos T, Sheldon T, Willis I. 2012. Brief communication Greenland's shrinking ice cover: "fast times" but not that fast. *Cryosphere* **6**: 533–537, doi: 10.5194/tc-6-533-2012.
- Kasten F, Young AT. 1989. Revised optical air mass tables and approximation formula. *Appl. Opt.* **28**: 4735–4738.
- Klok E, Greuell W, Oerlemans J. 2003. Temporal and spatial variation of the surface albedo of Morteratschgletscher, Switzerland, as derived from 12 Landsat images. *J. Glaciol.* **49**: 491–502.
- Knap W, Brock B, Oerlemans J, Willis I. 1999a. Comparison of Landsat TM-derived and ground-based albedos of Haut Glacier d'Arolla, Switzerland. *Int. J. Remote Sens.* **20**: 3293–3310.
- Knap W, Reijmer C, Oerlemans J. 1999b. Narrowband to broad-band conversion of Landsat TM glacier albedos. *Int. J. Remote Sens.* **20**: 2091–2110.
- Knudsen NT, Hasholt B. 1999. Radio-echo sounding at the Mittivakkat Gletscher, Southeast Greenland. *Arct. Antarct. Alp. Res.* **31**(3): 321–328.
- Knudsen NT, Hasholt B. 2008. Mass balance observations at Mittivakkat Glacier, Ammassalik Island, Southeast Greenland 1995–2006. *Geogr. Tidsskr. Dan. J. Geogr.* **108**(1): 111–120.
- Liang S, Fang H, Chen M, Shuey CJ, Walthall C, Daughtry C, Morisette J, Schaaf C, Strahler A. 2002. Validation MODIS land surface reflectance and albedo products: methods and preliminary results. *Remote Sens. Environ.* **83**: 149–162.
- Liang S, Stroeve J, Box J. 2005. Mapping daily snow/ice short-wave broadband albedo for Moderate Resolution Imaging Spectroradiometer (MODIS): the improved direct retrieval algorithm and validation with Greenland in situ measurements. *J. Geophys. Res.* **110**: D10109, doi: 10.1029/2004JD005493.

- Liston GE, Hiemstra CA. 2011. The changing cryosphere: pan-Arctic snow trends (1979–2009). *J. Clim.* **24**: 5691–5712, doi: 10.1175/JCLI-D-11-00081.1.
- Lucht W. 1998. Expected retrieval accuracies of bidirectional reflectance and albedo from EOS-MODIS and MISR angular sampling. *J. Geophys. Res.* **103**: 8763–8778.
- Lucht W, Schaaf CB, Strahler AH. 2000. An algorithm for the retrieval of albedo from space using semiempirical BRDF models. *IEEE Trans. Geosci. Remote Sens.* **38**: 977–998.
- Mernild SH, Liston GE. 2010. The influence of air temperature inversion on snow melt and glacier surface mass-balance simulations, SW Ammassalik Island, SE Greenland. *J. Appl. Meteorol. Clim.* **49**(1): 47–67.
- Mernild SH, Liston GE, Hasholt B, Knudsen NT. 2006. Snow distribution and melt modeling for Mittivakkat Glacier, Ammassalik Island, SE Greenland. *J. Hydrometeorol.* **7**: 808–824.
- Mernild SH, Hansen BU, Jakobsen BH, Hasholt B. 2008. Climatic conditions at the Mittivakkat Glacier catchment (1994–2006), Ammassalik Island, SE Greenland, and in a 109 years term perspective (1898–2006). *Geogr. Tidsskr. Dan. J. Geogr.* **108**(1): 51–72.
- Mernild SH, Knudsen NT, Lipscomb WH, Yde JC, Malmros JK, Jakobsen BH, Hasholt B. 2011. Increasing mass loss from Greenland's Mittivakkat Gletscher. *Cryosphere* **5**: 341–348, doi: 10.5194/tc-5-341-2011.
- Mernild SH, Malmros JK, Yde JC, Knudsen NT. 2012. Multi-decadal marine and land-terminating glacier retreat in Ammassalik region, Southeast Greenland. *Cryosphere* **6**: 625–639, doi: 10.5194/tc-6-625-2012.
- Mernild SH, Knudsen NT, Hoffman MJ, Yde JC, Lipscomb WL, Hanna E, Malmros JK, Fausto RS. 2013a. Volume and velocity changes at Mittivakkat Gletscher, Southeast Greenland, 1994–2012. *J. Glaciol.* **59**(216): 660–670, doi: 10.3189/2013JoG13J017.
- Mernild SH, Pelto M, Malmros JK, Yde JC, Knudsen NT, Hanna E. 2013b. Identification of ablation rate, ELA, AAR, and net mass balance using transient snowline variations on two Arctic glaciers. *J. Glaciol.* **59**(216): 649–659, doi: 10.3189/2013JoG12J221.
- Mernild SH, Hanna E, McConnell JR, Sigl M, Beckerman AP, Yde JC, Cappelen J, Steffen K. 2014. Greenland precipitation trends in a long-term instrumental climate context (1890–2012): Evaluation of coastal and ice core records. *Int. J. Climatol.*, doi: 10.1002/joc.3986.
- Oerlemans J, Giesen R, van den Broeke MR. 2009. Retreating alpine glaciers: increased melt rates due to accumulation of dust (Vadret de Morteratsch, Switzerland). *J. Glaciol.* **55**: 729–736.
- Qu X, Hall A. 2007. What controls the strength of snow-albedo feedback? *J. Clim.* **20**: 3971–3981, doi: 10.1175/jcli4186.1.
- Salomon JG, Crystal B, Schaaf CB, Strahler AH, Gao F, Jin Y. 2006. Validation of the MODIS bidirectional reflectance distribution function and albedo retrievals using combined observations from the Aqua and Terra platforms. *IEEE Trans. Geosci. Remote Sens.* **44**(6): 1555–1565, doi: 10.1109/TGRS.2006.871564.
- Schaaf C, Gao F, Strahler A, Lucht W, Li X, Tsang T, Strugnell N, Zhang X, Jin Y, Muller J-P, Lewis P, Barnesley M, Hobson P, Disney M, Roberts G, Dunderdale M, Doll C, d'Entremont R, Hu B, Liang S, Privette J, Roy D. 2002. First operational BRDF, albedo nadir reflectance products from MODIS. *Remote Sens. Environ.* **83**: 135–148.
- Schaaf C, Wang Z, Strahler AH. 2011. Commentary on Wang and Zender – MODIS snow albedo bias at high solar zenith angles relative to theory and to in situ observations in Greenland. *Remote Sens. Environ.* **115**(5): 1296–1300.
- Six D, Wagnon P, Sicart J, Vincent C. 2009. Meteorological controls on snow and ice ablation for two very contrasted months on Saint-Sorlin Glacier (France). *Ann. Glaciol.* **50**: 66–72.
- Steffen K, Box JE, Abdalati W. 1996. Greenland Climate Network: GC-Net. In CRREL 96-27 Special Report on Glaciers, Ice Sheets and Volcanoes (Tribute to M. Meier), Colbeck SC (ed). Cold Reg. Res. and Dev. Cent.: Hanover, NH, 98–103.
- Stibal M, Šabacká M, Žárský J. 2013. Biological processes on glacier and ice sheet surfaces. *Nat. Geosci.* **5**: 771–774, doi: 10.1038/ngeo1611.
- Strahler AH, Muller J-P, Lucht W, Shhaaf CB, Tsang T, Gao F, Li X, Lewis P, Barnesley MJ. 1999. MODIS BRDF/Albedo Product: algorithm theoretical basis document, version 5.0. MODIS Report, MOD43, 53 pp.
- Stroeve J. 2001. Assessment of Greenland albedo variability from the advanced very high resolution radiometer Polar Pathfinder data set. *J. Geophys. Res. Atmos.* **106**(D24): 33989–34006, doi: 10.1029/2001jd900072.
- Stroeve J, Box JE, Gao F, Liang S, Nolin A, Schaaf C. 2005. Accuracy assessment of the MODIS 16-day albedo product for snow: comparison with Greenland in situ measurements. *Remote Sens. Environ.* **94**: 46–60.
- Stroeve J, Box JE, Haran T. 2006. Evaluation of the MODIS (MOD10A1) daily snow albedo product over the Greenland ice sheet. *Remote Sens. Environ.* **105**: 155–171, doi: 10.1016/j.rse.2006.06.009.
- Stroeve J, Box JE, Wang Z, Schaaf C, Barrett A. 2013. Re-evaluation of MODIS MCD43 Greenland albedo accuracy and trends. *Remote Sens. Environ.* **138**: 199–214, doi: 10.1016/j.rse.2013.07.023.
- Takeuchi N, Kohshima S, Katsumoto S. 2001. Structure, formation, and darkening process of albedo-reducing material (Cryoconite) on a Himalayan glacier: a granular algal mat growing on the glacier. *Arct. Antarct. Alp. Res.* **33**(2): 115–122.
- Tedesco M, Kokhanovsky A. 2007. The semi-analytical snow retrieval algorithm and its application to MODIS data. *Remote Sens. Environ.* **111**(2-3): 228–241.
- Tedesco M, Fettweis X, Mote T, Whar J, Alexander P, Box JE, Wouters B. 2013. Evidence and analysis of 2012 Greenland records from spaceborne observations, a regional climate model and reanalysis data. *Cryosphere* **7**: 615–630, doi: 10.5194/tc-7-615.
- Trabant DC, Mayo LR. 1985. Estimations and effects of interannual accumulation on five glaciers in Alaska. *Ann. Glaciol.* **6**: 113–117.
- Wang X, Zender CS. 2010. MODIS snow albedo bias at high solar zenith angles relative to theory and to in situ observations in Greenland. *Remote Sens. Environ.* **114**: 563–575.
- Wang MD, Masek J, Wu A, Nagol J, Xiong X, Levy R, Vermote E, Wolfe R. 2012. Impact of sensor degradation on the MODIS NDVI time series. *Remote Sens. Environ.* **119**: 55–61.
- Warren SG. 1982. Optical-properties of snow. *Rev. Geophys.* **20**: 67–89, doi: 10.1029/RG020i001p00067.
- Weiss A, Norman JM. 1985. Partitioning solar radiation into direct and diffuse, visible and near-infrared components. *Agric. For. Meteorol.* **34**: 205–213, doi: 10.1016/0168-1923(85)90020-6.
- Wright P, Bergin M, Dibb J, Lefer B, Domine F, Carman T, Carmagnola C, Dumont M, Courville Z, Schaff C, Wang Z. 2014. Comparing MODIS daily snow albedo to spectral albedo field measurements in Central Greenland. *Remote Sens. Environ.* **140**: 118–129.
- Yallop ML, Anesio AM, Perkins RG, Cook J, Telling J, Fagan D, MacFarlane J, Stibal M, Barker G, Bellas C, Hodson A, Tranter M, Wadham J, Roberts NW. 2012. Photophysiology and albedo-changing potential of the ice algal community on the surface of the Greenland ice sheet. *ISME J.* **6**: 2302–2313.
- Yde JC, Knudsen NT. 2007. 20th-century glacier fluctuation on Disko Island (Qeqertarsuaq), Greenland. *Ann. Glaciol.* **46**: 209–214.
- Zege EP, Katsev IL, Malinka AV, Prikhach AS, Heygster G, Wiebe H. 2011. Algorithm for retrieval of the effective snow grain size and pollution amount from satellite measurements. *Remote Sens. Environ.* **115**: 2647–2685, doi: 10.1016/j.rse.2011.06.001.
- Zemp M, Thibert E, Huss M, Stumm D, Rolstad Denby C, Nuth C, Nussbaumer SU, Moholdt G, Mercer A, Mayer C, Joerg PC, Jansson P, Hynek B, Fischer A, Escher-Vetter H, Elvehøy H, Andreassen LM. 2013. Uncertainties and reanalysis of glacier mass balance measurements. *Cryosphere* **7**: 1227–1245.

[8]

Mernild, S. H., Liston, G. E., Kane, D. L., Hasholt, B. and Knudsen, N. T. 2008. Snow, runoff, and mass balance modelling for the entire Mittivakkat Glacier (1998–2006), Ammassalik Island, SE Greenland. *Geografisk Tidsskrift-Danish Journal of Geography*, 108(1), 121–136.

Reprinted with permission from Taylor & Francis





# Snow, runoff, and mass balance modeling for the entire Mittivakkat Glacier (1998–2006), Ammassalik Island, SE Greenland

Sebastian H. Mernild, Glen E. Liston, Douglas L. Kane, Niels T. Knudsen & Bent Hasholt

---

## Abstract

*SnowModel*, a physically-based snow evolution modeling system that includes four submodels – *MicroMet*, *EnBal*, *SnowPack*, and *SnowTran-3D* – was used to simulate eight full-year (1998/99 through 2005/06) evolutions of snow accumulation, blowing snow sublimation, evaporation, snow and ice surface melt, runoff, and mass changes on the entire Mittivakkat Glacier (31 km<sup>2</sup>) in south-east Greenland. Meteorological observations from two meteorological stations inside the glacier catchment were used as model input, and glaciological mass balance observations were used for model calibration (1998/99 through 2001/02) and validation (2002/03 through 2005/06) of winter snow simulations. As confirmed by observations, the spatially modeled end-of-winter snow water equivalent (SWE) accumulation increased with elevation up to 700–800 m a.s.l. in response to elevation, topography, and dominating wind direction, and maximum snow deposition occurred on the lee side of the ridge east and south of the glacier. Simulated end-of-summer cumulative runoff decreased with elevation and minimum runoff occurred on the shadowed side of the ridge east and south of the glacier. The modeled test period averaged annual mass balance was 65 mm w.eq. y<sup>-1</sup> or ~8% more than the observed. For the simulation period, the glacier net mass balance varies from -199 to -1,834 mm w.eq. y<sup>-1</sup>, averaging -900(±470) mm w.eq. y<sup>-1</sup>. The glacier averaged annual modeled precipitation ranged from 1,299 to 1,613 mm w.eq. y<sup>-1</sup>, evaporation and sublimation from 206 to 289 mm w.eq. y<sup>-1</sup>, and runoff from 1,531 to 2,869 mm w.eq. y<sup>-1</sup>. The model simulated Mittivakkat Glacier net loss of 900 mm w.eq. y<sup>-1</sup> contributes approximately 42% to the average simulated runoff of 2,140 mm w.eq. y<sup>-1</sup>, indicating a mean specific runoff of 67.8 l s<sup>-1</sup> km<sup>-2</sup>.

## Keywords

*Ammassalik Island; Arctic; Glacier; Greenland; Modeling; Runoff; Snow; SnowModel; Water balance.*

Sebastian H. Mernild (Corresponding author)

International Arctic Research Center and Water & Environmental Research Center, University of Alaska Fairbanks, Alaska, USA

E-mail: fxs@uaf.edu

Glen E. Liston

Cooperative Institute for Research in the Atmosphere, Colorado State University, Colorado, USA

Douglas L. Kane

Water & Environmental Research Center, University of Alaska Fairbanks, Alaska, USA

Niels T. Knudsen

Department of Earth Science, University of Aarhus, Denmark

Bent Hasholt

Department of Geography & Geology, University of Copenhagen, Denmark

*Geografisk Tidsskrift-Danish Journal of Geography*  
108(1):121-136, 2008

The earth's climate is changing. The global mean surface air temperature has increased approximately 0.6°C over the past century (Lemke et al. 2007). In this period, the six warmest years have all occurred since 1998, and the 15 warmest years since 1988 (Hansen et al. 2007), with the largest air temperature changes in winter (Box 2002; Sturm et al. 2005). The Arctic climate has warmed substantially from the end of the Little Ice Age (LIA) to the present (Serreze et al. 2000). According to Chylek et al.

(2006), Greenland temperatures have increased most dramatically during two periods, with warming rates during 1920–1930 being about 50% higher than those in 1995–2005. At the Ammassalik region in coastal south-eastern Greenland, the period 1936–1946 (-1.8°C) was the warmest 10-year period since the end of the LIA, followed by a cooling period until the late 1980s and afterwards, a warming period. The 1995–2004 (-2.0°C) was the warmest 10-year period within the last approximately



60 years (Mernild et al. 2007a). This warming has been accompanied by an increase in precipitation of approximately  $1\% \text{ decade}^{-1}$  (ACIA, 2005). The Arctic is undergoing a system-wide response to the altered climatic state, and the effects of a warmer and wetter climate on the terrestrial cryospheric and hydrologic components are already becoming apparent in the high-latitude hydrological cycle on hemispheric, regional, local, and micro scales as documented by e.g. Serreze et al. (2000), Vorosmarty et al. (2001), Moritz et al. (2002), Hanna et al. (2005); Hinzman et al. (2005), and Mernild et al. (2007a, 2007b). It appears that the first-order impacts on the terrestrial regions of the Arctic expected in connection with a warming climate result from a longer thawing period (e.g. Hinzman et al., 2005; Mernild et al., 2007a, 2007b). A longer snow-free season and greater winter insulation produces secondary impacts that cause, for example, greater melt of glacier snow and ice and deeper thaw of the active layer (Hinzman et al., 2005). Snow and glacier ice are reservoirs of water from a hydrological perspective. Basins with a substantial glacier component consistently display an increasing trend in runoff, presumably due to increases in glacier melt. River basins without significant glaciers tend to show a decreasing runoff. Previous studies on e.g. Svalbard by Killingtonveit (2004) and in the circumpolar Arctic by e.g. Kane and Yang (2004) have shown that glaciers have a dominant influence on the water balance compared to non-glaciated areas, often producing surpluses of melting and runoff exceeding precipitation.

Throughout the Arctic, much of the winter precipitation falls in solid form under windy conditions (e.g. Liston and Sturm 2002). As winter progresses, the solid precipitation accumulates on the ground and is frequently redistributed during blowing snow events. A further consequence of this blowing snow is that significant portions (10–50%) of snow cover can be returned to the atmosphere by sublimation of windborne snow particles (e.g. Liston and Sturm 1998, 2002, 2004; Essery et al. 1999; Pomeroy and Essery 1999; Hasholt et al. 2003; Mernild et al. 2006a). As spring and summer progress, the variation, duration, and intensity of snow and glacier melt increase in response to variations in weather and climate (e.g. insulation, temperature inversions, and wind speed) and surface characteristics (e.g. albedo, roughness). The moisture in this system also changes phase (solid, liquid, and vapour) throughout the year as part of various physical processes and in response to the available surface energy fluxes. All of these seasonally changing processes

directly impact the cryospheric and the seasonal evolution of the high-latitude hydrological cycle (e.g. Kane 1997; Liston and Sturm 2002).

Across the Arctic, precipitation gauges significantly underestimate solid precipitation because of aerodynamic errors at the precipitation gauging station (e.g. Woo et al. 1982; Yang et al. 1998; Allerup et al. 1998, 2000a, 2000b; Liston and Sturm 2002, 2004). In addition, due to the generally rough terrain, harsh climatic conditions, and remote locations of Arctic glaciers, extensive snow distribution, snowmelt, and glacier melt measurements have typically not been possible. The use of gauging stations that underestimate the true amount of solid precipitation, limited numbers of Arctic meteorological stations, and limited winter and summer glacier mass balance measurements lead us to conclude that we have few quality observations related to the spatial and temporal distribution of snow precipitation, snow-blowing sublimation, and surface melt across much of the glaciated Arctic. On Ammassalik Island, SE Greenland, information on climate, glacier conditions, and runoff were absent before the 1933 expedition by Milthers. During the International Geophysical Year (IGY) in 1957–58 (also known as the Third International Polar Year (IPY)), measurements of meteorology and terrestrial runoff were carried out at the Mittivakkat Glacier catchment for the first time. In 1972, the Sermilik Research Station was established. Since then, an extensive monitoring program to study climate landscape processes, interactions, and trends has been ongoing. Studies of simultaneous effects of climate in the form of observed glacier mass balance changes and runoff are carried out so changes in climate can be directly linked to short and long-term trends. Presently, the Mittivakkat Glacier catchment is the only catchment in all of east Greenland (along the approximately 3,000 km coast) where a permanent glacier monitoring program is in place together with automatic meteorological and hydrometric monitoring stations. The lack of measurements of such key climate system components is a serious impediment to hydrological research efforts. Thus, there is a clear need to explore issues associated with data sparseness and modeling capabilities.

The goal of this study is to apply and test a state-of-the-art modeling system, SnowModel (Liston and Elder 2006a, Mernild et al. 2006a, Liston et al. 2007), over the entire Mittivakkat Glacier complex in southeast Greenland. We performed the model simulations with the following objectives: 1) to simulate spatial winter processes related to snow accumulation, snow redistribution by

**Table 1:** Observed winter, summer, and net mass balance for the Mittivakkat Glacier observation area (17.6 km<sup>2</sup>) (1995/96 through 2005/06). Winter mass balance observations are carried out in late May and in early June and summer mass balance observations in late August.

Observed winter balance for the Mittivakkat Glacier mass balance observation area (mm w.eq)													
Altitude (m a.s.l.)	Area (km <sup>2</sup> )	1995/1996	1996/1997	1997/1998	1998/1999	1999/2000	2000/2001	2001/2002	2002/2003	2003/2004	2004/2005	2005/2006	1995–2006
>800	0.771	2,000	1,600	1,050	800	950	1,250	1,350	No data	No data	1,150	1,150	1,260(±360)
700–800	2.467	2,050	1,950	1,150	1,050	1,300	1,350	1,450	No data	No data	1,300	1,300	1,430(±340)
600–700	3.994	1,800	1,650	1,200	1,100	1,500	1,350	1,520	No data	No data	1,200	1,060	1,380(±260)
500–600	2.702	1,700	1,550	1,200	1,050	1,450	1,300	1,550	No data	No data	1,000	1,150	1,330(±250)
400–500	3.160	1,200	1,200	1,150	950	1,300	1,200	1,150	No data	No data	850	1,000	1,110(±150)
300–400	2.351	1,000	950	1,070	900	900	950	950	No data	No data	450	750	790(±150)
200–300	1.439	850	850	1,000	800	800	750	850	No data	No data	350	580	760(±190)
<200	0.536	900	800	950	750	900	750	950	No data	No data	200	750	770(±230)
130–899	17.600	1,510	1,410	1,140	980	1,230	1,180	1,280	No data	No data	920	1,010	1,180(±140)
Observed summer balance for the Mittivakkat Glacier mass balance observation area (mm w.eq)													
Altitude (m a.s.l.)	Area (km <sup>2</sup> )	1995/1996	1996/1997	1997/1998	1998/1999	1999/2000	2000/2001	2001/2002	2002/2003	2003/2004	2004/2005	2005/2006	1995–2006
>800	0.771	-1,000	-1,100	-1,700	-750	-1,000	-1,550	-250	No data	No data	-1,750	-780	-1,140(±400)
700–800	2.467	-1,050	-1,250	-1,800	-1,030	-1,250	-1,850	-550	No data	No data	-1,900	-910	-1,340(±380)
600–700	3.994	-1,150	-1,450	-1,900	-1,250	-1,500	-2,100	-1,350	No data	No data	-2,200	-1,220	-1,610(±340)
500–600	2.702	-1,300	-1,700	-2,100	-1,550	-1,750	-2,050	-1,900	No data	No data	-2,550	-1,530	-1,860(±280)
400–500	3.160	-1,650	-2,000	-2,380	-1,900	-2,250	-1,950	-2,300	No data	No data	-2,950	-1,750	-2,120(±300)
300–400	2.351	-1,900	-2,350	-2,750	-2,450	-2,900	-2,050	-2,500	No data	No data	-3,500	-2,050	-2,490(±370)
200–300	1.439	-2,400	-2,650	-3,380	-3,130	-3,600	-3,100	-2,900	No data	No data	-4,250	-2,650	-3,120(±420)
<200	0.536	-3,000	-2,950	-4,500	-3,850	-4,250	-4,250	-3,300	No data	No data	-4,750	-3,500	-3,790(±550)
130–899	17.600	-1,500	-1,810	-2,310	-1,750	-2,060	-2,140	-1,780	No data	No data	-2,740	-1,590	-1,960(±310)
Observed net mass balance for the Mittivakkat Glacier mass balance observation area (mm w.eq)													
Altitude (m a.s.l.)	Area (km <sup>2</sup> )	1995/1996	1996/1997	1997/1998	1998/1999	1999/2000	2000/2001	2001/2002	2002/2003	2003/2004	2004/2005	2005/2006	1995–2006
>800	0.771	1,000	500	-650	50	-50	-300	1,100	1,050	50	-600	370	220(±560)
700–800	2.467	1,000	700	-650	20	50	-500	900	950	-450	-600	390	140(±600)
600–700	3.994	650	200	-700	-150	0	-750	170	750	-700	-1,000	-160	-150(±510)
500–600	2.702	400	-150	-900	-500	-300	-750	-350	550	-850	-1,550	-250	-430(±440)
400–500	3.160	-450	-800	-1,230	-950	-950	-750	-1,150	250	-1,100	-2,100	-700	-910(±370)
300–400	2.351	-900	-1,400	-1,680	-1,550	-2,000	-1,100	-1,550	-200	-1,550	-3,050	-1,000	-1,480(±480)
200–300	1.439	-1,550	-1,800	-2,380	-2,330	-2,800	-2,350	-2,050	-850	-2,500	-3,900	-1,950	-2,230(±530)
<200	0.536	-2,100	-2,150	-3,550	-3,100	-3,350	-3,500	-2,350	-1,450	-3,500	-4,550	-3,000	-2,940(±690)
130–899	17.600	10	-400	-1,170	-770	-830	-960	-500	350	-1,060	-1,820	-580	-740(±430)

wind, and snow sublimation on the glacier in order to estimate the end-of-winter snow water equivalent (SWE); 2) to simulate the spatial glacier snowmelt and glacier ice melt in order to estimate the yearly glacier runoff; 3) to model the annual glacier winter, summer, and net mass balance from 1998 through 2006 and compare these modeled outputs with available observational datasets; and 4) to simulate the water balance components for the entire Mittivakkat Glacier, including the freshwater runoff contribution to the ocean.

## Study area

### Physical settings and climate

The Mittivakkat Glacier (65°42'N, 37°48'W) is a temperate glacier (Knudsen and Hasholt, 1999) situated on Ammassalik Island, approximately 15 km northwest of the town of Tasiilaq (Ammassalik) and 50 km east of the eastern margin of the Greenland Ice Sheet. It is separated from the mainland by the 10–15 km wide Sermilik Fjord. The

Mittivakkat Glacier has several outlets and covers 31 km<sup>2</sup> (Figure 1a) with an elevation ranging from approximately 160 to 930 m a.s.l. The area surrounding the glacier is characterized by strong alpine relief, and varies in elevation from 0 to 973 m a.s.l., with the highest altitudes east and south of the glacier (Figure 1a). Since the first observation in 1933, there has been an almost continuous recession of the Mittivakkat Glacier of around 1.3 km (approximately 18 m y<sup>-1</sup>). Since 1898/99, in 89 out of 105 balance years, the Mittivakkat Glacier had a negative estimated net mass balance (Mernild et al. 2007a). From 1995/96 through 2005/06, the observed winter, summer, and net mass balances were 1,180±(140), -1,960±(310), and -740±(430) mm w.eq. (Table 1). Over the same time period, the equilibrium line altitude (ELA, where annual ablation equals annual accumulation) moved up the glacier from approximately 550 to 700 m a.s.l. (Table 1). Avalanches are rare near the glacier.

There are two primary meteorological stations within the simulation domain: Station Nunatak (515 m a.s.l., representative of the ELA of the Mittivakkat glacier) and Sta-

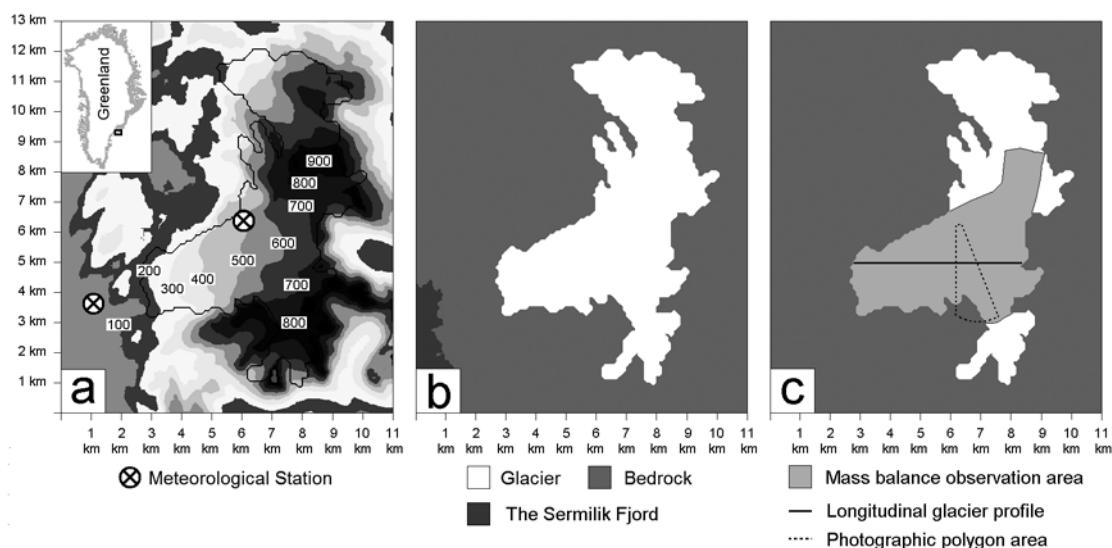


**Figure 1:** Mittivakkat Glacier simulation domain (31 km<sup>2</sup>): (a) topography (100 m contour interval); (b) surface characteristics; and (c) observation area (17.6 km<sup>2</sup>) with location of longitudinal profile and photographic polygon area. Also shown in (a) are the two meteorological tower stations: Station Nunatak (515 m a.s.l.) and Station Coast (25 m a.s.l.). The inset figure in (a) indicates the general location of the Mittivakkat Glacier in eastern Greenland. The domain coordinates can be converted to UTM by adding 548 km to the west–east origin (easting) and 7281 km to the south–north origin (northing) and converting to meters.

tion Coast (25 m a.s.l., representative of the coastal area) (Figure 1a). Station Nunatak is located at the highest peak on a small nunatak (~5 m from the glacier in the dominant wind directions). Station Coast includes a site located on a rock hill close to the coast. The Mittivakkat Glacier area climate is an ET (tundra) climate according to the Köppen classification system. Based on data from these stations, the mean annual air temperature (MAAT) (2.0 m) (1998–2006) is -2.4, -0.8, and -1.8°C for Station Nunatak, Station Coast, and the glacier (derived from Micrometeorological Model (MicroMet) air temperature forcing fields). The maximum monthly average area air temperature is 5.4°C in July and the minimum is -8.1°C in February. The mean annual area relative humidity is 83% (2.0 m) (1998–2006) (derived from MicroMet). The total annual precipitation (TAP) at Station Nunatak is 1,851 mm w.eq. (after applying a wind speed correction, due to the exposed station location on the nunatak (Mernild et al., 2006a)) and 1,428 mm w.eq. at Station Coast (1998–2006) (no wind speed correction was needed or applied at Station Coast), indicating a positive orographic effect between the stations of 113 mm w.eq. 100 m<sup>-1</sup> (Mernild et al., 2008a). The opposite, a negative orographic effect of -52 mm w.eq. 100 m<sup>-1</sup>, occurs for liquid precipitation during the summer months (e.g. Mernild 2006; Mernild et al. 2007a). Approximately 65–85% of TAP falls as snow during a period that spans from approximately mid-Sep-

tember to late May. The mean annual wind speed is 3.7 and 4.1 m s<sup>-1</sup> for Station Nunatak and Station Coast (2.0 m) (1998–2006), respectively, mainly dominated by N and E winds during autumn, winter, and spring, and SW, S, and E winds during summer. Strong winds (neqqajaaq, similar to a foehn wind) occur during winter on the Mittivakkat Glacier, mainly coming from the E and NE, and often followed by katabatic winds (piteraqaq) from the Greenland Ice Sheet and channelled through the Sermilik Fjord in a northerly direction. Wind velocities during a piteraqaq can gust to 85 m s<sup>-1</sup>, causing severe blowing and drifting snow. Together, the factors of topography, precipitation, and wind result in significant winter snow redistribution.

## SnowModel

### *SnowModel description*

SnowModel (Liston and Elder 2006a) is a spatially distributed snowpack evolution modeling system specifically designed to be applicable over the wide range of snow landscapes, climates, and conditions found around the world. It is made up of four submodels: MicroMet defines the meteorological forcing conditions (Liston and Elder 2006b); EnBal calculates the surface energy exchanges, including melt (Liston 1995; Liston et al. 1999); SnowPack simulates snow depth and water equivalent

evolution (Liston and Hall 1995); and SnowTran-3D is a blowing snow model that accounts for snow redistribution by wind (Liston and Sturm 1998; 2002; Liston et al. 2007). While other distributed snow models exist (e.g. Tarboton et al. 1995; Marks et al. 1999; Winstral and Marks 2002), the SnowTran-3D component allows application in Arctic, alpine (that is, above treeline), and prairie environments that comprise 68% of seasonally snow-covered areas in the Northern Hemisphere (Liston 2004). SnowModel also simulates snow-related physical processes at spatial scales ranging from five meters to global and temporal scales ranging from 10 minutes to a whole season. Simulated processes include: 1) accumulation and loss from snow precipitation, blowing snow redistribution, and sublimation; 2) loading, unloading, and sublimation within forest canopies; 3) snow density evolution; and 4) snow pack ripening and melt. SnowModel was originally developed for glacier-free landscapes. For glacier surface mass balance studies on Eastern Greenland, SnowModel was modified to simulate glacier ice melt after winter snow accumulation had ablated (Mernild et al. 2006a, 2007c).

#### *Micromet*

MicroMet is a quasi-physically based meteorological distribution model (Liston and Elder 2006b) specifically designed to produce the high-resolution meteorological forcing distributions (air temperature, relative humidity, wind speed, wind direction, precipitation, solar and long-wave radiation, and surface pressure) required to run spatially distributed terrestrial models over a wide range of landscapes in a physically realistic manner. MicroMet uses elevation-related interpolations to modify air temperature, humidity, and precipitation following Kunkel (1989), Walcek (1994), Dodson and Marks (1997), and Liston et al. (1999). Temperature and humidity distributions are defined to be compatible with the observed lapse rates. Wind flow in complex topography is simulated following Ryan (1977) and Liston and Sturm (1998). Solar radiation variations are calculated using elevation, slope, and aspect relationships (Pielke 2002). Incoming long-wave radiation is calculated while taking into account cloud cover and elevation-related variations following Iziomon et al. (2003). Precipitation is distributed following Thornton et al. (1997). In addition, any data from more than one location, at any given time, are spatially interpolated over the domain using a Gaussian distance-dependent weighting function and interpolated to the model grid using the Barnes objective analysis scheme (Barnes 1964,

1973; Koch et al. 1983). Liston and Elder (2006b) and Liston et al. (2007) have performed a rigorous validation of MicroMet using various observational datasets, data denial, and geographic domains. Further, MicroMet has been used to distribute observed and modeled meteorological variables over a wide variety of landscapes in the United States: Colorado (Greene et al. 1999), Wyoming (Hiemstra et al. 2002, 2006), Idaho (Prasad et al. 2001), and Arctic Alaska (Liston et al. 1999, 2002, 2007; Liston and Sturm 1998, 2002); Norway: Svalbard and central Norway (Bruland et al. 2004); East Greenland (Hasholt et al. 2003; Mernild et al. 2006a, 2006b, 2007c, 2008b); and near-coastal Antarctica (Liston et al. 1999).

#### *Enbal*

EnBal performs standard surface energy balance calculations (Liston 1995; Liston et al. 1999). This component simulates surface (skin) temperatures, and energy and moisture fluxes in response to observed and/or modeled near-surface atmospheric conditions provided by MicroMet. Surface latent and sensible heat flux and snowmelt calculations are made using a surface energy balance model of the form:

$$(1 - \alpha) Q_{si} + Q_{li} + Q_{le} + Q_h + Q_e + Q_c = Q_m, \quad (1)$$

where  $Q_{si}$  is the solar radiation reaching the earth's surface,  $Q_{li}$  is the incoming long-wave radiation,  $Q_{le}$  is the emitted long-wave radiation,  $Q_h$  is the turbulent exchange of sensible heat,  $Q_e$  is the turbulent exchange of latent heat,  $Q_c$  is the conductive energy transport,  $Q_m$  is the energy flux available for melt, and  $\alpha$  is the surface albedo. Details of each term in Equation 1 and the model solution are available in Liston (1995) and Liston et al. (1999). In the presence of snow or glacier ice, surface temperatures greater than 0°C indicate that energy is available for melting. This energy is computed by fixing the surface temperature at 0°C and solving Equation 1 for  $Q_m$ .

#### *Snowpack*

SnowPack is a single-layer, snowpack evolution model (Liston and Hall 1995) that describes snowpack changes in response to precipitation and melt fluxes defined by MicroMet and EnBal. Its formulation closely follows Anderson (1976) to define compaction-based snow density evolution, where the density evolves over time in response to snow temperature and the weight of overlying snow. A second density-modifying process results from snow melting. The melted snow reduces the snow depth



Symbol	Value	Parameter
$C_v$	0.50	Vegetation snow-holding depth (m) - Bedrock
	0.01	- Glacier
	0.01	- Lake
$t_c$	1,500	Terrain curvature (m)
$f$	500.0	Snow equilibrium fetch distance (m)
$U_{*t}$	0.25	Threshold wind-shear velocity ( $\text{m s}^{-1}$ )
$Z_0$	0.001	Snow surface roughness length (m)
$\alpha$		Surface albedo
	0.8	- Snow
	0.4	- Ice
$\rho$		Surface density ( $\text{kg m}^{-3}$ )
	280	- Snow
	910	- Ice
$dt$	1	Time step (day)
$dx = dy$	100	Grid cell increment used at different simulations (m)

**Table 2:** User-defined constants used in Snow-Model simulations (see Liston and Sturm (1998) for parameter definitions).

and is redistributed through the snowpack until a maximum snow density, assumed to be  $550 \text{ kg m}^{-3}$ , is reached (Liston and Hall 1995). This provides a simple method to account for heat and mass transfer processes, such as snowpack ripening, during spring melt. Any additional melt water is assumed to reach the ground or ice at the base of the snowpack and is defined as “runoff”. The density of new snow (precipitation) added to the snowpack is also defined following Anderson (1976).

### Snowtran-3D

SnowTran-3D (Liston and Sturm 1998; Liston et al. 2007) is a three-dimensional submodel that simulates snow depth evolution (deposition and erosion) resulting from windblown snow based on a mass balance equation that describes the temporal variation of snow depth at each grid cell within the simulation domain. SnowTran-3D’s primary components are a wind flow forcing field, a wind shear stress on the surface, snow transport by saltation, snow transport by turbulent suspension, sublimation of saltating and suspended snow, and accumulation and erosion at the snow’s surface (Liston and Sturm 2002). Simulated transport and blowing snow sublimation processes are influenced by the interactions among available snow, topography, and atmospheric conditions (Liston and Sturm 1998). SnowTran-3D simulates snow depth evolution and then uses the snow density simulated by SnowPack to convert it to the more hydrologically significant SWE depth. Deposition and erosion, which lead to changes in snow depth (Equation 2), are the result of changes in horizontal mass transport rates of saltation,  $Q_{\text{salt}}$  ( $\text{kg m}^{-1} \text{ s}^{-1}$ ), changes in horizontal mass transport rates of turbulent suspended snow,  $Q_{\text{turb}}$  ( $\text{kg m}^{-1} \text{ s}^{-1}$ ), sub-

limation of transported snow particles,  $Q_v$  ( $\text{kg m}^{-2} \text{ s}^{-1}$ ), and the water equivalent precipitation rate,  $P$  ( $\text{m s}^{-1}$ ). Combined, the time rate of change in snow depth,  $\zeta$  (m), is

$$\frac{d(\rho_s \zeta)}{dt} = \rho_w P - \left( \frac{dQ_{\text{salt}}}{dx} + \frac{dQ_{\text{turb}}}{dx} + \frac{dQ_{\text{salt}}}{dy} + \frac{dQ_{\text{turb}}}{dy} \right) + Q_v \quad (2)$$

where  $t$  (s) is time;  $x$  (m) and  $y$  (m) are the horizontal coordinates in the west–east and south–north directions, respectively; and  $\rho_s$  and  $\rho_w$  ( $\text{kg m}^{-3}$ ) are snow and water density, respectively. At each time step, Equation 2 is solved for each individual grid cell within the domain, and is coupled to the neighboring cells through the spatial derivatives ( $d/dx$ ,  $d/dy$ ). SnowTran-3D simulations have previously been compared against observations in glacier and glacier-free alpine, Arctic, and Antarctic landscapes (Greene et al. 1999; Liston et al. 2000, 2007; Prasad et al. 2001; Hiemstra et al. 2002, 2006; Liston and Sturm 2002; Hasholt et al. 2003; Bruland et al. 2004; Mernild et al. 2006a, 2006b, 2007c, 2008b).

### SnowModel input

To solve the system of equations, SnowModel requires spatially distributed fields of topography and land cover types, and temporally varying meteorological data (air temperature (recorded at 2.0 m level), relative humidity (2.0 m), wind speed (2.0 m), wind direction (2.0 m), and SWE precipitation (surface level) obtained from point meteorological stations located within the simulation domain (Figure 1a). The simulations were performed on a one-day time step. Snow and ice melt and blowing snow are threshold processes and may not be accurately represented by a one-day time step. Unfortunately, computa-



**Table 3:** Mean monthly lapse rates based on air temperature (2 m) from Station Nunatak and Station Coast (1999 through 2004).

	Jan	Feb	Mar	Apr	May	Jun	Jul	Aug	Sep	Oct	Nov	Dec	Ave
Average air temperature lapse rate and standard deviation (°C 100 m <sup>-1</sup> )	-0.45	-0.51	-0.47	-0.30	-0.20	0.33	0.33	0.15	-0.31	-0.49	-0.51	-0.42	-0.24(±0.32)

tional resources did not permit the use of a smaller time increment. The simulations span the eight-year period of 1 September 1998 through 31 August 2006, and a split-sample test was applied for calibration (1998/99 through 2001/02) and validation (2002/03 through 2005/06) of the winter snow simulations (e.g. Klemes, 1985, 1986; Refsgaard and Knudsen, 1996; Refsgaard, 2000; Refsgaard and Henriksen, 2004). The calibration and validation periods were chosen arbitrarily. Summer ablation was not calibrated or tested.

Topographic data were obtained from a digital elevation model (DEM) based on a 1:100000-scale map with 25 m contour intervals (derived from 1981 aerial photos). A 100 m grid cell increment DEM was used that covered the 11 km by 13 km simulation domain, which included the Mittivakkat Glacier (Figure 1). Each grid cell within the domain was assigned a land cover type and classified as bedrock with a snow-holding depth of 0.50 m, as lake ice with a depth of 0.01 m, or as glacier with a snow-holding depth of 0.01 m (Mernild et al., 2006a) (Table 2). The snow-holding depth is the snow depth that must be exceeded before snow can be transported by wind. Each grid value of the snow-holding depth was assumed to be constant throughout the winter except for lakes, which were assumed to be unable to accumulate snow until after their surface was frozen (assumed to occur in the beginning of October; Hasholt et al. 2003). All fjord areas within the domain were excluded from the model simulations (Figure 1). Albedo was assumed to be 0.8 for snow. Realistically, snow albedo changes with time and surface characteristics (Pomeroy and Brun 2001). Model parameter values used in the simulations are provided in Table 2 (see Liston and Sturm (1998) for parameter definitions). Monthly lapse rates were also used as a model input (Table 3), with a minimum monthly lapse rate of -0.51°C 100 m<sup>-1</sup> for November and February, and a maximum monthly lapse rate of 0.33°C 100 m<sup>-1</sup> in June and July; these temperature increases with elevation are governed by summer sea breezes in daytime coming predominately from the S and SW (Mernild et al. 2006a).

In addition to the meteorological observations, during each of the eight study years, winter and summer mass balance measurements were made at the end of May and the end of August, respectively. During these field campaigns, snow depth, density, and ablation from snow and glacier ice were measured using cross-glacier stake lines spaced approximately 500 m apart; the distance between the stakes in each line was 200–250 m (Knudsen and Hasholt 2004). The assumed accuracy of each observed winter and summer mass balances is ±15%; however, larger errors might occur especially in glacier areas with many crevasses (Knudsen and Hasholt 1999). To determine the Mittivakkat Glacier snow cover variations on the upper glacier, automatic digital cameras positioned at Station Nunatak were used. Liquid (rain) precipitation was measured at both stations 0.45 m above the ground without wind corrections because the orifice of the gauge was located at approximately the same height as the local roughness elements. Solid (snow) precipitation was calculated from snow depth sounder observations that are assumed to have an accuracy of within ±10–15%. The noise was removed from the sounder data and the remaining snow depth increases were adjusted using a temperature-dependent snow density (from 67.9 to 217.6 kg m<sup>-3</sup>, on average, 85.8 kg m<sup>-3</sup>; Brown et al. 2003) and an hourly snowpack settling rate (Anderson 1976) to estimate the SWE precipitation.

SWE precipitation from Station Nunatak was calibrated using the Mittivakkat Glacier winter mass balance observations for the calibration period (1998/99 through 2001/02), because initial SnowModel simulations underestimated end-of-winter (31 May) glacier SWE depths by 25% (1998/99), 30% (1999/2000), 38% (2000/01), 18% (2001/02), and 28% (average 1998–2002) for the calibration period (for further details, see calibration iterative routines in Mernild et al. (2006a), which yielded a simulated Mittivakkat Glacier SWE depth on 31 May that was within 1% of the observed Mittivakkat Glacier winter mass balance observations). As suggested by the numerous wind events above 5 m s<sup>-1</sup> (a typical snow transport

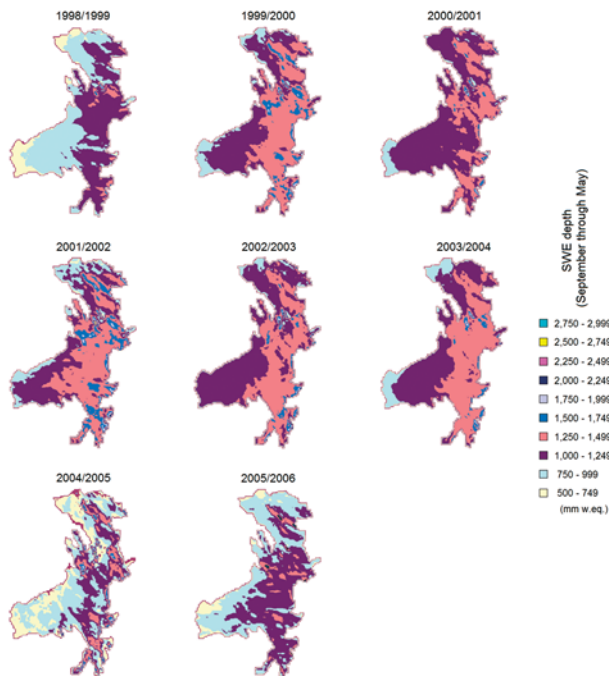


**Figure 2:** Spatial distribution of the snow water equivalent (SWE) depth (250 mm w.eq. interval) for the entire Mittivakkat Glacier at 31 May. The simulation period goes from September through May from 1998/99 to 2005/06.

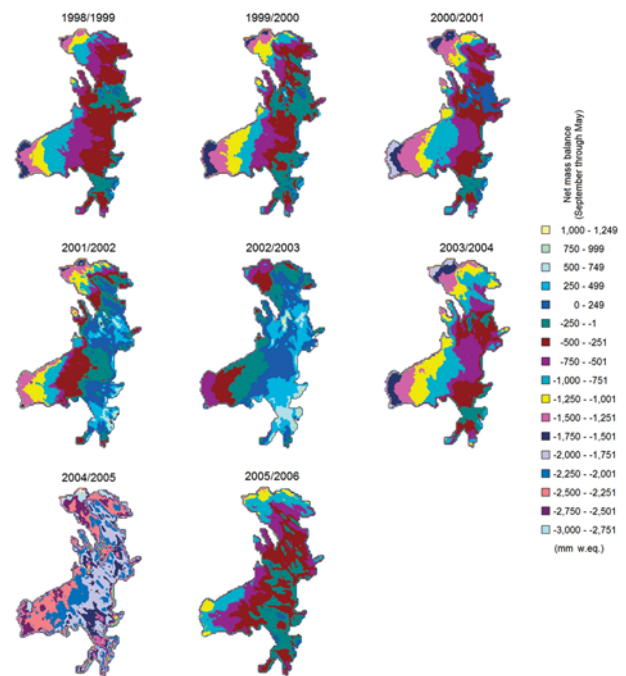


**Figure 4:** Spatial distribution net mass balance (250 mm w.eq. interval) for the entire Mittivakkat Glacier at 31 August. The simulation period goes from September through August (1998/1999 to 2005/06).

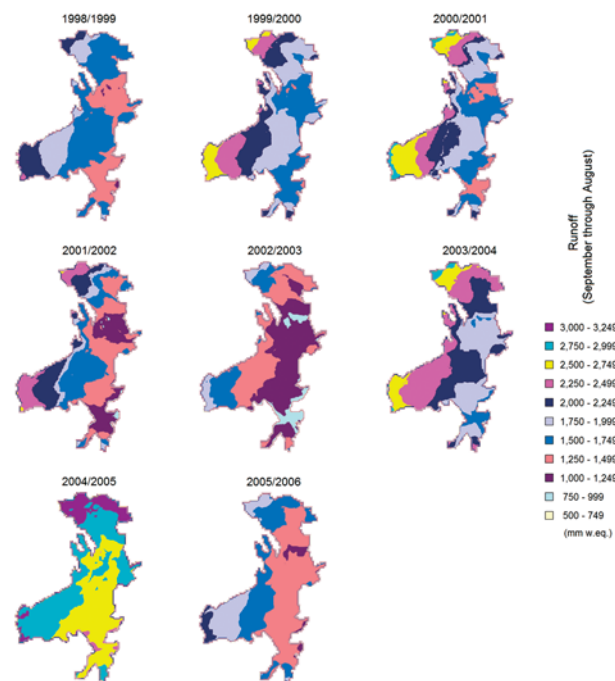


**Figure 3:** Spatial distribution of the cumulative runoff (250 mm w.eq. interval) for the entire Mittivakkat Glacier at 31 August. The simulation period goes from September through August (1998/1999 to 2005/06).

threshold; Liston and Sturm 1998) at the exposed station location on the nunatak (Figure 1a), the SWE precipitation was underestimated; the solid precipitation at Station Nunatak was redistributed by the wind and did not accumulate under the snow depth sounder that was used to reconstruct the precipitation history (Mernild et al., 2006a).

## Results

Table 4 shows observed and modeled winter, summer, and net mass balances for the observation area (17.6 km<sup>2</sup>) (Figure 1c) and modeled SWE precipitation, runoff, and net mass balance values (Figures 2, 3, and 4) for the entire Mittivakkat Glacier (31 km<sup>2</sup>). For the observation area, average modeled winter mass balance (September through May) of 1,100(±150) mm w.eq. is significant ( $R^2 = 0.99$ ;  $rmse = 17$ , where  $rmse$  is root mean squared error;  $p < 0.01$ , where  $p$  is the level of significance) with observed values of 1,140(±140) mm w.eq. (1998/99 to 2005/06). This indicates a SWE difference of less than 1% in accordance to the iterative calibration routines. The years 1998/99 through 2001/02 are used for calibration of the winter snow simulations and 2002/03 through 2005/06

**Table 4:** Validation of SnowModel simulations: observed and modeled winter, summer, and net mass balance from the Mitivakkat Glacier, Ammassalik Island (SE Greenland; 65°N) from 1995/96 to 2005/06. Winter mass balance observations are carried out in late May and in early June and summer mass balance observations in late August, while modeled winter values on 31 May and summer values on 31 August. \*Average calculated based on data from 1998/99 to 2001/02, 2004/05, and 2005/06.

The Mitivakkat Glacier Ammassalik Island (SE Greenland, 65°N)									
	Winter mass balance (mm w.eq.)			Summer mass balance (mm w.eq.)			Net mass balance (mm w.eq. y <sup>-1</sup> )		
	Observed (observation area, 17.6 km <sup>2</sup> )	Modeled (observation area, 17.6 km <sup>2</sup> ) (31 May)	Modeled (entire glacier, 31 km <sup>2</sup> ) (31 May)	Observed (observation area, 17.6 km <sup>2</sup> )	Modeled (observation area, 17.6 km <sup>2</sup> ) (31 August)	Modeled (entire glacier, 31 km <sup>2</sup> ) (31 August)	Observed (observation area, 17.6 km <sup>2</sup> )	Modeled (observation area, 17.6 km <sup>2</sup> ) (31 August)	Modeled (entire glacier, 31 km <sup>2</sup> ) (31 August)
1998/1999	980	960	980	-1,750	-1,690	-1,833	-770	-730	-853
1999/2000	1,230	1,240	1,250	-2,060	-2,020	-2,124	-830	-780	-874
2000/2001	1,180	1,190	1,210	-2,140	-2,060	-2,207	-960	-870	-997
2001/2002	1,280	1,270	1,260	-1,780	-1,690	-1,850	-500	-420	-590
2002/2003	No data	1,240	1,240	No data	-1,310	-1,439	350	-70	-199
2003/2004	No data	1,220	1,230	No data	-2,160	-2,320	-1,060	-940	-1,090
2004/2005	920	930	940	-2,740	-2,750	-2,774	-1,820	-1,820	-1,834
2005/2006	1,010	1,040	1,020	-1,590	-1,640	-1,751	-580	-600	-731
Average and standard deviation	1,100(±150)*	1,140(±140)	1,140(±140)	-2,010(±410)*	-1,920(±440)	-2,040(±410)	-770(±610)	-780(±500)	-900(±470)

for model validation. For the years 2002/03 and 2003/04, only annual net mass balance data were available. An extrapolation run over the entire glacier area shows an average modeled winter mass balance of 1,140(±140) mm w.eq. (1998/99 to 2005/06) (Table 4) and a variation in the end-of-winter SWE from 500–749 mm w.eq. at low-lying areas (below 300 m a.s.l.) up to 2,250–2,499 mm w.eq. in the upper part (around 800 m a.s.l.) (Figure 2). As confirmed by observations, the spatial modeled end-of-winter SWE accumulation on 100 m altitude intervals increases with elevation up to 700–800 m a.s.l. (illustrated end-of-winter 31 May 2005 on Figure 5b) in response to elevation, topography, and dominating wind direction. A significant correlation occurs between modeled SWE depth and the observed end-of-winter mass balance expressed using the 100 m altitude intervals: for 1998/99,  $R^2 = 0.95$ ,  $p < 0.01$ ; 1999/2000,  $R^2 = 0.94$ ,  $p < 0.01$ ; 2000/01,  $R^2 = 0.98$ ,  $p < 0.01$ ; 2001/02,  $R^2 = 0.96$ ,  $p < 0.01$ ; 2002/03,  $R^2 = 0.94$ ,  $p < 0.01$ ; 2003/04,  $R^2 = 0.95$ ,  $p < 0.01$ ; 2004/05,  $R^2 = 0.98$ ,  $p < 0.01$  (Figure 5b), and 2005/06,  $R^2 = 0.96$ ,  $p < 0.01$ , even though the maximum difference in SWE for each interval varies by up to 150 mm w.eq. (e.g. for the interval >800 m a.s.l., 1999/2000). Within SnowModel, SnowTran-3D simulates spatial snow deposition patterns in response to erosion and deposition. In Figure 2, the spatial variation in modeled SWE depths for 31 May 1999 through 2006 is illustrated. The SWE pattern illustrates an almost identical spatial yearly snow distribution from 1998/99 through 2005/06 with maximum SWE deposition values between 500 and 800 m a.s.l. on the lee side of the ridge east and south of the glacier (Figures 2 and 5b), because the majority of snow-transporting winds are from NE, E, and SE.

The observation area average modeled summer mass balance (June through August) of -1,920(±440) mm w.eq. (1998/99 to 2005/06) is significant ( $R^2 = 0.98$ ;  $rmse = 48$ ;  $p < 0.01$ ) with observed values of -2,010(±410) mm w.eq. (Table 4), showing a difference of approximately 5%. For the entire glacier, the average summer mass balance is -2,040(±410) mm w.eq. (1998/99 to 2005/06), varying from -1,439 mm w.eq. (2002/03) to -2,774 mm w.eq. (2004/05). End-of-summer minimum surface melt and runoff occurred on the shadow side of the ridge east and south of the glacier (Figure 3). The end-of-summer (31 August) snow cover and the location of modeled and observed ELA on the Mitivakkat glacier is a product of both snow accumulation and ablation processes. An example of the snow cover variation through the late part of the 2002/03 ablation season is shown in Figure 6 based on digital camera images from Station Nunatak. The observed ELA data were produced using glacier net mass balance measurements (Table 1). The modeled ELA location (identical with the snow line, the boundary between bare ice and snow cover on the glacier surface) for 2002/03 (the year with the lowest ablation) (Figure 5c), and for 2004/05 (the year with the highest ablation) (Figure 5d) were situated from approximately 400 m a.s.l. and upwards. The modeled average ELA location is confirmed by the 100 m altitude interval data from the observed net mass balance (Table 1), which indicates a 0 mm w.eq. net mass balance from approximate 400 m a.s.l. up the glacier to approximately 700 m a.s.l. through the simulation period 1998/99 to 2005/06. For the years 1997/98, 2000/01, and 2004/05, the observed net mass balance is completely negative (Table 1), indicating a non-existing ELA for the glacier these years. However, previous studies by Mernild

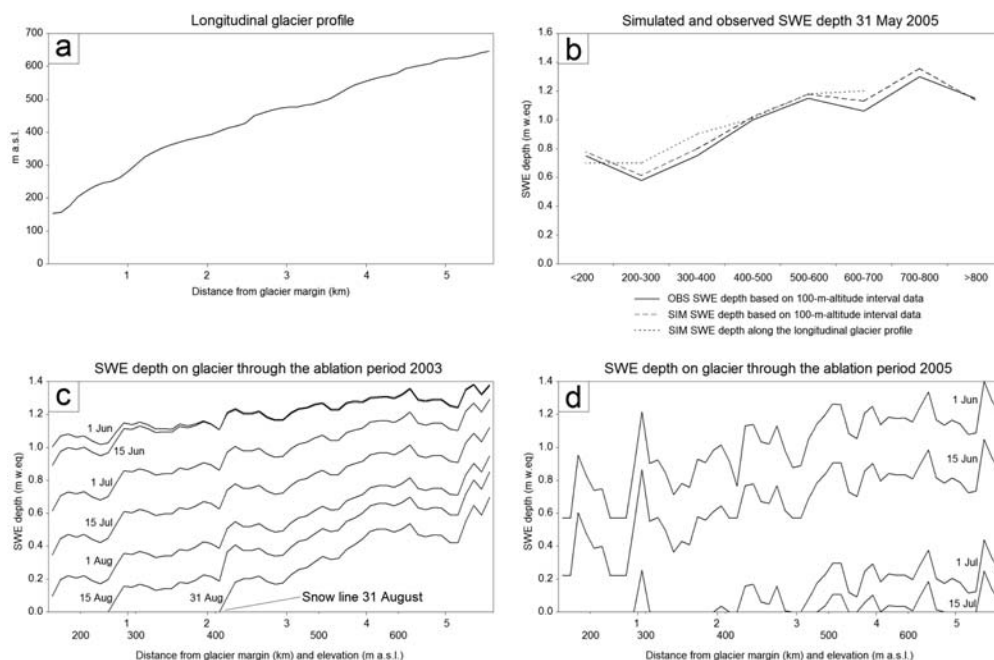


**Figure 5:**  
 (a) The Mittivakkat Glacier longitudinal surface profile (5.6 km) (for profile location see Figure 1c); (b) simulated and observed SWE depth 31 May 2005; (c) SWE depth variation through the 2003 ablation period (the ablation period (June through August) with the lowest ablation); and (d) SWE depth through the 2005 ablation period (the ablation period with the highest ablation).

et al. (2006a) have shown that some isolated snow patches remained on the glacier surface on August 31.

Table 4 presents an average modeled net mass balance (September through August) for the observation area (1998/99 to 2005/06) of  $-780(\pm 500)$  mm w.eq.  $y^{-1}$ . This corresponds significantly ( $R^2 = 0.97$ ;  $rmse = 162$ ;  $p < 0.01$ ) with the observed net mass balance of  $-770(\pm 610)$  mm w.eq.  $y^{-1}$  or a 10 mm w.eq.  $y^{-1}$  difference; however, the maximum difference between yearly observed and modeled values is 420 mm w.eq. (2002/03). The modeled test period averaged annual mass balance was 65 mm w.eq.  $y^{-1}$  (1998/99 to 2001/02), or  $\sim 8\%$  more than the observed values. For the entire glacier, the average net mass balance is  $-900(\pm 470)$  mm w.eq. (1998/99 to 2005/06), varying from  $-199$  mm w.eq. (2002/03) to  $-2,774$  mm w.eq. (2004/05). On Figure 4, the spatial variation in the modeled net mass balances for 31 August 1999 through 2006 is illustrated. The net mass balance pattern illustrates minimum values on the shadow side of the ridge east and south of the glacier, and decreasing values with increasing altitude.

## Discussion

During blowing snow events, sublimation of wind transported snow can play an important role in the high-latitude hydrological cycle. Previous Mittivakkat Glacier

studies (1997/98) (Hasholt et al. 2003) (1999–2004) (Mernild et al., 2006a) have shown that as much as 15% of the annual precipitation and 12% of solid precipitation may be returned to the atmosphere by sublimation. During the investigation period 1998/99–2005/06, modeled annual sublimation averaged 10% (approximately 135 mm w.eq.) of the solid precipitation inputs and approximately 7% of the modeled ablation for the entire Mittivakkat Glacier. The sublimation losses are low at the Mittivakkat Glacier compared to many previous studies in Arctic North America and Greenland (e.g. Pomeroy and Gray 1995; Pomeroy et al. 1997; Liston and Sturm 1998; Essery et al. 1999; Pomeroy and Essery 1999; Liston and Sturm, 2004), where approximately 5–50% of the annual solid precipitation was returned to the atmosphere by sublimation. Blowing snow sublimation rates are mainly dependent upon air temperature, humidity deficit, wind speed, and particle size distribution (e.g. Schmidt 1972, 1982; Tabler 1975; Pomeroy and Gray 1995; Liston and Sturm 2002; Hasholt et al. 2003). In our relatively coastal domain, high wind speeds are generally coincident with high relative humidity, and therefore, sublimation has played a lesser role (around only 7%) in the glacier mass balance budget. Previous studies show significant snow redistribution; in Arctic North America within the first 300 m of fetch, 35–85% of annual snowfall is removed by wind erosion, and the amount increases with wind speed (e.g. Pomeroy et al. 1993). The wind redistribution processes



influence snow depths over distances of tens of centimetres to hundreds of meters. On Ammassalik Island, previous blowing snow model simulations (Hasholt et al. 2003; Mernild et al., 2006a) found significant snow redistribution from east-facing slopes to west-facing slopes, together with the greatest drift accumulation at the head of the Mittivakkat Glacier. Figure 5b shows good agreement between simulated and observed end-of-winter SWE depth in the long profile with the largest SWE accumulation located between 500 and 800 m a.s.l., which is consistent with previous observations and simulations. Above 800 m a.s.l., the SWE accumulation decrease mainly results from increasing wind redistribution of snow to the lower part of the glacier due to wind flow patterns over and around ridges and peaks (topographic characteristics). Even reasonable agreement occurs between the modeled and observed end-of-winter season spatially distributed SWE depths, with maximum depths on the upper glacier, mainly on the lee side of the ridge east and south of the glacier (Figures 2 and 5b).

The difference between modeled and observed annual mass balances for the observation area is mainly caused by differences in summer mass balances (Tables 4). For four out of six years, model ablation is underestimated. This variation in ablation is likely due to model limitations or the use of non-representative model input data. For example, SnowModel was not able to account for: 1) the high frequency of clouds or sea fog below approximately 150–250 m a.s.l.; 2) the occurrence of a persistent temperature inversion (below approximately 250–300 m a.s.l., based on near-surface measurements) in the western part of the Mittivakkat Glacier during summer; and 3) highly variable lapse rates in the mountains and over glaciers. Because of the adjacent rocks, air temperature data from Station Nunatak may be overestimated during times of low wind speed. Data from meteorological stations not located on the glacier surface may also be different from air temperatures over the glacier itself. Using air temperature data from Station Coast and Station Nunatak in modeling indicates positive lapse rates for the ablation period (for a temperature increase of approximately 1.5°C for the higher station). In reality, it also seems unlikely that two-meter air temperatures would increase with elevation over the glacier itself. Clearly, MicroMet/SnowModel would benefit from the ability to simulate the presence of surface temperature inversions. We expect this to be particularly important in snow- and ice-covered Arctic environments, including Greenland.

During summer (ablation period from June to August),

the ablation processes (phase-change processes) of evaporation/sublimation and melting dominated the watershed's snow and ice characteristics. As part of the Snow-Model simulations, melting from snow and glacier ice on Mittivakkat Glacier were computed, and redistributed through the snow pack. Any additional meltwater is assumed to reach the ground or ice at the base of the snow-pack. Figure 3 plots the spatial distribution of runoff on the Mittivakkat Glacier from 1998/99 through 2005/06. In some areas of the glacier (e.g. at the glacier terminus), as much as 3,000–3,249 mm w.eq.  $y^{-1}$  (2004/05) may occur. The amount of runoff decreases with increasing altitude, from an average of 2,500 mm w.eq.  $y^{-1}$  at the glacier margin to 1,500 mm w.eq.  $y^{-1}$  around highest elevations (Figure 3) and approximately 2,000 mm w.eq.  $y^{-1}$  at the ELA. Early in the melt season (June), runoff is mainly controlled by glacier snowmelt, whereas later in the season (July and August), when the snow cover is largely gone, the melt distribution and runoff is dominated by glacier ice melt.

Throughout the year, different surface processes (snow accumulation, snow redistribution, sublimation, and surface melting) on the Mittivakkat Glacier affect the high-latitude water balance (Equation 3). The yearly water balance equation for the glacier can be described by:

$$P - ET - R \pm \Delta S = 0 \pm \eta \quad (3)$$

where P is the precipitation input from snow and rain (and possible condensation); ET is evaporation and sublimation; R is runoff throughout the entire period of flow;  $\Delta S$  is a change in mass balance resulting from changes in glacier storage, and snowpack storage (including local snow redistribution and snow transport from nearby catchments). Storage also includes changes in supraglacial storage (lakes, pond, channels, etc.), englacial storage (pond and water table), and subglacial storage (cavities and lakes), which we did not account for in the model simulations. Here  $\eta$  is the water balance discrepancy (error). The error term should be 0 (or small) if the major components (P, ET, R, and  $\Delta S$ ) have been determined accurately. Table 5 presents the water balance elements (Equation 3): P, ET, R, and  $\Delta S$  for the entire Mittivakkat Glacier (September to August) from 1998/99 to 2005/06, showing an annual average precipitation of 1,490( $\pm 150$ ) mm w.eq.  $y^{-1}$ , a modeled evaporation and sublimation of 250( $\pm 30$ ) mm w.eq.  $y^{-1}$ , a modeled runoff of 2,140( $\pm 410$ ) mm w.eq.  $y^{-1}$ , and a modeled change in storage of -900( $\pm 470$ ) mm w.eq.  $y^{-1}$ . Previous arctic studies (e.g. Kane and Yang, 2004) showed



	Precipitation from rain and snow (P) (mm w.eq. y <sup>-1</sup> )	Evaporation and sublimation (ET) (mm w.eq. y <sup>-1</sup> )	Runoff (R) from snow/glacier melt and rain (mm w.eq. y <sup>-1</sup> ) *	Storage ( $\Delta S$ ) (mm w.eq. y <sup>-1</sup> )
1998/1999	1,299	206	1,946	-853
1999/2000	1,612	253	2,233	-874
2000/2001	1,604	289	2,312	-997
2001/2002	1,613	263	1,940	-590
2002/2003	1,549	217	1,531	-199
2003/2004	1,594	271	2,413	-1,090
2004/2005	1,256	221	2,869	-1,834
2005/2006	1,373	246	1,858	-731
Average and standard deviation	1,490( $\pm$ 150)	250( $\pm$ 30)	2,140( $\pm$ 410)	-900( $\pm$ 470)

**Table 5:** Surface water balance elements: corrected precipitation (P), modeled evaporation and sublimation (ET), modeled runoff (R), and modeled storage ( $\Delta S$ ) for the entire Mittivakkat Glacier (31 km<sup>2</sup>) from 1998/99 through 2005/06 (from September through August). \*The runoff does not include englacial and subglacial melting or changes in internal storage e.g. glacial bulk water release.

that glaciers have a dominant influence on the water balance compared to non-glacierized areas, often producing surplus of melting and runoff exceeding the precipitation. For the entire Mittivakkat Glacier, the negative storage indicates a glacier recession for the period, with an average glacier melt contribution of 900 mm w.eq. y<sup>-1</sup> (1998/99–2005/06), which contributes approximate 42% to the average simulated runoff of 2,140 mm w.eq. y<sup>-1</sup>, indicating a mean specific runoff of 67.8 l s<sup>-1</sup> km<sup>-2</sup>.

## Summary and conclusion

SnowModel, a physically based snow-evolution modeling system that accounts for the evolution of snow accumulation, distribution, blowing-snow sublimation, and melt was used to describe the variations in snow distribution and surface melt over a 31.0 km<sup>2</sup> arctic East Greenland glacier. The glacier area includes strong alpine relief, with elevations ranging from 160 at the outlet to 973 m a.s.l. at the highest peaks. Approximately 65–85% of TAP falls as snow from approximately mid-September to late May. The wind patterns around topography characteristics (ridge and peaks) allow significant wind redistribution of snow. High wind speeds in the area are generally coincident with high relative humidity and, therefore, water in the snow cover being returned to the atmosphere by sublimation played a relatively small role in the glacier mass balance budget. SnowModel was calibrated for four winter periods and tested against four others. Further, winter, summer, and net mass balances for the glacier were modeled. This research has quantified the interrelationships and interactions that exist within the individual glacier mass balance components (accumulation, glacier-distributed snow cover and ablation, and glacier-distributed surface melt fluxes) and the hydrological cycle's

seasonal components (runoff and storage changes). Snow cover was found to vary on the glacier at the end-of-winter period (31 May) with maximum SWE depths located at 500–800 m a.s.l., mainly on the lee side of the ridge east and south of the glacier. Above 800 m a.s.l. average SWE depth is decreasing, mainly associated with increasing wind distribution of snow based on wind flow pattern over and around ridges and peaks. The model simulations during the eight full-year (1998/99 through 2005/06), produced SWE depths that were essentially identical ( $p < 0.01$ ) to the winter mass balance observations, and ablation values significant ( $p < 0.01$ ) with summer mass balance observations. The difference between modeled and observed annual net mass balance estimates is mainly caused by differences in summer mass balance; in four out of six years, ablation is underestimated in the model. This divergence can be used as guide to understand the consequence of the meteorological station locations in the area and as a guide to develop model routines for simulating the temperature inversion layer, which appears to be a common feature of this area of Greenland. Runoff was found to vary on the glacier at the end-of-the ablation period (31 August) with maximum cumulative runoff at the glacier margin and minimum runoff on the shadow side of the ridge east and south of the glacier.

## Acknowledgements

We thank the reviewers for insightful reviews of this paper. This work was supported by grants from the University of Alaska Presidential IPY Postdoctoral Foundation and the University of Alaska Fairbanks Office of the Vice Chancellor for Research and carried out during the first author's IPY Post Doc. Program at the University of Alaska Fairbanks.

## References

- ACIA, (2005): Arctic Climate Impact Assessment. Cambridge University Press, 1042 p.
- Allerup, P., H. Madsen, and F. Vejen, (1998): Estimating true precipitation in arctic areas. Proc. Nordic Hydrological Conf., Helsinki, Finland, Nordic Hydrological Programme, NHP Rep. 44: 1–9.
- Allerup, P., H. Madsen, and F. Vejen, (2000a): Correction of precipitation based on off-site weather information. Atmos. Res., 53: 231–250.
- Allerup, P., H. Madsen, and F. Vejen, (2000b): Correction of observed precipitation in Greenland. Proc. Nordic Hydrological Conf., Uppsala, Sweden, NHF/NAH Nordic Association for Hydrology, 1–8.
- Anderson, E. A. (1976): A point energy balance model of a snow cover. NOAA Tech. Rep. NWS 19, 150 pp.
- Barnes, S. L. (1964): A technique for maximizing details in numerical weather map analysis. J. Appl. Meteor. 3: 396–409.
- Barnes, S. L., (1973): Mesoscale objective analysis using weighted timeseries observations. NOAA Tech. Memo. ERL NSSL-62, National Severe Storms Laboratory, Norman, OK, 60 pp.
- Box, J. E. (2002): Survey of Greenland instrumental temperature records: 1973–2001. Int. Climatol. 22: 1829–1847.
- Brown, R. D., B. Brasnett, and D. Robinson, (2003): Gridded North American monthly snow depth and snow water equivalent for GCM evaluation. Atmosphere-Ocean 41(1): 1–14.
- Bruland, O., G. E. Liston, J. Vonk, K. Sand, and A. Killingtveit, (2004): Modelling the snow distribution at two High-Arctic sites at Svalbard, Norway, and at a Sub-Arctic site in Central Norway. Nordic Hydrology 35(3): 191–208.
- Chylek, P., M. K., Dubey, and G. Lesins, (2006): Greenland warming of 1920–1930 and 1995–2005. Geophys. Res. Lett., 33, L11707, doi:10.1029/2006GL026510, 2006.
- Dodson, R., and D. Marks, (1997): Daily air temperature interpolation at high spatial resolution over a large mountainous region. Climate Res., 8: 1–20
- Essery, R. L. H., L. Li, and J. W. Pomeroy, (1999): A distributed model of blowing snow over complex terrain. Hydrol. Processes, 13: 2423–2438.
- Greene, E. M., Liston, G. E. and Pielke, R. A. (1999): Simulation of above treeline snowdrift formation using a numerical snowtransport model. Cold Reg. Sci. Technol. 30: 135–144.
- Hanna, H. P., Huybrechts, I. Janssens, J. Cappelen, K. Steffen, and A. Stephens, (2005): Runoff and mass balance of the Greenland ice sheet: 1958–2003. J. Geophys. Res. 110: 1–16.
- Hansen, J., R. Ruedy, M. Sato, and K. Lo, (2007): GISS 2007 Temperature analysis through November. <http://pubs.giss.nasa.gov/docs>.
- Hasholt, B., Liston, G. E. and Knudsen N. T. (2003): Snow distribution modelling in the Ammassalik region, southeast Greenland. Nordic Hydrol. 34: 1–16.
- Hinzman, L.D., N. D. Bettez, W. B. Bolton, F. S. Chapin, M. B. Dyurgerov, C. L. Fastie, B. Griffith, R. D. Hollister, A. Hope, H. P. Huntington, A. M. Jensen, G. J. Jia, T. Joergensen, D. L. Kane, D. R. Klein, G. Kofinas, A. H. Lynch, A. H. Lloyd, A. D. McGuire, F. E. Nelson, W. C. Oechel, T. E. Osterkamp, C. H. Racine, V. E. Romanovsky, R. S. Stone, D. A. Stow, M. Sturm, C. E. Tweedie, G. L. Vourlitis, M. D. Walker, D. A. Walker, P. J. Webber, J. M. Welker, K. S. Winker, and K. Yoshikawa, (2005): Evidence and implications of recent climate change in Northern Alaska and other Arctic regions. Climatic Change 72: 251–298.
- Hiemstra, C. A., Liston, G. E. and Reiners, W. A. (2002): Snow Redistribution by Wind and Interactions with Vegetation at Upper Treeline in the Medicine Bow Mountains, Wyoming. Arctic, Antarctic, and Alpine Research 34: 262–273.
- Hiemstra, C. A., G. E. Liston, and W. A. Reiners, (2006): Observing, modelling, and validating snow redistribution by wind in a Wyoming upper treeline landscape. Ecological Modelling 197: 35–51.
- Iziomon, M. G., H. Mayer, and A. Matzarakis, (2003): Downward atmospheric longwave irradiance under clear and cloudy skies: Measurement and parameterization. J. Atmos. Sol.-Terr. Phys. 65: 1107–1116.
- Kane, D. L. (1997): The Impact of Hydrologic Perturbation on Arctic Ecosystems Induced by Climate Change. Global Change and Arctic terrestrial Ecosystems. Ecological Studies 124: 63–81.
- Kane, D. L., and D. Yang, (2004): Overview of water balance determinations for high latitude watersheds. In Northern Research Basins Water Balance. Kane, D. L. and Yang, D. (eds.): Northern Research Basins Water Balance, IAHS Publication 290: 1–12.
- Killingtveit, Å. (2004): Water balance studies in two catchments on Spitsbergen, Svalbard. In Northern Research Basins Water Balance, D. L. Kane and D. Yang, Eds., IAHS Publication 290: 120–128.

- Klemes V. (1985): Sensitivity of water resources systems to climate variations. WPC Report 98, World Meteorological Organisation, Geneva.
- Klemes V. (1986): Operational testing of hydrological simulation models. *Hydrological Sciences Journal* 31: 13–24.
- Knudsen, N. T., and B. Hasholt, (1999): Radio-echo sounding at the Mittivakkat Gletscher, southeast Greenland. *Arc. Antarct. Alp. Res.* 31: 321–328.
- Knudsen, N. T., and B. Hasholt, (2004): Mass balance observations at Mittivakkat Glacier, southeast Greenland 1995–2002. *Nordic Hydrol.*, 35: 381–390.
- Koch, S. E., M. DesJardins, and P. J. Kocin, (1983): An interactive Barnes objective map analysis scheme for use with satellite and conventional data. *J. Climate Appl. Meteor.*, 22: 1487–1503.
- Kunkel, K. E. (1989): Simple procedures for extrapolation of humidity variables in the mountains western United States. *J. Climate* 2: 656–669.
- Lemke, P., J. Ren, R.B. Alley, I. Allison, J. Carrasco, G. Flato, Y. Fujii, G. Kaser, P. Mote, R.H. Thomas and T. Zhang, (2007): Observations: Changes in Snow, Ice and Frozen Ground. In: *Climate Change 2007: The Physical Science Basis. Contribution of Working Group I to the Fourth Assessment Report of the Intergovernmental Panel on Climate Change* [Solomon, S., D. Qin, M. Manning, Z. Chen, M. Marquis, K.B. Averyt, M. Tignor and H.L. Miller (eds.)]. Cambridge University Press, Cambridge, United Kingdom and New York, NY, USA.
- Liston, G. E. (1995): Local Advection of Momentum, Heat, and Moisture during the Melt of Patchy Snow Covers. *Journal of Applied Meteorology* 34(7): 1705–1715.
- Liston, G. E. (2004): Representing subgrid snow cover heterogeneities in regional and global models. *J. Climate* 17: 1381–1397.
- Liston, G. E., and Elder, K. (2006a): A distributed snow-evolution modeling system (SnowModel). *Journal of Hydrometeorology* 7: 1259–1276.
- Liston, G. E., and Elder, K. (2006b): A meteorological distribution system for high resolution terrestrial modeling (MicroMet). *Journal of Hydrometeorology*, 7: 217–234.
- Liston, G. E., and Hall, D. K. (1995): An energy-balance model of lake-ice evolution. *J. Glaciol.* 41: 373–382.
- Liston, G. E., R. B. Haehnel, M. Sturm, C. A. Hiemstra, S. Berezovskaya, and R. D. Tabler, 2007: Simulating complex snow distributions in windy environments using SnowTran-3D. *Journal of Glaciology* 53: 241–256.
- Liston, G. E., J. P. McFadden, M. Sturm, and R. A. Pielke Sr., (2002): Modeled changes in arctic tundra snow, energy, and moisture fluxes due to increased shrubs. *Global Change Biol.* 8: 17–32.
- Liston, G. E., and Sturm, M. (1998): A snow-transport model for complex terrain. *J. Glaciol.* 44: 498–516.
- Liston, G. E., and Sturm, M. (2002): Winter Precipitation Patterns in Arctic Alaska Determined from a Blowing-Snow Model and Snow-Depth Observations. *Journal of Hydrometeorology* 3: 646–659.
- Liston, G. E., and Sturm, M. (2004). The role of winter sublimation in the Arctic moisture budget. *Nordic Hydrology* 35(4–5): 325–334.
- Liston, G. E., Winther, J.-G., Bruland, O., Elvehøy, H. and Sand, K. (1999): Below surface ice melt on the coastal Antarctic ice sheet. *J. Glaciol.* 45(150): 273–285.
- Liston, G. E., Winther, J.-G., Bruland, O., Elvehøy, H., Sand, K. and Karlöf, L. (2000): Snow and blue-ice distribution patterns on the coastal Antarctic ice sheet. *Antarctic Science* 12(1): 69–79.
- Marks, D., J. Domingo, D. Susong, T. Link, and D. Garen, (1999): A spatially distributed energy balance snowmelt model for application in mountain basins. *Hydrol. Processes* 13: 1935–1959.
- Mernild, S. H., (2006): Freshwater Discharge from the coastal area outside the Greenland Ice Sheet, East Greenland, with focus on Mittivakkat, Ammassalik Island (Low Arctic) and Zackenberg (High Arctic). Ph.D. dissertation, University of Copenhagen, Institute of Geography. Pp. 394.
- Mernild, S. H., B. Hasholt, B. J. Jakobsen, B. U. Hansen, and D. Kane, (2007a): Climate, glacier mass balance, and runoff (1993–2005) Mittivakkat Glacier catchment, Ammassalik Island, SE Greenland, and in a long term perspective (1898–1993). *Hydrology Research*. In Press.
- Mernild, S. H., Hasholt, B. and Liston, G.E. (2006b): Water flow through Mittivakkat Glacier, Ammassalik Island, SE Greenland. *Geografisk Tidsskrift-Danish Journal of Geography* 106(1): 25–43.
- Mernild, S. H., G. E. Liston, and B. Hasholt, (2007c): Snow-Distribution and Melt Modeling for Glaciers in Zackenberg River Drainage Basin, NE Greenland. *Hydrological Processes*, 21: 3249–3263. DOI: 10.1002/hyp. 6500.
- Mernild, S. H., Hansen, B. U., Jakobsen, B. J., and Hasholt, B. (2008a): Climatic conditions at the Mitti-

- vakkat Glacier catchment (1994–2006), Ammassalik Island, SE Greenland, and in a 109 years term perspective (1898–2006). *Geografisk Tidsskrift-Danish Journal of Geography*, 108 (1): 49-70.
- Mernild, S. H., Liston, G. E., Hasholt, B. and Knudsen, N. T. (2006a): Snow-Distribution and Melt Modeling for Mittivakkat Glacier, Ammassalik Island, SE Greenland. *Journal of Hydrometeorology* 7: 808–824.
- Mernild, S. H., Liston, G. E., Himestra, C. A., Steffen, K. (2008b). Surface Melt Area and Water Balance Modeling on the Greenland Ice Sheet 1995–2005. *Journal of Hydrometeorology*. In press.
- Mernild, S. H., Sigsgaard, C. Rasch, M., Hasholt, B., Hansen, B. U. Stjernholm, M. and Petersen, D. (2007b): Climate, river discharge and suspended sediment transport in the Zackenberg River Drainage Basin and Young Sund/Tyrolerfjord, Northeast Greenland, 1995–2003. In Rysgaard, S. and Glud, R. N. (eds.), *Carbon cycling in Arctic Marine ecosystems: Case study Young Sound, Meddr. om Grønland, BioScience* 58: 24–43.
- Moritz, R. E., C. M. Bitz, and E. J. Steig, (2002): Dynamics of recent climate change in the Arctic, *Science* 297: 1497–1502.
- Pielke, R. A., Sr. (2002): *Mesoscale Meteorological Modeling*. Academic Press, 676 pp.
- Pomeroy, J. W., and E. Brun. (2001): Physical properties of snow. Pages 45-126 in H. G. Jones, J. W. Pomeroy, D. A. Walker, and R. W. Hoham, editors. *Snow Ecology: An Interdisciplinary Examination of Snow-Covered Ecosystems*. Cambridge University Press, Cambridge, U.K.
- Pomeroy, J. W. and R. L. H. Essery, (1999): Turbulent fluxes during blowing snow: Field test of model sublimation predictions. *Hydrol. Processes* 13: 2963–2975.
- Pomeroy, J. W., and D. M. Gray, (1995): Snowcover accumulation, relocation and management. National Hydrology Research Institute Science Rep. 7, Hydrological Science Division, HNRI Division of Hydrology, University of Saskatchewan, 144 pp.
- Pomeroy, J. W., D. M. Gray, and P. G. Landine, (1993): The Prairie Blowing Snow Model: Characteristics, validation, operation. *J. Hydrol.* 144: 165–192.
- Pomeroy, J. W., P. Marsh, and D. M. Gray, (1997): Application of distributed blowing snow model to the Arctic. *Hydrol. Processes* 11: 1450–1465.
- Prasad, R., D. G. Tarboton, G. E. Liston, C. H. Luce, and M. S. Seyfried, (2001): Testing a blowing snow model against distributed snow measurements at Upper Sheep Creek. *Water Resour. Res.* 37: 1341–1357.
- Refsgaard J. C. (2000): Towards a formal approach to calibration and validation of models using spatial data. In *Spatial Patterns in Catchment Hydrology: Observations and Modelling*, Gryson R, Blöschl G (eds). Cambridge University Press.
- Refsgaard J. C. and Henriksen, H. J. (2004): Modelling guidelines—terminology and guiding principles. *Advances in Water Resources* 27: 71–82.
- Refsgaard J. C. and Knudsen J. (1996): Operational validation and intercomparison of different types of hydrological models. *Water Resources Research* 32: 2189–2202.
- Ryan, B. C. (1977): A mathematical model for diagnosis and prediction of surface winds in mountains terrain. *J. Appl. Meteor.* 16: 1547–1564.
- Schmidt, R. A. (1972): Sublimation of wind-transported snow—A model. Research Paper RM-90, Rocky Mountain Forest and Range Experiment Station, Forest Service, U.S. Department of Agriculture, Fort Collins, CO, 24 pp.
- Schmidt, R. A. (1982): Vertical profiles of wind speed, snow concentration, and humidity in blowing snow. *Bound.-Layer Meteor.* 23: 223–246.
- Serreze, M. C., J. E. Walsh, F. S. Chapin III, M. Osterkamp, M. Dyurgerov, V. Romanovsky, W. C. Oechel, J. Morison, T. Zhang, and R. G. Barry, (2000): Observational evidence of recent change in the northern high-latitude environment. *Clim. Change* 46: 159–207.
- Sturm, M., J. Schimel, G. Michaelson, J. M. Welker, S. F. Oberbauer, G. E. Liston, J. Fahnestock, and V. E. Romanovsky, (2005): Winter biological processes could help convert Arctic tundra to shrubland. *Bio Science* 55(1): 17–26.
- Tabler, R. D. (1975): Estimating the transport and evaporation of blowing snow. Proc. Great Plains Agricultural Council: Snow Management on the Great Plains Symp., Bismarck, ND, Publication 73: 85–104.
- Tarboton, D. G., T. G. Chowdhury, and T. H. Jackson, (1995): A spatially distributed energy balance snowmelt model. *Biogeochemistry of Seasonally Snow-Covered Catchments*, K. A. Tonnessen, M. W. Williams, and M. Tranter, Eds., IAHS Publication 228: 141–155.
- Thornton, P. E., S. W. Running, and M. A. White, (1997): Generating surfaces of daily meteorological variables over large regions of complex terrain. *J. Hydrol.* 190: 214–251.

- Vorosmarty, C. J., L. D. Hinzman, B. J. Peterson, D. H. Bromwich, L. C. Hamilton, J. Morison, V. E. Romanovsky, M. Sturm, and R. S. Webb, (2001): The hydrological cycle and its role in Arctic and global environmental change: A rationale and strategy for synthesis study, 84 pp., Arct. Res. Consortium of the U.S., Fairbanks, Alaska.
- Walcek, C. J., (1994): Cloud cover and its relationship to relative humidity during a spring midlatitude cyclone. *Mon. Wea. Rev.* 122: 1021–1035.
- Winstral, A., and D. Marks, (2002): Simulating wind fields and snow redistribution using terrain-based parameters to model snow accumulation and melt over a semi-arid mountain catchment. *Hydrol. Processes* 16: 3585–3603.
- Woo, M. K., R. Heron, and P. Marsh, (1982): Basal Ice in High Arctic Snowpacks. *Arc. Alp. Res.* 14: 251–260.
- Yang, D., B. E. Goodison, J. R. Metcalfe, V. S. Golubev, R. Bates, T. Pangburn, and C. L. Hanson, (1998): Accuracy of NWS 8 standard nonrecording precipitation gauge: Results and application of WMO intercomparison. *J. Atmos. Oceanic Technol.* 15: 54–68.



[9]

Mernild, S. H. and Liston, G. E. 2010. The influence of air temperature inversion on snow melt and glacier surface mass-balance simulations, SW Ammassalik Island, SE Greenland.  
*Journal of Applied Meteorology and Climate*, 49(1), 47–67.

Reprinted with permission from American Meteorological Society

## The Influence of Air Temperature Inversions on Snowmelt and Glacier Mass Balance Simulations, Ammassalik Island, Southeast Greenland

SEBASTIAN H. MERNILD\*

*International Arctic Research Center, and Water and Environmental Research Center,  
University of Alaska Fairbanks, Fairbanks, Alaska*

GLEN E. LISTON

*Cooperative Institute for Research in the Atmosphere, Colorado State University, Fort Collins, Colorado*

(Manuscript received 25 June 2008, in final form 16 July 2009)

### ABSTRACT

In many applications, a realistic description of air temperature inversions is essential for accurate snow and glacier ice melt, and glacier mass-balance simulations. A physically based snow evolution modeling system (SnowModel) was used to simulate 8 yr (1998/99–2005/06) of snow accumulation and snow and glacier ice ablation from numerous small coastal marginal glaciers on the SW part of Ammassalik Island in SE Greenland. These glaciers are regularly influenced by inversions and sea breezes associated with the adjacent relatively low temperature and frequently ice-choked fjords and ocean. To account for the influence of these inversions on the spatiotemporal variation of air temperature and snow and glacier melt rates, temperature inversion routines were added to MircoMet, the meteorological distribution submodel used in SnowModel. The inversions were observed and modeled to occur during 84% of the simulation period. Modeled inversions were defined not to occur during days with strong winds and high precipitation rates because of the potential of inversion breakup. Field observations showed inversions to extend from sea level to approximately 300 m MSL, and this inversion level was prescribed in the model simulations. Simulations with and without the inversion routines were compared. The inversion model produced air temperature distributions with warmer lower-elevation areas and cooler higher-elevation areas than without inversion routines because of the use of cold sea-breeze-based temperature data from underneath the inversion. This yielded an up to 2 weeks earlier snowmelt in the lower areas and up to 1–3 weeks later snowmelt in the higher-elevation areas of the simulation domain. Averaged mean annual modeled surface mass balance for all glaciers (mainly located above the inversion layer) was  $-720 \pm 620$  mm w.eq.  $\text{yr}^{-1}$  (w.eq. is water equivalent) for inversion simulations, and  $-880 \pm 620$  mm w.eq.  $\text{yr}^{-1}$  without the inversion routines, a difference of 160 mm w.eq.  $\text{yr}^{-1}$ . The annual glacier loss for the two simulations was  $50.7 \times 10^6$  and  $64.4 \times 10^6$   $\text{m}^3$   $\text{yr}^{-1}$  for all glaciers—a difference of  $\sim 21\%$ . The average equilibrium line altitude (ELA) for all glaciers in the simulation domain was located at 875 and 900 m MSL for simulations with or without inversion routines, respectively.

---

\* Current affiliation: Computational Physics and Methods Group (CCS-2), Los Alamos National Laboratory, Los Alamos, New Mexico.

---

*Corresponding author address:* Dr. Sebastian H. Mernild, Climate, Ocean, and Sea Ice Modeling Group, Computational Physics and Methods (CCS-2), Los Alamos National Laboratory, Los Alamos, NM 87545.  
E-mail: mernild@lanl.gov

### 1. Introduction

Air temperature inversions—increasing temperatures with elevation—are present throughout the Arctic, covering a wide range of spatial and temporal domains. While these inversions can exist over a wide range of landscapes, and be the result of numerous processes and interactions, the inversion climatology literature mostly focuses on studies of single valley or basin locations (e.g., Putnins

1970; Kahl 1990; Kahl et al. 1992; Serreze et al. 1992; Kadygrov et al. 1999; Hansen et al. 2008). A realistic description of the spatiotemporal air temperature variation over complex topography influenced by air temperature inversions is essential for snow and ice melt calculations, glacier mass-balance estimates, river breakup simulations, ecological studies, water resource predictions, and for dispersion of pollutants in mountain and basin areas (e.g., Whiteman 1982; Chen et al. 1999; Singh 1999; Whiteman et al. 1999; Archer 2004; Lundquist and Cayan 2007; Kerminen et al. 2007; Barry 2008). Inversions occur when the coldest (and densest) air settles to the lowest topographic level and therefore temperatures increase with increasing elevation above the earth's surface (Anquetin et al. 1998). In contrast, periods without inversions may typically experience the moist adiabatic temperature decrease with an altitude of  $-0.65^{\circ}\text{C} (100 \text{ m})^{-1}$  (Marinec and Rango 1986; Oke 1987).

Air temperature inversions are present on local-to-regional scales, for example, during the passage of cold fronts, by radiative cooling of the surface, from advection, and from the invasion of cooler and increasingly moist onshore breezes (e.g., Streten et al. 1974; Oke 1987; Milionis and Davies 2008). Cold waters cause higher frequencies of inversion in high-latitude coastal regions, based on the local-to-regional wind systems (e.g., sea breezes) as a result of thermal differences between land and ocean (Hosler 1961; Milionis and Davies 2008). The height of the inversion base is attributed to the combined effects of topography (e.g., terrain-induced air motion), synoptic conditions (e.g., the thermal and dynamic structure of the atmosphere), and sea ice dynamics (e.g., Greenland 1979; Riordan et al. 1986; Hanna and Strimaitis 1990; Kahl 1990; Barry 2008; Milionis and Davies 2008).

Around Ammassalik Island in SE Greenland, summer inversions are common because of the effect of sea breezes. During winter at Ammassalik Island, both sea and land surfaces are typically visibly homogeneous with a covering of ice and snow, and snow, respectively: high albedo and low amounts of absorbed solar radiation therefore provide small differences in energy partitioning between the marine and terrestrial surfaces (Hansen et al. 2008). After terrestrial snowmelt in the spring, the land surface warms up, giving rise to a temperature gradient between the land and the still frozen sea. During daytime, cold and moist sea breezes affect the air temperature lapse rates in the coastal areas (e.g., Barry 2008; Mernild et al. 2008a). As spring and summer progress, the sea ice melts and the temperature differences between sea and land decrease, but the ocean temperatures still remain relatively low compared to the land. Because of the nearly continuous and relatively large solar radiation input during midsummer, the sea breeze can still exist, but

possibly in a slightly weaker version. Sea breezes have been found all over the coastal Arctic [e.g., along the Alaskan Beaufort and Arctic Sea coast (Kozo 1982a,b; Kahl 1990), the Canadian Arctic Sea coast (Weick and Rouse 1991; Kahl et al. 1992), Disko Island in west Greenland (Hansen et al. 2005), and Zackenberg in NE Greenland (Hansen et al. 2008)].

Air temperature is an important climatological parameter—a key driver for melt in high-latitude polar regions—and therefore also the most studied parameter. Still, along the coast and in Greenland's interior, because of the generally rough terrain, logistic constraints, and the remote locations, extensive air temperature observations have typically not been possible. Use of the few existing meteorological stations that measure air temperature and temperature of the atmosphere by radiosonde observations leads us to conclude that we have a limited knowledge about the distribution of air temperature and the effect of air temperature inversions on snow and ice cover throughout Greenland. The limited measurement of such a key climate system component is likely a serious impediment to hydrological research efforts. Thus, there is a clear need to explore issues associated with data sparseness and modeling capabilities.

The goal of this study is to understand the influence of temperature inversions on snow and glacier mass balance over the SW part of Ammassalik Island in SE Greenland, and to quantify their effects on snow and ice cover evolution. The aim of this study is to apply a well-tested approach and state-of-the-art modeling system, SnowModel (Liston and Elder 2006a; Mernild et al. 2006b; Liston et al. 2007), including its quasi-physically-based meteorological distribution model, MicroMet (Liston and Elder 2006b). We performed model simulations for an 8-yr period (1998/99–2005/06) with the following objectives: 1) to assess MicroMet–SnowModel meteorological driving data against independent observations; 2) to simulate the spatial air temperature distribution during periods without and with air temperature inversions; 3) to model the effect of inversions on winter snow accumulation, and summer ablation related to snowmelt and glacier-ice melt; and 4) to simulate the effect of air temperature inversions on the surface winter (defined herein to be September–May), summer (June–August), and annual mass balance for marginal glaciers near Greenland's east coast.

## 2. Study area

### a. Physical setting

Ammassalik Island (678 km<sup>2</sup>) is located in SE Greenland (65°N latitude; 37°W longitude) approximately 50 km east of the eastern margin of the Greenland Ice Sheet

(GrIS), separated from the mainland to the west by the 10–15-km-wide Sermilik Fjord, to the north by the Ikaasartivaq Fjord, to the east by the Ammassalik Fjord, and to the south by the North Atlantic Ocean (Fig. 1a). The simulation domain (485 km<sup>2</sup>) covers the SW part of the island—the area of potential interest for water resources for the town Tasiilaq. The glacier and lake areas are 61.9 km<sup>2</sup> (~13% of the simulation domain) and 24.6 km<sup>2</sup> (~5%), respectively (Fig. 1b). The observed average winter, summer, and annual mass balances for 1998/99–2005/06 for the Mittivakkat Glacier observation area (outlined in Fig. 1c; 17.6 km<sup>2</sup>) are, respectively, 1100 ± 150, −2010 ± 410, and −770 ± 610 mm water equivalent (w.eq.). Since 1898, 89 out of 105 mass-balance years show a negative Mittivakkat Glacier annual mass balance (Mernild et al. 2008b). Strong alpine relief characterizes the SW part of Ammassalik Island, with elevations ranging to above 1093 m MSL at the highest peaks (Fig. 1a). Proglacier valleys west on the island have an E–W orientation toward Sermilik Fjord, whereas east of Mittivakkat Glacier, valleys have a N–S orientation toward Ammassalik Fjord.

#### b. Meteorological stations and climate

There are three meteorological stations within the simulation domain: Station Nunatak (65°42'N; 37°49'W; 515 m MSL) is representative of glacier conditions, located on a small nunatak (~5 m from the glacier in the dominant wind directions) close to the equilibrium line altitude (ELA) on the NW part of Mittivakkat Glacier; Station Coast (65°41'N; 37°55'W; 25 m MSL) is representative of coastal/valley conditions located on a rock hill near Sermilik Fjord; and Station Tasiilaq (65°36'N; 37°38'W; 44 m MSL) is a standard synoptic World Meteorological Organization (WMO) meteorological station representative of coastal–fjord areas located on a hillside in the upper city limit of Tasiilaq (Fig. 1a) [technical specifications of Station Nunatak and Station Coast and the sensors can be found in Mernild et al. (2008a), and of Station Tasiilaq by contacting the Danish Meteorological Institute]. Ammassalik Island is considered to be low Arctic according to Born and Böcher (2001), and represents a relatively humid area of Greenland (Mernild et al. 2008a). Based on observed data from these stations, the mean annual air temperature (MAAT) (1998–2006) is −2.1°, −0.8°, and −0.1°C for Station Nunatak, Station Coast, and Station Tasiilaq, respectively (Mernild et al. 2008a). The maximum monthly air temperature averaged across the three stations is 6.7°C in July and the minimum is −7.3°C in February. Mean annual relative humidity is 82%. The total annual precipitation (TAP) is 1851 mm w.eq. yr<sup>−1</sup> at Station Nunatak, 1428 mm w.eq. yr<sup>−1</sup> at Station Coast, and 1254 mm w.eq. yr<sup>−1</sup> at Station Tasiilaq

(Mernild et al. 2008a), indicating a positive orographic effect between the coastal stations and Station Nunatak. The mean annual wind speed is 3.8, 4.0, and 2.3 m s<sup>−1</sup> for Station Nunatak, Station Coast, and Station Tasiilaq, respectively (Mernild et al. 2008a), while the average summer (June–August) and winter wind speed (September–May) across the three stations are 2.1 and 3.8 m s<sup>−1</sup>, respectively.

#### c. Air temperature inversion analysis

Air temperature inversions are common in the coastal areas around the Ammassalik Island, including the lower part of the Mittivakkat Glacier; these inversions affect air temperature lapse rates in the area and the associated snow and ice melt processes.

Twice-daily radiosonde observations recorded at 0000 and 1200 UTC time at Station Tasiilaq (1996–2005) were used to estimate the frequency of air temperature inversions (Table 1). For Station Tasiilaq, air temperature and elevation above sea level were recorded at different atmospheric pressure levels: at the terrain surface (52 m MSL), 925 hPa (average elevation and standard deviation: 631 ± 108 m MSL), 850 hPa (1329 ± 114 m MSL), and 700 hPa (2871 ± 141 m MSL). Because the 925-hPa level has an average elevation of 631 m MSL, many of the shallow coastal area inversions that actually occur are not captured by the radiosonde data. During summer (June–August), inversions were present an average of 30% of the time, and 20% of the time during the rest of the year (winter).

To improve our understanding of air temperature inversions in the Ammassalik Island area, observed climate data from Station Coast (2 m), Station Nunatak (2 m), and Station Tasiilaq (2 m) were analyzed during periods where Station Tasiilaq radiosonde observations (1995–2006) existed. No statistically significant difference occurred in observed surface relative humidity, air temperature, and wind speed at the three meteorological stations between the periods without or with radiosonde-observed inversion layers. This is likely because the 2-m climate on the Ammassalik Island is influenced by a combination of local-to-regional meteorological conditions: 1) local meteorological conditions based on variations in topography, the sea-breeze effect, and the presence of marginal glaciers producing katabatic winds, for example, on the Mittivakkat Glacier; and 2) overall meteorological conditions from the GrIS and the surrounding fjords/ocean. Even the difference in radiosonde wind speed data between the periods without or with radiosonde-observed inversion layers was insignificant (and around 1–2 m s<sup>−1</sup>) for the lower part of the atmosphere (below 925 hPa) (Table 2).

In addition, field observations were performed June–August 2005 and 2006, near Station Coast, to learn more

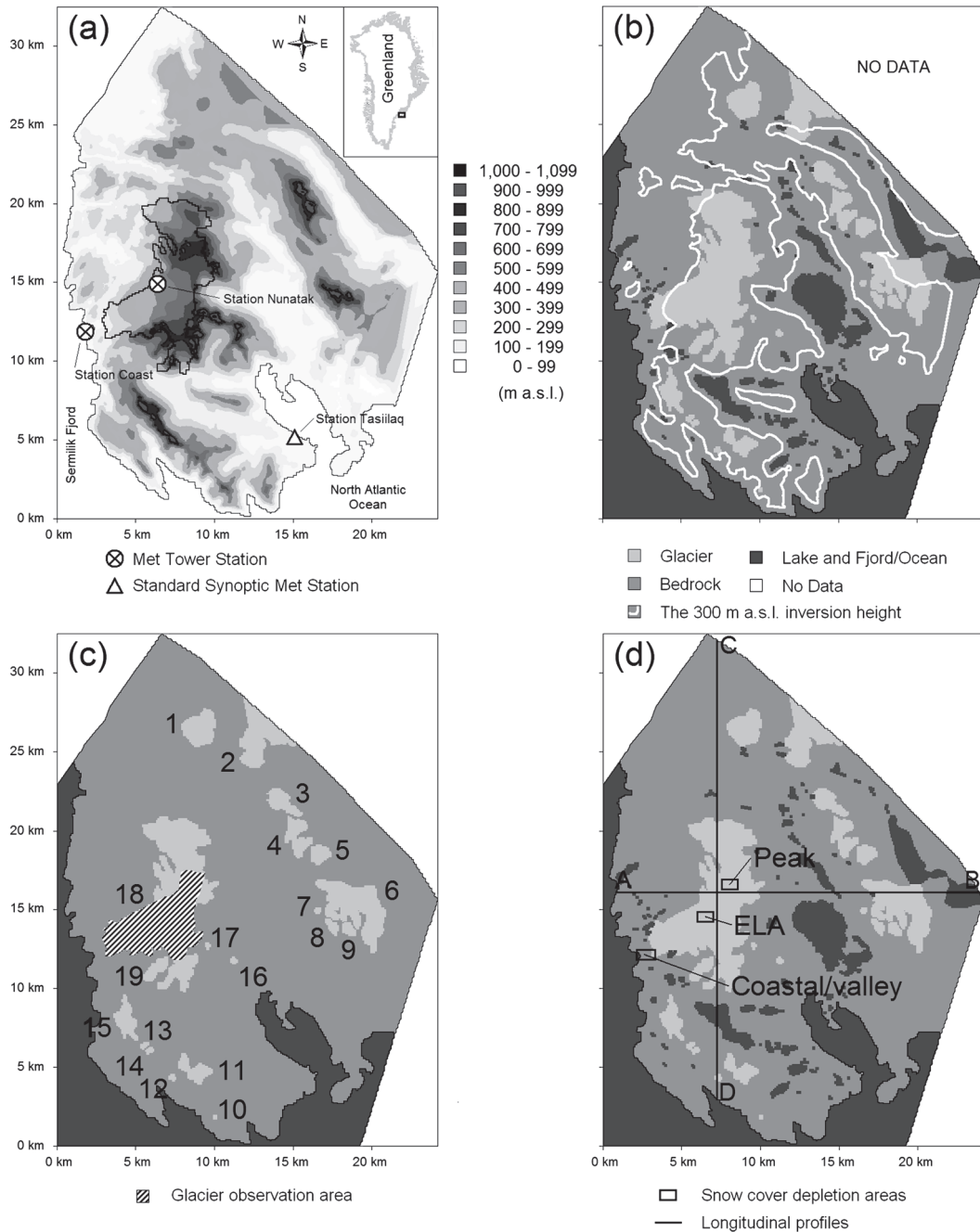


FIG. 1. Southwest Ammassalik Island simulation domain: (a) topography (gray shades, 100-m contour interval), the entire Mittivakkat Glacier complex outlined by the black line, and the three meteorological tower stations: Station Nunatak (515 m MSL), Station Coast (25 m MSL), and Station Tasiilaq (44 m MSL; a standard synoptic WMO meteorological station operated by the Danish Meteorological Institute); (b) surface characteristics including inversion height; (c) glacier numbers and glacier observation area at the Mittivakkat Glacier (17.6 km<sup>2</sup>); and (d) location of the snow cover depletion areas and longitudinal profiles A–B and C–D. The inset figure in (a) indicates the general location of the Mittivakkat Glacier in eastern Greenland. The domain coordinates can be converted to UTM by adding 548 km to the west–east origin (easting) and 7272 km to the south–north origin (northing) and converting to meters.



TABLE 1. The average monthly occurrence of air temperature inversions at Station Tasiilaq (1996–2005) and near Station Coast (June–August 2005 and 2006). Winter observations near Station Coast were not conducted because of the harsh climatic conditions and logistical constraints.

	Jan	Feb	Mar	Apr	May	Jun	Jul	Aug	Sep	Oct	Nov	Dec	Avg
Inversion Station Tasiilaq (%)	24	23	22	18	20	28	32	29	14	15	17	23	22
Inversion near Station Coast (%)	—	—	—	—	—	84	80	87	—	—	—	—	84

about the inversions in this area (Fig. 2). Vertical hand-carried temperature observations near Station Coast (June–August 2005 and 2006) (Figs. 1a and 2) were used to estimate inversion frequency and elevation. These observations found a summer average inversion presence 84% of the time (Table 1), or 2.8 times the frequency captured by the radiosonde data. These observations also showed that the tops of the air temperature inversions were located at approximately 300 m MSL (Fig. 2). Clearly the radiosonde data are only capturing the deepest inversions, and there are many inversions that exist in the natural system that are not represented by the radiosonde observations. While we do not have the observations to quantify it, we expect that the winter radiosonde records also frequently miss the presence of low-level inversions.

In Fig. 2, the vertical temperature profiles show the summer variations and average distribution with elevation. The inversion frequency found near Station Coast is almost identical with values found other places in the Arctic. By comparison, frequencies of 85%–99% were found for Alaskan and Canadian Arctic stations (Kahl 1990; Kahl et al. 1992; Kadygrov et al. 1999), and 91% for the Arctic Ocean based on nearly 30 000 analyzed radiosonde temperature observations (Kahl et al. 1996). In winter, the occurrence of inversions at Station Tasiilaq was lower compared to summer conditions, probably because 1) the sea and land surfaces have much the same temperature since they are both covered more or less continuously in ice and snow and local temperature differences in the heating of sea and land is minimal; and 2) wind speeds are slightly higher in winter (between 1.3 and 2.9 m s<sup>-1</sup>) (Table 2). We also know that radiational cooling is greatest during winter, and this likely increase the chances of inversions and possibly increases the occurrence of relatively shallow inversions that are not detectable by the radiosonde observations.

### 3. SnowModel

#### a. SnowModel description

SnowModel (Liston and Elder 2006a) is a spatially distributed snowpack evolution modeling system specifi-

cally designed to be applicable over the wide range of snow landscapes and climates found around the world. It is made up of four submodels: MicroMet (a quasi-physically-based meteorological distribution model) defines the meteorological forcing conditions (Liston and Elder 2006b); EnBal calculates the surface energy exchanges, including melt (Liston 1995; Liston et al. 1999); SnowPack simulates heat and mass transfer processes, and snow depth and water equivalent evolution (Liston and Hall 1995); and SnowTran-3D is a blowing-snow model that accounts for snow redistribution by wind (Liston and Sturm 1998, 2002; Liston et al. 2007). SnowModel simulates snow-related physical processes at spatial scales ranging from 5 m to global and temporal scales ranging from 10 min to a whole season. SnowModel was originally developed for glacier-free landscapes. For glacier-surface mass-balance studies, SnowModel was modified to simulate glacier-ice melt after winter snow accumulation had ablated (Mernild et al. 2006b, 2007).

To solve the system of equations, SnowModel requires spatially distributed fields of topography and land cover types, and temporally varying meteorological data (air temperature, relative humidity, wind speed, wind direction, and precipitation) obtained from the two meteorological stations: Station Nunatak and Station Coast located within the simulation domain (Fig. 1a). Model simulations used a 100-m grid increment. The simulations were performed using a 1-day time step and spanned the 8-yr period from 1 September 1998 through 31 August 2006. Snow and ice melt and blowing snow are threshold processes and may not be accurately represented by a 1-day time step. Unfortunately, computational resources did not allow using a smaller time increment for the entire simulation domain. Therefore, daily simulated melt and blowing-snow processes were tested against hourly simulated values from the Mittivakkat Glacier subdomain (1998/99–2005/06) and remain significant ( $p < 0.01$ , where  $p$  is the level of significance), with an average difference of 2%, 3%, and 8% for the winter, summer, and annual mass balance, respectively (Table 3).

Topographic data over the SW part of the Ammassalik Island were obtained from a digital elevation model

TABLE 2. Station Coast and Station Nunatak observed daily wind speed ( $W_s$ ) and precipitation ( $P$ ), and Station Tasiilaq radiosonde observed wind speed. The table shows the average and frequency of wind speed below and above  $8 \text{ m s}^{-1}$  for the three stations, and precipitation below and above  $10 \text{ mm w.eq.}$  for Station Coast and Station Nunatak. Further, average summer (June–August) and winter (September–May) wind speed and average wind speed during periods with radiosonde observed inversion and no inversion are shown. The radiosonde observations are conducted at different pressure levels (1996–2005): terrain surface ( $52 \text{ m MSL}$ ),  $925 \text{ hPa}$  ( $631 \pm 108 \text{ m MSL}$ ),  $850 \text{ hPa}$  ( $1329 \pm 114 \text{ m MSL}$ ), and  $700 \text{ hPa}$  ( $2871 \pm 141 \text{ m MSL}$ ).

	Station Coast				Station Nunatak			
	2 m above terrain surface		2 m above terrain surface		2 m above terrain surface		2 m above terrain surface	
	(25 m MSL)		(25 m MSL)		(515 m MSL)		(515 m MSL)	
Wind speed interval ( $\text{m s}^{-1}$ )	<8	>8	<8	>8	<8	>8	<8	>8
Avg wind speed ( $\text{m s}^{-1}$ )	$3.5 \pm 2.0$	$10.6 \pm 3.3$	$3.1 \pm 1.7$	$10.7 \pm 2.3$				
Frequency (%)	92	8	91	9				
	Station Coast				Station Nunatak			
	0.45 m above terrain surface		0.45 m above terrain surface		0.45 m above terrain surface		0.45 m above terrain surface	
	(25 m MSL)		(25 m MSL)		(515 m MSL)		(515 m MSL)	
Precipitation interval (mm w.eq.)	<10	>10	<10	>10	<10	>10	<10	>10
Precipitation (mm w.eq.)	$3.6 \pm 2.7$	$21.2 \pm 14.6$	$3.7 \pm 2.6$	$19.5 \pm 9.4$				
Frequency (%)	90	10	91	9				
Frequency (%), avg, and std dev for days both with wind speed $>8 \text{ m s}^{-1}$ and precipitation $>10 \text{ mm w.eq.}$	F: 2 Ws: $10.1 \pm 2.8$ P: $20.2 \pm 11.0$		F: 2 Ws: $10.6 \pm 2.1$ P: $21.3 \pm 10.8$					
Frequency (%) of days with wind speed $<8 \text{ m s}^{-1}$ and precipitation $<10 \text{ mm w.eq.}$	84		84					
	Radiosonde		Radiosonde		Radiosonde		Radiosonde	
	Terrain surface		925 hPa		850 hPa		700 hPa	
	(52 m MSL)		(631 $\pm$ 108 m MSL)		(1329 $\pm$ 114 m MSL)		(2871 $\pm$ 141 m MSL)	
Wind speed interval ( $\text{m s}^{-1}$ )	<8	>8	<8	>8	<8	>8	<8	>8
Avg wind speed ( $\text{m s}^{-1}$ )	$2.8 \pm 1.4$	$12.0 \pm 4.2$	$4.3 \pm 1.8$	$12.2 \pm 4.1$	$4.9 \pm 1.7$	$13.8 \pm 5.1$	$5.1 \pm 1.8$	$14.5 \pm 6.0$
Frequency (%)	92	8	75	25	54	46	43	57
Avg summer wind speed ( $\text{m s}^{-1}$ ) (June–August)	$2.4 \pm 2.0$		$7.7 \pm 0.9$		$9.4 \pm 4.4$		$9.9 \pm 4.9$	
Avg winter wind speed ( $\text{m s}^{-1}$ ) (September–May)	$3.7 \pm 3.4$		$9.5 \pm 4.5$		$11.7 \pm 6.1$		$12.8 \pm 6.9$	
Diff between winter and summer wind speed ( $\text{m s}^{-1}$ )	1.3		2.2		2.3		2.9	
Avg wind speed during periods with radiosonde observed inversion ( $\text{m s}^{-1}$ )	$2.7 \pm 2.5$		$7.8 \pm 2.9$		$9.4 \pm 4.0$		$10.8 \pm 5.3$	
Avg wind speed during periods with no radiosonde observed inversion ( $\text{m s}^{-1}$ )	$3.7 \pm 3.6$		$9.7 \pm 4.5$		$11.9 \pm 5.8$		$13.8 \pm 6.5$	
Diff in wind speed between periods with radiosonde and no radiosonde observed inversion ( $\text{m s}^{-1}$ )	1.0		1.9		2.5		3.0	

(DEM) (100-m gridcell increment). Each grid cell was assigned a land cover type and classified as bedrock with a snow-holding depth (the snow depth that must be exceeded before snow can be transported by wind) of  $0.50 \text{ m}$  (Mernild et al. 2006b, 2007), as lake ice with a depth of  $0.01 \text{ m}$ , or as glacier with a snow-holding

depth of  $0.01 \text{ m}$  (Fig. 1b; Table 4) (Liston and Sturm 2002; Mernild et al. 2006b). Albedo was assumed to be  $0.8$  for snow and  $0.4$  for ice. Realistically, snow and ice albedo change with time and surface characteristics (e.g., Pomeroy and Brun 2001). Model parameter values used in the simulations are provided in Table 4.

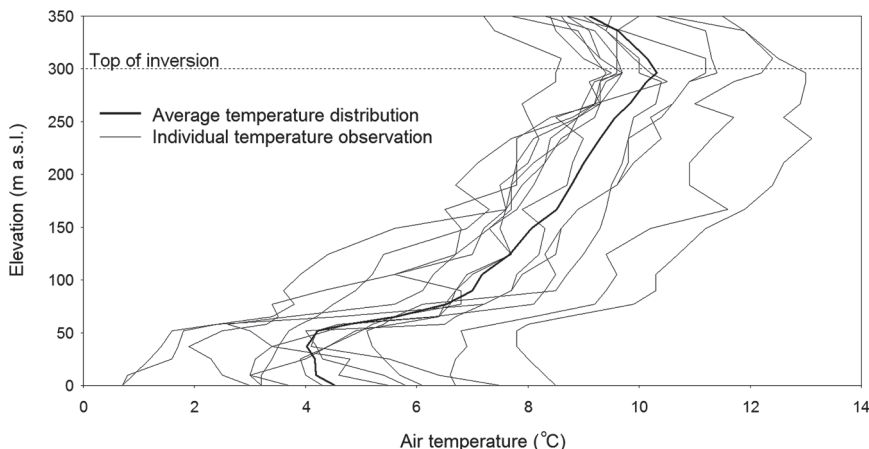


FIG. 2. Vertical observed air temperature distribution near Station Coast during daytime with different weather conditions: sunny, foggy, cloudy, and rainy conditions from June through August 2005 and 2006. Air temperature was measured at approximately every 20 m of elevation. The dotted line indicates the top of the observed temperature inversion level at 300 m MSL used for the model simulations.

*b. SnowModel modifications for air temperature inversions*

The submodels that make up SnowModel were all originally developed without routines for air temperature inversion simulations; in its original form, MicroMet provided air temperature distributions whose values decrease with elevation using elevation-related interpolations that are compatible with the observed lapse rates and follow Kunkel (1989), Walcek (1994), Dodson and Marks (1997), and Liston et al. (1999). Thus, for this Ammassalik Island study, the following MicroMet–

SnowModel modifications were implemented to account for the sea-breeze-related inversions found in this area: 1) routines were included for distributing inversion air temperatures, and 2) the height of the temperature inversion layer was defined and temperature lapse rates below and above the inversion layer were added. Together this allowed SnowModel to simulate the influence of spatiotemporal inversion patterns on air temperature distributions and snow and ice melt across the simulation domain. Air temperature distribution calculations with temperature inversion were made using

TABLE 3. Observed and SnowModel Analysis 1 simulated daily and hourly winter, summer, and annual mass balance for the Mittivakkat Glacier observation area (17.6 km<sup>2</sup>) (1998/99–2005/06). Winter mass-balance observations were carried out in late May and in early June, summer mass-balance observations in late August, modeled winter mass balance 31 May, and modeled summer mass balance 31 Aug. The annual mass-balance calculations span the period from 1 Sep through 31 Aug of the next year. Observed data are based on Knudsen and Hasholt (2008) and Mernild et al. (2008e).

	1998/99	1999/00	2000/01	2001/02	2002/03	2003/04	2004/05	2005/06	Avg
Obs winter mass balance (mm w.eq.)	980	1230	1180	1280	No data	No data	920	1010	1100 ± 150
Modeled winter mass balance, 31 May (daily time step) (mm w.eq.)	960	1240	1190	1270	1240	1220	930	1040	1140 ± 140
Modeled winter mass balance, 31 May (hourly time step) (mm w.eq.)	930	1200	1230	1240	1280	1190	890	1000	1120 ± 150
Obs summer mass balance (mm w.eq.)	–1750	–2060	–2140	–1780	No data	No data	–2740	–1590	–2010 ± 410
Modeled summer mass balance, 31 Aug (daily time step) (mm w.eq.)	–1690	–2020	–2060	–1690	–1310	–2160	–2750	–1640	–1920 ± 440
Modeled summer mass balance, 31 Aug (hourly time step) (mm w.eq.)	–1720	–2070	–2130	–1750	–1410	–2290	–2800	–1570	–1970 ± 450
Obs annual mass balance (mm w.eq. yr <sup>–1</sup> )	–770	–830	–960	–500	350	–1060	–1820	–580	–770 ± 610
Modeled annual mass balance (daily time step) (mm w.eq. yr <sup>–1</sup> )	–730	–780	–870	–420	–70	–940	–1820	–600	–780 ± 500
Modeled annual mass balance (hourly time step) (mm w.eq. yr <sup>–1</sup> )	–790	–870	–900	–510	–130	–1100	–1910	–570	–850 ± 520

TABLE 4. User-defined constants used in the SnowModel simulations [see Liston and Sturm (1998) for parameter definitions].

Symbol	Value	Parameter
$C_v$		Vegetation snow-holding depth (equal surface roughness length) (m)
	0.50	Bedrock
	0.01	Lake ice
	0.01	Glacier ice
$f$	500.0	Snow equilibrium fetch distance (m)
$U_{*t}$	0.25	Threshold wind shear velocity ( $\text{m s}^{-1}$ )
$Z_0$	0.01	Snow surface roughness length (m)
$dt$	1	Time step (day)
$dx = dy$		Gridcell increment (km)
$\alpha$	0.1	Ammassalik Island simulation area
		Surface albedo
	0.8	Snow
$\rho$	0.4	Ice
		Surface density ( $\text{kg m}^{-3}$ )
$\rho_s$	280	Snow
	910	Ice
$I$	550	Saturated snow density ( $\text{kg m}^{-3}$ )
	300	Elev of air temperature inversion (m MSL)

$$T_{\text{inv}}(z) = T_{z=0} + \int_{z=0}^{E_{\text{inv}}} \Delta T_{\text{lapse below}} dz + \int_{E_{\text{inv}}}^z \Delta T_{\text{lapse above}} (z - E_{\text{inv}}), \quad (1)$$

where  $T_{\text{inv}}$  is the air temperature distributed by the inversion routines,  $T_{z=0}$  is the temperature at sea level,  $\Delta T$  are the air temperature lapse rates below and above the inversion layer,  $E_{\text{inv}}$  is the defined inversion elevation, and  $z$  is the elevation ranging from sea level to the highest terrain in the simulation domain.

### c. SnowModel testing

Prior to performing SnowModel sensitivity simulations using the temperature inversion routines, test simulations were performed over our domain of interest using the original MicroMet temperature lapse-rate formulation. To assess the performance of the SnowModel–MicroMet distributed meteorological data, simulated meteorological data (without the inversion routines) were tested against independent observations not used in MicroMet. Station Tasiilaq (Fig. 1a) was used for comparisons spanning September 1998–August 2006. The validation station was located approximately 15 km from the stations used in MicroMet to drive SnowModel. In strong alpine terrain/mountainous areas air temperature variability is

complicated because it encompasses such a broad range of temporal and spatial scales (Lundquist and Cayan 2007). However, validations of MicroMet-simulated meteorological data indicate substantial correlation with independent observed meteorological data from Station Tasiilaq (Fig. 3). MicroMet-generated air temperature values accounted for 87% of the variance in the observed 1998–2006 daily averaged dataset, indicating a significant ( $p < 0.01$ ) justification of the MicroMet temperature routines. Wind speed, precipitation, and relative humidity have less strong correlations, but remain significant ( $p < 0.01$ ) and respectable (around 50% variance) representations of Station Tasiilaq meteorological processes. This validation is limited because it employs only one independent station located near sea level, however, based on its previous applications and testing in areas having strong topographic relief (e.g., Liston and Elder 2006a; Mernild et al. 2008d), we assume that MicroMet satisfactorily represents the Ammassalik Island meteorological conditions.

To assess the performance of SnowModel accumulation and ablation routines, distributed observed point snow and SWE depths, time lapse photographs, and satellite images were used for validation with satisfactory results: a difference of a maximum 7% occurred between observed snow and SWE values and modeled values [for further information see Mernild et al. (2006b,a, 2007, 2008c–e, 2009)]. Further, winter, summer, and annual mass-balance observations from the Mittivakkat Glacier observation area ( $17.6 \text{ km}^2$ ; Fig. 1c) were used to assess the model performance (without the inversion routines) for the end-of-winter accumulation (31 May) and the end-of-summer ablation (31 August) (Table 3). A split-sample test (e.g., Klemes 1985, 1986; Refsgaard and Knudsen 1996; Refsgaard 2000; Refsgaard and Henriksen 2004) was applied for calibration (1998/99–2001/02) and validation (2002/03–2005/06) of the simulated end-of-winter and summer mass balance. For the validation period a high degree of similarity between average modeled and observed winter, summer, and annual mass balance occurred (Table 3). For the winter, summer, and annual mass balance, an average difference of 20 ( $\sim 2\%$ ), 30 ( $\sim 1\%$ ), and 80 ( $\sim 10\%$ )  $\text{mm w.eq. yr}^{-1}$  occurred, respectively. These differences are within the uncertainties of the observed winter, summer, and annual mass-balance values; still, the annual variation between the modeled and observed mass balance could be up to 420  $\text{mm w.eq. yr}^{-1}$  (2002/03). For further information about the calibration and validation procedures see Mernild et al. (2006b, 2008e).

### d. SnowModel simulations

To perform SnowModel simulations using the new temperature inversion representation, a methodology to

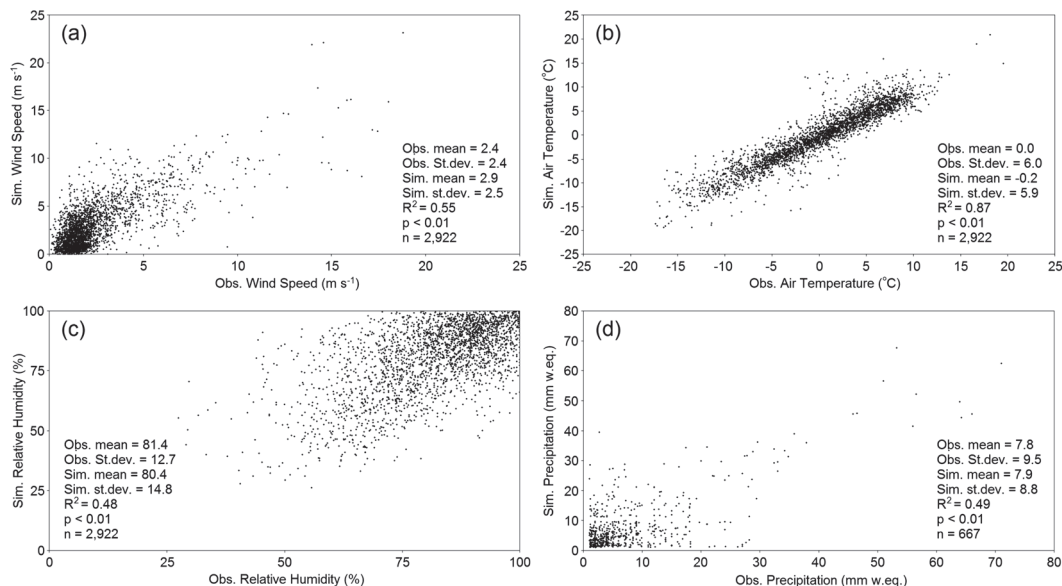


FIG. 3. A comparison between mean daily-observed meteorological data (a) wind speed, (b) air temperature, (c) relative humidity, and (d) precipitation, and mean daily SnowModel–MicroMet Analysis 1 simulated meteorological data for Station Tasiilaq (1998–2006) (for station location see Fig. 1a). Only precipitation values >1 mm w.eq. were included.

define inversion presence, absence, height, and strength needed to be defined throughout the 8-yr simulation period. Unfortunately, our high-resolution inversion observations only exist during summer. To extend our summer observations into winter, and define a representative winter inversion frequency, we assumed, for the reasons given in section 2c, that inversions occurred during winter at the same frequency as they did during summer (84%). In addition, our radiosonde analysis and other published literature suggest that inversions are less likely to occur during strong winds and high-precipitation rates. High-precipitation rates are typically associated with higher wind speeds, humidity increases, and other factors that reduce the likelihood of an inversion (e.g., Oke 1987; Stull 1988). We also know it is possible to have precipitation during an inversion. In the model simulations that follow, we assumed inversions would be

present during days with no precipitation, and also during days when the precipitation was < 10 mm w.eq. day<sup>-1</sup> and/or when the wind speed was < 8 m s<sup>-1</sup>. These thresholds were defined by analyzing our Station Coast and Station Nunatak atmospheric forcing datasets during the 8-yr simulation period (Table 2). During 16% of the time no-inversion days occurred.

Because the available observations were not detailed enough to provide a full understanding of the inversion height and strength within and around Ammassalik Island, a sensitivity analysis was conducted on the Mittivakkat Glacier to see the influence of changing the inversion layer level in 100-m increments, from 100 through 500 m MSL (Table 5). The effect—per 100 m increase in elevation level—on the Mittivakkat Glacier winter, summer, and annual mass-balance averaged values was -50 mm w.eq. (100 m)<sup>-1</sup> (5%), 88 mm w.eq. (100 m)<sup>-1</sup>

TABLE 5. SnowModel Analysis 2 simulated winter, summer, and annual mass balance for the Mittivakkat Glacier observation area (17.6 km<sup>2</sup>) for different inversion elevations. Simulations were conducted for inversions at 100-m intervals going from 0 through 500 m MSL. The simulations span the period from 1 Sep 2000 through 31 Aug 2001.

	No inversion	100 m MSL inversion layer	200 m MSL inversion layer	300 m MSL inversion layer	400 m MSL inversion layer	500 m MSL inversion layer
Mittivakkat Glacier winter mass balance (mm w.eq.)	1190	1140	1080	1030	980	940
Mittivakkat Glacier summer mass balance (mm w.eq.)	-2060	-1960	-1830	-1730	-1660	-1610
Mittivakkat Glacier annual mass balance ( $\Delta S$ ) (mm w.eq. yr <sup>-1</sup> )	-870	-820	-750	-700	-680	-670



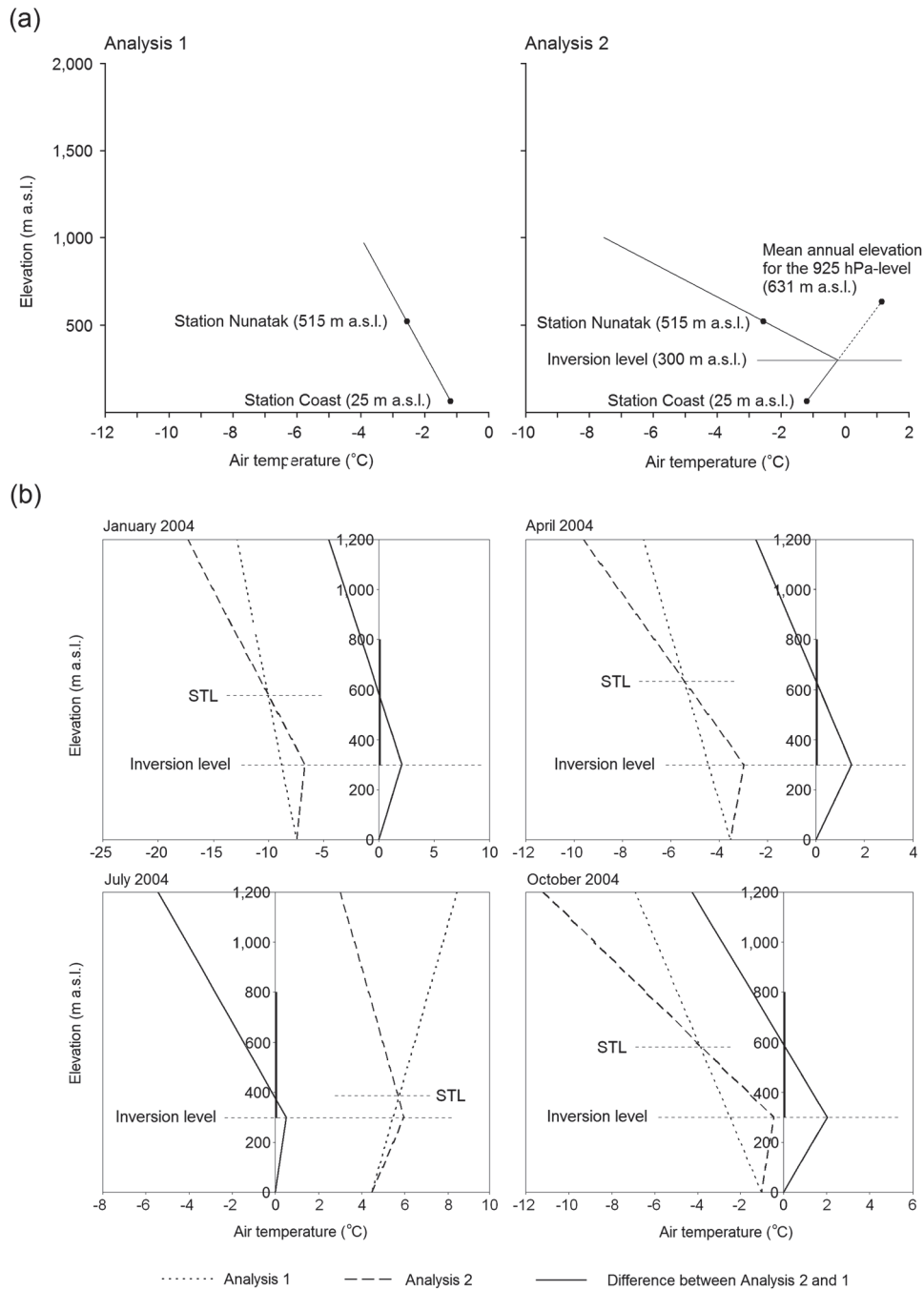


FIG. 4. (a) Schematic illustration of the Analysis (left) 1 and (right) 2 air temperature lapse-rate routines. For Analysis 2, the air temperature inversion level was set at 300 m MSL according to observations (see Fig. 2). In general, for Analysis 2, the air temperature increased with height up to the inversion level, and above the air temperature decreased. (b) An example of the average air temperature distribution with increasing elevation for Analysis 1 and 2 for the months of January, April, July, and October 2004. A negative difference between Analysis 1 and 2 indicates that Analysis 1 estimated air temperature is below Analysis 2 estimated values. Inversion-level and STL is illustrated. Further, a thick line is shown on the ordinate to illustrate the main glacier elevations (ranging from 300 to 800 m MSL).

TABLE 6. Average monthly lapse rates for Analysis 1 and 2. For Analysis 2, lapse rates are defined both below ( $\Delta T_{\text{lapsebelow}}$ ) and above ( $\Delta T_{\text{lapseabove}}$ ) the top of the air temperature inversion layer. During Analysis 2 simulation periods with no inversion, Analysis 1 lapse rates were used. Lapse rates are based on air temperature data for the period 1999–2004 (see Fig. 4 for a schematic illustration).

	Jan	Feb	Mar	Apr	May	Jun	Jul	Aug	Sep	Oct	Nov	Dec	Avg
Analysis 1													
$[\text{°C (100 m)}^{-1}]$ (1999–2004) (Mernild et al. 2006b)	−0.45	−0.51	−0.47	−0.30	−0.20	0.33	0.33	0.15	−0.31	−0.49	−0.51	−0.42	−0.24
Analysis 2													
$\Delta T_{\text{lapsebelow}}$ the inversion layer $[\text{°C (100 m)}^{-1}]$	0.25	0.19	0.23	0.19	0.16	0.46	0.95	0.29	0.24	0.20	0.20	0.19	0.30
Analysis 2													
$\Delta T_{\text{lapseabove}}$ the inversion layer $[\text{°C (100 m)}^{-1}]$	−1.19	−1.34	−0.97	−0.74	−0.32	−0.44	−0.63	−0.45	−0.94	−1.19	−1.23	−0.87	−0.86

(5%), and 38 mm w.eq.  $(100 \text{ m})^{-1}$  (5%), respectively. Because of the small influence on the accumulation and ablation processes of the choice of the elevation level, we assume that the choice of the 300 m MSL level is appropriate given what we do know about inversions in this area. However, in the natural system we do expect variations in inversion level to occur under the influence of variations in topography and local climate (e.g., wind speed), and distance from the ocean and marginal glaciers.

Therefore, to determine the influence of temperature inversions on winter snow accumulation and summer ablation, and to simulate their effects on the surface winter, summer, and annual mass balance for the glaciers near Greenland's east coast, two simulations were performed: the first was conducted without accounting for temperature inversions (Analysis 1), and the second (Analysis 2) assumed temperature inversions occurred up to a height of 300 m MSL and were assumed to be present 84% of the time during the simulation period. The no-inversion cases were defined by days with precipitation rates  $>10 \text{ mm w.eq. day}^{-1}$  and/or winds  $>8 \text{ m s}^{-1}$ .

Monthly average air temperature lapse rates for Analysis 1 were estimated and used based on air temperature observations (2 m) from Station Coast (25 m MSL) and (2 m) from Station Nunatak [515 m MSL; see Mernild et al. (2006b) for further information]. For Analysis 1, a minimum monthly lapse rate of  $-0.51 \text{°C (100 m)}^{-1}$  occurred for November and February, and a maximum monthly lapse rate of  $0.33 \text{°C (100 m)}^{-1}$  in June and July; these temperature increases with elevation are governed by summer sea breezes in daytime coming predominantly from the S and SW (Mernild et al. 2006b, 2008a). Air temperature data from Station Coast and Station Nunatak indicated positive lapse rates for the ablation period (a temperature increase of approximately  $1.5 \text{°C}$  for the higher station). In reality, for Analysis 1, it seems unlikely that 2-m air temperatures would increase with elevation over the glacier itself (Mernild et al. 2006b).

For Analysis 2, lapse rates up to the fixed inversion layer (300 m MSL) and the 300 m MSL air temperature were calculated based on Station Coast observed air temperatures and Station Tasiilaq radiosonde 925-hPa (average elevation 631 m MSL) recorded air temperatures. Above the fixed inversion layer (300 m MSL) lapse rates were estimated based on the 300 m MSL inversion layer calculated air temperature and the Station Nunatak observed air temperature (see Fig. 4 for a schematic illustration of the Analysis 1 and 2 air temperature lapse rate routines and Table 6 for average monthly lapse rates). For January, February, October, and November the lapse rates above the fixed inversion layer are steeper than the adiabatic lapse rate of  $-0.98 \text{°C (100 m)}^{-1}$  (Table 6). Realistically, this would represent unstable conditions that could not be maintained in the atmosphere. At present, no temperature observations are available at higher catchment elevations for validation of the estimated upper lapse rates. The model simulates up to  $\sim 2.9 \text{°C}$  colder conditions at peaks. Therefore, a sensitivity analysis was conducted illustrating  $<1\%$  difference in glacier mass balance whether the Table 6 upper lapse rates or the adiabatic lapse rates were used for the months January, February, October, and November. Further, the use of different sites for the radiosonde and meteorological observations might also only create minor uncertainties.

#### 4. Results and discussion

Figure 5a illustrates the spatial modeled daily mean air temperature distribution for the coldest day, 21 February 2002, for Analysis 1 of  $-20.3 \text{°C}$  (without inversion) and 2 of  $-21.1 \text{°C}$ , showing a spatial variation in air temperature of  $6.1 \text{°C}$  within the simulation domain for Analysis 1, ranging from  $-18.2 \text{°C}$  to  $-24.3 \text{°C}$ . For Analysis 2 the variation was greater,  $8.8 \text{°C}$ , varying from  $-17.3 \text{°C}$  to  $-26.1 \text{°C}$ . In the low-lying areas (e.g., below 453 m MSL for February), the Analysis 1 simulated air temperature was relatively low in comparison with the Analysis 2

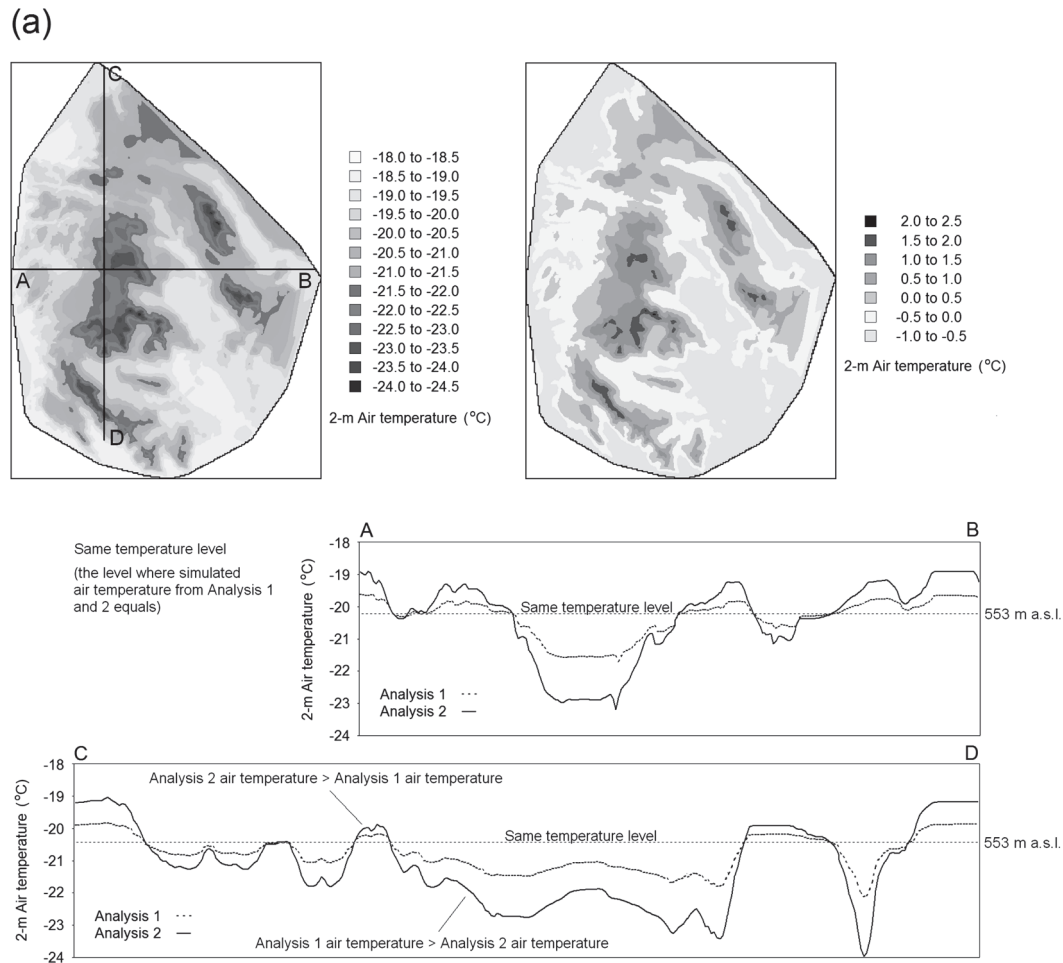


FIG. 5. (a) SnowModel–MicroMet spatial simulated 2-m air temperature for the Ammassalik Island, for the coldest day during the simulation period (21 Feb 2002): (top left) Analysis 1 simulated spatial air temperature; (top right) the spatial difference in air temperature between Analysis 1 and 2, where negative temperatures indicate Analysis 1 estimated values are below Analysis 2 estimated values; (middle) the Analysis 1 and 2 modeled temperatures at the A–B longitudinal profile; (bottom) the Analysis 1 and 2 modeled temperatures at the C–D longitudinal profile. At the longitudinal profiles, the STL (553 m MSL) is shown. For the profile locations see Fig. 1d. (b) As in (a), but for the warmest day during the simulation period (13 Jul 2005). At the longitudinal profiles, the STL (494 m MSL) is shown. For the profile locations see Fig. 1d.

simulated temperature, and vice versa. The level where simulated temperature from Analysis 1 and 2 is equal (e.g., at the 453 m MSL level for February) is called the “same temperature level” (STL). The temperature variations and the STL are clearly illustrated on the longitudinal temperature profiles in Fig. 5a, where the profiles cross each other. A similar spatial trend occurred for the warmest day, 13 July 2005, for Analysis 1 (19.8°C) and Analysis 2 (18.4°C) (Fig. 5b). For July, the STL was situated at 494 m MSL, almost equal to the February level. The STL was almost stable at the same altitude for winter and summer, but during breakup (April and May) and freeze-up (September and October) the STL and the temperature distribution appears to be more complex

because of, for example, variations in air temperature lapse rates influenced by the presence of periodic snow cover at the meteorological stations and sea ice dynamics at the Sermilik Fjord near Station Coast (see Fig. 4b for April and October). On average, for the accumulation period (September–May), the spatially distributed simulation area air temperature was 0.5°C lower for Analysis 1 than Analysis 2. For the ablation period (June–August), the Analysis 1 modeled simulation area temperature averaged 0.6°C higher than Analysis 2 simulated values.

The effect of Analysis 1 (routines without inversion) and 2 (with inversion) distributed air temperature is shown in Fig. 6 for three randomly chosen snow cover

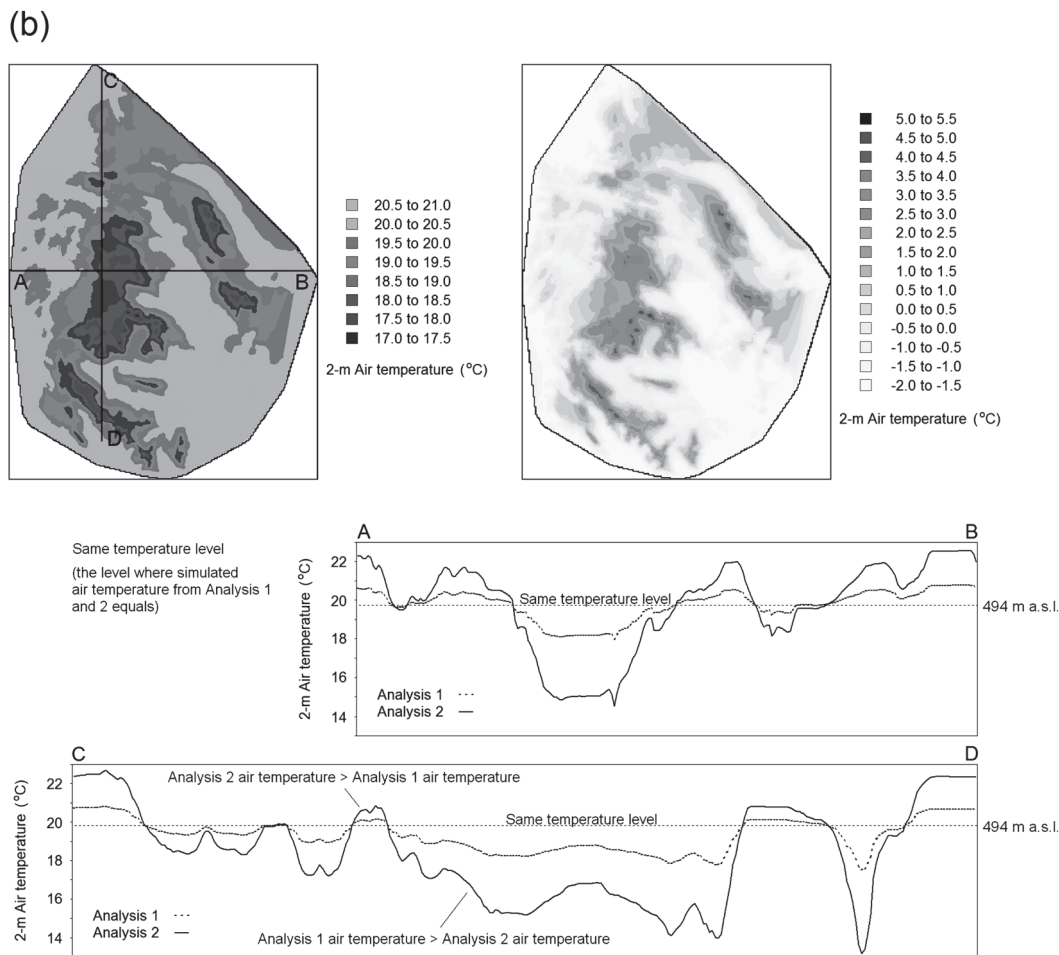


FIG. 5. (Continued)

depletion areas at the Mittivakkat Glacier: an area representative of the meteorological coastal–valley conditions that spans the elevation from 4 to 200 m MSL, an area representative of glacier conditions (from 489 to 615 m MSL), and an area representative of the mountain-peak conditions (from 679 to 941 m MSL). The snow cover extent is a product of both snow accumulation and ablation processes (phase change processes) of evaporation–sublimation and melting, which are strongly influenced by the air temperature distribution. Within SnowModel, SnowTran-3D simulates spatial blowing-snow deposition patterns in response to erosion and deposition, and EnBal calculates energy flux available for snowmelt. In Fig. 6, the 2003 (the year with the lowest ablation) Analysis 1 modeled valley snowmelt (ablation) started on day of year (DOY) 151 (31 May)—12 days later than the Analysis 2 estimated start of snowmelt. The 12-days earlier snowmelt modeled by Analysis 2 captured the effect of representing inversions in the simulations. Further, for Analysis 1, 25% of the snow cover extent

was melted away at DOY 175, 50% at DOY 181, and 75% at DOY 187. For Analysis 2, this occurred on DOY 169, 176, and 184, respectively, indicating a 3–6-day faster snowmelt for the valley (low-lying areas) under conditions of air temperature inversions. For 2005 (the year with the greatest ablation) the trend was similar. However, the Analysis 2 snowmelt occurred 1–3 days before, indicating a reduced effect of the inversions on melting during years with high ablation. For the glacier depletion area the trend is opposite: Analysis 1 snowmelt occurred earlier for both 2003 and 2005. For 2003 (Analysis 1), 25% of the snow cover extent was melted away at DOY 155, 50% at DOY 162, and 75% at DOY 207. For Analysis 2, the DOY are 162, 173, and 225, respectively. On average, throughout the ablation period, an approximately 1–2-week later Analysis 2 snowmelt occurred. For 2005 the trend was similar, however a later snowmelt extent of 1–4 days is indicated. For the peak depletion area, the melt trend equals the one from the glacier area; however, melt occurs later during the

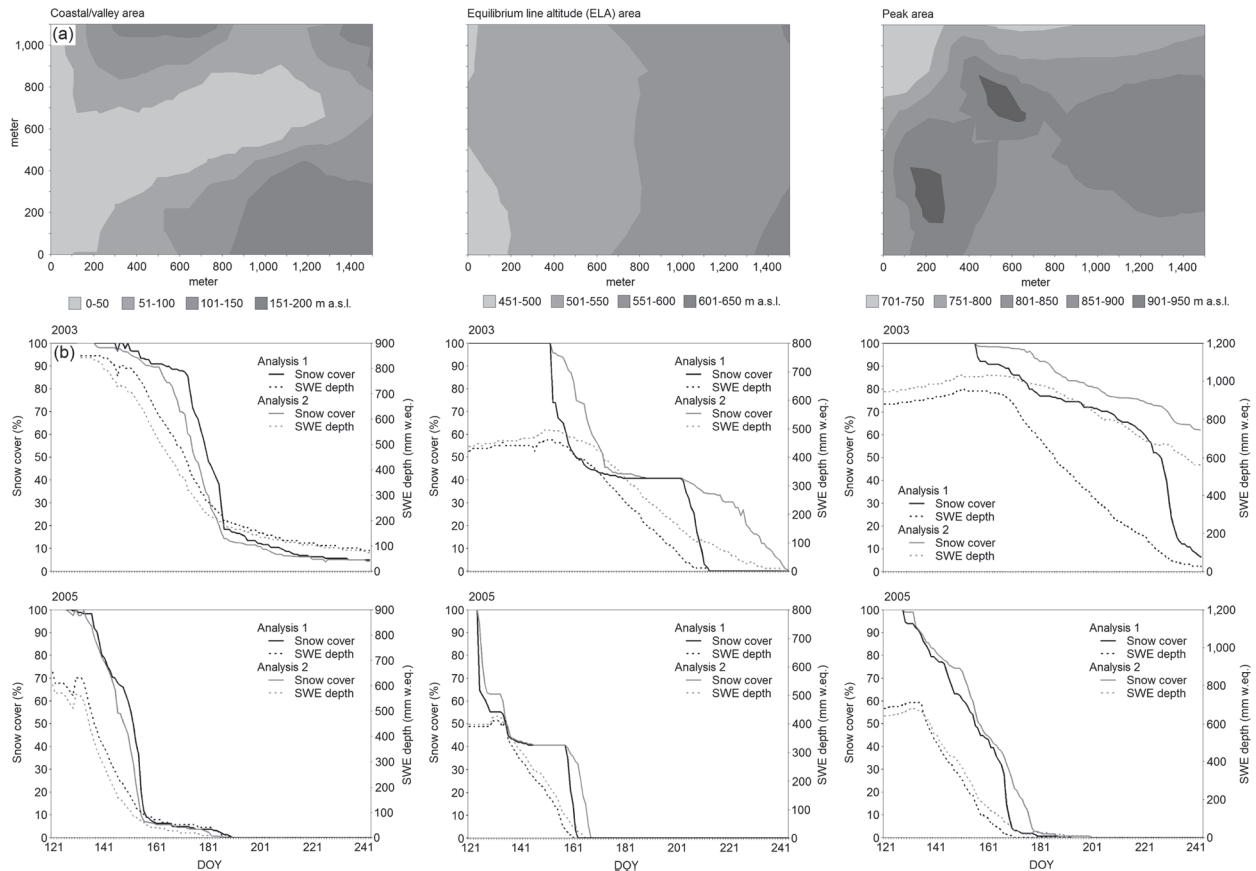


FIG. 6. (a) Digital elevation for the three snow cover depletion areas ( $1.1 \text{ km} \times 1.5 \text{ km}$ ;  $1.65 \text{ km}^2$ ): the (from left to right) coastal–valley area, glacier area, and peak area. (b) For the same areas, snow cover depletion and SWE depth curves for (top) 2003 (the year with the lowest ablation) and (bottom) 2005 (the year with the greatest ablation) both for Analysis 1 and 2, for the period 1 May (DOY 121)–31 Aug (DOY 243). For location of the three depletion areas see Fig. 1d.

ablation season because of the higher elevations. Analysis 1 snowmelt occurred earlier for both 2003 and 2005. For 2003 (Analysis 1), 25% of the snow cover extent was melted away at DOY 191, 50% at DOY 228, and 75% at DOY 232. For Analysis 2, only 25% of melted snow cover extent was reached (DOY 220) within the period from May to the end of August. On average, a 3–5-week later and slower snowmelt occurred for Analysis 2. For 2005, the peak area trend was similar; however a later and slower Analysis 2 snowmelt extent of between 2 and 4 days occurred. In general, for both Analysis 1 and 2, the start date of continuous snowmelt was delayed with increasing elevation. However, for the glacier depletion area, 25% of the snow cover was melted away approximately 2–3 weeks before the low-lying coastal–valley area. This is because the coastal area is influenced by cold sea breezes during the ablation period. Furthermore, in the early ablation period (June), runoff (including high spring flow rates) is mainly controlled by snowmelt whereas later in the season (July and August) when the

snow cover is largely gone, runoff is dominated by perennial snow patches, rain events, and glacier-ice melt from marginal glaciers like the Mittivakkat Glacier. On average (1999–2004) the change (loss) in, for example, the Mittivakkat Glacier snow and ice storage explains between 30% and 60% of the runoff (Mernild 2006).

The influence of distributed air temperature representation on average SWE depth, for all three depletion cover areas from May through August for 2003 and 2005, is further illustrated in Fig. 6. The difference in average SWE depth varied up to 53 mm w.eq. between Analysis 1 and 2. However, for the 2003 peak area, the difference was 294 mm w.eq. in terms of average SWE depth. In the coastal–valley area, Analysis 2 modeled SWE depth was less than Analysis 1, and vice versa for the high elevated areas (the glacier and the peak areas). This is due to the temporal and spatial air temperature distributions shown in Figs. 5a and 5b.

The spatial variations in modeled snow cover extent, and whether snow cover is present or absent on



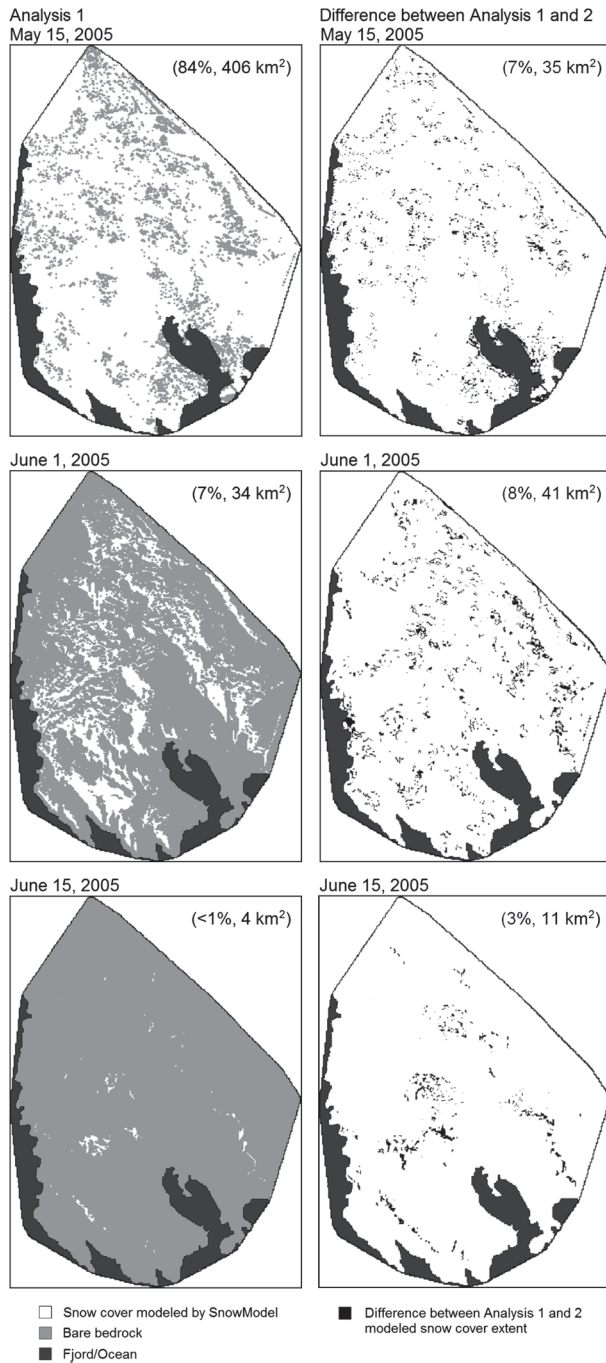


FIG. 7. SnowModel spatial simulated snow cover extent for the SW part of the Ammassalik Island for (top) 15 May, (middle) 1 Jun, and (bottom) 15 Jun 2005 for (left) Analysis 1 and (right) the difference between Analysis 1 and 2. The percentage and area of snow cover extent is also shown for each time step.

Ammassalik Island, is illustrated as an example from 15 May through 15 June 2005 (the year with the greatest ablation) (Fig. 7). Modeled snow cover extent indicates that snow is present on glaciers, mainly on leeward south-

TABLE 7. Analysis 1 and 2 SnowModel simulated average winter, summer, and annual mass balance for glaciers on the SW part of the Ammassalik Island for the 8-yr period 1998/99–2005/06. For glacier information see Table 8.

	1998/99	1999/00	2000/01	2001/02	2002/03	2003/04	2004/05	2005/06	Avg
Analysis 1									
Winter mass balance (mm w.eq.)	970 ± 160	1240 ± 240	1230 ± 110	1230 ± 270	1230 ± 150	1230 ± 160	930 ± 270	1000 ± 210	1130 ± 240
Summer mass balance (mm w.eq.)	-1650 ± 220	-2020 ± 310	-2200 ± 200	-1850 ± 340	-1460 ± 200	-2340 ± 270	-2820 ± 190	-1750 ± 200	-2010 ± 480
Annual mass balance (mm w.eq. yr <sup>-1</sup> )	-670 ± 370	-780 ± 500	-970 ± 290	-620 ± 600	-230 ± 350	-1110 ± 430	-1890 ± 450	-750 ± 400	-880 ± 620
Analysis 2									
Winter mass balance (mm w.eq.)	870 ± 310	1070 ± 240	1090 ± 190	1150 ± 320	1130 ± 220	1090 ± 220	770 ± 210	930 ± 230	1010 ± 270
Summer mass balance (mm w.eq.)	-1480 ± 170	-1740 ± 180	-1780 ± 130	-1490 ± 340	-1090 ± 140	-2030 ± 140	-2610 ± 240	-1640 ± 170	-1730 ± 480
Annual mass balance (mm w.eq. yr <sup>-1</sup> )	-610 ± 300	-670 ± 310	-690 ± 200	-310 ± 600	40 ± 290	-940 ± 320	-1810 ± 380	-710 ± 390	-720 ± 620

TABLE 8. A description of the glaciers in the simulation domain by number, name, area, and elevation based on the 100-m gridcell increment. The Glacier numbers refers to Fig. 1c.

Glacier no.	Glacier name	Glacier area (km <sup>2</sup> )	Glacier elev range (m MSL)	Avg glacier elev (m MSL)
1	Glacier 530	3.29	350–523	466
2	Glacier 783*	8.16	148–501	372
3	Glacier 1050	1.70	411–959	586
4	Glacier 1054	2.00	409–895	664
5	Glacier 769	1.02	370–637	504
6	Glacier 390	8.88	50–854	360
7	Sofias Fjeld Glacier 1	0.09	587–753	682
8	Sofias Fjeld Glacier 2	0.39	668–901	771
9	Sofias Fjeld Glacier 3	0.45	584–926	761
10	Itsajjivit Glacier	0.04	330–362	348
11	Ymer Glacier	1.56	314–650	503
12	Uunnguttoq Glacier	0.10	345–457	408
13	Glacier 938 NW	0.11	679–481	571
14	Glacier 938 SE	0.11	721–568	647
15	Glacier 588	1.82	325–683	540
16	Glacier 962	0.10	654–808	714
17	Vegas Fjeld Glacier	0.07	530–719	604
18	Mittivakkat Glacier	31.00	136–950	583
19	Glacier 894	1.07	471–826	659

\* Glacier 783 (number 2) is part of a bigger glacier complex extending outside the simulation domain.

facing slopes, and mostly in the valleys, because of the blowing-snow redistribution since the majority of snow-transporting winds are from the NE, N, and SE. For 15 May, Analysis 1 indicates a snow cover extent of 84% (406 km<sup>2</sup>), and an approximately 7% (~35 km<sup>2</sup>) spatial discrepancy between Analysis 1 and 2 (Fig. 7), a discrepancy mainly pronounced in the northwest-, north-, and northeast-facing slopes. This is probably due to the shadow effect of the mountains, and on south-facing slopes according to snow erosion, accumulation, and ablation. For 1 and 15 June, the snow cover extent was 7% (34 km<sup>2</sup>) and <1% (4 km<sup>2</sup>), and the spatial discrepancy 8% (41 km<sup>2</sup>) and 3% (11 km<sup>2</sup>), respectively. Figure 7 illustrates that the spatial snow cover extent for the entire SW part of Ammassalik Island is nearly identical with the variations in snow cover extent illustrated at the three randomly chosen depletion curve examples in Fig. 6.

Throughout the year, different surface processes (snow accumulation, snow redistribution, blowing-snow sublimation, surface evaporation, and melting) on snow and glaciers ice affect the surface glacier mass balance and the high-latitude water balance. The yearly water balance equation for a glacier can be described by

$$P - (E + SU) - R \pm \Delta S = 0 \pm \eta, \quad (2)$$

where  $P$  is the precipitation input from snow and rain (and possible condensation),  $E$  is evaporation,  $SU$  is sublimation (including blowing-snow sublimation),  $R$  is runoff, and  $\Delta S$  is change in glacier storage due to, for example, change in mass balance (including snow trans-

port from nearby bedrock areas). Glacier storage also includes changes in supraglacial storage (lakes, pond, channels, etc.), englacier storage (ponds and the water table), and subglacier storage (cavities and lakes)—glacier storage components not accounted for in this study. Here,  $\eta$  is the water balance discrepancy (error). The error term should be 0 (or small) if the major components ( $P$ ,  $E$ ,  $SU$ ,  $R$ , and  $\Delta S$ ) have been determined accurately. Dividing the water balance into two different periods—an accumulation period (September–May; winter period) where accumulation processes (precipitation and snow redistribution, influenced by blowing-snow sublimation) are dominant, and an ablation period (June–August; summer period) where ablation processes (evaporation, sublimation, and melting) are dominant—is commonly used when the conditions of glaciers are presented.

During blowing-snow events, sublimation of wind transported snow can play an important role in the high-latitude hydrological cycle. During the investigation period 1998/99–2005/06, modeled annual sublimation for the Mittivakkat Glacier averaged 10% (approximately 135 mm w.eq.) of the solid precipitation inputs for Analysis 1, and 11% (approximately 147 mm w.eq.) for Analysis 2. For the entire simulation domain it is approximately 11% of the solid precipitation for both Analysis 1 and 2. The sublimation losses are low at Ammassalik Island relative to many previous studies in Arctic North America and Greenland (e.g., Pomeroy and Gray 1995; Pomeroy et al. 1997; Liston and Sturm 1998; Essery et al. 1999; Pomeroy and Essery 1999; Liston

and Sturm 2004), where approximately 5%–50% of the annual solid precipitation was returned to the atmosphere by sublimation. Blowing snow sublimation rates are mainly dependent upon air temperature, humidity deficit, wind speed, and particle size distribution (e.g., Schmidt 1972, 1982; Tabler 1975; Pomeroy and Gray 1995; Liston and Sturm 2002). In our coastal domain, high wind speeds are generally coincident with high relative humidity, and therefore, sublimation has played a lesser role in the snow and glacier mass balance budget, whether it is modeled by Analysis 1 or 2.

In Table 7 the average winter, summer, and annual mass balances for the glaciers in the SW part of the Ammassalik are shown for both Analysis 1 and 2 (1998/99–2005/06). The glaciers are located above the inversion layer, mainly from 300 to 800 m MSL (for additional glacier information see Table 8). The average modeled winter mass balance is  $1130 \pm 240$  (Analysis 1) and  $1010 \pm 270$  mm w.eq. (Analysis 2), indicating a significant difference (97.5% quantile) of 120 mm w.eq. (or 12%). The difference in average modeled winter mass balance is sensitive to changes in temperature, since colder air can carry less precipitable moisture. For the glaciers lying above the STL level, the Analysis 1 simulated average winter air temperature is relatively higher than the average winter temperature simulated by Analysis 2. The interannual variation in average winter balance for both Analysis 1 and 2 from 1998/99 through 2005/06 was almost similar (Fig. 8a), illustrating a nonsignificant decreasing trend of  $-14$  and  $-11$  mm w.eq.  $\text{yr}^{-1}$ , respectively. The average modeled summer mass balances for Analysis 1 and 2 were  $-2010 \pm 480$  and  $-1730 \pm 480$  mm w.eq., respectively (Table 7), indicating a significant difference (97.5% quantile) of 280 mm w.eq. (16%). The interannual variation in average summer mass balance throughout the simulation period indicated a nonsignificant increasing loss of  $50$  mm w.eq.  $\text{yr}^{-1}$  (Analysis 1) and  $63$  mm w.eq.  $\text{yr}^{-1}$  (Analysis 2) (Fig. 8a). Based on simulated winter and summer balance values, the average annual glacier mass balance was  $-880 \pm 620$  and  $-720 \pm 620$  mm w.eq.  $\text{yr}^{-1}$  for Analysis 1 and 2, respectively, indicating a significant difference (97.5% quantile) of 160 mm w.eq. (22%) (Table 7). Throughout the simulation period the average annual mass balance indicated a nonsignificant increasing loss of  $64$  and  $74$  mm w.eq.  $\text{yr}^{-1}$  for Analysis 1 and 2, respectively (Fig. 8a), a loss related to the increased MAAT of the area of  $0.09^\circ\text{C yr}^{-1}$  (1998–2006). An example of the spatial modeled negative annual mass balance is shown in Fig. 9 for a collection of glaciers varying in size, elevation, aspect, and location for the year 2003/04 for both Analysis 1 and 2; they indicate the highest annual mass-loss rates at low elevations and, in general, for

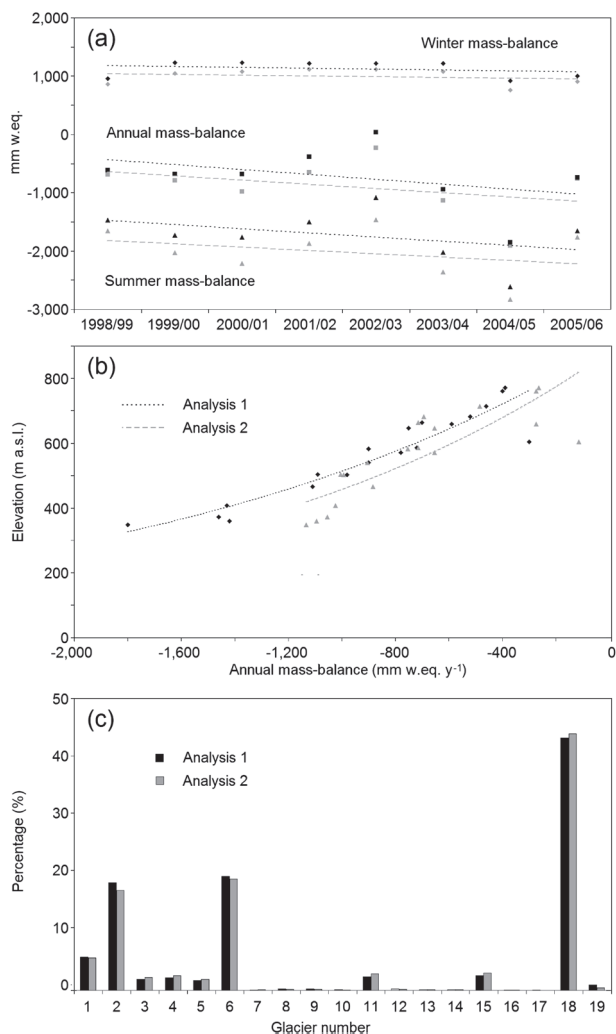


FIG. 8. (a) Analysis 1 and 2 SnowModel simulated average winter, summer, and annual mass balance for all glaciers in the simulation domain from 1998/99 through 2005/06, except for glacier 2 (Glacier 783), which is part of a larger glacier complex ranging outside the domain; (b) Analysis 1 and 2 average modeled glacier annual mass balance plotted against the average glacier elevation; (c) Analysis 1 and 2 change in average glacier storage (%).

Analysis 1. The spatial variation in average annual mass balance (1998/99–2005/06) is shown in Tables 7 and 9. The Itsaqjivit Glacier (Glacier 10) had on average the lowest annual mass balance of  $-1800 \pm 550$  mm w.eq.  $\text{yr}^{-1}$  (Analysis 1), while the Vegas Fjeld Glacier (Glacier 17) had the highest annual mass balance of  $-300 \pm 530$  mm w.eq.  $\text{yr}^{-1}$  (Fig. 1c). These mass-balance variations are primarily related to the differences in elevation and aspect. For Analysis 2 the values were, respectively  $-1190 \pm 700$  and  $-90 \pm 660$  mm w.eq.  $\text{yr}^{-1}$  (Table 9), indicating the average annual mass balances were negative for all glaciers in both Analysis 1 and 2. In Fig. 8b,

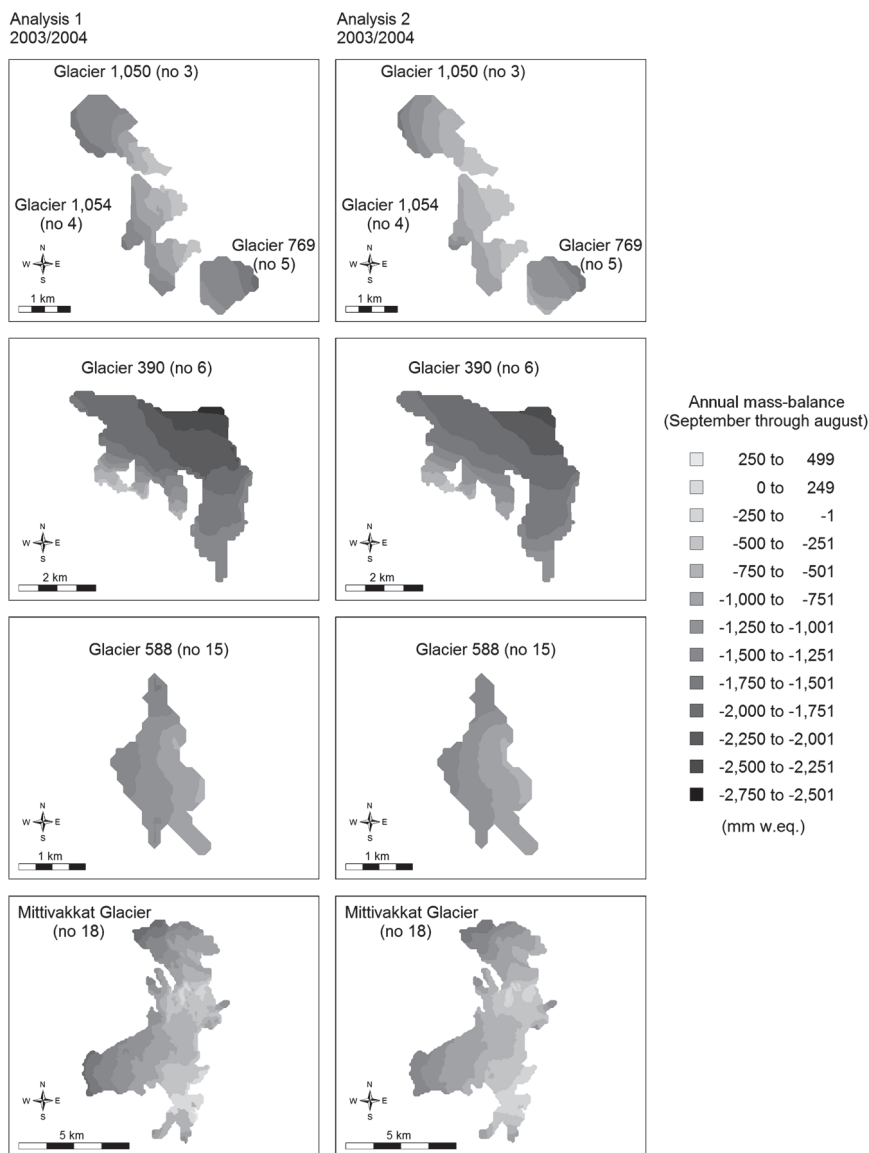


FIG. 9. SnowModel simulated spatial annual mass balance for different glaciers on Ammassalik Island for the period 2003/04 based on Analysis 1 and 2. The glaciers refer to the numbers in Table 8 and Fig. 1c.

the average negative glacier annual mass balance is shown in relation to the average glacier elevation. This indicates that the average ELA (the ELA is defined as the elevation where the annual mass balance is zero, or where accumulation equals ablation) for the glaciers is located at 900 m MSL for Analysis 1 and at 875 m MSL for Analysis 2, showing a change in location of ELA of 25 m MSL. This is mainly due to changes in ablation of 280 mm w.eq. rather than changes in accumulation of 120 mm w.eq. (Table 7). Annual mass-balance observations from the Mittivakkat Glacier show that the average ELA was close at 700 m MSL, varying in elevation

between 400 m MSL and up to more than 900 m MSL through the period from 1995/96 to 2005/06 (Knudsen and Hasholt 2008). This is in the range of simulated ELA elevation estimated by Analysis 1 and 2.

A negative glacier annual mass balance may be important from a water resource perspective. For the town Tasiilaq (Fig. 1a) the simulation domain is of potential interest for water resources. In Table 9 and Fig. 8c, the absolute values/percentages of the glacier mass loss ( $\text{mm w.eq. yr}^{-1}$  and  $\text{m}^3 \text{y}^{-1}$ ) (Analysis 1) indicates that Glacier 2 (Glacier 783), 6 (Glacier 930), and 18 (Mittivakkat Glacier) are the main contributors with

TABLE 9. Analysis 1 and 2 modeled annual mass-balance change ( $\Delta S$ ) for the glaciers on SW Ammassalik Island from 1998/99 through 2005/06 (from September through August). The glacier numbers refer to the numbers in Table 8 and Fig. 1c.

	Analysis 1 modeled annual mass balance ( $\Delta S$ )		Analysis 2 modeled annual mass balance ( $\Delta S$ )	
	mm w.eq. yr <sup>-1</sup>	m <sup>3</sup> yr <sup>-1</sup> (%)	mm w.eq. yr <sup>-1</sup>	m <sup>3</sup> yr <sup>-1</sup> (%)
Glacier 1	-1100 ± 480	-3 651 900 (5.7)	-860 ± 380	-2 832 700 (5.6)
Glacier 2	-1460 ± 520	-11 913 600 (18.5)	-1070 ± 500	-8 698 600 (17.2)
Glacier 3	-720 ± 480	-1 224 000 (1.9)	-650 ± 550	-1 111 800 (2.2)
Glacier 4	-700 ± 480	-1 400 000 (2.2)	-630 ± 540	-1 268 000 (2.5)
Glacier 5	-1090 ± 520	-1 111 800 (1.7)	-960 ± 610	-977 200 (1.9)
Glacier 6	-1420 ± 510	-12 609 600 (19.6)	-1090 ± 620	-9 688 100 (19.1)
Glacier 7	-520 ± 450	-46 800 (<0.1)	-600 ± 530	-54 200 (0.1)
Glacier 8	-390 ± 290	-152 100 (0.2)	-230 ± 560	-87 800 (0.2)
Glacier 9	-400 ± 530	-180 000 (0.3)	-230 ± 650	-107 500 (0.2)
Glacier 10	-1800 ± 550	-72 000 (0.1)	-1190 ± 700	-47 700 (<0.1)
Glacier 11	-980 ± 490	-1 528 800 (2.4)	-930 ± 540	-1 452 400 (2.9)
Glacier 12	-1430 ± 580	-143 000 (0.2)	-1040 ± 610	-103 600 (0.2)
Glacier 13	-780 ± 710	-85 800 (0.1)	-620 ± 630	-67 700 (0.1)
Glacier 14	-750 ± 470	-82 500 (0.1)	-610 ± 580	-67 100 (0.1)
Glacier 15	-900 ± 490	-1 638 000 (2.5)	-870 ± 510	-1 522 900 (3.0)
Glacier 16	-460 ± 470	-46 000 (<0.1)	-420 ± 600	-41 800 (<0.1)
Glacier 17	-300 ± 530	-21 000 (<0.1)	-90 ± 660	-6 100 (<0.1)
Glacier 18	-900 ± 470	-27 900 000 (43.3)	-720 ± 580	-22 289 000 (44.0)
Glacier 19	-590 ± 80	-631 300 (1.0)	-430 ± 570	-233 200 (0.5)
Avg and tot	-880 ± 620	-64 438 200 (100)	-690 ± 620	-50 657 400 (100)

values around  $11.9 \times 10^6 \text{ m}^3 \text{ yr}^{-1}$  (~19% of total loss),  $12.6 \times 10^6 \text{ m}^3 \text{ yr}^{-1}$  (~20%), and  $27.9 \times 10^6 \text{ m}^3 \text{ yr}^{-1}$  (~43%), respectively. For Analysis 2, the values are less and around  $8.7 \times 10^6 \text{ m}^3 \text{ yr}^{-1}$  (~17%),  $9.7 \times 10^6 \text{ m}^3 \text{ yr}^{-1}$  (~19%), and  $22.3 \times 10^6 \text{ m}^3 \text{ yr}^{-1}$  (~44%), respectively. Modeled changes in glacier annual mass balance for Analysis 1 and 2 were  $-64.4 \times 10^6 \text{ m}^3 \text{ yr}^{-1}$  and  $-50.7 \times 10^6 \text{ m}^3 \text{ yr}^{-1}$ , respectively, indicating a maximum difference of ~21% (Table 9) for conditions with and without air temperature inversions.

Air temperature inversions are commonplace throughout the Arctic. Therefore, a pilot study like this can be used as a guide to emphasize the importance of 1) including air temperature inversion routines in climate models to improve snow and ice melt calculations, and to improve, more specifically, GrIS climate change simulations; and 2) detailed radiosonde observations in space and time, for example, around the GrIS to collect comprehensive information about temperature distributions, including inversion, since inversion according to Huybrechts et al. (1991) depends on latitude. As a first step, these model estimates show, for example, an up to ~21% difference in glacier annual mass balance for simulations without or with air temperature inversions. This quantity, when projected over the entire GrIS ablation zone, is expected to affect GrIS surface mass-balance, freshwater runoff, and water resource predictions in important ways, and advocates the need to represent air temperature inversions in GrIS mass balance calculations and predictions.

## 5. Summary and conclusions

In Arctic coastal areas, air temperature inversions are a common feature. The physically based snow evolution modeling system (SnowModel) was modified with routines to account for the spatial distribution of air temperature inversions, and to describe the subsequent effect on snow accumulation, and snow and glacier ice ablation over the SW part of the Ammassalik Island in East Greenland. Based on vertical air temperature observations, the top of the temperature inversion layer was found to be approximately 300 m MSL, and was present in 84% of the summer observations. The observations were not detailed enough to provide a full annual understanding of the inversion height, strength, and thickness within and around all of Ammassalik Island. But, using a combination of observational datasets and physical understanding of the natural system, we justifiably assumed inversions were present 84% of the time with an inversion level of 300 m MSL throughout the 8-yr simulation period. Inversion absence was assumed when wind speeds were greater than  $8 \text{ m s}^{-1}$  and/or precipitation rates were greater than  $10 \text{ mm w.eq. day}^{-1}$ . Sensitivity simulations were performed that changed the inversion level by 100 m over a 100–500-m range. These yielded uncertainties of 5% in both winter and summer glacier mass balance, and further justified our choice of an observation-based 300-m inversion level for the rest of our model simulations. These Ammassalik Island simulations showed that ignoring routines for air temperature



inversion in Arctic coastal climate, snow, ice, and runoff modeling studies could create errors in snowmelt date, indicating an earlier or later snowmelt date by up to 1–3 weeks. The model simulations (1998/99–2005/06) yielded useful insights into the average glacier annual mass-balance consequences from a water resource perspective, representing a ~21% difference in mass-balance loss without or with inversion routines of  $64.4 \times 10^6$  and  $50.7 \times 10^6 \text{ m}^3 \text{ yr}^{-1}$ , respectively. Therefore, in many Arctic coastal landscapes we expect that a realistic description of temperature inversion is essential for accurate snow and glacier ice melt and glacier mass-balance simulations.

*Acknowledgments.* We extend a very special thanks to Jessica D. Lundquist, University of Washington, and the two anonymous reviewers for their insightful critique of this article. Thanks are given to the Cooperative Institute for Research in the Atmosphere, Colorado State University, for hosting the first author during October 2007 and February 2008, and the Faculty of Science and Institute of Low Temperature Science, Hokkaido University, Japan, for hosting the first author from April through July 2008. Thanks are also given to the Department of Geography and Geology, University of Copenhagen, for providing the input data, and to the Danish Meteorological Institute for providing WMO synoptic meteorological data from the station in Tasiilaq. This work was supported by grants from the University of Alaska Presidential IPY Postdoctoral Foundation, the University of Alaska Fairbanks (UAF) Office of the Vice Chancellor for Research, Office of the Director at the International Arctic Research Center, UAF, and the Water Environmental Research Center, UAF, and was carried out during the first author's IPY Post-Doctoral Program at the UAF.

#### REFERENCES

- Anquetin, S., C. Guilbaud, and J.-P. Chollet, 1998: The formation and destruction of inversion layers within a deep valley. *J. Appl. Meteor.*, **37**, 1547–1560.
- Archer, D., 2004: Hydrological implications of spatial and altitudinal variation in temperature in the upper Indus basin. *Nord. Hydrol.*, **35**, 209–222.
- Barry, R. G., 2008: *Mountain Weather and Climate*. 3rd ed. Cambridge University Press, 506 pp.
- Born, E. W., and J. Böcher, 2001: *The Ecology of Greenland*. Ministry of Environment and Natural Resources, 429 pp.
- Chen, J., S. C. Sauners, T. R. Crow, R. J. Naiman, K. D. Brosofske, G. D. Morz, B. L. Brookshire, and J. F. Franklin, 1999: Microclimate in forest ecosystem and landscape ecology. *Bio-science*, **49**, 288–297.
- Dodson, R., and D. Marks, 1997: Daily air temperature interpolation at high spatial resolution over a large mountainous region. *Climate Res.*, **8**, 1–20.
- Essery, R. L. H., L. Li, and J. W. Pomeroy, 1999: A distributed model of blowing snow over complex terrain. *Hydrol. Processes*, **13**, 2423–2438.
- Greenland, D. E., 1979: Modelling air pollution potential for mountain resorts. Institute of Arctic and Alpine Research, Occasional Paper 32, Boulder, CO, University of Colorado, 96 pp.
- Hanna, S. R., and D. G. Strimaitis, 1990: Rugged terrain effects on diffusion. *Atmospheric Processes over Complex Terrain, Meteor. Monogr.*, No. 45, Amer. Meteor. Soc., 109–143.
- Hansen, B. U., B. Elberling, O. Humlum, and N. Nielsen, 2005: Meteorological trends (1991–2004) at Arctic Station, Central West Greenland (69°15'N) in a 130 years perspective. *Dan. J. Geogr.*, **106** (1), 45–56.
- , and Coauthors, 2008: Present day climate at Zackenberg. *Adv. Ecol. Res.*, **40**, 115–153.
- Hosler, C. R., 1961: Low level inversion frequency in the contiguous United States. *Mon. Wea. Rev.*, **89**, 319–339.
- Huybrechts, P., A. Letreguilly, and N. Reeh, 1991: The Greenland ice sheet and greenhouse warming. *Palaeogeogr. Palaeoclimatol. Palaeoecol.*, **89**, 399–412.
- Kadyrov, E. N., A. S. Viazankin, E. R. Westwater, and K. B. Widener, 1999: Characteristics of the low-level temperature inversion at the North Slope of Alaska on the base of microwave remote sensing data. *Proc. Ninth ARM Science Team Meeting*, San Antonio, TX, Dept. of Energy, 1–7.
- Kahl, J. D., 1990: Characteristic of the low-level temperature inversion along the Alaska Arctic Coast. *Int. J. Climatol.*, **10**, 537–548.
- , M. D. Serreze, and R. C. Schnell, 1992: Tropospheric low-level temperature inversions in the Canadian Arctic. *Atmos.–Ocean*, **30**, 511–529.
- , D. A. Martinez, and N. A. Zaitseva, 1996: Long-term variability in the low-level inversion layer over the Arctic Ocean. *Int. J. Climatol.*, **16**, 1297–1313.
- Kerminen, V., and Coauthors, 2007: Development of particle number size distribution near a major road in Helsinki during an episodic inversion situation. *Atmos. Environ.*, **41**, 1759–1767.
- Klemes, V., 1985: Sensitivity of water resources systems to climate variations. WPC Rep. 98, World Meteorological Organization, 56 pp.
- , 1986: Operational testing of hydrological simulation models. *Hydrol. Sci. J.*, **31**, 13–24.
- Knudsen, N. T., and B. Hasholt, 2008: Mass balance observations of the Mittivakkat Glacier, Ammassalik Island, Southeast Greenland 1995–2006. *Dan. J. Geogr.*, **108** (1), 111–120.
- Kozo, T. L., 1982a: An observational study of sea breezes along the Alaskan Beaufort Sea Coast: Part I. *J. Appl. Meteor.*, **21**, 891–905.
- , 1982b: A mathematical model of sea breezes along the Alaskan Beaufort Sea Coast: Part II. *J. Appl. Meteor.*, **21**, 906–924.
- Kunkel, K. E., 1989: Simple procedures for extrapolation of humidity variables in the mountainous western United States. *J. Climate*, **2**, 656–669.
- Liston, G. E., 1995: Local advection of momentum, heat, and moisture during the melt of patchy snow covers. *J. Appl. Meteor.*, **34**, 1705–1715.
- , and D. K. Hall, 1995: An energy-balance model of lake-ice evolution. *J. Glaciol.*, **41**, 373–382.
- , and M. Sturm, 1998: A snow-transport model for complex terrain. *J. Glaciol.*, **44**, 498–516.
- , and —, 2002: Winter precipitation patterns in arctic Alaska determined from a blowing-snow model and snow-depth observations. *J. Hydrometeorol.*, **3**, 646–659.

- , and —, 2004: The role of winter sublimation in the Arctic moisture budget. *Nord. Hydrol.*, **35**, 325–334.
- , and K. Elder, 2006a: A meteorological distribution system for high-resolution terrestrial modelling (MicroMet). *J. Hydrometeorol.*, **7**, 217–234.
- , and —, 2006b: A distributed snow evolution modeling system (SnowModel). *J. Hydrometeorol.*, **7**, 1259–1276.
- , J.-G. Winther, O. Bruland, H. Elvehøy, and K. Sand, 1999: Below surface ice melt on the coastal Antarctic ice sheet. *J. Glaciol.*, **45** (150), 273–285.
- , R. B. Haehnel, M. Sturm, C. A. Hiemstra, S. Berezovskaya, and R. D. Tabler, 2007: Simulating complex snow distributions in windy environments using SnowTran-3D. *J. Glaciol.*, **53**, 241–256.
- Lundquist, L. D., and D. R. Cayan, 2007: Surface temperature patterns in complex terrain: Daily variations and long-term change in the central Sierra Nevada, California. *J. Geophys. Res.*, **112**, D11124, doi:10.1029/2006JD007561.
- Marinec, J., and A. Rango, 1986: Parameter values for snowmelt runoff modelling. *J. Hydrol.*, **84**, 197–219.
- Mernild, S. H., 2006: Freshwater discharge from the coastal area outside the Greenland Ice Sheet, East Greenland, with focus on Mittivakkat, Ammassalik Island (low Arctic) and Zackenberg (high Arctic). Ph.D. dissertation, Institute of Geography, Faculty of Science, University of Copenhagen, 394 pp.
- , B. Hasholt, and G. E. Liston, 2006a: Water flow through Mittivakkat Glacier, Ammassalik Island, SE Greenland. *Dan. J. Geogr.*, **106** (1), 25–43.
- , G. E. Liston, B. Hasholt, and N. T. Knudsen, 2006b: Snow-distribution and melt modeling for Mittivakkat Glacier, Ammassalik Island, SE Greenland. *J. Hydrometeorol.*, **7**, 808–824.
- , —, and —, 2007: Snow-distribution and melt modeling for glaciers in Zackenberg River drainage basin, NE Greenland. *Hydrol. Processes*, **21**, 3249–3263, doi:10.1002/hyp.6500.
- , B. U. Hansen, B. H. Jakobsen, and B. Hasholt, 2008a: Climatic conditions at the Mittivakkat Glacier catchment (1994–2006), Ammassalik Island, SE Greenland, and in a 109 years term perspective (1898–2006). *Dan. J. Geogr.*, **108** (1), 49–70.
- , D. L. Kane, B. U. Hansen, B. H. Jakobsen, B. Hasholt, and N. T. Knudsen, 2008b: Climate, glacier mass balance, and runoff (1993–2005) Mittivakkat Glacier catchment, Ammassalik Island, SE Greenland, and in a long term perspective (1898–1993). *Hydrol. Res.*, **39** (4), 239–256.
- , G. E. Liston, and B. Hasholt, 2008c: East Greenland freshwater runoff to the North Atlantic Ocean 1999–2004 and 2071–2100. *Hydrol. Processes*, **22**, 4571–4586, doi:10.1002/hyp.7061.
- , —, C. A. Hiemstra, and K. Steffen, 2008d: Surface melt area and water balance modeling on the Greenland Ice Sheet 1995–2005. *J. Hydrometeorol.*, **9**, 1191–1211.
- , —, D. L. Kane, B. Hasholt, and N. T. Knudsen, 2008e: Spatial snow distribution, runoff, and mass balance modelling for entire Mittivakkat Glacier (1998–2006), Ammassalik Island, SE Greenland. *Dan. J. Geogr.*, **108** (1), 125–140.
- , —, C. A. Hiemstra, and K. Steffen, 2009: Record 2007 Greenland Ice Sheet surface melt extent and runoff. *Eos, Trans. Amer. Geophys. Union*, **90**, doi:10.1029/2009EO020002.
- Milionis, A. E., and T. D. Davies, 2008: A comparison of temperature inversion statistics at a coastal and a non-coastal location influenced by the same synoptic regime. *Theor. Appl. Climatol.*, **94**, 225–239.
- Oke, T. R., 1987: *Boundary Layer Climates*. 2nd ed. Routledge, 435 pp.
- Pomeroy, J. W., and D. M. Gray, 1995: Snowcover accumulation, relocation and management. National Hydrology Research Institute Science Rep. 7, Hydrological Science Division, University of Saskatchewan, 144 pp.
- , and R. L. H. Essery, 1999: Turbulent fluxes during blowing snow: Field test of model sublimation predictions. *Hydrol. Processes*, **13**, 2963–2975.
- , and E. Brun, 2001: Physical properties of snow. *Snow Ecology: An Interdisciplinary Examination of Snow-Covered Ecosystems*, H. G. Jones et al., Eds., Cambridge University Press, 45–126.
- , P. Marsh, and D. M. Gray, 1997: Application of distributed blowing snow model to the Arctic. *Hydrol. Processes*, **11**, 1450–1465.
- Putnins, P., 1970: The climate of Greenland. *Climates of the Polar Regions*, S. Orvig, Ed., Vol. 12, *World Survey of Climatology*, Elsevier, 3–112.
- Refsgaard, J. C., 2000: Towards a formal approach to calibration and validation of models using spatial data. *Spatial Patterns in Catchment Hydrology: Observations and Modelling*, R. Gryson and G. Bloschl, Eds., Cambridge University Press, 329–354.
- , and J. Knudsen, 1996: Operational validation and inter-comparison of different types of hydrological models. *Water Resour. Res.*, **32**, 2189–2202.
- , and H. J. Henriksen, 2004: Modelling guidelines—terminology and guiding principles. *Adv. Water Resour.*, **27**, 71–82.
- Riordan, A. J., J. M. Davis, and R. B. Kiess, 1986: The morning inversion near the ground and its daytime transition at two rural sites in the Carolinas. *J. Climate Appl. Meteorol.*, **25**, 239–256.
- Schmidt, R. A., 1972: Sublimation of wind-transported snow—A model. Research Paper RM-90, Rocky Mountain Forest and Range Experiment Station, Forest Service, U.S. Department of Agriculture, Fort Collins, CO, 24 pp.
- , 1982: Vertical profiles of wind speed, snow concentration, and humidity in blowing snow. *Bound.-Layer Meteorol.*, **23**, 223–246.
- Serreze, M. C., J. D. Kahl, and R. C. Schnell, 1992: Low-level temperature inversions of the Eurasian Arctic and comparisons with Soviet drifting station data. *J. Climate*, **5**, 615–629.
- Singh, P., 1999: A temperature lapse rate study in Western Himalayas. *Hydrol. J. Indian Assoc. Hydrol.*, **14**, 156–163.
- Streten, N. A., N. Ishikawa, and G. Wendler, 1974: Some observations of the local wind regime on an Alaskan Arctic Glacier. *Arch. Meteor. Geophys. Bioklimatol. Ser. B*, **22**, 337–350.
- Stull, R. B., 1988: *An Introduction to Boundary Layer Meteorology*. Kluwer Academic, 666 pp.
- Tabler, R. D., 1975: Estimating the transport and evaporation of blowing snow. *Proc. Snow Management on the Great Plains Symp.*, Publication 73, Bismarck, ND, Great Plains Agricultural Council, 85–104.
- Walcek, C. J., 1994: Cloud cover and its relationship to relative humidity during a spring midlatitude cyclone. *Mon. Wea. Rev.*, **122**, 1021–1035.
- Weick, E. J., and W. R. Rouse, 1991: Advection in the coastal Hudson Bay Lowlands, Canada. II. Impact of atmospheric divergence on the surface energy balance. *Arct. Alp. Res.*, **23**, 338–348.
- Whiteman, C. D., 1982: Breakup at temperature inversions in deep mountain valleys: Part I. Observations. *J. Appl. Meteorol.*, **21**, 270–289.
- , X. Bian, and S. Zhong, 1999: Wintertime evolution of the temperature inversion in the Colorado Plateau basin. *J. Appl. Meteorol.*, **38**, 1103–1117.

[10]

Liston, G. E. and Mernild, S. H. 2012. Greenland freshwater runoff. Part I: A runoff routing model for glaciated and non-glaciated landscapes (HydroFlow).  
*Journal of Climate*, 25(17), 5997–6014.

Reprinted with permission from American Meteorological  
Society

# Greenland Freshwater Runoff. Part I: A Runoff Routing Model for Glaciated and Nonglaciated Landscapes (HydroFlow)

GLEN E. LISTON

*Cooperative Institute for Research in the Atmosphere, Colorado State University, Fort Collins, Colorado*

SEBASTIAN H. MERNILD

*Climate, Ice Sheet, Ocean, and Sea Ice Modeling Group, Los Alamos National Laboratory, Los Alamos, New Mexico*

(Manuscript received 12 October 2011, in final form 16 March 2012)

## ABSTRACT

A gridded linear-reservoir runoff routing model (HydroFlow) was developed to simulate the linkages between runoff production from land-based snowmelt and icemelt processes and the associated freshwater fluxes to downstream areas and surrounding oceans. HydroFlow was specifically designed to account for glacier, ice sheet, and snow-free and snow-covered land applications. Its performance was verified for a test area in southeast Greenland that contains the Mittivakkat Glacier, the local glacier in Greenland with the longest observed time series of mass-balance and ice-front fluctuations. The time evolution of spatially distributed gridcell runoffs required by HydroFlow were provided by the SnowModel snow-evolution modeling system, driven with observed atmospheric data, for the years 2003 through 2010. The spatial and seasonal variations in HydroFlow hydrographs show substantial correlations when compared with observed discharge coming from the Mittivakkat Glacier area and draining into the adjacent ocean. As part of its discharge simulations, HydroFlow creates a flow network that links the individual grid cells that make up the simulation domain. The collection of networks that drain to the ocean produced a range of runoff values that varied most strongly according to catchment size and percentage and elevational distribution of glacier cover within each individual catchment. For 2003–10, the average annual Mittivakkat Glacier region runoff period was  $200 \pm 20$  days, with a significant increase in annual runoff over the 8-yr study period, both in terms of the number of days (30 days) and in volume ( $54.9 \times 10^6 \text{ m}^3$ ).

## 1. Introduction

Recent evidence indicates the Arctic climate, cryosphere, and hydrological cycle are changing (Hinzman et al. 2005; Lemke et al. 2007; Ettema et al. 2009). Long-term temperature observations show warming trends of variable strength throughout the Arctic and Greenland (Serreze et al. 2000; Allison et al. 2009; Box et al. 2010), with an average increase almost twice the global average rate in the past 100 years (Solomon et al. 2007). Fluctuations in mass balance and freshwater runoff from the Greenland Ice Sheet (GrIS), and from glaciers and ice caps peripheral to the GrIS, follow these climate fluctuations (Hanna et al. 2008; Rignot et al. 2008; Ettema

et al. 2009). The associated glacial responses have been observed and marked by glaciers retreating and thinning along the periphery of the Ice Sheet (Krabill et al. 2000, 2004; Weidick and Bennike 2007). In general, approximately half of the mass loss from the GrIS originates from iceberg calving. These can be thought of as point sources unevenly distributed along the coastline. For example, the Helheim Glacier in southeast Greenland and Jakobshavn Glacier in west Greenland are two of the most prolific GrIS calving outlet glaciers (Rignot and Kanagaratnam 2006; Lemke et al. 2007). The other half of GrIS mass loss comes from surface melting and subsequent runoff into the ocean. These fluxes are nonuniformly distributed along the Greenland coast (Mernild and Liston 2012). For East Greenland, approximately 60% of the runoff originates from the GrIS, and approximately 40% from the land area and glaciers peripheral to the Ice Sheet (Mernild et al. 2008b). These peripheral ice masses are quite numerous in Greenland,

---

*Corresponding author address:* Dr. Glen E. Liston, Cooperative Institute for Research in the Atmosphere, Colorado State University, Fort Collins, CO 80523-1375.  
E-mail: glen.liston@colostate.edu



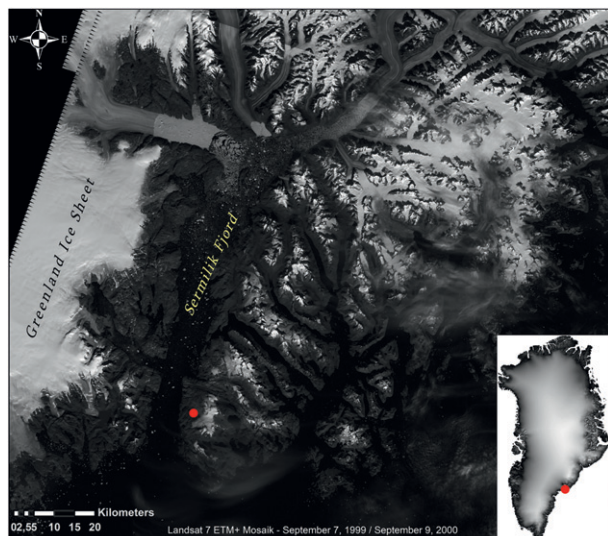


FIG. 1. Landsat 7 ETM+ mosaic showing examples of peripheral glaciers in East Greenland, from the Mittivakkat Glacier, Ammassalik Fjord region: acquired on 7 Sep 1999 and 15 Aug 2000. The Mittivakkat Glacier is located to the right and below the red dot. Landsat scene identifiers LE72310141999250AGS00 and LE72320142000228AGS00. The inset figure indicates the general location (red dot) in East Greenland.

with as many as 5297 glaciers existing in the southwest quarter between  $59^{\circ}$  and  $71^{\circ}\text{N}$  and  $43^{\circ}$  and  $53^{\circ}\text{W}$  (Weidick et al. 1992), and many more than that in northwestern, northern, and eastern Greenland (Fig. 1).

Greenland calving and runoff contributions to the surrounding oceans is likely playing a role in controlling ocean salinity, sea ice dynamics, global eustatic sea level rise, and thermohaline circulation (THC) in the Greenland–Iceland–Norwegian Seas (ACIA 2005; Su et al. 2006; Lemke et al. 2007; Allison et al. 2009). Model simulations of future climate scenarios suggest a warmer Greenland overall (Fettweis et al. 2008; Stendel et al. 2008; Mernild et al. 2010a, 2011b), and the associated accelerating runoff and calving could perturb the THC by reducing the ocean density contrasts that drive the circulation (Rahmstorf et al. 2005). Therefore, quantifying melt-related freshwater fluxes from Greenland snow, glacier, and ice sheet surfaces to the surrounding oceans is expected to play an important role in improving our climate system understanding and representations.

Presently, detailed information about the spatial and temporal runoff distribution to the oceans from nonglaciated and glaciated areas of Greenland are limited (Mernild and Liston 2012). Discharge at catchment outlets represents an integrated response of the upstream watershed to precipitation and other hydrometeorologic

processes like snow and glacier melt and to glaciohydrologic processes such as englacial bulk water storage and release. For glaciated areas, the physical mechanisms controlling water flow across the glacier and ice sheet surfaces must be accounted for if physically based simulations of the temporally evolving runoff distribution are to be realistic.

The purpose of this study was to develop *HydroFlow* and verify its performance for glacier, ice sheet, and snow-free and snow-covered land applications, with the ultimate goal of providing a tool that can simulate the linkages between runoff production from land-based liquid precipitation and snowmelt and icemelt processes, and the associated freshwater fluxes to surrounding oceans. To quantify spatial and temporal runoff distributions over a wide range of snow- and ice-covered and snow- and ice-free landscapes, the modeling system needs to account for individual drainage basins and streamflow networks within the entire domain of interest, and to track rain- and meltwater-related flow from snow-covered ice, snow-free ice, snow-covered land, and snow-free land, to the ocean.

After developing the *HydroFlow* gridded linear-reservoir runoff routing model for application in glaciated and nonglaciated areas, it was applied to a test area in southeast Greenland. This area contains the Mittivakkat Glacier, the local glacier in Greenland with the longest observed time series of mass-balance (since 1995) and ice-front fluctuations (since 1931) (Knudsen and Hasholt 2008; Mernild et al. 2011a). The spatial and seasonal variations in *HydroFlow* hydrographs were compared with observed discharge data coming from the Mittivakkat Glacier area and draining into the adjacent ocean.

To provide the time evolution of spatially distributed gridcell runoffs required by *HydroFlow*, a new, multi-layer version of *SnowModel* (Liston and Elder 2006a,b; Mernild et al. 2006b) was driven with observed atmospheric data. *SnowModel* is a physically based, spatially distributed, meteorological and snow and ice evolution modeling system that has been used, tested, and verified in domains around the world where snow and/or ice are dominant features of the environment. *SnowModel* simulates the snow and ice cover evolution in response to blowing and drifting snow processes, snowpack growth and densification, snowmelt and icemelt fluxes, variations in liquid and solid precipitation, and other features important for describing seasonal snow evolution in snow-covered, ice-covered, and ice-free landscapes. The *SnowModel*-produced gridcell runoffs were used as inputs to *HydroFlow*, which routed the runoffs through the watersheds of interest and into the surrounding ocean.



## 2. HydroFlow: A gridded linear-reservoir runoff routing model

To assist in verifying gridcell runoffs generated by SnowModel, and to transport water across land and ice to adjacent oceans, a linear-reservoir runoff routing scheme called HydroFlow was developed. Watershed discharge is an important integrator of the hydrologic cycle and is generally measured more accurately than the other moisture budget components. Observed discharge data represent a readily available and valuable contribution for verifying modeled balances between precipitation, snowmelt, icemelt, evaporation, sublimation, soil moisture changes, transpiration, and runoff. A key output of SnowModel (and virtually any land surface hydrology model) simulations is water available for runoff at each grid cell at each model time step. For the case of SnowModel, these are primarily associated with snowmelt and icemelt and liquid precipitation fluxes and moisture redistribution within the snow and ice cover. To relate these gridcell runoffs to watershed hydrographs, a linear-reservoir runoff routing model (HydroFlow) that routes SnowModel-computed grid-cell runoffs through the coincident runoff drainage networks is required. The HydroFlow hydrographs can then be compared with observed discharge values, thus providing a measure of model-simulated regional water balances over time scales ranging from individual storms and melt events to seasonal and annual cycles.

A fundamental premise of the HydroFlow linear-reservoir runoff routing model is that the catchment(s) of interest (i.e., the simulation domain) can be divided into a grid of rectangular model cells that cover the entire domain and are linked via a topographically controlled flow network. Each grid cell acts as a linear reservoir that transfers water from itself and the upslope cells to the downslope cell. HydroFlow assumes that there are two transfer components (or transfer functions) within each model grid cell: a slow-response flow and a fast-response flow. Each of these transfer functions have different time scales associated with them and represent the wide range of physical processes associated with the horizontal moisture transport through and across the landscape. The slow time scale accounts for the time it takes runoff at each individual grid cell, usually produced from liquid precipitation or snowmelt and/or icemelt, to enter the routing network. The moisture is then transported through the flow network at a rate associated with the fast time scale. Associated with these slow and fast time scales are different water transport mechanisms: the slow time scale generally accounts for transport within the snow and ice matrices (for the case of glaciers and ice

sheets) and soil (for the case of snow-covered and snow-free land), and the fast time scale generally represents some kind of channel flow, such as that represented by supraglacial, englacial, or subglacial flow (for the case of glaciers and ice sheets) and river and stream channels (for the case of snow-covered and snow-free land).

Applying conservation of mass principles to a routing model grid box yields the following continuity equation:

$$\frac{dS}{dt} = \frac{dS_f}{dt} + \frac{dS_s}{dt} + \sigma, \quad (1)$$

where  $S$  is the total storage,  $S_f$  is the fast time-scale storage,  $S_s$  is the slow time-scale storage,  $t$  is time, and  $\sigma$  represents storage components assumed negligible in this application. The contributions to the fast and slow storage terms are given by

$$\frac{dS_f}{dt} = Q_{fi} + Q_s - Q_f \quad (2)$$

and

$$\frac{dS_s}{dt} = Q_m - Q_s, \quad (3)$$

where  $Q_f$  is the fast-response flow,  $Q_s$  is the slow-response flow,  $Q_m$  is the melt-generated runoff at an individual model grid cell (e.g., the slow time scale, gridbox runoff produced by each SnowModel grid cell; this could also include rain), and  $Q_{fi}$  is the fast time-scale inflow from any adjacent grid cells.

To solve these equations the relationship between storage and outflow must be defined. While nonlinear relationships between storage and flow have been developed (Singh 1988), their use is not justified for the simple approach considered in this model. This model does not consider channel streamflow routing, instead it assumes each grid cell is a linear storage reservoir (i.e., storage is proportional to outflow),

$$S(t) = k(t)Q(t), \quad (4)$$

where  $k$  has dimensions of time equal to the typical residence or transient time of a fluid element passing through the reservoir or model grid cell. The  $k$  parameter is a function of such things as travel distance (which is a function of model grid size), surface slope, surface roughness, characteristics of the material the fluid is flowing through and over, and stream length, width, and depth. The time dependence of  $k$  in this formulation allows for the evolution of the snow-ice matrix within the simulation domain; on a glacier or ice sheet, for

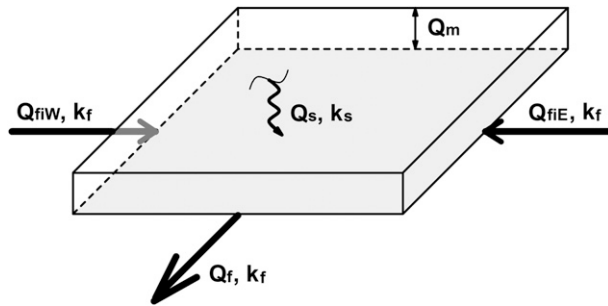


FIG. 2. Schematic showing the local, SnowModel-generated layer of water available for runoff in a grid cell ( $Q_m$ ), the slow transport of water within that grid cell to the routing network ( $Q_s$ ), inflow from nearby grid cells ( $Q_{fi}$ ), and the slow and fast transformation functions ( $k_s$  and  $k_f$ ). The magnitudes of  $Q_s$  and  $Q_f$  are provided by Eqs. (11) and (10), respectively.

example, as last winter's snow cover melts away to reveal the ice below, the meltwater source and residence-time coefficients change. After substitution, the original set of equations becomes

$$\frac{d(k_f Q_f)}{dt} = Q_{fi} + Q_s - Q_f \quad (5)$$

and

$$\frac{d(k_s Q_s)}{dt} = Q_m - Q_s, \quad (6)$$

where  $k_f$  and  $k_s$  are the fast-response and slow-response transfer functions, respectively. This set of equations, when applied to each grid box of the runoff routing model, is connected via the flow network through the presence of the  $Q_{fi}$  term. To illustrate the two-dimensional character of the contributing flow network,  $Q_{fi}$  can be expanded to yield

$$Q_{fi} = Q_{fiN} + Q_{fiNE} + Q_{fiE} + Q_{fiSE} + Q_{fiS} \\ + Q_{fiSW} + Q_{fiW} + Q_{fiNW}, \quad (7)$$

where the subscripts N, NE, E, SE, S, SW, W, and NW indicate the compass direction of the adjacent connecting grid box. One of the right-hand-side terms will be zero (the one corresponding to the outflow boundary), and possibly all eight will be zero (for the case of a grid box located at the head of a watershed), depending on the gridded representation of the flow network. Figure 2 provides a schematic illustrating the relationship between the HydroFlow grid network connectivity, gridcell water production, slow and fast transfer functions, inflow from upslope grid boxes, and gridcell outflow.

Equations (5)–(7) describe a coupled system of ordinary differential equations whose solution yields a discharge hydrograph for each grid cell (e.g., Liston et al. 1994). These model equations typically involve steady-state terms that do not grow significantly with time, together with rapidly decaying transient terms [depending on the magnitude of  $k(t)$ ]. The steady-state terms typically result from the slow time-scale flow components, while the transient terms are due to the fast time-scale flow. The presence of significantly different time coefficients in the system of equations and, for the case where the total integration time is much greater than the model time coefficients, leads to a class of problems called “stiff systems” of differential equations. In such problems it is critical that the numerical solution be able to resolve the steady-state portion of the system without becoming dominated by errors encountered in resolving the transient part. While this problem can be overcome by a reduction of the time step, frequently the time step must be made so small that round-off errors may dominate the solution and the computational expense becomes unreasonable. Further discussion of stiff differential equation characteristics was provided by Shampine and Gear (1979) and Byrne and Hindmarsh (1987), and an ordinary differential equation solution scheme capable of handling the “stiffness” issue was presented by Brown et al. (1989).

An alternative solution to Eqs. (5)–(7) can be found by recognizing that a more general form of these equations,

$$\frac{d(kQ)}{dt} = I - Q, \quad (8)$$

has the solution

$$Q_t = Q_{t-1} \exp\left(-\frac{\Delta t}{k}\right) + I_t \left[1 - \exp\left(-\frac{\Delta t}{k}\right)\right], \quad (9)$$

where  $I$  represents the inflow contributions from gridcell runoff, the flow network, and/or slow storage flow (Nielsen and Hansen 1973),  $\Delta t$  is the model time increment, and  $t$  and  $t - 1$  are the current and previous time steps, respectively. Equation (9) can be solved for any grid cell whose up-network inputs are known. Given knowledge of which grid cells flow into down-network grid cells, and first solving the grid cells at the head of a watershed (the grid cells that make up the watershed boundary) where there are no inflows, and continuing to solve grid cells that are fed with cells that have already have a solution, the entire solution matrix can be solved at any given time step.

In the context of Eqs. (5) and (6), Eq. (9) becomes

$$Q_{f,t} = Q_{f,t-1} \exp\left(-\frac{\Delta t}{k_f}\right) + (Q_{fi,t} + Q_{s,t}) \left[1 - \exp\left(-\frac{\Delta t}{k_f}\right)\right] \quad (10)$$

and

$$Q_{s,t} = Q_{s,t-1} \exp\left(-\frac{\Delta t}{k_s}\right) + Q_{m,t} \left[1 - \exp\left(-\frac{\Delta t}{k_s}\right)\right], \quad (11)$$

respectively, where Eq. (11) is solved before Eq. (10). The solution of Eqs. (10) and (11) also require initial flow conditions. In this Greenland snowmelt and icemelt application, these are first assumed to be zero at the end of winter, then full annual integrations are iteratively performed and the initial conditions adjusted until the end-of-integration-year flow closely matches the prescribed initial conditions.

To solve the gridded linear-reservoir runoff routing system given by Eqs. (7), (10), and (11), grid-specific, time evolving, residence time coefficients,  $k$ , must also be defined. These residence times for land, glaciers, and ice sheets are a function of many things, including surface slope; density of surface depression storage (e.g., supraglacial lakes); distance traveled; deviations from a straight path; snow, ice, and soil porosity; snow temperature (cold content); density of supraglacial and englacial crevasses and moulins; seasonal changes in supraglacial, englacial, subglacial channel dimensions and roughness; the hydrostatic water pressure; channel dimensions and roughness in proglacial rivers; the occurrence of snow dams during breakup season; and soils and land-cover characteristics (Hock and Jansson 2005). In its most basic form, the residence time coefficient,  $k$ , can be defined as

$$k = D/V, \quad (12)$$

where  $D$  is distance or average length dimension of the grid cells, and  $V$  is velocity.

In the Greenland snow, ice, and land system there are four dominant surfaces where runoff occurs: snow-covered ice, snow-free ice, snow-covered land, and snow-free land. For each of these surfaces there are both slow and fast residence-time coefficients or velocities. For the model simulations presented herein, the slow velocities,  $V_s$ , were defined to be 0.12, 0.20, 0.10, and 0.08 m s<sup>-1</sup>, for snow-covered ice, snow-free ice, snow-covered land,

and snow-free land, respectively, based on Mittivakkat Glacier field observations (Mernild 2006; Mernild et al. 2006b). Observed snow-free land values are greater than those typically found in porous media flow (Todd 1980), presumably because of the predominance of bedrock and large gravels in this area (Mernild et al. 2006b).

To define the fast velocities,  $V_f$ , the slow velocities were modified according to the formula,

$$V_f = \alpha V_s \Gamma, \quad (13)$$

where  $\alpha$  is a scaling parameter that accounts for all factors influencing flow speed that have not been directly considered in this formulation (e.g., snow and ice porosity, channel flow), and  $\Gamma$  is surface slope. The surface slope was scaled such that it produced a correction of 0.4 for a slope of 5°, a correction of 1.0 for a slope of 15° (Mernild et al. 2006a), and a correction of 2.4 for a slope of 45°. In practice,  $\alpha$  was an adjustable parameter determined by the value that yielded a best fit to available discharge data. Because the snow distribution over ice and land varies in time and space owing to accumulation and ablation processes, the velocities and associated time coefficients also have a spatial and temporal evolution.

Note that, because of the  $\exp(-\Delta t/k)$  terms in Eqs. (10) and (11), the relative magnitudes of  $\Delta t$  and  $k$  strongly control the shape of the simulated hydrographs ( $\Delta t$  and  $k$  have the same time units). In practice, a  $\Delta t/k$  ratio  $\gg 1$  produces virtually no time delay in the flow (the transport is instantaneous and each grid cell accumulates all gridcell runoff and flow from all up-network grid cells at each time step), and if this ratio is  $\ll 1$ , then the flow never changes (it always equals the initial conditions). Intermediate ratio values produce an attenuated representation of all runoff and flow from up-network. Therefore, the time step used in the SnowModel integration (i.e., the local runoff time step) should be roughly compatible with, or less than, the time scale of the flow and transport processes represented by the applied residence-time scale.

### 3. Model simulations

#### a. SnowModel

Running the HydroFlow runoff routing model requires gridded runoffs over the domain of interest. Because of the length scale dependence in Eq. (12), the model automatically accounts for residence-time adjustments associated with differences in grid size. These gridded runoffs were provided by SnowModel (Liston and Elder 2006a), a spatially distributed snow-evolution modeling system designed for application in all landscapes, climates, and conditions where snow and ice

occurs. It is an aggregation of four submodels: EnBal (Liston 1995; Liston et al. 1999) calculates surface energy exchanges; SnowPack (Liston and Hall 1995) simulates snow depth and water-equivalent evolution; SnowTran-3D (Liston and Sturm 1998; Liston et al. 2007) accounts for snow redistribution by wind; and SnowAssim (Liston and Hiemstra 2008) is available to assimilate field and remote sensing datasets (not used in this study).

SnowModel is designed to run on grid increments of 1 m to 200 m and temporal increments of 10 min to 1 day. It can be applied using much larger grid increments (up to 10s of km) if the inherent loss in high-resolution (subgrid) information (Liston 2004; Liston and Hiemstra 2011a,b; Mernild and Liston 2012) is acceptable. In this application, processes simulated by SnowModel include accumulation from snow precipitation; blowing-snow redistribution and sublimation; snow-density evolution; and snowpack ripening and melt. SnowModel incorporates first-order physics required to simulate snow evolution within each of the global snow classes defined by Sturm et al. (1995) and G. E. Liston and M. Sturm (2012, unpublished manuscript). Required SnowModel inputs include time series fields of precipitation, wind speed and direction, air temperature, and relative humidity obtained from meteorological stations and/or an atmospheric model located within or near the simulation domain; and spatially distributed, time-invariant fields of topography and land-cover type.

SnowModel was originally developed for glacier- and ice-free landscapes. For glacier and GrIS surface mass-balance studies, SnowModel was modified to simulate glacier/ice melt after the winter snow accumulation had ablated (Mernild et al. 2006b), and routines were added to account for the time-evolving, spatial variations in snow albedo (Mernild et al. 2010c). In addition, in the application described herein, the role of surface meltwater percolating into, and refreezing within, snow and firn layers, makes an important contribution to the evolution of snow and ice densities and moisture available for runoff. Accounting for this requires a multilayer snow and ice model that simulates refreezing of meltwater as a function of snow and ice permeability and cold content (the temperature below freezing). To account for this, a multilayer snowpack model (SnowPack-ML) was implemented and coupled with the snow and ice temperature model of Liston et al. (1999) (Fig. 3).

#### b. MicroMet

Meteorological forcings required by SnowModel were provided by MicroMet (Liston and Elder 2006b), a quasi-physically-based, high-resolution (e.g., 1-m to 10-km horizontal grid increment), meteorological distribution model. MicroMet is a data assimilation

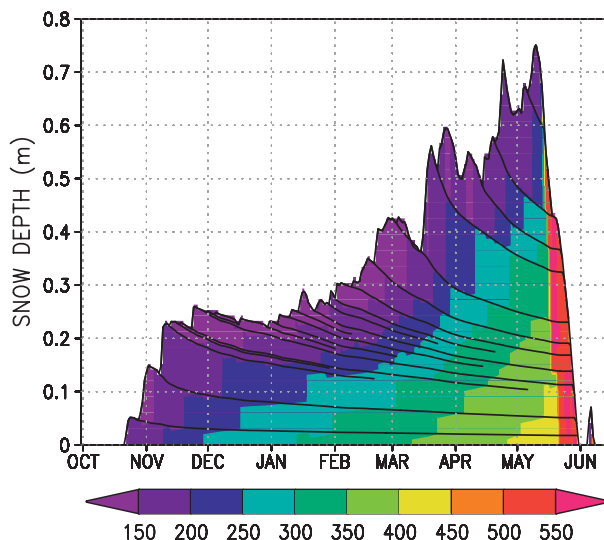


FIG. 3. Example SnowModel multilayer snowpack (SnowPack-ML) layers and snow density ( $\text{kg m}^{-3}$ ) evolution.

and interpolation model that utilizes meteorological station datasets and/or gridded atmospheric model or analyses datasets. MicroMet minimally requires screen-height air temperature, relative humidity, wind speed and direction, and precipitation data. The model uses known relationships between meteorological variables and the surrounding landscape (primarily topography) to distribute those variables over any given landscape in physically plausible and computationally efficient ways. At each time step, MicroMet calculates and distributes air temperature, relative humidity, wind speed, wind direction, incoming solar radiation, incoming longwave radiation, surface pressure, and precipitation, and makes them accessible to SnowModel.

MicroMet and SnowModel have been used to distribute observed and modeled meteorological variables and evolve snow distributions over complex terrain in Colorado, Wyoming, Idaho, Oregon, Alaska, Arctic Canada, Siberia, Japan, Tibet, Chile, Germany, Austria, Norway, Greenland, and Antarctica as part of a wide variety of terrestrial modeling studies (e.g., Liston and Sturm 1998, 2002; Greene et al. 1999; Liston et al. 2000, 2002, 2007, 2008; Hiemstra et al. 2002, 2006; Prasad et al. 2001; Hasholt et al. 2003; Bruland et al. 2004; Liston and Winther 2005; Mernild et al. 2006b, 2008b, 2010a, 2011b; Liston and Hiemstra 2008, 2011a,b; Mernild and Liston 2010, 2012).

#### c. Simulation domain, model configuration, and meteorological forcing

The Mittivakkat Glacier ( $31 \text{ km}^2$ ;  $65^{\circ}42'N$ ,  $37^{\circ}48'W$ ) is a local glacier (peripheral to the GrIS), located on



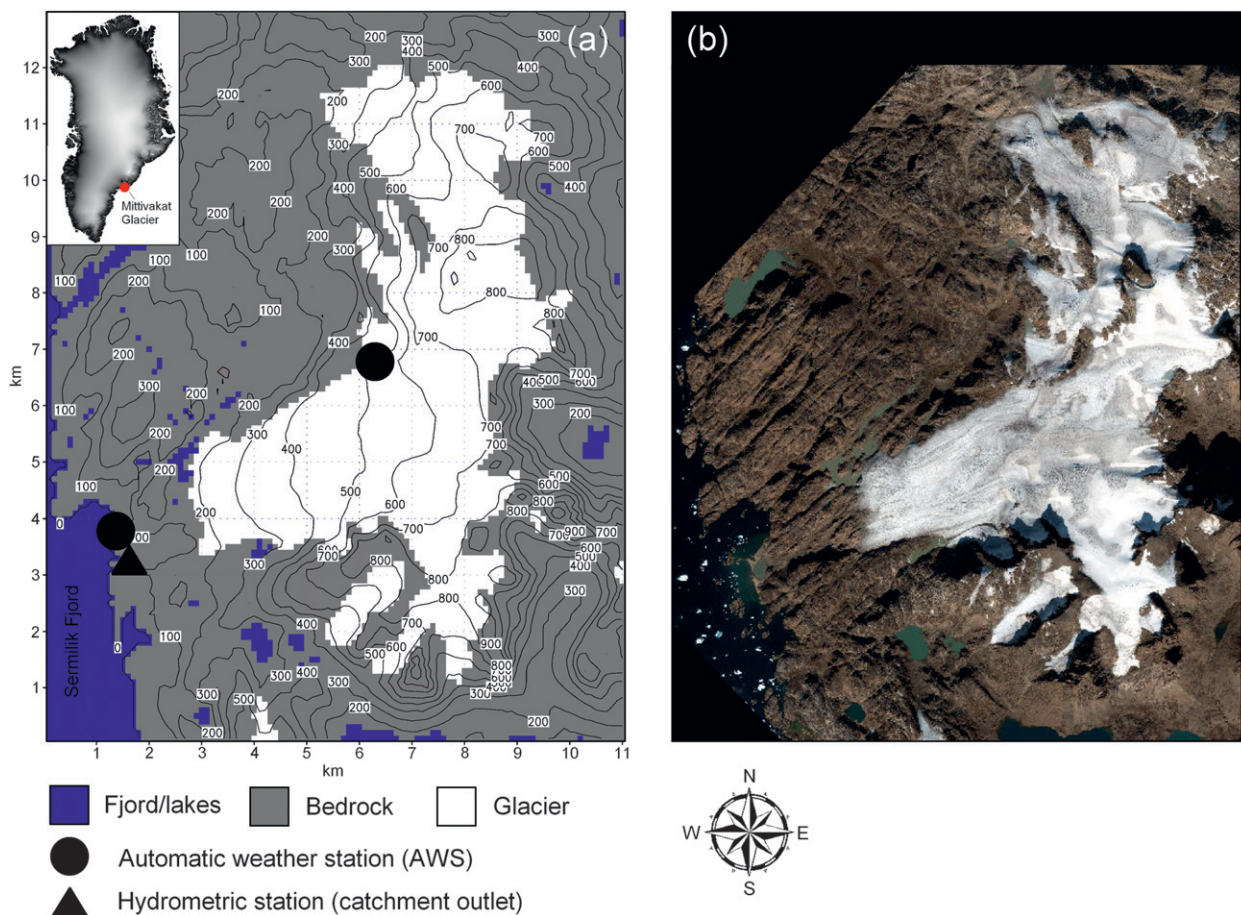


FIG. 4. (a) The Mittivakkat Glacier simulation domain, in southeast Greenland, with topography (100-m contour interval) and land cover characteristics. Also shown are the two automatic weather stations, Station Nunatak (515 m MSL) and Station Coast (25 m MSL), and the hydrometric station at the A4 catchment outlet (for locations of the different catchment outlets see Fig. 6). The inset figure indicates the general location of the Mittivakkat Glacier region (red dot) in southeast Greenland. The domain coordinates can be converted to UTM by adding 548 km to the west–east origin (easting) and 7281 km to the south–north origin (northing) and converting to meters. (b) September 2005 QuickBird image of the glacier and surrounding landscape.

Ammassalik Island in southeast Greenland. The model simulation domain (Fig. 4) includes the glacier and the surrounding area and ranges in elevation from sea level to 973 m MSL. The entire Mittivakkat Glacier complex (ranging from approximately 160 to 930 m MSL) has several river and stream outlets that drain through proglacier valleys into Sermilik Fjord.

Starting in 1931, Mittivakkat Glacier has been observed at regular intervals using aerial photography, and since that time the glacier terminus has retreated approximately 1300 m. Mittivakkat Glacier is the only local glacier in Greenland for which there exist long-term observations of surface mass balance (WGMS 2009). In 1995 an annual surface-mass-balance program for the glacier was initiated (Knudsen and Hasholt 2002). In 13 of the last 15 years, the Mittivakkat Glacier had a negative surface mass balance, with an average of

$-0.87 \pm 0.66$  m water equivalent (w.eq.)  $\text{yr}^{-1}$ , and a cumulative net mass balance of  $-13.0 \pm 1.9$  m w.eq. (Mernild et al. 2011a). This corresponds to a 15-yr 11% decrease of the total ice volume determined in 1994 by Knudsen and Hasholt (1999). For the last eight years (2002/03 through 2009/10; corresponding to the study period described herein), the average mass balance was  $-1.05 \pm 0.81$  m w.eq.  $\text{yr}^{-1}$ , with a winter balance of  $1.03 \pm 0.14$  m w.eq.  $\text{yr}^{-1}$ , and a summer balance of  $-2.01 \pm 0.63$  m w.eq.  $\text{yr}^{-1}$  (Table 1). At present, Mittivakkat Glacier is significantly out of equilibrium with present-day climate, and will likely lose approximately 70% of its current area and approximately 80% of its volume, even in the absence of further climate changes (Mernild et al. 2011a).

The mean annual air temperature for the Mittivakkat Glacier region (1994–2006) was  $-1.7^{\circ}\text{C}$ . Mean annual



TABLE 1. Mittivakkat Glacier surface mass balance observations for the 8-year period 2002/03 through 2009/10 [individual mass balance data for the entire available 15-year observation period can be found in Knudsen and Hasholt (2008) and Mernild et al. (2011a)].

	2002/03	2003/04	2004/05	2005/06	2006/07	2007/08	2008/09	2009/10	Average $\pm$ std dev
Observed Mittivakkat Glacier summer mass balance, June through August (m w.eq.)	—	—	0.92	0.98	—	1.18	—	—	1.03 $\pm$ 0.14*
Observed Mittivakkat Glacier winter mass balance, September through May (m w.eq.)	—	—	-2.74	-1.59	—	-1.70	—	—	-2.01 $\pm$ 0.63*
Observed Mittivakkat Glacier net mass balance, September through August (m w.eq.)	0.34	-1.07	-1.82	-0.58	-1.58	-0.52	-1.01	-2.16	-1.05 $\pm$ 0.81

\* Calculated winter and summer average mass balances and standard deviation were based on values from 2004/05, 2005/06, and 2007/2008.

relative humidity and wind speed were 83% and  $3.9 \text{ m s}^{-1}$ . The corrected (following Allerup et al. 1998, 2000) mean total annual precipitation (TAP) was  $1550 \text{ mm w.eq. yr}^{-1}$  (Mernild et al. 2008a).

SnowModel was used to simulate gridcell snow evolution, surface energy fluxes, snowmelt and icemelt, and runoff, for the 8-yr period 2002/03 through 2009/10. These runoffs were then used to drive HydroFlow to simulate runoff hydrographs spanning the 8-yr simulation period for each grid cell within the simulation domain. The simulation covered an 11-km by 13-km ( $143 \text{ km}^2$ ) domain centered on the Mittivakkat Glacier, including its coastal zone along Sermilik Fjord (Fig. 4). The model simulation was performed using a 100-m horizontal grid increment (14 300 grid cells) and 1-day time step. Topographic data used in the model simulation were obtained from a digital elevation model (DEM) based on a 1:100000-scale map with a 25-m contour interval (Mernild et al. 2006b). Each grid cell was classified into SnowModel land cover classes (Liston and Elder 2006a) as bedrock, fjord/lakes, or glacier using a QuickBird satellite image acquired September 2005 (Fig. 4).

To solve the HydroFlow coupled system of equations, watershed flow-accumulation networks must be defined over the domain of interest. In this Greenland application, every nonocean grid cell within the simulation domain is part of a defined watershed, and each watershed has a single flow outlet into either the simulation domain boundary (for the case where the boundary is a land grid cell) or the ocean (Fig. 5). The Terrain Analysis Programs for the Environmental Sciences-Grid Version (TAPES-G) (Gallant and Wilson 1996), in conjunction with the 100-m grid increment simulation domain DEM, was used to define the individual watersheds and the associated grid connectivity within each watershed (Fig. 6). The TAPES-G implementation allows the user to define the domain area and grid size.

Atmospheric data to drive the model simulations were provided by two automatic weather stations within the domain: Station Nunatak (515 m MSL; representative of the glacier) and Station Coast (25 m MSL; representative of the coastal and valley areas). At these stations wind speed, wind direction, air temperature, and relative humidity were recorded at 2-m levels every hour, and resampled to mean daily values. Liquid precipitation (rain) was measured at both stations 0.45 m above the ground; a height equal to the local roughness elements (i.e., rocks) (for additional information about

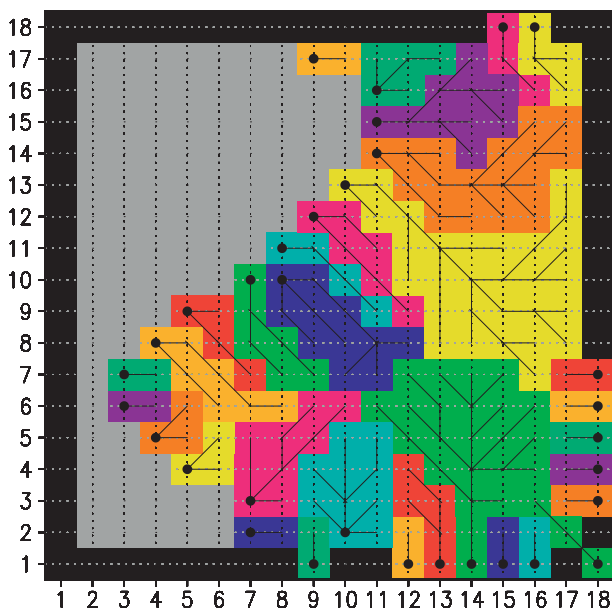


FIG. 5. Example flow network calculated from hypothetical gridded topography and ocean-mask datasets to illustrate the HydroFlow network configuration over the simulation domain. Computational domain boundary cells are black, gray cells are ocean. Other colors represent individual drainage basins, each of which drains either into the domain boundary or the ocean. Basin outlet points are indicated by black dots and the drainage network by black lines.

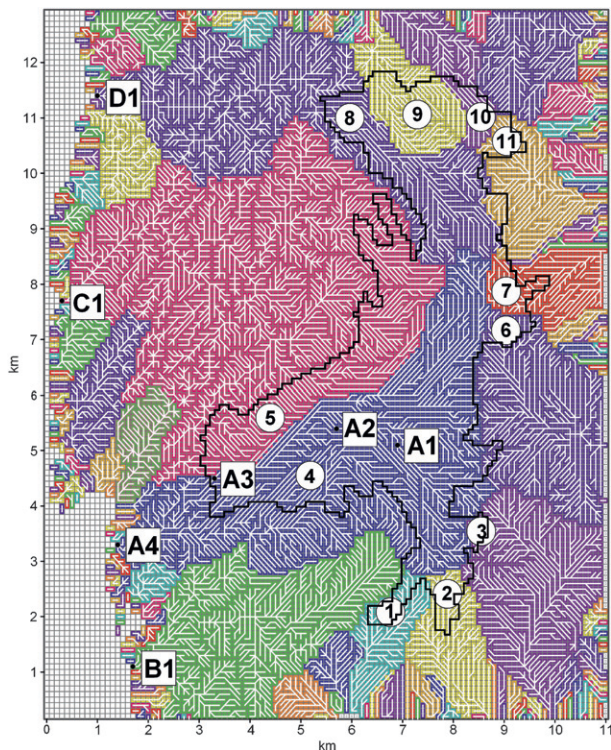


FIG. 6. Mittivakkat Glacier complex (represented by the bold black line) and simulation domain including individual glacier basins (Area 1 to 11) (represented by different colors), stream/river flow network (represented by white lines), and locations B1, A4, C1, D1, A3, A2, and A1 for the simulated hydrographs.

the meteorological stations, see Mernild et al. 2008a). Solid precipitation (e.g., snowfall) was calculated from snow depth sounder observations, assumed to have an accuracy of within  $\sim 10\%$ – $15\%$ , adjusted according to routines described by Mernild et al. (2006b) and Liston and Hiemstra (2008). SnowModel has been applied and tested within the Mittivakkat Glacier region, and substantial correlations have been found when model outputs were compared with independent in situ observations of meteorological variables, snow depths and distributions, and glacier mass balances (Hasholt et al. 2003; Mernild et al. 2006b, 2010b; Mernild and Liston 2010). In light of the considerable MicroMet and SnowModel modeling work already done in the Mittivakkat Glacier area, we concluded that the combination of MicroMet and SnowModel simulated gridcell runoffs were of sufficient quality, without any additional adjustments, to drive the HydroFlow simulations.

#### 4. Results

The Mittivakkat Glacier complex and its surrounding landscape, including the simulated individual drainage

catchments and flow network, are illustrated in Fig. 6. HydroFlow (using TAPES-G) divided the glacier into 11 individual drainage basins (Fig. 6 and Table 2), and the entire simulation domain was divided into approximately 300 individual subcatchments peripheral to the glacier, where approximately 150 of these subcatchments drain directly into Sermilik Fjord. The eleven drainage basins covering Mittivakkat Glacier ranged in size from  $0.4 \text{ km}^2$  (Area 3, covering 1% of the glacier area) to  $13.6 \text{ km}^2$  (Area 4, covering 44% of the glacier area), and the three largest basins (Areas 4, 5, and 8) drained approximately 80% of the glacier area into Sermilik Fjord through the watershed outlets A4, C1, and D1 (Table 2, Figs. 6 and 7).

The size of the HydroFlow-estimated Mittivakkat Glacier watershed was compared with maps and field observations (Mernild and Hasholt 2006; Mernild et al. 2006a; Knudsen and Hasholt 2008). The drainage area upstream of location A4, for example, was previously estimated to be  $18.4 \text{ km}^2$  with 78% glacier cover ( $14.3 \text{ km}^2$ ). In HydroFlow, the area upstream of A4 was  $19.0 \text{ km}^2$  with 72% glacier cover ( $13.6 \text{ km}^2$ ). Compared to previous observational studies, HydroFlow reproduced the location of the watershed divides reasonably well and, based on the 100-m grid increment DEM, the size of the defined drainage area is assumed to be within an error of a few percent. Even though HydroFlow reproduced the individual catchments, we are aware, based on tracer observations, that glacier subsurface (englacial and subglacial) water flow between neighboring glacier basins (e.g., to/from Areas 4 and 5) occurs due to englacial fractures such as crevasses and moulins (Mernild 2006, Mernild et al. 2006a). The subsurface exchange between neighboring basins is expected to have only a minor influence on the outlet hydrographs (Mernild et al. 2010b).

For the watersheds upstream of locations A4, C1, and D1 (Fig. 6) the percentage of simulated drainage area covered by Mittivakkat Glacier ranged from 21% ( $6.0 \text{ km}^2$ , Area 5) to 72% ( $13.6 \text{ km}^2$ , Area 4) (Table 2). In this region, watershed runoff is largely an integrated response of snow and glacier melt and liquid precipitation. Previous studies (e.g., Hasholt and Mernild 2008) have shown that it is appropriate to assume an insignificant contribution from subsurface flow occurs in the glacier-free areas of this bedrock dominated landscape (Fig. 7). Therefore, runoff from different catchments was strongly influenced by the fraction of glacier coverage where high runoff volumes were associated with glacier cover at low elevations. In Fig. 8 for example, the 2003 biweekly spatial distribution of seasonal cumulative runoff, produced by SnowModel at each grid cell, for Mittivakkat Glacier and the bedrock

TABLE 2. HydroFlow simulated Mittivakkat Glacier basins and catchment areas for the simulation domain (see Fig. 6 for the location of the catchments and catchment outlets). Average specific runoff is shown for the outlets B1, A4, C1, and D1 (2002/03–2009/10).

	Mittivakkat Glacier basin											Total
	1	2	3	4	5	6	7	8	9	10	11	
Mittivakkat Glacier basin (km <sup>2</sup> ) and percentage of total glacier area (%)	0.5 (2)	0.6 (2)	0.4 (1)	13.6 (44)	6.0 (19)	0.5 (2)	0.9 (3)	4.4 (14)	2.2 (7)	0.7 (2)	1.2 (4)	31.0 (100)
Catchment area at the outlet to Sermilik Fjord (km <sup>2</sup> ), and percentage of area covered by glacier (%)	—	—	—	19.0 (72)	28.4 (21)	—	—	13.7 (32)	—	—	—	—
Outlet corresponding to the upstream Mittivakkat Glacier basin	—	—	—	A4	C1	—	—	D1	—	—	—	—
	Catchment outlet											
	B1			A4			C1			D1		
Specific runoff (L s <sup>-1</sup> km <sup>-2</sup> )	47*			68			43			52		

\* The drainage area upstream for outlet location B1 is 9.8 km<sup>2</sup>.

peripheral to the glacier, is illustrated for 1 June through 15 August (for 31 August 2003, see Mernild et al. 2008c). At the low lying glacier margins more than 1600 mm w.eq. runoff was simulated, and runoff from snow cover (and some rain) on bedrock was approximately 900 mm w.eq.

As part of the HydroFlow routing of these (Fig. 8) gridcell runoffs, it assumes there are two runoff components within each HydroFlow grid cell: a within-gridcell slow-response runoff and a fast-response runoff associated with the overland flow network. Each of these is associated with a residence or transient time ( $k$ ) describing how long it takes a fluid element to pass through a model grid cell. To solve the system of equations, grid-specific, time evolving, residence time coefficients,  $k$ , were defined using Mittivakkat Glacier field measurements (Mernild 2006; Mernild et al. 2006a). These field observations included tracer measurements for snow-covered ice, snow-free ice, snow-covered land, and snow-free land at the beginning and the end of the ablation period (see the  $k$  values listed in section 2). Figure 9 provides the 2003 time evolution of fast-time-scale  $k$  values over the simulation domain. Shown are the changes in water residence times resulting from changes in snow- and ice-covered fractions for glacier and glacier-free areas of the domain. As the snow on land melts free, the residence times increase in response to the water flowing through the tortuous rock-debris flow paths (e.g., Figure 7), and as the glacier surface becomes snow-free, the residence times are reduced.

The seasonal variability in HydroFlow simulated runoff at outlet A4 was compared, in detail, with

observed runoff time series for the two years when we have the most observed runoff data: 2003 (the year with the second lowest cumulative runoff of  $25.1 \times 10^6$  m<sup>3</sup>) and 2010 (the year with the highest cumulative runoff of  $52.8 \times 10^6$  m<sup>3</sup>) (Figs. 10a and 10b), yielding  $r^2$  (square of the linear correlation coefficient) values of 0.77 and 0.63, respectively, and Nash–Sutcliffe coefficient (NSC) (Nash and Sutcliffe 1970) values of 0.61 and 0.60, respectively. If the NSC is 1, then the model is a perfect fit to the observations. If NSC is less than 1, decreasing values represent a decline in goodness of fit, where 0 and negative values represent major deviations between the modeled and observed data. Note that these goodness-of-fit measures could be improved with additional calibration of the fast-response and slow-response transfer functions; something we did not attempt. The other years with runoff observations yielded  $r^2$  values of 0.59 for 2004 and 0.62 for 2009.

In general, the simulated runoff variations and peaks reproduced available discharge observations ( $r^2 = 0.77$  and 0.63), both in time and volume. For 2003 and 2010 the difference between simulated and observed runoff was  $\sim 12\,000$  m<sup>3</sup> (analog to a mean discharge difference of  $0.14$  m<sup>3</sup> s<sup>-1</sup>) and  $\sim 2200$  m<sup>3</sup> ( $0.03$  m<sup>3</sup> s<sup>-1</sup>), respectively, where positive numbers mean the model is overestimating observed control values, and vice versa. Further, comparison of simulated and observed peak runoff values indicate a maximum difference of  $\sim 267\,000$  m<sup>3</sup> (analog to a maximum discharge difference of  $3.10$  m<sup>3</sup> s<sup>-1</sup>) for 2003 and  $\sim 453\,000$  m<sup>3</sup> ( $5.25$  m<sup>3</sup> s<sup>-1</sup>) for 2010 (Figs. 10a and 10b). Overall, for the two analyzed years HydroFlow is able to reproduce mean and peak control values reasonably well.



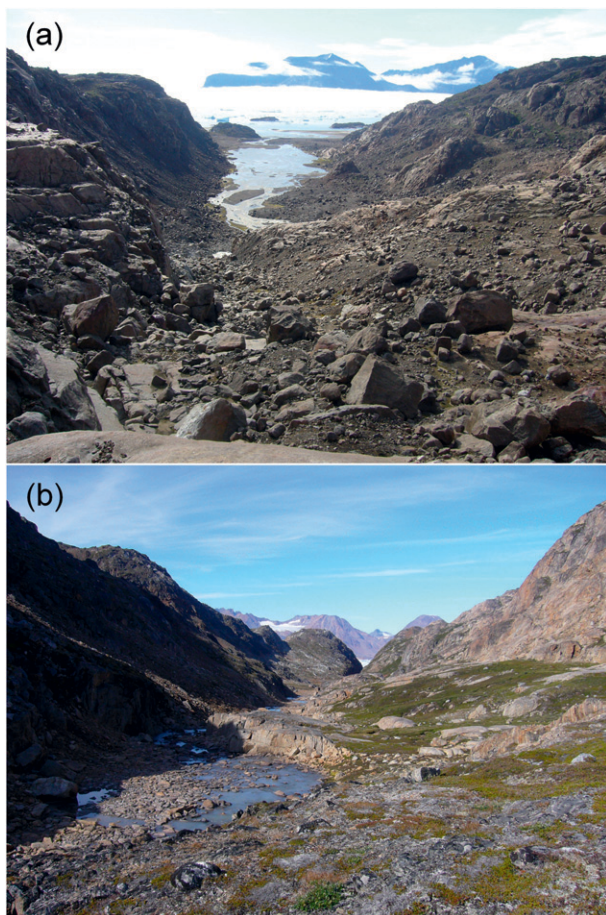


FIG. 7. Catchment outlets to Sermilik Fjord: (a) A4 and (b) D1. The photos were taken looking west toward Sermilik Fjord, and the distances from the foregrounds to the coast is approximately 2 km (photos: S. H. Mernild, August 2010).

Figures 10c and 10d display the within-catchment runoff variability by plotting the hydrographs at locations A1 through A4 for 2003 and 2010. Consistent with the model formulation, the hydrographs for both 2003 and 2010 increased in volume and runoff period downstream as the flow network progressed downbasin from point A1 through A4. This occurs in response to both decreasing elevation and increasing drainage area. Further, seasonal runoff variations were similar for all four locations, with the most pronounced being at the outlet (A4) and the least pronounced being upstream (A1).

The simulated runoff values at the B1, A4, C1, and D1 catchment outlets (Figs. 10e and 10f), display the spatial variation in coastal runoff contributions from these primary catchments that drain into Sermilik Fjord. At regional scales the spatial variation in runoff was closely associated with variations in glacier cover, size of the drainage area, and travel distance within each

catchment (Figs. 10e and 10f). The watersheds upstream of outlets A4 and C1 produced the greatest runoff contribution to Sermilik Fjord.

The 2003–10 mean cumulative annual discharge ( $\text{m}^3$ ) into Sermilik Fjord from catchment outlets B1, A4, C1, and D1 are illustrated in Fig. 11a. Figure 11b displays the mean cumulative annual discharge ( $\text{m}^3$ ) from all of the catchment outlets along the eastern coast of the simulation domain (they all feed into Sermilik Fjord) for 2003 and 2010. The dominance of the B1, A4, C1, and D1 outlets are clear in Fig. 11b. Also shown is the percentage of total annual discharge represented by the B1, A4, C1, and D1 outlets. In 2003 and 2010, 84% and 90%, respectively, of the eastern coastal discharge came from outlets B1, A4, C1, and D1. Averaged over the 2003–10 simulation period, outlets B1, A4, C1, and D1 contributed approximately 90% of the annual discharge ( $128.9 \pm 34.1 \times 10^6 \text{ m}^3 \text{ yr}^{-1}$  with a standard deviation of  $\pm 34.1 \times 10^6 \text{ m}^3 \text{ yr}^{-1}$ ) to Sermilik Fjord. Taken individually, the average contributions from C1 ( $38.5 \pm 22.2 \times 10^6 \text{ m}^3 \text{ yr}^{-1}$ ) and A4 ( $40.9 \pm 13.7 \times 10^6 \text{ m}^3 \text{ yr}^{-1}$ ) were each approximately 30% of the total, and contributions from B1 ( $14.7 \pm 5.8 \times 10^6 \text{ m}^3 \text{ yr}^{-1}$ ) and D1 ( $22.4 \pm 8.0 \times 10^6 \text{ m}^3 \text{ yr}^{-1}$ ) were each approximately 15% of the total. For the watersheds without glacier cover (these comprised approximately 90% of the catchments) the cumulative annual discharge to the ocean was relatively low, in the range of  $1.0 \times 10^4$  to  $1.0 \times 10^5 \text{ m}^3 \text{ y}^{-1}$ . This uneven spatial distribution of runoff to the ocean (Fig. 11b) is expected to occur throughout East Greenland where the strip of land between the GrIS and ocean contains thousands of individual glaciers, ice caps, and ice-free areas peripheral to the Ice Sheet (Fig. 1).

Another way to compare runoff contributions from different catchments is by looking at specific runoff (runoff volume per unit drainage area per time,  $\text{L km}^{-2} \text{ s}^{-1}$ ; to convert to  $\text{mm yr}^{-1}$  multiply by 31.6). For the Mittivakkat Glacier region the specific runoff averaged from 43 to  $68 \text{ L km}^{-2} \text{ s}^{-1}$  (Table 2); the highest values were for outlet A4, due to its high percentage (72%) of contributing area glacier cover. Previous independent model simulations presented an average (1994–2004) value of  $63 \text{ L km}^{-2} \text{ s}^{-1}$  for the catchment upstream of outlet A4 (Mernild and Hasholt 2006); the same order of magnitude as the value simulated by HydroFlow (Table 2). Furthermore, due to the high percentage of glacier cover upstream of location A4, variations in annual Mittivakkat Glacier net mass balance from 2002/03 through 2009/10 had a significant impact on annual runoff variations ( $r^2 = 0.56$ ;  $p < 0.01$ , where  $p$  is the level of significance), indicating that, on average, approximately 35% of the simulated runoff was explained by the Mittivakkat Glacier net loss. This value is

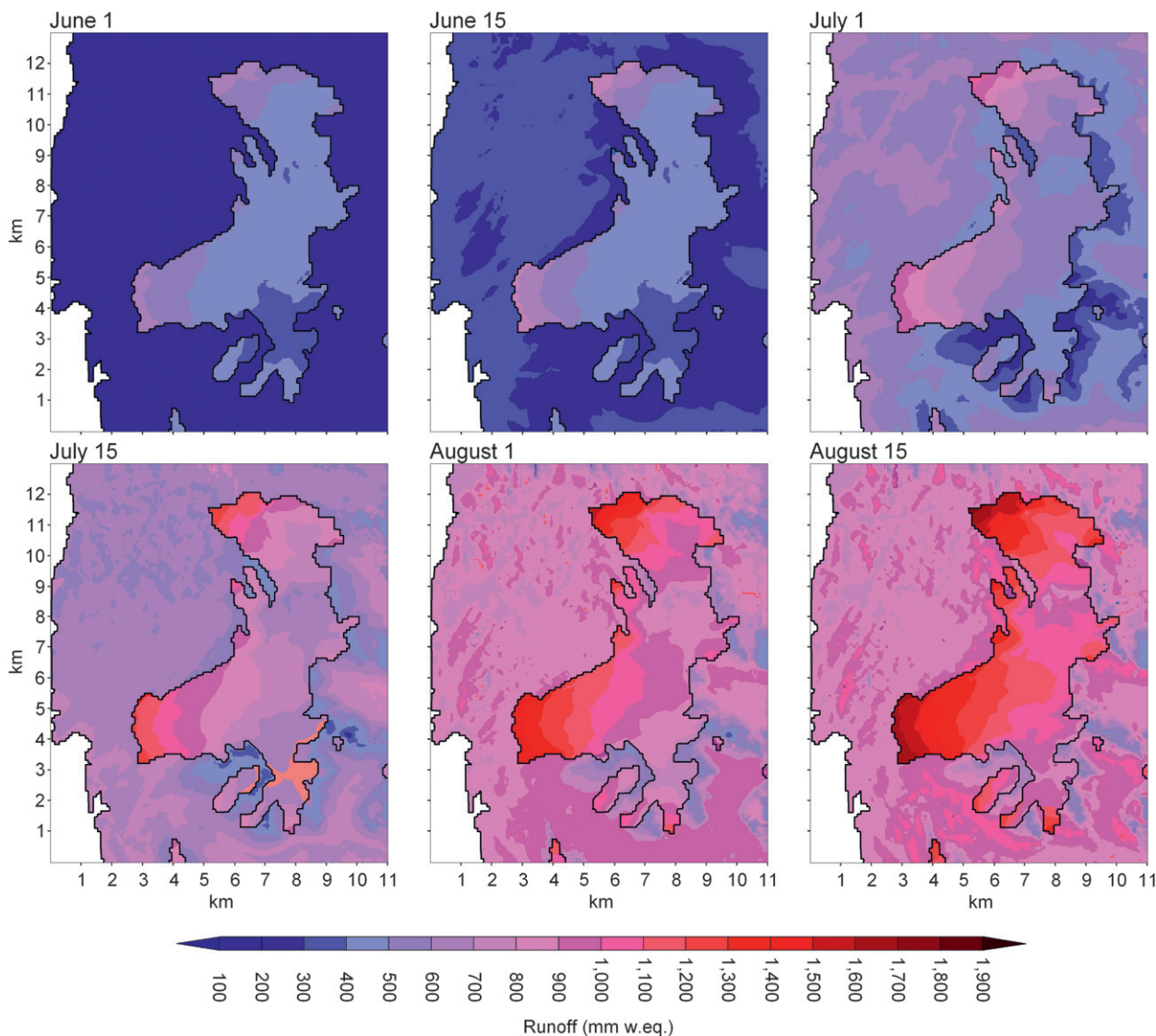


FIG. 8. Simulated, biweekly, cumulative, SnowModel grid-cell runoff distribution for the Mittivakkat Glacier region for 2003 from 1 June through 15 August. For 31 August (end of the ablation period), the spatial runoff distribution can be seen in Mernild et al. (2008c).

expected to be lower for catchment outlets C1 and D1 due to the lower percentage of glacier coverage upslope of those locations.

For 2003 through 2010 the seasonal runoff distribution was simulated for the four main outlets: B1, A4, C1, and D1 (Fig. 12). Considering all four outlets, the average runoff period was  $200 \pm 20$  days (from approximately mid-May through mid-November). During the 8-yr study, the Mittivakkat Glacier region runoff period increased by approximately 30 days ( $p < 0.01$ , estimated from linear regression over the eight year study period). Not only did the runoff period increase for the Mittivakkat Glacier region, but the number of days with runoff volumes greater than average ( $1.3 \times 10^5 \text{ m}^3 \text{ day}^{-1}$ ;

2003–10) also increased. The number of days with runoff greater than average increased from approximately 70 days in 2003 to approximately 85 days in 2010 (nonsignificant), indicating, in general, more days with greater discharge to the ocean. More significantly ( $p < 0.01$ ), the mean annual volume of runoff to the fjord increased by  $54.9 \times 10^6 \text{ m}^3$  for the period 2003 through 2010. This enhanced runoff, both in number of runoff days and in volume, support the conclusion of Mernild et al. (2011a) that the Mittivakkat Glacier is out of equilibrium with present-day climate, and significant losses in glacier area and volume are expected in the future, even in the absence of further climate changes.



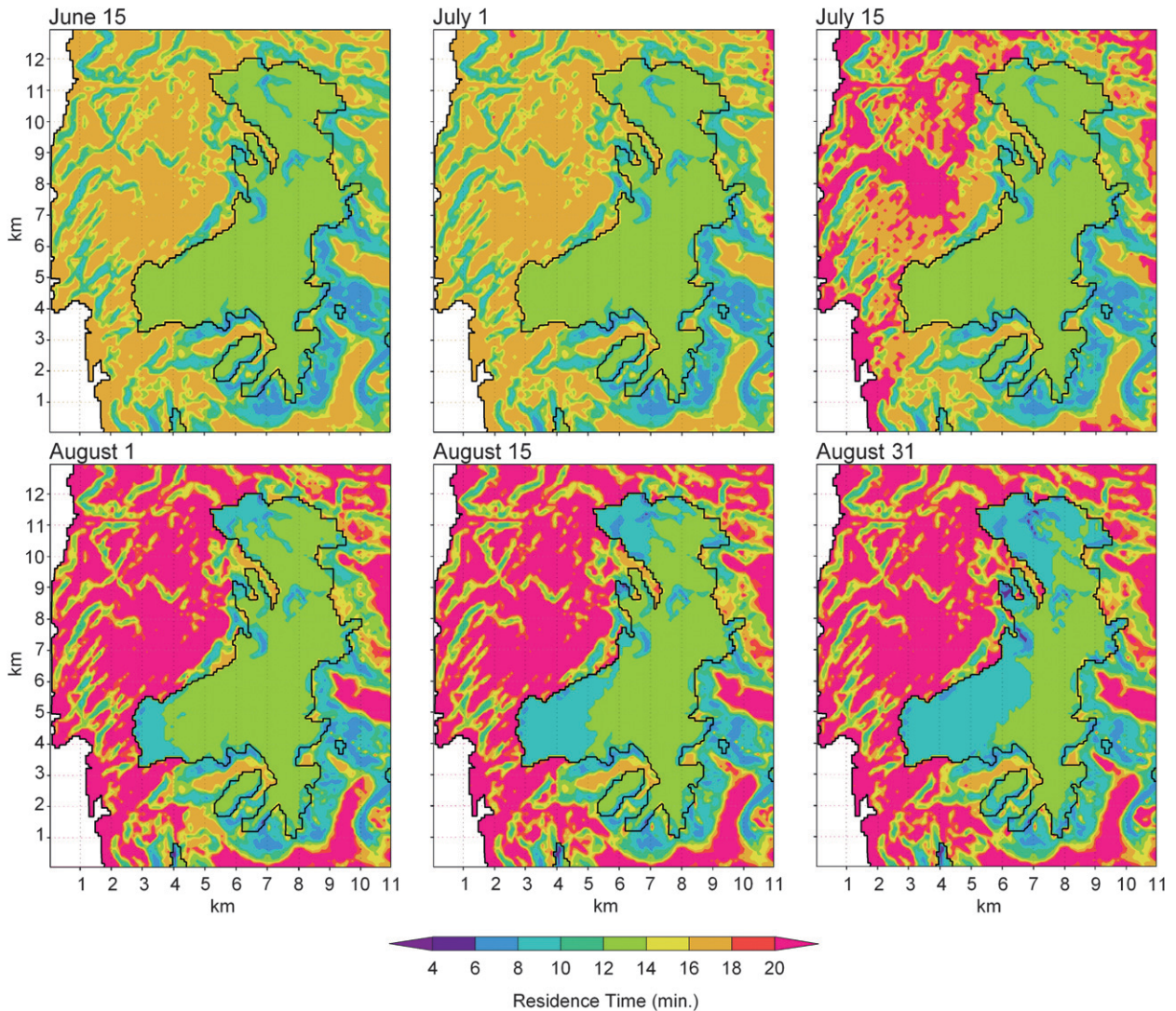


FIG. 9. Biweekly fast-time-scale residence time coefficient ( $k_f$ ) distributions for the Mittivakkat Glacier region, from 15 June through 31 August 2003. Note the different times plotted in this figure and Fig. 8; because of delayed melt in 2003 the 1 June distribution is identical to that on 15 June.

## 5. Discussion and conclusions

Linear reservoir models have been previously applied to simulate glacier runoff discharge (see Jansson et al. 2003; Hock and Jansson 2005). In most recent applications, the glacier of interest is typically divided into two or three reservoirs according to their surface characteristics (e.g., Hock and Noetzi 1997; Hannah and Gurnell 2001; Schaefli et al. 2005; de Woul et al. 2006): one reservoir covers the snow-free area of the glacier; a second reservoir covers the seasonally snow-covered area of the glacier; and a third reservoir (if used) is applied to the area above the previous year's equilibrium line (the firn reservoir). The areas covered by the first two reservoirs

change as the snow melts and exposes the ice below, and typically the coefficients associated with each reservoir's time scale do not change throughout the simulation period.

In contrast, HydroFlow treats each model grid cell as a linear reservoir, each with its own temporally evolving residence-time coefficients. This means that the runoff routing model is much more general and, through its coupling with SnowModel, is able to take advantage of available information related to the snow and ice evolution. For example, HydroFlow automatically accounts for when (in these simulations, the day) a model grid cell becomes snow free and only glacier ice remains, and the associated time scale changes for that grid cell. In

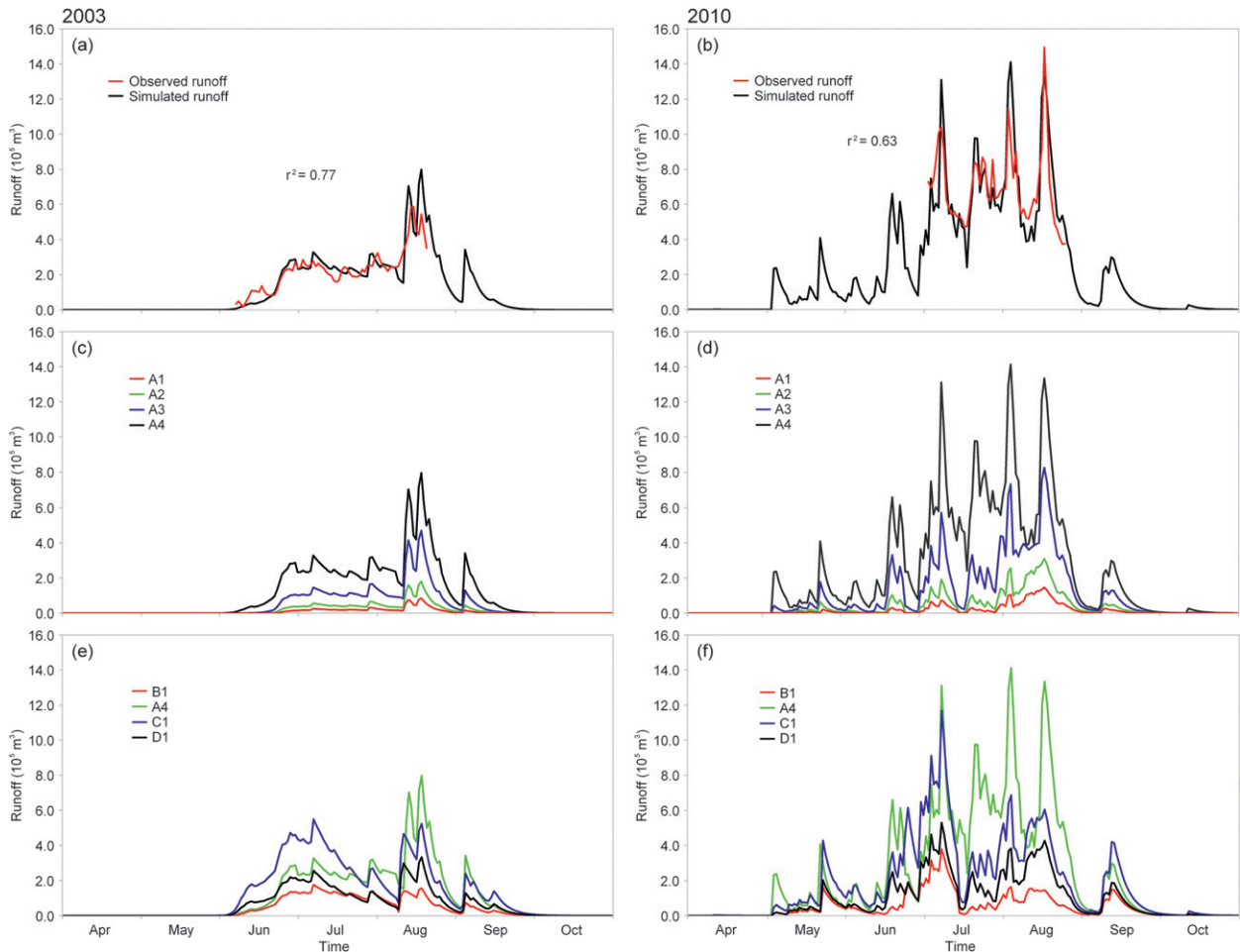


FIG. 10. (a) Observed and simulated runoff at location A4 for 2003 (the year with the second lowest cumulative runoff) and (b) 2010 (the year with the highest cumulative runoff) ( $r^2$  = square of the linear correlation coefficient), the observation period is shorter than the simulation period; (c),(d) simulated hydrographs at different locations upstream for outlet A4; and (e),(f) simulated hydrographs at outlets B1, A4, C1, and D1 to the Sermilik Fjord (for outlet locations see Fig. 6).

addition, the coupling of SnowModel with HydroFlow automatically accounts for runoff differences in response to the spatial and temporal variations in snowmelt and icemelt fluxes at each grid cell and on each day of the simulation. These can be caused by, for example, variations in slope and aspect, wind fields, albedo, temperature distributions, and elevation differences (all accounted for as part of the SnowModel integrations). A further application of this coupled modeling system is to use MicroMet to downscale atmospheric forcing variables produced by regional climate model (RCM) simulations and use those to drive SnowModel and HydroFlow integrations over catchments with limited meteorological forcing data or as part of climate change studies (e.g., Mernild et al. 2010a, 2011b). It is also possible to drive HydroFlow with gridded runoff data from other land surface hydrology observation and/or modeling systems.

One source of uncertainty in the HydroFlow simulations results from processes occurring within the watershed of interest that are not included in the modeling system. While the improvements included in HydroFlow can be thought of as a step forward in runoff simulations for snowmelt and icemelt on glaciers, ice sheets, and snow-covered land, there are still numerous water-transport-related processes that are not explicitly included in the model simulations. HydroFlow for example, as with most other models, omits processes such as temporal variations in 1) englacial bulk water storage and release, including drainage from glacial surges and drainage of glacial-dammed water (long-term build-up of storage followed by short-term release); 2) melt contributions from internal glacial deformation, geothermal heat, basal sliding, and the internal drainage system as it evolves during the melt season; 3) englacial water flow between neighboring catchments; and

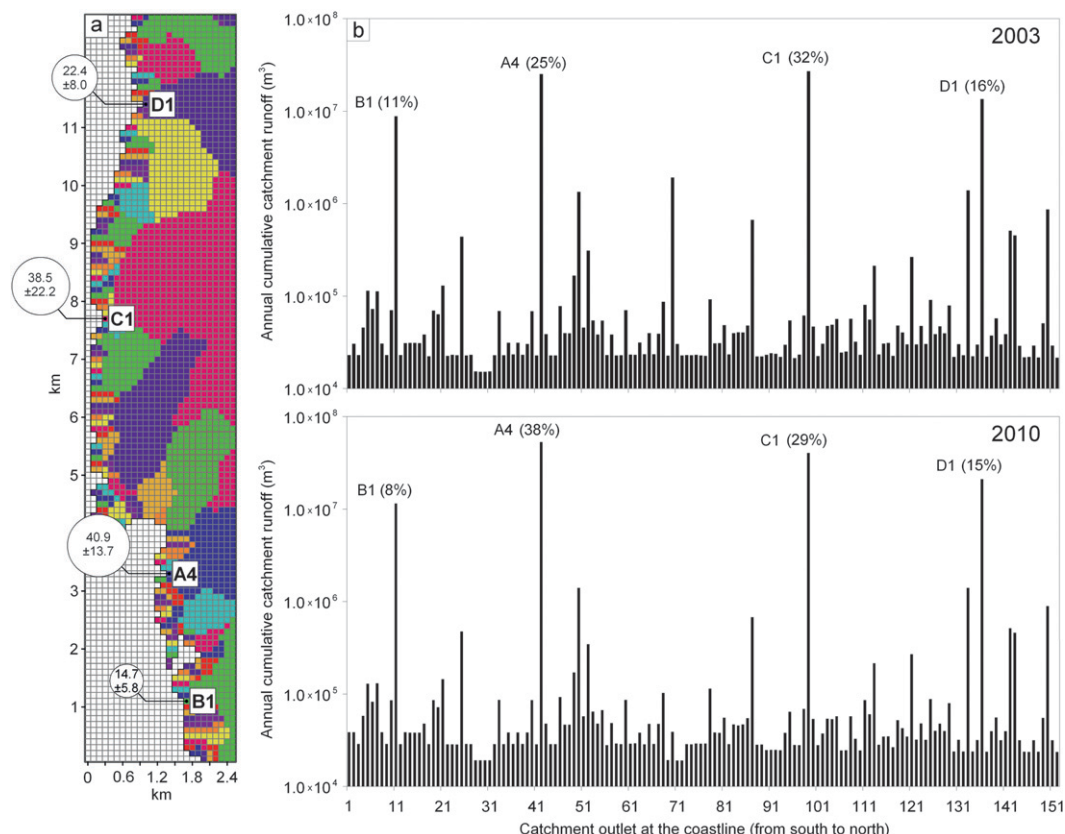


FIG. 11. (a) 2003–10 mean and standard deviation of annual simulated cumulative runoff to the Sermilik Fjord from catchment outlets D1, C1, A4, and B1 ( $10^6 \text{ m}^3 \text{ y}^{-1}$ ) and (b) spatial runoff distribution to Sermilik Fjord for 2003 and 2010. The percentages indicate the fraction of annual discharge into Sermilik Fjord from outlets D1, C1, A4, and B1. Note the ordinate logarithmic scale.

4) open channel streamflow routing. In addition, Snow-Model is not a dynamic glacier model, and routines for simulating changes in glacier area, size, surface elevation, and seasonal variations in the internal drainage system, are not yet represented within the modeling system.

Uncertainty in the simulated runoff discharges also occurs as a result of oversimplifications of the processes represented within the modeling system and due to simplified representations of the atmospheric forcing (e.g., air temperature and precipitation). At present, physically based glacier runoff models are simple representations of a complex natural system (e.g., Hock and Jansson 2005). But, with the HydroFlow routines for estimating drainage area, watershed divides, the flow-accumulation network, the time evolution and spatial distribution of different water transport mechanisms, and the runoff transient times, we are now able to provide information about the temporal and spatial variability in runoff at each point within the catchment including the watershed outlet and at every watershed, large and small, within the

simulation domain. A further advantage of this spatially distributed modeling approach is that it also allows detailed analyses of within-watershed runoff-related processes such as those associated with solute transport and sediment erosion and accumulation (Hasholt and Mernild 2006). While good model performance at gauging stations does not ensure good performance at sites upstream of those stations (Refsgaard 1997), the nested watersheds within the simulation domain considered herein have similar physical and climatological conditions as the outlets of the main catchments. Therefore, we expect similar behavior in them also. In addition, the physically based representations contained within MicroMet and SnowModel make them appropriate tools to simulate rainwater and snowmelt and icemelt fluxes, and using them to drive HydroFlow, for both gauged and ungauged basin applications. At the largest scale the combination of MicroMet, Snow-Model, and HydroFlow provides the ability to estimate the time evolution and spatial distribution of runoff into adjacent oceans.



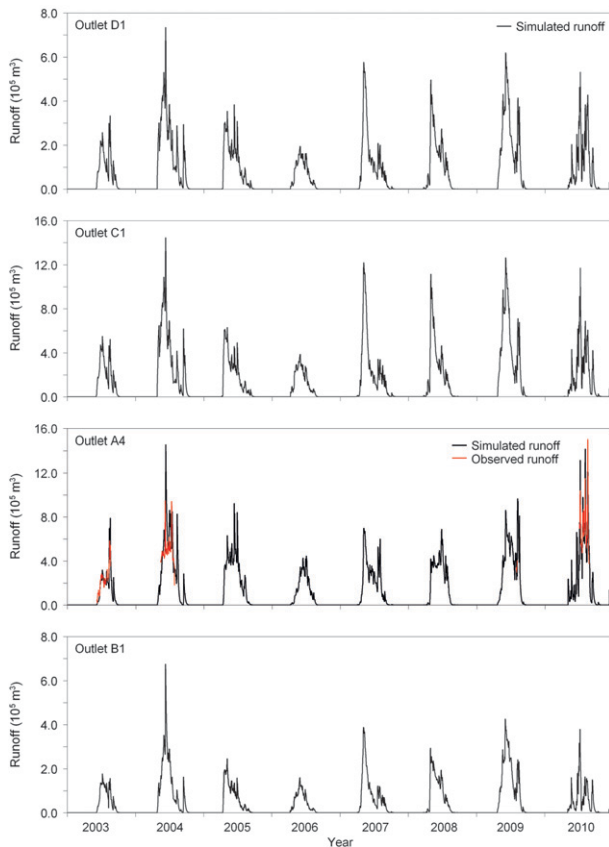


FIG. 12. Simulated runoff hydrographs at the outlets D1, C1, A4, and B1 for the period 2003 through 2010 (for outlet locations see Fig. 6). For outlet A4 available observed runoff is included (no data available from 2005 through 2008). Note the different scales on the ordinate.

Over recent decades, transforming glacier meltwater and liquid precipitation into hydrographs by modeling glacier hydrology has improved in parallel with our increased understanding of the role of snow and ice in the hydrological system. A fundamental premise of the HydroFlow runoff routing model presented herein is that the simulation domain can be divided into individual drainage basins, each with its own river/streamflow network that can track rain and meltwater from snow and ice across and through snow-covered and snow-free glaciers, ice sheets, and land to surrounding oceans. The spatial distribution of catchment runoff to Sermilik Fjord from the Mittivakkat Glacier region was strongly influenced by catchment size and variations in glacier elevation range and areal coverage. For the majority of catchments without glacier cover (approximately 90%) the cumulative annual runoff ranged from  $1.0 \times 10^4$  to  $1.0 \times 10^5 \text{ m}^3 \text{ yr}^{-1}$ , corresponding to approximately 850–1100  $\text{mm yr}^{-1}$ . For catchments with glacier cover the annual runoff was as high as  $40.9 \times 10^6 \text{ m}^3 \text{ yr}^{-1}$ , corresponding to approximately

2100  $\text{mm yr}^{-1}$  (and contributed approximately 90% of the domain runoff to Sermilik Fjord). A similar uneven discharge pattern to the ocean is expected to be present throughout Greenland because, like the Mittivakkat Glacier region, the land area between the GrIS and ocean includes numerous individual glaciers and ice caps peripheral to the Ice Sheet (Fig. 1).

**Acknowledgments.** The authors thank Jens Christian Refsgaard, Sveta Stuefer, Kazuyoshi Suzuki, Hans Thodsen, and Amy Tidwell for their insightful review of an early version of this paper. This work was supported by NASA Grant NNX08AV21G; Norwegian Research Council Grant 192958/S60, titled Updating Methodology in Operational Runoff Models; a consortium of Norwegian hydropower companies lead by Statkraft; grants provided by the Climate Change Prediction Program and Scientific Discovery for Advanced Computing (SciDAC) program within the U.S. Department of Energy Office of Science; and by the Los Alamos National Laboratory (LANL) Director's Fellowship. LANL is operated under the auspices of the National Nuclear Security Administration of the U.S. Department of Energy under Contract DE-AC52-06NA25396. We also thank the Department of Geography and Geology, University of Copenhagen, for providing the observed meteorological and runoff data, and Jeppe Malmros, University of Copenhagen, for the graphic design of Fig. 1.

## REFERENCES

- ACIA, 2005: *Arctic Climate Impact Assessment*. Cambridge University Press, 1042 pp.
- Allerup, P., H. Madsen, and F. Vejen, 1998: Estimating true precipitation in Arctic areas. *Proc. Nordic Hydrological Conf.*, Helsinki, Finland, Nordic Hydrological Programme, 1–9.
- , —, and —, 2000: Correction of precipitation based on off-site weather information. *Atmos. Res.*, **53**, 231–250.
- Allison, I., and Coauthors, 2009: *The Copenhagen Diagnosis: Updating the World on the Latest Climate Science*. The University of New South Wales Climate Change Research Centre (CCRC), 60 pp.
- Box, J. E., J. Cappelen, D. Decker, X. Fettweis, T. Mote, M. Tedesco, and R. S. W. Van de Wal, cited 2010: Greenland ice sheet. [Available online at [http://www.arctic.noaa.gov/reportcard/greenland\\_ice\\_sheet.html](http://www.arctic.noaa.gov/reportcard/greenland_ice_sheet.html).]
- Brown, P. N., G. D. Byrne, and A. C. Hindmarsh, 1989: VODE: A variable coefficient ODE solver. *SIAM J. Sci. Stat. Comput.*, **10**, 1038–1051.
- Bruland, O., G. E. Liston, J. Vonk, and A. Killingtveit, 2004: Modelling the snow distribution at two High-Arctic sites at Svalbard, Norway, and at a Sub-Arctic site in Central Norway. *Nord. Hydrol.*, **35**, 191–208.
- Byrne, G. D., and A. C. Hindmarsh, 1987: Stiff ODE solvers: A review of current and coming attractions. *J. Comput. Phys.*, **70**, 1–62.

- de Woul, M., R. Hock, M. Braun, T. Thorsteinsson, T. Jóhannesson, and S. Halldórsdóttir, 2006: Firm layer impact on glacial runoff: A case study at Hofsjökull, Iceland. *Hydrol. Processes*, **20**, 2171–2185.
- Ettema, J., M. van den Broeke, E. van Meijgaard, M. J. van de Berg, J. L. Bamber, J. E. Box, and R. C. Bales, 2009: Higher surface mass balance of the Greenland ice sheet revealed by high resolution climate modeling. *Geophys. Res. Lett.*, **36**, L12501, doi:10.1029/2009GL038110.
- Fettweis, X., E. Hanna, H. Gallee, P. Huybrechts, and M. Erpicum, 2008: Estimation of the Greenland ice sheet surface mass balance for the 20th and 21st centuries. *Cryosphere*, **2**, 117–129.
- Gallant, J. C., and J. P. Wilson, 1996: TAPES-G: A grid-based terrain analysis program for the environmental sciences. *Comput. Geosci.*, **22**, 713–722.
- Greene, E. M., G. E. Liston, and R. A. Pielke Sr., 1999: Simulation of above treeline snowdrift formation using a numerical snow-transport model. *Cold Reg. Sci. Technol.*, **30**, 135–144.
- Hanna, E., and Coauthors, 2008: Increased runoff from melt from the Greenland Ice Sheet: A response to global warming. *J. Climate*, **21**, 331–341.
- Hannah, D. M., and A. M. Gurnell, 2001: A conceptual, linear reservoir runoff model to investigate melt season changes in cirque glacier hydrology. *J. Hydrol.*, **246**, 123–141.
- Hasholt, B., and S. H. Mernild, 2006: Glacial erosion and sediment transport in the Mittivakkat Glacier catchment, Ammassalik island, southeast Greenland, 2005. *IAHS Publ.*, **306**, 45–55.
- , and —, 2008: Hydrology, sediment transport, and water resources of Ammassalik Island, SE Greenland. *Dan. J. Geogr.*, **108**, 73–95.
- , G. E. Liston, and N. T. Knudsen, 2003: Snow distribution modelling in the Ammassalik Region, South East Greenland. *Nord. Hydrol.*, **34**, 1–16.
- Hiemstra, C. A., G. E. Liston, and W. A. Reiners, 2002: Snow redistribution by wind and interactions with vegetation at upper treeline in the Medicine Bow Mountains, Wyoming, USA. *Arct. Antarct. Alp. Res.*, **34**, 262–273.
- , —, and —, 2006: Observing, modelling, and validating snow redistribution by wind in a Wyoming upper treeline landscape. *Ecol. Modell.*, **197**, 35–51.
- Hinzman, L. D., and Coauthors, 2005: Evidence and implications of recent climate change in Northern Alaska and other Arctic regions. *Climatic Change*, **72**, 251–298.
- Hock, R., and C. Noetzi, 1997: Areal melt and discharge modeling of Storglaciären, Sweden. *Ann. Glaciol.*, **24**, 211–216.
- , and P. Jansson, 2005: Modeling glacier hydrology. *Encyclopedia of Hydrological Sciences*, Vol. 4, M. G. Anderson and J. McDonnell, Eds., John Wiley & Sons, Ltd, 2647–2655.
- Jansson, P., R. Hock, and T. Schneider, 2003: The concept of glacier storage: A review. *J. Hydrol.*, **282**, 116–129.
- Knudsen, N. T., and B. Hasholt, 1999: Radio-echo sounding at the Mittivakkat Gletscher, Southeast Greenland. *Arct. Antarct. Alp. Res.*, **31**, 321–328.
- , and —, 2002: Mass balance observations at Mittivakkat Gletscher, Southeast Greenland 1995–2002. *Nord. Hydrol.*, **35**, 381–390.
- , and —, 2008: Mass balance observations at Mittivakkat Glacier, Ammassalik Island, Southeast Greenland 1995–2006. *Dan. J. Geogr.*, **108**, 111–120.
- Krabill, W., and Coauthors, 2000: Greenland ice sheet: High-elevation balance and peripheral thinning. *Science*, **289**, 428–430.
- , and Coauthors, 2004: Greenland Ice Sheet: Increased coastal thinning. *Geophys. Res. Lett.*, **31**, L24402, doi:10.1029/2004GL021533.
- Lemke, P., and Coauthors, 2007: Observations: Changes in snow, ice and frozen ground. *Climate Change 2007: The Physical Science Basis*, S. Solomon et al., Eds., Cambridge University Press, 337–383.
- Liston, G. E., 1995: Local advection of momentum, heat, and moisture during the melt of patchy snow covers. *J. Appl. Meteor.*, **34**, 1705–1715.
- , 2004: Representing subgrid snow cover heterogeneities in regional and global models. *J. Climate*, **17**, 1381–1397.
- , and D. K. Hall, 1995: An energy balance model of lake ice evolution. *J. Glaciol.*, **41**, 373–382.
- , and M. Sturm, 1998: A snow-transport model for complex terrain. *J. Glaciol.*, **44**, 498–516.
- , and —, 2002: Winter precipitation patterns in arctic Alaska determined from a blowing-snow model and snow-depth observations. *J. Hydrometeorol.*, **3**, 646–659.
- , and J.-G. Winther, 2005: Antarctic surface and subsurface snow and ice melt fluxes. *J. Climate*, **18**, 1469–1481.
- , and K. Elder, 2006a: A distributed snow-evolution modeling system (SnowModel). *J. Hydrometeorol.*, **7**, 1259–1276.
- , and —, 2006b: A meteorological distribution system for high-resolution terrestrial modeling (MicroMet). *J. Hydrometeorol.*, **7**, 217–234.
- , and C. A. Hiemstra, 2008: A simple data assimilation system for complex snow distributions (SnowAssim). *J. Hydrometeorol.*, **9**, 989–1004.
- , and —, 2011a: Representing grass- and shrub-snow-atmosphere interactions in climate system models. *J. Climate*, **24**, 2061–2079.
- , and —, 2011b: The changing cryosphere: Pan-Arctic snow trends (1979–2009). *J. Climate*, **24**, 5691–5712.
- , Y. C. Sud, and E. F. Wood, 1994: Evaluating GCM land surface hydrology parameterizations by computing river discharges using a runoff routing model: Application to the Mississippi basin. *J. Appl. Meteor.*, **33**, 394–405.
- , J.-G. Winther, O. Bruland, H. Elvehøy, and K. Sand, 1999: Below-surface ice melt on the coastal Antarctic ice sheet. *J. Glaciol.*, **45**, 273–285.
- , —, —, —, and L. Karlöf, 2000: Snow and blue-ice distribution patterns on the coastal Antarctic ice sheet. *Antarct. Sci.*, **12**, 69–79.
- , J. P. McFadden, M. Sturm, and R. A. Pielke Sr., 2002: Modeled changes in arctic tundra snow, energy, and moisture fluxes due to increased shrubs. *Global Change Biol.*, **8**, 17–32.
- , R. B. Haehnel, M. Sturm, C. A. Hiemstra, S. Berezovskaya, and R. D. Tabler, 2007: Simulating complex snow distributions in windy environments using SnowTran-3D. *J. Glaciol.*, **53**, 241–256.
- , C. A. Hiemstra, K. Elder, and D. W. Cline, 2008: Meso-cell study area (MSA) snow distributions for the Cold Land Processes Experiment (CLPX). *J. Hydrometeorol.*, **9**, 957–976.
- Mernild, S. H., 2006: The internal drainage system of the lower Mittivakkat Glacier, Ammassalik Island, SE Greenland. *Dan. J. Geogr.*, **106**, 13–24.
- , and B. Hasholt, 2006: Climatic control on river discharge simulations, Mittivakkat Glacier catchment, Ammassalik Island, SE Greenland. *Nord. Hydrol.*, **37**, 327–346.
- , and G. E. Liston, 2010: The influence of air temperature inversions on snowmelt and glacier mass-balance simulations, Ammassalik Island, SE Greenland. *J. Appl. Meteor. Climatol.*, **49**, 47–67.
- , and —, 2012: Greenland freshwater runoff. Part II: Distribution and trends, 1960–2010. *J. Climate*, **25**, 6015–6035.



- , B. Hasholt, and G. E. Liston, 2006a: Water flow through Mittivakkat Glacier, Ammassalik Island, SE Greenland. *Dan. J. Geogr.*, **106**, 25–43.
- , G. E. Liston, B. Hasholt, and N. T. Knudsen, 2006b: Snow-distribution and melt modeling for Mittivakkat Glacier, Ammassalik Island, Southeast Greenland. *J. Hydrometeorol.*, **7**, 808–824.
- , B. U. Hansen, B. H. Jakobsen, and B. Hasholt, 2008a: Climatic conditions at the Mittivakkat Glacier catchment (1994–2006), Ammassalik Island, SE Greenland, and in a 109 years term perspective (1898–2006). *Dan. J. Geogr.*, **108**, 51–72.
- , G. E. Liston, and B. Hasholt, 2008b: East Greenland freshwater runoff to the North Atlantic Ocean 1999–2004 and 2071–2100. *Hydrol. Processes*, **22**, 4571–4586, doi:10.1002/hyp.7061.
- , —, D. L. Kane, N. T. Knudsen, and B. Hasholt, 2008c: Snow, runoff, and mass balance modeling for the entire Mittivakkat Glacier (1998–2006), Ammassalik Island, SE Greenland. *Dan. J. Geogr.*, **108**, 121–136.
- , —, C. A. Hiemstra, and J. H. Christensen, 2010a: Greenland Ice Sheet surface mass-balance modeling in a 131-year perspective 1950–2080. *J. Hydrometeorol.*, **11**, 3–25.
- , and Coauthors, 2010b: Freshwater flux to Sermilik Fjord, SE Greenland. *Cryosphere*, **4**, 453–465, doi:10.5194/tc-4-453-2010.
- , G. E. Liston, K. Steffen, and P. Chylek, 2010c: Meltwater flux and runoff modeling in the ablation area of the Jakobshavn Isbræ, West Greenland. *J. Glaciol.*, **56**, 20–32.
- , N. T. Knudsen, W. H. Lipscomb, J. C. Yde, J. K. Malmros, B. H. Jakobsen, and B. Hasholt, 2011a: Increasing mass loss from Greenland's Mittivakkat Gletscher. *Cryosphere*, **5**, 341–348, doi:10.5194/tc-5-341-2011.
- , G. E. Liston, C. A. Hiemstra, J. H. Christensen, M. Stendel, and B. Hasholt, 2011b: Surface mass-balance and runoff modeling using HIRHAM4 RCM at Kangerlussuaq (Søndre Strømfjord), West Greenland, 1950–2080. *J. Climate*, **24**, 609–623.
- Nash, J. E., and J. V. Sutcliffe, 1970: River flow forecasting through conceptual models, Part I—A discussion of principles. *J. Hydrol.*, **10**, 282–290.
- Nielsen, S. A., and E. Hansen, 1973: Numerical simulation of the rainfall-runoff process on a daily basis. *Nord. Hydrol.*, **4**, 171–190.
- Prasad, R., D. G. Tarboton, G. E. Liston, C. H. Luce, and M. S. Seyfried, 2001: Testing a blowing snow model against distributed snow measurements at Upper Sheep Creek, Idaho, USA. *Water Resour. Res.*, **37**, 1341–1357.
- Rahmstorf, S., and Coauthors, 2005: Thermohaline circulation hysteresis: A model intercomparison. *Geophys. Res. Lett.*, **32**, L23605, doi:10.1029/2005GL023655.
- Refsgaard, J. C., 1997: Parameterisation, calibration and validation of distributed hydrological models. *J. Hydrol.*, **198**, 69–97.
- Rignot, E., and P. Kanagaratnam, 2006: Changes in the velocity structure of the Greenland Ice Sheet. *Science*, **315**, 1559–1561.
- , J. E. Box, E. Burgess, and E. Hanna, 2008: Mass balance of the Greenland ice sheet from 1958 to 2007. *Geophys. Res. Lett.*, **35**, L20502, doi:10.1029/2008GL035417.
- Schaeffli, B., B. Hingray, M. Niggli, and A. Musy, 2005: A conceptual glacio-hydrological model for high mountainous catchments. *Hydrol. Earth Syst. Sci.*, **9**, 95–109.
- Serreze, M. C., and Coauthors, 2000: Observational evidence of recent change in the northern high-latitude environment. *Climatic Change*, **46**, 159–207.
- Shampine, L. F., and C. W. Gear, 1979: A user's view of solving stiff ordinary differential equations. *SIAM Rev.*, **21**, 1–17.
- Singh, V. P., 1988: *Hydrologic Systems*. Vol. 1. *Rainfall-Runoff Modeling*, Prentice-Hall, 480 pp.
- Solomon, S., D. Qin, M. Manning, M. Marquis, K. Averyt, M. M. B. Tignor, H. L. Miller Jr., and Z. Chen, Eds., 2007: *Climate Change 2007: The Physical Science Basis*. Cambridge University Press, 996 pp.
- Stendel, M., J. H. Christensen, and D. Petersen, 2008: Arctic climate and climate change with a focus on Greenland. *Adv. Ecol. Res.*, **40**, 13–43, doi:10.1016/S0065-2504(07)00002-5.
- Sturm, M., J. Holmgren, and G. E. Liston, 1995: A seasonal snow cover classification system for local to global applications. *J. Climate*, **8**, 1261–1283.
- Su F., J. C. Adam, K. E. Trenberth, and D. P. Lettenmaier, 2006: Evaluation of surface water fluxes of the pan-Arctic land region with a land surface model and ERA-40 reanalysis. *J. Geophys. Res.*, **111**, D05110, doi:10.1029/2005JD006387.
- Todd, D. K., 1980: *Groundwater Hydrology*. 2nd ed. John Wiley & Sons, 535 pp.
- Weidick, A., and O. Bennike, 2007: Quaternary glaciation history and glaciology of Jakobshavn Isbræ and the Disko Bugt region, West Greenland: A review. *GEUS Bulletin*, Vol. 14, Geological Survey of Denmark and Greenland, 78 pp.
- , C. E. Bøggild, and N. T. Knudsen, 1992: Glacier inventory of west Greenland. National Snow and Ice Data Center, Boulder, CO, digital media. [Available online at <http://nsidc.org/data/g01375.html>.]
- WGMS, 2009: Glacier mass balance bulletin. World Glacier Monitoring Service Bulletin 10, 96 pp.

[11]

Mernild, S. H., Malmros, J. K., Yde, J. C., and Knudsen, N. T.  
2012. Multi-decadal marine and land-terminating glacier retreat  
in Ammassalik region, Southeast Greenland.  
The Cryosphere, 6, 625–639, doi:10.5194/tc-6-625-2012.

Reprinted with permission from Copernicus Publications



# Multi-decadal marine- and land-terminating glacier recession in the Ammassalik region, southeast Greenland

S. H. Mernild<sup>1</sup>, J. K. Malmros<sup>2</sup>, J. C. Yde<sup>3</sup>, and N. T. Knudsen<sup>4</sup>

<sup>1</sup>Climate, Ocean, and Sea Ice Modeling Group, Los Alamos National Laboratory, New Mexico, USA

<sup>2</sup>Department of Geography and Geology, University of Copenhagen, Denmark

<sup>3</sup>Sogn og Fjordane University College, Sogndal, Norway

<sup>4</sup>Department of Geoscience, Aarhus University, Aarhus, Denmark

Correspondence to: S. H. Mernild (mernild@lanl.gov)

Received: 26 January 2012 – Published in The Cryosphere Discuss.: 7 February 2012

Revised: 9 May 2012 – Accepted: 15 May 2012 – Published: 6 June 2012

**Abstract.** Landsat imagery was applied to elucidate glacier fluctuations of land- and marine-terminating outlet glaciers from the Greenland Ice Sheet (GrIS) and local land-terminating glaciers and ice caps (GIC) peripheral to the GrIS in the Ammassalik region, Southeast Greenland, during the period 1972–2011. Data from 21 marine-terminating glaciers (including the glaciers Helheim, Midgaard, and Fenris), the GrIS land-terminating margin, and 35 GIC were examined and compared to observed atmospheric air temperatures, precipitation, and reconstructed ocean water temperatures (at 400 m depth in the Irminger Sea). Here, we document that net glacier recession has occurred since 1972 in the Ammassalik region for all glacier types and sizes, except for three GIC. The land-terminating GrIS and GIC reflect lower marginal and areal changes than the marine-terminating outlet glaciers. The mean annual land-terminating GrIS and GIC margin recessions were about three to five times lower than the GrIS marine-terminating recession. The marine-terminating outlet glaciers had an average net frontal retreat for 1999–2011 of  $0.098 \text{ km yr}^{-1}$ , which was significantly higher than in previous sub-periods 1972–1986 and 1986–1999. For the marine-terminating GrIS, the annual areal recession rate has been decreasing since 1972, while increasing for the land-terminating GrIS since 1986. On average for all the observed GIC, a mean net frontal retreat for 1986–2011 of  $0.010 \pm 0.006 \text{ km yr}^{-1}$  and a mean areal recession of around 1 % per year occurred; overall for all observed GIC, a mean recession rate of  $27 \pm 24 \%$  occurred based on the 1986 GIC area. Since 1986, five GIC melted away in the Ammassalik area.

## 1 Introduction

The Greenland Ice Sheet (GrIS) – land- and marine-terminating outlet glaciers on the periphery of the GrIS – and local land-terminating glaciers and ice caps (GIC) peripheral to the GrIS have undergone rapid changes over the last decades. Most notable changes are thinning, leading to destabilization and accelerated retreat of GrIS marine-terminating glaciers (Joughin et al., 2004, 2010; Howat et al., 2005, 2008; Rignot and Kanagaratnam, 2006; Moon and Joughin, 2008; Nick et al., 2009), and increasing mass loss, thinning, and retreat of land-terminating GIC (Yde and Knudsen, 2007; Mernild et al., 2011a; Radić and Hock, 2011).

The underlying mechanisms of GrIS marine-terminating glacier dynamics remain somehow unclear (Straneo et al., 2010; Johannessen et al., 2011). The frontal recessions at the calving front are highly due to changes in the force balance due to thinning, reduced resistive force, and speed-up based on warming of oceanic subsurface waters and warming of the atmosphere, where warm subsurface waters are suggested by Luthcke et al. (2006), Velicogna and Wahr (2006), Holland et al. (2008), Howat et al. (2008), Thomas et al. (2009), van den Broeke et al. (2009), Velicogna (2009), Murray et al. (2010), Rignot et al. (2010), Straneo et al. (2010), and Andresen et al. (2011) to play a significant role. However, Johannessen et al. (2011) stated, based on statistical correlations, that penetration of snow and ice melt water to the glacier bed might play an important role, influencing the GrIS sliding and dynamic processes. The mechanisms suggested for land-terminating GIC recession are less complex. In the Ammassalik region, Southeast Greenland, studies of GIC have shown that mass loss and margin retreat have

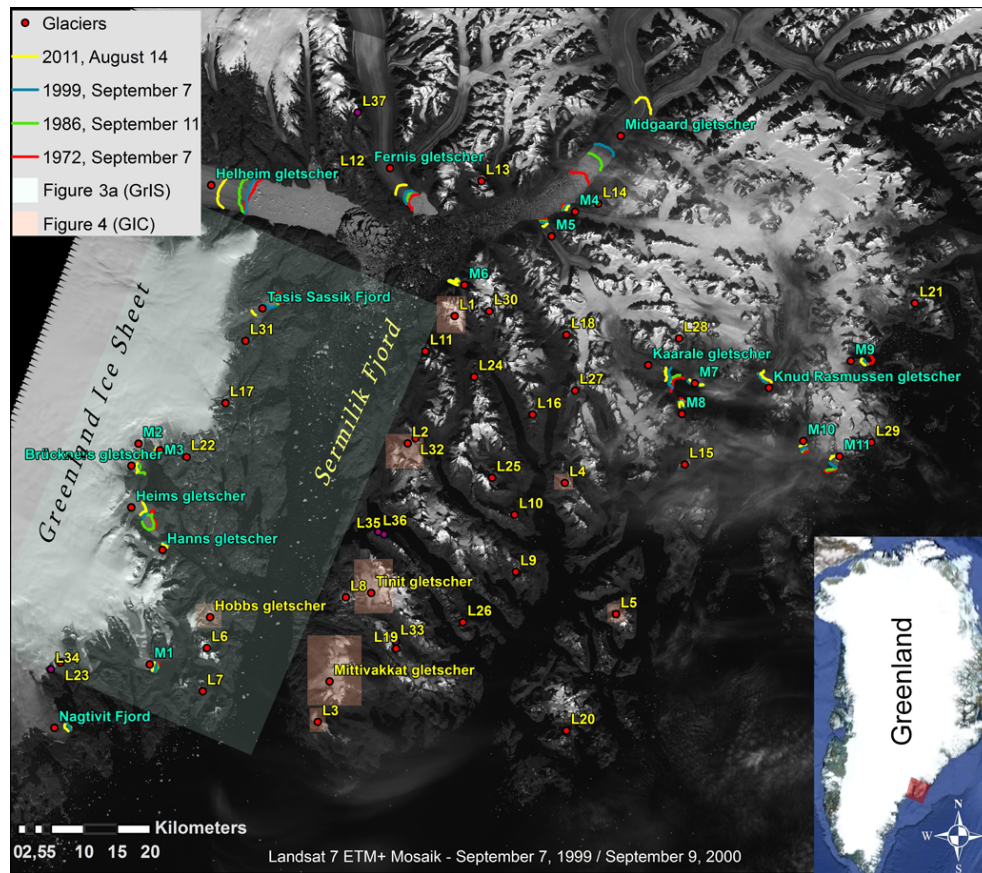


**Fig. 1.** The Ammassalik region, including the Sermilik Fjord and parts of the southeastern sector of the GrIS. The marine-terminating glacier margins are marked with positions (lines) for each of the survey years: 1972 (red color), 1986 (green), 1999 (blue), and 2011 (yellow) (the location names are written in turquoise). The 35 local land-terminating glaciers and ice caps (GIC) peripheral to the GrIS are written in yellow, where eight are marked with shaded areas; marginal changes for those eight GIC and the GrIS are illustrated in detail. The GIC marked with L33–L37 are examples of GIC that melted away during 1986–2011. The inset figure indicates the general location of the Ammassalik region in Southeast Greenland (source: Landsat 7 ETM+ Mosaik, 7 September 1999/9 September 2000).

been driven mainly by higher surface temperatures (increasing surface ablation) and decreasing precipitation (decreasing snow accumulation) since the mid-1900s (Mernild et al., 2011a).

The glacier contribution to sea-level rise from Greenland marine-terminating glaciers has been analyzed by satellite. Howat and Eddy (2011) identified changes in ice-frontal positions from 210 GrIS marine-terminating glaciers with fronts wider than 1 km (spanning nearly four decades, 1972–2010). These results show a trend of accelerated recession, where 90 % of the observed glaciers receded between 2000 and 2010. Box and Decker (2011) identified areal changes at 39 of the widest Greenland marine-terminating glaciers (2000–2010). Collectively, the 39 glaciers lost a cumulative area of 1368 km<sup>2</sup>. For the Ammassalik region – a region including the Ammassalik Island, the Sermilik Fjord (the largest fjord system in Southeast Greenland) and its surrounding landscape – only frontal changes of major GrIS marine-terminating glaciers, such as Helheim, Fernis, and

Midgaard glaciers, have been observed in earlier studies; however, at least 21 marine-terminating glaciers have been identified; all 21 were included in this study (Fig. 1).

For the land-terminating GIC in Greenland, margin retreat has been sparsely observed (Yde and Knudsen, 2007), and the only currently published time series of whole glacier in-situ mass balance observations (since 1995/1996) is from the Mittivakkat Gletscher, located in the Ammassalik region (WGMS, 2009; Mernild et al., 2011a), even though thousands of individual GIC are located on the land-strip between the GrIS and ocean, of which several hundred are situated in the Ammassalik region (Mernild et al., 2012). Thus, there is a need for more information about contemporary glacier fluctuations of Greenlandic GIC and their coupling to climate change.

The ability to assess GrIS and GIC margin changes in the Ammassalik region has been improved through the use of Landsat imagery dating back to 1972. The imagery gives us the possibility to map “snapshots” and the averaged

**Table 1.** Satellite platform, sensors, band information, scenes used in the analysis, and uncertainties related to the satellite classification process.

Platform	Landsat 1	Landsat 5	Landsat 7	Terra
Sensor and bands	Landsat MSS (bands 2–7)	Landsat TM (bands 1–5, and 7)	Landsat ETM+ (bands 1–5, and 7)	ASTER GDEM Version 2
Ground resolution	~60 m	30 m	30 m, 15 m panchromatic	30 m
Precision error	±30 m (horizontal)	±15 m (horizontal)	±15 m, 7.5 m panchromatic (horizontal)	~ ±12.5 m (vertical)
Scenes	M1251013_01319720907	L5231014_01419860911 L71232013_01320110814 L71232014_01420110814 L71232014_01420070904 L71231014_01420070913	L71231014_01419990907	20111017145633_1819068388
Survey years and dates	7 September 1972	11 September 1986	7 September 1999 13 September 2007 14 August 2011	–
Uncertainties related to the satellite classification process				
Image co-registration error	MSS to TM: 39.86 m		TM to ETM+: 11.33 m	
GPS vs. Image classification error	Number of GCP used: 27		Overall difference between satellite-derived and GPS margin observations: 22 m	
Classification error	For snow patches: overestimate by 3.4 %		For debris covered terrain and shadow regions: underestimate by 1.8 %	

behaviour of glacier changes for the past four decades for the identified marine-terminating glaciers, the GrIS land-terminating margin, and the GIC during a period of climate warming. The average multi-decadal glacier recession in the Ammassalik region (65° N, 37° W) was examined, rather than the annual range of variability, even though recent observations suggest that major changes in the dynamics of Greenland marine-terminating glaciers take place over timescales of 3–10 yr (Howat et al., 2007; Nick et al., 2009; Andresen et al., 2011; Johannessen et al., 2011), rather than over several decades or centuries as previously believed (Truffer and Fahnestock, 2007).

Here, on approximately decadal scale we examine net frontal position and area fluctuations using multispectral Landsat satellite data, observing 21 marine-terminating glaciers from 1972–2011, land-terminating glacier frontal positions for parts of the GrIS, and of 35 GIC from 1986–2011 for the Ammassalik region – a region including the thermodynamic transition zone from the North Atlantic Ocean into the Arctic Ocean through the Denmark Strait. Changes were considered in the context of meteorological observations and reconstructed ocean water temperature time series. As part of the study, the cumulative net area changes for the marine-terminating glaciers were examined. Finally, we investigate differences in marginal change rates between the marine and the terrestrial glacier environments.

## 2 Data and methods

The Landsat and Advanced Spaceborne Thermal and Reflection Radiometer (ASTER) Global Digital Elevation Model Version 2 (GDEM v2) scenes were selected and acquired through WIST (<http://reverb.echo.nasa.gov/reverb/redirect/wist>; EOSDIS, 2009): Landsat 1 carried the four-band Multispectral Scanner (MSS); Landsat 5 carried the seven-band Thematic Mapper (TM); and Landsat 7 carried the eight-band Enhanced Thematic Mapper Plus (ETM+), having a ground resolution of ~60, 30, and 30 m (15 m in the panchromatic band 8), respectively. The ASTER GDEM v2 provides a ground resolution of 30 m (Table 1) and is used to estimate minimum, mean, and maximum GIC elevations.

Data were obtained from seven relatively cloud-free scenes (>25 % cloud free) covering the Ammassalik region at the end of the ablation period (mid-August through mid-September) for the time series analysis (i.e., 1972, 1986, 1999, 2007, and 2011, Table 1). For 1972 the GrIS and GIC land-terminating margin analyses were omitted due to difficulties in separating ice cover from snow cover; the year 1972 was one of the coldest years during the study period, and the year with the lowest satellite-derived melt extent cover for GrIS (Mernild et al., 2011b). For 2011, scenes from 2007 were used for filling gaps, due to the ETM+ sensor Scan Line Instrument (SLI) malfunction. Because of the four year gap between 2007 and 2011, the gap-filled procedure was used only when absolutely necessary to



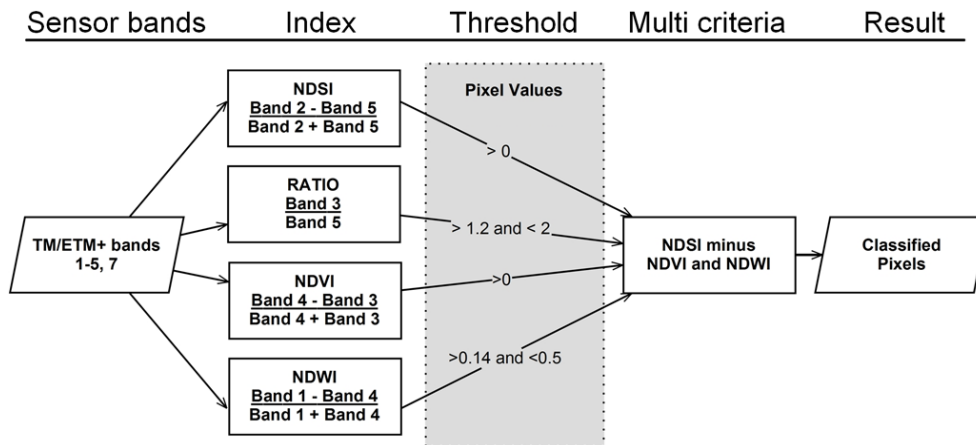


**Fig. 2.** An example of the multi-criteria analysis for the Landsat 5 TM and Landsat 7 ETM+ scenes. For the latter the corresponding values were 1999 NDSI  $> 0$ , NDWI  $> 0.16$  and  $< 0.45$ , and NDVI  $< 0$ , and for 2011 NDSI  $> 0$ , NDWI  $> 0.15$  and  $< 0.5$ , and NDVI  $< 0$ . Band ratios were the same for all scenes. The analysis was carried out using the tool BandMath in ENVI<sup>TM</sup>.

minimize misclassification. All imagery and features were projected in WGS84, UTM Zone 24N, and the selected scenes were radiometrically calibrated using the Landsat calibration tool in ENVI<sup>TM</sup> software package (<http://www.itvis.com/ProductServices/ENVI.aspx>), converting the band values to “At Surface Reflectance”. The individual bands (TM and ETM+ bands 1–5, and 7, and MSS bands 2–7) were standardized using the ENVI<sup>TM</sup> Dark Subtract (DS) tool before ratio and indices were calculated. Standard pixel errors associated with the different scenes and sensors were  $\pm 30$  m (MSS),  $\pm 15$  m (TM),  $\pm 15$  m (7.5 m panchromatic) (ETM+), and  $\pm 30$  m (ASTER GDEM v2). The error associated with the ASTER GDEM v2 is expected to be  $\sim \pm 12.9$  m vertically (Table 1); however, larger uncertainty might occur vertically in steep terrain and in areas of poor contrasts (Tachikawa et al., 2011).

The image co-registration errors associated with the individual sensor types were 39.86 m (MSS-TM) and 11.33 m (TM-ETM+) (due to the root mean square, RMS), based on 27 near-sea ground control points (GCP) for each sensor type (Table 1). The supervised classification process used for the 1986, 1999, and 2011 scenes was based on a multi-criteria analysis involving the calculation of a set of indices (Fig. 2): normalized difference snow index (NDSI; Dozier and Warren, 1982); normalized difference water index (NDWI; Gao, 1996); NDVI (normalized difference vegetation index; Rouse et al., 1973); and RATIO bands 3/5 TM/ETM+. The RATIO was used in reference due to better performance than the NDSI index in mountainous areas (like the Ammassalik region) capturing ice and snow covered areas influenced by shadows and debris (Paul, 2004). The NDVI was used to filter out vegetation and the NDWI to identify and filter out lakes in the margin area of the GrIS and GIC. The resulting classifications were converted to (1) polygon files and cleaned up manually in ESRI<sup>TM</sup> ArcMap by

visual inspection, (2) poly-line files for visual presentation; and (3) point shapes with a 30-m distribution along the lines and used to examine the mean and median center of the margin distribution for each year. The 1972 scene was not included in the classification process since the spectral bands of the Landsat 1 MSS sensor used different wavelengths and band distribution than both the TM and ETM+ sensors, and thus is not eligible for this type of snow/ice classification. The raw model precision errors for each year compared with the cleaned up classification were found to be 5.2% (overestimate by 3.4% due to snow patches and underestimate by 1.8% due to heavily debris covered terrain and shadow regions) overall, with 1999 being the most troublesome year (Table 1).

The GrIS and GIC margin positions were digitized for each of the years, and the distance between the margins was calculated at the dominant glacier’s flow direction using a centerline method approach. The expected errors related to the classification and determination of the glacier margin positions are shown in Table 1.

The selection of the 35 GIC was randomly chosen: (1) following the regional distribution due to size, aspect, and elevation, and (2) trying to avoid area where the 2011 scene SLI failure could influence the classification. The 2007 scene gap-fill was used in reference only when absolutely necessary.

The Landsat-derived 2011 (14 August) GIC margin was validated for the Mittivakkat Gletscher against the 2011 (9 August) GPS-observed margin; only the lower elevated margin of the Mittivakkat Gletscher was observed. The location of the observed margin was obtained from portable single-frequency GPS measurements having a relative uncertainty of about  $\pm 5$  m (Mernild et al., 2011a). Overall, the RMS difference between the 2011 satellite and GPS margin observations was 22 m (Fig. 3 and Table 1).

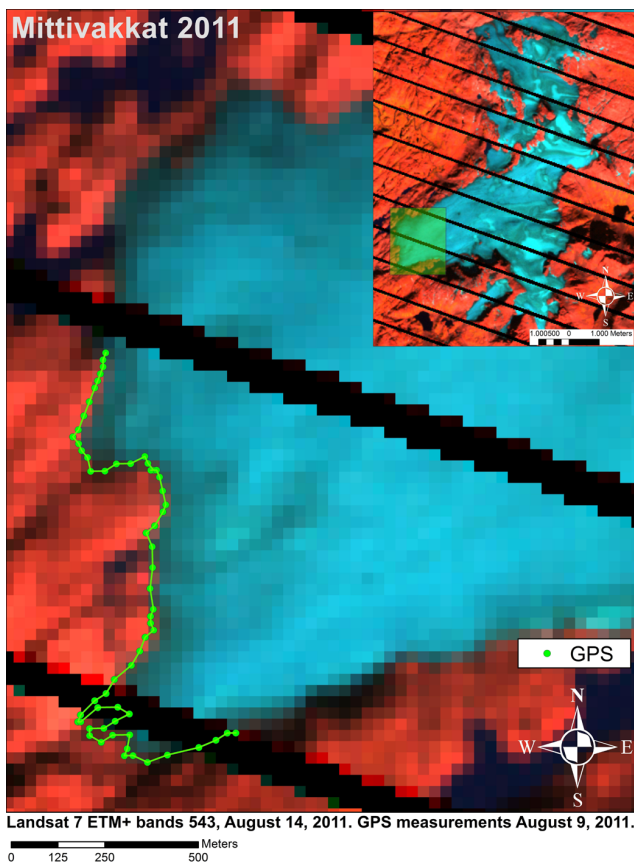


**Fig. 3.** A comparison between the Landsat-derived Mittivakkat Gletscher margin and the observed margin based on portable GPS observations (green line with dots) for August 2011. The inset figure indicates the location of the observed margin at Mittivakkat Gletscher. The oblique black lines are due to the SLI malfunction.

The observed meteorological data, air temperature and precipitation were obtained from the Danish Meteorological Institute (DMI) station in Tasiilaq for 1972–2011, located less than 10 km from the Sermilik Fjord outlet, and reconstructed ocean subsurface water temperatures at 400 m depth in the Irminger Sea were used as a proxy for the variability of the subsurface warm Atlantic water in the Sermilik Fjord (Johannessen et al., 2011).

### 3 Results and discussion

#### 3.1 Marine-terminating glaciers

For the Ammassalik region, the 21 observed marine-terminating glaciers, on average for the survey period 1972–2011, receded at a net rate of  $0.053 \pm 0.113 \text{ km yr}^{-1}$  (here and below, the  $\pm$  standard deviations are included) with a median of  $0.025 \text{ km yr}^{-1}$  (Table 2). For 1999–2011, the mean net recession rate was  $0.098 \pm 0.171 \text{ km yr}^{-1}$ , which is in accordance with the mean net recession rate of  $0.11 \text{ km yr}^{-1}$

for 210 GrIS marine-terminating outlet glaciers (2000–2010) determined by Howat and Eddy (2011). For the sub-periods the fraction of marine-terminating glaciers in net recession increased from 57 % (1972–1986), 86 % (1986–1999) to 100 % (1999–2011), indicating complete marine-terminating glacier retreat for the Ammassalik region since 1999. For Southeast Greenland, Howat and Eddy (2011) estimated an increasing fraction of net retreat from 55 % (1972–1985), 73 % (1985–2000) to 89 % (2000–2010) ( $n = 38$ ). For the last period, this was almost in the same order of magnitude as the fraction of glacier recession determined for the Ammassalik region.

On an individual glacier scale, Midgaard, Helheim, Tasis Sassik Fjord, Heims, and Fenris had (as listed) the five highest net recession rates of  $0.365 \text{ km yr}^{-1}$  (this equals a net frontal recession of 14.3 km),  $0.155 \text{ km yr}^{-1}$  (6.0 km),  $0.130 \text{ km yr}^{-1}$  (5.1 km),  $0.075 \text{ km yr}^{-1}$  (2.8 km), and  $0.065 \text{ km yr}^{-1}$  (2.6 km), respectively (Fig. 4) for 1972–2011. All five glaciers are outlets from the GrIS, receiving ice from the interior of the ice sheet, having the largest GrIS catchment areas within the Ammassalik region and probably also the greatest ice thickness and therefore more susceptible to enhanced submarine melting via warmer water intruding beneath the ice, than the other observed outlet glaciers (due to their shallow depth of the glacier bases). Overall for the Ammassalik region, 80 % of the marine-terminating glaciers receded at rates less than  $0.050 \text{ km yr}^{-1}$  (Fig. 4), and Thomas et al. (2009) suggested that outlet glaciers without deep beds are changing far more slowly. The mean net recession rates during the period 1972–2011 for the glaciers Midgaard, Helheim, and Fenris compared well with the recession rates determined by Howat and Eddy (2011) for 1972–2010.

For the sub-periods, the 21 observed marine-terminating glaciers had mean frontal recession rates of  $0.031 \pm 0.056$  and  $0.029 \pm 0.060 \text{ km yr}^{-1}$  for 1972–1986 and 1986–1999, respectively (significantly similar, 97.5 % quartile). For 1999–2011, the mean recession rate increased to  $0.098 \pm 0.171 \text{ km yr}^{-1}$ , which was significantly higher (95 % quartile) than the two previous sub-periods, and about 3.2 times higher than the 1972–1986 rate. The same trend occurred for the median recession rates, where the 1999–2011 rate was 5.4 times higher than for 1972–1986 (Table 2). The high mean rates for 1999–2011 were mainly due to the recession at the glaciers Midgaard, Helheim, F5, and Fenris, whereas both Midgaard Gletscher and Helheim Gletscher were outside the 75 % percentiles (Fig. 5a). Also, for 1972–1986 and 1986–1999 Midgaard Gletscher and Helheim Gletscher were considered as outliers. The maximum net advance rate in the dataset was observed for Helheim Gletscher of  $0.100 \text{ km yr}^{-1}$  (1986–1999). A maximum net recession rate was observed for Midgaard Gletscher of  $0.700 \text{ km yr}^{-1}$  (1999–2011) (Figs. 1 and 5a). For the Ammassalik region in general, the mean recession rate has increased since 1972 (Fig. 5a). Howat and Eddy (2011), for the GrIS outlet glaciers, noted a transition from stable and

**Table 2.** Frontal position change rate statistics for the period 1972–2011 for the GrIS marine-terminating glaciers in the Ammassalik region, mean annual air temperature and precipitation anomaly from the DMI meteorological station in Tasiilaq, and mean annual reconstructed ocean water temperature anomaly at 400 m depth in the Irminger Sea (Johannessen et al., 2011).

Range	Number of GrIS marine-terminating glaciers	Mean annual air temperature anomaly and standard deviation ( $^{\circ}\text{C yr}^{-1}$ )	Mean annual precipitation anomaly and standard deviation (mm w.e. $\text{yr}^{-1}$ )	Mean annual reconstructed ocean water temperature anomaly and standard deviation ( $^{\circ}\text{C yr}^{-1}$ )	Glacier fraction in net retreat (%)	Mean change rate and standard deviation ( $\text{km yr}^{-1}$ )	Median change rate ( $\text{km yr}^{-1}$ )	Maximum advance rate ( $\text{km yr}^{-1}$ )	Maximum recession rate ( $\text{km yr}^{-1}$ )
1972–1986	21	$-0.63 \pm 0.78$	$69 \pm 212$	$-0.12 \pm 0.30$	57	$-0.031 \pm 0.056$	-0.007	0.005	-0.223
1986–1999	21	$-0.33 \pm 0.63$	$-17 \pm 238$	$-0.06 \pm 0.49$	86	$-0.029 \pm 0.060$	-0.009	0.100	-0.187
1999–2011	21	$1.08 \pm 0.59$	$-62 \pm 163$	$0.23 \pm 0.43^*$	100	$-0.098 \pm 0.171$	-0.038	-0.003	-0.758
1972–2011	21	–	–	–	100	$-0.053 \pm 0.113$	-0.025	0.100	-0.758

\* Data are missing from 1995 and 1996, and only present until 2009.

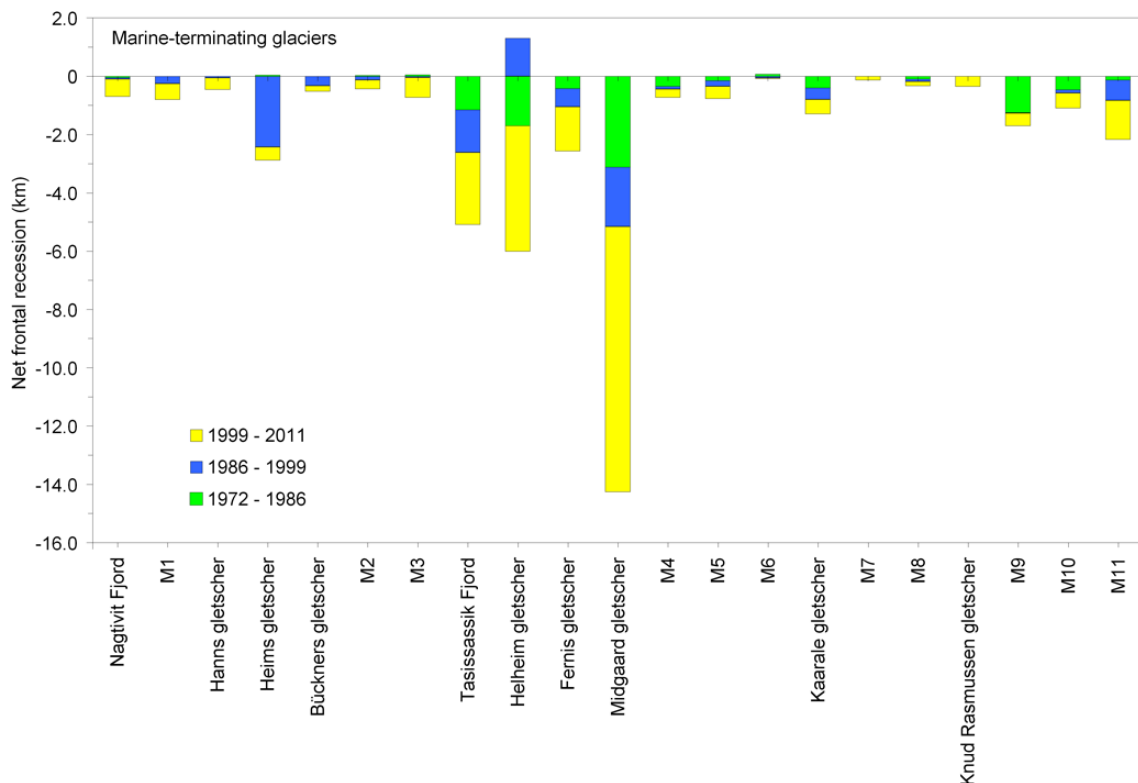


**Fig. 4.** Satellite-derived net frontal recession for the 21 marine-terminating glaciers in the Ammassalik region for the sub-periods 1972–1986 (green), 1986–1999 (blue), and 1999–2011 (yellow). For glacier locations, see Fig. 1.

small fluctuations in glacier frontal positions (1972–1985) to moderately widespread recession in the southeast and western parts of GrIS (1985–2000), followed by an accelerated net recession in all regions of the ice sheet (2000–2010).

Since 1972, the 21 marine-terminating glaciers showed a cumulative net area loss of  $281 \text{ km}^2$ , with mean annual

area loss rates of  $7.2 \text{ km}^2 \text{ yr}^{-1}$  (Fig. 6). The largest individual marine-terminating area loss occurred at Midgaard Gletscher of  $130 \text{ km}^2$  (equal to 46% of the cumulative net area exposure in the Ammassalik region), followed by Helheim Gletscher of  $67 \text{ km}^2$  (equal to 24%). About 70% of the glaciers had an area loss less than

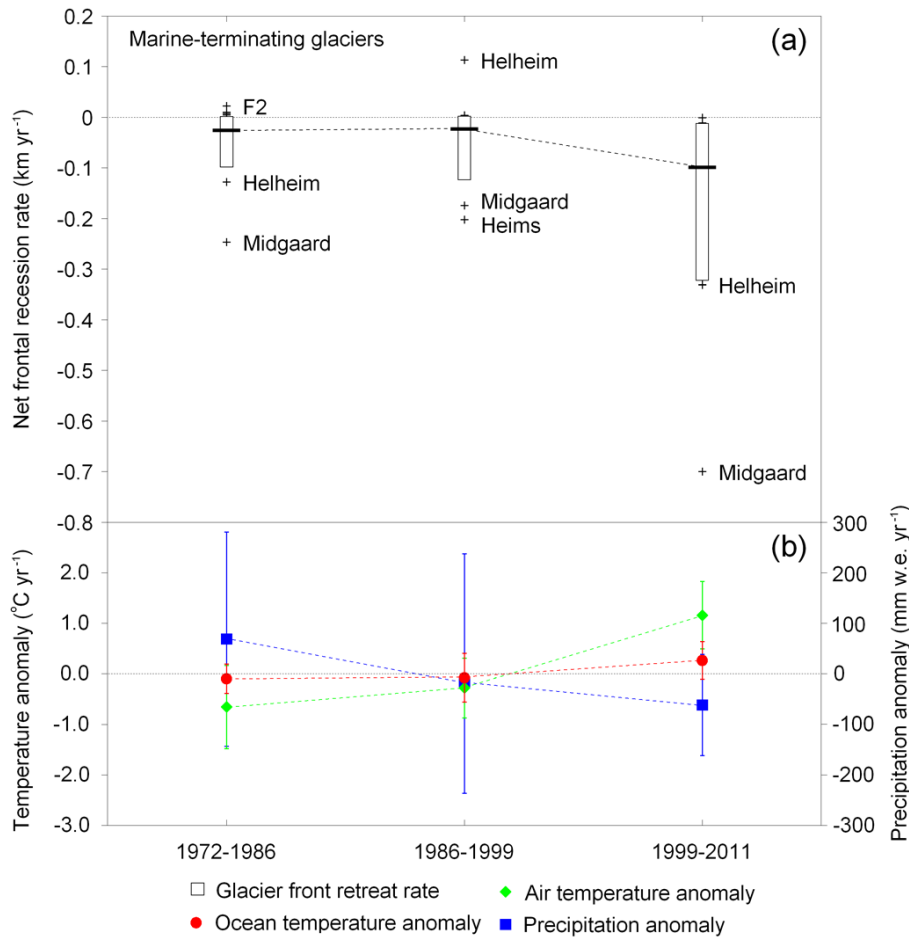


**Fig. 5.** (a) Box plots of frontal-position change for the sample 21 marine-terminating glaciers in the Ammassalik region with measurements in each of the 1972–1986, 1986–1999, and 1999–2011 survey periods. The edges of the boxes denote 25 % and 75 % percentiles and the vertical line mean. Data points outside this range are considered outliers and are plotted as crosses and labeled; (b) mean annual air temperature anomaly (observed at the DMI meteorological station in Tasiilaq), mean annual ocean water temperature anomaly at 400 m depth in the Irminger Sea (Johannessen et al., 2011), mean annual precipitation anomaly (uncorrected) (observed at the DMI meteorological station in Tasiilaq) and standard deviations are shown.

4 km<sup>2</sup> during the period 1972–2011. Also, the 21 observed marine-terminating glaciers had a trend towards lower annual area loss rates (Fig. 6): for the sub-periods 1972–1986, 1986–1999, and 1999–2011, the mean area loss rates were 8.5 km<sup>2</sup> yr<sup>-1</sup> (equal to 118 km<sup>2</sup> and 0.40 km<sup>2</sup> yr<sup>-1</sup> glacier<sup>-1</sup>), 6.8 km<sup>2</sup> yr<sup>-1</sup> (88 km<sup>2</sup> and 0.32 km<sup>2</sup> yr<sup>-1</sup> glacier<sup>-1</sup>), and 6.3 km<sup>2</sup> yr<sup>-1</sup> (75 km<sup>2</sup> and 0.30 km<sup>2</sup> yr<sup>-1</sup> glacier<sup>-1</sup>), respectively (Fig. 6), indicating decreasing area loss rates since 1972. This is probably because the side fjords to the Sermilik Fjord decreased in width the further up the fjord the marine-terminating moves. When looking at the mean GrIS outlet glaciers (Midgaard, Helheim, Tasis Sassik Fjord, Heims, and Fenris (*n* = 5)) and the non-GrIS outlet glaciers (*n* = 16), they both had a mean trend towards lower annual area loss rates (Fig. 6); however, the absolute mean area loss rates were higher for the GrIS outlet

glaciers. This suggests that outlet glaciers without deep beds are retreating far more slowly.

Box and Decker (2011) measured area change at 39 of the widest GrIS marine-terminating glaciers based on Moderate Resolution Imaging Spectroradiometer (MODIS) between 2000 and 2010, including the glaciers Midgaard, Helheim, and Fenris. Overall for the 39 glaciers, they exposed a cumulated net area of 1368 km<sup>2</sup>. On individual glacier scale, the observed area loss rates for the glaciers Midgaard, Helheim, and Fenris were -2.9, -2.0, and -0.4 km<sup>2</sup> yr<sup>-1</sup> for 1999–2011, respectively, compared to -3.6, -2.5, and -0.3 km<sup>2</sup> yr<sup>-1</sup> for 2000–2010 determined by Box and Decker (2011). The Landsat-derived area loss rates were in the same range as Box and Decker (2011) (97.5 % quartile), and both studies indicated that the clearest pattern of area exposure happened at the Midgaard Gletscher in the Sermilik

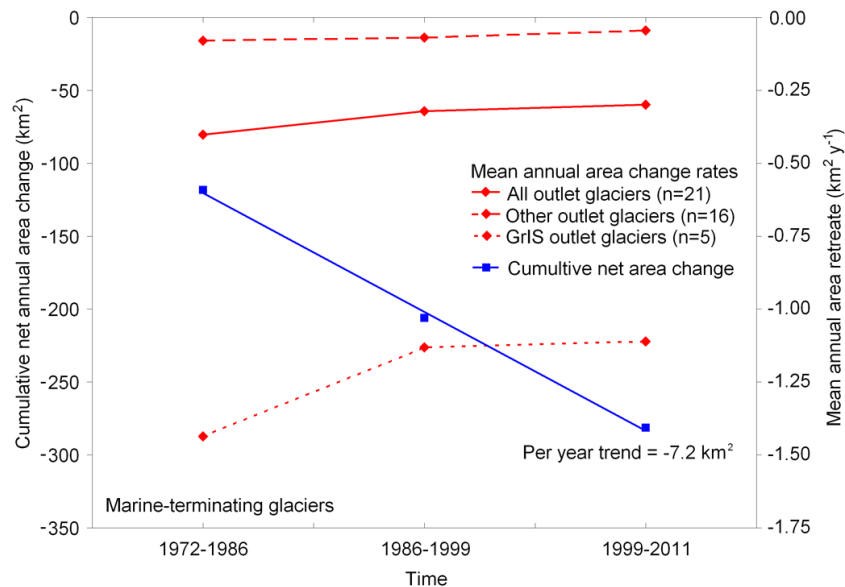


**Fig. 6.** Mean annual area change rates and cumulative net area change for all 21 marine-terminating glaciers, the five GrIS outlet glaciers, and other sixteen outlet glaciers for the Ammassalik region 1972–2011.

Fjord, even compared with the entire Southeast Greenland according to Box and Decker (2011).

Several authors (e.g., Holland et al., 2008; Murray et al., 2010; Straneo et al., 2010; Andresen et al., 2011) suggest that ocean warming and warm subsurface waters caused large changes to submarine melting, marine-terminating glacier frontal positions and thinning, reduced resistive stress and ice discharge acceleration. In recent decades the 21 marine-terminating glaciers in the Ammassalik region have experienced increasing frontal recession rates and decreasing area exposure rates that are synchronous with both increasing mean annual air temperature (MAAT) ( $\sim 0.06^{\circ}\text{C yr}^{-1}$ , significant at  $p < 0.01$ , where  $p$  is level of significance) from the DMI meteorological station in Tasiilaq and reconstructed annual ocean water temperature ( $\sim 0.12^{\circ}\text{C yr}^{-1}$ , significant  $p < 0.025$ ; at 400 m depth in the Irminger Sea penetrating into the Sermilik Fjord and exposing the lower part of glaciers such as Helheim and Fenris to warm waters with temperatures up to  $4^{\circ}\text{C}$ ; Johannessen et al., 2011) (Figs. 5b and 6). The mean glacier retreat was more widespread for 1999–2011 (approximately the first decade of the 21st century) than for the earlier sub-periods (1972–1986 and 1986–1999). The observed accelerated recession of the marine-terminating glaciers in the Ammassalik region coincided with the onset of a warming trend in the sub-polar North Atlantic Ocean (Myers et al., 2007; Straneo et al., 2010), likely initiated by the influx of warmer deep water originating in the Irminger Sea (Holland et al., 2008; Hanna et al., 2009). This supports the hypothesis that ocean warming associated with shifts in the Irminger and East Greenland currents caused increasing submarine melt at the ice-ocean interface, and retreat, thinning, and acceleration as the

loss of resistive stress at the terminus recedes (Joughin et al., 2010). However, oceanographic studies have demonstrated that although subtropical ocean waters reach glacial fjords in Southeast Greenland, there is no proof that they come into direct contact with glaciers (Walsh et al., 2012). Mechanisms driving the circulation of warmer North Atlantic waters are, however, still not well understood (e.g., Straneo et al., 2010). On the other hand, Johannessen et al. (2011) have argued (due to statistical correlation) that, based on annual frontal positions of Helheim Gletscher, 24 % of the ice-front fluctuations could be accounted for by ocean temperatures and 56 % by air temperatures, even though changes in frontal positions were influenced by a number of local factors, e.g., up-glacier ice dynamics and bed geometry. Overall, several studies using a range of different methods show that GrIS marine-terminating glaciers recede and mass loss might be influenced by atmospheric and probably more importantly by oceanographic impacts, especially in the southeastern part of the GrIS (Luthcke et al., 2006; Velicogna and Wahr, 2006; van den Broeke, 2009; Velicogna, 2009).

### 3.2 The land-terminating ice sheet

In Fig. 7 the GrIS land-terminating margin and changes within the Ammassalik region are illustrated for 1986, 1999, and 2011. Since 1986 the GrIS area has decreased in size within the Ammassalik region from  $1166\text{ km}^2$  (1986),  $1153\text{ km}^2$  (1999) to  $1124\text{ km}^2$  (2011), indicating a net area loss of 4 % (equal to an area exposure rate of  $0.15\% \text{ yr}^{-1}$ ) (Table 3). As such for the land-terminating GrIS, the area exposure rates were  $1.0\text{ km}^2 \text{ yr}^{-1}$  ( $13\text{ km}^2$ ) and  $2.4\text{ km}^2 \text{ yr}^{-1}$  ( $29\text{ km}^2$ ) for the sub-periods 1986–1999 and 1999–2011,



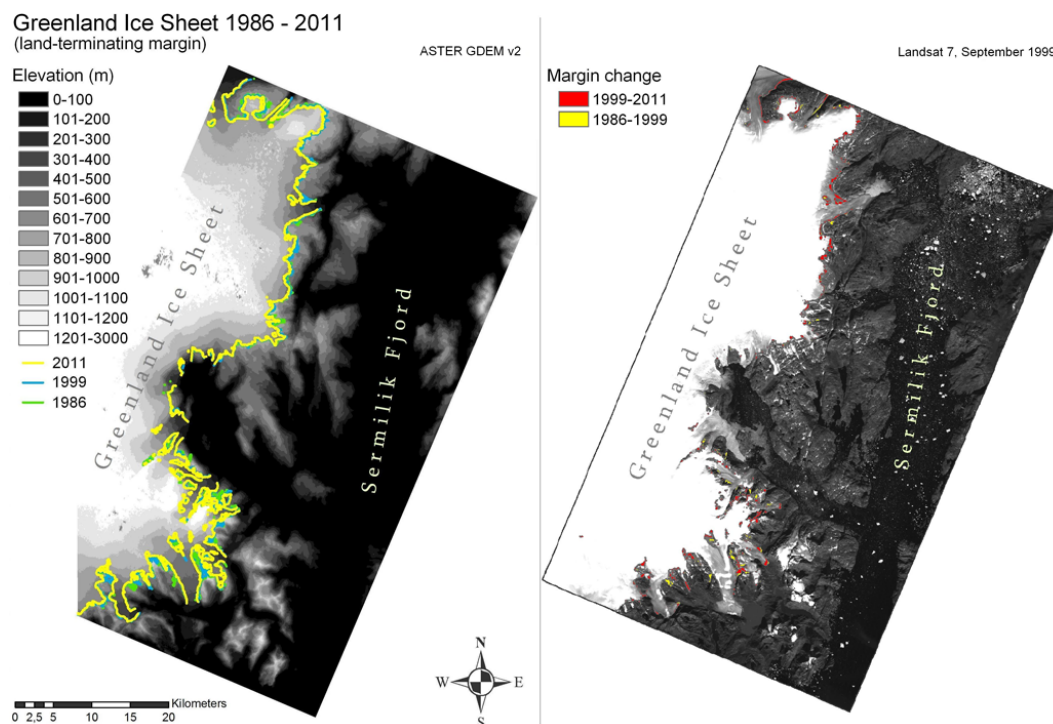


**Fig. 7.** The location of the GrIS land-terminating margin for the survey years 1986 (green), 1999 (blue), and 2011 (yellow) in the Ammassalik region, and the marginal changes between the survey years. The topography has black and gray shaded colors (source: ASTER GDEM v2 and Landsat 7).

**Table 3.** GrIS land-terminating margin-position change rate statistics for each survey year and period for the Ammassalik region.

Years	GrIS margin length for the highlighted section in Ammassalik region (km)	GrIS area for the section for the highlighted section in Ammassalik region (km <sup>2</sup> )	Area in percentage related to the 1986 area (%)
1986	686	1166	100
1999	589	1153	99
2011	544	1124	96
	GrIS mean margin change rate (km yr <sup>-1</sup> )	GrIS mean margin change (km)	
1986–1999	−0.010	−0.127	
1999–2011	−0.026	−0.316	
1986–2011	−0.018	−0.443	

respectively, indicating an increasing trend in area exposure since 1986. The land-terminating area exposure was unevenly distributed for the GrIS (Fig. 7). A division of the ice sheet into 100-m elevation bands indicated that the largest GrIS area recession occurred at the elevation between 701–800 m a.s.l. for both survey periods, with rates of 0.22 km<sup>2</sup> yr<sup>-1</sup> (1986–1999) and 0.50 km<sup>2</sup> yr<sup>-1</sup> (1999–2011) (Figs. 7 and 8). Along with this area reduction, the GrIS land-terminating margin decreased ~20 % in total length from 686 km (1986) to 544 km (2011), because the 2011 margin

was less curved – had fewer land-terminating outlets – than in 1986 and 1999. When the area recession is compared to changes in margin length, the largest GrIS area length recession ratio occurred at the elevation >800 m a.s.l., most pronounced for the period 1999–2011 (Fig. 8). The spatial area recession seems to be highly influenced by local topography, hypsometry, shadow effects, climate variability, glacier dynamic processes within the GrIS, increasing ELA elevation (the ELA is the spatially averaged elevation of the equilibrium line, defined as the set of points on the glacier surface

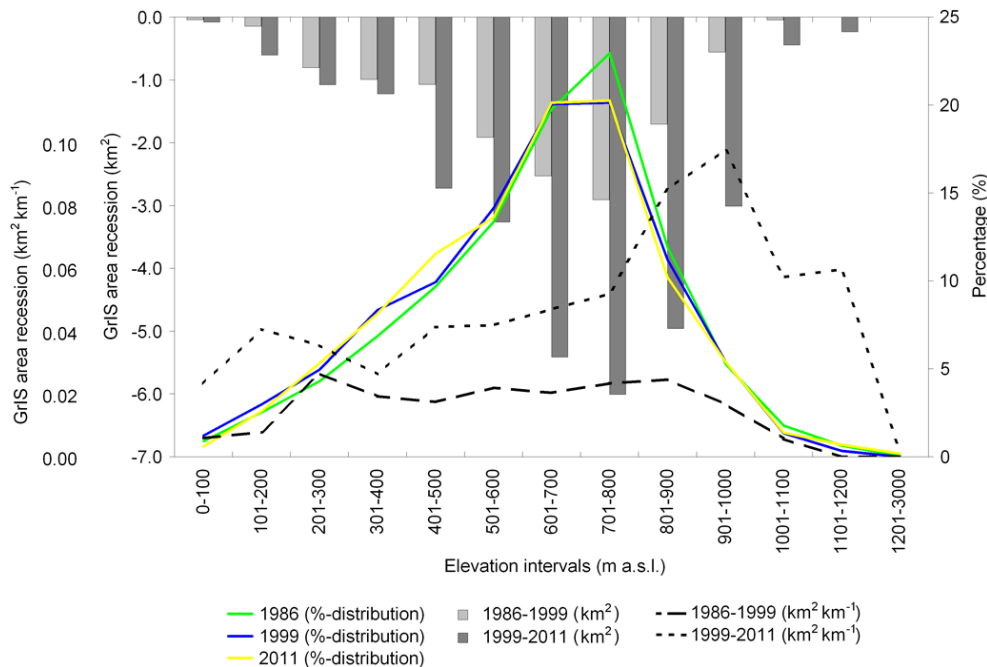


**Fig. 8.** GrIS land-terminating area recession rates for different elevation intervals, Ammassalik region, for the sub-periods 1986–1999 (light gray) and 1999–2011 (dark gray), area recession rate related to changes in margin length for 1986–1999 (black dashed line, long dashed) and 1999–2011 (black dashed line, short dashed), and the percentage of margin elevation for the different elevation intervals for the years 1986 (green), 1999 (blue), and 2011 (yellow) (see Fig. 7 for location of the margin).

where the net mass balance is zero), and the margin elevation distribution, where approximately 20 % of the margin was located between 701–800 m a.s.l. (1986–2011) (Fig. 8).

The mean net recession rate of the GrIS land-terminating margin was  $0.018 \pm 0.009 \text{ km yr}^{-1}$  (equal to a net recession of 0.443 km) for 1986–2011, comprised of a mean recession rate of  $0.010 \text{ km yr}^{-1}$  (0.127 km) for 1986–1999, and  $0.026 \text{ km yr}^{-1}$  (0.316 km) for 1999–2011 (Table 3). This land-terminating recession rate for the GrIS over this period of 1986–2011 is about three times lower the mean rate of recession of the marine-terminating GrIS. Sohn et al. (1998) measured recession rates of the GrIS land-terminating margin near Jakobshavn Isbræ, West Greenland, of  $0.016\text{--}0.040 \text{ km yr}^{-1}$ , averaging  $0.026 \text{ km yr}^{-1}$  for 1962–1992. This may suggest that the recession rate can be expected to be within this order of magnitude along many parts of the GrIS land-terminating margin.

Net GrIS land-terminating marginal recession for the Ammassalik region, including increasing area exposure, occurred for the period 1972–2011, during a period of increasing MAAT ( $\sim 0.06 \text{ }^\circ\text{C yr}^{-1}$ ) and decreasing annual precipitation ( $-7.0 \text{ mm water equivalent (w.e.) yr}^{-1}$ , significant at  $p < 0.025$ ; Fig. 5b) – probably heading towards future warmer and drier conditions in the region (Mernild et al., 2011a). The average increase in MAAT generally favors surface ablation (evaporation, sublimation, and melt), and an earlier start of the ablation season by decreasing the “cold

content” of the snowpack (Bøggild et al., 2005; Mernild et al., 2011a), whereas a decrease in annual precipitation may lead to earlier exposure of glacier ice melt and summer firn surface of previous years (having a lower albedo than fresh snow, promoting increased solar absorption). Therefore, the combination of increasing air temperature and decreasing precipitation is likely to increase ablation and GrIS margin thinning and recession, and if MAAT and precipitation continue to follow these trends, then it is expected that the GrIS land-terminating margin will continue its recession, leading to increased area exposure. However, changes in the hypsometric distribution along the GrIS margin may influence recession rates on a decadal timescale.

### 3.3 Land-terminating glaciers and ice caps

Peripheral to the GrIS, 35 land-terminating GIC were chosen (Fig. 1) to assess area exposure for the Ammassalik region for 1986, 1999, and 2011 based on Landsat imagery. In Fig. 9 the size, mean elevation, and aspect distribution are illustrated for the 35 GIC, indicating that the majority of the GIC is below  $5 \text{ km}^2$ , located between 400–800 m a.s.l., and facing south, west, and northwest. The GIC are non-surging glaciers located south of the East Greenland surge cluster (Jiskoot et al., 2003). For the Ammassalik region, the observed GIC indicated a relative mean area exposure of  $4 \pm 18 \%$  for 1986–1999, and  $27 \pm 24 \%$  for 1986–2011, which is equal to a mean net area exposure rate of  $0.04 \text{ km}^2 \text{ yr}^{-1}$  per glacier

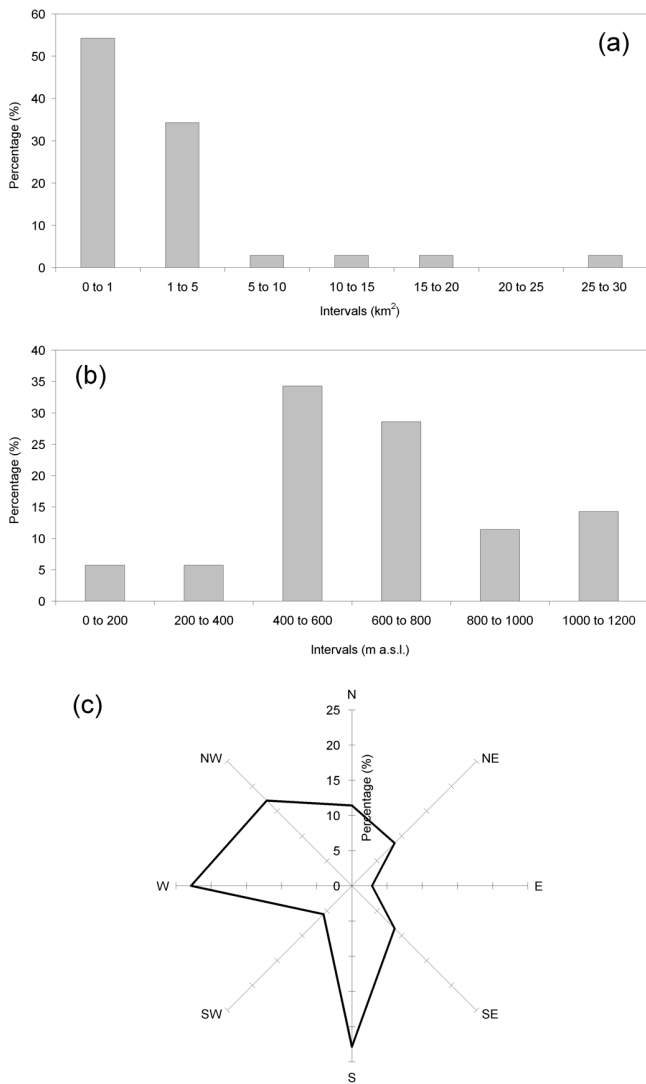


**Fig. 9.** Distribution of the 35 observed land-terminating GIC: (a) size; (b) mean elevation; and (c) aspect.

(or  $1.07 \text{ yr}^{-1}$  per glacier) (Fig. 10a and b). For small GIC ( $n = 32$ ;  $< 10 \text{ km}^2$ ), the net area exposure rate was on average  $1.08 \text{ \% yr}^{-1}$ , and for large GIC ( $n = 3$ ;  $> 10 \text{ km}^2$ ) was a comparable rate of  $0.81 \text{ \% yr}^{-1}$ . For 1986–1999, eleven individual GIC (around 30%, mostly below  $2 \text{ km}^2$ ) had a net increase in area, while for 1986–2011 there were only three GIC all facing towards the west (L11, L14, and L9; and around 10% – all less than  $1 \text{ km}^2$ ) (Fig. 10b). As illustrated in Fig. 10c, GIC having a mean elevation height higher than  $705 \text{ m a.s.l.}$  had in general a net area increase from 1986 to 1999, while glaciers with a mean elevation lower than  $705 \text{ m a.s.l.}$  had a net area decrease (based on the significant linear regression;  $r^2 = 0.38$ ;  $p < 0.01$ ). The height of  $705 \text{ m a.s.l.}$  was around the observed average ELA of  $690 \text{ m a.s.l.}$  at the Mittivakkat Gletscher in the late 1990s (Knudsen and Hasholt, 2004; Mernild et al., 2011a; Table 2).

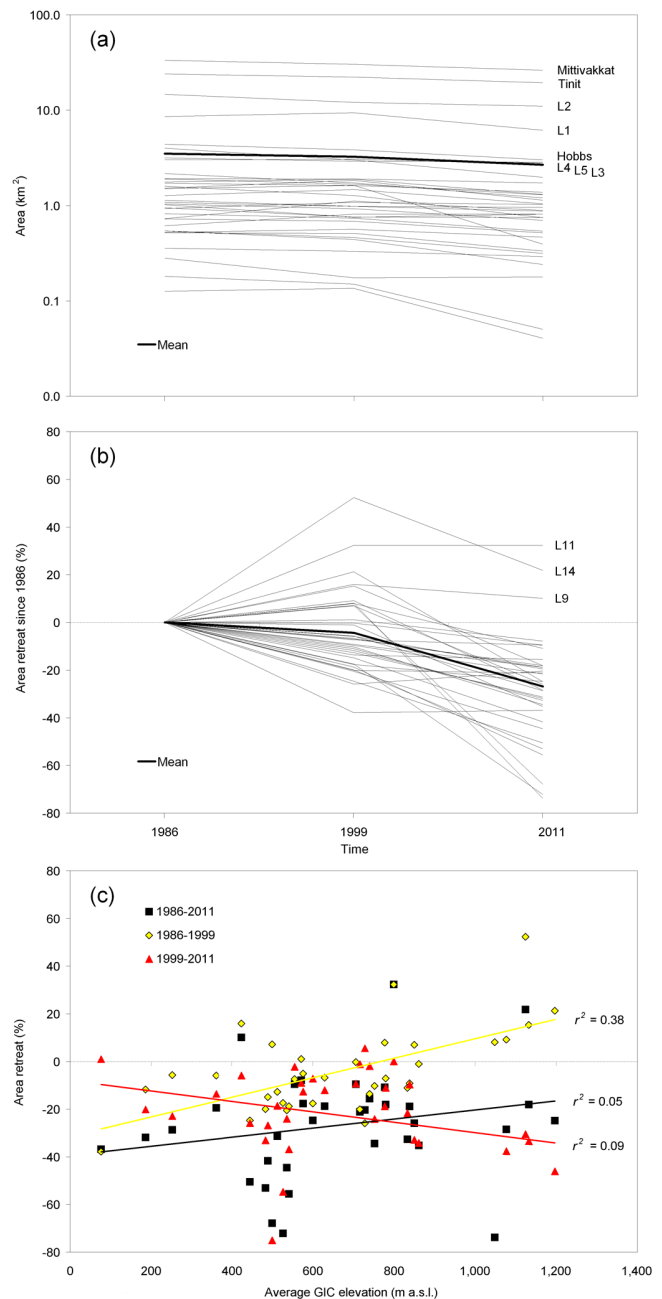


**Fig. 10.** (a) Land-terminating GIC area for the 35 observed GIC (Mittivakkat, Hobbs, Tinit, and L1–L32 glaciers) for 1986, 1999, and 2011 (the listed glaciers are illustrated as an example in Fig. 11); (b) relative GIC area change since 1986 (the named glaciers are the ones with area increase); and (c) relative GIC area change in relation to variations in mean elevation GIC height for 1986–1999, 1999–2011, and overall for 1986–2011.

For 1999–2011 the linear regression shown in Fig. 10c indicates the opposite trend for GIC in the Ammassalik region: an increase in area recession for GIC at high elevation ranges, and vice versa. This shift in trend occurred simultaneously with an increase in the average observed ELA for the

**Table 4.** Characteristics of land-terminating GIC L33–L37 in the Ammassalik region, which have melted away during the period 1986–2011 (see Fig. 1 for location of the doomed glaciers).

GIC	Minimum elevation (m a.s.l.)	Maximum elevation (m a.s.l.)	Mean elevation (m a.s.l.)	Aspect	Area 1986 (km <sup>2</sup> )	Area 1999 (km <sup>2</sup> )	Area 2011 (km <sup>2</sup> )
L33	507	792	634	E	0.178	0.050	0
L34	462	538	513	E	0.041	0.034	0
L35	846	910	893	W	0.036	0	0
L36	777	896	841	W	0.076	0.016	0
L37	1107	1145	1117	SW	0.018	0.029	0

Mittivakkat Gletscher to 750 m a.s.l. Overall for 1986–2011, the observed GIC faced a general net area loss that was highest at low elevations, and vice versa (based on the linear regression; Fig. 10c). However, as previously mentioned, three minor GIC (<1 km<sup>2</sup>) had a net area gain during this 25-yr period, indicating that glacier fluctuations may vary on local scales.

Since the GIC on average had a mean net area exposure rate of about 1 % yr<sup>-1</sup>, it may be expected that GIC in the Ammassalik region could melt substantially in the 21st century under ongoing climate change. For the period 1986–2011, there are examples of five glaciers that completely melted away: all located at different mean elevations within the region from 460 to 1110 m a.s.l., and with different aspects facing from east to west (Table 4). The recession seems therefore not to be limited to low elevated areas only, but more likely to occur for north-facing GIC. Also, in Fig. 11, examples of eight GIC are shown to illustrate the spatial changes in margin location from 1986 to 2011.

For the largest GIC – the Mittivakkat Gletscher (26.2 km<sup>2</sup> in 2011) – the area extent had diminished about 18 % since 1986 (lower than the mean GIC area exposure for the Ammassalik region of 27 ± 24 %). The terminus has retreated by 1.6 km (0.015 km yr<sup>-1</sup>) since the maximum extent of the Little Ice Age around 1900, by 1.3 km (0.017 km yr<sup>-1</sup>) since 1931 (Humlum and Christiansen, 2008; Mernild et al., 2011a), and by 0.3 km (0.013 km yr<sup>-1</sup>) since 1986. This is almost of the same magnitude as the GIC of the Ammassalik region's mean net recession rate of 0.010 ± 0.006 km yr<sup>-1</sup> (1986–2011), and of the regional GrIS land-terminating margin of 0.018 ± 0.009 km yr<sup>-1</sup> (see Sect. 3.2): the mean Ammassalik GIC land-terminating recession rate (1986–2011) is about five times lower than the mean GrIS marine-terminating recession rate. Also, for Mittivakkat Gletscher the annual mass balance measured continuously since 1995/1996 illustrates a 16-yr average mass loss of 0.970 ± 0.190 m w.e. yr<sup>-1</sup>, and an accumulation-area ratio (AAR: the ratio of the accumulation area to the area of the entire glacier) of ~0.10 (updated from Mernild et al., 2011a), indicating that the glacier is significantly out of balance with the current climate. The glacier will likely lose at least 70 % of its current area extent and 80 % of its volume even in the

absence of further climate changes (Mernild et al., 2011a). Since the initiation of the mass balance observation program in 1995/1996, Mittivakkat Gletscher had in 14 out of 16 yr a negative surface mass balance, while the general climatic trend in the region has been towards higher temperatures, less winter precipitation, and more negative glacier mass balances and continuous marginal recession (Fig. 11). Consecutive record glacier mass loss occurred for the years 2009/2010 and 2010/2011 of -2.16 and -2.45 m w.e. yr<sup>-1</sup>, respectively. The 2011 mass loss was not only the largest annual loss of volume in the history of the mass balance observational program, but also the largest annual loss in simulations of glacier mass balance changes back to 1898 (Mernild et al., 2008). The marginal recession, mass balance and AAR observations suggest that recent Mittivakkat mass losses, which have been driven largely by higher surface temperatures and less solid precipitation, are representative of the broader region, which includes the 35 observed GIC in Figs. 10 and 11 – glaciers of different sizes and elevation ranges. This is confirmed since the Mittivakkat Gletscher net area exposure rate closely follows the average rates for the Ammassalik region.

Glacier fluctuations and area exposure have been studied in other parts of Greenland. North of the Ammassalik region, in central East Greenland (68–72° N) land-terminating GIC peripheral to the GrIS have receded at a mean rate of 0.010 km yr<sup>-1</sup> for a wide range of glacier sizes (2002–2009) (Kargel et al., 2012). Also, on Disko Island in West Greenland, Yde and Knudsen (2007) estimated mean GIC terminus retreat rates of 0.008 km yr<sup>-1</sup> for non-surgingly GIC, and 0.020 km yr<sup>-1</sup> for quiescent phase surge-type GIC, reflecting a higher non-climatic-driven recession rate after glacier surges. These studies are in accordance with the findings for the Ammassalik region and indicate that the current mean recession rate for GIC in Greenland (probably excluding North Greenland where no data are currently available) is likely to be on the order of 0.008–0.010 km yr<sup>-1</sup>.

#### 4 Summary and conclusion

The satellite observations show net glacier recession since 1972 for the Ammassalik region for all glacier types and sizes, both at the marine-terminating and land-terminating



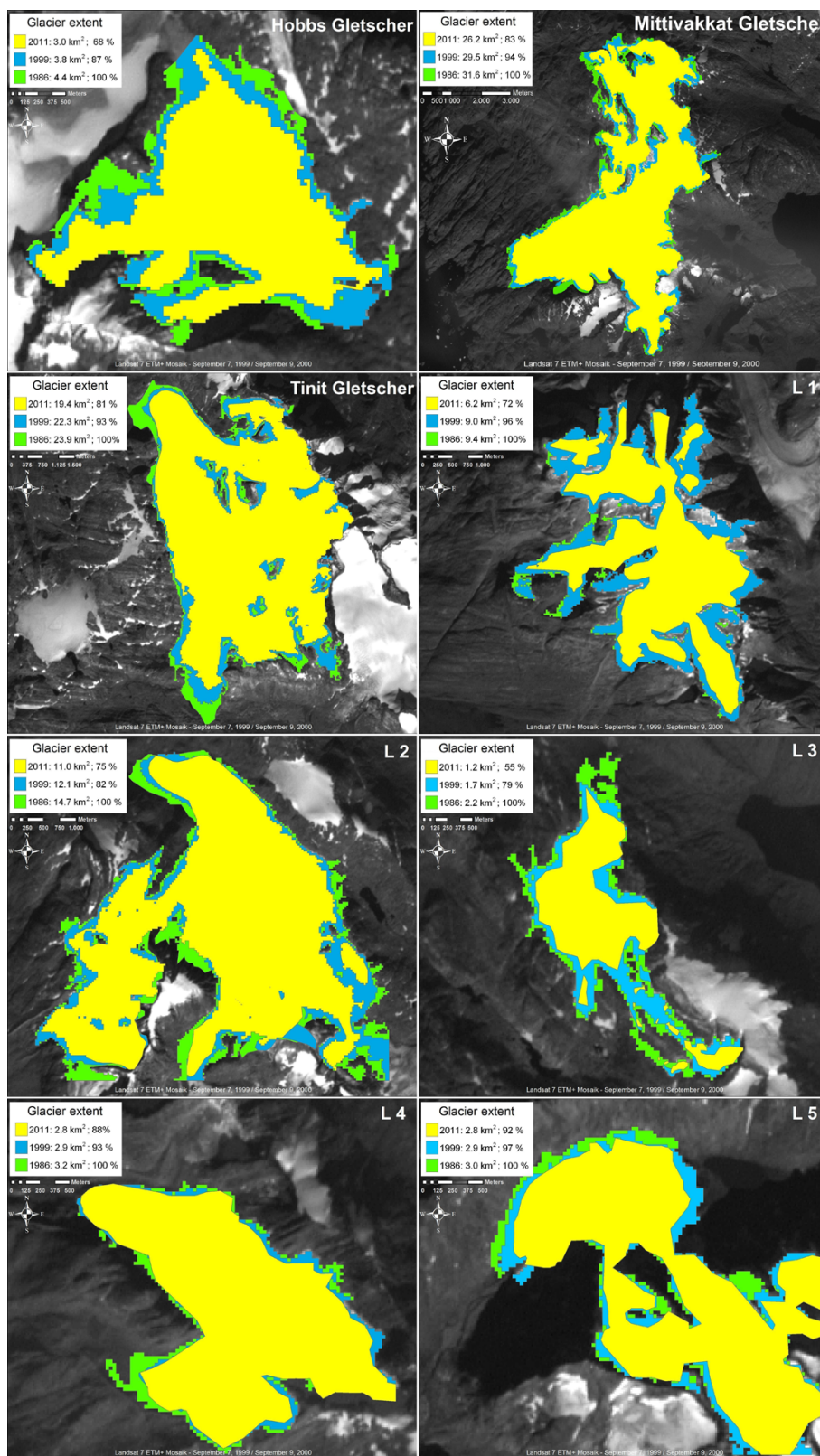


**Fig. 11.** The margin location of eight land-terminating GIC (peripheral to the GrIS) in the Ammassalik region: Hobbs, Mittivakkat, Tinit, and L1–L5 glaciers for the survey years 1986 (green), 1999 (blue), and 2011 (yellow) estimated from Landsat images. The location of the individual glaciers is shown in Fig. 1 (source: Landsat 7 ETM+ Mosaik, 7 September 1999/9 September 2000).



GrIS, and land-terminating GIC. However, the land-terminating GrIS and GIC reflect slower area exposure rates than the faster marine-terminating outlet glaciers. This could likely be due to a combination of effects, as the marine-terminating GrIS was influenced by the onset of a sea-water warming trend in the North Atlantic Ocean (Myers et al., 2007; Straneo et al., 2010), and by atmospheric impacts from regional trends in MAAT and precipitation, while GIC were only influenced by the latter. For the marine-terminating GrIS outlet glaciers the mean annual area exposure rate has decreased since 1972, whereas it has increased for the land-terminating GrIS margin since 1986, even though both parts of the GrIS have undergone substantial area changes in the past decades. The observed land-terminating GrIS and GIC indicate a net area recession of 4 % (equal to an area exposure rate of  $0.15 \text{ \% yr}^{-1}$ ) and  $27 \pm 24 \text{ \%}$  (around  $1 \text{ \% yr}^{-1}$ ), respectively, and margin recession rates of  $0.018 \pm 0.009$  and  $0.010 \pm 0.006 \text{ km yr}^{-1}$ . These mean net margin recession rates are about three to five times lower than the GrIS marine-terminating margin rates. If these GIC recession trends were extrapolated, it would indicate that a substantial amount of the GIC in the Ammassalik region might melt away within the 21st century under ongoing climate warming. So far, five GIC in the Ammassalik region have melted away since 1986.

**Acknowledgements.** The authors thank Matthew Hecht, Mauri Pelto, and the anonymous reviewers for their insightful review of this paper. We also thank Ola M. Johannessen for providing the reconstructed ocean water data. This work was partly supported by the Earth System Modeling program and by the Scientific Discovery for Advanced Computing (SciDAC) program within the US Department of Energy's Office of Science and by a Los Alamos National Laboratory (LANL) Director's Fellowship. LANL is operated under the auspices of the National Nuclear Security Administration of the US Department of Energy under Contract No. DE-AC52-06NA25396, and partly from the European Community's Seventh Framework Programme under grant agreement No. 262693. S. H. M. and J. K. M. compiled the satellite images, analyzed the data, and wrote the manuscript. J. C. Y. and N. T. K. contributed to the discussion of results and writing of the text.

Edited by: E. Hanna

## References

- Andresen, C. S., Straneo, F., Riebergaard, M. H., Bjørk, A. A., Andersen, T. J., Kuijpers, A., Nørgaard-Pedersen, N., Kjær, K. H., Schjøth, F., Weckstrom, K., and Ahlstrøm A. P.: Rapid response of Helheim Glacier in Greenland to climate variability over the past century, *Nat. Geosci.*, 5, 37–41, doi:10.1038/NCEO1349, 2011.
- Box, J. E. and Decker, D. T.: Greenland marine-terminating glacier area changes: 2000–2010, *Ann. Glaciol.*, 52, 91–98, 2011.
- Bøggild, C. E., Forsberg, R., and Reeh, N.: Melt: Water in a transect across the Greenland ice sheet, *Ann. Glaciol.*, 40, 169–173, 2005.
- Dozier, J. and Warren, S. G.: Effect of viewing Angle on the Infrared Brightness Temperature of Snow, *Water Resour. Res.*, 18, 1424–1434, 1982.
- Earth Observing System Data and Information System (EOSDIS): Earth Observing System ClearingHouse (ECHO)/Warehouse Inventory Search Tool (WIST) Version 10.X. Greenbelt, MD: EOSDIS, Goddard Space Flight Center (GSFC) NASA, 2009.
- Gao, B.-C.: NDWI – A Normalized Difference Water Index for Remote Sensing of Vegetation Liquid Water From Space, *Remote Sens. Environ.*, 58, 257–266, 1996.
- Hanna, E., Cappelen, J., Fettweis, X., Huybrechts, P., Luckman, A., and Ribergaard, M. H.: Hydrologic response of the Greenland ice sheet: the role of oceanographic warming, *Hydrol. Process.*, 23, 7–30, 2009.
- Holland, D. M., Thomas, R. H., de Young, B., Ribergaard, M. H., and Lyberth, B.: Acceleration of Jakobshavn Isbrae triggered by warm subsurface ocean waters, *Nat. Geosci.*, 1, 659–662, 2008.
- Howat, I. M. and Eddy, A.: Multi-decadal retreat of Greenland's marine-terminating glaciers, *J. Glaciol.*, 57, 389–396, 2011.
- Howat, I. M., Joughin, I., Tulaczyk, S., and Gogineni, S.: Rapid retreat and acceleration of Helheim Glacier, East Greenland, *Geophys. Res. Lett.*, 32, L22502, doi:10.1029/2005GL024737, 2005.
- Howat, I. M., Joughin, I., and Scambos, T. A.: Rapid Changes in Ice Discharge from Greenland Outlet Glaciers, *Science*, 315, 1559–1561, 2007.
- Howat, I. M., Joughin, I., Fahnestock, M., Smith, B. E., and Scambos, T.: Synchronous retreat and acceleration of southeast Greenland outlet glaciers 2000–2006: ice dynamic and coupling to climate, *J. Glaciol.*, 54, 646–660, 2008.
- Humlum, O. and Christiansen, H. H.: Geomorphology of the Ammassalik Island, SE Greenland, *Geogr. Tidssk.*, 108, 5–20, 2008.
- Jiskoot, H., Murray, T., and Luckman, A.: Surge potential and drainage-basin characteristics in East Greenland, *Ann. Glaciol.*, 36, 142–148, 2003.
- Johannessen, O. M., Korabely, A., Miles, V., Miles, M. W., and Solberg, K. E.: Interaction Between the Warm Subsurface Atlantic Water in the Sermilik Fjord and Helheim Glacier in Southeast Greenland, *Surv. Geophys.*, 32, 387–396, doi:10.1007/s10712-011-9130-6, 2011.
- Joughin, I., Abdalati, W., and Fahnestock, M. A.: Large fluctuations in speed on Greenland's Jakobshavn Isbrae glacier, *Nature*, 432, 608–610, 2004.
- Joughin, I., Smith, B. E., Howat, I. M., Scambos, T., and Moon, T.: Greenland Flow variability from ice-sheet-wide velocity mapping, *J. Glaciol.*, 56, 415–430, 2010.
- Knudsen, N. T. and Hasholt, B.: Mass balance observations at Mittivakkat Glacier, southeast Greenland 1995–2002, *Nord. Hydrol.*, 35, 381–390, 2004.
- Kargel, J. S., Ahlstrøm, A. P., Alley, R. B., Bamber, J. L., Benham, T. J., Box, J. E., Chen, C., Christoffersen, P., Citterio, M., Cogley, J. G., Jiskoot, H., Leonard, G. J., Morin, P., Scambos, T., Sheldon, T., and Willis, I.: Brief communication Greenland's shrinking ice cover: “fast times” but not that fast, *The Cryosphere*, 6, 533–537, doi:10.5194/tc-6-533-2012, 2012.
- Luthcke, S., Zwally, H. J., Abdalati, W., Rowlands, D. D., Ray, R. D., Nerem, R. S., Lemoine, F. G., McCarthy, J. J., and Chinn, D. S.: Recent Greenland mass loss by drainage system from satellite gravity observations, *Science*, 314, 1286–1289, 2006.

- Mernild, S. H., Kane, D. L., Hansen, B. U., Jakobsen, B. H., Hasholt, B., and Knudsen, N. T.: Climate, glacier mass balance, and runoff (1993–2005) for the Mittivakkat Glacier catchment, Ammassalik Island, SE Greenland, and in a long term perspective (1898–1993), *Hydrol. Res.*, 39, 239–256, 2008.
- Mernild, S. H., Knudsen, N. T., Lipscomb, W. H., Yde, J. C., Malmros, J. K., Hasholt, B., and Jakobsen, B. H.: Increasing mass loss from Greenland's Mittivakkat Gletscher, *The Cryosphere*, 5, 341–348, doi:10.5194/tc-5-341-2011, 2011a.
- Mernild, S. H., Mote, T., and Liston, G. E.: Greenland Ice Sheet surface melt extent and trends, 1960–2010, *J. Glaciol.*, 57, 621–628, 2011b.
- Mernild, S. H., Hanna, E., Knudsen, N. T., Yde, J. C., and Seidenkrantz, M.-S.: The climate impact on observed land terminating glaciers and ice caps in Northern North Atlantic, *J. Climate*, in review, 2012.
- Moon, T. K. and Joughin, I.: Retreat and advance of Greenland tide-water glaciers from 1992 to 2007, *J. Geophys. Res.*, 113, F02022, doi:10.1029/2007JF000927, 2008.
- Myers, P., Kulan, N., and Ribergaard, M. H.: Irminger Water variability in the West Greenland Current, *Geophys. Res. Lett.*, 34, L17601, doi:10.1029/2007GL030419, 2007.
- Murray, T., Scharrer, K., James, T. D., Dye, S. R., Hanna, E., Booth, A. D., Selmes, N., Luckman, A., Hughes, A. L. C., Cook, S., and Huybrechts, P.: Ocean regulation hypothesis for glacier dynamics in southeast Greenland and implications for ice sheet mass changes, *J. Geophys. Res.*, 115, F03026, doi:10.1029/2009JF001522, 2010.
- Nick, F., Vieli, M. A., Howat, I. M., and Joughin, I.: Large-scale changes in Greenland outlet glacier dynamics triggered at the terminus, *Nat. Geosci.*, 2, 110–114, doi:10.1038/NGEO394, 2009.
- Paul, F.: The New Swiss Glacier Inventory 2000 – Application of remote sensing and GIS, Ph.D. thesis, Department of Geography, University of Zurich, 198 pp., 2004.
- Radić, V. and Hock, R.: Regionally differentiated contribution of mountain glaciers and ice caps to future sea-level rise, *Nat. Geosci.*, 4, 91–94, 2011.
- Rignot, E. and Kanagaratnam, P.: Changes in the velocity structure of the Greenland Ice Sheet, *Science*, 311, 986–990, 2006.
- Rignot E., Knoppes, M., and Velicogna, I.: Rapid submarine melting of the calving faces of West Greenland glaciers, *Nat. Geosci.*, 3, 187–191, 2010.
- Rouse, J. W., Haas, R. H., Schell, J. A., and Deering, D. W.: Monitoring vegetation systems in the Great Plains with ERTS, Third ERTS Symposium, NASA SP-351, I, 309–317, 1973.
- Sohn, H.-G., Jezek, K. C., and van der Veen, C. J.: Jakobshavn Glacier, West Greenland: 30 years of spaceborne observations, *Geophys. Res. Lett.*, 25, 2699–2702, 1998.
- Straneo, F., Hamilton, G. S., Sutherland, D. A., Sterns, L. A., Davidson, F., Hammill, M. O., Stenson, G. B., and Rosing-Asvid, A.: Rapid circulation of warm subtropical waters in a major glacial fjord in East Greenland, *Nat. Geosci.*, 3, 182–222, 2010.
- Tachikawa, T., Kaku, M., Iwasaki, A., Gesch, D., Oimoen, M., Zhang, Z., Danielson, J., Krieger, T., Curtis, B., Haase, J., Abrams, M., Crippen, R., and Carabajal, C.: ASTER Global Digital Elevation Model Version 2 – Summary of Validation Results, NASA Land Processes Distributed Active Archive Center and the Joint Japan-US ASTER Science Team ([https://igskmncnwb001.cr.usgs.gov/aster/GDEM/Summary\\_GDEM2\\_validation\\_report\\_final.pdf](https://igskmncnwb001.cr.usgs.gov/aster/GDEM/Summary_GDEM2_validation_report_final.pdf)), 2011.
- Thomas, R., Frederick, E., Krabill, W., Manizade, S., and Martin, C.: Recent changes on Greenland outlet glaciers, *J. Glaciol.*, 55, 147–162, 2009.
- Truffer, M. and Fahnestock, M.: Rethinking ice sheet time scales, *Science*, 315, 1508–1510, 2007.
- van den Broeke, M., Bamber, J., Ettema, J., Rignot, E., Schrama, E., van de Berg, W., van Meijgaard, E., Velicogna, I., and Wouters, B.: Partitioning Recent Greenland Mass Loss, *Science*, 326, 984–986, 2009.
- Velicogna, I.: Increasing rates of ice mass loss from the Greenland and Antarctic ice sheets revealed by GRACE, *Geophys. Res. Lett.*, 36, L19503, doi:10.1029/2009GL040222, 2009.
- Velicogna, I. and Wahr, J.: Acceleration of Greenland ice mass loss in spring 2004, *Nature*, 443, 329–331, 2006.
- Walsh, K. M., Howat, I. M., Ahn, Y., and Enderlin, E. M.: Changes in the marine-terminating glaciers of central east Greenland, 2000–2010, *The Cryosphere*, 6, 211–220, doi:10.5194/tc-6-211-2012, 2012.
- WGMS: Glacier Mass Balance Bulletin, Bulletin No. 10 (2006–2007), edited by: Haerberli, W., Gartner-Roer, I., Hoelzle, M., Paul, F., and Zemp, M., ICSU(WDS)/IUGG(IACS)/UNEP/UNESCO/WMO, World Glacier Monitoring Service, Zurich, 96 pp., 2009.
- Yde, J. C. and Knudsen, N. T.: 20th-century glacier fluctuation on Disko Island (Qeqertarsuaq), Greenland, *Ann. Glaciol.*, 46, 209–214, 2007.

[12]

Mernild, S. H., Lipscomb, W. H., Bahr, D. B., Radić, V., and Zemp, M. 2013. Global glacier retreat: A revised assessment of committed mass losses and sampling uncertainties. *The Cryosphere*, 7, 1565–1577, doi:10.5194/tc-7-1565-2013.

Reprinted with permission from Copernicus Publications



# Global glacier changes: a revised assessment of committed mass losses and sampling uncertainties

S. H. Mernild<sup>1,2</sup>, W. H. Lipscomb<sup>3</sup>, D. B. Bahr<sup>4,5</sup>, V. Radic<sup>6</sup>, and M. Zemp<sup>7</sup>

<sup>1</sup>Climate, Ocean and Sea Ice Modeling Group, Computational Physics and Methods, Los Alamos National Laboratory, Los Alamos, NM 87545, USA

<sup>2</sup>Glaciology and Climate Change Laboratory, Center for Scientific Studies/Centro de Estudios Científicos (CECs), Chile

<sup>3</sup>Climate, Ocean and Sea Ice Modeling Group, Fluid Dynamics and Solid Mechanics, Los Alamos National Laboratory, Los Alamos, NM 87545, USA

<sup>4</sup>Institute of Arctic and Alpine Research, University of Colorado, Boulder, CO 80309, USA

<sup>5</sup>Institut für Geographie, Universität Innsbruck, Innrain 52, 6020 Innsbruck, Austria

<sup>6</sup>Department of Earth and Ocean Sciences, University of British Columbia, Vancouver, Canada

<sup>7</sup>Department of Geography, University of Zurich, Zurich, Switzerland

Correspondence to: S. H. Mernild (mernild@cecs.cl)

Received: 9 April 2013 – Published in The Cryosphere Discuss.: 7 May 2013

Revised: 12 August 2013 – Accepted: 20 August 2013 – Published: 2 October 2013

**Abstract.** Most glaciers and ice caps (GIC) are out of balance with the current climate. To return to equilibrium, GIC must thin and retreat, losing additional mass and raising sea level. Because glacier observations are sparse and geographically biased, there is an undersampling problem common to all global assessments. Here, we further develop an assessment approach based on accumulation-area ratios (AAR) to estimate committed mass losses and analyze the undersampling problem. We compiled all available AAR observations for 144 GIC from 1971 to 2010, and found that most glaciers and ice caps are farther from balance than previously believed. Accounting for regional and global undersampling errors, our model suggests that GIC are committed to additional losses of  $32 \pm 12\%$  of their area and  $38 \pm 16\%$  of their volume if the future climate resembles the climate of the past decade. These losses imply global mean sea-level rise of  $163 \pm 69$  mm, assuming total glacier volume of 430 mm sea-level equivalent. To reduce the large uncertainties in these projections, more long-term glacier measurements are needed in poorly sampled regions.

## 1 Introduction

Averaged over a typical year, glaciers accumulate snow at upper elevations and ablate snow and ice at lower elevations. When the total accumulation is equal, on average, to the total ablation, a glacier is in balance with its local climate. If accumulation exceeds ablation over a period of years to decades, glaciers must thicken and advance; if ablation exceeds accumulation, glaciers must thin and retreat. Most of the Earth's glaciers are retreating (e.g., Meier et al., 2007; Bahr et al., 2009; WGMS, 2012).

Glacier annual mass balance has been measured by direct field methods for about 340 glaciers and ice caps (GIC), of which about 70 have uninterrupted records of 20 years or more (Dyurgerov, 2010; WGMS, 2012). This is a very small fraction of the Earth's estimated 200 000 or more GIC (Arendt et al., 2012). Globally integrated GIC mass changes cannot be measured directly, but must be estimated by up-scaling observations from a small number of glaciers and ice caps. Several analyses (Dyurgerov and Meier, 2005; Kaser et al., 2006; Meier et al., 2007; Cogley, 2009a, 2012) based on direct and geodetic measurements suggest that GIC mass loss is currently raising global mean sea level by about  $1 \text{ mm yr}^{-1}$ . This is about one-third of the total rate of sea-level rise inferred from satellite altimetry, with ocean thermal

expansion and ice-sheet mass loss accounting for most of the remainder (Cazenave and Llovel, 2010). GRACE gravity measurements from 2003 to 2010 suggest a smaller GIC sea-level contribution of about  $0.4 \text{ mm yr}^{-1}$ , excluding GIC peripheral to the Greenland and Antarctic ice sheets (Jacob et al., 2012). These GRACE estimates, however, have large regional uncertainties and rely on the performance of global hydrologic models. Gardner et al. (2013) recently combined satellite gravimetry and altimetry with local glaciological measurements to estimate that the Earth's GIC raised sea level by  $0.71 \pm 0.08 \text{ mm yr}^{-1}$  during the period 2003–2009.

Several modeling studies have projected global-scale transient glacier mass changes in response to forcing from climate models (e.g., Raper and Braithwaite, 2006; Radić and Hock, 2011; Marzeion et al., 2012; Slangen et al., 2012). Based on output from 10 global climate models prepared for the Fourth Assessment Report of the Intergovernmental Panel on Climate Change (IPCC AR4), sea level is projected to rise by  $124 \pm 37 \text{ mm}$  during the 21st century from GIC mass loss, with the largest contributions from Arctic Canada, Alaska, and Antarctica (Radić and Hock, 2011). Another study (Marzeion et al., 2012) used 15 global climate models prepared for the IPCC Fifth Assessment Report (AR5) to project that GIC mass loss by 2100 will range from  $148 \pm 35 \text{ mm}$  to  $217 \pm 47 \text{ mm}$ , depending on the emission scenario. For model calibration and validation, these studies used direct and geodetic mass balance observations available for much fewer than 1 % of the Earth's glaciers. Undersampling is a significant problem for these studies and for all methods that project global sea-level rise from GIC.

Bahr et al. (2009, henceforth BDM) developed an alternative approach for projecting global glacier volume changes. This approach is based on the accumulation-area ratio (AAR), the fractional glacier area where accumulation exceeds ablation. For a glacier in balance with the climate, the AAR is equal to its equilibrium value,  $\text{AAR}_0$ . Glaciers with  $\text{AAR} < \text{AAR}_0$  will retreat from lower elevations, typically over several decades or longer, until the AAR returns to the equilibrium value. In the extreme case  $\text{AAR} = 0$ , there is no accumulation zone and the glacier must disappear completely (Pelto, 2010). From the ratio  $\alpha = \text{AAR} / \text{AAR}_0$ , BDM derived  $p_A$  and  $p_V$ , the fractional changes in area  $A$  and volume  $V$  required to reach equilibrium with a given climate. They showed that for a given glacier or ice cap,  $p_A = \alpha - 1$  and  $p_V = \alpha^\gamma - 1$ , where  $\gamma$  is the exponent in the glacier volume–area scaling relationship,  $V \propto A^\gamma$  (Bahr et al., 1997). Data and theory suggest  $\gamma = 1.25$  for ice caps and  $\gamma = 1.375$  for glaciers. Using AAR observations of  $\sim 80$  GIC during the period 1997–2006 (Dyurgerov et al., 2009), BDM computed a mean AAR of  $44 \pm 2 \%$ , with  $\text{AAR} < \text{AAR}_0$  for most GIC. They estimated that even without additional warming, the volume of glaciers must shrink by  $27 \pm 5 \%$ , and that of ice caps by  $26 \pm 8 \%$ , to return to equilibrium.

The AAR method provides physics-based estimates of committed GIC area and volume changes, and complements techniques such as mass balance extrapolation (Meier et al., 2007) and numerical modeling (Oerlemans et al., 1998; Raper and Braithwaite, 2006). Compared to direct mass balance measurements, AARs are relatively easy and inexpensive to estimate with well-timed aerial and satellite images, which could potentially solve the undersampling problem. Here we adopt the BDM approach and develop it further. Instead of assuming that a sample of fewer than 100 observed GIC, mostly in Europe and western North America, is representative for the global mean, we test the foundations of this assumption and quantify its uncertainties. We aim not only to provide a revised estimate of committed global-scale glacier mass losses but also to assess the sampling errors associated with the limited number of available AAR observations.

## 2 Data and methods

We compiled a data set of AAR (%) and mass balance ( $\text{kg m}^{-2} \text{ yr}^{-1}$ ) for 144 GIC (125 glaciers and 19 ice caps) from 1971 to 2010, mainly from the World Glacier Monitoring Service (WGMS, 2012) but with additional data from Dyurgerov and Meier (2005), Bahr et al. (2009), and individual investigators. (See Sheet A in the supplementary material.) Thus we expanded and updated the data set used by BDM. We found that the BDM data set generally omits AARs for glaciers with net ablation at all elevations (hence  $\text{AAR} = 0$ ) in a particular year. Including these values lowers the mean AAR. Figure 1 shows the locations of GIC in the updated data set, and Fig. 2 shows the number of GIC with AAR observations in each year.

These data were distilled from a larger data set that included several dozen additional glaciers in the WGMS database. For each glacier or ice cap we computed  $\text{AAR}_0$  by linear regression of the AAR with mass balance (Fig. 3 and Sheet B of the supplementary material). We retained only those GIC for which the linear relationship is statistically significant ( $p < 0.10$ , based on a linear regression  $t$  test) in order to remove GIC with short time series and those for which AAR methods are not applicable. Instances of  $\text{AAR} = 0$  and  $\text{AAR} = 100 \%$  were excluded from the regressions (but included for the broader analysis), since AAR and mass balance are not related linearly when net ablation occurs at all elevations or when net accumulation occurs at all elevations. Following Dyurgerov et al. (2009), we assumed that  $\text{AAR}_0$  does not change in time.

We then computed annual, pentadal, and decadal averages of AAR and  $\alpha$  for selected regions (Fig. 1) and for the full data set, along with the fractional change in area  $p_A$  and volume  $p_V$  required for GIC to reach equilibrium with a given climate (see Appendices A and B for details). The arithmetic mean AAR and  $\alpha$  have fallen during each decade since the 1970s (Fig. 4). We found a decadal-average  $\alpha < 1$ , implying



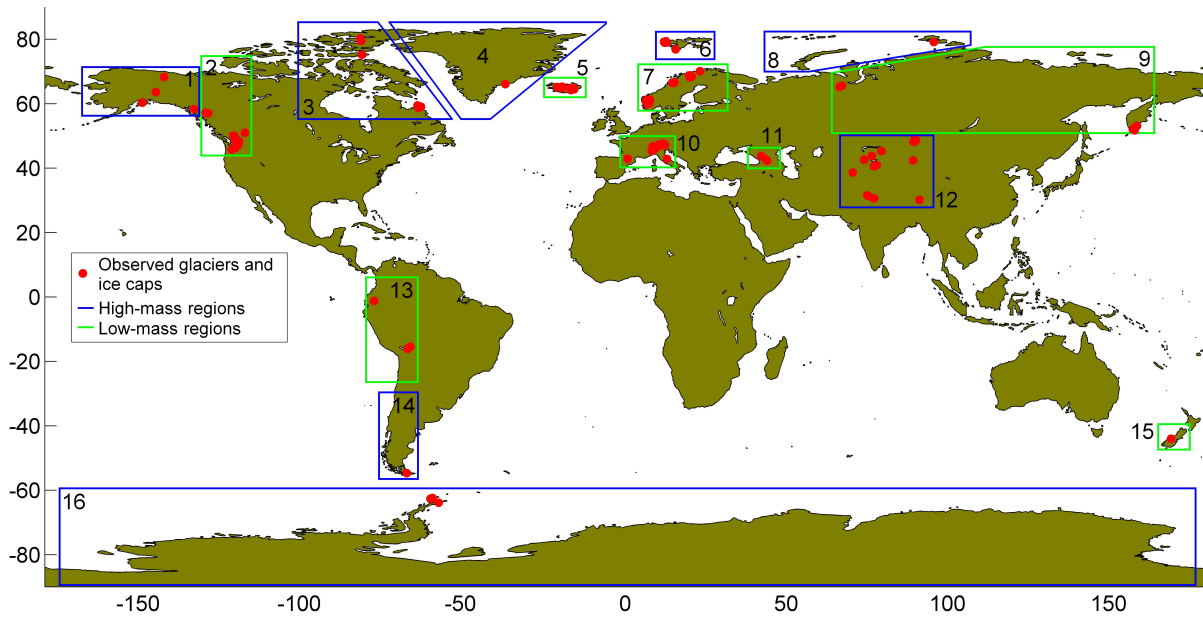


**Fig. 1.** Locations of the 144 glaciers and ice caps (GIC) in the updated data set. The data are divided into 16 regions: (1) Alaska, (2) western Canada/US, (3) Arctic Canada, (4) Greenland, (5) Iceland, (6) Svalbard, (7) Scandinavia, (8) the Russian Arctic, (9) North Asia, (10) central Europe, (11) the Caucasus, (12) central Asia, (13) the northern Andes, (14) the southern Andes, (15) New Zealand, and (16) Antarctica. The data set contains 38 GIC in high-mass regions (ice volume  $V > 5000 \text{ km}^3$ , outlined in blue) and 106 GIC in low-mass regions ( $V < 5000 \text{ km}^3$ , outlined in green). Volume estimates are from Radić et al. (2013).

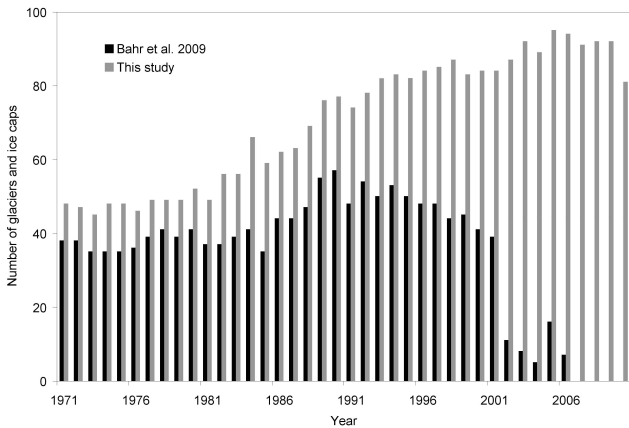


**Fig. 2.** Number of glaciers and ice caps with AAR observations per year in the Bahr et al. (2009) data set (black) and in the updated data set used in this study (grey).

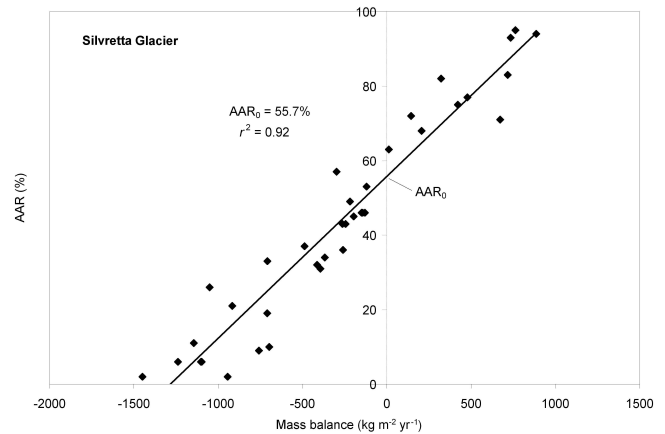


**Fig. 3.** Linear regression of AAR against mass balance for Silvretta Glacier, Swiss Alps. The y intercept is  $AAR_0$ , the equilibrium value of AAR. Each diamond represents one year of data.

future retreat if recent climate conditions continue, for 93 out of 96 GIC with observations during the 2000s. The mean AAR for 2001–2010 is  $34 \pm 3 \%$ . This is well below BDM’s estimate of  $44 \pm 2 \%$ , indicating that the observed GIC are farther from balance than previously reported. (Here and below, error ranges computed from our data set correspond to a 95 % confidence interval, or 1.96 times the standard error. Uncertainty ranges in other published work may not be directly comparable. BDM, for example, expressed uncertain-

ties as plus or minus one standard error, corresponding to a 68 % confidence interval.)

GIC observations are sparse and geographically biased, thus complicating any extrapolation of global glacier mass loss from the available data. Direct AAR and mass-balance measurements have focused on small to mid-sized glaciers in accessible regions such as the Alps, Scandinavia, and the western US and Canada (Fig. 1). Based on Radić et al. (2013), we divided the Earth’s glaciated regions into eight

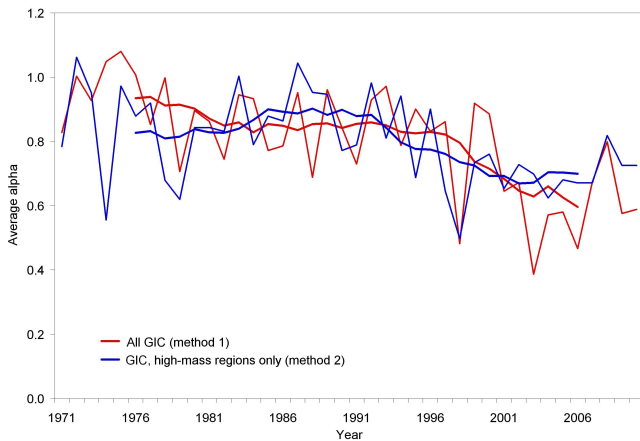


**Fig. 4.** Annual average  $\alpha = \text{AAR} / \text{AAR}_0$  for the full data set (thin red line) and for the GIC in high-mass regions only (thin blue line), 1971–2010. The thick red and blue lines are 10 yr running means. Both the full data set and the high-mass-only data sets have significant ( $p < 0.01$ ) negative trends during the periods 1971–2010 and 1991–2010. The 1971–1990 trends are not significant ( $p > 0.10$ ).

high-mass regions (each with an ice volume  $V > 5000 \text{ km}^3$ ) and eight low-mass regions ( $V < 5000 \text{ km}^3$ ). The data set includes 38 GIC in high-mass regions (Arctic Canada, Antarctica, Alaska, Greenland, the Russian Arctic, central Asia, Svalbard, and the southern Andes) and 106 GIC in low-mass regions (Iceland, western Canada/US, the northern Andes, central Europe, Scandinavia, North Asia, the Caucasus, and New Zealand). The high-mass regions collectively contain about 97 % of the Earth's glacier mass.

Area is not correlated significantly ( $p > 0.10$ ) with AAR or  $\alpha$  for observed GIC spanning a range of  $\sim 0.1$  to  $1000 \text{ km}^2$  (Fig. 5), suggesting that glacier size is not a large source of bias. Geographic bias, on the other hand, could be important. In our data set, only 23 of 96 GIC with observed AAR during the period 2001–2010 are in high-mass regions. Table 1 shows the decadal mean  $\alpha$  for each of 14 regions with one or more GIC in the 2001–2010 data set. Among regions with at least three observed GIC, the highest values are in Alaska ( $\alpha = 0.89 \pm 0.28$ ) and Antarctica ( $\alpha = 0.89 \pm 0.28$ ), with the lowest values in Svalbard ( $\alpha = 0.49 \pm 0.15$ ) and central Europe ( $\alpha = 0.47 \pm 0.06$ ). Three regions with low glacier mass (central Europe, Scandinavia, and western Canada/US) contain more than half the GIC in the data set and have relatively low  $\alpha$ . These regional differences suggest that the full data set may not be spatially representative and that projections based on the arithmetic mean  $\alpha$  could overestimate committed GIC losses.

To show how geographical bias and undersampling can affect estimates of global glacier mass balance and AAR, we applied three different averaging methods: (1) the arithmetic mean for the full data set; (2) the arithmetic mean for the GIC in high-mass regions only; and (3) a mean obtained by up-

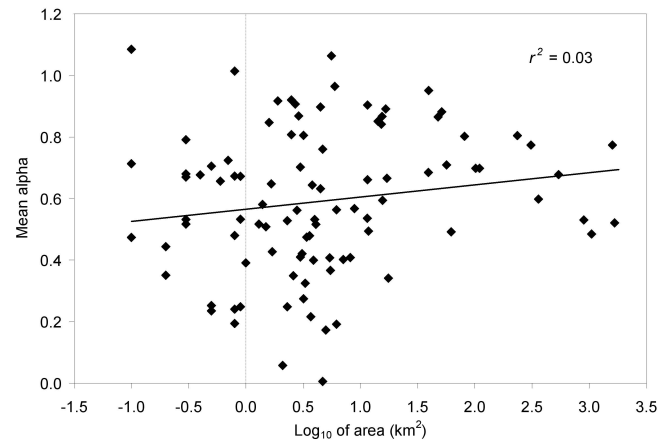


**Fig. 5.** Linear relation between the log of area ( $\text{km}^2$ ) and the 2001–2010 mean  $\alpha = \text{AAR} / \text{AAR}_0$  for 96 GIC with observations in the past decade. Each diamond represents one glacier or ice cap. The correlation between  $\alpha$  and the log of area, although slightly positive ( $r^2 = 0.03$ ), is insignificant ( $p > 0.10$ ), suggesting that a bias toward smaller glaciers does not imply a bias in  $\alpha$ .

**Table 1.** Regional mean values of  $\alpha = \text{AAR} / \text{AAR}_0$  for 2001–2010\*.

Region	Mean $\alpha$
Alaska (3)	$0.89 \pm 0.28$
W. Canada/US (19)	$0.57 \pm 0.06$
Arctic Canada (2)	$0.60 \pm 0.35$
Greenland (1)	$0.34 \pm 0.51$
Iceland (10)	$0.72 \pm 0.09$
Svalbard (6)	$0.49 \pm 0.15$
Scandinavia (18)	$0.53 \pm 0.06$
Central Europe (19)	$0.47 \pm 0.06$
Caucasus (2)	$0.81 \pm 0.32$
Central Asia (7)	$0.80 \pm 0.16$
Northern Andes (4)	$0.71 \pm 0.21$
Southern Andes (1)	$0.71 \pm 0.51$
New Zealand (1)	$0.92 \pm 0.47$
Antarctic (3)	$0.89 \pm 0.28$
<i>Global (96)</i>	<i><math>0.68 \pm 0.12</math></i>

\* Error ranges give 95 % confidence interval. The number of observed GIC per region is shown in parentheses. The global mean is obtained by method 3.

scaling the regional mean values, with each value weighted by the region's GIC area or volume. Because method 3 assumes GIC to be representative only of their regions and not of the entire Earth, it is the least likely to be geographically biased. This method, however, is limited to the past decade, because several high-mass regions had no observations in earlier decades.

The method 3 errors are dominated by errors in a few large undersampled regions, including Arctic Canada, Antarctica, Greenland, and Alaska. We estimated regional errors by

subsampling GIC in two well-represented regions – central Europe and western Canada/US – and computing the difference between the mean  $\alpha$  of each subsample and of the full sample (see Appendix B). The spread of differences as a function of subsample size (Fig. 6) gives an estimate of the error  $\delta\alpha$  in poorly sampled regions with small area (e.g., New Zealand, Caucasus, and Svalbard). For poorly sampled regions with large area (e.g., Greenland, Arctic Canada, the Russian Arctic, and Antarctica, whose glaciers experience different climate regimes within the region) we carried out the same analysis but using two combined regions: (1) central Europe and Scandinavia, and (2) western Canada/US and Alaska. All errors are derived as root-mean-square errors (RMSE) at 95 % confidence interval.

Figure 7 shows pentadal average global glacier mass balance for 1971–2010 as estimated by each method (see Sheet D of the supplementary material), along with the estimates of Kaser et al. (2006), Cogley (2012), and Gardner et al. (2013). (No published benchmarks exist for global average  $\alpha$ . However,  $\alpha$  and mass balance are closely correlated, as shown in Fig. 8, suggesting that a method that is representative for mass balance is also representative for  $\alpha$ .) The multi-decade time series in Fig. 7 show significant trends toward more negative mass balance. The estimates of Cogley (2012) are based on both geodetic and direct measurements and are more negative by 100–200 kg m<sup>-2</sup> yr<sup>-1</sup> than the direct-only estimates from Kaser et al. (2006), probably because the direct measurements exclude rapidly thinning calving glaciers (Cogley, 2009a). Gardner et al. (2013), who combined satellite observations with local glaciological measurements, estimated a mass balance of  $-350 \pm 40$  kg m<sup>-2</sup> yr<sup>-1</sup> for 2003–2009, more than 100 kg m<sup>-2</sup> yr<sup>-1</sup> less negative than the other published estimates for the past decade. They found that local measurements tend to be negatively biased compared to satellite-based measurements.

Method 1 (the mean of all observed GIC) gives a post-2000 mass balance more negative than the published estimates, suggesting a bias due to high melt rates in over-represented low-mass regions. Method 2 (the mean from high-mass regions) agrees closely with the direct-based estimates of Kaser et al. (2006) and, as expected, gives a less negative mass balance than the direct-plus-geodetic estimates of Cogley (2012). Method 3 (based on regional upscaling) agrees closely with method 2 in 2001–2005 and 2006–2010, but with large uncertainty ranges due to propagation of errors from undersampled high-mass regions. Both method 2 and method 3 give mass balances more negative than that of Gardner et al. (2013) during the past decade.

This comparison suggests that to a good approximation, methods 2 and 3 are globally representative for glacier mass balance (and hence  $\alpha$ ), but with two caveats. First, the direct-plus-geodetic results of Cogley (2012) imply that the exclusion of calving glaciers could result in a positive bias of 100 to 200 kg m<sup>-2</sup> yr<sup>-1</sup>. On the other hand, the results of Gardner et al. (2013) suggest that mass loss in-

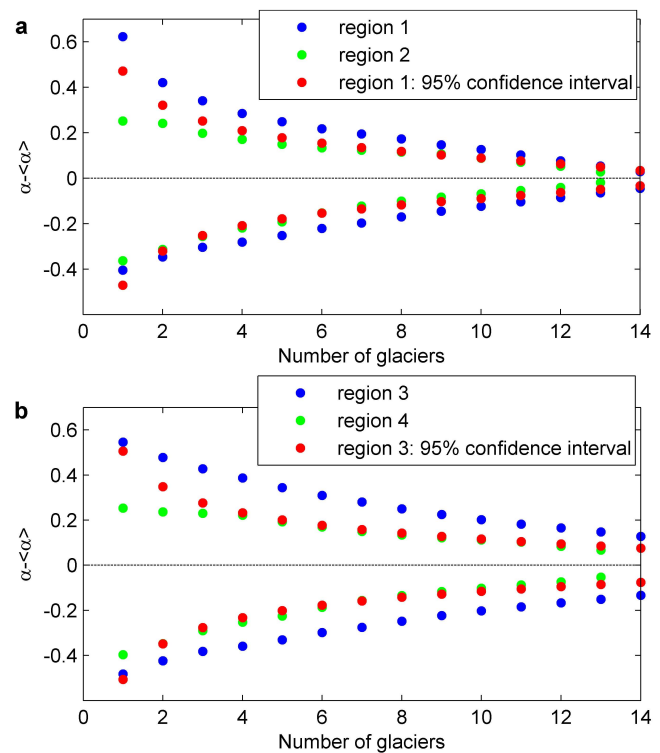


**Fig. 6.** Spread of decadal mean  $\alpha$  as a function of subsample size in well-sampled regions. This plot shows the maximum difference between subsample mean  $\alpha$  and reference  $\langle\alpha\rangle$  as a function of the number of glaciers in the subsample for (a) two well-sampled regions: region 1, central Europe; and region 2, western Canada/US. (b) The same regions but extended: region 3, central Europe and Scandinavia; and region 4, western Canada/US and Alaska. The reference  $\langle\alpha\rangle$  is the mean of the full sample, which includes glaciers with continuous AAR series during the period 2001–2010. In red is the difference range at 95 % confidence interval ( $1.96 \times$  standard deviation) for region 1 and region 3.

ferred from direct measurements is negatively biased compared to satellite measurements. The Gardner et al. (2013) estimate of  $350 \pm 40$  kg m<sup>-2</sup> yr<sup>-1</sup> for 2003–2009 is 100 to 150 kg m<sup>-2</sup> yr<sup>-1</sup> less negative than our method 2 and 3 estimates for the past decade. A mass-balance bias of 100 kg m<sup>-2</sup> yr<sup>-1</sup> would be associated with biases of about 0.06 in  $p_A$  and 0.08 in  $p_V$  (Fig. 8).

### 3 Results and discussion

To estimate committed GIC area and volume losses based on present-day climate, we applied method 3 to observations of  $\alpha$  from 2001 to 2010. A window of about a decade is optimal because it is long enough to average over interannual variability but short compared to glacier dynamic timescales. We adjusted for geographic bias by weighting each regional mean value by the region's total GIC area (for computing  $p_A$ ) or volume (for computing  $p_V$ ), based on Radić et al. (2013).

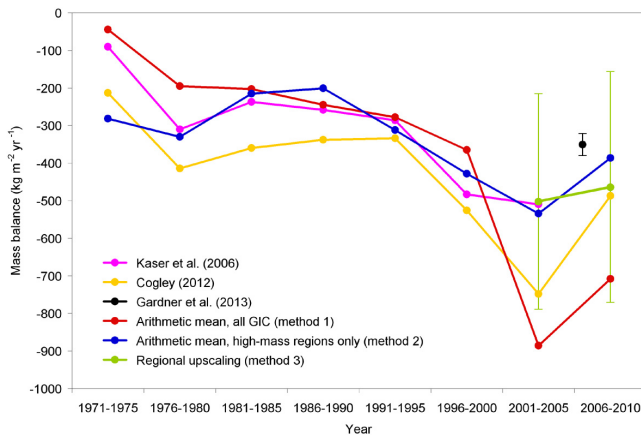


**Fig. 7.** Pentadal average mass balance, 1971–2010. Estimated global average GIC mass balance ( $\text{kg m}^{-2} \text{yr}^{-1}$ ) at 5 yr intervals from published estimates and from this data set: (1) Kaser et al. (2006), based on direct glacier measurements (purple); (2) Cogley (2012), based on direct plus geodetic measurements (yellow); (3) Gardner et al. (2013), with 95 % confidence interval for 2003–2009 (black); (4) arithmetic mean of all GIC in the 1971–2010 data set (method 1, red); (5) arithmetic mean of GIC in the eight high-mass regions of Fig. 1 (method 2, blue); (6) average based on area-weighted upscaling of regional means (method 3, green) including error bars at 95 % confidence interval.

Errors were estimated based on the number of observed GIC per region, and are dominated by a few underrepresented regions (see Appendix B). We found  $\alpha = 0.68 \pm 0.12$  for 2001–2010, implying committed area losses of  $32 \pm 12\%$  and volume losses of  $38 \pm 16\%$  if climate conditions of 2001–2010 continue in the future. The resulting sea-level rise scales linearly with the initial glacier volume. Assuming a total GIC volume of 430 mm sea-level equivalent (SLE) (Huss and Farinotti, 2012), these committed glacier losses would raise global mean sea level by  $163 \pm 69$  mm. Using a larger value of 522 mm SLE (Radić et al., 2013), global mean sea level would rise by  $198 \pm 84$  mm.

Method 2 yields similar estimates. The mean  $\alpha$  during the period 2001–2010 for GIC in high-mass regions is  $0.70 \pm 0.10$ , implying committed area losses of  $30 \pm 10\%$  and volume losses of  $37 \pm 12\%$  (where the error estimates are based on the assumption that these GIC are globally representative). The close agreement with method 3 suggests that method 2 does not have a large geographic bias with respect to  $\alpha$ .

The Earth is expected to warm further (e.g., Meehl et al., 2007), making it likely that long-term GIC area and volume losses will exceed estimates based on the climate of the past decade. From method 2, there is a significant negative trend ( $p < 0.01$ , based on a  $t$  test) in average annual  $\alpha$  of  $-0.0052 \pm 0.0033 \text{ yr}^{-1}$  from 1971 to 2010 (Fig. 4). The trend is nearly identical for the subset of GIC with observations in all four decades, implying that the changing com-

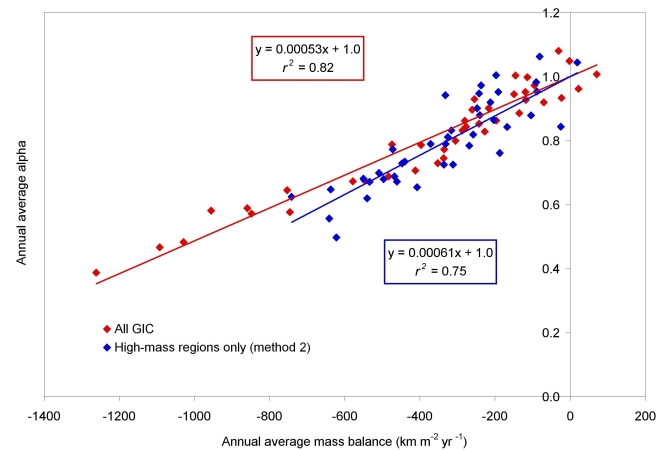


**Fig. 8.** Linear relation between average mass balance and average  $\alpha$  for the period 1971–2010. Each diamond represents the average of all GIC observations for one year. The red diamonds denote averages over the full data set, and the blue diamonds denote averages over the GIC in high-mass regions only. The regression lines are forced to pass through the point  $(x, y) = (0, 1)$ . Both correlations are significant ( $p < 0.01$ ), as determined from the squared correlation coefficient,  $r^2$ . A change in mass balance of  $100 \text{ kg m}^{-2} \text{ yr}^{-1}$  is associated with a change in  $\alpha$  of about 0.06.

position of the data set does not substantially bias the trend. The trend in  $\alpha$  has been much steeper since 1990; there is a significant negative trend ( $p < 0.01$ , based on a  $t$  test) of  $-0.0078 \pm 0.0082 \text{ yr}^{-1}$  for 1991–2010, whereas the 1971–1990 trend is not significantly different from zero ( $p > 0.10$ ). By extrapolating these trends, we can estimate the losses required to equilibrate with the climate of future decades. Taking  $\alpha = 0.68 \pm 0.12$  as the 2005 value and extending the 40 yr trend, the average would fall by  $0.18 \pm 0.12$  over 35 yr, reaching  $0.50 \pm 0.17$  by 2040. The Earth's GIC would then be committed to losing  $50 \pm 17\%$  of their area and  $60 \pm 20\%$  of their volume (see Appendix A). Relative to present-day GIC volume, which is decreasing by about 2 % per decade, the losses would be somewhat greater. These error ranges may understate the true uncertainties because of natural interdecadal variability, and because the method 2 data set may not be globally representative.

Glacier area and volume losses will occur on decade-to-century timescales. The AAR method does not directly predict rates of retreat and thinning, but theory (Jóhannesson et al., 1989) predicts that the volume response time for a typical glacier with a mean thickness of 100–500 m is on the order of 100 years. Scaling analysis (Bahr and Radić, 2012) implies that glaciers thinner than 500 m contain a majority of the Earth's total glacier volume (see Appendix C), suggesting that a large fraction of committed glacier volume losses will occur within a century. However, larger GIC with longer response times will continue to lose mass and raise sea level after 2100.





**Fig. 9.** Brewster Glacier, New Zealand, at the end of the 2008 ablation season. The glacier area is 2.5 km<sup>2</sup>. The 2008 glacier mass balance is  $-1653 \text{ kg m}^{-2} \text{ yr}^{-1}$ , and the AAR is 10 %, with net accumulation limited to small white patches of remaining snow. Grey firn areas (i.e., snow from previous years) generally lie in the ablation zone, as does the bare (blue) ice. The photo illustrates the difficulty of determining a specific elevation at which a glacier is in equilibrium. Photo taken by A. Willsman (Glacier Snowline Survey, National Institute of Water and Atmospheric Research Ltd (NIWA), New Zealand), 14 March 2008.

This analysis has focused on global ice losses and sea-level rise, but glacier retreat and thinning will also have regional impacts associated with changes in seasonal runoff (Immerzeel et al., 2010; Kaser et al., 2010) and glacier hazards (Kääb et al., 2005). In some regions, fractional area and volume ice losses will exceed the global average. Assuming that the observed GIC are regionally representative, GIC in central Europe will lose  $64 \pm 7 \%$  of their volume if future climate resembles the climate of the past decade (which included several record heat waves). We also project substantial volume losses in Scandinavia ( $56 \pm 7 \%$ ), western Canada/US ( $53 \pm 7 \%$ ) and Iceland ( $35 \pm 11 \%$ ). Projections elsewhere are less certain because of the smaller sample sizes.

#### 4 Conclusions

AARs are declining faster than most glaciers and ice caps (GIC) can respond dynamically. As a result, committed area and volume losses far exceed the losses observed to date. Based on regional upscaling of AAR observations from 2001 to 2010, we conclude that the Earth's glaciers and ice caps will ultimately lose  $32 \pm 12 \%$  of their area and  $38 \pm 16 \%$  of their volume if the future climate resembles the climate of the past decade. Committed losses could increase substantially during the next few decades if the climate continues to warm.

These relative losses are larger than those estimated by BDM, reflecting the lower AARs in data that have become available since the earlier study. Our projections, however, have large uncertainties (40 % relative error in the projected mass loss) that are dominated by underrepresented high-mass regions, including Arctic Canada, Antarctica, Greenland, and Alaska.

To reduce the uncertainties, more observations are needed in poorly sampled regions. Direct mass-balance and AAR measurements are inherently labor intensive and limited in coverage. AARs can be estimated, however, from aerial and satellite observations of the end-of-summer snowline (e.g., Fig. 9 and Rabatel et al., 2013). Deriving AAR<sub>0</sub> from observations requires mass-balance measurements for about a decade, but BDM found that the global mean AAR<sub>0</sub> can be used for most GIC with only moderate loss of precision. Huss et al. (2013) recently showed that simple mass balance modeling, combined with terrestrial and airborne/spaceborne AAR observations, can be used to determine glacier mass changes. Also, AAR methods could be extended to tidewater glaciers, incorporating calving as well as surface processes.

#### Appendix A

##### Means and errors of $\alpha$ , $p_A$ , and $p_V$

The first section of Sheet C in the supplementary material (*All GIC – alpha, p<sub>A</sub>, p<sub>V</sub>*) shows values of  $\alpha = \text{AAR} / \text{AAR}_0$  for the full data set. For each year  $i$ , the annual mean  $\alpha$  is found by averaging over  $N_i$  values:

$$\bar{\alpha}_i = \frac{\sum_{n=1}^{N_i} \alpha_{ni}}{N_i}, \quad (\text{A1})$$

where  $\alpha_{ni}$  denotes the value for glacier  $n$  in year  $i$ . The variance for each year is computed as

$$\sigma_i^2 = \frac{1}{N_i - 1} \sum_{n=1}^{N_i} (\alpha_{ni} - \bar{\alpha}_i)^2, \quad (\text{A2})$$

resulting in a standard error of

$$\delta\alpha_i = \frac{\sigma_i}{\sqrt{N_i}}. \quad (\text{A3})$$

The annual values and running 10 yr means are shown in Fig. 4.

Arithmetic means for the full data set were computed for four 10 yr windows: 1971–1980, 1981–1990, 1991–2000, and 2001–2010. For the full data set we computed a mean  $\alpha$  of  $0.93 \pm 0.06$ ,  $0.85 \pm 0.06$ ,  $0.83 \pm 0.07$ , and  $0.59 \pm 0.05$  during the 1970s, 1980s, 1990s, and 2000s, respectively. Let us suppose that for a given glacier  $n$ , we have measurements in  $M_n$  out of 10 yr ( $1 \leq M_n \leq 10$ ). In order for each measurement to be weighted equally, glaciers with more measurements receive greater weight than those with fewer measurements. Thus the decadal mean for the data set is computed as



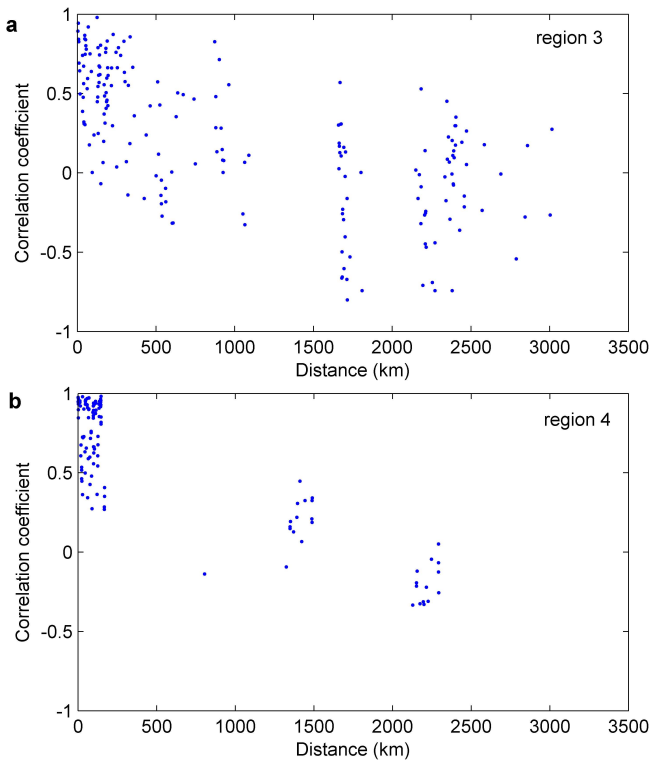


**Fig. A1.** Correlation between  $\alpha$  time series (2001–2010) of any two glaciers in a region versus the distance between the two glaciers. **(a)** Region 3: central Europe (15 glaciers) and Scandinavia (5 glaciers); **(b)** region 4: western Canada/US (14 glaciers) and Alaska (2 glaciers).

$$\bar{\alpha} = \frac{\sum_{n=1}^N f_n \bar{\alpha}_n}{N_f}, \tag{A4}$$

where  $f_n = M_n/10$ ,  $\bar{\alpha}_n$  is given by

$$\bar{\alpha}_n = \frac{\sum_{i=1}^{M_n} \alpha_{ni}}{M_n}, \tag{A5}$$

and

$$N_f = \sum_{n=1}^N f_n. \tag{A6}$$

Equation (A4) is equivalent to the arithmetic mean of all measurements, with each measurement weighted equally. We can think of  $N_f$  as the equivalent number of glaciers; it is equal to the total number of measurements divided by the number of years. The variance is given by

$$\sigma^2 = \frac{1}{N_f - 1} \sum_{n=1}^N f_n (\bar{\alpha}_n - \bar{\alpha})^2, \tag{A7}$$

and the standard error is

$$\delta\alpha = \frac{\sigma}{\sqrt{N_f}}. \tag{A8}$$

The arithmetic mean AAR and its standard error, shown in the second section of Sheet C for 2001–2010 only, are computed analogously.

The next sections of Sheet C show the 2001–2010 arithmetic mean values of  $p_A$  and  $p_V$  for the full data set. BDM showed that for a given glacier or ice cap,  $p_A = \alpha - 1$  and  $p_V = \alpha^\gamma - 1$ , where  $\alpha = \text{AAR}/\text{AAR}_0$  and  $\gamma$  is the exponent in the glacier volume–area scaling relationship,  $V = cA^\gamma$  (Bahr et al., 1997). Data and theory suggest  $\gamma = 1.25$  for ice caps and  $\gamma = 1.375$  for glaciers. Thus  $p_V$  depends on  $\gamma$  but not on the poorly constrained constant  $c$ , and  $p_A$  is independent of both  $c$  and  $\gamma$ . We compute means of  $p_A$  and  $p_V$  first for glaciers, then separately for ice caps. (In the text below, we generally refer to “glaciers”, but the same analysis applies to ice caps with the appropriate value of  $\gamma$ .) For a single glacier we have  $\bar{p}_{An} = \bar{\alpha}_n - 1$  and  $\bar{p}_{Vn} = \bar{\alpha}_n^\gamma - 1$ , where  $\bar{\alpha}_n$  is the mean value of  $\alpha$  for glacier  $n$  over the decade. Let us suppose we have at least one  $\alpha$  value during the decade for each of  $N$  glaciers. To give greater weight to glaciers with more measurements, we compute the decadal mean  $\bar{p}_A$  and  $\bar{p}_V$  as

$$\bar{p}_A = \frac{\sum_{n=1}^N f_n \bar{\alpha}_n}{N_f} - 1 \tag{A9}$$

and

$$\bar{p}_V = \frac{\sum_{n=1}^N f_n \bar{\alpha}_n^\gamma}{N_f} - 1. \tag{A10}$$

The variance associated with  $p_A$  is

$$\sigma_{p_A}^2 = \frac{1}{N_f - 1} \sum_{n=1}^N f_n (\bar{\alpha}_n - \bar{\alpha})^2, \tag{A11}$$

and the variance associated with  $p_V$  is

$$\sigma_{p_V}^2 = \frac{1}{N_f - 1} \sum_{n=1}^N f_n (\bar{\alpha}_n^\gamma - \bar{\alpha}^\gamma)^2. \tag{A12}$$

The standard errors are

$$\delta p_A = \frac{\sigma_{p_A}}{\sqrt{N_f}} \tag{A13}$$

and

$$\delta p_V = \frac{\sigma_{p_V}}{\sqrt{N_f}}. \tag{A14}$$

If these data are taken to be globally representative, as assumed by BDM, then we compute that the Earth’s glaciers

must lose  $44 \pm 6\%$  of their area and  $51 \pm 7\%$  of their volume, and ice caps must lose  $32 \pm 9\%$  of their area and  $38 \pm 10\%$  of their volume, in order to reach equilibrium with the climate of the past decade. As discussed in the main text, however, the data are likely to be geographically biased.

To assess the data for size biases, we plotted the mean value of  $\alpha$  for each glacier against the log of glacier area. As shown in Fig. 5, the correlation is slightly positive ( $r^2 = 0.03$ ) but statistically insignificant ( $p < 0.10$ ). The correlation between  $\alpha$  and glacier area is also insignificant. A positive correlation between glacier area and the change in  $\alpha$  (relative to the equilibrium value of 1.0) would be expected in the following case: if (1) larger glaciers have greater elevation ranges than smaller glaciers; (2) for a given lifting of the equilibrium line altitude (ELA), the AAR decreases less for glaciers with large elevation ranges than for glaciers with small elevation ranges; and (3) the average lifting of the ELA in a warming climate is independent of glacier size. The lack of a significant correlation between glacier area and  $\alpha$  suggests that one or more of these assumptions does not apply to the observed GIC. We checked for area-range bias (i.e., the first assumption) by comparing plots of glacier area vs. elevation range for (1) the observed GIC and (2) more than 100 000 GIC in the World Glacier Inventory (Cogley et al., 2009b). We did not find evidence of a significant bias.

Sheet E in the supplementary material (*High mass regions*) is similar to Sheet C except that it includes only the 38 GIC in high-mass regions: Arctic Canada, Antarctica, Alaska, Greenland, the Russian Arctic, central Asia, Svalbard, and the southern Andes. The first three sections show AAR, mass balance, and  $\alpha$ , respectively. Decadal mean values of  $\alpha$ ,  $p_A$ , and  $p_V$  as well as the associated standard errors are shown for 2001–2010. These are the “method 2” averages cited in the text. The arithmetic mean and 10 yr running mean are shown in Fig. 4, and the 40 yr linear trend (1971–2010) and two 20 yr linear trends (1971–1990 and 1991–2010) of the mean values are given in Sheet E. We used a  $t$  test to determine significance. The 1970–2009 and 1990–2009 trends are significantly negative at the 1% level, whereas the 1970–1989 trend is not significantly different from zero at the 10% level. In the last section of Sheet E, we repeated the annual mean and trend calculations for the 11 GIC in high-mass regions with observations in all four decades to assess the effect on the trends of the changing composition of the data set. The trends are similar to those computed for all 38 GIC.

To estimate future values of the global mean  $\alpha$ , we took  $\alpha_{\text{global}} = 0.68 \pm 0.12$  (the global mean value estimated for 2001–2010, given in Section 3) as a best estimate for 2005. We applied the 40 yr trend ( $-0.0052 \pm 0.0033 \text{ yr}^{-1}$ ) given in Sheet E for the 38 high-mass GIC (method 2). Extending this trend for 35 yr gives a change of  $-0.18 \pm 0.12$ , resulting in  $\alpha_{\text{global}} = 0.50 \pm 0.17$  by 2040. (It is possible that the downward trend in  $\alpha$  would slow as  $\alpha$  reaches 0 for an increasing number of glaciers. With this 35 yr mean trend, however, only three of 96 glaciers with data in 2001–2010 would have

$\alpha = 0$  by 2040, with a negligible effect on the results.) We set  $p_V \text{ global} = (\bar{\alpha}_{\text{global}})^{\bar{\gamma}} - 1$ , with  $\bar{\gamma} = 1.31 \pm 0.05$  to reflect an uncertain partitioning of volume between glaciers and ice caps. The error  $\delta p_V \text{ global} = 0.20$  was calculated as

$$(\delta p_V)^2 = \left( \frac{\partial p_V}{\partial \alpha} \right)_{\bar{\alpha}}^2 (\delta \alpha)^2 + \left( \frac{\partial p_V}{\partial \gamma} \right)_{\bar{\gamma}}^2 (\delta \gamma)^2. \quad (\text{A15})$$

## Appendix B

### Regional calculations

Sheet F (*Regional mass balance*) shows the average mass balance during the period 2001–2010 for each of 14 regions (Table 1), the estimated GIC area in the region (Radić et al., 2013), and the corresponding fraction of the Earth’s total GIC area. For the past decade the data set has no observations from the Russian Arctic, which contains an estimated 8% of global GIC area, or from North Asia, which contains much less than 1%. For purposes of regional upscaling, we used Svalbard (which is climatically similar) as a surrogate for the Russian Arctic, and we neglected North Asia. Thus the regional area fractions are relative to a global total that omits the small GIC area in North Asia. The global average mass balance is computed as

$$b_{\text{global}} = \sum_n w_{An} b_n, \quad (\text{B1})$$

where  $w_{An}$  is the fractional area weight for region  $n$ , and  $b_n$  is the mean mass balance. Sheet F shows the global average mass balance computed for the full decade, for each of two pentads, and for the period 2003–2009 (corresponding to Gardner et al., 2013).

Sheet G (*Regional alpha*) shows regional mean values of  $\alpha$  in 2001–2010 for the same 14 regions (Table 1 in the main text) based on Radić et al. (2013). Again, Svalbard is used as a surrogate for the Russian Arctic, and North Asia is neglected. Decadal mean  $\alpha$  for each glacier and ice cap are shown in Sheet G. Measurements of  $\alpha$  are averaged, with each measurement weighted equally, to obtain the regional means  $\bar{\alpha}_n$ . The estimated area and volume losses per region are  $\bar{p}_{An} = \bar{\alpha}_n - 1$  and  $\bar{p}_{Vn} = (\bar{\alpha}_n)^{\bar{\gamma}_n} - 1$ , where  $\bar{\gamma}_n$  is estimated as described below. The upscaled global estimates are obtained by summing over regions, with each regional value weighted by the estimated total GIC area in the region (for  $\alpha$  and  $p_A$ ) and total volume (for  $p_V$ ):

$$p_A \text{ global} = \sum_n w_{An} \bar{p}_{An}, \quad (\text{B2})$$

$$p_V \text{ global} = \sum_n w_{Vn} \bar{p}_{Vn}. \quad (\text{B3})$$

The upscaled values, with errors, are shown in Sheet G. The regional area and volume weights,  $w_{An}$  and  $w_{Vn}$ , are also shown in Sheet G.

The errors for these global estimates are given by

$$(\delta p_{A \text{ global}})^2 = \sum_n (w_{An} \delta p_{An})^2, \quad (\text{B4})$$

$$(\delta p_{V \text{ global}})^2 = \sum_n (w_{Vn} \delta p_{Vn})^2, \quad (\text{B5})$$

where  $\delta p_{An}$  and  $\delta p_{Vn}$  are the regional errors. For each region we have  $\delta p_{An} = \delta \alpha_n$ , where  $\delta \alpha_n$  (shown in column V) is estimated by the following method. We subsampled GIC in two well-represented regions, central Europe and western Canada/US. For 2001–2010 we considered  $n = 15$  glaciers with continuous records in central Europe, and  $n = 14$  glaciers with continuous records in western Canada/US. The full samples per region provide reference mean values  $\langle \alpha \rangle$  for each region. For each region we computed means for all possible subsamples containing 1 to  $n - 1$  glaciers. For a subsample of one glacier, regional  $\alpha$  is equal to  $\alpha$  from each glacier, and therefore this subsample gives the largest range of possible values. We also calculated the regional mean  $\alpha$  for all possible subsamples of two glaciers, three glaciers, and so on. For each subsample size, Fig. 6a shows the maximum range of results (i.e., subsampled regional  $\alpha$  minus the reference  $\langle \alpha \rangle$ ). The range is largest for a subsample of one glacier and slowly decreases as we approach the maximum of 14 glaciers (and would reach zero for the total of 20 in this case). For each subsample size we computed the standard deviation of the  $\alpha$  values. Figure 6a shows the 95 % confidence interval ( $1.96 \times$  standard deviation), which provides an estimate of  $\delta \alpha_n$  in poorly sampled regions with small spatial area (Iceland, Svalbard, the northern Andes, the Caucasus, and New Zealand). For regions containing more than 10 glaciers with observed AAR (central Europe, Scandinavia and western Canada/US) we assigned an error based on a subsample size of 12. (A number  $> 10$  was chosen arbitrarily, but the error does not decline significantly for sample sizes  $> 10$ ; any number from 11 to 14 would give a similar error estimate.) Based on the data from central Europe, which has a wider spread of differences than western Canada/US, the errors (values of  $n$  shown in parentheses) are as follows: Iceland (10),  $\delta \alpha = 0.09$ ; Svalbard (6),  $\delta \alpha = 0.15$ ; the northern Andes (4),  $\delta \alpha = 0.21$ ; Caucasus (2),  $\delta \alpha = 0.32$ ; New Zealand (1),  $\delta \alpha = 0.47$ ; and central Europe (19), Scandinavia (18), and western Canada/US (18),  $\delta \alpha = 0.06$ .

For poorly sampled regions covering large spatial area (central Asia, Alaska, Antarctica, Arctic Canada, the southern Andes, and Greenland), we carried out the same analysis but using two combined regions: (1) central Europe and Scandinavia, and (2) western Canada/US and Alaska (Fig. 6b). Thus, in addition to  $n = 15$  glaciers from central Europe we included  $n = 5$  glaciers from Scandinavia, and in addition to  $n = 14$  glaciers from western Canada/US we included  $n = 2$  glaciers from Alaska. For each of these two extended regions we carried out a correlation analysis.

Although there are a few correlations of  $\sim 0.5$  for glaciers  $> 1500$  km apart, most time series of  $\alpha$  are not significantly correlated when the distance between glaciers exceeds  $\sim 300$  km (Fig. A1). Therefore, the glacier sampling in the combined regions is representative for poorly sampled regions covering large spatial areas whose glaciers experience different climatic regimes within the region. Based on the data from central Europe and Scandinavia (which has a wider spread of differences than western Canada/US and Alaska), the errors at 95 % confidence interval (values of  $n$  shown in parentheses) are as follows: central Asia (7),  $\delta \alpha = 0.16$ ; Alaska and Antarctica (3),  $\delta \alpha = 0.28$ ; Arctic Canada (2),  $\delta \alpha = 0.35$ ; and Greenland and the southern Andes (1),  $\delta \alpha = 0.51$ .

Since  $p_V$  is a function of both  $\alpha$  and  $\gamma$ , the regional errors  $\delta p_{Vn}$  depend on both  $\delta \alpha_n$  and  $\delta \gamma_n$ :

$$(\delta p_{Vn})^2 = \left( \frac{\partial p_V}{\partial \alpha} \right)_{\bar{\alpha}_n}^2 (\delta \alpha_n)^2 + \left( \frac{\partial p_V}{\partial \gamma} \right)_{\bar{\gamma}_n}^2 (\delta \gamma_n)^2, \quad (\text{B6})$$

where  $\bar{\alpha}$  and  $\bar{\gamma}$  are best estimates. Evaluating the derivatives, this becomes

$$(\delta p_{Vn})^2 = \left( \bar{\gamma}_n \bar{\alpha}_n^{\bar{\gamma}_n - 1} \right)^2 (\delta \alpha_n)^2 + \left( \bar{\alpha}_n^{\bar{\gamma}_n} \ln(\bar{\alpha}_n) \right)^2 (\delta \gamma_n)^2. \quad (\text{B7})$$

We estimated  $\bar{\gamma}_n$  and  $\delta \gamma_n$  as follows. Drawing from existing glacier inventories (Cogley, 2009b), we tabulated the total number of GIC and the number of ice caps in each region. Regions with relatively few ice caps (less than 1 % of the total number of GIC in the regional inventory) were assumed to have most of their volume contained in glaciers. For these regions we assumed  $\bar{\gamma} = 1.36 \pm 0.02$ , where the error corresponds roughly to the difference between the observed value of 1.36 for valley glaciers and the theoretical value (Bahr et al., 1997) of 1.375. For regions where at least 1 % of the GIC are classified as ice caps, we assumed  $\bar{\gamma} = 1.31 \pm 0.05$  to reflect an uncertain partitioning of volume between glaciers and ice caps. (Because ice caps can be much larger than typical glaciers, a relatively small number of ice caps can contain a substantial fraction of a region's volume. BDM, for example, estimated that 53 % of total GIC volume is contained in ice caps and 47 % in glaciers, although there are many more glaciers than ice caps.) A more complete analysis would use scaling relationships to estimate the total glacier and ice cap volume in each region. Existing inventories, however, do not contain complete lists of glaciers and ice caps in all regions, nor do all GIC fall clearly into one category or the other.

Although the partitioning between glaciers and ice caps is only approximate, our results are not sensitive to the details of this partitioning. The errors  $\delta p_{Vn}$  are dominated by the term containing  $\delta \alpha_n$  (the first term on the right-hand side of Eq. B6), with much smaller contributions from the term containing  $\delta \gamma_n$  (the second term on the right-hand side of Eq. B6).

## Appendix C

### Glacier volume response times

The volume response time for a glacier, defined as the timescale for exponential adjustment to a new steady-state volume following a mass-balance perturbation, can be estimated as  $\tau_V \sim H/|b_T|$ , where  $H$  is a thickness scale (e.g., mean glacier thickness) and  $b_T$  is the mass balance at the terminus (Jóhannesson et al., 1989). For typical glaciers with thicknesses of 100 to 500 m and terminus melt rates of 1 to 5 m yr<sup>-1</sup>, the response time is on the order of 100 yr. The mean terminus melt rate for our data set is  $\sim 3$  m yr<sup>-1</sup>, as shown in Sheet I (*Terminus mass balance*).

Bahr and Radić (2012) showed that the fraction of total volume contained in glaciers of area less than  $A_{\min}$  is given to a good approximation by

$$\Theta = \left( \frac{A_{\min}}{A_{\max}} \right)^{\gamma - \beta + 1}, \quad (\text{C1})$$

where  $A_{\max}$  is the area of the largest glaciers;  $\gamma = 1.375$  is the exponent in the volume–area scaling relationship  $V \propto A^\gamma$ ; and  $\beta = 2.1$  is the exponent in the power law  $N(A) \propto A^{-\beta}$ , which predicts the number of glaciers  $N$  of size  $A$ . Volume–area scaling implies  $h \propto A^{\gamma-1}$ , where  $h$  is the mean ice thickness. Therefore,

$$\Theta = \left( \frac{h_{\min}}{h_{\max}} \right)^{\frac{\gamma - \beta + 1}{\gamma - 1}}. \quad (\text{C2})$$

The largest glaciers and ice caps have a thickness of about 1000 m. Setting  $h_{\min} = 500$  m and  $h_{\max} = 1000$  m in Eq. (A24), we obtain  $\Theta = 0.60$ , implying that approximately 60 % of total glacier volume resides in glaciers thinner than 500 m. This analysis suggests that glaciers with response times on the order of a century or less contain a majority of the Earth's total glacier volume.

## Appendix D

### Contributing investigators

The principal investigators for the glaciers and ice caps in the WGMS database are listed in WGMS (2012) and earlier bulletins. We have supplemented the WGMS database with data compiled by Mark Dyurgerov (Dyurgerov et al., 2005; Bahr et al., 2009). In addition, we thank the following investigators for providing us with data not previously in the WGMS database:

- Pedro Skvarca: *Bahia Del Diablo*
- Andrea Fischer and Gerhard Markl: *Hintereisferner, Jamtalferner, Kesselwandferner*

- Heinz Slupetzky: *Sonnblickkees*
- Ludwig N. Braun: *Vernagtferner*
- Reinhard Böhm and Wolfgang Schöner: *Goldbergkees, Kleinfleißkees, Wurtenkees*
- Javier C. Mendoza Rodríguez and Bernard Francou: *Charquini Sur, Zongo*
- Alex Gardner: *Devon Ice Cap NW*
- Graham Cogley: *White*
- Bolívar Cáceres Correa and Bernard Francou: *Antizana 15 Alpha*
- Niels Tvis Knudsen: *Mittivakkat*
- Finnur Pálsson, Helgi Björnsson, and Hannes Haraldsson: *Brúarjökull, Eyjabakkajökull, Köldukvíslarjökull, Langjökull S. Dome, Tungnaárjökull*
- Þorsteinn Þorsteinsson: *Hofsjökull N, Hofsjökull E, Hofsjökull SW*
- Luca Carturan: *Carèser*
- Luca Mercalli: *Ciardoney*
- Gian Carlo Rossi and Gian Luigi Franchi: *Malavalle, Pendente*
- Bjarne Kjølmoen: *Álfotbreen, Breidalblikkbrea, Gråfjellsbrea, Langfjordjøkelen, Nigardsbreen*
- Hallgeir Elvehøy: *Austdalsbreen, Engabreen, Hardangerjøkulen*
- Liss M. Andreassen: *Gråsubreen, Hellstugubreen, Storbreen*
- Jack Kohler: *Austre Brøggerbreen, Kongsvegen, Midtre Lovénbreen*
- Piotr Glowacki and Dariusz Puczko: *Hansbreen*
- Ireneusz Sobota: *Waldemarbreen*
- O.V. Rototayeva: *Garabashi*
- Yu K. Narozhniy: *Leviy Aktru, Maliy Aktru, and No. 125*
- Miguel Arenillas: *Maladeta*
- Peter Jansson: *Mårmaglaciären, Rabots glaciär, Riukojietna, Storglaciären*
- Giovanni Kappenberger and Giacomo Casartelli: *Basòdino*
- Martin Funk and Andreas Bauder: *Gries, Silvretta*

- Mauri Pelto: *Columbia (2057), Daniels, Easton, Foss, Ice Worm, Lower Curtis, Lynch, Rainbow, Sholes, Yawning, Lemon Creek*
- Jon Riedel: *Noisy Creek, North Klawatti, Sandalee, Silver*
- Rod March and Shad O’Neel: *Gulkana, Wolverine*
- William R. Bidlake: *South Cascade*

**Supplementary material related to this article is available online at <http://www.the-cryosphere.net/7/1565/2013/tc-7-1565-2013-supplement.zip>.**

*Acknowledgements.* We thank principal investigators and their teams, along with the WGMS staff, for providing AAR and mass-balance data. We also thank Daniel Farinotti, Ben Marzeion, and Mauri Pelto for insightful reviews, and we thank Graham Cogley, Alex Gardner, Matthias Huss, and Georg Kaser for helpful data and feedback. This work was supported partly by a Los Alamos National Laboratory (LANL) Director’s Fellowship and by the Earth System Modeling program of the Office of Biological and Environmental Research within the US Department of Energy’s Office of Science. LANL is operated under the auspices of the National Nuclear Security Administration of the US Department of Energy under contract No. DE-AC52-06NA25396, and partly by the European Community’s Seventh Framework Programme under grant agreement No. 262693.

Edited by: J. O. Hagen

## References

- Arendt, A. A., Bolch, T., Cogley, J. G., Gardner, A., Hagen, J.-O., Hock, R., Kaser, G., Pfeffer, W. T., Moholdt, G., Paul, F., Radić, V., Andreassen, L., Bajracharya, S., Beedle, M., Berthier, E., Bhambri, R., Bliss, A., Brown, I., Burgess, E., Burgess, D., Cawkwell, F., Chinn, T., Copland, L., Davies, B., de Angelis, H., Dolgova, E., Filbert, K., Forester, R., Fountain, A., Frey, H., Giffen, B., Glasser, N., Gurney, S., Hagg, W., Hall, D., Haritashya, U. K., Hartmann, G., Helm, C., Herreid, S., Howat, I., Kapustin, G., Khromova, T., Kienholz, C., Koenig, M., Kohler, J., Kriegel, D., Kutuzov, S., Lavrentiev, I., LeBris, R., Lund, J., Manley, W., Mayer, C., Miles, E., Li, X., Menounos, B., Mercer, A., Moelg, N., Mool, P., Nosenko, G., Negrete, A., Nuth, C., Pettersson, R., Racoviteanu, A., Ranzi, R., Rastner, P., Rau, F., Rich, J., Rott, H., Schneider, C., Seliverstov, Y., Sharp, M., Sigurdsson, O., Stokes, C., Wheate, R., Winsvold, S., Wolken, G., Wyatt, F., and Zhelyzhina, N.: Randolph Glacier Inventory [v2.0]: a Dataset of Global Glacier Outlines, digital media, available at: [http://www.glims.org/RGI/RGI\\_Tech\\_Report\\_V2.0.pdf](http://www.glims.org/RGI/RGI_Tech_Report_V2.0.pdf), Global Land Ice Measurements from Space, Boulder, Colorado, 2012.
- Bahr, D. B. and Radić, V.: Significant contribution to total mass from very small glaciers, *The Cryosphere*, 6, 763–770, doi:10.5194/tc-6-763-2012, 2012.
- Bahr, D. B., Meier, M. F., and Peckham, S. D.: The physical basis of glacier volume-area scaling, *J. Geophys. Res.*, 102, 20355–20362, 1997.
- Bahr, D. B., Dyurgerov, M., and Meier, M. F.: Sea-level rise from glaciers and ice caps: A lower bound, *Geophys. Res. Lett.*, 36, L03501, doi:10.1029/2008GL036309, 2009.
- Cazenave, A. and Llovel, W.: Contemporary sea level rise, *Annu. Rev. Mar. Sci.*, 2, 145–173, 2010.
- Cogley, J. G.: Geodetic and direct mass-balance measurements: comparison and joint analysis, *Ann. Glaciol.*, 50, 96–100, 2009a.
- Cogley, J. G.: A more complete version of the World Glacier Inventory, *Ann. Glaciol.*, 50, 32–38, 2009b.
- Cogley, J. G.: The Future of the World’s Glaciers, in: *The Future of the World’s Climate*, edited by: Henderson-Sellers, A. and McGuffie, K., 197–222, Elsevier, Amsterdam, 2012.
- Dyurgerov, M. B.: Data of Glaciological Studies – Reanalysis of Glacier Changes: From the IGY to the IPY, 1960–2008, Publication No. 108, Institute of Arctic and Alpine Research, Boulder, Colorado, 2010.
- Dyurgerov, M. B. and Meier, M. F.: *Glaciers and the Changing Earth System: A 2004 Snapshot*, Occas. Paper 58, 117 pp., Institute of Arctic and Alpine Research, Boulder, Colorado, 2005.
- Dyurgerov, M. B., Meier, M. F., and Bahr, D. B.: A new index of glacier area change: a tool for glacier monitoring, *J. Glaciol.*, 55, 710–716, 2009.
- Gardner, A. S., Moholdt, G., Cogley, J. G., Wouters, B., Arendt, A. A., Wahr, J., Berthier, E., Hock, R., Pfeffer, W. T., Kaser, G., Ligtenberg, S. R. M., Bolch, T., Sharp, M. J., Hagen, J. O., van den Broeke, M. R., and Paul, F. A.: Reconciled estimate of glacier contributions to sea level rise: 2003 to 2009, *Science*, 340, 852–857, 2013.
- Huss, M. and Farinotti, D.: Distributed ice thickness and volume of all glaciers around the world, *J. Geophys. Res.*, 117, F04010, doi:10.1029/2012JF002523, 2012.
- Huss, M., Sold, L., Hoelzle, M., Stokvis, M., Salzmann, N., Farinotti, D., and Zemp, M.: Towards remote monitoring of sub-seasonal glacier mass balance, *Ann. Glaciol.*, 54, 85–93, doi:10.3189/2013AoG63A427, 2013.
- Immerzeel, W. W., van Beek, L. P. H., and Bierkens, M. F. P.: Climate change will affect the Asian water towers, *Science*, 328, 1382–1385, 2010.
- Jacob, T., Wahr, J., Pfeffer, W. T., and Swenson, S.: Recent contributions of glaciers and ice caps to sea level rise, *Nature*, 482, 514–518, 2012.
- Jóhannesson, T., Raymond, C., and Waddington, E.: Time-scale for adjustment of glaciers to changes in mass balance, *J. Glaciol.*, 35, 355–369, 1989.
- Kääb, A., Reynolds, J. M., and Haeberli, W.: Glacier and permafrost hazards in high mountains, in: *Global Change and Mountain Regions: An Overview of Current Knowledge*, edited by: Huber, U. M., Bugmann, H. K. M., and Reasoner, M. A., Springer, Dordrecht, the Netherlands, 225–234, 2005.
- Kaser, G., Cogley, J. G., Dyurgerov, M. B., Meier, M. F., and Ohmura, A.: Mass balance of glaciers and ice caps: Consensus estimates for 1961–2004, *Geophys. Res. Lett.*, 33, L19501, doi:10.1029/2006GL027511, 2006.



- Kaser, G., Großhauser, M., and Marzeion, B.: Contribution potential of glaciers to water availability in different climate regimes, *P. Natl. Acad. Sci. USA*, 107, 20223–20227, 2010.
- Marzeion, B., Jarosch, A. H., and Hofer, M.: Past and future sea-level change from the surface mass balance of glaciers, *The Cryosphere*, 6, 1295–1322, doi:10.5194/tc-6-1295-2012, 2012.
- Meehl, G. A. and Stocker, T. F.: Global climate projections, in: *Climate Change 2007: The Physical Science Basis, Contribution of Working Group I to the Fourth Assessment Report of the Intergovernmental Panel on Climate Change*, edited by: Solomon, S., Qin, D., Manning, M., Marquis, M., Averyt, K., Tignor, M. M. B., Miller Jr., H. L., and Chen, Z., Cambridge University Press, Cambridge, 2007.
- Meier, M. F., Dyurgerov, M. B., Rick, U. K., O’Neel, S., Pfeffer, W. T., Anderson, R. S., Anderson, S. P., and Glazovsky, A. F.: Glaciers dominate eustatic sea-level rise in the 21st century, *Science*, 317, 1064–1067, 2007.
- Oerlemans, J., Anderson, B., Hubbard, A., Hybrechts, P., Jóhannesson, T., Knap, W. H., Schmeits, M., Stroeven, A. P., van de Wal, R. S. W., Wallinga, J., and Zuo, Z.: Modelling the response of glaciers to climate warming, *Clim. Dynam.*, 14, 267–274, 1998.
- Pelto, M. S.: Forecasting temperate alpine glacier survival from accumulation zone observations, *The Cryosphere*, 4, 67–75, doi:10.5194/tc-4-67-2010, 2010.
- Rabatel, A., Letréguilly, A., Dedieu, J.-P., and Eckert, N.: Changes in glacier Equilibrium-Line Altitude (ELA) in the western Alps over the 1984–2010 period: evaluation by remote sensing and modeling of the morpho-topographic and climate controls, *The Cryosphere Discuss.*, 7, 2247–2291, doi:10.5194/tcd-7-2247-2013, 2013.
- Radić, V. and Hock, R.: Regionally differentiated contribution of mountain glaciers and ice caps to future sea-level rise, *Nat. Geosci.*, 4, 91–94, 2011.
- Radić, V., Bliss, A., Breedlow, A. C., Hock, R., Miles, E., and Cogley, J. G.: Regional and global projections of twenty-first century glacier mass changes in response to climate scenarios from global climate models, *Clim. Dynam.*, doi:10.1007/s00382-013-1719-7, 2013.
- Raper, S. C. B. and Braithwaite, R. J.: Low sea level rise projections from mountain glaciers and icecaps under global warming, *Nature*, 439, 311–313, 2006.
- Slangen, A. B. A., Katsman, C. A., van de Wal, R. S. W., Vermeersen, L. L. A., and Riva, R. E. M.: Towards regional projections of twenty-first century sea-level change based on IPCC SRES scenarios, *Clim. Dynam.*, 38, 1191–1209, 2012.
- World Glacier Monitoring Service (WGMS): *Fluctuations of Glaciers 2005-2010 (Vol. X)*, edited by: Zemp, M., Frey, H., Gärtner-Roer, I., Nussbaumer, S. U., Hoelzle, M., Paul, F., and Haeberli W., ICSU (WDS) / IUGG (IACS) / UNEP / UNESCO / WMO, Zurich, Switzerland, 336 pp., Publication based on database version: doi:10.5904/wgms-fog-2012-11, 2012.

[13]

Mernild, S. H., Hanna, E., Yde, J. C., Seidenkrantz, M.-S., Wilson, R., and Knudsen, N. T. 2014. Atmospheric and oceanic influence on mass-balance trends of northern North Atlantic region land-terminating glaciers. *Geografiska Annaler: Series A, Physical Geography*, 96, 561–577, doi:10.1111/geoa.12053.

Reprinted with permission from Wiley

# ATMOSPHERIC AND OCEANIC INFLUENCE ON MASS BALANCE OF NORTHERN NORTH ATLANTIC REGION LAND-TERMINATING GLACIERS

SEBASTIAN H. MERNILD<sup>1,2</sup>, EDWARD HANNA<sup>3</sup>, JACOB C. YDE<sup>4</sup>, MARIT-SOLVEIG SEIDENKRANTZ<sup>5</sup>, RYAN WILSON<sup>1</sup> and NIELS TVIS KNUDSEN<sup>6</sup>

<sup>1</sup>Glaciology and Climate Change Laboratory, Center for Scientific Studies/Centro de Estudios Científicos (CECs), Chile

<sup>2</sup>Climate, Ocean, and Sea Ice Modeling Group, Los Alamos National Laboratory, New Mexico, USA

<sup>3</sup>Department of Geography, University of Sheffield, Sheffield, UK

<sup>4</sup>Faculty of Engineering and Science, Sogn og Fjordane University College, Sogndal, Norway

<sup>5</sup>Centre for Past Climate Studies, Department of Geoscience, and Arctic Research Centre, Aarhus University, Aarhus, Denmark

<sup>6</sup>Department of Geoscience, Aarhus University, Aarhus, Denmark

Mernild, S.H., Hanna, E., Yde, J.C., Seidenkrantz, M.-S., Wilson, R. and Knudsen, N.T., 2014. Atmospheric and oceanic influence on mass balance of northern North Atlantic region land-terminating glaciers. *Geografiska Annaler: Series A, Physical Geography*, 96, 561–577. doi:10.1111/geoa.12053

**ABSTRACT.** In this study, observed annual mass-balance data series from 1970 to 2009 for 29 land-terminating glaciers and ice caps in the northern North Atlantic region are presented to highlight their spatio-temporal variability. The glaciers and ice caps mass-balance data are compared with various zonal latitude bands of regional near-surface air temperature time series, large-scale atmospheric and oceanic circulation indices, as well as with North Icelandic sea-surface temperature records, since variations in mass-balance conditions are related both to variations in surface weather conditions and to atmospheric and oceanic circulations. The purpose is to explore statistical and physical relations based on the hypothesis that the general atmospheric and sea-surface warming trends are potential drivers of the ongoing regional glaciers and ice caps mass change. Our analysis shows that the mean observed northern North Atlantic glaciers and ice caps annual mass balance was mostly negative during the first decade of the twenty-first century, with a variability in glaciers and ice caps loss from c. 860 mm water equivalent yr<sup>-1</sup> for Southeast Greenland and Iceland to c. 380 mm water equivalent yr<sup>-1</sup> for Svalbard and Scandinavia. For Iceland and Scandinavia, variations in the North Atlantic oscillation seem to be important for mass-balance conditions, whereas overall for the entire northern North Atlantic region the mass-balance time series was significantly correlated with both NASA's Goddard Institute for Space Studies regional near-surface air temperature and Atlantic multidecadal oscillation time series, individually.

**Key words:** Atlantic multidecadal oscillation, climate change, climate indices, glaciers and ice caps, Greenland Blocking Index, North Atlantic oscillation

## Introduction

The annual mass balance of *glaciers and ice caps (GIC)* is dependent on changes in surface ablation and accumulation (Meier 1965; Kaser *et al.* 2006). In the Arctic, the mean annual surface air temperature has increased by twice the rate of the global surface air temperature in the past 100 years (e.g. Hansen *et al.* 2010). Around 20% of the estimated global GIC surface area is located in the northern North Atlantic region (Arendt *et al.* 2012; Radić *et al.* 2013). This makes the understanding of GIC mass-balance conditions in the northern North Atlantic particularly important, due to their significance to surface albedo, land–atmosphere heat exchange, and contribution to global sea-level rise. In fact, the GIC mass balance has on average shown greater mass loss from the early 1970s to mid/late 2000s (e.g. Kaser *et al.* 2006; Cogley 2012; Mernild *et al.* 2013b).

A way to understand the GIC mass-balance conditions from a climate change perspective could be to compare GIC mass-balance time series with various large-scale climatic indices, each describing a different part of the ocean–atmosphere system. Here, the significance of near-surface air temperature changes is tested through comparison with the

*Goddard Institute for Space Studies (GISS)* near-surface air temperature anomalies for various latitude bands, for example, 90–24° N and 90–64° N (Hansen *et al.* 2010; Erlykin *et al.* 2012). The role of *sea-surface temperature (SST)* and ocean circulation changes are studied through comparison with the *Atlantic multidecadal oscillation (AMO)* (updated from Kaplan *et al.* 1998). The AMO is an expression of fluctuating mean SST in the North Atlantic region, illustrating alternating multi-decadal periods of cool and warm SST anomalies throughout the North Atlantic Ocean (Schlesinger and Ramankutty 1994; Kerr 2000; Knudsen *et al.* 2011, 2014). According to Chylek *et al.* (2009), Arctic surface air temperatures (on land) are highly correlated with the AMO, suggesting that the Atlantic Ocean thermohaline circulation is linked to the Arctic temperature variability on a multi-decadal time scale. The overall trend in mean *Greenland Ice Sheet (GrIS)* melt extent seems to correlate with the smoothed trends of AMO (Mernild *et al.* 2011b). For the Alps, however, the mass balance is significantly anti-correlated with the AMO (Huss *et al.* 2010). Also, the *North Icelandic sea-surface Temperature (NICE SST)* records (Hanna *et al.* 2006; an area-averaged monthly time series constructed from three north Icelandic stations primarily focusing on the island of Grimsey located off Iceland's north coast) are used, where the NICE SST index expresses more localized temperature variability than the AMO. But as the region north of Iceland is strongly influenced by the varying strength of southward flowing Polar waters and northward transport of warm Atlantic water of subtropical origin, the NICE SST index could also be used as an index of the overall North Atlantic ocean circulation.

Atmospheric circulation indices are good measures of airflow and jet-stream variability (e.g. Overland *et al.* 2012) and have also been found to be important for GrIS mass-balance change (Hanna *et al.* 2013a, 2013b). The best described of these indices is the *North Atlantic oscillation (NAO)*; Hurrell and van Loon 1997) and the *Arctic oscillation (AO)*, which both represent large-scale regional North Atlantic and Arctic phenomena related to the Northern Hemispheric Northern Annular Mode (Feldstein and Franzke 2006). The AO describes sea-level pressure modulations in the strength of the polar vortex (Thompson and Wallace 1998), while the Atlantic expression of this is defined using the NAO index: i.e. the mean sea-level pressure difference between the Azores High and Icelandic Low (Hurrell and van Loon 1997). The AO and NAO

have been proven to, for example, influence the following: moisture transport from the North Atlantic to Northwest Europe (Dickson *et al.* 2000; Rogers *et al.* 2001); Northwest European winter storms (Hanna *et al.* 2008); surface air temperature anomalies (Hurrell 1996); inflow of warm Atlantic water into the Arctic Ocean (Dickson *et al.* 2000); winter precipitation over Scandinavian GIC (Reichert *et al.* 2001); mass balance of Scandinavian mountain glaciers; and changes in ocean circulation and precipitation in the larger North Atlantic region (Pohjola and Rogers 1997; Nesje *et al.* 2000; Rasmussen and Conway 2005; Seidenkrantz *et al.* 2007, 2008; Trouet *et al.* 2009, 2011; Marzeion and Nesje 2012; Olsen *et al.* 2012; Sicre *et al.* 2014). For example, Nesje *et al.* (2000) examined eight Scandinavian and two Svalbard glaciers and found that variations in NAO are best statistically correlated with mass-balance variations on maritime glaciers in southern Norway. The NAO also influences the climate of the continental European Alps (e.g. Beniston and Jungo 2002) and subsequently the GIC surface mass balances in this region (Marzeion and Nesje 2012).

The *Greenland blocking index (GBI)*, a Greenland-specific measurement of air circulation changes (Fang 2004; Hanna *et al.* 2012), which is defined as the normalized values of the 500 hPa mean geopotential height over the GBI domain 60–80° N and 20–80° W, is in contrast a more Greenland-specific indicator of atmospheric circulation than the NAO and may be expected to have a more pronounced impact on this area. GBI has previously been linked to GrIS runoff and mass changes by Hanna *et al.* (2013b), and to record melting of the GrIS surface in the summer 2012 (Hanna *et al.* 2013a).

In the study described herein, analyses of the statistical relationships and physical relations between land-terminating GIC mass balances in the northern North Atlantic region and large-scale atmospheric and oceanic circulation indices were evaluated, all in an effort to improve our understanding of the linkages. The goal is to, first, estimate individual mean annual land-terminating GIC annual mass-balance time series (1979–2009) from Southeast Greenland (comprising a section around the Sermilik Fjord), Iceland, Scandinavia, Svalbard, and the northern North Atlantic; second, map statistical relationships and physical relations (1970–2009) between the land-terminating GIC mass-balance time series and the GISS zonal mean annual near surface air temperature, mean annual

AMO index, mean winter NAO index, mean winter AO index, mean annual GBI, and mean annual NiCeSST; and third, analyze the range in correlation between indices.

This study is different from related studies by evaluating the relations between mesoscale climate (i.e. atmospheric circulation) and GIC mass-balance conditions in the northern North Atlantic region over larger temporal and spatial scales, and by including more climatic indices (in comparison to Brazel *et al.* 1992; Pohjola and Rogers 1997; Hodge *et al.* 1998; Bitz and Battisti 1999; Nesje *et al.* 2000; Marzeion and Nesje 2012). Studies by McCabe and Fountain (1995) and McCabe *et al.* (2000), for example, performed similar atmospheric circulation and mass balance analysis but included only a single glacier in the North Cascade Mountain Range and winter mass balance of Northern Hemisphere GIC, respectively.

It is important to emphasize that this paper only addresses the links between land-terminating GIC

mass-balance and large-scale climatic indices, and does not include marine-terminating glaciers, where mass-balance changes are additionally influenced by subaqueous melt.

## Study area, data, and methods

### Study area

The northern North Atlantic basin covers the Greenland Sea, Iceland Sea, Norwegian Sea, Barents Sea, Denmark Strait, and Fram Strait, and is surrounded by East Greenland, Iceland, Svalbard, and Norway (Fig. 1). The terrestrial landscape adjacent to the northern North Atlantic basin is characterized by strong relief with valleys and fjords, and ice-covered areas. The Randolph Glacier Inventory (e.g. Radić *et al.* 2013) reports ice-covered areas peripheral to the GrIS (between the ice sheet margin and the ocean) of 87 800 km<sup>2</sup>, Iceland 11 100 km<sup>2</sup>, Svalbard 34 000 km<sup>2</sup>, and Scandinavia 2900 km<sup>2</sup>.

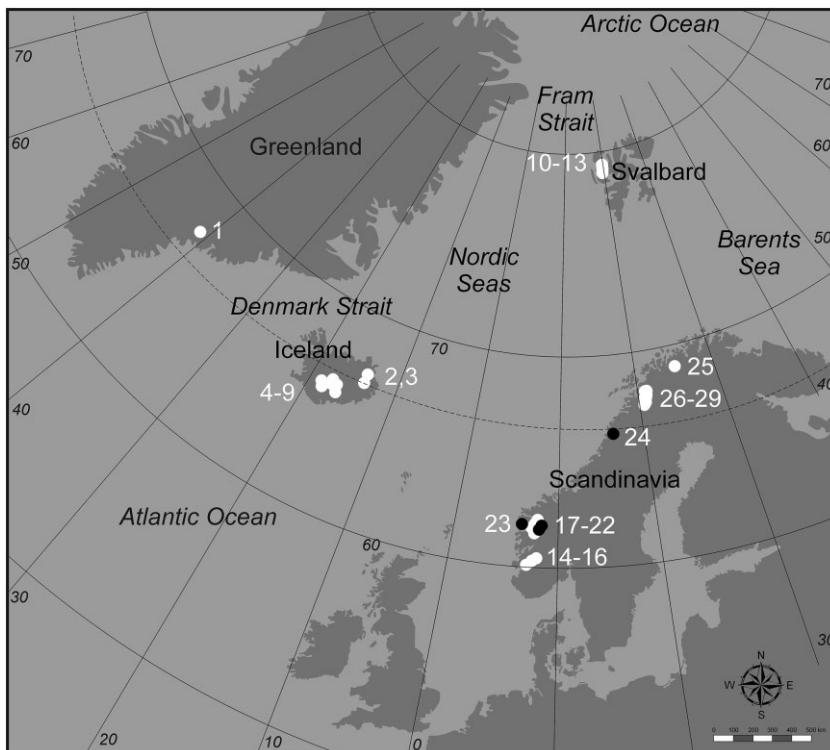


Fig. 1. Location of the observed GIC in the northern North Atlantic region (filled circles). Black dots indicate GIC with a positive cumulative mass balance since 1970 (see Fig. 3); white dots represent GIC with a negative cumulative mass balance since 1970. Numbers refer to the GIC specifications provided in Table 1.



### Dataset

Observations of annual mass balance ( $B_a$ ), winter mass balance ( $B_w$ ), and summer mass balance ( $B_s$ ) for land-terminating GIC from Southeast Greenland, Iceland, Svalbard, and Scandinavia (Figs 2 and 3), were obtained from the World Glacier Monitoring Service (WGMS) database (<http://www.wgms.ch>), and updated with time series from Dyurgerov and Meier (2005), Dyurgerov (2010), and Mernild *et al.* (2013b). In total,  $B_a$  data from 29 land-terminating GIC were used, the only long-term mass balance observed GIC in the region (Fig. 1 and Table 1), which is a minor fraction of the northern North Atlantic region's several thousands of GIC. Out of the 29 GIC, one was located in Southeast Greenland (in the Sermilik Fjord region), eight in Iceland, four in Svalbard (from the western part), and 16 in Scandinavia. Seventeen of these GIC have uninterrupted  $B_a$  records lasting at least 20 years. The number of GIC in the  $B_a$  dataset varied from 10 to 29 per year throughout the period 1970–2009, where 36% of the annual  $B_a$  were present from

1970 to 1979, 43% from 1980 to 1989, 79% from 1990 to 1999, and 96% from 2000 to 2009. The observed GIC vary in size from 2.3 km<sup>2</sup> to 1600 km<sup>2</sup> (Table 1); the relatively large GIC in Iceland distorts the surface area distribution. The observed GIC have a mean area of 130 km<sup>2</sup> and a median area of 6 km<sup>2</sup>, whereas approximately 80% of the observed GIC were smaller than 100 km<sup>2</sup>. For Iceland, the mean and median areas were 460 km<sup>2</sup> and 270 km<sup>2</sup>, respectively. For the  $B_w$  and  $B_s$  datasets, observations from 13 GIC were used from Scandinavia.

### Methods

The mean annual area-weighted mass-balance ( $\bar{B}_a$ ) time series were calculated for 1970–2009 (Fig. 4) based on available GIC data, and the following weighting function:

$$\bar{B}_a = \frac{\sum_{n=1}^N B_a A_n}{A_{total}} \quad (1)$$

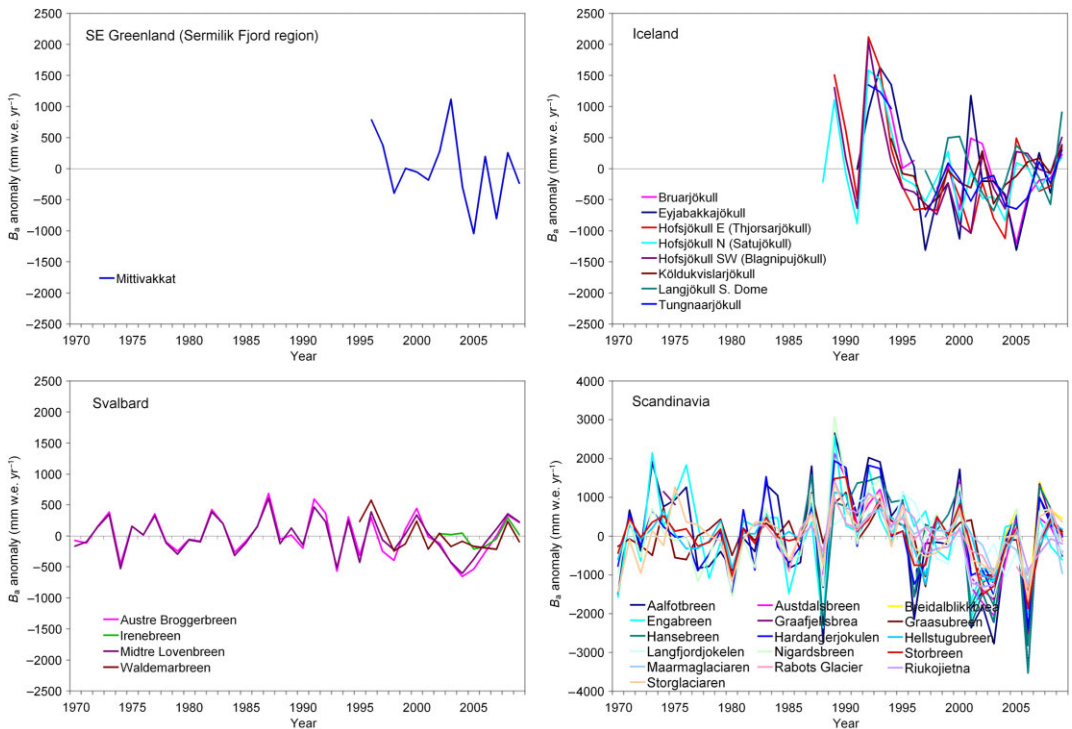


Fig. 2. Time series of observed  $B_a$  (annual mass balance) anomaly for the period 1970–2009 for GIC located in Southeast Greenland (Sermilik Fjord region), Iceland, Svalbard, and Scandinavia. Note the different scale on the ordinate for Scandinavia.

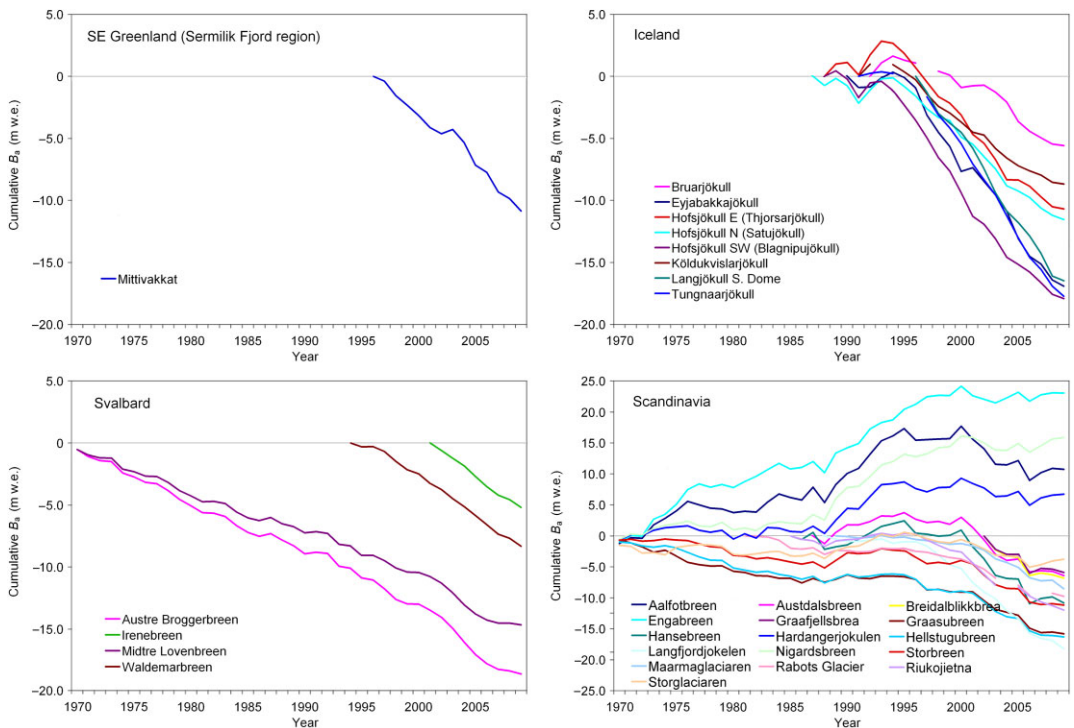


Fig. 3. Time series of cumulative observed  $B_a$  for the period 1970–2009 for GIC located in Southeast Greenland, Iceland, Svalbard, and Scandinavia. The location of the four Scandinavian GIC with a positive cumulative mass balance for the 1970–2009 interval are illustrated with black color (filled circles) on Figure 1. Note the different scale on the ordinate for Scandinavia.

where  $B_a$  is the specific individual observed GIC annual mass balance,  $A_n$  is individual GIC area cover, and  $A_{total}$  is the total GIC area cover for the observed GIC. The observed individual GIC areas were obtained from the WGMS database (based on the most updated dataset) and held constant due to the lack of area change observations throughout the period. This may induce a bias into the  $\bar{B}_a$  time series by underestimating the GIC area compared with reality. Mass-balance anomaly and cumulative  $B_a$  time series are shown for each individual GIC (Figs 2 and 3), and decadal  $\bar{B}_a$  means were calculated over several periods, for example, 1970–1979, 1980–1989, etc. as well as for the entire 1970–2009 period for each region (Table 2). In order to smooth out the annual variability's 10-year running mean, values are shown in different figures.

While McCabe *et al.* (2000) used a principal components analysis approach, we decided to follow the procedure used by Nesje *et al.* (2000) that the correlations between the  $\bar{B}_a$ ,  $B_a$ ,  $B_w$ , and  $B_s$  and

the climate indices should be calculated based on linear regression (henceforth the statistical relations are based on linear correlation). Furthermore, the statistical relationships were calculated on decadal scales and for 1970–2009 based on annual values.

To test for possible relations, all correlation trends labeled as “significant” are significant at or above the 5% level ( $p < 0.05$ ; where  $p$  is the significance level, indicating there is less than 5% probability that such a correlation between the two time series was produced by chance; see, for example, Table 3. Such calculations are based on the null hypothesis).

#### Uncertainties and representativeness

Direct  $B_a$  observations are subject to uncertainties. According to Zemp *et al.* (2013) the methodological uncertainty of  $B_a$  estimates on a single glacier are typically in the range of  $\pm 340$  mm water equivalent (w.e.)  $\text{yr}^{-1}$ , respectively, due to measurement and analytic errors. For Svalbard, a spatial variation in

Table 1. Geographic and glaciological characteristics of the 29 observed GIC in the northern North Atlantic, including mean  $B_a$  and standard errors for both the entire observational period and for the 2000–2009 interval, and  $B_a$  differences between the entire observational period and 2000–2009. For GIC locations, see Fig. 1.

Number	Location (country)	Glacier name	Latitude and longitude	Area (km <sup>2</sup> )	Observation period	Average $B_a$ for the observation period, including standard error (mm w.e. yr <sup>-1</sup> )	Average $B_a$ , for 2000–2009, including standard error (mm w.e. yr <sup>-1</sup> ). The differences between 2000–2009 and the entire observation period (mm w.e. yr <sup>-1</sup> ) and the standard error of the difference between the means of the samples are illustrated in the brackets
1	Southeast Greenland/ Sermilik Fjord region	Mittivakkat	65.67 N; 37.83 W	15.9	1996–2009	-776 ± 153	853 ± 191 (-77 ± 245)
2	Iceland	Brúarjökull	64.67 N; 16.17 W	1600.0	1993–2009, excl. 1997	-349 ± 156	-569 ± 162 (-220 ± 225)
3	Iceland	Eyjabakkajökull	64.65 N; 15.58 W	110.0	1991–2009	-891 ± 194	-1128 ± 229 (-237 ± 300)
4	Iceland	Hofsjökull E (Thjorsarjökull)	64.80 N; 18.58 W	235.9	1989–2009	-509 ± 191	-853 ± 171 (-334 ± 252)
5	Iceland	Hofsjökull N (Satujökull)	64.95 N; 18.92 W	81.5	1988–2009	-525 ± 143	-799 ± 116 (-274 ± 184)
6	Iceland	Hofsjökull SW (Blagnipujökull)	64.72 N; 19.05 W	51.5	1989–2009	-853 ± 164	-1028 ± 168 (-175 ± 235)
7	Iceland	Köldukvislarjökull	64.58 N; 17.83 W	310.0	1992–2009, excl. 1993	-510 ± 120	-572 ± 93 (-62 ± 152)
8	Iceland	Langjökull S. Dome	64.62 N; 18.07 W	900.0	1997–2009	-267 ± 132	-1270 ± 159 (-3 ± 206)
9	Iceland	Tungnaárjökull	64.62 N; 18.07 W	360.0	1986, 1992–1994, 1997–2009	-1041 ± 169	-1358 ± 98 (-317 ± 195)
10	Svalbard	Austra Brøggerbreen	78.88 N; 11.83 E	6.2	1970–2009	-467 ± 51	-567 ± 118 (-100 ± 128)
11	Svalbard	Irenebreen	78.65 N; 12.10 E	4.1	2002–2009	-652 ± 55	-652 ± 55 <sup>a</sup>
12	Svalbard	Midtre Lovénbreen	78.88 N; 12.07 E	5.5	1970–2009	-367 ± 47	-426 ± 105 (-59 ± 115)
13	Svalbard	Waldemarbreen	78.67 N; 12.00 E	2.6	1995–2009	-557 ± 62	-618 ± 55 (-61 ± 83)
14	Norway	Breidablikkbrea	60.10 N; 6.40 E	3.6	2003–2009	-973 ± 453	-973 ± 453 <sup>a</sup>
15	Norway	Gráfjellsbrea	60.10 N; 6.40 E	8.9	1974–1975, 2003–2009	-566 ± 501	-846 ± 501 (-280 ± 598)
16	Norway	Hardangerjøkulen	60.53 N; 7.37 E	17.1	1970–2009	168 ± 160	-113 ± 366 (-281 ± 399)
17	Norway	Ålfotbreen	61.75 N; 5.65 E	4.5	1970–2009	268 ± 231	-498 ± 550 (-766 ± 596)
18	Norway	Austdalsbreen	61.80 N; 7.35 E	11.8	1988–2009	-291 ± 241	-828 ± 369 (-537 ± 441)
19	Norway	Gråsubreen	61.65 N; 8.60 E	2.3	1970–2009	-396 ± 96	-680 ± 229 (-284 ± 248)
20	Norway	Hellstugubreen	61.57 N; 8.43 E	3.0	1970–2009	-408 ± 96	-722 ± 227 (-314 ± 246)
21	Norway	Nigardsbreen	61.72 N; 7.13 E	47.8	1970–2009	397 ± 157	149 ± 340 (-248 ± 375)
22	Norway	Storbreen	61.52 N; 8.13 E	5.4	1970–2009	-280 ± 110	-667 ± 279 (-387 ± 300)
23	Norway	Hansebreen	61.75 N; 5.68 E	3.1	1986–2009	-451 ± 298	-1089 ± 527 (-638 ± 605)
24	Norway	Engabreen	66.65 N; 13.85 E	39.6	1970–2009	577 ± 176	41 ± 331 (-536 ± 375)
25	Norway	Langfjordjøkul	70.12 N; 21.77 E	3.7	1989–2009	-868 ± 176	-1356 ± 218 (-488 ± 280)
26	Sweden	Mårmaglaciären	68.05 N; 18.41 E	4.0	1990–2009	-427 ± 120	-718 ± 194 (-291 ± 228)
27	Sweden	Rabots Glaciär	67.90 N; 18.55 E	3.9	1982–2009, excl. 2004 and 2007	-376 ± 115	-782 ± 231 (-406 ± 236)
28	Sweden	Riukojietna	68.08 N; 18.08 E	4.7	1986–2009, excl. 2004	-521 ± 155	-1075 ± 207 (-554 ± 250)
29	Sweden	Storglaciären	67.90 N; 18.57 E	3.2	1970–2009	-95 ± 111	-264 ± 246 (-169 ± 270)
Mean	-	-	-	-	-	-448 ± 167	-734 ± 241 (-286 ± 184)

<sup>a</sup> The differences in average between 2000–2009 and the entire observation period are not calculated, due to no observation being available before 2002.

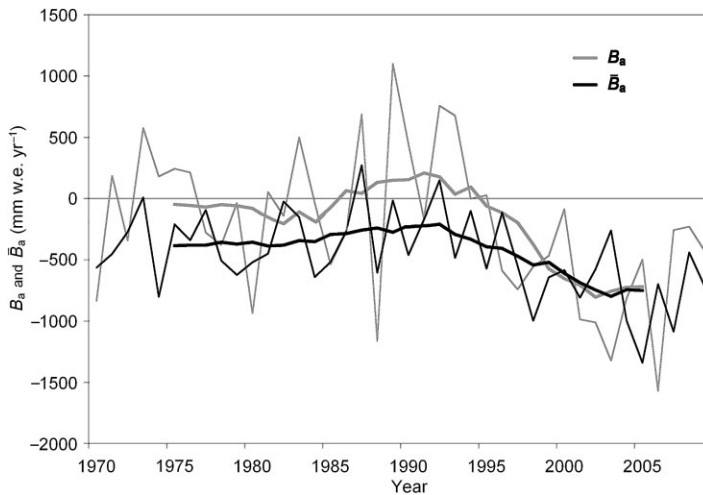


Fig. 4. Time series of  $B_a$  and  $\bar{B}_a$  for the northern North Atlantic region (1970–2009). The bold lines are 10-year running means.

Table 2. Means and standard errors of  $\bar{B}_a$  for Southeast Greenland, Iceland, Svalbard, and Scandinavia. For each period  $n = 10$ , except  $n = 4$  over 1996–1999 for the third period for Southeast Greenland. The fifth column gives the mean over the full period  $n = 14$  for Southeast Greenland,  $n = 20$  for Iceland,  $n = 40$  for Svalbard and Scandinavia.

Glaciated regions	$\bar{B}_a$ 1970–1979 (mm w.e. yr <sup>-1</sup> )	$\bar{B}_a$ 1980–1989 (mm w.e. yr <sup>-1</sup> )	$\bar{B}_a$ 1990–1999 (mm w.e. yr <sup>-1</sup> )	$\bar{B}_a$ 2000–2009 (mm w.e. yr <sup>-1</sup> )	Mean $\bar{B}_a$ (mm w.e. yr <sup>-1</sup> )
Southeast Greenland/ Sermilik Fjord region	–	–	$-583 \pm 252$	$-853 \pm 191$	$-776 \pm 153$
Iceland	–	–	$-320 \pm 250$	$-867 \pm 91$	$-594 \pm 144$
Svalbard	$-424 \pm 85$	$-333 \pm 84$	$-415 \pm 111$	$-534 \pm 87$	$-426 \pm 42$
Scandinavia	$346 \pm 217$	$272 \pm 355$	$565 \pm 198$	$-240 \pm 317$	$236 \pm 162$

Table 3.  $r^2$  values between  $\bar{B}_a$  and the different indices for individual decades (1970–1979, 1980–1989, etc.) and for 1970–2009. Significant correlations ( $p < 0.05$ ) are shown in bold.

Indices		1970–1979	1980–1989	1990–1999	2000–2009	1970–2009
GISS zonal mean annual near surface air temperature	90–24° N 90–64° N	0.19 <b>0.48</b>	0.01 <b>0.41</b>	<b>0.58</b> <b>0.38</b>	<b>0.28</b> 0.14	<b>0.26</b> <b>0.31</b>
AMO index		<0.01	0.08	<b>0.73</b>	0.11	<b>0.25</b>
Mean winter NAO index		0.09	0.01	<0.01	0.01	0.02
Mean winter AO Index		0.15	0.09	0.01	0.24	0.04
GBI		<0.01	<0.01	<0.01	0.13	0.05
NIceSST		0.15	0.04	0.04	0.06	0.07

geodetic balances has been illustrated between 1965–1990 and 2003–2007, with most negative balances occurring for GIC located in the south and least negative in the northeast (Nuth *et al.* 2010). As the only long-term GIC mass-balance observations are in the western part of Svalbard (Fig. 1), the observed  $B_a$  are not fully representative of Svalbard

as a region, and might be biased towards local trends for the smaller GIC in the western part. For Southeast Greenland, however, only one glacier has been observed, the Mittivakkat Gletscher: a glacier which is representative of GIC conditions in a broader region, i.e. the Sermilik Fjord region (Mernild *et al.* 2011a, 2012a). Mittivakkat is the

only long-term mass-balance observed glacier in Greenland (Mernild *et al.* 2013a, 2013b, 2013c).

## Results and discussion

### *Observed mass-balance conditions around northern North Atlantic*

In Fig. 2 the time series of the  $B_a$  1970–2009 anomaly are shown for each individual GIC grouped by Southeast Greenland, Iceland, Svalbard, and Scandinavia. For the four observed regions, the  $B_a$  time series generally show higher mass loss over time and insignificant mean mass loss trends for Southeast Greenland, Scandinavia, and Svalbard, and significant for Iceland ( $p < 0.025$ ). Overall, for the 29 GIC, the 2000–2009 mean observed  $B_a$  loss of  $734 \pm 241$  mm w.e. yr<sup>-1</sup> (henceforth, the  $\pm$  standard errors are included) was on average  $286 \pm 184$  mm w.e. yr<sup>-1</sup> greater than the 1970–2009 mean (Table 1). In Fig. 3 the time series for cumulative  $B_a$  1970–2009 are shown for each individual GIC, also grouped by Southeast Greenland, Iceland, Svalbard, and Scandinavia. For the observed GIC in Scandinavia the picture is diverse, showing both negative (in the range of  $-3.8 \pm 3.4$  to  $-18.2 \pm 3.7$  m w.e.; identical to  $-3.8 \pm 3.4 \times 10^3$  to  $-18.2 \pm 3.7 \times 10^3$  mm w.e.), and positive ( $6.7 \pm 6.4$  to  $23.1 \pm 7.0$  m w.e.) cumulative  $B_a$  since 1970. However, after 2000 the positive cumulative  $B_a$  seems to be decreasing or even reversing. For the three other regions all observed GIC had negative cumulative  $B_a$  records since 1970 in the range from  $-5.6 \pm 2.5$  to  $-17.9 \pm 3.4$  m w.e. (Iceland),  $-5.2 \pm 0.4$  to  $-18.7 \pm 2.1$  m w.e. (Svalbard) and  $-10.9 \pm 2.1$  m w.e. (Southeast Greenland) (Fig. 3). The observed Scandinavian GIC with positive cumulative  $B_a$  are classified as ice caps (according to the WGMS database) and as maritime (coastal) GIC (according to Hurrell and van Loon, 1997), and located within a maximum distance of 130 km from the North Atlantic coastline. Nesje *et al.* (2000) observed that Scandinavian maritime GIC gained mass from 1988 to 1998, while more continental Scandinavian GIC lost mass in the same time interval, mainly because maritime GIC  $B_a$  are more dominated by  $B_w$  (winter accumulation from lows coming from the Atlantic Ocean) than  $B_s$ . These findings by Nesje *et al.* (2000) were confirmed in the present study by the  $B_a$ ,  $B_w$ , and  $B_s$  observations for maritime and continental Scandinavian GIC for the period 1970–2009, where  $r^2$  values (square of the linear correlation coefficient) of 0.67 (0.61) occurred between  $B_w$  and  $B_a$  ( $B_s$  and  $B_a$ ) for maritime

GIC, and of 0.23 (0.70) respectively for continental GIC.

### *Weighted mass balance*

In Fig. 4, the 10-year running mean time series (1970–2009) of the  $B_a$  arithmetic mean observations for the northern North Atlantic region show positive  $B_a$  from 1986 to 1995 but negative before and after, with the greatest loss in mass balance after 1995. For the  $B_a$  time series the first half (1970–1989) of the observation period was influenced by the GIC conditions mainly in Svalbard and Scandinavia, and for the second half (1990–2009) by conditions in Southeast Greenland, Iceland, Svalbard, and Scandinavia (due to the percentage of available  $B_a$  data stated in the section *Dataset*). For the 10-year running means of the  $\bar{B}_a$  time series,  $\bar{B}_a$  was negative throughout the period averaging  $-455 \pm 54$  mm w.e. yr<sup>-1</sup>, less negative in the late 1980s and early 1990s, averaging  $-180 \pm 102$  mm w.e. yr<sup>-1</sup> and most negative for the first decade of the twenty-first century (2000–2009), with an average of  $-750 \pm 101$  mm w.e. yr<sup>-1</sup> (Fig. 4). For the first decade of the twenty-first century (2000–2009) the  $\bar{B}_a$  and  $B_a$  time series (based on annual values) indicated no significant difference (97.5% quantile) here and henceforth based on the null hypothesis. The  $\bar{B}_a$  fluctuation patterns in the northern North Atlantic GIC presented here are similar to the GrIS trends described by Rignot *et al.* (2008), who found the GrIS to be in balance in the 1970s and 1980s with subsequent rapid mass loss afterwards as the temperature increased over high latitudes.

In Fig. 5 available  $\bar{B}_a$  data for 1970–2009 are illustrated for Southeast Greenland, Iceland, Svalbard, and Scandinavia. For Scandinavia the  $\bar{B}_a$  10-year running means were on average positive until 1998 and negative thereafter. For Southeast Greenland, Iceland, and Svalbard the 10-year running means were consistently negative and most negative for the first decade of the twenty-first century. A comparison of annual means and their variance for the last decade (2000–2009) indicates that  $\bar{B}_a$  time series for Southeast Greenland ( $-853 \pm 191$  mm w.e. yr<sup>-1</sup>) and Iceland ( $-867 \pm 91$  mm w.e. yr<sup>-1</sup>) (Table 2) were not significantly different (97.5% quantile), both at the mean level of  $c. -860$  mm w.e. yr<sup>-1</sup>. For Svalbard ( $-534 \pm 87$  mm w.e. yr<sup>-1</sup>) and Scandinavia ( $-240 \pm 317$  mm w.e. yr<sup>-1</sup>) (Table 2) the average  $\bar{B}_a$  values were also not significantly different (97.5% quan-



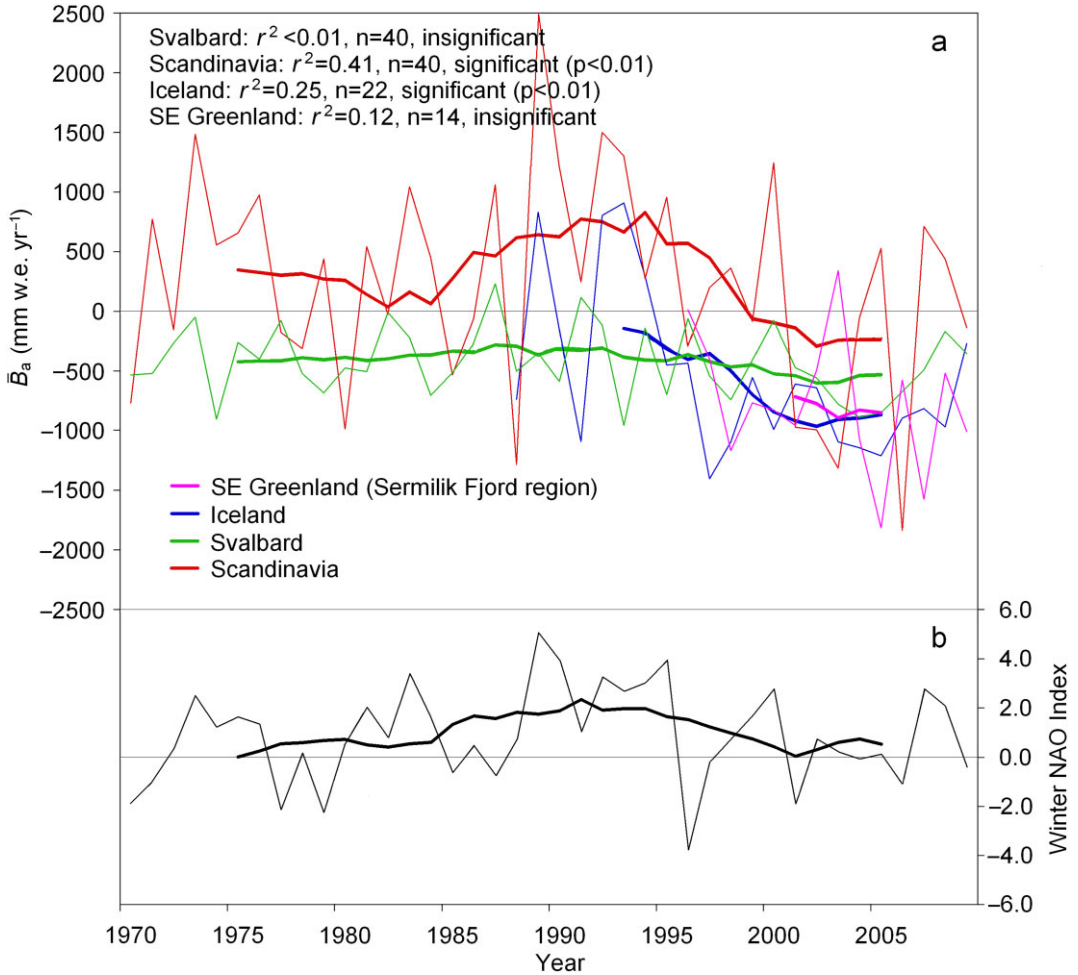


Fig. 5. (a)  $\bar{B}_a$  time series for Southeast Greenland, Iceland, Svalbard, and Scandinavia (1970–2009); and (b) time series of mean winter (December–March) NAO Index. The bold lines are 10-year running means.

tile) with a mean rate of *c.*  $-380 \text{ mm w.e. yr}^{-1}$  (Fig. 5). The difference in average  $\bar{B}_a$  (2000–2009) between Southeast Greenland and Iceland on the one hand, and Scandinavia and Svalbard on the other hand was significant (97.5% quantile), indicating on average more than two times less  $\bar{B}_a$  loss for GIC in Scandinavia and Svalbard than for GIC in Iceland and Southeast Greenland. The GIC, which form the basis for the mass-balance observations in Scandinavia and Svalbard, are located at latitudes from  $60^\circ \text{ N}$  through  $77^\circ \text{ N}$  (Table 1), i.e. up to  $4^\circ$  latitude further south than GIC in Iceland. Therefore the difference in  $\bar{B}_a$  loss observed between Southeast Greenland and Iceland, and Scandinavia and Svalbard appears not to be a simple function of

latitude, but may instead be explained by differences in climate, weather, and ocean conditions, such as polar jet stream changes (e.g. Overland *et al.* 2012) and corresponding variability in atmospheric wind and moisture transport (Dickson *et al.* 2000; Rogers *et al.* 2001). NAO is an atmospheric phenomenon which is known to, for example, influence the following: moisture transport from the North Atlantic onto Northwest Europe (Dickson *et al.* 2000; Rogers *et al.* 2001); Northwest European windstorms (Hanna *et al.* 2008); hemispheric surface air temperature anomalies (Hurrell 1996); coastal southern Greenland temperatures (Hanna and Cappelen 2003); the inflow of warm Atlantic-derived water into the Arctic Ocean (Dickson *et al.*

2000); winter precipitation over Scandinavian GIC (and subsequent  $B_w$ ) (Reichert *et al.* 2001); and the seesaw pattern in temperature and precipitation in the North Atlantic region. Therefore, it is also a potential candidate for explaining the northeast–southwest differences in  $\bar{B}_a$  response.

Regarding the use of NAO to explain the differences in  $\bar{B}_a$  within the northern North Atlantic region between the northeastern–southwestern parts, the NAO index for 1970–2009 (Fig. 5) shows a positive 10-year running mean for this period (although with a more negative trend for the last decade). This illustrates generally relatively mild and moist winter conditions for Northwest Europe, and thus a greater fraction than normal of the precipitation fell as liquid precipitation (depending on the 0°C isotherm altitude), whereas conditions over Greenland and Northeast Canada were primarily relatively cold and dry (Hurrell and van Loon 1997; Hanna and Cappelen 2003). We compared the annual Southeast Greenland, Iceland, Svalbard, and Scandinavia  $\bar{B}_a$  records with variations in winter NAO in order to test the statistical relationship: the winter season (December–March) is when the NAO is strongest, so these months tend to dominate the annual NAO index signal. A comparison between the NAO index and  $\bar{B}_a$  for Southeast Greenland, Iceland, Svalbard, and Scandinavia illustrates correlations (1970–2009) of  $r^2 = 0.12$  (insignificant), 0.25 (significant;  $p < 0.01$ ),  $< 0.01$  (insignificant), and 0.41 (significant;  $p < 0.01$ ), respectively, where 25–41% of the annual variability in  $\bar{B}_a$  for Iceland and Scandinavia can be explained by variations in NAO. These statistical correlations between  $\bar{B}_a$  and NAO conditions may explain the general  $\bar{B}_a$  difference, at least between Iceland and Scandinavia. In relatively dry winters, the diminished end-of-winter snow accumulation melts relatively fast during the spring warming (Iceland conditions). This will promote ablation of the underlying older ice; the ice surface albedo facilitates a stronger radiation-driven mass loss due to the lower albedo for ice than for snow (Stroeve *et al.* 2005). Conversely, for relatively wet winters (Scandinavia conditions) the enhanced end-of-winter snow accumulation, especially when coupled with frequent summer precipitation snow events, keeps the albedo high (Mernild and Liston 2012). In wet/snowy years, it therefore generally takes longer to melt the snowpack than in less wet/snowy years, thus delaying the start of ablation of the underlying ice. Also, the greater than normal liquid precipitation fraction during warm years tends to increase snow pack ablation since

heat is introduced by rain and by lowering the surface albedo.

The effects of volcanic ash fallout and glacier surge dynamics on mass balance are not accounted for in this study and may compromise the analyses of some of the observed Icelandic and Svalbard glaciers. Glacier surging is a cyclic flow instability that is characterized by a relatively short ( $< 1\text{--}10$  yr) marked increase in velocity followed by a long (20 to  $> 200$  yr) quiescent phase of slow velocity and rebuilding. The coupling between surge-type glaciers and  $B_a$  is not straightforward since  $B_a$  depends on changes in the hypsometry of a glacier and, therefore, on where a glacier is in its surge cycle (Yde and Paasche 2010). Recent glacier surges are likely to have negative effect on  $B_a$ , whereas glaciers that are well into their quiescent phase are likely to experience a positive effect on  $B_a$  (Nuth *et al.* 2010). In the northern North Atlantic, surge-type glaciers are clustered into three distinct regions (East Greenland, Svalbard, and Iceland) while no surge activity has ever been recorded in Scandinavia. Of the GIC in the dataset (Table 1), Mittivakkat Gletscher in Southeast Greenland is a key glacier representative of the region (Mernild *et al.* 2011a, 2012a). It is a non-surging glacier located south of the East Greenland surge cluster (Jiskoot *et al.* 2003). In Svalbard, surge-type glaciers are widely distributed (Jiskoot *et al.* 2000) but for the Svalbard GIC included in the dataset none have a known surge history. On the contrary, all Icelandic GIC in the dataset have experienced surge events in recent centuries (Björnsson *et al.* 2003; Evans 2011).

#### *Northern North Atlantic weighted mass balance*

To test the possible statistical relationship between the northern North Atlantic region GIC mass balance and various atmospheric and ocean circulation indices and temperature data, we compared the time series of  $\bar{B}_a$  (only based on annual values, even though the 10-year running means illustrated in Fig. 6a–f are showing on average almost similar trends) for 1970–2009 and on decadal timescale (1970–1979, 1980–1989, etc.). On a decadal scale, calculations of statistical relations showed significant correlations between  $\bar{B}_a$  and GISS zonal near surface air temperature for areas 90–24° N: 1990–1999 ( $r^2 = 0.58$ ) and 2000–2009 (0.28), and 90–64° N: 1970–1979 (0.48), 1980–1989 (0.41), and 1990–1999 (0.38), and between  $\bar{B}_a$  and the AMO index (1990–1999) (0.73) (Table 3). In contrast, for the overall period 1970–2009 the statistical relations on

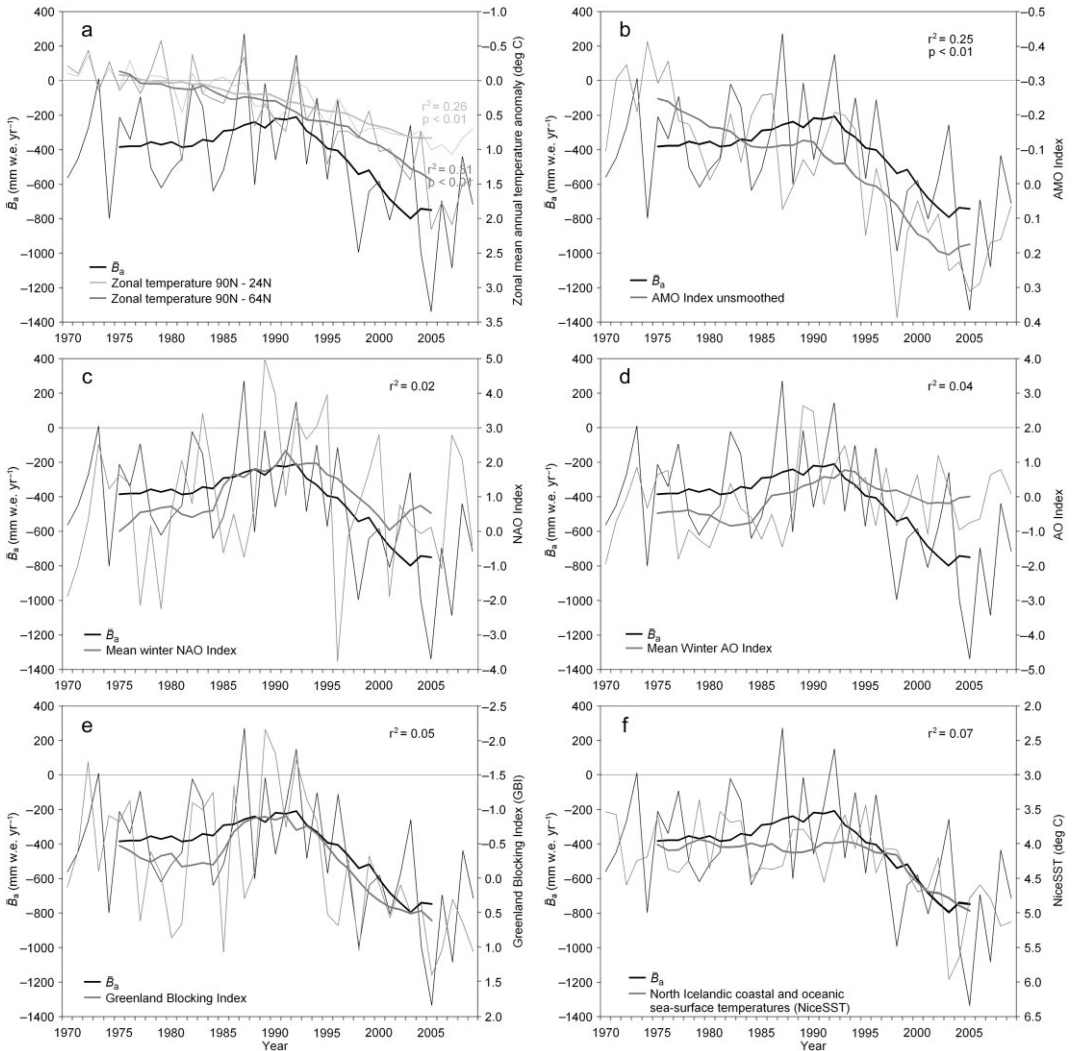


Fig. 6. Time series of  $\bar{B}_a$  1970–2009 compared with (a) GISS zonal near surface air temperature anomaly; (b) unsmoothed AMO index; (c) mean winter (December–March) NAO index; (d) mean winter (January–March) AO index; (e) GBI; and (f) reconstructed NiceSST. Where correlations are significant,  $p$ -values are added. The bold lines are 10-year running means. Note the inverse scales for the second ordinate on (a), (b), (e) and (f).

annual values showed significant correlations with GISS (90–24° N and 90–64° N) of 0.26–0.31 ( $p < 0.01$ ) and AMO of 0.25 ( $p < 0.01$ ) (Table 3), where a relatively high  $\bar{B}_a$  loss corresponded to a relatively high (warm) zonal surface air temperature and SST, and positive AMO index (Fig. 6). Insignificant correlations were found with winter NAO, AO, GBI, and NiceSST. In Table 4 the physical explanations between changes in indices and related climate processes (like cold/mild and dry/wet conditions) and subsequent changes in  $\bar{B}_a$  conditions

are illustrated. Regarding AMO, it is a physically based SST index known to be linked to continental-near surface temperatures, which are physically related to  $B_s$  and subsequent  $\bar{B}_a$ . A positive AMO index indicates relatively high surface air temperature and less precipitation at high latitudes (subsequent relatively high  $\bar{B}_a$  loss), and a negative AMO index corresponds to relatively low surface air temperature and a higher precipitation (subsequent relatively low  $\bar{B}_a$  loss). As an example, it could be noted for the AMO index that high GIC mass-balance loss

Table 4. Physical links between variations in indices and temperature data and the impacts on climate parameters in the northern North Atlantic region and subsequent GIC mass balances. The sign > indicates relatively small GIC mass-balance loss, and >> indicates relatively greater GIC mass-balance loss.

Indices or temperature data	Variability in indices and temperature data	Impact on climate parameters in the northern North Atlantic region	Mass balance	Reference
GISS zonal mean annual near surface air temperature AMO index	Increasing surface air temperature	Increasing ablation	from > to >> loss	e.g. Hock (2003)
	Positive AMO	Relatively less precipitation and relatively high surface air temperature	>> loss	e.g. Mernild <i>et al.</i> (2012b)
	Negative AMO	Relatively high precipitation and relatively low surface air temperature	> loss	e.g. Mernild <i>et al.</i> (2012b)

Table 5.  $r^2$  values between the climatic and oceanic indices and temperature data 1970–2009. Significant correlations ( $p < 0.05$ ) are illustrated in bold.

Indices or temperature data		GISS zonal mean annual near surface air temperature		AMO index	Winter NAO index	Winter AO Index	GBI
		90–24° N	90–64° N				
		GISS zonal mean annual near surface air temperature	90–24° N				
	90–64° N	<b>0.83</b>	–	–	–	–	–
AMO index		<b>0.76</b>	<b>0.57</b>	–	–	–	–
Winter NAO index		0.02	0.01	<0.01	–	–	–
Winter AO Index		0.04	0.03	<0.01	<b>0.55</b>	–	–
GBI		<b>0.20</b>	<b>0.20</b>	<b>0.12</b>	<0.01	<0.01	–
NIceSST		<b>0.21</b>	<b>0.23</b>	<b>0.18</b>	0.04	<0.01	<b>0.18</b>

occurs during periods when the North Atlantic and Northwest Europe are characterized by positive temperature anomalies (e.g. Trenberth *et al.* 2007; Hansen *et al.* 2010). Despite the seemingly modest changes in the AMO index of *c.* 0.2, the AMO anomalies are stable and their timescale is sufficient to exert a significant influence on the climatic variability in the northern North Atlantic region (e.g. Polonsky 2011).

These statistical relationships might indicate inter-annual variability in the linkage between  $\bar{B}_a$  and the atmosphere and ocean surface circulation processes, and that GIC annual  $\bar{B}_a$  may partly be controlled by synoptic-scale atmosphere and ocean circulation changes (for GISS 26–31% of the variability in  $\bar{B}_a$  could be explained by the zonal temperatures, and 25% by AMO), and partly probably by local to meso-scale climatic variations, with both sets of factors affecting trends in, for example, near surface air temperature, radiation, and snow accumulation patterns.

For Iceland and Scandinavia (Fig. 5) the mean winter NAO index however correlates significantly

with the  $\bar{B}_a$ , indicating that the NAO is a useful predictor of GIC Iceland and Scandinavia mass-balance variations. On an annual scale for the northern North Atlantic, the lowest  $r^2$  values of 0.02 and 0.04 occurred between  $\bar{B}_a$  and the NAO index and  $\bar{B}_a$  and the AO index (Table 3), respectively, even though Meier *et al.* (2003) have previously shown a strong correlation between AO and  $B_w$ .

#### *Correlations between temperature data/indices and multiple linear regression*

Based on the different atmospheric and ocean circulation indices and temperature datasets: GISS zonal mean annual near surface air temperature 90–24° N and 90–64° N, AMO index, mean winter NAO index, mean winter AO index, GBI, and NIceSST, a matrix is shown in Table 5, illustrating (in)significant correlations. Significant correlations occurred, for example, between the AMO index and the GISS zonal surface air temperature, and NIceSST, whereas insignificant correlations

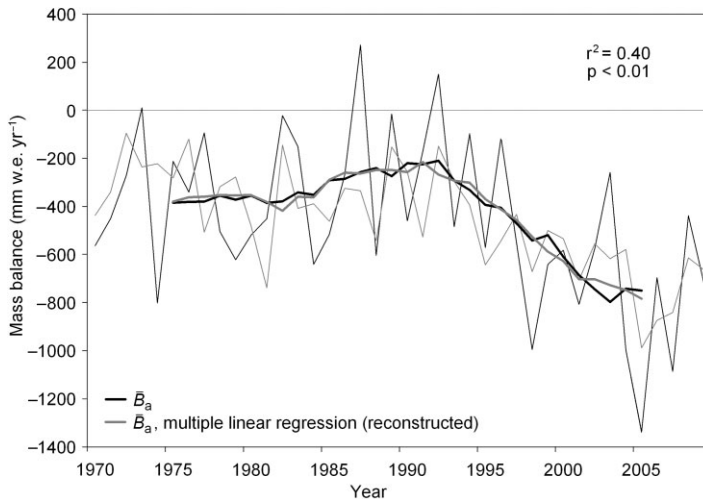


Fig. 7. Time series of  $\bar{B}_a$  and reconstructed  $\bar{B}_a$  based on multiple linear regression (1970–2009). The bold lines are 10-year running means.

Table 6.  $r^2$  values, maximum residual, and root mean square residual for the multiple linear regressions (the reconstructed  $\bar{B}_a$  time series can be found in Fig. 7) estimated based on a different number of indices. Significant correlations ( $p < 0.05$ ) are illustrated in bold.

	Mean 1970–2009		
	$r^2$ values	Maximum annual residual (mm w.e. yr <sup>-1</sup> )	Root mean square residual (mm w.e. yr <sup>-1</sup> )
All seven indices	<b>0.40</b>	-610	262
Combinations of six indices	<b>0.28–0.40</b>	607–842	262–271
Combinations of five indices	<b>0.28–0.40</b>	586–840	262–286
Combinations of four indices	<b>0.12–0.40</b>	586–894	262–316
Combinations of three indices	<b>0.09–0.39</b>	572–897	263–321
Combinations of two indices	0.03– <b>0.39</b>	563–897	264–331

occurred between AMO and winter NAO or winter AO (NAO and AO are both surface pressure-based indices). Between NAO and AO the correlation was significant (Table 5).

Further, based on these annual relations between the atmospheric and ocean circulation indices and temperature datasets, a North Atlantic region  $\bar{B}_a$  time series (hindcast) was reconstructed and compared with actual observations (Fig. 7). The  $r^2$  value of the reconstructed time series was 0.40 ( $p < 0.01$ ; significant) compared with observations showing a root mean square residual of 262 mm w.e. yr<sup>-1</sup>. If indices/temperature datasets are omitted, one by one (Table 6), the different combinations of, for example, six, five, four indices/temperature datasets, etc., indicates a clear lowering and a greater range in the  $r^2$  values from

0.28–0.40 based on the combination of six indices to 0.03–0.39 based on the combination of two indices. Based on the combination of the two indices GISS 90–24° N and Winter NAO, an  $r^2$  value of 0.39 occurred. These data show that including all seven indices rather than only GISS 90–24° N and Winter NAO does not significantly improve the maximum correlation between the reconstructed time series and the observed time series. Also, an increase and a greater range in the root mean square residuals occurred from 262–271 mm w.e. yr<sup>-1</sup> based on the combination of six indices to 264–331 mm w.e. yr<sup>-1</sup> based on the combination of two indices. Furthermore, the GISS 90–24° N and Winter NAO exhibit the lowest root mean square residuals of 264 mm w.e. yr<sup>-1</sup> based on a combination of two



indices. Therefore, in future studies, for example, the combination of GISS 90–24° N and Winter NAO might be preferred, as the *best* model, to hindcast changes in the North Atlantic region mass-balance time series, since the combination of an increasing number of indices (three, four, five, etc.) does not improve the maximum correlation and the minimum residual significantly.

Thus, although the use of annual indices/temperature datasets may still lack accuracy due to, for example, incomplete representation by numerical models, neglected climate feedbacks, GIC area and hypsometry changes, and glacier surge activity, which are issues all having an impact on the analyses, the multiple linear regression prediction model (based on the combination of GISS 90–24° N and Winter NAO) captures the overall trends and variations in the  $\bar{B}_a$  time series from 1970 to 2009 (Fig. 7).

## Conclusions

To explore atmospheric and oceanic influence on the mass balance of land-terminating GIC in the northern North Atlantic region, we used correlation analysis, based on known physical relations. Our findings show that since 1970,  $\bar{B}_a$  (mean annual area-weighted mass balance) in the northern North Atlantic has generally been more negative during the first decade of the twenty-first century (2000–2009), with an average of  $-750 \pm 101$  mm w.e. yr<sup>-1</sup>. For Iceland and Scandinavia individually  $\bar{B}_a$  statistically correlated significantly with the mean winter NAO index, as the latter is a signature of the North Atlantic airflow and moisture transport into Northwest Europe. The average positive NAO index (1970–2009) contributed to relatively mild and wet winters in Northwest Europe and cold and dry winters in Greenland and Northeast Canada, partly explaining the differences in  $\bar{B}_a$  between Southeast Greenland and Iceland (c.  $-860$  mm w.e. yr<sup>-1</sup>) and Svalbard and Scandinavia (c.  $-380$  mm w.e. yr<sup>-1</sup>), based on variations in end-of-winter snow accumulation, surface albedo, and melt rates. This indicates on average more than twice less  $\bar{B}_a$  loss for GIC in Scandinavia and Svalbard than for GIC in Iceland and Southeast Greenland. Overall, on a northern North Atlantic annual timescale, the statistical relationship between  $\bar{B}_a$  and the GISS zonal near surface air temperature for the areas 90–24° N and 90–64° N, and  $\bar{B}_a$  and the ocean circulation index AMO are significant.

## Acknowledgements

This work was supported by the Chilean Government through the Centers of Excellence Base Financing Program of CONICYT, the Earth System Modeling program by the Scientific Discovery for Advanced Computing (SciDAC) program within the US Department of Energy's Office of Science and by the Los Alamos National Laboratory. LANL is operated under the auspices of the National Nuclear Security Administration of the US Department of Energy under Contract No. DE-AC52-06NA25396, and partly from the European Community's Seventh Framework Programme under grant agreement No. 262693 (project GLAMOSEG-II). It is also a contribution to the OCEANHEAT project funded by the Danish Council for Independent Research Natural Science (Project No. 12-126709/FNU), and the EU FP7 project "Past4Future" (Project No. 243908). Thanks are given to reviewers for their valuable comments and to the World Glacier Monitoring Service for providing GIC mass-balance data. We thank the Icelandic Meteorological Office and Trausti Jonsson for help in updating the NiCeSST dataset and data used therein. NASA GISS data can be downloaded from <http://data.giss.nasa.gov/gistemp/tabledata/ZonAnn.Ts+dSST.txt>, AMO: <http://www.esrl.noaa.gov/psd/data/time-series/AMO/>, NAO: [http://gcmd.nasa.gov/records/GCMD\\_NCAR\\_NAO.html](http://gcmd.nasa.gov/records/GCMD_NCAR_NAO.html), and AO: [http://www.cpc.ncep.noaa.gov/products/precip/CWlink/daily\\_ao\\_index/ao.shtml](http://www.cpc.ncep.noaa.gov/products/precip/CWlink/daily_ao_index/ao.shtml).

*Sebastian H. Mernild, Ryan Wilson, Glaciology and Climate Change Laboratory, Center for Scientific Studies/Centro de Estudios Científicos (CECs), Av. Arturo Prat 514, 5110466 Valdivia, Chile*

*Email: mernild@cecs.cl and rwilson@cecs.cl*

*Edward Hanna, Department of Geography, University of Sheffield, Sheffield S10 2TN, UK*

*Email: e.hanna@sheffield.ac.uk*

*Jacob C. Yde, Faculty of Engineering and Science, Høgskulen i Sogn og Fjordane, Postboks 133, 6851 Sogndal, Norway*

*Email: jacob.yde@hisf.no*

*Marit-Solveig Seidenkrantz, Centre for Past Climate Studies, and Arctic Research Centre, Department of Geoscience, Aarhus University, Høegh-Guldbergs Gade 2, 8000 Aarhus C, Denmark*

*Email: mss@geo.au.dk*

*Niels Tvis Knudsen, Department of Geoscience, Aarhus University, Høegh-Guldbergs Gade 2, 8000 Aarhus C, Denmark*

*Email: ntk@geo.au.dk*

## References

- Arendt, A., Bolch, T., Cogley, J.G., Gardner, A., Hagen, J.-O., Hock, R., Kaser, G., Pfeffer, W.T., Moholdt, G., Paul, F., Radic, V., Andreassen, L., Bajracharya, S., Beedle, M., Berthier, E., Bhambri, R., Bliss, A., Brown, I., Burgess, E., Burgess, D., Cawkwell, F., Chinn, T., Copland, L., Davies, B., de Angelis, H., Dolgova, E., Filbert, K., Forester, R., Fountain, A., Frey, H., Giffen, B., Glasser, N., Gurney, S., Hagg, W., Hall, D., Haritashya, U.K., Hartmann, G., Helm, C., Herreid, S., Howat, I., Kapustin, G., Khromova, T., Kienholz, C., Koenig, M., Kohler, J., Kriegel, D., Kutuzov, S., Lavrentiev, I., LeBris, R., Lund, J., Manley, W., Mayer, C., Miles, E., Li, X., Menounos, B., Mercer, A., Moelg, N., Mool, P., Nosenko, G., Negrete, A., Nuth, C., Petterson, R., Racoviteanu, A., Ranzi, R., Rastner, P., Rau, F., Rich, J., Rott, H., Schneider, C., Seliverstov, Y., Sharp, M., Sigursson, O., Stokes, C., Wheate, R., Winsvold, S., Wolken, G., Wyatt, F. and Zhelyzhina, N., 2012. Randolph Glacier Inventory [v2.0]: A Dataset of Global Glacier Outlines. Global Land Ice Measurements from Space, Boulder Colorado, USA, Digital Media (with area corrections downloaded 2012).
- Beniston, M. and Junco, P., 2002. Shifts in the distributions of pressure, temperature and moisture and changes in the typical weather patterns in the Alpine region in response to the behaviour of the North Atlantic Oscillation. *Theoretical and Applied Climatology*, 71, 29–42.
- Bitz, C.C. and Battisti, D.S., 1999. Interannual to decadal variability in climate and the glacier mass balance in Washington, western Canada, and Alaska. *Journal of Climate*, 12, 3181–3196.
- Björnsson, H., Pálsson, F., Sigurdsson, O. and Flowers, G.E., 2003. Surges of glaciers in Iceland. *Annals of Glaciology*, 36, 82–90.
- Brazel, A.J., Chambers, F.B. and Kalkstein, L.S., 1992. Summer energy balance on West Gulkana Glacier, Alaska, and linkages to a temporal synoptic index. *Zeitschrift für Geomorphologie*, 86, 15–34.
- Chylek, P., Folland, C., Lesins, G., Wang, M. and Dubey, M., 2009. Arctic air temperature change amplification and the Atlantic multidecadal oscillation. *Geophysical Research Letters*, 36, L14801. doi:10.1029/2009GL038777
- Cogley, J.G., 2012. The future of the world's glaciers. In: Henderson-Sellers, A. and McGuffie, K. (eds), *The Future of the World's Climate*. Elsevier, Amsterdam. 197–222.
- Dickson, R.R., Osborn, T.J., Hurrell, J.W., Meincke, J., Blindheim, J., Adlandsvik, B., Vinje, T., Alekseev, G. and Maslowski, W., 2000. The Arctic Ocean response to the North Atlantic Oscillation. *Journal of Climate*, 13, 2671–2696.
- Dyrgerov, M.B., 2010. *Data of glaciological studies – reanalysis of glacier changes: from the IGY to the IPY, 1960–2008*. Publication No. 108, Institute of Arctic and Alpine Research, University of Colorado.
- Dyrgerov, M.B. and Meier, M.F., 2005. *Glaciers and the changing Earth system: a 2004 snapshot*. Occasional Paper No. 58, Institute of Arctic and Alpine Research, University of Colorado.
- Erylkin, A.D., Wolfendale, A.W. and Hanna, E., 2012. Global warming – some perspectives. *Journal of Environmental Science and Engineering*, B1, 2 (4), 499–509.
- Evans, D.J.A., 2011. Glacial landsystems of Satujökull, Iceland: a modern analogue for glacial landsystem overprinting by mountain icecaps. *Geomorphology*, 129, 225–237.
- Fang, Z.-F., 2004. Statistical relationship between the northern hemisphere sea ice and atmospheric circulation during wintertime. In: Zhu, X. (ed.), *Observation, Theory and Modeling of Atmospheric Variability*. World Scientific Series on Meteorology of East Asia. World Scientific Publishing Company, Singapore. 131–141.
- Feldstein, S.B. and Franzke, C., 2006. Are the northern oscillation and the northern annular mode distinguishable? *Journal of Atmospheric Sciences*, 63, 2915–2930.
- Hanna, E. and Cappelen, J., 2003. Recent cooling in coastal southern Greenland and relation with the North Atlantic Oscillation. *Geophysical Research Letters*, 30 (3), 1132. doi:10.1029/2002GL015797.
- Hanna, E., Cappelen, J., Allan, R., Jónsson, T., le Blancq, F., Lillington, T. and Hickey, K., 2008. New insights into North European and North Atlantic surface pressure variability, storminess and related climatic change since 1830. *Journal of Climate*, 21, 6739–6766. doi:10.1175/2008JCLI2296.1.
- Hanna, E., Fettweis, X., Mernild, S.H., Cappelen, J., Ribergaard, M.H., Shuman, C. A., Steffen, K., Wood, L. and Mote, T.L., 2013a. Atmospheric and oceanic climate forcing of the exceptional Greenland ice sheet surface melt in summer 2012. *International Journal of Climatology*, 34, 1022–1037. doi:10.1002/joc.3743.
- Hanna, E., Jones, J.M., Cappelen, J., Mernild, S.H., Wood, L., Steffen, K. and Huybrechts, P., 2013b. The influence of North Atlantic atmospheric and oceanic forcing effects on 1900–2010 Greenland summer climate and ice melt/runoff. *International Journal of Climatology*, 33, 862–880. doi: 10.1002/joc.3475.
- Hanna, E., Jónsson, T., Ólafsson, J. and Valdimarsson, H., 2006. Icelandic coastal sea-surface temperature records constructed: putting the pulse on air-sea-climate interactions in the northern North Atlantic. Part 1: Comparison with HadISST1 open ocean surface temperatures and preliminary analysis of long-term patterns and anomalies of SSTs around Iceland. *Journal of Climate*, 19, 5652–5666.
- Hanna E, Mernild S.H., Cappelen, J. and Steffen K., 2012. Recent warming in Greenland in a long-term instrumental (1881–2012) climatic context. Part 1: evaluation of surface air temperature records. *Environmental Research Letters*, 7, 045404. doi:10.1088/1748-9326/7/4/045404.
- Hansen, J., Ruedy, R., Sato, M. and Lo, K., 2010. Global surface temperature change. *Reviews of Geophysics*, 48, RG4004.
- Hock, R., 2003. Temperature index melt modelling in mountain areas. *Journal of Hydrology*, 282 (1–4), 104–115.
- Hodge, S.M., Trabant, D.C., Krimmel, R.M., Heinrichs, T.A., March, R.S. and Josberger, E.G., 1998. Climate variations and changes in mass of three glaciers in western North America. *Journal of Climate*, 11, 2161–2179.
- Hurrell, J.W., 1996. Influence of variations in extratropical wintertime teleconnections on Northern Hemisphere temperature. *Geophysical Research Letters*, 23, 665–668.

- Hurrell, J.W. and van Loon, H., 1997. Decadal variations in climate associated with the North Atlantic oscillation, *Climate Change*, 36, 301–326.
- Huss, M., Hock, R., Bauder, A. and Funk, M., 2010. 100-year mass changes in the Swiss Alps linked to the Atlantic multidecadal oscillation, *Geophysical Research Letters*, 30 (10). doi:10.1029/2010GL042616.
- Jiskoot, H., Murray, T. and Boyle, P., 2000. Controls on the distribution of surge-type glaciers in Svalbard. *Journal of Glaciology*, 46, 412–422.
- Jiskoot, H., Murray, T. and Luckman A., 2003. Surge potential and drainage-basin characteristics in East Greenland. *Annals of Glaciology*, 36, 142–148.
- Kaplan, A., Cane, M.A., Kushnir, Y. and Clement, A.C., 1998. Analyses of global sea surface temperatures 1856–1991. *Journal of Geophysical Research*, 103, 18575–18589.
- Kaser, G., Cogley, J.C., Dyurgerov, M.B., Meier, M.F. and Ohmura, A., 2006. Mass balance of glaciers and ice caps: consensus estimates for 1961–2004. *Geophysical Research Letters*, 33, 1–5.
- Kerr, R.A., 2000. A North Atlantic climate pacemaker for the centuries. *Science*, 288, 1984–1985.
- Knudsen, M.F., Jacobsen, B.H., Seidenkrantz, M.-S. and Olsen, J., 2014. Evidence for external forcing of the Atlantic multidecadal oscillation since the termination of the Little Ice Age. *Nature Communications*, 5, 3323. doi:10.1038/ncomms4323.
- Knudsen M.F., Seidenkrantz, M.-S., Jacobsen, B.H. and Kuijpers, A., 2011. Tracking the Atlantic multidecadal oscillation through the last 8,000 years. *Nature Communications*, 2, 178. doi:10.1038/ncomms1186.
- Marzeion, B. and Nesje, A., 2012. Spatial patterns of North Atlantic oscillation influence on mass balance variability of European glaciers. *The Cryosphere*, 6, 661–673.
- McCabe, G.J. and Fountain, A.G., 1995. Relations between atmospheric circulation and the mass balance of South Cascade Glacier, Washington. *Arctic and Alpine Research*, 27, 226–233.
- McCabe, G.J., Fountain, A.G. and Dyurgerov, M., 2000. Variability in winter mass balance of northern hemisphere glaciers and relations with atmospheric circulation. *Arctic, Antarctic and Alpine Research*, 32, 64–72.
- Meier, M.F., 1965. Glaciers and climate. In: Wright, H.E. and Frey, D.G. (eds), *The Quaternary of the United States*. Princeton University Press, Princeton, New Jersey. 795–805.
- Meier, M.F., Dyurgerov, M.B. and McCabe, G.J., 2003. The health of glaciers: recent changes in glacier regime. *Climate Change*, 59 (1–2), 123–135. doi:10.1023/A:1024410528427.
- Mernild, S.H., Knudsen, N.T., Hoffman, J.K., Yde, J.C., Lipscomb, W.L., Hanna, E., Malmros, J.K. and Fausto, R.S., 2013a. Volume and velocity changes at Mittivakkat Gletscher, Southeast Greenland, 1994–2012. *Journal of Glaciology*, 59 (216), 1–11. doi:10.3189/2013JoG13J017.
- Mernild, S.H., Knudsen, N.T., Lipscomb, W.H., Yde, J.C., Malmros, J.K., Jakobsen, B.H. and Hasholt, B., 2011a. Increasing mass loss from Greenland's Mittivakkat Gletscher. *The Cryosphere*, 5, 341–348. doi:10.5194/tc-5-341-2011.
- Mernild, S.H., Lipscomb, W.H., Bahr, D.B., Radić, V. and Zemp, M., 2013b. Global glacier retreat: a revised assessment of committed mass losses and sampling uncertainties. *The Cryosphere*, 7, 1565–1577. doi:10.5194/tc-7-1565-2013.
- Mernild, S.H. and Liston, G.E., 2012. Greenland freshwater runoff. Part II: Distribution and trends, 1960–2010. *Journal of Climate*, 25 (17), 6015–6035.
- Mernild, S.H., Malmros, J.K., Yde, J.C. and Knudsen, N.T., 2012a. Multi-decadal marine and land-terminating glacier retreat in Ammassalik region, Southeast Greenland. *The Cryosphere*, 6, 625–639. doi:10.5194/tc-6-625-2012.
- Mernild, S.H., Mote, T. and Liston, G.E., 2011b. Greenland Ice Sheet surface melt extent and trends, 1960–2010. *Journal of Glaciology*, 57 (204), 621–628.
- Mernild, S.H., Pelto, M., Malmros, J.K., Yde, J.C., Knudsen, N.T. and Hanna, E., 2013c. Identification of ablation rate, ELA, AAR, and net mass balance using transient snow-line variations on two Arctic glaciers. *Journal of Glaciology*, 59 (216), 1–11. doi:10.3189/2013JoG12J221.
- Mernild, S.H., Seidenkrantz, M.-S., Chylek, P., Liston, G.E. and Hasholt, B., 2012b. Climate-driven fluctuations in freshwater to Sermilik Fjord, East Greenland, during the last 4000 years. *The Holocene*, 22 (2), 155–164. doi:10.1177/0959683611431215.
- Nesje, A., Lie, O. and Dahl, S.O., 2000. Is the North Atlantic Oscillation reflected in Scandinavian glacier mass balance records? *Journal of Quaternary Science*, 15, 587–601.
- Nuth, C., Moholdt, G., Kohler, J., Hagen, J.O. and Käab, A., 2010. Svalbard glacier elevation changes and contribution to sea level rise. *Journal of Geophysical Research*, 115, F01008. doi:10.1029/2008JF001223.
- Olsen, J., Anderson, N.J. and Knudsen, M.S., 2012. Variability of the North Atlantic oscillation over the past 5,200 years. *Nature Geoscience*, 5, 808–812. doi:10.1038/ngeo1589.
- Overland, J.E., Francis, J., Hanna, E. and Wang, M., 2012. The recent shift in early summer arctic atmospheric circulation. *Geophysical Research Letters*, 39, L19804. doi:10.1029/2012GL053268.
- Pohjola, V.A. and Rogers, J.C., 1997. Atmospheric circulation and variations in Scandinavian glacier mass balance. *Quaternary Res.*, 47, 29–36. doi:10.1006/qres.1996.1859.
- Polonsky, A.B., 2011. Global warming, Atlantic multidecadal oscillation, thermohaline catastrophe and their impact on climate of the North Atlantic region. In: Kogan et al. (eds), *NATO Science for Peace and Security Series C: Environmental Security*. Springer Science + Business Media. 124–138. doi:10.1007/978-90-481-9618-0\_15.
- Radić, V., Bliss, A., Breedlow, A.C., Hock, R., Miles, E. and Cogley, J.G. 2013. Regional and global projections of twenty-first century glacier mass changes in response to climate scenarios from global climate models. *Climate Dynamics*, 42: 37–58. doi:10.1007/s00382-013-1719-7.
- Rasmussen, L.A. and Conway, H., 2005. Influence of upper-air conditions on glaciers in Scandinavia. *Annals of Glaciology*, 42, 402–408. doi:10.3189/172756405781812727.
- Reichert, B.K., Bengtsson, L. and Oerlemans, J., 2001. Mid-latitude forcing mechanisms for glacier mass balance

- investigated using general circulation models. *Journal of Climate*, 14, 3767–3784.
- Rignot, E., Box, J.E., Burgess, E. and Hanna, E., 2008. Mass balance of the Greenland ice sheet from 1958–2007. *Geophysical Research Letters*, 35, L20502. doi:10.1029/2008GL035417.
- Rogers, A.N., Bromwich, D.H., Sinclair, E.N. and Cullather, R.I., 2001. The atmospheric hydrological cycle over the Arctic basins from reanalysis. Part II: Interannual variability. *Journal of Climate*, 14, 2414–2429.
- Schlesinger, M.E. and Ramankutty, N., 1994. An oscillation in the global climate system of period 65–70 years. *Nature*, 367, 723.
- Seidenkrantz, M.-S., Aagaard-Sørensen, S., Møller, H.S., Kuijpers, A., Jensen, K.G. and Kunzendorf, H., 2007. Hydrography and climatic change during the last 4.400 years in Ameralik Fjord, SW Greenland. *The Holocene*, 17 (3), 387–401.
- Seidenkrantz, M.-S., Roncaglia, L., Fischel, A., Heilmann-Clausen, C., Kuijpers, A. and Moros, M., 2008. Variable North Atlantic climate seesaw patterns documented by a late Holocene marine record from Disko Bugt, West Greenland. *Marine Micropalaeontology*, 68, 66–83. doi:10.1016/j.marmicro.2008.01.006.
- Sicre, M.-A., Weckström, K., Seidenkrantz, M.-S., Kuijpers, A., Benetti, M., Massé, M., Ezat, U., Schmidt, S., Bouloubassi, I., Olsen, J., Khodri, M. and Mignot, J., 2014. Labrador current variability over the last 2000 years. *Earth and Planetary Science Letters*, 400, 26–32. doi:10.1016/j.epsl.2014.05.016.
- Stroeve, J., Box, J.E., Gao, F., Liang, S., Nolin, A. and Schaaf, C., 2005. Accuracy assessment of the MODIS 16-day albedo product for snow: comparisons with Greenland in situ measurements. *Remote Sensing of Environment*, 94, 46–60.
- Thompson, D.W.J. and Wallace, J.M., 1998. The Arctic oscillation signature in the wintertime geopotential height and temperature fields. *Geophysical Research Letters*, 25, 1297–1300.
- Trenberth, K.E., Jones, P.D., Ambenje, P., Bojariu, R., Easterling, D., Klein tank, A., Parker, D., Rahimzadeh, F., Renwick, J.A., Rusticucci, M., Soden, B. and Zhai, P., 2007. Observations: surface and atmospheric climate change. In: Solomon, S., Qin, D., Manning, M., Chen, Z., Marquis, M., Averyt, K.B., Tignor, M. and Miller, H.L. (eds), *Climate Change 2007: The Physical Science Basis*. Contribution of Working Group I to the Fourth Assessment Report of the Intergovernmental Panel on Climate Change Cambridge University Press, Cambridge, UK and New York, USA.
- Trouet, V., Esper, J., Graham, N.E., Baker, A., Scourse, J.D. and Frank, D.C., 2009. Persistent positive North Atlantic oscillation mode dominated the medieval climate anomaly. *Science*, 324, 78–80.
- Trouet, V., Scourse, J.D. and Raible, C.C., 2011. North Atlantic storminess and Atlantic meridional overturning circulation during the last millennium: reconciling contradictory proxy records of NAO variability. *Global and Planetary Change*, 84, 48–55. doi:10.1016/j.gloplacha.2011.10.003.
- Yde, J.C. and Paasche, Ø., 2010. Reconstructing climate change: not all glaciers suitable. *EOS Transactions AGU*, 91, 189–190.
- Zemp, M., Thibert, E., Huss, M., Stumm, D., Rolstad Denby, C., Nuth, C., Nussbaumer, S.U., Moholdt, G., Mercer, A., Mayer, C., Joerg, P.C., Jansson, P., Hynek, B., Fischer, A., Escher-Vetter, H., Elvehøy, H. and Andreassen, L.M., 2013. Uncertainties and re-analysis of glacier mass balance measurements. *The Cryosphere*, 7, 1227–1245.

*Manuscript received 11 Nov, 2013, revised and accepted 9 Jun, 2014*

[14]

Mernild, S. H., Liston, G. E., and Hiemstra, C. A. 2014  
Northern Hemisphere glaciers and ice caps surface mass balance  
and contribution to sea-level rise.  
*Journal of Climate*, 27(15), 6051–6073, doi.org/10.1175/JCLI-  
D-13-00669.1.

Reprinted with permission from American Meteorological  
Society



# Northern Hemisphere Glacier and Ice Cap Surface Mass Balance and Contribution to Sea Level Rise

SEBASTIAN H. MERNILD

*Climate, Ocean, and Sea Ice Modeling Group, Computational Physics and Methods, Los Alamos National Laboratory, Los Alamos, New Mexico, and Glaciology and Climate Change Laboratory, Center for Scientific Studies, Valdivia, Chile*

GLEN E. LISTON

*Cooperative Institute for Research in the Atmosphere, Colorado State University, Fort Collins, Colorado*

CHRISTOPHER A. HIEMSTRA

*U.S. Army Cold Regions Research and Engineering Laboratory, Fort Wainwright, Alaska*

(Manuscript received 4 November 2013, in final form 6 May 2014)

## ABSTRACT

Mass changes and mass contribution to sea level rise from glaciers and ice caps (GIC) are key components of the earth's changing sea level. GIC surface mass balance (SMB) magnitudes and individual and regional mean conditions and trends (1979–2009) were simulated for all GIC having areas greater or equal to 0.5 km<sup>2</sup> in the Northern Hemisphere north of 25°N latitude (excluding the Greenland Ice Sheet). Recent datasets, including the Randolph Glacier Inventory (RGI; v. 2.0), the NOAA Global Land One-km Base Elevation Project (GLOBE), and the NASA Modern-Era Retrospective Analysis for Research and Applications (MERRA) products, together with recent SnowModel developments, allowed relatively high-resolution (1-km horizontal grid; 3-h time step) simulations of GIC surface air temperature, precipitation, sublimation, evaporation, surface runoff, and SMB. Simulated SMB outputs were calibrated against 1422 direct glaciological annual SMB observations of 78 GIC. The overall GIC mean annual and mean summer air temperature, runoff, and SMB loss increased during the simulation period. The cumulative GIC SMB was negative for all regions. The SMB contribution to sea level rise was largest from Alaska and smallest from the Caucasus. On average, the contribution to sea level rise was  $0.51 \pm 0.16$  mm sea level equivalent (SLE) yr<sup>-1</sup> for 1979–2009 and ~40% higher  $0.71 \pm 0.15$  mm SLE yr<sup>-1</sup> for the last decade, 1999–2009.

## 1. Introduction

Most glaciers and ice caps (GIC) are shrinking in response to climate change, with observations showing significant declines in mass balances over the last few decades. At present, GIC are large contributors to eustatic sea level rise, and important regulators of water availability around the world (e.g., Kaser et al. 2006; Meier et al. 2007; Cogley 2009, 2012; Hock et al. 2009; Hirabayashi et al. 2010; Leclercq et al. 2011; Marzeion et al. 2012; Gardner et al. 2013; Mernild et al. 2013a).

Direct glaciological GIC surface mass balance (SMB) observations are scarce and sparsely distributed; only ~340 GIC have been observed worldwide, of which nearly 70 have continuous records of 20 years or more (Dyurgerov 2010; WGMS 2012). This is a minor fraction of the earth's 200 000 or more estimated GIC (Radić and Hock 2010; Arendt et al. 2012), and this substantial gap leaves us with limited information about Northern Hemisphere GIC conditions.

In the search for long-term trends given the absence of broader SMB sampling, upscaling, satellite, and modeling approaches have attempted to estimate global mean GIC mass changes and their associated mass contribution to sea level rise (e.g., Kaser et al. 2006; Hock et al. 2009; Marzeion et al. 2012; Gardner et al. 2013; Mernild et al. 2013a). Kaser et al. (2006) used direct

---

*Corresponding author address:* Dr. Sebastian H. Mernild, Glaciology and Climate Change Laboratory, Center for Scientific Studies/Centro de Estudios Científicos (CECs), 5110466 Valdivia, Chile.  
E-mail: smernild@gmail.com

glaciological observations from 1961 to 2004 to illustrate that global mean GIC mass balance conditions were slightly below zero around 1970, but became more negative during the past last quarter century through 2004. They estimated a GIC mass contribution to sea level rise of  $0.77 \pm 0.26$  mm sea level equivalent (SLE)  $\text{yr}^{-1}$  (1991–2004), which constituted  $\sim 20\%$ – $30\%$  of the observed sea level rise for 1993–2005. Mernild et al. (2013a) reported, based on direct glaciological SMB and accumulation-area ratio (AAR: the ratio of the accumulation area to the area of the entire glacier) observations (1971–2010), taking into account the sparse and geographically biased GIC distribution, that GIC (i) were heading toward more negative annual SMB during the first half (2001–05) of the first decade of the twenty-first century [SMB conditions have not been sustained during the most recent 5-yr period (2006–10), in which GIC losses have been more moderate, though still large] and (ii) are committed to additional losses of  $38\% \pm 16\%$  of their volume if the future climate resembles the climate of the past decade. These losses imply a global GIC mean sea level rise of  $163 \pm 69$  mm SLE.

Gardner et al. (2013) used satellite gravimetry, altimetry, and glaciological records to estimate GIC mass changes and mass contribution to sea level rise (2003–09). Their satellite-based estimates were, in general, less negative than glaciological observations, with a global GIC mass budget equal to  $0.71 \pm 0.08$  mm SLE  $\text{yr}^{-1}$  (or  $29\% \pm 13\%$  of the observed sea level rise). Hock et al. (2009) employed a simplified monthly global grid-based degree-day approach ( $1^\circ \times 1^\circ$ ) where the model related summer balances to positive degree-day sums, and winter balances to the sum of daily precipitation when temperatures were below freezing; GIC mass changes and associated mass contribution to sea level rise of  $0.79 \pm 0.34$  mm SLE  $\text{yr}^{-1}$  were reported for 1961–2004. Marzeion et al. (2012) simulated SMB for individual GIC based on the Randolph Glacier Inventory (RGI v. 1.0, the first globally complete digital GIC database inventory, Arendt et al. 2012) and monthly climate forcing (air temperature and precipitation), where air temperature was used as a proxy for the energy available for melt. Routines adjusting for annual GIC surface area and volume changes were included. For 1902–2009, the simulated global GIC mass loss sum corresponded to  $114 \pm 5$  mm SLE, equal to an average of  $1.06$  mm SLE  $\text{yr}^{-1}$ .

These examples of estimated global GIC mass balance conditions and mass loss contributions to sea level rise vary depending on approaches and time periods: 1) data from direct glaciological observations are constrained by undersampling and geographic biases; 2) remote sensing data are limited to short and relatively recent periods; and 3) modeling approaches are problematic

because of coarse-scale spatial and temporal resolutions of the physical processes driving GIC changes. Fortunately, modeling capabilities have grown in recent years along with the emergence of remotely sensed datasets such as the RGI. Now it is possible to simulate global GIC surface processes, allowing us to improve our understanding of climate change impacts on global GIC surface conditions associated with latitude, topography, and other regional influences.

In this study, SnowModel (Liston and Elder 2006a,b) was used to simulate Northern Hemisphere GIC surface temperature, precipitation, evaporation, sublimation, surface runoff, and SMB on rescaled 1-km RGI GIC data. SnowModel is a spatially distributed meteorological snow and ice evolution modeling system; in this application it downscaled reanalysis atmospheric forcing data with a 3-h temporal resolution to simulate the GIC snow and ice evolution. Direct glaciological observations for the period 1979–2009 were used to evaluate model performance.

The purpose of this study is to simulate and analyze, at the highest achievable spatial and temporal resolutions, GIC SMB changes and SMB contribution to sea level rise, including variations in GIC surface air temperature, precipitation, sublimation, evaporation, and surface runoff in the Northern Hemisphere for Arctic and glaciated mountain regions [specifically, for the 15 glacier regions north of  $25^\circ\text{N}$ , defined by Radić and Hock (2010), not including the Greenland Ice Sheet] (Fig. 1). Our goals entail mapping and understanding the climatic impact on individual and regional GIC conditions from September 1979 through August 2009. We considered SMB losses, including internal processes related to the snowpack such as refreezing of meltwater, neglecting mass loss from dynamic activities, melting from internal glacier ice deformation, melting from changes in the internal drainage system, subglacial geothermal melting, and subglacial frictional melting due to basal ice motion.

## 2. Model description

### a. SnowModel

SnowModel is a spatially distributed snow and ice evolution model driven by meteorological data (Liston and Elder 2006a,b), designed for application in all climates and landscapes where snow and ice are present. SnowModel is an aggregation of six submodels: MicroMet, a quasi-physically based high-resolution meteorological distribution model (Liston and Elder 2006b); Enbal, an energy surface exchange and melt model (Liston 1995; Liston et al. 1999); SnowTran-3D, a surface model for snow redistribution by wind (Liston and Sturm 1998, 2002;

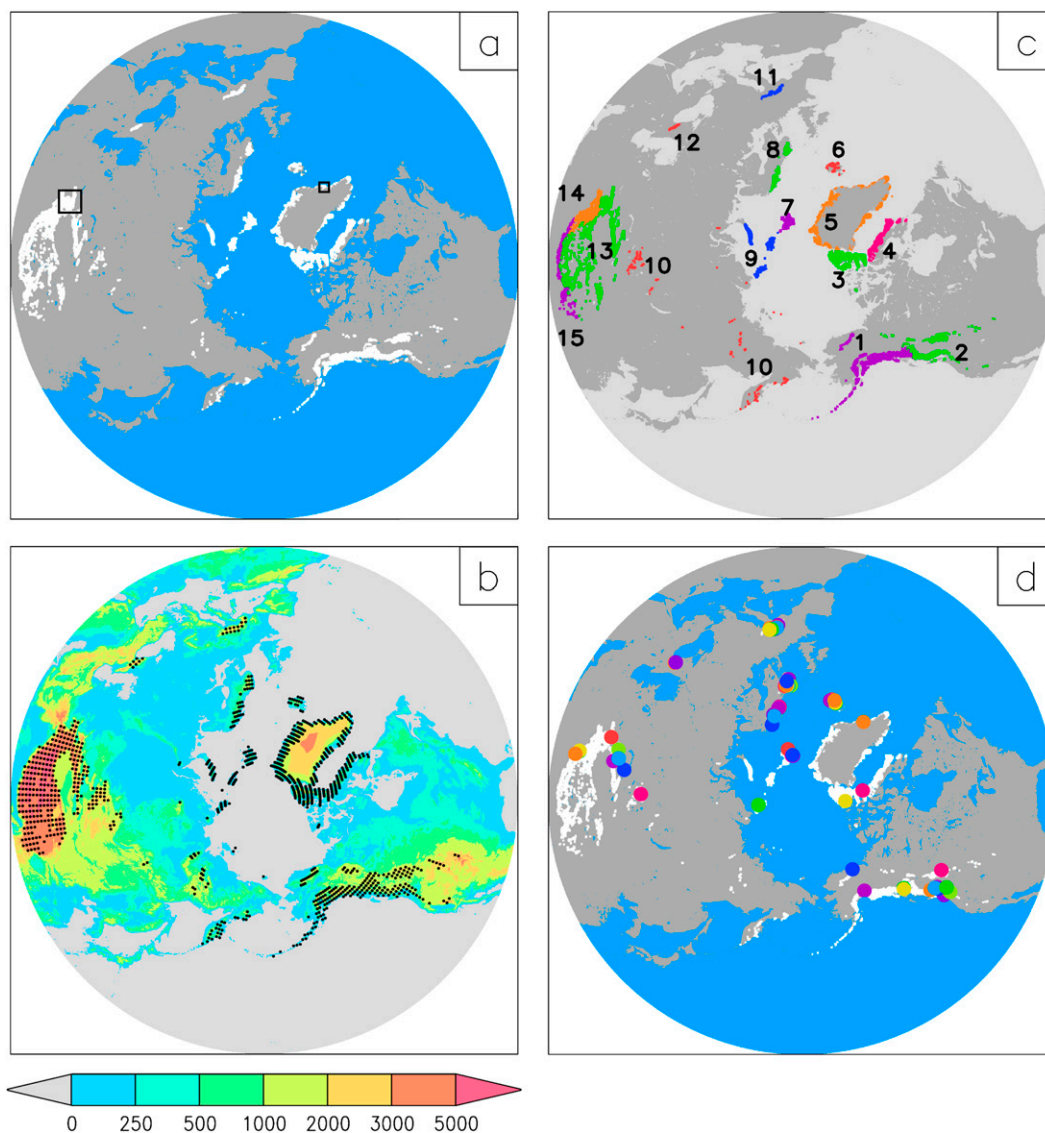


FIG. 1. The Northern Hemisphere (above 25°N). (a) Land-cover distribution, where GIC (land ice; except for the Greenland Ice Sheet) are illustrated in white color, land surface in gray, and ocean and lakes in blue. Also, two specific regions (see black bold squares): southeast Greenland and the Himalayas are illustrated as examples showing the spatial distribution of temperature, precipitation, sublimation and evaporation, and runoff mean and trends (see Fig. 5). (b) Locations of MERRA atmospheric forcing grid points used in the model simulations (black dots; to improve clarity only every other grid point was plotted in  $x$  and  $y$ , i.e., 25% of the grid points used are shown), with the color background showing topography (m, color increment is not linear). (c) Glacier regions 1 to 15 divided using the regional demarcations defined by Radić and Hock (2010). Each region has a different color and number associated with it: 1) Alaska; 2) western Canada and the United States; 3) Arctic Canada (North); 4) Arctic Canada (South); 5) Greenland; 6) Iceland; 7) Svalbard; 8) Scandinavia; 9) Arctic Russia; 10) North Asia; 11) Central Europe; 12) Caucasus; 13) Central Asia (North); 14) Central Asia (South); and 15) Central Asia (West) (regions 13, 14, and 15 are also known as the High Mountain Asia region). (d) Locations of the 78 mass-balance observed GIC, illustrated with different colors.

Liston et al. 2007); SnowPack-ML, a multilayer snowpack model simulating refreezing of meltwater as a function of snow and ice permeability and cold content (Liston and Mernild 2012); HydroFlow, a gridded linear-reservoir

runoff routing model (not used in this study; Liston and Mernild 2012; Mernild and Liston 2012), and SnowAssim, a model available to assimilate field observed datasets (Liston and Hiemstra 2008).

SnowModel downscales and simulates meteorological conditions, surface energy balance, and moisture exchanges including snow and glacier melt, blowing-snow redistribution and sublimation, multilayer heat- and mass-transfer processes within the snow (e.g., snowpack temperature and density evolution, and snowpack ripening), and surface freshwater runoff, where runoff is defined to be the water that flows from the bottom of the simulated snowpack into the supraglacial, englacial, and subglacial regions or to the proglacial drainage system. For the simulations, SnowModel requires temporally varying fields of air temperature, water-equivalent precipitation, relative humidity, wind speed, and wind direction obtained from direct observations within/near the model simulation domain, and/or from atmospheric models (e.g., reanalysis or general circulation model data) within/near the domain. Further, spatially distributed time-invariant fields of topography and land cover are required [for further and more detailed information about SnowModel see, e.g., Mernild and Liston (2010) and Mernild et al. (2006, 2010a,b, 2011a,b)]. SnowModel, including its submodels, has previously been tested and used in Alaska, Colorado, Wyoming, Arctic Canada, Greenland, Norway (Svalbard), and northern Japan, comparing simulated snow accumulation/distribution and snow and glacier ice ablation and runoff processes with observations (e.g., Hiemstra et al. 2002, 2006; Hasholt et al. 2003; Bruland et al. 2004; Liston and Hiemstra 2008, 2011; Suzuki et al. 2011).

### *b. Model configuration, simulation domain, and meteorological forcing*

SnowModel GIC surface processes, including precipitation, snow accumulation, sublimation, evaporation, runoff, and SMB, were simulated for the 30-yr period, September 1979 through August 2009, using a 3-h time step, covering a  $7235 \text{ km} \times 7235 \text{ km}$  domain centered on the North Pole, having a spherical area of  $\sim 41.1 \times 10^6 \text{ km}^2$  (Fig. 1). In these calculations the mass balance year was assumed to be 1 September–31 August. Topography was obtained from the National Oceanic and Atmospheric Administration (NOAA) Global Land One-km Base Elevation Project (GLOBE) (Hastings et al. 1999), which provided a 1-km digital elevation model (DEM) for the domain (Fig. 1b). The GIC cover distribution was obtained from the RGI v. 2.0 (Figs. 1a,c); GIC from the RGI polygons were resampled to 1-km grid increments, and included in the glacier-cover file if the individual grid cells were covered by 50% or more of glacier ice, giving 543 389 GIC covered grid cells north of  $25^\circ\text{N}$  (Fig. 1a). Most of these GIC grids ( $\sim 75\%$ ) were located in the Arctic region (regions 1–10) and  $\sim 25\%$  in the high mountain regions (regions 11–15). The GIC

cover ranges in latitude from  $27.1^\circ$  to  $83.6^\circ\text{N}$ , and the topography from sea level to 8557 m above mean sea level (MSL), where peak elevations were located in the border region between Nepal and Tibet (region 15: Central Asia, West; Fig. 1c) in the area called High Mountain Asia (HMA).

Using a 1-km grid increment means that minor GIC ( $<0.5 \text{ km}^2$ ) were ignored from the simulations, and therefore one might expect an underestimation of GIC area. To assess the effect of resampling, the GIC area cover for the Alaska region was compared using 1-km ( $90\,793 \text{ km}^2$ ) and 100-m resolution ( $90\,637 \text{ km}^2$ ) data. Going to a coarser resolution for Alaska resulted in a GIC area overestimate of  $156 \text{ km}^2$ . Similar analyses could yield either slight over- or underestimates for the other glacierized regions, assuming an uncertainty in GIC area of  $\sim 0.2\%$ , similar to the one estimated for Alaska.

Atmospheric forcings were provided by the National Aeronautics and Space Administration (NASA) Modern-Era Retrospective Analysis for Research and Applications (MERRA) products (Bosilovich 2008; Bosilovich et al. 2008, 2011; Cullather and Bosilovich 2011; Rienecker et al. 2011; Robertson et al. 2011). MERRA is a reanalysis dataset that has the specific goal of improving the representation of water cycle processes and features while taking advantage of modern satellite-era datasets (Liston and Hiemstra 2011), and was used for this study due to its high resolution. The MERRA dataset used in this study covers the period 1979 through 2009 on an hourly time step and on a  $2/3^\circ$  longitude by  $1/2^\circ$  latitude grid.

For the simulations described herein, SnowModel was modified to only include MERRA grid points for the Northern Hemisphere grid cells that included glacier ice. This substantially improved computational efficiency and explains the discontinuous distribution of atmospheric data points illustrated in Fig. 1b. Further, to improve the computational efficiency and still resolve the diurnal cycle and the associated energy-related processes, the hourly MERRA time steps of 10-m air temperature, specific humidity,  $u$  and  $v$  wind components, and precipitation were aggregated to 3-hourly values (Liston and Hiemstra 2011). For the incoming solar radiation, MicroMet (Liston and Elder 2006b) used its submodels to generate these fields, considering the influence of cloud cover, topographic slope, and aspect on incoming solar radiation. The MicroMet solar radiation model was compared against observations provided by the NASA Cold Land Processes Field Experiment (CLPX) on an hourly time scale, yielding an  $r^2$  value (square of the linear correlation coefficient) of 0.87 for the hourly data, and captured the observed seasonal variations (Liston and Elder 2006b). SnowModel ingested MERRA and MicroMet meteorological forcing



variables and it simulated the time evolution and spatial distribution of energy and water fluxes, incoming solar radiation, incoming longwave radiation, emitted longwave radiation, sensible heat flux, latent heat flux, conductive heat flux, albedo, surface (skin) temperature, precipitation, snow depth, sublimation and evaporation, snow and ice surface melt, runoff, and GIC surface mass balance terms. The 3-hourly SnowModel simulated parameters were aggregated (averaged or summed, depending on the variable) to daily, annual, or decadal values over the 30-yr period for spatial and temporal analyses.

### 3. Datasets and calibration

#### a. Observed GIC dataset

Direct glaciological observations were used for calibration of simulated GIC SMB conditions. In Mernild et al. (2013a; see their supplementary material) direct glaciological observations from 105 GIC in the Northern Hemisphere north of 25°N that were greater than 1.0 km<sup>2</sup> (equal to the size of the grid increment) [updated from Dyurgerov and Meier (2005), the World Glacier Monitoring Service database (WGMS 2012), and directly from principal investigators] were listed covering the period 1971–2010. A geographical comparison between the 105 GIC latitudinal and longitudinal grids, and the presence of the GIC in the RGI v. 2.0 (using a buffer distance of 1 km), found that the locations of 78 out of 105 GIC could be identified and confirmed in the resampled 1-km grid RGI dataset (for the GIC not identified, 90% were <5.0 km<sup>2</sup>). These 78 GIC (including their 1422 direct glaciological annual SMB observations for 1979–2009) were used for calibration (see Fig. 1d) and had the following geographic distribution: 3 GIC (in region 1), 11 (2), 3 (3), 1 (5), 10 (6), 6 (7), 21 (8), 1 (9), 11 (11), 2 (12), 6 (13), 2 (14), and 1 (15). No available (long-term) direct glaciological SMB observations were available for Arctic Canada South (region 4) and North Asia (region 10) for model calibration: for example, for region 4 only short-term GIC SMB observations occurred (in 1982–84 from the Hidden, Minaret, Abraham, and Superguksoak glaciers, and in 1980, 1982, and 1984 from Barnes Ice Cap Southern Dome Northern slope) (G. Cogley 2014, personal communication). Approximately 30% of the observed GIC time series had records for all 30 years, and approximately 70% had uninterrupted records of 10 years or more, indicating a variation in the annual number of SMB observations from 35–39 for 1979–87 to 44–53 for 1988–2009.

For all 78 GIC the observed midrange elevation was calculated:  $Z_{\text{mid}} = (Z_{\text{max}} - Z_{\text{min}})/2$  (WGMS 1989),

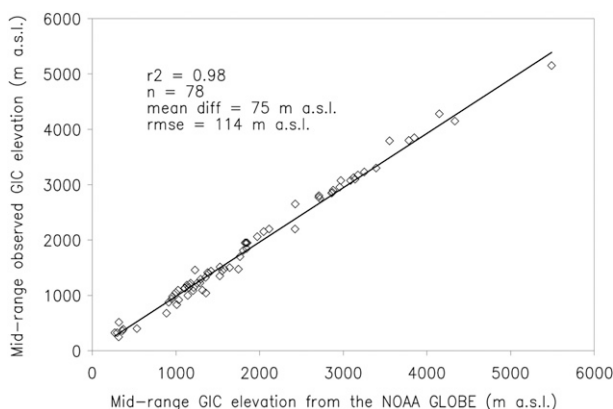


FIG. 2. Midrange comparison between observed GIC elevations and the NOAA GLOBE DEM GIC elevations.

where  $Z_{\text{max}}$  is the maximum GIC elevation and  $Z_{\text{min}}$  the minimum elevation, and compared against  $Z_{\text{mid}}$  estimated from the SnowModel topographic grid [i.e., NOAA GLOBE digital elevation model (DEM), Hastings et al. 1999]. In Fig. 2, a linear regression illustrates a sufficient  $r^2$  value of 0.98 between observed GIC  $Z_{\text{mid}}$  and SnowModel DEM GIC  $Z_{\text{mid}}$ , with a mean difference of 75 m MSL (with the observed mean value being lower than the SnowModel DEM) and a rms error (rmse) of 114 m MSL. Based on this correlation and the rmse in  $Z_{\text{mid}}$  between the 78 GIC (varying in elevation from around sea level to above 5000 m MSL) and the SnowModel DEM, we are confident that our GIC elevation estimates are appropriate for GIC SMB simulations.

#### b. Calibration dataset

Estimation of precipitation conditions in mountainous regions is one of the greatest challenges in mountain hydrology (e.g., Bhutiyani 1999). Bosilovich et al. (2008) analyzed precipitation outputs from an early version of the MERRA reanalysis system and concluded that MERRA precipitation fields were an improvement over the previous reanalyses. However, since the major uncertainties in GIC SMB calculations are related to uncertainties in observed and estimated solid precipitation and the associated snow accumulation processes (e.g., Woo et al. 1982; Yang et al. 1998; Allerup et al. 1998, 2000a,b; Liston and Sturm 2002, 2004; Rasmussen et al. 2012) rather than in ablation processes, GIC SMB adjustments were made to the SnowModel precipitation inputs (i.e., the MERRA precipitation values) to correct identified SMB biases. Initial simulations used the original MERRA precipitation, where simulated GIC SMB time series were compared with observed GIC SMB time series for each of the 78 GIC. Because of the difference in SMB, we calculated a mean precipitation



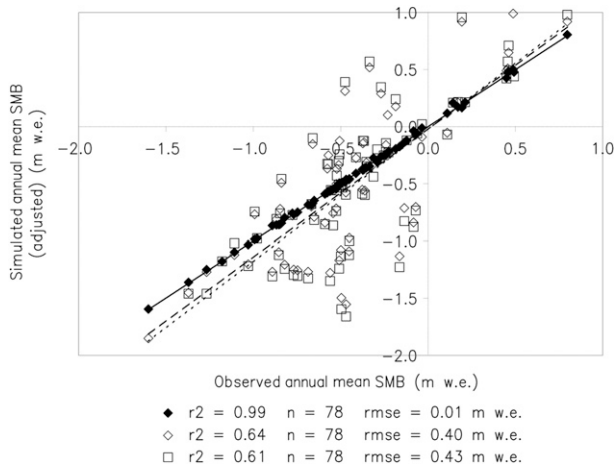


FIG. 3. Linear relationship between GIC observed and simulated mean annual SMB, where simulated SMB was conducted based on individual GIC precipitation adjustments (black diamonds and black trend line), mean regional GIC precipitation adjustments (white diamonds and large dashed trend line), and leave-one-out cross validation estimated GIC precipitation adjustments (white square and short dashed trend line).

adjustment factor based on each individual GIC that, when multiplied by the original MERRA precipitation, yielded a new simulated GIC SMB that was roughly similar to the observed GIC SMB [similar precipitation adjustment/assimilation procedures have been used sufficient in Mernild et al. (2006) for simulating SMB conditions on a glacier in east Greenland and in Liston and Hiemstra (2008)]. In Fig. 3, linear regressions between observed and simulated mean annual GIC SMB based on 1) individual GIC precipitation adjustments, 2) mean regional precipitation adjustments, and 3) precipitation adjustments calculated from the leave-one-out cross validation are illustrated. For the regression between observed GIC and simulated GIC based on individual precipitation adjustments the  $r^2$  value and rmse were 0.99 and 0.01 m w.e. (water equivalent), respectively, and based on mean regional precipitation adjustments 0.64 and 0.40 m w.e. Applying the mean regional precipitation adjustment factors will then lead to greater model errors compared to using individual GIC precipitation adjustment factors. However, since the regional mean precipitation adjustment factors cannot be considered independent of the observed SMB values, a leave-one-out cross validation was conducted for each of the regions that have  $n \geq 2$  GICs with SMB observations (regions 1–3, 6–8, and 11–14). In Fig. 3, the linear regressions between observed and simulated mean annual GIC SMB (estimated from the leave-one-out cross validation) are illustrated, showing an  $r^2$  value of 0.61 and rmse of 0.43 m w.e., similar to the regression

TABLE 1. Regional breakdown of mean precipitation adjustment factors and standard deviations for each of the 15 regions.

Region	Mean precipitation adjustment factor	Standard deviation
1: Alaska	0.70	0.10
2: Western Canada and United States	0.79	0.28
3: Arctic Canada, North	0.57	0.22
4: Arctic Canada, South	0.57	No value
5: Greenland	0.56	No value
6: Iceland	0.32	0.21
7: Svalbard	0.80	0.33
8: Scandinavia	0.79	0.22
9: Arctic Russia	0.18	No value
10: North Asia	0.18	No value
11: Central Europe	0.76	0.18
12: Caucasus	0.55	0.21
13: Central Asia, North	1.06	0.23
14: Central Asia, South	0.37	0.18
15: Central Asia, West	1.06	No value
Mean	0.61	0.22

estimated from the mean regional precipitation adjustments. Given the latter comparison, we are confident that SnowModel is appropriate for simulating annual mean (able to account for roughly 60% of the variance in SMB) and 30-yr mean GIC SMB conditions for observed and nonobserved GIC located in the 13 (out of 15) regions with GIC SMB observations (even though model routines for evaporation, sublimation, and runoff were not validated individually against observations, but only restricted to a SMB validation).

Using these individual GIC precipitation adjustment factors, regional mean adjustment factors were calculated by averaging the factors contained within each specific region (Table 1). These regional precipitation correction factors were used in each corresponding region and the corrected precipitation for the SnowModel GIC SMB simulations presented herein. The mean regional precipitation adjustment factors averaged  $0.61 \pm 0.22$  (Table 1), indicating an average initial overestimation (before adjustment) of SnowModel-MERRA simulated GIC SMB. In Kotlarski et al. (2010), uncorrected gridded ALP-IMP [<http://www.zamg.ac.at/ALP-IMP/>; Climatic Research Unit (CRU)] data annual precipitation showed a positive bias of 17%. SnowModel-MERRA overestimations in GIC SMB might be attributed to general precipitation lapse rates missing specific local/regional variability in precipitation lapse rates for mountain regions where GIC are located, overestimating (underestimating) the fraction of snow (rain), where the fraction of precipitation being rainfall was not contributing to the mass balance. For regions with one or less observed GIC SMB time series (e.g., Arctic Canada South, Greenland, and North Asia), a surrogate was used for

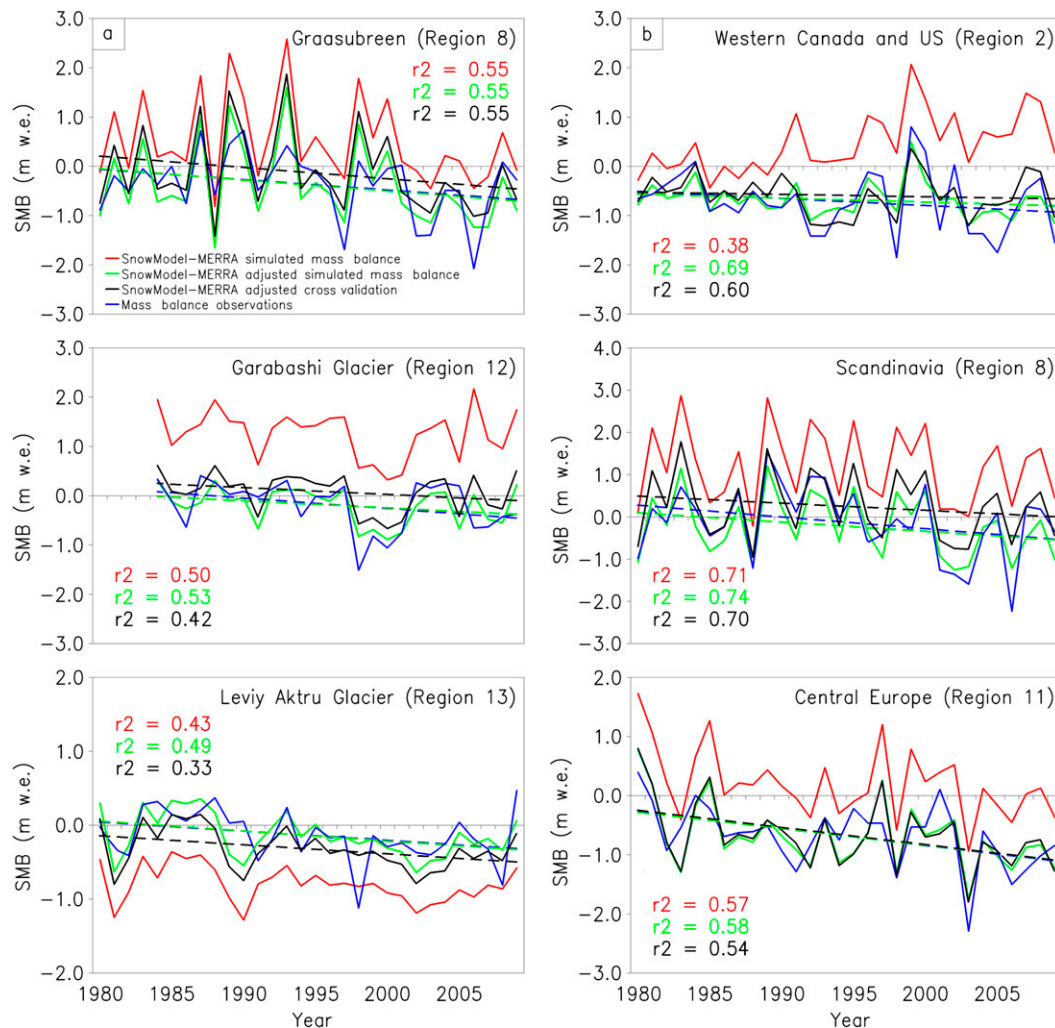


FIG. 4. Examples of annual simulated GIC SMB, precipitation-adjusted SMB, and observed SMB time series: (a) for three individual GIC located in three different regions (each GIC was picked randomly among the GIC from where observations covers the entire simulation period 1979 to 2009) and (b) on a regional scale from three randomly picked regions: western Canada and the United States (region 2; number of observed GIC  $n = 11$ ), Scandinavia (region 8,  $n = 21$ ), and central Europe (region 11,  $n = 11$ ). Trend lines are shown for both the observed and the precipitation-adjusted SMB time series (all are significant). The  $r^2$  values illustrate the correlation between mass balance observations and SnowModel-MERRA simulated mass balance (red color), and SnowModel-MERRA calibrated simulated mass balance (green color).

calibration. For example, for the regions Arctic Canada South and North Asia adjustment values from Arctic Canada North and Arctic Russia, respectively, were used because of the climatically similar conditions. For Greenland GIC, because of the climatic variability and teleconnection between east and west Greenland (e.g., Box 2002; Hanna et al. 2013; Mernild et al. 2014), precipitation adjustment values from Greenland's surrounding regions (Arctic Canada North, Arctic Canada South, Svalbard, and Iceland) were used. As an example, three randomly chosen individual GIC time series are shown (Fig. 4a) that include Graasubreen (region 8), Garabashi Glacier (region 12),

and Leviy Aktru (region 13) covering  $>25$  years of SMB observations compared with uncalibrated and calibrated simulated SMB time series. Mean regional SMB time series are shown (Fig. 4b) for observed GIC, and also for three randomly chosen regions (western Canada and the United States, Scandinavia, and Central Europe). Variability occurs between observed and simulated SMB time series and the observed and calibrated SMB time series (Fig. 4). For example, SnowModel was able to account for 55% of the variance in SMB for Graasubreen (Fig. 4a), also after cross validation. For Garabashi Glacier and Leviy Aktru, for example, SnowModel was able after cross

validation to account for 42% and 33% of the variance in SMB, respectively (Fig. 4a). In addition, the 30-yr average SMB (Fig. 4) and their trend lines are significant in these comparisons ( $p < 0.05$ , based on a linear regression  $t$  test).

#### 4. GIC surface water balance components

The yearly GIC water mass balance equation [Eq. (1)] can be described as follows from the hydrological method:

$$P - (E + Su) - R \pm \Delta S = 0 \pm \eta, \quad (1)$$

where  $P$  is precipitation input from snow and rain (and possible condensation),  $E$  is evaporation (liquid to gas phase flux of water),  $Su$  is sublimation (solid to gas phase with no intermediate liquid stage),  $R$  is surface runoff,  $\Delta S$  is change in storage ( $\Delta S$  is also referred to as SMB) from changes in glacier storage and snowpack storage. The parameter  $\eta$  is the water balance discrepancy (error). The error term should be 0 (or small if the components  $P$ ,  $E$ ,  $Su$ ,  $R$ , and  $\Delta S$  have been determined accurately. Here,  $\Delta S$  is calculated as the residual value.

### 5. Results and discussion

#### a. Decadal GIC conditions

Table 2 presents regional breakdowns for all 15 glacierized regions of simulated mean GIC surface air temperature [mean annual air temperature (MAAT)] and mean summer air temperature [June–August (JJA)] and surface hydrological conditions (precipitation, sublimation, evaporation, surface runoff, and SMB) on decadal scales and for the entire simulation period. Mass gain (accumulation) is calculated as positive and mass loss (ablation) is considered negative for the GIC. The 30-yr domain average (1979–2009) simulated GIC MAAT was  $-10.3^\circ \pm 0.1^\circ\text{C}$ . [Here and below, the standard errors correspond to a 95% confidence interval, or 1.96 times the standard error. The errors are random and normally distributed; therefore, the standard error propagation can be used. For calculation of standard error, see Mernild et al. (2013a; see their supplemental material, sheet F).] This varies regionally from  $-3.9^\circ \pm 0.4^\circ\text{C}$  in Scandinavia to  $-19.3^\circ \pm 0.3^\circ\text{C}$  in Arctic Canada (northern and southern regions) (Table 2). For the Arctic GIC area (regions 1–10) the change in simulated MAAT from the first decade (1979–89) to the last decade (1999–2009) was greater than elsewhere, where Svalbard, Greenland, and Arctic Russia faced the highest MAAT changes of  $1.5^\circ\text{C}$  (equal to a significant linear average trend of  $0.06^\circ\text{C yr}^{-1}$

from 1979 to 2009),  $1.2^\circ\text{C}$  ( $0.06^\circ\text{C yr}^{-1}$ ; significant), and  $1.2^\circ\text{C}$  ( $0.05^\circ\text{C yr}^{-1}$ ; significant), respectively. Regions such as western Canada and the United States and the Caucasus all faced the smallest MAAT change of  $0.3^\circ\text{C}$  ( $0.02^\circ\text{C yr}^{-1}$ ; insignificant), which is significantly below the mean Northern Hemisphere GIC air temperature increase of  $0.8^\circ \pm 0.4^\circ\text{C}$  ( $0.04^\circ\text{C yr}^{-1}$ ; significant) (Table 2). Besides MAAT we also looked into mean JJA air temperature conditions. Regarding mean JJA air temperature the 30-yr domain average was  $-0.4^\circ \pm 0.1^\circ\text{C}$ , and varied from  $3.9^\circ \pm 0.4^\circ\text{C}$  in Scandinavia to  $-4.0^\circ \pm 0.2^\circ\text{C}$  in Greenland (Table 2). The change in simulated mean JJA air temperature from the first decade to the last decade varied from  $0.2^\circ\text{C}$  ( $0.01^\circ\text{C yr}^{-1}$ ; insignificant) in Central Asia North to  $1.0^\circ\text{C}$  ( $0.05^\circ\text{C yr}^{-1}$ ; significant) in Arctic Canada North. In general for the domain the linear average trend for JJA ( $0.03^\circ\text{C yr}^{-1}$ ; significant) (1979–2009) was lower than the trend for MAAT ( $0.04^\circ\text{C yr}^{-1}$ ; significant), indicating greater changes in air temperature during winter compared with summer (Table 2). These variations in air temperatures show fidelity with air temperature anomaly patterns (1979–2004) identified by Overland et al. (2004), and follow the general surface air temperature trend, where temperature rise during recent decades has been more pronounced at high latitudes (e.g., Hansen et al. 2010) and during winter (e.g., Hanna et al. 2012).

Regarding the SnowModel-adjusted simulated GIC precipitation conditions, the 30-yr domain average (1979–2009) was  $1.64 \pm 0.03$  m w.e., varying regionally, on average, from  $0.26 \pm 0.01$  m w.e. in Arctic Russia to  $3.68 \pm 0.14$  m w.e. in western Canada and the United States. Regional patterns were more diverse than the regional GIC air temperature patterns, showing both positive and negative regional GIC precipitation trends between the first and last decades (Table 2). At higher elevations and coastal mountain ranges adjacent to warmer ocean waters (e.g., western Canada and the United States, and Scandinavia), annual precipitation was, in general, higher than interior continental GIC (Table 2). On a mean regional scale between the first and last decades, simulated GIC precipitation conditions varied between a decrease of  $-0.65$  m w.e. ( $-0.032$  m w.e.  $\text{yr}^{-1}$ ; significant) for central Europe to a regional increase of  $0.16$  m w.e. ( $0.002$  m w.e.  $\text{yr}^{-1}$ ; insignificant) for Alaska (Table 2), highlighting regional differences influenced by meteorological conditions.

General circulation models (GCMs) have often been used to address precipitation questions for past, present, and future conditions (e.g., Walsh et al. 2008; Finniss et al. 2009a,b). These studies generally find that higher temperatures lead to increases in precipitation. However, in this study the GIC domain-average simulated precipitation change between the first and last decades

was  $-0.05$  m w.e. ( $< -0.001$  m w.e. yr $^{-1}$ ; insignificant) (Table 2). A decreasing trend in precipitation is not uncommon in (site specific) observations; for example, Hinzman et al. (2005) reported long-term precipitation trends of  $-1.29$  cm decade $^{-1}$  for Barrow, Alaska, where Rawlins et al. (2006) found snowfall trends of  $-0.3$  cm decade $^{-1}$  for the former Soviet Union. In general, MERRA showed remarkably similar precipitation trends with other reanalyses in comparison with the Global Precipitation Climatology Project (e.g., Liston and Hiemstra 2011).

SnowModel-simulated GIC 30-yr domain-average sublimation and evaporation was  $0.12 \pm 0.00$  m w.e., without significant changes between the first and last decades (Table 2). Regarding GIC sublimation and evaporation loss, one cluster of regions has significantly higher values than others. For the cold and dry high mountain regions in Central Asia (all regions)—also known as High Mountain Asia (the largest glacierized region outside the Arctic and Antarctica)—sublimation and evaporation varied on a regional scale, averaging from  $0.27 \pm 0.01$  to  $0.33 \pm 0.00$  m w.e. (1979–2009). Owing to a combination of relatively cold and dry climatic conditions in HMA (e.g., Benn and Evans 2002), the loss from sublimation was higher compared with less cold and dry regions in the simulation domain. For the GIC regions outside HMA, the 30-yr average GIC sublimation and evaporation loss varied between  $0.03 \pm 0.00$  and  $0.16 \pm 0.00$  m w.e. (Table 2).

Regarding GIC runoff, SnowModel-simulated 30-yr domain-average runoff was  $1.90 \pm 0.06$  m w.e. (Table 2). On a decadal time scale, runoff increased on average for all 15 regions throughout the simulation period from  $1.73 \pm 0.04$  m w.e. in 1979–89 to  $2.06 \pm 0.07$  m w.e. in 1999–2009, equal to a trend of  $0.016$  m w.e. yr $^{-1}$  (significant) (Table 2). Overall, for the 15 individual regions simulated, GIC runoff rose significantly for 10 regions and insignificantly for western Canada and the United States, Arctic Russia, North Asia, Central Europe, and Central Asia South (Table 2). The 30-yr mean regional GIC runoff varied from  $0.57 \pm 0.06$  m w.e. in Arctic Canada North to  $3.91 \pm 0.16$  m w.e. in western Canada and the United States, illustrating a heterogeneous regional GIC runoff distribution for the Northern Hemisphere.

The GIC SMB [Eq. (1)] patterns illustrated in Table 2 show a 30-yr domain-average loss of  $-0.38 \pm 0.07$  m w.e., which was smallest for the first decade ( $-0.19 \pm 0.03$  m w.e.) and largest for the last decade ( $-0.57 \pm 0.11$  m w.e.), equal to a trend of  $0.018$  m w.e. yr $^{-1}$  (significant). Variability among regions yielded an average SMB ranging from  $-0.64 \pm 0.10$  m w.e. (1979–2009) in Central Asia South to  $-0.15 \pm 0.07$  m w.e. (1979–2009) in Arctic Canada North. Further, annual time series of

the regional-average GIC surface hydrological conditions (precipitation, runoff, and SMB) are illustrated in Fig. 5 for three randomly chosen regions: western Canada and the United States, Scandinavia, and central Europe. For all three regions the linear trend in annual GIC SMB and precipitation decreased, while runoff increased (1979–2009). As one would expect, all three regions exhibit interplay among the variables. For example, the annual variability in regional-averaged runoff can be related to the annual precipitation conditions, since snowfall (end-of-winter snow accumulation) is negatively correlated with runoff. This link has been confirmed in earlier studies by, for example, Hanna et al. (2008) and Mernild et al. (2009). This indicates that years with low GIC surface runoff were synchronous with years of relatively high end-of-winter snow accumulation. More surface meltwater was retained in a thicker snowpack, reducing GIC runoff; however, maritime regions with high snowfall might have high summer runoff, as the regions in general are warm and wet. For Alaska, Greenland, and North Asia, a positive correlation was present between surface runoff and end-of-winter snow accumulation. Given the important role snow plays in GIC surface energy and moisture budgets, quantifying changes and variations in snow cover (e.g., thickness, duration, albedo, and timing; all components of the natural system simulated and accounted for by SnowModel) are essential for a comprehensive understanding of GIC surface runoff and mass balance changes. Therefore, we assume this modeling assessment to be a step forward compared with earlier GIC modeling studies (e.g., Hock et al. 2009; Marzeion et al. 2012), in the sense that the detailed resolution presented herein includes the diurnal cycle and its associated energy-related processes, which are important for a more detailed physical understanding of GIC runoff and end-of-winter snow accumulation and subsequent SMB conditions.

#### *b. Spatial latitude and elevation distribution*

From Fig. 1, GIC are unevenly distributed across the Northern Hemisphere and have been divided into 15 glacierized regions, located in both maritime and continental climate conditions. Even though this climate variability exists among regions, a pronounced pattern in the location—that is, in the latitude–elevation distribution—of GIC occurred, where GIC at high latitudes, in general, were located at relatively low elevations, and vice versa for low latitudes (Fig. 6).

The latitude–elevation distributed GIC MAAT (1979–2009) (Fig. 6a) showed a characteristic diagonal pattern, including both vertical and horizontal temperature gradients. Changes in simulated MAAT from the first decade to the last decade, highlighted on average by

TABLE 2. Regional breakdown of surface GIC conditions: mean and standard error (error ranges correspond to a 95% confidence interval) for annual air temperature (MAAT), June–August (JJA) mean air temperatures, precipitation ( $P$ ), sublimation and evaporation ( $Su+E$ ), runoff ( $R$ ), and mass balance (SMB) for all simulated GIC within each region from 1979 through 2009, and on the decadal scale. Significant trends ( $p < 0.05$ ) for the 1979–2009 period are highlighted in bold.

Region and area	Parameters	1979/80 to 1988/89	1989/90 to 1998/99	1999/00 to 2008/09	Mean 1979 to 2009	Mean change from the first to the last decade and mean linear trends from 1979 to 2009 (shown in brackets; $^{\circ}\text{C yr}^{-1}$ and $\text{m yr}^{-1}$ ) (trends are calculated based on a linear regression $t$ test)
1: Alaska (90 800 km <sup>2</sup> )	MAAT ( $^{\circ}\text{C}$ )	$-6.5 \pm 0.4$	$-6.5 \pm 0.3$	$-6.2 \pm 0.5$	$-6.4 \pm 0.2$	0.3 (0.01)
	JJA ( $^{\circ}\text{C}$ )	$2.0 \pm 0.5$	$2.6 \pm 0.5$	$2.6 \pm 0.8$	$2.4 \pm 0.3$	0.6 (0.03)
	$P$ (m w.e.)	$2.93 \pm 0.33$	$2.75 \pm 0.25$	$3.09 \pm 0.22$	$2.93 \pm 0.16$	0.16 (0.002)
	$Su+E$ (m w.e.)	$0.08 \pm 0.00$	$0.07 \pm 0.00$	$0.08 \pm 0.00$	$0.08 \pm 0.00$	0.00 (0.000)
	$R$ (m w.e.)	$3.06 \pm 0.23$	$3.35 \pm 0.19$	$3.54 \pm 0.27$	$3.31 \pm 0.15$	0.48 ( <b>0.020</b> )
2: Western Canada and United States (14 400 km <sup>2</sup> )	SMB (m w.e.)	$-0.20 \pm 0.29$	$-0.66 \pm 0.24$	$-0.52 \pm 0.36$	$-0.46 \pm 0.18$	$-0.32 (-0.017)$
	MAAT ( $^{\circ}\text{C}$ )	$-4.8 \pm 0.5$	$-4.5 \pm 0.5$	$-4.5 \pm 0.4$	$-4.6 \pm 0.3$	0.3 (0.02)
	JJA ( $^{\circ}\text{C}$ )	$3.6 \pm 0.4$	$3.9 \pm 0.6$	$4.1 \pm 0.7$	$3.9 \pm 0.3$	0.5 (0.03)
	$P$ (m w.e.)	$3.76 \pm 0.16$	$3.73 \pm 0.27$	$3.56 \pm 0.26$	$3.68 \pm 0.14$	$-0.20 (-0.006)$
	$Su+E$ (m w.e.)	$0.08 \pm 0.00$	$0.08 \pm 0.00$	$0.08 \pm 0.00$	$0.08 \pm 0.00$	0.00 (0.000)
3: Arctic Canada, North (105 000 km <sup>2</sup> )	$R$ (m w.e.)	$3.70 \pm 0.20$	$4.00 \pm 0.28$	$4.02 \pm 0.30$	$3.91 \pm 0.16$	0.32 (0.014)
	SMB (m w.e.)	$-0.02 \pm 0.29$	$-0.34 \pm 0.46$	$-0.54 \pm 0.38$	$-0.30 \pm 0.22$	$-0.51 (-0.021)$
	MAAT ( $^{\circ}\text{C}$ )	$-19.8 \pm 0.4$	$-19.5 \pm 0.4$	$-18.7 \pm 0.4$	$-19.3 \pm 0.3$	1.1 ( <b>0.06</b> )
	JJA ( $^{\circ}\text{C}$ )	$-3.8 \pm 0.5$	$-3.6 \pm 0.7$	$-2.8 \pm 0.5$	$-3.4 \pm 0.3$	1.0 ( <b>0.05</b> )
	$P$ (m w.e.)	$0.45 \pm 0.06$	$0.47 \pm 0.05$	$0.45 \pm 0.04$	$0.45 \pm 0.03$	0.01 ( $< -0.001$ )
4: Arctic Canada, South (40 900 km <sup>2</sup> )	$Su+E$ (m w.e.)	$0.03 \pm 0.00$	$0.04 \pm 0.00$	$0.04 \pm 0.00$	$0.04 \pm 0.00$	0.00 (0.000)
	$R$ (m w.e.)	$0.37 \pm 0.05$	$0.58 \pm 0.05$	$0.74 \pm 0.05$	$0.57 \pm 0.06$	0.37 ( <b>0.018</b> )
	SMB (m w.e.)	$0.04 \pm 0.10$	$-0.15 \pm 0.06$	$-0.33 \pm 0.08$	$-0.15 \pm 0.07$	$-0.37 (-0.018)$
	MAAT ( $^{\circ}\text{C}$ )	$-19.8 \pm 0.6$	$-19.5 \pm 0.4$	$-18.7 \pm 0.3$	$-19.3 \pm 0.3$	1.1 ( <b>0.06</b> )
	JJA ( $^{\circ}\text{C}$ )	$-2.7 \pm 0.4$	$-2.6 \pm 0.6$	$-2.1 \pm 0.4$	$-2.5 \pm 0.3$	0.6 (0.03)
5: Greenland (88 000 km <sup>2</sup> )	$P$ (m w.e.)	$0.62 \pm 0.06$	$0.66 \pm 0.05$	$0.69 \pm 0.06$	$0.66 \pm 0.03$	0.07 ( <b>0.004</b> )
	$Su+E$ (m w.e.)	$0.03 \pm 0.00$	$0.04 \pm 0.00$	$0.03 \pm 0.00$	$0.03 \pm 0.00$	0.00 (0.000)
	$R$ (m w.e.)	$0.80 \pm 0.07$	$1.20 \pm 0.10$	$1.35 \pm 0.07$	$1.12 \pm 0.10$	0.55 ( <b>0.026</b> )
	SMB (m w.e.)	$-0.21 \pm 0.10$	$-0.58 \pm 0.10$	$-0.69 \pm 0.10$	$-0.49 \pm 0.09$	$-0.48 (-0.022)$
	MAAT ( $^{\circ}\text{C}$ )	$-16.2 \pm 0.4$	$-15.7 \pm 0.4$	$-15.0 \pm 0.4$	$-15.6 \pm 0.3$	1.2 ( <b>0.06</b> )
6: Iceland (11 100 km <sup>2</sup> )	JJA ( $^{\circ}\text{C}$ )	$-4.4 \pm 0.3$	$-4.1 \pm 0.4$	$-3.5 \pm 0.3$	$-4.0 \pm 0.2$	0.9 ( <b>0.04</b> )
	$P$ (m w.e.)	$0.39 \pm 0.07$	$0.47 \pm 0.05$	$0.49 \pm 0.05$	$0.45 \pm 0.04$	0.10 ( <b>0.005</b> )
	$Su+E$ (m w.e.)	$0.08 \pm 0.00$	$0.09 \pm 0.00$	$0.08 \pm 0.00$	$0.08 \pm 0.00$	0.00 (0.000)
	$R$ (m w.e.)	$0.45 \pm 0.12$	$0.61 \pm 0.05$	$0.80 \pm 0.03$	$0.62 \pm 0.07$	0.36 ( <b>0.019</b> )
	SMB (m w.e.)	$-0.14 \pm 0.13$	$-0.22 \pm 0.04$	$-0.39 \pm 0.05$	$-0.25 \pm 0.06$	$-0.25 (-0.013)$
7: Svalbard (33 800 km <sup>2</sup> )	MAAT ( $^{\circ}\text{C}$ )	$-6.1 \pm 0.3$	$-5.7 \pm 0.2$	$-5.1 \pm 0.4$	$-5.6 \pm 0.2$	1.0 ( <b>0.05</b> )
	JJA ( $^{\circ}\text{C}$ )	$-0.2 \pm 0.4$	$-0.1 \pm 0.4$	$-0.4 \pm 0.4$	$0.0 \pm 0.2$	0.6 ( <b>0.03</b> )
	$P$ (m w.e.)	$1.68 \pm 0.11$	$1.62 \pm 0.09$	$1.76 \pm 0.13$	$1.68 \pm 0.06$	0.08 (0.003)
	$Su+E$ (m w.e.)	$0.08 \pm 0.00$	$0.09 \pm 0.00$	$0.08 \pm 0.00$	$0.08 \pm 0.00$	0.00 (0.000)
	$R$ (m w.e.)	$1.80 \pm 0.17$	$2.01 \pm 0.24$	$2.40 \pm 0.23$	$2.07 \pm 0.15$	0.60 ( <b>0.028</b> )
8: Scandinavia (2800 km <sup>2</sup> )	SMB (m w.e.)	$-0.20 \pm 0.17$	$-0.48 \pm 0.24$	$-0.73 \pm 0.15$	$-0.47 \pm 0.13$	$-0.52 (-0.025)$
	MAAT ( $^{\circ}\text{C}$ )	$-12.0 \pm 1.0$	$-11.3 \pm 0.6$	$-10.5 \pm 0.5$	$-11.2 \pm 0.5$	1.5 ( <b>0.06</b> )
	JJA ( $^{\circ}\text{C}$ )	$-2.5 \pm 0.4$	$-2.3 \pm 0.3$	$-2.0 \pm 0.3$	$-2.3 \pm 0.2$	0.5 ( <b>0.03</b> )
	$P$ (m w.e.)	$0.69 \pm 0.04$	$0.76 \pm 0.05$	$0.84 \pm 0.07$	$0.76 \pm 0.04$	0.15 ( <b>0.006</b> )
	$Su+E$ (m w.e.)	$0.04 \pm 0.00$	$0.04 \pm 0.00$	$0.04 \pm 0.00$	$0.04 \pm 0.00$	0.00 (0.000)
8: Scandinavia (2800 km <sup>2</sup> )	$R$ (m w.e.)	$1.15 \pm 0.12$	$1.64 \pm 0.07$	$1.93 \pm 0.24$	$1.57 \pm 0.11$	0.45 ( <b>0.019</b> )
	SMB (m w.e.)	$-0.14 \pm 0.12$	$-0.43 \pm 0.11$	$-0.45 \pm 0.25$	$-0.34 \pm 0.11$	$-0.30 (-0.014)$
	MAAT ( $^{\circ}\text{C}$ )	$-4.3 \pm 0.4$	$-4.0 \pm 0.4$	$-3.3 \pm 0.3$	$-3.9 \pm 0.2$	1.0 ( <b>0.04</b> )
	JJA ( $^{\circ}\text{C}$ )	$3.6 \pm 0.8$	$3.6 \pm 0.6$	$4.5 \pm 0.6$	$3.9 \pm 0.4$	0.9 (0.04)
	$P$ (m w.e.)	$3.57 \pm 0.42$	$3.79 \pm 0.34$	$3.27 \pm 0.38$	$3.54 \pm 0.23$	$-0.30 (-0.015)$
8: Scandinavia (2800 km <sup>2</sup> )	$Su+E$ (m w.e.)	$0.06 \pm 0.00$	$0.07 \pm 0.00$	$0.06 \pm 0.00$	$0.06 \pm 0.00$	0.00 (0.000)
	$R$ (m w.e.)	$3.48 \pm 0.17$	$3.56 \pm 0.33$	$4.01 \pm 0.26$	$3.68 \pm 0.17$	0.53 ( <b>0.025</b> )
	SMB (m w.e.)	$0.03 \pm 0.48$	$0.17 \pm 0.34$	$-0.81 \pm 0.48$	$-0.20 \pm 0.29$	$-0.84 (-0.040)$



TABLE 2. (Continued)

Region and area	Parameters	1979/80 to 1988/89	1989/90 to 1998/99	1999/00 to 2008/09	Mean 1979 to 2009	Mean change from the first to the last decade and mean linear trends from 1979 to 2009 (shown in brackets; °C yr <sup>-1</sup> and m yr <sup>-1</sup> ) (trends are calculated based on a linear regression <i>t</i> test)
9: Arctic Russia (51 800 km <sup>2</sup> )	MAAT (°C)	-14.7 ± 0.5	-14.8 ± 0.5	-13.5 ± 0.5	-14.4 ± 0.4	1.2 ( <b>0.05</b> )
	JJA (°C)	-3.6 ± 0.3	-3.4 ± 0.3	-3.2 ± 0.1	-3.4 ± 0.1	0.4 (0.02)
	<i>P</i> (m w.e.)	0.26 ± 0.01	0.25 ± 0.02	0.27 ± 0.02	0.26 ± 0.01	0.01 (<0.001)
	Su+ <i>E</i> (m w.e.)	0.04 ± 0.00	0.04 ± 0.00	0.04 ± 0.00	0.04 ± 0.00	0.00 (0.000)
	<i>R</i> (m w.e.)	0.37 ± 0.13	0.45 ± 0.12	0.45 ± 0.14	0.42 ± 0.07	0.08 (0.003)
10: North Asia (2800 km <sup>2</sup> )	SMB (m w.e.)	-0.15 ± 0.13	-0.24 ± 0.12	-0.21 ± 0.15	-0.20 ± 0.08	-0.06 (-0.003)
	MAAT (°C)	-12.3 ± 0.5	-12.0 ± 0.3	-11.8 ± 0.4	-12.0 ± 0.2	0.5 ( <b>0.03</b> )
	JJA (°C)	2.0 ± 0.4	2.4 ± 0.5	2.9 ± 0.3	2.4 ± 0.3	0.9 ( <b>0.04</b> )
	<i>P</i> (m w.e.)	0.60 ± 0.02	0.60 ± 0.02	0.64 ± 0.02	0.61 ± 0.01	0.04 ( <b>0.002</b> )
	Su+ <i>E</i> (m w.e.)	0.07 ± 0.00	0.07 ± 0.00	0.07 ± 0.00	0.07 ± 0.00	0.00 (0.000)
11: Central Europe (2000 km <sup>2</sup> )	<i>R</i> (m w.e.)	0.93 ± 0.07	0.92 ± 0.10	1.01 ± 0.07	0.95 ± 0.05	0.08 (0.003)
	SMB (m w.e.)	-0.40 ± 0.07	-0.39 ± 0.09	-0.44 ± 0.06	-0.41 ± 0.04	-0.04 (-0.001)
	MAAT (°C)	-6.9 ± 0.4	-6.5 ± 0.3	-6.3 ± 0.4	-6.5 ± 0.2	0.6 ( <b>0.03</b> )
	JJA (°C)	0.4 ± 0.5	0.8 ± 0.4	1.3 ± 0.6	0.8 ± 0.3	0.9 ( <b>0.04</b> )
	<i>P</i> (m w.e.)	2.89 ± 0.15	2.68 ± 0.22	2.24 ± 0.35	2.60 ± 0.17	-0.65 (- <b>0.032</b> )
12: Caucasus (1100 km <sup>2</sup> )	Su+ <i>E</i> (m w.e.)	0.14 ± 0.01	0.14 ± 0.01	0.14 ± 0.01	0.14 ± 0.00	0.00 (0.000)
	<i>R</i> (m w.e.)	2.83 ± 0.33	2.91 ± 0.25	3.12 ± 0.21	2.95 ± 0.15	0.29 (0.015)
	SMB (m w.e.)	-0.08 ± 0.34	-0.38 ± 0.27	-1.62 ± 0.41	-0.49 ± 0.24	-0.93 (- <b>0.046</b> )
	MAAT (°C)	-7.7 ± 0.2	-7.8 ± 0.5	-7.4 ± 0.3	-7.6 ± 0.2	0.3 (0.02)
	JJA (°C)	0.5 ± 0.4	0.7 ± 0.6	1.2 ± 0.5	0.8 ± 0.3	0.7 ( <b>0.04</b> )
13: Central Asia, North (64 400 km <sup>2</sup> )	<i>P</i> (m w.e.)	1.98 ± 0.13	1.96 ± 0.13	2.01 ± 0.16	1.98 ± 0.08	0.03 (0.005)
	Su+ <i>E</i> (m w.e.)	0.15 ± 0.01	0.16 ± 0.01	0.16 ± 0.01	0.16 ± 0.00	0.00 (0.000)
	<i>R</i> (m w.e.)	2.13 ± 0.12	2.29 ± 0.18	2.46 ± 0.19	2.29 ± 0.10	0.33 ( <b>0.020</b> )
	SMB (m w.e.)	-0.31 ± 0.16	-0.48 ± 0.15	-0.61 ± 0.09	-0.47 ± 0.09	-0.30 (- <b>0.015</b> )
	MAAT (°C)	-9.9 ± 0.3	-9.8 ± 0.2	-9.6 ± 0.2	-9.8 ± 0.1	0.3 ( <b>0.02</b> )
14: Central Asia, South (21 800 km <sup>2</sup> )	JJA (°C)	-1.0 ± 0.3	-0.8 ± 0.4	-0.8 ± 0.3	-0.9 ± 0.2	0.2 (0.01)
	<i>P</i> (m w.e.)	2.03 ± 0.10	2.00 ± 0.10	1.98 ± 0.09	2.00 ± 0.05	-0.05 (0.002)
	SU+ <i>E</i> (m w.e.)	0.34 ± 0.01	0.33 ± 0.01	0.33 ± 0.01	0.33 ± 0.00	-0.02 (<- <b>0.001</b> )
	<i>R</i> (m w.e.)	1.93 ± 0.09	2.01 ± 0.10	2.06 ± 0.06	2.00 ± 0.05	0.13 ( <b>0.006</b> )
	SMB (m w.e.)	-0.25 ± 0.09	-0.35 ± 0.07	-0.40 ± 0.11	-0.33 ± 0.06	-0.15 (- <b>0.007</b> )
15: Central Asia, West (33 800 km <sup>2</sup> )	MAAT (°C)	-12.1 ± 0.4	-12.1 ± 0.3	-11.5 ± 0.2	-11.9 ± 0.2	0.6 ( <b>0.02</b> )
	JJA (°C)	-2.5 ± 0.7	-2.5 ± 0.6	-1.8 ± 0.6	-2.3 ± 0.4	0.7 (0.02)
	<i>P</i> (m w.e.)	0.81 ± 0.06	0.85 ± 0.07	0.67 ± 0.04	0.78 ± 0.04	-0.14 (- <b>0.006</b> )
	Su+ <i>E</i> (m w.e.)	0.28 ± 0.01	0.28 ± 0.01	0.26 ± 0.01	0.27 ± 0.01	-0.02 (<- <b>0.001</b> )
	<i>R</i> (m w.e.)	1.13 ± 0.14	1.08 ± 0.15	1.23 ± 0.11	1.15 ± 0.08	0.10 (0.004)
Overall, north of 25°N	SMB (m w.e.)	-0.59 ± 0.15	-0.50 ± 0.16	-0.82 ± 0.12	-0.64 ± 0.10	-0.23 (-0.009)
	MAAT (°C)	-8.3 ± 0.3	-8.1 ± 0.3	-7.7 ± 0.3	-8.0 ± 0.2	0.6 ( <b>0.04</b> )
	JJA (°C)	-1.2 ± 0.2	-1.0 ± 0.3	-0.8 ± 0.2	-1.0 ± 0.1	0.4 ( <b>0.02</b> )
	<i>P</i> (m w.e.)	2.24 ± 0.12	2.19 ± 0.16	2.24 ± 0.19	2.22 ± 0.09	-0.01 (<- <b>0.001</b> )
	Su+ <i>E</i> (m w.e.)	0.33 ± 0.00	0.32 ± 0.01	0.31 ± 0.01	0.32 ± 0.00	-0.01 (<- <b>0.001</b> )
Overall, north of 25°N	<i>R</i> (m w.e.)	2.20 ± 0.07	2.37 ± 0.10	2.47 ± 0.07	2.34 ± 0.06	0.27 ( <b>0.013</b> )
	SMB (m w.e.)	-0.28 ± 0.11	-0.50 ± 0.10	-0.55 ± 0.24	-0.44 ± 0.10	-0.26 (- <b>0.014</b> )
	MAAT (°C)	-10.6 ± 0.1	-10.4 ± 0.1	-9.8 ± 0.1	-10.3 ± 0.1	0.8 ( <b>0.04</b> )
	JJA (°C)	-0.7 ± 0.1	-0.4 ± 0.3	-0.1 ± 0.2	-0.4 ± 0.1	0.6 ( <b>0.03</b> )
	<i>P</i> (m w.e.)	1.66 ± 0.05	1.65 ± 0.03	1.61 ± 0.05	1.64 ± 0.03	-0.05 (<- <b>0.001</b> )
Overall, north of 25°N	Su+ <i>E</i> (m w.e.)	0.12 ± 0.00	0.12 ± 0.00	0.12 ± 0.00	0.12 ± 0.00	0.00 (0.000)
	<i>R</i> (m w.e.)	1.73 ± 0.04	1.90 ± 0.07	2.06 ± 0.07	1.90 ± 0.06	0.33 ( <b>0.016</b> )
	SMB (m w.e.)	-0.19 ± 0.03	-0.37 ± 0.06	-0.57 ± 0.11	-0.38 ± 0.07	-0.37 (- <b>0.018</b> )

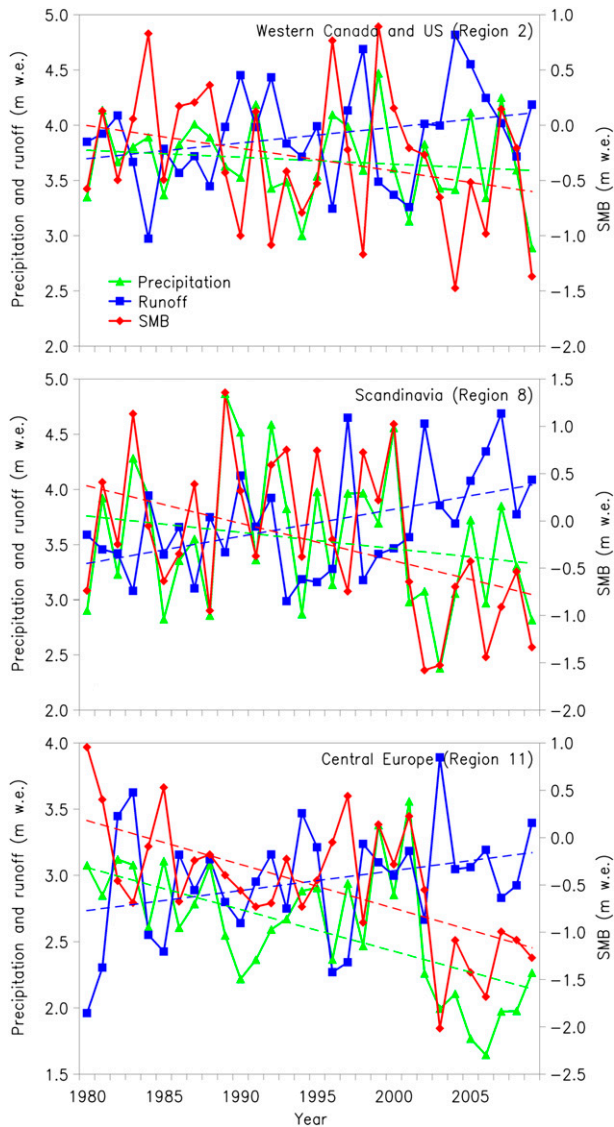


FIG. 5. An example of mean annual regional GIC simulated precipitation, runoff, and SMB time series for all GIC in three randomly picked regions: western Canada and the United States (region 2), Scandinavia (region 8), and Central Europe (region 11) for 1979 to 2009 (in Table 2 significant trends for each parameter are highlighted in bold).

the increasing MAAT for all GIC, were most pronounced at high latitudes, as expected from observations (Hansen et al. 2010) (insignificant changes are shown in gray color). Enclaves of decreasing GIC MAAT occurred (Fig. 6a), for example, at the Karakoram Range ( $\sim 35^{\circ}$ – $38^{\circ}$ N), Kamchatka ( $\sim 58^{\circ}$ – $60^{\circ}$ N), the southern part of Alaska ( $\sim 53^{\circ}$ – $60^{\circ}$ N), and for several Arctic areas.

In addition to surface air temperature, precipitation (snow accumulation) is a key climate system variable that is important for understanding GIC SMB conditions. The 30-yr mean annual latitude–elevation distributed GIC

precipitation sum (Fig. 6b) indicates a more heterogeneous precipitation pattern for GIC (compared to the diagonal MAAT pattern) that is likely influenced by topography, orography, distance from large bodies of water, and climate conditions. This is especially true of GIC located in southeast Alaska and western Canada and the United States ( $\sim 51^{\circ}$ – $61^{\circ}$ N), and the eastern and southern part of the region Central Asia (West) in HMA ( $28^{\circ}$ – $29^{\circ}$ N), which had remarkably higher mean annual precipitation sums compared to GIC at equivalent latitudes. Changes in mean annual GIC precipitation totals from the first to last decades are heterogeneously distributed as well, indicating clusters of GIC facing both decreasing and increasing precipitation trends (Fig. 6b). Clusters of GIC where the precipitation increases were greatest were found in parts of southeast Alaska and western Canada and the United States, the eastern and southern part of the region Central Asia (West), Svalbard (around  $78^{\circ}$ – $79^{\circ}$ N), and in the Karakoram Range. On the other hand, clusters where precipitation decreased at a maximum rate were found in Central Asia, and in the eastern and southern part of the region Central Asia (West) (Fig. 6b).

The 30-yr mean annual latitude–elevation distributed GIC sublimation and evaporation sum during 1979–2009 are illustrated in Fig. 6c. Specifically for HMA, the simulated sublimation and evaporation sum was high, due to the cold and dry climatic conditions (see also section 5a for further information). The greatest changes in annual GIC sublimation and evaporation sum (between the first and last decades) occurred as well for HMA, where on average it changed  $-0.01$  m w.e. for HMA, equal to a mean trend of  $< -0.001$  m w.e.  $\text{yr}^{-1}$  (Table 2). For GIC outside HMA, changes in sublimation and evaporation were lower and almost in the same range (Fig. 6c).

From a hydrological perspective, GIC represents water storage available for river runoff when melting in spring and summer. Runoff is an important parameter for water availability around the world (e.g., Huss 2011; Immerzeel et al. 2012) and for addressing water resource issues associated with drinking water, irrigation, and hydropower production. In regions where snow and ice melt are key components of the hydrologic cycle, around 30%–40% of the annual runoff can be explained by GIC net mass loss, as observed in southeast Greenland (Mernild and Hasholt 2006; Liston and Mernild 2012). The latitude–elevation distributed 30-yr mean annual GIC runoff sum (1979–2009) is heterogeneously distributed (Fig. 6d), where two GIC clusters ( $25^{\circ}$ – $28^{\circ}$ N and  $50^{\circ}$ – $62^{\circ}$ N) had maximum simulated runoff values ( $> 3.5$  m w.e.); these are located in the same areas where maximum precipitation occurred. For latitudes between the two maximum GIC runoff clusters, simulated runoff seems to be roughly influenced by the characteristic

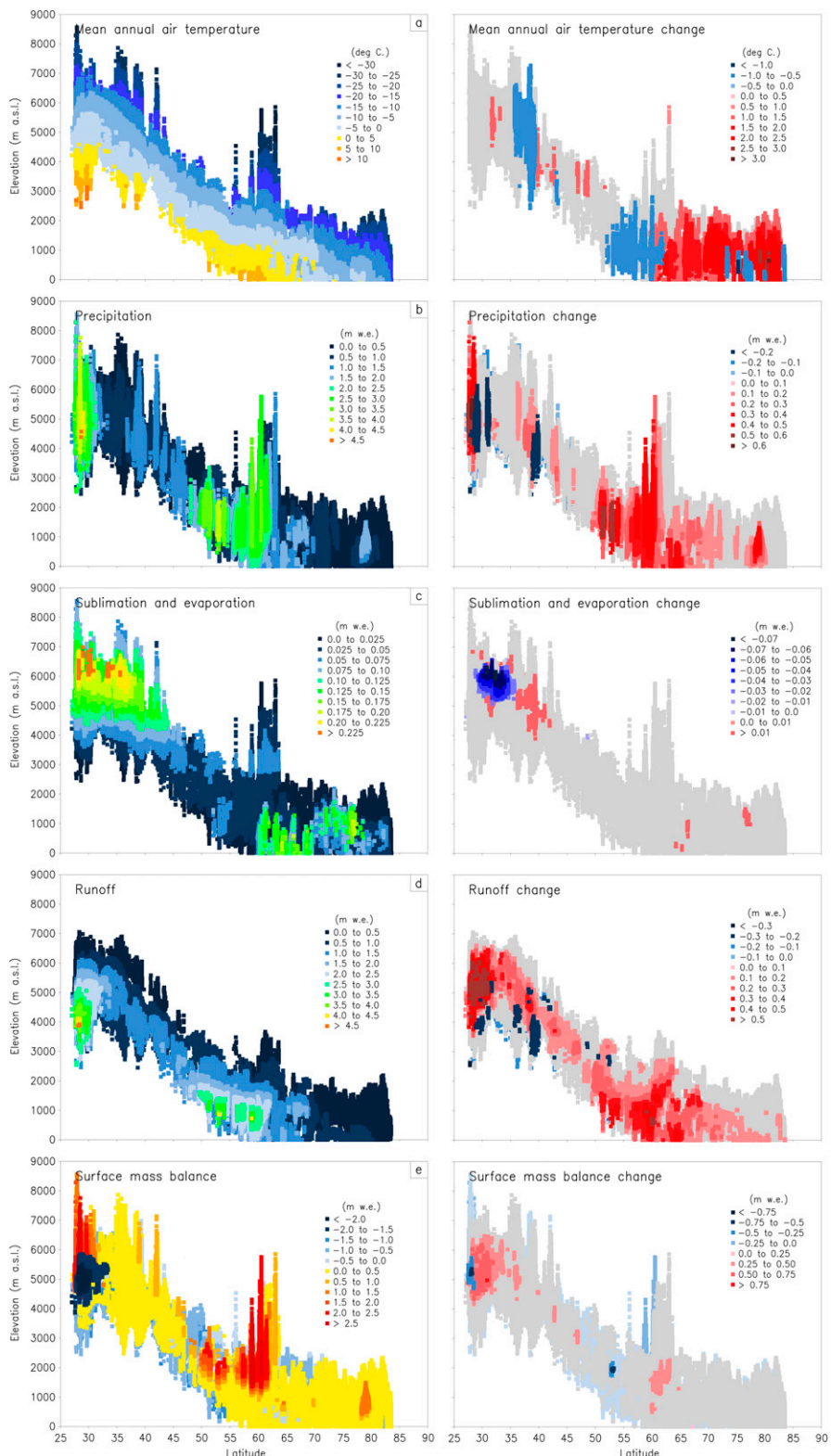


FIG. 6. Latitude vs elevation for mean (1979–2009) and changes (1979–89 minus 1999–2009): (a) MAAT, (b) precipitation, (c) sublimation and evaporation, (d) runoff, and (e) SMB for all individual GIC covered grid cells ( $n = 543\,389$ ). Insignificant changes (in the right column) are highlighted in gray color.

TABLE 3. The percentage distribution of GIC SMB decreasing and increasing annual trends for 1979–89, 1989–99, and 1999–2009.

			1979–89		1989–99		1999–2009	
Decreasing trend	Insignificant	All slopes	47%	57%	48%	52%	36%	40%
	Significant ( $p < 0.05$ )	0.00 to $-0.05$ m w.e. yr $^{-1}$	8%		3%		3%	
		$-0.05$ to $-0.10$ m w.e. yr $^{-1}$	2%		1%		1%	
		$> -0.10$ m w.e. yr $^{-1}$	0.5%		0.4%		<0.1%	
Increasing trend	Insignificant	All slopes	40%	43%	44%	48%	54%	60%
	Significant ( $p < 0.05$ )	0.00 to $0.05$ m w.e. yr $^{-1}$	2%		3%		5%	
		$0.05$ to $0.10$ m w.e. yr $^{-1}$	1%		1%		1%	
		$> 0.10$ m w.e. yr $^{-1}$	0.2%		0.2%		<0.1%	

latitude–elevation diagonal temperature patterns, except for the area located higher than  $\sim 70^\circ\text{N}$ . Here, probably due to the relatively low temperatures—MAAT is typically below freezing and the ablation period is relatively short—changes in runoff seem less pronounced in response to changes in elevation, compared to lower latitudes. Regarding changes in runoff from the first decade to the last decade, the latitude–elevation distributed runoff indicates clusters of both increasing and decreasing GIC runoff.

These GIC simulations allow us to map and analyze MAAT, precipitation, sublimation and evaporation, and runoff conditions and therefore [based on Eq. (1)] to estimate GIC SMB conditions in the Northern Hemisphere at higher resolution and with more physical realism than ever done before. The simulated GIC latitude–elevation distributed SMB (1979–2009) (Fig. 6e) shows clusters of maximum mass gain in southeast Alaska, western Canada and the United States, and Svalbard. For HMA, both maximum SMB gain and loss were simulated; this is also true of the Karakoram Range, where observed mass gain for the early twenty-first century has been confirmed by Gardelle et al. (2012). Regarding changes in SMB from the first to the last decades, a heterogeneous latitude–elevation pattern occurred with enclaves of maximum loss and gain. Clusters of maximum loss were located in HMA and the western United States and Canada, while clusters of maximum gain were located in HMA, including in the Karakoram Range. Behind these heterogeneous conditions in SMB change (Fig. 6e), a shift occurred toward a lower (higher) percentage of decreasing (increasing) GIC SMB trends (Table 3). Increasing annual SMB trends occurred for 43% of the domain in 1979–89 and 60% in 1999–2009 while decreasing trends occurred for 57% in 1979–89 and 40% in 1999–2009. Roughly 10% of all the increasing and decreasing trends were significant.

### c. Examples of spatial GIC simulations

SnowModel simulated 30-yr mean and trend distribution of GIC air temperature and surface hydrological

conditions are illustrated for two areas—the Sermilik Fjord area in southeast Greenland (Fig. 7, including the Mittivakkat Gletscher, the longest mass balance observed glacier in Greenland) and the eastern Karakoram Range in the Himalayas (Fig. 8; an area containing some of the longest valley glaciers, the Siachen and Biafo Glaciers, outside the Arctic). The Mittivakkat Gletscher was used as an independent verification of the simulated results. For the Mittivakkat Gletscher the simulated 30-yr MAAT was  $-1.6^\circ \pm 0.2^\circ\text{C}$  for 1979–2009 and  $-1.3^\circ \pm 0.2^\circ\text{C}$  for 1994–2009 (Fig. 7), which for the latter period was indistinguishable (97.5% quantile, based on the null hypothesis) from observed surface MAAT 1994–2009 (MAAT data obtained from two adjacent meteorological stations, Station Coast and Station Nunatak, which were merged) of  $-1.5^\circ \pm 0.1^\circ\text{C}$  [for location of the stations, see Mernild et al. (2008a) and Hanna et al. (2012)]. The simulated (adjusted) 8-yr average Station Nunatak precipitation (1999–2006) was  $1.56 \pm 0.19$  m w.e. and indistinguishable from observed precipitation, averaging  $1.85 \pm 0.18$  m w.e. (97.5% quantile, based on the null hypothesis) (Mernild et al. 2008b). (Nunatak is a meteorological station operated by University of Copenhagen, located at 515 m MSL close to the northwestern margin of Mittivakkat and at the equilibrium-line altitude.) Mittivakkat Gletscher simulated 30-yr average sublimation and evaporation, and runoff, were  $0.07 \pm 0.00$  and  $1.56 \pm 0.15$  m w.e. (Figs. 7c,d), respectively. For Mittivakkat, during the 1995–2009 SMB observation period the mean annual observed SMB was  $-0.76 \pm 0.32$  m w.e. (Mernild et al. 2011a,c, 2013b), which was indistinguishable (97.5% quantile; based on the null hypothesis) from the SnowModel-simulated Mittivakkat Gletscher mean annual SMB of  $-0.64 \pm 0.24$  m w.e. Overall for the Mittivakkat Gletscher, precipitation increased an average of  $9$  mm w.e. yr $^{-1}$  (significant), MAAT  $0.05^\circ\text{Cyr}^{-1}$  (significant), and runoff  $10$  mm w.e. yr $^{-1}$  (insignificant) (Fig. 7e).

In Figs. 8a–d, the spatial variability is also shown as an example from the eastern Karakoram Range. It is clear



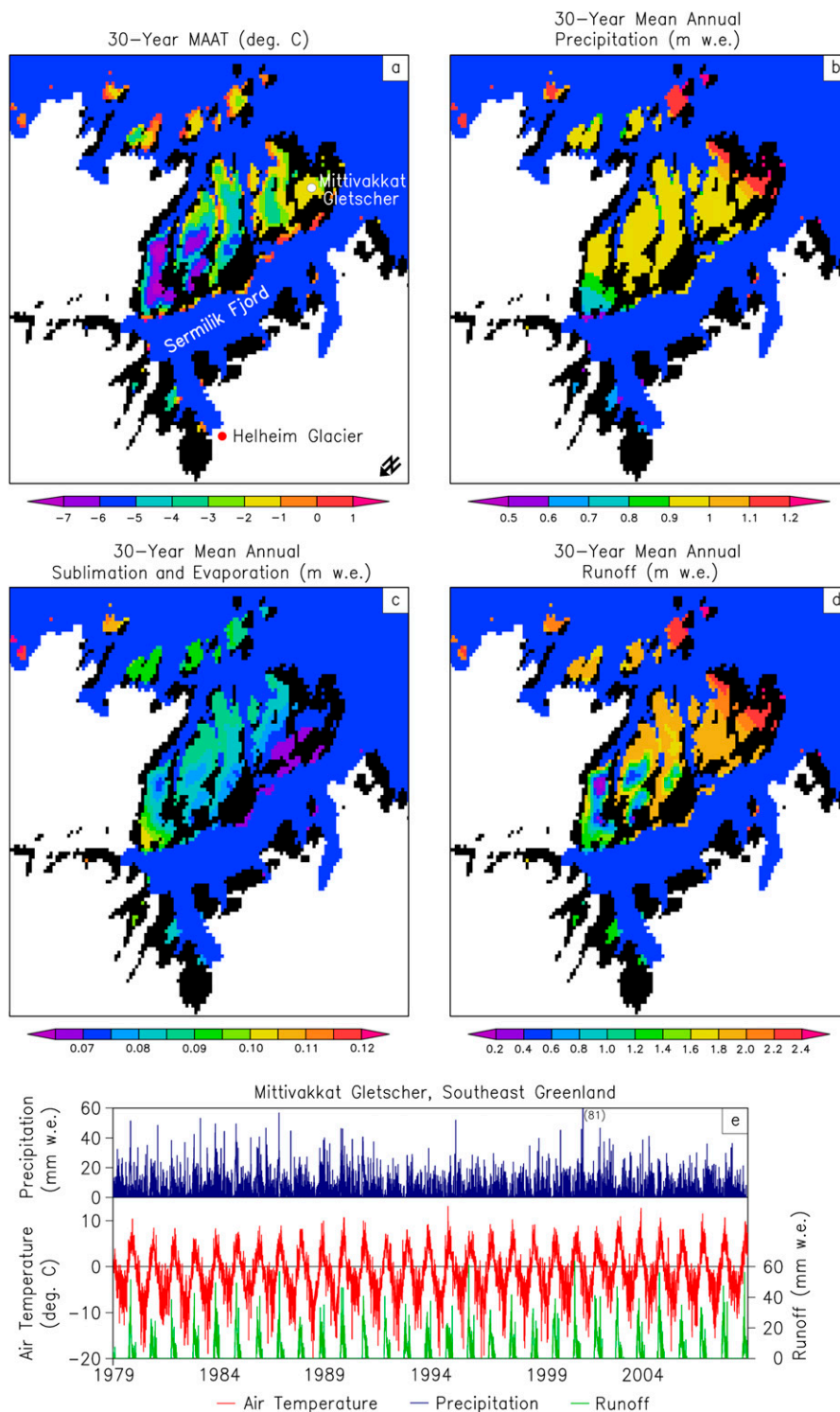


FIG. 7. An example of the spatial distribution of 30-yr mean (1979–2009) for GIC in the Sermilik Fjord area, southeast Greenland (region 5): (a) MAAT, (b) precipitation, (c) sublimation and evaporation, (d) runoff, and (e) daily time series of air temperature, precipitation, and runoff for the Mittivakkat Gletscher [65°42'N, 37°48'W; see white dot in (a)], the only long-term observed mountain glacier in Greenland. The domain is  $x = 121$  km and  $y = 135$  km, and the distance between Mittivakkat Glacier and Helheim Glacier is  $\sim 80$  km [Helheim is illustrated with a red dot in (a)]. The black color indicates nonglacier areas, white is the Greenland Ice Sheet, and the dark blue color is fjords and ocean. The overall regional location is illustrated in Fig. 1a.



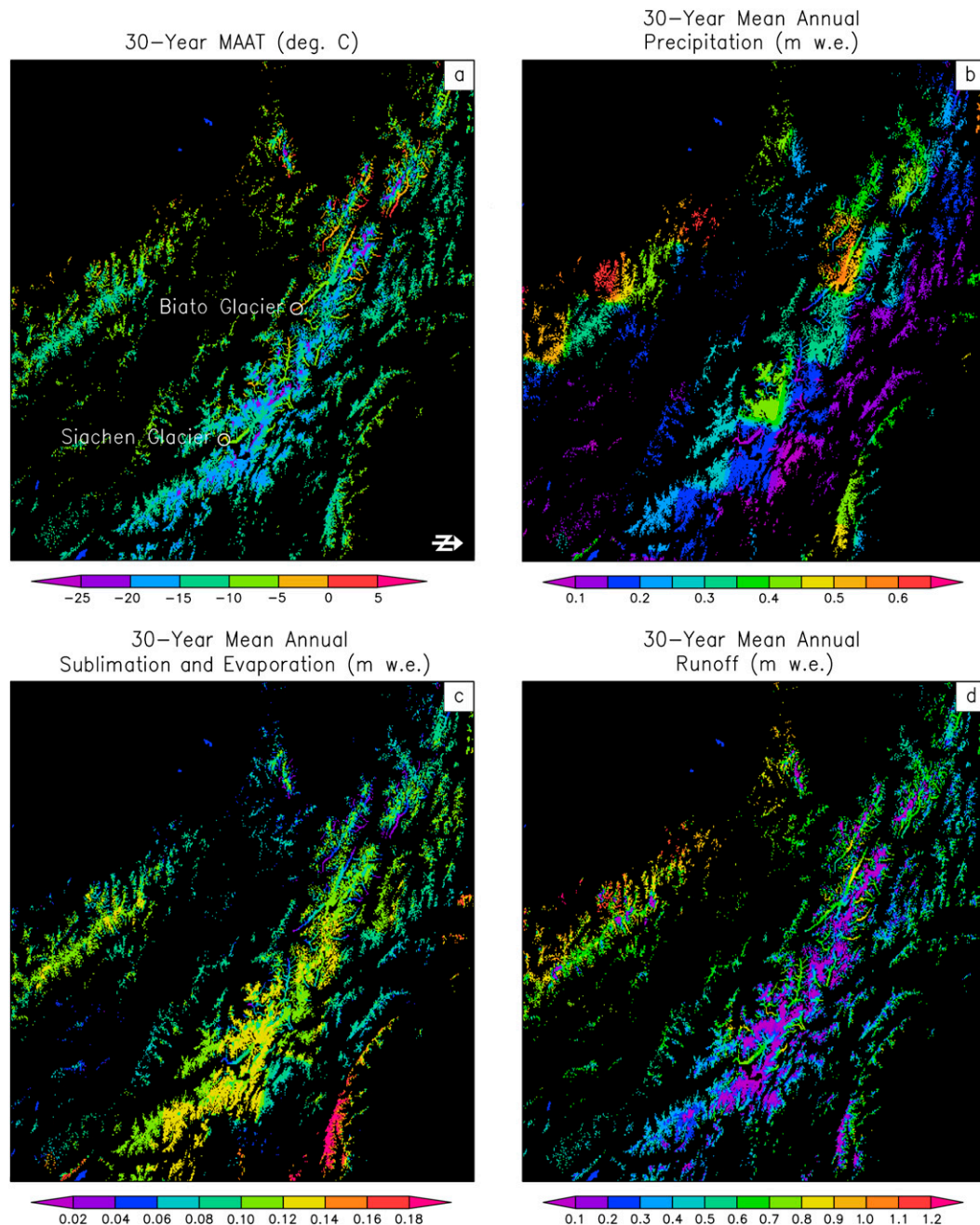


FIG. 8. As in Fig. 7, but for the Karakoram Range, spanning the borders of Pakistan, India, and China. The location of the Siachen ( $35^{\circ}25'N$ ,  $77^{\circ}06'E$ ) and Biafo Glaciers ( $35^{\circ}52'N$ ,  $75^{\circ}42'E$ ) are illustrated with white circles in (a), the distance between Siachen and Biafo Glaciers is  $\sim 140$  km, and the overall regional location is provided in Fig. 1a. The domain is  $x = 500$  km and  $y = 450$  km. The black color indicates nonglacier areas.

from the simulations that in this steep mountainous region the relatively low-elevation GIC are facing the highest MAAT and runoff along with the lowest snowfall, and that the opposite is true for the relatively high-elevation GIC (1979–2009). This is expected, but we also note that GIC in this area are experiencing a relatively

high mean annual ablation rate from sublimation and evaporation of more than  $0.18$  m w.e., equivalent to  $\sim 40\%$  of the annual precipitation. This ratio is in the same range as the sublimation/evaporation to precipitation ratio found in many regions of the Arctic (Liston and Sturm 1998, 2002, 2004).

TABLE 4. Regional breakdown of mean and standard error (error ranges correspond to a 95% confidence interval) of SMB and SMB contribution to sea level rise for 1979–2009 and 1999–2009.

Region	Annual volumetric SMB budget (km <sup>3</sup> ) (1979–2009)	Annual SMB contribution to sea level rise (mm SLE), and regional percentage (%) of overall contribution (1979–2009)	Annual volumetric SMB budget (km <sup>3</sup> ) (1999–2009)	Annual SMB contribution to sea level rise (mm SLE), and regional percentage (%) of overall contribution (1999–2009)	Percentage difference between 1979–2009 and 1999–2009 (%)
1: Alaska	-41.8 ± 16.5	0.12 ± 0.05 (23%)	-47.2 ± 19.1	0.13 ± 0.05 (19%)	13
2: Western Canada and United States	-4.3 ± 3.2	0.01 ± 0.01 (2%)	-7.7 ± 3.0	0.02 ± 0.01 (3%)	80
3: Arctic Canada, North	-15.8 ± 7.5	0.04 ± 0.02 (8%)	-34.7 ± 4.9	0.10 ± 0.01 (14%)	120
4: Arctic Canada, South	-20.1 ± 3.8	0.06 ± 0.01 (11%)	-28.2 ± 2.4	0.08 ± 0.01 (11%)	40
5: Greenland	-22.0 ± 5.3	0.06 ± 0.02 (12%)	-34.3 ± 2.6	0.09 ± 0.01 (13%)	56
6: Iceland	-5.2 ± 1.5	0.01 ± 0.00 (3%)	-8.1 ± 1.0	0.02 ± 0.00 (3%)	55
7: Svalbard	-11.2 ± 3.7	0.03 ± 0.01 (6%)	-15.2 ± 4.9	0.04 ± 0.01 (6%)	36
8: Scandinavia	-0.6 ± 0.8	<0.01 ± 0.00 (<1%)	-2.3 ± 0.8	0.01 ± 0.00 (<1%)	305
9: Arctic Russia	-10.4 ± 3.9	0.03 ± 0.01 (<1%)	-10.9 ± 4.6	0.03 ± 0.01 (4%)	5
10: North Asia	-1.2 ± 0.1	<0.01 ± 0.00 (6%)	-1.2 ± 0.1	<0.01 ± 0.00 (<1%)	7
11: Central Europe	-1.0 ± 0.5	<0.01 ± 0.00 (<1%)	-3.3 ± 0.5	0.01 ± 0.00 (1%)	230
12: Caucasus	-0.5 ± 0.1	<0.01 ± 0.00 (<1%)	-0.7 ± 0.1	<0.01 ± 0.00 (<1%)	30
13: Central Asia, North	-21.3 ± 3.7	0.06 ± 0.01 (11%)	-25.8 ± 4.2	0.07 ± 0.01 (10%)	21
14: Central Asia, South	-14.0 ± 2.1	0.04 ± 0.01 (8%)	-17.9 ± 1.5	0.05 ± 0.00 (7%)	28
15: Central Asia, West	-14.9 ± 3.4	0.04 ± 0.01 (8%)	-18.6 ± 4.7	0.05 ± 0.01 (7%)	25
Overall Northern Hemisphere	-184.3 ± 56.1	0.51 ± 0.16	-256.1 ± 54.3	0.71 ± 0.15	39

#### d. Regional SMB contribution to sea level rise

Sea level rise is dominated by melt-related mass losses from GIC and ice sheets, ice sheet and glacier calving, and ocean thermal expansion (e.g., Cogley 2012; Marzeion et al. 2012; Gardner et al. 2013; Vaughan et al. 2013; Mernild et al. 2013a). In Table 4, the regional SMB of the Northern Hemisphere GIC budget is displayed for 1979–2009 and 1999–2009. Here we emphasize the acceleration of the GIC SMB contribution to sea level rise for the first decade of the new millennium (2000–09), which was the warmest observed decade both globally and in Greenland (Hansen et al. 2010; Mernild et al. 2014). Our simulations show a regional variability in SMB (insignificant linear trends occurred for regions 9, 10, and 14; elsewhere the trends were significant) and a cumulative negative SMB for all regions (Fig. 9), with the largest negative cumulative SMB in High Mountain Asia (especially from Central Asia South, with -19.2 m w.e.) and Central Europe (-14.8 m w.e.). In contrast, the smallest negative cumulative SMB loss was from Arctic Russia (-6.0 m w.e.) and Arctic Canada North (-4.5 m w.e.). When integrating the regional GIC SMB over the regional GIC areas, the annual overall Northern Hemisphere GIC volumetric SMB budget for all 15 individual glacierized regions aggregated -184.3 ± 28.6 km<sup>3</sup> for 1979–2009, and -256.1 ± 27.7 km<sup>3</sup> for

1999–2009, with the greatest annual regional volumetric SMB budgets (1979–2009) from Alaska (-41.8 ± 8.4 km<sup>3</sup>) and Greenland (-22.0 ± 2.7 km<sup>3</sup>) and the smallest from Caucasus (-0.5 ± 0.1 km<sup>3</sup>) and Scandinavia (-0.6 ± 0.4 km<sup>3</sup>). Gardner et al. (2013) confirmed the geographical distribution of the peak mass loss from Alaska and the lowest loss from the Caucasus, even though the Alaska mass budget from Gardner et al. included both GIC SMB and calving contributions.

When converting the GIC SMB budget to sea level equivalent the ocean surface area was set to be constant (3.61 × 10<sup>8</sup> km<sup>2</sup>), which did not account for land area isostasy, coastline changes, grounding line migration, or influence from general sea level rise. For simplicity, we assumed the GIC mass losses contributed instantaneously to sea level rise (i.e., no changes in evaporation and water storage along proglacial hydrological flow paths were assumed to occur). On average, the Northern Hemisphere GIC SMB simulations indicated that the annual volumetric SMB contribution to sea level rise was 0.51 ± 0.16 mm SLE for 1979–2009 and 0.71 ± 0.15 mm SLE for 1999–2009 (Table 4), equal to an increase of ~40% for the last decade compared to the mean for the entire simulation period. A trend toward a higher GIC sea level contribution has been recently confirmed by the Intergovernmental Panel on Climate Change (IPCC) (Vaughan et al. 2013). The greatest

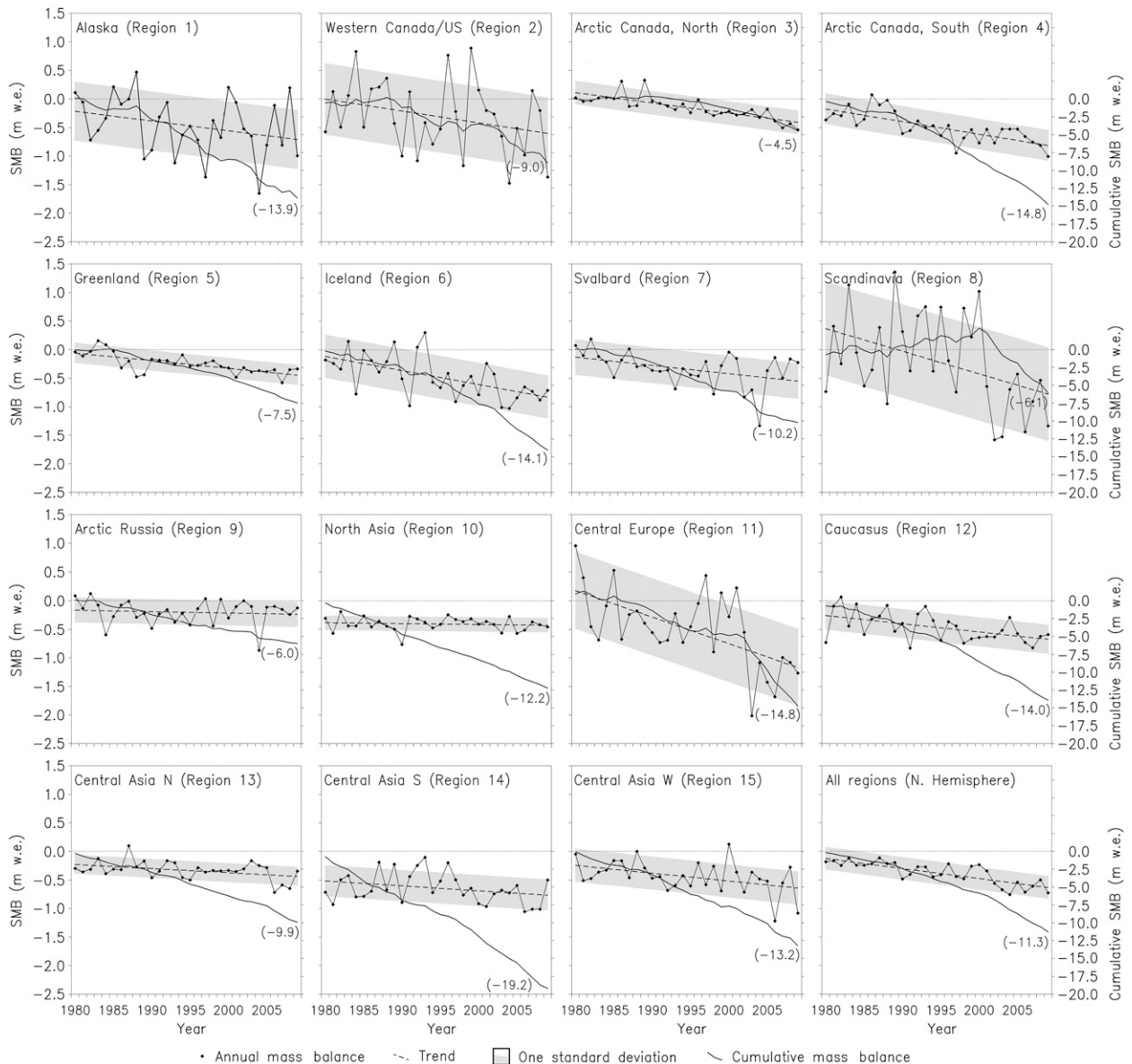


FIG. 9. Regional breakdown of GIC SMB and cumulative SMB time series for 1979–2009, including linear regression (in Table 2 significant SMB conditions are highlighted in bold).

regional mean annual contribution to sea level rise was from Alaska of  $0.12 \pm 0.05$  mm SLE (1979–2009) and  $0.13 \pm 0.05$  mm SLE (1999–2009) (Table 4), accounting for  $\sim 20\%$  of the overall Northern Hemisphere GIC contribution to sea level rise.

In other studies, Marzeion et al. (2012) estimated for 1902–2009 the global GIC mass loss sum to be  $114 \pm 5$  mm SLE, equal to an annual average of 1.06 mm SLE; Kaser et al. (2006) found  $0.77 \pm 0.26$  mm SLE (1991–2004), Gardner et al. (2013) calculated  $0.71 \pm 0.08$  mm SLE (2003–09), and Hock et al. (2009) estimated  $0.50 \pm 0.18$  mm SLE (1961–2004). The calculated GIC mass

balance contribution to sea level rise clearly varies depending on the method used. SnowModel simulations only calculate SMB loss from Northern Hemisphere GIC (from  $\sim 75\%$  of the global GIC area; Radić et al. 2014). Therefore, global GIC SMB contribution to sea level rise would likely be higher than the mean annual SnowModel-estimated  $0.71 \pm 0.15$  mm SLE (1999–2009) when adding SMB contributions for the Southern Hemisphere GIC, loss rates from calving GIC and ice sheets, and loss rates from subglacial geothermal melting and subglacial frictional melting due to basal ice motion. No attempt here has been made to calculate and include these other contributions.

### *e. Model limitations and perspectives*

The GIC simulations presented a detailed and more physically realistic representation of energy balance, snow and ice ablation, snowpack evolution, and runoff processes at relatively high temporal and spatial resolution compared with many previous studies. SnowModel capabilities present a contrast with studies that largely relied on air temperature as a proxy for the energy available for melt. In addition, to properly understand GIC surface processes in Arctic and mountainous regions, subdiurnal model time steps are required owing to the subdaily variability in solar radiation and its associated energy-related SMB processes. Over virtually all snow and ice GIC surfaces, the incoming solar radiation is the primary source of energy melting snow and ice by an order of magnitude more than that provided by sensible heat flux associated with air temperature (Liston and Hiemstra 2011). These improved temporal and spatial issues could be part of the reason for the differences among previously published model results.

The use of constant GIC area, thus neglecting any SMB feedback from GIC retreat, thinning, and subsequent changing hypsometry, etc., is also a weakness in the GIC SMB simulations. We know from satellite observations (e.g., Landsat), of the Sermilik Fjord region of southeast Greenland (Mernild et al. 2012) that GIC peripheral to the Greenland Ice Sheet had a mean area recession rate of  $27\% \pm 24\%$  from 1986 to 2011 (during this same period five glaciers completely melted away). Analyses from the pan-Arctic region of historical data and aerial and satellite images from the late twentieth century to the present have suggested that mean GIC area retreats occurred in the range of 3% to 63% (e.g., Glazovsky and Macheret 2006; M. D. Ananicheva and G. Kapustin 2010, unpublished manuscript; Bolch et al. 2010; Andreassen et al. 2012). The use of constant GIC area (a GIC snapshot from the 2000s) might underestimate the volumetric SMB budget, mostly in the beginning of the simulation period. On the other hand, is it not clear if a change in GIC area over the last 30 years can be resolved on a 1-km grid.

Also in these SnowModel simulations, owing to the relatively large grid increment (1 km), blowing snow processes were not included. On GIC, sublimation can occur both from the static surface and from blowing-snow particles. The static-surface sublimation of snow (in nature and SnowModel) depends on surface air temperature, the moisture deficit of the air, wind speed, and other components of the surface energy balance (Liston and Hiemstra 2011). In this study the sublimation part from blowing snow is not included. In previous Arctic and alpine studies it has been found that the total amount of estimated sublimation (from static

and blowing-snow particles) varied between 10% and 50% of the total winter precipitation (Liston and Sturm 1998, 2002, 2004; Hiemstra et al. 2002).

SnowModel assumed one-way atmospheric forcing, where the atmospheric conditions were prescribed at each time step without regard for whether the snow and ice distribution and properties might be different than that in the original MERRA reanalysis. In the natural system the atmospheric variables would be modified in response to differences and changes in surface conditions (Liston and Hiemstra 2011); such interactions were not accounted for in the simulations described herein.

This model study and its associated analyses have not addressed how GIC SMB may change in the future. Numerous studies have examined future trends (e.g., Marzeion et al. 2012; Radić et al. 2014). These studies generally project GIC to lose additional mass and to reduce the current volume, suggesting additional GIC mass contributions to sea level rise in the coming decades.

Our analysis of this Northern Hemisphere high spatial resolution GIC dataset has also suggested the possibility (cf. Fig. 6) of using it to establish a new GIC classification system. This classification system, based on seasonal and annual GIC climate, mass balance, and runoff conditions, could provide insights into local-area GIC conditions and a way to distinguish GIC conditions among the earth's 200 000 or more estimated GIC to highlight commonalities among GIC located in different geographical regions. By the way of example, consider the Alaska region (region 1, Fig. 1c); within this region are glaciers exhibiting maritime SMB characteristics and other glaciers exhibiting Arctic SMB features. As another example, the western Canada and the United States region (region 2, Fig. 1c) includes both warm, wet maritime glaciers and cold, dry continental glaciers. From an SMB perspective both of these regions include glaciers at both ends of the spectrum in terms of accumulation and ablation. The datasets presented herein contain the information required to develop an improved classification scheme based on glacier SMB structures and characteristics. Previously, GIC have been classified by their morphological shape and geophysical conditions (e.g., Rau et al. 2005; Cuffey and Paterson 2010), but a GIC classification system based on climate, mass balance, and runoff is now possible and could be of scientific and computational interest to glaciologists, hydrologists, and ecologists, since GIC are clear regulators of water availability and substantial contributors to eustatic sea level rise. In addition to this proposed GIC classification approach, an examination of the Southern Hemisphere GIC conditions needs to be addressed, when RGI GIC uncertainties have been resolved for South America.



## 6. Conclusions

The merging of atmospheric forcing dataset (i.e., MERRA) and the first complete global glaciers and ice caps (GIC) digital inventory (i.e., Randolph Glacier Inventory, v. 2.0) with a high-resolution (1-km horizontal grid increment and 3-h time step) snow and ice evolution modeling tool (SnowModel) allowed us to map and analyze the spatial GIC surface hydrological conditions and variations between glacierized regions in the Northern Hemisphere (north of 25°N; not including the Greenland Ice Sheet). We have investigated the GIC surface mass balance (SMB) and SMB contribution to sea level rise, including variations in GIC surface air temperature, precipitation, sublimation, evaporation, and surface runoff for the 30-yr period 1979–2009. SnowModel-simulated GIC SMB outputs were calibrated against direct glaciological SMB observations, showing agreement between simulations and observations. Using available SMB observations from the earth's 200 000 or more estimated GIC (Radić and Hock 2010; Arendt et al. 2012), high-resolution SMB simulations were used to improve our understanding of Northern Hemisphere GIC SMB conditions for all GIC having areas over 0.5 km<sup>2</sup>. Model simulations and calculations were performed on a 1-km grid and included 543 389 GIC grid cells.

Overall, GIC MAAT increased an average between the first and last decade of  $0.8^{\circ} \pm 0.1^{\circ}\text{C}$  (equal to a significant annual linear average trend of  $0.04^{\circ}\text{C yr}^{-1}$ ) for the simulation period, showing a characteristic diagonal latitude–elevation pattern and an average temperature increase most pronounced at high latitudes. In addition, for total annual GIC precipitation, the latitude–elevation pattern was heterogeneous with clusters of GIC receiving less/more precipitation than GIC at same latitudes, due to local topographic, orographic, and climatic influences. Average GIC runoff and SMB loss increased for all regions, including both latitude–elevation and regional variability, where the annual SMB contribution to sea level rise for the last decade (1999–2009) averaged  $0.71 \pm 0.15$  mm SLE, and was ~40% greater than the 30-yr mean of  $0.51 \pm 0.16$  mm SLE.

These simulations provide an improvement over previous model studies in assessing the Northern Hemisphere GIC SMB conditions because of its relatively high temporal and spatial resolution and its physically based representations of the governing processes. The simulations and analyses highlight conditions and changes ranging from individual GIC to regional and continental scales. Our current understanding of the local variability in GIC behavior is limited in areas where we have no observations, and

therefore this study and its associated GIC database allows us to examine, classify, and distinguish GIC SMB conditions among Earth's 200 000 or more GIC.

*Acknowledgments.* This work was supported in part by the Earth System Modeling program and by the Scientific Discovery for Advanced Computing (SciDAC) program within the U.S. Department of Energy's Office of Science, and by a Los Alamos National Laboratory (LANL) (LANL is operated under the auspices of the National Nuclear Security Administration of the U.S. Department of Energy under Contract DE-AC52-06NA25396). Additional support was provided from the European Community's Seventh Framework Programme under Grant Agreement 262693. We thank the NASA Goddard Earth Sciences (GES) Data and Information Services Center (DISC) and Global Modeling and Assimilation Office (GMAO) for providing the MERRA datasets, and NOAA for providing the Global Land One-km Base Elevation Project (GLOBE) digital elevation model. Request of data should be addressed to the first author.

## REFERENCES

- Allerup, P., H. Madsen, and F. Vejen, 1998: Estimating true precipitation in Arctic areas. *Nordic Hydrological Programme Rep.* 44, 1–9.
- , —, and —, 2000a: Correction of precipitation based on off-site weather information. *Atmos. Res.*, **53**, 231–250, doi:10.1016/S0169-8095(99)00051-4.
- , —, and —, 2000b: Correction of observed precipitation in Greenland. *Proc. Nordic Hydrological Conf.*, Uppsala, Sweden, NHF/NAH Nordic Association for Hydrology, 1–8.
- Andreassen, L. M., S. H. Winsvold, F. Paul, and J. E. Hausberg, 2012: *Inventory of Norwegian Glaciers*. L. M. Andreassen and S. H. Winsvold, Eds., Norwegian Water Resources and Energy Directorate, 242 pp.
- Arendt, A., and Coauthors, 2012: Randolph Glacier Inventory (v2.0): A dataset of global glacier outlines. Global Land Ice Measurements from Space, Boulder Colorado, digital media (with area corrections downloaded 2012). [Available online at <http://www.glims.org/RGI/>.]
- Benn, D. I., and D. J. A. Evans, 2002: *Glaciers and Glaciation*. Arnold, 734 pp.
- Bhutiyan, M. R., 1999: Mass-balance studies on Siachen Glacier in the Nubra Valley, Karakoram Himalaya, India. *J. Glaciol.*, **45** (149), 112–118.
- Bolch, T., B. Menounos, and R. Wheate, 2010: Landsat-based inventory of glaciers in western Canada, 1985–2005. *Remote Sens. Environ.*, **114**, 127–137, doi:10.1016/j.rse.2009.08.015.
- Bosilovich, M. G., 2008: NASA's Modern Era Retrospective Analysis for Research and Applications: Integrating Earth observations. *Earthzine*. [Available online at <http://www.earthzine.org/2008/09/26/nasas-modern-era-retrospective-analysis/>.]
- , J. Chen, F. R. Robertson, and R. F. Adler, 2008: Evaluation of global precipitation re-analyses. *J. Appl. Meteor. Climatol.*, **47**, 2279–2299, doi:10.1175/2008JAMC1921.1.



- , R. R. Franklin, and J. Chen, 2011: Global energy and water budgets in MERRA. *J. Climate*, **24**, 5721–5739, doi:10.1175/2011JCLI4175.1.
- Box, J. E., 2002: Survey of Greenland instrumental temperature records: 1873–2001. *Int. J. Climatol.*, **22**, 1829–1847, doi:10.1002/joc.852.
- Bruland, O., G. E. Liston, J. Vonk, and A. Killingtveit, 2004: Modelling the snow distribution at two high Arctic sites at Svalbard, Norway, and at a sub-Arctic site in central Norway. *Nord. Hydrol.*, **35**, 191–208.
- Cogley, J. G., 2009: Geodetic and direct mass-balance measurements: Comparison and joint analysis. *Ann. Glaciol.*, **50**, 96–100, doi:10.3189/172756409787769744.
- , 2012: The future of the world's glaciers. *The Future of the World's Climate*, 2nd ed., A. Henderson-Sellers and K. McGuffie, Eds., Elsevier, 205–218, doi:10.1016/B978-0-12-386917-3.00008-7.
- Cuffey, K. M., and W. S. B. Paterson, 2010: *The Physics of Glaciers*. 4th ed. Elsevier, 708 pp.
- Cullather, R. I., and M. G. Bosilovich, 2011: The moisture budget of the polar atmosphere in MERRA. *J. Climate*, **24**, 2861–2879, doi:10.1175/2010JCLI4090.1.
- Dyurgerov, M. B., 2010. Data of glaciological studies—Reanalysis of glacier changes: From the IGY to the IPY, 1960–2008. Publication 108, Institute of Arctic and Alpine Research, 116 pp.
- , and M. F. Meier, 2005: Glaciers and the changing Earth system: A 2004 snapshot. Occasional Paper 58, Institute of Arctic and Alpine Research, Boulder, Colorado, 117 pp.
- Finnis, J., J. Cassano, M. Holland, M. C. Serreze, and P. Uotila, 2009a: Synoptically forced hydroclimatology of major Arctic watersheds in general circulation models. Part 1: The Mackenzie River Basin. *Int. J. Climatol.*, **29**, 1226–1243, doi:10.1002/joc.1753.
- , —, —, —, and —, 2009b: Synoptically forced hydroclimatology of major Arctic watersheds in general circulation models. Part 2: Eurasian watersheds. *Int. J. Climatol.*, **29**, 1244–1261, doi:10.1002/joc.1769.
- Gardelle, J., E. Berthier, and Y. Arnaud, 2012: Slight mass gain of Karakoram glaciers in the early twenty-first century. *Nat. Geosci.*, **5**, 322–325, doi:10.1038/ngeo1450.
- Gardner, A. S., and Coauthors, 2013: A reconciled estimate of glacier contributions to sea level rise: 2003 to 2009. *Science*, **340**, 852–857, doi:10.1126/science.1234532.
- Glazovsky, A., and Y. Macheret, 2006: Glaciation in north and central Eurasia in present time (in Russian with English summary). *Eurasian Arctic*, V. M. Kotlyakov, Eds., Nauka, 97–114 and 438–445.
- Hanna, E., and Coauthors, 2008: Increased runoff from melt from the Greenland Ice Sheet: A response to global warming. *J. Climate*, **21**, 331–341, doi:10.1175/2007JCLI1964.1.
- , S. H. Mernild, J. Cappelen, and K. Steffen, 2012: Recent warming in Greenland in a long-term instrumental (1881–2012) climatic context: I. Evaluation of surface air temperature records. *Environ. Res. Lett.*, **7**, 045404, doi:10.1088/1748-9326/7/4/045404.
- , J. M. Jones, J. Cappelen, S. H. Mernild, L. Wood, K. Steffen, and P. Huybrechts, 2013: Discerning the influence of North Atlantic atmospheric and oceanic forcing effects on 1900–2010 Greenland summer climate and melt. *Int. J. Climatol.*, **33**, 862–880, doi:10.1002/joc.3475.
- Hansen, J., R. Ruedy, M. Sato, and K. Lo, 2010: Global surface temperature change. *Rev. Geophys.*, **48**, RG4004, doi:10.1029/2010RG000345.
- Hasholt, B., G. E. Liston, and N. T. Knudsen, 2003: Snow distribution modelling in the Ammassalik region, South East Greenland. *Nord. Hydrol.*, **34**, 1–16.
- Hastings, D. A., and Coauthors, 1999: The Global Land One-km Base Elevation (GLOBE) digital elevation model, version 1.0. NOAA, National Geophysical Data Center, digital media. [Available online at <http://www.ngdc.noaa.gov/mgg/topo/globe.html>.]
- Hiemstra, C. A., G. E. Liston, and W. A. Reiners, 2002: Snow redistribution by wind and interactions with vegetation at upper treeline in the Medicine Bow Mountains, Wyoming, USA. *Arct. Antarct. Alp. Res.*, **34**, 262–273, doi:10.2307/1552483.
- , —, and —, 2006: Observing, modelling, and validating snow redistribution by wind in a Wyoming upper treeline landscape. *Ecol. Modell.*, **197**, 35–51, doi:10.1016/j.ecolmodel.2006.03.005.
- Hinzman, L. D., and Coauthors, 2005: Evidence and implications of recent climate change in northern Alaska and other arctic regions. *Climatic Change*, **72**, 251–298, doi:10.1007/s10584-005-5352-2.
- Hirabayashi, Y., P. Döll, and S. Kanae, 2010: Global-scale modeling of glacier mass balances for water resources assessments: Glacier mass changes between 1948 and 2006. *J. Hydrol.*, **390**, 245–256, doi:10.1016/j.jhydrol.2010.07.001.
- Hock, R., M. de Woul, V. Radić, and M. Dyurgerov, 2009: Mountain glaciers and ice caps around Antarctica make a large sea-level rise contribution. *Geophys. Res. Lett.*, **36**, L07501, doi:10.1029/2008GL037020.
- Huss, M., 2011: Present and future contribution of glacier storage change to runoff from macroscale drainage basins in Europe. *Water Resour. Res.*, **47**, W07511, doi:10.1029/2010WR010299.
- Immerzeel, W., L. van Beek, M. Konz, A. Shrestha, and M. F. P. Bierkens, 2012: Hydrological response to climate change in a glacierized catchment in the Himalayas. *Climatic Change*, **110**, 721–736, doi:10.1007/s10584-011-0143-4.
- Kaser, G., J. G. Cogley, M. B. Dyurgerov, M. F. Meier, and A. Ohmura, 2006: Mass balance of glaciers and ice caps: Consensus estimates for 1961–2004. *Geophys. Res. Lett.*, **33**, L19501, doi:10.1029/2006GL027511.
- Kotlarski, S., F. Paul, and D. Jacob, 2010: Forcing a distributed glacier mass balance model with the regional climate model REMO. Part I: Climate model evaluation. *J. Climate*, **23**, 1589–1606, doi:10.1175/2009JCLI2711.1.
- Leclercq, P. W., J. Oerlemans, and J. G. Cogley, 2011: Estimating the glacier contribution to sea-level rise for the period 1800–2005. *Surv. Geophys.*, **32**, 519–535, doi:10.1007/s10712-011-9121-7.
- Liston, G. E., 1995: Local advection of momentum, heat, and moisture during the melt of patchy snow covers. *J. Appl. Meteor.*, **34**, 1705–1715, doi:10.1175/1520-0450-34.7.1705.
- , and M. Sturm, 1998: A snow-transport model for complex terrain. *J. Glaciol.*, **44**, 498–516.
- , and —, 2002: Winter precipitation patterns in Arctic Alaska determined from a blowing-snow model and snow-depth observations. *J. Hydrometeorol.*, **3**, 646–659, doi:10.1175/1525-7541(2002)003<0646:WPPIAA>2.0.CO;2.
- , and —, 2004: The role of winter sublimation in the Arctic moisture budget. *Nord. Hydrol.*, **35**, 325–334.
- , and K. Elder, 2006a: A distributed snow-evolution modeling system (SnowModel). *J. Hydrometeorol.*, **7**, 1259–1276, doi:10.1175/JHM548.1.
- , and —, 2006b: A meteorological distribution system for high-resolution terrestrial modeling (MicroMet). *J. Hydrometeorol.*, **7**, 217–234, doi:10.1175/JHM486.1.

- , and C. A. Hiemstra, 2008: A simple data assimilation system for complex snow distributions (SnowAssim). *J. Hydrometeorol.*, **9**, 989–1004, doi:10.1175/2008JHM871.1.
- , and —, 2011: The changing cryosphere: Pan-Arctic snow trends (1979–2009). *J. Climate*, **24**, 5691–5712, doi:10.1175/JCLI-D-11-00081.1.
- , and S. H. Mernild, 2012: Greenland freshwater runoff. Part I: A runoff routing model for glaciated and nonglaciated landscapes (HydroFlow). *J. Climate*, **25**, 5997–6014, doi:10.1175/JCLI-D-11-00591.1.
- , J.-G. Winther, O. Bruland, H. Elvehøy, and K. Sand, 1999: Below surface ice melt on the coastal Antarctic ice sheet. *J. Glaciol.*, **45**, 273–285, doi:10.3189/002214399793377130.
- , R. B. Haehnel, M. Sturm, C. A. Hiemstra, S. Berezovskaya, and R. D. Tabler, 2007: Simulating complex snow distributions in windy environments using SnowTran-3D. *J. Glaciol.*, **53**, 241–256.
- Marzeion, B., A. H. Jarosch, and M. Hofer, 2012: Past and future sea-level change from the surface mass balance of glaciers. *Cryosphere*, **6**, 1295–1322, doi:10.5194/tc-6-1295-2012.
- Meier, M. F., M. B. Dyurgerov, U. K. Rick, S. O’Neel, W. T. Pfeffer, R. S. Anderson, S. P. Anderson, and A. F. Glazovsky, 2007: Glaciers dominate eustatic sea-level rise in the 21st century. *Science*, **317**, 1064–1067, doi:10.1126/science.1143906.
- Mernild, S. H., and B. Hasholt, 2006: Climatic control on river discharge simulations, Mittivakkat Glacier catchment, Ammassalik Island, southeast Greenland. *Nord. Hydrol.*, **37**, 327–346, doi:10.2166/nh.2006.018.
- , and G. E. Liston, 2010: The influence of air temperature inversion on snow melt and glacier surface mass-balance simulations, Ammassalik Island, southeast Greenland. *J. Appl. Meteor. Climatol.*, **49**, 47–67, doi:10.1175/2009JAMC2065.1.
- , and —, 2012: Greenland freshwater runoff. Part II: Distribution and trends, 1960–2010. *J. Climate*, **25**, 6015–6035, doi:10.1175/JCLI-D-11-00592.1.
- , —, B. Hasholt, and N. T. Knudsen, 2006: Snow distribution and melt modeling for Mittivakkat Glacier, Ammassalik Island, Southeast Greenland. *J. Hydrometeorol.*, **7**, 808–824, doi:10.1175/JHM522.1.
- , B. U. Hansen, B. H. Jakobsen, and B. Hasholt, 2008a: Climatic conditions at the Mittivakkat Glacier catchment (1994–2006), Ammassalik Island, SE Greenland, and in a 109 years term perspective (1898–2006). *Geogr. Tidsskrift, Dan. J. Geogr.*, **108**, 51–72, doi:10.1080/00167223.2008.10649574.
- , D. L. Kane, B. U. Hansen, B. H. Jakobsen, B. Hasholt, and N. T. Knudsen, 2008b: Climate, glacier mass balance, and runoff (1993–2005) for the Mittivakkat Glacier catchment, Ammassalik Island, SE Greenland, and in a long term perspective (1898–1993). *Hydrol. Res.*, **39**, 239–256, doi:10.2166/nh.2008.101.
- , G. E. Liston, C. A. Hiemstra, K. Steffen, E. Hanna, and J. H. Christensen, 2009: Greenland Ice Sheet surface mass-balance modeling and freshwater flux for 2007, and in a 1995–2007 perspective. *Hydrol. Processes*, **23**, 2470–2484, doi:10.1002/hyp.7354.
- , —, —, and J. H. Christensen, 2010a: Greenland Ice Sheet surface mass-balance modeling in a 131-yr perspective 1950–2080. *J. Hydrometeorol.*, **11**, 3–25, doi:10.1175/2009JHM1140.1.
- , —, K. Steffen, and P. Chylek, 2010b: Meltwater flux and runoff modeling in the ablation area of the Jakobshavn Isbræ, West Greenland. *J. Glaciol.*, **56**, 20–32, doi:10.3189/002214310791190794.
- , —, C. A. Hiemstra, J. H. Christensen, M. Stendel, and B. Hasholt, 2011a: Surface mass-balance and runoff modeling using HIRHAM4 RCM at Kangerlussuaq (Søndre Strømfjord), West Greenland, 1950–2080. *J. Climate*, **24**, 609–623, doi:10.1175/2010JCLI3560.1.
- , T. Mote, and G. E. Liston, 2011b: Greenland Ice Sheet surface melt extent and trends, 1960–2010. *J. Glaciol.*, **57**, 621–628, doi:10.3189/002214311797409712.
- , N. T. Knudsen, W. H. Lipscomb, J. C. Yde, J. K. Malmros, B. H. Jakobsen, and B. Hasholt, 2011c: Increasing mass loss from Greenland’s Mittivakkat Gletscher. *Cryosphere*, **5**, 341–348, doi:10.5194/tc-5-341-2011.
- , J. K. Malmros, J. C. Yde, and N. T. Knudsen, 2012: Multi-decadal marine- and land-terminating glacier retreat in the Ammassalik region, southeast Greenland. *Cryosphere*, **6**, 625–639, doi:10.5194/tc-6-625-2012.
- , W. H. Lipscomb, D. B. Bahr, V. Radić, and M. Zemp, 2013a: Global glacier retreat: A revised assessment of committed mass losses and sampling uncertainties. *Cryosphere*, **7**, 1565–1577, doi:10.5194/tc-7-1565-2013. [Supplementary material is available at <http://www.the-cryosphere.net/7/1565/2013/tc-7-1565-2013-supplement.zip>.]
- , N. T. Knudsen, M. J. Hoffman, J. C. Yde, W. L. Lipscomb, E. Hanna, J. K. Malmros, and R. S. Fausto, 2013b: Volume and velocity changes at Mittivakkat Gletscher, southeast Greenland, 1994–2012. *J. Glaciol.*, **59**, 660–670, doi:10.3189/2013JoG13J017.
- , E. Hanna, J. C. Yde, J. Cappelen, and J. K. Malmros, 2014: Coastal Greenland air temperature extremes and trends 1890–2010: Annual and monthly analysis. *Int. J. Climatol.*, **34**, 1472–1487, doi:10.1002/joc.3777.
- Overland, J. E., M. C. Spillane, D. B. Percival, M. Y. Wang, and H. O. Mofjeld, 2004: Seasonal and regional variation of pan-Arctic surface air temperature over the instrumental record. *J. Climate*, **17**, 3263–3282, doi:10.1175/1520-0442(2004)017<3263:SARVOP>2.0.CO;2.
- Radić, V., and R. Hock, 2010: Regional and global volumes of glaciers derived from statistical upscaling of glacier inventory data. *J. Geophys. Res.*, **115**, F01010, doi:10.1029/2009JF001373.
- , A. Bliss, A. C. Beedlow, R. Hock, E. Miles, and J. G. Cogley, 2014: Regional and global projection of twenty-first century glacier mass changes in response to climate scenarios from global climate models. *Climate Dyn.*, **42**, 37–58, doi:10.1007/s00382-013-1719-7.
- Rasmussen, R., and Coauthors, 2012: How well are we measuring snow?: The NOAA/FAA/NCAR winter precipitation test bed. *Bull. Amer. Meteor. Soc.*, **93**, 811–829, doi:10.1175/BAMS-D-11-00052.1.
- Rau, F., F. Mauz, S. Vogt, S. J. S. Khalsa, and B. Raup, 2005: Illustrated GLIMS Glacier Classification Manual—Glacier Classification Guidance for the GLIMS Glacier Inventory, version 1 (2005-02-10), 36 pp. [Available online at [http://www.glims.org/MapsAndDocs/assets/GLIMS\\_Glacier-Classification-Manual\\_V1\\_2005-02-10.pdf](http://www.glims.org/MapsAndDocs/assets/GLIMS_Glacier-Classification-Manual_V1_2005-02-10.pdf).]
- Rawlins, M. A., C. J. Willmott, A. Shiklomanov, E. Linder, S. Froking, R. B. Lammers, and C. J. Vorosmarty, 2006: Evaluation of trends in derived snowfall and rainfall across Eurasia and linkages with discharge to the Arctic Ocean. *Geophys. Res. Lett.*, **33**, L07403, doi:10.1029/2005GL025231.
- Rienecker, M. M., and Coauthors, 2011: MERRA: NASA’s Modern-Era Retrospective Analysis for Research and Applications. *J. Climate*, **24**, 3624–3648, doi:10.1175/JCLI-D-11-00015.1.

- Robertson, F. R., M. G. Bosilovich, J. Chen, and T. L. Miller, 2011: The effect of satellite observing system changes on MERRA water and energy fluxes. *J. Climate*, **24**, 5197–5217, doi:[10.1175/2011JCLI4227.1](https://doi.org/10.1175/2011JCLI4227.1).
- Suzuki, K., and Coauthors, 2011: Impact of land-use changes on snow in a forested region with heavy snowfall in Hokkaido, Japan. *Hydrological Sci. J.*, **56** (3), 443–467, doi:[10.1080/02626667.2011.565008](https://doi.org/10.1080/02626667.2011.565008).
- Vaughan, D. G., and Coauthors, 2013: Observations: Cryosphere. *Climate Change 2103: The Physical Science Basis*, T. F. Stocker, et al., Cambridge University Press, 317–382.
- Walsh, J. E., W. L. Chapman, V. Romanovsky, J. H. Christensen, and M. Stendel, 2008: Global climate model performance over Alaska and Greenland. *J. Climate*, **21**, 6156–6174, doi:[10.1175/2008JCLI2163.1](https://doi.org/10.1175/2008JCLI2163.1).
- Woo, M. K., R. Heron, and P. Marsh, 1982: Basal ice in High Arctic snowpacks. *Arct. Alp. Res.*, **14**, 251–260, doi:[10.2307/1551157](https://doi.org/10.2307/1551157).
- WGMS, 1989: World glacier inventory: Status 1988. W. Haeberli et al., Eds., World Glacier Monitoring Service, 458 pp.
- , 2012: Fluctuations of glaciers 2005–2010 (Vol. X). M. Zemp et al., Eds., World Glacier Monitoring Service, 336 pp. [Publication based on database version, doi:[10.5904/wgms-fog-2012-11](https://doi.org/10.5904/wgms-fog-2012-11).]
- Yang, D., B. E. Goodison, J. R. Metcalfe, V. S. Golubev, R. Bates, T. Pangburn, and C. L. Hanson, 1998: Accuracy of NWS 8" standard nonrecording precipitation gauge: Results and application of WMO intercomparison. *J. Atmos. Oceanic Technol.*, **15**, 54–68, doi:[10.1175/1520-0426\(1998\)015<0054:AO NSNP>2.0.CO;2](https://doi.org/10.1175/1520-0426(1998)015<0054:AO NSNP>2.0.CO;2).

[15]

Mernild, S. H., Liston, G. E., Hiemstra C. A., and Steffen, K.  
2008. Surface Melt Area and Water Balance Modeling on the  
Greenland Ice Sheet 1995–2005.  
Journal of Hydrometeorology, 9(6), 1191–1211.

Reprinted with permission from American Meteorological  
Society

# Surface Melt Area and Water Balance Modeling on the Greenland Ice Sheet 1995–2005

SEBASTIAN H. MERNILD

*International Arctic Research Center and Water and Environmental Research Center, University of Alaska Fairbanks, Fairbanks, Alaska*

GLEN E. LISTON AND CHRISTOPHER A. HIEMSTRA

*Cooperative Institute for Research in the Atmosphere, Colorado State University, Fort Collins, Colorado*

KONRAD STEFFEN

*Cooperative Institute for Research in the Environmental Sciences, University of Colorado, Boulder, Colorado*

(Manuscript received 15 August 2007, in final form 5 May 2008)

## ABSTRACT

SnowModel, a physically based snow-evolution modeling system that includes four submodels—MicroMet, EnBal, SnowPack, and SnowTran-3D—was used to simulate variations in Greenland [including the Greenland Ice Sheet (GrIS)] surface snow and ice melt, as well as water balance components, for 1995–2005. Meteorological observations from 25 stations inside and outside the GrIS were used as model input. Winter and summer mass balance observations, spatial snow depth observations, and snowmelt depletion curves derived from time-lapse photography from the Mittivakkat and Zackenberg glacierized catchments in East Greenland were used to validate the performance of SnowModel. Model results compared well with observed values, confirming the robustness of the model. The yearly modeled GrIS interior nonmelt area differs from satellite observations by a maximum of  $\sim 68\,000\text{ km}^2$  (or  $\sim 6\%$ ) in 2004, and the lowest uncertainties ( $< 8000\text{ km}^2$ , or  $< 1\%$ ) occur for the years with the smallest (2005) and most extensive (1996) nonmelt areas. Modeled surface melt occurred at elevations reaching 2950 m MSL for 2005, while the equilibrium line altitude (ELA) fluctuates from 1640 to 600 m MSL. The modeled interannual variability in the nonmelt area also agrees with observation records ( $R^2 = 0.96$ ), yielding simulated GrIS nonmelt covers of 71% for 1996 and 50% for 2005. On average, the simulated nonmelt area decreased  $\sim 6\%$  from 1995 to 2005; this trend is similar to observed values. An average surface mass balance (SMB) storage of  $138(\pm 81)\text{ km}^3\text{ yr}^{-1}$ , a GrIS loss of  $257(\pm 81)\text{ km}^3\text{ yr}^{-1}$ , and a runoff contribution to the ocean of  $392(\pm 58)\text{ km}^3\text{ yr}^{-1}$  occurred for the period 1995–2005. Approximately 58% and 42% of the runoff came from the GrIS western and eastern drainage areas, respectively. The modeled average specific runoff from the GrIS was  $6.71\text{ s}^{-1}\text{ km}^{-2}\text{ yr}^{-1}$ , which, over the simulation period, represents a contribution of  $\sim 1.1\text{ mm yr}^{-1}$  to global sea level rise.

## 1. Introduction

Greenland is the world's largest island, and the Greenland Ice Sheet (GrIS) is the Northern Hemisphere's largest terrestrial permanent ice- and snow-covered area. Ice mass and snow cover serve as water reservoirs that are highly vulnerable to ongoing climatic variations and change (e.g., Hanna et al. 2005; Hinzman et al. 2005). The climate is changing: The average surface air temperature north of  $60^\circ\text{N}$  has increased by

$\sim 0.09^\circ\text{C decade}^{-1}$ , and this change is conspicuous in winter months (e.g., Box 2002; Sturm et al. 2005). The climate has warmed substantially since the end of the Little Ice Age, and significantly in the last 30 yr (Serreze et al. 2000). This warming was accompanied by an increase in precipitation of  $\sim 1\%$   $\text{decade}^{-1}$  (ACIA 2005). The Arctic is undergoing a system-wide response to climatic change, and the effect of a warmer and wetter climate on terrestrial cryospheric and hydrological processes and their components have already been documented on hemispheric, regional, local, and micro-scales (e.g., Serreze et al. 2000; Vorosmarty et al. 2001; Moritz et al. 2002; Hinzman et al. 2005; Mernild et al. 2007b,d).

Since Benson (1962) and Bauer (1968) first estimated GrIS mass balance components, a number of studies

---

*Corresponding author address:* Dr. Sebastian H. Mernild, International Arctic Research Center and Water and Environmental Research Center, University of Alaska Fairbanks, P.O. Box 750292, Fairbanks, AK 99775-0292.  
E-mail: fxs@uaf.edu



using a variety of methods (e.g., airborne and satellite laser altimetry, positive-degree and energy-balance models) have followed. Recent studies have documented GrIS mass-balance loss up to  $238(\pm 36)$   $\text{km}^3 \text{yr}^{-1}$  with an increasing trend of loss over the last several years (e.g., van de Wal 1996; Ohmura et al. 1999; Reeh et al. 1999; Janssens and Huybrechts 2000; Church et al. 2001; Mote 2003; Hanna et al. 2005; Chen et al. 2006; Luthcke et al. 2006; Ramillien et al. 2006; Velicogna and Wahr 2006). Modeling studies have shown that every 1-K rise in surface air temperature produces 20%–50% more Greenland ice melt (Oerlemans 1991; Braithwaite and Olesen 1993; Janssens and Huybrechts 2000; Hanna et al. 2005). Available satellite data show an attendant 47%  $\text{K}^{-1}$  increase in GrIS snowmelt extent (Abdalati and Steffen 1997b; Hanna et al. 2005), so a predicted rise in air temperature of 2–5 K would approximately double melt rates and increase water storage losses. These changes in storage affect runoff to the Arctic Ocean, the only ocean with a contributing land area greater than its surface area (Barry and Serreze 2000). Previous GrIS runoff estimates detected GrIS mass losses via runoff. For example, Janssens and Huybrechts (2000) showed losses of  $281 \text{ km}^3 \text{yr}^{-1}$  (1953–2003), Mote (2003) showed  $278 \text{ km}^3 \text{yr}^{-1}$  (1988–99), Hanna et al. (2005) showed  $324 \text{ km}^3 \text{yr}^{-1}$  (1993–98) and  $372(\pm 37) \text{ km}^3 \text{yr}^{-1}$  (1998–2003), and Box et al. (2006) found  $373 \text{ km}^3 \text{yr}^{-1}$  (1998–2004). Together, these sources indicate a trend of increasing GrIS runoff through the last decades. Changes in freshwater runoff to the ocean (or more specifically to the Greenland–Iceland–Norwegian Seas) play an important role in determining the global ocean thermohaline circulation, salinity, ice sea dynamics (Broecker et al. 1985; Broecker and Denton 1990; Su et al. 2006), global sea level rise (Dowdeswell et al. 1997; ACIA 2005; Box et al. 2006), and plans for hydroelectric power schemes (Hock and Jansson 2005; Mernild and Hasholt 2006), as well as the influx of sediment and nutrients to the ocean (Rysgaard et al. 2003; Hasholt et al. 2006).

Rough terrain, harsh climatic conditions, and remote location are commonly cited reasons for lack of knowledge and data for Greenland. Logistical constraints make it difficult to collect extensive observations of snow distribution, sublimation (surface and blowing-snow), evaporation, and snow and glacier-melt observations; collecting runoff measurements has typically been considered impossible. Only a few quality observations related to the spatial and temporal distributions of snow have been reported. Furthermore, the use of gauging stations that underestimate solid precipitation amounts, scattered Arctic meteorological stations, and limited winter and summer GrIS mass-balance obser-

vations produce sparse and unreliable data related to the spatial and temporal distributions of snow precipitation, sublimation, and surface melt across much of the GrIS. Such key climate-system components are essential to hydrological research efforts, and there is a clear need to explore issues associated with data sparseness and modeling capabilities.

This study attempts to improve our quantitative understanding of GrIS surface melt distributions and its related water balance components, particularly changes in surface mass balance (SMB) and freshwater runoff. The goal of this study was to apply a well-tested approach—a state-of-the-art modeling system, SnowModel (Liston and Elder 2006a; Mernild et al. 2006b)—to Greenland, including the GrIS. SnowModel was first tested at a local-to-regional scale using independent in situ observations from two long-term automatic meteorological and hydrometric monitoring catchments located in East Greenland between the GrIS and the ocean (Fig. 1). The model configuration was then adjusted to run over all of Greenland and tested using independent GrIS meteorological observations, satellite images, and equilibrium line altitude (ELA) studies. We performed model simulations for a 10-yr period, (1995–2005) with the following objectives: 1) assess MicroMet–SnowModel meteorological driving data against independent observations; 2) compare year-round simulated snow evolution components (snow accumulation, snow redistribution by wind, surface and blowing-snow sublimation, evaporation, and snow and ice melt) with independent in situ observations from the Mittivakkat and Zackenberg catchments, East Greenland; 3) quantify the yearly maximum and the 1995–2005 interannual variability in the GrIS surface melt cover (and the nonmelt area in the GrIS interior); 4) estimate and analyze the GrIS water balance components, including the SMB and GrIS mass balance; 5) simulate the interannual variability in GrIS specific runoff and the runoff separation to the GrIS western and eastern drainage areas; and 6) calculate the GrIS runoff contribution to global sea level rise.

## 2. Study area

### *Physical settings and climate*

Greenland is roughly 2600 km long from the northernmost point at Cape Morris Jesup ( $83^\circ\text{N}$ ) to the southern tip at Cape Farwell ( $60^\circ\text{N}$ ). The island is dominated by the largest ice sheet in the Northern Hemisphere, the GrIS ( $1.834 \times 10^6 \text{ km}^2$ ), which covers approximately 85% of the island. The ice sheet's maximum altitude is more than 3200 m MSL. (Fig. 1). The maximum width of the ice-free land strip is 200 km. The

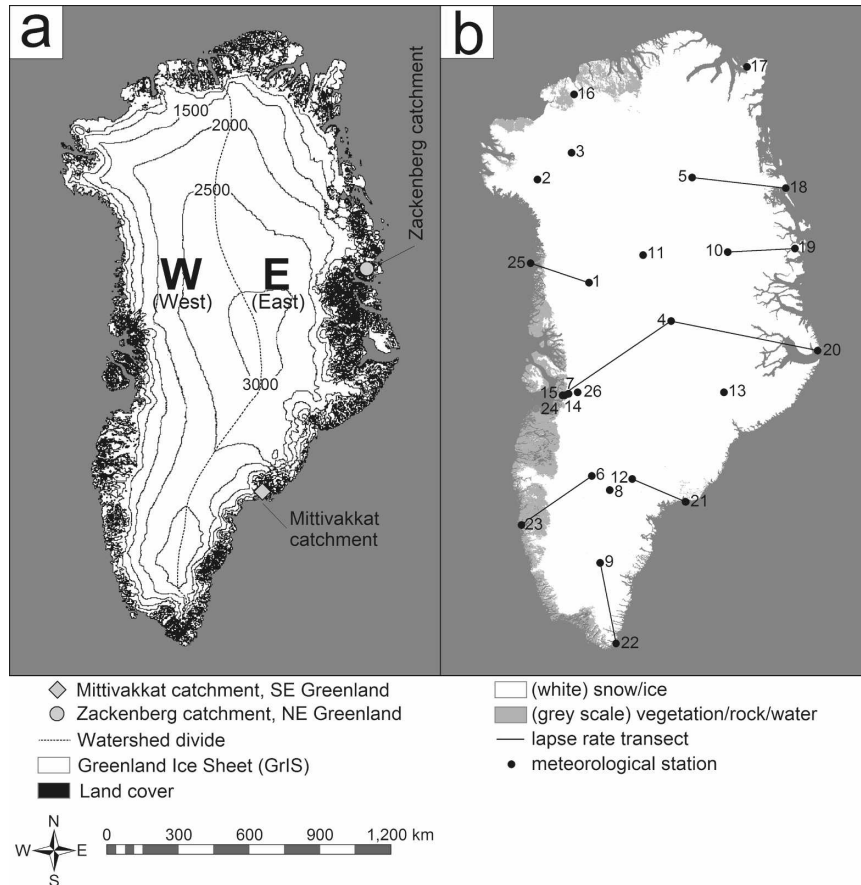


FIG. 1. Greenland simulation domain: (a) topography (500-m contour interval), a division of the GrIS into a western and an eastern drainage area based on surface topography, and the location of the Mittivakkat catchment and the Zackenberg catchment; and (b) the location of the coastal and GrIS meteorological tower stations, designation of snow-ice and vegetation-rock-water surface cover, and the eight air temperature lapse rate transects between the following meteorological stations: 22 and 9, 21 and 12, 20 and 4, 19 and 10, 18 and 5, 25 and 1, 15 and 4, and 23 and 6.

majority of the land strip is mountainous and includes numerous marginal glaciers and ice caps, and a number of fjords that reach the interior.

The Mittivakkat (Ammassalik Island, SE Greenland, 65°N) and the Zackenberg (NE Greenland, 74°N) catchments are the only two areas on the East Greenland land strip permanently instrumented for automatic collection of meteorological, hydrometric, and snow monitoring (Fig. 1a). Additional glacier observations regularly occur at Mittivakkat glacier (Knudsen and Hasholt 2004; Mernild et al. 2006b, 2008). These catchments are not connected to the GrIS. The Mittivakkat catchment is 18.4 km<sup>2</sup>, characterized by strong topographic relief, and ranges in elevation from 0 to 973 m MSL. Roughly 78% (14.4 km<sup>2</sup>) of the catchment is covered by parts of the Mittivakkat Glacier, a temperate glacier ranging from approximately 160 to 930 m MSL in elevation (Mernild et al. 2006b).

The Zackenberg catchment covers 512 km<sup>2</sup> and is characterized by high-relief mountainous landscapes. Its elevation ranges from 0 to 1450 m MSL, from wide valleys to extensive glaciated plateaus mainly above 1000 m MSL. Roughly 20% (101 km<sup>2</sup>) of the catchment is covered by glaciers.

The climate in Greenland is arctic; that is, the average air temperature for the warmest month is below 10°C everywhere—except for the fjords in the south that fall into the subarctic zone where temperatures dip only slightly below this limit (Born and Böcher 2001). In the northern parts of the GrIS, winter air temperatures can drop below −70°C, while on the East Greenland land strip, summer temperatures can briefly rise above 25°C (Mernild et al. 2007a). The mean annual air temperature (MAAT) varies from 1.3° to −16.9°C from south to north. The simulation data period (1995–2005) shows a MAAT warming of ~1.8°C (based on

TABLE 1. Meteorological input data for the Greenland SnowModel simulations. Meteorological station data on the GrIS (stations 1–15, and 26) were provided by the Steffen Research Group at CIRES, coastal meteorological station data (stations 16–18 and 20–25) by the DMI, and the Zackenberg meteorological station (station number 19) by the Danish Polar Center (DPC), the Greenland Survey (ASIAQ), the GeoBasis (Danish National Environmental Research Center, NERI), and the Department of Geography and Geology, University of Copenhagen.

Meteorological station No.	Meteorological station name	Location	Data time period	Altitude (m MSL)
1	NASA-U	73°50'31"N, 49°29'54"W	1 Jan 1998–29 May 2005	2369
2	GITS	77°08'16"N, 61°02'24"W	7 May 1999–14 May 2005	1869
3	Humboldt	78°31'36"N, 56°49'50"W	2 Jan 1998–23 Jun 2005	1995
4	Summit	72°34'47"N, 38°30'18"W	1 Sep 1999–31 Aug 2005	3208
5	Tunu-N	78°00'59"N, 33°59'00"W	17 May 1996–7 Nov 2003	2052
6	DYE-2	66°28'48"N, 46°16'44"W	25 May 1996–15 Nov 2003	2165
7	JAR1	69°29'51"N, 49°41'16"W	20 Jun 1996–10 Dec 2005	962
8	Saddle	65°59'58"N, 44°30'03"W	20 Apr 1997–10 Oct 2004	2456
9	South Dome	63°08'56"N, 44°49'02"W	23 Apr 1996–12 Oct 2004	2901
10	NASA-E	75°00'02"N, 29°59'50"W	3 May 1997–23 Oct 2004	2614
11	NGRIP	75°05'59"N, 42°19'57"W	9 Jul 1997–29 Dec 2004	2950
12	NASA-SE	66°28'45"N, 42°29'56"W	24 Apr 1998–25 May 2005	2393
13	KAR	69°41'58"N, 33°00'21"W	18 May 1998–7 Jun 2005	2579
14	JAR2	69°25'09"N, 50°03'55"W	2 Jun 1999–31 Aug 2005	542
15	JAR3	69°23'40"N, 50°18'36"W	1 Jan 2001–24 May 2004	283
16	Hall Land	81°41'00"N, 59°57'00"W	1 Sep 1995–31 Aug 1996	105
17	Station Nord	81°36'00"N, 16°39'00"W	1 Sep 1995–31 Aug 2005	36
18	Danmarkshavn	76°46'00"N, 18°40'00"W	1 Sep 1995–31 Aug 2005	11
19	Zackenberg	74°28'10"N, 20°34'20"W	1 Sep 1997–31 Aug 2005	43
20	Ittoqqortoormiit	70°29'00"N, 21°57'00"W	1 Sep 1995–31 Aug 2005	66
21	Tasiilaq	65°36'00"N, 37°38'00"W	1 Sep 1995–31 Aug 2005	44
22	Ikerassuaq	60°03'00"N, 43°10'00"W	1 Sep 1995–31 Aug 2005	88
23	Nuuk	64°10'00"N, 51°45'00"W	1 Sep 1995–31 Aug 2005	80
24	Aasiaat	68°42'00"N, 52°45'00"W	1 Sep 1995–31 Aug 2005	88
25	Kitsissorsuit	74°02'00"N, 57°49'00"W	1 Sep 1995–31 Aug 2005	40
26	Swiss Camp	69°34'03"N, 49°19'17"W	1 Jan 1995–16 Aug 2006	1140

data from the 10 coastal meteorological stations; Fig. 1 and Table 1, stations 16–25). In southern and southeastern Greenland, the annual precipitation is  $\sim 2500$  mm w.eq. yr<sup>-1</sup> (where w.eq. means water equivalent), while the northern areas receive little precipitation (Ohmura and Reeh 1991; Born and Böcher 2001; Serreze and Barry 2005). Many of the island's characteristics cause considerable contrast in its weather conditions, including complex coastal topography, elevation, distance from the coastal area, marginal glaciers and ice caps, and the GrIS, which makes the climate vary considerably even over short distances. Temperature inversions are a common feature for Greenland coastal areas (Mernild et al. 2007a,c; Hansen et al. 2008) and for the GrIS (Putnins 1970).

### 3. SnowModel

#### a. SnowModel description

SnowModel (Liston and Elder 2006a) is a spatially distributed snowpack evolution modeling system specifically designed to be applicable over the wide range

of snow landscapes, climates, and conditions found around the world. It is made up of four submodels: MicroMet defines the meteorological forcing conditions (Liston and Elder 2006b); EnBal calculates the surface energy exchanges, including melt (Liston 1995; Liston et al. 1999); SnowPack simulates snow depth and water-equivalent evolution (Liston and Hall 1995); and SnowTran-3D is a blowing-snow model that accounts for snow redistribution by wind (Liston and Sturm 1998; 2002; Liston et al. 2007). While other distributed-snow models exist (e.g., Tarboton et al. 1995; Marks et al. 1999; Winstral and Marks 2002), the SnowTran-3D component allows application in Arctic, alpine (i.e., above treeline), and prairie environments that compose 68% of the seasonally snow-covered areas in the Northern Hemisphere (Liston 2004). SnowModel also simulates snow-related physical processes at spatial scales ranging from 5 m to global and temporal scales ranging from 10 min to a whole season. Simulated processes include 1) accumulation and loss from snow precipitation, blowing-snow redistribution, and sublimation; 2) loading, unloading, and sublimation within forest cano-

pies; 3) snow-density evolution; and 4) snowpack ripening and melt. SnowModel was originally developed for glacier-free landscapes. For glacier surface mass balance studies on eastern Greenland, SnowModel was modified to simulate glacier-ice melt after winter snow accumulation had ablated (Mernild et al. 2006b, 2007c).

#### 1) MICROMET

MicroMet is a quasi-physically based meteorological distribution model (Liston and Elder 2006b) designed specifically to produce the high-resolution meteorological forcing distributions (air temperature, relative humidity, wind speed, wind direction, precipitation, solar and longwave radiation, and surface pressure) required to run spatially distributed terrestrial models over a wide range of landscapes in a physically realistic manner. MicroMet uses elevation-related interpolations to modify air temperature, humidity, and precipitation following Kunkel (1989), Walcek (1994), Dodson and Marks (1997), and Liston et al. (1999). Temperature and humidity distributions are defined to be compatible with the observed lapse rates. Wind flow in complex topography is simulated following Ryan (1977) and Liston and Sturm (1998). Solar radiation variations are calculated using elevation, slope, and aspect relationships (Pielke 2002). Incoming longwave radiation is calculated while taking into account cloud cover (Walcek 1994; Liston and Elder 2006b) and elevation-related variations following Iziomon et al. (2003). Precipitation is distributed following Thornton et al. (1997). In addition, any data from more than one location, at any given time, are spatially interpolated over the domain using a Gaussian distance-dependent weighting function and interpolated to the model grid using the Barnes objective analysis scheme (Barnes 1964, 1973; Koch et al. 1983). Liston and Elder (2006b) and Liston et al. (2007) performed a rigorous validation of MicroMet using various observational datasets, data denial, and geographic domains. Further, MicroMet has been used to distribute observed and modeled meteorological variables over a wide variety of landscapes in the United States—Colorado (Greene et al. 1999), Wyoming (Hiemstra et al. 2002, 2006), Idaho (Prasad et al. 2001), and Arctic Alaska (Liston et al. 1999, 2002, 2007; Liston and Sturm 1998, 2002); Norway—Svalbard and central Norway (Bruland et al. 2004); East Greenland (Hasholt et al. 2003; Mernild et al. 2006a,b, 2007c); and near-coastal Antarctica (Liston et al. 1999).

#### 2) ENBAL

EnBal performs standard surface energy balance calculations (Liston 1995; Liston et al. 1999). This compo-

nent simulates surface (skin) temperatures, and energy and moisture fluxes in response to observed and/or modeled near-surface atmospheric conditions provided by MicroMet. Surface latent and sensible heat flux and snowmelt calculations are made using a surface energy balance model of the form

$$(1 - \alpha)Q_{si} + Q_{li} + Q_{le} + Q_h + Q_e + Q_c = Q_m, \quad (1)$$

where  $Q_{si}$  is the solar radiation reaching Earth's surface,  $Q_{li}$  is the incoming longwave radiation,  $Q_{le}$  is the emitted longwave radiation,  $Q_h$  is the turbulent exchange of sensible heat,  $Q_e$  is the turbulent exchange of latent heat,  $Q_c$  is the conductive energy transport,  $Q_m$  is the energy flux available for melt, and  $\alpha$  is the surface albedo. Details of each term in Eq. (1), and the model solution, are available in Liston (1995) and Liston et al. (1999). In the presence of snow or glacier ice, surface temperatures greater than 0°C indicate that energy is available for melting. This energy is computed by fixing the surface temperature at 0°C and solving Eq. (1) for  $Q_m$ .

#### 3) SNOWPACK

SnowPack is a single-layer, snowpack-evolution and runoff-retention model that describes snowpack changes in response to precipitation and melt fluxes defined by MicroMet and EnBal (Liston and Hall 1995; Liston and Elder 2006a). Its formulation closely follows Anderson (1976). In SnowPack, the density changes with time in response to snow temperature and the weight of the overlying snow (Liston and Elder 2006a). A second density-modifying process results from snow melting. The melted snow reduces the snow depth and percolates through the snowpack. If the snow temperature is below freezing, any percolating/liquid water refreezes and is stored in the snow (in the "pores") as internal refreezing. When saturated snow density is reached, assumed to be 550 kg m<sup>-3</sup> (Liston and Hall 1995), actual runoff occurs. This provides a method of accounting for heat and mass transfer processes, such as snowpack ripening, during spring melt. The density of new snow from additional accumulation is defined following Anderson (1976) and Liston and Hall (1995). Static-surface (nonblowing snow) sublimation calculated in EnBal is used to adjust the snowpack depth; blowing-snow sublimation is calculated in SnowTran-3D (Liston and Elder 2006a).

#### 4) SNOWTRAN-3D

SnowTran-3D (Liston and Sturm 1998; Liston et al. 2007) is a three-dimensional submodel that simulates snow depth evolution (deposition and erosion) result-

ing from wind-blown snow based on a mass-balance equation that describes the temporal variation of snow depth at each grid cell within the simulation domain. SnowTran-3D's primary components are a wind-flow forcing field, a wind shear stress on the surface, snow transport by saltation, snow transport by turbulent suspension, sublimation of saltating and suspended snow, and accumulation and erosion at the snow's surface (Liston and Sturm 2002). Simulated transport and blowing-snow sublimation processes are influenced by the interactions among available snow, topography, and atmospheric conditions (Liston and Sturm 1998). SnowTran-3D simulates snow depth evolution; then uses the snow density simulated by SnowPack to convert to the more hydrologically significant snow-water equivalent (SWE) depth. Deposition and erosion, which lead to changes in snow depth [Eq. (2)], are the result of changes in horizontal mass-transport rates of saltation,  $Q_{\text{salt}}$  ( $\text{kg m}^{-1} \text{s}^{-1}$ ); changes in horizontal mass-transport rates of turbulent suspended snow,  $Q_{\text{turb}}$  ( $\text{kg m}^{-1} \text{s}^{-1}$ ); sublimation of transported snow particles,  $Q_v$  ( $\text{kg m}^{-2} \text{s}^{-1}$ ); and the water-equivalent precipitation rate,  $P$  ( $\text{m s}^{-1}$ ). Combined, the time rate of change in snow depth,  $\zeta$  (m), is

$$\frac{d(\rho_s \zeta)}{dt} = \rho_w P - \left( \frac{dQ_{\text{salt}}}{dx} + \frac{dQ_{\text{turb}}}{dx} + \frac{dQ_{\text{salt}}}{dy} + \frac{dQ_{\text{turb}}}{dy} \right) + Q_v, \quad (2)$$

where  $t$  (s) is time;  $x$  (m) and  $y$  (m) are the horizontal coordinates in the west–east and south–north directions, respectively; and  $\rho_s$  and  $\rho_w$  ( $\text{kg m}^{-3}$ ) are snow and water density, respectively. At each time step, Eq. (2) is solved for each individual grid cell within the domain and is coupled to the neighboring cells through the spatial derivatives ( $d/dx$ ,  $d/dy$ ). SnowTran-3D simulations have previously been compared against observations in glacier and glacier-free alpine, Arctic, and Antarctic landscapes (Greene et al. 1999; Liston et al. 2000, 2007; Prasad et al. 2001; Hiemstra et al. 2002, 2006; Liston and Sturm 2002; Hasholt et al. 2003; Bruland et al. 2004; Mernild et al. 2006a,b, 2007c).

### b. SnowModel input

To solve this system of equations, SnowModel requires spatially distributed fields of topography, and land-cover and meteorological data (air temperature, relative humidity, wind speed, wind direction, and precipitation), obtained from stations located within the simulation domain. For this study, data are obtained from 26 meteorological stations (Fig. 1b and Table 1). Sixteen stations, operated by the Cooperative Institute for Research in Environmental Sciences (CIRES), Uni-

versity of Colorado, Boulder, Colorado, are located on the GrIS at altitudes from 283 to 3208 m MSL. Four were located along the ice sheet crest (2500–3200 m MSL), eight stations are close to the 2000-m contour line (1800–2500 m MSL), and four stations are positioned in the ablation area (280–1200 m MSL). The Danish Meteorological Institute (DMI) operates nine, and the GeoBasis program, in cooperation with the Danish National Environmental Research Center and the Department of Geography and Geology, University of Copenhagen, operates one peripheral low-elevation station located below 110 m MSL. Simulations were performed on a daily time step. Admittedly, snow and ice melt and blowing snow are threshold processes that may not be accurately represented by this time step; however, computational constraints prohibited higher temporal-resolution simulations. For the SnowModel test areas—the Mittivakkat and the Zackenberg catchments—the simulations span the 10-yr period from 1995 through 2005, and the start and end of a year are designated as 1 September and 31 August of the next year to appropriately separate the accumulation and ablation components of the glacier mass balance annual cycle. For the GrIS, water balance components were simulated based on the calendar year for better comparison with previous studies.

Greenland topographic data for the model simulations were provided by Bamber et al. (2001) who applied “correction” elevations derived by satellite imagery to an existing radar-altimetry digital elevation model (DEM). The image-derived correction was determined from a high-resolution (625 m) grid of slopes inferred from the regional slope-to-brightness relationship of 44 Advanced Very High Resolution Radiometer (AVHRR) images covering all of Greenland (Scambos and Haran 2002). For the model simulations, this DEM was aggregated to a 5-km grid-cell increment and clipped to yield a  $2830 \times 1740 \text{ km}^2$  simulation domain that encompassed all of Greenland. The GrIS terminus was confirmed or estimated by using aerial photos and maps (1:250000 Geodetic Institute, Denmark). For the SnowModel test areas (Mittivakkat and the Zackenberg catchments) a 100-m grid-cell increment DEM was used (for further detail see Mernild et al. 2006a,b, 2007c), to capture small-scale features such as drifts. Relatively finescale features are absent from the coarser GrIS-scale simulations at 5-km resolution.

Each grid cell within the domains was assigned a U.S. Geological Survey (USGS) Land Use/Land Cover System class (Fig. 1b) according to the North American Land Cover Characteristics Database, version 2.0 [available online at the USGS Earth Resources Observation and Science (EROS) Data Center's Distributed



Active Archive Center Web site: [http://edcdaac.usgs.gov/glcc/na\\_int.html](http://edcdaac.usgs.gov/glcc/na_int.html)]. The snow-holding depth (the snow depth that must be exceeded before snow can be transported by wind) and canopy gap fraction (the solar radiation reaching the snow surface below the canopy) were assumed to be constant during the 10-yr simulation period (Table 2). The albedo was assumed to be 0.8 for snow. Realistically, snow albedo changes with time and surface characteristics (Pomeroy and Brun 2001); thus, the model will likely underestimate the energy available for surface melting. When the snow is melted, GrIS surface ice conditions are used. User-defined constants for SnowModel are shown in Table 2 [for parameter definitions, see Liston and Sturm (1998, 2002) and Liston and Elder (2006a)]. All fjord and ocean areas within the domain were excluded from model simulations (Fig. 1b).

Solid and liquid precipitation measurements at the DMI meteorological stations (Fig. 1b and Table 1; stations 16–18 and 20–25) were calculated from Helman–Nipher shield observations corrected according to Allerup et al. (1998, 2000). Solid (snow) precipitation was calculated from snow-depth sounder observations (Fig. 1b and Table 1; station 19) after the sounder data noise was removed; these data are assumed to be accurate within  $\pm(10\%–15\%)$  (Mernild et al. 2007c). The snow-depth sounder observations were fractionated into liquid (rain) precipitation and solid (snow) precipitation at different air temperatures based on observations from different locations on Svalbard (Førland and Hanssen-Bauer 2003). For air temperatures below  $-1.5^{\circ}\text{C}$ , sounder data were considered to represent solid precipitation and for temperatures above  $3.5^{\circ}\text{C}$  precipitation is considered liquid; for temperatures between these limits, the snow and rain fraction is calculated by linear interpolation. Snow-depth increases at relative humidity  $<80\%$  and at wind speed  $>10\text{ m s}^{-1}$  were removed to better distinguish between the proportions of real snow accumulation based on precipitation events and blowing snow redistribution (Mernild et al. 2007c). Remaining snow-depth increases were adjusted using a temperature-dependent snow density (Brown et al. 2003) and an hourly snowpack settling rate for estimating the mm w.e.q. (Anderson 1976).

Temperature inversions with cold, low clouds or sea fog coming from the ocean dominate the coastal climate (approximately 300–400 m MSL). This study's use of data from meteorological stations located both in low-lying coastal areas and on the GrIS contributes to a more detailed understanding of the altitudinal air temperature distribution within the simulation domain. Unfortunately, this information is not detailed enough

TABLE 2. User-defined constants used in the SnowModel simulations [see Liston and Sturm (1998) for parameter definitions].

Symbol	Value	Parameter
$C_v$		Vegetation snow-holding depth (equal surface roughness length; m)
	0.50	Barren
	0.15	Grassland
	1.00	Mixed forest
	0.50	Mixed tundra
	0.30	Shrubland
	0.01	Snow
	0.01	Ice
	0.50	Wooded tundra
	0.50	Wooded wetland
	0.01	Water (ocean and lake)
$f$	500.0	Snow equilibrium fetch distance (m)
$U_{*t}$	0.25	Threshold wind shear velocity ( $\text{m s}^{-1}$ )
$dt$	1	Time step (day)
$dx = dy$		Grid-cell increment used at different simulations (km)
	0.1	Model validation at Mittivakkat and Zackenberg catchments
$\alpha$	5.0	Entire Greenland simulation
		Surface albedo
	0.8	Snow
$\rho$	0.4	Ice
		Surface density ( $\text{kg m}^{-3}$ )
	280	Snow
	910	Ice

to provide a full understanding of the inversion height, strength, and thickness on Greenland. Average monthly lapse rates (1997–2005) based on air temperature observations from eight different transects all around Greenland were used as a model input (Fig. 1, Table 3). Transects lay between low-lying meteorological stations located in the land strip area almost at sea level and stations on the GrIS. The minimum monthly lapse rate of  $-8.26^{\circ}\text{C km}^{-1}$  occurred in February, and the maximum ( $-5.77^{\circ}\text{C km}^{-1}$ ) occurred in June. The low winter lapse rate is followed by a high standard deviation and vice versa for the summer (Table 3), due to the relatively cold and variable winter temperatures at the GrIS interior.

To assess the performance of upscaled SnowModel–MicroMet distributed meteorological data, simulated meteorological data were tested against observations not used in MicroMet. The Swiss Camp station (Table 1), located on the GrIS (Fig. 1), was used for comparisons spanning 1995–2005. The validation station was located 40 km from the nearest station (JAR1) used in MicroMet to drive SnowModel.

### c. SnowModel validation

Few quality observations for spatial in situ snow evolution, snow and ice surface melt, and glacier net mass

TABLE 3. Mean monthly air temperature lapse rates and standard deviation based on data from eight transects laid between meteorological stations in the Greenland coastal area and on the GrIS (from 1997 through 2005). See Fig. 1b for transect locations.

	Jan	Feb	Mar	Apr	May	Jun	Jul	Aug	Sep	Oct	Nov	Dec	Ave
Avg air temperature lapse rate and std dev ( $^{\circ}\text{C km}^{-1}$ )	-7.84 ( $\pm 1.97$ )	-8.26 ( $\pm 1.78$ )	-7.80 ( $\pm 1.30$ )	-6.98 ( $\pm 1.09$ )	-6.69 ( $\pm 1.08$ )	-5.77 ( $\pm 0.98$ )	-6.89 ( $\pm 1.00$ )	-6.42 ( $\pm 0.87$ )	-7.70 ( $\pm 1.12$ )	-8.62 ( $\pm 1.28$ )	-8.65 ( $\pm 1.87$ )	-7.94 ( $\pm 1.93$ )	-7.46 ( $\pm 1.36$ )

balance are available. SnowModel accumulation and ablation routines were tested by visual inspection, cumulative values, and simple linear regression (Tables 4–6). Unfortunately, the only available observations for validation were collected outside the GrIS, from two well-instrumented and reliable long-term automatic stations collecting meteorological and hydrometric data in the Mittivakkat and Zackenberg catchments of East Greenland. These catchments supplied independent, in situ observations on glacier surface mass balance, snow-depth distribution, and snow cover extent used to validate SnowModel snow accumulation and ablation routines on local-to-regional scales before the routines were upscaled for all of Greenland, including the GrIS.

### 1) GLACIER SURFACE MASS BALANCE OBSERVATIONS AT MITTIVAKKAT

Modeled end-of-winter (31 May) spatial SWE depths and end-of-summer ablation (31 August) were validated against observed SWE depths (winter glacier mass balance) and ablation values (summer glacier mass balance) from the 14.4 km<sup>2</sup> Mittivakkat glacier test area (Table 4). The validation was conducted for the 10-yr period 1995/96–2004/05 at the end of May and the end of August. During these field campaigns, snow depth, snow density, and ablation from snow and glacier ice were measured using cross-glacier stake lines spaced approximately 500 m apart; the stakes in each line were set 50–100 m apart for snow accumulation (in total 230 measurements) and 200–250 m apart for snow and ice ablation measurements (in total 60 measurements). The accuracy levels of the observed winter and summer mass balances are each assumed to be within ~15%; however, larger errors might occur, especially in glacier areas with many crevasses (Knudsen and Hasholt 1999, 2004; Mernild et al. 2006a).

### 2) SNOW OBSERVATIONS AT ZACKENBERG

Approximately 2000 end-of-winter snow-depth measurements were made at the end of May or beginning of June for 2004 and 2005 in the 16.8 km<sup>2</sup> Zackenberg valley site (Table 5; Mernild et al. 2007c). Snow depth was measured approximately every 25–30 m using a global positioning system (GPS) MagnaProbe (Snow-Hydro, Fairbanks, Alaska; information online at www.snowhydro.com), a device that records snow depth and location. Average total snowpack snow density was measured at 40–50 different places in the valley each year (Mernild et al. 2007c). Spatial observations of average SWE depth were used to validate SnowModel winter components.

TABLE 4. Validation of SnowModel simulations: observed and modeled winter, summer, and net glacier mass balance from the Mittivakkat Glacier, Ammassalik Island (SE Greenland; 65°N) from 1995/96 to 2004/05. Validation was done for both 100-m (test area, 14.4 km<sup>2</sup>) and 5-km grid-cell increments (25.0 km<sup>2</sup>). Winter mass balance observations are carried out in late May and in early June, and summer mass balance observations in late August, while modeled winter values are taken on 31 May and summer values on 31 August. Both *R*<sup>2</sup> and *p* are estimated between the observed and modeled values. Observed data are based on information from previous studies by Knudsen and Hasholt (2004) and Mernild et al. (2006a).

The Mittivakkat Glacier, Ammassalik Island (SE Greenland, 65°N)									
	Winter mass balance (mm w.eq.)			Summer mass balance (mm w.eq.)			Net mass balance (mm w.eq. yr <sup>-1</sup> )		
	Observed	Modeled (31 May; 100-m grid-cell increment, 14.4 km <sup>2</sup> )	Modeled (31 May; 5-km grid-cell increment, 25.0 km <sup>2</sup> )	Observed	Modeled (31 Aug; 100-m grid-cell increment, 14.4 km <sup>2</sup> )	Modeled (31 Aug; 5-km grid-cell increment, 25.0 km <sup>2</sup> )	Observed	Modeled (Sep–Aug; 100-m grid-cell increment, 14.4 km <sup>2</sup> )	Modeled (Sep–Aug; 5-km grid-cell increment, 25.0 km <sup>2</sup> )
1995/96	1510	1470	1440	–1500	–1560	–1540	10	–90	–100
1996/97	1410	1390	1340	–1810	–1850	–1830	–400	–460	–490
1997/98	1140	1130	1110	–2310	–2270	–2280	–1170	–1140	–1170
1998/99	980	960	960	–1750	–1690	–1700	–770	–730	–740
1999/2000	1230	1200	1160	–2060	–2000	–1990	–830	–800	–830
2000/01	1180	1240	1190	–2140	–2010	–2030	–960	–770	–840
2001/02	1280	1250	1210	–1780	–1660	–1650	–500	–410	–440
2002/03	1400	1240	1200	–1050	–1270	–1250	–350	–30	–50
2003/04	No data	1260	1210	No data	–2120	–2100	–1070	–860	–890
2004/05	920	930	900	–2740	–2720	–2720	–1820	–1690	–1820
Avg and std dev	1228 (±197)	1207 (±168)	1172 (±159)	–1904 (±485)	–1915 (±407)	–1909 (±414)	–786 (±485)	–698 (±492)	–737 (±520)
<i>R</i> <sup>2</sup>	—	0.92	0.92	—	0.95	0.96	—	0.93	0.94
Level of signi- ficance ( <i>p</i> )	—	<0.01	<0.01	—	<0.01	<0.01	—	<0.01	<0.01

### 3) PHOTOGRAPHIC SNOW-COVER OBSERVATIONS AT ZACKENBERG VALLEY

Zackenberg snow cover distributions have been observed from 1 June through the ablation period (1 June–31 August) by photographs taken once every day at solar noon (Table 5). Traditionally, determining snow-cover extent has been based on point measurements; however, such measurements will not always detect significant area snow-cover variations. Therefore, since 1995, a digital camera has been placed on a hillside 477 m MSL overlooking the Zackenberg Valley

(16.8 km<sup>2</sup>) taking daily oblique photos to quantify the evolution of spatial snow-cover distributions. These photographs were transformed into digital orthophotos and used to perform snow-cover mapping (for technical specifications see Hinkler et al. 2003). Snow-cover distribution for the test area was converted into depletion curves to illustrate the daily ablation from 1 June, typically illustrating a laterally reversed S-shaped curve as a result of gradual snow-cover decrease. Depletion curves based on daily values from 1996 through 2005 were used to validate the SnowModel summer components. For brevity, the data in Table 6 only show results

TABLE 5. Validation of SnowModel simulations: observed and modeled winter snow depths from the Zackenberg valley (NE Greenland; 74°N) from 2003/04 to 2004/05. Validation was done for both 100-m (test area, 16.8 km<sup>2</sup>) and 5-km grid-cell increments (25.0 km<sup>2</sup>). Snow depth (SWE) observations are carried out in late May and in early June, while modeled snow-depth values are determined on 31 May.

The Zackenberg valley, Zackenberg (NE Greenland, 74°N)			
	Observed SWE depth (mm w.eq.)	Modeled SWE depth (31 May; mm w.eq.; 100-m grid-cell increment, 16.8 km <sup>2</sup> )	Modeled SWE depth (31 May; mm w.eq.; 5-km grid-cell increment, 25.0 km <sup>2</sup> )
2003/04	221	207	201
2004/05	177	166	171

TABLE 6. Validations of SnowModel routines were done on a daily basis. Here, the observed and modeled snow cover extents (%) are shown every 10th day through the ablation period (from 1 Jun through 31 Aug) from the Zackenberg valley (NE Greenland; 74°N) from 1996 through 2005. Validations were done for both 100-m (test area, 16.8 km<sup>2</sup>) and 5-km grid-cell increments (25.0 km<sup>2</sup>). Observed snow cover is based on data from J. Hinkler et al. (2007; personal communication). Both  $R^2$  and  $p$  are estimated between observed and modeled values.

The Zackenberg valley, Zackenberg (NE Greenland, 74°N)									
	1996			1997			1998		
	Observed	Modeled (100-m grid-cell increment, 16.8 km <sup>2</sup> )	Modeled (5-km grid-cell increment, 25.0 km <sup>2</sup> )	Observed	Modeled (100-m grid-cell increment, 16.8 km <sup>2</sup> )	Modeled (5-km grid-cell increment, 25.0 km <sup>2</sup> )	Observed	Modeled (100-m grid-cell increment, 16.8 km <sup>2</sup> )	Modeled (5-km grid-cell increment, 25.0 km <sup>2</sup> )
1 Jun	78	81	85	99	98	100	96	99	100
10 Jun	39	43	31	93	90	100	88	90	85
20 Jun	16	19	31	78	75	79	74	74	75
1 Jul	4	5	10	26	25	54	50	52	54
10 Jul	3	2	10	13	15	10	29	26	54
20 Jul	<1	<1	0	6	5	10	9	10	0
1 Aug	<1	<1	0	4	2	0	4	4	0
10 Aug	<1	<1	0	3	2	0	2	1	0
20 Aug	<1	<1	0	<1	1	0	<1	1	0
$R^2$	—	0.99	0.95	—	0.99	0.95	—	0.99	0.95
Level of significance ( $p$ )	—	<0.01	<0.01	—	<0.01	<0.01	—	<0.01	<0.01
	1999			2000			2001		
	Observed	Modeled (100-m grid-cell increment, 16.8 km <sup>2</sup> )	Modeled (5-km grid-cell increment, 25.0 km <sup>2</sup> )	Observed	Modeled (100-m grid-cell increment, 16.8 km <sup>2</sup> )	Modeled (5-km grid-cell increment, 25.0 km <sup>2</sup> )	Observed	Modeled (100-m grid-cell increment, 16.8 km <sup>2</sup> )	Modeled (5-km grid-cell increment, 25.0 km <sup>2</sup> )
1 Jun	100	100	100	83	84	100	—	97	100
10 Jun	98	100	100	56	58	46	—	89	85
20 Jun	94	96	100	18	21	21	83(*)	84	85
1 Jul	70	68	64	5	8	10	29	32	31
10 Jul	31	33	64	2	3	10	5	7	10
20 Jul	19	22	10	2	2	0	3	4	10
1 Aug	10	13	10	1	1	0	<1	<1	0
10 Aug	7	10	10	<1	1	0	<1	<1	0
20 Aug	4	5	0	<1	<1	0	<1	<1	0
$R^2$	—	0.99	0.92	—	0.99	0.95	—	0.99	0.99
Level of significance ( $p$ )	—	<0.01	<0.01	—	<0.01	<0.01	—	<0.01	<0.01
	2002			2003			2004		
	Observed	Modeled (100-m grid-cell increment, 16.8 km <sup>2</sup> )	Modeled (5-km grid-cell increment, 25.0 km <sup>2</sup> )	Observed	Modeled (100-m grid-cell increment, 16.8 km <sup>2</sup> )	Modeled (5-km grid-cell increment, 25.0 km <sup>2</sup> )	Observed	Modeled (100-m grid-cell increment, 16.8 km <sup>2</sup> )	Modeled (5-km grid-cell increment, 25.0 km <sup>2</sup> )
1 Jun	95	95	100	79	80	85	94	94	100
10 Jun	84	81	90	59	62	64	65	73	75
20 Jun	52	47	36	21	22	10	23	30	21
1 Jul	19	17	15	4	6	10	8	10	21
10 Jul	8	6	15	1	2	0	5	5	0
20 Jul	5	3	0	<1	1	0	3	4	0
1 Aug	4	1	0	<1	<1	0	1	2	0
10 Aug	1	<1	0	<1	<1	0	<1	1	0
20 Aug	<1	<1	0	<1	<1	0	<1	<1	0
$R^2$	—	0.99	0.97	—	0.99	0.98	—	0.99	0.98
Level of significance ( $p$ )	—	<0.01	<0.01	—	<0.01	<0.01	—	<0.01	<0.01

TABLE 6. (Continued)

The Zackenberg valley, Zackenberg (NE Greenland, 74°N)			
	2005		
	Observed	Modeled (100-m grid-cell increment, 16.8 km <sup>2</sup> )	Modeled (5-km grid-cell increment, 25.0 km <sup>2</sup> )
1 Jun	86	84	90
10 Jun	61	66	75
20 Jun	36	32	21
1 Jul	8	12	10
10 Jul	4	5	10
20 Jul	1	2	0
1 Aug	<1	1	0
10 Aug	<1	<1	0
20 Aug	<1	<1	0
R <sup>2</sup>	—	0.99	0.95
Level of significance ( <i>p</i> )	—	<0.01	<0.01

\* Note that 23 Jun is the first day with photographic data in 2001.

from the 1st, 10th, and 20th days in each month during the ablation period.

4) SURFACE MELT OBSERVED FROM SATELLITE IMAGES

Detection of surface melt at large spatial scales is effectively accomplished by using satellite microwave

data. The daily GrIS snowmelt extent is mapped (25-km grid-cell increment) using passive microwave satellite observations that discriminate wet from dry snow (Fig. 3; Abdalati and Steffen 1997a). The criterion for melt is 1% mean liquid water content by volume in the top meter of snow. The center part of the GrIS is the area where the melting threshold of the cross-well ground-penetrating radar (XGPR) microwave algorithm did not show any melt. The end-of-summer maximum observed spatial surface melt distribution at the GrIS was used to validate SnowModel melt simulations (Fig. 3).

4. Results and discussion

Validations of MicroMet-simulated GrIS meteorological data indicate substantial correlation with independent observed GrIS meteorological data from the Swiss Camp (Fig. 2). Critical MicroMet-generated air temperature, relative humidity, and precipitation values account for 84%, 63%, and 69%, respectively, of the variance in the observed 1995–2005 daily averaged dataset. The wind speed has less strong correlations, but the results remain respectable (>50% variance) for representations of GrIS meteorological processes. While this validation is limited because it employs only one independent station, a rare commodity, it indicates that MicroMet satisfactorily represents GrIS conditions.

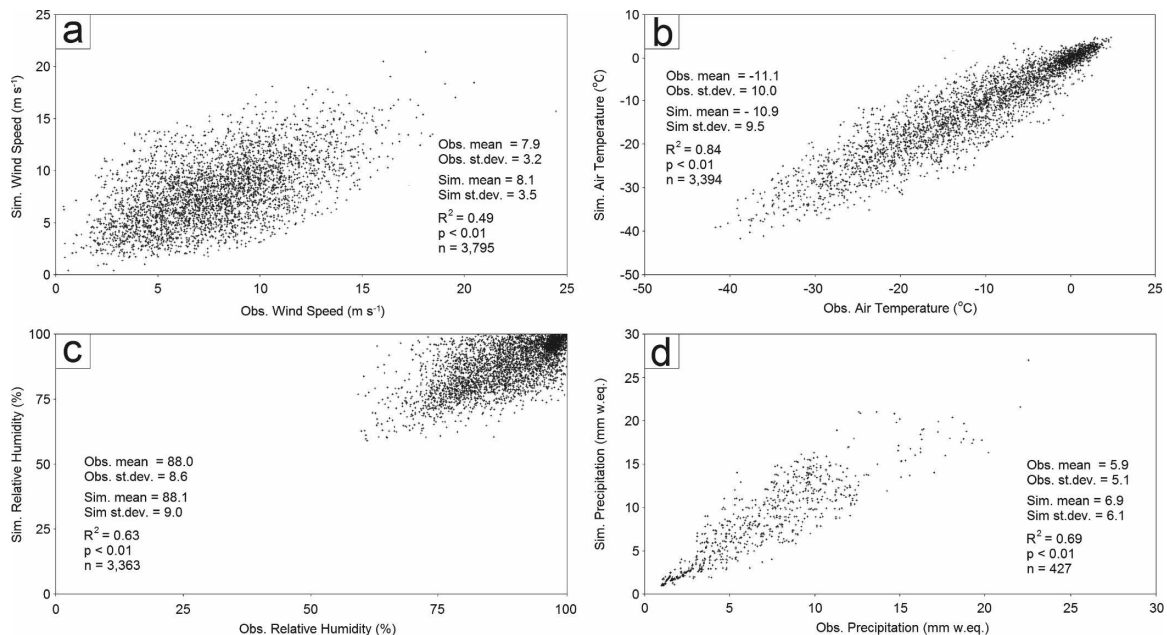


FIG. 2. A comparison between daily observed meteorological data [(a) mean wind speed, (b) mean air temperature, (c) mean relative humidity, and (d) precipitation and SnowModel–MicroMet-simulated meteorological data for the Swiss Camp on the GrIS (1995–2005) (for station info, see Table 1). Only precipitation values >1 mm w.eq. were included.



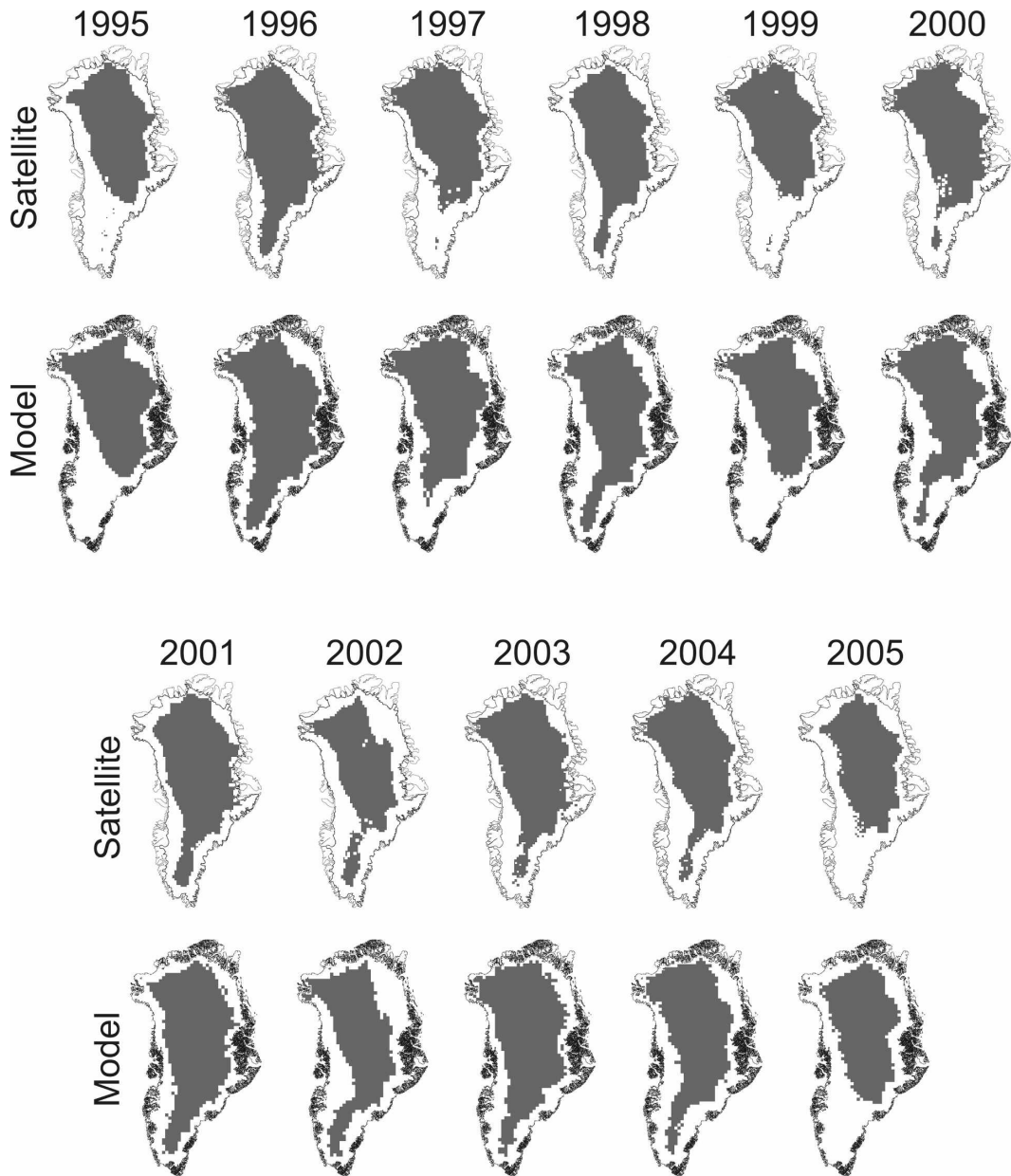


FIG. 3. The 1995–2005 Greenland melt extent based on satellite observations [the surface melt zone (lightest area), where summer warmth turns snow and ice around the edges of the ice sheet into slush and ponds of meltwater], and the 1995–2005 Greenland SnowModel-simulated surface melt zone (lightest area). The observed melt extent is based on satellite data provided by CIRES.

SnowModel was chosen for this study because of its robustness and ease of implementation over new simulation domains. This model demands rather limited input data, an important consideration in areas like Greenland, for which data are sparse due to rough terrain, harsh climatic conditions, and its remote location. It appears that our choice of a simple methodology provided estimates of the GrIS surface melt distribution and related water balance components that agree

well with observed values and previous studies. Nevertheless, it is important to keep in mind the limitation for SnowModel results when tested against observations collected from the strip of land surrounding the GrIS and not from the GrIS itself. SnowModel tests were conducted both for 100-m and 5-km grid cells, showing acceptable results (Tables 4–6).

Table 4 presents the modeled winter mass balance for the accumulation period (September–May), the

modeled summer mass balance for the ablation period (June–August), and the modeled mass-balance data (100-m grid cell) for the Mittivakkat Glacier test area for the years 1995/96–2004/05. The average modeled winter mass balance was 1207( $\pm$ 168) mm w.eq. (Table 4). This corresponds well with the observed winter mass balance of 1228( $\pm$ 197) mm w.eq., or a 21-mm w.eq. ( $\sim$ 2%) difference. The modeled winter mass balance shows significant correlation with observed values (1995–2005):  $R^2 = 0.92$ ,  $p < 0.01$  (where  $p$  is the level of significance), covering a maximum variation between modeled and observed values of 160 mm w.eq. for 2002/03 (Table 4). The average modeled summer mass balance was  $-1915(\pm 407)$  mm w.eq., which corresponds to an observed summer mass balance of  $-1904(\pm 485)$  (Table 4), or an 11 mm w.eq. (approximately  $<1\%$ ) difference. The maximum variation between modeled and observed values was 220 mm w.eq. for 2002/03 (Table 4). The modeled summer mass balance shows significant correlation with observed values (1995–2005):  $R^2 = 0.95$ ,  $p < 0.01$ . The average modeled net mass balance was  $-698(\pm 492)$  mm w.eq.  $\text{yr}^{-1}$ , an underestimation of 88 mm w.eq.  $\text{yr}^{-1}$  compared to the observations ( $\sim 11\%$  difference). The average simulated mass loss was less than the observed value. The modeled net mass balance shows significant correlation with observed values (1995–2005):  $R^2 = 0.93$ ,  $p < 0.01$ . The maximum yearly net mass balance difference between the observed and modeled values was 320 mm w.eq.  $\text{yr}^{-1}$  for 2002/03.

At the Zackenberg test area, the end-of-winter SWE depth (31 May) was modeled for 2003/04 and 2004/05 (100-m grid cell) and yielded average SWE depths of 207- and 166-mm w.eq., respectively (Table 5). The average modeled and observed end-of-winter SWE depths indicate a maximum SWE depth difference of 14 mm w.eq., or  $\sim 6\%$  (Table 5). SnowModel over- and under-performed randomly in response to both elevation and topographic influences—characteristics (ridge and hills), and to finescale snow-depth variations not captured by the 100-m DEM. Our analysis of the snow-cover extent in the Zackenberg test area for the ablation period (June–August 1996–2005) inferred inter- and intra-annual variations. The modeled snow-cover extent (100-m grid cell) shows significant correlation with observed values (based on time-lapse photography) for the ablation periods ( $R^2 = 0.99$ ,  $p < 0.01$ ; Table 6), even though the maximum variation between the modeled and observed snow cover extents through the ablation periods was 8%, or approximately 1.3 km<sup>2</sup> (at 10 June 2004; Table 6). Snow-cover extent is a product of both snow accumulation and ablation processes (phase-change processes like evaporation, sublimation,

and melting). Within SnowModel, SnowTran-3D simulates spatial snow deposition patterns in response to erosion and deposition, and EnBal calculates the energy flux available for snowmelt. Table 6 illustrates the modeled snow-cover variation through June–August 1996–2005, showing that 80%–100% of the test area was snow covered on 1 June, 50% of the snow cover extent had melted away by mid-June to early July, and 95% melted by early July to late August. The model variations were very similar to the recorded observations.

All three tests of the SnowModel winter and summer snow-evolution components developed for the Mittivakkat and Zackenberg catchments indicated good agreement between observed and simulated values (100-m grid cell). Further, the snow validation, while not from areas on the GrIS, do indicate that the SnowModel results are representing key physical snow accumulation and ablation processes and that the models can calculate reasonable estimates of the mass balance on a finescale (100-m grid cell).

Figure 3 plots both the spatially satellite-observed melt and modeled end-of-summer snow and ice surface melt (any melt amount) and nonmelt extents for the GrIS from 1995 to 2005. There is a high degree of similarity in the nonmelt distributions. In some areas the discrepancy between modeled and satellite-observed melt and nonmelt boundaries can be up to 160 km (1996), especially in northeastern Greenland, where the distance between meteorological stations is great. This discrepancy might also be due to the 1-day simulation time step; hourly variations in surface melt are not represented in the simulations, the fixed albedo used for snow and ice, and temporal and spatial uncertainties in satellite observations. Modeled nonmelt areas of the GrIS are, on average, underestimated by  $\sim 3\%$  (1995–2005; see Fig. 4), confirming the robustness of the ablation processes in SnowModel. The modeled GrIS surface melt area is, therefore, on average overestimated by  $\sim 29\,000$  km<sup>2</sup>  $\text{yr}^{-1}$  when compared with satellite observations. Observed interannual variability ranges from  $\sim 68\,000$  km<sup>2</sup> (or  $\sim 6\%$ ) in 2004 to  $<8000$  km<sup>2</sup> (or  $<1\%$ ) in 1996 and 2005; these 2 yr represent the extreme low (2005) and high (1996) nonmelt areas (Fig. 4). Simulated interannual variability for the nonmelt area agrees ( $R^2 = 0.96$ ) with the observations, illustrating that the nonmelt area can vary from year to year from as high as 71% (1996) to as low as 50% (2005). On average, the simulated nonmelt area decreased  $\sim 6\%$  in size from 1995 through 2005 ( $R^2 = 0.09$ ;  $p < 0.25$ ), indicating an increasing GrIS surface melt area, due to a significant average increase ( $R^2 = 0.76$ ,  $p < 0.01$ ) in the annual temperature anomaly of  $\sim 1.8^\circ\text{C}$  (Table 7).

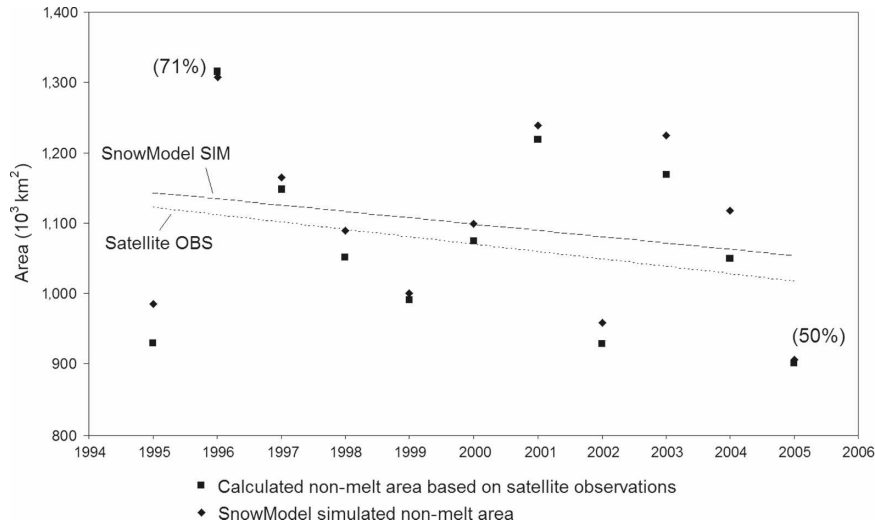


FIG. 4. Time series for the SnowModel-simulated and satellite-observed nonmelt areas located at the inner part of the GrIS from 1995 through 2005. Maximum and minimum percentages of the SnowModel-simulated nonmelt area in relation to the total GrIS area are illustrated.

For 2005, the modeled surface melt occurred at elevations as high as 2950 m MSL.

The melt index (defined as the melting area above the 2000-m GrIS contour line times the number of melting days) was further used to map snow-melt changes (Fig. 5). The index varies from  $0.42 \times 10^6 \text{ km}^2 \times \text{days}$  (1996) to  $3.31 \times 10^6 \text{ km}^2 \times \text{days}$  (1999), on average increasing  $\sim 0.57 \times 10^6 \text{ km}^2 \times \text{days}$  from 1995 through 2005 ( $R^2 = 0.07$ ,  $p < 0.25$ ). The low 1996 melt index indicates good agreement with the high observed nonmelting area (71%) for 1996 (Figs. 3 and 4). The smallest nonmelting area (50%) and highest temperature anomaly ( $1.12^\circ\text{C}$ ; Table 7) occurred in 2005; however, the 2005 melt index ( $2.75 \times 10^6 \text{ km}^2 \times \text{days}$ ) is only second largest after 1999 ( $3.29 \times 10^6 \text{ km}^2 \times \text{days}$ ; Fig. 5). The trends in modeled melt-index results are consistent with values found by Tedesco (2007) (Fig. 5).

Figure 6 illustrates the ELA for the western and eastern GrIS regions along a latitude line from  $60^\circ$  to  $81^\circ\text{N}$ . The ELA is defined as the elevation where the SMB equals zero. Therefore, the ELA provides a useful metric for the accumulation and the ablation's net influence on the SMB. Regional variations between the western and eastern parts of the GrIS are due to changes in local topography. On the western GrIS, the ELA varies from 810 m MSL ( $81^\circ\text{N}$ ) to 1640 ( $63^\circ\text{N}$ ), averaging 1260 m MSL (Fig. 6a), and on the eastern GrIS it varies from 600 m MSL ( $81^\circ\text{N}$ ) to 1400 ( $69^\circ\text{N}$ ), averaging 1130 m MSL (Fig. 6b). The modeled ELA is lower with increased latitude (Figs. 6a and 5b), which is consistent with the parameterization of Zwally and Giovinetto

(2001) (also in Box et al. 2004). The trend in average ELA from 1995 through 2005 is shown on Fig. 6c. The lowest average modeled ELA occurs in 1996 (western GrIS, 670 m MSL; eastern GrIS, 550 m MSL), a year with extensive observed nonmelt area. In contrast, the highest ELA developed in 2005 (western GrIS, 1690 m MSL; eastern GrIS, 1610 m MSL), a year with the smallest nonmelt area (Figs. 3 and 4). The general trend for 1995–2005 is an increase in average ELA in the western GrIS of  $\sim 42 \text{ m MSL yr}^{-1}$  ( $R^2 = 0.25$ ,  $p < 0.10$ ) and of  $\sim 45 \text{ m MSL yr}^{-1}$  ( $R^2 = 0.26$ ,  $p < 0.10$ ) in the eastern GrIS (Fig. 6c).

Throughout the year, different surface processes such as snow accumulation and redistribution, sublimation, evaporation, and surface melt affect the GrIS water balance. The yearly water balance equation for the GrIS can be described by

$$P - (E + \text{SU}) - R \pm \Delta S = 0 \pm \eta, \quad (3)$$

where  $P$  is the precipitation input from snow and rain (and possible condensation),  $E$  is evaporation [liquid to gas phase (atmosphere) flux of water vapor],  $\text{SU}$  is sublimation (snow blowing; solid to gas phase with no intermediate liquid stage),  $R$  here is runoff, and  $\Delta S$  is change in storage ( $\Delta S$  is also referred as the SMB) from changes in glacier storage and snowpack storage. Here,  $\eta$  is the water balance discrepancy (error). The error term should be 0 (or small) if the major components ( $P$ ,  $E$ ,  $\text{SU}$ ,  $R$ , and  $\Delta S$ ) have been determined accurately. Here, a change in storage is calculated by the residual value.

TABLE 7. Surface water balance elements: corrected precipitation ( $P$ ), modeled evaporation ( $E$ ), modeled sublimation (SU), modeled runoff ( $R$ ), and storage ( $\Delta S$ ) (also referred as SMB) for the GrIS from 1995 through 2005 (change in storage is calculated by the residual value), and the annual temperature anomaly.

Year	Corrected precipitation	Evaporation ( $E$ ; mm w.eq. yr <sup>-1</sup> )	Sublimation (SU; mm w.eq. yr <sup>-1</sup> )	Runoff ( $R$ )	Ablation ( $E + SU + R$ ; mm w.eq. yr <sup>-1</sup> )	Storage ( $\Delta S$ ; mm w.eq. yr <sup>-1</sup> )	Annual temp anomaly (°C yr <sup>-1</sup> )
	from rain and snow ( $P$ ; mm w.eq. yr <sup>-1</sup> )			from snow/glacier melt and rain (mm w.eq. yr <sup>-1</sup> )*			
1995	322	29	29	217	275	47	-1.13
1996	376	26	30	151	207	169	-0.33
1997	352	32	22	186	240	112	-0.77
1998	326	33	30	262	325	1	-0.18
1999	339	27	26	192	245	94	-0.74
2000	346	29	27	195	251	95	0.43
2001	363	28	31	210	269	94	-0.05
2002	356	30	28	238	296	60	0.45
2003	365	30	30	260	320	45	0.93
2004	321	38	32	201	271	50	0.28
2005	327	29	28	214	271	56	1.12
Avg, std dev	345(±19)	31(±3)	28(±3)	211(±31)	270(±35)	75(±44)- 138(±81) km <sup>3</sup> yr <sup>-1</sup> **	0.00
Min	321	26	22	151	207	1	-1.13
Max	376	38	32	262	325	169	1.12
Range	55	12	10	111	118	168	2.25
Avg change	-7	+3	+3	+34	+40	-47	+1.9
$R^2$	0.02	1	0.09	0.12	0.18	0.12	0.76
RMS	345	30	29	214	272	86	0.68
Level of significance ( $p$ )	<0.25	<0.25	<0.25	<0.25	<0.10	<0.25	<0.01
$R^2$ and $p$ (linear regression: between $P$ , $E$ , SU, $R$ , or $E + SU + R$ , and $\Delta S$ )	0.44, <0.01	0.29, <0.05	0.09, <0.25	0.79, <0.01	0.83, <0.01	—	—

\* The runoff does not include englacial and subglacial melting or changes in internal storage (e.g., glacial bulk water release). Losses from calving and geothermal heating are also omitted.  
 \*\* Changes in modeled surface storage are given in km<sup>3</sup> yr<sup>-1</sup>. For the other water balance components, see values in km<sup>3</sup> yr<sup>-1</sup> in Table 10.

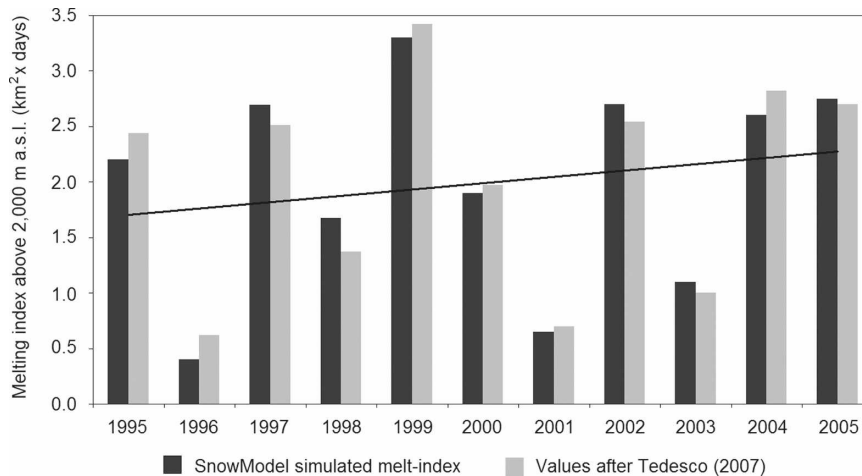


FIG. 5. Simulated melt index above 2000 m MSL on the GrIS including the trendline. The melt index is defined as the melting area times the number of melting days. The unit on the abscissa is km<sup>2</sup> × days in millions. The total GrIS area equal to or greater than 2000 m in elevation is 1 084 317 km<sup>2</sup>.

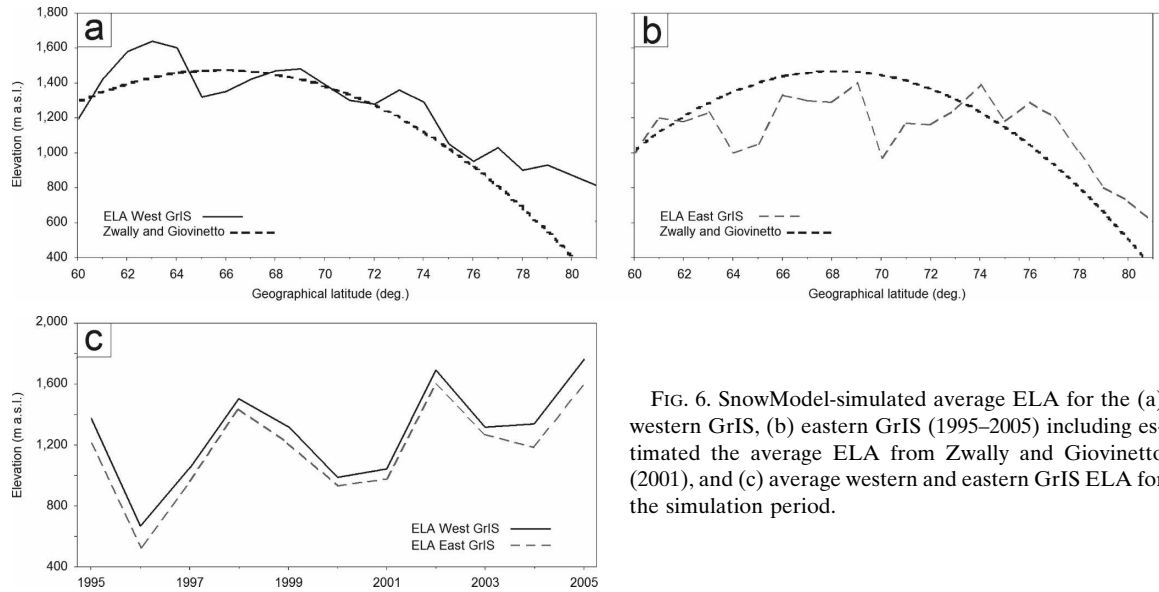


FIG. 6. SnowModel-simulated average ELA for the (a) western GrIS, (b) eastern GrIS (1995–2005) including estimated average ELA from Zwally and Giovinetto (2001), and (c) average western and eastern GrIS ELA for the simulation period.

Sublimation can play an important role in the high-latitude hydrological cycle during the year. Previous Mittivakkat Glacier studies (Hasholt et al. 2003; Mernild et al. 2006b, 2008), Zackenberg glacier studies (Mernild et al. 2007c), and GrIS studies (Box and Steffen 2001) have all shown that as much as 12%–23% of the annual precipitation may be returned to the atmosphere by sublimation. In Arctic North America, studies by Liston and Sturm (1998, 2004), Essery et al. (1999), and Pomeroy and Essery (1999) indicate that 5%–50% of the annual solid precipitation was returned to the atmosphere by sublimation. For the GrIS (1995–2005), modeled annual sublimation averaged  $28(\pm 3)$  mm w.eq. yr<sup>-1</sup>, which equaled  $52(\pm 6)$  km<sup>3</sup> yr<sup>-1</sup>, or ~10% of the solid precipitation input for the GrIS (Tables 7 and 10). SnowModel results were slightly lower than Box and Steffen's (2001) observed GrIS values of  $62(\pm 23)$  to  $120(\pm 65)$  km<sup>3</sup> yr<sup>-1</sup>. In our GrIS simulation domain, low air temperatures coincide with high relative humidity, and, therefore, sublimation has played a lesser role in the surface high-latitude water budget.

Table 7 presents the surface modeled water balance

components [Eq. (3)] for the GrIS from 1995 through 2005. The SMB is governed by accumulation (snow precipitation) and by ablation (evaporation, sublimation, and runoff). Net snow accumulation occurs over the GrIS interior while net surface ablation dominates the terminus/low-lying parts of the GrIS (Figs. 3 and 5). The interannual variability in precipitation and ablation causes sizeable SMB fluctuations with correlations of  $R^2 = 0.44$ ,  $p < 0.01$ , and  $R^2 = 0.83$ ,  $p < 0.01$ , respectively (Table 7). SMB fluctuations were largely tied to changes in ablation processes, mainly runoff. In 1998 the SMB was 1 mm w.eq. yr<sup>-1</sup> (Table 7), because of high ablation (325 mm w.eq. yr<sup>-1</sup>), of which 262 mm w.eq. yr<sup>-1</sup> was runoff. The same year featured a  $-0.18$  temperature anomaly and relatively low precipitation (326 mm w.eq. yr<sup>-1</sup>). Other relatively low SMB values are found in 1995, 2002, 2003, 2004, and 2005, and are also due to a high runoff-related flux into the ocean. The absolute maximum SMB of 169 mm w.eq. yr<sup>-1</sup> occurred in 1996 due to high precipitation, 376 mm w.eq. yr<sup>-1</sup>, and concurrent low ablation (207 mm w.eq. yr<sup>-1</sup>, where 151 mm w.eq. was runoff). The Table 7 estimated SMB conditions are in agreement with

TABLE 8. Specific runoff ( $L s^{-1} km^{-2}$ ) and contribution from the GrIS to the global sea level change from 1995 through 2005. The specific runoff values do not include hydroglacio processes such as the sudden release of bulk water.

	1995	1996	1997	1998	1999	2000	2001	2002	2003	2004	2005	Avg and std dev
Specific runoff ( $L s^{-1} km^{-2} yr^{-1}$ )	6.9	4.8	5.9	8.3	6.1	6.2	6.7	7.5	8.2	6.4	6.8	$6.7(\pm 1.0)$
Runoff from GrIS as a contribution to global sea level change (mm w.eq. yr <sup>-1</sup> )	1.1	0.8	1.0	1.4	1.0	1.0	1.1	1.2	1.3	1.1	1.1	1.1



TABLE 9. A separation of the SnowModel-simulated GrIS runoff into western and eastern drainage areas showing contributions to the Arctic Ocean from 1995 through 2005.

	1995	1996	1997	1998	1999	2000	2001	2002	2003	2004	2005	Avg and std dev
Modeled runoff from the western GrIS drainage area; mm w.eq. yr <sup>-1</sup> and % of total runoff	130.2 (60%)	92.1 (61%)	106.0 (57%)	154.6 (59%)	111.4 (58%)	109.2 (56%)	115.5 (55%)	133.3 (56%)	150.8 (58%)	110.6 (58%)	122.0 (57%)	121.4(±19.2) (58%)
Modeled runoff from the eastern GrIS drainage area; mm w.eq. yr <sup>-1</sup> and % of total runoff	86.8 (40%)	59.9 (39%)	80.0 (43%)	107.4 (41%)	80.6 (42%)	85.8 (44%)	94.8 (45%)	104.7 (44%)	109.2 (42%)	90.4 (42%)	92.0 (43%)	90.0(±14.5) (42%)

Hanna et al. (2005, 2008) and Box et al. (2006), indicating that SMB on average is 11% (9 mm w.eq. yr<sup>-1</sup> or 17 km<sup>3</sup> yr<sup>-1</sup>) lower than the Box et al. (2006) (1995–2004) simulated values. Integrated over the GrIS, the 11-yr precipitation rate indicates a nonsignificant decreasing trend of ~7 mm w.eq. The ablation increase averages ~40 mm w.eq. ( $R^2 = 0.18$ ,  $p < 0.10$ ), and runoff alone increases by ~34 mm w.eq. ( $R^2 = 0.12$ ,  $p < 0.25$ ) (Table 7). As the precipitation decreases combined with an increasing runoff, the net effect of these parameters indicates an increasing average SMB loss on 47 mm w.eq. for 1995–2005 ( $R^2 = 0.12$ ,  $p < 0.25$ ). The mean annual runoff of 211(±31) mm w.eq. yr<sup>-1</sup>, equals 392(±58) km<sup>3</sup> yr<sup>-1</sup> and a specific runoff of 6.7 l s<sup>-1</sup> km<sup>-2</sup> yr<sup>-1</sup> (Table 8). The calculated runoff was similar to those estimated by Hanna et al. (2005), 372 km<sup>3</sup> yr<sup>-1</sup> for the period 1998–2003, and by Box et al. (2006), 396 km<sup>3</sup> yr<sup>-1</sup> (1995–2004). Our simulated runoff was 46 km<sup>3</sup> yr<sup>-1</sup> (11%) higher than Hanna et al.'s (2005) estimated runoff for the same period (1998–2003), and 3 km<sup>3</sup> yr<sup>-1</sup> (<1%) lower than Box et al.'s (2006) estimated runoff for the period 1995–2004.

The SnowModel-simulated runoff was spatially separated into a western and an eastern GrIS drainage area contribution. Around 58% of the runoff drains from the western GrIS area, 227(±32) km<sup>3</sup> yr<sup>-1</sup>, and 42%

from the eastern GrIS area, 165(±26) km<sup>3</sup> yr<sup>-1</sup> (Fig. 1, Table 9). Serreze et al. (2006) reported values of freshwater export from the Arctic Ocean to the Greenland Sea of 4700 km<sup>3</sup> yr<sup>-1</sup> (2300 km<sup>3</sup> yr<sup>-1</sup> as sea ice and 2400 km<sup>3</sup> yr<sup>-1</sup> as upper-ocean freshwater). Using these values as the most reliable estimate for freshwater export to the Greenland Sea, the eastern GrIS and the total GrIS runoff amounts of 165 km<sup>3</sup> yr<sup>-1</sup> and 392 km<sup>3</sup> yr<sup>-1</sup> (1995–2005) contribute ~4% and ~8% of the total freshwater input to the Greenland Sea, respectively. From the standpoint of a global eustatic sea level rise, the 1995–2005 GrIS runoff contribution is ~1.1 mm w.eq. yr<sup>-1</sup> (Table 8).

Table 10 shows the GrIS water balance (1995–2005), including values for SMB, bottom melting [yielding an estimated 17 mm w.eq. yr<sup>-1</sup>, or 32 km<sup>3</sup> yr<sup>-1</sup>; values from Church et al. (2001)], and iceberg calving [yielding an estimated 191 mm w.eq. yr<sup>-1</sup>, or 357 km<sup>3</sup> yr<sup>-1</sup> (1996–2005); values from Rignot and Kanagaratnam (2006)]. SnowModel is a surface model and only produces first-order effects of climate change; it does not include glacio–hydro–dynamic routines. This study suggests (Table 10) that the GrIS is losing mass: 133 mm w.eq. yr<sup>-1</sup>, or 257 km<sup>3</sup> yr<sup>-1</sup> of GrIS mass was lost on average during 1995–2005. Losses ranged from 83 (1996) to 394 km<sup>3</sup> yr<sup>-1</sup> (1998). Our results span the 80 km<sup>3</sup> yr<sup>-1</sup> overall

TABLE 10. Average water balance components for the GrIS from 1995 through 2005. The change in storage is calculated by the residual value.

	Corrected precipitation from rain and snow ( $P$ )	Evaporation ( $E$ )	Sublimation ( $SU$ )	Runoff ( $R$ ) from snow/glacier melt and rain	Iceberg calving	Bottom melting	Storage ( $\Delta S$ )
Avg and std dev (mm w.eq. yr <sup>-1</sup> )	345(±19)	31(±3)	28(±3)	211(±31)	191	17(±2)*	-133(±44)
(km <sup>3</sup> yr <sup>-1</sup> )	634(±35)	58(±6)	52(±6)	392(±58)	357**	32(±3)	-257(±81)

\* Bottom melting by geothermal heating from Church et al.(2001) is recalculated from km<sup>3</sup> yr<sup>-1</sup> to mm w.eq. yr<sup>-1</sup>.

\*\* Iceberg calving (1996–2005) from Rignot and Kanagaratnam (2006) is recalculated from km<sup>3</sup> yr<sup>-1</sup> to mm w.eq. yr<sup>-1</sup>.

GrIS volume loss during 1997–2003 estimated by airborne laser altimetry (Krabill et al. 2000, 2004; Thomas et al. 2006) and the mass losses of 111–248 km<sup>3</sup> yr<sup>-1</sup> for 2002–2006 generated by the Gravity Recovery and Climate Experiment (GRACE) results (Chen et al. 2006; Luthcke et al. 2006; Ramillien et al. 2006; Velicogna and Wahr 2006).

The disparity between the SnowModel-simulated surface melt extent and the passive microwave satellite-observed melt extent can be used as a guide to understanding where additional meteorological stations might be deployed within the simulation domain to improve the model simulations. This disparity can also be useful in developing model routines for simulating the temperature inversion layer, which is a common Arctic feature. Air temperature inversion test simulations will first be conducted on the Mittivakkat catchment before routines are automated, and upscaled for greater catchments, for example, the GrIS.

## 5. Summary and conclusions

This study presents simulations of the GrIS surface melt area and water-balance components for the period 1995–2005. Our SnowModel simulations have been validated against independent in situ observations (accumulation and ablation observations) made on the land between the GrIS and the ocean in eastern Greenland. This simulated GrIS series yielded useful insights into the present conditions on the ice sheet and the interannual variability of water-balance components. There is a high degree of agreement between these GrIS simulations and the recorded observations, and both indicate an increasing surface melt area during the simulation period. Further, simulation values for GrIS surface change, runoff, SMB, and GrIS loss are in line with previous modeling and satellite studies. Runoff increased over the simulation period, while a reduction in the GrIS mass balance occurred. The runoff has likely been a factor in global sea level rise, contributing ~1.1 mm w.eq. yr<sup>-1</sup> to the eustatic sea level rise (not considering ocean loss by evaporation or the contribution from thermal expansion).

*Acknowledgments.* This work was supported by grants from the University of Alaska Presidential IPY Postdoctoral Foundation, and the University of Alaska Fairbanks (UAF) Office of the Vice Chancellor for Research and conducted during the first author's IPY postdoctoral fellowship at the UAF. A special thanks goes to the Cooperative Institute for Research in the Atmosphere (CIRA), Colorado State University, for hosting the first author in February and October

2007; to Cooperative Institute for Research in Environmental Sciences (CIRES), University of Colorado at Boulder, for hosting the first author from November 2007 through February 2008; and to the Faculty of Science, Hokkaido University, Sapporo, Japan, for hosting the first author from April through July 2008. Furthermore, the authors thank President's Professor of Climate Change and Chief Scientist John Walsh, International Arctic Research Center (IARC), UAF, for his review of the paper. A special thanks to Dr. Theodore Scambos, CIRES, University of Colorado, for providing a satellite picture and the Greenland Digital Elevation Model.

## REFERENCES

- Abdalati, W., and K. Steffen, 1997a: Snowmelt on the Greenland Ice Sheet as derived from passive microwave satellite data. *J. Climate*, **10**, 165–175.
- , and —, 1997b: The apparent effects of the Mt. Pinatubo eruption on the Greenland ice sheet melt extent. *Geophys. Res. Lett.*, **24**, 1795–1797.
- ACIA, 2005: *Arctic Climate Impact Assessment*. Cambridge University Press, 1042 pp.
- Allerup, P., H. Madsen, and F. Vejen, 1998: Estimating true precipitation in arctic areas. *Proc. Nordic Hydrological Conf.*, Helsinki, Finland, Nordic Hydrological Programme Rep. 44, 1–9.
- , —, and —, 2000: Correction of precipitation based on off-site weather information. *Atmos. Res.*, **53**, 231–250.
- Anderson, E. A., 1976: A point energy balance model of a snow cover. NOAA Tech. Rep. NWS 19, 150 pp.
- Bamber, J., S. Ekholm, and W. Krabill, 2001: A new, high-resolution digital elevation model of Greenland fully validated with airborne laser altimeter data. *J. Geophys. Res.*, **106B**, 6733–6746.
- Barnes, S. L., 1964: A technique for maximizing details in numerical weather map analysis. *J. Appl. Meteor.*, **3**, 396–409.
- , 1973: Mesoscale objective analysis using weighted time series observations. NOAA Tech. Memo. ERL NSSL-62, National Severe Storms Laboratory, Norman, OK, 60 pp.
- Barry, R. G., and M. C. Serreze, 2000: Atmospheric components of the arctic ocean freshwater balance and their interannual variability. *The Freshwater Budget of the Arctic Ocean*, E. L. Lewis et al., Eds., Kluwer Academic, 45–56.
- Bauer, A., 1968: Nouvelle estimation du bilan de masses de L'Inlandsis du Groenland. *Deep-Sea Res.*, **14**, 13–17.
- Benson, C. S., 1962: Stratigraphic studies in the snow and firn of Greenland Ice Sheet. U.S. Army SIPRE Research Rep. 70, 93 pp.
- Born, E. W., and J. Böcher, 2001: *The Ecology of Greenland*. Ministry of Environment and Natural Resources, Nuuk, Greenland, 429 pp.
- Box, J. E., 2002: Survey of Greenland instrumental temperature records: 1973–2001. *Int. Climatol.*, **22**, 1829–1847.
- , and K. Steffen, 2001: Sublimation estimates for the Greenland ice sheet using automated weather station observations. *J. Geophys. Res.*, **106** (D24), 33 965–33 982.
- , D. H. Bromwich, and L.-S. Bai, 2004: Greenland ice sheet surface mass balance 1991–2000: Application of Polar MMS

- mesoscale model and in situ data. *J. Geophys. Res.*, **109**, D16105, doi:10.1029/2003JD004451.
- , and Coauthors, 2006: Greenland ice sheet surface mass balance variability (1988–2004) from calibrated Polar MM5 output. *J. Climate*, **19**, 2783–2800.
- Braithwaite, R. J., and O. B. Olesen, 1993: Seasonal variation of ice ablation at the margin of the Greenland ice sheet and its sensitivity to climate change, Qamanarassup sermia, West Greenland. *J. Glaciol.*, **39**, 267–274.
- Broecker, W. S., and G. H. Denton, 1990: The role of ocean-atmosphere reorganization in glacial cycles. *Quat. Sci. Rev.*, **9**, 305–341.
- , D. M. Peteet, and D. Rind, 1985: Does the ocean-atmosphere system have more than one stable mode of operation. *Nature*, **315**, 21–26.
- Brown, R. D., B. Brasnett, and D. Robinson, 2003: Gridded North American monthly snow depth and snow water equivalent for GCM evaluation. *Atmos.–Ocean*, **41**, 1–14.
- Bruland, O., G. E. Liston, J. Vonk, K. Sand, and A. Killingtveit, 2004: Modelling the snow distribution at two high-Arctic sites at Svalbard, Norway, and at a sub-Arctic site in central Norway. *Nord. Hydrol.*, **35**, 191–208.
- Chen, J. L., C. R. Wilson, and B. D. Tapley, 2006: Satellite gravity measurements confirm accelerated melting of Greenland ice sheet. *Science*, **313**, 1958–1960.
- Church, J. A., J. M. Greory, P. Huybrechts, M. Kuhn, C. Lambeck, M. T. Nguan, D. Qin, and P. L. Woodworth, 2001: Change in sea level. *Climate Change 2001: The Scientific Basis*, J. T. Houghton et al., Eds., Cambridge University Press, 639–694.
- Dodson, R., and D. Marks, 1997: Daily air temperature interpolation at high spatial resolution over a large mountainous region. *Climate Res.*, **8**, 1–20.
- Dowdeswell, J. A., and Coauthors, 1997: The mass balance of circum-Arctic glaciers and recent climate change. *Quat. Res.*, **48**, 1–4.
- Essery, R. L. H., L. Li, and J. W. Pomeroy, 1999: A distributed model of blowing snow over complex terrain. *Hydrol. Processes*, **13**, 2423–2438.
- Førland, E. J., and I. Hanssen-Bauer, 2003: Climate variations and implications for precipitations types in the Norwegian Arctic. Norwegian Meteorological Institute Rep. 24/02, 21 pp.
- Greene, E. M., G. E. Liston, and R. A. Pielke, 1999: Simulation of above treeline snowdrift formation using a numerical snowtransport model. *Cold Reg. Sci. Technol.*, **30**, 135–144.
- Hanna, E., P. Huybrechts, I. Janssens, J. Cappelen, K. Steffen, and A. Stephens, 2005: Runoff and mass balance of the Greenland ice sheet: 1958–2003. *J. Geophys. Res.*, **110**, D13108, doi:10.1029/2004JD005641.
- , and Coauthors, 2008: Increased runoff from melt from the Greenland Ice Sheet: A response to global warming. *J. Climate*, **21**, 331–341.
- Hansen, B. U., and Coauthors, 2008: Present day climate at Zackenberg. *High-Arctic Ecosystem Dynamics in a Changing Climate: Ten Years of Monitoring and Research at Zackenberg Research Station, Northeast, Greenland*, H. Meltofte et al., Eds., Advances in Ecological Research, Vol. 40, Elsevier, 111–149.
- Hasholt, B., G. E. Liston, and N. T. Knudsen, 2003: Snow distribution modelling in the Ammassalik region, southeast Greenland. *Nord. Hydrol.*, **34**, 1–16.
- , N. Bobrovitskaya, J. Bogen, J. McNamara, S. H. Mernild, D. Milbourn, and D. E. Walling, 2006: Sediment transport to the Arctic Ocean and adjoining cold oceans. *Nord. Hydrol.*, **37**, 413–432.
- Hiemstra, C. A., G. E. Liston, and W. A. Reiners, 2002: Snow redistribution by wind and interactions with vegetation at upper treeline in the Medicine Bow Mountains, Wyoming. *Arct. Antarct. Alp. Res.*, **34**, 262–273.
- , —, and —, 2006: Observing, modelling, and validating snow redistribution by wind in a Wyoming upper treeline landscape. *Ecol. Modell.*, **197**, 35–51.
- Hinkler, J., S. B. Pedersen, M. Rasch, and B. U. Hansen, 2003: Automatic snow cover monitoring at high temporal and spatial resolution, using images taken by a standard digital camera. *Int. J. Remote Sens.*, **23**, 4669–4682.
- Hinzman, L. D., and Coauthors, 2005: Evidence and implications of recent climate change in northern Alaska and other Arctic regions. *Climatic Change*, **72**, 251–298.
- Hock, R., and P. Jansson, 2005: Modelling glacier hydrology. *Encyclopedia of Hydrological Science*, M. Andersen, Ed., John Wiley, 1–9.
- Iziomon, M. G., H. Mayer, and A. Matzarakis, 2003: Downward atmospheric longwave irradiance under clear and cloudy skies: Measurement and parameterization. *J. Atmos. Sol.-Terr. Phys.*, **65**, 1107–1116.
- Janssens, I., and P. Huybrechts, 2000: The treatment of meltwater retention in mass-balance parameterisation of the Greenland Ice Sheet. *Ann. Glaciol.*, **31**, 133–140.
- Knudsen, N. T., and B. Hasholt, 1999: Radio-echo sounding at the Mittivakkat Gletscher, southeast Greenland. *Arct. Antarct. Alp. Res.*, **31**, 321–328.
- , and —, 2004: Mass balance observations at Mittivakkat Glacier, southeast Greenland 1995–2002. *Nord. Hydrol.*, **35**, 381–390.
- Koch, S. E., M. DesJardins, and P. J. Kocin, 1983: An interactive Barnes objective map analysis scheme for use with satellite and conventional data. *J. Climate Appl. Meteor.*, **22**, 1487–1503.
- Krabill, W. E., and Coauthors, 2000: Greenland ice sheet: High-elevation balance and peripheral thinning. *Science*, **289**, 428–430.
- , and Coauthors, 2004: Greenland Ice Sheet: Increased coastal thinning. *Geophys. Res. Lett.*, **31**, L24402, doi:10.1029/2004GL021533.
- Kunkel, K. E., 1989: Simple procedures for extrapolation of humidity variables in the mountainous western United States. *J. Climate*, **2**, 656–669.
- Liston, G. E., 1995: Local advection of momentum, heat, and moisture during the melt of patchy snow covers. *J. Appl. Meteor.*, **34**, 1705–1715.
- , 2004: Representing subgrid snow cover heterogeneities in regional and global models. *J. Climate*, **17**, 1381–1397.
- , and D. K. Hall, 1995: An energy-balance model of lake-ice evolution. *J. Glaciol.*, **41**, 373–382.
- , and M. Sturm, 1998: A snow-transport model for complex terrain. *J. Glaciol.*, **44**, 498–516.
- , and —, 2002: Winter precipitation patterns in arctic Alaska determined from a blowing-snow model and snow-depth observations. *J. Hydrometeorol.*, **3**, 646–659.
- , and —, 2004: The role of winter sublimation in the Arctic moisture budget. *Nord. Hydrol.*, **35**, 325–334.
- , and K. Elder, 2006a: A distributed snow-evolution modeling system (SnowModel). *J. Hydrometeorol.*, **7**, 1259–1276.

- , and —, 2006b: A meteorological distribution system for high-resolution terrestrial modeling (MicroMet). *J. Hydrometeorol.*, **7**, 217–234.
- , J.-G. Winther, O. Bruland, H. Elvehøy, and K. Sand, 1999: Below surface ice melt on the coastal Antarctic ice sheet. *J. Glaciol.*, **45**, 273–285.
- , —, —, —, —, and L. Karlöf, 2000: Snow and blue-ice distribution patterns on the coastal Antarctic ice sheet. *Antarct. Sci.*, **12**, 69–79.
- , J. P. McFadden, M. Sturm, and R. A. Pielke Sr., 2002: Modeled changes in arctic tundra snow, energy, and moisture fluxes due to increased shrubs. *Global Change Biol.*, **8**, 17–32.
- , R. B. Haehnel, M. Sturm, C. A. Hiemstra, S. Berezovskaya, and R. D. Tabler, 2007: Simulating complex snow distributions in windy environments using SnowTran-3D. *J. Glaciol.*, **53**, 241–256.
- Luthcke, S. B., and Coauthors, 2006: Recent Greenland ice mass loss by drainage system from satellite gravity observations. *Science*, **314**, 1286–1289.
- Marks, D., J. Domingo, D. Susong, T. Link, and D. Garen, 1999: A spatially distributed energy balance snowmelt model for application in mountain basins. *Hydrol. Processes*, **13**, 1935–1959.
- Mernild, S. H., and B. Hasholt, 2006: Climatic control on river discharge simulations from the Mittivakkat Glacier catchment, Ammassalik Island, SE Greenland. *Nord. Hydrol.*, **37**, 327–346.
- , —, and G. E. Liston, 2006a: Water flow through Mittivakkat Glacier, Ammassalik Island, SE Greenland. *Dan. J. Geogr.*, **106**, 25–43.
- , G. E. Liston, B. Hasholt, and N. T. Knudsen, 2006b: Snow-distribution and melt modeling for Mittivakkat Glacier, Ammassalik Island, SE Greenland. *J. Hydrometeorol.*, **7**, 808–824.
- , B. Hasholt, D. L. Kane, B. U. Hansen, B. H. Jakobsen, and N. T. Knudsen, 2007a: Climate, glacier mass balance, and runoff 1993–2005, and in a long term perspective (106 year), Mittivakkat Glacier catchment, Ammassalik Island, SE Greenland. *Hydrol. Res.*, **39**, 239–256.
- , —, and G. E. Liston, 2007b: Climatic control on river discharge simulations, Zackenberg River drainage basin, NE Greenland. *Hydrol. Processes*, **22**, 1932–1948, doi:10.1002/hyp.6777.
- , G. E. Liston, and B. Hasholt, 2007c: Snow-distribution and melt modeling for glaciers in Zackenberg River drainage basin, NE Greenland. *Hydrol. Processes*, **21**, 3249–3263, doi:10.1002/hyp.6500.
- , C. Sigsgaard, M. Rasch, B. Hasholt, B. U. Hansen, M. Stjernholm, and D. Petersen, 2007d: Climate, river discharge and suspended sediment transport in the Zackenberg River drainage basin and Young Sund/Tyrolerfjord, northeast Greenland, 1995–2003. *Carbon Cycling in Arctic Marine Ecosystems: Case Study Young Sound*, S. Rysgaard and R. N. Glud, Eds., Meddr. om Grønland—BioScience, Vol. 58, 24–43.
- , G. E. Liston, D. L. Kane, B. Hasholt, and N. T. Knudsen, 2008: Spatial snow distribution, runoff, and mass balance modelling for entire Mittivakkat Glacier (1998–2006), Ammassalik Island, SE Greenland. *Dan. J. Geogr.*, **108**, 121–136.
- Moritz, R. E., C. M. Bitz, and E. J. Steig, 2002: Dynamics of recent climate change in the Arctic. *Science*, **297**, 1497–1502.
- Mote, T. L., 2003: Estimation of runoff rates, mass balance, and elevation changes on the Greenland ice sheet from passive microwave observations. *J. Geophys. Res.*, **108**, 4052, doi:10.1029/2001JD002032.
- Oerlemans, J., 1991: The mass balance of the Greenland ice sheet: Sensitivity to climate change as revealed by energy-balance modelling. *Holocene*, **1**, 40–49.
- Ohmura, A., and N. Reeh, 1991: New precipitation and accumulation maps for Greenland. *J. Glaciol.*, **37** (125), 140–148.
- , P. Calanca, M. Wild, and M. Anklin, 1999: Precipitation, accumulation and mass balance of the Greenland Ice Sheet. *Z. Gletscherkunde Glazialgeol.*, **35**, 1–20.
- Pielke, R. A., Sr., 2002: *Mesoscale Meteorological Modeling*. Academic Press, 676 pp.
- Pomeroy, J. W., and R. L. H. Essery, 1999: Turbulent fluxes during blowing snow: Field test of model sublimation predictions. *Hydrol. Processes*, **13**, 2963–2975.
- , and E. Brun, 2001: Physical properties of snow. *Snow Ecology: An Interdisciplinary Examination of Snow-Covered Ecosystems*, H. G. Jones et al., Eds., Cambridge University Press, 45–126.
- Prasad, R., D. G. Tarboton, G. E. Liston, C. H. Luce, and M. S. Seyfried, 2001: Testing a blowing snow model against distributed snow measurements at Upper Sheep Creek. *Water Resour. Res.*, **37**, 1341–1357.
- Putnins, P., 1970: The climate of Greenland. *Climates of the Polar Regions*, S. Orvig, Ed., World Survey of Climatology, Vol. 12, Elsevier, 3–112.
- Ramillien, G., A. Lombard, A. Cazanave, E. R. Ivins, M. Llubes, F. Remy, and R. Biancali, 2006: Interannual variations of the mass balance of the Antarctic and Greenland ice sheet from GRACE. *Global Planet. Change*, **53**, 198–208.
- Reeh, N., C. Mayer, H. Miller, H. H. Thomson, and A. Weidick, 1999: Present and past climate control on fjord glaciations in Greenland: Implications for IRD-deposition in the sea. *Geophys. Res. Lett.*, **26**, 1039–1042.
- Rignot, E., and P. Kanagaratnam, 2006: Changes in the velocity structure of the Greenland Ice Sheet. *Science*, **311**, 986–990.
- Ryan, B. C., 1977: A mathematical model for diagnosis and prediction of surface winds in mountainous terrain. *J. Appl. Meteorol.*, **16**, 1547–1564.
- Rysgaard, S., T. Vang, M. Stjernholm, B. Rasmussen, A. Windelin, and S. Kiilsholm, 2003: Physical conditions, carbon transport, and climate change impacts in a northeast Greenland fjord. *Arct. Antarct. Alp. Res.*, **35**, 301–312.
- Scambos, T., and T. Haran, 2002: An image-enhanced DEM of the Greenland Ice Sheet. *Ann. Glaciol.*, **34**, 291–298.
- Serreze, M. C., and R. G. Barry, 2005: *The Arctic Climate System*. Cambridge Atmospheric and Space Science Series, Cambridge University Press, 424 pp.
- , and Coauthors, 2000: Observational evidence of recent change in the northern high-latitude environment. *Climatic Change*, **46**, 159–207.
- , and Coauthors, 2006: The large-scale freshwater cycle of the Arctic. *J. Geophys. Res.*, **111**, C11010, doi:10.1029/2005JC003424.
- Sturm, M., J. Schimel, G. Michaelson, J. M. Welker, S. F. Oberbauer, G. E. Liston, J. Fahnestock, and V. E. Romanovsky, 2005: Winter biological processes could help convert Arctic tundra to shrubland. *Bioscience*, **55**, 17–26.
- Su, F., J. C. Adam, K. E. Trenberth, and D. P. Lettenmaier, 2006: Evaluation of surface water fluxes of the pan-Arctic land region with a land surface model and ERA-40 reanalysis. *J. Geophys. Res.*, **111**, D05110, doi:10.1029/2005JD006387.

- Tarboton, D. G., T. G. Chowdhury, and T. H. Jackson, 1995: A spatially distributed energy balance snowmelt model. *Biogeochemistry of Seasonally Snow-Covered Catchments*, K. A. Tonnessen, M. W. Williams, and M. Tranter, Eds., IAHS Publ. 228, 141–155.
- Tedesco, M., 2007: A new record in 2007 for melting in Greenland. *Eos, Trans. Amer. Geophys. Union*, **88**, 383.
- Thomas, R. E., F. W. Krabill, S. Manizade, and C. Martin, 2006: Progressive increase in ice loss from Greenland. *Geophys. Res. Lett.*, **33**, L10503, doi:10.1029/2006GL026075.
- Thornton, P. E., S. W. Running, and M. A. White, 1997: Generating surfaces of daily meteorological variables over large regions of complex terrain. *J. Hydrol.*, **190**, 214–251.
- Van de Wal, R. S. W., 1996: Mass balance modelling of the Greenland Ice Sheet: A comparison of an energy balance and a degree-day model. *Ann. Glaciol.*, **23**, 36–45.
- Velicogna, I., and J. Wahr, 2006: Acceleration of Greenland ice mass loss in spring 2004. *Nature*, **443**, 329–331.
- Vorosmarty, C. J., and Coauthors, 2001: The hydrological cycle and its role in Arctic and global environmental change: A rationale and strategy for synthesis study. Arctic Research Consortium of the United States, Fairbanks, AK, 84 pp.
- Walcek, C. J., 1994: Cloud cover and its relationship to relative humidity during a spring midlatitude cyclone. *Mon. Wea. Rev.*, **122**, 1021–1035.
- Winstral, A., and D. Marks, 2002: Simulating wind fields and snow redistribution using terrain-based parameters to model snow accumulation and melt over a semi-arid mountain catchment. *Hydrol. Processes*, **16**, 3585–3603.
- Zwally, J. H., and M. B. Giovinetto, 2001: Balance mass flux and ice velocity across the equilibrium line in drainage systems of Greenland. *J. Geophys. Res.*, **106** (33), 717–728.



[16]

Mernild, S. H., Mote, T., and Liston, G. E. 2011. Greenland Ice Sheet surface melt extent and trends, 1960–2010. *Journal of Glaciology*, 57(204), 621–628.

Reprinted with permission from International Glaciological Society

# Greenland ice sheet surface melt extent and trends: 1960–2010

Sebastian H. MERNILD,<sup>1</sup> Thomas L. MOTE,<sup>2</sup> Glen E. LISTON<sup>3</sup>

<sup>1</sup>*Climate, Ocean and Sea Ice Modeling Group, Computational Physics and Methods, Los Alamos National Laboratory, Los Alamos, New Mexico 87545, USA*

*E-mail: mernild@lanl.gov*

<sup>2</sup>*Department of Geography, University of Georgia, Athens, Georgia 30602-2502 USA*

<sup>3</sup>*Cooperative Institute for Research in the Atmosphere, Colorado State University, Fort Collins, Colorado 80523-1375, USA*

**ABSTRACT.** Observed meteorological data and a high-resolution (5 km) model were used to simulate Greenland ice sheet surface melt extent and trends before the satellite era (1960–79) and during the satellite era through 2010°. The model output was compared with passive microwave satellite observations of melt extent. For 1960–2010 the average simulated melt extent was  $15 \pm 5\%$ . For the period 1960–72, simulated melt extent decreased by an average of 6%, whereas 1973–2010 had an average increase of 13%, with record melt extent in 2010. The trend in simulated melt extent since 1972 indicated that the melt extent in 2010 averaged twice that in the early 1970s. The maximum and mean melt extents for 2010 were 52% ( $\sim 9.5 \times 10^5 \text{ km}^2$ ) and 28% ( $\sim 5.2 \times 10^5 \text{ km}^2$ ), respectively, due to higher-than-average winter and summer temperatures and lower-than-average winter precipitation. For 2010, the southwest Greenland melt duration was 41–60 days longer than the 1960–2010 average, while the northeast Greenland melt duration was up to 20 days shorter. From 1960 to 1972 the melting period (with a >10% melt extent) decreased by an average of  $3 \text{ days a}^{-1}$ . After 1972, the period increased by an average of  $2 \text{ days a}^{-1}$ , indicating an extended melting period for the ice sheet of about 70 days: 40 and 30 days in spring and autumn, respectively.

## INTRODUCTION

The Greenland ice sheet (GrIS) is the largest reservoir of permanent snow and ice in the Northern Hemisphere ( $\sim 7 \text{ m}$  sea-level equivalent) and is highly sensitive to climate changes (e.g. Bamber and others, 2001; Box and others, 2006). Satellite-based observations indicate that in 2007 and 2010 the GrIS had record surface melt extent (Mote, 2007; Tedesco, 2007; Steffen and others, 2008; Tedesco and others, 2011; J.E. Box and others, <http://www.arctic.noaa.gov/reportcard/greenland.html>) accompanied by unusually high freshwater runoff to the ocean (Mernild and Hasholt, 2009). The extent and duration of surface melting are important for a number of reasons. An altered melting regime can produce substantial differences in surface albedo and energy and moisture balances, especially because wet snow absorbs up to three times more incident solar energy than dry snow (Steffen, 1995). Further, an altered melt regime can influence the ice sheet's surface mass balance (SMB) and runoff and its dynamic and subglacial sliding processes. Mechanisms that link climate, surface hydrology, internal drainage and ice dynamics are poorly understood, and numerical ice-sheet models do not simulate these changes realistically (Nick and others, 2009). This was one of the main reasons why the Intergovernmental Panel on Climate Change (IPCC) Fourth Assessment Report (AR4; Solomon and others, 2007) did not include future predictions for GrIS mass loss contribution related to global sea-level rise. Without a deeper understanding of the surface/dynamic-sliding interactions and the subsequent hydrodynamic response of ice sheets, neither a best estimate nor an upper bound of future sea-level rise is reliable. Therefore, to quantify and predict GrIS mass loss, including runoff conditions, knowledge about its long-term variations in surface melt extent and trends, including the temporal and spatial distributions, melt intensity and duration, needs to be further developed. This surface meltwater runoff represents

about half the annual mass loss from the GrIS (Zwally and Giovinetto, 2001; Rignot and Kanagaratnam, 2006), with iceberg calving generating approximately the other half.

In this paper, we examine the duration, extent and magnitude of the GrIS surface melting from 1960 through 2010. Melting is simulated using SnowModel, a spatially distributed meteorological snow and ice model (Liston and Elder, 2006a,b; Mernild and Liston, 2010) forced with observed meteorological data for the period when reliable forcing data are available. We compare results with observations during the satellite era (1979–2010) and we simulate GrIS melting conditions and trends from 1960 to 2010. Further, we examine whether the 2010 record melt season lies outside the natural melt variability since 1960.

## METHODOLOGY AND DATA

SnowModel (Liston and Elder, 2006a,b; Mernild and others, 2006) is a spatially distributed system for modeling meteorological conditions, snow evolution, snow and ice melting and runoff, given surface meteorological forcing. It simulates surface energy and moisture exchanges, including snow and glacier melt, multi-layer heat- and mass-transfer processes in snow (e.g. snowpack temperature and density evolution) and ice hydrological features such as meltwater routing from the surface through snow, firn and glacial ice. SnowModel routines have been described and tested by, for example, Liston and Elder (2006a,b), Liston and others (2007), Liston and Hiemstra (2008, in press), Mernild and others (2008, 2009, 2010, 2011) and Mernild and Liston (2010) and used successfully in a variety of snow and glacier environments, including the Arctic and Antarctic.

Atmospheric forcing required by SnowModel is provided by MicroMet (Liston and Elder, 2006b), which assimilates and interpolates time series of air temperature, relative humidity, wind speed and direction and precipitation from

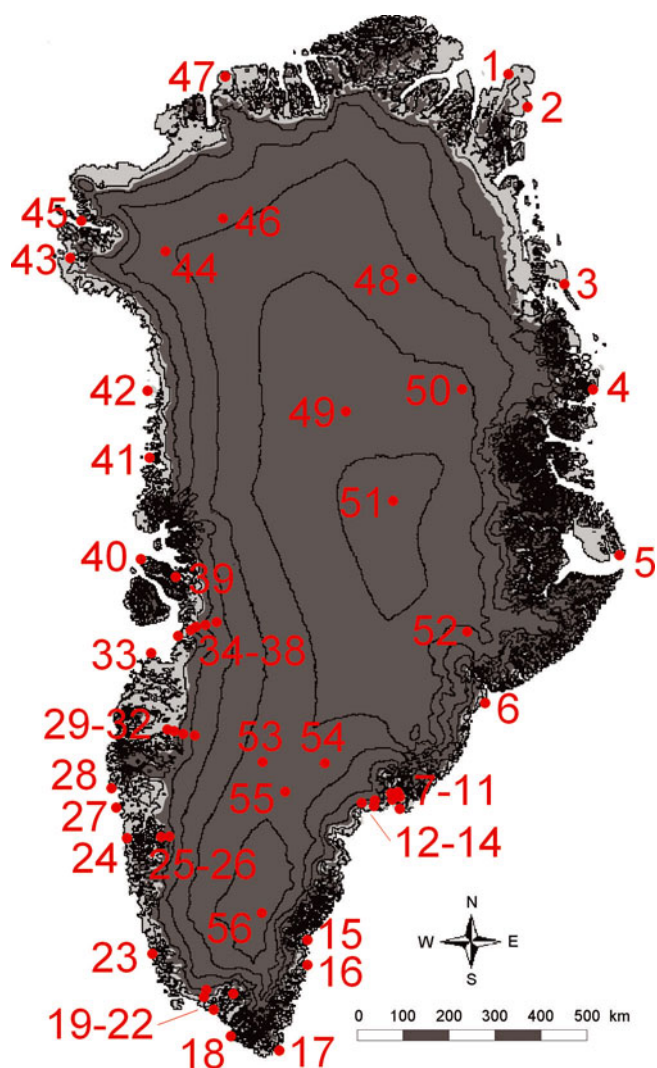


**Fig. 1.** Greenland simulation domain with topography (500 m contour interval) and the location of the coastal and GrIS meteorological tower stations (red dots). Station specifications are provided in Table 1.

surface meteorological stations near or within the simulation domain. MicroMet uses known relationships between meteorological variables and the surrounding landscape (e.g. topography and surface characteristics) to distribute these variables in physically plausible and computationally efficient ways (e.g. Liston and others, 2007; Liston and Hjemstra, 2011). Data are interpolated horizontally to a regular grid using a Barnes objective analysis scheme (Barnes, 1964, 1973; Koch and others, 1983) that applies a Gaussian distance-dependent weighting function. Interpolation weights are determined objectively as a function of data spacing and distribution. At each time-step, air temperature, solar radiation, albedo, outgoing longwave radiation, latent heat flux, sensible heat flux, snowmelt, sublimation, snowmelt runoff, snow depth and snow water equivalent are calculated and made accessible to SnowModel. The SnowModel simulated melt extent (for each daily time-step) was determined by summing the number of gridcells where simulated melt occurred.

Melt simulations were performed on daily time-steps based on: (1) a 5 km digital elevation model (Bamber and others, 2001) and land cover from the US Geological Survey (USGS) North American Land Cover Characteristics

Database, version 2.0 ([http://edcdaac.usgs.gov/glcc/na\\_int.html](http://edcdaac.usgs.gov/glcc/na_int.html)) and (2) observed atmospheric forcing data from 56 meteorological stations located both in coastal areas and on the GrIS (Fig. 1; Table 1). The simulations covered the period September 1959 through December 2010. User-defined constants used in the simulations are listed by Mernild and others (2009).

Using the increase in microwave emissivity as liquid water forms in previously dry snow (Stiles and Ulaby, 1980), passive microwave satellite sensors were used to determine surface and near-surface melt occurrence for comparison with the SnowModel results. A microwave emission model was used to determine the brightness temperature ( $T_B$ ) associated with 1% volumetric water content each year for locations across the GrIS using the dynamic threshold algorithm given by Mote and Anderson (1995). These modeled  $T_B$  values are used as threshold values to distinguish melt from non-melt during the summer of a given year. While Mote and Anderson (1995) used the 37 GHz frequency, this study used the 18 GHz scanning multichannel microwave radiometer (SMMR) and 19.35 GHz Special Sensor Microwave/Imager (SSM/I), following Mote (2007).

The 18 GHz horizontally polarized channel from SMMR (January 1979 to June 1987; <http://nsidc.org/data/nsidc-0007.html>) and 19.35 GHz channel from SSM/I (July 1987 to September 2010; <http://nsidc.org/data/nsidc-0001.html>)  $T_B$  data were extracted from the US National Snow and Ice Data Center polar stereographic daily grids with a nominal 25 km gridcell increment. The emission model simulated the  $T_B$  values associated with melt for each gridcell each year. The melt area was determined by summing the total area covered by cells where the observed  $T_B$  exceeded the modeled threshold  $T_B$ . A comparison of SSM/I melt occurrence with infrared land surface temperatures from the Moderate Resolution Imaging Spectroradiometer (MODIS) in 2006 and 2007 showed that the SSM/I indicated 5–8% greater melt area; the two products agreed for 93% of non-cloud-contaminated cells.

## RESULTS AND DISCUSSION

Since 1960, the maximum modeled GrIS melt extent has been in 2010 and the minimum in 1972 (Fig. 2a). For 2010, the maximum melt extent was  $\sim 9.5 \times 10^5 \text{ km}^2$ , or 52% of the GrIS surface. This slightly exceeded the previous record of 51% set in 2007 and was significantly above the 51 year average of 34%. The modeled standard deviation in melt extent from 1960 to 2010 was 9% ( $\sim 6.2 \pm 1.7 \times 10^5 \text{ km}^2$ ). For 1972, a melt extent of 17% ( $\sim 3.1 \times 10^5 \text{ km}^2$ ) was simulated (Fig. 2a). In contrast to the simulated values, the satellite-derived area that underwent melting was more extensive in 2002 than in 2010 (Fig. 3a), indicating surface melt on 80% ( $\sim 13.2 \times 10^5 \text{ km}^2$ ) of the ice sheet. The SSM/I satellite-derived maximum 2002 melt extent is different from the results based on cross-polarized gradient ratio (XPGR) algorithms (Abdalati and Steffen, 1997; Steffen and others, 2008 and updated), where 2010 was a record year, close to values from 2007 (personal communication from K. Steffen, 2010). A possible reason for the extremely high SSM/I satellite-observed 2002 melt extent might be the greater sensitivity of the dynamic threshold algorithm to melt onset compared with the XPGR algorithm (Anderson and others, 1996). Furthermore, while the dynamic threshold algorithm

**Table 1.** Meteorological input data for the GrIS melt extent simulations. Stations were operated and data were provided by the Danish Meteorological Institute (DMI), University of Colorado at Boulder (CU), Geological Survey of Denmark and Greenland (GEUS), University of Copenhagen (UC) and University of Utrecht (UU). Parameters are Ta: air temperature; Rh: relative humidity; Ws: wind speed; Wd: wind direction; and P: precipitation. For station locations see Figure 1

Station No.	Station name	Grid	Altitude m a.s.l.	Data period	Parameters	Operated by
1	Station Nord	81°36'00" N, 16°39'00" W	36	1 Sept 1961 to 9 Jul 2007	Ta, Rh, Ws,Wd, P	DMI
2	Henrik Krøyer Holme	80°39'00" N, 13°43'00" W	10	1 Sept 1985 to current	Ta, Rh, Ws,Wd	DMI
3	Danmarkshavn	76°46'00" N, 18°40'00" W	11	1 Sept 1959 to current	Ta, Rh, Ws,Wd, P	DMI
4	Daneborg	74°18'00" N, 20°13'00" W	44	1 Sept 1959 to current	Ta, Rh, Ws,Wd, P	DMI
5	Ittoqqortoormiit	70°29'00" N, 21°57'00" W	66	1 Nov 1980 to current	Ta, Rh, Ws,Wd, P	DMI
6	Aputiteeq	67°47'00" N, 32°18'00" W	13	1 Sept 1959 to 9 Feb 1987	Ta, Rh, Ws,Wd, P	DMI
7	Tasiilaq	65°36'00" N, 37°38'00" W	44	1 Sept 1959 to current	Ta, Rh, Ws,Wd, P	DMI
8	Sermilik, Station Coast_L	65°41'00" N, 37°55'00" W	25	25 Jun 1993 to current	Ta, Rh, Ws,Wd	UC, IGG*
9	Sermilik, Station Coast_U	65°40'20" N, 37°54'10" W	190	1 Aug 2009 to current	Ta, Rh, Ws,Wd	UC, IGG
10	Sermilik, Station Nunatak	65°42'00" N, 37°49'00" W	515	1 Jun 1997 to current	Ta, Rh, Ws,Wd	UC, IGG
11	MIT	65°41'33" N, 37°49'34" W	460	3 May 2009 to 29 Oct 2010	Ta, Rh, Ws	GEUS
12	TAS_L	65°38'00" N, 38°54'00" W	270	26 Jun 2006 to 12 Feb 2010	Ta, Rh,Ws, Wd	GEUS
13	TAS_U	65°42'00" N, 38°52'00" W	580	16 Apr 2004 to 26 Oct 2010	Ta, Rh, Ws,Wd	GEUS
14	KULU	65°45'00" N, 38°36'00" W	880	20 Jun 1999 to 13 Sept 2000	Ta, Rh, Ws,Wd	CU, CIRES (GC-NET)†
15	Timmiarmiut	62°32'00" N, 42°08'00" W	10	1 Sept 1959 to 30 Jun 1979	Ta, Rh, Ws,Wd, P	DMI
16	Ikermiuarsuk	61°56'00" N, 42°04'00" W	39	18 Jun 1980 to current	Ta, Rh, Ws,Wd	DMI
17	Ikerassuaq	60°03'00" N, 43°10'00" W	88	1 Sept 1959 to current	Ta, Rh, Ws,Wd, P	DMI
18	Nanortalik	60°08'00" N, 45°13'00" W	21	2 Jan 1961 to current	Ta, Rh, Ws,Wd, P	DMI
19	Qaqortoq	60°43'00" N, 46°03'00" W	32	1 Jan 1961 to current	Ta, Rh, Ws,Wd, P	DMI
20	Mitt. Narsarsuaq	61°10'00" N, 45°25'00" W	27	1 Jan 1961 to current	Ta, Rh, Ws,Wd, P	DMI
21	QAS_L	61°01'54" N, 45°50'54" W	310	9 May 2003 to 31 Jul 2010	Ta, Rh, Ws,Wd	GEUS
22	QAS_U	61°10'42" N, 46°49'00" W	890	7 Aug 2008 to 19 Jul 2010	Ta, Rh, Ws,Wd	GEUS
23	Paamiut	62°00'00" N, 49°40'00" W	13	1 Sept 1959 to current	Ta, Rh, Ws,Wd, P	DMI
24	Nuuk	64°10'00" N, 51°45'00" W	80	1 Sept 1959 to current	Ta, Rh, Ws,Wd, P	DMI
25	NUK_L	64°28'54" N, 49°31'42" W	560	20 Aug 2007 to 30 Oct 2010	Ta, Rh, Ws,Wd	GEUS
26	NUK_U	64°29'54" N, 49°15'54" W	1140	20 Aug 2007 to 26 Oct 2010	Ta, Rh, Ws,Wd	GEUS
27	Sioralik	65°01'00" N, 52°33'00" W	14	16 Jun 1983 to current	Ta, Rh, Ws,Wd	DMI
28	Mitt. Maniitsoq	65°25'00" N, 52°56'00" W	28	6 Dec 2000 to current	Ta, Rh, Ws,Wd	DMI
29	Kangerlussuaq	67°01'00" N, 50°42'00" W	50	1 May 1973 to current	Ta, Rh, Ws,Wd, P	DMI
30	Station S5	67°06'00" N, 50°07'00" W	490	1 Sept 2006 to 18 Aug 2010	Ta, Rh, Ws	UU
31	Station S6	67°05'00" N, 49°23'00" W	1020	1 Sept 2006 to 14 Jul 2010	Ta, Rh, Ws	UU
32	Station S9	67°03'00" N, 48°14'00" W	1520	1 Sept 2006 to 14 Aug 2010	Ta, Rh, Ws	UU
33	Aasiaat	68°42'00" N, 52°45'00" W	43	1 Jan 1959 to current	Ta, Rh, Ws,Wd, P	DMI
34	Mitt. Ilulissat	69°14'00" N, 51°04'00" W	29	15 Aug 1991 to current	Ta, Rh, Ws,Wd	DMI
35	JAR1	69°29'51" N, 49°41'16" W	962	20 Jun 1996 to 12 May 2010	Ta, Rh, Ws,Wd	CU, CIRES (GC-NET)
36	JAR2	69°25'09" N, 50°03'55" W	542	2 Jun 1999 to 14 May 2010	Ta, Rh, Ws,Wd	CU, CIRES (GC-NET)
37	JAR3	69°23'40" N, 50°18'36" W	283	1 Jan 2001 to 24 May 2004	Ta, Rh, Ws,Wd	CU, CIRES (GC-NET)
38	Swiss Camp	69°34'03" N, 49°19'17" W	1.140	1 Jan 1995 to 10 May 2010	Ta, Rh, Ws,Wd	CU, CIRES (GC-NET)
39	Uummanaq	70°40'00" N, 52°07'00" W	39	1 Jan 1961 to 30 Jun 2006	Ta, Rh, Ws,Wd, P	DMI
40	Nuussuaq	70°41'00" N, 54°37'00" W	27	1 Jan 1961 to current	Ta, Rh, Ws,Wd, P	DMI
41	Upernavik	72°47'00" N, 56°10'00" W	120	25 Oct 2000 to current	Ta, Rh, Ws,Wd	DMI
42	Kitsissorsuit	74°02'00" N, 57°49'00" W	40	10 Sept 1981 to current	Ta, Rh, Ws,Wd	DMI
43	Pituffik	76°32'00" N, 68°45'00" W	77	1 Jan 1974 to 27 Nov 2006	Ta, Rh, Ws,Wd, P	DMI
44	GITS	77°08'16" N, 61°02'24" W	1869	7 Jun 1995 to 2 May 2007	Ta, Rh, Ws,Wd	CU, CIRES (GC-NET)
45	Qaanaaq	77°28'00" N, 69°13'00" W	16	10 Aug 1995 to 13 Oct 2004	Ta, Rh, Ws,Wd	DMI
46	Humboldt	78°31'36" N, 56°49'50" W	1995	22 Jun 1995 to 30 Apr 2008	Ta, Rh, Ws,Wd	CU, CIRES (GC-NET)
47	Hall Land	81°41'00" N, 59°57'00" W	105	30 Aug 1982 to 6 Sept 2007	Ta, Rh, Ws,Wd	DMI
48	Tunu-N	78°00'59" N, 33°59'00" W	2052	17 May 1995 to 1 May 2008	Ta, Rh, Ws,Wd	CU, CIRES (GC-NET)
49	NorthGRIP	75°05'59" N, 42°19'57" W	2950	9 Jul 1997 to 8 May 2010	Ta, Rh, Ws,Wd	CU, CIRES (GC-NET)
50	NASA-E	75°00'02" N, 29°59'50" W	2614	3 May 1997 to 2 May 2008	Ta, Rh, Ws,Wd	CU, CIRES (GC-NET)
51	Summit	72°34'47" N, 38°30'18" W	3208	14 May 1995 to 16 Aug 2010	Ta, Rh, Ws,Wd	CU, CIRES (GC-NET)
52	KAR	69°41'58" N, 33°00'21" W	2579	18 May 1998 to 7 Jun 2005	Ta, Rh, Ws,Wd	CU, CIRES (GC-NET)
53	DYE-2	66°28'48" N, 46°16'44" W	2165	25 May 1995 to 30 Apr 2010	Ta, Rh, Ws,Wd	CU, CIRES (GC-NET)
54	NASA-SE	66°28'45" N, 42°29'56" W	2393	24 Apr 1998 to 29 Apr 2010	Ta, Rh, Ws,Wd	CU, CIRES (GC-NET)
55	Saddle	65°59'58" N, 44°30'03" W	2456	20 Apr 1997 to 26 Apr 2009	Ta, Rh, Ws,Wd	CU, CIRES (GC-NET)
56	South Dome	63°08'56" N, 44°49'02" W	2901	23 Apr 1997 to 30 Jun 2008	Ta, Rh, Ws,Wd	CU, CIRES (GC-NET)

\*Institute for Geography and Geology, University of Copenhagen.

†Cooperative Institute for Research in Environmental Sciences (Greenland Climate Network).



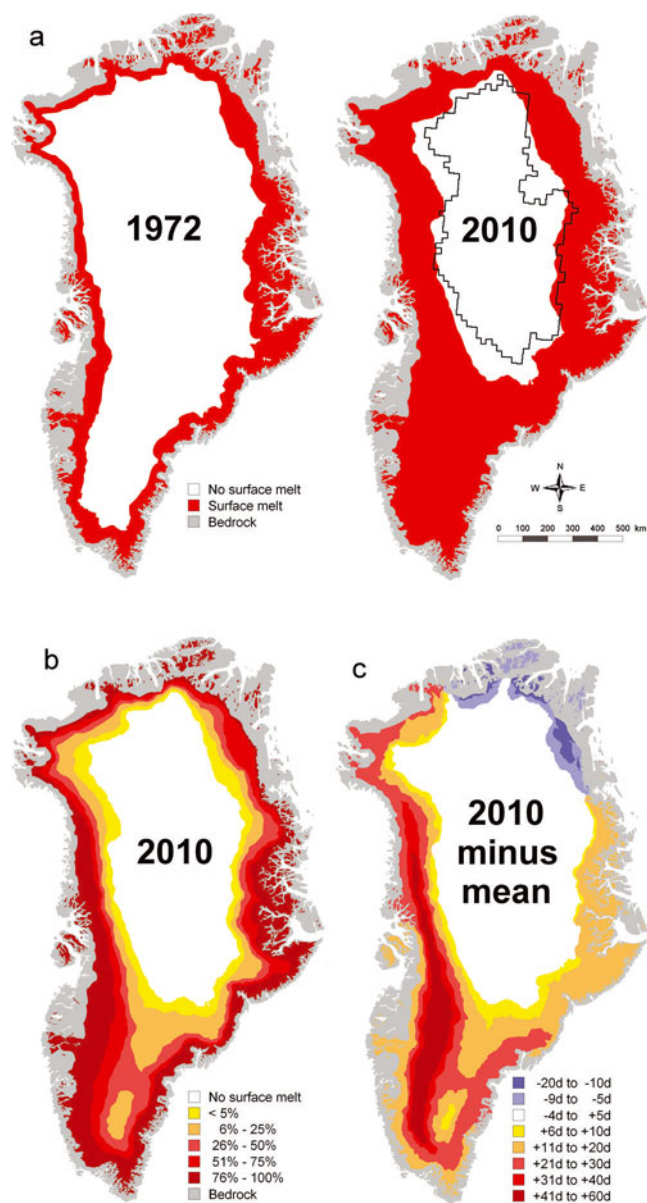


**Fig. 2.** (a) Maximum simulated GrIS surface melt extent for 1972 (the year with minimum melt extent within the time series 1960–2010) and 2010 (the year with maximum melt extent). The satellite-derived boundary between melting and melt-free areas is shown for 2010 (bold black curve). (b) Simulated 2010 melt frequency in percentage of total melt days. (c) The difference between 2010 simulated melt duration and the 1960–2010 mean, in days.

used here showed a slightly greater total area underwent melt in 2002, it also showed that 2007 and 2010 had more frequent melt and longer melt seasons than 2002. For 2010, simulated surface melting occurred at elevations as high as 3000 m a.s.l., whereas for 1972 surface melting occurred only up to 2400 m a.s.l. Simulated melt extent was distributed largely as expected, with no melting at higher elevations in the interior of the GrIS (Fig. 2a), while marginal regions had surface melt 76–100% of the time during the summer (May to September), with melting most pronounced in southwest Greenland (Fig. 2b).

In Figure 2a, the maximum simulated 2010 melt extent is compared with satellite-derived melt extent. The simulated boundary between melting and melt-free areas is highly consistent with the satellite-derived boundary, with an

average discrepancy of  $40 \pm 35$  km. The discrepancy was larger (up to  $\sim 160$  km) in the northeast and northwest and in the southern part of the interior. Differences between satellite-derived and simulated results were most pronounced where the distance between meteorological stations was largest. However, the general correspondence between simulations and observations supports the use of SnowModel for analyzing melting conditions before the satellite era (1960–79) when reliable atmospheric forcing data are available.

The difference between the 2010 melt duration and the 1960–2010 mean is illustrated in Figure 2c. The melt duration in 2010 was 41–60 days longer than the 1960–2010 average, with the largest differences occurring at the southwestern and western margins of the ice sheet at elevations up to  $\sim 2000$  m a.s.l. According to meteorological observations and US National Centers for Environmental Prediction/US National Center for Atmospheric Research (NCEP/NCAR) reanalysis data, this melting was consistent with anomalous warm airflow from the south during spring and summer, and record high winter air temperature leading to warm pre-melt conditions (Box and others, <http://www.arctic.noaa.gov/reportcard/greenland.html>), along with somewhat lower-than-average winter precipitation. Low winter snowfall led to earlier exposure of glacier ice and of the previous year's summer snow surface; these surfaces have a lower albedo than fresh snow, promoting greater solar absorption and increased melting (Oke, 1987; Douville and others, 1995). For example, at Nuuk ( $64.2^\circ$  N along Greenland's west coast) the 2009/10 winter, spring and summer were the warmest since record-keeping began in 1873. Similarly, Aasiaat ( $69.0^\circ$  N along Greenland's west coast) had its warmest year since record-keeping began in 1951 (Box and others, <http://www.arctic.noaa.gov/reportcard/greenland.html>), and Greenland's winter precipitation in 2009/10 was  $\sim 35\%$  below the 1960–2010 average.

Melt durations in low-elevation areas along the southeast and east margins were up to 30 and 20 days longer than average, respectively. Along the northeastern portion of the ice-sheet margin, where winter temperatures were lower than average, the 2010 melt duration was up to 20 days less than the long-term average, probably due to regional variability in the atmospheric circulation and a late start to the melt season because of a greater cold content of the snowpack. As a whole, the 2010 GrIS melt duration was  $14 \pm 16$  days longer than the 1960–2010 average, with a longer than average melt season on 89% of the GrIS. Because our model simulations were performed at relatively high resolution, the spatial heterogeneity in duration was greater than that of coarser-resolution satellite observations as described, for example, by Mote (2007 and updated) and Box and others (<http://www.arctic.noaa.gov/reportcard/greenland.html>). Overall, however, the simulated melt duration was consistent with the pattern identified by Box and others (<http://www.arctic.noaa.gov/reportcard/greenland.html>, fig. GL3) for 1979–2010 (Fig. 2c).

For 1960–2010, time series of simulated maximum melt extent showed interannual variability superimposed on a period from 1960 to 1972 that can be approximated by a linear decreasing trend ( $p < 0.10$ , where  $p$  is level of significance) of 7% ( $\sim 1.2 \times 10^5$  km<sup>2</sup>) of the total area of the GrIS (Fig. 3a). After 1972, the maximum melt extent increased significantly ( $p < 0.01$ ) by 22% ( $\sim 3.7 \times 10^5$  km<sup>2</sup>) of the GrIS area, consistent overall with the increase in GrIS



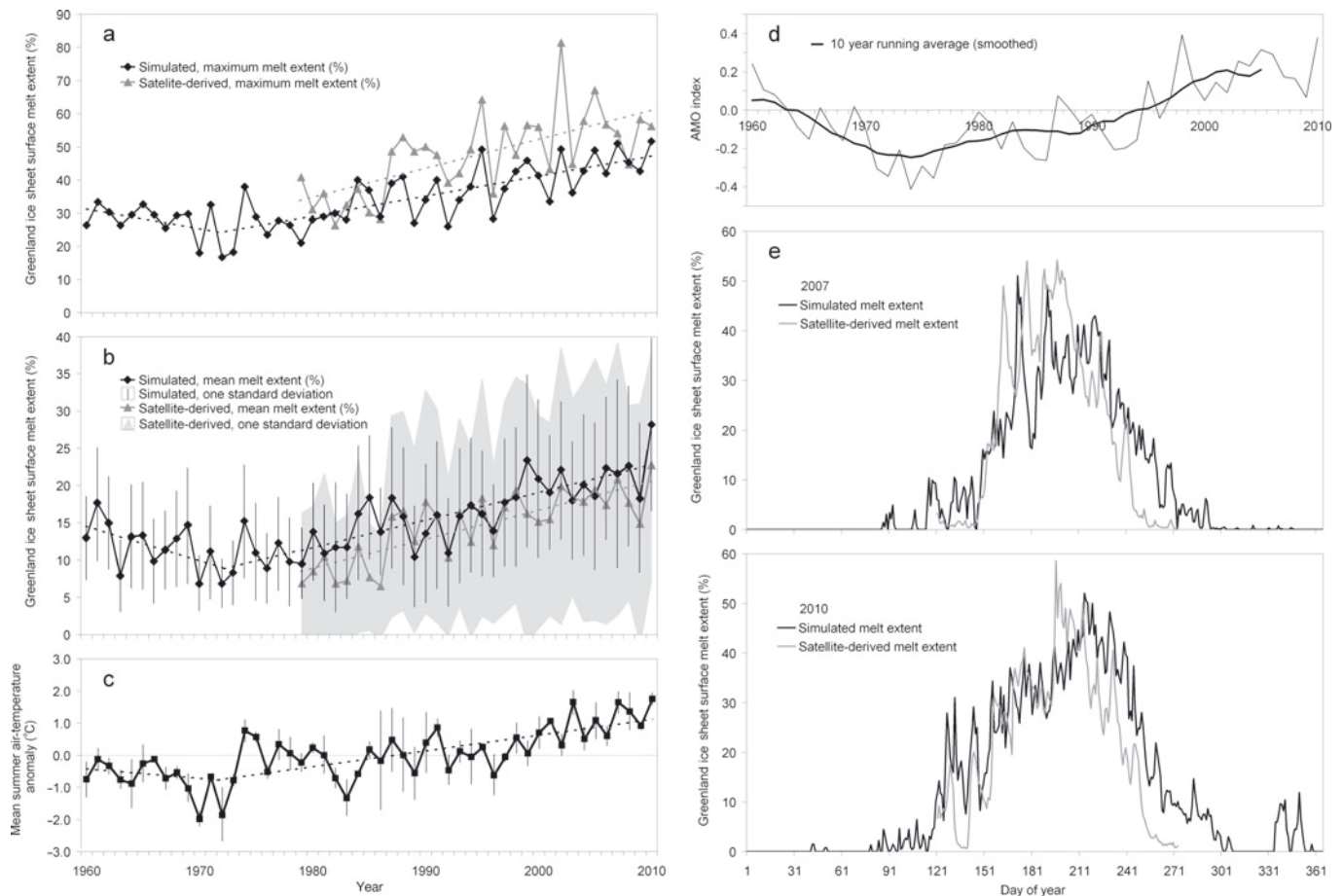


**Fig. 3.** (a) Time series of simulated annual maximum GrIS melt extent (1960–2010) and satellite-derived maximum melt extent (1979–2010). (b) Time series of seasonal mean (May through September) simulated (1960–2010) and satellite-derived (1979–2010) GrIS melt extent and standard deviation. (c) Mean Greenland summer air temperature anomaly with standard deviation (1960–2010). (d) Unsmoothed and smoothed Atlantic multi-decadal oscillation index (<http://www.esrl.noaa.gov/psd/data/timeseries/AMO/>). (e) Simulated and satellite-derived seasonal melt extent in 2007 and 2010.

maximum melt extent estimated by Fettweis and others (2011). Likewise, the satellite-derived maximum melt extent (Fig. 3a) increased significantly ( $p < 0.01$ ) by 27% ( $\sim 4.4 \times 10^5 \text{ km}^2$ ) from 1979 to 2010 and is in general agreement with the SnowModel results. The correlation between satellite-derived maximum melt extent and the simulated maximum melt extent is  $r^2 = 0.56$  (based on linear regression; where  $r^2$  is the explained variance), indicating a statistical significance at the 95% level ( $p < 0.05$ ; i.e. there is <5% probability that such a correlation between the two time series can be produced by chance) and an rmse of 55%.

The maximum melt extents shown in Figures 2 and 3a are snapshots of surface melt. For studying seasonal climate impacts on SMB and runoff, it can be more appropriate to study the mean of integrated seasonal melt extent, as shown in Figure 3b. The simulated mean annual melt extent was  $15 \pm 5\%$  (1960–2010), and the simulated mean melt extent of  $17 \pm 4\%$  ( $\sim 3.0 \pm 0.7 \times 10^5 \text{ km}^2$ ) (1979–2010) is significant (97.5% quantile) compared with the satellite-derived melt extent of  $15 \pm 5\%$  ( $\sim 2.6 \pm 0.8 \times 10^5 \text{ km}^2$ ) and within one standard deviation of the observed values (Fig. 3b). For the mean modeled melt extent, a significant ( $p < 0.01$ ) decreasing trend amounting to 6% of the GrIS area ( $\sim 1.1 \times 10^5 \text{ km}^2$ ) occurred from 1960 to 1972. After 1972, the GrIS exhibited a reversal of this trend, with a significantly increasing trend in melt extent of 13% of the GrIS area ( $2.4 \times 10^5 \text{ km}^2$ ) found

in the simulations (1972–2010;  $p < 0.01$ ) and a slightly smaller increase of 12% ( $\sim 2.0 \times 10^5 \text{ km}^2$ ) derived from the satellite observations (1979–2010;  $p < 0.01$ ), meaning that larger areas of dry snow were turned into percolation facies. The simulated melt extent since 1972 indicates that the melt extent in 2010 averaged more than twice that of the early 1970s. Many studies have demonstrated that the GrIS melt extent is greater than in the past (Mote, 2007; Tedesco, 2007; Hanna and others, 2008; Steffen and others, 2008; Mernild and others, 2009, 2010; Fettweis and others, 2011; Tedesco and others, 2011; Box and others, <http://www.arctic.noaa.gov/reportcard/greenland.html>) and SnowModel results offer additional confirmation of these trends at a higher resolution. The increase in melt extent is associated with an observed rise in Greenland mean summer air temperature of  $2.3^\circ\text{C}$  for 1972–2010 (Fig. 3c) and with a rise in coastal Greenland summer temperatures of  $1.7^\circ\text{C}$  based on available long-term weather-station data for 1991–2006 (Hanna and others, 2008). Furthermore, the overall trends in mean melt extent (Fig. 3b) seem to correlate with the smoothed trends of the Atlantic multi-decadal oscillation (AMO) index (Fig. 3d). From 1960 to the beginning of the 1970s the smoothed AMO index decreased on average and thereafter it increased towards 2010, analogous with the trends in melt extent for the GrIS. Chylek and others (2010) showed that the Arctic detrended temperatures were highly correlated with AMO,

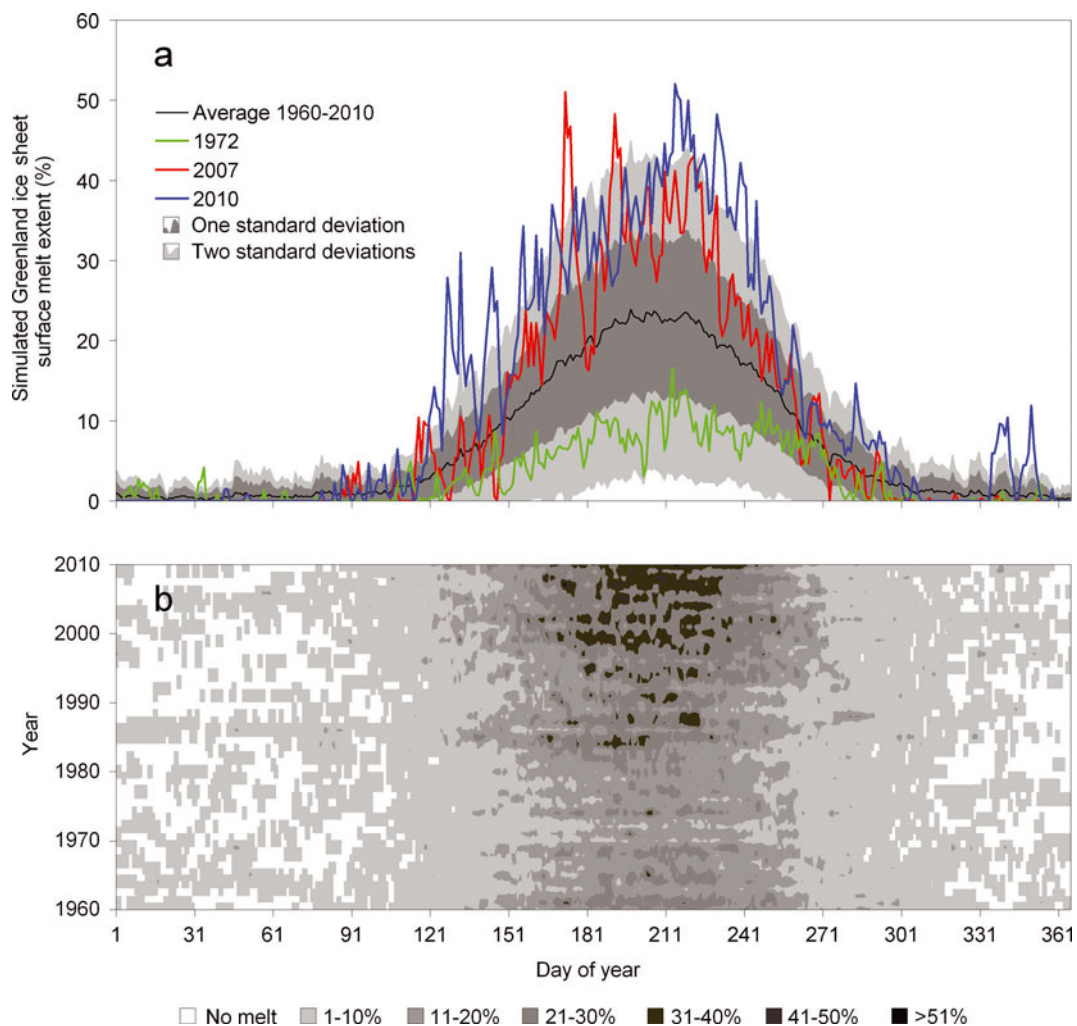


**Fig. 4.** (a) Time series of maximum daily simulated GrIS melt extent from 1972, 2007, 2010 and average 1960–2010, including standard deviations. (b) Maximum daily simulated GrIS melt extent from January through December for 1960–2010.

suggesting the Atlantic Ocean as a possible source of Arctic climate variability.

The impacts from major episodic volcanic eruptions (e.g. Agung, Indonesia (1963), El Chichón, Mexico (1982) and Pinatubo, Philippines (1991)) do not appear to have a significant impact on melt extent variations (Fig. 3b), even though, as stated by Hanna and others (2005), global dust veils generated by volcanic activity might cool the polar regions and suppress ice-sheet melt.

According to simulations, the GrIS had the lowest mean melt extent of 7% ( $\sim 1.2 \times 10^5 \text{ km}^2$ ) in 1972 and the highest mean melt extent in 2010; the satellite observations also affirm that 2010 was a record year with respect to mean melt extent (Fig. 3b). The simulated minimum mean melt extent was due to a 1972 mean summer (June–August) temperature  $\sim 0.7 \pm 0.3^\circ\text{C}$  below the 1972–2000 baseline, and the maximum melt extent was due to a 2010 record high mean temperature  $\sim 1.9 \pm 0.6^\circ\text{C}$  above the baseline (Fig. 3) in combination with the lower than average winter precipitation. For 2010, the simulated mean melt extent was 28% ( $\sim 5.2 \times 10^5 \text{ km}^2$ ) of the total ice-sheet area and the satellite-observed melt extent was 23% ( $\sim 4.2 \times 10^5 \text{ km}^2$ ).

The interannual variability in simulated GrIS mean melt extent occurred simultaneously with observed variations in Greenland mean summer air temperatures (at a level of  $r^2 = 0.65$ ,  $p < 0.05$ ,  $\text{rmse} = 14\%$ ) (Fig. 3c). In Figure 3e, time

series of seasonal simulated and observed melt extent are shown for 2007 and 2010 (the previous and present record melting years). The variability in seasonal simulated and observed melt extent was very similar. However, by the end of the season in mid-August, the simulations for both years relative to the observations are overestimated by an average of  $11 \pm 5\%$  of the GrIS area. The average seasonal cycle for 1960–2010 indicated that melt extent in the extreme years 2007 and 2010 was about one to two standard deviations greater than average, and that 1972 (the year with minimum melt extent) was one to two standard deviations lower than average (Fig. 4a).

The trend in seasonal melt extent for the simulation period is shown in Figure 4b. From 1960 to 1972 the melting period (with a  $>10\%$  melt extent) decreased by an average of  $3 \text{ days a}^{-1}$ . After 1972 the period of  $>10\%$  melt extent increased by an average of  $2 \text{ days a}^{-1}$ , culminating in an extended melting period of  $\sim 70$  days: 40 days in spring and 30 days in spring and autumn (Fig. 4b). Not only did the melting period increase for the GrIS, but also the number of days with a maximum melt extent greater than 30%. The number of days with a melt extent greater than 30% increased from  $\sim 25$  days in 1972 to  $\sim 80$  days in 2010, indicating an increasing melt index for the GrIS, where the melt index is defined as the melting area times the number of melting days (Tedesco, 2007).

## CONCLUSION

Our findings show that GrIS melt extent reveals unambiguously that the melt period decreased from 1960 to 1972 (before satellite observations were available) and increased thereafter at a rate of 2 days  $a^{-1}$ , giving an extended melting period of 70 days, beginning 40 days earlier in spring and ending 30 days later in autumn. This increased melt period included record melt extent in 2010 and abnormally long melt duration, 41–60 days greater than average (1960–2010) at the southwestern and western margin of the ice sheet, supporting the hypothesis that 2010 was an unusually warm and dry year. Simulations of the GrIS melt extent, such as those presented here, will be crucial for understanding SMB, including runoff conditions, since surface meltwater runoff represents about half of the annual mass loss from the GrIS (Zwally and Giovinetto, 2001; Rignot and Kanagaratnam, 2006), with iceberg calving generating most of the other half.

## ACKNOWLEDGEMENTS

We thank J.E. Box and two anonymous reviewers for insightful critiques of this paper. This work was supported by grants from the Climate Change Prediction Program and the Scientific Discovery for Advanced Computing (SciDAC) program within the US Department of Energy's Office of Science, the Los Alamos National Laboratory (LANL) Director's Fellowship, LANL Institute for Geophysics and Planetary Physics, and NASA grant No. NNX08AP34A. LANL is operated under the auspices of the National Nuclear Security Administration of the US Department of Energy under contract No. DE-AC52-06NA25396. We thank the Program for Monitoring of the Greenland Ice Sheet (PROMICE; <http://www.promice.org>), the Geological Survey of Denmark and Greenland, the Danish Meteorological Institute, the University of Utrecht, the Greenland Climate Network, the University of Colorado at Boulder (<http://cires.colorado.edu/science/groups/steffen/gcnet/>) and the Department of Geography and Geology, University of Copenhagen, for providing meteorological data for this study.

## REFERENCES

- Abdalati, W. and K. Steffen. 1997. The apparent effects of the Mt Pinatubo eruption on the Greenland ice-sheet melt extent. *Geophys. Res. Lett.*, **24**(14), 1795–1797.
- Anderson, M.R., T. Mote and W. Abdalati. 1996. A comparison of passive microwave techniques for detecting snowpack melt on the Greenland ice sheet. In Colbeck, S.C., ed. *Glaciers, ice sheets and volcanoes: a tribute to Mark F. Meier*. Hanover, NH, Cold Regions Research and Engineering Laboratory, 5–9. (CRREL Special Report 96-27.)
- Bamber, J.L., S. Ekholm and W.B. Krabill. 2001. A new, high-resolution digital elevation model of Greenland fully validated with airborne laser altimeter data. *J. Geophys. Res.*, **106**(B4), 6733–6745.
- Barnes, S.L. 1964. A technique for maximizing details in numerical weather map analysis. *J. Appl. Meteorol.*, **3**(4), 396–409.
- Barnes, S.L. 1973. Mesoscale objective map analysis using weighted time-series observations. *NOAA Tech. Mem.* ERL NSSL-62.
- Box, J.E. and 8 others. 2006. Greenland ice sheet surface mass balance variability (1988–2004) from calibrated polar MM5 output. *J. Climate*, **19**(12), 2783–2800.
- Chylek, P., C.K. Folland, G. Lesins and M.K. Dubey. 2010. Twentieth century bipolar seesaw of the Arctic and Antarctic surface air temperatures. *Geophys. Res. Lett.*, **37**(8), L08703. (10.1029/2010GL042793.)
- Douville, H., J.F. Royer and J.F. Mahfouf. 1995. A new snow parameterization for the Météo-France climate model. Part 1. Validation in stand-alone experiments. *Climate Dyn.*, **12**(1), 21–35.
- Fettweis, X., M. Tedesco, M. van den Broeke and J. Ettema. 2010. Melting trends over the Greenland ice sheet (1958–2009) from spaceborne microwave data and regional climate models. *Cryos. Discuss.*, **4**(4), 2433–2473.
- Fettweis, X., M. Tedesco, M. van den Broeke and J. Ettema. 2011. Melting trends over the Greenland ice sheet (1958–2009) from spaceborne microwave data and regional climate models. *Cryosphere*, **5**(20), 359–375.
- Hanna, E., P. Huybrechts, I. Janssens, J. Cappelens, K. Steffen and A. Stephens. 2005. Runoff and mass balance of the Greenland ice sheet: 1958–2003. *J. Geophys. Res.*, **110**(D13), D13108. (10.1029/2004JD005641.)
- Hanna, E. and 8 others. 2008. Increased runoff from melt from the Greenland Ice Sheet: a response to global warming. *J. Climate*, **21**(2), 331–341.
- Koch, S.E., M. desjardins and P.J. Kocin. 1983. An interactive Barnes objective map analysis scheme for use with satellite and conventional data. *J. Climate Appl. Meteorol.*, **22**(9), 1487–1503.
- Liston, G.E. and K. Elder. 2006a. A distributed snow-evolution modeling system (SnowModel). *J. Hydromet.*, **7**(6), 1259–1276.
- Liston, G.E. and K. Elder. 2006b. A meteorological distribution system for high-resolution terrestrial modeling (MicroMet). *J. Hydromet.*, **7**(2), 217–234.
- Liston, G.E. and C.A. Hiemstra. 2008. A simple data assimilation system for complex snow distributions (SnowAssim). *J. Hydromet.*, **9**(5), 989–1004.
- Liston, G.E. and C.A. Hiemstra. In press. The changing cryosphere: pan-Arctic snow trends (1979–2009). *J. Climate*.
- Liston, G.E., R.B. Haehnel, M. Sturm, C.A. Hiemstra, S. Berezovskaya and R.D. Tabler. 2007. Simulating complex snow distributions in windy environments using SnowTran-3D. *J. Glaciol.*, **53**(181), 241–256.
- Mernild, S.H. and B. Hasholt. 2009. Observed runoff, jökulhlaups and suspended sediment load from the Greenland ice sheet at Kangerlussuaq, West Greenland, 2007 and 2008. *J. Glaciol.*, **55**(193), 855–858.
- Mernild, S.H. and G.E. Liston. 2010. The influence of air temperature inversions on snow melt and glacier surface mass-balance simulations, Ammassalik Island, Southeast Greenland. *J. Appl. Meteorol. Climatol.*, **49**(1), 47–67. (10.1175/2009JAMC2065.1.)
- Mernild, S.H., G.E. Liston, B. Hasholt and N.T. Knudsen. 2006. Snow distribution and melt modeling for Mittivakkat Glacier, Ammassalik Island, Southeast Greenland. *J. Hydromet.*, **7**(4), 808–824.
- Mernild, S.H., G.E. Liston, C.A. Hiemstra and K. Steffen. 2008. Surface melt area and water balance modeling on the Greenland ice sheet 1995–2005. *J. Hydromet.*, **9**(6), 1191–1211.
- Mernild, S.H., G.E. Liston, C.A. Hiemstra, K. Steffen, E. Hanna and J.H. Christensen. 2009. Greenland ice sheet surface mass-balance modelling and freshwater flux for 2007, and in a 1995–2007 perspective. *Hydrol. Process.*, **23**(17), 2470–2484.
- Mernild, S.H., G.E. Liston, C.A. Hiemstra and J.H. Christensen. 2010. Greenland Ice Sheet surface mass-balance modeling in a 131-year perspective 1950–2080. *J. Hydromet.*, **11**(1), 3–25.
- Mernild, S.H., G.E. Liston, C.A. Hiemstra, J.H. Christensen, M. Stendem and B. Hasholt. 2011. Surface mass-balance and runoff modeling using HIRHAM4 RCM at Kangerlussuaq, (Søndre Strømfjord), West Greenland, 1950–2080. *J. Climate*, **24**(3), 609–623.

- Mote, T.L. 2007. Greenland surface melt trends 1973–2007: evidence of a large increase in 2007. *Geophys. Res. Lett.*, **34**(22), L22507. (10.1029/2007GL031976.)
- Mote, T.L. and M.R. Anderson. 1995. Variations in snowpack melt on the Greenland ice sheet based on passive-microwave measurements. *J. Glaciol.*, **41**(137), 51–60.
- Nick, F.M., A. Vieli, I.M. Howat and I. Joughin. 2009. Large-scale changes in Greenland outlet glacier dynamics triggered at the terminus. *Nature Geosci.*, **2**(2), 110–114.
- Oke, T.R. 1987. *Boundary layer climates. Second edition.* London, Methuen.
- Rignot, E. and P. Kanagaratnam. 2006. Changes in the velocity structure of the Greenland Ice Sheet. *Science*, **311**(5673), 986–990.
- Solomon, S. and 7 others, eds. 2007. *Climate change 2007: the physical science basis. Contribution of Working Group I to the Fourth Assessment Report of the Intergovernmental Panel on Climate Change.* Cambridge, etc., Cambridge University Press.
- Steffen, K. 1995. Surface energy exchange at the equilibrium line on the Greenland ice sheet during onset of melt. *Ann. Glaciol.*, **21**, 13–18.
- Steffen, K. and 6 others. 2008. Rapid changes in glaciers and ice sheets and their impacts on sea level. In *Abrupt climate change.* Reston, VA, US Geological Survey, 29–66. (US Climate Change Science Program: Synthesis and Assessment Product 3.4.)
- Stiles, W.H. and F.T. Ulaby. 1980. The active and passive microwave response to snow parameters. 1. Wetness. *J. Geophys. Res.*, **85**(C2), 1037–1044.
- Tedesco, M. 2007. A new record in 2007 for melting in Greenland. *Eos*, **88**(39), 383.
- Tedesco, M. and 7 others. 2011. The role of albedo and accumulation in the 2010 melting record in Greenland. *Environ. Res. Lett.*, **6**, 014005. (10.1088/1748-9326/6/1/014005.)
- Zwally, H.J. and M.B. Giovinetto. 2001. Balance mass flux and ice velocity across the equilibrium line in drainage systems of Greenland. *J. Geophys. Res.*, **106**(D24), 33,717–33,728.

MS received 7 January 2011 and accepted in revised form 11 April 2011

[17]

Mernild, S. H. and Liston, G. E. 2012. Greenland freshwater runoff. Part II: Distribution and trends, 1960–2010. *Journal of Climate*, 25(17), 6015–6035.

Reprinted with permission from American Meteorological Society



## Greenland Freshwater Runoff. Part II: Distribution and Trends, 1960–2010

SEBASTIAN H. MERNILD

*Climate, Ocean, and Sea Ice Modeling Group, Computational Physics and Methods, Los Alamos National Laboratory, Los Alamos, New Mexico*

GLEN E. LISTON

*Cooperative Institute for Research in the Atmosphere, Colorado State University, Fort Collins, Colorado*

(Manuscript received 11 October 2011, in final form 4 June 2012)

### ABSTRACT

Runoff magnitudes, the spatial patterns from individual Greenland catchments, and their changes through time (1960–2010) were simulated in an effort to understand runoff variations to adjacent seas and to illustrate the capability of SnowModel (a snow and ice evolution model) and HydroFlow (a runoff routing model) to link variations in terrestrial runoff with ocean processes and other components of Earth's climate system. Significant increases in air temperature, net precipitation, and local surface runoff lead to enhanced and statistically significant Greenland ice sheet (GrIS) surface mass balance (SMB) loss. Total Greenland runoff to the surrounding oceans increased 30%, averaging  $481 \pm 85 \text{ km}^3 \text{ yr}^{-1}$ . Averaged over the period, 69% of the runoff to the surrounding seas originated from the GrIS and 31% came from outside the GrIS from rain and melting glaciers and ice caps. The runoff increase from the GrIS was due to an 87% increase in melt extent, 18% from increases in melt duration, and a 5% decrease in melt rates ( $87\% + 18\% - 5\% = 100\%$ ). In contrast, the runoff increase from the land area surrounding the GrIS was due to a 0% change in melt extent, a 108% increase in melt duration, and an 8% decrease in melt rate. In general, years with positive Atlantic multidecadal oscillation (AMO) index equaled years with relatively high Greenland runoff volume and vice versa. Regionally, runoff was greater from western than eastern Greenland. Since 1960, the data showed pronounced runoff increases in west Greenland, with the greatest increase occurring in the southwest and the lowest increase in the northwest.

### 1. Introduction

Long-term temperature observations show warming trends of variable strength throughout the Arctic, and ample evidence indicates that the Arctic hydrological cycle, including that for Greenland and the Greenland ice sheet (GrIS), is changing (e.g., Serreze et al. 2000; Hinzman et al. 2005; Hanna et al. 2008; Ettema et al. 2009; Mernild et al. 2010). Since the early 1990s, the increase in GrIS surface runoff has followed atmospheric warming (Hanna et al. 2008), explaining half of the recent mass loss of the GrIS (van den Broeke 2009), a mass loss that by 2100 may contribute up to 54 cm sea

level equivalent (SLE) (Pfeffer et al. 2008), since model simulations of future climate scenarios point to higher temperatures in this region (Solomon et al. 2007). In addition to the sea level contribution, terrestrial runoff from Greenland is also important for ocean density, the Atlantic meridional overturning circulation (AMOC) (Rahmstorf et al. 2005), and their impacts on the climate system (Bryden et al. 2005).

Model studies have shown that the AMOC may be sensitive to changes in terrestrial freshwater; freshening the surface waters in the northern North Atlantic inhibits deep convection feeding the deep southward branch of the AMOC (e.g., Bryan 1986; Rahmstorf 1995). The AMOC carries warm upper waters into far-northern latitudes and returns cold deep waters southward across the equator. This transport of heat makes a substantial contribution to, for example, the climate of continental Europe, and any slowdown in the overturning circulation could have implications for climate change (Bryden

---

*Corresponding author address:* Dr. Sebastian H. Mernild, Climate, Ocean, and Sea Ice Modeling Group, Computational Physics and Methods (CCS-2), Los Alamos National Laboratory, Los Alamos, NM 87545.  
E-mail: mernild@lanl.gov

et al. 2005). One of the potential freshwater sources that might have an effect on the AMOC is enhanced freshwater runoff from Greenland.

In spite of the critical role runoff from Greenland plays in Earth's climate system, there has been limited quantitative information about the spatial and temporal patterns of drainage basins and associated freshwater flux from Greenland, including the GrIS, to the adjacent seas. In addition, information about changes in Greenland spatial runoff patterns, as well as temporal changes spanning years to decades, is still lacking. Only a few watersheds in Greenland [e.g., Mittivakkat in southeast Greenland (65°N) (Mernild and Hasholt 2006; Liston and Mernild 2012), Zackenberg in northeast Greenland (74°N) (Hasholt et al. 2008; Mernild et al. 2008a; Jensen and Rasch 2010), and Kangerlussuaq in west Greenland (67°N) (Mernild et al. 2011a; Hasholt et al. 2012)] include runoff observations. Unfortunately, even these observational datasets have limitations and, taken together, transfer less than 1% of the Greenland runoff to the surrounding oceans. The Zackenberg discharge (volumetric water flow rate expressed, e.g., as  $\text{m}^3 \text{s}^{-1}$ ) dataset spans 15 years, the Mittivakkat dataset covers 12 years, and the Kangerlussuaq dataset only covers 4 years. For these three locations, the observations only span parts of the runoff season, ranging between one week and approximately three months. In addition, the Zackenberg, Mittivakkat, and Kangerlussuaq data suffer from difficulties measuring accurate runoff values due to, for example, seasonal and interannual changes in bed profile. Kangerlussuaq is particularly problematic because of the strong turbulence and presence of hydraulic jumps at the measurement point, which makes the location less than ideal for measuring precise discharge quantities. For example, the updated runoff values from Kangerlussuaq appear to include uncertainties of up to 125% when compared to independent acoustic Doppler current profiler (ADCP) observations (Hasholt et al. 2012). These uncertainties are due to inaccurate soundings of the observed cross section profile at the catchment outlet because the level of the bed can vary dramatically in response to changes in sand deposition and erosion throughout the runoff season. A study by Rennermalm et al. (2012) confirms that changing bed elevations over time, a phenomenon observed at several Watson River tributaries upstream of Kangerlussuaq, are associated with discharge uncertainties of up to 14%–47%. In addition, the updated Kangerlussuaq runoff time series were only compared against four ADCP point observations (Hasholt et al. 2012) and not against the full range of independent observations required for a statistically rigorous analysis. With these weaknesses

in mind, the limited river discharge values available for Greenland should be used with caution, especially if one is trying to understand the role Greenland runoff plays in Earth's climate system.

A recent study by Rignot and Kanagaratnam (2006) estimated GrIS drainage basins areas (related to GrIS calving fluxes), and Lewis and Smith (2009) estimated a hydrological drainage network for the GrIS. Lewis and Smith (2009) suggested that the GrIS drainage-network routes varying amounts of water to the GrIS edge and that the spatially averaged GrIS annual volumetric runoff production, regionally speaking, is highest in southwest and lowest in northeast Greenland, with greater hydrologic activity in western regions than in eastern regions, for a given latitude.

In the study described herein, detailed analyses of both simulated runoff magnitudes and spatial patterns from individual Greenland catchments, as well as runoff changes through time, were performed and evaluated—all in an effort to understand the climate impact and whether changes in melt rates, melt area, and melt duration were the main reason for the increase in runoff from Greenland to the adjacent seas. In addition, this study introduces modeling tools capable of providing the missing connection between terrestrial water fluxes and ocean circulation features such as the AMOC. This climate-feature connection represents a critical link between Greenland snow and ice melt, ocean processes, and the associated interactions and feedbacks within Earth's climate system.

Here, we examined the GrIS surface mass balance conditions (surface hydrological conditions), including GrIS and Greenland surface runoff, the spatial distribution of Greenland runoff to the adjacent seas, and their changes from 1960 through 2010. This was accomplished by coupling the HydroFlow runoff routing model (Liston and Mernild 2012) with SnowModel, a spatially distributed, meteorological and snow and ice evolution model (Liston and Elder 2006a, 2006b; Mernild et al. 2006b). The coupled modeling system was run over the GrIS and all surrounding land and peripheral glaciers and ice caps for the period 1960 through 2010 (Fig. 1a). As part of the model simulations, HydroFlow divided all of Greenland, including the GrIS, into individual drainage basins (Fig. 1b) and simulated the associated grid connectivity—its water routing network—within each individual watershed. SnowModel and HydroFlow were then forced with observed meteorological data, and the overall trends and annual variability in air temperature and runoff were related to both variations and trends in the Atlantic multidecadal oscillation (AMO) index (e.g., Folland et al. 1986; Schlesinger and Ramankutty 1994; Kerr 2000; Chylek et al. 2009, 2010) to illustrate the impact from

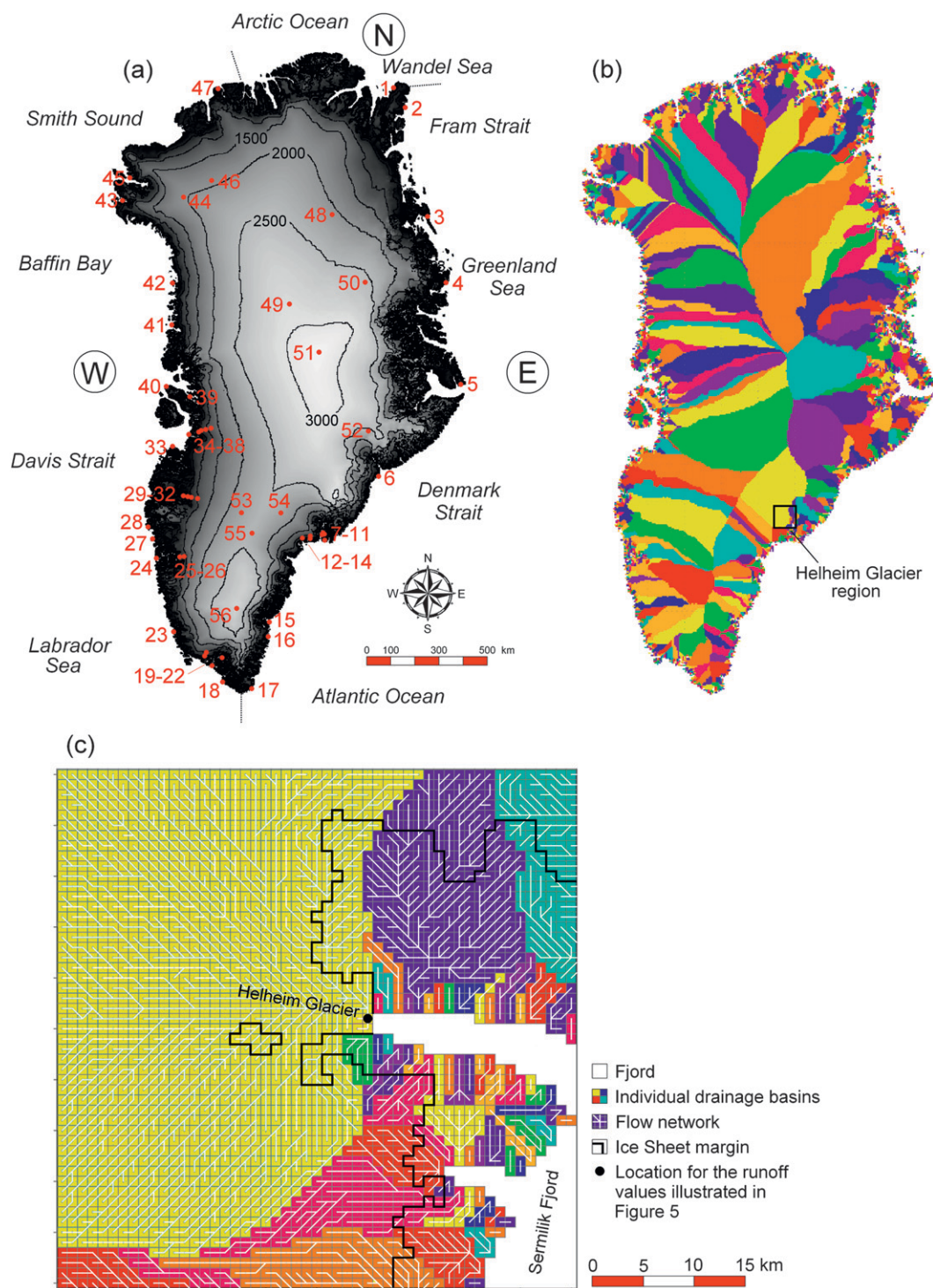


FIG. 1. (a) Greenland simulation domain with topography (500-m contour interval), the location of the coastal and GrIS meteorological tower stations (red dots; station specifications are provided in Table 1), and names of the surrounding seas and oceans. Greenland has been divided into three regions (east, west, and north) based on what oceans and seas watershed runoff flow into (see dashed lines and circles). The GrIS is marked with a color scale from gray to white (related to elevation), and the area outside the GrIS with black. (b) Simulated individual Greenland drainage basins (represented by multiple colors). Also, a specific region is illustrated from where examples of catchment runoff and hydrographs are illustrated (see bold square). (c) A closeup example of the individual drainage basins and flow network for the Helheim Glacier region, at the innermost part of the Sermilik Fjord, southeast Greenland, including the location for the runoff values and hydrographs illustrated in Fig. 5.

regional weather systems and the impacts from major episodic volcanic eruptions as part of an effort to understand the runoff response to natural forcings. Further, we examined whether the spatial runoff distribution from the warmest decade on record (2001–10) (Hansen et al. 2010) was different than the runoff distribution from both the average of 1960–69 and the average of 1960–2010.

## 2. Methodology and data

### a. HydroFlow

The HydroFlow runoff routing model (Liston and Mernild 2012) was developed and tested to simulate the linkages between surface runoff production from rainfall and land-based snowmelt and icemelt processes and the associated freshwater fluxes to down-slope areas and adjacent seas. HydroFlow is a spatially distributed model that divides the simulation domain into individual drainage basins, linking each grid cell within each drainage basin via an eight-compass-direction water-flow routing network. The water flow is transported through the routing network via linear reservoirs. For runoff routing, HydroFlow assumes that different transport mechanisms exist within each individual model grid cell: a slow-response runoff system (representing the time it takes for any available snow and ice melt, including liquid precipitation, to be transported within a model grid cell to the fast-response reservoir) and a fast-response system (representing flow processes such as those represented by supraglacial, englacial, subglacial, and proglacial water transport) that moves water down network. As part of the modeling system, locally generated runoff from snow-covered ice, snow-free ice, snow-covered land, and snow-free land all have different residence times associated with them and evolve with time as the snow and ice melts: this is taken into account as part of the runoff routing simulations (Liston and Mernild 2012). The equations solved by HydroFlow are

$$Q_{f,t} = Q_{f,t-1} \exp\left(-\frac{\Delta t}{k_f}\right) + (Q_{fi,t} + Q_{s,t}) \left[1 - \exp\left(-\frac{\Delta t}{k_f}\right)\right] \quad (1)$$

and

$$Q_{s,t} = Q_{s,t-1} \exp\left(-\frac{\Delta t}{k_s}\right) + Q_{m,t} \left[1 - \exp\left(-\frac{\Delta t}{k_s}\right)\right], \quad (2)$$

where  $Q_f$  is the fast-response flow;  $Q_s$  is the slow-response flow;  $Q_m$  is the meltwater- and rainwater-generated runoff at an individual model grid cell (e.g., the slow-time-scale gridbox runoff produced by each SnowModel grid cell);  $Q_{fi}$  is the fast time-scale inflow from any adjacent grid cells;  $k_f$  and  $k_s$  are the fast-response and slow-response transfer functions, respectively;  $\Delta t$  is the model time increment; and  $t$  and  $t - 1$  are the current and previous time steps, respectively.

This set of equations, when applied to each grid box of the runoff routing model, is connected via the flow network through the presence of the  $Q_{fi}$  term. To solve the HydroFlow water routing equations, individual watersheds and the associated grid connectivity within each watershed must be defined. Expanding  $Q_{fi}$ , to highlight the network connectivity, yields

$$Q_{fi} = Q_{fiN} + Q_{fiNE} + Q_{fiE} + Q_{fiSE} + Q_{fiS} + Q_{fiSW} + Q_{fiW} + Q_{fiNW}, \quad (3)$$

where the subscripts N, NE, E, SE, S, SW, W, and NW indicate the compass direction of the adjacent connecting grid box. One of the right-hand side terms will be zero (the one corresponding to the outflow boundary), and possibly all eight will be zero (for the case of a grid box located at the head of a watershed), depending on the gridded representation of the flow network.

Equations (1)–(3) describe a coupled system of equations whose solution yields a discharge hydrograph for each grid cell. These equations can be solved for any grid cell whose up-network inputs are known. Given knowledge of which grid cells flow into down-network grid cells, and first solving the grid cells at the head of a watershed (the grid cells that make up the watershed boundary) where there are no inflows and continuing to solve grid cells that are fed with cells that have already have a solution, the entire solution matrix can be solved at any given time step. As part of the flow network generation, only a single flow outlet into the ocean is allowed for each individual watershed. Also, conservation of mass principles between inflow, storage change, transit times, and outflow from each cell in the routing network must be defined to simulate the catchment runoff and generate discharge hydrographs for the routing grid cells. The residence time/flow velocity of a fluid element passing through the model grid cells depends on, for example, travel distance (e.g., grid cell size); surface slope and roughness (e.g., density of depression storage such as supraglacial lakes, crevasses, and moulins); characteristics of the snow and ice matrix that the fluid is flowing through and over (e.g.,



temperature or cold content and porosity); temporal evolution of the snow and ice matrix; and changes in supraglacial, englacial, and subglacial channel dimensions. Since the terrestrial snow distribution and associated characteristics vary in space and time, the transit time of each fluid element also have temporal and spatial evolutions.

In HydroFlow, the individual basins, watershed divides, and the flow network were controlled exclusively by surface topography. In Lewis and Smith (2009), the potential GrIS subbasins and the associated hydrologic flow network were identified based on the hydraulic potentiometric surface, which accounts for the effects of ice overburden pressure (i.e., hydrostatic pressure), and the surface and bedrock topography (Cuffey and Paterson 2010),

$$\varphi \cong \rho_i g (h_s + 0.1y), \quad (4)$$

where  $\varphi$  is the elevation of the potentiometric surface,  $\rho_i$  is the ice density,  $g$  is the gravitational constant,  $h_s$  is the GrIS surface elevation, and  $y$  is the bedrock elevation.

Since the bedrock elevation is multiplied by a factor of 0.1 in Eq. (4), the role of bedrock topography on controlling the potentiometric surface and the associated flow direction is secondary. Identification of the flow network and subbasins by Lewis and Smith were therefore dominated by differences in surface topography unless elevation differences in the bedrock topography were sufficiently greater than the differences in surface topography. Therefore, defining the flow network using strictly surface topographic controls (based on 5-km grid cells), as done in the current application, appears to be acceptable owing to the smoothness of the surfaces.

A detailed description and schematic illustrations of HydroFlow, including flow paths and storage changes, can be found in Liston and Mernild (2012). The performance of HydroFlow was verified against runoff observations from a Mittivakkat Glacier test area, an area that included snow-free and snow-covered glacier surfaces, and snow-free and snow-covered land peripheral to the GrIS in southeast Greenland. HydroFlow successfully simulated flow conditions and spatial runoff distribution to the adjacent ocean, with simulated runoff variations, including peaks, reproducing observed runoff ( $r^2$  between 0.63 and 0.77) in both timing and volume (Liston and Mernild 2012).

#### *b. SnowModel simulation setup and data analysis*

HydroFlow requires temporally evolving, gridded inputs of rainfall and snowmelt and icemelt runoff, over the simulation domain. In this study, these contributions

were provided by SnowModel (Liston and Elder 2006a,b; Mernild et al. 2006b), a spatially distributed modeling system that simulates meteorological conditions, surface energy, and moisture exchanges including snow and glacier melt, multilayer heat- and mass-transfer processes within the snow (e.g., snowpack temperature and density evolution), and surface runoff. Required SnowModel inputs include temporally varying fields of precipitation, wind speed and direction, air temperature, and relative humidity obtained from meteorological stations located within the simulation domain and spatially distributed, time-invariant fields of topography and land-cover type. Gridded meteorological forcings required by SnowModel were provided by MicroMet (Liston and Elder 2006b), a quasi-physically based high-resolution (e.g., 10-m to 10-km horizontal grid increment) meteorological distribution model. MicroMet is a data assimilation and interpolation model. The model uses known relationships between meteorological variables and the surrounding landscape (primarily topography) to distribute those variables over any given landscape in physically plausible and computationally efficient ways. At each time step, MicroMet calculates and distributes air temperature, relative humidity, wind speed, wind direction, incoming solar radiation, incoming longwave radiation, surface pressure, and precipitation and makes them accessible to SnowModel.

Previously, SnowModel and its various submodels, MicroMet (Liston and Elder 2006b), EnBal (Liston 1995; Liston et al. 1999), SnowTran-3D (Liston and Sturm 1998, 2002; Liston et al. 2007), and SnowPack-ML (Liston and Hall 1995; Liston and Mernild 2012), have been used successfully to simulate snow and ice accumulation and ablation processes throughout the Arctic, including Greenland (Mernild et al. 2006a; Liston et al. 2007; Mernild and Liston 2010; Liston and Hiemstra 2011). Specifically, for the GrIS, SnowModel has been tested and sufficient explained variances were found when comparing model output against independent in situ observations of meteorological variables (Mernild et al. 2008c, 2010), passive microwave-derived melt extent (Mernild et al. 2008c, 2009, 2011b), Moderate Resolution Imaging Spectroradiometer (MODIS) satellite-derived melt extent (Mernild et al. 2010), and runoff (Mernild et al. 2011a). Therefore, based on these studies, the combination of MicroMet and SnowModel generated gridcell runoffs are assumed to be of sufficient quality to drive the HydroFlow simulations presented herein.

SnowModel and HydroFlow simulations were performed for Greenland using a 5-km grid increment and daily time step over the period September 1959 through



TABLE 1. Meteorological input data for the Greenland runoff simulations. The stations were operated and data provided by Danish Meteorological Institute (DMI), University of Colorado at Boulder (CU), Geological Survey of Denmark and Greenland (GEUS), University of Copenhagen/Institute of Geography and Geology (UC/IGG), and University of Utrecht (UU). The abbreviations indicate  $T_a$ : air temperature, RH: relative humidity, Ws: wind speed, Wd: wind direction, and  $P$ : precipitation. Observed precipitation at the DMI meteorological station was corrected following Allerup et al. (1998, 2000). See Fig. 1 for station locations.

Meteorological station	Meteorological station name	Grid	Altitude (m MSL)	Data period	Parameters	Operator
1	Station Nord	81°36'00"N, 16°39'00"W	36	1 Sep 1961–9 Jul 2007	$T_a$ , RH, Ws, Wd, $P$	DMI
2	Henrik Krøyer Holme	80°39'00"N, 13°43'00"W	10	Since 1 Sep 1985	$T_a$ , RH, Ws, Wd	DMI
3	Danmarkshavn	76°46'00"N, 18°40'00"W	11	Since 1 Sep 1959	$T_a$ , RH, Ws, Wd, $P$	DMI
4	Danaborg	74°18'00"N, 20°13'00"W	44	Since 1 Sep 1959	$T_a$ , RH, Ws, Wd, $P$	DMI
5	Ittoqqortoormiit	70°29'00"N, 21°57'00"W	66	Since 1 Nov 1980	$T_a$ , RH, Ws, Wd, $P$	DMI
6	Aputiteeq	67°47'00"N, 32°18'00"W	13	1 Sep 1959–9 Feb 1987	$T_a$ , RH, Ws, Wd, $P$	DMI
7	Tasiilaq	65°36'00"N, 37°38'00"W	44	Since 1 Sep 1959	$T_a$ , RH, Ws, Wd, $P$	DMI
8	Sermilik, Station Nunatak	65°41'00"N, 37°55'00"W	515	Since 25 Jun 1993	$T_a$ , RH, Ws, Wd	UC/IGG
9	Sermilik, Station Coast_U	65°40'20"N, 37°54'10"W	190	Since 1 Aug 2009	$T_a$ , RH, Ws, Wd	UC/IGG
10	Sermilik, Station Coast_L	65°42'00"N, 37°49'00"W	25	Since 1 Jun 1997	$T_a$ , RH, Ws, Wd	UC/IGG
11	MIT	65°41'33"N, 37°49'34"W	460	3 May 2009–29 Oct 2010	$T_a$ , RH, Ws	GEUS
12	TAS_L	65°38'00"N, 38°54'00"W	270	26 Jun 2006–12 Feb 2010	$T_a$ , RH, Ws, Wd	GEUS
13	TAS_U	65°42'00"N, 38°52'00"W	580	16 Apr 2004–26 Oct 2010	$T_a$ , RH, Ws, Wd	GEUS
14	KULU	65°45'00"N, 38°36'00"W	880	20 Jun 1999–13 Sep 2000	$T_a$ , RH, Ws, Wd	CU/CIRES (GC-NET)
15	Timmarmiut	62°32'00"N, 42°08'00"W	10	1 Sep 1959–30 Jun 1979	$T_a$ , RH, Ws, Wd, $P$	DMI
16	Ikermiarsuk	61°56'00"N, 42°04'00"W	39	Since 18 Jun 1980	$T_a$ , RH, Ws, Wd	DMI
17	Ikerassuaq	60°03'00"N, 43°10'00"W	88	Since 1 Sep 1959	$T_a$ , RH, Ws, Wd, $P$	DMI
18	Nanortalik	60°08'00"N, 45°13'00"W	21	Since 2 Jan 1961	$T_a$ , RH, Ws, Wd, $P$	DMI
19	Qaortoq	60°43'00"N, 46°03'00"W	32	Since 1 Jan 1961	$T_a$ , RH, Ws, Wd, $P$	DMI
20	Mitt. Narsarsuaq	61°10'00"N, 45°25'00"W	27	Since 1 Jan 1961	$T_a$ , RH, Ws, Wd, $P$	GEUS
21	QAS_L	61°01'54"N, 45°50'54"W	310	9 May 2003–31 Jul 2010	$T_a$ , RH, Ws, Wd	GEUS
22	QAS_U	61°10'42"N, 46°49'00"W	890	7 Aug 2008–19 Jul 2010	$T_a$ , RH, Ws, Wd	GEUS
23	Paamiut	62°00'00"N, 49°40'00"W	13	Since 1 Sep 1959	$T_a$ , RH, Ws, Wd, $P$	DMI
24	Nuuk	64°10'00"N, 51°45'00"W	80	Since 1 Sep 1959	$T_a$ , RH, Ws, Wd, $P$	DMI
25	NUK_L	64°28'54"N, 49°31'42"W	560	20 Aug 2007–30 Oct 2010	$T_a$ , RH, Ws, Wd	GEUS
26	NUK_U	64°29'54"N, 49°15'54"W	1140	20 Aug 2007–26 Oct 2010	$T_a$ , RH, Ws, Wd	GEUS
27	Sioralik	65°01'00"N, 52°33'00"W	14	Since 16 Jun 1983	$T_a$ , RH, Ws, Wd	DMI
28	Mitt. Manitssoq	65°25'00"N, 52°56'00"W	28	Since 6 Dec 2000	$T_a$ , RH, Ws, Wd, $P$	DMI
29	Kangerlussuaq	67°01'00"N, 50°42'00"W	50	Since 1 May 1973	$T_a$ , RH, Ws	UU
30	Station S5	67°06'00"N, 50°07'00"W	490	1 Sep 2006–18 Aug 2010	$T_a$ , RH, Ws	UU
31	Station S6	67°05'00"N, 49°23'00"W	1020	1 Sep 2006–14 Jul 2010	$T_a$ , RH, Ws	UU
32	Station S9	67°03'00"N, 48°14'00"W	1520	1 Sep 2006–14 Aug 2010	$T_a$ , RH, Ws	UU
33	Aasiaat	68°42'00"N, 52°45'00"W	43	Since 1 Jan 1959	$T_a$ , RH, Ws, Wd, $P$	DMI
34	Mitt. Ilulissat	69°14'00"N, 51°04'00"W	29	Since 15 Aug 1991	$T_a$ , RH, Ws, Wd	DMI
35	JAR1	69°29'51"N, 49°41'16"W	962	20 Jun 1996–12 May 2010	$T_a$ , RH, Ws, Wd	CU/CIRES (GC-NET)
36	JAR2	69°25'09"N, 50°03'55"W	542	2 Jun 1999–14 May 2010	$T_a$ , RH, Ws, Wd	CU/CIRES (GC-NET)
37	JAR3	69°23'40"N, 50°18'36"W	283	1 Jan 2001–24 May 2004	$T_a$ , RH, Ws, Wd	CU/CIRES (GC-NET)
38	Swiss camp	69°34'03"N, 49°19'17"W	1140	1 Jan 1995–10 May 2010	$T_a$ , RH, Ws, Wd	CU/CIRES (GC-NET)

TABLE 1. (Continued)

Meteorological station	Meteorological station name	Grid	Altitude (m MSL)	Data period	Parameters	Operator
39	Uummannaq	70°40'00"N, 52°07'00"W	39	1 Jan 1961–30 Jun 2006	$T_a$ , RH, Ws, Wd, $P$	DMI
40	Nuussuaq	70°41'00"N, 54°37'00"W	27	Since 1 Jan 1961	$T_a$ , RH, Ws, Wd, $P$	DMI
41	Upernavik	72°47'00"N, 56°10'00"W	120	Since 25 Oct 2000	$T_a$ , RH, Ws, Wd	DMI
42	Kitsissorsuit	74°02'00"N, 57°49'00"W	40	Since 10 Sep 1981	$T_a$ , RH, Ws, Wd	DMI
43	Pituffik	76°32'00"N, 68°45'00"W	77	1 Jan 1974–27 Nov 2006	$T_a$ , RH, Ws, Wd, $P$	DMI
44	GITS	77°08'16"N, 61°02'24"W	1869	7 Jun 1995–2 May 2007	$T_a$ , RH, Ws, Wd	CU/CIRES (GC-NET)
45	Qaanaq	77°28'00"N, 69°13'00"W	16	10 Aug 1995–13 Oct 2004	$T_a$ , RH, Ws, Wd	DMI
46	Humboldt	78°31'36"N, 56°49'50"W	1995	22 Jun 1995–30 Apr 2008	$T_a$ , RH, Ws, Wd	CU/CIRES (GC-NET)
47	Hall Land	81°41'00"N, 59°57'00"W	105	30 Aug 1982–6 Sep 2007	$T_a$ , RH, Ws, Wd	DMI
48	Tunu-N	78°00'59"N, 33°59'00"W	2052	17 May 1995–1 May 2008	$T_a$ , RH, Ws, Wd	CU/CIRES (GC-NET)
49	NGRIP	75°05'59"N, 42°19'57"W	2950	9 Jul 1997–8 May 2010	$T_a$ , RH, Ws, Wd	CU/CIRES (GC-NET)
50	NASA-E	75°00'02"N, 29°59'50"W	2614	3 May 1997–2 May 2008	$T_a$ , RH, Ws, Wd	CU/CIRES (GC-NET)
51	Summit	72°34'47"N, 38°30'18"W	3208	14 May 1995–16 Aug 2010	$T_a$ , RH, Ws, Wd	CU/CIRES (GC-NET)
52	KAR	69°41'58"N, 33°00'21"W	2579	18 May 1998–7 Jun 2005	$T_a$ , RH, Ws, Wd	CU/CIRES (GC-NET)
53	DYE-2	66°28'48"N, 46°16'44"W	2165	25 May 1995–30 Apr 2010	$T_a$ , RH, Ws, Wd	CU/CIRES (GC-NET)
54	NASA-SE	66°28'45"N, 42°29'56"W	2393	24 Apr 1998–29 Apr 2010	$T_a$ , RH, Ws, Wd	CU/CIRES (GC-NET)
55	Saddle	65°59'58"N, 44°30'03"W	2456	20 Apr 1997–26 Apr 2009	$T_a$ , RH, Ws, Wd	CU/CIRES (GC-NET)
56	South Dome	63°08'56"N, 44°49'02"W	2901	23 Apr 1997–30 Jun 2008	$T_a$ , RH, Ws, Wd	CU/CIRES (GC-NET)

December 2010. Digital elevation model (DEM) data were provided by Bamber et al. (2001), and land-cover data were obtained from the U.S. Geological Survey (USGS) North American Land Cover Characteristics Database, version 2.0, updated with Landsat satellite-derived surface characteristics (Mernild et al. 2012a) (resolving glaciers having a glacier size greater than 30 m  $\times$  30 m). Glaciers and ice caps were classified as glacier cover in the land-cover file if the individual grid cells were covered by more than 50% of glacier ice. SnowModel was forced with observed atmospheric data from 56 meteorological stations located both in coastal areas and on the GrIS, shown in Fig. 1 and Table 1, (Mernild et al. 2011b). The number of meteorological stations varied from 10 (1960) to 45 (2006) per year between 1960 and 2010 (Table 1). The increase in number of meteorological stations over time likely increased the simulated regional variability. MicroMet (Liston and Elder 2006b) uses a Barnes objective analysis scheme that applies a Gaussian distance-dependent weighting function as part of its horizontal interpolations. In addition, elevation-related lapse rates are applied to the distributed temperature fields. For these reasons, the relatively small number of meteorological stations present during the early part of the simulations does not necessarily imply a degradation in simulated meteorological fields. We therefore assume the station increase does not significantly influence the trends and that the general trends that we produce and describe herein are valid. A detailed description of the model configuration and user-defined constants used in these Greenland simulations are available from Mernild et al. (2009, 2011b).

The spatial distribution of runoff was simulated for Greenland, including the runoff from each of the Greenland individual drainage basins and the routing of that runoff to the surrounding oceans. In addition, Greenland has been divided into eight 45° sectors, or regions, centered on the four cardinal and four ordinal directions (i.e., north, northeast, east, southeast, etc.) to illustrate the regional runoff distribution. The origin of these sectors is located at approximately the center of Greenland at 71.8914°N, 41.7181°W.

The simulated increase in Greenland runoff to the surrounding oceans was compared against increases in melt rates, melt area (melt extent values are illustrated in Fig. 3b of Mernild et al. 2011b), and melt duration or period (based on linear regression) to quantify the relative contributions of these three factors. In addition, calculated changes in Greenland runoff were compared with changes in Greenland runoff duration, also based on linear regression. Also, an additional

analysis of the source of the Greenland runoff increase to the surrounding oceans over the period 1960–2010 was conducted. We applied a linear regression to the time series of annual total Greenland runoff, total GrIS runoff, maximum Greenland melt extent, Greenland melt duration, and Greenland average melt rate and calculated the change in those regressions (based on the linear regression slope) over the 50-yr period (based on decadal averages). These results were scaled so that they totaled 100% and are used to provide a relative measure of melt extent, melt duration, and melt rate in governing the changes in Greenland runoff.

### 3. Results and discussion

#### *a. Individual Greenland drainage basins and flow network*

The Greenland simulation domain, individual modeled drainage catchments, and an example of the simulated flow network for the Helheim Glacier region in southeast Greenland are illustrated in Fig. 1. HydroFlow divided the GrIS into ~400 individual drainage basins and all of Greenland (including the GrIS basins) into ~3150 individual basins (Fig. 1b). Each of these basins includes their own flow network that drains runoff to downslope areas and into the adjacent seas (Fig. 1c). For Greenland, the individual simulated drainage basins range in area from 50 to 154 800 km<sup>2</sup> (averaging ~700 km<sup>2</sup>) (Fig. 1b) with 85% of the drainage basins equal to or less than 250 km<sup>2</sup>; these relatively small basins cover 10% of the total Greenland area and are mainly located in the land area between the GrIS and the oceans. A drainage-network study by Lewis and Smith (2009) identified 293 distinct GrIS hydrological basins ranging in area from 185 to 117 000 km<sup>2</sup>, values on a similar order of magnitude to those estimated by HydroFlow, even though Lewis and Smith omitted basins less than 100 km<sup>2</sup>.

The size and the shape of the HydroFlow simulated GrIS drainage basins (Fig. 1b) were compared with drainage basins estimated by Rignot and Kanagaratnam (2006). A comparison of the 20 greatest GrIS drainage basins was carried out only since the catchment division by Rignot and Kanagaratnam did not include midsize or minor catchments. Overall, HydroFlow reproduced the location of the watershed divides and the area of the greatest drainage basins reasonably well. When compared to Rignot and Kanagaratnam (2006), the sizes of the HydroFlow simulated drainage areas were generally within an error of less than 10%, and only one of the areas fell within an error of 30%.

#### *b. Climate and GrIS surface mass balance*

In Fig. 2a, the simulated mean annual air temperatures (MAAT) for Greenland are illustrated. Figure 2a also includes the mean summer temperatures for June–August (JJA); these are the temperatures largely associated with summer ablation, including the processes associated with evaporation, sublimation, and surface runoff. Figure 2b displays the AMO index series for 1960–2010 (<http://www.esrl.noaa.gov/psd/data/timeseries/AMO/>), and Fig. 2c presents the GrIS modeled net precipitation, surface mass balance, and runoff to adjacent seas. From 1960 to 2010 the Greenland mean summer air temperature and MAAT increased an average of 1.9° and 1.2°C (Fig. 2a), respectively. However, before the mid-1980s the trend in mean summer temperature correlates significantly with MAAT and was in antiphase, meaning JJA was on average increasing while MAAT was on average decreasing ( $r^2 = 0.11$  and  $p < 0.1$ , where  $r^2$  is the explained variance and  $p$  is level of significance), and hereafter the trends were in phase (significant) ( $r^2 = 0.94$ ,  $p < 0.01$ ) and increasing (Fig. 2a). Since the mid-1980s, mean summer temperature and MAAT increased an average of 1.5° and 2.2°C, respectively. Hanna et al. (2008) found an increase in coastal Greenland summer temperatures for 1991–2006 of 1.8°C, based on observations. Furthermore, the overall variations in SnowModel simulated mean summer temperature explains the variance significantly ( $r^2 = 0.65$ ,  $p < 0.01$ ), with the smoothed trends of the AMO index (Fig. 2b) [similar conditions between summer temperature and AMO variations was confirmed in Hanna et al. (2012)]. From 1960 to the mid-1970s, the smoothed AMO index decreased on average and thereafter it increased through 2010, corresponding with the trend in simulated mean summer temperature for Greenland. A study by Chylek et al. (2010) showed that Arctic temperatures were highly correlated with the AMO index, suggesting the Atlantic Ocean as a possible source of Arctic climate variability. This was also the case for the simulated Greenland MAAT for which the explained variance was significant for the periods after the mid-1980s (1986–2010:  $r^2 = 0.95$ ,  $p < 0.01$ ) and before that time (1960–85:  $r^2 = 0.18$ ,  $p < 0.01$ ); however, the latter period had a higher  $r^2$  value (explained more of the variance).

Figure 2c presents time series (1960–2010) of simulated GrIS surface hydrological conditions: net precipitation (precipitation minus evaporation and sublimation), surface runoff, and surface mass balance (SMB) on an annual basis for the calendar year (1 January–31 December). Mass gain (accumulation) is calculated as positive and mass loss (ablation) is considered negative for the GrIS. The average 1960–2010 simulated GrIS net precipitation

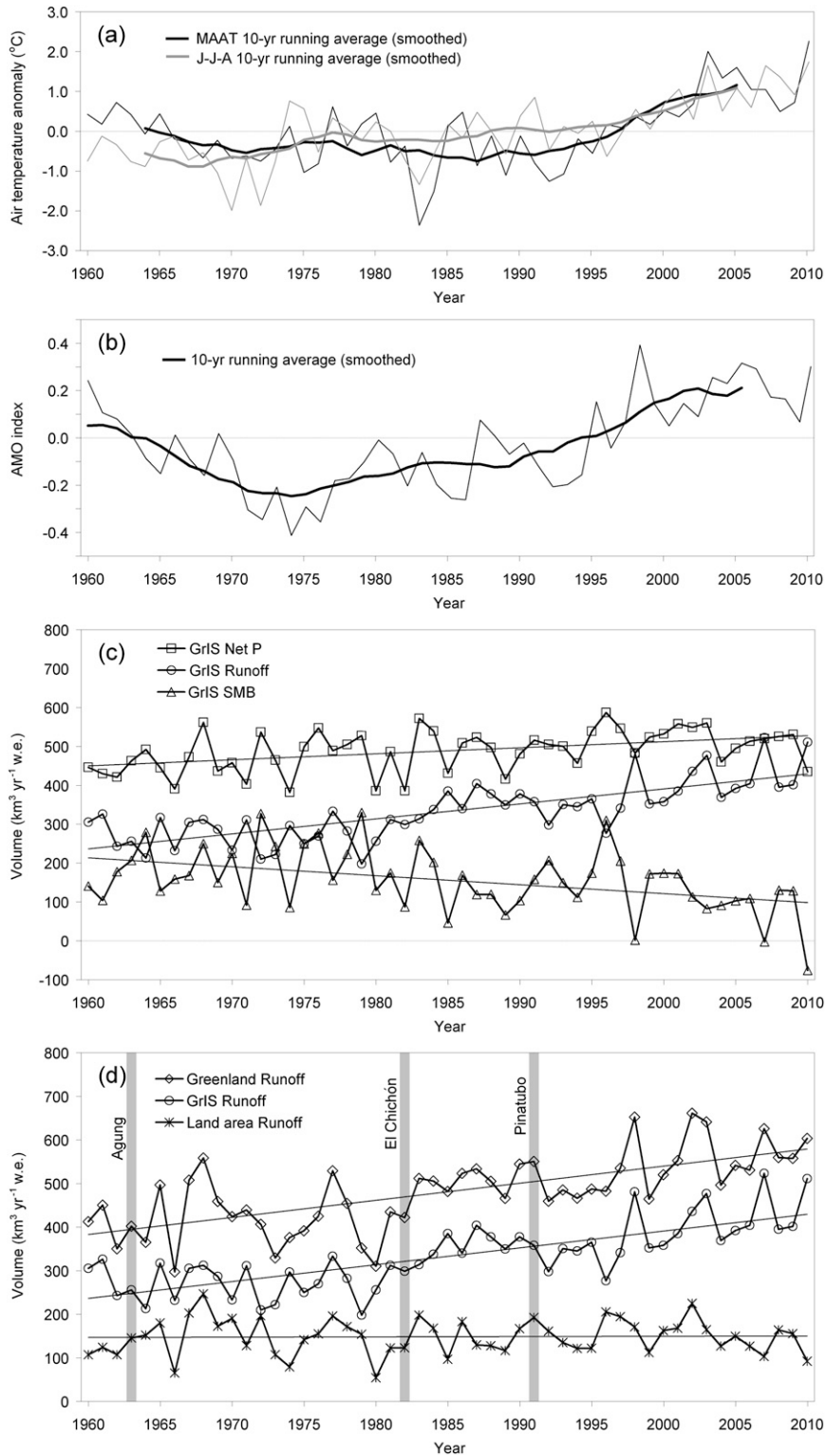


FIG. 2. (a) Simulated mean summer (JJA) and mean annual air temperature (MAAT) Greenland anomaly time series for 1960–2010; (b) unsmoothed and smoothed (10-yr running average) Atlantic multidecadal oscillation (AMO) index; (c) GrIS simulated net precipitation  $P$ , surface mass balance ( $SMB = \Delta S$ ), and surface runoff  $R$  time series for 1960–2010; and (d) simulated surface GrIS runoff, land strip area (area outside the GrIS) runoff, and Greenland runoff time series for 1960–2010. The Agung (1963; Bali), El Chichón (1982; Mexico), and Mt. Pinatubo (1991; Philippines) volcanic eruptions are marked in (d).

was  $489 \pm 53 \text{ km}^3 \text{ yr}^{-1}$  (here and below, the  $\pm$  standard deviations are included), varying from  $456 \pm 46 \text{ km}^3 \text{ yr}^{-1}$  in 1960–69 to  $516 \pm 38 \text{ km}^3 \text{ yr}^{-1}$  in 2000–10 (Table 2). The simulated average GrIS net precipitation was just below the range of recently reported average net precipitation values: all reporting a similar average trend in precipitation as SnowModel toward higher annual values (Box et al. 2006; Hanna et al. 2005, 2008; Fettweis 2007; Fettweis et al. 2008; Ettema et al. 2009). Averaged for the GrIS, 85% of the SnowModel simulated precipitation fell as snow with the rest falling as rain.

On a decadal time scale, SnowModel simulated GrIS surface runoff varied an average of  $261 \pm 45 \text{ km}^3 \text{ yr}^{-1}$  ( $0.7 \pm 0.2 \text{ mm SLE yr}^{-1}$ ) in 1970–79 to  $429 \pm 57 \text{ km}^3 \text{ yr}^{-1}$  ( $1.2 \pm 0.2 \text{ mm SLE yr}^{-1}$ ) in 2000–10 (Table 2). Overall, for the period 1960–2010, GrIS simulated net precipitation and surface runoff rose significantly, averaging  $1.5$  ( $r^2 = 0.19, p < 0.01$ ) and  $3.8 \text{ km}^3 \text{ yr}^{-2}$  ( $r^2 = 0.58, p < 0.01$ ), respectively, leading to an enhanced significant SMB loss of  $2.3 \text{ km}^3 \text{ yr}^{-2}$  ( $r^2 = 0.17, p < 0.01$ ) (Table 2), average trends identical to previous studies by, for example, Box et al. (2006), Fettweis (2007), Hanna et al. (2008), and Ettema et al. (2009). These values closely follow air temperature fluctuations (Fig. 2a), indicating that surface mass loss increased as climate warmed with no suggestion of deceleration (Fig. 2c). The described trends for GrIS simulated net precipitation, runoff, and SMB are expected in a warmer climate (Fig. 2c and Table 2) due to enhanced snow accumulation in the relatively cold GrIS interior (where the increase in MAAT was still below freezing); enhanced melt/runoff season and surface melt extent (Fig. 3a); and enhanced ablation at lower elevations, including the GrIS margin areas.

The increase in simulated surface runoff led to a cumulative GrIS runoff loss of  $16\,970 \text{ km}^3$  (equal to  $47.1 \text{ mm SLE}$ ) (1960–2010), with an annual average surface runoff of  $333 \pm 75 \text{ km}^3 \text{ yr}^{-1}$  ( $0.9 \pm 0.2 \text{ mm SLE yr}^{-1}$ ) (Table 2), just above the range of recently reported average runoff values by, for example, Box et al. (2006), Fettweis (2007), Hanna et al. (2008) (updated), Ettema et al. (2009), and Mernild et al. (2010). The differences between these simulated average surface runoff values were likely primarily due to the different model representations of meltwater retention and refreezing within the snowpack for areas above  $\sim 2000 \text{ m}$  above mean sea level (MSL). In the simulations presented herein, a multilayer snowpack model (Snowpack-ML) (Liston and Mernild 2012) was coupled to SnowModel and used to simulate the amount of percolation and internal refreezing (storage) from surface snowmelt and rain within the snow and firn layers, making an important contribution to the evolution of snow and ice densities,

snow temperatures (cold content: temperatures below freezing), and moisture available for runoff (Liston and Mernild 2012). These simulations produced an internal refreezing value of 25% ( $129 \pm 29 \text{ km}^3 \text{ yr}^{-1}$ ) (Table 2), which is in the same range produced by the single-layer snowpack model used by Hanna et al. (2002, 2005, 2008) but below the value of 45% estimated by Ettema et al. (2009). If routines for retention and internal refreezing in the snowpack are not included in the simulations, runoff available for internal glacier drainage would be overestimated by approximately 25%–45% (e.g., Hanna et al. 2008; Ettema et al. 2009), depending on the simulation model and/or method.

For the GrIS, subtracting the simulated average surface runoff from the net precipitation yielded a surface mass gain, with an average annual GrIS SMB of  $156 \pm 82 \text{ km}^3 \text{ yr}^{-1}$  (1960–2010) (Table 2), a mean value just below recent reported values by, for example, Box et al. (2006), Fettweis (2007), Hanna et al. (2008), and Ettema et al. (2009). The GrIS SMB decadal variability ranged from  $220 \pm 86 \text{ km}^3 \text{ yr}^{-1}$  in 1970–79 to  $86 \pm 72 \text{ km}^3 \text{ yr}^{-1}$  in 2000–10. The simulations showed the largest (most positive) SMB near the beginning of the simulation period, with a subsequent mass loss as temperatures and runoff increased.

For the GrIS, during 1960–2010 the accumulation zone covered an average of 90% of the total GrIS area, and the ablation zone an average of 10%. In contrast, the simulated area generating surface runoff covered an average of 12% and surface melt an average of 15% of the GrIS (Fig. 3a). A maximum SnowModel simulated ablation zone width of 125 km occurred in the southwest region of the GrIS and was almost as wide for the northeast GrIS. In contrast, the narrowest ablation zone had a maximum width of 10–20 km and occurred in both the northwest and the southeast regions of the GrIS, a distribution predominantly following elevation changes and the spatial variability in precipitation (data simulated in this study but not illustrated). Therefore, the widest ablation zones occurred in relatively low precipitation regions, and the narrowest zones occurred in the high precipitation areas. The spatial variability in simulated GrIS ablation zones were in general agreement with Ettema et al. (2009).

### c. Greenland surface runoff

Figure 2d presents the time series of simulated Greenland runoff (1960–2010) and individual runoff contributions from the GrIS and from the land area—including thousands of glaciers and ice caps—located between the ice sheet and the surrounding oceans. The 1960–2010 average, simulated Greenland runoff was  $481 \pm 85 \text{ km}^3 \text{ yr}^{-1}$  ( $1.3 \pm 0.2 \text{ mm SLE yr}^{-1}$ ), varying from



TABLE 2. Decadal mean and standard deviation of GrIS simulated net precipitation ( $P_{\text{net}}$ ), runoff ( $R$ ), and surface mass balance (SMB) (change in storage,  $\Delta S$ ), internal GrIS storage, and Greenland runoff from 1960 through 2010. Also provided are the differences between mean Greenland runoff 2000–10 minus 1960–69 and 2000–10 minus 1960–2010.

	1960–69	1970–79	1980–89	1990–99	2000–10 <sup>a</sup>	Avg 1960–2010	Annual change 1960–2010	2000–10 minus 1960–69	2000–10 minus 1960–2010
GrIS net precipitation ( $P_{\text{net}}$ ) ( $\text{km}^3 \text{ yr}^{-1}$ )	456 ± 47	481 ± 55	475 ± 66	514 ± 38	516 ± 38	489 ± 53	1.5 <sup>b</sup>	60	27
GrIS surface runoff ( $R$ ) ( $\text{km}^3 \text{ yr}^{-1}$ ) and (mm SLE $\text{yr}^{-1}$ )	280 ± 40 (0.2 ± 0.2)	261 ± 45 (0.7 ± 0.2)	337 ± 44 (0.9 ± 0.2)	355 ± 54 (1.0 ± 0.2)	429 ± 57 (1.2 ± 0.2)	333 ± 75 (0.9 ± 0.2) (16 970) <sup>c</sup>	3.8 <sup>b</sup>	150 (50%)	97 (30%)
GrIS SMB ( $\Delta S$ ) ( $\text{km}^3 \text{ yr}^{-1}$ )	176 ± 55	220 ± 86	138 ± 65	159 ± 80	86 ± 72	156 ± 82	-2.3 <sup>b</sup>	-90	-70
GrIS mean melt extent (% $\text{yr}^{-1}$ ) (Mermild et al. 2011b)	13 ± 3	10 ± 3	14 ± 3	16 ± 3	21 ± 3	17 ± 4	—	—	—
GrIS internal storage ( $\text{km}^3 \text{ yr}^{-1}$ ) (the difference between surface melt and rain and surface runoff)	118 ± 19	114 ± 19	120 ± 15	132 ± 17	161 ± 21	129 ± 29 (25%) <sup>d</sup>	—	—	—
Land area runoff ( $R$ ) ( $\text{km}^3 \text{ yr}^{-1}$ )	150 ± 53	152 ± 39	132 ± 42	158 ± 34	143 ± 36	148 ± 41	0.1 <sup>b</sup>	—	—
Greenland runoff ( $R$ ) ( $\text{km}^3 \text{ yr}^{-1}$ )	430 ± 80 (65%) <sup>e</sup>	413 ± 56 (65%) <sup>e</sup>	469 ± 67 (72%) <sup>e</sup>	513 ± 60 (69%) <sup>e</sup>	572 ± 53 (75%) <sup>e</sup>	481 ± 85 (70%) <sup>e</sup>	3.9 <sup>b</sup>	142 (30%)	91 (20%)
Greenland runoff ( $R$ ) equivalent to global sea level change (mm w.e. SLE $\text{yr}^{-1}$ ) <sup>f</sup>	1.2 ± 0.2	1.1 ± 0.2	1.3 ± 0.2	1.4 ± 0.2	1.6 ± 0.2	1.3 ± 0.2	—	—	—

<sup>a</sup> The average values are based on 11 years of data; otherwise, only 10 years are used for each decade from 1960–69 through 1990–99.

<sup>b</sup> The unit is  $\text{km}^3 \text{ yr}^{-2}$ .

<sup>c</sup> Total 1960–2010 GrIS surface runoff ( $\text{km}^3$ ).

<sup>d</sup> The percentage of surface meltwater stored as retention/refreezing within the snowpack.

<sup>e</sup> Percentage (%) of Greenland runoff coming from the GrIS.

<sup>f</sup> For the global sea level calculations, a global sea level area of  $361 \times 10^6 \text{ km}^2$  was used.

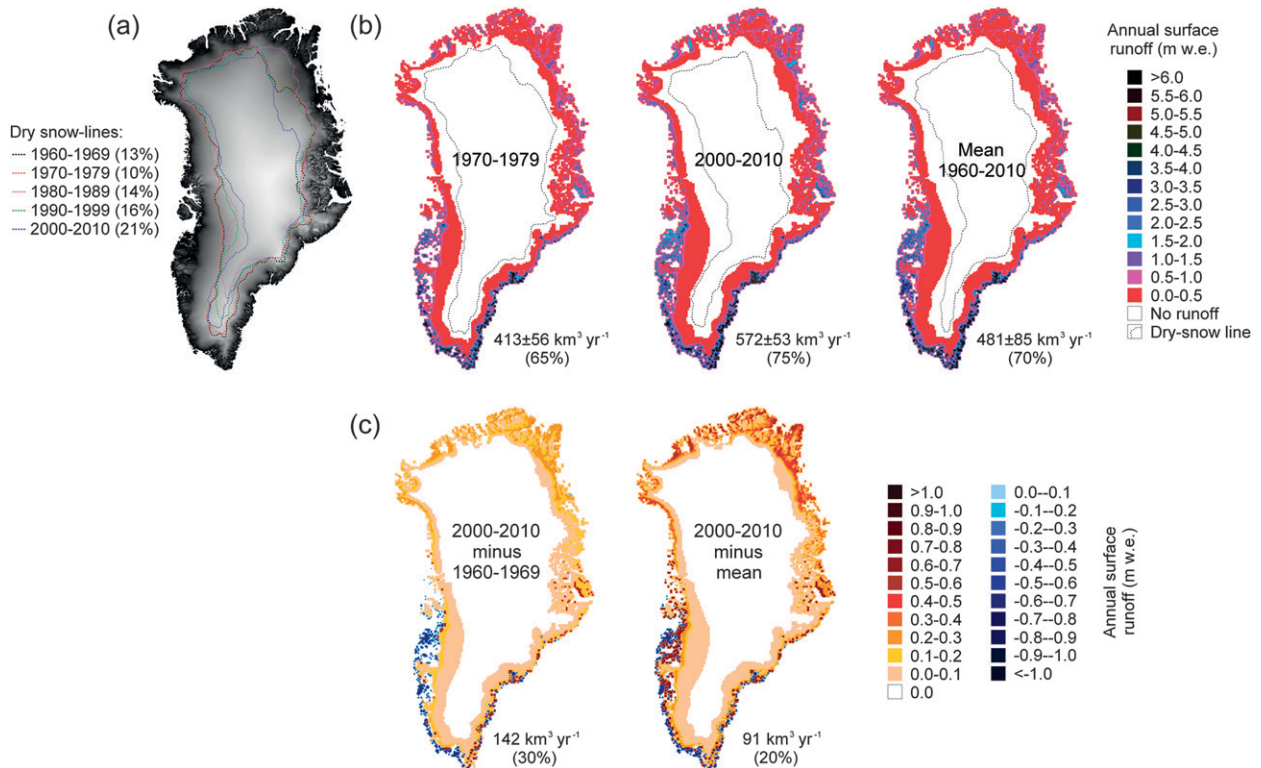


FIG. 3. (a) Mean annual simulated GrIS dry-snow line (dotted lines; the maximum average decadal boundary between melt and no melt on the glacier surface) (for definition, see Cuffey and Paterson 2010) on decadal intervals from 1960–69 through 2000–10. The percentages in brackets express the average annual melt extent on decadal scale for GrIS (time series of simulated mean melt extent 1960–2010 can be found in Mernild et al. 2011b). (b) Annual average simulated Greenland spatial surface runoff on decadal intervals for the decade with the lowest (1970–79) and highest (2000–10) runoff and mean (1960–2010). (c) The difference between the 2000–10 annual simulated Greenland runoff and the 1960–69 runoff and between the 2000–10 annual simulated runoff and the 1960–2010 mean.

$413 \pm 56 \text{ km}^3 \text{ yr}^{-1}$  ( $1.1 \pm 0.2 \text{ mm SLE yr}^{-1}$ ) in 1960–69 to  $572 \pm 53 \text{ km}^3 \text{ yr}^{-1}$  ( $1.6 \pm 0.2 \text{ mm SLE yr}^{-1}$ ) in 2000–10, following the trends in air temperature and precipitation (Table 2 and Figs. 2a,b). The runoff simulations indicated that 69% of the runoff to the surrounding seas originated from the GrIS and 31% originated from the land area (Table 2; for division between the GrIS and the land area, see Fig. 1a). For the land area, the trend in simulated runoff was constant (Fig. 2d), and the average runoff was  $148 \pm 41 \text{ km}^3 \text{ yr}^{-1}$  (Table 2). A possible reason for the minimal change in slope of the land-area runoff ( $0.1 \text{ km}^3 \text{ yr}^{-1}$ ) in the Fig. 2d curve is because the glaciers and ice caps are already melting all summer, and an enhanced melt season and melt extent were therefore not possible. In contrast, simulated GrIS runoff, on average, has increased  $3.9 \text{ km}^3 \text{ yr}^{-1}$  since 1960 (Table 2), and there has been enhanced surface melt extent (Fettweis et al. 2011; Mernild et al. 2011b). Runoff values resolved previously for all of east Greenland indicated a 60% origin from the GrIS and 40% from the land area (Mernild et al. 2008b): these east Greenland runoff values are similar

to the Greenland runoff values simulated in the current study.

In Fig. 2d, 1960–2010 simulated runoff time series from both the GrIS and all of Greenland are illustrated. The impact on runoff variability due to major episodic volcanic eruptions, such as Agung (1963), El Chichón (1982), and Mt. Pinatubo (1991) (Fig. 2d), and in the years immediately after do not appear to be systematic. For the year immediately after Agung and Pinatubo, simulated annual runoff values decreased, and they increased after El Chichón. The simulated Greenland runoff variations seems to be due to a combination of annual variations in both temperature and precipitation that are controlled by factors other than volcanic activity. Hanna et al. (2005) stated that global dust veils generated by volcanic activity might cool the polar regions and suppress ice sheet melt, but clearly there are other aspects of the climate system that may offset the volcanic signal. In contrast, the general climate forcing conditions captured by variations in the smooth AMO index time series (Fig. 2b) can be traced in the overall Greenland runoff pattern (Fig. 2d). In

general, years with positive AMO index equaled years with relatively high Greenland simulated runoff volume (and relatively high mean summer temperatures), and years with negative AMO index had low runoff volume, with a significant explained variance ( $r^2 = 0.73$ ,  $p < 0.01$ ) between the AMO index and Greenland runoff.

For Greenland, the spatial distribution of simulated surface runoff is illustrated at the decadal scale for the decade with the lowest (1970–79) and highest (2000–10) runoff and for 1960–2010 in Fig. 3b. Generally, relatively high average surface runoff values were simulated for the southwest and southeast regions of Greenland, and sporadic high values were simulated in the north region with maximum values of 4–6 m water equivalent (w.e.)  $\text{yr}^{-1}$ . Elsewhere, runoff was less with lowest values in the northeast and northwest regions of less than 0.5 m w.e.  $\text{yr}^{-1}$  (Fig. 3b). This spatial simulated surface runoff distribution is largely in agreement with values from Lewis and Smith (2009). This regional pattern in surface runoff can be largely explained by the spatial distribution of precipitation since snowfall (end-of-winter accumulation) and surface runoff are negatively correlated through surface albedo, snow depth, and snow characteristics (e.g., snow cold content) (Hanna et al. 2008; Ettema et al. 2009; Mernild et al. 2009). For dry precipitation regions (west and northeast Greenland), the relatively low end-of-winter snow accumulation melts relatively fast during spring warmup. After the winter snow accumulation (albedo 0.50–0.80) has ablated, the ice surface albedo (0.40) promotes a stronger radiation-driven ablation and surface runoff, owing to the lower ice albedo. For wet precipitation regions (southeast and northwest Greenland) the relatively high end-of-winter snow accumulation, combined with frequent summer snow precipitation events, keeps the albedo high. Therefore, in wet regions it generally takes a longer time to melt the snowpack compared to dry regions before ablating the underlying glacier ice. For glaciers, ice caps, and the GrIS snowpack retention and refreezing processes suggest that regions with relatively high surface runoff are synchronous with relatively low end-of-winter snow accumulation because more meltwater was retained in the thicker snowpack, reducing runoff to the internal glacier drainage system (Hanna et al. 2008; Mernild et al. 2009).

In Fig. 3c, the simulated spatial surface runoff distribution for Greenland is illustrated for both 2000–10 minus 1960–69 and 2000–10 minus 1960–2010. For the GrIS the mean difference in surface runoff between 1960–69 and 2000–10 averaged  $150 \text{ km}^3 \text{ yr}^{-1}$  (an increase of 50%), associated with a simulated precipitation

increase of  $60 \text{ km}^3 \text{ yr}^{-1}$  and a SMB loss of  $90 \text{ km}^3 \text{ yr}^{-1}$  (Table 2). Spatially, the difference in simulated GrIS runoff between 1960–69 and 2000–10 was as large as  $0.8 \text{ m w.e. yr}^{-1}$  near the ice sheet margin (Fig. 3c). For the land strip area, the differences in surface runoff were more diverse because of the distribution of local glaciers and ice caps. Generally, for the land area in the southwest region, surface runoff had a difference of up to  $-1.0 \text{ m w.e. yr}^{-1}$  (between 1960–69 and 2000–10), while in the southeast region, for a given latitude, the runoff differences were more variable. Here the difference in surface runoff was less pronounced compared to the southwest areas with differences of only up to  $-0.6 \text{ m w.e. yr}^{-1}$ . However, differences in simulated surface runoff of up to  $1.0 \text{ m w.e. yr}^{-1}$  occurred, mainly from local glaciers and ice caps. In north Greenland, simulated surface runoff differed by up to  $0.4 \text{ m w.e. yr}^{-1}$  (Fig. 3c). For the land area, the difference in surface runoff during the last five decades was generally quite diverse with both positive and negative differences in runoff (Fig. 3c). These values were highly dependent on the location, distribution, elevation, and size of the local glaciers and ice caps compared to the more homogeneous and positive runoff differences simulated for the GrIS.

The last decade (2000–10) has been the warmest decade on record (Hansen et al. 2010) with simulated MAAT and mean summer temperature  $1.1^\circ$  and  $1.0^\circ\text{C}$  above average, respectively, for the last five decades (Fig. 2a). For the GrIS, the 2000–10 simulated net precipitation was  $27 \text{ km}^3 \text{ yr}^{-1}$  and surface runoff was  $97 \text{ km}^3 \text{ yr}^{-1}$  (30%) above the 1960–2010 average, leading to a SMB of  $70 \text{ km}^3 \text{ yr}^{-1}$  below average (Table 2). For the GrIS, surface runoff values of up to  $0.9 \text{ m w.e. yr}^{-1}$  above average occurred (Fig. 3c). On a regional scale the 2000–10 minus the 1960–2010 runoff distribution generally resulted in a lower than average simulated surface runoff from nonglaciated land areas in the southeast and southwest regions. For glaciated areas, however, surface runoff was generally above this same average, with up to  $1.0 \text{ m w.e. yr}^{-1}$  in the southeast and southwest regions. For example, in northeast and north Greenland, surface runoff (2000–10) was as much as  $0.7 \text{ m w.e. yr}^{-1}$  greater than the 50-yr average (1960–2010) for the land strip area. A possible explanation for these relatively high, above average, simulated surface runoff values in northeast and north Greenland could be due to changes in the sea ice extent and thickness in the Arctic Ocean and Greenland Sea (Mernild et al. 2011b), and the influence of these changes are captured by the Greenland meteorological station network used to force the model simulations.

#### d. Spatial runoff distribution from Greenland to adjacent seas

In Fig. 1b, Greenland was divided into individual drainage basins. In addition, the western half (1 133 000 km<sup>2</sup>; 53% of the total area) and eastern half of Greenland (1 005 000 km<sup>2</sup>; 47%) were defined based on the main Greenland watershed divide running north to south. Regionally, the average Greenland 1960–2010 simulated runoff to the adjacent seas was greater in the western half of Greenland, 263 km<sup>3</sup> yr<sup>-1</sup> (equals 55% of the total Greenland runoff), than in the eastern half of Greenland, 218 km<sup>3</sup> yr<sup>-1</sup> (45%) (indicating an insignificant regional difference).

In Fig. 4, the spatial simulated runoff distribution from Greenland to the adjacent seas is illustrated (where each radial bar in the Greenland runoff figure represents the accumulated runoff contribution from 10 adjacent, individual drainage catchments). The individual drainage catchments route varying amounts of runoff to the surrounding seas. The 1960–2010 average simulated discharge for these drainage catchments varied from <0.01 to 10.1 km<sup>3</sup> yr<sup>-1</sup> (Fig. 4a). The spatial variability in catchment runoff to the surrounding seas also varied according to catchment size, ice sheet and glacier elevation range, and ice sheet and glacier areal coverage within each individual catchment. For approximately half of the simulated runoff values (colored radial bars) in Fig. 4a, runoff ranged from <0.01 to 1.0 km<sup>3</sup> yr<sup>-1</sup> (1960–2010) and contributed 15% of the total Greenland runoff. In contrast, 15% of the catchments (Fig. 4a)—catchments having a relatively large ice sheet and/or glacier areal coverage—had a mean annual runoff greater than 2.5 km<sup>3</sup> yr<sup>-1</sup> and contributed 40% of the Greenland runoff to the adjacent seas.

In Fig. 4 and in the following discussion, regionally, the average Greenland 1960–2010 simulated runoff to the adjacent seas was greatest from the south sector (88 km<sup>3</sup> yr<sup>-1</sup>) and southwest sector (82 km<sup>3</sup> yr<sup>-1</sup>) and lowest from the east sector (45 km<sup>3</sup> yr<sup>-1</sup>) and southeast sector (49 km<sup>3</sup> yr<sup>-1</sup>) (Fig. 4a). The regional distribution of runoff to the surrounding oceans appears to be in general agreement with the study by Lewis and Smith (2009). Also, Greenland has been divided into three regions based on which oceans and seas watershed runoff flows into (Fig. 1a): the average 1960–2010 simulated runoff to Fram Strait, the Nordic Seas, Denmark Strait, and the Atlantic Ocean (called the eastern oceans and seas of Greenland) was 191 km<sup>3</sup> yr<sup>-1</sup> (40%); to Smith Sound, Baffin Bay, Davis Strait, and the Labrador Sea (called the western seas and oceans of Greenland) was 237 km<sup>3</sup> yr<sup>-1</sup> (49%); and to the Wandel Sea and Arctic Ocean (called the northern seas and oceans of Greenland) 53 km<sup>3</sup> yr<sup>-1</sup> (11%).

In Figs. 4b and 4c, the differences in spatial catchment runoff from Greenland to the surrounding seas for both average 2000–10 minus average 1960–69 and average 2000–10 minus average 1960–2010 are illustrated. Over the last five decades, runoff increased by 142 km<sup>3</sup> yr<sup>-1</sup> (an increase of 30%) for Greenland (Table 2 and Fig. 4b), with an insignificant increase of 77 km<sup>3</sup> yr<sup>-1</sup> for the western half of Greenland and 65 km<sup>3</sup> yr<sup>-1</sup> for the eastern half of Greenland. The greatest change in runoff was in the south (26 km<sup>3</sup> yr<sup>-1</sup>) and southwest sectors (24 km<sup>3</sup> yr<sup>-1</sup>), and the least change was in the east sector (13 km<sup>3</sup> yr<sup>-1</sup>). For the eastern oceans and seas of Greenland the simulated runoff increased by 63 km<sup>3</sup> yr<sup>-1</sup>, for the western seas and oceans by 61 km<sup>3</sup> yr<sup>-1</sup>, and for the northern seas and oceans by 18 km<sup>3</sup> yr<sup>-1</sup>. On an individual catchment scale, runoff increased up to 3.0 km<sup>3</sup> yr<sup>-1</sup> (Fig. 4b) and was influenced by the catchment size, local climate variability (air temperature and precipitation), and fraction of glacier cover. Further, for the warmest decade on record, 2000–10 (Hansen et al. 2010), Greenland runoff was 91 km<sup>3</sup> yr<sup>-1</sup> above the 1960–2010 average (Table 2). This time period had the greatest change in the east (17 km<sup>3</sup> yr<sup>-1</sup>) and southwest (16 km<sup>3</sup> yr<sup>-1</sup>) sectors, the least change in the east Greenland sector (8 km<sup>3</sup> yr<sup>-1</sup>), and at the individual catchment scale was up to 1.9 km<sup>3</sup> yr<sup>-1</sup> greater than average (Fig. 4c). Also, for the eastern oceans and seas of Greenland the runoff was 41 km<sup>3</sup> yr<sup>-1</sup> above the 1960–2010 average, for the western seas and oceans 39 km<sup>3</sup> yr<sup>-1</sup> above average, and for the northern seas and oceans 11 km<sup>3</sup> yr<sup>-1</sup> above.

The length of the simulated discharge season at regional scales (for the eight sectors) was highest in the southern sectors (averaging approximately 4–6 months) and lowest in the northern sectors (averaging approximately 2–3 months) (Fig. 4a). The increase in length of discharge season between 1960–69 and 2000–10 ranged from 11 days in the north sector to 27 days in the south and southwest sectors (Fig. 4b).

The simulated changes (or increase) in Greenland runoff to the surrounding oceans can, in general, be the result of three issues: 1) changes in GrIS melt rates ( $r^2 = 0.03$ ,  $p > 0.10$ ), 2) changes in GrIS melt area (maximum extent area) ( $r^2 = 0.41$ ,  $p < 0.01$ ), 3) and changes in GrIS melt duration or period ( $r^2 = 0.21$ ,  $p < 0.01$ ). In addition, changes in Greenland runoff compared reasonably with changes in Greenland runoff duration ( $r^2 = 0.68$ ;  $p < 0.01$ ), even though this is not directly related to the production of water like the other three, but it is related to the timing (influenced by, e.g., the snow cold content and snow depth) of how long it takes for the water to reach the ocean. The explained variance between Greenland runoff and runoff duration is relatively high compared to the



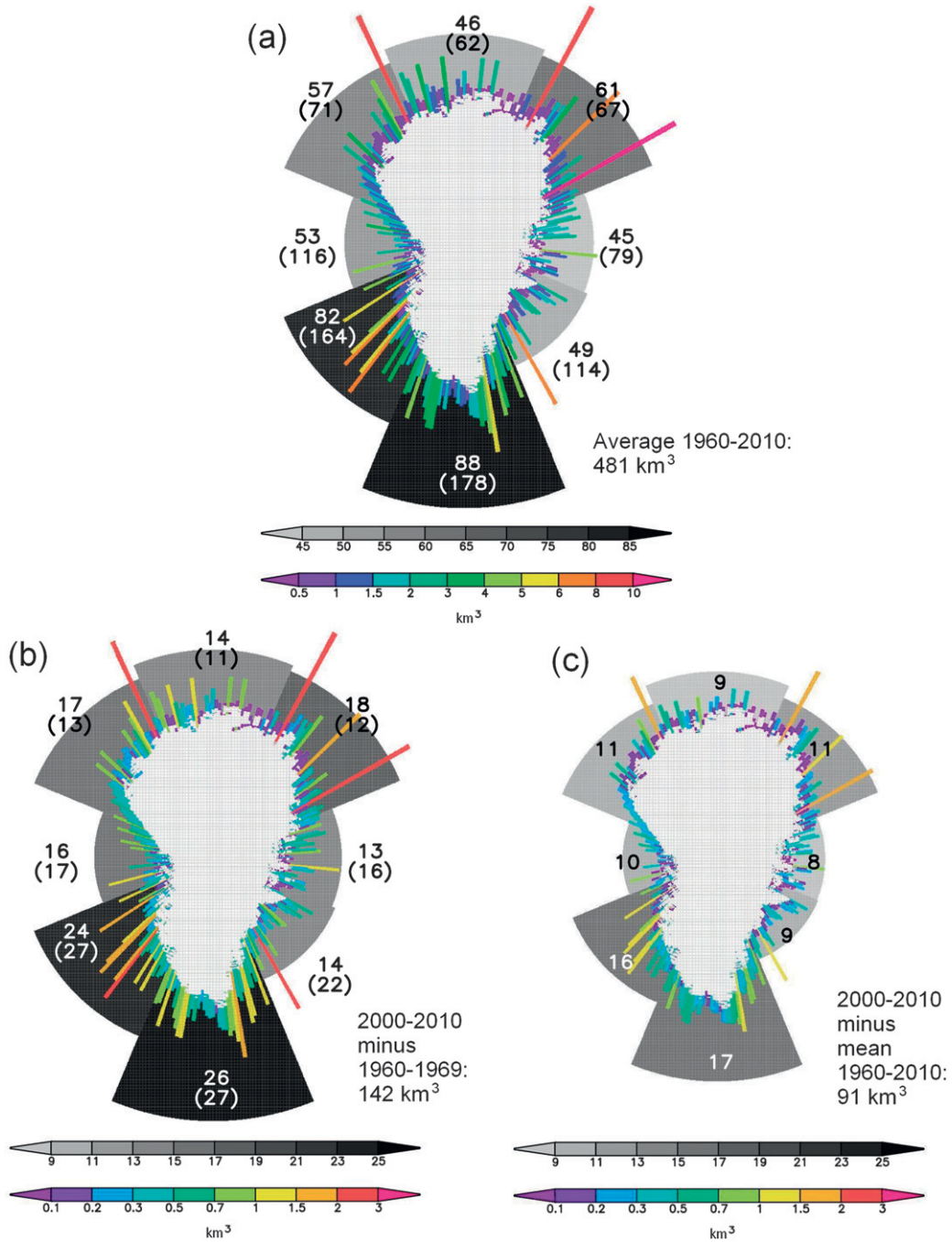


FIG. 4. Spatial distribution of simulated runoff from Greenland's individual drainage basins [each radial colored bar represents the accumulated runoff of 10 catchments located side by side (in total there are 316 radial bars); this was done to simplify the presentation of spatial runoff trends, since 85% of all catchments are equal or below 250 km<sup>2</sup>], and from the eight sectors (north, northeast, east, etc.) to the adjacent seas: (a) mean annual Greenland runoff for 1960–2010, where the numbers in brackets indicate the length of the discharge season (in days) for each region; (b) the difference between 2000–10 mean annual Greenland runoff and the 1960–69 runoff, where the numbers in brackets indicate the increase in the length (in days) of the discharge season for each region; and (c) the difference between 2000–10 mean annual Greenland runoff and the 1960–2010 mean. The regional runoff numbers for each sector have been used to scale radial distance of each gray wedge from the coast to the outside of the wedge and not from the center of Greenland to the outside of the wedge. So, for example, the 53 and 57 wedge in Fig. 4a ends are a similar distance from the coast but have very different total wedge sizes [and 49 and 45 are similar (Fig. 4a) because the coast is a similar distance from the center of the projection]. Greenland is slightly distorted from our traditional view in this radial projection.



explained variance between Greenland runoff and the climate-forcing impacts on GrIS melt conditions. This is likely because runoff at the outlet represents an integrated response of the upstream watershed to precipitation and other hydrometeorological processes like snow and glacier melt, to snow cold content, and to glaciohydrological processes like englacial bulk water storage and release, instead of just the climate impact on snow and ice conditions. In addition, this analysis suggests that increases in GrIS melt extent plays a relatively larger role in the simulated runoff increases than do the melt rate and melt duration changes.

As an additional analysis of the source of the Greenland runoff increase to the surrounding oceans over the period 1960–2010, we again assume that the increases are due, in general, to changes in 1) melt rates, 2) melt areas, and/or 3) melt duration. Because each of these is directly proportional to the total runoff (e.g., if the melt rates double, assuming all else is held constant, the runoff doubles), we assume that their contributions are proportional to their individual changes, under the constraint that their total contributions sum to equal the calculated runoff change. Applying linear regressions indicated that 103% of the Greenland runoff increase was due to increases in melt extent, 18% was due to increases in melt duration, and that there was a runoff reduction of 22% due to a decrease in melt rates. Note, that the runoff reduction due to the decreasing melt rates was more than compensated by the increase in melt extent and melt duration ( $103\% + 18\% - 22\% = 100\%$ ). During this period (also based on decadal averages), the runoff from all of Greenland increased by 30% while, in contrast, GrIS runoff increased by 50% (Table 2).

Continuing with this relatively simple attribution analysis procedure, for the GrIS itself, 87% of the GrIS runoff increase was due to increases in melt extent, 18% was due to increases in melt duration, and a reduction of 5% occurred because of a decrease in melt rates ( $87\% + 18\% - 5\% = 100\%$ ). For the land area surrounding the GrIS, the weak increase in runoff (almost horizontal trend in Fig. 2d) to the surrounding oceans over the period 1960–2010 was due to a 0% change in melt extent, with a 108% increase due to an increase in melt duration and a runoff reduction of 8% due to a decrease in melt rates ( $0\% + 108\% - 8\% = 100\%$ ). In summary, the strong increase in GrIS runoff was largely due to increases in melt extent, while the relatively small increase in land area runoff was mainly due to changes in melt duration. This and the air temperature increases noted in Fig. 2a further suggests that the increase in discharge from Greenland to the surrounding oceans is primarily the result of increasing air temperatures that allow melt to occur over more area of the GrIS.

This can also be shown using absolute runoff and runoff extent values. To quantify the absolute contributions between increasing runoff and increasing runoff extent, specific runoff can be used (runoff volume per unit drainage area per time,  $\text{L s}^{-1} \text{km}^{-2}$ ; to convert to  $\text{mm yr}^{-1}$ , multiply by 31.6). For the GrIS, melt occurring at higher and colder altitudes and latitudes means that the average specific runoff was decreasing, with absolute values of the specific runoff varying an average of  $64 \text{ L s}^{-1} \text{km}^{-2}$  in 1970–79 to  $41 \text{ L s}^{-1} \text{km}^{-2}$  in 2000–10. This indicates that the increase in runoff area extent has increased faster than the increasing runoff amount.

Here, the observed temperature increases have had a much larger contribution to increasing the available melt area than they do in increasing Greenland melt rates. The energy available to melt snow and ice in Greenland comes primarily from the incoming solar radiation component of the surface energy budget, and the air temperature distributions largely just define where and when the snow and ice melts (Marks and Dozier 1992; Liston and Hiemstra 2011).

#### *e. A case example: Runoff distribution from Helheim glacier drainage basin*

In Fig. 5a, the simulated MAAT and mean summer temperatures for June–August for the Helheim glacier drainage basin outlet in southeast Greenland are illustrated for 1960–2010 (see geographical location in Fig. 1c). Figure 5b displays the precipitation distribution time series for 1960–2010, Fig. 5c the modeled annual watershed runoff, Fig. 5d the daily average runoff on decadal intervals, and Fig. 5e the daily simulated runoff time series for 1960–2010. From 1960 to 2010 the Helheim mean summer air temperature and MAAT increased an average of  $0.3^\circ$  and  $0.8^\circ\text{C}$ , respectively, indicating less changes in temperature than the average trends for Greenland (Fig. 2a). As for Greenland in general, the trends in mean summer temperature and MAAT for Helheim before the mid-1980s were significant ( $r^2 = 0.23$ ,  $p < 0.01$ ) and was, in general, in antiphase, meaning JJA was on average decreasing while MAAT was on average increasing, and hereafter the trends were in phase (significant) ( $r^2 = 0.72$  and  $p < 0.01$ ) and increasing (Fig. 2a). Also for Helheim, the precipitation was almost in antiphase with the JJA temperature anomaly (Figs. 5a and 5b); during relatively dry years at Helheim (precipitation below average); for example, before 1970 and after 1995, the temperature was generally above average and between these years the temperature was generally below average (Figs. 5a,b): a similar pattern for Sermilik Fjord from 1900 to 2008 is illustrated in Mernild et al. (2012b). The variability

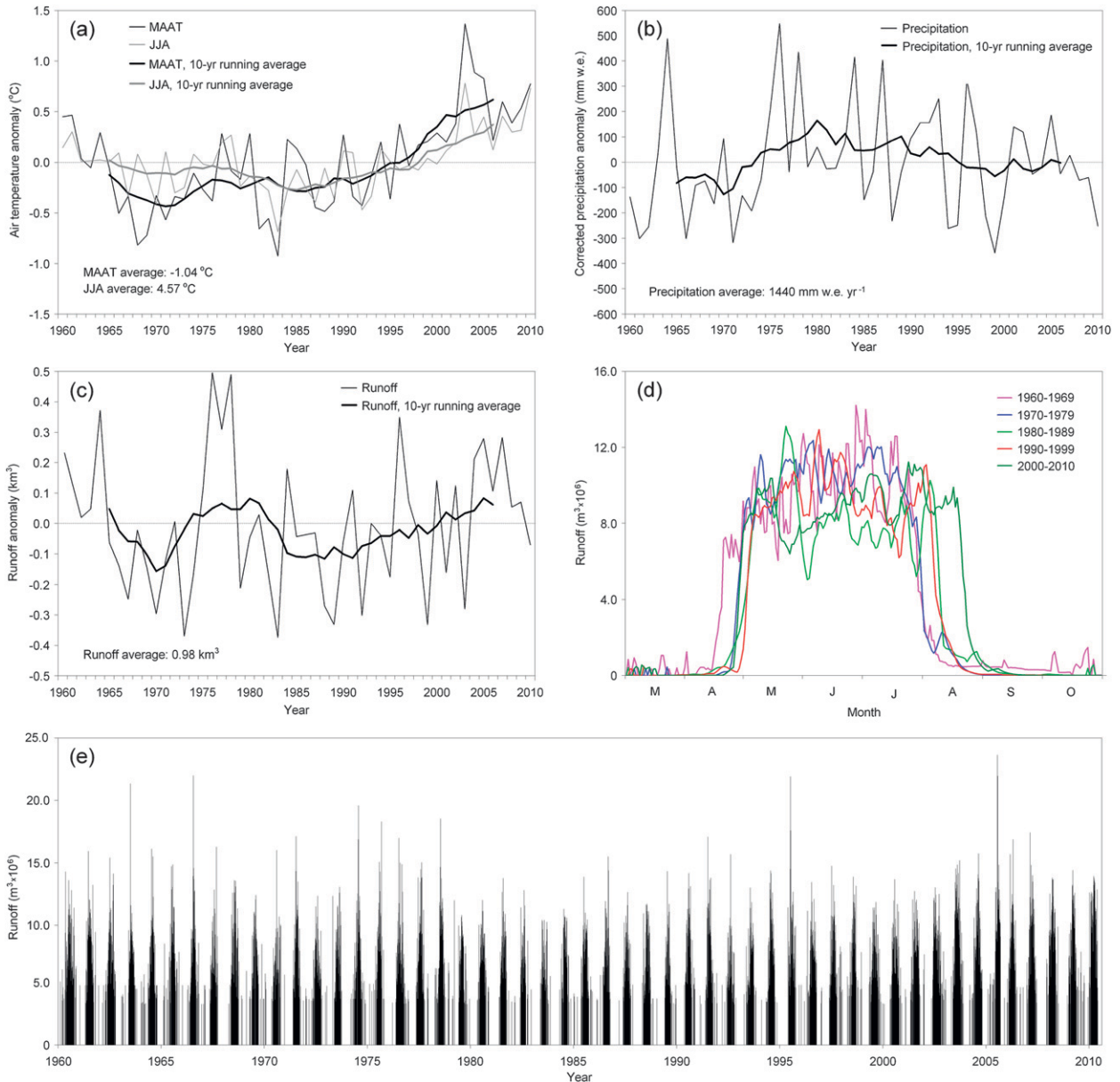


FIG. 5. (a) An example of Helheim Glacier catchment outlet mean summer (JJA) and mean annual air temperature (MAAT) anomaly time series for 1960–2010; (b) corrected annual precipitation anomaly 1960–2010; (c) simulated annual runoff anomaly 1960–2010; (d) daily average simulated Helheim Glacier catchment runoff (5-day running mean) on decadal intervals from 1960–69 through 2000–10; and (e) daily simulated Helheim Glacier catchment runoff from 1960 through 2010. The geographical location is illustrated in Fig. 1c.

between temperature and precipitation may be explained by deep Icelandic lows associated with stronger westerly winds bringing dry and relatively warm air masses to southeast Greenland during positive NAO scenarios (Bromwich et al. 1999; Hurrell and Deser 2009)—a pattern linked with a positive AMO index (Fig. 2b).

These runoff variations are due to a combined effect of climate impacts from temperature (snow and ice

melt) and precipitation (rain and snow) (Fig. 5c). Here, simulated runoff is illustrated in Figs. 5c–e. Clearly, the amount of runoff changed over time, together with the date of breakup and the runoff period. The displayed runoff (Figs. 5c,e) indicates definite seasonal, interannual, and decadal cycles. For example, it appears as though, in the illustrated 10-yr running average (Fig. 5c), the variability in runoff before 1973 ( $r^2 = 0.85$ ,  $p < 0.01$ ) and after 1986 ( $r^2 = 0.92$ ,  $p < 0.01$ ) were dominated by changes in

MAAT followed atmospheric warming (Fig. 5a), and between 1973 and 1986 by the changes in precipitation ( $r^2 = 0.71, p < 0.01$ ) (Fig. 5b). In addition, Fig. 5d shows an approximately 4-week shift in length of discharge season as the decades progress. The daily discharge hydrographs for the 50-yr simulation period (Fig. 5e) highlight the detailed interannual variations in runoff simulated as part of these MicroMet/SnowModel/HydroFlow model simulations.

#### 4. Conclusions

We have investigated the impact of changes in Greenland weather and climate conditions on surface hydrological processes and runoff for the 50-yr period 1960–2010. This included quantifying the spatial distribution and trends of meltwater and rainwater discharge into the adjacent seas from both the GrIS and the land, ice cap, and glacier areas between the GrIS and surrounding oceans. The merging of observed atmospheric forcing datasets with SnowModel—a snow and ice evolution system—and HydroFlow—a runoff routing system—allowed a detailed (5-km, daily) analysis and mapping of spatial variations in Greenland discharge to the adjacent seas and provided insights into the regional distribution of runoff features and quantities. Individual drainage catchments (~3150), each with an individual flow network, were estimated for Greenland before simulating runoff to downflow areas and the surrounding oceans. Given the severe dearth of Greenland discharge observations, runoff simulations are crucial for understanding Greenland spatial and temporal runoff variations; this runoff explains half of the recent mass loss of the GrIS (van den Broeke 2009).

Overall, Greenland has warmed and the runoff has increased during the last 50 years with the greatest runoff increase occurring in southwest Greenland and lower runoff increases occurring in northeast Greenland. The spatial runoff distributions show greater hydrological activity in southwest Greenland and lowest for the northeast Greenland region, supporting the hypothesis that discharges into the adjacent seas are greatest in regions where snowfall (end-of-winter snow accumulation) is generally low and discharge is least in regions where snowfall is high. These processes and relationships are crucial for understanding the spatial distribution of runoff to the surrounding oceans, and the linkages among a changing climate and the associated changes in runoff magnitudes and distributions.

The Greenland simulations showed distinct regional-scale runoff variability throughout the simulation domain. A similar uneven runoff pattern is expected to be

present throughout the pan-Arctic because, like Greenland, the pan-Arctic landscape has numerous individual mountain glaciers and ice caps dominating the local to regional freshwater budget, including the spatial distribution of runoff to the oceans and the contribution to present rates of global sea level rise. Gardner et al. (2011) confirmed that mountain glaciers and ice caps are contributing significantly to present rates of sea level rise and will continue to do so during the next century and beyond. In addition, the Canadian Arctic Archipelago could potentially play a key role in future sea level changes. It is located off the northwestern shore of Greenland and contains one-third of the global volume of land-based ice outside the ice sheets (Radić and Hock 2010). Its contribution to sea level rise remains largely unknown.

In addition to this Greenland application, SnowModel and HydroFlow could be used to address water resource issues associated with irrigation and drinking water in regions where snow and glacier melt are key components of the hydrologic cycle, such as the Andes and the Tibetan Plateau and its surrounding mountain ranges. The state of the Tibetan Plateau region's hydrosphere and cryosphere affects a considerable portion of the world's population, principally the inhabitants of South and East Asia (Joswiak et al. 2011); the future economic and social health and development of these populations depends critically upon snow- and ice-related hydrologic resources, especially runoff. Other potential applications of these tools include using them to estimate water supply potential for hydropower production in snow-covered and glaciated areas like Greenland and throughout the pan-Arctic and using them to quantify present and future glacier mass balance values from Earth's estimated 300 000–400 000 glaciers and ice caps (Dyurgerov and Meier 2005).

In the future, under an expected warmer climate regime, the GrIS margin, including its outlet glaciers, will retreat farther inland. Under these conditions, surface runoff from the ice sheet, local glaciers, and ice caps will likely dominate calving as the primary Greenland mass loss mechanism. This makes it crucial to understand future changes in runoff, the spatial distribution of that runoff to the seas surrounding Greenland, and the associated contribution to global sea level rise since glaciers will continue to melt and contribute to sea level rise throughout the next century and beyond (e.g., Gardner et al. 2011).

Understanding the linkages among Greenland local meltwater and runoff, freshwater discharge into the surrounding oceans, ocean circulation features such as the AMOC, and other components of the climate system will provide critical insights into the workings of the

Greenland climate system and its interactions with the rest of Earth's atmosphere, hydrosphere, and cryosphere. Historically, the representation of Greenland freshwater discharge into the oceans has been either nonexistent or unrealistically simplistic. For example, ocean models have traditionally placed the freshwater runoff flux directly into the midocean areas (Weijer et al. 2012) rather than accurately accounting for the spatial and temporal distributions of actual Greenland runoff. With their ability to transport freshwater from the interior and margins of Greenland to the surrounding seas, models such as SnowModel and HydroFlow are now available to fill this gap in climate-system representation. As a consequence, these tools are expected to make valuable contributions toward answering scientific questions related to future Greenland spatial runoff distributions, freshwater discharge into the surrounding oceans, contributions to sea level rise, and other climate-related impacts associated with changes in climate features such as ocean salinity and density stratification, ocean temperature, sea ice distributions, ocean circulation patterns such as the AMOC, and the attendant feedbacks to the atmosphere and the rest of the climate system.

*Acknowledgments.* We extend a very special thanks to the two anonymous reviewers for their insightful critique of this article. This work was supported by the Climate Change Prediction Program and Scientific Discovery for Advanced Computing (SciDAC) program within the U.S. Department of Energy Office of Science, Los Alamos National Laboratory (LANL) Director's Fellowship, LANL Institute for Geophysics and Planetary Physics, and NASA Grant NNX08AV21G. LANL is operated under the auspices of the National Nuclear Security Administration of the U.S. Department of Energy under Contract DE-AC52-06NA25396. Thanks are given to the Program for Monitoring of the Greenland Ice Sheet (PROMICE), Geological Survey of Denmark and Greenland; the Danish Meteorological Institute; the University of Utrecht; the Greenland Climate Network, University of Colorado at Boulder; and the Department of Geography and Geology, University of Copenhagen for providing meteorological station observations.

#### REFERENCES

- Allerup, P., H. Madsen, and F. Vejen, 1998: Estimating true precipitation in arctic areas. *Nordic Hydrological Programme Rep.* 44, 9 pp.
- , —, and —, 2000: Correction of precipitation based on off-site weather information. *Atmos. Res.*, **53**, 231–250.
- Bamber, J. L., S. Ekholm, and W. B. Krabil, 2001: A new, high-resolution digital elevation model of Greenland fully validated with airborne altimetry data. *J. Geophys. Res.*, **106**, 6733–6745.
- Box, J. E., and Coauthors, 2006: Greenland ice sheet surface mass balance variability (1988–2004) from calibrated Polar MM5 output. *J. Climate*, **19**, 2783–2800.
- Bromwich, D. H., Q.-S. Chen, Y. Li, and R. L. Cullather, 1999: Precipitation over Greenland and its relation to the North Atlantic Oscillation. *J. Geophys. Res.*, **104**, 22 103–22 115.
- Bryan, F. O., 1986: High-latitude salinity effects and interhemispheric thermohaline circulations. *Nature*, **323**, 301–304.
- Bryden, H. L., H. R. Longworth, and S. A. Cunningham, 2005: Slowing of the Atlantic meridional overturning circulation at 25°N. *Nature*, **438**, 655–657, doi:10.1038/nature04385.
- Chylek, P., C. K. Folland, G. Lesins, M. K. Dubey, and M. Wang, 2009: Arctic air temperature change amplification and the Atlantic multidecadal oscillation. *Geophys. Res. Lett.*, **36**, L14801, doi:10.1029/2009GL038777.
- , —, —, and —, 2010: Twentieth century bipolar seesaw of the Arctic and Antarctic surface air temperatures. *Geophys. Res. Lett.*, **37**, L08703, doi:10.1029/2010GL042793.
- Cuffey, K. M., and W. S. B. Paterson, 2010: *The Physics of Glaciers*. 4th ed. Elsevier, 707 pp.
- Dyrugerov, M. B., and M. F. Meier, 2005: Glaciers and the changing earth system: A 2004 snapshot. University of Colorado at Boulder INSTAAR Occasional Paper 58, 116 pp.
- Ettema, J., M. R. van den Broeke, E. van Meijgaard, W. J. van den Berg, J. L. Bamber, J. E. Box, and R. C. Bales, 2009: Higher surface mass balance of the Greenland ice sheet revealed by high-resolution climate modeling. *Geophys. Res. Lett.*, **36**, L12501, doi:10.1029/2009GL038110.
- Fettweis, X., 2007: Reconstruction of the 1979–2006 Greenland ice sheet surface mass balance using the regional climate model MAR. *Cryosphere*, **1**, 21–40.
- , E. Hanna, H. Gallee, P. Huybrechts, and M. Ericpicum, 2008: Estimation of the Greenland ice sheet surface mass balance during 20th and 21st centuries. *Cryosphere*, **2**, 117–129.
- , M. Tedesco, M. R. van den Broeke, and J. Ettema, 2011: Melting trends over the Greenland ice sheet (1958–2009) from spaceborne microwave data and regional climate models. *Cryosphere*, **5**, 359–375.
- Folland, C. K., T. Palmer, and D. E. Parker, 1986: Sahel rainfall and worldwide sea temperatures. *Nature*, **320**, 602–607.
- Gardner, A. S., and Coauthors, 2011: Sharply increased mass loss from glaciers and ice caps in the Canadian Arctic Archipelago. *Nature*, **473**, 357–360, doi:10.1038/nature10089.
- Hanna, E., P. Huybrechts, and T. Mote, 2002: Surface mass balance of the Greenland ice sheet from climate-analysis data and accumulation/runoff models. *Ann. Glaciol.*, **35**, 67–72.
- , —, I. Janssens, J. Cappelen, K. Steffen, and A. Stephens, 2005: Runoff and mass balance of the Greenland ice sheet: 1958–2003. *J. Geophys. Res.*, **110**, D13108, doi:10.1029/2004JD005641.
- , and Coauthors, 2008: Increased runoff from melt from the Greenland ice sheet: A response to global warming. *J. Climate*, **21**, 331–341.
- , J. M. Jones, J. Cappelen, S. H. Mernild, L. Wood, K. Steffen, and P. Huybrechts, 2012: The influence of North Atlantic atmospheric and oceanic forcing effects on 1900–2010 Greenland summer climate and ice melt/runoff. *Int. J. Climatol.*, doi:10.1002/joc.3475, in press.
- Hansen, J., R. Ruedy, M. Sato, and K. Lo, 2010: Global surface temperature change. *Rev. Geophys.*, **48**, RG4004, doi:10.1029/2010RG000345.



- Hasholt, B., and Coauthors, 2008: Hydrology and transport of sediment and solutes at Zackenberg. *High-Arctic Ecosystem Dynamics in a Changing Climate: Ten Years of Monitoring and Research at Zackenberg Research Station, Northeast Greenland*, H. Meltofte et al., Eds., Advances in Ecological Research, Vol. 40, Academic Press, 111–149.
- , A. B. Mikkelsen, M. H. Nielsen, and M. A. D. Larsen, 2012: Observations of runoff and sediment and dissolved loads from the Greenland ice sheet at Kangerlussuaq, west Greenland, 2007 to 2010. *Z. Geomorphol.*, in press.
- Hinzman, L. D., and Coauthors, 2005: Evidence and implications of recent climate change in northern Alaska and other Arctic regions. *Climatic Change*, **72**, 251–298.
- Hurrell, J. W., and C. Deser, 2009: North Atlantic climate variability: The role of the Northern Atlantic Oscillation. *J. Mar. Syst.*, **78**, 28–41.
- Jensen, L. M., and M. Rasch, 2010: Zackenberg Ecological Research operations, 15th annual report, 2009. Aarhus University National Environmental Research Institute Rep., 134 pp.
- Joswiak, M., T. Yao, and D. Joswiak, 2011: Moving forward on glacier retreat. *Eos, Trans. Amer. Geophys. Union*, **92**, 188, doi:10.1029/2011EO220006.
- Kerr, R. A., 2000: A North Atlantic climate pacemaker for the centuries. *Science*, **288**, 1984–1985.
- Lewis, S. M., and L. C. Smith, 2009: Hydrological drainage of the Greenland ice sheet. *Hydrol. Processes*, **23**, 2004–2011, doi:10.1002/hyp.7343.
- Liston, G. E., 1995: Local advection of momentum, heat, and moisture during the melt of patchy snow covers. *J. Appl. Meteor.*, **34**, 1705–1715.
- , and D. K. Hall, 1995: An energy-balance model of lake-ice evolution. *J. Glaciol.*, **41**, 373–382.
- , and M. Sturm, 1998: A snow-transport model for complex terrain. *J. Glaciol.*, **44**, 498–516.
- , and —, 2002: Winter precipitation patterns in arctic Alaska determined from a blowing-snow model and snow-depth observations. *J. Hydrometeorol.*, **3**, 646–659.
- , and K. Elder, 2006a: A distributed snow-evolution modeling system (SnowModel). *J. Hydrometeorol.*, **7**, 1259–1276.
- , and —, 2006b: A meteorological distribution system for high-resolution terrestrial modeling (MicroMet). *J. Hydrometeorol.*, **7**, 217–234.
- , and C. A. Hiemstra, 2011: The changing cryosphere: Pan-Arctic snow trends (1979–2009). *J. Climate*, **24**, 5691–5712.
- , and S. H. Mernild, 2012: Greenland freshwater runoff. Part I: A runoff routing model for glaciated and nonglaciated landscapes (HydroFlow). *J. Climate*, **25**, 5997–6014.
- , J.-G. Winther, O. Bruland, H. Elvehøy, and K. Sand, 1999: Below surface ice melt on the coastal Antarctic ice sheet. *J. Glaciol.*, **45**, 273–285.
- , R. B. Haehnel, M. Sturm, C. A. Hiemstra, S. Berezovskaya, and R. D. Tabler, 2007: Simulating complex snow distributions in windy environments using SnowTran-3D. *J. Glaciol.*, **53**, 241–256.
- Marks, D., and J. Dozier, 1992: Climate and energy exchange at the snow surface in the alpine region of the Sierra Nevada, 2, Snow cover energy balance. *Water Resour. Res.*, **28**, 3043–3054.
- Mernild, S. H., and B. Hasholt, 2006: Climatic control on river discharge simulations, Mittivakkat Glacier catchment, Ammassalik Island, SE Greenland. *Nord. Hydrol.*, **37** (4–5), 327–346.
- , and G. E. Liston, 2010: The influence of air temperature inversions on snowmelt and glacier mass balance simulations, Ammassalik Island, southeast Greenland. *J. Appl. Meteor. Climatol.*, **49**, 47–67.
- , B. Hasholt, and G. E. Liston, 2006a: Water flow through Mittivakkat Glacier, Ammassalik Island, SE Greenland. *Danish J. Geogr.*, **106**, 25–43.
- , G. E. Liston, B. Hasholt, and N. T. Knudsen, 2006b: Snow-distribution and melt modeling for Mittivakkat Glacier, Ammassalik Island, southeast Greenland. *J. Hydrometeorol.*, **7**, 808–824.
- , B. Hasholt, and G. E. Liston, 2008a: Climatic control on river discharge simulations, Zackenberg River drainage basin, northeast Greenland. *Hydrol. Processes*, **22**, 1932–1948, doi:10.1002/hyp.6777.
- , G. E. Liston, and B. Hasholt, 2008b: East Greenland freshwater runoff to the Greenland-Iceland-Norwegian Seas 1999–2004 and 2071–2100. *Hydrol. Processes*, **22**, 4571–4586, doi:10.1002/hyp.7061.
- , —, C. A. Hiemstra, and K. Steffen, 2008c: Surface melt area and water balance modeling on the Greenland ice sheet 1995–2005. *J. Hydrometeorol.*, **9**, 1191–1211.
- , —, —, E. Hanna, and J. H. Christensen, 2009: Greenland ice sheet surface mass-balance modeling and freshwater flux for 2007, and in a 1995–2007 perspective. *Hydrol. Processes*, **23**, 2470–2484, doi:10.1002/hyp.7354.
- , —, —, and J. H. Christensen, 2010: Greenland ice sheet surface mass-balance modeling in a 131-yr perspective, 1950–2080. *J. Hydrometeorol.*, **11**, 3–25.
- , —, —, —, M. Stendel, and B. Hasholt, 2011a: Surface mass-balance and runoff modeling using HIRHAM4 RCM at Kangerlussuaq (Søndre Strømfjord), west Greenland, 1950–2080. *J. Climate*, **24**, 609–623.
- , T. Mote, and G. E. Liston, 2011b: Greenland ice sheet surface melt extent and trends, 1960–2010. *J. Glaciol.*, **57**, 621–628.
- , J. K. Malmros, N. T. Knudsen, and J. C. Yde, 2012a: Multi-decadal marine- and land-terminating glacier retreat in the Ammassalik region, southeast Greenland. *Cryosphere*, **6**, 625–639.
- , M.-S. Seidenkrantz, P. Chytle, G. E. Liston, and B. Hasholt, 2012b: Climate-driven fluctuations in freshwater to Sermilik Fjord, east Greenland, during the last 4000 years. *Holocene*, **22**, 155–164, doi:10.1177/0959683611431215.
- Pfeffer, W. T., J. T. Harper, and S. O'Neil, 2008: Kinematic constraints on glacier contribution of 21st-century sea-level rise. *Science*, **321**, 1340–1343.
- Radić, V., and R. Hock, 2010: Regional and global volumes of glaciers derived from statistical upscaling of glacier inventory data. *J. Geophys. Res.*, **115**, F01010, doi:10.1029/2009JF001373.
- Rahmstorf, S., 1995: Bifurcations of the Atlantic thermohaline circulation in response to changes in the hydrological cycle. *Nature*, **378**, 145–149.
- , and Coauthors, 2005: Thermohaline circulation hysteresis: A model intercomparison. *Geophys. Res. Lett.*, **32**, L23605, doi:10.1029/2005GL023655.
- Rennermalm, A. K., L. C. Smith, V. W. Chu, R. R. Forster, J. E. Box, and B. Hagedorn, 2012: Proglacial river stage, discharge, and temperature datasets from the Akuliarusiarsuup Kuaa River northern tributary, southwest Greenland, 2008–2011. *Earth Syst. Sci. Data*, **4**, 1–12, doi:10.5194/essd-4-1-2012.



- Rignot, E., and P. Kanagaratnam, 2006: Changes in the velocity structure of the Greenland ice sheet. *Science*, **311**, 986–990.
- Schlesinger, M. E., and N. Ramankutty, 1994: An oscillation in the global climate system of period 65–70 years. *Nature*, **367**, 723.
- Serreze, M. C., and Coauthors, 2000: Observational evidence of recent change in the northern high-latitude environment. *Climatic Change*, **46**, 159–207.
- Solomon, S., D. Qin, M. Manning, M. Marquis, K. Averyt, M. M. B. Tignor, H. L. Miller Jr., and Z. Chen, Eds., 2007: *Climate Change 2007: The Physical Science Basis*. Cambridge University Press, 996 pp.
- van den Broeke, M. R., and Coauthors, 2009: Partitioning recent Greenland mass loss. *Science*, **326**, 984–986.
- Weijer, W., M. E. Maltrud, M. W. Hecht, H. A. Dijkstra, and M. A. Kliphuis, 2012: Response of the Atlantic Ocean circulation to Greenland Ice Sheet melting in a strongly-eddy ocean model. *Geophys. Res. Lett.*, **39**, L09606, doi:10.1029/2012GL051611.

[18]

Mernild, S. H., Liston, G. E., Hiemstra, C. A. and Christensen, J. H. 2010. Greenland Ice Sheet surface mass-balance modeling in a 131-year perspective 1950–2080. *Journal of Hydrometeorology*, 11(1), 3–25.

Reprinted with permission from American Meteorological Society

# Greenland Ice Sheet Surface Mass-Balance Modeling in a 131-Yr Perspective, 1950–2080

SEBASTIAN H. MERNILD\*

*International Arctic Research Center, and Water and Environmental Research Center,  
University of Alaska Fairbanks, Fairbanks, Alaska*

GLEN E. LISTON AND CHRISTOPHER A. HIEMSTRA

*Cooperative Institute for Research in the Atmosphere, Colorado State University, Fort Collins, Colorado*

JENS H. CHRISTENSEN

*Danish Climate Centre, Danish Meteorological Institute, Copenhagen, Denmark*

(Manuscript received 17 December 2008, in final form 25 August 2009)

## ABSTRACT

Fluctuations in the Greenland ice sheet (GrIS) surface mass balance (SMB) and freshwater influx to the surrounding oceans closely follow climate fluctuations and are of considerable importance to the global eustatic sea level rise. A state-of-the-art snow-evolution modeling system (SnowModel) was used to simulate variations in the GrIS melt extent, surface water balance components, changes in SMB, and freshwater influx to the ocean. The simulations are based on the Intergovernmental Panel on Climate Change scenario A1B modeled by the HIRHAM4 regional climate model (RCM) using boundary conditions from the ECHAM5 atmosphere–ocean general circulation model (AOGCM) from 1950 through 2080. In situ meteorological station [Greenland Climate Network (GC-Net) and World Meteorological Organization (WMO) Danish Meteorological Institute (DMI)] observations from inside and outside the GrIS were used to validate and correct RCM output data before they were used as input for SnowModel. Satellite observations and independent SMB studies were used to validate the SnowModel output and confirm the model's robustness. The authors simulated an ~90% increase in end-of-summer surface melt extent ( $0.483 \times 10^6 \text{ km}^2$ ) from 1950 to 2080 and a melt index (above 2000-m elevation) increase of 138% ( $1.96 \times 10^6 \text{ km}^2 \times \text{days}$ ). The greatest difference in melt extent occurred in the southern part of the GrIS, and the greatest changes in the number of melt days were seen in the eastern part of the GrIS (~50%–70%) and were lowest in the west (~20%–30%). The rate of SMB loss, largely tied to changes in ablation processes, leads to an enhanced average loss of  $331 \text{ km}^3$  from 1950 to 2080 and an average SMB level of  $-99 \text{ km}^3$  for the period 2070–80. GrIS surface freshwater runoff yielded a eustatic rise in sea level from  $0.8 \pm 0.1$  (1950–59) to  $1.9 \pm 0.1 \text{ mm}$  (2070–80) sea level equivalent (SLE)  $\text{yr}^{-1}$ . The accumulated GrIS freshwater runoff contribution from surface melting equaled 160-mm SLE from 1950 through 2080.

## 1. Introduction

The Greenland Ice Sheet (GrIS) is the Northern Hemisphere's largest terrestrial permanent ice- and snow-

---

\* Current affiliation: Climate, Ocean, and Sea Ice Modeling Group, Computational Physics and Methods, Los Alamos National Laboratory, Los Alamos, New Mexico.

---

*Corresponding author address:* Dr. Sebastian H. Mernild, Climate, Ocean, and Sea Ice Modeling Group, Computational Physics and Methods (CCS-2), Los Alamos National Laboratory, Mail Stop B296, Los Alamos, NM 87545.  
E-mail: mernild@lanl.gov

covered area and a reservoir of water, from a hydrological perspective (e.g., Box et al. 2006; Fettweis 2007; Richter-Menge et al. 2007; Mernild et al. 2008d, 2009a,b), containing between 7.0-m and 7.4-m global sea level equivalent (SLE) (Warrick and Oerlemans 1990; Gregory et al. 2004; Lemke et al. 2007). It is essential to predict and assess the impact of future climate on the GrIS, which is believed to be influenced by human activities (Albritton et al. 2001). We must establish the present and future state of the GrIS surface melt extent and surface mass balance (SMB), including freshwater flux, to detect warning signs indicative of its future response

(Hanna et al. 2008). Variability in mass balance closely follows climate fluctuations; the mass balance was close to equilibrium during the relatively cold 1970s and 1980s and lost mass rapidly as the climate warmed in the 1990s and 2000s with no indication of deceleration (Rignot et al. 2008). The GrIS is a useful indicator to ongoing climatic variations and changes, and it is suggested that the GrIS responds more quickly to climate perturbations than previously thought, particularly near the margin in southern Greenland (Velicogna and Wahr 2006).

The climate appears to be changing. Observations indicate that the most pronounced temperature increase occurs at higher northern latitudes, which have increased at almost twice the global average rate in the past 100 years (Alley et al. 2007). Since 1957 air temperature for the Arctic has increased more than 2°C (available online at <http://www.giss.nasa.gov/>). The warming was accompanied by an increase in precipitation of  $\sim 1\%$  decade<sup>-1</sup> (ACIA 2005). Simulations by atmosphere–ocean models for areas north of 60°N project an increased mean surface air temperature of 2.5°C by the mid-twenty-first century and 4.5°–5.0°C by the end of the twenty-first century (ACIA 2005; Alley et al. 2007).

A response to an altered climate has already been observed on the GrIS, manifested by thinning along its periphery (primarily in the south) and a slight thickening of  $\sim 2$ –5 cm yr<sup>-1</sup> in the interior (e.g., Krabill et al. 1999, 2000, 2004; Johannessen et al. 2005; Thomas et al. 2006; Zwally et al. 2005). Changes in air temperature result in large changes in the surface melt extent. The GrIS passive microwave satellite-derived surface melt extent increased  $17.6 \times 10^3$  (1973–2007; Mote 2007) and  $40.0 \times 10^3$  km<sup>2</sup> yr<sup>-1</sup> (1992–2005, Tedesco 2007); for 2007 a record GrIS melt extent occurred (e.g., Mernild et al. 2009a,b). Further, for the area above 2000-m elevation the 2007 melt index, defined as the melting area times the number of melting days, was 153% greater than the average for the period 1988–2006, setting a new record (Mote 2007; Tedesco 2007; Mernild et al. 2009b). In contrast to 2007, snowmelt over the whole GrIS in 2008 was not significant at high elevations. Melt extent in 2008 was, however, above the 1979–2007 average, with the 2008 updated melt extent trend of approximately  $16 \times 10^3$  km<sup>2</sup> yr<sup>-1</sup> (Tedesco et al. 2008).

Numerous GrIS mass-balance studies using airborne laser altimetry and models (the positive-degree approach and energy balance) suggest a balance ranging between 25 and  $-60$  km<sup>3</sup> water equivalent (w.eq.) yr<sup>-1</sup> (1961–2003), from  $-50$  to  $-100$  km<sup>3</sup> w.eq. yr<sup>-1</sup> (1993–2003) and a reduction at even higher rates between 2003 and 2005 to a loss of  $\sim 270$  km<sup>3</sup> w.eq. yr<sup>-1</sup> in 2007 (Lemke et al. 2007; Rignot et al. 2008; Mernild et al.

2009b). Analyses of the Gravity Recovery and Climate Experiment (GRACE) satellite data show mass loss of 75–129 km<sup>3</sup> w.eq. yr<sup>-1</sup> (2003–05) and losses ranging from 150 to 270 km<sup>3</sup> w.eq. yr<sup>-1</sup> (2002–07) (Velicogna and Wahr 2005, 2006; Chen et al. 2006; Lutchke et al. 2006; Ramillien et al. 2006). This indicates an accelerating GrIS mass loss in the 1990s up through the beginning of the twenty-first century, equivalent to a net global eustatic sea level rise of  $\sim 0.5$  mm SLE yr<sup>-1</sup> (Velicogna and Wahr 2006).

Nearly half of the mass lost from the GrIS originates by surface melting and subsequent freshwater runoff into the ocean. The other half is from iceberg calving and geothermal melting (e.g., Lemke et al. 2007; Mernild et al. 2008c). Calculated runoff losses are provided by Janssens and Huybrechts (2000), 281 km<sup>3</sup> yr<sup>-1</sup> (1953–2003); Mote (2003), 278 km<sup>3</sup> yr<sup>-1</sup> (1988–99); Box et al. (2006), 396 km<sup>3</sup> yr<sup>-1</sup> (1995–2004); Hanna et al. (2008), 351 km<sup>3</sup> yr<sup>-1</sup> (1995–2007); Fettweis (2007), 304 km<sup>3</sup> yr<sup>-1</sup> (1979–2006); Mernild et al. (2008d), 392 km<sup>3</sup> yr<sup>-1</sup> (1995–2005); and Mernild et al. (2009a,b), 397 km<sup>3</sup> yr<sup>-1</sup> (1995–2007). Increases indicate an accelerating GrIS runoff, probably playing a potential role in ocean salinity, sea ice dynamics, the global eustatic sea level rise (e.g., Dowdeswell et al. 1997; ACIA 2005; Box et al. 2006; Alley et al. 2007), and thermohaline circulation (THC) of the Greenland–Iceland–Norwegian Seas (e.g., Broecker et al. 1985; Broecker and Denton 1990; Su et al. 2006). Accelerating GrIS runoff could perturb the THC by reducing the density contrast driving the circulation (Rahmstorf et al. 2005). Any weakening of the circulation in response to increased GrIS runoff induced by global warming (Gregory et al. 2005; Swingedouw et al. 2006) could reduce heat inflow to the Greenland–Iceland–Norwegian Seas and subsequently reduce the warming in the region, including northwest Europe.

This study attempts to improve our quantitative understanding of the past, present, and future (131-yr perspective, 1950–2080) GrIS surface melt extent and its related water balance components. Specifically, we address changes in the SMB and the influx of freshwater to the ocean as a contribution to the global eustatic sea level rise. The goal of this study is to apply a well-tested approach—a state-of-the-art snow-evolution modeling system, SnowModel (e.g., Liston and Elder 2006a,b; Liston et al. 2007; Mernild et al. 2006b, 2008c)—to the GrIS for the period from 1950 through 2080 based on the Intergovernmental Panel on Climate Change (IPCC) A1B climate scenario. The climate scenario is used in a high-resolution regional climate model (RCM)HIRHAM4 developed by the Danish Meteorological Institute (DMI) (Christensen et al. 1996; Stendel et al. 2008). The RCM output data was calibrated and tested using in situ

meteorological observations obtained from the GrIS [Greenland Climate Network (GC-Net); 1995–2005] and the coast [World Meteorological Organization (WMO) DMI meteorological stations] before being used as meteorological forcings for SnowModel. SnowModel was tested by coincident passive microwave satellite images and SMB studies. We performed the GrIS model simulations for the 131-yr period (1950–2080) with the following objectives: 1) assess the HIRHAM4 RCM meteorological driving data against in situ meteorological observations; 2) quantify the GrIS end-of-summer maximum surface melt extent and long-term trends; 3) estimate and analyze the GrIS water balance components, including the SMB and freshwater runoff; and 4) quantify the GrIS freshwater runoff and accumulated runoff contribution to global sea level rise.

## 2. Study area

Greenland is the world's largest island, and the GrIS the Northern Hemisphere's largest terrestrial permanent ice- and snow-covered area ( $1.834 \times 10^6 \text{ km}^2$ ), which covers approximately 85% of the island (Fig. 1). Greenland is roughly 2600 km long, up to approximately 950 km wide, and the ice sheet's maximum altitude is more than 3200 m MSL. The total ice sheet volume is  $2.85 \times 10^6 \text{ km}^3$ , equivalent to an average global sea level rise between 7.0 and 7.4 m SLE (Warrick and Oerlemans 1990; Gregory et al. 2004; Lemke et al. 2007).

The climate in Greenland is arctic (Born and Böcher 2001). In the northern parts of the GrIS, winter air temperatures can drop below  $-70^\circ\text{C}$ , whereas on the east Greenland land strip, summer temperatures can briefly rise above  $25^\circ\text{C}$  (Mernild et al. 2008b). The observed GrIS mean annual air temperature (MAAT) is  $-13.3^\circ\text{C}$ , covering a nonsignificant MAAT warming of  $\sim 1.8^\circ\text{C}$  for the period 1995–2005 (based on data from the 10 coastal meteorological stations, Fig. 1; Table 1, stations 16–25). In southern and southeastern Greenland, the observed annual precipitation is  $\sim 2400 \text{ mm w.eq. yr}^{-1}$ , while the northern desertlike areas hardly receive any precipitation ( $< 200 \text{ mm w.eq. yr}^{-1}$ ) (e.g., Born and Böcher 2001; Serreze and Barry 2005). Many of the island's characteristics cause considerable contrast in its weather conditions—including complex coastal topography, elevation, distance from the coastal area, marginal glaciers, and ice caps—and the GrIS, which makes the climate vary appreciably even over short distances. Temperature inversions are a common feature for Greenland coastal areas (Hansen et al. 2008; Mernild et al. 2008a) and for the GrIS (Putnins 1970).

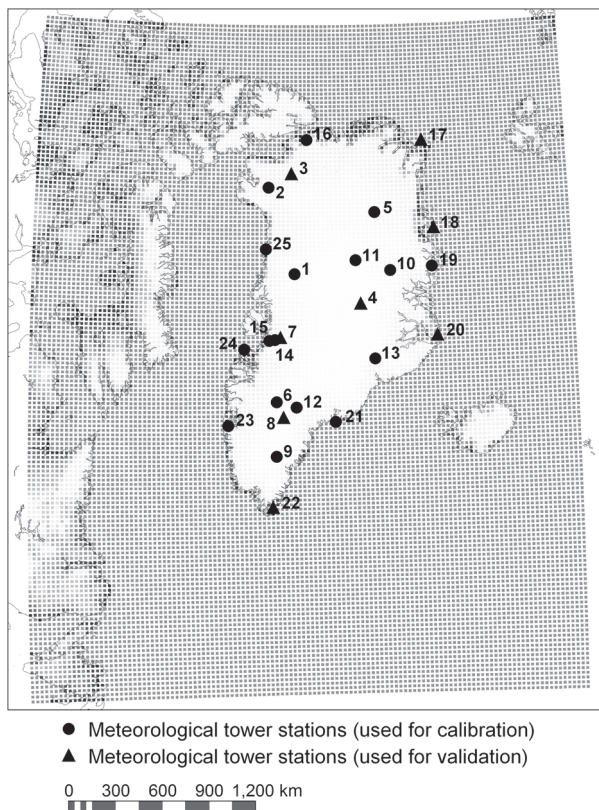


FIG. 1. The HIRHAM4 RCM Greenland simulation domain, including the GrIS, and the location of the meteorological stations (used for calibration and validation): the GC-Net meteorological stations from the GrIS and the WMO meteorological stations near the coast. The figure is based on a study by Stendel et al. (2008).

## 3. Models and methods

Throughout the Arctic, rough terrain, harsh climatic conditions, and remote locales are commonly cited reasons for lacking knowledge and adequate data. Furthermore, logistical constraints make it difficult to collect extensive observations of snow, sublimation, evaporation, and snow and glacier melt. Collecting runoff measurements have typically been considered impossible. Also, scattered Arctic meteorological stations and limited winter and summer GrIS mass-balance observations have resulted in sparse and unreliable data related to the spatial and temporal distribution of snow precipitation, sublimation, surface snow and ice melt across much of the GrIS, and runoff to the ocean. Such key components are essential to hydrological research efforts, and there is a clear need to explore issues associated with data sparseness and modeling capabilities.

Likewise, there are several kinds of uncertainties related to climate projections using simulations with coupled atmosphere–ocean GCMs (AOGCMs). Apart from uncertainties in future greenhouse gas and aerosol



TABLE 1. Meteorological input data for the Greenland SnowModel simulations. Meteorological station data on the GrIS (Station numbers 1–15 and 26) were provided by the Cooperative Institute for Research in Environmental Sciences, University of Colorado at Boulder; coastal meteorological station data (station numbers 16–18 and 20–25) by DMI; and the Zackenberg meteorological station (station number 19) by the Danish National Environmental Research Institute and the University of Copenhagen.

Station number	Station name	Location	Data period	Altitude (m MSL)	Station used for calibration (C) or validation (V)
1	NASA-U	73°50'31"N, 49°29'54"W	1 Jan 1998 to 29 May 2005	2369	C
2	GITS	77°08'16"N, 61°02'24"W	7 May 1999 to 14 May 2005	1869	C
3	Humboldt	78°31'36"N, 56°49'50"W	2 Jan 1998 to 23 Jun 2005	1995	V
4	Summit	72°34'47"N, 38°30'18"W	1 Sep 1999 to 31 Aug 2005	3208	V
5	Tunu-N	78°00'59"N, 33°59'00"W	17 May 1996 to 7 Nov 2003	2052	C
6	DYE-2	66°28'48"N, 46°16'44"W	25 May 1996 to 15 Nov 2003	2165	C
7	JAR1	69°29'51"N, 49°41'16"W	20 Jun 1996 to 10 Dec 2005	962	V
8	Saddle	65°59'58"N, 44°30'03"W	20 Apr 1997 to 10 Oct 2004	2456	V
9	South Dome	63°08'56"N, 44°49'02"W	23 Apr 1996 to 12 Oct 2004	2901	C
10	NASA-E	75°00'02"N, 29°59'50"W	3 May 1997 to 23 Oct 2004	2614	C
11	NGRIP	75°05'59"N, 42°19'57"W	9 Jul 1997 to 29 Dec 2004	2950	C
12	NASA-SE	66°28'45"N, 42°29'56"W	24 Apr 1998 to 25 May 2005	2393	C
13	KAR	69°41'58"N, 33°00'21"W	18 May 1998 to 7 Jun 2005	2579	C
14	JAR2	69°25'09"N, 50°03'55"W	2 Jun 1999 to 31 Aug 2005	542	C
15	JAR3	69°23'40"N, 50°18'36"W	1 Jan 2001 to 24 May 2004	283	C
16	Hall Land	81°41'00"N, 59°57'00"W	1 Sep 1995 to 31 Aug 1996	105	C
17	Station Nord	81°36'00"N, 16°39'00"W	1 Sep 1995 to 31 Aug 2005	36	V
18	Danmarkshavn	76°46'00"N, 18°40'00"W	1 Sep 1995 to 31 Aug 2005	11	V
19	Zackenberg	74°28'10"N, 20°34'20"W	1 Sep 1997 to 31 Aug 2005	43	C
20	Ittoqqortoormiit	70°29'00"N, 21°57'00"W	1 Sep 1995 to 31 Aug 2005	66	V
21	Tasiilaq	65°36'00"N, 37°38'00"W	1 Sep 1995 to 31 Aug 2005	44	C
22	Ikerassuaq	60°03'00"N, 43°10'00"W	1 Sep 1995 to 31 Aug 2005	88	V
23	Nuuk	64°10'00"N, 51°45'00"W	1 Sep 1995 to 31 Aug 2005	80	C
24	Aasiaat	68°42'00"N, 52°45'00"W	1 Sep 1995 to 31 Aug 2005	88	C
25	Kitsissorsuit	74°02'00"N, 57°49'00"W	1 Sep 1995 to 31 Aug 2005	40	C

emissions and their conversion to radiative forcings, there are uncertainties in global and, in particular, regional climate responses to these forcings owing to, for example, different parameterizations [discussed in detail by Stocker et al. (2001)]. There is also large natural variability on the regional scale (consider, e.g., the North Atlantic Oscillation), so it is difficult to determine which part of the response of a model is due to anthropogenic forcing and to natural variability (solar, volcanic, but also unforced), respectively.

This implies that there is no single “best” model to use in an assessment of Arctic (or Greenland) climate changes, although some models clearly perform better than others (e.g., Christensen et al. 2007b; Walsh et al. 2008). However, most of the uncertainties mentioned in the previous paragraph can be quantified by using ensembles of model simulations rather than one particular model. Here, we are limited by the availability of one realization of a downscaling experiment only, where the behavior of the driving GCM model is amazingly realistic in describing present-day conditions in the Arctic in general and around Greenland in particular (Walsh et al. 2008; Stendel et al. 2008).

#### a. Choosing the model configuration

To assess how representative our results may be, given our particular regional–global model setup, we note as an important starting point that the ECHAM5 GCM is one of the best performing state-of-the-art models when it comes to representing the present climate. Walsh et al. (2008) in their study of GCMs participating in the most recent Coupled Model Intercomparison Project (CMIP) found that for Greenland, the Arctic, and the Northern Hemisphere, the ECHAM5 model outperforms most other IPCC class models with respect to all three parameters studied: temperature, precipitation, and mean sea level pressure. In the presence of sea ice, snow coverage, and frozen grounds, the interpretation of a climate change signal from GCM simulations is very sensitive to the realism of simulated present-day conditions (e.g., see Christensen et al. 2007b, 2008). Visual inspection of temperature bias maps in Walsh et al. (2008, Fig. 8) documents that sea ice coverage for present-day conditions in the Arctic is very well depicted by ECHAM5, whereas most other GCMs tend to show severe biases reflecting either too much or too little sea ice in many

locations of the Arctic. In Christensen et al. (2007b), the climate change signal for 21 CMIP models (including ECHAM5) are displayed. As pointed out in Christensen et al. (2008), it is interesting to note, however, that the projected climate signals to some degree are caused by quite different mechanisms. Observing in an extract of the performance of the model from Walsh et al. (2008), they found a common feature for most of the models, reflected by the ensemble mean, of a clear tendency to simulate too much sea ice in the Barents Sea in winter, with the ECHAM5 model being a clear exception. At the same time, the greatest warming by the end of the century is simulated exactly over this region in the ensemble mean as well as by the individual models. In the National Center for Atmospheric Research and Geophysical Fluid Dynamics Laboratory models, for example, this is partly reflecting the present-day bias, while in the ECHAM5 model, this apparently cannot be the case. Furthermore, in general, the largest warming occurs in the area with too much ice (strong cold bias) under present-day conditions. Thus to some extent, the results at the regional scale are clearly subject to systematic errors in present-day simulations. Using an ensemble of models masks this deficiency. Therefore, maps of warming must be carefully analyzed and cannot be used at face value in a region with nonlinear feedbacks, such as in the presence and absence of sea ice.

Given these caveats, we are confident that ECHAM5-based simulations are as good as any possible simulation based on a random choice of a GCM. If all GCMs were used for downscaling, the resulting distribution would partly (perhaps even largely) be due to outlier models with a poor representation of Arctic and Greenland climate (especially sea ice) conditions. It is beyond the scope of the present paper to quantify in more detail the uncertainty of our results owing to of the GCM-RCM choice made here.

### *b. HIRHAM4 RCM*

The IPCC A2 and B2 climate scenarios (available online at <http://www.ipcc.ch>) have been used in the HIRHAM4 RCM (Christensen et al. 1996, 2001; Bjørge et al. 2000; Christensen and Christensen 2007) for several climate change time-slice experiments for present and future conditions, with the third climate configuration of the Met Office Unified Model (HadCM3) AOGCM (Gordon et al. 2000; Pope et al. 2000) or ECHAM4 AOGCM (Roeckner et al. 1996; Christensen et al. 2007a,b) as boundary conditions. These simulation areas cover central and northern Europe. The performance of the model for arctic conditions has been found to be state of the art in many aspects (e.g., Christensen and Kuhry 2000; Dethloff et al. 2002; Kilsholm et al.

2003). In a recent HIRHAM4 study Stendel et al. (2008) has set up the model to conduct a transient climate change experiment representing the period 1950–2080 for the IPCC scenario A1B, covering Greenland and adjacent sea areas (Fig. 1). This A1B scenario was run on a 25-km grid cell increment with 19 vertical levels, using boundary conditions from ECHAM5 AOGCM (Roeckner et al. 2003). While high-resolution regional climate simulations to date mainly have been run as time-slice experiments, we present results of a transient simulation covering 1950–2080. All forcing data have been taken from the transient ECHAM5–Max Planck Institute Ocean Model (MPI-OM1) run. The A1B experiment, as described in the IPCC Fourth Assessment Report (AR4), runs (runs were done in a worldwide coordination with a clearly defined common model setup) begin in 2000, and the AOGCM uses outputs from a detailed simulation of the twentieth-century experiment as initial conditions in 2000 (e.g., Randall et al. 2007).

Of course, it would be desirable to investigate an ensemble of RCM simulations [different RCMs forced by different GCMs or at realizations of a single GCM, as done in the PRUDENCE project, see Christensen et al. (2007a)]. This was, however, impossible owing to the lack of computer capacity, so we had to restrict ourselves to this particular configuration. The results from Walsh et al. (2008) indicate that the chosen GCM is a sensible choice when only one realization can be offered. Déqué et al. (2007) indicates that the role of choosing a particular ensemble member is insignificant compared with choosing the GCM.

### *c. SnowModel description*

SnowModel (Liston and Elder 2006a) is a spatially distributed snowpack evolution modeling system specifically designed to be applicable over the wide range of snow landscapes, climates, and conditions found around the world. It is made up of four submodels: MicroMet defines the meteorological forcing conditions (Liston and Elder 2006b); EnBal calculates the surface energy exchanges, including melt (Liston 1995; Liston et al. 1999); SnowPack simulates snow depth and water equivalent evolution (Liston and Hall 1995); and SnowTran-3D is a blowing-snow model that accounts for snow redistribution by wind (Liston and Sturm 1998, 2002; Liston et al. 2007). Although other distributed snow models exist (e.g., Tarboton et al. 1995; Marks et al. 1999; Winstral and Marks 2002), the SnowTran-3D component allows for application in arctic, alpine (i.e., above treeline), and prairie environments that make up 68% of seasonally snow-covered areas in the Northern Hemisphere (Liston 2004). SnowModel also simulates snow-related physical processes at spatial scales ranging from 5 m to global and

temporal scales ranging from 10 min to a whole season. Simulated processes include 1) accumulation and loss from snow precipitation, and blowing-snow redistribution; 2) loading, unloading, and blowing-snow sublimation; 3) snow density evolution; and 4) snowpack ripening and melt. SnowModel was originally developed for glacier-free landscapes. For glacier surface mass-balance studies, SnowModel was modified to simulate glacier ice melt after winter snow accumulation had ablated (Mernild et al. 2006b, 2007).

### 1) MICROMET

MicroMet is a quasi-physically based meteorological distribution model (Liston and Elder 2006b) specifically designed to produce the high-resolution meteorological forcing distributions (air temperature, relative humidity, wind speed, wind direction, precipitation, solar and longwave radiation, and surface pressure) required to run spatially distributed terrestrial models over a wide range of landscapes in a physically realistic manner. MicroMet uses elevation-related interpolations to modify air temperature, humidity, and precipitation following Kunkel (1989), Walcek (1994), Dodson and Marks (1997), and Liston et al. (1999). Temperature and humidity distributions are defined to be compatible with the observed lapse rates. Wind flow in complex topography is simulated following Ryan (1977) and Liston and Sturm (1998). Solar radiation variations are calculated using elevation, slope, and aspect relationships (Pielke 2002). Incoming longwave radiation is calculated while taking into account cloud cover and elevation-related variations following Iziomon et al. (2003). Precipitation is distributed following Thornton et al. (1997). In addition, any data from more than one location, at any given time, are spatially interpolated over the domain using a Gaussian distance-dependent weighting function and interpolated to the model grid using the Barnes objective analysis scheme (Barnes 1964, 1973; Koch et al. 1983). Liston and Elder (2006b) and Liston et al. (2007) have performed a rigorous validation of MicroMet using various observational datasets, data denial, and geographic domains. Furthermore, MicroMet has been used to distribute observed and modeled meteorological variables over a wide variety of landscapes in the United States: Colorado (Greene et al. 1999), Wyoming (Hiemstra et al. 2002, 2006), Idaho (Prasad et al. 2001), and arctic Alaska (Liston et al. 2002, 2007; Liston and Sturm 1998, 2002); Norway: Svalbard and central Norway (Bruland et al. 2004); east Greenland (Mernild et al. 2006b, 2007); the Greenland ice sheet (Mernild et al. 2008c,d, 2009a,b); and near-coastal Antarctica (Liston et al. 1999; Liston and Winther 2005). As an example, the GrIS validations of MicroMet-simulated meteorological

data indicate substantial correlation with independently observed GrIS meteorological data from, for example, the Swiss camp [located within 50 km from JAR1 (station 7) at 1140 m MSL (Table 1, Fig. 1)]. MicroMet-generated air temperature, relative humidity, and precipitation values account for 84%, 63%, and 69%, respectively, of the variance in the observed 1995–2005 daily averaged dataset. The wind speed has less strong correlations, but the results remain respectable (>50% variance) for representations of GrIS meteorological processes (Mernild et al. 2008d).

### 2) ENBAL

EnBal performs standard surface energy balance calculations (Liston 1995, Liston et al. 1999). This component simulates surface (skin) temperatures and energy and moisture fluxes in response to observed and/or modeled near-surface atmospheric conditions provided by MicroMet. Surface latent and sensible heat fluxes and snowmelt calculations are made using a surface energy balance model of the form:

$$(1 - \alpha)Q_{si} + Q_{li} + Q_{le} + Q_h + Q_e + Q_c = Q_m, \quad (1)$$

where  $Q_{si}$  is the solar radiation reaching the earth's surface,  $Q_{li}$  is the incoming longwave radiation,  $Q_{le}$  is the emitted longwave radiation,  $Q_h$  is the turbulent exchange of sensible heat,  $Q_e$  is the turbulent exchange of latent heat,  $Q_c$  is the conductive energy transport,  $Q_m$  is the energy flux available for melt, and  $\alpha$  is the surface albedo. Details of each term in Eq. (1) and the model solution are available in Liston (1995) and Liston et al. (1999). In the presence of snow or glacier ice, surface temperatures greater than 0°C indicate that energy is available for melting. This energy is computed by fixing the surface temperature at 0°C and solving Eq. (1) for  $Q_m$ . Energy transports toward the surface are defined to be positive.

### 3) SNOWPACK

SnowPack is a single-layer snowpack evolution and runoff/retention model that describes snowpack changes in response to precipitation and melt fluxes defined by MicroMet and EnBal (Liston and Hall 1995; Liston and Elder 2006a). Its formulation closely follows Anderson (1976). In SnowPack, the density changes with time in response to snow temperature and weight of overlying snow (Liston and Elder 2006a). A second density-modifying process results from snow melting. The melted snow reduces the snow depth and percolates through the snowpack. If the snow temperature is below freezing, any percolating/liquid water refreezes and is stored in the snow (in the “pores”) as internal refreezing.

When saturated snow density is reached, assumed to be  $550 \text{ kg m}^{-3}$  (Liston and Hall 1995), actual runoff occurs. This provides a method to account for heat and mass transfer processes, such as snowpack ripening, during spring melt. The density of new snow from additional accumulation is defined following Anderson (1976) and Liston and Hall (1995). Static-surface (nonblowing snow) sublimation calculated in EnBal is used to adjust the snowpack depth; blowing-snow sublimation is calculated in SnowTran-3D (Liston and Elder 2006a).

#### 4) SNOWTRAN-3D

SnowTran-3D (Liston and Sturm 1998; Liston et al. 2007) is a three-dimensional submodel that simulates snow depth evolution (deposition and erosion) resulting from windblown snow based on a mass-balance equation that describes the temporal variation of snow depth at each grid cell within the simulation domain. SnowTran-3D's primary components are a wind flow forcing field, a wind shear stress on the surface, snow transport by saltation, snow transport by turbulent suspension, sublimation of saltating and suspended snow, and accumulation and erosion at the snow's surface (Liston and Sturm 2002). Simulated transport and blowing-snow sublimation processes are influenced by the interactions among available snow, topography, and atmospheric conditions (Liston and Sturm 1998). SnowTran-3D simulates snow depth evolution and then uses the snow density simulated by SnowPack to convert it to the more hydrologically significant snow water equivalent (SWE) depth. Deposition and erosion, which lead to changes in snow depth [Eq. (2)], are the result of changes in horizontal mass transport rates of saltation  $Q_{\text{salt}}$  ( $\text{kg m}^{-1} \text{ s}^{-1}$ ), changes in horizontal mass transport rates of turbulent suspended snow  $Q_{\text{turb}}$  ( $\text{kg m}^{-1} \text{ s}^{-1}$ ), sublimation of transported snow particles  $Q_v$  ( $\text{kg m}^{-2} \text{ s}^{-1}$ ), and the water equivalent precipitation rate  $P$  ( $\text{m s}^{-1}$ ). Combined, the time rate of change in snow depth  $\zeta$  (m) is

$$\frac{d(\rho_s \zeta)}{dt} = \rho_w P - \left( \frac{dQ_{\text{salt}}}{dx} + \frac{dQ_{\text{turb}}}{dx} + \frac{dQ_{\text{salt}}}{dy} + \frac{dQ_{\text{turb}}}{dy} \right) + Q_v, \quad (2)$$

where  $t$  (s) is time;  $x$  (m) and  $y$  (m) are the horizontal coordinates in the west–east and south–north directions, respectively; and  $\rho_s$  and  $\rho_w$  ( $\text{kg m}^{-3}$ ) are snow and water density, respectively. At each time step Eq. (2) is solved for each individual grid cell within the domain and is coupled to the neighboring cells through the spatial derivatives ( $d/dx$ ,  $d/dy$ ). SnowTran-3D simulations have previously been compared against observations in glacier and glacier-free alpine, Arctic, and Antarctic land-

scapes (Greene et al. 1999; Liston et al. 2007; Prasad et al. 2001; Hiemstra et al. 2002, 2006; Liston and Sturm 2002; Bruland et al. 2004; Mernild et al. 2006b, 2007, 2008c,d, 2009a,b).

#### 5) SNOWMODEL INPUT

To solve the equations, SnowModel requires spatially distributed fields of topography and land cover in addition to temporally distributed point meteorological data (air temperature, relative humidity, wind speed, wind direction, and precipitation). Meteorological data was obtained from the HIRHAM4 RCM model (1950–2080) based on the IPCC scenario A1B and from observations from meteorological stations located within the simulation domain (1995–2005). For this study, observed data are obtained from 25 meteorological stations: 15 stations from the GC-Net, 9 from the WMO station from the near coast operated by the DMI, and 1 by the Danish National Environmental Research Institute and the University of Copenhagen (Fig. 1 and Table 1). Simulations were performed on a one-day time step, although snow and ice melt and blowing snow are threshold processes that may not be accurately represented by this time step. We recognize that the use of daily averaged atmospheric forcing variables, instead of hourly values, will produce a smoothing of the natural system. Therefore, daily simulated melt (ablation) and blowing-snow processes (accumulation) were tested against hourly simulated ablation and accumulation values from a test area, the Mittivakkat Glacier ( $31 \text{ km}^2$ ) in southeast Greenland (Mernild and Liston 2010), and remain significant ( $p < 0.01$ , where  $p$  is level of significance), with an average difference of 2%, 3%, and 8% for the glacier winter, summer, and net mass balances, respectively.

Snow precipitation measurements include uncertainties, especially under windy and cold conditions (e.g., Yang et al. 1999; Liston and Sturm 2002, 2004; Serreze and Barry 2005). Solid and liquid precipitation measurements at the DMI meteorological stations (Fig. 1 and Table 1, stations 16–18 and 20–25) were calculated from Helman–Nipher shield observations corrected according to Allerup et al. (1998, 2000). Solid (snow) precipitation was calculated from snow depth sounder observations at the other stations (Fig. 1 and Table 1) after sounder data noise was removed; these data are assumed to be accurate within  $\pm 10\%$ – $15\%$  (Mernild et al. 2007, 2009b). Snow depth sounder observations were partitioned into liquid (rain) and solid (snow) precipitation at different air temperatures based on methods employed at Svalbard (Førland and Hanssen-Bauer 2003). For air temperatures below  $-1.5^\circ\text{C}$ , sounder data were considered to represent solid precipitation and for temperatures above  $3.5^\circ\text{C}$  precipitation is considered liquid; linear interpolation was



used to calculate snow and rain fractions at temperatures between these limits. Snow depth increases at relative humidity  $<80\%$  and wind speed  $>10 \text{ m s}^{-1}$  were removed to better distinguish between the proportions of real snow accumulation based on precipitation events and blowing-snow redistribution (Mernild et al. 2007, 2009b). Remaining snow depth increases were adjusted using a temperature-dependent snow density (Brown et al. 2003) and hourly snowpack settling.

Greenland topographic data for the model simulations were provided by Bamber et al. (2001), who applied “correction” elevations derived by satellite imagery to an existing radar-altimetry digital elevation model (DEM). The image-derived correction was determined from a high-resolution (625 m) grid of slopes inferred from the regional slope-to-brightness relationship of 44 Advanced Very High Resolution Radiometer images covering all of Greenland (Scambos and Haran 2002). For the model simulations, this time-invariant DEM was aggregated to a 5-km gridcell increment and clipped to yield a  $2830 \text{ km} \times 1740 \text{ km}$  simulation domain that encompassed all of Greenland. The GrIS terminus was confirmed or estimated by using aerial photos and maps (1:250 000, Geodetic Institute, Denmark).

SnowModel is a surface model producing first-order effects of climate change; it does not include glacio-hydrodynamic and sliding routines. Using a time-invariant DEM could be inappropriate. Therefore, a 1950–2080 assessment of GrIS volume, area, and maximum and average heights was performed using the simulation code for polythermal ice sheets (SICOPOLIS) (Greve 1997a,b, 2005), a state-of-the-art 3D dynamic/thermodynamic shallow-ice approximation model. On the basis of the IPCC A1B scenario for the period, there was a small change in the GrIS. By 2080 the volume differed 3% ( $5.01 \times 10^4 \text{ km}^3$ ), melt area changed 8% ( $4.88 \times 10^4 \text{ km}^2$ ), and heights shifted  $<1\%$  (maximum height: 17 m and average height:  $3 \pm (8) \text{ m}$ ). These discrepancies fall well within the uncertainties of this study. Furthermore, for this study there is only a one-way nesting between HIRHAM4 (the atmosphere) and SnowModel (the surface), not taking into account, for example, the positive albedo feedback associated with snowmelt and the fact that wet snow absorbs as much as three times more incident solar energy than dry snow (Steffen 1995).

Each grid cell within the domains was assigned a U.S. Geological Survey land use/land cover system class according to the North American Land Cover Characteristics Database, Version 2.0 [available from the USGS Earth Resources Observatin and Science (EROS) Center’s Distributed Active Archive Center, Sioux Falls, South Dakota]. The snow-holding depth (the snow depth

TABLE 2. User-defined constants used in the SnowModel simulations (see Liston and Sturm 1998) for parameter definitions).

Symbol	Value	Parameter
$C_v$		Vegetation snow-holding depth (equal surface roughness length) (m)
	0.50	Barren
	0.15	Grassland
	1.00	Mixed forest
	0.50	Mixed tundra
	0.30	Shrubland
	0.01	Snow
	0.01	Ice
	0.50	Wooded tundra
	0.50	Wooded wetland
$f$	0.01	Water (ocean and lake)
	500.0	Snow equilibrium fetch distance (m)
$U_{*t}$	0.25	Threshold wind shear velocity ( $\text{m s}^{-1}$ )
$dt$	1	Time step (day)
$dx = dy$		Gridcell increment used at different simulations (km)
	0.1	Model validation at Mittivakkat and Zackenberg catchments
	5.0	Entire Greenland simulation
$\alpha$		Surface albedo
	0.8	Snow
	0.4	Ice
$\rho$		Surface density ( $\text{kg m}^{-3}$ )
	280	Snow
	910	Ice

that must be exceeded before snow can be transported by wind) was assumed to be constant. Albedo was assumed to be 0.8 for snow (Table 2). Realistically, snow albedo changes with time and surface characteristics (Pomeroy and Brun 2001); thus, the model will likely underestimate energy available for surface melting. Therefore, SnowModel simulations with a fixed snow albedo of 0.8 was tested against simulated variable snow albedo from a test area, the Jakobshavn Isbræ drainage area in west Greenland [for information about the variable albedo routines see Mernild et al. (2009c)], indicating a mean annual variable snow albedo of 0.7 and a difference of up to  $\sim 15\%$  in SMB and runoff. When the snow is ablated, GrIS surface ice conditions are used. Ice albedo was invariant and assumed to be 0.4. The GrIS ablation zone is characterized by lower albedo on the margin and an increase in albedo toward the equilibrium line altitude (ELA), where a veneer of ice and snow dominate the surface (Boggild et al. 2006). The emergence and melting of old ice in the ablation zone creates surface layers of dust (black carbon particles) that were originally deposited with snowfall higher on the ice sheet. This debris cover is often augmented by locally derived windblown sediment (Boggild et al.



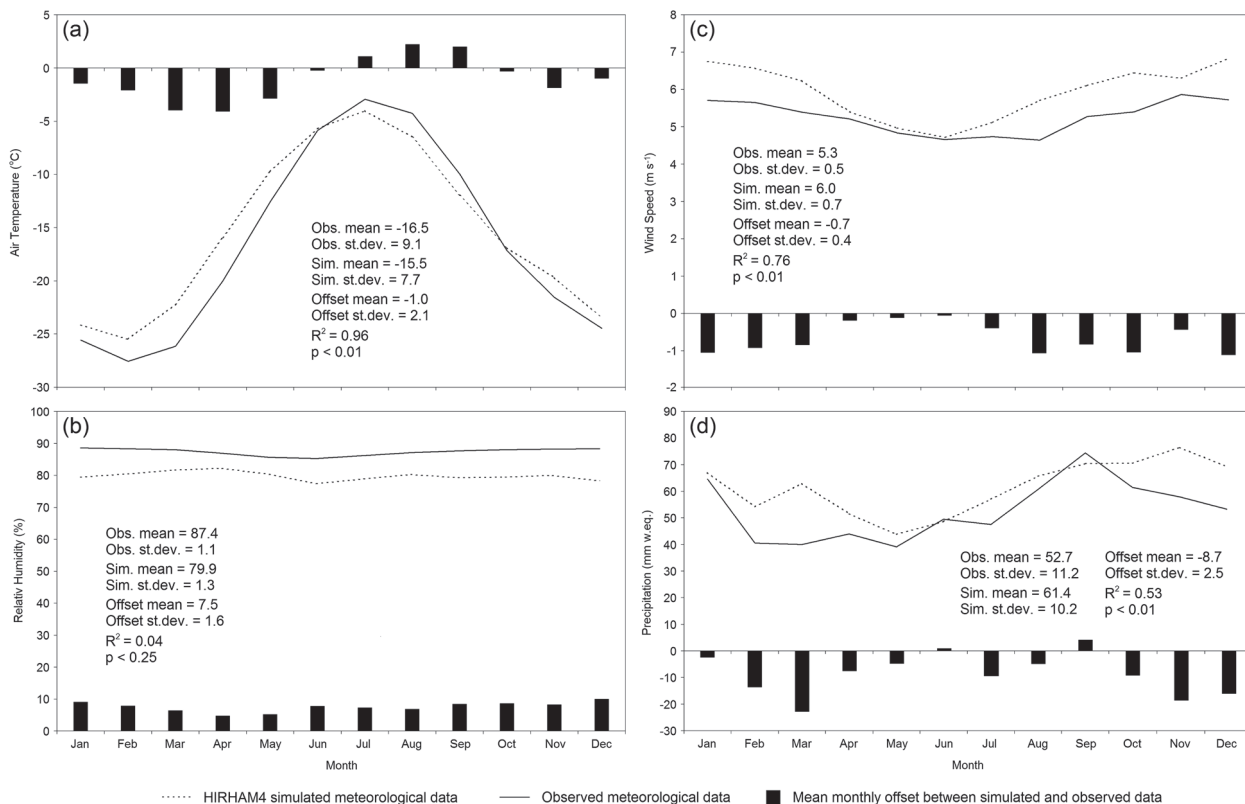


FIG. 2. Observed and HIRHAM4 RCM simulated meteorological data (25-km grid cell): (a) air temperature, (b) relative humidity, (c) wind speed, and (d) precipitation for the period 1995–2005 (see Fig. 1 and Table 1 for stations used for calibration). The mean monthly offset between the observed and the modeled values is illustrated and used for calibration of HIRHAM RCM modeled values for the period 1950–2080.

2006). Particles on or melting into the ice change the area-average albedo, increasing melt. User-defined constants for SnowModel are shown in Table 2 [for parameter definitions see Liston and Sturm (1998, 2002)]. All fjord and ocean areas within the domain were excluded from model simulations. Further, changes in glacier storage based on changes in supraglacial storage (lakes, pond, channels, etc.), englacial storage (ponds and the water table), subglacial storage (cavities and lakes), meltwater routing, evolution of a runoff drainage system, and changes based on iceberg calving, tidal response where ice meets ocean, and geothermal melting are not calculated in the SnowModel simulations, even though they might influence the contribution of runoff.

d. Satellite images

Detection of surface melt at large spatial scales is effectively accomplished by using satellite microwave data. The daily GrIS snowmelt extent is mapped (25-km gridcell increment) using passive microwave satellite observations that discriminate wet from dry snow. The

criterion for melt is 1% mean liquid water content by volume in the top meter of snow (Abdalati and Steffen 1997). The center part of the GrIS is the area where the melting threshold of the cross-well ground-penetrating radar microwave algorithm did not show any melt. The end-of-summer maximum observed spatial surface melt distribution at the GrIS was used to validate SnowModel melt simulations.

e. HIRHAM4 RCM validation and uncertainty

Before the HIRHAM4 RCM output data can be trusted for use as input data for further modeling, it needs to be tested and calibrated against observed meteorological data since RCM output biases can be large. Stendel et al. (2007) provide some basic validation of the current simulation. However, because HIRHAM is running in a full climate mode, that is, the driving GCM only knows about the state of the atmosphere–ocean system from the external drivers (sun, aerosols, and greenhouse gases), whether actually realized (1950–2000) or projected (2001–80) we need for our purpose to tie in this single realization with the observed

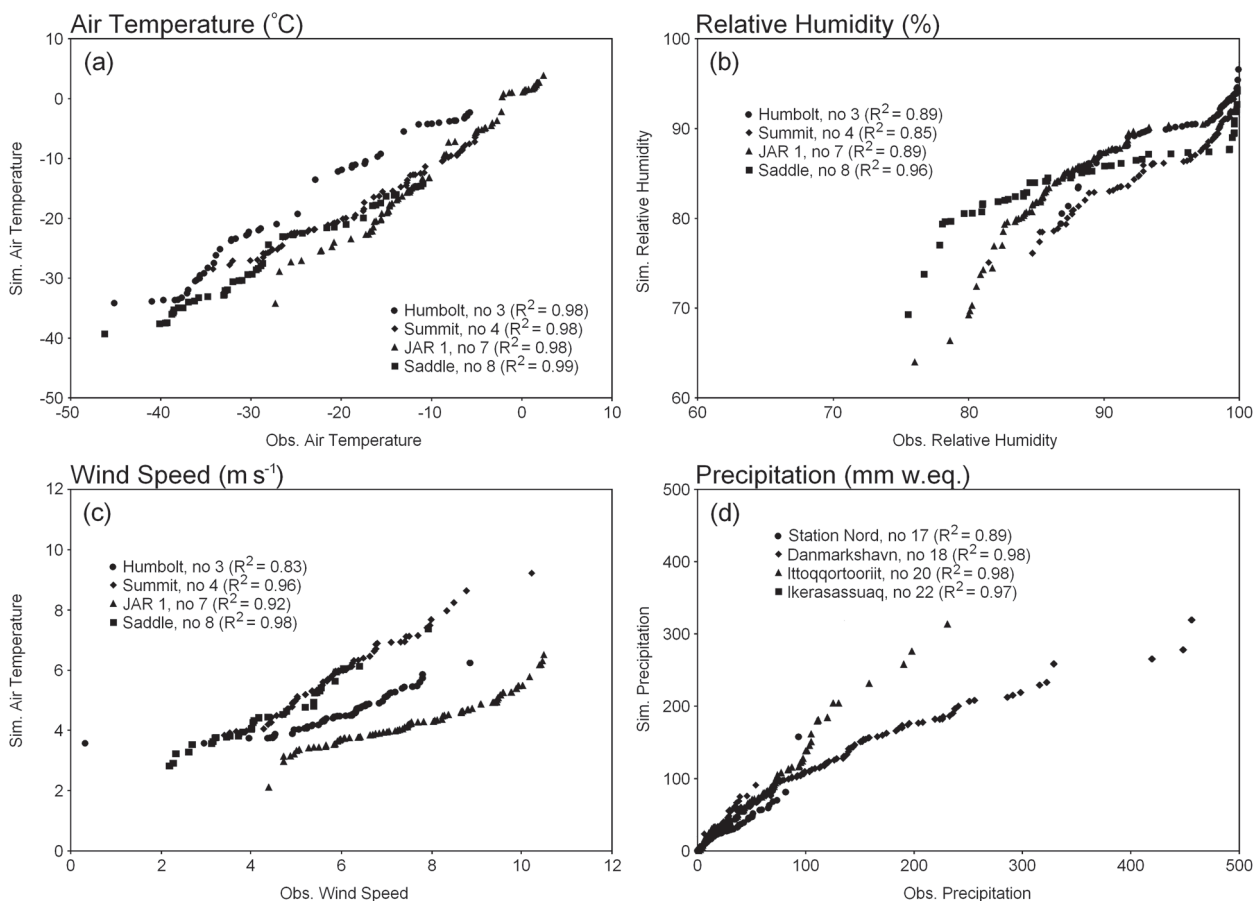


FIG. 3. Comparison between ranked monthly observed meteorological data and ranked HIRHAM4-MicroMet-SnowModel simulated data for the period 1995–2005: (a) mean air temperature, (b) mean relative humidity, (c) mean wind speed, and (d) precipitation. For air temperature, relative humidity, and wind speed four meteorological stations at different elevations on the GrIS were used—Humbolt (No. 3), Summit (No. 4), JAR1 (No. 7), and Saddle (No. 8)—and for precipitation four meteorological stations at different latitude were used—Station Nord (No. 17), Danmarkshavn (No. 18), Ittoqqortoormiit (No. 20), and Ikerasassuaq (No. 22). Only monthly precipitation values above 0 mm w.eq. were included. For additional station information and data period, see Table 1.

climate system. We have excellent data for verifying SnowModel covering the period 1995–2005. For a bias adjustment or calibration of the HIRHAM results a 10-yr period is relatively short; however, we have assessed the role of this short period by an additional calibration in which the model years were 1980–90 and the observed years 1995–2005. The resulting offset in precipitation is on average 42 mm w.eq. (or 7%) and the temperature difference was 1.5°C (or 10%) for 1980–90 with respect to the calibration period 1995–2005. Relative humidity and wind are both insignificantly changed. Mean monthly offset between the RCM modeled output and the observed meteorological data were further estimated for the period 1995–2005 (see Fig. 2 and Table 1 for station information). These mean monthly (1995–2005) offset values were added to the daily RCM meteorological parameters to correct each variable (air

temperature, relative humidity, wind speed, and corrected precipitation) for the 1950–2080 period before being used as meteorological forcings for SnowModel. To assess the performance of the adjusted SnowModel simulated spatial distributed meteorological data the spatial distributed meteorological data were tested against in situ meteorological observations (with data not used for calibration) spanning 1995–2005 (see Table 1 for stations used for calibration and validation). We have ranked the data for each period and compared the ranked numbers. This illustrates the ability of HIRHAM to capture the span of realized parameters for the period of concern and, therefore, also gives a rough estimate about the calibration method. Ideally we should use longer periods and address classical climatological values, but this is beyond the scope of the present work, and some of the results are provided elsewhere (e.g., Stendel

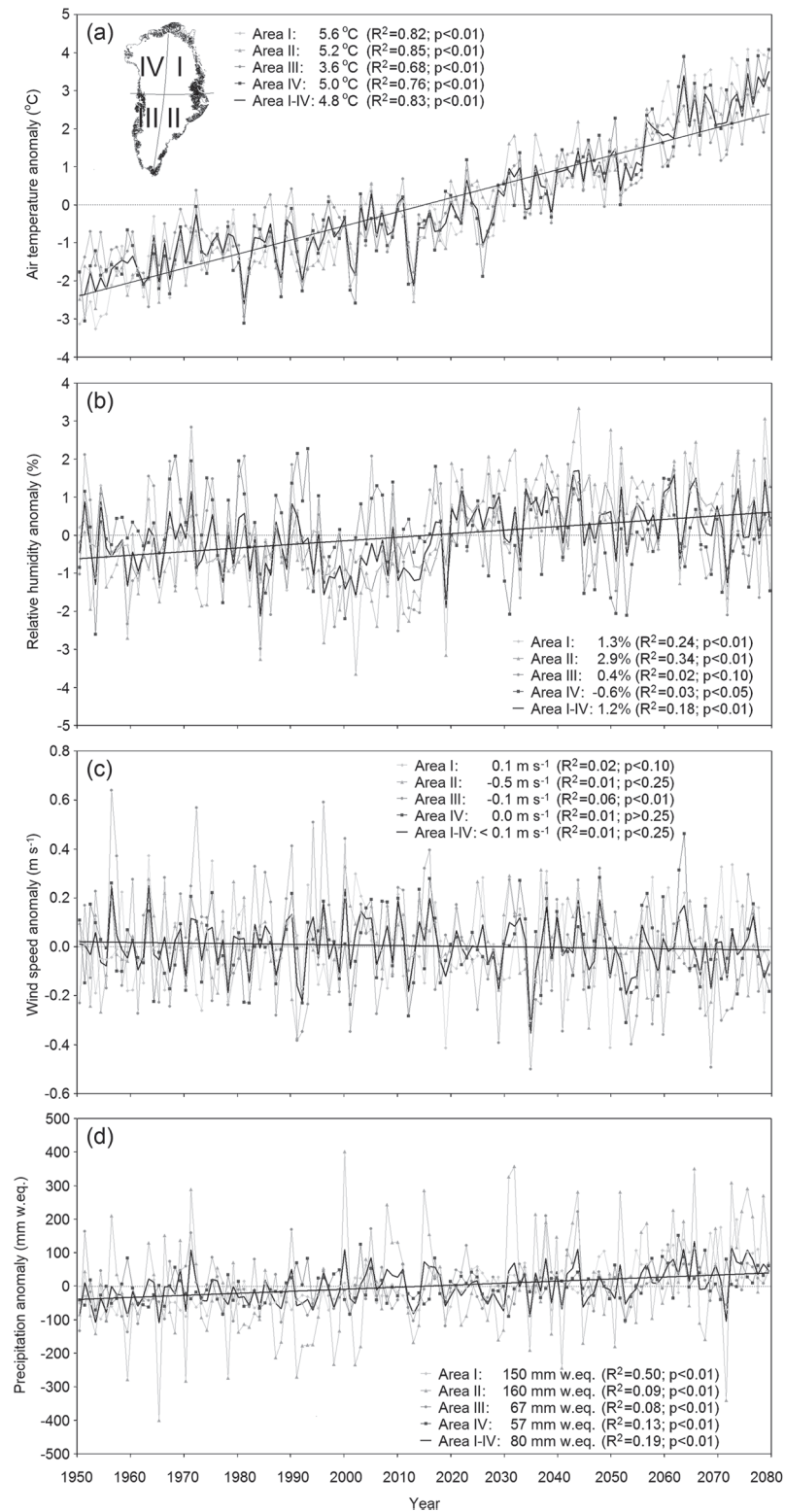


FIG. 4. HIRHAM4 RCM-calibrated anomaly time series and average changes for the GrIS subareas I to IV from 1950 through 2080 for (a) air temperature, (b) relative humidity, (c) wind speed, and (d) precipitation. For all four parameters the zero line is included, and  $R^2$  and  $p$  (level of significance). The inset in (a) indicates the division of the GrIS into subareas I-IV.

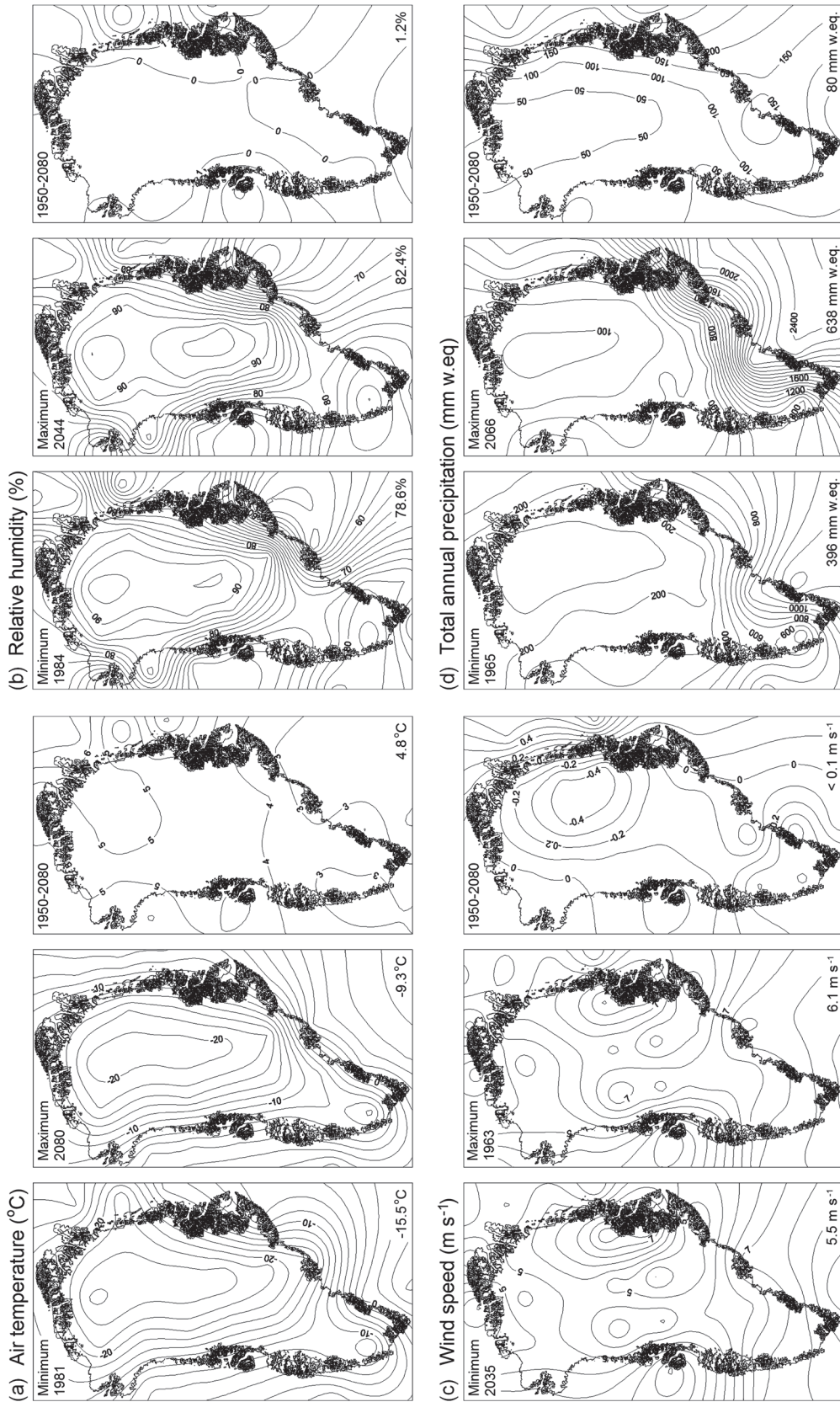


FIG. 5. Greenland HIRHAM4 RCM calibrated annual minimum average, annual maximum average, and average annual trend difference from 1950 through 2080 for the parameters (a) air temperature, (b) relative humidity, (c) wind speed, and (d) precipitation. Years for the annual minimum and maximum are indicated for each parameter.



TABLE 3. Simulated rank-ordered GrIS mean summer air temperature (Jun–Aug) and summer anomaly from 1950–2080.

Rank	Year	Absolute summer air temperature (°C)	Summer anomaly (°C)
1	2074	0.58	2.71
2	2078	0.46	2.59
3	2076	0.42	2.55
4	2080	0.17	2.29
5	2066	0.08	2.21
6	2063	−0.13	2.00
7	2075	−0.21	1.91
8	2060	−0.37	1.76
9	2073	−0.39	1.74
10	2069	−0.41	1.71
122	1992	−3.43	−1.31
123	1952	−3.46	−1.34
124	2018	−3.50	−1.38
125	1954	−3.58	−1.46
126	1965	−3.59	−1.47
127	1960	−3.60	−1.47
128	1951	−3.61	−1.48
129	1953	−3.63	−1.51
130	1950	−3.66	−1.53
131	1963	−3.88	−1.75
1950–2080 average and standard deviation		−2.12 ± 1.06	0.00
Minimum		0.58	−1.75
Maximum		−3.88	2.71
Range		4.46	4.46
Average change (°C)			3.14

et al. 2007). Validations of the simulated GrIS meteorological data (air temperature, relative humidity, and wind speed) indicate substantial correlation with in situ-observed meteorological data from different meteorological stations on the GrIS—JAR1, Humbolt, Saddle, and Summit—at different elevations and with in situ-observed precipitation from outside the GrIS—Station Nord, Danmarkshavn, Ittoqqortoormiit, and Ikerasassuaq—at different latitudes (see Fig. 3 and Table 1 for station information). Modeled air temperature values account for 98%–99% of the variance in the observed 1995–2005 mean monthly dataset. The relative humidity, corrected precipitation, and wind speed have the same or slightly fewer strong correlations, but results remain respectable for relative humidity (between 85% and 96%), wind speed (between 83% and 98%), and for precipitation (between 89% and 98%) for representations of the GrIS meteorological processes (Figs. 3a–3d).

The most obvious model bias is the systematic dry bias of the simulated near-surface humidity, particularly when humidity is high. This is related to a general difficulty of representing coastal climate on model land points in HIRHAM (Stendel et al. 2008). For precipitation, we note that, with the exception of Danmarkshavn, the model

captures the span of observed precipitation rather well (perhaps surprisingly so), given the short period of comparison. For temperature, the annual cycle is clearly the dominant feature in the explained variance. However, we also note that the agreement over the full span of temperatures is within what seems to be acceptable for our purpose (see, however, Stendel et al. 2008).

#### f. SnowModel validation and uncertainty

Few quality observations for spatial in situ snow-evolution, snow and ice surface melt, and glacier net mass-balance are available in Greenland, including from the GrIS. SnowModel accumulation and ablation routines have been tested quantitatively [simulations based on observed meteorological data; for further information see Mernild et al. (2006a,b, 2007, 2008d)] at local scale (from east and west Greenland) and regional scale (from the GrIS) using observations from snow pit depths; glacier winter, summer, and net mass balances; depletion curves; photographic time lapses; satellite images (microwave satellite-derived melt extent); and different parameterizations such as melt index and ELA. A maximum discrepancy between modeled and observed SWE depths of 7%, glacier mass balances of 7%, snow cover extent of 7%, and GrIS melt discrepancy between melt and nonmelt boundaries of 32(±24) km occurs (Mernild et al. 2009a,b). However, in northeastern Greenland, the discrepancy can be up to 160 km where the distances among meteorological stations is far (Fig. 1). In this study, SnowModel-simulated melt extent were compared against concurrent passive microwave satellite-derived melt extent and previous GrIS SMB studies.

SnowModel, like all models, possesses uncertainties owing to processes not represented by the modeling system. For example, routines for simulating the air temperature inversion layer and variable snow and ice albedo are not yet included. In addition, changes in the GrIS area, size, and height according to glacier dynamical processes and subglacial geothermal bottom melting and sliding are not calculated in the model routines. Based on the uncertainties in the modeled results from previous Greenland SnowModel simulations, including the GrIS, it is reasonable to assume that this GrIS SMB study is influenced with a similar maximum uncertainty of 7% for SWE depth, snow cover extent, and SMB components (Mernild et al. 2006a,b, 2007, 2008d).

## 4. Results and discussion

### a. Regional climate model trends 1950–2080

The regional climate model adjusted meteorological data for the 1950–2080 GrIS (air temperature, relatively



TABLE 4. Decadal GrIS MAAT; surface melt extent; melt index (above 2000 m MSL); precipitation  $P$ ;  $E + SU$ , where  $E$  is evaporation and  $SU$  is sublimation; runoff  $R$ ; change in storage  $\Delta S$ ; ELA, specific runoff (Rs), runoff equivalent to a global sea level rise from 1950 through 2080. The runoff values do not include hydroglacio processes, such as sudden release of bulk water.

	1950–59	1960–69	1970–79	1980–89	1990–99	2000–09
MAAT ( $^{\circ}\text{C}$ )	$-14.8 \pm 0.4$	$-14.3 \pm 0.5$	$-13.9 \pm 0.4$	$-14.1 \pm 0.7$	$-13.8 \pm 0.5$	$-13.5 \pm 0.7$
Passive microwave satellite-derived surface melt extent ( $10^6 \text{ km}^2$ )	—	—	—	0.484	0.678	0.774 <sup>b</sup>
Surface melt extent ( $10^6 \text{ km}^2$ and %)	0.469 (26)	0.510 (28)	0.586 (32)	0.617 (34)	0.737 (40)	0.797 (43)
Melt index above 2000 m MSL ( $\text{km}^2 \times \text{days } 10^6$ )	$1.42 \pm 1.34$	$1.48 \pm 1.27$	$1.51 \pm 1.20$	$1.72 \pm 1.29$	$1.52 \pm 1.14$	$1.63 \pm 1.28$
ELA (m MSL)	$1158 \pm 343$	$1151 \pm 274$	$1257 \pm 201$	$1312 \pm 295$	$1238 \pm 356$	$1367 \pm 281$
$P$ ( $\text{km}^3 \text{ yr}^{-1}$ )	$600.1 \pm 68.7$	$635.9 \pm 67.8$	$683.1 \pm 92.5$	$618.7 \pm 47.9$	$637.1 \pm 55.6$	$663.7 \pm 62.0$
$E + SU$ ( $\text{m}^3 \text{ yr}^{-1}$ )	$137.6 \pm 17.5$	$109.4 \pm 16.0$	$142.3 \pm 14.4$	$143.2 \pm 16.5$	$148.2 \pm 15.1$	$135.4 \pm 14.0$
$R$ ( $\text{km}^3 \text{ yr}^{-1}$ )	$284.7 \pm 36.1$	$270.6 \pm 39.5$	$299.5 \pm 25.9$	$314.5 \pm 53.5$	$353.8 \pm 59.7$	$425.4 \pm 48.1$
Ablation ( $E+SU+R$ ), $\text{K m}^3 \text{ yr}^{-1}$	$422.3 \pm 45.7$	$380.0 \pm 46.1$	$441.8 \pm 31.6$	$457.7 \pm 53.3$	$502.0 \pm 64.8$	$560.8 \pm 45.5$
$\Delta S$ ( $\text{Km}^3 \text{ yr}^{-1}$ )	$177.8 \pm 71.7$	$255.9 \pm 73.2$	$241.3 \pm 96.3$	$161.0 \pm 53.7$	$135.1 \pm 89.4$	$102.9 \pm 71.6$
$R_s$ ( $1 \text{ s}^{-1} \text{ km}^{-2} \text{ yr}^{-1}$ )	$4.9 \pm 0.6$	$5.2 \pm 0.7$	$5.2 \pm 0.4$	$5.4 \pm 0.9$	$6.1 \pm 1.0$	$7.4 \pm 0.8$
Runoff equivalent to the global sea level change ( $\text{mm SLE yr}^{-1}$ )	$0.79 \pm 0.10$	$0.75 \pm 0.11$	$0.83 \pm 0.05$	$0.87 \pm 0.18$	$0.98 \pm 0.16$	$1.18 \pm 0.16$
Accumulated runoff equivalent to the global sea level change ( $\text{mm SLE yr}^{-1}$ )	7.9	15.4	23.7	32.4	42.2	54.0

<sup>a</sup> The average values are based on 11 years of data, otherwise only 10 years are used for each decade from 1950 to 1959 through 2060 to 2069.

<sup>b</sup> Average passive microwave satellite-derived surface melt extent for the period 2000–07.

<sup>c</sup> Average passive microwave satellite-derived surface melt extent for the period of 1980–2007.

humidity, wind speed, and precipitation) are illustrated in Figs. 4a–d. The GrIS is divided into four subareas (I–IV, Fig. 4a). The greatest changes in predicted MAAT of  $5.6^{\circ}\text{C}$  occurs in northeast Greenland (area I) (significant,  $p < 0.01$ ); this is likely due to the projected change in sea ice extent and thickness, particularly off the east coast of Greenland. The lowest warming,  $3.6^{\circ}\text{C}$ , occurs in area III (significant  $p < 0.01$ ), southwest Greenland (Fig. 4a), where sea surface temperatures are changing only marginally (see Stendel et al. 2008). Overall, MAAT increased a significant  $4.8^{\circ}\text{C}$  from 1950 through 2080 (Fig. 4a). Patterns of annual minimum average (1981) and annual maximum average (2080) temperature distribution (Fig. 5a) show the variable extent of low interior temperatures ( $< -20^{\circ}\text{C}$ ) and higher temperatures in coastal Greenland ( $> 0^{\circ}\text{C}$ ). Temporally, the average change in summer (June–August) temperature—temperatures affecting the ablation processes—is  $3.1^{\circ}\text{C}$  (significant,  $p < 0.01$ ). Six of the coldest summers occurred in the first decade (1950–59), while the six warmest summers were in the last decade (2070–80) of

the simulations (Table 3). We note here that this behavior underlines the general aspect of the simulation, namely, that the steady warming despite decadal variations is quite robust, which is not likely to be altered if another ECHAM5 ensemble member had been chosen. The average change in summer temperature ( $3.1^{\circ}\text{C}$ ) is below the average change in MAAT ( $4.8^{\circ}\text{C}$ ). A winter (December–February) average change of  $5.9^{\circ}\text{C}$  (significant,  $p < 0.01$ ) is sizeable. Identical seasonal trends were identified in observations by Box (2002) and Sturm et al. (2005) from the 1970s through 1990s.

From 1950 to 2080 relative humidity increased  $1.2\%$  on average (significant,  $p < 0.01$ ) (Figs. 4b and 5b). Average wind speed decreased slightly,  $< 0.1 \text{ m s}^{-1}$  (insignificant,  $p < 0.25$ ); the largest reduction,  $-0.2$  to  $-0.5 \text{ m s}^{-1}$ , occurs on the GrIS northeastern interior (Figs. 4c and 5c). Modeled precipitation increased  $80 \text{ mm w.eq.}$  on the GrIS (significant,  $p < 0.01$ ), with the lowest gain of  $57 \text{ mm w.eq.}$  in northwest Greenland (area IV) and the greatest increase of  $160 \text{ mm w.eq.}$  in southeast Greenland (significant,  $p < 0.01$ ) (area II, Figs. 4d and 5d)

TABLE 4. (Extended)

2010–19	2020–29	2030–39	2040–49	2050–59	2060–69	2070–80 <sup>a</sup>	Average and standard deviation
$-13.5 \pm 0.6$	$-13.0 \pm 0.5$	$-12.4 \pm 0.5$	$-11.9 \pm 0.3$	$-11.5 \pm 0.6$	$-10.5 \pm 0.6$	$-10.1 \pm 0.5$	$-12.9 \pm 1.5$ 0.645 <sup>c</sup>
0.838 (46)	0.882 (48)	0.874 (48)	0.934 (51)	0.995 (54)	0.956 (52)	1.025 (56)	0.792 $\pm$ 0.194
$1.76 \pm 1.45$	$2.25 \pm 1.27$	$2.51 \pm 1.42$	$2.71 \pm 1.31$	$2.58 \pm 1.30$	$2.64 \pm 1.43$	$3.38 \pm 1.41$	$2.09 \pm 1.62$
$1328 \pm 454$	$1575 \pm 268$	$1608 \pm 428$	$1754 \pm 309$	$1790 \pm 314$	$1919 \pm 430$	$2056 \pm 413$	$1520 \pm 776$
$692.8 \pm 99.3$	$650.0 \pm 39.9$	$690.9 \pm 102.0$	$698.3 \pm 96.1$	$691.8 \pm 69.5$	$762.4 \pm 83.0$	$770.2 \pm 100.6$	$677.3 \pm 89.7$
$149.1 \pm 20.0$	$165.5 \pm 15.2$	$170.8 \pm 19.4$	$177.6 \pm 16.8$	$179.9 \pm 16.9$	$189.3 \pm 19.4$	$201.8 \pm 18.9$	$157.7 \pm 25.7$
$443.4 \pm 39.0$	$482.1 \pm 26.5$	$480.9 \pm 35.9$	$529.2 \pm 37.0$	$589.7 \pm 66.1$	$573.0 \pm 63.3$	$667.7 \pm 47.6$	$442.1 \pm 134.4$
$592.5 \pm 52.6$	$647.6 \pm 33.8$	$651.7 \pm 48.7$	$706.8 \pm 45.2$	$769.6 \pm 72.9$	$762.3 \pm 72.1$	$869.5 \pm 60.6$	$597.3 \pm 152.7$
$100.3 \pm 92.1$	$2.4 \pm 32.8$	$39.2 \pm 89.1$	$-8.5 \pm 75.8$	$-77.8 \pm 84.0$	$0.1 \pm 111.1$	$-99.3 \pm 103.1$	$79.3 \pm 128.9$
$7.7 \pm 0.7$	$8.3 \pm 0.5$	$8.3 \pm 0.6$	$9.1 \pm 0.6$	$10.2 \pm 1.1$	$9.9 \pm 1.1$	$11.5 \pm 0.8$	$7.6 \pm 2.3$
$1.23 \pm 0.06$	$1.34 \pm 0.07$	$1.33 \pm 0.09$	$1.47 \pm 0.10$	$1.63 \pm 0.08$	$1.59 \pm 0.12$	$1.85 \pm 0.08$	$1.22 \pm 0.37$
66.3	79.6	92.9	107.6	123.9	139.8	160.4	160.4

due to projected changes in cyclonic systems. The overall trend for predicted climate (1950–2080) is warmer and wetter, where MAAT will increase from  $-14.8^\circ$  (1950–59) to  $-10.1^\circ\text{C}$  (2070–80) and average precipitation from 600 (1950–59) to 770 mm w.eq. yr<sup>-1</sup> (2070–80) (Table 4).

#### b. SnowModel melt extent simulations

The simulated end-of-summer GrIS melt extent is illustrated in Figs. 6a–6c. To examine annual melt extent spatial variation, 1996 and 2007 were selected randomly from the observation period (1979–2007) and the assessment indicates a reasonable degree of similarity between the observed (passive microwave) and modeled melt distributions (Fig. 6a). The differences among spatial annual simulated and observed GrIS melt boundaries average  $51(\pm 34)$  km with a maximum distance of  $\sim 180$  km. Modeled end-of-summer maximum melt extent from the observation period are, on average, overestimated by  $\sim 10\%$  (Table 4) when compared with satellite observations. The interannual discrepancy, likely due to a fixed albedo for snow and ice and a mismatch in modeled and observed resolutions, ranges from  $\sim 303$   $600$  km<sup>2</sup> ( $\sim 17\%$ ) in 1998 to  $\sim 7200$  km<sup>2</sup> ( $\sim 1\%$ ) in 1991.

The GrIS-simulated surface melt and nonmelt extent are further shown on a decadal basis for the period 1950–59 through 2070–80 (Fig. 6b). The average 1950–59 end-of-summer melt extent was 30% ( $0.542 \times 10^6$  km<sup>2</sup>) and 56% for 2070–80 ( $1.025 \times 10^6$  km<sup>2</sup>), indicating an average maximum difference of  $\sim 90\%$  ( $0.483 \times 10^6$  km<sup>2</sup>). The greatest difference in melt extent occurs in the southern part of the GrIS. To the northwest (area IV) and northeast (area I) of the GrIS, the changes in melt extent are less pronounced (Fig. 6b). Further, for 1950–59 and 2070–80, surface melt occurred at elevations as high as 2550 and 3050 m MSL, respectively. The distribution of the amount of simulated melt days is further shown for the periods 1950–59 and 2070–80 (Fig. 6b), indicating a significant average increase of 28 melt days for the GrIS ( $R^2 = 0.74$ ,  $p < 0.01$ ). For the period 1950–59 the maximum number of melt days was 126 increasing to 242 for 2070–80. The greatest number of melt days is seen in the southeastern part of the GrIS (area II). The largest change ( $\sim 50\%$ – $70\%$ ) in the number of melt days was visible in the eastern part (areas I and II) of the GrIS and is lower ( $\sim 20\%$ – $30\%$ ) to the west (areas III and IV) for 1950–2080 (Fig. 6b). The reason is likely the projected change in sea ice extent and thickness in adjacent seas.

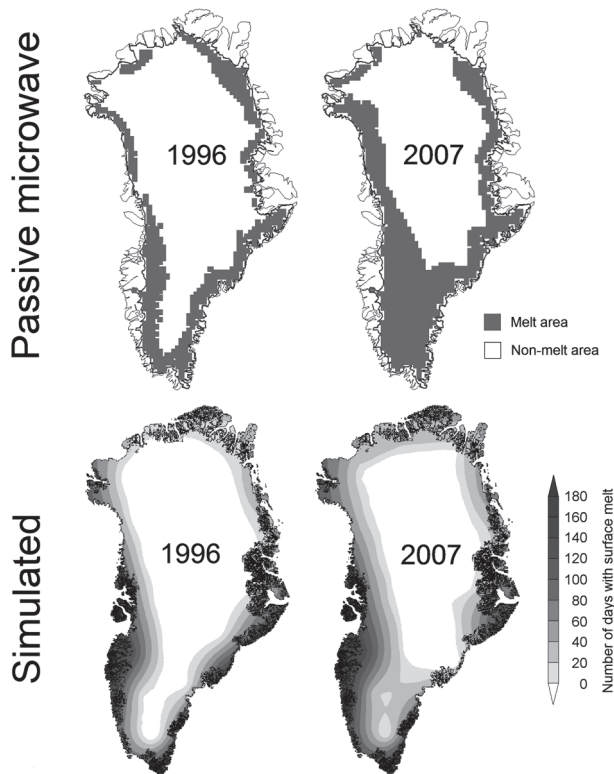


FIG. 6a. The GrIS maximum melt extent based on satellite-derived passive microwave observations and SnowModel simulations for the years 1996 (second lowest melt extent since the satellite observations began in 1979; only 1992 is smaller than the 1996 melt extent) and 2007 (greatest melt extent since the satellite observations began). The simulated melt extent includes number of days with surface melt.

A time series of the simulated end-of-summer GrIS surface melt extent from 1950 through 2080 is illustrated in Fig. 6c. The percentage of total modeled melt extent is shown for four years: 1961, the year with the lowest melt extent in the simulation period (1950–2080); 1983, lowest melt extent since the satellite observations began in 1979; 2007, greatest melt extent since the satellite observations began; and 2077, the year with the highest melt extent in the simulation period. Simulated melt extent varies from  $0.389 \times 10^6 \text{ km}^2$  (21% of the total GrIS area) in 1961 to  $1.204 \times 10^6 \text{ km}^2$  (66%) in 2077, indicating an increasing GrIS melt extent through the period.

### c. Water balance components

Throughout the year, surface processes such as snow accumulation and redistribution, evaporation, sublimation (including blowing-snow sublimation), and surface melt affect the GrIS water balance [Eq. (3)]. The yearly water balance equation for the GrIS can be described by

$$P - (E + \text{SU}) - R \pm \Delta S = 0 \pm \eta, \quad (3)$$

where  $P$  is the precipitation input from snow and rain (and possible condensation),  $E$  is evaporation (liquid to gas phase (atmosphere) flux of water vapor),  $\text{SU}$  is sublimation (snow blowing; solid to gas phase with no intermediate liquid stage),  $R$  is runoff, and  $\Delta S$  is change in storage ( $\Delta S$  is also referred as SMB) from changes in glacier storage and snowpack storage. Here  $\eta$  is the water balance discrepancy (error). The error term should be 0 (or small) if the major components ( $P$ ,  $E$ ,  $\text{SU}$ ,  $R$ , and  $\Delta S$ ) have been determined accurately. Here, a change in storage is calculated as the residual value.

The RCM–SnowModel SMB precipitation for 1995–2004 falls within the range of other studies (Table 5). The greatest average difference is  $15 \text{ km}^3 \text{ yr}^{-1}$ ; it is not surprising given vast uncertainties in measuring snow precipitation. Measuring snow precipitation typically includes errors, especially under windy and cold conditions (e.g., Yang et al. 1999; Liston and Sturm 2002, 2004; Serreze and Barry 2005). Snowfall in the Arctic is most often connected with strong winds and typically takes the form of fine snowflakes (Sturm et al. 1995). As a result, wind easily lifts and redistributes the snowflakes according to exposure and local topography, and it is sometimes difficult to distinguish between a period of snowfall and a period of drifting snow.

RCM–SnowModel simulated GrIS runoff estimate (1995–2004, Table 5) was highest compared to the other studies. The maximum difference was  $59 \text{ km}^3 \text{ yr}^{-1}$  and the minimum difference was  $3 \text{ km}^3 \text{ yr}^{-1}$ . SnowModel runoff routines take retention and internal refreezing into account when meltwater penetrates through the snowpack. These routines do have a significant effect on the SMB runoff. The role of meltwater retention in terms of the overall GrIS mass balance indicates that runoff is overestimated between 20% and 29% if no retention/refreezing routines are included (1995–2004) (Mernild et al. 2008c). The overestimation corresponds with previous values of  $\sim 25\%$  estimated by the Janssens and Huybrechts (2000) single-layer snowpack model (used by, e.g., Hanna et al. 2002, 2005, 2008; Table 5). The lack of retention/refreezing routines in SnowModel [used in this paper and Mernild et al. (2008d), Table 5] leads to an overestimation of ocean runoff, a consequent overestimation of global sea level rise, and may explain the larger difference among SnowModel simulated runoff and the other studies.

For SMB (1995–2004), the average RCM–SnowModel simulated values were lowest,  $32 \text{ km}^3 \text{ yr}^{-1}$  lower than Mernild et al. (2008d; a study based on observed data only) and  $51 \text{ km}^3 \text{ yr}^{-1}$  lower than Box et al. (2006). Compared with the study by Hanna et al. (2008), the RCM–SnowModel SMB was  $207 \text{ km}^3 \text{ yr}^{-1}$  lower. The lower SnowModel-simulated GrIS SMB values are due

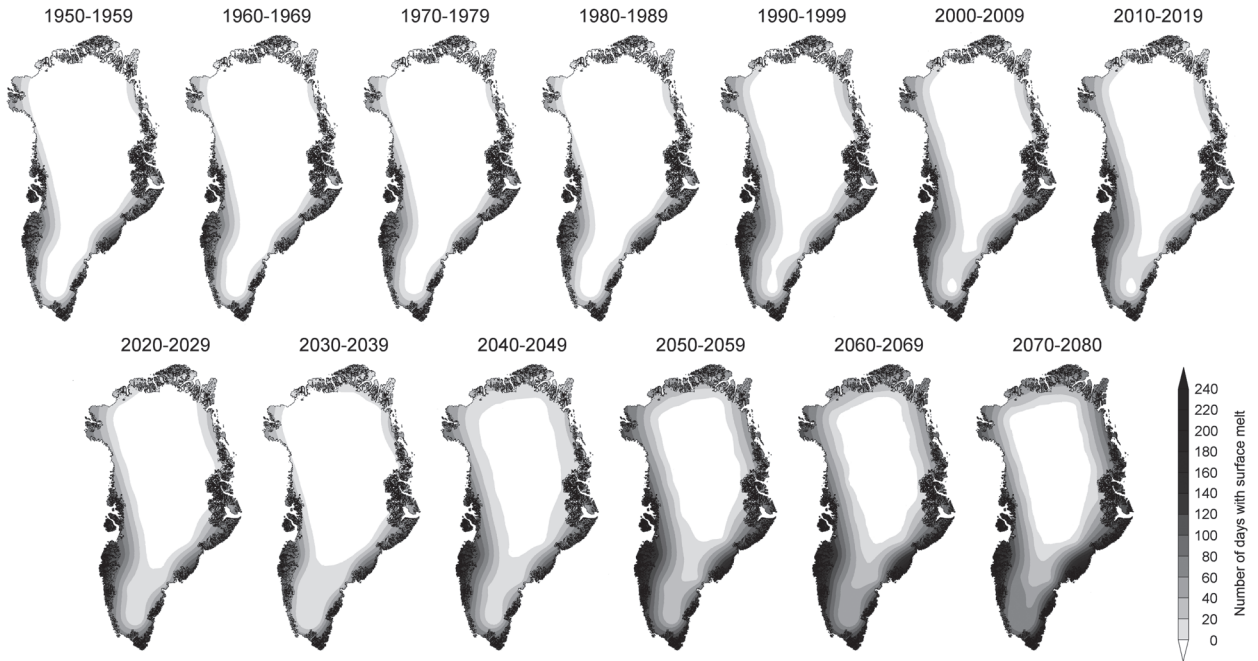


FIG. 6b. Average maximum decadal melt extent from 1950–1959 through 2070–80, including the number of days with surface melt.

to the incorporation of evaporation and sublimation values of  $142 \text{ km}^3 \text{ yr}^{-1}$  in the SMB calculations [see Eq. (1)], where sublimation alone accounts for  $64 \text{ km}^3 \text{ yr}^{-1}$  on average: a value in the lower end of the Box and Steffen (2001) observed GrIS sublimation values of  $62(\pm 23)$  to  $120(\pm 65) \text{ km}^3 \text{ yr}^{-1}$  (1995–2000). SnowModel simulated evaporation and sublimation accounted for 26% of the total GrIS ablation processes, indicating variations in the range from 134 in 2003 to  $153 \text{ km}^3 \text{ yr}^{-1}$  in 1999.

Table 4 presents the decadal GrIS surface melt conditions and the water balance components [Eq. (3)] for

the period 1950–2080. The melt index (the area above 2000-m elevation where the greatest changes in melting occur) increased 138% ( $1.96 \times 10^6 \text{ km}^2 \times \text{days}$ ), and the end-of-summer maximum melt extent grew 89% ( $4.83 \times 10^5 \text{ km}^2$ ). The trend in melt extent is illustrated in Fig. 6c. Over time, more of the GrIS surface area melted increasing from  $0.542 \times 10^6$  (1950–59) to  $1.025 \times 10^6 \text{ km}^2$  (2070–80), and the melting occurred for a longer duration during the ablation season. Increasing decadal temperatures largely explain the variance between MAAT and melt extent ( $R^2 = 0.79$ ) and melt index ( $R^2 = 0.89$ ),

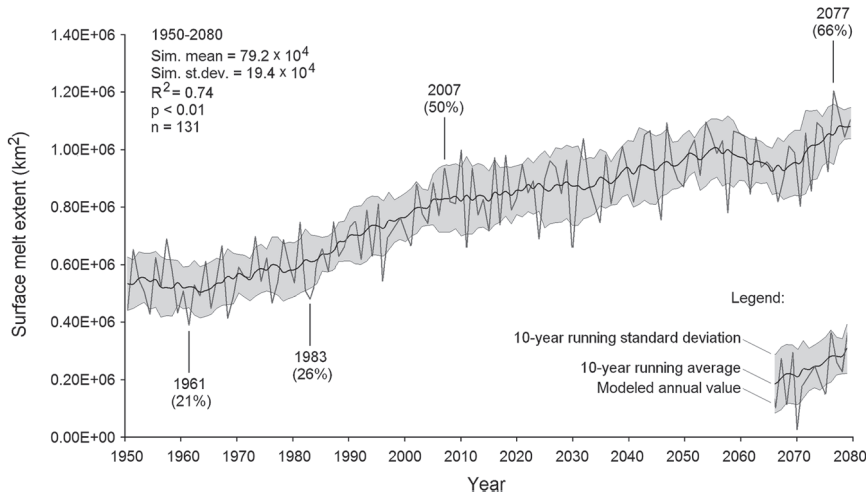


FIG. 6c. Time series for the simulated GrIS surface melt extent from 1950 through 2080. The percentage of total modeled melt extent is shown for the four years: 1961, 1983, 2007, and 2077.

TABLE 5. Different GrIS surface water balance studies, including parameters  $P$ ,  $R$ , and  $\Delta S$  for the period 1995–2004, compared with the present HIRHAM4 RCM–SnowModel study.

Parameters ( $\text{km}^3 \text{ yr}^{-1}$ )	Box et al. (2006)	Fettweis (2007)	Hanna et al. (2008)	Mernild et al. (2008d)	RCM–SnowModel
$P$	$654.0 \pm 36.4$	$641.2 \pm 59.9$	$655.4 \pm 53.5$	$635.9 \pm 35.2$	$650.2 \pm 53.5$
$R$	$395.7 \pm 61.1$	$367.2 \pm 92.2$	$339.3 \pm 63.0$	$387.4 \pm 63.3$	$398.5 \pm 45.5$
$\Delta S$	$160.3 \pm 69.4$	$263.3 \pm 138.5$	$316.1 \pm 116$	$141.0 \pm 84.7$	$109.3 \pm 88.9$

indicating that rising temperatures influence the ablation processes and melt conditions.

Modeled ELA provides a useful metric of accumulation and ablation's net influence on the SMB (Table 4). On the GrIS from 1950–2080, the decadal ELA is changing in elevation from 1150 to 2060 m MSL, an average elevation increase of  $\sim 70$  m MSL decade $^{-1}$ . Values of ELA correlate highly with MAAT ( $R^2 = 0.94$ ,  $p < 0.01$ ) and with precipitation ( $R^2 = 0.73$ ,  $p < 0.01$ ) (Table 4). Location of the ELA is largely tied to changes in MAAT and subsequent changes in melt extent and melt index. The spatial location of ELA is influenced by local topography, regional variations in precipitation regimes, dominant cyclonic systems, and latitude.

The SMB trend from 1950 to 2080 (Fig. 7; Table 4) integrates accumulation (snow precipitation) and ablation (evaporation, sublimation, and runoff) over the GrIS. It is the manifestation of increased precipitation and ablation.

Interannual variability in precipitation and ablation caused sizeable SMB fluctuations with correlations of

$R^2 = 0.46$ ,  $p < 0.01$  and  $R^2 = 0.93$ ,  $p < 0.01$ , respectively (Table 4). SMB fluctuations were largely tied to changes in ablation processes. Fluctuation patterns illustrated in Fig. 7, which were almost identical to the trends described by Rignot et al. (2008), indicated the highest balance in the 1970s and early 1980s with subsequent rapid losses as temperatures warmed. In Table 4 the interdecadal trend and variability in precipitation ( $R^2 = 0.73$ ,  $p < 0.01$ ), evaporation/sublimation ( $R^2 = 0.85$ ,  $p < 0.01$ ), runoff ( $R^2 = 0.94$ ,  $p < 0.01$ ), and SMB ( $R^2 = 0.86$ ,  $p < 0.01$ ) rates possessed significantly high correlations throughout the simulation period. Precipitation rose  $133 \text{ km}^3$ , evaporation/sublimation  $73 \text{ km}^3$ , and runoff  $391 \text{ km}^3$ —leading to enhanced average SMB losses of  $331 \text{ km}^3$  (Fig. 7). Throughout the simulation period the decadal SMB varied from  $256$  (1960–69) to  $-99 \text{ km}^3 \text{ yr}^{-1}$  (2070–80), averaging  $79(\pm 129) \text{ km}^3 \text{ yr}^{-1}$  (Table 4). SMB values below zero (negative SMB value) occur from the period 2040–49 through 2070–80 (Table 4). A negative SMB developed in response to high ablation values

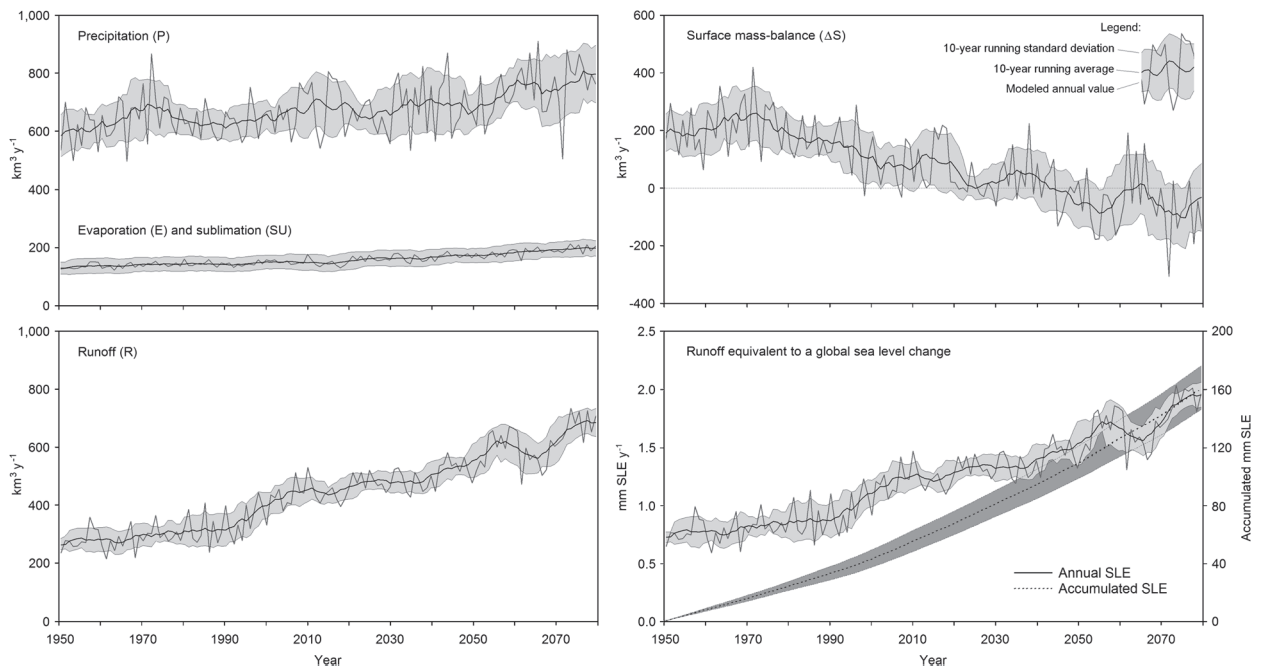


FIG. 7. Time series for the simulated GrIS  $P$ ,  $E + \text{SU}$ ,  $\Delta S$ ,  $R$ , and annual and accumulated contribution to the global sea level change for the period of 1950–2080.



(Table 4), ranging from an average of  $706 \text{ km}^3 \text{ yr}^{-1}$  (of which 74% was runoff) for 2040–49 to  $870 \text{ km}^3 \text{ yr}^{-1}$  (of which 77% was runoff) in 2070–80. Our SMB is similar to the Fettweis et al. (2008) SMB loss estimates generated from mean SMB values of 24 AOGCMs (using projections of temperature and precipitation anomalies from AOGCMs) performed for the IPCC Fourth Assessment Report for 2010–80. The RCM–SnowModel simulated SMB is, on average,  $\sim 180 \text{ km}^3 \text{ yr}^{-1}$  below the AOGCMs mean values and is similar to the lowest AOGCMs 2080 projected SMB of  $-100 \text{ km}^3 \text{ yr}^{-1}$ .

Sublimation plays an important role in the annual high-latitude hydrological cycle. Previous GrIS studies (e.g., Box and Steffen 2001; Mernild et al. 2008d) have shown that as much as 12%–23% of the annual precipitation may be returned to the atmosphere by sublimation. In arctic North America, studies by Liston and Sturm (1998, 2004), Essery et al. (1999), and Pomeroy and Essery (1999) indicate that 5%–50% of the annual solid precipitation was returned to the atmosphere by sublimation. For the GrIS (1950–2080), modeled annual sublimation averaged  $74 \text{ km}^3 \text{ yr}^{-1}$ , which is  $\sim 47\%$  of the total average for evaporation and sublimation of  $158 \text{ km}^3 \text{ yr}^{-1}$  (Table 4) and is 12% of the total precipitation of  $677 \text{ km}^3 \text{ yr}^{-1}$ . SnowModel simulated results were in the lower end of the Box and Steffen (2001) observed GrIS sublimation values of  $62(\pm 23)$  to  $120(\pm 65) \text{ km}^3 \text{ yr}^{-1}$  (12%–23% of the total precipitation), even though the observed values are from the period 1995–2000.

The average GrIS runoff from the period 1950 through 2080 is  $442(\pm 134) \text{ km}^3 \text{ yr}^{-1}$  (Table 4, Fig. 7). During this time runoff accelerated  $\sim 30 \text{ km}^3 \text{ decade}^{-1}$  to a runoff value of  $668 \text{ km}^3 \text{ yr}^{-1}$  (2070–80). The average GrIS runoff of  $442 \text{ km}^3 \text{ yr}^{-1}$  is comparable to approximately 1000 icebergs (density  $917 \text{ kg m}^3$ ) with dimensions  $1 \text{ km} \times 1 \text{ km}$  and an ice thickness 500 m. The GrIS runoff equals a specific runoff of  $7.6(\pm 2.3) \text{ l s}^{-1} \text{ km}^{-2} \text{ yr}^{-1}$ , equivalent to an average rise in global eustatic sea level of  $1.2 \text{ mm SLE yr}^{-1}$ , changing from  $0.8 \pm 0.1$  (1950–59) to  $1.9 \pm 0.1 \text{ mm SLE yr}^{-1}$  (2070–80) (Table 4 and Fig. 7). The accumulated GrIS freshwater runoff is 160 mm SLE from 1950 through 2080. In addition to enhanced runoff, GrIS may shed mass by iceberg calving and geothermal melting. Thus, simulated GrIS freshwater runoff might underestimate the mass lost by half (Lemke et al. 2007; Mernild et al. 2008c).

In terms of our general satisfaction with these model results, it is important to be clear about the assumptions and potential deficiencies of this modeling study. In these simulations we have assumed a mean monthly offset value corrected to each meteorological variable, a time-invariant DEM, a fixed albedo for snow and ice,

and no routines for the influence of air temperature inversions on snowmelt and glacier mass-balance simulations. We also recognize that the use of daily averaged atmospheric forcing variables will produce a smoothing of the natural system compared with higher temporal resolutions. Our understanding of the GrIS freshwater flux to the ocean is still far from complete. Detailed climate–cryospheric interactions are being examined at finer scales at the GrIS Kangerluassuaq drainage area, west Greenland, to estimate the freshwater influx to the ocean before upscaling routines to the entire GrIS.

## 5. Summary and conclusions

These GrIS simulations reveal continued warming and dramatically increased ablation amount and extent from 1950 to 2080. Over the period of simulation, surface runoff increased from 285 (1950–59) to  $668 \text{ km}^3 \text{ yr}^{-1}$  (2070–80). The GrIS freshwater runoff will be a factor in global sea level rise, equivalent to an average rise of  $1.2 \text{ mm SLE yr}^{-1}$ , and a cumulative increase of around 160 mm SLE in this particular model setup under an IPCC A1B emission scenario.

Realistic simulations are required to better predict GrIS SMB loss and the impacts of this loss for the North Atlantic Ocean since it plays an important role in determining the global thermohaline circulation, salinity, sea ice dynamics, and the global eustatic sea level rise. There is a high degree of agreement between GrIS simulations and recorded observations as well as simulated GrIS SMB values and previous modeling studies. However, SnowModel does not yet include routines for variable snow albedo and for the influence of air temperature inversions on snowmelt and glacier mass-balance simulations. These improvements are forthcoming and will likely bolster modeling efforts. In this work, we have not considered feedback processes from a changing GrIS to the atmosphere, which are also likely to influence simulated surface air temperatures and thereby impact the resulting melt rates.

Another uncertainty that we have partly ignored here is the spread in model projections of the climate of the future. We acknowledge that more than 20 IPCC-type GCMs have been analyzed with respect to their projection in climate change, that is, by the IPCC (Christensen et al. 2007b), showing a wide range of results with the Arctic exhibiting an even higher lack of confidence than any other region. We attribute a substantial part of this uncertainty to imperfections of various models, particularly with respect to the representation of arctic processes. In our work, we employed only one model, which we have identified as one of (if not) the best GCMs in representing present climate conditions, ECHAM5. This model simulates a future

climate not far diverged from the ensemble mean of 21 IPCC class models. Our results presented here are representative of state-of-the-art modeling, but are not comprehensive in assessing the entire range of possibilities.

*Acknowledgments.* Very special thanks to the three anonymous reviewers for their insightful critique of this article. This work was supported by grants from the University of Alaska Presidential IPY Postdoctoral Foundation and the University of Alaska Fairbanks (UAF) Office of the Vice Chancellor for Research and conducted during the first author's IPY Post Doctorate Program at the UAF. Special thanks to the faculty of science and Institute of Low Temperature Science, Hokkaido University, Japan, for hosting the first author from April through July 2008 and to Colorado State University, Cooperative Institute for Research in the Atmosphere, for hosting the first author through September and October 2008, and February 2009. Thanks to Martin Stendel and John Cappelen at the Danish Meteorological Institute (DMI) for providing HIRHAM4 RCM data and WMO meteorological data obtained from the near coast, and to the Cooperative Institute for Research in Environmental Science (CIRES), University of Colorado at Boulder, for providing meteorological data from the Greenland Climate Network (GC-Net) automatic weather stations. Also, thanks to Theodore Scambos, CIRES, University of Colorado at Boulder, for providing the Greenland digital elevation model.

#### REFERENCES

- Abdalati, W., and K. Steffen, 1997: The apparent effects of the Mt. Pinatubo eruption on the Greenland ice sheet melt extent. *Geophys. Res. Lett.*, **24**, 1795–1797.
- ACIA, 2005: *Arctic Climate Impact Assessment*. Cambridge University Press, 1042 pp.
- Albritton, D. L., and Coauthors, 2001: Summary for policy makers. *Climate Change 2001: The Scientific Basis*, J. T. Houghton et al., Eds., Cambridge University Press, 1–83.
- Allerup, P., H. Madsen, and F. Vejen, 1998: Estimating true precipitation in arctic areas. *Proc. Nordic Hydrological Conf.*, Helsinki, Finland, Nordic Hydrological Programme Rep. 44, 1–9.
- , —, and —, 2000: Correction of precipitation based on off-site weather information. *Atmos. Res.*, **53**, 231–250.
- Alley, R. B., and Coauthors, 2007: Summary for policymakers. *Climate Change 2007: The Physical Science Basis*, S. Solomon et al., Eds. Cambridge University Press, 1–18.
- Anderson, E. A., 1976: A point energy balance model of a snow cover. NOAA Tech. Rep. NWS 19, 150 pp.
- Bamber, J., S. Ekholm, and W. Krabill, 2001: A new, high-resolution digital elevation model of Greenland fully validated with airborne laser altimeter data. *J. Geophys. Res.*, **106**, 6733–6746.
- Barnes, S. L., 1964: A technique for maximizing details in numerical weather map analysis. *J. Appl. Meteor.*, **3**, 396–409.
- , 1973: Mesoscale objective analysis using weighted time series observations. NOAA Tech. Memo. ERL NSSL-62, 60 pp.
- Bjørge, D., J. E. Haugen, and T. E. Nordeng, 2000: Future climate in Norway. DNMI Research Rep. 103, Norwegian Meteorological Institute, 41 pp.
- Boggild, C. E., S. G. Warren, R. E. Brandt, and K. J. Brown, 2006: Effects of dust and black carbon on albedo of the Greenland ablation zone. *Eos, Trans. Amer. Geophys. Union*, (Fall Meeting Suppl.), Abstract U22A-05.
- Born, E. W., and J. Böcher, 2001: The ecology of Greenland. Ministry of Environment and Natural Resources Rep., 429 pp.
- Box, J. E., 2002: Survey of Greenland instrumental temperature records: 1973–2001. *Int. Climatol.*, **22**, 1829–1847.
- , and K. Steffen, 2001: Sublimation estimates for the Greenland ice sheet using automated weather station observations. *J. Geophys. Res.*, **106** (D24), 33 965–33 982.
- , and Coauthors, 2006: Greenland ice sheet surface mass balance variability (1988–2004) from calibrated Polar MM5 output. *J. Climate*, **19**, 2783–2800.
- Broecker, W. S., and G. H. Denton, 1990: The role of ocean-atmosphere reorganization in glacial cycles. *Quat. Sci. Rev.*, **9**, 305–341.
- , D. M. Peteet, and D. Rind, 1985: Does the ocean-atmosphere system have more than one stable mode of operation? *Nature*, **315**, 21–26.
- Brown, R. D., B. Brasnett, and D. Robinson, 2003: Gridded North American monthly snow depth and snow water equivalent for GCM evaluation. *Atmos.–Ocean*, **41**, 1–14.
- Bruland, O., G. E. Liston, J. Vonk, K. Sand, and A. Killingtveit, 2004: Modelling the snow distribution at two High-Arctic sites at Svalbard, Norway, and at a Sub-Arctic site in Central Norway. *Nord. Hydrol.*, **35**, 191–208.
- Chen, J. L., C. R. Wilson, and D. B. Tapley, 2006: Satellite gravity measurements confirm accelerated melting of Greenland ice sheet. *Science*, **313**, 1958–1960.
- Christensen, J. H., and P. Kuhry, 2000: High-resolution regional climate model validation and permafrost simulation for the East European Russian Arctic. *J. Geophys. Res.*, **105**, 29 647–29 658.
- , and O. B. Christensen, 2007: A summary of the PRUDENCE model projections of changes in European climate by the end of this century. *Climatic Change*, **81**, 7–30.
- , —, P. Lopez, E. van Meijgaard, and M. Botzet, 1996: The HIRHAM4 regional atmospheric climate model. DMI Scientific Rep. 96-4, 51 pp.
- , —, J.-P. Schultz, S. Hagemann, and M. Botzet, 2001: High resolution physiographic data set for HIRHAM4: An application to a 50 km horizontal resolution domain covering Europe. DMI Technical Rep. 01–15, 21 pp.
- , T. R. Carter, M. Rummukainen, and G. Amanatidis, 2007a: Evaluating the performance and utility of regional climate models: The PRUDENCE project. *Climatic Change*, **81**, 1–6.
- , and Coauthors, 2007b: Regional climate projections. *Climate Change 2007: The Physical Science Basis*, S. Solomon et al., Eds., Cambridge University Press, 848–940.
- , M. Stendel, P. Kuhry, V. Romanovsky, and J. Walsh, 2008: Does permafrost deserve attention in comprehensive climate models? *Proc. Ninth Int. Conf. on Permafrost*, Fairbanks, AK, University of Alaska Fairbanks, 247–250.
- Déqué, M., and Coauthors, 2007: An intercomparison of regional climate simulations for Europe: Assessing uncertainties in model projections. *Climatic Change*, **81**, 53–70.

- Dethloff, K., and Coauthors, 2002: Recent Greenland accumulation estimated from regional climate model simulations and ice core analysis. *J. Climate*, **15**, 2821–2832.
- Dodson, R., and D. Marks, 1997: Daily air temperature interpolation at high spatial resolution over a large mountainous region. *Climate Res.*, **8**, 1–20.
- Dowdeswell, J. A., and Coauthors, 1997: The Mass balance of Circum-Arctic Glaciers and Recent Climate Change. *Quat. Res.*, **48**, 1–14.
- Essery, R. L. H., L. Li, and J. W. Pomeroy, 1999: A distributed model of blowing snow over complex terrain. *Hydrol. Processes*, **13**, 2423–2438.
- Fettweis, X., 2007: Reconstruction of the 1979–2006 Greenland ice sheet surface mass balance using the regional climate model MAR. *Cryosphere*, **1**, 21–40.
- , E. Hanna, H. Gallée, P. Huybrechts, and M. Erpicum, 2008: Estimation of the Greenland ice sheet surface mass balance for the 20th and 21st centuries. *Cryosphere*, **2**, 117–129.
- Førland, E. J., and I. Hanssen-Bauer, 2003: Climate variations and implications for precipitations types in the Norwegian arctic. Norwegian Meteorological Institute Rep. 24/02, 21 pp.
- Gordon, C., C. Cooper, C. A. Senior, H. Banks, J. M. Gregory, T. C. Johns, J. F. B. Mitchell, and R. A. Wood, 2000: The simulation of SST, sea ice extents and ocean heat transports in a version of the Hadley Centre coupled model without flux adjustments. *Climate Dyn.*, **16**, 147–168.
- Greene, E. M., G. E. Liston, and R. A. Pielke, 1999: Simulation of above treeline snowdrift formation using a numerical snow-transport model. *Cold Reg. Sci. Technol.*, **30**, 135–144.
- Gregory, J. M., P. Huybrechts, and S. C. B. Raper, 2004: Threatened loss of the Greenland ice-sheet. *Nature*, **428**, 616.
- , and Coauthors, 2005: A model intercomparison of changes in the Atlantic thermohaline circulation in response to increasing atmospheric CO<sub>2</sub> concentration. *Geophys. Res. Lett.*, **32**, L12703, doi:10.1029/2005GL023209.
- Greve, R., 1997a: A continuum-mechanical formulation for shallow polythermal ice sheets. *Philos. Trans. Roy. Soc. London*, **A355**, 921–974.
- , 1997b: Application of a polythermal three-dimensional ice sheet model to the Greenland ice sheet: Response to a steady-state and transient climate scenarios. *J. Climate*, **10**, 901–918.
- , 2005: Relation of measured basal temperatures and the spatial distribution of the geothermal flux for the Greenland ice sheet. *Ann. Glaciol.*, **42**, 424–432.
- Hanna, E., P. Huybrechts, and T. Mote, 2002: Surface mass balance of the Greenland ice sheet from climate-analysis data and accumulation/runoff models. *Ann. Glaciol.*, **35**, 67–72.
- , —, I. Janssens, J. Cappelen, K. Steffen, and A. Stephens, 2005: Runoff and mass balance of the Greenland ice sheet: 1958–2003. *J. Geophys. Res.*, **110**, D13108, doi:10.1029/2004JD005641.
- , and Coauthors, 2008: Increased runoff from melt from the Greenland ice sheet: A response to global warming. *J. Climate*, **21**, 331–341.
- Hansen, B. U., and Coauthors, 2008: Present Day Climate at Zackenberg. *Adv. Ecol. Res.*, **40**, 115–153.
- Hiemstra, C. A., G. E. Liston, and W. A. Reinert, 2002: Snow Redistribution by Wind and Interactions with Vegetation at Upper Treeline in the Medicine Bow Mountains, Wyoming. *Arct. Antarct. Alp. Res.*, **34**, 262–273.
- , —, and —, 2006: Observing, modelling, and validating snow redistribution by wind in a Wyoming upper treeline landscape. *Ecol. Modell.*, **197**, 35–51.
- Iziomon, M. G., H. Mayer, and A. Matzarakis, 2003: Downward atmospheric longwave irradiance under clear and cloudy skies: Measurement and parameterization. *J. Atmos. Sol.-Terr. Phys.*, **65**, 1107–1116.
- Janssens, I., and P. Huybrechts, 2000: The treatment of meltwater retention in mass-balance parameterisations of the Greenland ice sheet. *Ann. Glaciol.*, **31**, 133–140.
- Johannessen, O. M., K. Khvorostovsky, M. W. Miles, and L. P. Bobylev, 2005: Recent ice-sheet growth in the interior of Greenland. *Science Express*, **310**, 1013–1016, doi:10.1126/science.1115356.
- Kiilsholm, S., J. H. Christensen, K. Dethloff, and A. Rinke, 2003: Net accumulation of the Greenland ice sheet: High resolution modeling of climate changes. *Geophys. Res. Lett.*, **30**, 1485, doi:10.1029/2002GL015742.
- Koch, S. E., M. DesJardins, and P. J. Kocin, 1983: An interactive Barnes objective map analysis scheme for use with satellite and conventional data. *J. Climate Appl. Meteor.*, **22**, 1487–1503.
- Krabill, W., and Coauthors, 1999: Rapid Thinning of Parts of the Southern Greenland Ice Sheet. *Science*, **283**, 1522–1524, doi:10.1126/science.283.5407.1522.
- , and Coauthors, 2000: Greenland Ice Sheet: High-elevation balance and peripheral thinning. *Science*, **289**, 428–430, doi:10.1126/science.289.5478.428.
- , and Coauthors, 2004: Greenland Ice Sheet: Increased coastal thinning. *Geophys. Res. Lett.*, **31**, L24402, doi:10.1029/2004GL021533.
- Kunkel, K. E., 1989: Simple procedures for extrapolation of humidity variables in the mountainous western United States. *J. Climate*, **2**, 656–669.
- Lemke, P., and Coauthors, 2007: Observations: Changes in snow, ice and frozen ground. *Climate Change 2007: The Physical Science Basis*, S. Solomon et al., Eds., Cambridge University Press, 338–384.
- Liston, G. E., 1995: Local advection of momentum, heat, and moisture during the melt of patchy snow covers. *J. Appl. Meteor.*, **34**, 1705–1715.
- , 2004: Representing subgrid snow cover heterogeneities in regional and global models. *J. Climate*, **17**, 1381–1397.
- , and D. K. Hall, 1995: An energy-balance model of lake-ice evolution. *J. Glaciol.*, **41**, 373–382.
- , and M. Sturm, 1998: A snow-transport model for complex terrain. *J. Glaciol.*, **44**, 498–516.
- , and —, 2002: Winter precipitation patterns in arctic Alaska determined from a blowing-snow model and snow-depth observations. *J. Hydrometeorol.*, **3**, 646–659.
- , and —, 2004: The role of winter sublimation in the Arctic moisture budget. *Nord. Hydrol.*, **35**, 325–334.
- , and J.-G. Winther, 2005: Antarctic surface and subsurface snow and ice melt fluxes. *J. Climate*, **18**, 1469–1481.
- , and K. Elder, 2006a: A distributed snow-evolution modeling system (SnowModel). *J. Hydrometeorol.*, **7**, 1259–1276.
- , and —, 2006b: A meteorological distribution system for high-resolution terrestrial modeling (MicroMet). *J. Hydrometeorol.*, **7**, 217–234.
- , J.-G. Winther, O. Bruland, H. Elvehøy, and K. Sand, 1999: Below surface ice melt on the coastal Antarctic ice sheet. *J. Glaciol.*, **45**, 273–285.
- , J. P. McFadden, M. Sturm, and R. A. Pielke Sr., 2002: Modeled changes in arctic tundra snow, energy, and moisture fluxes due to increased shrubs. *Global Change Biol.*, **8**, 17–32.
- , R. B. Haehnel, M. Sturm, C. A. Hiemstra, S. Berezovskaya, and R. D. Tabler, 2007: Simulating complex snow distributions

- in windy environments using SnowTran-3D. *J. Glaciol.*, **53**, 241–256.
- Lutckhe, S. B., and Coauthors, 2006: Recent Greenland ice mass loss by drainage system from satellite gravity observations. *Science*, **314**, 1286–1289.
- Marks, D., J. Domingo, D. Susong, T. Link, and D. Garen, 1999: A spatially distributed energy balance snowmelt model for application in mountain basins. *Hydrol. Processes*, **13**, 1935–1959.
- Mernild, S. H., and G. E. Liston, 2010: The influence of air temperature inversions on snowmelt and glacier mass balance simulations, Ammassalik Island, southeast Greenland. *J. Appl. Meteor. Climatol.*, in press.
- , B. Hasholt, and G. E. Liston, 2006a: Water flow through Mittivakkat Glacier, Ammassalik Island, SE Greenland. *Dan. J. Geogr.*, **106**, 25–43.
- , G. E. Liston, B. Hasholt, and N. T. Knudsen, 2006b: Snow distribution and melt modeling for Mittivakkat Glacier, Ammassalik Island, southeast Greenland. *J. Hydrometeorol.*, **7**, 808–824.
- , —, and —, 2007: Snow-distribution and melt modelling for glaciers in Zackenberg river drainage basin, north-eastern Greenland. *Hydrol. Processes*, **21**, 3249–3263, doi:10.1002/hyp.6500.
- , B. Hasholt, B. H. Jakobsen, and B. U. Hansen, 2008a: Climatic conditions at the Mittivakkat Glacier catchment (1994–2006), Ammassalik Island, SE Greenland, and in a 109-year perspective (1898–2006). *Dan. J. Geogr.*, **108**, 51–72.
- , —, and G. Liston, 2008b: Climatic control on river discharge simulations, Zackenberg River drainage basin, northeast Greenland. *Hydrol. Processes*, **22**, 1932–1948, doi:10.1002/hyp.6777.
- , G. E. Liston, and B. Hasholt, 2008c: East Greenland freshwater runoff to the Greenland-Iceland-Norwegian Seas 1999–2004 and 2071–2100. *Hydrol. Processes*, **22**, 4571–4586, doi:10.1002/hyp.7061.
- , —, C. A. Hiemstra, and K. Steffen, 2008d: Surface melt area and water balance modeling on the Greenland ice sheet 1995–2005. *J. Hydrometeorol.*, **9**, 1191–1211.
- , —, —, and —, 2009a: Record 2007 Greenland Ice Sheet surface melt extent and runoff. *Eos, Trans. Amer. Geophys. Union*, **90**, doi:10.1029/2009EO020002.
- , —, —, —, E. Hanna, and J. H. Christensen, 2009b: Greenland Ice Sheet surface mass-balance modelling and freshwater flux for 2007, and in a 1995–2007 perspective. *Hydrol. Processes*, **23**, 2470–2484, doi:10.1002/hyp.7354.
- , —, K. Steffen, and P. Chylek, 2009c: Meltwater flux and runoff modeling in the ablation area of the Jakobshavn Isbræ, West Greenland. *J. Glaciol.*, in press.
- Mote, T. L., 2003: Estimations of runoff rates, mass balance, and elevation changes on the Greenland ice sheet from passive microwave observations. *J. Geophys. Res.*, **108**, 4056, doi:10.1029/2001JD002032.
- , 2007: Greenland surface melt trends 1973–2007: Evidence of a large increase in 2007. *Geophys. Res. Lett.*, **34**, L22507, doi:10.1029/2007GL031976.
- Pielke, R. A., Sr., 2002: *Mesoscale Meteorological Modeling*. Academic Press, 676 pp.
- Pomeroy, J. W., and R. L. H. Essery, 1999: Turbulent fluxes during blowing snow: Field test of model sublimation predictions. *Hydrol. Processes*, **13**, 2963–2975.
- , and E. Brun, 2001: *Physical properties of snow*. *Snow Ecology: An Interdisciplinary Examination of Snow-Covered Ecosystems*, H. G. Jones, et al., Eds., Cambridge University Press, 45–118.
- Pope, V. D., M. L. Gallani, P. R. Rowntree, and R. A. Stratton, 2000: The impact of new physical parametrizations in the Hadley Centre climate model—HadAM3. *Climate Dyn.*, **16**, 123–146.
- Prasad, R., D. G. Tarboton, G. E. Liston, C. H. Luce, and M. S. Seyfried, 2001: Testing a blowing snow model against distributed snow measurements at Upper Sheep Creek. *Water Resour. Res.*, **37**, 1341–1357.
- Putnins, P., 1970: The climate of Greenland. *Climates of the Polar Regions*, S. Orvig, Ed., Vol. 12, *World Survey of Climatology*, Elsevier Science, 3–112.
- Rahmstorf, S., and Coauthors, 2005: Thermohaline circulation hysteresis: A model intercomparison. *Geophys. Res. Lett.*, **32**, L23605, doi:10.1029/2005GL023655.
- Ramillien, G., A. Lombard, A. Cazanave, E. R. Ivins, M. Llubes, F. Remy, and R. Biancalà, 2006: Interannual variations of the mass balance of the Antarctic and Greenland ice sheet from GRACE. *Global Planet. Change*, **53**, 198–208.
- Randall, D. A., and Coauthors, 2007: Climate models and their evaluation. *Climate Change 2007: The Physical Science Basis*, S. Solomon, et al., Eds., Cambridge University Press, 589–662.
- Richter-Menge, J., and Coauthors, 2007: Greenland ice sheet mass balance. Arctic Report Card 2007, NOAA Rep., 45 pp. [Available online at [http://www.arctic.noaa.gov/report07/ArcticReportCard\\_full\\_report.pdf](http://www.arctic.noaa.gov/report07/ArcticReportCard_full_report.pdf).]
- Rignot, E., J. E. Box, E. Burgess, and E. Hanna, 2008: Mass balance of the Greenland ice sheet from 1958 to 2007. *Geophys. Res. Lett.*, **35**, L20502, doi:10.1029/2008GL035417.
- Roeckner, E., and Coauthors, 1996: The atmospheric general circulation model ECHAM-4: Model description and simulation of present-day climate. Max-Planck-Inst. Für Meteorologie Rep. 218, 94 pp.
- , and Coauthors, 2003: The atmospheric general circulation model ECHAM 5. Part I: Model description. Max-Planck-Inst. Für Meteorologie 349, 140 pp.
- Ryan, B. C., 1977: A mathematical model for diagnosis and prediction of surface winds in mountains terrain. *J. Appl. Meteorol.*, **16**, 1547–1564.
- Scambos, T., and T. Haran, 2002: An image-enhanced DEM of the Greenland Ice Sheet. *Ann. Glaciol.*, **34**, 291–298.
- Serreze, M. C., and R. G. Barry, 2005: *The Arctic Climate System*. Cambridge University Press, 385 pp.
- Steffen, K., 1995: Surface energy exchange during the onset of melt at the equilibrium line altitude of the Greenland ice sheet. *Ann. Glaciol.*, **21**, 13–18.
- Stendel, M., V. E. Romanovsky, J. H. Christensen, and T. Sazonova, 2007: Using dynamical downscaling to close the gap between global change scenarios and local permafrost dynamics. *Global Planet. Change*, **56**, 203–214.
- , J. H. Christensen, and D. Petersen, 2008: Arctic Climate and Climate Change with a Focus on Greenland. *Adv. Ecol. Res.*, **40**, 13–43, doi:10.1016/S0065-2504(07)00002-5.
- Stocker, T. F., and Coauthors, 2001: Physical climate processes and feedbacks. *Climate Change 2001: The Scientific Basis*, J. T. Houghton, et al., Eds., Cambridge University Press, 417–470.
- Sturm, M., J. Holmgren, and G. E. Liston, 1995: Seasonal snow cover classification system for local to global applications. *J. Climate*, **8**, 1261–1283.
- , J. Schimel, G. Michaelson, J. M. Welker, S. F. Oberbauer, G. E. Liston, J. Fahnestock, and V. E. Romanovsky, 2005: Winter biological processes could help convert Arctic tundra to shrubland. *Bioscience*, **55**, 17–26.



- Su, F., J. C. Adam, K. E. Trenberth, and D. P. Lettenmaier, 2006: Evaluation of surface water fluxes of the pan-Arctic land region with a land surface model and ERA-40 reanalysis. *J. Geophys. Res.*, **111**, D05110, doi:10.1029/2005JD006387.
- Swingedouw, D., P. Braconnot, and O. Marti, 2006: Sensitivity of the Atlantic Meridional Overturning Circulation to the melting from northern glaciers in climate change experiments. *Geophys. Res. Lett.*, **33**, L07711, doi:10.1029/2006GL025765.
- Tarboton, D. G., T. G. Chowdhury, and T. H. Jackson, 1995: A spatially distributed energy balance snowmelt model. *Biogeochemistry of Seasonally Snow-Covered Catchments*, IAHS Publication 228, IAHS, 141–155.
- Tedesco, M., 2007: 2006 Greenland Ice Sheet snowmelt from spaceborne microwave brightness temperatures. *Eos, Trans. Amer. Geophys. Union*, **88**, doi:10.1029/2007EO220003.
- , X. Fettweis, M. Broeke, R. Wal, and P. Smeets, 2008: Extreme snowmelt in northern Greenland during summer 2008. *Eos, Trans. Amer. Geophys. Union*, **89**, doi:10.1029/2008EO410004.
- Thomas, R., E. Frederick, W. Krabill, S. Manizade, and C. Martin, 2006: Progressive increase in ice loss from Greenland. *Geophys. Res. Lett.*, **33**, L10503, doi:10.1029/2006GL026075.
- Thornton, P. E., S. W. Running, and M. A. White, 1997: Generating surfaces of daily meteorological variables over large regions of complex terrain. *J. Hydrol.*, **190**, 214–251.
- Velicogna, I., and J. Wahr, 2005: Greenland mass balance from GRACE. *Geophys. Res. Lett.*, **32**, L18505, doi:10.1029/2005GL023955.
- , and —, 2006: Acceleration of Greenland ice mass loss in spring 2004. *Nature*, **443**, 329–331.
- Walcek, C. J., 1994: Cloud cover and its relationship to relative humidity during a spring midlatitude cyclone. *Mon. Wea. Rev.*, **122**, 1021–1035.
- Walsh, J. E., W. L. Chapman, V. Romanovsky, J. H. Christensen, and M. Stendel, 2008: Global climate model performance over Alaska and Greenland. *J. Climate*, **21**, 2156–2174.
- Warrick, R., and J. Oerlemans, 1990: Sea level rise. *Climate Change: The IPCC Scientific Assessment*, J. T. Houghton, G. J. Jenkins, and J. J. Ephraums, Eds., Cambridge University Press, 261–281.
- Winstral, A., and D. Marks, 2002: Simulating wind fields and snow redistribution using terrain-based parameters to model snow accumulation and melt over a semi-arid mountain catchment. *Hydrol. Processes*, **16**, 3585–3603.
- Yang, D., S. Ishida, B. E. Goodison, and T. Gunther, 1999: Bias correction of precipitation data for Greenland. *J. Geophys. Res.*, **104** (D6), 6171–6181.
- Zwally, J. H., M. Giovinetto, J. Li, H. Cornejo, M. Beckley, A. Brenner, J. Saba, and D. Yi, 2005: Mass changes of the Greenland and Antarctic ice sheets and shelves and contributions to sea-level rise: 1992–2002. *J. Glaciol.*, **51**, 509–527.



[19]

Mernild, S. H., Howat, I. M., Ahn, Y., Liston, G. E., Steffen, K.,  
Jakobsen, B. H., Hasholt, B., Fog, B., and van As, D. 2010.  
Freshwater flux to Sermilik Fjord, SE Greenland.  
The Cryosphere, 4, 453–465, doi:10.5194/tc-4-453-2010.

Reprinted with permission from Copernicus Publications

## Freshwater flux to Sermilik Fjord, SE Greenland

S. H. Mernild<sup>1</sup>, I. M. Howat<sup>2</sup>, Y. Ahn<sup>2</sup>, G. E. Liston<sup>3</sup>, K. Steffen<sup>4</sup>, B. H. Jakobsen<sup>5</sup>, B. Hasholt<sup>5</sup>, B. Fog<sup>5</sup>, and D. van As<sup>6</sup>

<sup>1</sup>Climate, Ocean, and Sea Ice Modeling Group, Computational Physics and Methods (CCS-2), Los Alamos National Laboratory, New Mexico, USA

<sup>2</sup>Byrd Polar Research Center and School of Earth Sciences, Ohio State University, Ohio, USA

<sup>3</sup>Cooperative Institute for Research in the Atmosphere, Colorado State University, Colorado, USA

<sup>4</sup>Cooperative Institute for Research in Environmental Sciences, University of Colorado, Colorado, USA

<sup>5</sup>Department of Geography and Geology, University of Copenhagen, Denmark

<sup>6</sup>Geological Survey of Denmark and Greenland, Denmark

Received: 29 June 2010 – Published in The Cryosphere Discuss.: 30 July 2010

Revised: 13 October 2010 – Accepted: 16 October 2010 – Published: 26 October 2010

**Abstract.** Terrestrial inputs of freshwater flux to Sermilik Fjord, SE Greenland, were estimated, indicating ice discharge to be the dominant source of freshwater. A freshwater flux of  $40.4 \pm 4.9 \times 10^9 \text{ m}^3 \text{ y}^{-1}$  was found (1999–2008), with an 85% contribution originated from ice discharge (65% alone from Helheim Glacier), 11% from terrestrial surface runoff (from melt water and rain), 3% from precipitation at the fjord surface area, and 1% from subglacial geothermal and frictional melting due to basal ice motion. The results demonstrate the dominance of ice discharge as a primary mechanism for delivering freshwater to Sermilik Fjord. Time series of ice discharge for Helheim Glacier, Midgård Glacier, and Fenris Glacier were calculated from satellite-derived average surface velocity, glacier width, and estimated ice thickness, and fluctuations in terrestrial surface freshwater runoff were simulated based on observed meteorological data. These simulations were compared and bias corrected against independent glacier catchment runoff observations. Modeled runoff to Sermilik Fjord was variable, ranging from  $2.9 \pm 0.4 \times 10^9 \text{ m}^3 \text{ y}^{-1}$  in 1999 to  $5.9 \pm 0.9 \times 10^9 \text{ m}^3 \text{ y}^{-1}$  in 2005. The sub-catchment runoff of the Helheim Glacier region accounted for 25% of the total runoff to Sermilik Fjord. The runoff distribution from the different sub-catchments suggested a strong influence from the spatial variation in glacier coverage, indicating high runoff volumes, where glacier cover was present at low elevations.

### 1 Introduction

Global atmospheric temperatures showed a warming trend since the 1970s, and all years during the present century (2001–2008) have been among the warmest since the beginning of instrumental records (Allison et al., 2009). Surface air temperature observations reveal the strongest increase occurring over Northern Hemisphere land areas (40–70° N) since the 1970s; an increase almost twice the global average rate (IPCC, 2007), accompanied by a  $\sim 1\%$  decade<sup>-1</sup> increase in precipitation (ACIA, 2005). However, for the past decades the strongest increases in temperature have been over the Arctic Ocean in autumn and winter, in response to loss of the insulating Arctic sea ice cover (Screen and Simmonds, 2010).

There is clear evidence of increased melting of the Greenland Ice Sheet (GrIS) and marginal glaciers in Greenland since the mid-1990s (e.g., Mote, 2007; Tedesco, 2007; Knudsen and Hasholt, 2008; Steffen et al., 2008), and rapid mass loss has been observed and simulated (e.g., Hanna et al., 2008; Allison et al., 2009; Khan et al., 2010). In a warming climate, we would expect an accelerating freshwater flux: ice discharge (calving) and runoff to the ocean, manifested by, e.g., decreasing ocean salinity, and increasing global eustatic sea level rise (e.g., ACIA, 2005; Box et al., 2006; IPCC, 2007; Mernild et al. 2011). A few freshwater runoff measurements are available for Greenland from the 1990s at the Sermilik Research Station, Sermilik Fjord (65° N), SE Greenland (Fig. 1), and at the Zackenberg Research Station, Young Sund/Tyroler Fjord (74° N), NE Greenland, and shorter term measurements are available



Correspondence to: S. H. Mernild  
(mernild@lanl.gov)

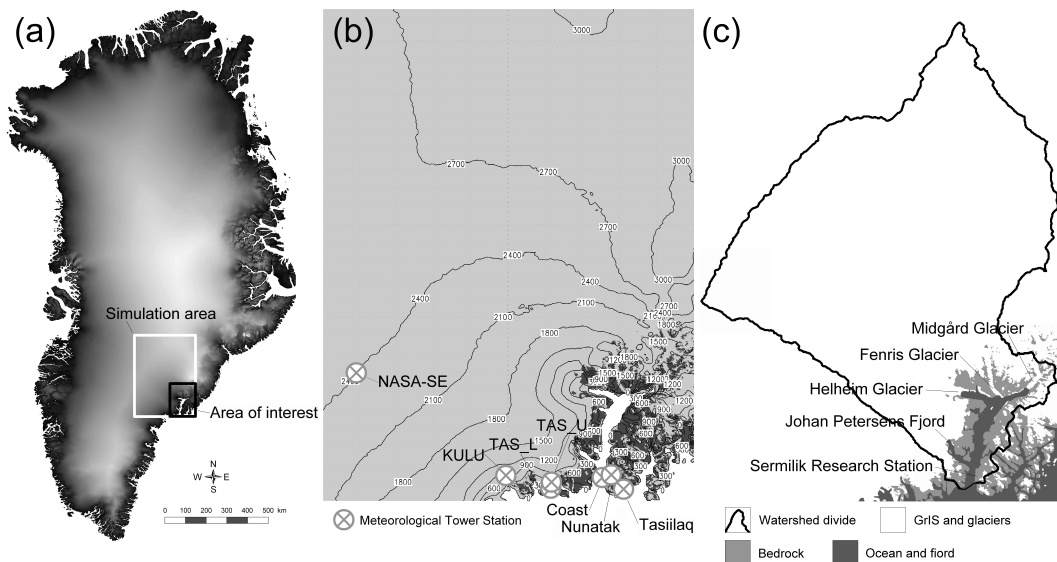


**Fig. 1.** (a) Greenland, including the Sermilik Fjord simulation domain ( $120\,350\text{ km}^2$ ) and area of interest ( $18\,750\text{ km}^2$ ) in South East Greenland; (b) Sermilik Fjord with topography (300-m contour interval) and meteorological stations (see Table 1 for station information); and (c) MODIS satellite-derived surface characteristics (30 August 2009), including catchment ( $58\,045\text{ km}^2$ ), watershed divide, and locations of GrIS outlet glaciers. The surface watershed divide is estimated based on the program RiverTools (<http://www.rivertools.com/>): a GIS application for analysis and visualization of digital terrain, watersheds, and river network.

from Kangerlussuaq (Søndre Strømfjord), Kangerlussuaq Fjord ( $67^\circ\text{ N}$ ), W Greenland, since 2007, and from Kobberfjord ( $64^\circ\text{ N}$ ), W Greenland, since 2008 (e.g., Mernild and Hasholt, 2006, 2009; Jensen and Rasch, 2009). These data series are important tools for assessing and quantifying the impact of climate change and variability on freshwater runoff from glaciated landscapes such as Greenland.

The first documentation of glaciers in the Sermilik Fjord catchment basin was carried out in 1933, and in 1970 the Sermilik Research Station was established close to the Mittivakkat Glacier to study the control of climate on a low-arctic (Born and Böcher, 2001), partly glaciated landscape. An automated terrestrial monitoring program was initiated for the Mittivakkat Glacier catchment in 1993, which presents today the longest continuous monitoring program in E Greenland. Data on observed climate conditions have been presented by Mernild et al. (2008a) and Jakobsen et al. (2008). Seasonal and annual observations on the Mittivakkat Glacier include: winter, summer, and net mass-balance (Knudsen and Hasholt, 2004, 2008), freshwater runoff (e.g., Hasholt, 1980; Hasholt and Mernild, 2004, 2008), and sediment transport (Hasholt and Walling, 1992; Busskamp and Hasholt, 1996; Hasholt and Mernild, 2008). Modeling studies for this region include seasonal and annual climate processes (Mernild and Liston, 2010), snow cover distribution (Hasholt et al., 2003; Mernild et al., 2006a), glacier surface mass-balance (Mernild et al., 2006a, 2008b), and runoff (Mernild and Hasholt, 2006; Mernild et al., 2008b).

This collection of extensive observations and model results from the Mittivakkat Glacier catchment was used to simulate the terrestrial surface runoff for the Sermilik Fjord (the study does not include ocean fluxes). Not only runoff but also ice discharge from e.g., the Helheim Glacier (one of the most conspicuous calving outlet glaciers from the GrIS) at the innermost part of the fjord, seems to be an important source of freshwater for both, the Sermilik Fjord and the Irminger Sea. We present a 10-year time series (1999–2008) of freshwater flux to the Sermilik Fjord in order to assess variability and trend thereof due to changes in air temperature, net precipitation (hereafter referred to as precipitation), and ice dynamics. In particular, we address the simulated temporal and spatial distribution of terrestrial surface freshwater runoff to the fjord and also on a sub-catchment scale. The runoff was simulated in SnowModel (Liston and Elder, 2006a; Mernild et al., 2006a) – a state-of-the-art modeling system, based on in situ meteorological data within the Sermilik Fjord area. Runoff was initially simulated for the Mittivakkat Glacier catchment area of  $\sim 18\text{ km}^2$  and tested against observed runoff data from the Mittivakkat Glacier catchment outlet which is the only place in the Sermilik Fjord where runoff is observed. The simulated runoff was bias corrected against runoff observations, before runoff simulations were scaled up to the entire Sermilik Fjord catchment area. The following objectives are addressed: (1) assess the performance of SnowModel by comparing simulated runoff against observed runoff for the Mittivakkat Glacier catchment; (2) simulate the spatial runoff variability and

quantify whether the annual freshwater runoff to the Sermilik Fjord has been increasing throughout the simulation period; (3) compare simulated runoff with observed Helheim ice discharge to illustrate the respective distribution from each freshwater source; and (4) merge different sources of freshwater input, e.g., simulated runoff, simulated precipitation over the fjord with satellite-derived ice discharge and geothermal and frictional melting due to basal ice motion to quantify the freshwater flux to the Sermilik Fjord.

## 2 Study area

### 2.1 Physical settings and climate

The Sermilik Fjord catchment (58 045 km<sup>2</sup>) is located on the east coast of Greenland (65° N, 37° W), connected to the Irminger Sea (Fig. 1a). The fjord is 1103 km<sup>2</sup> in area, 85 km in length, and the largest fjord system in SE Greenland. The catchment drains a part of the GrIS, including the Helheim, Fenris, and Midgård Glaciers (the three major outlet glaciers in Sermilik Fjord catchment), and marginal glaciers, among these the Mittivakkat Glacier on Ammassalik Island (see Figs. 1c and 3a for location), where long-term monitoring of climate, mass-balance, and runoff was observed (Mernild and Hasholt, 2006; Knudsen and Hasholt, 2008). The Sermilik Fjord catchment ranges in elevation from sea level to ~2900 m a.s.l. The lower parts of the terrain (elevation below 700–1000 m a.s.l.) are dominated by exposed bedrock, sporadic thin soil layers, and sparse vegetation. Landscapes above 700–1000 m a.s.l. are mostly covered by glaciers and the GrIS (Fig. 1c). For the purposes of this study, the Sermilik Fjord catchment has been divided into seven sub-catchments, each draining into specific parts of the fjord. These areas also represent characteristic variations in glacier ice coverage from approximately 10% (area 2) to 87% (area 4) (Figs. 1c and 4f).

The Sermilik Fjord region represents one of the most humid parts of Greenland (the zone of largest annual precipitation is located ~200 km further south). The simulated mean annual air temperature (MAAT, 2-m above the surface) for the full catchment including the GrIS was  $-4.8^{\circ}\text{C}$  (1999–2008), varying from around the freezing point at the near coastal stations (Tasiilaq and Coast Stations) to around  $-19^{\circ}\text{C}$  on the GrIS (Station NASA-SE) (Fig. 2a). The total annual simulated precipitation (corrected after Allerup et al., 1998, 2000; for further information about the detailed precipitation correction procedures, see Mernild et al., 2009, 2010a) varied from ~1200 to ~1800 mm w.eq. y<sup>-1</sup> within the catchment. Our simulated precipitation values were almost in the same order of magnitude compared to spatial values (1958–2007 average) from Ettema et al. (2009) of 1000 up to 3000 mm w.eq. y<sup>-1</sup>. Mean annual catchment relative humidity and wind speed were 83% and 4.1 m s<sup>-1</sup>, respectively.

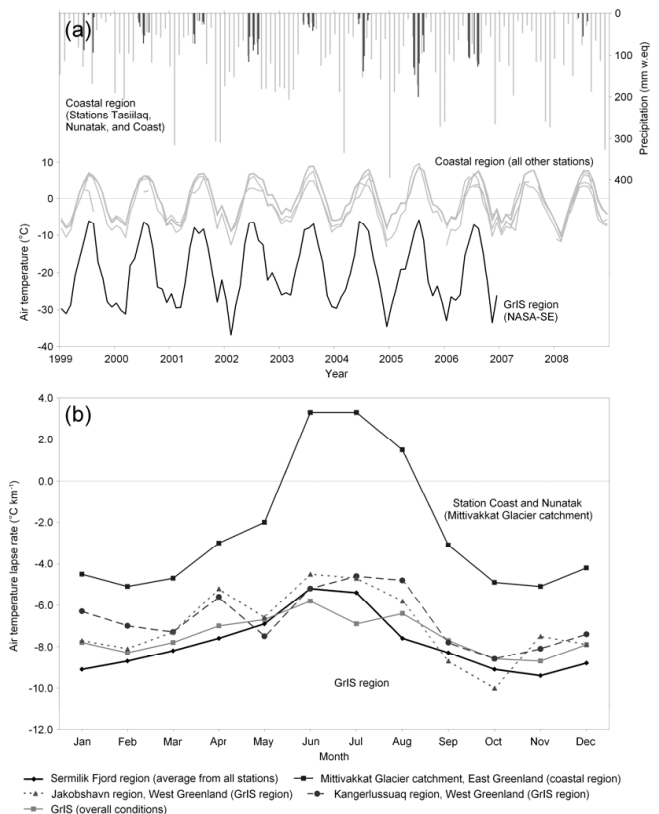


**Fig. 2.** (a) Time series of observed mean monthly air temperature from coastal (Station Tasiilaq, Coast, Nunatak, TAS\_U, TAS\_L, and KULU) and GrIS stations (NASA-SE). Observed cumulative monthly precipitation from coastal stations (Tasiilaq; light color, and Coast and Nunatak (June, July, and August); dark colors) are illustrated; and (b) mean monthly air temperature lapse rates for all the meteorological stations in the simulation domain, for Station Coast and Nunatak (Mernild et al., 2006), and for different areas around the GrIS are illustrated (Mernild et al., 2009).

During summer, the low lying coastal areas, on, e.g., Ammassalik Island (approximately below 300 m a.s.l.), are influenced by air temperature inversions which are common in Arctic coastal landscapes, due to the effect of sea breezes associated with thermal differences between land and the frequently ice-choked fjord and ocean (e.g., Kozo, 1982; Weick and Rouse, 1991; Mernild and Liston, 2010). The climate and its seasonal variability are illustrated in Fig. 2b using positive summer air temperature lapse rates in the near coastal areas. Apart from this temperature inversion in the lower lying near coastal areas during summer, observed air temperature data from all seven stations in the Sermilik Fjord catchment (Fig. 1) showed constantly negative mean monthly temperature lapse rates, very similar to the high-elevation GrIS temperature lapse rates (Fig. 2a) (e.g., Steffen and Box, 2001; Mernild et al., 2009).

**Table 1.** Meteorological input data for the Sermilik Fjord simulation based on meteorological station data on the GrIS: KULU and NASA-SE (provided by University of Colorado at Boulder) and TAS\_L and TAS\_U (by Geological Survey of Denmark and Greenland (GEUS)), and from the outside the GrIS: Station Tasiilaq (by Danish Meteorological Institute (DMI)) and Station Coast and Station Nunatak (by University of Copenhagen, Department of Geography and Geology). The abbreviations indicate: (*Ta*) air temperature, (RH) relative humidity, (Ws) wind speed, (Wd) wind direction, and (*P*) precipitation. For station locations see Fig. 1b.

Meteorological station	Location	Grid	Elevation (m.a.s.l.)	Data period	Parameters	Operated by
KULU	GrIS	65°45' N; 39°36' W	880	20 Jun 1999 – 13 Sep 2000	<i>Ta</i> , RH, Ws, and Wd	University of Colorado at Boulder
NASA-SE	GrIS	66°28' N; 42°30' W	2390	1 Jan 1999 – 25 May 2005	<i>Ta</i> , RH, Ws, and Wd	University of Colorado at Boulder
TAS_L	GrIS	65°38' N; 38°54' W	270	26 Jun 2006 – 31 Dec 2008	<i>Ta</i> , RH, Ws, and Wd	GEUS
TAS_U	GrIS	65°42' N; 38°52' W	580	16 Apr 2004 – 31 Dec 2008	<i>Ta</i> , RH, Ws, and Wd	GEUS
Tasiilaq	Outside GrIS	65°36' N; 37°38' W	44	1 Sep 1998 – 31 Aug 2009	<i>Ta</i> , RH, Ws, Wd, and <i>P</i>	DMI
Coast	Outside GrIS	65°41' N; 37°55' W	25	1 Jan 1999 – 31 Dec 2008	<i>Ta</i> , RH, Ws, Wd, and <i>P</i>	University of Copenhagen
Nunatak	Outside GrIS	65°42' N; 37°49' W	515	1 Jan 1999 – 31 Dec 2008	<i>Ta</i> , RH, Ws, Wd, and <i>P</i>	University of Copenhagen

### 3 Model description and satellite data

#### 3.1 SnowModel and model simulations

SnowModel (Liston and Elder, 2006a), is a spatially-distributed snow-evolution, ice melt, and runoff modeling system designed to be applicable over a wide range of snow and glacier landscapes, and climates found around the world, where snow and ice variations play an important role in hydrological cycling (Mernild et al., 2006a; Mernild and Liston, 2010). For a detailed description of SnowModel, including its subprograms and tests see Liston and Elder (2006a, b), Liston et al. (2008), Liston and Hiemstra (2008), and Mernild and Liston (2010): *MicroMet* is a quasi-physically based meteorological distribution model, which defines the meteorological forcing conditions, *EnBal* calculates the surface energy exchanges, including melt, *SnowPack* simulates heat- and mass-transfer processes and snow-depth and water equivalent evolution, and *SnowTran-3D* is a blowing-snow model that accounts for snow redistribution by wind. SnowModel is a surface model simulating first-order effects of atmospheric forcing on snow, glacier ice, and runoff, but processes related to glacier dynamics are not included.

#### 3.2 Input data, model bias correction, and uncertainties

Meteorological data of air temperature, relative humidity, wind speed, wind direction, and precipitation were obtained from seven meteorological stations at different elevations within the simulation domain (Fig. 1b). Four stations were located on the GrIS, and three outside the GrIS in the coastal region (Table 1). Simulations were performed on a one-day time step, based on lapse rates, generated using observed data from all seven stations (Fig. 2b). The simulation period spans from 1 September 1998 through 31 August 2009, whereas output values were simulated for calendar years (1999–2008). Air temperature and precipitation data are summarized in Fig. 2a.

The Greenland topographic data at 625-m resolution from Bamber et al. (2001) was used with the image-derived correction published by Scambos and Haran (2002), and interpolated to a 500-m grid increment covering a 400.5 by 300.5 km simulation domain for the Sermilik Fjord catchment (Fig. 1a). The location of the Sermilik Fjord coast line, GrIS terminus, and marginal glaciers were estimated by using Moderate Resolution Imaging Spectroradiometer (MODIS) satellite images (observed on 30 August 2009). User-defined constants for SnowModel are shown in Mernild et al. (2009), and parameter definitions are given in Liston and Sturm (1998).

SnowModel simulated runoff was tested and bias corrected against observed runoff from the outlet of the Mittivakkat Glacier catchment for the period 1999–2005 (different observed runoff periods were used, due to variations in field campaign from year to year; Fig. 3a). The cumulative simulated runoff was initially underestimated by 34–43%, averaging 38% according to runoff observations (Fig. 2). Therefore, a linear regression ( $r^2 = 0.95$ ; where  $r^2$  is the explained variance) was used for runoff correction as shown in Fig. 3a. The corrected cumulative annual Mittivakkat Glacier runoff is illustrated in Fig. 3b. This underestimation of runoff is expected to be a mixture of various causes, where the first three are expected to be the main reasons: (1) uncertainties associated with model inputs (e.g., Mernild and Liston 2010); (2) unrepresented or poorly-represented processes in SnowModel (Liston and Elder 2006a, b); (3) uncertainties related to runoff observations (Hasholt et al., 2006; Mernild and Hasholt, 2009); and (4) englacial and subglacial water flow to/from neighboring glacier sub-catchments (see Mernild 2006, Mernild et al., 2006b; a description of the Mittivakkat Glacier watershed divides can be seen in Mernild and Hasholt (2006).



The assumed accuracy of single outlet discharge measurements is within 5–10%, whereas calculated stage-discharge values might deviate up to 25% from simultaneous manual measurements. However, long-term discharges (monthly and annual) are typically accurate within approximately 5–15% (Hasholt et al., 2006; Mernild and Hasholt, 2009). Statistical analysis from previous SnowModel studies on snow distributions, snow and glacier melt, and runoff from marginal glaciers in Greenland and the GrIS (e.g., Mernild et al., 2006a, 2009), along with uncertainties in observed discharge used for calibration, indicates that simulated influx of runoff to the Sermilik Fjord might be influenced by the same order of uncertainties: We assume an error of 10–25%. This includes uncertainties related to not using routines for air temperature inversion in low lying near coastal areas (Mernild and Liston, 2010) and the associated influence on snow and glacier ice melt and glacier mass-balance simulations; unfortunately no radiosonde data exist for the inner part of the Sermilik Fjord.

Even though SnowModel underestimated runoff by 38% on average before bias-correction, it is currently probably the most physically realistic model for simulating snow and ice melt, and water balance components, including freshwater runoff from snow- and ice-covered regions. The model demands limited input data, an important consideration in the Sermilik Fjord and other Arctic areas, for which data are sparse due to rough terrain, harsh climatic conditions, and remote location.

### 3.3 Satellite-derived ice discharge

Time series of ice flux to the calving front, which will equal the sum of ice lost to calving and melt at the calving face, and which we term discharge, for Helheim Glacier, Midgård Glacier, and Fenris Glacier were calculated from observed average surface velocity, glacier width and estimated ice thickness. Speeds were measured from automated Repeat-Image Feature Tracking (RIFT) using pairs of orthorectified images from: (1) Landsat 7 Enhanced Thematic Mapper Plus (panchromatic band) distributed by the United States Geological Survey; (2) visible to near-infrared bands of the Advanced Spaceborne Thermal Emissivity and reflection Radiometer (ASTER) distributed by the NASA Land Processes Distributed Active Archive (LP DAAC); and (3) SPOT-5 panchromatic images distributed through the SPIRIT program. Landsat and ASTER images have a pixel resolution of 15 m and the 5 m SPOT-5 images were down-sampled to 15 m for RIFT processing. The Multi-Image/Multi-Chip (MIMC) RIFT algorithm (Ahn and Howat, 2010) was used to measure surface displacements every 100 m. Individual displacement vectors were then averaged over a 1-km wide band near the front of the glacier to provide a time series of average velocity at the ice front. Errors in this velocity estimate are the sum of the ambiguity cross-correlation peak (typically 5 m) and errors in image co-registration, which can

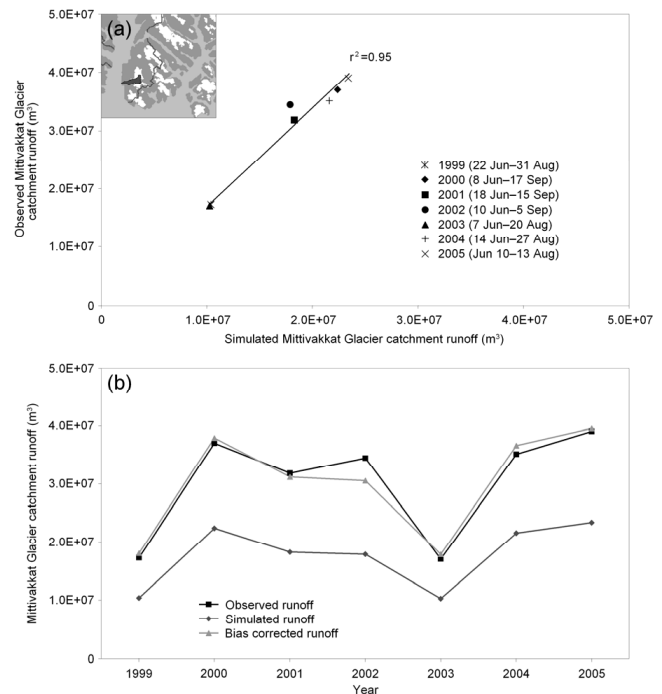


**Fig. 3.** (a) Observed and simulated Mittivakkat Glacier catchment runoff from 1999–2005. The linear regression (forced through zero) was used for bias correction of the Sermilik Fjord simulated runoff. Be aware that the annual observed runoff periods are different. The inset figure indicates the general location of the Mittivakkat Glacier catchment (black polygon) within sub-catchment area 1 (for a general location of the sub-catchments see Fig. 4a) inside the Sermilik Fjord catchment; and (b) observed, simulated, and bias corrected runoff from the Mittivakkat Glacier catchment from 1999–2005.

vary from several meters to several 10's of meters, following manual registration correction procedures, depending on the image pair. Due to the high speeds observed, we assumed that speed was constant with ice depth. Averaged glacier width over the region of velocity sampling was obtained from 15-m Landsat imagery.

Ice thickness for Helheim Glacier was obtained in 2001 and 2008 by the University of Kansas Coherent Radar Depth Sounder (CoRDS) (Gogineni et al., 2001; Howat et al., 2005). For Fenris and Midgård glaciers, for which no thickness data are available, ice thickness at the start of the time series was estimated from the height of the calving front assuming a grounded ice front at hydrostatic equilibrium and densities of ice and sea water of 910 and 1027 kg m<sup>3</sup>, respectively. We assume an error of  $\pm 50$  m in this thickness estimate. Changes in ice thickness through time were then measured from repeat ASTER digital elevation models produced by the LP DAAC and vertically co-registered using tie points over ice-free terrain. These data have a relative error of  $\pm 10$  m in the vertical (Fujisada et al., 2005). Overall, we assume an ice discharge error of 15–25%.

### 3.4 Geothermal and frictional melting due to basal ice motion

The upper-bounds for the melt water generated through melting at the ice bed due to: (a) geothermal heating; and (b) frictional heating due to basal ice motion were estimated. For (a), it was liberally assumed that the bed was at the melting temperature over all regions with surface elevations below 1200 m a.s.l., and area of 2300 km<sup>2</sup>. A typical geothermal heat flux of 0.05 W m<sup>-2</sup> gives a basal melt rate of 5 mm w.eq. y<sup>-1</sup> (Cuffey and Paterson, 2010, p. 118) for ice at the melting temperature, totaling approximately 0.01 × 10<sup>9</sup> m<sup>3</sup> y<sup>-1</sup> produced by geothermal heating over this area, which was two orders of magnitude less than the contributions from runoff and ice discharge, and can therefore be ignored (Tables 2 and 3). For (b), the maximum rate of basal melt due to frictional heating caused by ice sliding over the bed is Eq. (1):

$$m = (tb \times ub) / (\rho \times L_f) \quad (1)$$

where,  $tb$  is the basal shear stress,  $ub$  is sliding speed,  $\rho$  is the ice density, and  $L_f$  is the latent heat of freezing/melting. Again, it was assumed that the bed was at the melting temperature over the drainage area with surface elevations below 1200 m a.s.l. We also assumed that 100% of the ice motion needed to maintain mass balance (i.e., the balance velocity) was accomplished through basal sliding in this region. Balance velocities were obtained from Bamber et al. (2000). Finally, we assumed that the basal drag was equal to the driving stress, which we calculated from the ice thickness and surface elevation maps from Bamber et al. (2000, 2001). From this we obtain a total melt volume rate of approximately 0.5 × 10<sup>9</sup> m<sup>3</sup> y<sup>-1</sup>, which is approximately 1% of the average total freshwater flux (Table 3).

## 4 Results and discussion

### 4.1 Terrestrial surface runoff to Sermilik Fjord

Annual (1999–2008) cumulative simulated runoff from all seven sub-catchments, and from the entire catchment, to Sermilik Fjord is shown in Fig. 4b. Total runoff to Sermilik Fjord for the modeled decade averaged  $4.6 \pm 0.7 \times 10^9$  m<sup>3</sup> y<sup>-1</sup>, from a minimum of  $2.9 \pm 0.4 \times 10^9$  m<sup>3</sup> y<sup>-1</sup> in 1999 to a maximum of  $5.9 \pm 0.9 \times 10^9$  m<sup>3</sup> y<sup>-1</sup> in 2005; these values were expected to be among the highest since the simulation period included the warmest years since the beginning of instrumental records. For the simulation period, data showed an average insignificant increase in runoff of  $1.0 \times 10^9$  m<sup>3</sup> ( $r^2 = 0.14$ ,  $p < 0.25$ ; where  $p$  level of significance) (Fig. 4b), due to a combination of both increasing annual precipitation ( $r^2 = 0.13$ ) and increasing mean annual summer air temperature (June through August) ( $r^2 = 0.32$ ), influencing the

melting snow and ice conditions. An increase in precipitation for the Sermilik Fjord catchment of  $\sim 15\%$  decade<sup>-1</sup>, which was above the average increase of  $\sim 1\%$  decade<sup>-1</sup> for the Arctic in general, estimated by ACIA (2005).

For the simulation period, 2007 showed the largest satellite-derived GrIS cumulative melt extent followed by 2005 (Steffen et al., 2008), but also the largest melt index – defined as the melting area times the number of melting days for areas above 2000 m in elevation (Tedesco, 2007) – followed by 2005 as the fourth highest for the simulation period. The largest amount of modeled runoff to the Sermilik Fjord occurred in 2005, and not in 2007 (Fig. 4b). This discrepancy between the GrIS melting conditions and the Sermilik Fjord runoff conditions was due to a record high annual precipitation for 2005 of  $\sim 180$  mm w.eq. y<sup>-1</sup> combined with the second highest mean annual summer air temperatures of 2.2 °C (Fig. 2a). The record high 2005 precipitation combined with the relatively high percentage of rain ( $\sim 65\%$  of the total annual precipitation) was the reason why less precipitation accumulated as snow during winter, and more streamed directly into the fjord as runoff. The connection between snow melting, melt water retention and refreezing within the snowpack, and runoff is described, e.g., in Hanna et al. (2008), Mernild et al. (2009) related to the variation in annual snow accumulation/precipitation.

Weather conditions for SE Greenland, including the Sermilik Fjord, are affected by low-pressure systems (e.g., Tsukernik et al., 2007), especially the associated wind and precipitation which varies due to year-to-year changes in the storm tracks. Most low pressure centers arrive from directions between south and west, steered by the “polar vortex”, an upper level cyclone. During winter these are normally centered over the Canadian Cold Pole and during summers they are less pronounced and centered over the Arctic Ocean (Hansen et al., 2008). Therefore, it should be kept in mind, even though maximum melting conditions occurred for the GrIS as in 2007, local variability in precipitation can be the reason for annual runoff peaks, as illustrated for the Sermilik Fjord catchment for 2005.

On a sub-catchment scale, the interannual runoff variability generally followed the variability of the overall runoff to the fjord, showing lowest runoff values in 1999 and highest values in 2005 (Fig. 4b). In Fig. 4b the spatial distribution of runoff to the Sermilik Fjord is illustrated, displaying that sub-area 7 contributed, on average, the lowest annual runoff volume of  $0.4 \pm 0.1 \times 10^9$  m<sup>3</sup> y<sup>-1</sup>, and sub-area 4 the highest value of  $1.4 \pm 0.2 \times 10^9$  m<sup>3</sup> y<sup>-1</sup>. Besides the general effect of precipitation and summer air temperatures on runoff from all sub-catchments, both the percentage of glacier cover and its hypsometry within each sub-catchment strongly influenced simulated runoff within the region. Generally, sub-catchments showing high fractions of glacier cover and glaciers at low elevations show stronger positive runoff effects during years with high temperatures (Fig. 4c).

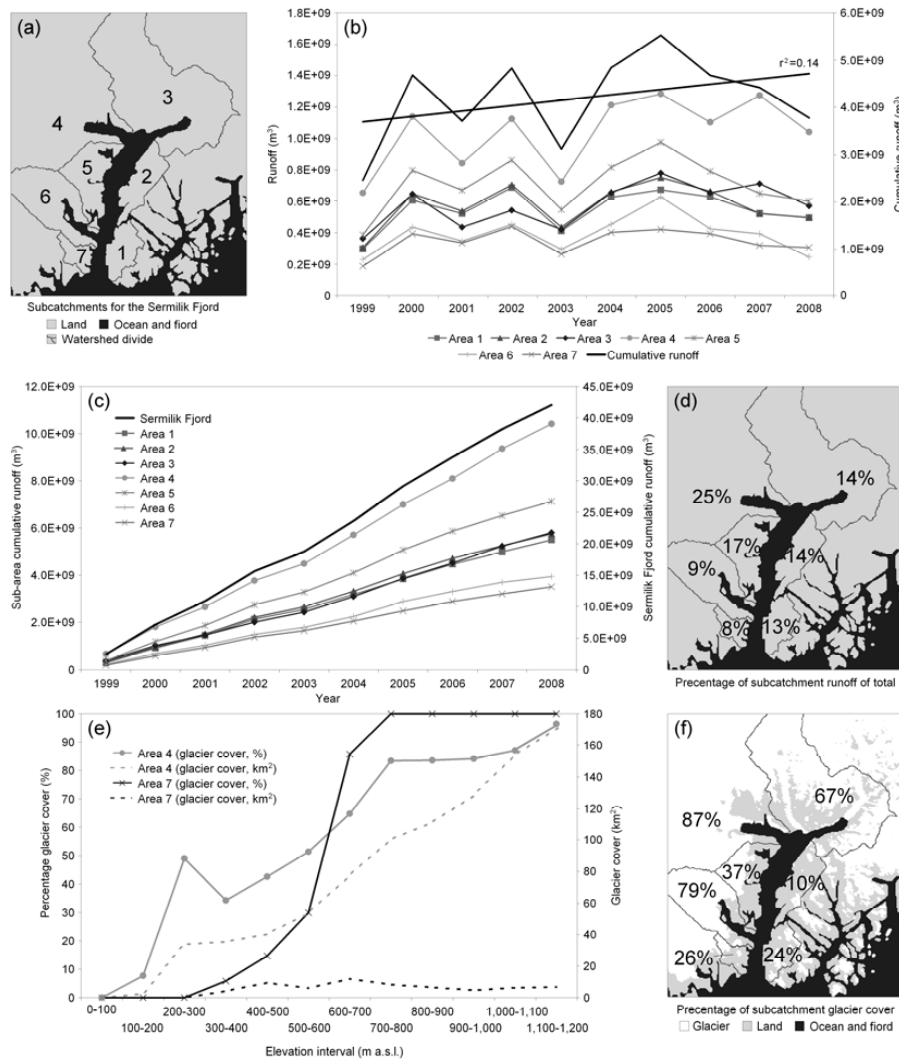


**Fig. 4.** (a) Area of interest including the seven sub-catchments for the Sermilik Fjord (simulated in River Tools); (b) time series (1999–2008) of annual sub-catchment simulated runoff and annual cumulative runoff, including trend line (linear) for cumulative runoff; (c) cumulative sub-catchment runoff and overall runoff; (d) percentage of sub-catchment runoff of total runoff; (e) glacier cover distribution in percentage and square kilometer within the elevations from where runoff occurred for the sub-catchment with the lowest cumulative runoff (sub-catchment 7) and the highest (sub-catchment 4); and (f) the percentage of sub-catchment glacier cover within the area of interest.

The Sermilik Fjord accumulated catchment and sub-catchment runoff (1999–2008) are illustrated in Fig. 4c, showing an overall cumulative freshwater runoff volume of  $46.0 \pm 6.9 \times 10^9 \text{ m}^3$ . The lowest cumulative runoff contribution occurred from sub-area 7, with a total of  $3.5 \pm 0.5 \times 10^9 \text{ m}^3$ , which equalled about 8% of the overall freshwater runoff to the fjord. The highest contribution of  $10.4 \pm 1.6 \times 10^9 \text{ m}^3$  came from sub-area 4 – the Helheim sub-catchment –, which equalled about 25% of the overall runoff. The percentage of cumulative freshwater runoff from the other sub-areas (area 1–3 and 5–6) averaged from 9% to 17% of the overall runoff (Fig. 4d). Obviously sub-catchments with the greatest glacier coverage, combined with the highest percentage of glaciers at low elevations, were the sub-areas

where the greatest freshwater runoff contribution to the fjord occurred, and vice versa. In Fig. 4e the differences between sub-catchments 4 and 7 in glacier cover ( $\text{km}^2$ ) and in glacier cover (%) within each 100-m elevation interval are shown. Area 4 was the sub-catchment having the greatest glacier area of  $910 \text{ km}^2$  from where runoff occurred:  $\sim 30\%$  of the area was located below 500–600 m a.s.l. Area 7 was, however, a sub-catchment having a glacier cover of only  $65 \text{ km}^2$  of which only  $\sim 10\%$  was found below 500–600 m a.s.l. Areas 1–3 and 5–6 represent a mixture of the main characteristics found in areas 4 and 7. Even though areas 3 and 6 both have a relatively high glacier cover of 67% and 79%, respectively, the cumulative runoff only accounted for 14% and 9% of the overall runoff to the fjord (Fig. 4d). The reason for these

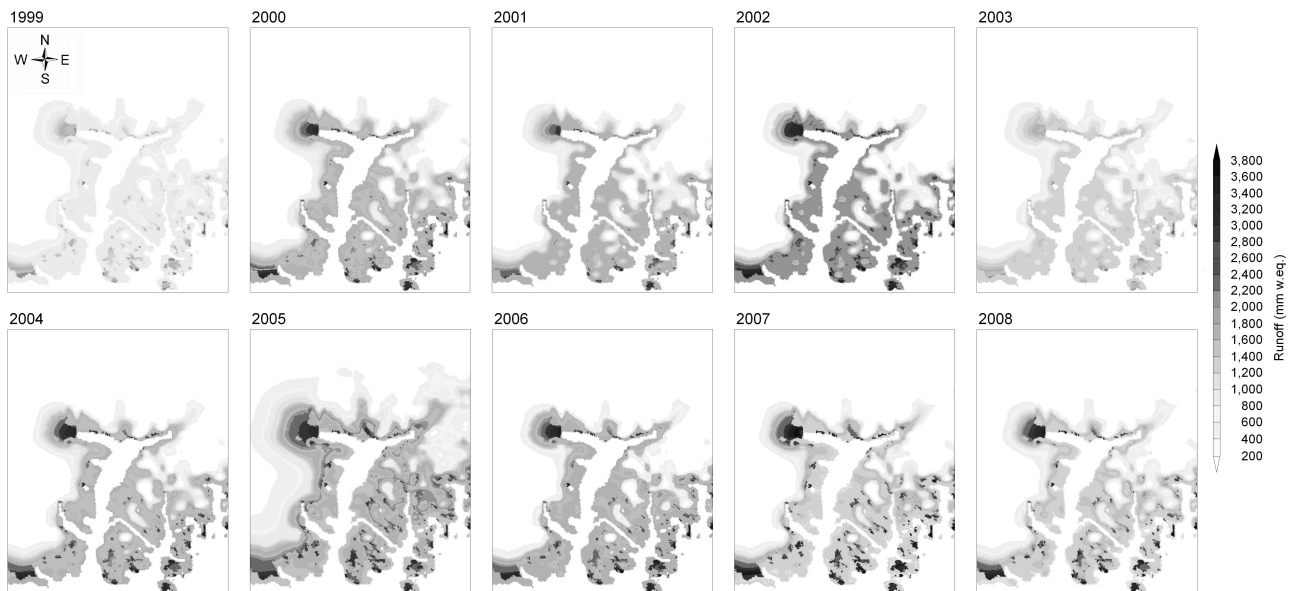


**Fig. 5.** Spatial simulated annual cumulative runoff within the area of interest to the Sermilik Fjord for 1999–2008.

relatively low percentages of runoff values from sub-area 3 and 6 were due to the high elevated glacier cover within each sub-catchment. For sub-area 5 the situation was however different: In area 5 the amount of runoff accounted for 17% of the overall runoff to Sermilik Fjord, even though the sub-catchment area and the glacier cover area were relatively low. The reason for the relatively high runoff volume from sub-area 5 was because of the low elevated glacier cover in the sub-area.

In Fig. 5 the spatial distributions of annual cumulative runoff to Sermilik Fjord are illustrated for 1999 through 2008. Those parts of the fjord catchment exhibiting glaciers covering low altitudes, e.g., both marginal glaciers and the Helheim glacier terminus showed the highest simulated runoff values. At the Helheim glacier terminus the areally-averaged annual maximum runoff ranged from  $\sim 1.8$  m w.eq. in 2003 to more than  $\sim 3.8$  m w.eq. in 2007. Simulated runoff values which seemed to be in line with previously published values, e.g., by Ettama et al. (2008), and consistent with previous GrIS runoff simulations by Mernild et al. (2009). The amount of simulated runoff decreased with increasing altitude, on average by  $\sim 250$  mm w.eq.  $100$  m $^{-1}$  from the ice margin all the way to the boundary where runoff occurs (Fig. 5); for the Jakobshavn drainage area, W Greenland ( $69^\circ$  N), the value was similar with  $\sim 220$  mm w.eq.  $100$  m $^{-1}$  (Mernild et al., 2010b). On the GrIS within the Sermilik Fjord catchment (for a latitude range of  $65$ – $66^\circ$  N) this annual runoff boundary line was located about 25–40 km from the GrIS terminus at an elevation of 1140 m a.s.l. to 1600 m a.s.l., averaging  $1150 \pm 140$  m a.s.l.

#### 4.2 Freshwater flux to Sermilik Fjord

To account for the freshwater flux to the Sermilik Fjord, not only terrestrial surface runoff needs to be addressed, but also: (1) ice discharge influenced by GrIS dynamical processes (as described by Howat et al., 2005, 2008) and temperature of near-coastal ocean currents (Holland et al., 2008; Straneo et al., 2010); (2) seasonal changes in internal drainage system due to melting; (3) runoff from subglacial geothermal melting and frictional melting due to basal ice motion; (4) submarine melting at tidewater glacier margins; and (5) precipitation (e.g., rain and snow accumulation on sea ice) at the Sermilik Fjord surface area. Unfortunately, seasonal changes in internal drainage system was omitted, due to missing data (values probably insignificant related to the overall terrestrial freshwater flux budget to the Sermilik Fjord), while submarine melting at tidewater glacier margins was integrated in the ice discharge values. Contributions of ice discharge from minor GrIS outlet glaciers, e.g., glaciers located in Johan Petersens Fjord were ignored due to lack of available data (only a minor production of icebergs has been observed; personal communication, N. T. Knudsen, 2010), while ice discharge from the three major outlet glaciers: the Helheim Glacier, Fenris Glacier, and Midgård Glacier at the innermost part of the fjord were included (Figs. 6 and 7). Based on satellite-derived observations, the Helheim average ice discharge for the period 1999–2008, was estimated to be  $25.9 \pm 2.6 \times 10^9$  m $^3$  w.eq.  $y^{-1}$  (Tables 2 and 3), and for the Fenris and Midgård Glaciers ice discharge were  $2.5 \pm 0.5$  and  $5.5 \pm 1.0 \times 10^9$  m $^3$  w.eq.  $y^{-1}$ , respectively (Table 3 and Fig. 6). In Fig. 6 an example of variations in surface ice velocity, ice thickness, and

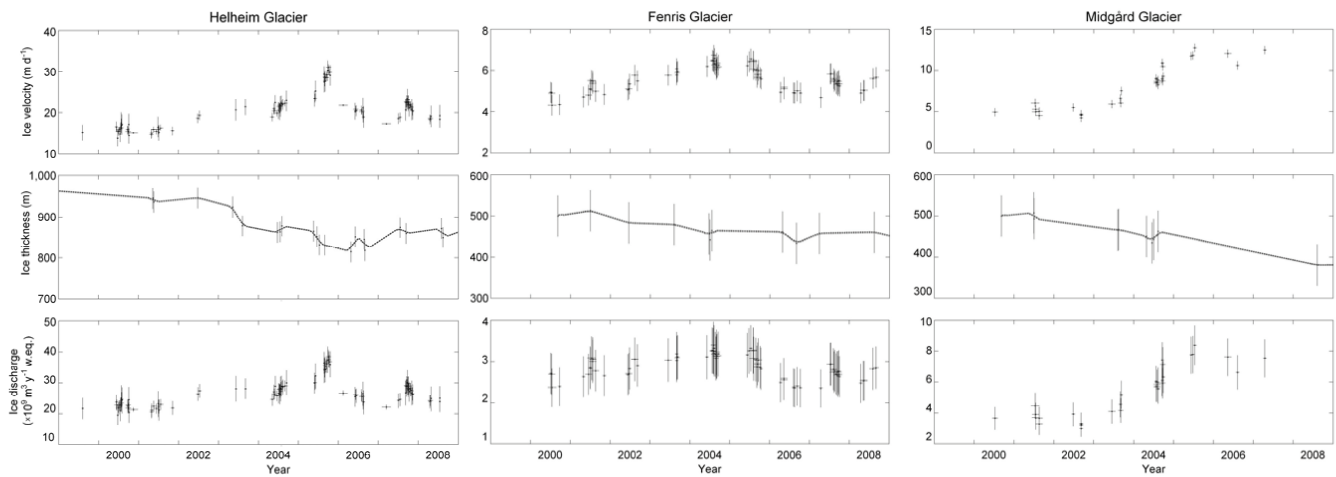


**Fig. 6.** Satellite-derived time series for the period 1998–2008 of ice velocity, ice thickness, and ice discharge at a stationary flux gate within 3 km of the most-retreated front position of the three major outlet glaciers: Helheim Glacier, Fenris Glacier, and Midgård Glacier draining into the Sermilik Fjord. Ice thickness observations (denoted by vertical error bars) were linearly interpolated, denoted by the curve, and multiplied by constant glacier width and observations of ice velocity and the ratio of water and ice densities (0.91) to obtain discharge of water. Ice discharge data for Helheim Glacier reported here are updated from Howat et al. (2005, 2007). Fenris and Midgård Glaciers are located in sub-area 3 and Helheim in sub-area 4.

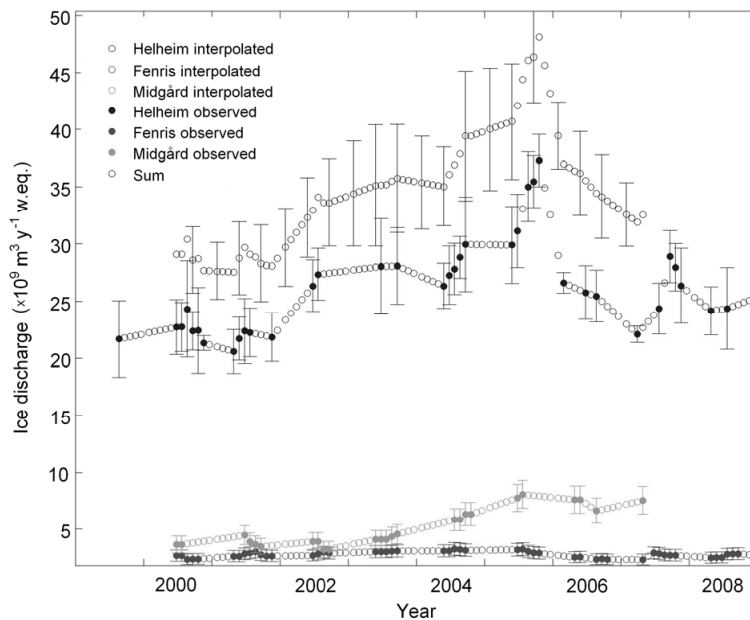


**Fig. 7.** Average monthly ice discharge observations (closed circle) and linearly-interpolated values (open circle) for Helheim Glacier, Fenris Glacier, and Midgård Glacier, and sum of the three glaciers for the period 1999 through 2008.

ice discharge for the Helheim Glacier, Fenris Glacier, and Midgård Glacier are illustrated, showing substantial variations in velocity, ice thickness, and discharge, with a general increase in velocity and discharge after 2002 and peaking in 2005 and 2006. Due to both decreased ice velocity and thickness, ice discharge at Helheim Glacier decreased to earlier levels by 2007 (Howat et al., 2007). However, for the simulation period, ice discharge from the three ma-

ior outlet glaciers showed an average significant increase of  $13.2 \times 10^9 \text{ m}^3 \text{ w.eq.}$  ( $r^2 = 0.49$ ;  $p < 0.01$ ) (Fig. 7). Mean annual ice discharge values were combined with annual Snow-Model simulated precipitation at the Sermilik Fjord surface area, terrestrial surface runoff, and subglacial geothermal and frictional melting, to deduce the freshwater flux: (1) from the Helheim Glacier catchment (Table 2), but also; (2) to the entire Sermilik Fjord (Table 3). Calculations



**Table 2.** Freshwater flux from the Helheim Glacier catchment based on SnowModel simulated freshwater runoff and satellite-derived ice discharge.

	1999	2000	2001	2002	2003	2004	2005	2006	2007	2008	Mean
SnowModel simulated runoff from the Helheim Glacier catchment including error (sub-area 4), $10^9 \text{ m}^3 \text{ y}^{-1}$	$0.7 \pm 0.1$	$1.1 \pm 0.2$	$0.8 \pm 0.1$	$1.1 \pm 0.2$	$0.7 \pm 0.1$	$1.2 \pm 0.2$	$1.3 \pm 0.2$	$1.1 \pm 0.2$	$1.3 \pm 0.2$	$1.0 \pm 0.2$	$1.0 \pm 0.2$ (4%)
Satellite-derived ice discharge from the Helheim Glacier including error, $10^9 \text{ m}^3 \text{ y}^{-1}$	$21.7 \pm 3.3$	$22.7 \pm 2.5$	$21.8 \pm 2.2$	$26.8 \pm 2.3$	$28.1 \pm 3.8$	$28.0 \pm 2.5$	$33.8 \pm 2.8$	$25.9 \pm 1.8$	$25.9 \pm 2.1$	$24.3 \pm 2.8$	$25.9 \pm 2.6$ (96%)
Freshwater flux from the Helheim Glacier catchment, $10^9 \text{ m}^3 \text{ y}^{-1}$	$22.4 \pm 3.4$	$23.8 \pm 2.7$	$22.6 \pm 2.3$	$27.9 \pm 2.5$	$28.8 \pm 3.9$	$29.2 \pm 2.7$	$35.1 \pm 3.0$	$27.0 \pm 2.0$	$27.2 \pm 2.3$	$25.3 \pm 3.0$	$26.9 \pm 2.8$

**Table 3.** Freshwater flux to the Sermilik Fjord based on SnowModel simulated freshwater runoff, precipitation at the Sermilik Fjord surface area, subglacial geothermal melting and subglacial frictional melting due to basal ice motion, and satellite-derived ice discharge from the Helheim Glacier, Fenris Glacier, and Midgård Glacier (the three major outlet glaciers in Sermilik Fjord catchment). Mean freshwater flux to the Sermilik Fjord is calculated based on mean values from each input component.

	1999	2000	2001	2002	2003	2004	2005	2006	2007	2008	Mean
SnowModel simulated terrestrial runoff to the Sermilik Fjord including error, $10^9 \text{ m}^3 \text{ y}^{-1}$	$2.9 \pm 0.4$	$5.1 \pm 0.8$	$4.1 \pm 0.6$	$5.2 \pm 0.8$	$3.5 \pm 0.5$	$5.2 \pm 0.8$	$5.9 \pm 0.9$	$5.1 \pm 0.8$	$4.8 \pm 0.7$	$4.2 \pm 0.6$	$4.6 \pm 0.7$ (11%)
SnowModel simulated precipitation (e.g., rain and snow accumulation on sea ice) at the Sermilik Fjord surface area ( $1103 \text{ km}^2$ ) including error, $10^9 \text{ m}^3 \text{ y}^{-1}$	$0.9 \pm 0.1$	$1.2 \pm 0.1$	$1.7 \pm 0.1$	$1.7 \pm 0.1$	$1.4 \pm 0.1$	$1.4 \pm 0.1$	$1.8 \pm 0.1$	$1.4 \pm 0.1$	$1.5 \pm 0.1$	$1.3 \pm 0.1$	$1.4 \pm 0.1$ (3%)
Subglacial geothermal melting, $10^9 \text{ m}^3 \text{ y}^{-1}$	0.01	0.01	0.01	0.01	0.01	0.01	0.01	0.01	0.01	0.01	0.01 (>0.03%)
Subglacial frictional melting due to basal ice motion, $10^9 \text{ m}^3 \text{ y}^{-1}$	0.5	0.5	0.5	0.5	0.5	0.5	0.5	0.5	0.5	0.5	0.5 (1%)
Satellite-derived ice discharge from the Helheim Glacier including error, $10^9 \text{ m}^3 \text{ y}^{-1}$	$21.7 \pm 3.3$	$22.7 \pm 2.5$	$21.8 \pm 2.2$	$26.8 \pm 2.3$	$28.1 \pm 3.8$	$28.0 \pm 2.5$	$33.8 \pm 2.8$	$25.9 \pm 1.8$	$25.9 \pm 2.1$	$24.3 \pm 2.8$	$25.9 \pm 2.6$ (65%)
Satellite-derived ice discharge from the Fenris Glacier including error, $10^9 \text{ m}^3 \text{ y}^{-1}$	–	$2.3 \pm 0.5$	$2.5 \pm 0.5$	$2.6 \pm 0.5$	$2.8 \pm 0.5$	$2.9 \pm 0.5$	$2.8 \pm 0.5$	$2.2 \pm 0.5$	$2.5 \pm 0.5$	$2.4 \pm 0.5$	$2.5 \pm 0.5$ (6%)
Satellite estimated ice discharge from the Midgård Glacier including error, $10^9 \text{ m}^3 \text{ y}^{-1}$	–	$3.7 \pm 0.7$	$3.9 \pm 0.8$	$3.6 \pm 0.7$	$4.2 \pm 0.8$	$6.1 \pm 1.0$	$7.9 \pm 1.2$	$7.3 \pm 1.2$	$7.5 \pm 1.2$	–	$5.5 \pm 1.0$ (14%)
Freshwater flux to the Sermilik Fjord, $10^9 \text{ m}^3 \text{ y}^{-1}$	–	$35.5 \pm 4.6$	$34.5 \pm 4.2$	$40.4 \pm 4.4$	$40.5 \pm 5.7$	$44.1 \pm 4.9$	$52.7 \pm 5.5$	$42.4 \pm 4.4$	$42.7 \pm 4.6$	–	$40.4 \pm 4.9$

showed a freshwater flux averaging  $26.9 \pm 2.8 \times 10^9 \text{ m}^3 \text{ y}^{-1}$  from the Helheim Glacier sub-catchment, and a flux of  $40.4 \pm 4.9 \times 10^9 \text{ m}^3 \text{ y}^{-1}$  to the Sermilik Fjord for 1999–2008. The suggested freshwater flux entering the Sermilik Fjord of  $40.4 \pm 4.9 \times 10^9 \text{ m}^3 \text{ y}^{-1}$ , equaled 5% of the freshwater flux of  $786 \times 10^9 \text{ m}^3 \text{ y}^{-1}$  (1995–2007) from the entire GrIS to the ocean (Mernild et al., 2009). For the Helheim Glacier catchment, around  $25.9 \pm 2.6 \times 10^9 \text{ m}^3 \text{ y}^{-1}$  (96%) originated from satellite-derived ice discharge, and  $1.0 \pm 0.2 \times 10^9 \text{ m}^3 \text{ y}^{-1}$  (4%) from SnowModel simulated runoff. For Sermilik Fjord  $4.6 \pm 0.7 \times 10^9 \text{ m}^3 \text{ y}^{-1}$  (11%) out of a freshwater flux of  $40.4 \pm 4.9 \times 10^9 \text{ m}^3 \text{ y}^{-1}$ , originated from the SnowModel simulated runoff,  $1.4 \pm 0.1 \times 10^9 \text{ m}^3 \text{ y}^{-1}$  (3%) from

the SnowModel simulated precipitation at the Sermilik Fjord surface area,  $33.9 \pm 4.1 \times 10^9 \text{ m}^3 \text{ y}^{-1}$  (85%) from ice discharge, and  $0.5 \times 10^9 \text{ m}^3 \text{ y}^{-1}$  (1%) from subglacial frictional melting due to basal ice motion (Table 3). In general, ice discharge represented 65%, 14%, and 6% of the total freshwater flux from Helheim, Midgård, and Fenris glaciers, respectively (Table 3). For GrIS in total, around half of the mass loss originated by surface melting and subsequent freshwater runoff into the ocean, and the other half from iceberg calving and geothermal melting (e.g., Rignot and Kanagaratnam 2006, Lemke et al. 2007, Mernild et al. 2008c).

The Helheim Glacier represents one of the major outlet glaciers from the GrIS, which dominated 65% of the freshwater flux into Sermilik Fjord. Runoff only forms a minor part (11%) of the overall freshwater flux to the fjord. Similar conditions were found for the Jakobshavn drainage area (2000–2007), where 7% of the average annual freshwater flux originated from surface runoff (Mernild et al., 2010b). For two of the major GrIS outlet glacier sub-catchments (Helheim and Jakobshavn) it can be concluded that runoff was a minor contributor to the freshwater flux, which was highly dominated by ice discharge.

## 5 Summary and conclusion

The amount of freshwater runoff reaching the ocean from marginal glaciers, the GrIS, and ice free landscapes depends on the precipitation and storage changes in reservoirs of ice, snow, and water on land. In many places around Greenland, glaciers calve directly into the sea and the overall flux of freshwater from specific catchments, e.g., the Sermilik Fjord catchment, will be influenced by or even dominated by a discharge of calving ice. At the Sermilik Fjord catchment, 85% of the average annual freshwater flux of  $40.4 \pm 4.9 \times 10^9 \text{ m}^3 \text{ y}^{-1}$  (1999–2008) originated from ice discharge (65% alone from the Helheim Glacier), 11% from terrestrial surface runoff, 3% from net precipitation at the fjord area, and 1% from subglacial frictional melting. Ice discharge is the primary mechanism for delivering freshwater to Sermilik Fjord. In period of a warmer climate, as for example during the recent decade an increase in runoff ( $r^2 = 0.14$ ) and ice discharge ( $r^2 = 0.49$ ) occurred. The Sermilik Fjord increasing runoff was caused by both increasing mean annual summer air temperature and precipitation: even though maximum melting conditions occurred in 2007, local variability in precipitation can be the reason for annual runoff peaks, as illustrated for the Sermilik Fjord for 2005.

*Acknowledgements.* Special thanks to the Danish Meteorological Institute, the Cooperative Institute for Research in Environmental Sciences (CIRES), University of Colorado at Boulder, the Department of Geography and Geology, University of Copenhagen, and the Geological Survey of Denmark and Greenland (GEUS) for use of observed meteorological data. Further, thanks to the Department of Geography and Geology, University of Copenhagen, for use of observed runoff data. Thanks are also given to Byrd Polar Research Center, Ohio State University, for use of satellite-derived ice discharge. This work was supported by grants from the Climate Change Prediction Program within the US Department of Energy's Office of Science. Los Alamos National Laboratory is operated under the auspices of the National Nuclear Security Administration of the US Department of Energy under Contract No. DE-AC52-06NA25396.

Edited by: S. Dery

## References

- ACIA: Arctic Climate Impact Assessment, Cambridge University Press, 1042 pp., 2005.
- Ahn, Y. and Howat, I. M.: Efficient, automated glacier surface velocity measurements from repeat images using multi-image/multi-chip (MIMC) feature tracking, *IEEE T. Geosci. Remote*, revised, 2010.
- Allerup, P., Madsen, H., and Vejen, F.: Estimating true precipitation in Arctic areas, *Proc. Nordic Hydrological Conf.*, Helsinki, Finland, Nordic Hydrological Programme Rep. 44, 1–9, 1998.
- Allerup, P., Madsen, H., and Vejen, F.: Correction of precipitation based on off-site weather information. *Atmos. Res.*, 53, 231–250, 2000.
- Allison, I., Bindoff, N. L., Bindschadler, R. A., Cox, P. M., de Noblet, N., England, M. H., Francis, J. E., Gruber, N., Haywood, A. M., Karoly, D. J., Kaser, G., Le Quéré, C., Lenton, T. M., Mann, M. E., McNeil, B. I., Pitman, A. J., Rahmstorf, S., Rignot, E., Schellnhuber, H. J., Schneider, S. H., Sherwood, S. C., Somerville, R. C. J., Steffen, K., Steig, E. J., Visbeck, M., and Weaver, A. J.: *The Copenhagen Diagnosis: Updating the World on the Latest Climate Science*, The University of New South Wales Climate Change Research Centre (CCRC), Sydney, Australia, 60 pp., 2009.
- Bamber, J., Ekholm, S., and Krabill, W.: A new, high-resolution digital elevation model of Greenland fully validated with airborne laser altimeter data, *J. Geophys. Res.*, 106, 6733–6746, 2001.
- Bamber J., Hardy, R. J., and Joughin, I.: An analysis of balance velocities over the Greenland Ice Sheet and comparison with synthetic aperture radar interferometry, *J. Glaciol.*, 46(152), 10, 67–74, 2000.
- Born, E. W. and Böcher, J.: *The Ecology of Greenland*, Nuuk, Ministry of Environment and Natural Resources, 429 pp. 2001.
- Box, J. E., Bromwich, D. H., and Veenhuis, B. A., et al.: Greenland Ice Sheet surface mass balance variability (1998–2004) from calibrated polar MM5 output, *J. Climate*, 19, 2783–2800, 2006.
- Buskamp, R. and Hasholt, B.: Coarse bed load transport in a glacial valley, Sermilik, South East Greenland, *Z. Geomorphol.*, 40, 349–358, 1996.
- Cuffey, K. M. and Paterson, W. S. B.: *The Physics of Glaciers*, 4<sup>th</sup> edn., Butterworth-Heinemann, Oxford, 704 pp., 2010.
- Ettema, J., van den Broeke, M., van Meijgaard, E., van de Berg, M. J., Bamber, J. L., Box, J. E., and Bales, R. C.: Higher surface mass balance of the Greenland Ice Sheet revealed by high resolution climate modeling, *Geophys. Res. Lett.*, 36, L12501, doi:10.1029/2009GL038110, 2009.
- Gogineni, S., Tammana, D., Braaten, D., et al.: Coherent radar ice thickness measurements over Greenland Ice Sheet, *J. Geophys. Res.*, 106, 33761–33772, 2001.
- Hanna, E., Huybrechts, P., Steffen, K., et al.: Increased runoff from melt from the Greenland Ice Sheet: a response to global warming, *J. Climate*, 21, 331–341, 2008.
- Hansen, B. U., Sigsgaard, C., Rasmussen, L., Cappelen, J., Hinkler, J., Mernild, S. H., Petersen, D., Tamstorf, M., Rasch, M., and Hasholt, B.: Present day climate at Zackenberg, *Adv. Ecol. Res.*, 40, 115–153, 2008.
- Hasholt, B.: Morphological and hydrological possibilities for the development of water power at Angmassalik – a case study of applied physical geography, *Geogr. Tidsskr.*, 80, 57–62, 1980.

- Hasholt, B., Bobrovitskaya, N., Bogen, J., McNamara, J., Mernild, S. H., Milbourn, D., and Walling, D. E.: Sediment transport to the Arctic Ocean and adjoining cold oceans, *Nord. Hydrol.*, 37(4–5), 413–432, 2006.
- Hasholt, B., Liston, G. E., and Knudsen, N. T.: Snow-distribution modelling in the Ammassalik Region, South East Greenland, *Nord. Hydrol.*, 34(1/2), 1–16, 2003.
- Hasholt, B. and Mernild, S. H.: Estimation of water balance in and around the Mittivakkat Glacier basin, Ammassalik Island, Southeast Greenland, in: *Northern Research Basins Water Balance*, edited by: Kane, D. L. and Yang, D., Wallingford, UK, IAHS, 129–142, publications no. 290, ISBN 1-901502-82-1, 2004.
- Hasholt, B. and Mernild, S. H.: Hydrology, sediment transport, and water resources of Ammassalik Island, SE Greenland, *Geogr. Tidsskr.*, 108(1), 73–95, 2008.
- Hasholt, B., Mernild, S. H., Sigsgaard, C., Elberling, B., Petersen, D., Jakobsen, B. H., Hansen, B. U., Hinkler, J., and Søgaaard, H.: Hydrology and transport of sediment and solutes at Zackenberg, in: *High-Arctic Ecosystem Dynamics in a Changing Climate: Ten Years of Monitoring and Research at Zackenberg Research Station, Northeast Greenland*, edited by: Meltofte, H., Christensen, T. R., Elberling, B., Forchhammer, M. C., and Rasch, M.: Hydrology and transport of sediment and solutes at Zackenberg, *Adv. Ecol. Res.*, 40, 111–149, 2008.
- Hasholt, B. and Walling, D. E.: Use of caesium-137 to investigate sediment sources and sediment delivery in a small glacierized mountain drainage basin in eastern Greenland, in: *Erosion, Debris Flows and Environment in Mountain Regions*, IAHS, Publ. 209, 87–99, 1992.
- Holland, D. M., Thomas, R. H., de Young, B., Ribergaard, M. H., and Lyberth, B.: Acceleration of Jakobshavn Isbræ triggered by warm subsurface ocean waters, *Nat. Geosci.*, 1(10), 659–664, 2008.
- Howat, I. M., Joughin, I., Tulaczyk, S., and Gogineni, S.: Rapid retreat and acceleration of Helheim Glacier, East Greenland, *Geophys. Res. Lett.*, 32, L22502, doi:10.1029/2005GL024737, 2005.
- Howat, I. M., Joughin, I., and Scambos, T.: Rapid changes in ice discharge from Greenland outlet glaciers, *Science*, 315, 1559, doi:10.1126/science.1138478, (advanced publication in *Science Express* on 8 February 2007), 2007.
- IPCC: Summary for policymakers, in: *Climate Change 2007, The Physical Science Basis, Contribution of Working Group I to the Fourth Assessment Report of the Intergovernmental Panel on Climate Change*, edited by: Solomon, S., Qin, D., Manning, M., Chen, Z., Marquis, M., Averyt, K. B., Tignor, M., and Miller, H. L., Cambridge University Press, Cambridge, UK and New York, USA, 2007.
- Jakobsen, B. H., Fredskild, B., and Pedersen, J. B. T.: Holocene changes in climate and vegetation in the Ammassalik area, East Greenland, recorded in lake sediment and soil profiles, *Geogr. Tidsskr.*, 108(1), 21–50, 2008.
- Jensen, L. M. and Rasch, M.: Zackenberg Ecological Research Operations, 14<sup>th</sup> Annual Report 2008, National Environmental Research Institute, Aarhus University, Denmark, 116 pp., 2009.
- Jujisada, H., Bailey, G. B., Kelly, G. G., Hara, S., and Abrams, M. J.: ASTER DEM performance, *IEEE T. Geosci. Remote*, 43(12), 2707–2714, 2005.
- Khan, S. A., Wahr, J., Bevis, M., Velicogna, I., and Kendrick, E.: Spread of ice mass into Northwest Greenland observed, *Geophys. Res. Lett.*, 37, L06501, doi:10.1029/2010GL042460, 2010.
- Kozo, T. L.: An observational study of sea breezes along the Alaskan Beaufort Sea Coast: Part I, *J. Appl. Meteorol.*, 21, 891–905, 1982.
- Knudsen, N. T. and Hasholt, B.: Mass balance observations at the Mittivakkat Gletscher, Southeast Greenland 1995–2002, *Nord. Hydrol.*, 35(4–5), 381–390, 2004.
- Knudsen, N. T. and Hasholt, B.: Mass balance observations at Mittivakkat Glacier, Ammassalik Island, Southeast Greenland 1995–2006, *Geogr. Tidsskr.*, 108(1), 111–120, 2008.
- Lemke, P., Ren, J., Alley, R. B., Allison, I., Carrasco, J., Flato, G., Fujii, Y., Kaser, G., Mote, P., Thomas, R. H., and Zhang, T.: Observations: Changes in Snow, Ice and Frozen Ground, in: *Climate Change 2007: The Physical Science Basis. Contribution of Working Group I to the Fourth Assessment Report of the Intergovernmental Panel on Climate Change*, edited by: Solomon, S., Qin, D., Manning, M., Chen, Z., Marquis, M., Averyt, K. B., Tignor, M., and Miller, H. L., Cambridge University Press, Cambridge, United Kingdom and New York, NY, USA, 2007.
- Liston, G. E. and Elder, K.: A distributed snow-evolution modeling system (SnowModel), *J. Hydrometeorol.*, 7, 1259–1276, 2006a.
- Liston, G. E. and Elder, K.: A meteorological distribution system for high-resolution terrestrial modeling (MicroMet), *J. Hydrometeorol.*, 7, 217–234, 2006b.
- Liston, G. E. and Hiemstra, C. A.: A simple data assimilation system for complex snow distributions (SnowAssim), *J. Hydrometeorol.*, 9, 989–1004, 2008.
- Liston, G. E. and Sturm, M.: A snow-transport model for complex terrain, *J. Glaciol.*, 44, 498–516, 1998.
- Mernild, S. H.: The internal drainage system of the lower Mittivakkat Glacier, Ammassalik Island, SE Greenland, *Geogr. Tidsskr.*, 106(1), 13–24, 2006.
- Mernild, S. H., Hansen, B. U., Jakobsen, B. H., and Hasholt, B.: Climatic conditions at the Mittivakkat Glacier catchment (1994–2006), Ammassalik Island, SE Greenland, and in a 109 years term perspective (1898–2006), *Geogr. Tidsskr.*, 108(1), 51–72, 2008a.
- Mernild, S. H. and Hasholt, B.: Climatic control on river discharge simulations, Mittivakkat Glacier catchment, Ammassalik Island, SE Greenland, *Nord. Hydrol.*, 37(4–5), 327–346, 2006.
- Mernild, S. H. and Hasholt, B.: Observed runoff, jökulhlaups, and suspended sediment load from the Greenland Ice Sheet at Kangerlussuaq, West Greenland, for 2007 and 2008, *J. Glaciol.*, 55(193), 855–858, 2009.
- Mernild, S. H., Hasholt, B., and Liston, G. E.: Water flow through Mittivakkat Glacier, Ammassalik Island, SE Greenland, *Geogr. Tidsskr.*, 106(1), 25–43, 2006b.
- Mernild, S. H. and Liston, G. E.: The influence of air temperature inversion on snow melt and glacier surface mass-balance simulations, SW Ammassalik Island, SE Greenland, *J. Appl. Meteorol. Clim.*, 49(1), 47–67, 2010.
- Mernild, S. H., Liston, G. E., Hasholt, B., and Knudsen, N. T.: Snow distribution and melt modeling for Mittivakkat Glacier, Ammassalik Island, SE Greenland, *J. Hydrometeorol.*, 7, 808–824, 2006a.
- Mernild, S. H., Liston, G. E., Hiemstra, C. A., Christensen, J. H., Stendel, M. and Hasholt, B.: Surface mass-balance and runoff modeling using HIRHAM4 RCM at Kangerlussuaq (Søndre Strømfjord), West Greenland, 1950–2080, in press, *J. Climate*,

- 2011.
- Mernild, S. H., Liston, G. E., Hiemstra, C. A., and Steffen, K.: Surface Melt Area and Water Balance Modeling on the Greenland Ice Sheet 1995–2005, *J. Hydrometeorol.*, 9(6), 1191–1211, 2008c.
- Mernild, S. H., Liston, G. E., Hiemstra, C. A., Steffen, K., Hanna, E., and Christensen, J. H.: Greenland Ice Sheet surface mass-balance modeling and freshwater flux for 2007, and in a 1995–2007 perspective, *Hydrol. Process.*, 23(17), 2470–2484, doi:10.1002/hyp.7354, 2009.
- Mernild, S. H., Liston, G. E., Kane, D. L., Hasholt, B., and Knudsen, N. T.: Spatial snow distribution, runoff, and mass balance modelling for entire Mittivakkat Glacier (1998–2006), Ammassalik Island, SE Greenland, *Geogr. Tidsskr.*, 108(1), 121–136, 2008b.
- Mernild, S. H., Liston, G. E., Hiemstra, C. A., and Christensen, J. H.: Greenland Ice Sheet surface mass-balance modeling in a 131-year perspective 1950–2080, *J. Hydrometeorol.*, 11(1), 3–25, 2010a.
- Mernild, S. H., Liston, G. E., Steffen, K., and Chylek, P.: Meltwater flux and runoff modeling in the ablation area of the Jakobshavn Isbræ, West Greenland, *J. Glaciol.*, 56(195), 20–32, 2010b.
- Mote, T. L.: Greenland surface melt trends 1973–2007: evidence of a large increase in 2007, *Geophys. Res. Lett.*, 34, L22507, doi:10.1029/2007GL031976, 2007.
- Rignot, E., and Kanagaratnam P.: Changes in the Velocity Structure of the Greenland Ice Sheet, *Science*, 315, 1559–1561, 2006.
- Rysgaard, S. and Glud, R. N.: Carbon cycling in Arctic marine ecosystems: case study young sound, *Meddr. om Grønland, Bioscience*, 58, 24–43, 2007.
- Scambos, T. and Haran, T.: An image-enhanced DEM of the Greenland ice sheet, *Ann. Glaciol.*, 34, 291–298, 2002.
- Screen, J. A. and Simmonds, I.: The central role of diminishing sea ice in recent Arctic temperature amplification. *Nature*, 464: 1334–1337, 2010.
- Steffen, K. and Box, J. E.: Surface climatology of the Greenland ice sheet: Greenland Climate Network 1995–1999, *J. Geophys. Res.*, 106, 33951–33964, doi:10.1029/2001JD900161, 2001.
- Steffen, K., Clark, P. U., Cogley, J. G., Holland, D., Marshall, S., Rignot, E., and Thomas, R.: Rapid changes in glacier and ice sheet and their impacts on sea level, in: *Abrupt Climate Change, a Report by the US Climate Change Science Program and the Subcommittee on Global Change Research*, US Geological Survey, reston, VA, 60–142, 2008.
- Straneo, F., Hamilton, G. S., Sutherland, D. A., Stearne, L. A., Davidson, F., Hammill, M. O., Stenson, G. B., and Rosing-Asvid, A.: Rapid circulation of warm subtropical waters in a major glacial fjord in East Greenland, *Nat. Geosci.*, 3(3), 182–186, 2010.
- Tedesco, M.: A new record in 2007 for melting in Greenland, *EOS T. Am. Geophys. Un.*, 88(39), 383 pp., 2007.
- Tsukernik, M., Kindig, D. N., and Serreze, M. C.: Characteristics of winter cyclone activity in the northern North Atlantic: Insights from observations and regional modeling, *J. Geophys. Res.*, 112, C03101, doi:10.1029/2006JD007184, 2007.
- Velicogna, I. and Wahr, J.: Acceleration of Greenland ice mass loss in spring 2004, *Nature*, 443, 329–331, 2006.
- Weick, E. J. and Rouse, W. R.: Advection in the coastal Hudson Bay Lowlands, Canada, II, Impact of atmospheric divergence on the surface energy balance, *Arctic Alpine Res.*, 23, 338–348, 1991.